Nagar Yuwak Shikshan Sanstha's

Yeshwantrao Chavan College of Engineering

(An Autonomous Institution affiliated to Rashtrasant Tukadoji Maharaj Nagpur University)

Hingna Road, Wanadongri, Nagpur - 441 110

NAAC Accredited with 'A++' Grade

Ph.: 07104-242919, 242623, 242588

Summary of 3.4.3

Number of research papers per teacher in CARE Journals notified on UGC website during the year

Year	2022
Number	129
No. of Teachers	328
No. of papers per Teachers	0.3932

Supporting Documents

1.   Proof of Papers in the Journals notified on UGC website

Dr. U. P. Waghe

(Principal)

Proof of Papers in the Journals

Parametric investigation and economic design of slender steel fibre reinforced concrete beams using shear resisting mechanisms approach

Bichitra Singh Negi [a,b,*], Kranti Jain [b], R.R. Dighade [c]

[a] Department of Civil Engineering, Dev Bhoomi Uttarakhand University, Dehradun, 248007, Uttarakhand, India
[b] Department of Civil Engineering, National Institute of Technology, Srinagar, Pauri Garhwal-246174, Uttarakhand, India
[c] Department of Civil Engineering, Yeshwantrao Chavan College of Engineering, Nagpur, Maharashtra, India

ARTICLE INFO

ABSTRACT

The shear resisting mechanisms (SRM) in slender steel fibre reinforced concrete (SFRC) beam (without stirrups) comprised of four shear resisting mechanisms (uncracked concrete in the compression zone, the dowel action of the longitudinal reinforcement bars, the aggregate interlocking through the aggregates protruding at the critical diagonal shear crack, and the steel fibres bridging the diagonal crack). These shear resisting mechanisms are interrelated to each other and very complex to quantify. However, parametric analysis is one of the methods which can easily be applied and quantify their interconnection. As a result, the parametric analysis has been carried out in this research with the main focus on the effect of influential parameters on shear strength, shear resisting mechanisms, and the interrelationship between them. Thus, the SRM model has been again verified and validated through the results of parametric investigation. Furthermore, the SRM based model has been further modified, and a cost analysis for economic beam design was performed. Finally, design recommendations from the standpoint of practical application have been proposed.

1. Introduction

Steel fibre reinforced concrete (SFRC) beam's shear strength has been experimentally investigated globally over the last few decades, and the results show that these beams have superior shear strength than traditional reinforced concrete (RC) beams [1–4]. Furthermore, steel fibres have been found to be effective in controlling crack growth and improving shear stress transfer across cracks. This increase in shear strength has led to the conclusion that the use of steel fibres could partially or completely replace traditional transverse reinforcement. The placing of transverse reinforcement can be time-consuming and expensive on-site, so replacing it with fibres is simple, less time-consuming, and less expensive.

Furthermore, the *fib* model code [5] stated that steel fibres improve shear strength by increasing the concrete contribution, when the SFRC is considered as a separate composite material. Finally, *ACI* 318–08 [6], as confirmed by *ACI* 318–19 [7], allows the use of steel fibres (with a minimum fibre volume fraction of 0.75 %) as minimum shear reinforcement in concrete up to normal strength.

Sturm et al. [8] strongly recommended that conservative and reliable methods for predicting shear strength be developed due to the catastrophic nature of shear failure. Lantsoght [9] examines the shear capacity of SFRC beams and discovers that the majority of approaches are based on empirical relations that are difficult to apply to a new set of databases.

Mechanics-based models are typically divided into two types: 1) Models based on modified field compression theory (MCFT) [10–12]; 2) Models based on critical shear crack stresses [13–14]. The shear resisting mechanisms (SRM)-based model belongs to the second type, in which the uncracked concrete in the compressed zone and the cracked region below the neutral axis control the development of stresses along the critical shear crack.

Shear resistance in RC beams (without stirrups) is attributed to the contribution of uncracked concrete in the compression zone, aggregate interlocking, and longitudinal reinforcement bar dowel action [15–17]. However, the SRM based model for SFRC beams differs from that of RC beams in that the contribution of steel fibres to shear strength is a separate parameter. It demonstrates that shear transfer in SFRC beams without stirrups is governed by four shear resisting mechanisms (i.e., contribution of uncracked concrete, aggregate interlocking, dowel action and the steel fibres). However, the presence of steel fibres affects the other shear resisting mechanisms because steel fibres play a dual role in shear resistance. Steel fibres primary function is to transfer tensile stress

---

Nomenclature

Notations

a	= shear span, mm
b, b_w	= effective width of beam, mm
c_s	= side concrete cover to stirrups used for binding the longitudinal reinforcement, mm
d, d_e	= effective depth, mm
d_g	= maximum aggregate size, mm
d_o	= effective depth of cross-section (d), but not less than 100 mm, mm
d_{by}	= diameter of shear reinforcement, mm
d_f	= diameter of fibre, mm
f_c'	= concrete compressive strength, MPa
f_t	= tensile strength of concrete, MPa
f_s	= tensile stress of longitudinal steel, MPa
f_y	= yield strength of longitudinal steel, MPa
G_s	= modulus of rigidity, MPa
k_{fc}	= coefficient for effect of concrete compressive strength,
k_t	= factor account for duration of loading (0.6 and 0.4 for short- and long-term loading),
L_c	= crack length in the horizontal direction, mm
l_f	= length of steel fibre, mm
N	= number of fibres bridging the crack,
s	= normalized slip/ sliding, mm
s_y	= shear reinforcement spacing, mm
V_{agg}	= shear force resisted by aggregate interlock, kN
V_{cc}	= shear force resisted by compressed concrete, kN
V_d	= shear force resisted by dowel, kN
V_f	= fibre volume fraction, %
V_{fr}	= shear force resisted by bridging action of fibres, kN
v_u	= ultimate shear strength, MPa
x	= depth of neutral axis from extreme compression fibres, mm
α_1	= coefficient depending upon compressive strength,
α, Θ	= angle of inclination between longitudinal and shear reinforcement,
β_1	= coefficient depending upon compressive strength,
ρ	= longitudinal reinforcement ratio,
ρ_y	= ratio of the amount of transverse reinforcement to the effective cover area,
σ_d	= stress due to longitudinal bar, MPa
σ_f	= average tensile stress resisted by the fibres bridging unit area of the inclined crack, MPa

across the critical shear crack via the pull-out effect, and their secondary function is to act as a barrier to further crack growth. Steel fibre incorporation also changes the depth of uncracked concrete (compressed concrete), inclined crack length, crack width, and shear crack angle, resulting in a change in the contribution of concrete, aggregate interlocking, and dowel action to shear resistance.

Although the literature [3,17–20] suggests that compressed concrete and steel fibres contribute significantly to shear resistance, however the dowel action and aggregate interlock play a minor role. Negi and Jain [21], on the other hand, investigate and proposed the contribution of each shear resisting mechanism. As the dependent parameters change, the contribution proportion of shear resisting mechanisms may change. As a result, a detailed theoretical investigation with parametric analysis is required to determine the effect of various parameters.

The primary goal of this study is to determine the impact of four influential parameters on the shear strength and shear resisting mechanism of SFRC beams. The SRM-based model was used to perform parametric analysis on SFRC beams. Furthermore, the SRM-based model is modified to obtain the economic beam design, and design recommendations are made based on the cost analysis.

2. Research significance

The parametric analysis provided by the SRM model enables researchers to determine the actual behaviour of each mechanism in terms of shear strength. It also aids in determining the effect of four major parameters (fibre volume fraction, concrete compressive strength, longitudinal reinforcement amount, and shear span to depth ratio) on shear strength and shear resisting mechanisms. This allows the researchers to understand the actual internal shear behaviour of the SFRC beams and to optimize them. The cost analysis assists investigators in determining the amount of longitudinal steel reinforcement and grade of concrete to be used to achieve the desired shear strength, and thus assists in determining the most cost-effective beam design. As a result, this investigation may be useful in the development of appropriate code guidelines, allowing the SFRC to be used as a structural concrete globally.

3. Overview of shear resisting mechanisms

Shear failure typically begins as an inclined flexural shear crack from the tension fibres of the beam and extends to the member's most compressive fibre. The actual shape of the shear crack is curved [3,18,21–22], but for the numerical modelling, an idealized critical shear cracked section [3,9,19,23–24] just before shear failure has been assumed.

As shown in Fig. 1, the crack extends from the tension face of the member to the centroid of longitudinal reinforcement (a). further, the crack then extends (as diagonal tension failure) with an inclination 'Θ' with the longitudinal axis and is assumed to be straight up to an uncracked concrete depth 'c' below the uppermost compression face. Negi and Jain [21] calculated the shear strength of an SFRC beam without transverse reinforcement (V_u) and expressed it mathematically as:

$$V_u = V_{cc} + V_d + V_{agg} + V_{fr} \tag{1}$$

Eq. (1) states that the shear strength of slender SFRC beams without stirrups consists of four individual mechanisms (action of compressed concrete, dowel action, aggregate interlocking, and resistance by steel fibres), and the expressions for those individual mechanisms are given in Eqs. (2)–(5).
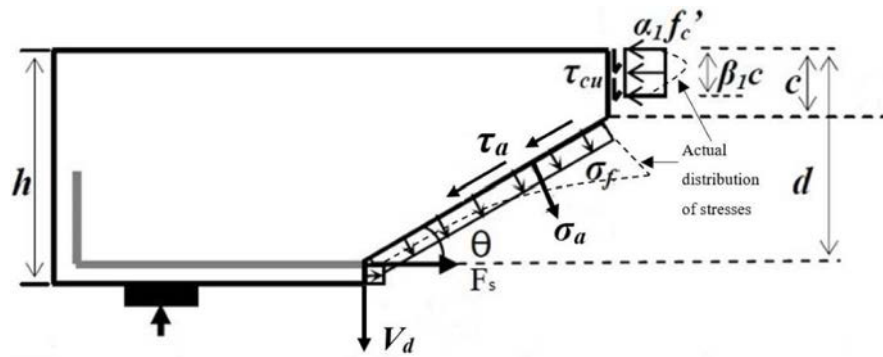
$$V_{cc} = 0.11 f_c' \beta_1 c b \tag{2}$$

$$V_d = \frac{E_s}{2(1+\nu)} \left(\frac{s}{w}\right) A_s \sin\phi \tag{3}$$

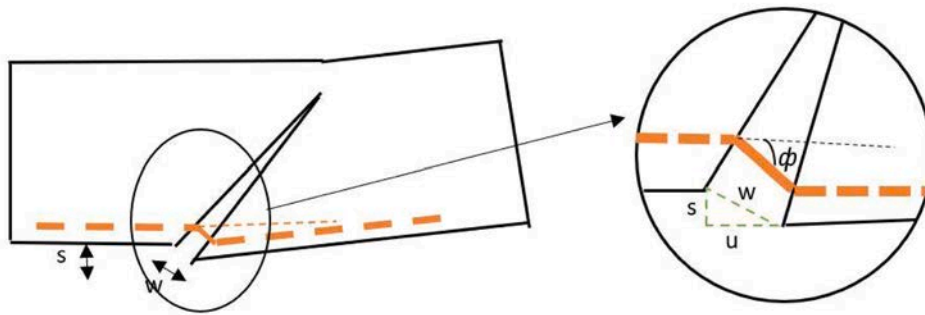$$V_{agg} = \frac{C_f}{4} \left(\sigma_{agg}\cot\theta + \tau_{agg}\right)(h-c)b \tag{4}$$

$$V_{fr} = \sigma_f b(d-c)\cot\theta \tag{5}$$

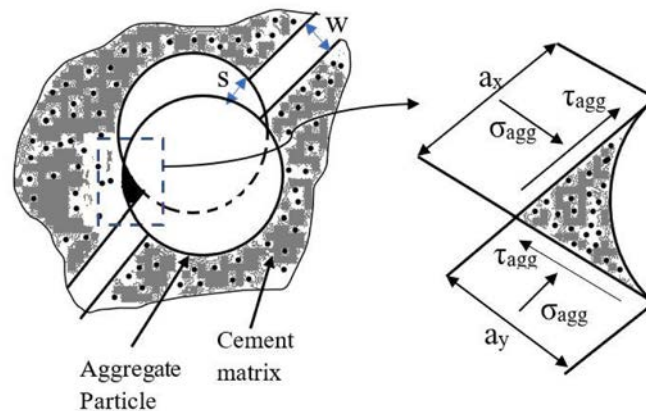As a result, the final form of the shear strength equation for slender SFRC beams is:

$$V_u = 0.11 f_c' \beta_1 c b + \frac{E_s}{2(1+\nu)} \left(\frac{s}{w}\right) A_s \sin\phi + \frac{1}{4} \left(\sigma_{ag}\cot\theta + \tau_{ag}\right)(h-c)b + 2\tau\frac{l_f}{d_f}b(d-c)\cot\theta \tag{6}$$

(a) Failure Pattern and stresses in SFRC beam

(b) Schematic representation for dowel action

(c) Two-phase model for aggregate interlocking

Fig. 1. Typical diagram for investigation of Shear Resisting Mechanisms [21].

The parameters used in the Eq. (6) are as follows: V_u represents the ultimate shear force, in kN; f_c' is concrete compressive strength, in MPa; β_1 is a coefficient depending upon compressive strength of concrete; c is the depth of compression zone, in mm; b is the width of beam, in mm; E_s is the modulus of elasticity of steel, in MPa; υ is the poisson ratio of steel; s is the slip in beam, in mm; w is the shear crack width, in mm; A_s cross-section area of longitudinal steel bar, in mm^2; σ_{ag} and τ_{ag} are the normal and shear stress developed through the contact area of a single aggregates respectively, in MPa; h is depth of beam, in mm; τ is average fibre–matrix interfacial bond stress, in MPa; l_f/d_f is the aspect ratio of fibres; and Θ indicates the angle of inclination of shear crack, in degree.

4. Parametric analysis using the SRM equations

Fibre volume fraction, shear span-to-depth ratio, member depth, longitudinal reinforcement ratio, compressive strength, fibre types, fibre orientation, and other parameters all influence shear strength and shear resisting mechanisms in slender SFRC beams without stirrups. Changing these parameters can improve the shear strength of SFRC beams significantly, but the extent of improvement varies depending on the beam. In this section, the effect of the most influential parameters on shear strength (fibre volume fraction, concrete compressive strength, amount of longitudinal reinforcement, and shear span-to-depth ratio) was considered and analyzed using the SRM-based model. These four

parameters were chosen because they are relevant to concrete ingredient materials and shear resisting mechanisms. The following is a detailed parametric investigation:

Effect of fibre volume fraction (V_f): The literature has suggested that the fibre volume fraction has significant effect on the shear strength [3–4,18,25–26]. The present study examines the effect of fibre volume fraction on the ultimate shear strength, depth of compression zone and each shear resisting mechanisms, for normal- and medium strength concrete at different fibre length. For the analysis, the beams of Jain [27] have been considered, having different concrete strength and different length of fibres. Table 1 lists the specifies of the beams that were taken into consideration for the parametric investigation. The analysis from the SRM model shows that the shear strength of SFRC beams without stirrups increases with the increase in fibre volume fraction, Fig. 2 (a). It is also found from the Fig. 2 (a), that the normal strength SFRC matrices with 35 mm fibre length has more shear strength than the matrices with 60 mm fibre length. However, it is reversed in case of medium strength concrete, where the 60 mm length fibres perform well than 35 mm length fibres. It implies that the short length steel fibres perform well with normal strength concrete while the long steel fibres are efficient with medium strength concrete. The SRM model also reveals that a change in the fibre volume fraction results in a varied behaviour of the shear resisting mechanisms. As fibre volume increases, shear resistance contribution from compressed concrete and steel fibres also increases, however, decreases the shear resistance contribution from dowel action and aggregate interlocking. The increase in contribution of steel fibres is due to two main reasons: (a) the increase in the number of fibres crossing the critical diagonal shear crack; (b) Shift in the depth of uncracked compressed zone (maximum up to 6 % decrease), Fig. 2 (b); which results into larger tension zone. The change in compressed concrete contribution is dependent on uncracked compressed zone depth and compressive strength. Even there is decrease in 'c', but there is also small increase in compressive strength (f_c'), attributed to overall increase in the concrete contribution. This increased compressive strength; working of the fibres and the aggregate interlocking on the same crack length, increases the fibre contribution and reduced the aggregate interlocking. In case of dowel action, the decrease in contribution is due to reduction in the tension force required for balancing the compressive force of uncracked compressed zone, Fig. 2(c). In the Fig. 2 (c), beams from the experimental investigation of Jain [27] and Arslan et al. [17] has been taken and the percentage contribution of each shear resisting mechanisms have been investigated. The first part of Fig. 2(c) having beam ID- D, E, F is for normal strength concrete while the second part (Beam ID- K, L, P) is for medium strength concrete. It is shown from the figure, that even the concrete strength changed but the trend of shear resisting mechanisms is similar, although the percentage increase or decrease in contribution may change. It is mentioned in the literature [3,28–29] that the more fibre volume fraction can affect the workability of concrete and hence reduce the shear strength, therefore the obtained results may vary for matrices with high fibre volume fraction.

Effect of compressive strength (f_c'): The concrete compressive strength is one of the most influencing parameters affecting the shear strength of SFRC beams. The SRM model shows that the shear strength is directly proportional to concrete compressive strength, Fig. 3(a). It is observed from the figure that the shear strength can increase up to 100 %, when the concrete compressive strength changes from normal to high strength, keeping the constant volume fraction of 0.75. However, the percentage contribution of concrete decreases as the compressive strength increases from normal strength (26 MPa) to medium strength (53 MPa), which results into a large reduction (25 % to 35 %) in the

Table 1
Details of the various parameters used for parametric analysis.

Investigators	Beam ID	V_f (%)	f_c' (MPa)	ρ (%)	a/d
Jain [27]	D	0.75	26.70	2.67	3.5
	E	1	25.05		
	F	1.5	27.72		
	G	0.5	24.94		
	H	0.75	27.54		
	AA	0.5	48.70		
	K	0.75	53.75		
	L	1	54.30		
	P	1.5	62.22		
Arslan et al. [17]	A2.5F1.0	1.0	24.53	1.34	2.5
	A3.5F1.0	1.0	20.21		3.5
	A3.5F2.0	2.0	21.43		3.5
	A3.5F3.0	3.0	27.91		3.5
	A4.5F1.0	1.0	24.53		4.5
Swamy [31]	3TLF-2	1.0	34.50	1.55	3.4
	2TLF-2		33.10	2.76	
	1TLF-2		40.90	4.31	
Mansur et al. [30]	B2	0.5	29.10	1.34	2.8
	B3				3.6
	4/0.5/3.5				3.5
Kwak et al. [3]	FHB3-3	0.75	68.60	1.48	3
	FHB1-4		62.60		4

uncracked compressed zone depth and hence reduces the contribution of dowel action. This reduction in 'c' increases the inclined shear crack length and hence increases the percentage contribution of steel fibres and aggregate interlocking, Fig. 3(b). It is also found that the matrices with 35 mm length fibres gives higher shear strength than the matrices with 60 mm length fibres, although the percentage increase in the shear strength with increase in compressive strength is more for 60 mm length fibres than the 35 mm length fibres, Fig. 3(a).

From the above analysis (Fig. 3), it is concluded that the major portion of shear force is taken by the compressed concrete, irrespective of concrete strength, however the steel fibre contribution has enhanced for concrete of more strength. The contribution of aggregate interlocking and dowel action has significant range for normal-strength concrete, which become very less with increase in concrete compressive strength.

Effect of longitudinal reinforcement ratio (ρ): The dowel action is one of the important SRM contributing in resisting the shear force. The increase in shear strength is about 8 % to 11 % for every 0.5 % increase in longitudinal reinforcement ratio, for the normal and medium strength concrete, respectively, Fig. 4(a). The beam D, G are of normal-strength concrete and the beam K, M are of medium-strength concrete, however the fibre length for D, K is 35 mm while the fibre length for G, M is 60 mm. For the longitudinal reinforcement ratio of 0.75 %, the achieved shear strength is maximum for the normal-strength beam with 35 mm length fibres, however the minimum shear strength achieved for normal-strength concrete with 60 mm length fibres which may be due to the reduction in workability of concrete matrix containing long length fibres. Therefore, the beam G always predicts less shear strength than the beams D, K and M. At ρ of 2.5 % the three beams D, K and M have shown approximately similar shear strength and the point act as a transition point because beyond this point, the shear strength for medium-strength concrete beam is more than the normal-strength concrete beam. However, the common trend shows that the shear strength is increases with increase in longitudinal reinforcement, Fig. 4(a). For analyzing the shear resisting mechanisms, beams from the experimental investigation of Swamy [31] have been considered, Fig. 4(b). It is observed that the change in longitudinal reinforcement ratio from 1.55 % to 4.31 %,
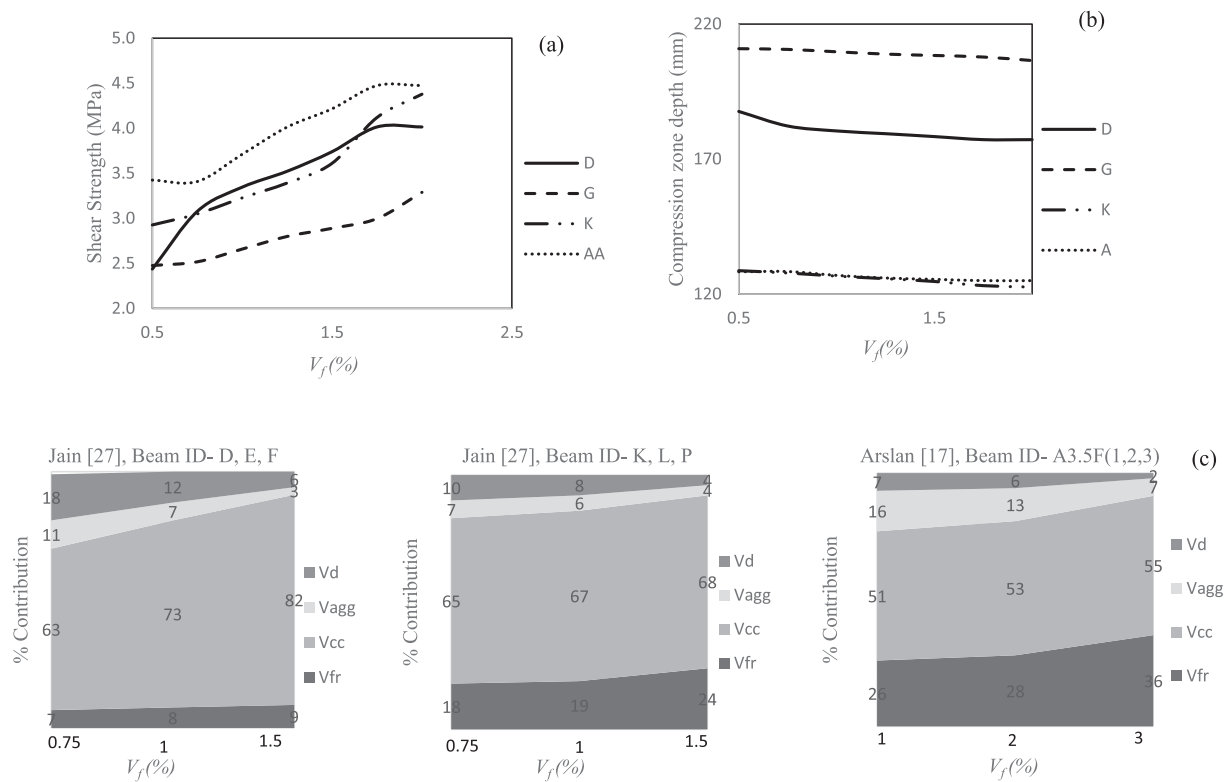
Fig. 2. Effect of Fibre volume fraction (V_f %) on (a) Shear strength; (b) Compression depth; and (c) % Contribution of each shear resisting mechanism.

results into the increase in contribution from the compressed concrete and dowel action by 82 % and 67 %, respectively, however the decrease in the contribution due to aggregate interlocking and steel fibres is about 67 % each. It is well established from the above analysis that the percentage contribution of compressed concrete and the dowel action are directly inter-related to each other. Since the increase in ρ (%) increase the contribution of dowel action, resulting into the increase in un-cracked compressed zone depth and hence the concrete contribution, Fig. 4(b). Due to this the shear crack length get reduced which further reduces the contribution of aggregate interlocking and the steel fibres.

Effect of *a/d* ratio: The incorporation of steel fibres in concrete changes the failure mode of a beam, since the fibres act as the shear reinforcement. As per Mansur et al. [30], the shear span to depth ratio (*a/d*) seems to decrease as the fibre volume fraction increases, however from the theoretical aspect, the effect of changing the *a/d* of SFRC is expected to affects the arching action only and hence the shear strength. From the analysis, it is found that the *a/d* ratio has significant effect on the shear strength, Fig. 5(a), although it does change the percentage contribution of shear resisting mechanisms, Fig. 5(b). The beams of Arslan [17] have been consider for measuring the change in shear strength with the *a/d* ratio, and it is found that the shear strength decreases significantly (33 %) with the increases in *a/d* ratio from 2.5 to 3.5, however the decrease in shear strength is less (10 %) for *a/d* variation from 3.5 to 4.5, Fig. 5(a).

This parametric analysis shows that the SRM model behaves well for the considered important parameters. Some of the results achieved are similar to the results available in the literature while the other results show some advanced interesting fact regarding the behaviour of these factors (like depth of compression zone, behaviour of shear resisting

mechanisms and their interdependency) and overall strength, with the change in the influential parameter. This shows that the SRM model is good for further analysis.

5. Cost analysis using SRM

The cost of the RC/ SFRC structure significantly depends on two components i.e., concrete and steel reinforcement. Therefore, for the cost analysis, the SRM model has been modified in such a way that the final solution is dependent on the two basic parameters only (concrete and steel reinforcement). As *ACI* 318–19 [7] mentioned the provision of using steel fibres in place of minimum shear reinforcement, considering the minimum fibre volume fraction as 0.75 %, therefore the volume fraction of steel fibres has been kept constant as 0.75 %. Also, the expression for the coefficients α and β are dependent on the compressive strength of concrete (f_c'), respectively. Therefore, β can be expressed in term of f_c', although its values change as the value to f_c' changed. The depth of compressed concrete zone (c) and crack width (w) has been determined by analyzing the beam database of 168 beams considered during the validation of SRM model and the average value for the different strength concrete has been obtained.

5.1. Modification of SRM model for normal-strength concrete

The average computed value for depth of compressed concrete zone and shear crack width is obtained as 0.5*d* and 0.21 mm, respectively and the coefficients *β* value is equal to 0.85. Therefore, the modified model for normal-strength concrete is obtained as follows:

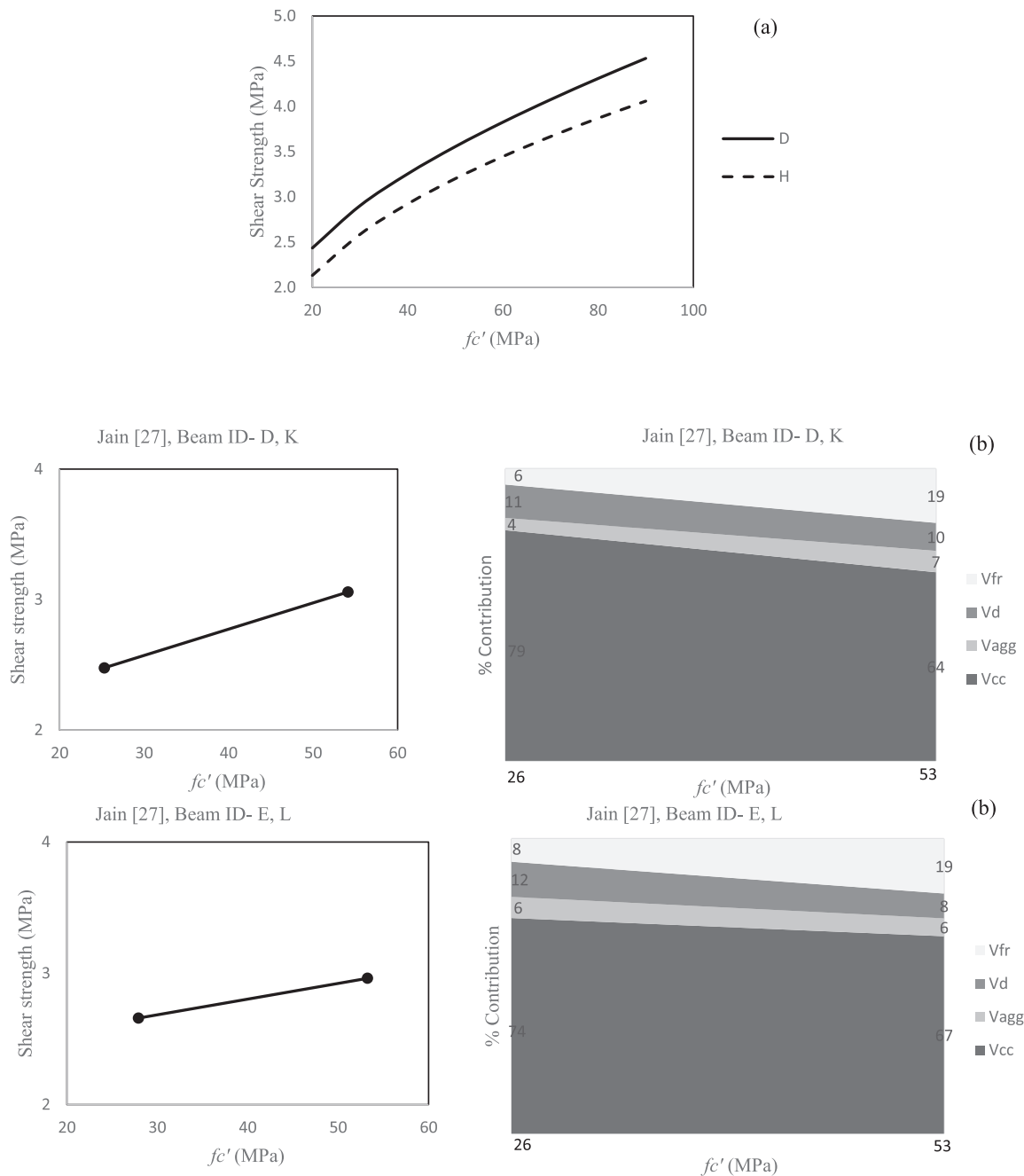i) Contribution of compressed concrete (V_{cc}):

Fig. 3. Effect of concrete compressive strength (*fc'*) on (a) Shear strength; (b) Shear strength and the shear resisting mechanisms for beam D and K of Jain [27]. (Continue) Effect of concrete compressive strength (*fc'*) on (a) Shear strength; (b) Shear strength and the shear resisting mechanisms for beam of Jain [27].

$$V_{cc} = 0.11 f'_c \beta_1 cb$$
$$= 0.11 \times 0.85 \times 0.5d \times f'_c b$$
$$= 0.046 f'_c bd$$

ii) Contribution of dowel action (V_d):

$$V_d = \frac{E_s}{2(1+\nu)} \left(\frac{s}{w}\right) A_s \sin\phi$$
$$= \frac{2 \times 10^5}{2(1+0.3)} \left(\frac{0.08}{0.21}\right) \times \frac{\rho bd}{100} \times \sin 22^0$$
$$= 0.11 \rho bd$$

iii) Contribution of aggregate Interlock (V_{agg}):

$$V_{agg} = \frac{1}{4} \left(\sigma_{agg}\cot\theta + \tau_{agg}\right)(h-c)b$$

Since the aggregate interlock is more dominant in the inclined shear crack region and have negligible contribution from the interlocking below the longitudinal reinforcement. Therefore, the contribution due to aggregate interlocking can be expressed as:

$$V_{agg} = \frac{1}{4} \left(\sigma_{agg}\cot\theta + \tau_{agg}\right)(d-c)b$$

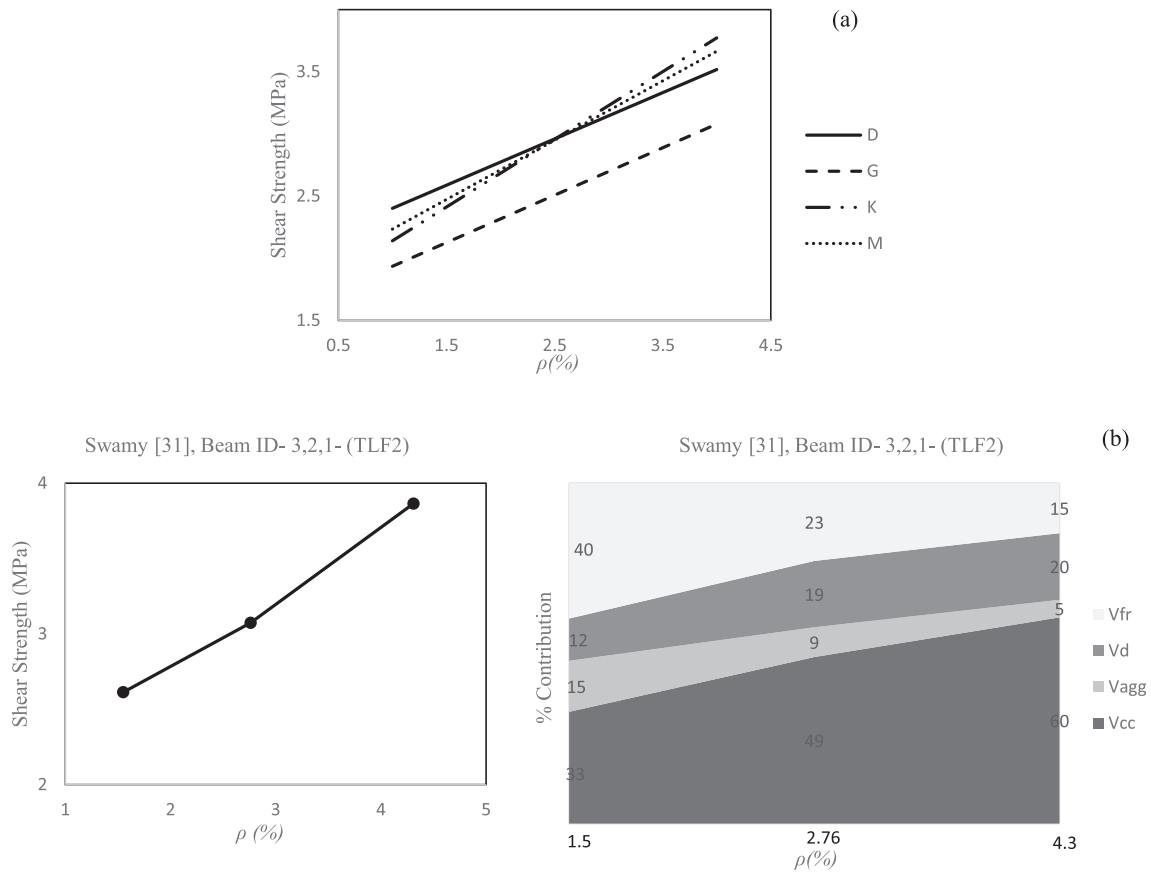Shear stresses due to aggregate interlocking are given by:

Fig. 4. Effect of amount of flexural reinforcement on (a) Shear strength; (b) Shear strength and shear resisting mechanism for beam of Swamy [31].

$$\tau_{agg} = 2\tau_0 \left(1 - \sqrt{\frac{2w}{d_a}}\right) r \frac{a_3 + a_4|r|^3}{1 + a_4 r^4}$$

$$= 2 \times 0.25 f_c' \times \left(1 - \sqrt{\frac{2 \times 0.21}{10}}\right) \times \left(\frac{0.08}{0.21}\right) \times \left(\frac{\frac{2.45}{.25 f_c'} + 2.44\left(1 - \frac{4}{0.25 f_c'}\right)\left(\frac{0.08}{0.21}\right)^3}{1 + 2.44\left(1 - \frac{4}{0.25 f_c'}\right)\left(\frac{0.08}{0.21}\right)^4}\right)$$

$$= 0.15 f_c' \left(\frac{\frac{9.8}{f_c'} + 0.135\left(1 - \frac{16}{f_c'}\right)}{1 + 0.051\left(1 - \frac{16}{f_c'}\right)}\right)$$

The normal stresses between the aggregate due to interlocking is given by:

$$\sigma_{agg} = -0.62\sqrt{w}\ \frac{r}{(1 + r^2)^{0.25}}\tau_{agg}$$

$$= -0.62\sqrt{0.21}\ \frac{\frac{0.08}{0.21}}{\left(1 + \left(\frac{0.08}{0.21}\right)^2\right)^{0.25}}\tau_{agg}$$

$$= -0.104\tau_{agg}$$

Therefore, the modified model for aggregate interlocking is:

$$V_{agg} = \frac{1}{4}\left(-0.104\tau_{agg}\cot 32^0 + \tau_{agg}\right)(d - 0.5d)b$$

$$= 0.104\tau_{agg}bd$$

$$= 0.104 \times 0.15 f_c' \left(\frac{\frac{9.8}{f_c'} + 0.135\left(1 - \frac{16}{f_c'}\right)}{1 + 0.051\left(1 - \frac{16}{f_c'}\right)}\right) bd$$

$$= 0.01563 f_c' \left(\frac{\frac{9.8}{f_c'} + 0.135\left(1 - \frac{16}{f_c'}\right)}{1 + 0.051\left(1 - \frac{16}{f_c'}\right)}\right) bd$$

iv) Contribution of Steel fibres (V_{fr}):

Arslan[17], Beam ID- A2.5F1.0b, A3.5F1.0,A4.5F1.0 (a)

Mansur[30], Beam ID- B2,B3 (b)

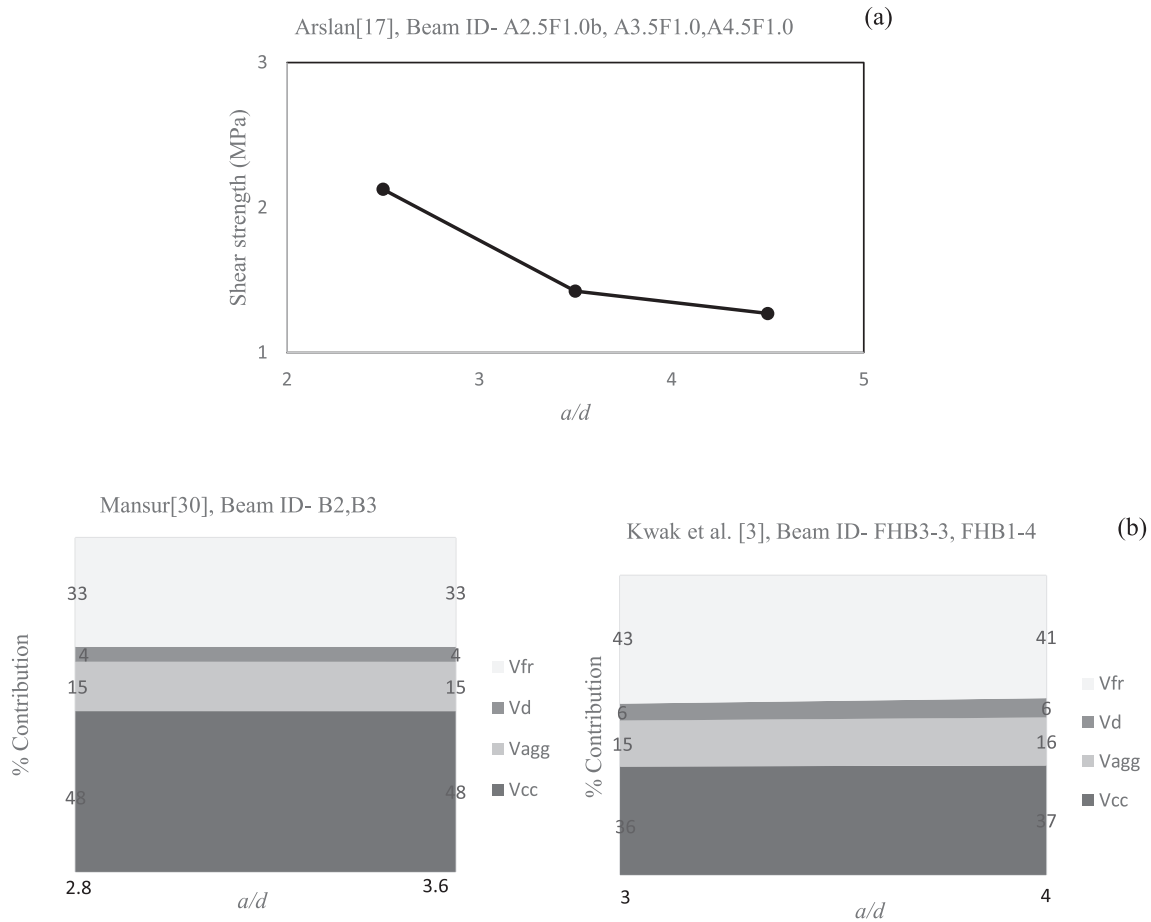Kwak et al. [3], Beam ID- FHB3-3, FHB1-4

Fig. 5. Effect of shear span to depth ratio (a/d) on (a) Shear strength; (b) Shear resisting mechanism.

$$V_{fr} = 2\tau \frac{l_f}{d_f} b(d-c)\cot\theta$$

$$= 2 \times 0.85\sqrt{f_c'}\left(\frac{l_f}{d_f}\right)b(0.5d)\cot32^0$$

$$= 0.00136\sqrt{f_c'}\left(\frac{l_f}{d_f}\right)bd$$

For the Dramix hooked-end steel fibres, having 35 mm and 60 mm length and aspect ratio of 65 and 80, respectively has been used for in the study. Therefore, the contribution of steel fibres is equal to:

$$V_{fr} = 0.088\sqrt{f_c'}bd \text{ for 35 mm length fibres}$$

$$V_{fr} = 0.1088\sqrt{f_c'}bd \text{ for 60 mm length fibres}$$

The ultimate shear strength capacity of steel fibre (v_u) for normal-strength ($\leq$28 MPa) [7] concrete beams are given by:
For 35 mm length fibres

$$v_u = 0.046f_c' + 0.11\rho + 0.01563f_c'\left(\frac{\frac{9.8}{f_c'} + 0.135\left(1 - \frac{16}{f_c'}\right)}{1 + 0.051\left(1 - \frac{16}{f_c'}\right)}\right) \quad (7)$$

For 60 mm length fibres

Table 2
Mixture proportion of concrete, adapted from Jain (27).

Ingredients	Weight (kg/m^3)		
	Normal-strength	Medium-strength	High-strength
Cement	394	511	486
Fine Aggregate, FA	860	810	834
Coarse aggregate, CA (4.75 mm-12.5 mm)	994	960	1023
Silica fume	–	–	49
Superplasticizer	–	2.81	5.83
Water	233	197	145
W/C ratio	0.59	0.39	0.28
Steel fibres	59	59	59

$$v_u = 0.046f_c' + 0.11\rho + 0.01563f_c'\left(\frac{\frac{9.8}{f_c'} + 0.135\left(1 - \frac{16}{f_c'}\right)}{1 + 0.051\left(1 - \frac{16}{f_c'}\right)}\right) + 0.1088\sqrt{f_c'} \quad (8)$$

Similarly, the shear strength models for medium and high-strength concrete have been developed and the final form is available in subsequent section.

Table 3
Prediction of shear strength capacity (MPa) and beam cost (in Rs.) from the modified SRM model.

| f_c' (MPa) \ ρ(%)	0.5	1.0	1.5	2.0	2.5	3.0	3.5	4.0
15	1.24	1.29	1.35	1.40	1.45	1.51	1.56	1.62
	1318	1628	1937	2247	2556	2866	3175	3485
20	1.53	1.58	1.64	1.69	1.75	1.80	1.86	1.91
	1318	1628	1937	2247	2556	2866	3175	3485
25	1.81	1.87	1.92	1.98	2.03	2.09	2.14	2.20
	1318	1628	1937	2247	2556	2866	3175	3485
30	2.09	2.14	2.20	2.25	2.31	2.36	2.42	2.47
	1318	1628	1937	2247	2556	2866	3175	3485
35	2.06	2.10	2.14	2.18	2.22	2.26	2.30	2.34
	1392	1702	2011	2321	2630	2940	3249	3559
40	2.23	2.27	2.31	2.35	2.39	2.43	2.47	2.51
	1392	1702	2011	2321	2630	2940	3249	3559
45	2.37	2.41	2.45	2.49	2.53	2.57	2.61	2.65
	1392	1702	2011	2321	2630	2940	3249	3559
50	2.50	2.54	2.58	2.62	2.66	2.70	2.74	2.78
	1392	1702	2011	2321	2630	2940	3249	3559
55	2.61	2.65	2.69	2.73	2.77	2.81	2.85	2.89
	1392	1702	2011	2321	2630	2940	3249	3559
60	2.62	2.64	2.67	2.70	2.73	2.75	2.78	2.81
	1416	1726	2035	2345	2654	2964	3273	3583
65	2.80	2.82	2.85	2.88	2.91	2.93	2.96	2.99
	1416	1726	2035	2345	2654	2964	3273	3583
70	2.97	3.00	3.03	3.05	3.08	3.11	3.14	3.16
	1416	1726	2035	2345	2654	2964	3273	3583
75	3.15	3.17	3.20	3.23	3.26	3.28	3.31	3.34
	1416	1726	2035	2345	2654	2964	3273	3583
80	3.32	3.35	3.38	3.40	3.43	3.46	3.49	3.51
	1416	1726	2035	2345	2654	2964	3273	3583
85	3.49	3.52	3.55	3.58	3.60	3.63	3.66	3.69
	1416	1726	2035	2345	2654	2964	3273	3583
90	3.67	3.69	3.72	3.75	3.78	3.80	3.83	3.86
	1416	1726	2035	2345	2654	2964	3273	3583

(a)

(b)
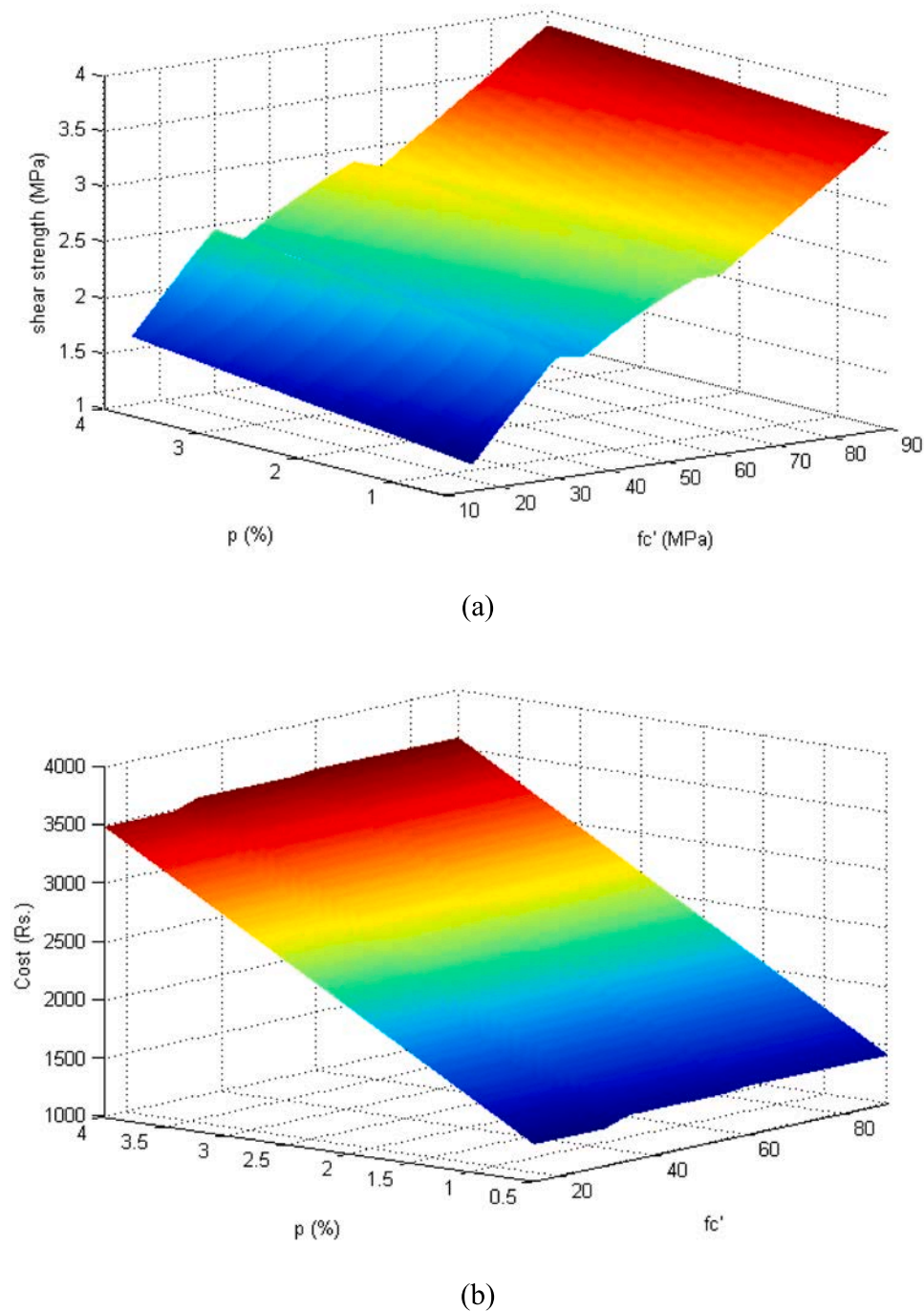
Fig. 6. Prediction of (a) Shear strength, (b) Beam cost (Rs.); for the different combination of *fc'* and *ρ*.

5.2. Modification of SRM for medium-strength concrete

For medium-strength concrete (28 MPa to 55 MPa) [7], the average computed value of compressed concrete zone depth and crack width is obtained as "0.45d" and 0.25 mm, respectively. Therefore, the modified model for medium-strength concrete is as follows:

For 35 mm length fibres

$$v_u = 0.05 f_c' \times \left(1.05 \right.$$

$$\left. - \frac{0.05 f_c'}{1000} \right) + 0.08\rho + 0.004 f_c' \left(\frac{\frac{9.8}{f_c'} + 0.08\left(1 - \frac{16}{f_c'}\right)}{1 + 0.025\left(1 - \frac{16}{f_c'}\right)} \right) + 0.097\sqrt{f_c'} \quad (9)$$

For 60 mm length fibres

$$v_u = 0.05 f'_c \times \left(1.05 \right.$$

$$\left. - \frac{0.05 f'_c}{1000} \right) + 0.08 \rho + 0.004 f'_c \left(\frac{\frac{9.8}{f'_c} + 0.08 \left(1 - \frac{16}{f'_c} \right)}{1 + 0.025 \left(1 - \frac{16}{f'_c} \right)} \right) + 0.12 \sqrt{f'_c} \qquad (10)$$

5.3. Modification of SRM model for medium-strength concrete

For high-strength concrete (>55 MPa) [7], the average computed value of compressed concrete zone depth and crack width is obtained as "0.4d" and 0.30 mm, respectively. Therefore, the modified model for high-strength concrete is expressed as follows:

For 35 mm length fibres

$$v_u = 0.0286 f'_c + 0.055 \rho + 0.0045 f'_c \left(\frac{\frac{9.8}{f'_c} + 0.046 \left(1 - \frac{16}{f'_c} \right)}{1 + 0.0123 \left(1 - \frac{16}{f'_c} \right)} \right) + 0.1061 \sqrt{f'_c}$$

$$(11)$$

For 60 mm length fibres

$$v_u = 0.0286 f'_c + 0.055 \rho + 0.0045 f'_c \left(\frac{\frac{9.8}{f'_c} + 0.046 \left(1 - \frac{16}{f'_c} \right)}{1 + 0.0123 \left(1 - \frac{16}{f'_c} \right)} \right) + 0.131 \sqrt{f'_c}$$

$$(12)$$

For the cost analysis, the mixture proportion for different grade concrete has been taken from the literature. In accordance with provision of *ACI* 318–19 [17], for the cost estimation from the present investigation, the considered the volume fraction of fibres is 0.75 %. The details of the mixtures proportion for each grade of concrete are given in Table 2. A beam of cross-sectional area of 150 mm × 300 mm and total length of 1770 mm has been considered.

The final output for the shear strength and the cost for all the different combination of concrete compressive strength and amount of longitudinal reinforcement, obtained from the modified models is tabulated in Table 3. The surface plot for the shear strength and the beam cost, are shown in Fig. 6(a) and (b), respectively. The detailed step-by-step procedure for obtaining the cost of the beam is presented in Appendix. It has been easily observed from the Table 3, that the same shear strength can be achieved with the different combination of concrete compressive strength and amount of longitudinal reinforcement, however there is a large variation in the cost. In Table 3 and Fig. 6 we can see that the shear strength obtained for normal-strength concrete beam with M25 concrete and $\rho = 0.5$ %, is 1.81 kN/m². Similar shear strength is obtained for M 20 grade concrete and $\rho = 3$ %, however the cost of beam in latter case is Rs. 2866. The percentage increase in cost for the beam of same shear strength = (2866–1318) × 100/1318 = 117 %. This indicates that the price of beam rises up to twice times for obtaining the same shear strength. In the same way, for M45 grade concrete and $\rho = 0.5$ %, the shear strength obtained is equal to 2.38 kN/m², same shear strength is also obtained for M 40 and $\rho = 2.5$ %, but the percentage increase in cost, for the same shear strength is about 89 %. Similarly, for M85 and $\rho = 0.5$ %, the shear strength obtained = 3.5 kN/m², same shear strength is obtained for M80 and $\rho = 4$ %, but the percentage increase in cost is equal to 150 %.

Therefore, it is concluded that the different combination of concrete grade and amount of longitudinal reinforcement can give same shear strength, and also, can get the cost prediction for these combinations to get economical beam design. Also, it is recommended from the analysis that, for achieving the more shear strength economically, the concrete strength has to be increased initially rather than the steel amount, also a minimum amount of fibres volume fraction (=0.75 %) has to includes in the concrete matrices, so that the fibres will mobilize in efficiently and proper workability of the matrices is also maintained.

6. Summary and conclusions

The purpose of this study is to obtain the effect of influential parameters (fibre volume fraction, concrete compressive strength, amount of longitudinal reinforcement ratio, and shear span to depth ratio) on the shear strength and the shear resisting mechanisms. These parameters have been already investigated in the literature for shear strength, but in addition to shear strength the novelty of this research is the effect of these parameters on the shear-resisting mechanisms and compressed concrete depth. So, the previously proposed SRM model has been again verified through parametric analysis for the shear strength variation. And, thus further cost analysis can be performed for the economic beam design. The conclusions drawn from the research are as follows:

- The parametric study indicates that the shear strength of slender SFRC beams is proportional to fibre volume fraction. The increase in fibre volume fraction, increases the number of fibres crossing the shear crack and reduces the depth of compressed concrete, resulting into the larger tension zone. The more the fibre volume fraction, the greater is the percentage contribution of steel fibre; compressed concrete and lesser is the percentage contribution of dowel action and aggregate interlocking. However, from the literature it is found that the workable limit fibre volume fraction for short fibres is 1.5 % and 1 % for long fibres. Therefore, the analysis is applicable to this range only.
- The concrete compressive strength found to be one of the influential parameters affecting the shear strength. When the compressive strength of concrete increases, the shear strength of SFRC also rises, or vice versa. However, approaching to shear resisting mechanism, the contribution of concrete decreases which is due to decline in depth of compressed concrete zone, which also lessens the dowel action contribution. On the opposite side, the percentage contribution of steel fibres rises with increase in the concrete compressive strength. When it comes to shear strength in normal-strength concrete, the aggregate interlocking and dowel action play a considerable role, but as concrete strength increases, these roles become less important.
- The increase in longitudinal reinforcement ratio increases the shear strength of SFRC beams, however the increase in shear strength is about 8 % to 11 % for every 0.5 % increase in longitudinal reinforcement ratio. Since the percentage contribution of dowel action directly depends on the longitudinal reinforcement ratio, it follows that as the longitudinal reinforcement ratio increases, so does the area of the compression zone, which causes the percentage contribution of compressed concrete to rise. As the tension zone area shrinks, steel fibres and aggregate interlocking become less important.
- One of the important factors influencing a beam's shear failure mechanism is the shear span-to-depth ratio. The parametric analysis reveals that the shear strength is inversely related to the shear span-to-depth ratio. Shear strength diminishes with an increase in shear span to depth ratio, but this loss is more pronounced for a/d ranges of 2.5 to 3.5 than 3.5 to 4.5. It is also found that the shear resisting mechanism is not significantly affected by the change in shear span-to-depth ratio.
- The SRM model has been modified for the case of normal-strength, medium-strength, and high-strength concrete for the purpose of practical application. The cost analysis of SFRC beams and the shear strength have been determined using the modified models. The cost study demonstrates that for two or more distinct combinations of concrete compressive strength and amount of longitudinal reinforcing, comparable shear strength can be attained. However, from the perspective of economic design, it is advised to utilize a beam with a

high-strength concrete grade and low amount of longitudinal reinforcement.

Since the theoretical model predict the internal shear resisting mechanisms and analyze the effect of important parameters on shear strength of the SFRC beams without stirrups, therefore, make it possible to the investigators for further optimization of the SFRC beams in shear without using any destructive procedure and hence it can be concluded that the SRM model proved to be easy, economic and less time-consuming process.

CRediT authorship contribution statement

Bichitra Singh Negi: Methodology, Investigation, Formal analysis, Writing – original draft. **Kranti Jain:** Investigation, Data curation, Supervision. **R.R. Dighade:** Formal analysis, Supervision.

Declaration of Competing Interest

The authors declare that they have no known competing financial interests or personal relationships that could have appeared to influence the work reported in this paper.

Data availability statement

Some or all data, models or code generated or used during the study are available from the corresponding author by request.

Appendix A. Supplementary data

Supplementary data to this article can be found online at https://doi.org/10.1016/j.istruc.2022.10.114.

References

[1] Aoude H, Belghiti M, Cook WD, Mitchell D. Response of steel fiber-reinforced concrete beams with and without stirrups. ACI Struct J 2012;109(3):359–67.

[2] Amin A, Foster SJ. Shear strength of steel fiber reinforced concrete beams with stirrups. Eng Struct 2016;111:323–32.

[3] Dinh HH, Parra-Montesinos GJ, Wight JK. Shear strength model for steel fiber reinforced concrete beams without stirrup reinforcement. J Struct Eng 2011;137 (10):1039–51.

[4] Kwak Y-K, Eberhard MO, Kim W-S, Kim J. Shear strength of steel fiber-reinforced concrete beams without stirrups. ACI Struct J 2002;99(4):530–8.

[5] *fib*. Model code 2010: final draft. Lausanne: International Federation for Structural Concrete; 2012.

[6] ACI Committee 318, 2008. Building Code Requirements for Structural Concrete (ACI 318-08) and Commentary (ACI 318R-08)," American Concrete Institute, Farmington Hills, MI, 465 pp.

[7] ACI Committee 318, 2019. Building Code Requirements for Structural Concrete (ACI 442 318-19) and Commentary (ACI 318R-19)," American Concrete Institute, Farmington 443 Hills, MI, USA.

[8] Sturm AB, Visintin P, Oehlers DJ. Mechanics of shear failure in fiber-reinforced concrete beams. J Struct Eng 2021;147(3):04020344.

[9] Lantsoght EOL. How do steel fibers improve the shear capacity of reinforced concrete beams without stirrups? Compos Part B Eng 2019;2019(175):107079.

[10] Minelli F, Vecchio FJ. Compression field modeling of fibre reinforced concrete members under shear loading". ACI Mater 2006;J.103 (2):244–52.

[11] Zhang F, Ding Y, Xu J, Zhang Y, Zhu W, Shi Y. Shear strength prediction for steel fiber reinforced concrete beams without stirrups. Eng Struct 2016;127:101–16.

[12] Barros JA, Foster SJ. An integrated approach for predicting the shear capacity of fiber reinforced concrete beams. Eng Struct 2018;174:346–57.

[13] Choi K-K, Hung-Gun P, Wight JK. Shear strength of steel fiber-reinforced concrete beams without web reinforcement. ACI Struct J 2007;104(1):12–21.

[14] Lee S-C, Cho J-Y, Vecchio FJ. Analysis of steel fiber-reinforced concrete elements subjected to shear. ACI Struct J 2016;113.

[15] Kim J, Park Y. Prediction of shear strength of reinforced concrete beams without web reinforcement. ACI Mater J 1996;93(3):213–22.

[16] Zararis PD. Shear strength and minimum shear reinforcement of reinforced concrete slender beams. ACI Struct J 2003;100(2):203–14.

[17] Arslan G, Keskin RSO, Ulusoy S. An experimental study on the shear strength of SFRC beams without stirrups. J Theor Appl Mech 2017;2017:55.

[18] Singh B, Jain K. An appraisal of steel fibers as minimum shear reinforcement in concrete beams (with Appendix). ACI Struct J 2014;111.

[19] Bi, J., Wang, Z., Zhao, Y., Huo, L., and Xie, Y. (2021). A mechanical model for shear design of steel fiber reinforced concrete beams without shear reinforcements. In Structures (Vol. 31, pp. 216-229). Elsevier.

[20] Negi BS, Jain K. Assessment of shear resisting mechanisms of steel fiber reinforced concrete beams. In: Proceedings of the Institution of Civil Engineers-Structures and Buildings; 2021. p. 1–17.

[21] Negi BS, Jain K. Shear resistant mechanisms in steel fiber reinforced concrete beams: an analytical investigation. Structures 2022;39(10):607–19.

[22] Shoaib A., Lubell A. S., and Bindiganavile V. S., (2012). Shear in Steel Fiber Reinforced Concrete Members without Stirrups. Structural Engineering Report No. 294, Department of Civil and Environmental Engineering, University of Alberta, 357 pp.

[23] Ashour SA, Hasanain GS, Wafa FF. Shear behavior of high-strength fiber reinforced concrete beams. ACI Mater J 1992;89(2):176–84.

[24] Khuntia M, Stojadinovic B, Goel SC. Shear strength of normal and high-strength fiber reinforced concrete beams without stirrups. ACI Struct J 1999;96(2):282–9.

[25] Sharma AK. Shear strength of steel fiber reinforced concrete beams. J Am Concr Inst 1986;83(4):624–8.

[26] Zarrinpour MR, Chao SH. Shear strength enhancement mechanisms of steel fibre-reinforced concrete slender beams. ACI Struct J 2017;114.

[27] Jain K. Shear Behaviour of Steel Fibrous Concrete Beams Without Stirrup Reinforcement". India: IIT Roorkee; 2013. Ph.D. Thesis.

[28] Sahoo DR, Sharma A. Effect of steel fibre content on behavior of concrete beams with and without stirrups. ACI Struct J 2014;111:1157–66.

[29] Jain, K., and Singh, B. (2016). Deformed steel fibres as minimum shear reinforcement—An investigation. In Structures (Vol. 7, pp. 126-137). Elsevier.

[30] Mansur MA, Ong KCG, Paramasivam P. Shear Strength of Fibrous Concrete Beams without Stirrups,". ASCE Journal of Structural Engineering 1986;112(9):2066–79.

[31] Swamy RN, Jones R, Chiam ATP. Influence of steel fibers on the shear resistance of lightweight concrete I-beams. ACI Struct J 1993;90(1):103–14.

scientific reports

Check for updates

OPEN   # Adsorption of Indigo Carmine Dye by Acacia nilotica sawdust activated carbon in fixed bed column

Tripti Gupta[1,6]✉, Khalid Ansari[2,6]✉, Dilip Lataye[3,6], Mahendra Kadu[1], Mohammad Amir Khan[4], Nabisab Mujawar Mubarak[5]✉, Rishav Garg[4] & Rama Rao Karri[5]

A continuous mode fixed-bed up-flow column adsorption analysis was conducted utilizing *Acacia nilotica* sawdust activated carbon (ASAC) as an adsorbent for the adsorption treatment of toxic Indigo Carmine Dye (ICD). The effect on the adsorption characteristics of ASAC of the influent ICD concentration, flow rate, and column bed depth has been investigated. According to the column study, the highest efficiency of ICD removal was approximately 79.01% at a preliminary concentration of 100 mg/L with a flow rate of 250 mL/h at a bed depth of 30 cm and adsorption power of 24.67 mg/g. The experimental work confirmed the dependency of break-through curves on dye concentration and flow rate for a given bed depth. Kinetic models were implemented by Thomas, Yoon–Nelson, and Bed-depth-service-time analysis along with error analysis to interpret experimental data for bed depth of 15 cm and 30 cm, ICD concentration of 100 mg/L and 200 mg/L and flow rate of 250 mL/h, and 500 mL/h. The analysis predicted the breakthrough curves using a regression basin. It indicated that all three models were comparable for the entire break-through curve depiction. The characteristic parameters determined by process design and error analysis revealed that the Thomas model was better followed by the BDST and Yoon–Nelson models in relating the procedure of ICD adsorption onto ASAC. B-E-T surface area and B-E-T pore volume of ASAC were 737.76 m^2/g and 0.2583 cm^3/g, respectively. S-E-M and X-R-D analysis reveal the micro-porous and amorphous nature of ASAC. F-T-I-R spectroscope indicate distinctive functional assemblies like -OH group, C–H bond, C–C bond, C–OH, and C–O groups on ASAC. It could be computed that the ASAC can be used efficiently as an alternative option for industrial wastewater treatment

Colorants and dyestuffs are commonly used in manufacturing and commercial industries, including clothing, rubber, pharmacy, leather, printing press, fruit, cosmetics, carpet, and paper. The textile industry ingests more than 80% of the entire production of dyestuff, creating it the principal consumer [1]. About 10–15% of textile industry dyes are discharged in streams, making the effluents aesthetically unpleasant. Discharge of such colored effluents is dangerous from an environmental and ecological point of view. Color obstructs sunlight dispersion, hinders photosynthesis action, and constrains the growth and metabolism of aquatic biota. The eradication of color from the effluent-carrying dye is a crucial challenge owing to difficulties in handling conventional and fied treatment methods to manage such wastewaters. Consequently, such techniques are ineffective but cannot be utilized to handle the large variety of organic pigment discharge efficiently.

Surface assimilation, or the deposit of impurities on the surface of a solid, is an attractive alternative treatment. Suitable for its convenience, simplicity of use, handling, sludge-free facility, and rejuvenation potential, it has become trendy and appealing, demonstrating an appropriate process for extracting non-biodegradable chemicals (specifial dyes) from wastewater[2]. Industrial activated carbon (AC) is a well-known adsorbent used

[1]Department of Civil Engineering, Shri Ramdeobaba College of Engineering and Management, Nagpur 440013, India. [2]Department of Civil Engineering, Yeshwantrao Chavan College of Engineering, Nagpur 441110, India. [3]Department of Civil Engineering, Visvesvaraya National Institute of Technology, Nagpur 440010, India. [4]Department of Civil Engineering, Galgotia College of Engineering, Knowledge Park I, Greater Noida, Uttar Pradesh 201310, India. [5]Petroleum and Chemical Engineering, Faculty of Engineering, Universiti Teknologi Brunei, Bandar Seri Begawan BE1410, Brunei Darussalam. [6]These authors contributed equally: Tripti Gupta, Khalid Ansari and Dilip Lataye. ✉email: guptatb@rknec.edu; ksansari@ycce.edu; mubark.yaseen@gmail.com

for admirable adsorption capabilities. However, it is expensive, and its rejuvenation makes it pricier in some world regions (e.g., Asia). Hence it is desirable to search for low-cost alternatives such as natural ingredients, agricultural by-products, or industrial waste as an adsorbent material. These products do not need any additional or expensive pre-treatment and should be regarded as possible adsorbents to eliminate dye-containing wastewater. These low-cost products provide acceptable output for diagnosing-colored effluents in laboratory measurements[3].

Several papers reported that manylow-cost materials such as natural, agricultural, or industrial wastes like Acacia nilotica sawdust activated carbon[4], orange peels activated carbon[5], chicken feathers[6], pongamia pinnata seed shell activated carbon[7], palm wood cellulose activated carbon[8],banana peels activated carbon[9], acacia glauca sawdust activated carbon[10], babul sawdust activated carbon[11], etc. have been considered to adsorb dyestuffs, heavy metals, and other impurities from solution as unconventional adsorbents. Mall et al. [12,13] provided a critical analysis of such minimum cost adsorbents to diagnose different wastewaters to remove several toxins carrying wastewaters. Sorption of different adsorbates using other adsorbent materials like boron by sepiolite [14], azo dye by jute fibers[15], phenolic compounds[16], methylene blue dye by zeolite [17], etc. in column mode is also described by some researchers. But dye adsorption (specifi ally Indigo Carmine Dye) by activated carbon of Acacia nilotica sawdust in column mode is hardly reported. Indigo Carmine is one of the dark blues colored poisonous and toxic, crystalline type of powdered dye having a chemical composition of $C_{16}H_8Na_2O_8S_2N_2$, molecular weight is 466.367 g/mol, and distinctive wavelength of 610 nm. It is very commonly used as a colorant and an indicator of pH in various activities. It has some drug allergies due to which it can damage the life of man [18], affects bones and chromosomes, and can cause dangerous hemodynamic effects on living beings [19]. Th s study investigates the efficacy of Acacia nilotica sawdust activated carbon (ASAC) foradsorptive elimination of poisonous Indigo-Carmine Dye (ICD) in a constant stable bed up-flow column.

The current study used a perspex column for continuous fixed-bed up-flow column analysis. The adsorbent of known weight for a given bed depth, i.e., Acacia nilotica sawdust activated carbon (ASAC), was packed with glass beads from the top and bottom. The adsorbate, Indigo Carmine Dye solution (ICD), was pumped at the appropriate fl w rates using a pump with a known initial concentration at natural pH. The fi al samples were taken at daily interims at the column's output, along with the concentrations were determined using a spectrophotometer.

Materials and methods

The objective of the present research work is to utilize Acacia nilotica sawdust activated carbon (ASAC) as an adsorbent for the adsorptive treatment of toxic Indigo Carmine Dye (ICD) bearing wastewater. For this purpose, continuous mode fi ed-bed up-fl w column adsorption analysis is conducted. The effect of the adsorption characteristics of ASAC on the influent ICD concentration, flow rate, and column bed depth has been investigated.

Adsorbent preparation and adsorbent characterization (ASAC).

For continuous fi ed-bed up-fl w column study, the adsorbent material,i.e., carbon activated babool sawdust for the removal of ICD, was prepared by chemically activating the material with ortho-phosphoric acid. The plant chosen for the study is the Acacia nilotica tree. Acacia nilotica is a scientific name for the evergreen Babool tree. It is native to Africa, the Middle East, the Indian subcontinent and across Asia. It is locally available and found abundantly. Th s plant is not directly utilized as an adsorbent in the present research work. The sawdust of babool tree which is a waste material from sawmills and hence of marginal cost has been considered here to prepare the adsorbent. Sawmill and timber industries are commonly available sources of sawdust or wood waste. Secondly the plant is locally available and found abundantly across Asia. In addition to this, Acacia nilotica tree/sawdust/wood waste is not listed as vulnerable/rare/endangered/indeterminate. The cost-effective low cost raw sawdust material, obtained from the local saw mill (M/s Gopal Timber Mill) in a quantity of 0.5 kg, was crushed and sieved according to the protocol outlined in Part 4 of Bureau of Indian Standards IS-2720[20] to get a uniform size in the range of 250–500 μ. It is then rinsed with doubly distillate water, naturally dehydrated, and incubated in an oven at 105 °C for around 2 h. After this, char is obtained by mixing 25 mL of ortho-phosphoric acid, i.e., H_3PO_4, in 50 g dehydrated sawdust in a 0.5:1 volume to weight ratio. To complete the activation and carbonization, the char was placed in a muffl furnace for around 1 h at 450 °C. The carbon was then rinsed with doubly distillate water for 2 h, dried at 378 K, and used in the new adsorption column analysis as Acacia nilotica sawdust activated carbon (ASAC)[4].

Characterization of adsorbent ASAC includes Brunauer, Emmett and Teller (B-E-T) surface area and (B-E-T) pore volume analysis, scanning electron microscope (S-E-M) analysis, Fourier transform infrared (F-T-I-R), spectroscopy, and X-ray diffraction (X-R-D) technique. Adsorption is a surface process. It robustly depends on the adsorbent's surface characteristics. The area-volume, morphology, chemistry and constitution of the ASAC surface were premeditated by B-E-T, S-E-M, F-T-I-R, and X-R-D analysis.

Adsorbate (ICD) preparation.

Analytical reagents were used in the current research. Indigo Carmine Dye (ICD) was acquired from a scientific store-Upper India, Nagpur. Standard 1000 mg/L stock solution was obtained by dissolving 1 g powdered ICD in 1000 mL doubly distillate water. Dilution of a standard stock of 1000 mg/L concentration yielded desired solutions of 100 mg/L and 200 mg/L concentrations. A double-beam Shimadzu ultraviolet–visible spectrophotometer was used to calculate the wavelength at an absorbance of 610 nm. (Model No. 2450).

Column study.

Continuous fl w analysis fully explores the concentration differential, which is believed to be a prime factor for adsorption, resulting in more optimal use of the adsorbent potential and improved effluent performance [21]. The schematic diagram showing the set-up of the column study is shown in Fig. 1.
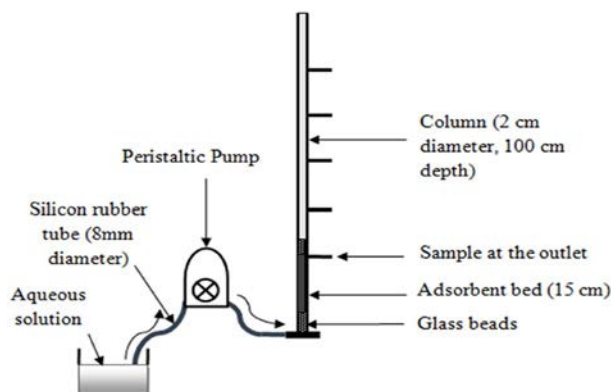
Figure 1. Experimental setup of column study.

Effect of study	Column bed depth (cm)	Influent dye concentration (mg/L)	Flow rate (mL/h)
Influent dye concentration	15	100	250
		200	
	15	100	500
		200	
	30	100	250
		200	
	30	100	500
		200	
Flow rate	15	100	250
			500
	15	200	250
			500
	30	100	250
			500
	30	200	250
			500
Column bed depth	15	100	250
	30		
	15	200	250
	30		
	15	100	500
	30		
	15	200	500
	30		

Table 1. Operational conditional for ASAC in fixed bed study.

ICD adsorption in the fixed bed system. The fixed bed adsorption analysis was performed using perspex glass columns and consists of internal diameters of 2 cm and lengths of 100 cm. The experiments were conducted using doubly distillate water at natural flow and continued till the bed reached the exhaustion point of all the pH of respective solutions. Table 1 shows the operating conditions for each set.

The predetermined flow rates of 250–500 mL/h, the predetermined ICD concentration of 100–200 mg/L and the predetermined column bed depth of 15–30 cm were adopted in the present research work in order to examine the effect on the adsorption performance and to establish optimum conditions for the adsorption of ICD in a column by ASAC.

Results and discussion

Continuous flow analysis is a successful periodic desorption mechanism. The breakthrough curve is the efficiency of a continual adsorption sample or a fixed-bed column. A break-through curve happens if the outflow agglomeration from a column bed is (3–5) % of the inflow agglomeration[22]. The breakthrough curve is drawn based

Columnbed depth (cm)	Flowrate (mL/h)	Concentration (mg/L)	Break-through time tb (min)	Exhaust time text (min)	Percentage removal (%)	Adsorption capacity (mg/g)
15	250	100	240	1350	74.48	25.13
		200	90	660	57.35	23.43
30	250	100	570	2670	79.01	24.67
		200	240	1320	65.79	22.45
15	500	100	120	810	68.38	25.69
		200	45	570	47.35	21.99
30	500	100	270	1560	75.50	21.24
		200	120	1290	58.43	21.05

Table 2. The effects of preliminary ICD concentration on the ASAC break-through curve.
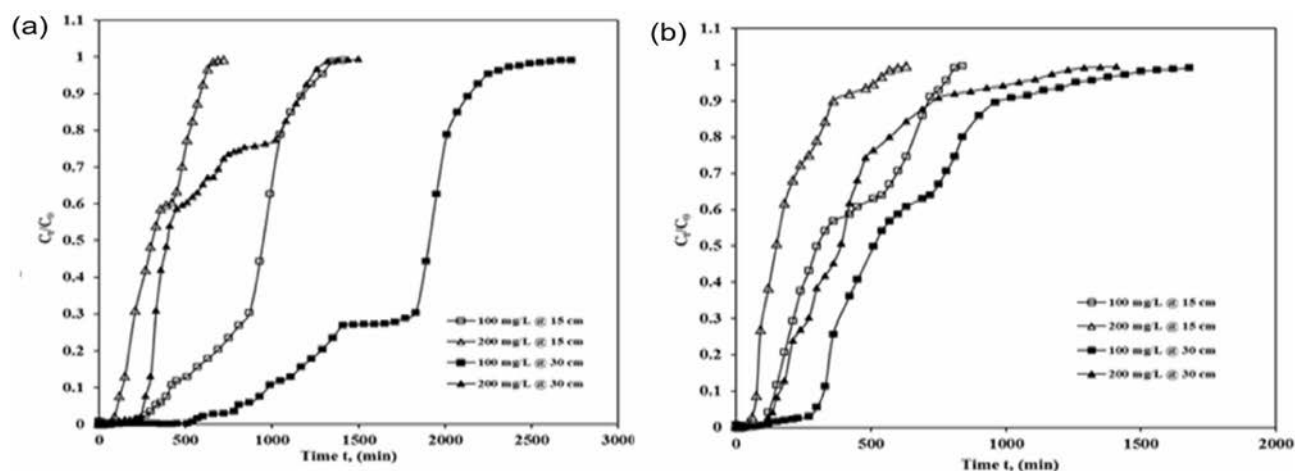
Figure 2. Break-through curve showing effect of concentration of ICD sorption by ASAC (z = 15 cm and 30 cm, C_0 = 100 mg/L and 200 mg/L, at (**a**) Q = 250 mL/h and (**b**) Q = 500 mL/h).

on lapse time by plotting output concentration against initial concentration, flow rate, bed width, and column diameter. In a fixed bed study, the adsorbent closest to the contaminated water saturates first, where maximum adsorption occurs initially. As time passes, these adsorption areas advance until they enter the bed exit [23]. As the adsorption areas migrate through the column, the adsorbate concentration equals the feed concentration at the exit.

Impact of ICD concentration on ASAC break-through plots. Break-through time (t_b) effect on initial concentration on ICD adsorption on the ASAC's fixed-bed column was investigated, and measurements were conceded out at the preliminary stage of 100–200 mg/L concentration with a maintained flow discharge of 250 mL/h and 500 mL/h with column bed depths of 15 cm and 30 cm. The obtained results are depicted in Table 2.

It was observed that break-through time generally occurred faster by rising in preliminary ICD concentration. The break-through time and exhaust time of ASAC were observed to increase with the decrease in initial ICD concentration, whereas the percent removal and adsorption capacity reduced with an increase in initial ICD concentration. ASAC's adsorption capacity decreases, and column percentage removal capacity also decreases because of the inadequate residence time of the column's dye solution. For bed depth of 15 cm and the constant flow of 250 mL/h, the break-through and exhaust times for 100 mg/L and 200 mg/L were 240 min, 90 min and 1350 min, and 660 min, respectively. Likewise, for the constant flow of 250 mL/h, the percentage removal and the adsorption capacity for 100 mg/L and 200 mg/L were found to be 74.48%, 57.35% and 25.12 mg/g, 23.43 mg/g, respectively (as shown in Table 2 and Fig. 2a).

Similarly, in the case of a depth of 30 cm and the constant flow of 250 mL/h, the break-through time and exhaust time for 100 mg/L and 200 mg/L were 570 min, 240 min, 2670 min, and 1320 min, respectively. Likewise, for the constant flow of 250 mL/h, the percentage removal and the adsorption capacity for 100 mg/L and 200 mg/L were found to be 79.01%, 65.79% and 24.67 mg/g, 22.45 mg/g, respectively (as shown in Table 2 and Fig. 2a).

Similar trends were observed for the depth of 15 cm and constant flow of 500 mL/h, for which the break-through time and exhaust time for 100 mg/L and 200 mg/L were found to be 120 min, 45 min, 810 min, and 570 min, respectively. Likewise, for the constant flow of 500 mL/h, the percentage removal and the adsorption capacity for 100 mg/L and 200 mg/L were found to be 68.38%, 47.35%, and 25.69 mg/g, 21.99 mg/g, respectively (as shown in Table 2 and Fig. 2b). Again, similar trends were observed for the depth of 30 cm constant

4

Column bed depth(cm)	Concentration (mg/L)	Flowrate (mL/h)	Break-through time tb (min)	Exhaust time text (min)	Percentage removal (%)	Adsorption capacity (mg/g)
15	100	250	240	1350	74.48	25.13
		500	120	810	68.38	22.69
30	100	250	570	2670	79.01	24.67
		500	270	1560	75.50	21.24
15	200	250	90	660	57.35	23.43
		500	45	570	47.35	21.99
30	200	250	240	1320	65.79	22.45
		500	120	1290	58.43	21.05

Table 3. Effects of flow rate on the break-through plots of ASAC.
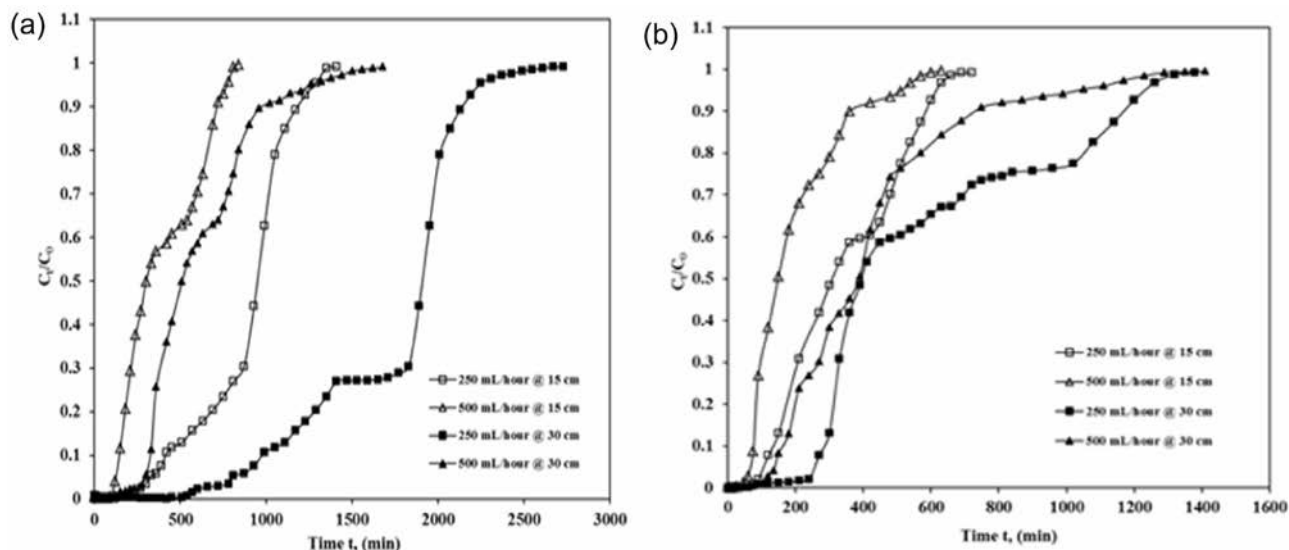
Figure 3. Break-throughplot showing effect of flow rate of ICD sorption by ASAC ($z = 15$ cm and 30 cm, $Q = 250$ mL/h and 500 mL/h, at (**a**) $C_0 = 100$ mg/L and (**b**) $C_0 = 200$ mg/L).

flow of 500 mL/h, for which the break-through time and exhaust time for 100 mg/L and 200 mg/L were found to be 270 min, 120 min, 1560 min, 1290 min, respectively. Likewise, for the constant flow of 500 mL/h, the percentage removal and the adsorption capacity for 100 mg/L and 200 mg/L were found to be 75.50%, 58.43%, and 21.24 mg/g, 21.05 mg/g, respectively (as shown in Table 2 and Fig. 2b). This may be because the higher the concentration gradient, the greater the drive strength for adsorption, ensuing in a lower potential for sorption and less break-through time [17]. The percentage removal capacity of the column has declined as the initial dye concentration has improved. Because of the increase in initial concentration, the ICD loading over the given bed depth also increased. The adsorbent sites got blocked over time, and an early breakpoint was initiated with increased concentration [24].

Impact of flow rate on ASAC break-throughplots. The consequence of flow rate on break-through time for ICD adsorption on fied ASAC beds was tested at various flow rates of 250 ml/h along with with500 mL/h for100 mg/L and 200 mg/L and column bed depths of 15 cm and 30 cm. Table 3, displays the obtained data. Break-through time rises when the flow rate increases and exhaust or saturation time reduces quickly. A higher curve slope shows a substantially reduced in external resistance to mass transfer[24]. For a column bed depth of 15 cm along with the starting ICD concentration of 100 mg/L, the break-throughtime declines from 240 to 120 min, and exhaust time also decreases from 1350 to 810 min when the flow increases from 250 to 500 mL/h (as shown in Fig. 3a). Likewise, in the case of 30 cm of depth, for the starting ICD concentration of 100 mg/L, the break-through time declines from 570 to 270 min, and exhaust time also slows down from 2670 to 1560 min when the flow increases from 250 to 500 mL/h (as shown in Fig. 3a).

A similar pattern was found in the case of 15 cm of column bed depth and 200 mg/L ICD concentration. The break-through time also decreases from 90 to 45 min, and exhaust time also falls from 660 to 570 min as the flow rises from 250 to 500 mL/h (as shown in Fig. 3b). In the case of 30 cm of column bed depth and 200 mg/L ICD concentration, a related form of the pattern was also observed with the break-through time, which also falls from 240 to 120 minand the exhaust time also decreases from 1320 to 1290 min as the flow grows from 250 to 500 mL/h (as shown in Fig. 3b).
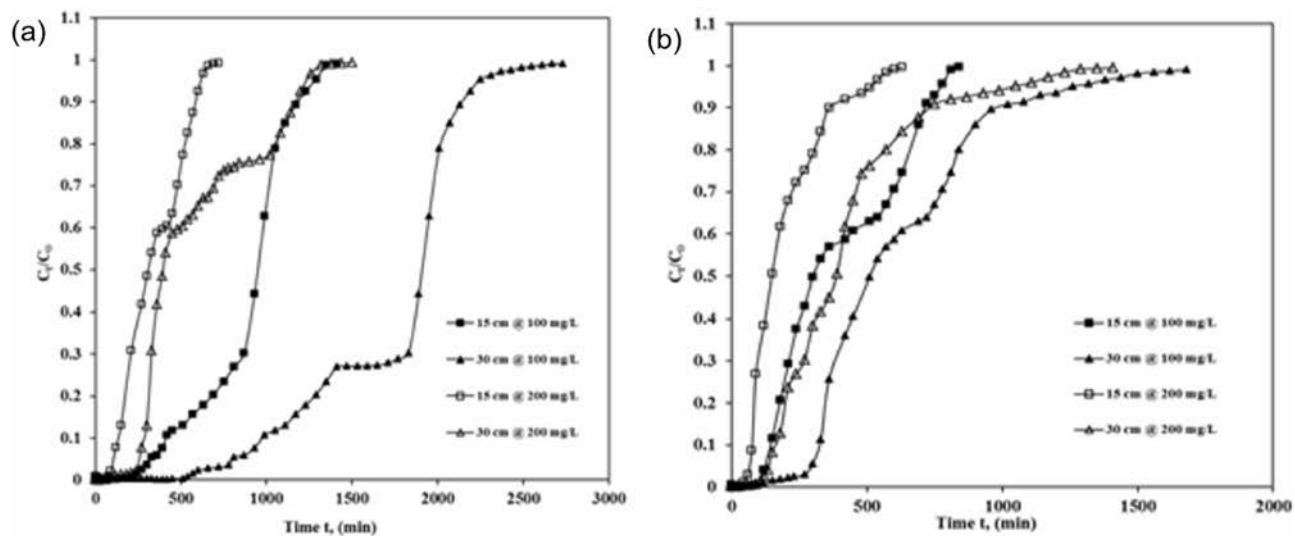
Figure 4. Break-through plot showing effect of bed depth on ICD sorption by ASAC (z = 15 cm and 30 cm, C_0 = 100 mg/L and 200 mg/L at (**a**) Q = 250 mL/h; (**b**) Q = 500 mL/h).

Concentration (mg/L)	Flowrate (mL/h)	Column bed depth(cm)	Break-through time tb (min)	Exhaust time (min)	Percentage removal (%)	Adsorption capacity (mg/g)
100	250	15	240	1350	74.48	25.13
		30	570	2670	79.01	24.67
200	250	15	90	660	57.35	23.43
		30	240	1320	65.79	22.45
100	500	15	120	810	68.38	22.69
		30	270	1560	75.50	21.24
200	500	15	45	570	47.35	21.99
		30	120	1290	58.43	21.05

Table 4. Effects of column bed depth on the break-through plot of ASAC.

The break-through plot steepens when fl w rises, and hence break-through time reduces. Th s rapid decrease in the breakpoint time for all adsorbents is due to increased fl w velocity and a reduction in resident contact time in the adsorption field [24]. This is because the residence time in the bed is not extended sufficiently for equilibrium to achieve the precise fl w rate. Therefore, the interaction time between the solute and adsorbent at higher concentrations is much shorter, consequently lowering the break-through time. It is also observed that when the influent solution's flow rate rises from 250 to 500 mL/h (as shown in Table 3), ASAC's adsorption capability decreases, and column percentage removal capacity declines because of the inadequate residence time of column's dye solution [17]. The solute residence period within the column is a significant parameter for building a packed bed column. Not all of the solute in the solution receives adequate residence time with a high fl w rate, resulting in inefficient use of adsorption ability [25,26].

Impact of column bed depth on ASAC break-through plot. The sequel of column bed depth on adsorption column parameters was explored by adjusting the bed height of ASAC by 15 cm and 30 cm, using initial ICD concentrations of 100 mg/L and 200 mg/L and fl w rates of 250 mL/h and 500 mL/h. The break-through curves and results obtained are shown in Fig. 4 and Table 4.

It was noticed that both break-through and exhaust time increase with the rise in-depth. In the case of a 250 mL/h fl w, the break-through time expands from 240 to 570 min for a fi st-time ICD concentration of 100 mg/L, and the exhaust time also extends from 1350 to 2670 min. The break-through time expanded from 90 to 240 min for the ICD concentration of 200 mg/L, and exhaust time also increased from 660 to 1320 min bed height extends from 15 to 30 cm, respectively (as shown in Fig. 4a). Similar kind of trends are seen in the case of a fl w rate of 500 mL/h; the break-through time for 100 mg/L increased from 120 to 270 min, with exhaust time also rising from 810 to 1560 min, and the break-through time for 200 mg/L increased from 45 to 120 min and the exhaust time also enlarged from 570 to 1290 min as bed height raised from 15 to 30 cm respectively (Fig. 4b).

Bed depth of 15 cm and 30 cm is adopted in the present research work, Th s Bed depth of 15 cm and 30 cm is predetermined to establish optimum conditions for the sorption performance of ICD onto ASAC. Th s is because, time of break-through and the time of exhaustion increases with the increasing bed depth (as shown in Table 4). It was observed that at the lowest bed depth, there is no suffici t time for ICD ions to diffuse into the holes

Column bed depth z (cm)	Concentration (mg/L)	Flow rate (mL/h)	Break through time tb (min)	k_T (L/mg/min)	q_{total} (mg)	q_{exp} (mg/g)	q_{calc} (mg/g)	R²	S.S
15	100	250	240	0.00006957	366.07	25.13	25.02	0.949	3.97 E−03
15	200		90	0.00007488	282.51	23.43	23.42	0.911	1.85 E−02
30	100	250	570	0.00004273	718.72	24.67	23.71	0.953	1.35 E−02
30	200		240	0.00003095	478.41	22.45	18.37	0.860	3.19 E−02
15	100	500	120	0.00011827	329.45	22.69	25.97	0.860	2.64 E−02
15	200		45	0.00007987	319.75	21.99	30.82	0.852	3.50 E−02
30	100	500	270	0.00005764	500.19	21.24	20.81	0.910	1.63 E−02
30	200		120	0.00003195	439.30	21.05	28.69	0.888	1.52 E−02

Table 5. Parameters of Thomas plot for ICD sorption onto ASAC.

of ASAC. The performance of column efficiency also improved with bed height owing to a rise in the measure of adsorbent material that offers more vacancies and newer zones for ICD dye adsorption. But the adsorption capacity of the column decreases with increased bed height, as shown in Table 4.

Kinetics in column adsorption study and Error analysis. To scrutinize the performance in the uninterrupted adsorption phase of ICD onto ASAC, three kinetic plots, i.e., Bed-depth-service-time, Yoon–Nelson and Thomas plots, and the error analysis by least-square of errors system were measured obtained for the ICD sorption onto ASAC.

Thomas modelling of break-throughplots. The Thomas model defies and calculates break-through plots and column effici cy. Th s model has been extracted from the premise that the drive strength has reverse action kinetics and undertakes Langmuir's desorption/adsorption and insignifi ant radial/axial scattering kinetics[27]. The Thomas plot measuring various concentrations is given in (Eq. 1.)

$$\frac{C_t}{C0} = \frac{1}{1 + \exp\left(\frac{k_T q_0 m}{Q} - kTC0t\right)} \tag{1}$$

Thomas' equation's linear form is given as (Eq. 2)

$$In\left(\frac{C_0}{Ct} - 1\right) = \frac{k_T q_0 m}{Q} - kTC0t \tag{2}$$

C_0 is the concentration of influent ICD (mg/L), C_t is the concentration of effluent ICD (mg/L), k_T is the Thomas rate constant (L/mg/min), q_0 is the equilibrium ICD uptake per gram of ASAC (mg/g), Q is the fl w rate (mL/h), m is the ASAC volume (g), and *t* is time (min). A linear plot of ln $[(C_0/C_t) − 1]$ against time *t* was used to measure k_T and q_0 values from the intersection and slope. Table 5 and Fig. 5 show the model's parameters as well as the correlation coefficient.

The investigational column statistics were applied to the Thomas model equation to obtain (k_T), i.e., Thomas rate constant and (q_0) maximum adsorption capacity. The relative parameters and regression coeffici t (R²) were determined using a correlation basin. The results of relative parameters and values of error analysis by the least-square of errors method (S.S) (that is less than or up to 0.004) are also listed in Table 5. The correlation coeffici t for regression was between 0.852 and 0.953, so there is a substantial correlation between *t* and C_t/C_0.

Table 5 depicts that with the rise from 100 to 200 mg/L of ICD concentrations, the value of q_{exp} decreases while the Thomas rate constant k_T increases. This may be because of the original concentration contrast between the solution dye and the adsorbent dye and the driving force for adsorbent adsorption[21]. Therefore, the higher drive strength to achieve a lower ICD concentration results in better column motion. Similarly, as the fl w rate expanded from 250 to 500 mL/h, the rate of q_{exp} decreased while the rate of k_T increased. The rate of q_{exp} improved noticeably as the depth (z) amplifi d from 15 to 30 cm, while the rate of k_T decreased. Thus, lesser influent ICD concentration, lesser fl w rate, and greater or higher depth will improve the effici cy of the column for ICD adsorption on ASAC. Thomas rate constant and contrast of adsorption capacity values acquired from experimental data and calculations showed that they were signifi antly close for given situations that specify the Thomas model's applicability.

Yoon–Nelson modelling of break-throughplots. The Yoon–Nelson plot[28] was worn to learn the break-through action of ICD adsorption on ASAC. It takes into account the hypothesis that a decrease in the sorption probability rate is relative to adsorbate sorption and adsorbate break-through probability[28].

The Yoon–Nelson kinetic plot for the column is given as (Eq. 3):

$$\frac{C_t}{C0} = \frac{1}{1 + \exp\left[k_{YN}(\tau - t)\right]} \tag{3}$$

The linear plotof one component structure is presented as(Eq. 4):
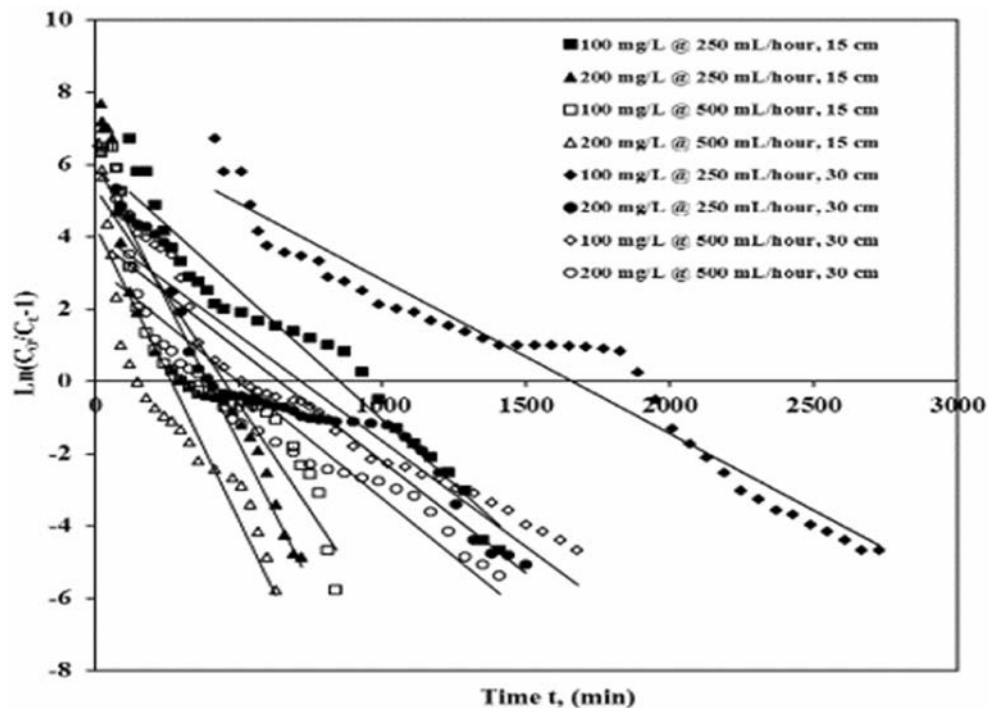
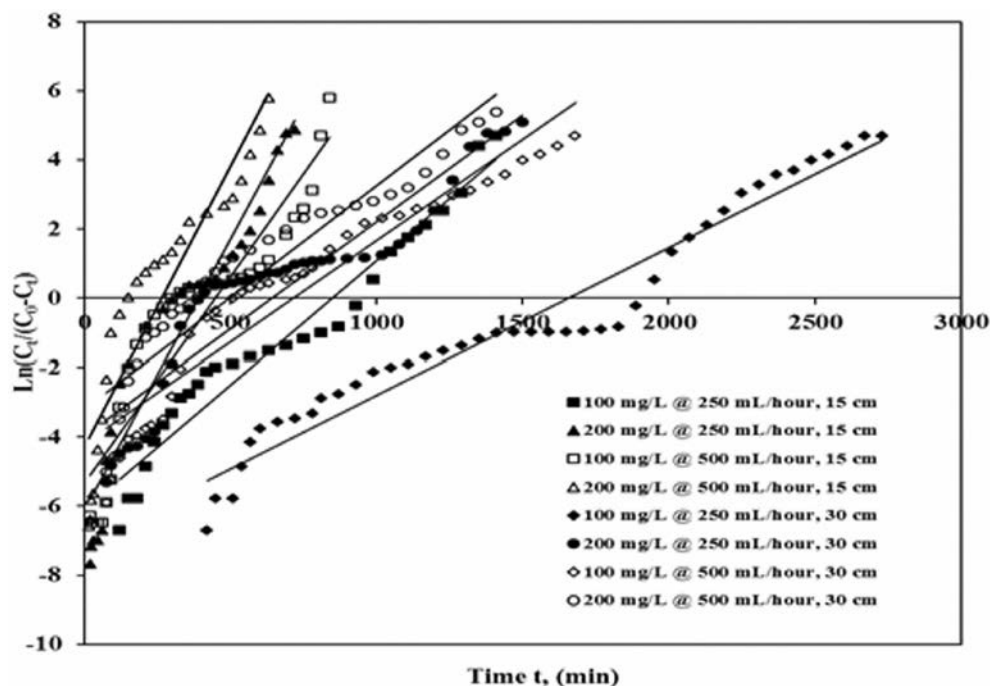**Figure 5.** Thomas break-through plot of ICD sorption by ASAC (z = 15 cm and 30 cm, C_0 = 100 mg/L and 200 mg/L, Q = 250 mL/h and 500 mL/h).

Column bed depth, z (cm)	Concentration (mg/L)	Flow rate (mL/h)	Break-through time, tb (min)	q_{total} (mg)	q_{exp} (mg/g)	q_{calc} (mg/g)	k_{YN} (L/min)	τ (min)	R^2	S.S
15	100	250	240	366.07	25.13	25.02	0.0070	869.43	0.949	4.27 E−03
15	200		90	282.51	23.43	23.42	0.0150	408.07	0.911	2.09 E−02
30	100	250	570	718.72	24.67	23.71	0.0043	1639.81	0.953	1.57 E−02
30	200		240	478.41	22.45	18.37	0.0062	640.29	0.860	3.46 E−02
15	100	500	120	329.45	22.69	25.97	0.0119	449.85	0.860	2.95 E−02
15	200		45	319.75	21.99	30.82	0.0160	268.44	0.852	4.00 E−02
30	100	500	270	500.19	21.24	20.81	0.0058	720.93	0.910	1.77 E−02
30	200		120	439.30	21.05	28.69	0.0064	499.70	0.888	1.62 E−02

Table 6. Parameters of Yoon–Nelson plot for ICD sorption onto ASAC.

$$In\left(\frac{Ct}{C_0 - Ct}\right) = k_{YN}t - \tau k_{YN} \qquad (4)$$

As C_0 is the influent ICD concentration (mg/L), C_t is the effluent ICD concentration (mg/L), k_{YN} is the Yoon–Nelson rate constant (L/min), is the time needed for 50% adsorbate break-through (min), along with t is the sampling time (min).

A linearized design of $ln\ [C_t/(C_0 − Ct)]$ against sample time (t) was worn to compute k_{YN} along with the slope and intercept. In Table 6 and Fig. 6, the parameters of the model and the coeffici ts of correlation are presented.

When a basic hypothetical Yoon–Nelson model was applied to ASAC (Table 6) to understand the break-throughbehaviour of ICD by obtaining the values of constant time τ and k_{YN}, the Yoon–Nelson rate constant k_{YN} improved along with 50% adsorbate break-through time (τ) falls with the grows in influent ICD concentration and flow rate for a given column bed depth. With the bed volume, i.e., fl w rate increasing from 250 to 500 mL/h, the value has expanded, while the standard of k_{YN} has reduced. Table 6 also shows that the break-through time decreases for a given column depth as the flow rate (Q) increases from 250 to 500 mL/h, and the influent ICD concentration (C_0) increases from 100 to 200 mg/L. In all cases, the regression correlation coefficient R^2 was found to be nearly close to unity.

The total quantity of adsorbate (q_{total}) decreases as the influent ICD concentration and fl w rate increase. Though all the parameters obtained in a model satisfy the Yoon–Nelson hypothesis, an increase in k_{YN} values with a decrease in τ values and slightly higher S.S values compared to other models may slightly deviate (negligible) internal significance of this model to a marginal extent.
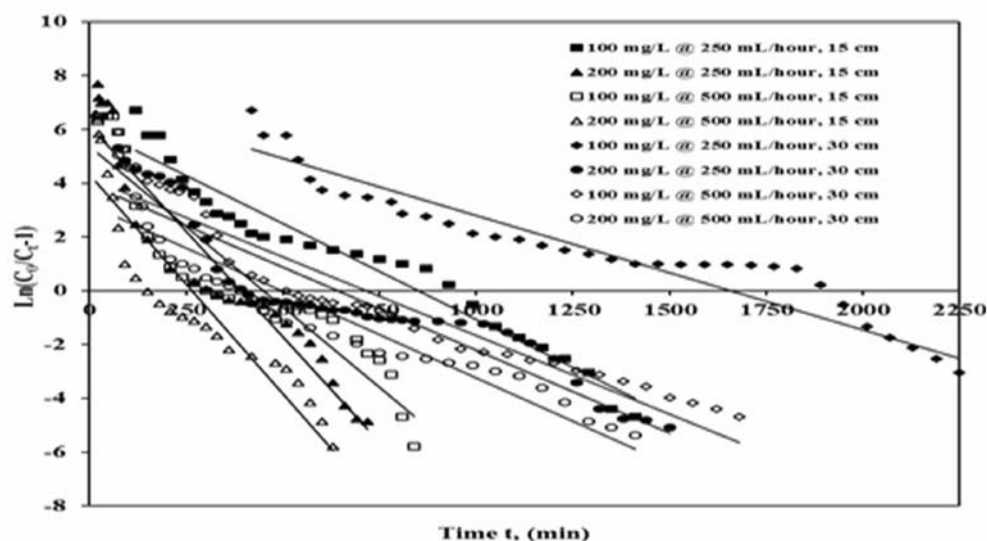
Figure 6. Yoon–Nelson break-through plot of ICD sorption by ASAC ($z = 15$ cm and 30 cm, $C_0 = 100$ mg/L and 200 mg/L, Q = 250 mL/h and 500 mL/h).

Column bed depth z (cm)	Concentration (mg/L)	Flow rate (mL/h)	Break through time tb (min)	q_{total} (mg)	q_{exp} (mg/g)	q_{calc} (mg/g)	k_a (L/mg/min)	N_0 (mg/L)	R^2	S.S
15	100	250	240	366.07	25.13	25.02	6.95719E−05	29,159.29	0.949	4.11 E-−3
15	200		90	282.51	23.43	23.42	7.48848E−05	27,246.29	0.911	1.92 E−02
30	100	250	570	718.72	24.67	23.71	4.2737E−05	54,996.83	0.953	1.45 E−02
30	200		240	478.41	22.45	18.37	3.09524E−05	42,751.69	0.860	3.27 E−02
15	100	500	120	329.45	22.69	25.97	1.18272E−04	30,174.46	0.860	2.74 E−02
15	200		45	319.75	21.99	30.82	7.98771E−05	35,846.73	0.852	3.65 E−02
30	100	500	270	500.19	21.24	20.81	5.76453E−05	48,357.83	0.910	1.68 E−02
30	200		120	439.30	21.05	28.69	3.19508E−05	66,729.58	0.888	1.57E−02

Table 7. Parameter of BDST plot for ICD sorption on ASAC.

Bed-depth-service-time analysis (BDST) modelling of break-through plots. The hypothesis of the BDST plot depicts that the pace of sorption is synchronized by the reaction between adsorbate (ICD) and adsorbent (ASAC)[29]. BDST is a common researchplot for forecasting the connection between depth and time concerning concentrations and various sorption characteristics. The BDST plot is indicated as (Eq. 5):

$$\frac{C_t}{C0} = \frac{1}{1 + \exp\left(\frac{k_a N_0 Z}{u} - k_a C0 t\right)}$$ (5)

The adsorption capacity by the BDST model is expressed as (Eq. 6):

$$q_0 = \frac{N_0 Z Q}{um}$$ (6)

C_0 is the infl w ICD concentration (mg/L), C_t is the outfl w ICD concentration (mg/L), k_a is the BDST model rate constant (L/mg/min), N_0 is the saturation concentration (mg/L), z is the bed depth (centimetre), and u is the influent linear velocity (centimetre/min), where t is the sampling time (min) q_0 represents the equilibrium ICD uptake per gram of adsorbent (mg/g), Q means the fl w rate (mL/h).

Also, m represents the volume of adsorbent (ASAC) in the column (g). As C_t/C_0 is plotted against sampling time (t) and column bed width, a straight line is obtained (z). The BDST model measures the adsorption power, saturation concentration, and BDST rate constant (k_a). The model parameters, total adsorbed quantity (q_{total}) and the correlation coefficients are presented in Table 7 and Fig. 7.

Figure 7. BDSTbreak-through plot of ICD sorption by ASAC (z = 15 cm and 30 cm, C_0 = 100 mg/L and 200 mg/L, Q = 250 mL/h and 500 mL/h).

The result (Table 7; Fig. 7) shows that break-through time reduces with the rise in influent ICD concentration and fl w rate for a given depth of column bed. While the k_a and N_0 values increase with the same. The BDST model variables will continue to advance the methods for different fl w rates and other influential dye concentrations without additional laboratory experiments. To measure the column output at new feasible fl w rates and influent dye concentrations, the BDST equation was used at either flow rate or influent ICD concentration. The error analysis values obtained by the least square method (S.S) were smaller than those obtained by the Yoon–Nelson, and robust predictions were found for adjusting feed concentration and fl w rate. In every one ofthe cases, the regression coeffici t R^2 was approximately equal to one, indicating the signifi ance andrationality of the BDST model for the current system.

Columns with a wide range of possible flow rates and concentrations can be generated using the model and measured constants.These outcomes show that the optimized conditions can be utilized to estimate adsorption efficiency on ASAC under desirable operating conditions for the ICD adsorption process.

Error analysis. As diverse equations are considered to calculate linear regression correlation coeffici ts (R^2) values, these values may signifi antly influence the accuracy throughout the linear regression examination; subsequently, the nonlinear regression investigation can be a superior alternative in evading such errors. As a result, the parameters of various kinetic models were determined using nonlinear correlation coeffici ts examination and the least square of errors procedure [17]. Error analysis was conducted to validate which model gives better results. The relative formula for error analysis by least-square of errors method (S.S) is provided by the following equation (Eq. 7) and respectively shown in Tables 5, 6, and 7 for Thomas, Yoon–Nelson, and BDST model

$$S.S. = \frac{\sum \left[(C_t/C_0)_c - (C_t/C_0)_e \right]^2}{N} \tag{7}$$

Here $(C_t/C_0)_c$ is the ratio of effluent to influent ICD concentrations calculated using Thomas, Yoon–Nelson and BDST plots, and $(C_t/C_0)_e$ is the ratio of effluent to influent ICD concentrations calculated using experimentation conditions[30,31]. N is the number of experimental data points. It is important to evaluate the data using S.S according to the coefficients (R^2) criteria to validate the most suitable and best-fitting kinetic model.

Figure 8 shows profiles measured and projected by Thomas, Yoon–Nelson and BDST models. It shows experimental break-throughplots comparison of ICDonto ASAC for column bed depth z = 15 cm and 30 cm, fl w rate Q = 250 mL/h (Fig. 8a) and 500 mL/h (Fig. 8b), influent ICD concentration C_0 = 100 mg/L and 200 mg/L).

Figure 8 break-throughplot comparison of ICD onto ASAC (z = 15 cm and 30 cm, C_0 = 100 mg/L and 200 mg/L at (a) Q = 250 mL/h (b) Q = 500 mL/h). It was clear from the figu es (Fig. 8) that the contract between the experimental points and the estimated normalized ICD concentrations was signifi antly strong. All three models were suitable for adsorption processes in continuous fi ed-bed adsorption systems where internal and external diffusions are not the limiting and restricting stage[21,32]. The column kinetic study revealed that the experimental break-through plots compared satisfactorily with the break-through profiles calculated by Thomas, Yoon–Nelson, and BDST models. The correlation coeffi ents showed that every one ofthe threemodels matches the experimental results well and is equivalent to one another. But if comparing the values of factors, constants, and error analysis obtained by the least square method (S.S) for all the three models, it could be considered that BDST best followed the Thomas model along with the Yoon–Nelson models in relating the development of ICD adsorption onto ASAC.
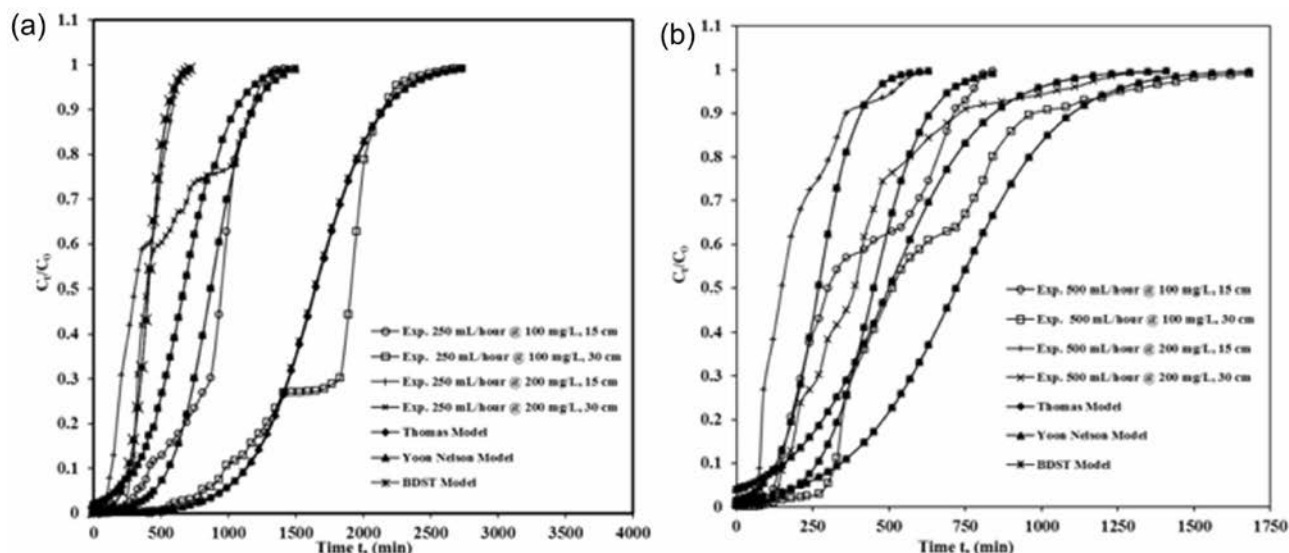
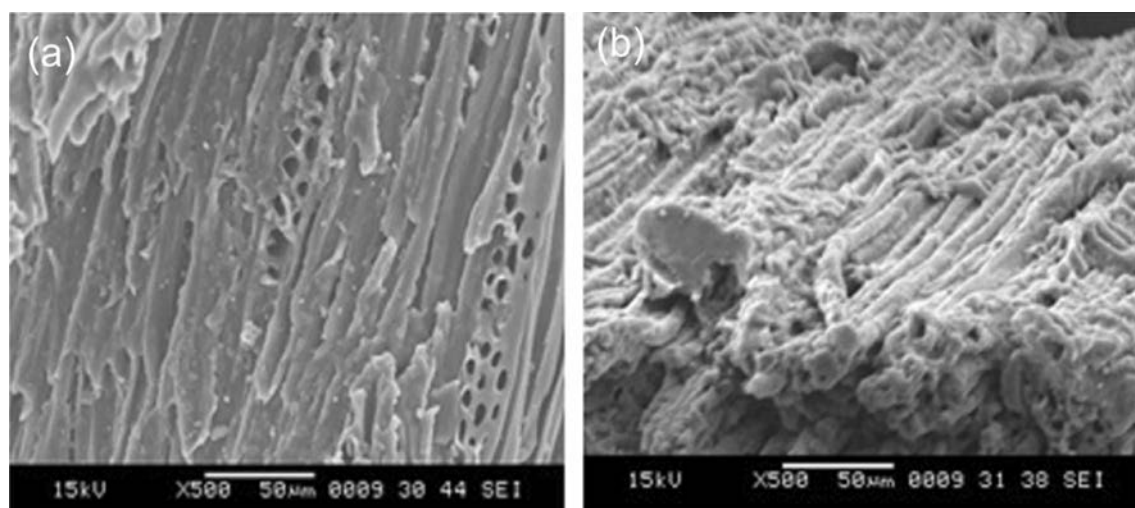**Figure 8.** Thomas, Yoon–Nelson and BDST models profiles.

Figure 9. S-E-M pictures of (**a**) raw ASAC and (**b**) ICD laden ASAC.

B–E–T surface area and B–E–T pore volume. B–E–T surface area and B–E–T pore volume of ASAC were analyzed using Brunauer, Emmett and Teller (B–E–T) method by ASTMD-3663-03. The standard test was conducted using ASAP 2020 (Micrometrics, USA) surface area and porosity analyzer. The $B–E–T$ surface area and $B–E–T$ pore volume of raw sawdust were 543.28 m^2/g and 0.1925 cm^3/g respectively. At the same time, $B–E–T$ surface area and $B–E–T$ pore volume of ASAC were obtained to be 737.76 m^2/g and 0.2583 cm^3/g, respectively. Th s rise in $B–E–T$ surface area and $B–E–T$ pore volume is due to the physico-chemical activation of raw sawdust into activated carbon (ASAC).

S-E-M, F-T-I-R and X-R-D analysis. S-E-M analysis explains the surface morphology and porosity of ASAC. ASAC laden with ICD was tested at 15 kV, 500× magnifi ations using a scanning electron microscope. From the picture of raw and laden ASAC (Fig. 9), it was noticed that the nature of ASAC is micro-porous. Such micro-pores are answerable for the biosorption of ICD onto the surface of ASAC. Such porosity is responsible for entering ICD molecules to penetrate the ling hemicellulose composition. They intermingle with the ASAC surface and diverse functional bonds [11,17].

The F-T-I-R spectroscopes are usually worn-out to recognize the distinguishing functional assemblies with excellent sorption capability. F-T-I-R spectroscopy monitors the chemistry of the ASAC surface and ICD-ASAC surface [11,17]. F-T-I-R spectroscopes of raw ASAC and ICD-laden ASAC are depicted in Fig. 10. Th s spectroscope shows the occurrence of distinguishing functional assemblies onto ASAC. The summit stretched in raw ASAC at 3670.06 cm^{-1} because of the –OH assembly, which vaguely shifts to 3682.03 cm^{-1} after ICD sorption onto ASAC. The group stretched in raw ASAC at 2933 cm^{-1} depicts well-built C–H links that swing faintly in ICD-laden ASAC to 2898 cm^{-1}. The summit stretched in raw ASAC at 2160 cm^{-1} describes the occurrence of a weak C–C
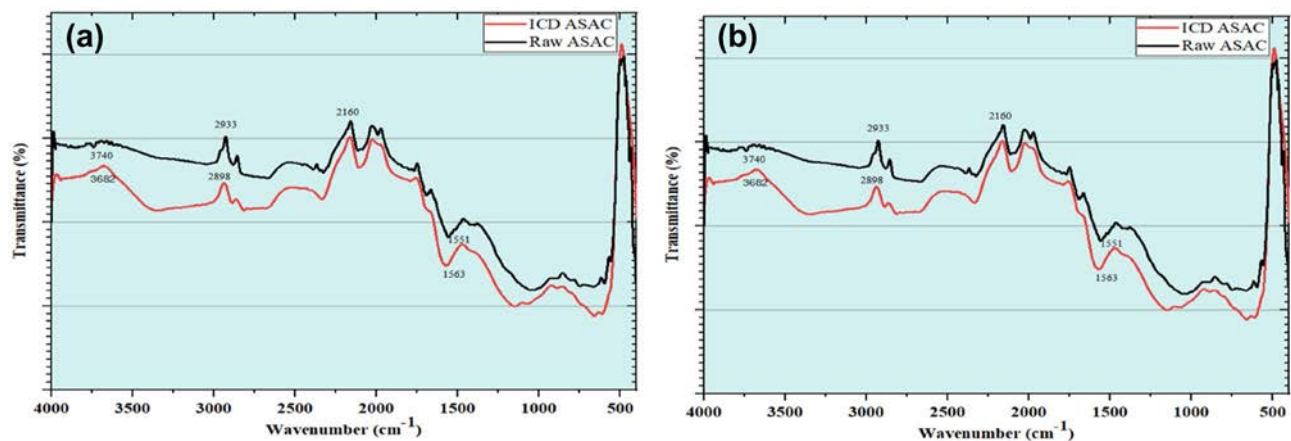
Figure 10. F-T-I-Rspectroscope of raw ASAC and ICD laden ASAC.
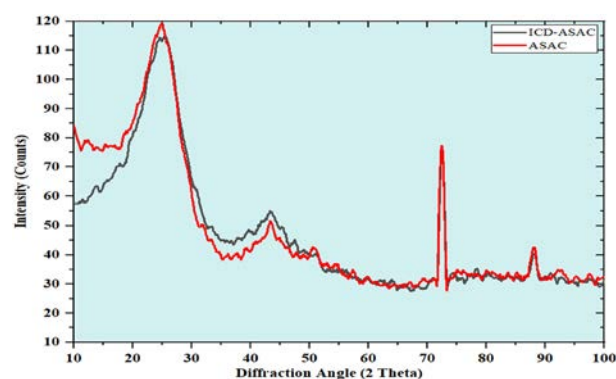
Figure 11. X-R-D spectrum of raw ASAC and ICD laden ASAC.

linkage thatdoes not swing after ICD adsorption. Similarly, the summit at 1551 cm^{-1} for raw ASAC swings to 1563 cm^{-1} for ICD laded ASAC[33]. This depicts the strong occurrence of C–OH and C–O groups. This swinging of summits validates the sorption of ICD onto ASAC.

X-R-D technique is a tool to analyze the crystalline or amorphous constitution of the adsorbents. The adsorption process may lead to changes in the adsorbent's constitution. Hence, understanding the molecular constitution and crystalline/amorphous constitution of the ASAC would provide valuable information regarding adsorption. Figure 11 shows the X-R-D spectra of raw ASAC and ICD-laden ASAC[34–36]. From Fig. 11, before the adsorption of ICD onto ASAC, the surface of ASAC showed hollow peaks, which indicated its amorphous nature. After adsorption with ICD, a reduction in the porous structure of the ASAC can be observed.

Conclusion

The present study shows the utilization of ASAC as an effective solution for removing ICD from wastewater. A continuous study of the fixed bed adsorption column on ASAC for the treatment of ICD discovered that ASAC could be used as an adsorbent material in industrial wastewater treatment to remove dyes from the solution. The adsorption of ICD for a given column bed depth was influenced by the flow rate and the ICD concentration. It was found that break-through and exhaust time occurred faster for shallower bed depths (15 cm) and increased gradually as column depth increased (30 cm). It was also observed that with an increase in initial dye solution concentration (from 100 to 200 mg/L) and flow rate (from 250 to 500 mL/h), break-through time and exhaust time decreased. The percentage removal efficiency and adsorption capacity of ASAC increase for lower initial ICD concentration and flow rate. The column study revealed that the maximum removal efficiency of ICD and adsorption capacity of ASAC was found to be about 47.35% and 21.99 mg/g, respectively, at lower column depth (15 cm), which increased respectively to 79.01% and 24.67 mg/g at higher column depth (30 cm), with the initial dye concentration reduced from 200 to 100 mg/L, allowing flow rate to reduce from 500 to 250 mL/h. The column kinetic study and error analysis also depicted that the experimental break-through plots compared satisfactorily with the break-through profiles calculated by Thomas, Yoon–Nelson and BDST models. Through comparing the values of variables, constants, and error analysis for all three models in relating the mechanism of ICD adsorption onto ASAC, it was also discovered that Thomas was better approached over BDST and Yoon–Nelson models. The comparison of correlation coefficients shows that all three models match the experimental results well and are equal in fixed-bed adsorption systems. The $B–E–T$ surface area and $B–E–T$ pore volume of raw sawdust were 543.28 m^2/g and 0.1925 cm^3/g respectively. Whereas $B–E–T$ surface area and $B–E–T$ pore volume of ASAC were

found to be 737.76 m²/g and 0.2583 cm³/g, respectively. Th s rise in *B–E–T* surface area and *B–E–T* pore volume is due to physico-chemical activation of raw sawdust into activated carbon (ASAC). *S-E-M* analysis and *X-R-D* analysis reveal the micro-porous and amorphous nature of ASAC. *F-T-I-R* spectroscopes indicate distinctive functional assemblies like –OH group, C–H bond, C–C bond, C–OH, and C–O groups on ASAC.It could be computed that the *Acacia nilotica* sawdust activated column can be considered as an alternative treatment option for industrial (specifi ally dye bearing) wastewater.

Data availability

The datasets used and analysed during the current study are available from the corresponding author on reasonable request.

References

1. Sujatha, M., Geetha, A., Sivakumar, P. & Palanisamy, P. N. Orthophosphoric acid activated babul seed carbon as an adsorbent for the removal of methylene blue. *E. J. Chem.* **5**, 742–753 (2008).
2. Zumriye, A. Application of biosorption for the removal of organic pollutants: A review. *Process Biochem.* **40**, 997–1026 (2005).
3. Ismail, I., Akar, T., Ozcan, S., Ozcan, A. & Tunali, S. Biosorption kinetics and isotherm studies of acid red 57 by dried cephalosporiumaphidicola cells from aqueous solutions. *Biochem. Eng. J.* **31**, 197–203 (2006).
4. Gupta, T. & Lataye, D. Adsorption of indigo carmine dye onto Acacia nilotica (babool) sawdust activated carbon. *J. ASCE Hazard. Toxic Radioact. Waste.* **21**, 4017013–4017014 (2017).
5. Dhorabe, P., Lataye, D. & Ingole, R. S. Adsorptive removal of 4-nitrophenol from aqueous solution by activated carbon prepared from waste orange peels. *J. Hazard. Toxic Radioact. Waste* **21**, 4016015–4016015 (2016).
6. Mittal, A. & Kurup, L. Utilization of hen feathers for the adsorption of indigo carmine from simulated effluents. *J. Environ. Prot. Sci.* **1**, 92–100 (2007).
7. Meshram, M. & Lataye, D. Adsorption of methylene blue dye onto activated carbon prepared from pongamia pinnata seed shell. *E. Shikimic Acid Metab. Metabolites* **3**, 1216–1220 (1993).
8. Wagh, P. & Shrivastava, V. Removal of indigo carmine dye by using palm wood cellulose activated carbon in aqueous solution: A kinetic and equilibrium. *Int. J. Latest Technol. Eng. Manage. Appl. Sci.* **4**, 1–9 (2015).
9. Ingole, R. L. D. & Dhorabe, P. Adsorption of phenol onto banana peels activated carbon. *KSCE J. Civ. Eng.* **21**, 100–110 (2017).
10. Dhorabe, P., Lataye, D. & Ingole, R. Removal of 4-nitrophenol from aqueous solution by adsorption onto activated carbon prepared from acacia glauca sawdust. *Water Sci. Technol.* **73**, 955–966 (2016).
11. Lataye, D. G. T. Removal of crystal violet and methylene blue dyes using activated carbon of acacia nilotica sawdust. *Ind. J. Chem. Tech.* **26**, 52–68 (2019).
12. Lataye, D., Mishra, I. & Mall, I. Removal of 4-picoline from aqueous solution by adsorption onto bagasse fly ash and rice husk ash: Equilibrium, thermodynamic and desorption study. *J. Environ. Eng.* **20**, 1048–1057 (2011).
13. Mall, I., Upadhyay, S. & Sharma, Y. A review on economical treatment of wastewaters effluents by adsorption. *Int. J. Environ. Stud.* **51**, 77–124 (1996).
14. Kavak, D. & Ozturk, N. Adsorption of boron from aqueous solution by sepiolite: II column studies. *II UluslararasıBorSempozyumu.* **23**(25), 495–500 (2014).
15. Roy, A., Chakraborty, S., Kundu, S. & Majumder, A. B. S. Lignocellulosic jute fiber as a bio adsorbent for the removal of azo dye from its aqueous solution: Batch and column studies. *J. Appl. Polym. Sci.* **129**, 15–27 (2013).
16. Sulaymon, A. & Ahmed, K. Competitive adsorption of furfural and phenolic compounds onto activated carbon in fi ed bed column. *Environ. Sci. Technol.* **42**, 392–397 (2007).
17. Gupta, T., Siddh, S. & Khungar, H. Adsorptive removal of direct-red-28 dye from contaminated water using subabool timber wood waste. *Helix* **9**, 5691–5695 (2019).
18. Naitoh, J. & Fox, B. M. Severe hypotension, bronchospasm and urticaria from intravenous indigo carmine. *Urol. J.* **44**, 271–272 (1994).
19. Yang, J., Monk, T. & White, P. Acute hemodynamic effects of indigo carmine in the presence of compromised cardiac function. *J. Clin. Anesth.* **3**, 320–323 (1991).
20. Indian Standard methods of test for soil: Part 4—Grain Size Analysis, vol. **4** (New Delhi India, 1985).
21. Zumriye, A. & Ferda, G. Biosorption of phenol by immobilized activated sludge in a continuous packed bed: Prediction of breakthrough curves. *Process Biochem.* **39**, 599–613 (2014).
22. Chen, J., Yoon, J. & Yiacoumi, S. Effects of chemical and physical properties of influent on copper sorption onto activated carbon fixed-bed columns. *Carbon* **41**, 1635–1644 (2003).
23. Hunge, P., Ansari, K., Gupta, T. & Waghmare, C. Use of pressure reducing valve for preventing pipeline rupture: A case study. *Helix* **9**(6), 5748–5752 (2019).
24. Gupta, V., Mittal, A., Krishnan, L. & Gajbe, V. Adsorption kinetics and column operations for the removal and recovery of malachite green from wastewater using bottom ash. *Sep. Purif. Technol.* **40**, 87–96 (2004).
25. Tamilselvi, S. & Asaithambi, M. Column mode adsorption studies of acid dye using a novel adsorbent. *Rasayan J. Chem.* **8**, 84–91 (2015).
26. Gupta, T. & Lataye, D. Adsorption of indigo carmine and methylene blue dye: Taguchi's design of experiment to optimize removal efficiency. *Sadhana Ind. Acad. Sci.* **43**, 1–13 (2018).
27. Thomas, H. Heterogeneous ion exchange in a flowing system. *J. Am. Chem. Soc.* **66**, 1664–1666 (1994).
28. Yoon, Y. & Nelson, J. A theoretical model for respirator cartridge service life. *Am. Ind. Hyg. Assoc. J.* **45**, 509–516 (1984).
29. Nithya, K., Sathish, A. & Senthil, P. Magnetite encapsulated alginates tailored material for the sustainable treatment of electroplating industrial wastewater: Column dynamics and mass transfer studies. *Clean. Technol. Environ. Policy* **23**, 89–102 (2021).
30. Julin, C., Yunhai, W., Yanpingj, P. & Shengxin, Y. Dynamic adsorption of anionic dyes by apricot shell activated carbon. *Desalin. Water Treat.* **53**, 25 (2015).
31. Runping, H. *et al.* Use of rice husk for the adsorption of congo red from aqueous solution in column mode. *Biores. Technol.* **99**, 2938–2946 (2008).
32. Gupta, T. & Ansari, K. Adsorption study on DR28 dye by subabul timber waste using Taguchi's laboratory test. *Helix* **9**, 5696–5700 (2019).
33. Ansari, K. *et al.* Experimental evaluation of industrial mushroom waste substrate using hybrid mechanism of vermicomposting and effective microorganisms. *Materials* **20**, 2963–2963 (2022).
34. Nagaraja, S. *et al.* Influence of heat treatment and reinforcements on tensile characteristics of aluminium AA 5083/silicon carbide/fly ash composites. *Materials* **14**, 25 (2021).

35. Ansari, K. & Shrikhande, A. N. Feasibility on grey water treatment by electrocoagulation process; a review. *Int. J. Emerg. Technol.* **10**, 85–92 (2019).
36. Raja, K. C. P., Thaniarasu, I., Elkotb, M. A., Ansari, K. & Saleel, C. A. Shrinkage study and strength aspects of concrete with foundry sand and coconut shell as a partial replacement for coarse and fine aggregate. *Materials* **14**, 25 (2021).

Author contributions

Conceptualization, T.G., K.A., M.K., D.L.; methodology, K.A., T.G., M.A.; software, N.M.M.; validation, K.A., T.G.; formal analysis, T.G., M.A.; investigation, K.A., T.G.; resources, T.G., M.A., D.L.; data curation, T.G., K.A.; writing—original draft preparation, T.G., K.A., N.M.M., M.A., M.K., R.R.K.; writing—review and editing, T.G., K.A., D.L.; visualization, M.A., N.M.M., D.L., T.G.; supervision, K.A., T.G.; project administration, all authors have read and agreed to the published version of the manuscript.

Competing interests

The authors declare no competing interests.

Additional information

Correspondence and requests for materials should be addressed to T.G., K.A. or N.M.M.

Reprints and permissions information is available at www.nature.com/reprints.

Publisher's note Springer Nature remains neutral with regard to jurisdictional claims in published maps and institutional affiliations.

Article

Optimization and Operational Analysis of Domestic Greywater Treatment by Electrocoagulation Filtration Using Response Surface Methodology

Khalid Ansari [1,2,*], Avinash Shrikhande [1], Mohammad Abdul Malik [3], Ahmad Aziz Alahmadi [4], Mamdooh Alwetaishi [5], Ali Nasser Alzaed [6] and Ahmed Elbeltagi [7]

[1] Department of Civil Engineering, Kavikulguru Institute of Technology and Science, Ramtek 441106, India
[2] Department of Civil Engineering, Yeshwantrao Chavan College of Engineering, Nagpur 441110, India
[3] Engineering Management Department, College of Engineering, Prince Sultan University, Riyadh 11586, Saudi Arabia
[4] Department of Electrical Engineering, College of Engineering, Taif University, P.O. Box 11099, Taif 21944, Saudi Arabia
[5] Department of Civil Engineering, College of Engineering, Taif University, Taif 21974, Saudi Arabia
[6] Department of Architecture Engineering, College of Engineering, Taif University, P.O. Box 11099, Taif 21944, Saudi Arabia
[7] Agricultural Engineering Department, Faculty of Agriculture, Mansoura University, Mansoura 35516, Egypt
* Correspondence: khalidshamim86@rediffmail.com or ksansari@ycce.edu

Abstract: Greywater is the most sustainable option to address the growing need for fresh water. This study aimed to identify the optimal operation variables of an electro-coagulation filtration (ECF) system for treating domestic greywater, using different conditions (e.g., different electrode combinations (Al-Fe-Al-Fe), initial pH (6.8–8.4), operating time (10–60 min), and voltage (6–24 volts)). A statistical data analysis was performed to evaluate the experimental conditions for modeling the chemical oxygen demand (COD), the total dissolved solids (TDSs), turbidity, and chloride removal effectiveness, almost ranging from (85 to 94%), respectively, with energy consumption using the response surface methodology (RSM) and the ANOVA test. When comparing the experimental and predicted model values, it was proved that the model fairly describes the experimental values with the R^2 values determined >0.99 for COD, TDSs, turbidity, chloride, and energy consumption, suggesting a regression sustainability of the model. The sludge properties were characterized using scanning electron microscopy (SEM), energy-dispersive X-ray spectroscopy (EDX), and FTIR spectroscopy, which indicated the removal of organic matter during the ECF, similar in composition, independently of the different applied voltage values used. The results of this study suggest the ECF significantly reduces the pollutants load in greywater, showing the aluminum-iron-based electrodes as a viable option to treat greywater with optimal operational costs ranging from (0.12 to 0.4) US\$ m^{-3} under different voltage conditions and parameters. This study establishes a path for greywater treatment technology that is economical and environmentally responsible for wastewater management that leads to sustainability.

Keywords: electrocoagulation; greywater; filtration; operational cost; ANOVA test; optimization

1. Introduction

Growing freshwater stress, caused by the population rising has put attention to simple, cost-effective, and reliable treatment technologies [1] to address the water management challenges. In developing countries, population and economic development demands [2] have led to the search for alternate water resources and strengthening water reuse and recycling. Domestic greywater recycling has been identified with the potential

to overcome the consumption pattern and reduce human health risks and environmental pollution [3] because of its lower concentration of pollutants [4] from different sources. Greywater contributes 50–80% of the household wastewater volume [5], depending on lifestyle, age, residential types, consumption patterns, religious traditions, and washing habits [5,6]. Greywater from households includes a high concentration of organic matter, which is primarily caused by using soap or soap products for body washing; its quality varies, according to the source, the geographical region, demographics, and degree of occupancy. Certain types of greywater have low suspended particles, and turbidity levels, indicating that a greater proportion of the pollutants are dissolved [7,8]. Its generation and characteristics show different loads of organic matter, fats and surfactants, salts, solids, nutrients, and pathogens, requiring treatment before reusing [8]. Greywater treatment procedures are primarily determined by their volume, physicochemical and biological properties, the amount of energy required, and the purposes for which treated water will be utilized [9].

Studies from the last five decades have shown different approaches to greywater treatment, including physical, chemical, biological, and hybrid methods [7,10]. Processes, such as soil filters, ultra-filtration (UF) membranes, membranes bioreactors [9], up-flow anaerobic sludge blankets (UASB) [10], rotating biological contractors (RBC) [11], sequencing batch reactors (SBR), ion exchange, and constructed wetlands [12], have been tested for greywater treatment, and all of them require either a large space and/or a highly skilled operation and maintenance. In the last few years, the use of hybrid physicochemical technologies, such as electrocoagulation followed by a sand filtration process, has gained attention as an efficient and effective alternative technology with a simple arrangement, minimum chemical addition, decreased sludge production, and low energy consumption to remove pollutants [13]. Hybrid processes using ECF processes have been tested in the past [14,15] generating significantly less membrane fouling and a greater COD, turbidity, and color removal, compared to the process alone. Based on the researcher's background, electrocoagulation (EC) proves to be a leading technology for water and wastewater treatment, combining coagulation, flotation, adsorption, and electrochemistry [16,17], as shown in Figure 1, with the dissolution mechanism of anode metals producing metal hydroxides with water molecules, which act as coagulants and in cathodic, the reactions cause the coagulants to rise to the surface by the release of hydrogen gas [16], with the phenomenon of the neutralization of charges, resulting in efficiently filtering out contaminants, such as dyes, metals, solids in suspension, organic matter, etc. [17–20].

Hence, researchers focused on the numerous advantages of using the electrocoagulation process in large-scale applications, and the ability to handle a wide range of reaction conditions with effluent types, with a better ability to reduce retention time, and rapidly sediment the electrogenerated flocculants during the sedimentation, with a reduction in sludge production, and the reduction in space and capital costs [21,22].
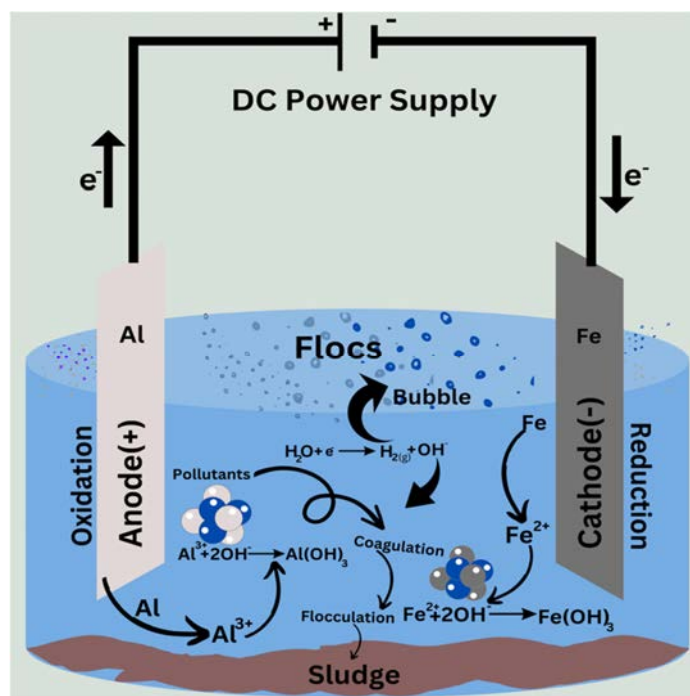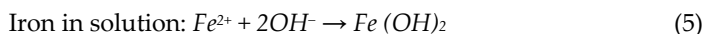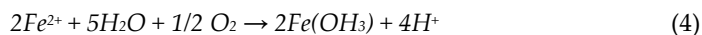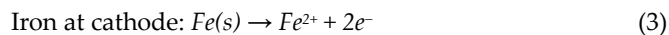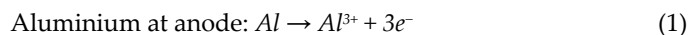
Figure 1. Systematic representation of the electrocoagulation process (EC).

According to Rakhmania et al., [21], the electrode material used is a critical factor influencing the efficiency of the EC process. Aluminium (Al) and iron (Fe) are the most often utilized electrodes in EC experiments, for eliminating pollutants, because they undergo dissolution to form amorphous metal hydroxides, such as Al^{3+} and Fe^{2+}, respectively, and are easily available at a cheap cost with the multivalent coagulant characteristic. Very few studies related to greywater, have been carried out with the application of EC and the results showed a remarkable increase in the removal efficiencies with Al-Fe-Al-Fe at pH 7.62, 98% turbidity (NTU), 98% COD (mg/L), 92% total phosphorus (mg/L), 84% total nitrogen (mg/L), and 99% total suspended solids (mg/L) [10]. According to Bote M., [13], the Al-Fe combination again showed the 87.5% COD removal at pH (9), with a current density of 45 (A/m²). Several studies [17–21], have reported a high EC efficiency in COD, BOD, and O&G [22] removal, using different electrode arrangements, mainly Al and Fe, with advantages in the low operational cost and a high bubble production [22]. The key reactions that rely on the characteristics of the solution are briefly presented in Equations (1) and (2) (which occur at the anode), Equations (3)–(5) (which occur at the cathode), [15].

$$\text{Aluminium at anode: } Al \rightarrow Al^{3+} + 3e^{-} \tag{1}$$

$$\text{Aluminium in solution: } Al^{3+} + 2OH^{-} \rightarrow Al\,(OH)_3 \tag{2}$$

$$\text{Iron at cathode: } Fe(s) \rightarrow Fe^{2+} + 2e^{-} \tag{3}$$

$$2Fe^{2+} + 5H_2O + 1/2\,O_2 \rightarrow 2Fe(OH_3) + 4H^{+} \tag{4}$$

$$\text{Iron in solution: } Fe^{2+} + 2OH^{-} \rightarrow Fe\,(OH)_2 \tag{5}$$

Based on the reaction analysis, H^2 gas and bubbles of O_2 gas simultaneously occur at the cathode and anode of the water electrolysis, resulting in a floc formation. Despite the evidence of EC improvement in the treatment efficiency, the major concern is identifying the best treatment conditions (e.g., electrode materials/arrangement, current density, power supply type, and operating time) for the specific applications [21,22]. According to

Bote M et al., [15], the optimization techniques for any process, such as the central composite design (CCD) was used to optimize the experimental condition by the response surface method (RSM), which is a reliable way to estimate the analytical statistical links between the independent factors and the response variables [23–29], helping to identify the optimal conditions and settings with relatively fewer trial experimental results [30–34], reducing the overall cost and time required for the procedure [35–38].

Furthermore, to the best of the author's knowledge, no information is available that addresses the hybrid mechanism of the ECF on greywater treatment, and only very few studies [10–20] target the estimation of the operational cost and sludge consumption to ascertain the effectiveness conditions, which helps to understand the novelty of this study. Therefore, the objective of this study is to investigate the treatment feasibility and characteristics of domestic greywater, using a hybrid ECF process, and optimized the process by RSM, to examine the overall efficiencies through the model simulation of the electrocoagulation filtration method, followed by an operational cost-enhancement with the application of recycling and reuse feasibility options for sustainable water management.

2. Materials and Methods

2.1. Samples

Twenty Greywater samples were collected from the bathtub or shower, hand basin, kitchen sinks, and laundry room sinks in residential areas in Nagpur, Maharashtra, India, in plastic buckets. The samples were shipped in polypropylene containers and maintained at 4 °C until characterization, as shown in Table 1 [22].

Table 1. Influents of the greywater characteristics.

Parameters	Minimum	Maximum	Average	Standard Deviation
pH	6.4	8.9	7.7	1.4
Turbidity (NTU)	36	88	36	12.6
TDSs (mg/L)	200	510	205	125
TSSs (mg/L)	39	190	88	56
COD (mg/L)	120	380	259	126
Chloride (mg/L)	10.9	56	32.6	8.9

2.2. Experimental Set-Up

Figure 2 shows the laboratory-scale setup used, including the EC reactors and filter media. The EC reactor [24 cm (height) × 20 cm (length) × 10 cm (width)], total volume 5.0 L, was made in 0.4 cm acrylic and used aluminium and iron sheets (18 cm (height) × 4.5 cm (width) × 0.02 cm (thickness)) as the electrode material separated by 3 cm. An auxiliary tank of identical proportions was compiled on either side of the reactors to eliminate the suspended stuff. The electrode configuration was in a monopolar parallel mode using a direct current (DC) power supply (model RPS 3005) with different operating conditions. In each run, 4.5 L of greywater were gently agitated at 130 rpm with four plates arranged vertically, immersed and covering an effective surface area of 82.5 cm² [22].

2.3. Filtration Media

A sand filter bed (60 cm in height, 10 cm wide, and 1.5 cm diameter) was also built with acrylic. In prior experiments, the sand and coconut shell activated carbon was washed, dried at 105 °C, sieved, and arranged with finer sand (effective size 0.2 to 0.5 mm) at the top, followed by granular activated carbon (effective size 0.2 to 0.6 mm) and gravel support (effective size 5 mm) at the bottom. The tests were carried out at room temperature. The effluents after the EC treatment were sent to filtering media (0.18 L/min) after

removing the precipitated flocs from the EC reactors, every 10 min for 60 min. The effluents were taken away so that the EC and filter could be tested while they were in use. The EC reactor and filter were cleaned after each run [22].
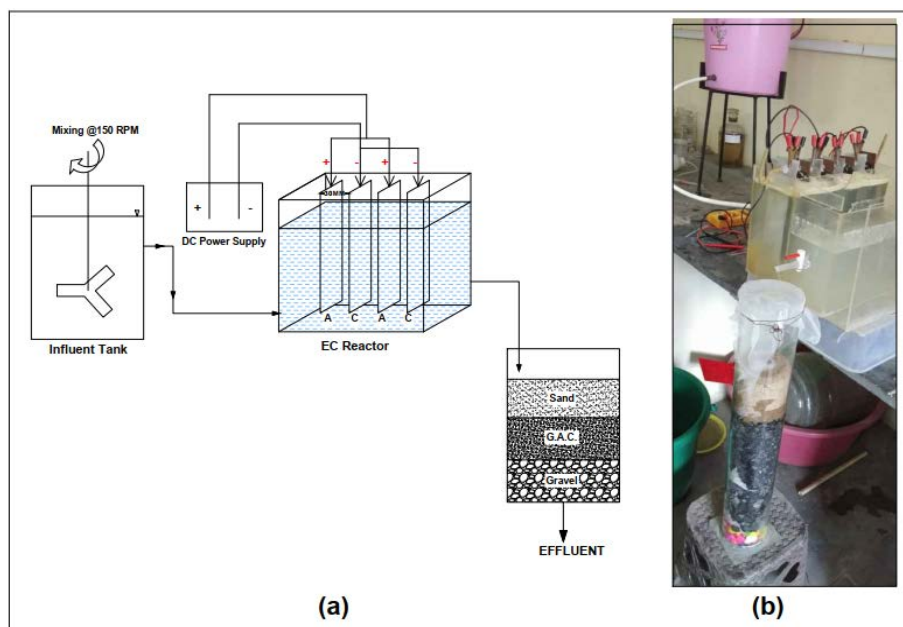

Figure 2. (**a**) ECF schematics, and (**b**) Experimental setup.

2.4. Analytical Studies

The performance of the hybrid EC reactor and filter bed was examined using the initial and final samples to emphasize the physiochemical characteristics of greywater, such as the chemical oxygen demand (COD), according to cuvette tests with a Hach Spectrophotometer (Hach, DR 2000, United States), total suspended solids (TSSs), total dissolved solids (TDSs), pH, turbidity, and chloride, according to the standard methods [23]. In this study, a JSM6380 LV scanning electron microscope (JEOL, Japan) with an accelerating voltage of 30.0 kV was utilized. To undertake the energy dispersive spectroscopy (EDS) study, the materials were gold-plated. The Fourier-transform infrared spectroscopy (FTIR) was used in a Bruker Vertex 70 spectrometer with OPUS 6.5 data handling and statistical analysis software was used to identify FTIR spectra (ATR).

2.5. Experiment Design Using the Response Surface Methodology (RSM)

The RSM was used to examine the connection between the removal efficiency and optimal process conditions [17–19]. The Design-Expert (version 13.0.5.0, Stat-Ease) software with the central composite design (CCD) application was used to determine the link between the variables and the response function [19]. Table 2 shows the three independent variables examined. The statistical tools were used to conduct the experimental design: analysis of variance (ANOVA), computational analysis, and three-dimensional response surface [27]. Three essential required input independent variables (a) voltage (6 to 24 volts), (b) reaction time (10–60 min), and (c) pH (6.8–8.4) for the Al-Fe-Al-Fe electrode combinations were tested and analyzed to calculate the most significant COD, TDSs, turbidity, and chloride removal effectiveness as a function of energy consumption. The input variables of the coded and real values for the selected variables were indicated using the RSM technique to operate the characteristics as the statistical significance and better evaluated through the ANOVA test [27].

Table 2. The levels and range of the independent variables.

Symbols	Independent Variables	Units	−1	0	+1
A	Voltage	Volts	6	12	24
B	Time	Min	10	30	60
C	pH	Unitless	6.8	7.6	8.4

To express the quality of the fitted models, the residual plots and coefficients of determination (R^2, adjusted R^2, and predicted R^2) were estimated [22,23]. To optimize the experiments, a software-based response surface prototype was used. Different versions (linear, quadratic, third-order polynomials, and two-factor interactions (2FI) were applied to fit the experimental data. The different algorithms obtained were then statistically examined to find the optimal model with the best actual, predicted, and adjusted R^2, low-predicted residual sum of squares, and no significant fit. Furthermore, the model's factors were evaluated using $p < 0.05$ value (probability) and F for (consistency) values using a 95% confidence level [20–22]. The lab tests were undertaken and compared to the model predictions to validate the model's outcomes, using different RSM conditions, using Equation (6) to express the system response as a percentage of the removal pollutants.

$$Yi = \beta 0 + \sum \beta iXi + \sum \beta iiXii2 + \sum \beta ijXiXj \tag{6}$$

where Yi is the relative removal efficiency, 0 for the model coefficient, i, ii, and i,j for the model coefficients, and Xi and Xj for the independent variables [20,21]. The RSM algorithm determines the coded values for the anticipated processes, such as Y1 (COD), Y2 (TDS), Y3 (chloride), Y4 (turbidity), and Y5 (electrode consumption).

The total number of experimental runs was decided, based on Equation (7)

$$N = 2^a + 2a + C = 20 \tag{7}$$

where N: total number of experimental runs; a: number of variables; C: number replicates to the center points.

3. Result and Discussion

The pH, operational duration, electrode type, and electrode spacing, are among the operational elements that affect the performance of the electrocoagulation filtration in eliminating the contaminants from greywater at different voltages. This enhances the efficacy of the EC, followed by the filtration in certain settings and systems. Using the following Equation (8), the effectiveness of the greywater removal was calculated [22].

$$\{RE\ (\%) = [(Xi - Xf)/Xi] \times 100\} \tag{8}$$

where Xi and Xf are the initial and final concentrations.

3.1. Effect of the Applied Voltage

The most crucial operational parameter that enhances the removal efficiency during the EC process is the applied voltage, which controls the reaction rate and the coagulant's production rate, resulting in the effect on the flocs formation and the operating cost of the electrocoagulation reactors [25,26]. To examine the impact of the voltage and the operating time of 60 min within the ECF process, the investigation was conducted at 6 V, 12 V, and 24 V, with an Al-Fe-Al-Fe electrode combination. It was observed when the voltage was applied, i.e., from 6 to 24 volts, the results highlight the increasing trends in the removal efficiency between 83 to 94%, for the COD, TDSs, chloride, and turbidity characteristics, due to the formation of $(OH)n$, which directly targets the flocs growth and charge neutralization of the Al^{3+} and Fe^{2+} ions during electrolysis [37–41].

3.2. Effect of the pH

Another critical factor in the greywater treatment is the pH, affecting the number of stable hydroxide species formed during the EC processes. Different types and numbers of electrodes and the influents' pH affect the pH during the treatment process. The pH properties of the hybrid electrodes at different voltages, (i.e., 6 to 24 volts), were examined to demonstrate the extreme elimination of the COD, turbidity, and other parameters, with the least electrode consumption [17]. From the observation, it is seen that the Al-Fe-Al-Fe combination produces a hydroxide sol that may adsorb the negative $H_2PO_4^-$ anions [17,28] and produce monomeric ions, such as $Al(OH)^2$, $Al(OH)_2^-$, $Al(OH)_3$, $Al(OH)_4^-$ and $Fe(OH)_2$, $Fe(OH)_3$ ions are capable for the quick assessment of hydrogen gas at the cathode [42] and its impact on the increase in the pollution removal performance at a pH of 6.8 to 8.4, showing the best performance.

3.3. Effect of the Operating Time

The EC also relies on the operating time it takes for dissolving the metal ions, to generate metal hydroxide species at the electrodes, which is a crucial step in the process [19]. The results in Table 3 showed that the COD (91%), TDSs (94.5%), turbidity (94.2%), and other parameters show appreciable removal efficiencies with the increase in the electrolysis reaction time from 10 to 60 min, which is due to an abundant discharge of coagulation metallic ions, such as Al^{3+} and Fe^{2+} ions at anode and cathode, were generated to destabilize the colloidal particles in the form of bubble production, based on the *Faraday Law* [19–21]. Hence, more flocs generation occurs, which increased the adsorption strength, resulting in a rise in the energy consumption over the electrolysis time [17], leading to an increase in the removal efficiency level of the pollutant contaminants.

Table 3. Experimental and the predicted responses for the various parameter levels.

	Voltage	Time	pH	Exp.	Pred.	Exp.	Pred.	Exp.	Pred.	Exp.	Pred.	Exp.	Pred.
Run	**Volts**	**min**		COD%		TDS%		Chloride%		Turbidity%		Electrode Consumption mg/Lit	
1	24	60	8.3	94.2	93.15	94.1	94.15	89.3	89.35	85.1	85.14	6.8	6.8
2	12	30	7.6	88.2	88.42	94.5	94.34	93.4	93.52	93.6	93.39	6.3	6.32
3	24	10	6.8	92.5	92.51	92.7	92.64	92.5	92.55	88.3	88.32	1.8	1.79
4	12	30	7.6	88.6	88.42	94.5	94.34	93.5	93.52	93.4	93.39	6.3	6.32
5	24	60	6.8	91.2	91.21	94.2	94.24	94.8	94.75	93.3	93.25	1.8	1.8
6	12	60	7.6	88.3	88.42	94.3	94.34	93.2	93.14	94.2	94.18	6.3	6.29
7	24	10	8.4	85.3	85.27	87.2	87.25	88.2	88.15	88.1	88.07	2.8	2.8
8	12	30	7.6	88.4	88.42	94.5	94.34	93.5	93.52	93.8	93.39	6.3	6.32
9	6	60	8.4	86.3	86.23	87.9	87.94	87.1	87.08	85.9	85.89	2.8	2.81
10	6	60	6.8	83.7	83.69	88.9	88.84	93.3	93.38	93.4	93.43	1.7	1.7
11	12	30	7.6	88.7	88.42	94.2	94.34	93.6	93.52	93.6	93.39	2.4	6.32
12	6	10	8.4	85.3	85.2	86.9	86.86	86.9	87	85.9	85.97	6.8	2.81
13	6	30	7.6	87.6	87.74	90.6	90.62	92.4	92.24	92.4	92.36	2.4	2.37
14	6	10	6.8	93.8	93.84	86.02	86.06	92.3	92.3	85.7	85.65	1.7	1.7
15	12	10	7.6	88.3	88.37	92.8	92.80	92.3	92.19	91.3	91.28	6.3	2.29
16	12	30	7.6	88.4	88.42	93.6	94.34	93.4	93.52	93.3	93.39	6.3	2.32
17	12	30	8.4	86.3	86.55	90.9	90.90	89.5	89.42	87.9	87.83	6.8	2.78
18	12	30	7.6	88.6	88.42	94.8	94.34	93.4	93.52	92.6	93.39	2.3	2.32
19	12	30	6.8	94.3	94.25	92.8	92.84	94.9	94.82	90.8	90.84	5.7	1.7
20	24	30	7.6	86.6	86.65	93.6	93.63	93.4	93.39	93.6	93.61	2.4	6.41

3.4. Effect of the Filter Media

In this ECF process, the physiochemical parameters, such as color, turbidity, heavy metal, pesticides, organic chemicals, TSSs, etc., were eliminated using a sand filter followed by activated carbon with staining and sedimentation capabilities to enhance the electrocoagulation process, based on the capacity of adsorbent surface area, porosity, and functional groups [42,43]. The sand filter is crucial for the solids removal and pH balance maintenance [42] and the activated carbon statute as catalyst media in the chemical reduction of the strong oxidants to innocuous byproducts, The purpose of the filter media is to overall increase the removal efficiency level for a sustainable onsite greywater treatment.

3.5. Experimental Results of the ANOVA Statistics

To summarize the 20 sets of runs, the actual (experimental) responses, and predicted responses, as shown in Figure 3 for the coded central composite design, fused in the greywater treatment by the electrocoagulation- filtration method, the following Tables 3–5 have been created. Y1 (COD), Y2 (TDSs), Y3 (chloride), Y4 (turbidity), and Y5 (electrode consumption), are all determined by three variables, as voltage (A), time (B), and pH (C). The Design-Expert software created the model quadratic regression Equations (9)–(13) [27].

Table 4. Statistical regression equation for the various parameter levels.

Responses	Regression Model	Equation
% Removal (COD) (Y1)	$+308.52650 + 0.041138 \times A - 0.092807 \times B - 52.85575 \times C - 0.001271(A \times B) + 0.048605(A \times C) + 0.014749(B \times C) - 0.014429A^2 - 0.000043B^2 + 3.09322C^2$	(9)
% Removal (TDSs) (Y2)	$-156.71153 + 2.97382 \times A + 0.314483 \times B + 60.53911 \times C - 0.001313(A \times B) - 0.21517(A \times C) - 0.021178(B \times C) - 0.037728A^2 - 0.001530B^2 - 3.85102C^2$	(10)
% Removal (Chloride) (Y3)	$-13.27855 + 0.163546 \times A + 0.210164 \times B + 30.03592 \times C + 0.001242 (A \times B) + 0.031250(A \times C) - 0.012500(B \times C) - 0.012480 \times A^2 - 0.001586 \times B^2 - 2.19809 \times C^2$	(11)
% Removal (Turbidity) (Y4)	$-290.37256 + 0.571890 \times A + 0.953617 \times B + 97.72627 \times C - 0.003163(A \times B) - 0.019764(A \times C) - 0.098269(B \times C) - 0.008583 \times A^2 - 0.001583 \times B^2 - 6.34378 \times C^2$	(12)
Electrode Consumption (Y5)	$-10.40679 + 0.003984 \times A + 0.003903 \times B + 2.65941 \times C + 3.65956(A \times B) - 0.003622 (A \times C) - 0.000032 (B \times C) + 0.000855 \times A^2 - 0.000053 \times B^2 - 0.127872 \times C^2$	(13)

Table 5. ANOVA quadratic model on the various parameter levels.

	COD		TDSs		Chloride		Turbidity		Electrode Consumption		
Source	Sum of Squares	*p*-Value	Sum of Squares	*p*-Value	Sum of Squares	*p*-Value	Sum of Squares	*p*-Value	Sum of Squares	*p*-Value	Remark
Model	155.89	<0.0001	181.91	<0.0001	112.7	<0.0001	203.71	<0.0001	2.85	<0.000	Significant
A-Voltage	3.61	<0.0001	20.87	<0.0001	3.98	<0.0001	2.31	0.0005	0.004	0.0795	
B-Time	0.0474	0.2523	4.44	<0.0001	3.22	<0.0001	14.62	<0.0001	3.00×10^{-8}	0.9958	
C-pH	134.06	<0.0001	24.54	<0.0001	71.04	<0.0001	37.67	<0.0001	2.77	<0.0001	
AB	0.6738	0.001	0.7198	0.0169	0.6439	<0.0001	4.17	<0.0001	5.59×10^{-6}	0.9433	
AC	1	0.0002	19.62	<0.0001	0.4139	0.0002	0.1656	0.2076	0.0056	0.0443	
BC	0.7015	0.0009	1.45	0.0023	0.5039	0.0001	31.14	<0.0001	3.38×10^{-6}	0.9559	
A²	2.88	<0.0001	19.68	<0.0001	2.15	<0.0001	1.02	0.0075	0.0101	0.0113	
B²	0.0018	0.8187	2.29	0.0005	2.46	<0.0001	2.45	0.0004	0.0027	0.137	
C²	10.78	<0.0001	16.7	<0.0001	5.44	<0.0001	45.32	<0.0001	0.0184	0.0019	
Residual	0.3214		0.8791		0.1341		0.9119		0.0105		
Lack of Fit	0.1531	0.9402	0.0241	0.9993	0.1007	0.1251	0.0236	0.9994	0.0022	0.9161	Not Significant
Pure Error	0.1683		0.855		0.0333		0.8883		0.0083		
Cor Total	156.21		182.79		112.83		204.62		2.86		

(**a**)

(**b**)

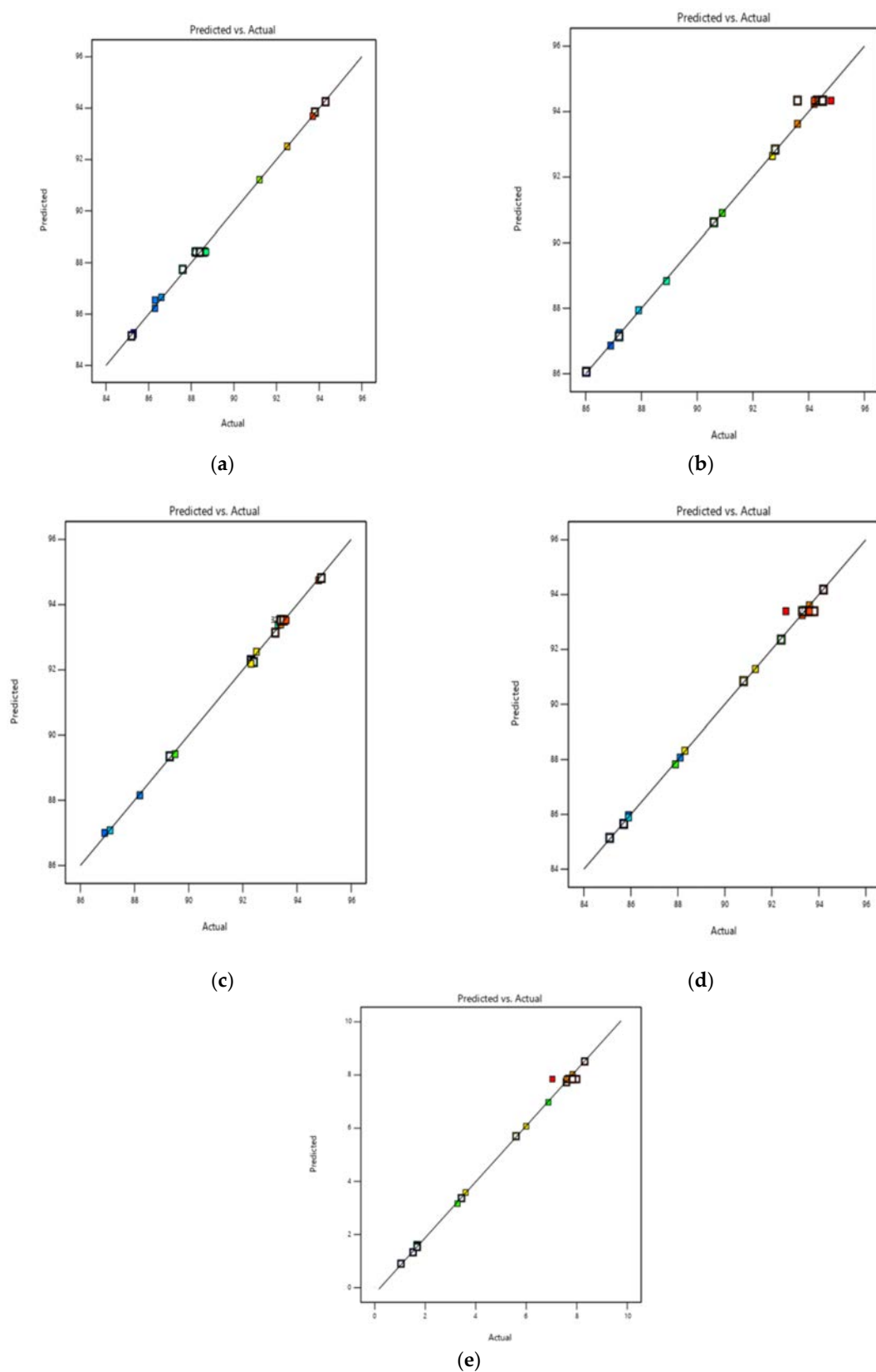(**c**)

(**d**)

(**e**)

Figure 3. Plot showing the actual versus predicted values of (**a**) COD, (**b**) TDSs, (**c**) chloride, (**d**) turbidity and (**e**) electrode consumption.

3.6. Validation of the Design

An investigation using the RSM technique was conducted to determine the best fit for the response function, to analyze the results of the EC and filtration processes regarding the error reduction and discover the best fit for the response function. Following the results shown in Table 6, the ANOVA (analysis of variance) was applied to decide the validity of the predicted model, as well as the multiple responses, which were tested for the COD, total dissolved solids (TDSs), turbidity, chloride, energy consumption, and operating cost reduction. The F-test was performed to determine whether the model was statistically significant. To obtain the correct result, the F-value of a model must be more important than the *p*-value of the model [27]. Statistically significant differences were found between the treatments for the COD, total dissolved solids (TDSs), chloride, turbidity, energy consumption, and operating cost, with the model F-values of 538.86, 229.91, 934, 248.21, 301.35, and 503.27, respectively. It was also found that for all five responses, the *p*-value was less than 0.0001, pointing out that the model is more correct and highly significant. The estimated lack of fit value for the model was shown to be not significant for all five responses, namely the COD, TDSs, turbidity, chloride, energy consumption, (*p*-value = 0.9402, 0.9993, 0.1251, 0.9994, and 0.9161, >0.05), indicating that the model is accepted, suitable, and considerable for the pollutant removal via the ECF processes [21,22]. The correlation between R^2, adjusted R^2, and predicted R^2 comes to 0.99, which again proves that the model is acceptable, as shown in Figure 4.

Table 6. The model's fit statistics and the ANOVA findings.

Parameter	COD Removal	TDS Removal	Chloride Removal	Turbidity Removal	Electrode Consumption
Model *F*-**value**	538.86	222.91	934	248.21	301.35
Adequate precision	71.75	39.47	95.45	42.33	48.41
C.V. %	0.2019	0.3237	0.1258	0.3325	1.41
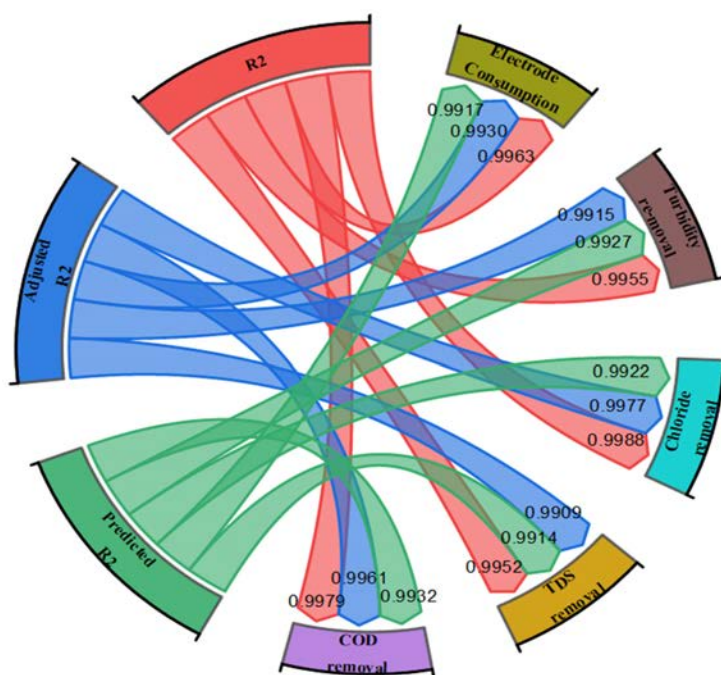
Figure 4. Chord Diagram showing the relation of R^2, adjusted R^2, and predicted R^2 with different responses.

3.7. Three Dimension Surface Plot

Figure 5 depicts, with the help of a three-dimensional surface plot, the matrix of the effect that applied voltage and operating duration have on the removal efficiency of the COD, TDSs, turbidity, chloride, energy consumption, and operating cost. The flag on the graph indicates the highest percentage of pollutants removed (94.3% COD, 94.8% TDSs, 94.9% chloride, and 94.2% turbidity), with an electrode consumption of 6.8 mg/L, is under ideal conditions. The graph's colour scheme alternates between blue and red, with blue representing the lowest value and red representing the highest [21,27].

(**a**)

(**b**)

(**c**)

(**d**)

(**e**)
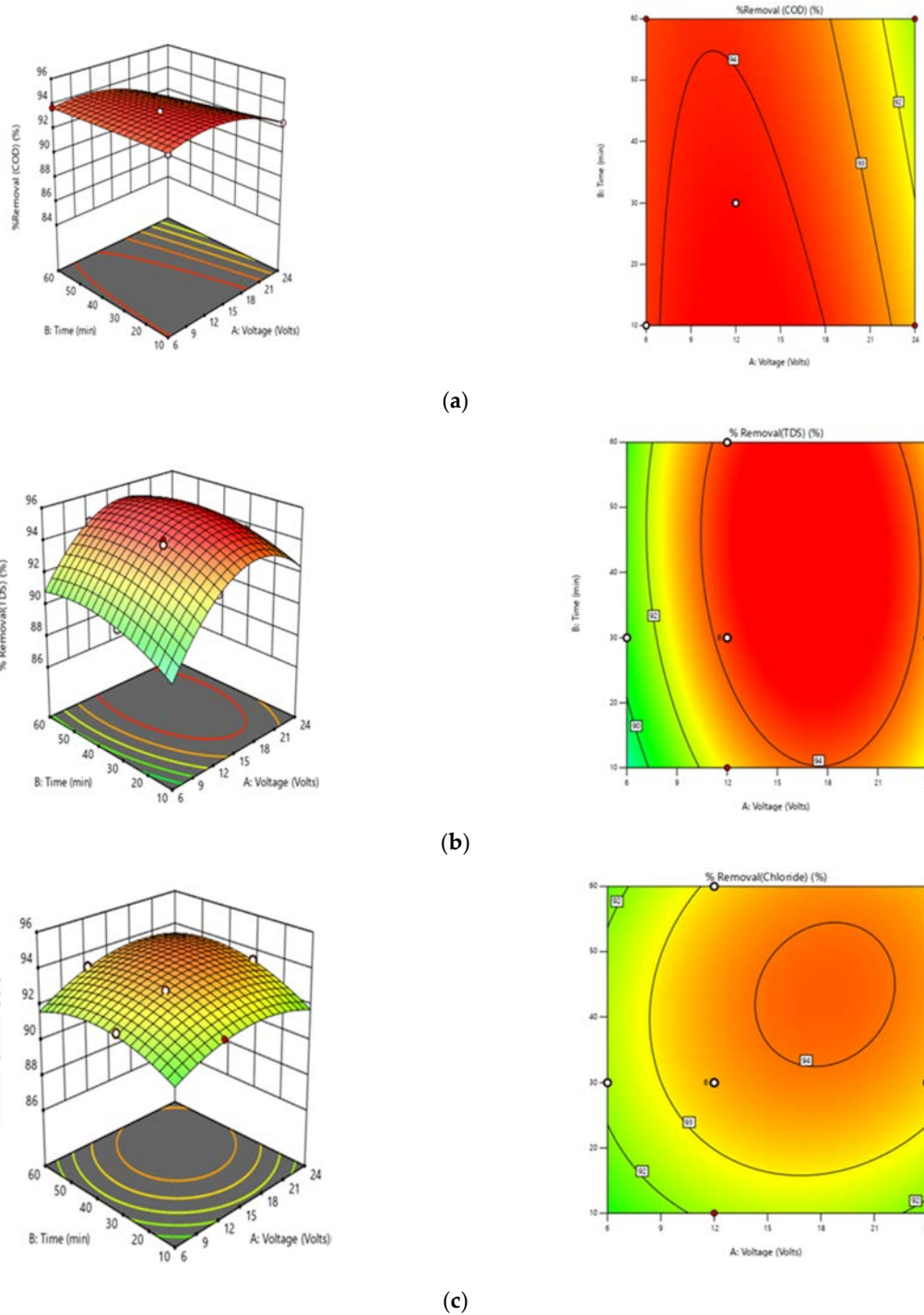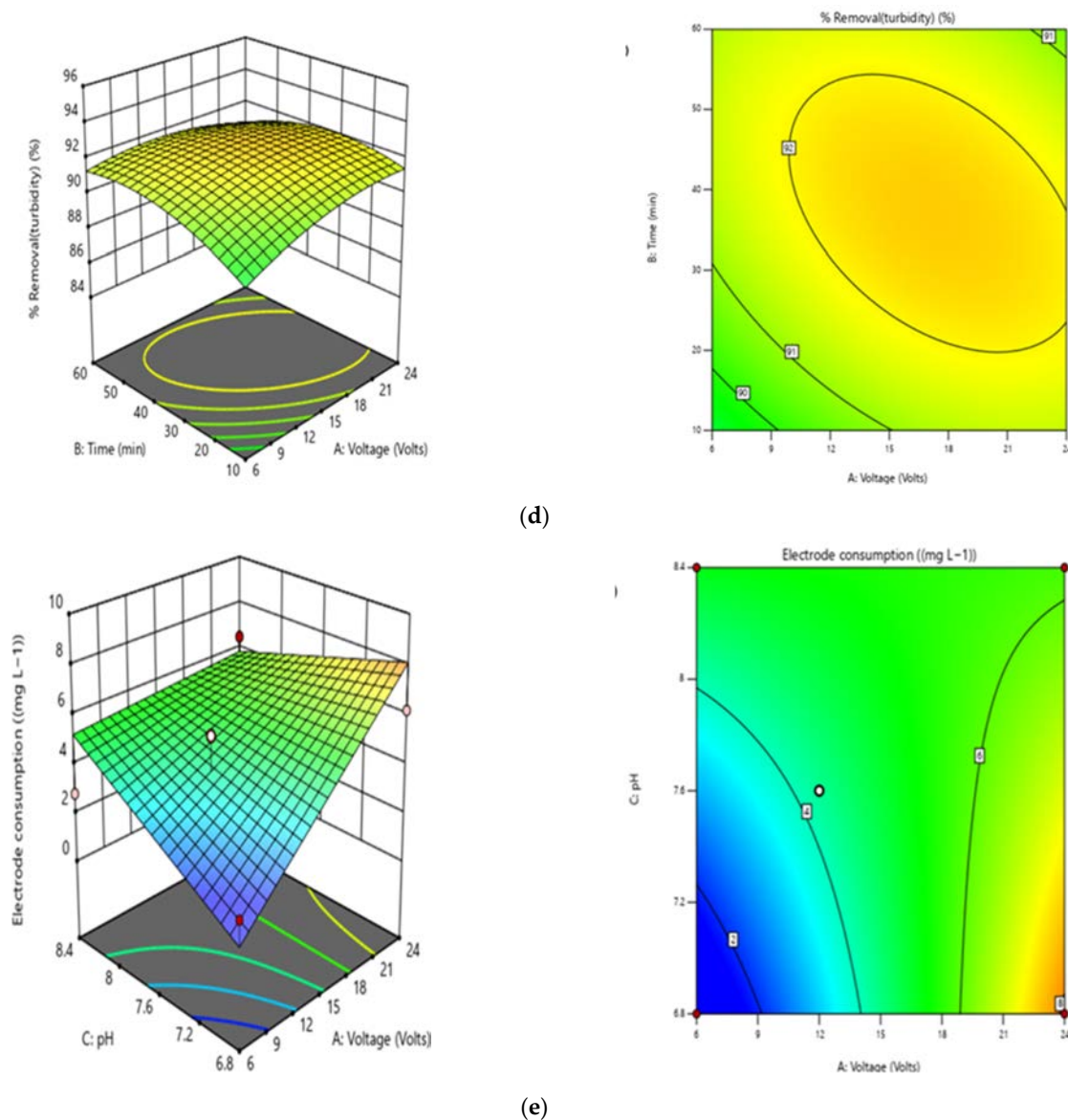
Figure 5. Three-dimensional surface and contour plot showing the effect of voltage and time on (**a**) COD, (**b**)TDSs, (**c**) chloride, (**d**) turbidity, (**e**) electrode consumption.

3.8. Optimization and Verification of the Model

The optimization and validation of the model demonstrated in Table 7, show that the efficiency of the electrocoagulation and the filtration processes using an Al-Fe-Al-Fe electrode combination with a different applied voltage, ranging from 6 to 24 volts, which results in the removal of organic matter and contaminants from greywater, is influenced by several factors, counting with the electrode materials type, applied voltage, pH, electrocoagulation time, and sludge produced in the cathode and anode. Hence, in the optimization process, the effect of applied voltage, electrocoagulation time, and pH were studied using the Al-Fe-Al-Fe electrode combinations.

Table 7. Optimization conditions for 6 to 24 volts.

Number	Voltage	Time	pH	Removal (%COD)	Removal (%TDS)	Removal (%Chloride)	Removal (%Turbidity)	Electrode Consumption	Desirability
1	6.00	55.00	7.800	87.119	90.761	91.07	92.592	1.484	0.644
2	12.000	57.45	7.7	92.000	94.260	94.796	94.651	1.875	0.859
3	24.0	54.50	7.900	94.351	94.421	94.888	93.118	4.5	0.495

4. Operational Cost

As per the researchers' output, the performance of the electrocoagulation filtration process is determined by the operational costs of the treatments, which is a disadvantageous approach, particularly in large-scale industrial applications [10,32]. Despite this, the technology has received little attention, with only a few studies published on the analysis of the operational costs. In the ECF process, the operating rate (OPc) includes the electrical energy consumed, the cost of the electrode uses, and the protectorate cost for the sludge disposal in landfills, filtration medium, and other fixed charges, which are projected to be 0.03 USD kg/m³ on average (USD 1 = INR 78.90) [33]. The cost of the electrical energy and electrode material and the cost of maintenance are used to calculate the operating cost, which is represented by Equations (14) and (15) shown below and expressed in Figure 6 [6,10,34,43]

$$OPc = Cost\ Energy + Cost\ Electrode + Cost\ Maintenance$$

$$Cost\ of\ energy, Cost\ Energy\ (kWh/m^3) = \{(U*i*to)/V\} \tag{14}$$

$$Cost\ of\ Electrode, Cost\ Electrode\ (kg/m^3) = \{(i*to*Mw)/(z*F*V)\} \tag{15}$$

where U = cell voltages (V); I = current (Amp); to = operating time (hrs); V = wetted volume of the reactor (m³); Mw = molecular wt. of Fe/Al (g/mol); z = amount of electrons involved in the EC process (2 for Fe and 3 for Al); F = faradays constant (96,485 C/mol); CD = current density (A), electrical consumption unit pricing for the Nagpur area (India) was set at USD 0.05/kWh, while the price of the electrode material was set at USD 0.51/kg for Fe and 1.39/kg for Al.
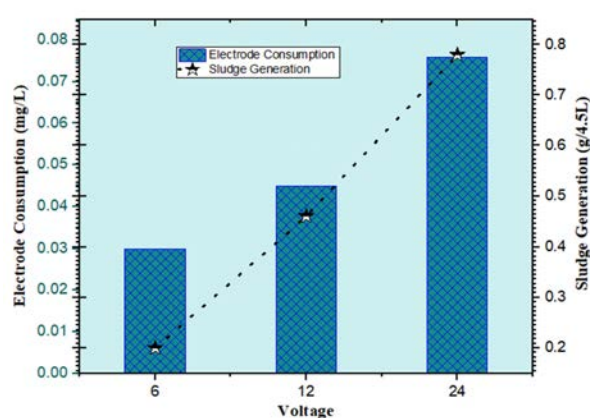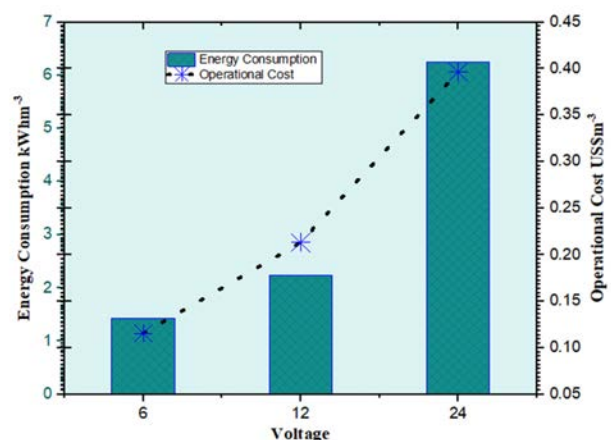
(**a**)   (**b**)

Figure 6. (**a**) Operational cost and energy consumption with respect to the voltage and (**b**) electrode consumption and sludge generation with respect to the voltage.

5. Sludge Characterization by the SEM, EDS, and FTIR Analyses

Sludge characterization facilitates the greywater recovery and pollution microstructural abatement, and examines the functional group by the SEM, EDX, and FTIR spectrum, after the obtained electrocoagulation treatment process at 6, 12, and 24 volts, as shown in Figure 7a–c. The sludge produced under various voltage distribution variations demonstrates that the scum particles created are highly agglomerated during the treatment process and the EDX analysis reflects the presence of the various elements with their atomic strength.

(**a**)   (**b**)

(**c**)
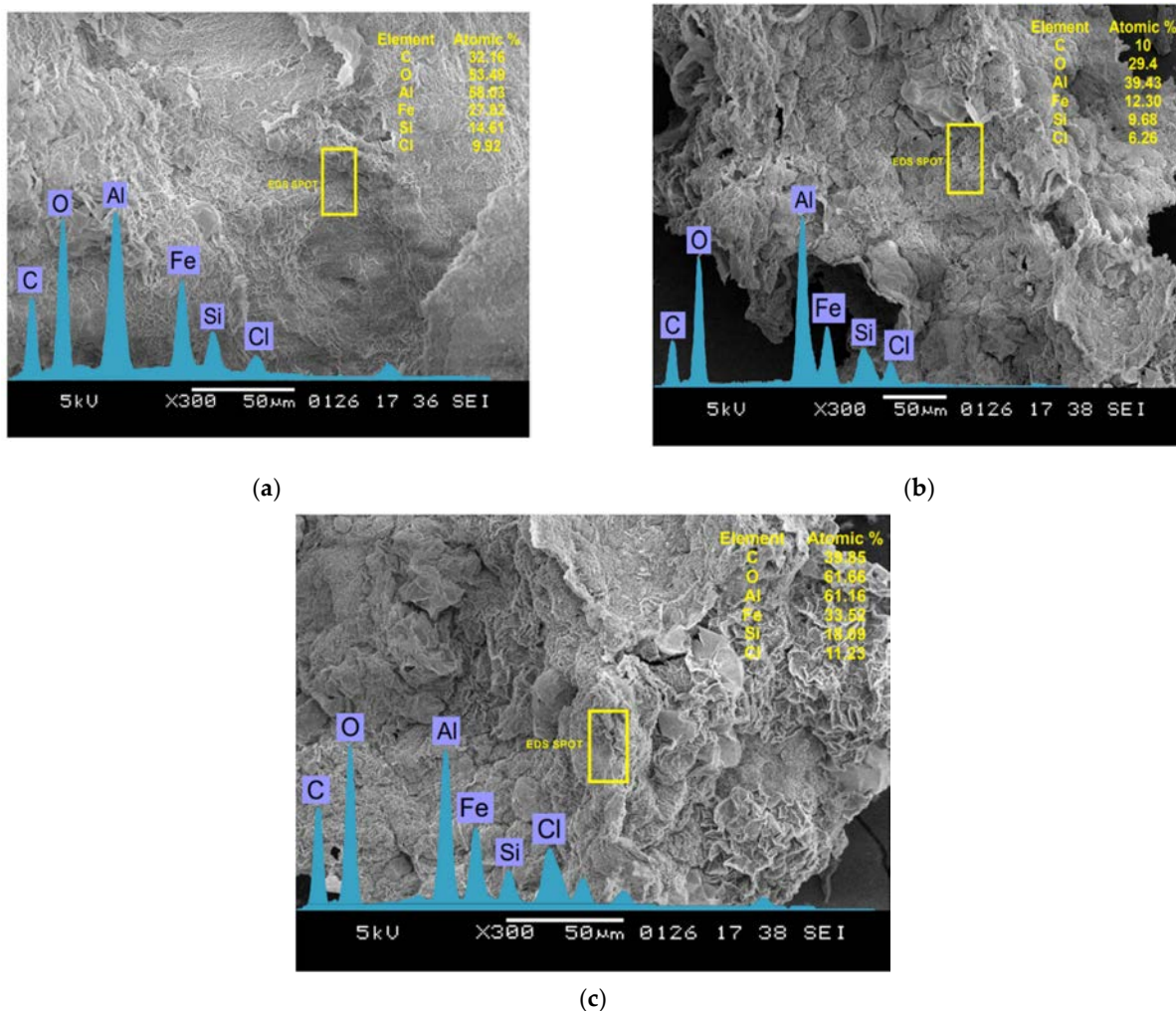
Figure 7. SEM and EDX microanalysis structure of the sludge generated during the ECF process at (**a**) 6 V, (**b**) 12 V, and (**c**) 24 V.

The presence of a high level of oxygen (29.4%, 53.49%, and 61.66%) and alumina (39.43%, 58.03%, and 61.16%) in 6, 12, and 24 volts, respectively, indicates the hydroxide contents in greywater during the coagulants and precipitate formation, obtained during the electrocoagulation process. Again, the presence of carbon and iron elements shows the adsorption mechanism which highlights the significant reduction of the organic pollutants from greywater with an increase in the atomic strength with an increase in the applied voltage. The FTIR analysis indicated, as reflected in Figure 8 shows, the changes in the wavenumber position to highlight the major peaks at 3639.6, 2409.5, 1484.7, and 691.5 (cm^{-1}), reflecting the functional group of Hydroxy, due to the O-H stretching, alkenyl C=C

stretching, C-H methylene and C-O bending stretching, indicating the elimination of greywater organic pollutants through the process of electrocoagulation [19,36,37,43]. The observed FTIR reflects that some slight changes in the amorphous nature were found with the different applied voltages. The sludge formed by the EC process, increases the operational costs and creates environmental issues with the disposal solutions, such as the electron metal ions, the operating treatment duration, the flow rate, the chemical composition, and so on, which are eliminated during the water purification. There hasn't been much research on the potential applications of EC sludge, nor has there been much research on its use in specific industries. However, there are a few studies that have been carried out on the use of sludge as fertilizers, pigments, building materials, absorbents, and catalysts, as well as a few studies on EC sludge valorization [44–46].
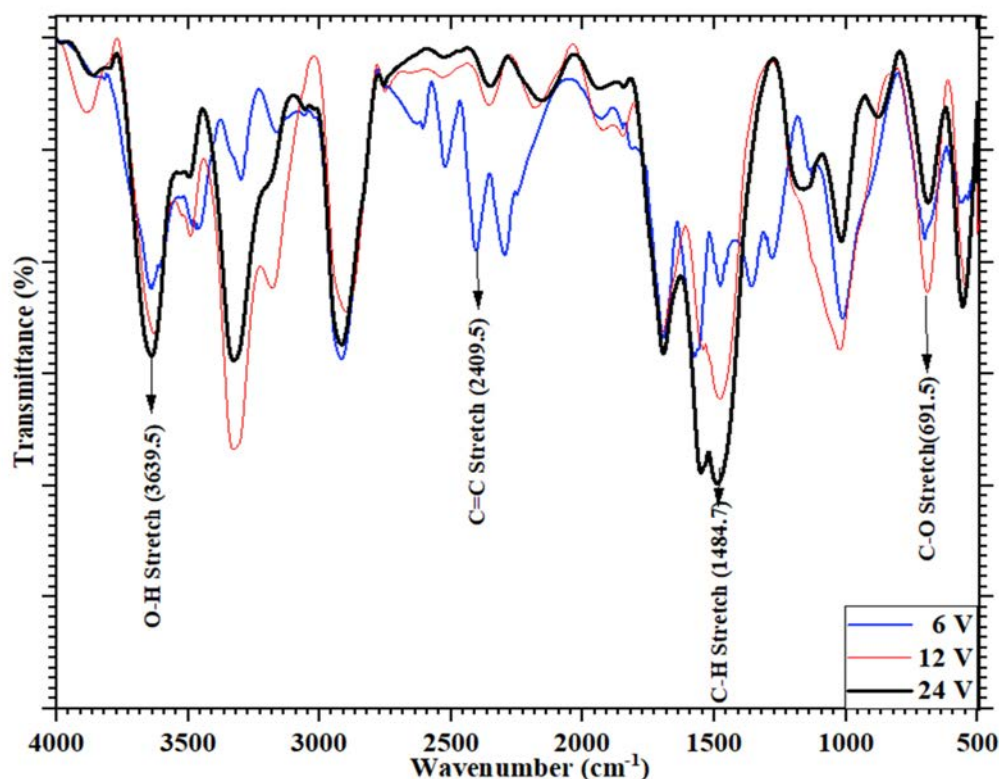
Figure 8. Sludge Characterization by the FTIR spectra with the different applied voltage.

6. Conclusions

The study examines the removal of the pollutant parameters of greywater, using the electrocoagulation filtration ECF technology of Al-Fe-Al-Fe electrode combination, at the varying applied voltages of 6, 12, and 24 volts. The results showed that the experimental removal efficiency, concerning initial pH, current density, and operating time, reaches (85 to 94)%. The statistical data analysis was utilized to check the experimental accuracy by using a central composite design to consider the values of the operating parameters at various factor intervals such as (voltage, time, and pH), on the elimination of the COD, TDSs, turbidity, chloride, with the utility of energy consumption with 20 sets of experimental run values provided by the RSM techniques. The findings show that the R^2 value (i.e., $R^2 > 0.97{\sim}0.99$) acquired from the ANOVA for all five responses consent that the suggested model is reliable and sustainable with strong evidence that the actual values and predicted values acquired are below 5% of the expected values. It was observed that the

operating cost for the different voltages, was between (0.12 to 0.40) USD/m^3. This concludes that the response surface method can optimize the greywater's long-term electrocoagulation filtration treatment. Finally, based on the experimental results and the optimization model, the ECF discharge greywater can be recycled and reused for non-potable consumption, such as gardening, the automobile sector, and lavatory flushing, applicable in rural, urban areas, and industries sectors with proper disinfected arrangements to remove the pollutant contaminants, in order to achieve a sustainable water management.

References

1. Moussa, D.T.; El-Naas, M.H.; Nasser, M.; Mj, A.-M. A comprehensive review of electro-coagulation for water treatment: Potentials and challenges. *J. Environ. Manag.* **2016**, *186*, 24–41.
2. Melhem, E.S.K. Grey water treatment by a continuous process of an electrocoagulation unit and a submerged membrane bioreactor system. *Chem. Eng. J.* **2012**, *198–199*, 201–210.
3. El-Khateeb, A.-S.H.; Shehata, M.A. Greywater treatment using different designs of sand filters. *Desalin. Water Treat.* **2014**, *52*, 5237–5242.
4. Antonopoulou, G.; Kirkou, A.; Stasinakis, A.S. Quantitative and qualitative greywater characterization in Greek households and investigation of their treatment using physicochemical methods. *Sci. Total Environ.* **2013**, *454–455*, 426–432.
5. Eriksson, E.; Auffarth, K.; Eilersen, A.M.; Henze, M.; Ledin, A. Household chemicals and personal care products as sources for xenobiotic organic compounds in grey wastewater. *Water SA* **2003**, *29*, 135–181.
6. Ghaitidak, D.M.; Yadav, K.D. Characteristics and treatment of greywater—A review. *Environ. Sci. Pollut. Res.* **2013**, *20*, 2795–2809.
7. Ansari, K.; Shrikhande, A.N. Feasibility on Grey Water Treatment by Electrocoagulation Process: A Review. *Int. J. Emerg. Technol.* **2019**, *10*, 92–99.
8. Pidou, M.; Avery, L.; Stephenson, T.; Jeffrey, P.; Parsons, S.; Liu, S.; Memon, F.; Jeffreson, B. Chemical solutions for greywater recycling. *Chemosphere* **2008**, *71*, 147–155.
9. Bracher, G.H.; Carissimi, E.; Wolff, D.B.; Graepin, C.; Hubner, A.P. Optimization of an electrocoagulation-flotation system for domestic wastewater treatment and reuse. *Environ. Technol.* **2020**, *42*, 2669–2679. https:// doi.org/10.1080/09593330.2019.1709905.
10. Fountoulakis, M.S.; Markakis, N.; Petousi, I.; Manios, T. Science of the total environment single house on-site grey water treatment using a submerged membrane bioreactor for toilet flushing. *Sci. Total Environ.* **2016**, *551–552*, 706–711. https://doi.org/10.1016/j.scitotenv. 2016.02.057.
11. Cecconet, D.; Callegari, A.; Hlavínek, P.; Capodaglio, A.G. Membrane bioreactors for sustainable, fit-for-purpose greywater treatment: A critical review. *Clean Technol. Environ. Policy* **2019**, *21*, 745–762. https:// doi.org/10.1007/s10098-019-01679-z.
12. Sibel, B.; Turkay, O. Domestic greywater treatment by electrocoagulation using hybrid electrode combinations. *J. Water Process Eng.* **2016**, *10*, 56–66.
13. Bote, M.E. Studies on electrode combination for COD removal from domestic wastewater using electrocoagulation. *Heliyon* **2021**, *7*, e08614.

14. Daghrir, R.; Drogui, P.; Blais, J.-F.; Guy, M. Hybrid process combining electrocoagulation and electro-oxidation processes for the treatment of restaurant wastewaters. *J. Environ. Eng.* **2012**, *138*. https://doi.org/10.1061/(ASCE)EE.1943-7870.0000579.

15. Lin, C.J.; Lo, S.L.; Kuo, C.Y.; Wu, C.H. Pilot-scale electrocoagulation with bipolar aluminum electrodes for on-site domestic greywater reuse. *J. Environ. Eng.* **2005**, *131*, 3.

16. Othmani, A.; Kadier, A.; Singh, R.; Igwegb, C.A.; Bouzid, M.; Aquatar, M.O.; Khanday, W.; Bote, M.; Damiri, F.; Gökkuş, O.; et al. A comprehensive review on green perspectives of electrocoagulation integrated with advanced processes for effective pollutants removal from water environment. *Environ. Res.* **2022**, *215*, 114294.

17. Bajpai, M.; Katoch, S. Techno-economical optimization using Box-Behnken (BB) design for COD and Chloride reduction from Hospital wastewater by electro-coagulation. *Water Environ. Res.* **2020**, *92*, 2140–2154. https://doi.org/10.1002/wer.1387.

18. Igwegbe, C.A.; Onukwuli, O.D.; Ighalo, J.O. Comparative analysis on the electrochemical reduction of colour, COD and turbidity from municipal solid waste leachate using aluminium, iron and hybrid electrodes. Sustain. *Water Resour. Manag.* **2021**, *7*, 39.

19. Bote, M.E.; Desta, W.M. Removal of Turbidity from Domestic Wastewater Using Elec-trocoagulation: Optimization with Response Surface Methodology. *Chem. Afr.* **2022**, *5*, 123–134.

20. Esfandyari, Y.; Saeb, K.; Tavana, A.; Rahnavard, A.; Fahimi, F.G. Effective removal of cefazolin from hospital wastewater by the electrocoagulation process. *Water Sci. Technol.* **2019**, *80*, 2422–2429.

21. Rakhmania; Kamyab, H.; Yuzir, M.A.; Al-Qaim, F.F.; Purba, L.D.A.; Riyadi, F.A. Application of Box-Behnken design to mineralization and color removal of palm oil mill effluent by electrocoagulation process. *Environ. Sci. Pollut. Res. Int.* **2021**, 1–13. https://doi.org/10.1007/s11356-021-16197-z.

22. Ansari, K.; Shrikhande, A.N. Impact of Different Mode of Electrode Connection on Performance of Hybrid Electrocoagulation Unit Treating Greywater. In *Recent Advancements in Civil Engineering*; Springer: Singapore, 2022; Volume 172, pp. 527–538.

23. APHA; AWWA. *Standard Methods for Examination of Water and Wastewater*, 22nd ed.; American Public Health Association: Washington, DC, USA, 2012; 1360p. ISBN 978-087553-013-0.

24. Akula, L.; Oruganti, R.; Bhattacharyya, D.; Kurilla, K.D. Treatment of Marigold Flower Processing Wastewater Using a Sequential Biological-Electrochemical Process. *Appl. Sci. Eng. Prog.* **2021**, *14*, 525–542. https://doi.org/10.14416/j.asep.2021.04.001.

25. Chakawa, S.; Aziz, M. Investigating the Result of Current Density, Temperature, and Electrolyte Concentration on COD: Subtraction of Petroleum Refinery Wastewater Using Response Surface Methodology. *Water* **2021**, *13*, 835.

26. Elazzouzi, M.; Haboubi, K.; El Elyoubi, M.; Kasmi, A. Development of a novel electrocoagulation anode for real urban wastewater treatment: Experimental and modeling study to optimize operative conditions. *Arab. J. Chem.* **2021**, *14*, 102912.

27. Bajpai, M.; Katoch, S.S.; Singh, M. Optimization and economical study of electro-coagulation unit using CCD to treat real graywater and its reuse potential. *Environ. Sci. Pollut. Res.* **2020**, *27*, 42040–42050.

28. Kakoi, B.; Kaluli, J.W.; Ndiba, P.; Thiong, G. Optimization of Maerua Decumbent bio-coagulant in paint industry wastewater treatment with response surface methodology. *J. Clean Prod.* **2017**, *164*, 1124–1134.

29. Naghdali, Z.; Sahebi, S.; Ghanbari, R.; Mousazadeh, M.; Jamali, H.A. Chromium removal and water recycling from electroplating wastewater through direct osmosis: Modeling and optimization by response surface methodology. *Environ. Health Eng. Manag.* **2019**, *6*, 113–120.

30. Aleboyeh, A.; Daneshvar, N.; Kasiri, M.B. Optimization of CI Acid Red 14 azo dye removal by electrocoagulation batch process with response surface methodology. *Process Intensif.* **2008**, *47*, 827–832.

31. Merzouk, B.; Gourich, B.; Sekki, A.; Madani, K.; Chibane, M. Removal turbidity and separation of heavy metals using electrocoagulation-electroflotation technique: A case study. *J. Hazard. Mater.* **2009**, *164*, 215–222.

32. Mansoorian, H.J.; Mahvi, A.H.; Jafari, A.J. Removal of lead and zinc from battery industry wastewater using electrocoagulation process: Influence of direct and alternating current by using iron and stainless steel rod electrodes. *Sep. Purif. Technol.* **2014**, *135*, 165–175.

33. Kuokkanen, V.; Kuokkanen, T.; Rämö, J.; Lassi, U. Electrocoagulation treatment of peat bog drainage water containing humic substances. *Water Res.* **2015**, *79*, 79–87.

34. Eyvaz, M.; Gürbulak, E.; Kara, S.; Yüksel, E. Preventing of cathode passivation/deposition in electrochemical treatment methods—A case study on winery wastewater with electrocoagulation. In *Modern Electrochemical Methods in Nano, Surface and Corrosion Science*; IntechOpen: London, UK, 2014; Volume 1.

35. Jadhav, M.V.; Mahajan, Y.S. Assessment of feasibility of natural coagulants in turbidity removal and modeling of coagulation process. *Desalin. Water Treat.* **2014**, *52*, 5812–5821.

36. Veli, S.; Arslan, A.; Bingöl, D. Application of response surface methodology to electroco-agulation treatment of hospital wastewater. *Clean Soil Air Water* **2016**, *44*, 1516–1522.

37. Kobya, M.; Akyol, A.; Demirbas, E.; Oncel, M.S. *Removal of Arsenic from Drinking Water by Batch and Continuous Electrocoagulation Processes Using Hybrid Al-Fe Plate*; Wiley: New York, NY, USA, 2013.

38. Devikar, S.; Ansari, K.; Waghmare, C.; Bhokar, M. Domestic Greywater Treatment by Hybrid Electrocoagulation and Filtration Method in Continuous Mode. In *Smart Technologies for Energy*; Springer: Berlin/Heidelberg, Germany, 2022; Volume 1, pp. 211–218.

39. Kobya, M.; Gengec, E.; Demirbas, E. Operating parameters and costs assessments of a real dye house wastewater effluent treated by a continuous electrocoagulation process. *Chem. Eng. Proc.* **2016**, *101*, 87–100.

40. Kuntal, A. et al. Characterization of greywater in an Indian middle-class household and investigation of physicochemical 612 treatment using electrocoagulation. *Sep. Purif. Technol.* **2014**, *130*, 160–166.

41. Ansari, K. et al. Experimental Evaluation of Industrial Mushroom Waste Substrate Using Hybrid Mechanism of Vermicomposting and Effective Microorganisms. *Materials* **2022**, *15*, 2963.

42. Jallouli, S.; Chouchene, K.; Ben Hmida, M.; Ksibi, M. Application of Sequential Combination of ElectroCoagulation/Electro-638 Oxidation and Adsorption for the Treatment of Hemodialysis Wastewater for Possible Reuse. *Sustainability* **2022**, *14*, 9597. https://doi.org/10.3390/ su14159597.

43. Villaseñor-Basulto, D.L.; Picos-Benítez, A.; Pacheco-Alvarez, M.; Pérez, T.; Bandala, E.R.; Peralta-Hernández, J.M. Tannery wastewater treatment using combined electrocoagulation and electro-Fenton processes. *J. Environ. Chem. Eng.* **2022**, *10*, 107290.

44. Gupta, T.; Ansari, K.; Lataye, D.; Kadu, M.; Khan, M.; Mubarak, N.; Garg, R.; Karri, R. Adsorption of Indigo Carmine Dye by Acacia nilotica sawdust activated carbon in fixed bed column. *Sci. Rep.* **2022**, *12*, 15522.

45. Rajaniemi, K.; Tuomikoski, S.; Lassi, U. Electrocoagulation Sludge Valorization—A Review. *Resources* **2021**, *10*, 127. https://doi.org/10.3390/resources10120127.

46. Aouni, A.; Fersi, C.; Ali, M.; Dhahbi, M. Treatment of textile wastewater by a hybrid electrocoagulation/nanofiltration process. *J. Hazard. Mater.* **2009**, *168*, 868–974.

Properties and Applications of Geopolymer Composites: A Review Study of Mechanical and Microstructural Properties

Ahmed Saeed [1,*], Hadee Mohammed Najm [2,*], Amer Hassan [2], Mohanad Muayad Sabri Sabri [3], Shaker Qaidi [4,5], Nuha S. Mashaan [6] and Khalid Ansari [7]

[1] Department of Civil Engineering, Southeast University, Nanjing 211189, China
[2] Department of Civil Engineering, Zakir Husain Engineering College, Aligarh Muslim University, Aligarh 202002, India
[3] Peter the Great St. Petersburg Polytechnic University, 195251 St. Petersburg, Russia
[4] Department of Civil Engineering, College of Engineering, University of Duhok, Duhok 42001, Iraq
[5] Department of Civil Engineering, College of Engineering, Nawroz University, Duhok 42001, Iraq
[6] Faculty of Science and Engineering, School of Civil and Mechanical Engineering, Curtin University, Bentley, WA 6102, Australia
[7] Department of Civil Engineering, Yashwantrao Chavan College of Engineering, Nagpur 441110, India
* Correspondence: alanessy2015@gmail.com (A.S.); gk4071@myamu.ac.in (H.M.N.)

Abstract: Portland cement (PC) is considered the most energy-intensive building material and contributes to around 10% of global warming. It exacerbates global warming and climate change, which have a harmful environmental impact. Efforts are being made to produce sustainable and green concrete as an alternative to PC concrete. As a result, developing a more sustainable strategy and eco-friendly materials to replace ordinary concrete has become critical. Many studies on geopolymer concrete, which has equal or even superior durability and strength compared to traditional concrete, have been conducted for this purpose by many researchers. Geopolymer concrete (GPC) has been developed as a possible new construction material for replacing conventional concrete, offering a clean technological choice for long-term growth. Over the last few decades, geopolymer concrete has been investigated as a feasible green construction material that can reduce CO_2 emissions because it uses industrial wastes as raw materials. GPC has proven effective for structural applications due to its workability and analogical strength compared to standard cement concrete. This review article discusses the engineering properties and microstructure of GPC and shows its merits in construction applications with some guidelines and suggestions recommended for both the academic community and the industrial sector. This literature review also demonstrates that the mechanical properties of GPC are comparable and even sometimes better than those of PC concrete. Moreover, the microstructure of GPC is significantly different from that of PC concrete microstructure and can be affected by many factors.

Keywords: geopolymer composites; clean technology; flexural strength; compressive strength

1. Introduction

Concrete is a widely utilised material in the building industry worldwide [1]; because of its low cost, durability, strength, and flexibility to be produced in any shape or size, it is considered the most extensively material used in building [2]. PC is one of the most energy-intensive building materials used in reinforced concrete applications, with current output estimated to be 2.60 billion tonnes (BT) per year worldwide and increasing by 5% annually. PC is made using the "two grinding and one calcining" technology, which uses limestone, clay, and other raw materials as inputs, with a calcination temperature of 1450 °C. Approximately one billion tonnes (BT) of limestone, 180 MT of clay, 50 MT of iron powder, 100 MT of coal, and 60 B KWh of energy are used annually by the cement industry in China [3]. A lot of carbon dioxide is released into the air during cement manufacturing

°C. Approximately one billion tonnes (BT) of limestone, 180 MT of clay, 50 MT of iron powder, 100 MT of coal, and 60 B KWh of energy are used annually by the cement industry in China [3]. A lot of carbon dioxide is released into the air during cement manufacturing (one tonne of cement production emits approximately one ton of CO_2). Extremely high carbon dioxide levels are released into the air during the cement manufacturing process (roughly one tonne of cement production releases one tonne of CO_2). This causes it to account for about 7% of all manufactured CO_2 emissions. Table 1 [4] summarises the amount of carbon dioxide released during the construction of various concrete elements.

Table 1. CO_2 emissions from different concrete volumes [4].

Strength (MPa)	Structural Member	Amount (m³)	Emission Factor (tCO₂₋e/m³)	Emissions (tCO₂⁻e)
15	Blinding	589	0.20	119
32	Footings	489	0.24	119
32	Slabs	1984	0.27	533
40	In situ column and wall	253	0.27	63
40	Precast walls	1067	0.33	351–1185

Additionally, Figure 1 presents the global trends in growing cement production. Limestone calcining and using a rotary kiln powered by fossil fuels to provide high heat contribute to substantial CO_2 emissions; this is a significant concern when utilising the PC. One of the most promising options is using geopolymers as a partial or complete substitute for cement [5,6].

Figure 1. Worldwide cement production in Metric Tonnes, 2010–2020 [7].

In 1979, Davidovits introduced the term geopolymer to refer to a group of mineral binders similar to zeolites within amorphous microstructure and chemical composition [8]. This material was previously used in the Roman Empire (Figure 2). An aluminosilicate precursor (Figure 3), made up of amorphous silica and alumina, and an activator (a dissolving agent) make up the geopolymers. The term "geopolymerisation" describes the transformation of zeolitic-like materials into an 3D aluminosilicate gel [9–12]. Generated binder performance is optimised through an alkaline polycondensation process involving silicates and aluminates [13]. It is common practice to use caustic alkalis of the MOH type or silicate of the R$_2$O(n)SiO$_2$-type in the synthesis of geopolymers. Such M OH type (NaOH), sodium carbonate (Na$_2$CO$_3$), potassium hydroxide (KOH), or sodium sulphate (Na$_2$SO$_4$) are common that contain the alkaline (KOH), or sodium by MOH [14].

In addition to the conventional activators, silica fume and rice husk ash have also been used as activator components in the synthesis of geopolymers [15].

(Na$_2$SO$_4$) are common activators that contain the alkali metal (M) indicated by MOH [14]. In addition to the conventional activators, silica fume and rice husk ash have also been used as activator components in the synthesis of geopolymers [15].

Figure 2. Manufacturing Process of GPCs in the Roman Kingdom [16].
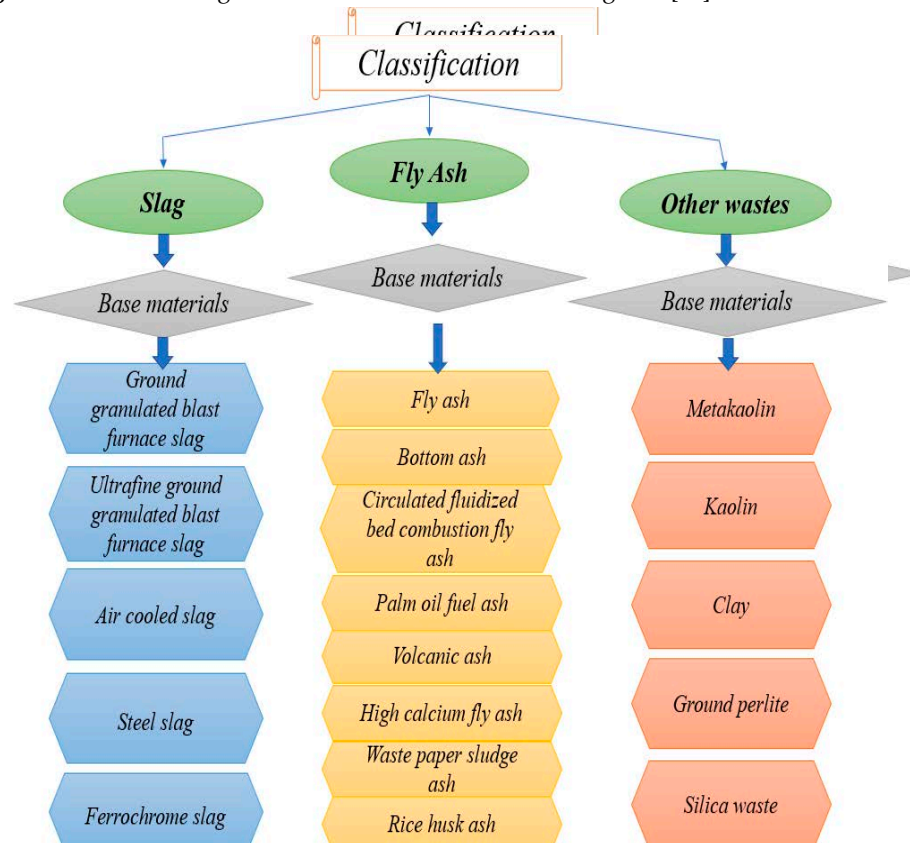
Figure 3. Raw materials used in geopolymer production.

Figure 3. Raw materials used in geopolymer production.

The environmental benefits of geopolymer concrete have led many to call it the "next generation" of concrete. It provides a novel approach to reducing CO₂ emissions in the construction industry by abolishing PC as a binder in concrete production [1,17,18]. Using geopolymer concrete not only has positive effects on the environment and human health but also provides a method for safely disposing of potentially hazardous materials [19]. In addition, research shows that the production of geopolymer concrete can reduce CO₂ emissions by about 22–72% compared to that of PC concrete at a similar cost [20]. In addition, tests [21–24] have confirmed that geopolymer concrete has exceptional mechanical properties. Geopolymer concrete (shown in Figure 4) is a sustainable building material depicted in a simplified diagram:
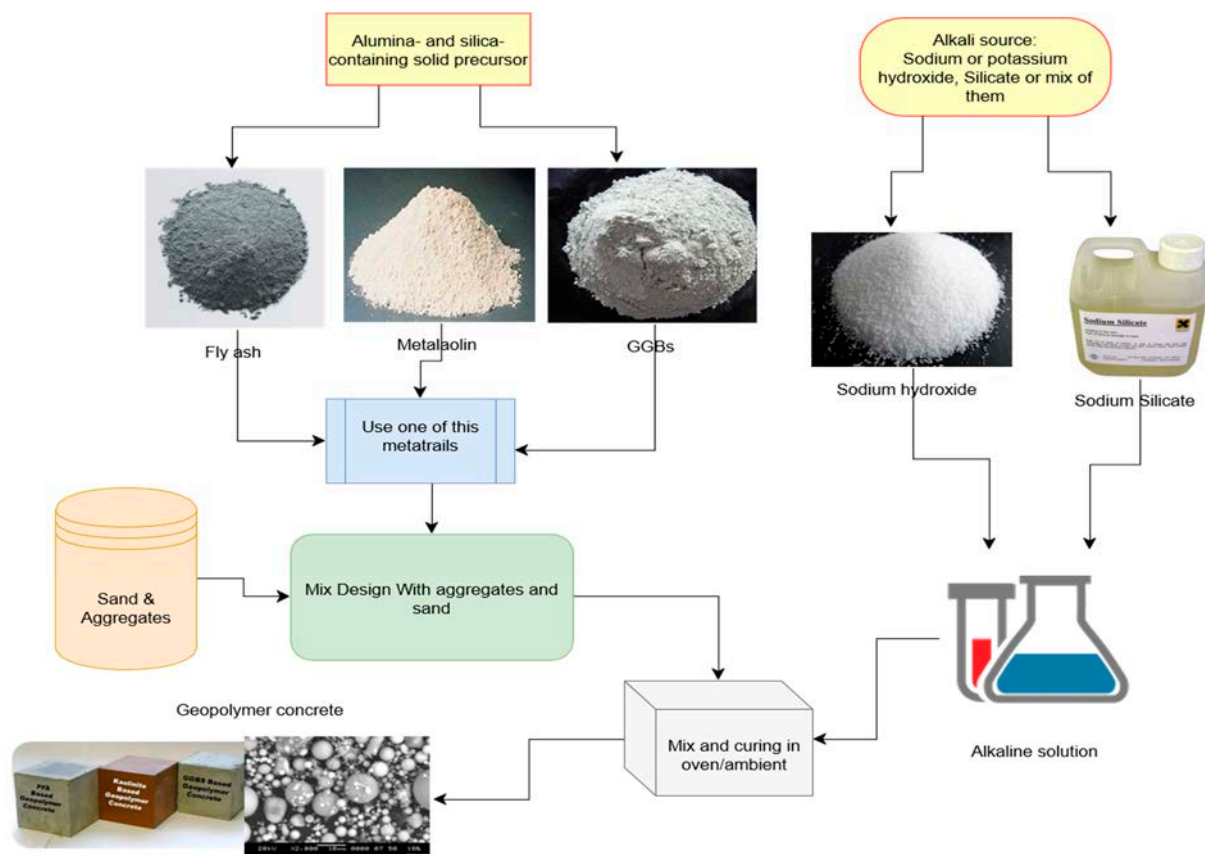
Figure 4. Geopolymer concrete production [25].

It was observed in the literature that there are many existing review studies to analysing the behaviour of geopolymer concrete [1–15,17,26–54]. However, previous review publications on geopolymer composite mortar/concrete highlighted mechanical or microstructural properties in the fresh and hardened states. However, they did not provide comprehensive information on this issue in a single paper. In addition, new studies that are relevant to the topic but were not discussed in earlier reviews were published. Therefore, this study provides a comprehensive overview of the most up-to-date studies on geopolymer concrete's mechanical and microstructural performance. It includes a review, analysis, and discussion of the literature on geopolymer concrete in its fresh and hardened states to aid in the education of researchers and the building industry.

1.1. Study Significance

The published literature papers were evaluated regarding the production of GPC and its mechanical behaviour. This paper discusses the mixed design, mechanical

Study Significance

The published literature papers were evaluated regarding the production of GPC and its mechanical behaviour. This paper discusses the mixed design, mechanical characteristics, and durability of GPC. Using the GPC as an alternative construction material is essential for environmental purposes. Before it can be used in construction, much research needs to be conducted on how structures behave with huge structural elements.

Therefore, this review article aims to provide inclusive information on GPC production, its economic benefits, durability, and environmental influences; the basic process for GPC production; and the factors affecting its mechanical properties.

2. Geopolymer Mortar (GPM)

Classic cement mortar is often utilised as a standard binding and repairing material in various engineering structures. Many scholars have addressed GPM's viability and potential applications as a suitable replacement for regular cement mortar [35]. Sathon-saowaphak was the first to investigate geopolymer mortar and studied the properties of bottom ash fineness, ash/liquid alkali ratio, $NaOH/Na_2SiO_3$ ratio, NaOH dosage, water to ash ratio, and superplasticiser on the behaviour in terms of workability and compressive strength of GPM [36]. Geopolymer mortar has a mechanical strength of 24–58 MPa, and adding NaOH solution improves the workability performance of GPM without reducing strength. According to the results of Detphan and Chindaprasirt [24], who prepared GPC using rice husk ash and fly ash and activated by NaOH and $NaSiO_3$ solution as a liquid for the mix, they found that the maximum strength of GPM is acquired by employing a Na_2SiO_3-to-NaOH mass ratio of four. Moreover, more discussion about geopolymer mortar properties is reported in the following sections.

2.1. Fresh Geopolymer Mortar Properties

2.1.1. Fresh Geopolymer Mortar Workability

The workability of fresh GPM is crucial in determining the hardened GPM quality. The concentration ratio of NaOH determines the geopolymer mortar's workability and the Na_2SiO_3 to NaOH. The flowability of modern mortars is typically controlled with the addition of water, which does not compromise the mortar's strength [37]. Flow, which a flow test may evaluate, is frequently used to determine whether mortar is workable. The term "flow" is widely used to describe how well new mortars work, and it is given as a percentage of the starting base diameter as per the ASTM C1437 standard [38]. Some testing instruments include a flow mould, measuring tape, tamper, flow table, and trowel. The flow test determines a material's consistency, filling ability, and workability. Sathon-saowaphak [36] studied the effect of bottom ash (BA) fineness on mortar workability and suggested that ground bottom ash might be employed as a raw material for the production of geopolymer. When the fineness of BA was increased, the workability of the mortar was improved. (Figure 5), as well as the impact of various liquid ratios of alkaline/ash. The workability of the mixes improved as the liquid alkaline/ash ratio was raised, as seen in Figure 6.

Bhowmick and Ghosh [39] determine the impact of fly ash/sand ratios and the influence of SiO_2/Na_2O ratio inactivators on GPM workability. They found that the flow value percentage increases with the fly ash/sand ratio, and the fresh geopolymer mortar's flowability increases as the SiO_2/Na_2O ratio in the activator increases, as shown in Figures 7 and 8.

(% retained on sieve No.325)
Figure 5. The flow of mortar with various BA fineness [36].

Figure 5. The flow of mortar with various BA fineness [36].

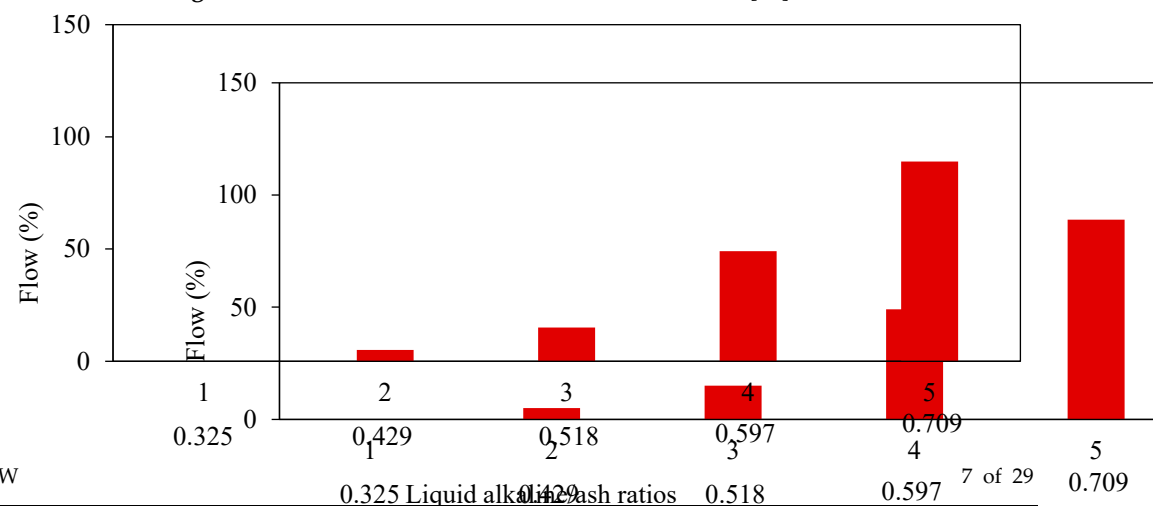**Figure 5.** The flow of mortar with various BA fineness [36].

Figure 6. The flow of mortar with various liquid alkaline-to-ash ratios [36].

Figure 6. The flow of mortar with various liquid alkaline-to-ash ratios [36].
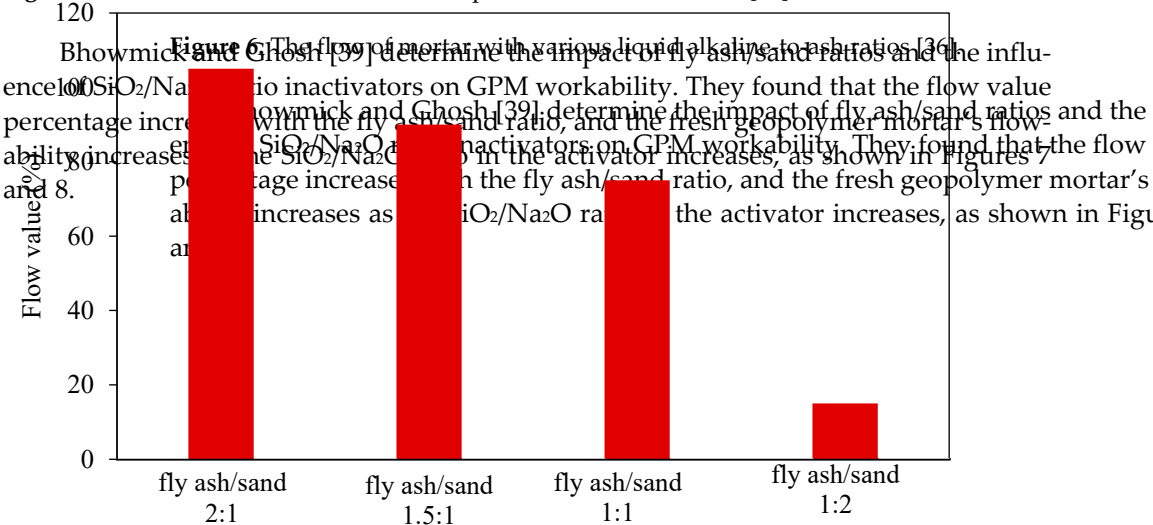
Figure 6. The flow of mortar with various liquid alkaline-to-ash ratios [36].

Bhowmick and Ghosh [39] determine the impact of fly ash/sand ratios and the influence of SiO_2/Na_2O ratio inactivators on GPM workability. They found that the flow value percentage increases with the fly ash/sand ratio, and the fresh geopolymer mortar's flowability increases as the SiO_2/Na_2O ratio in the activator increases, as shown in Figures 7 and 8.

Figure 7. Flow values vs. fly ash/sand ratio [39].

fly ash/sand 2:1 | fly ash/sand 1.5:1 | fly ash/sand 1:1 | fly ash/sand 1:2
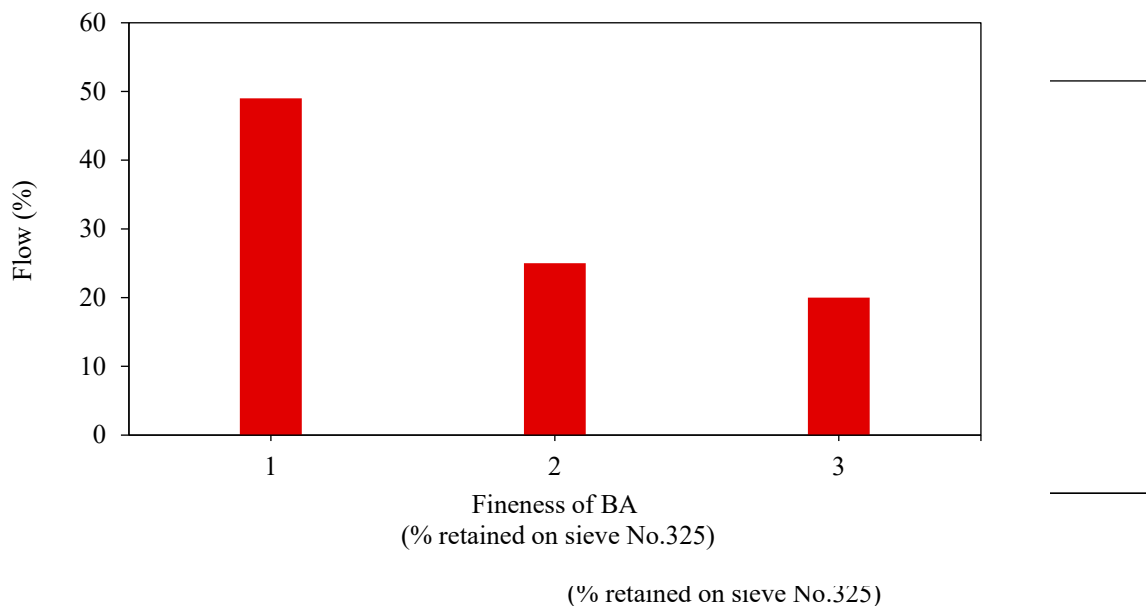
Figure 7. Flow value vs. fly ash/sand ratio [39].

Figure 8. Flow value vs. SiO$_2$/Na$_2$O ratio in activator [39].

2.1.2. Fresh Geopolymer Mortar Setting Time

Fresh mortar setting time is critical for transporting, casting, and compacting the mortar within the time restriction. The Vicat needle device can be utilised to test the setting times per the BS EN 480-2 and ASTM C 807-13 standards [40,41]. The first and final setting times are calculated using the needle's depth as a reference point, which ranges between 2.5 and 4 mm [41,42]. In order to determine the influence of time after mixing on dielectric properties before heat curing, cast specimens were kept in a laboratory at 28 to 29 °C while being protected from moisture loss by a vinyl sheet geopolymer. The dielectric characteristics of GPM were then measured after being mixed for 24 h [42]. Jumrat et al. [42] investigated the setting time of the specimen's mixture with the addition of water to obtain the standard flow. The results demonstrate that the weight proportions of NS/NH and FA/AS do not affect the initial and final setup periods. The setting time reduces as NS/NH and FA/AS weight ratios increase, as shown in Figure 9 [24]. By increasing the molarity of NaOH, the initial and final setting times of GPM can be greatly decreased [43].

The setting time reduction in GPM has been attributed to the increased use of PCs. As seen in Figure 10, increased NaOH concentrations caused geopolymer mortars to take longer to set [44].

Figure 9. GPM setting times at different mixture proportions [42].

Figure 10. Effect of NaOH molarity on GPM setting times [43].

2.2. Geopolymer Mortar Mechanical Properties

2.2.1. Geopolymer Mortar Compressive Strength

Numerous types of source materials are employed as base materials for producing geopolymers. The raw materials used and the proportioning factors impact the strength of GPM. A. Effanimanesh et al. [45] tried to compare the compressive strength of GPM at the ages of 7 and 28 days, using two different mixed materials (PC mortar, slag, and zeolite). The findings revealed that the compressive strength of GPM increased by up to 48% in the first 7 days compared to the cement mortar after 28 days.

Yusuf et al. [46] studied the effect of blending silica-rich (MK) and palm oil fuel ash (POFA) on the strength of GPM. They indicated that the Weibull distribution is suitable for analysing the blended GPM. Low calcium FA, GGBFS, and POFA can be combined to manufacture GPM under the standard condition that their percentage should be suitable.

Ismail et al. [47] studied the compressive strengths of GPM with sisal fibre (SF), coconut fibre (CF), and glass fibre (GF).

Ismail et al. [47] investigated the early strength characteristics of a GPM made from palm oil fuel and ash–metakaolin, with various degrees of NaOH and Na$_2$SiO$_3$ medium showed increasing PC replacement levels and NaOH concentrations as well as increasing mortar compressive strengths.

Phoo et al. [44], who studied the compressive strength of GPM with different NaOH dosages (6, 10, and 14 mol/dm³), found that high calcium FA GPM comprised of PC type I and ash–metakaolin with various degrees of NaOH and Na$_2$SiO$_3$ medium.

A. De Rossi [48] discovered that the strength of geopolymer mortars was affected by the use of construction and demolition waste (CDW) fine aggregates. GPM was formed by combining biomass FA waste and MK as a binder, sodium hydroxide as an activator, alkali sodium silicate solution, and CDW as fine aggregates. Except for the mortar created with particles of 1.0–2.0 mm, when the maximum strength was acquired with sand, CDW was used as aggregate. For CDW–geopolymer mortars, the values were 21 MPa (1.0–2.0 mm), 34 MPa (0.5–1.0 mm), and 40 MPa (0.5–2.0 mm). The mixed fraction had the highest strength values due to the maximum packing density. Table 2 illustrates the effect of various additives on the behaviour of geopolymer mortar.

Table 2. Effect of different additives on geopolymer concrete compressive strength.

Ref.	Additives	Remarks
Erfanimanesh et al. [45]	PC mortar, slag, and zeolite	The compressive strength of GPM increased by up to 48% in the first seven days compared to the cement mortar after 28 days.
Tanakorn Phoo [44]	NaOH dosages	A high NaOH dosage increases mortar compressive strengths.
Mohammad Ismail et al. [47]	palm oil fuel and ash metakaolin	The high volume of palm oil fuel and ash metakaolin replacement has been found to reduce compressive strength at an early curing age.
Yusuf et al. [46]	blending silica-rich MK and palm oil fuel ash	The Weibull distribution is suitable for analysing the blended GPM.
Ismail et al. [47]	sisal fibre (SF), coconut fibre (CF), and glass fibre (GF)	The compressive strengths of GPM reinforced with SF, CF and GF both dropped a lot more than those reinforced with SF.
De Rossi [48]	construction and demolition waste (CDW)	The mixed fraction had the highest strength values due to the maximum packing density.

2.2.2. Geopolymer Mortar Flexural Strength

In cement mortars, compressive and flexural strength are tightly linked. However, due to the incredible fragility of the geopolymer and its firm adherence to the aggregate particles, geopolymer mortars have high flexural strength but poor compressive strength [49]. With the addition of sand concentration to 77%, the flexural strength of GPM improves and reaches its maximal value, which slowly decreases because there is an insufficient binder to hold the grains together [20]. Thus, these findings indicate the formation of coarse pores and increased porosity. The alkali activator solution type and curing temperature impact GPM's flexural strength considerably [50]. According to the results of Huseien et al. [50], the GPM with a curing temperature of 28 °C has higher flexural strength than mortars with curing temperatures of 60 °C and 90 °C. Additionally, the activator solution of sodium aluminosilicate hydrate has lower flexural strength than the sodium hydroxide solution [51]. Li et al. [52] studied the influence of curing conditions on the strength of Class-C FA geopolymer at W/F0.35, where he concluded "For Class-C FA GPM with a water/ash ratio of 0.35 (CF35-C), the findings showed that before the age of 7 d, the non-standard curing shows much higher flexural strength than the standard curing. After steam curing for 24 h and 6 h, flexural strength increased sharply at the age of 1 d; then, strength developed slowly". Atis et al. [53] studied the flexural strength of GPM with various sodium concentrations and cured it for 24, 48, and 72 h at temperatures ranging from 45 °C to 116 °C. Atis et al. [53] showed the GPM containing 13% sodium after 24 h of heat curing at 116 °C had the maximum flexural strength, while the GPM incorporating 4.0% sodium after 24 h of heat curing at 106°C had the lowest flexural strength. Al-Majidi et al. [54] investigated the effect of Ground granulated blast-furnace slag (GGBFS) content on the ultimate flexural strength of GPM specimens cured at ambient temperature and variations in flexural strength with increasing GGBFS volume at curing ages of 7, 14, and 28 days; the results showed that at all ages, increasing the GGBFS content increased the ultimate flexural strength of GPM significantly. At 7 days, the flexural strength was improved by increasing the GGBFS content from 10 to 20, 30, and 40%, respectively. Flexural strength increased with longer curing durations, with flexural strength values for 10S, 20S, 30S, and 40S combinations rising at 14 and 28 days, respectively, compared to flexural strength values at 7 d. This is seen in Figure 11.

and 28 days; the results showed that at all ages, increasing the GGBFS content increased the ultimate flexural strength of GPM significantly. At 7 days, the flexural strength was improved by increasing the GGBFS content from 10 to 20, 30, and 40%, respectively. Flexural strength increased with longer curing durations, with flexural strength values for 10S, 20S, 30S, and 40S combinations rising at 14 and 28 days, respectively, compared to flexural strength values at 7 d. This is seen in Figure 11.
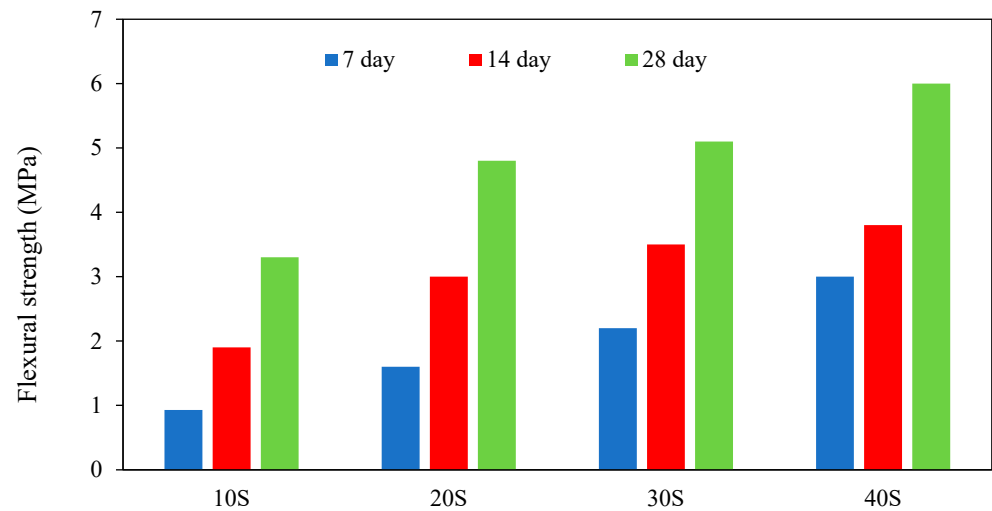
Figure 11. Influence of GGBFS volume on the ultimate flexural strength of GPM [54].

According to Erfanimanesh et al. [45], flexural strength comparison between GPM and PC mortar (Na_2CO_3 concentration was about 10% by weight of powder mixes (zeolite and slag), and 100% Fine Aggregate). GPM's flexural strength was tested using two distinct mix designs that used slag and zeolite as base ingredients. As shown in Figure 12, the geopolymer and the PC mortars had nearly comparable flexural strengths.

0% slag 0% zeolite 100% OPC
100% slag 0% zeolite 10% Na_2CO_3
75% slag 25% zeolite 10% Na_2CO_3
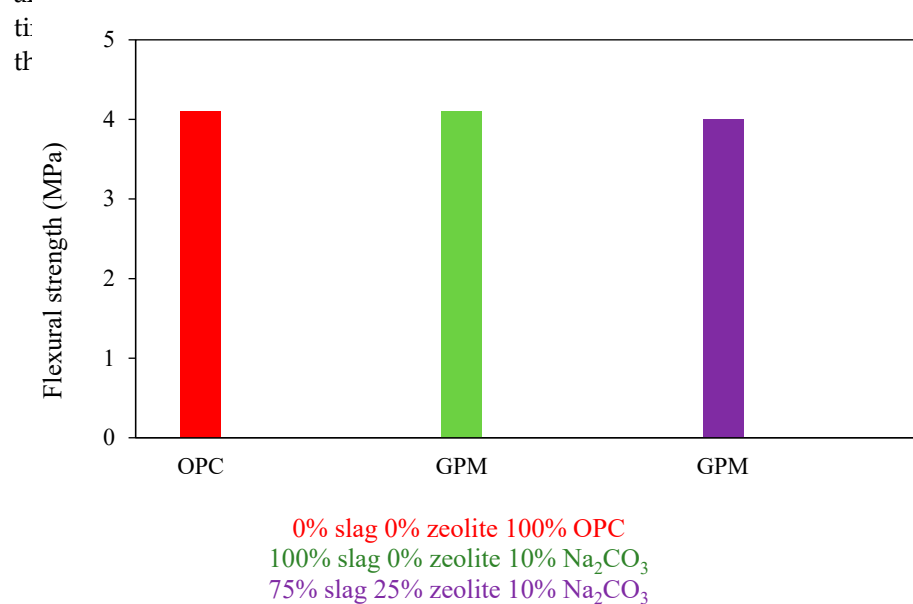
Figure 12. Flexural strength comparison between GPM and PCM.

Wongsa et al. [55] examined the properties of GPM comprising natural fibres and high levels of calcium fly ash. The primary materials in this investigation included coir or coconut fibre (CF), glass fibre (GF), and sisal fibre (SF). SF and CF were acquired from a plant farm in the Thai provinces of Prachuap Khiri Khan and Chon Buri, respectively. According to the results, utilising fibres enhanced GPM's flexural strength. In addition, the flexural strength of GPM tended to increase as the fibre content increased. Even though flexural strength increased with fibre content, the mixtures with more than 1% volume fraction had poor workability and were challenging to compact and cast. The flexural strength of GPM reinforced with natural fibre (CF and SF) varied from 5.3 to 6.6 MPa compared to CGM (3.2 MPa) and GPM reinforced with synthetic fibre (GF) (3.1–3.7 MPa), as shown in Figure 13.
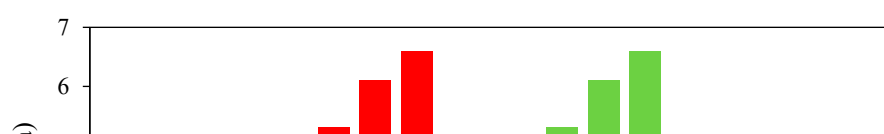
the flexural strength of GPM tended to increase as the fibre content increased. Even though flexural strengths increased with fibre content, the mixtures with more than 1% volume fraction had poor workability and were challenging to compact and cast. The flexural strength of GPM reinforced with natural fibre (CF and SF) varied from 5.3 to 6.6 MPa compared to CGM (3.2 MPa) and GPM reinforced with synthetic fibre (GF) (3.1–3.7 MPa) as shown in Figure 13.
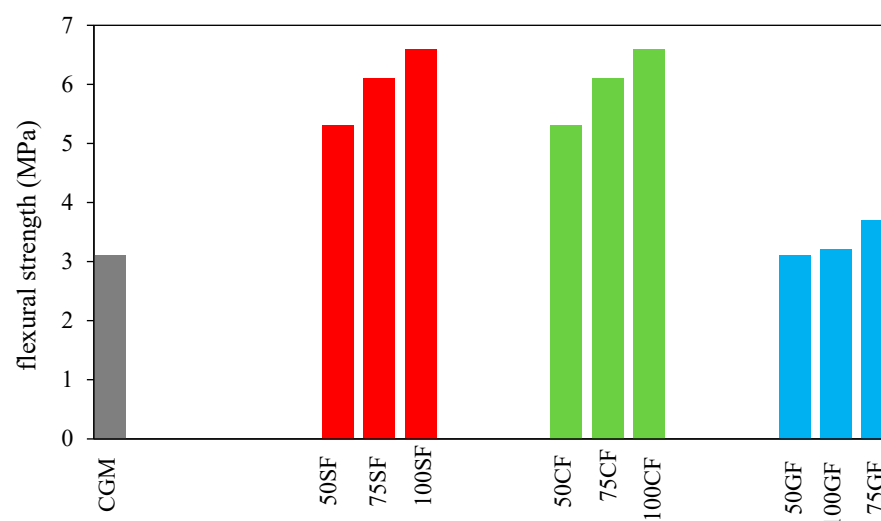
Figure 13. Flexural strength of GPM [55].

3. Geopolymer Concrete (GPC)

GPC is a cost-effective alternative that can be applied in place of standard cement. Thus, using GPC instead of PC cuts CO₂ emissions dramatically [25]. FA, MK, and GGBFS are examples of GPC sources, including Al and Si as rich materials [50]. GPC consists of three components: GGBFS, or MK, a source of aluminosilicates, such as FA; coarse and fine aggregate; and an activating solution consisting of sodium hydroxide and sodium silicate [20]. GGBS, FA, and MK, among other supplemental cementitious materials, are utilised as binders rather than cement. Using GGBS in combination with PC, FA, and palm oil fuel ash results in a high-strength GPC [16]. FA is the substance most frequently employed in the creation of GPCs as a single source of material [24]. Geopolymer concrete emits 20% less CO_2 than PC when (5–15%) Portland cement is substituted. This is because geopolymer concrete may attain an early compressive strength of 66 without needing external heat [20]. In order to create geopolymer paste, an inorganic polymeric binder, the source material must be combined with the activator, a solution of NaOH and Na_2SiO_3. Despite minimising the cost of GPC, no research on the availability and cost of GPC raw materials has been conducted globally. A global review of raw materials availability has been conducted, focusing on China and the U.S. The demand and cost of each raw material, including FA, SC, MK, NaOH, Na_2SiO_3, and silica fume, were analysed for China, the United States, and other major markets for which data are available. This study is essential to see if GPC can be a viable commercial alternative to PC concrete. Raw material supply is a pivotal impediment to widespread GPC adoption [23], so while the cost of each material is listed and briefly addressed, a more in-depth cost study was not conducted.

3.1. Fresh Properties of Geopolymer Concrete

3.1.1. Geopolymer Concrete Workability

Umniati et al. [29] highlighted that the workable flow of the GPC increases as the fly ash/sand ratio increases, and the sodium silicate solution's cohesion and slump ability improve when the SiO_2/Na_2O ratio rises [14]. Saranya et al. [23] also used the IS-1199:1959 slump cone test to find out how the different workable samples of GPC were. Due to its dense flow character, the slump value of GPC specimens was 72% higher than that of cement concrete. Steel fibres limit workability because they block the flow of concrete. Mehta et al. [30] studied the workability of GPP, and GPC was investigated at different molarities of NaOH and varied SiO_2/Al_2O_3 ratios by mass. Because the particles on the alkaline activator mixture grow as the dosage of NaOH increases, it is also noted that the dosage of NaOH considerably impacts the workability of GPC.

Hassan et al. [31] evaluated the workability of FA-based GPC using the slump cone test. Coarse and fine aggregate, alkaline liquid, FA, and water are used in GPC. Sodium silicate and sodium hydroxide are combined to make the alkaline liquid. As shown in Figure 14, the findings of the experiments showed that adding GGBS makes GPC less workable.

Sarker et al. [16] examined the feasibility of fly ash-based GPC for curing in ambient conditions. The experimental results showed that the slump and flow parameters are reduced in FA-based GPC when the slag blend increases. The behaviour becomes more visible as the percentage of the blend increases. As shown in Figure 15, S00, S10, S20, and

S30 represent combinations with slag contents of 0%, 10%, 20%, and 30%, respectively.

The steel and iron industries produce ground granulated blast furnace slag (GGBS).

According to Patilet et al. [57], using GGBS in concrete increases the material's workability, among other benefits. Geopolymer concrete made from ground granulated blast furnace
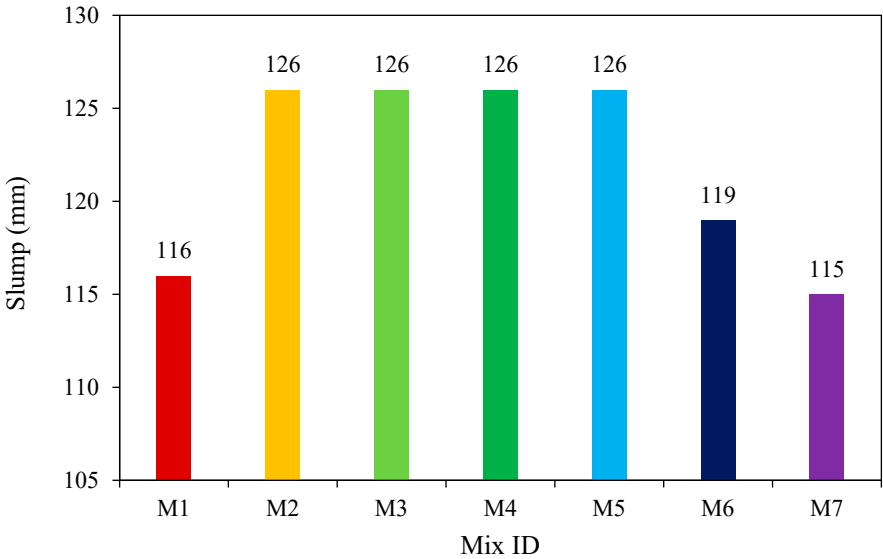
Figure 14. Variation in slump for different mixes (mm) [31].
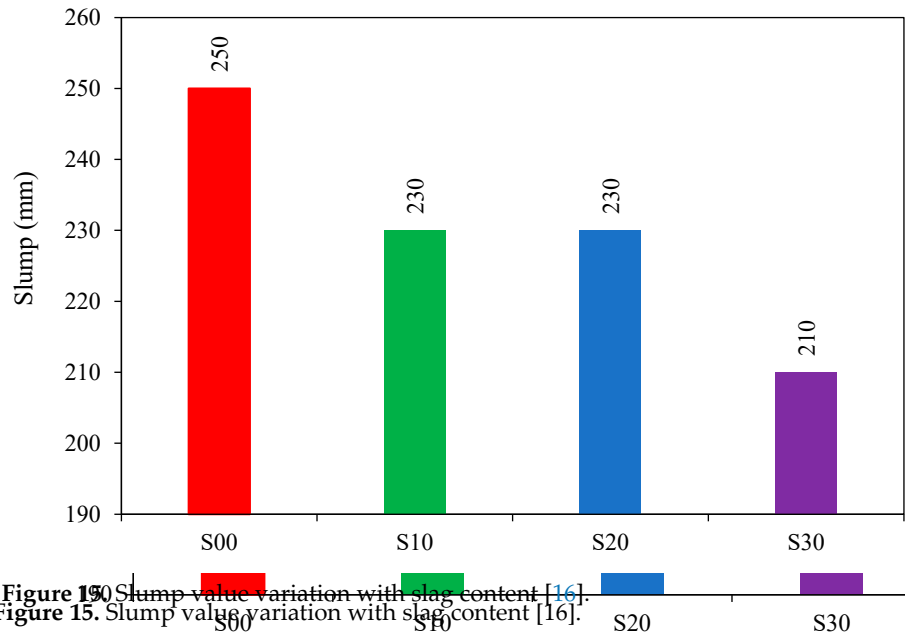
Figure 15. Slump value variation with slag content [16].

3.1.2. Geopolymer Concrete Setting Time

Setting time refers to the time that concrete can be cast, compacted, and transported [14]. As per ASTM C807 and the British Standards Institution (2009), the Vicat needle device determines the concrete setting time. Antoni et al. [32] observed that NaOH concentration influences the curing time of geopolymer concrete. They noticed that reducing the molarity of NaOH could effectively delay the setting of GPC. Because of the slower reac-

Fumed silica is a byproduct of the silicon and ferrosilicon alloy industries. Khater [59] states that due to its spherical shape, adding fumed silica in concrete increases its density and workability. With the activation of sodium silicate, fumed silica can form dihydrogen during synthesis and can be involved in modifying the chemistry and porosity of specimens.

3.1.2. Geopolymer Concrete Setting Time

Setting time refers to the time that concrete can be cast, compacted, and transported [14]. As per ASTM C807 and the British Standards Institution (2009), the Vicat needle device determines the concrete setting time. Antoni et al. [32] observed that NaOH concentration influences the curing time of geopolymer concrete. They noticed that reducing the molarity of NaOH could effectively delay the setting of GPC. Because of the slower reaction rate at a low ambient temperature of 20–24 °C, FA-based geopolymer paste takes more than 24 h to set. However, slag blending considerably reduces both the initial and final setting times.

When 10% slag is added to the binder, the initial setting time is lowered to 290 min, further reduced to 95 min, and 40 min when the slag concentration is increased to 20 and 30%. The discrepancy between the beginning and final setting times are reduced by increasing the slag concentration in GPP. As shown in Figure 16, the higher the proportion of slag, the faster the setting. With the rise in slag content, Figure 16 depicts the change in initial and final setting times and the difference in the period between the two. S00, S10, S20, and S30 indicate the addition of 0, 10, 20, and 30% GGBFS blends, respectively [16].

Brew et al. [60] produced quick-setting geopolymer concrete with fumed silica at ambient curing conditions. Waste management can be effectively performed by utilising fumed silica in GPC [61]. The addition of 20–30% fumed silica to geopolymer concrete can improve its setting time [62].
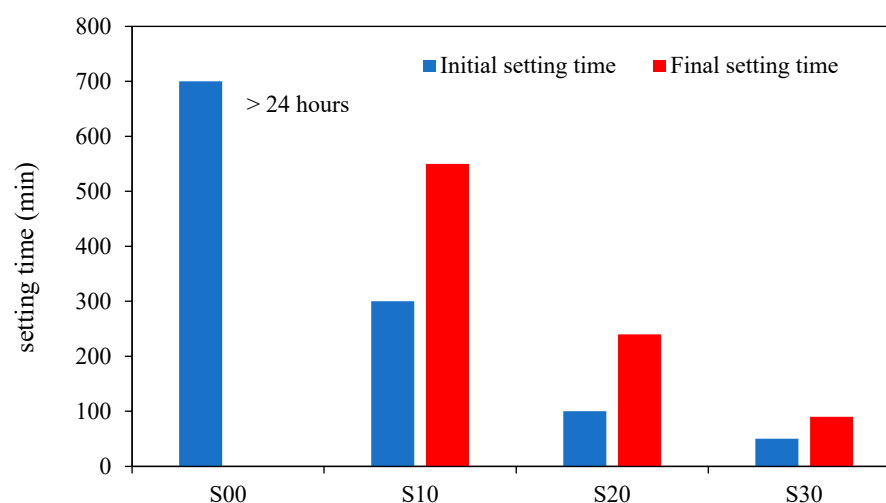
Figure 16. Slag variation during the initial and final setting times [16].

3.2. Mechanical Properties of Hardened Geopolymer Concrete

3.2.1. Compressive Strength

Compressive strength has usually expressed the behaviour of concrete in compression, and the initial elastic modulus represents the strength development with the shape and age of the stress–strain relationship. Lakshmi and Nagan [33] reported that the wet-mixing time, curing time, curing temperature, and particle size influence geopolymer concrete's compressive strength (ASTM C 39). Memon et al. [54] found that geopolymer concrete's compressive strength decreases dramatically when the added water content exceeds 12% of FA mass. After 1 d, heat-cured LCFA-based GPC reaches its maximal compressive strength with no additional increases in compressive strength over time [14]. When cured at 80–90 °C, about 91% of the final strength is formed in just a few hours. Nevertheless, as in PC concrete, GPC cured in an ambient environment setting becomes stronger over time.

Nevertheless, as in PC concrete, GPC cured in an ambient environment setting becomes stronger over time. All curing regimens (ambient temperature) achieve similar long-term strength findings. The amount of time needed to reach the mixture's maximal compressive strength depends on the curing temperature [14,63]. When employing GPC in the

All curing regimens (ambient temperature) achieve similar long-term strength findings. The amount of time needed to reach the mixture's maximal compressive strength depends on the curing temperature [14,63]. When employing GPC in the construction of concrete applications subjected to harsh environments, highly high compressive strengths and enhanced durability can be attained [64]. Similar to the relationship between the w/c ratio and the strength of PC concrete, it was found that the ratio of geopolymer particles to water was inversely correlated with the concrete's compressive strength. The entire mass of geopolymer solids [25] is comprised of binder, sodium hydroxide solids, and sodium silicate solids [27]. Ng et al. [65] provided that the ideal mass ratio for compressive strength in a geopolymer combination of fly ash and slag is 35:65. However, this ratio relies on the reactivity of the particular FA and GGBFS utilised. Bhowmick et al. [49] investigated the impact of FA/sand ratio, SiO_2/Na_2O ratio, and water/FA ratio on compressive strength, and according to the findings, the $Na_2SiO_3/NaOH$ ratio has an entirely different impact on GPC compressive strength than the SiO_2/Na_2O ratio. When the $Na_2SiO_3/NaOH$ molar ratio is set at 2.5, there is no significant increase in the compressive strength of GPC. The compressive strength of a structure significantly impacts its stability and safety. The curing conditions and the raw materials impact the compressive strength of FA/GGBS-based geopolymer concrete [66]. Erfanimanesh et al. [45] reported that the zeolite/slag ratio influenced the compressive strength of GPC, as shown in Figure 17. After 7 and 28 days, the GPCs had 30% and 25% higher compressive strengths than the PC concrete. As a result, the mechanical characteristics of the GPC samples were outstanding. Table 3 illustrates the effect of various additives on the behaviour of geopolymer concrete.

Table 3. Effect of different additives on geopolymer concrete compressive strength.

Ref.	Additives	Remarks
Demie, S et al. [67]	Superplasticizer	A high superplasticiser dose increases CS.
Phoo-Ngernkham et al. [68]	Ground granulated BFS	Compressive strength improves when GBFS dosage is increased.
Phoo-Ngernkham et al. [69]	PC mortar	GP composites were developed that have a more uniform and dense structure than concrete.
Islam, A et al. [70]	Ground granulated BFS, palm oil fuel ash	A 67 MPa CS was achieved by combining 30% POFA with 70% GGBS in FA-GP concrete.
Li, Z et al. [71]	Chitosan biopolymer	N-carboxymethyl chitosan's addition greatly enhanced strength and led to a slight boost in compressive strength.
Yang, T et al. [72]	Ground granulated BFS	The CS of GP mixtures can be increased through the addition of slag to the raw material, with a slag/FA dosage ratio of 0.8, resulting in the highest strength.
Rattanasak, U et al. [73]	Sulfate of calcium and sodium, calcium chloride, and sucrose	The final setting time is significantly prolonged by the presence of sugar. As a rule, admixtures boost CS quality.
Nath, S et al. [74]	GBFS, GCS	Partial replacement with GCS yielded a higher CS than partial replacement with GBFS.
Ding, Y.-C [75]	ground granulated BFS	48 MPa CSs were achieved with an M ratio of 0.96 SiO_2/Na_2O and a raw material composition of 70% GGBFS and 30% FA.
Zhang, M et al. [76]	Red mud	There is a decline in CS after 120 days. Safe aggregation of metals where they cannot exceed safe limits.
Kusbiantoro, A et al. [77]	Incinerated rice husk ash	Compressive and bond strength were enhanced when rice husk ash was added at an optimum dosage of 7%.
Torres-Carrasco et al. [78]	Waste glass	Supplemental silicon causes a rise in CS concentration. Typically, 15 g/100 mL is what's prescribed.

Figure 17. GPC and Portland cement concrete (PCC) compressive strength experiment data (10% Na₂CO₃ by weight of powder mixtures (slag and zeolite), 50% fine aggregate) [45].
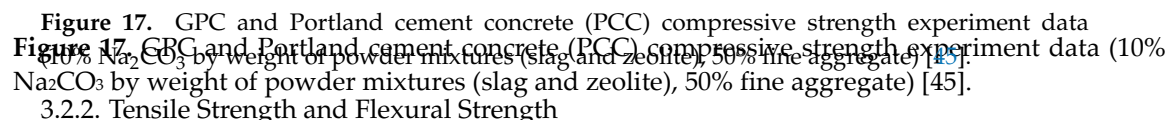
3.2.2. Tensile Strength and Flexural Strength

The splitting tensile strength (fsp) and the flexural strength (fr) of GPC increase in tandem with the compressive strength [79], and the compressive strength is proportional to the splitting tensile strength (fsp) and the flexural strength (fr). Test results by Hardijito [63] showed that the splitting tensile strength of geopolymer concrete is only a fraction of the compressive strength. However, there are some deviations from this general response described by some investigators. According to Ryu et al. [14], the rate of tensile strength increase shows as compressive strength increases. Replacing fly ash with GGBS was found to have a lower effect on splitting tensile and flexural strengths as compared with that compressive strength [80]. Tests by Oderji et al. [81] showed a reduction in flexural strength as the fly ash replacement with slag increased from 15% to 20%, knowing that there is a compressive strength enhancement with this modification. Hassan et al. [31] found that in contrast to the elastic modulus of GPC, preheating concrete at 75 °C for 26 h significantly increased compressive and flexural strengths. Other tests by Sarvanan and Elavenil [82] showed that in contrast to the compressive strength if 50% of fly ash is replaced with GGBS, there is a significant splitting tensile strength enhancement. The same observation was made for the elastic modulus property. Comparing data given by Partha et al. [83] with the others showed that using a special heat curing affects enhancing the flexure/compression ratio and, to a lesser degree, the tensile/compression ratio, as compared with the case of ambient temperature curing. Lee et al. [84] presented the tensile strength of the GPC experimental test was measured at 7, 14, and 28 days. Figure 18 demonstrates that when the ratio of sand to FA increases, the tensile strength steadily falls. The outcomes of experimental tests of geopolymer concrete tensile strength were compared by Zhuang et al. [85] based on the design strength of the ACI code, and findings suggest that the splitting tensile strength of GPC is comparable to that of the ACI design. According to Zhuang et al. [85], the tensile strength of the GPC was better than that of PC-quality concrete.

Figure 18. GPC tensile strength of different sand/fly ash ratios [84].
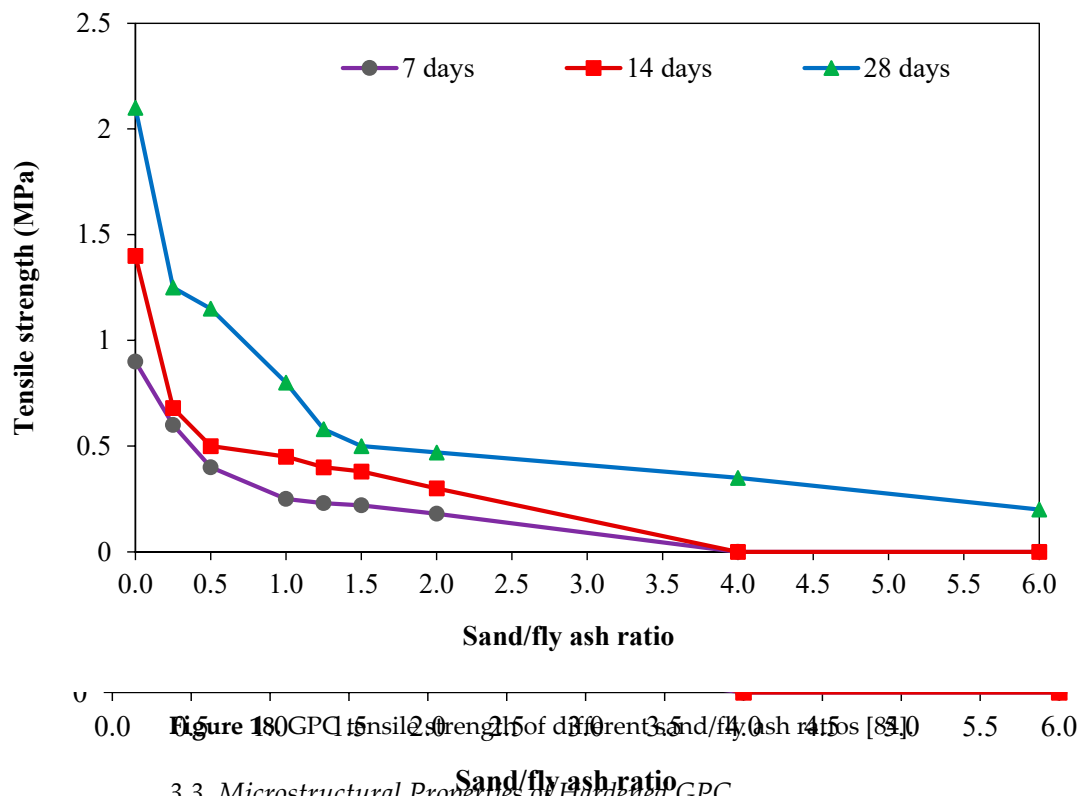
3.3. Microstructural Properties of Hardened GPC

3.3.1. X-ray Diffraction (XRD)

X-ray diffraction is a microstructural scanning test performed to investigate and identify a material's atomic and crystallographic nature. The XRD analysis test involves the irradiation of materials with entrant X-rays and then counting the intensities and scattering angles, which examines the position of the substance to identify its composition and identifies scattered intensity peaks. XRD is used in conjunction with other microstructural analyses such as optical light microscopy, electron microprobe microscopy, and scanning electron microscopy in geologic research, mainly if the sample to be analysed is a mixture. XRD data can identify each mineral in a sample and its concentration, different researchers have studied the XRD pattern of geopolymer concrete [66,84–95]. XRD data taken identify each mineral in a sample and its concentration, different researchers have studied the XRD pattern of geopolymer concrete [66,84–95]. The X-ray diffraction structure (XRD) pattern of geopolymer concrete is of a prevailing amorphous character, noticed by wide XRD peaks forming the shape of a "hill". Knumar et al. [9] shows the total diffraction (XRD) geopolymer concrete in its as-received condition. Amorphous character only seldom containing needle-shaped minority crystals".

Different researchers have studied the XRD pattern of geopolymer concrete [66,84–95]. The X-ray diffraction structure (XRD) pattern of geopolymer concrete is of a prevailing amorphous character, noticed by wide XRD peaks forming the shape of a "hill". Kumar et al. [9] shows the total diffraction (XRD) geopolymer concrete in its as-received condition. Amorphous character only seldom containing needle-shaped minority crystals".

Figure 19. XRD of geopolymer concrete [86].

3.3.2. Scanning Electron Micrograph (SEM) and Energy Dispersive X-ray (EDX)

3.3.2. Scanning Electron Micrograph (SEM) and Energy Dispersive X-ray (EDX)

SEM involves examining and scanning the material's surface with a focused beam of electrons through image analysis to measure and assess fine details. When electrons contact sample atoms, they provide multiple surface topography and composition signals, highlighting component failures, detecting particles, and analysing the interactions between substances and substrates.

Some studies have investigated the SEM and EDX test of GPC [88,96–99]. The microstructure of geopolymer-treated concrete appears more refined and denser than untreated concrete (Figure 20). Calcium hydroxide was not detected using EDX, but particles of non-reactant lime were present at levels similar to the control specimen. The main component of geopolymer cement is lime, which explains why it has these properties. Calcium, silicon, magnesium, and potassium peaks increase dramatically in the EDX elemental analysis of the geopolymer-modified PC concrete, which can be attributed to the high concentrations of these elements in the geopolymer cement (except potassium, which originates mostly from the alkaline activator).
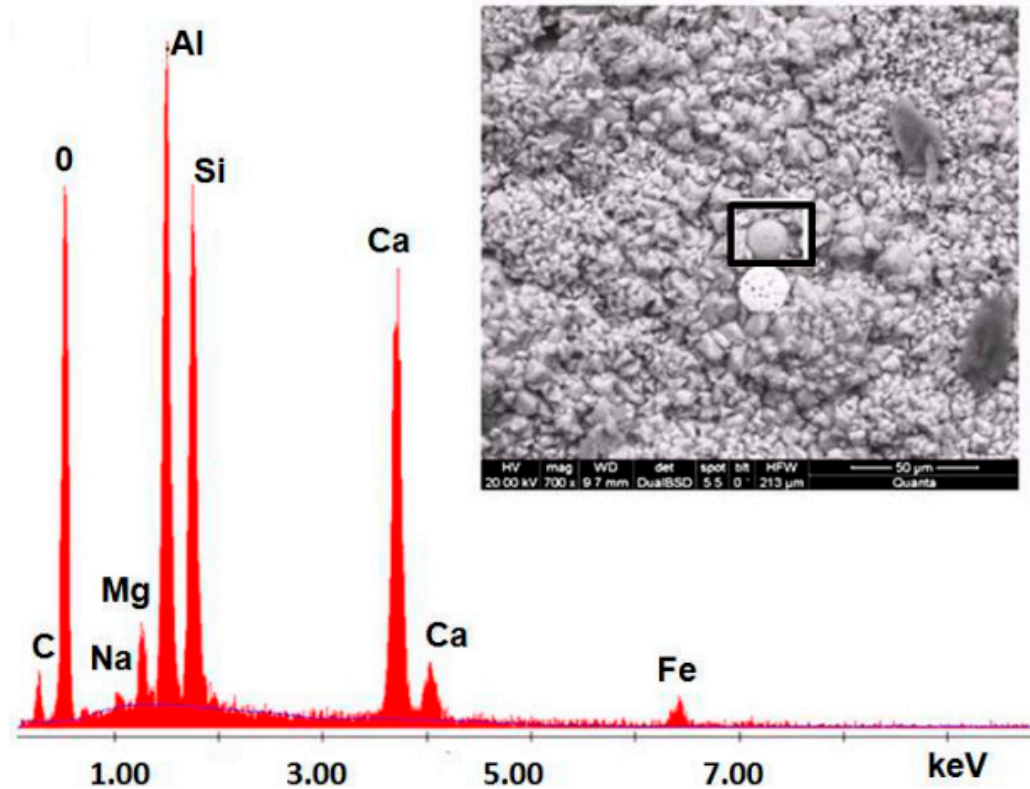
Figure 20. SEM and EDX curve showing the chemical composition of geopolymer concrete [99].

Jittabut et al. [88] showed that scanning electron microscopy (SEM) pictures of the failed specimens were taken to investigate the geopolymer concrete microstructure. Figure 21 shows micrographs of geopolymer concrete. The geopolymer concrete had that structure phases exist in the matrix GPCs. According to Han et al. [90], the microstructure investigation is absolute, thick, and unbroken, with a highly reactive microstructure. The polymerisation results were in good condition, with no breakdown or crystalline water.
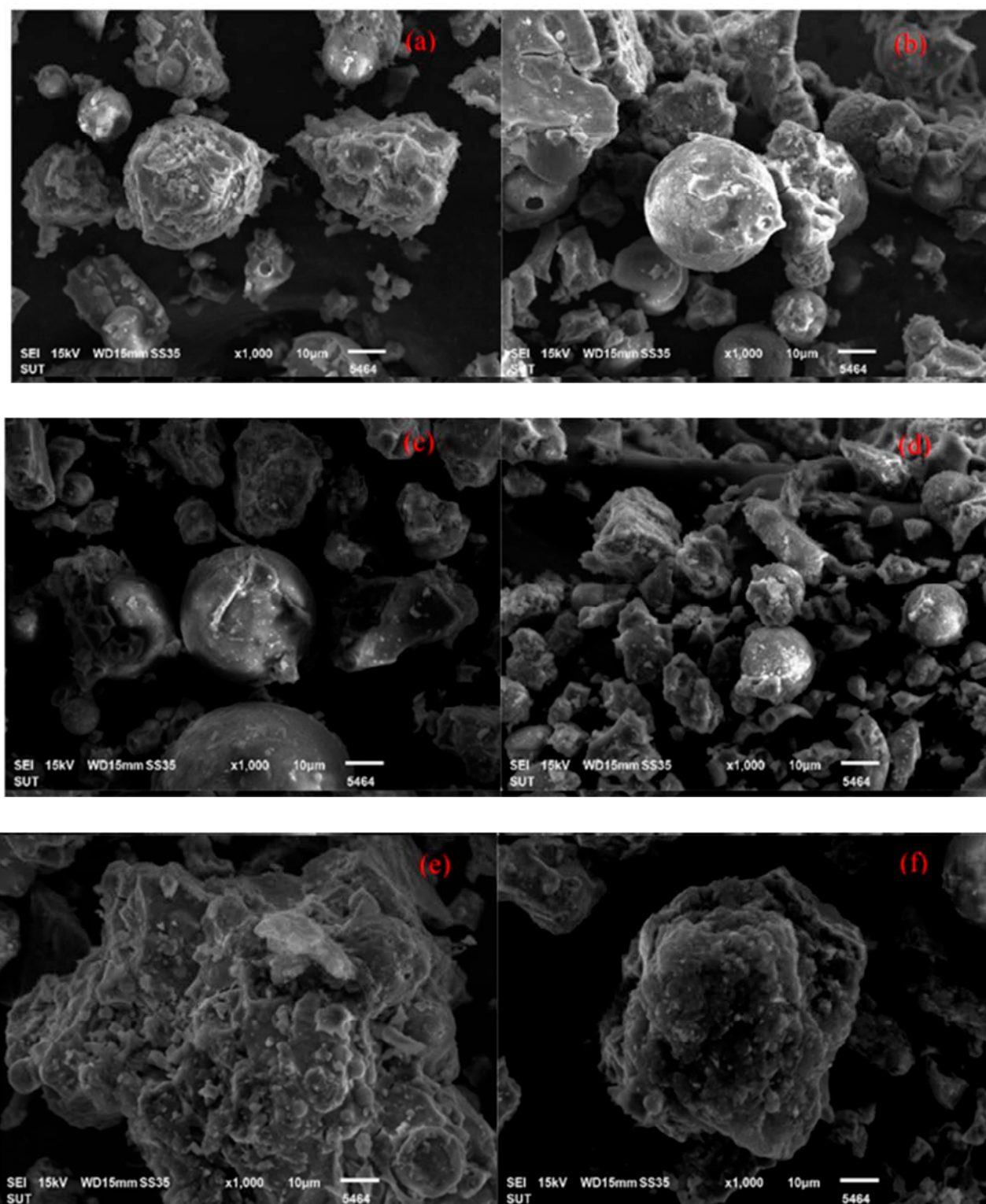
Figure 21. SEM images of a fracture surface of geopolymer nano-composite reinforced with carbon nanotubes (**a**) NaOH 10M control without MWCNTs (**b**) 10M control with CNTs 1 wt% (**c**) NaOH 15M control without MWCNTs (**d**) 15M control with MWCNTs 1 wt% (**e**) NaOH 20M control without MWCNTs and (**f**) 20M control with MWCNTs 1 wt%. [88].

3.3.3. Fourier Transform Infrared Spectroscopy (FTIR)

FTIR techniques are used to measure the infrared absorption, emission, and photo-conductivity of a solid, liquid, or gas and identify PHB functional categories. Very limited

FTIR techniques are used to measure the infrared absorption, emission, and photo-conductivity of a solid, liquid, or gas and identify PHB functional categories. Very limited studies have investigated the FTIR test of GPC [100–102]. Figure 22 represents the curing geopolymer sample spectra in the range of 4000 and 400 cm⁻¹. Rajini et al. [102] observed that the broad bands in geopolymer mixtures at roughly 3350–3570 cm⁻¹ are caused by the tensile vibrations of H–O–H bonds, whereas the broad bands at 1640–1646 cm⁻¹ are caused by the bending vibration of the water-associated-OH group.
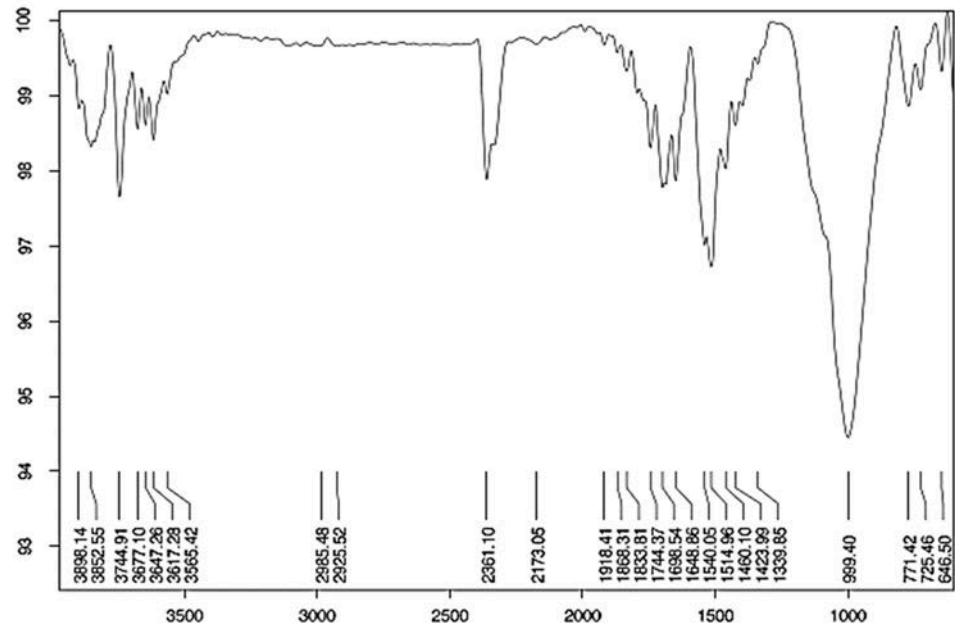
Figure 22. Fourier transform infrared spectroscopy (FTIR) of geopolymer concrete [102].

Salih, M. A. et al. [101] explain that "the spectra of raw geopolymer paste with different sodium silicate to sodium hydroxide ratios were distinguished with six groups of bands in the regions of 750–850 cm⁻¹, 900–1200 cm⁻¹, 1200–1300 cm⁻¹, 1300–1600 cm⁻¹, 1600–1700 cm⁻¹, and 2850–3700 cm⁻¹ (Figure 23). The first peak was observed at a wave number of 750–850 cm⁻¹ centred at 783 cm⁻¹, which may refer to the symmetric stretching vibration of Si–O–Si".
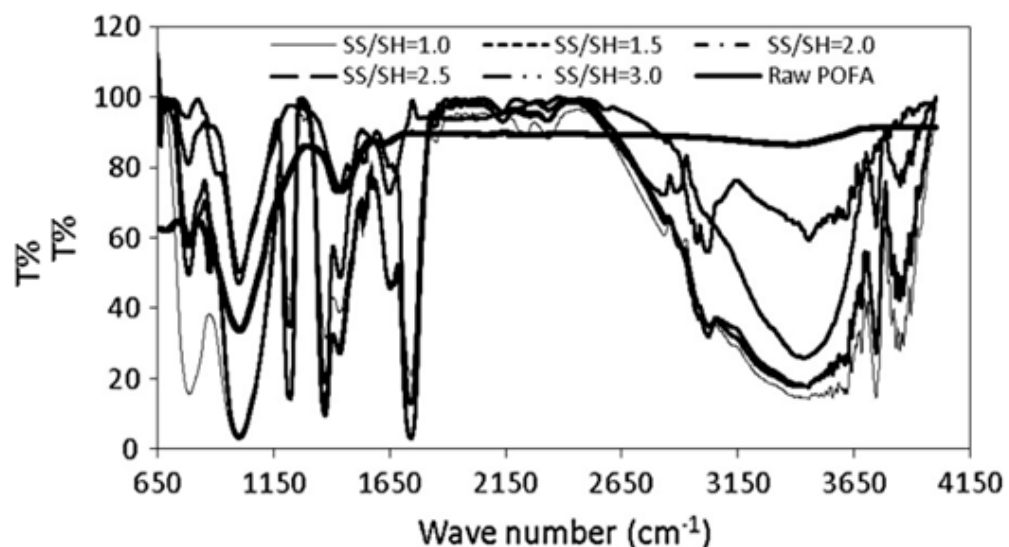
Figure 23. FTIR spectra of raw geopolymerized [101].

Figure 23. FTIR spectra of raw geopolymerized [101].

3.3.4. Differential Scanning Calorimetry (DSC)

DSC is an impressive scientific tool for pointing out various physical properties and thermal transitions of polymeric materials. Several distinctive features of the geopolymer pastes can be measured with DSC, which allows observation of exothermic and endothermic processes, in addition to glass transition temperatures (Tg).

Different researchers have studied the DSC analysis of geopolymer concrete [103–107]. Jamil, N. H. et al. [107] showed the geopolymer's range of thermograms (exothermal up) (Figure 24), where the geopolymer demonstrates some peaks in the matrix.
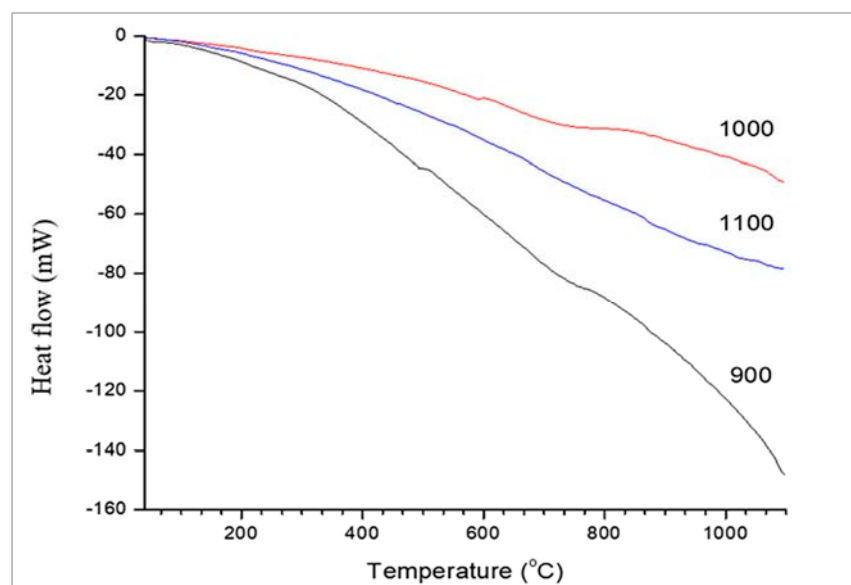
Figure 24. Differential scanning calorimetry (DSC) [107].

Figure 25 depicts the differential scanning calorimetry (DSC) thermograms of geopolymer paste after 28 days, which is akin to the results reported in previous works [101]. From what can be seen in the diagram, there was only one visible endothermic peak. The pastes with 1.5, 2:1.3, 2; and 3:1 sodium silicate to sodium hydroxide ratios had this major peak occurred at 175.57, 144.49, 149.40, 124.42, and 120.02 °C, respectively. Water being released from partially dehydrated C-S-H clusters may account for the peaks. For stoichiometric ratios of 1.0, 1.5, 2.0, 2.5, and 3.0 between sodium silicate and sodium hydroxide, the endothermic results were 388.03, 343.06, 384.09, 514.29, and 741.29 W/g, respectively.

3.3.5. Thermal Gravimetric Analysis (TGA)

TGA aids in the identification of several concrete phases, including calcite, portlandite, C-A-H, C-A-S-H, etc. The hydration reaction is often checked by measuring the CH content; if the CH level decreases, it indicates that CH has been consumed in the hydration reaction. Researchers from several fields have examined the geopolymer concrete TGA [108–111].

Figure 26 shows the TGA analysis of geopolymer concrete's thermogram. Rosas-Casarez et al. [94] emphasised the primary drop in slope between 0 °C and 1000 °C. In the temperature range of 0 to 120 °C, the dewatering operation resulted in a ten percent weight loss, which is the first substantial drop (number 1 in Figure 26). This process is related to free water that has been adsorbed on the sample's surface, water that can evaporate from the sample, and the sample's porosity. However, a current study on the loss of hydrated sodium aluminosilicate gel contradicts this notion. Between 120 and 200 °C, the presence of NASH gel contributes significantly to heat degradation (number 2 in Figure 26). Carbonate loss in mass between 450 and 800 °C may be attributable to carbonates synthesised in the outside environment (number 3 in Figure 26). This method

can be used as a comparative method between materials [112–117] by relating the water binding capacity for each compound against the effect of temperature. This allows for the differentiation and probing of structural variants and the presence of compounds in a material.
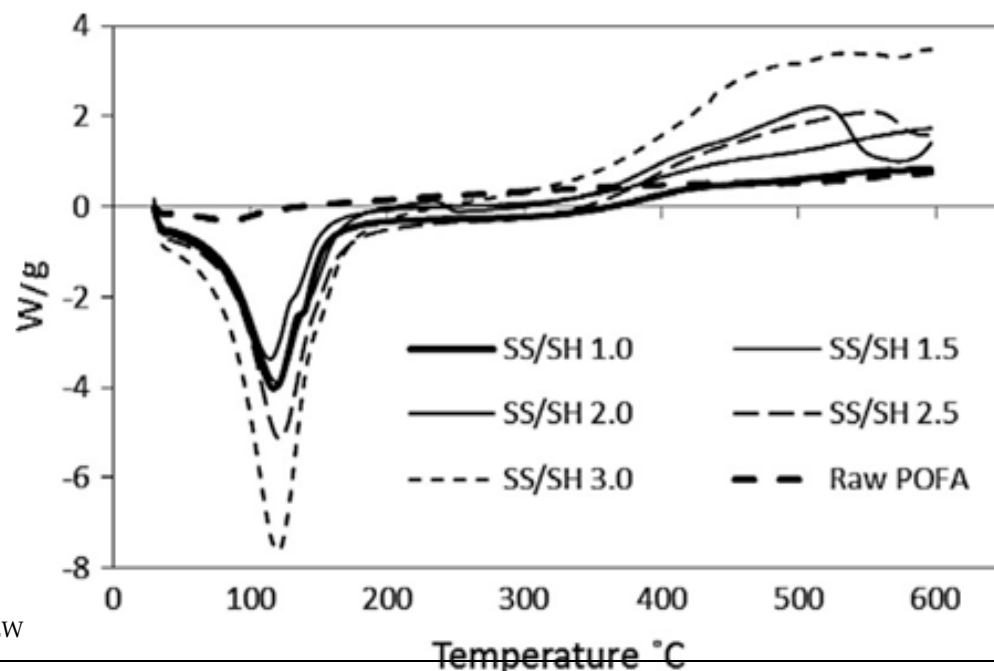
Figure 25. DSC diagrams of raw geopolymerized [101].
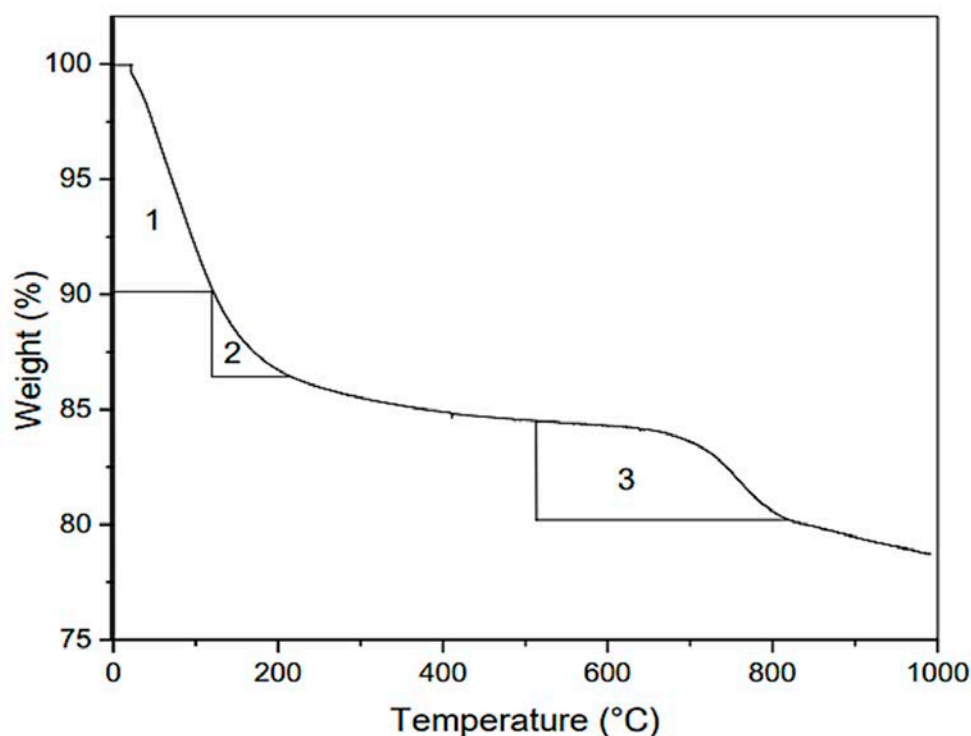
Figure 26. Thermogravimetric (TGA) analysis of geopolymer [94].

pacity for each compound against the effect of temperature. This allows for the differentiation and probing of structural variants and the presence of compounds in a material.

4. Scope and Future Research Work

Geopolymer concrete offers much potential in the construction industry. Even though geopolymer concrete has been researched very well in the last few years, several aspects should be covered, and extended data should be collected to understand the behaviour of geopolymer concrete before introducing it to the construction sector. The large-scale structural elements of GPC and the performance of reinforced geopolymer concrete should be investigated. Moreover, the behaviour of geopolymer materials in an aggressive

4. Scope and Future Research Work

Geopolymer concrete offers much potential in the construction industry. Even though geopolymer concrete has been researched very well in the last few years, several aspects should be covered, and extended data should be collected to understand the behaviour of geopolymer concrete before introducing it to the construction sector. The large-scale structural elements of GPC and the performance of reinforced geopolymer concrete should be investigated. Moreover, the behaviour of geopolymer materials in an aggressive environment, such as a marine environment, must be studied.

Research studies available on structural members of GPC are still lacking. Thus, more investigations need to be carried out on the structural behaviour under the different loading states, and proper modelling is essential, such as developing a proper relationship between the flexural strength, compressive strength, shear strength, and modulus of elasticity of GPC. Moreover, the elasticity and plasticity of geopolymer materials should be well studied to help structural engineers when they are designing buildings. Based on fundamental research, embarking on solid wastes to explore the preparation of varied characteristics of geopolymers in order to produce high-value-added application domains should be one of the primary paths of future geopolymer research development [91,92,111–132].

5. Conclusions

The mechanical properties and microstructural characteristics of geopolymer concrete were reviewed. From the above literature, the following are the final thoughts, along with suggestions for more research:

- Construction with geopolymer concrete is more durable and stronger than with PC concrete;
- Many factors, including curing conditions, the ratio of alkaline to the binder, and the type of activator, have an important impact on the mechanical properties of geopolymer concrete. Consequently, a proper mix design is required to achieve the target strength;
- Geopolymer concrete possesses all the potential characteristics for future applications in civil engineering because it is a green material and requires strength and durability properties for all types of projects in the construction industry;
- Even though it is known that GPC could be used as a replacement material and is a cleaner and more sustainable form of concrete, it is still not widely used in construction;
- Geopolymer concrete needs a standard code to be used more often in building structures;
- In terms of mechanical and microstructural performance, geopolymer concrete was better than PC concrete, especially after exposure to high temperatures;
- The effect of using geopolymer as a partial replacement for PC on the microstructure can be easily noticed; the microstructure has become significantly denser and more homogenous compared with the control specimen, while the number of voids has decreased;
- C-S-H gel and geopolymer gel enhance the mechanical and microstructural properties of precursors that are either high in Ca or contain a combination of Ca components.

Author Contributions: Conceptualisation, A.S., A.H., H.M.N., S.Q., M.M.S.S. and N.S.M.; methodology, A.S., A.H., H.M.N., M.M.S.S. and N.S.M.; software, A.S. and A.H.; validation, H.M.N., S.Q., M.M.S.S. and N.S.M.; formal analysis, A.S. and A.H.; investigation, A.S., A.H., H.M.N., S.Q., M.M.S.S. and N.S.M.; resources, A.S., A.H., H.M.N., M.M.S.S., N.S.M. and K.A.; data curation, A.S., A.H., H.M.N., M.M.S.S., S.Q., K.A. and N.S.M.; writing—original draft preparation, A.S. and A.H.; writing—review and editing, A.H., H.M.N., M.M.S.S. and N.S.M.; visualisation, A.S. and A.H.; supervision, A.S., A.H. and H.M.N.; project administration, M.M.S.S.; funding acquisition, M.M.S.S. All authors have read and agreed to the published version of the manuscript.

References

1. Amran, Y.M.; Alyousef, R.; Alabduljabbar, H.; El-Zeadani, M. Clean production and properties of geopolymer concrete; A review. *J. Clean. Prod.* **2020**, *251*, 119679. [CrossRef]
2. Basha, S.M.; Reddy, C.B.; Vasugi, K. Strength behaviour of geopolymer concrete replacing fine aggregates by M-sand and E-waste. *Int. J. Eng. Trends Technol.* **2016**, *40*, 401–407. [CrossRef]
3. Bhutta, A.; Farooq, M.; Zanotti, C.; Banthia, N. Pull-out behavior of different fibers in geopolymer mortars: Effects of alkaline solution concentration and curing. *Mater. Struct.* **2017**, *50*, 80. [CrossRef]
4. Castel, A.; Foster, S.; Ng, T.; Sanjayan, J.; Gilbert, R. Creep and drying shrinkage of a blended slag and low calcium fly ash geopolymer Concrete. *Mater. Struct.* **2016**, *49*, 1619–1628. [CrossRef]
5. Ahmed, H.U.; Mahmood, L.J.; Muhammad, M.A.; Faraj, R.H.; Qaidi, S.M.A.; Sor, N.H.; Mohammed, A.S.; Mohammed, A.A. Geopolymer concrete as a cleaner construction material: An overview on materials and structural performances. *Clean. Mater.* **2022**, *5*, 100111. [CrossRef]
6. Qaidi, S.M.A.; Tayeh, B.A.; Isleem, H.F.; de Azevedo, A.R.G.; Ahmed, H.U.; Emad, W. Sustainable utilisation of red mud waste (bauxite residue) and slag for the production of geopolymer composites: A review, Case Studies in Construction. *Materials* **2022**, *16*, e00994.
7. IEA. *Global Cement Production, 2010–2019*; IEA: Paris, France, 2020.
8. Chowdhury, S.; Mohapatra, S.; Gaur, A.; Dwivedi, G.; Soni, A. Study of various properties of geopolymer concrete–A review. *Mater. Today Proc.* **2021**, *46*, 5687–5695. [CrossRef]
9. Mohajerani, A.; Suter, D.; Jeffrey-Bailey, T.; Song, T.; Arulrajah, A.; Horpibulsuk, S.; Law, D. Recycling waste materials in geopolymer concrete. *Clean Technol. Environ. Policy* **2019**, *21*, 493–515. [CrossRef]
10. Ahmed, H.U.; Mohammed, A.S.; Qaidi, S.M.A.; Faraj, R.H.; Sor, N.H.; Mohammed, A.A. Compressive strength of geopolymer concrete composites: A systematic comprehensive review, analysis and modeling. *Eur. J. Environ. Civ. Eng.* **2022**, 1–46. [CrossRef]
11. Ahmed, S.N.; Sor, N.H.; Ahmed, M.A.; Qaidi, S.M.A. Thermal conductivity and hardened behavior of eco-friendly concrete incorporating waste polypropylene as fine aggregate. *Mater. Today Proc.* **2022**, *57*, 818–823. [CrossRef]
12. Aslam, F.; Zaid, O.; Althoey, F.; Alyami, S.H.; Qaidi, S.M.A.; de Prado Gil, J.; Martínez-García, R. Evaluating the influence of fly ash and waste glass on the characteristics of coconut fibers reinforced concrete. *Struct. Concr.* **2022**. [CrossRef]
13. Davidovits, J. Geopolymers. *J. Therm. Anal.* **1991**, *37*, 1633–1656. [CrossRef]
14. Ryu, G.S.; Lee, Y.B.; Koh, K.T.; Chung, Y.S. The mechanical properties of fly ash-based geopolymer concrete with alkaline activators. *Constr. Build. Mater.* **2013**, *47*, 409–418. [CrossRef]
15. Sreevidya, V. Investigations on the Flexural Behaviour of Ferro Geopolymer Composite Slabs. 2014. Available online: https://www.researchgate.net/publication/321050166_INVESTIGATIONS_ON_THE_FLEXURAL_BEHAVIOUR_OF_FERRO_GEOPOLYMER_COMPOSITE_SLABS (accessed on 1 September 2022).
16. Davidovits, J. False values on CO_2 emission for geopolymer cement/concrete published in scientific papers. *Tech. Pap.* **2015**, *24*, 1–9.
17. Gollakota, A.R.K.; Volli, V.; Shu, C.-M. Progressive utilisation prospects of coal fly ash: A review. *Sci. Total Environ.* **2019**, *672*, 951–989. [CrossRef] [PubMed]
18. Xiao, R.; Polaczyk, P.; Zhang, M.; Jiang, X.; Zhang, Y.; Huang, B.; Hu, W. Evaluation of glass powder-based geopolymer stabilised road bases containing recycled waste glass aggregate. *Transp. Res. Rec.* **2020**, *2674*, 22–32. [CrossRef]
19. Assi, L.; Carter, K.; Deaver, E.; Anay, R.; Ziehl, P. Sustainable concrete: Building a greener future. *J. Clean. Prod.* **2018**, *198*, 1641–1651. [CrossRef]
20. Assi, L.N.; Carter, K.; Deaver, E.; Ziehl, P. Review of availability of source materials for geopolymer/sustainable concrete. *J. Clean. Prod.* **2020**, *263*, 121477. [CrossRef]
21. van Jaarsveld, J.G.S.; van Deventer, J.S.J.; Lukey, G.C. The characterisation of source materials in fly ash-based geopolymers. *Mater. Lett.* **2003**, *57*, 1272–1280. [CrossRef]
22. Ahmad, J.; Majdi, A.; Elhag, A.B.; Deifalla, A.F.; Soomro, M.; Isleem, H.F.; Qaidi, S. A Step towards Sustainable Concrete with Substitution of Plastic Waste in Concrete: Overview on Mechanical, Durability and Microstructure Analysis. *Crystals* **2022**, *12*, 944. [CrossRef]
23. Ahmed, H.U.; Mohammed, A.A.; Rafiq, S.; Mohammed, A.S.; Mosavi, A.; Sor, N.H.; Qaidi, S.M.A. Compressive Strength of Sustainable Geopolymer Concrete Composites: A State-of-the-Art Review. *Sustainability* **2021**, *13*, 13502. [CrossRef]

24. Ahmed, H.U.; Mohammed, A.S.; Faraj, R.H.; Qaidi, S.M.A.; Mohammed, A.A. Compressive strength of geopolymer concrete modified with nano-silica: Experimental and modeling investigations. *Case Stud. Constr. Mater.* **2022**, *16*, e01036. [CrossRef]

25. Hassan, A.; Arif, M.; Shariq, M. Use of geopolymer concrete for a cleaner and sustainable environment–A review of mechanical properties and microstructure. *J. Clean. Prod.* **2019**, *223*, 704–728. [CrossRef]

26. Qaidi, S.M.A.; Atrushi, D.S.; Mohammed, A.S.; Ahmed, H.U.; Faraj, R.H.; Emad, W.; Tayeh, B.A.; Najm, H.M. Ultra-high-performance geopolymer concrete: A review. *Constr. Build. Mater.* **2022**, *346*, 128495. [CrossRef]

27. Hassan, A.; Arif, M.; Shariq, M. A review of properties and behaviour of reinforced geopolymer concrete structural elements-A clean technology option for sustainable development. *J. Clean. Prod.* **2020**, *245*, 118762. [CrossRef]

28. Habert, G.; D'Espinose De Lacaillerie, J.B.; Roussel, N. An Environmental Evaluation of Geopolymer Based Concrete Production: Reviewing Current Research Trends. *J. Clean. Prod.* **2011**, *19*, 1229–1238. [CrossRef]

29. Umniati, B.S.; Risdanareni, P.; Zein, F.T.Z. Workability Enhancement of Geopolymer Concrete through the Use of Retarder. *AIP Conf. Proc.* **2017**, *1887*, 020033.

30. Mehta, A.; Siddique, R. Properties of Low-Calcium Fly Ash Based Geopolymer Concrete Incorporating PC as Partial Re-placement of Fly Ash. *Constr. Build. Mater.* **2017**, *150*, 792–807. [CrossRef]

31. Hassan, A. Experimental Study of Fly Ash Based Geopolymer Concrete. *Int. J. Adv. Earth Sci. Eng.* **2018**, *7*, 635–648. [CrossRef]

32. Antoni, P.; Satria, J.; Sugiarto, A.; Hardjito, D. Effect of Variability of Fly Ash Obtained from the Same Source on the Characteristics of Geopolymer. *MATEC Web Conf.* **2017**, *97*, 01026. [CrossRef]

33. Lakshmi, R.; Nagan, S. Utilization of Waste e Plastic Particles in Cementitious Mixtures. *J. Struct. Eng. (Madras)* **2011**, *38*, 26–35.

34. Memon, F.A.; Nuruddin, M.F.; Demie, S.; Shafiq, N. Effect of Superplasticizer and Extra Water on Workability and Com-pressive Strength of Self-Compacting Geopolymer Concrete. *Res. J. Appl. Sci. Eng. Technol.* **2012**, *4*, 407–414.

35. Warid Wazien, A.Z.; Al Bakri Abdullah, M.M.; Abd Razak, R.; Mohd Remy Rozainy, M.A.Z.; Mohd Tahir, M.F.; Hussin, K. Potential of Geopolymer Mortar as Concrete Repairing Materials. *Mater. Sci. Forum* **2016**, *857*, 382–387. [CrossRef]

36. Sathonsaowaphak, A.; Chindaprasirt, P.; Pimraksa, K. Workability and Strength of Lignite Bottom Ash Geopolymer Mortar. *J. Hazard. Mater.* **2009**, *168*, 44–50. [CrossRef] [PubMed]

37. Chindaprasirt, P.; Chareerat, T.; Sirivivatnanon, V. Workability and Strength of Coarse High Calcium Fly Ash Geopolymer. *Cem. Concr. Compos.* **2007**, *29*, 224–229. [CrossRef]

38. *ASTM C 1437-07*; Standard Test Methods for Flow of Hydraulic Cement Mortar. ASTM International: West Conshohocken, PA, USA, 2008.

39. Bhowmick, A.; Ghosh, S. Effect of Synthesising Parameters on Workability and Compressive Strength of Fly Ash Based Geopoly-mer Mortar. *Int. J. Struct. Civ. Eng.* **2012**, *3*, 168–177.

40. *ASTM C1437-01*; Standard Test Method for Flow of Hydraulic Cement Mortar. ASTM International: West Conshohocken, PA, USA, 2001.

41. *BS EN 480-5*; Admixtures for Concrete, Mortar and Grout—Test Methods Part 5: Determination of Capillary Absorption. British Standard Institute: London, UK, 2005; Volume 3, pp. 480–485.

42. Jumrat, S.; Chatveera, B.; Rattanadecho, P. Dielectric Properties and Temperature Profile of Fly Ash-Based Geopolymer Mortar. *Int. Commun. Heat Mass Transf.* **2011**, *38*, 242–248. [CrossRef]

43. Saloma; Saggaff, A.; Hanafiah; Mawarni, A. Geopolymer Mortar with Fly Ash. *MATEC Web Conf.* **2016**, *78*, 01026. [CrossRef]

44. Phoo-ngernkham, T.; Sata, V.; Hanjitsuwan, S.; Ridtirud, C.; Hatanaka, S.; Chindaprasirt, P. Compressive Strength, Bending and Fracture Characteristics of High Calcium Fly Ash Geopolymer Mortar Containing Portland Cement Cured at Ambient Temperature. *Arab. J. Sci. Eng.* **2016**, *41*, 1263–1271. [CrossRef]

45. Erfanimanesh, A.; Sharbatdar, M.K. Mechanical and Microstructural Characteristics of Geopolymer Paste, Mortar, and Concrete Containing Local Zeolite and Slag Activated by Sodium Carbonate. *J. Build. Eng.* **2020**, *32*, 101781. [CrossRef]

46. Yusuf, T.O.; Ismail, M.; Usman, J.; Noruzman, A.H. Impact of Blending on Strength Distribution of Ambient Cured Me-takaolin and Palm Oil Fuel Ash Based Geopolymer Mortar. *Adv. Civ. Eng.* **2014**, *2014*, 658067. [CrossRef]

47. Ismail, M.; Yusuf, T.O.; Noruzman, A.H.; Hassan, I.O. Early Strength Characteristics of Palm Oil Fuel Ash and Metakaolin Blended Geopolymer Mortar. *Adv. Mater. Res.* **2013**, *690*, 1045–1048. [CrossRef]

48. De Rossi, A.; Ribeiro, M.J.; Labrincha, J.A.; Novais, R.M.; Hotza, D.; Moreira, R.F.P.M. Effect of the Particle Size Range of Construction and Demolition Waste on the Fresh and Hardened-State Properties of Fly Ash-Based Geopolymer Mortars with Total Replacement of Sand. *Process Saf. Environ. Prot.* **2019**, *129*, 130–137. [CrossRef]

49. Cyr, M.; Idir, R.; Poinot, T. Properties of Inorganic Polymer (Geopolymer) Mortars Made of Glass Cullet. *J. Mater. Sci.* **2012**, *47*, 2782–2797. [CrossRef]

50. Huseien, G.F.; Mirza, J.; Ismail, M.; Hussin, M.W. Influence of Different Curing Temperatures and Alkali Activators on Properties of GBFS Geopolymer Mortars Containing Fly Ash and Palm-Oil Fuel Ash. *Constr. Build. Mater.* **2016**, *125*, 1229–1240. [CrossRef]

51. Steinerova, M. Mechanical Properties of Geopolymer Mortars in Relation to Their Porous Structure. *Ceram. Silik.* **2011**, *55*, 362–372.

52. Li, X.; Wang, Z.; Jiao, Z. Influence of Curing on the Strength Development of Calcium-Containing Geopolymer Mortar. *Materials* **2013**, *6*, 5069–5076. [CrossRef]

53. Atiş, C.D.; Görür, E.B.; Karahan, O.; Bilim, C.; Ilkentapar, S.; Luga, E. Very High Strength (120 MPa) Class F Fly Ash Ge-opolymer Mortar Activated at Different NaOH Amount, Heat Curing Temperature and Heat Curing Duration. *Constr. Build. Mater.* **2015**, *96*, 673–678. [CrossRef]

54. Al-Majidi, M.H.; Lampropoulos, A.; Cundy, A.; Meikle, S. Development of Geopolymer Mortar under Ambient Temper-ature for in Situ Applications. *Constr. Build. Mater.* **2016**, *120*, 198–211. [CrossRef]

55. Wongsa, A.; Kunthawatwong, R.; Naenudon, S.; Sata, V.; Chindaprasirt, P. Natural Fiber Reinforced High Calcium Fly Ash Geopolymer Mortar. *Constr. Build. Mater.* **2020**, *241*, 118143. [CrossRef]

56. Lloyd, N.A.; Rangan, B.V. Geopolymer Concrete with Fly Ash. In Proceedings of the 2nd International Conference on Sustainable Construction Materials and Technologies, Ancona, Italy, 28–30 June 2010.

57. Patil, S.; Karikatti, V.; Chitawadagi, M. Granulated Blast-Furnace Slag (GGBS) based Geopolymer Concrete–Review. *Int. J. Adv. Sci. Eng.* **2018**, *5*, 879–885. [CrossRef]

58. Rajarajeswari, A.; Dhinakaran, G. Compressive strength of GGBFS based GPC under thermal curing. *Constr. Build. Mater.* **2016**, *126*, 552–559. [CrossRef]

59. Khater, H.M. Efect of fumed silica on the characterisation of the geopolymer materials. *Int. J. Adv. Struct. Eng.* **2013**, *5*, 12. [CrossRef]

60. Brew, D.R.M.; MacKenzie, K.J.D. Geopolymer synthesis using fumed silica and sodium aluminate. *J. Mater. Sci.* **2007**, *42*, 3990–3993. [CrossRef]

61. Bajpai, R.; Kailash, C.; Anshuman, S.; Kuldip, S.S.; Manpreet, S. Environmental impact assessment of fy ash and silica fume based geopolymer concrete. *J. Clean. Prod.* **2020**, *254*, 120147. [CrossRef]

62. Liu, Y.; Shi, C.; Zhang, Z.; Li, N.; Shi, D. Mechanical and fracture properties of ultra-high performance geopolymer concrete: Efects of steel fber and silica fume. *Cem. Concr. Compos.* **2020**, *112*, 103665. [CrossRef]

63. Rangan, B.; Hardjito, D. Studies on Fly Ash-Based Geopolymer Concrete. Ph.D. Thesis, Curtin University of Technology, Bentley, Australia, 2005.

64. Day, K.W. Properties of Concrete. In *Concrete Mix Design, Quality Control and Specification*; CRC Rress: Boca Raton, FL, USA, 2021.

65. Ng, T.S.; Foster, S.J. Development of High Performance Geopolymer Conscrete. In Proceedings of the Futures in Mechanics of Structures and Materials—20th Australasian Conference on the Mechanics of Structures and Materials (ACMSM20), Toowoomba, Australia, 2–5 November 2008.

66. Le, H.T.N.; Poh, L.H.; Wang, S.; Zhang, M.H. Critical Parameters for the Compressive Strength of High-Strength Concrete. *Cem. Concr. Compos.* **2017**, *82*, 202–216. [CrossRef]

67. Demie, S.; Nuruddin, M.F.; Shafiq, N. Effects of micro-structure characteristics of interfacial transition zone on the compressive strength of self-compacting geopolymer concrete. *Constr. Build. Mater.* **2013**, *41*, 91–98. [CrossRef]

68. Phoo-Ngernkham, T.; Maegawa, A.; Mishima, N.; Hatanaka, S.; Chindaprasirt, P. Effects of sodium hydroxide and sodium silicate solutions on compressive and shear bond strengths of FA–GBFS geopolymer. *Constr. Build. Mater.* **2015**, *91*, 1–8. [CrossRef]

69. Phoo-Ngernkham, T.; Sata, V.; Hanjitsuwan, S.; Ridtirud, C.; Hatanaka, S.; Chindaprasirt, P. High calcium fly ash geopolymer mortar containing Portland cement for use as repair material. *Constr. Build. Mater.* **2015**, *98*, 482–488. [CrossRef]

70. Islam, A.; Alengaram, U.J.; Jumaat, M.Z.; Bashar, I.I. The development of compressive strength of ground granulated blast furnace slag-palm oil fuel ash-fly ash based geopolymer mortar. *Mater. Des.* **2014**, *56*, 833–841. [CrossRef]

71. Li, Z.; Chen, R.; Zhang, L. Utilization of chitosan biopolymer to enhance fly ash-based geopolymer. *J. Mater. Sci.* **2013**, *48*, 7986–7993. [CrossRef]

72. Yang, T.; Yao, X.; Zhang, Z.; Wang, H. Mechanical property and structure of alkali-activated fly ash and slag blends. *J. Sustain. Cem. Mater.* **2012**, *1*, 167–178. [CrossRef]

73. Rattanasak, U.; Pankhet, K.; Chindaprasirt, P. Effect of chemical admixtures on properties of high-calcium fly ash geopolymer. *Int. J. Miner. Met. Mater.* **2011**, *18*, 364–369. [CrossRef]

74. Nath, S.; Kumar, S. Influence of iron making slags on strength and microstructure of fly ash geopolymer. *Constr. Build. Mater.* **2013**, *38*, 924–930. [CrossRef]

75. Ding, Y.-C.; Cheng, T.-W.; Dai, Y.-S. Application of geopolymer paste for concrete repair. *Struct. Concr.* **2017**, *18*, 561–570. [CrossRef]

76. Zhang, M.; Zhao, M.; Zhang, G.; Mann, D.; Lumsden, K.; Tao, M. Durability of red mud-fly ash based geopolymer and leaching behavior of heavy metals in sulfuric acid solutions and deionised water. *Constr. Build. Mater.* **2016**, *124*, 373–382. [CrossRef]

77. Kusbiantoro, A.; Nuruddin, M.F.; Shafiq, N.; Qazi, S.A. The effect of microwave incinerated rice husk ash on the compressive and bond strength of fly ash based geopolymer concrete. *Constr. Build. Mater.* **2012**, *36*, 695–703. [CrossRef]

78. Torres-Carrasco, M.; Puertas, F. Waste glass in the geopolymer preparation. Mechanical and microstructural characterisation. *J. Clean. Prod.* **2015**, *90*, 397–408. [CrossRef]

79. Rashad, A.M. Properties of alkali activated fly ash concrete blended with slag. *Iran. J. Mater. Sci. Eng.* **2013**, *10*, 57–64.

80. Abhilash, P.; Sashidhar, C.; Reddy, I.R. Strength properties of Fly ash and GGBS based Geo-polymer Concrete. *Int. J. ChemTech Res.* **2016**, *9*, 350–356.

81. Oderji, S.Y.; Chen, B.; Ahmad, M.R.; Shah, S.F.A. Fresh and hardened properties of one-part fly ash-based geopolymer binders cured at room temperature: Effect of slag and alkali activators. *J. Clean. Prod.* **2019**, *225*, 1–10. [CrossRef]

82. Sarvanan, S.; Elavenil, S. Strength properties of geopolymer concrete using M-sand by assessing their mechanical characteristics. *ARPN J. Eng. Appl. Sci.* **2018**, *13*, 4028–4041.

83. Partha, S.D.; Pradib, N.; Prabir, K.S. Strength and Permeation Properties of Slag Blended Fly Ash Based Geopolymer Concrete. *Adv. Mater. Res.* **2013**, *651*, 168–173. [CrossRef]

84. Lee, B.; Kim, G.; Kim, R.; Cho, B.; Lee, S.; Chon, C.M. Strength Development Properties of Geopolymer Paste and Mortar with Respect to Amorphous Si/Al Ratio of Fly Ash. *Constr. Build. Mater.* **2017**, *151*, 512–519. [CrossRef]

85. Zhuang, X.Y.; Chen, L.; Komarneni, S.; Zhou, C.H.; Tong, D.S.; Yang, H.M.; Yu, W.H.; Wang, H. Fly Ash-Based Geopolymer: Clean Production, Properties and Applications. *J. Clean. Prod.* **2016**, *125*, 253–267. [CrossRef]

86. Wong, L.S. Durability performance of geopolymer concrete: A review. *Polymers* **2022**, *14*, 868. [CrossRef]

87. Alomayri, T. The microstructural and mechanical properties of geopolymer composites containing glass microfibres. *Ceram. Int.* **2017**, *43*, 4576–4582. [CrossRef]

88. Pongsak, J.; Horpibulsuk, S. Physical and microstructure properties of geopolymer nanocomposite reinforced with carbon nanotubes. *Mater. Today Proc.* **2019**, *17*, 1682–1692.

89. Qaidi, S.; Najm, H.M.; Abed, S.M.; Ahmed, H.U.; Al Dughaishi, H.; Al Lawati, J.; Sabri, M.M.; Alkhatib, F.; Milad, A. Fly Ash-Based Geopolymer Composites: A Review of the Compressive Strength and Microstructure Analysis. *Materials* **2022**, *15*, 7098. [CrossRef]

90. Han, Q.; Zhang, P.; Wu, J.; Jing, Y.; Zhang, D.; Zhang, T. Comprehensive review of the properties of fly ash-based geopolymer with additive of nano-SiO_2. *Nanotechnol. Rev.* **2022**, *11*, 1478–1498. [CrossRef]

91. Arafa, S.; Milad, A.; Yusoff, N.I.M.; Al-Ansari, N.; Yaseen, Z.M. Investigation into the permeability and strength of pervious geopolymer concrete containing coated biomass aggregate material. *J. Mater. Res. Technol.* **2021**, *15*, 2075–2087. [CrossRef]

92. Milad, A.; Ali, A.S.B.; Babalghaith, A.M.; Memon, Z.A.; Mashaan, N.S.; Arafa, S.; Md Yusoff, N.I. Utilisation of waste-based geopolymer in asphalt pavement modification and construction—A review. *Sustainability* **2021**, *13*, 3330. [CrossRef]

93. Toniolo, N.; Rincón, A.; Roether, J.A.; Ercole, P.; Bernardo, E.; Boccaccini, A.R. Extensive reuse of soda-lime waste glass in fly ash-based geopolymers. *Constr. Build. Mater.* **2018**, *188*, 1077–1084. [CrossRef]

94. Rosas-Casarez, C.A.; Arredondo-Rea, S.P.; Gómez-Soberón, J.M.; Alamaral-Sánchez, J.L.; Corral-Higuera, R.; Chinchillas-Chinchillas MD, J.; Acuña-Agüero, O.H. Experimental study of XRD, FTIR and TGA techniques in geopolymeric materials. *Int. J. Adv. Comput. Sci. Appl* **2014**, *4*, 221–226.

95. Al Bakri, A.M.; Kamarudin, H.; Bnhussain, M.; Nizar, I.K.; Rafiza, A.R.; Zarina, Y. The processing, characterisation, and properties of fly ash based geopolymer concrete. *Rev. Adv. Mater. Sci.* **2012**, *30*, 90–97.

96. Xiao, S.; Cai, Y.; Guo, Y.; Lin, J.; Liu, G.; Lan, X.; Song, Y. Experimental Study on Axial Compressive Performance of Polyvinyl Alcohol Fibers Reinforced Fly Ash—Slag Geopolymer Composites. *Polymers* **2021**, *14*, 142. [CrossRef]

97. Korniejenko, K.; Kejzlar, P.; Louda, P. The Influence of the Material Structure on the Mechanical Properties of Geopolymer Composites Reinforced with Short Fibers Obtained with Additive Technologies. *Int. J. Mol. Sci.* **2022**, *23*, 2023. [CrossRef]

98. Chen, X.; Zhou, M.; Shen, W.; Zhu, G.; Ge, X. Mechanical properties and microstructure of metakaolin-based geopolymer compound-modified by polyacrylic emulsion and polypropylene fibers. *Constr. Build. Mater.* **2018**, *190*, 680–690. [CrossRef]

99. Hemalatha, T.; Ramaswamy, A. A review on fly ash characteristics—Towards promoting high volume utilization in developing sustainable concrete. *J. Clean. Prod.* **2017**, *147*, 546–559. [CrossRef]

100. Le, T.A.; Le, S.H.; Nguyen, T.N.; Nguyen, K.T. Assessment of the Rheological and Mechanical Properties of Geopolymer Concrete Comprising Fly Ash and Fluid Catalytic Cracking Residue as Aluminosilicate Precursor. *Appl. Sci.* **2021**, *11*, 3032. [CrossRef]

101. Salih, M.A.; Ali AA, A.; Farzadnia, N. Characterization of mechanical and microstructural properties of palm oil fuel ash geopolymer cement paste. *Constr. Build. Mater.* **2014**, *65*, 592–603. [CrossRef]

102. Rajini, B.; Rao, A.N.; Sashidhar, C. Micro-level studies of fly ash and GGBS–based geopolymer concrete using Fourier transform infra-red. *Mater. Today Proc.* **2021**, *46*, 586–589. [CrossRef]

103. Frydrych, M.; Hýsek, Š.; Fridrichová, L.; Le Van, S.; Herclík, M.; Pechočiaková, M.; Le Chi, H.; Louda, P. Impact of Flax and Basalt Fibre Reinforcement on Selected Properties of Geopolymer Composites. *Sustainability* **2019**, *12*, 118. [CrossRef]

104. Zhao, J.; Wang, K.; Wang, S.; Wang, Z.; Yang, Z.; Shumuye, E.D.; Gong, X. Effect of elevated temperature on mechanical properties of high-volume fly ash-based geopolymer concrete, mortar and paste cured at room temperature. *Polymers* **2021**, *13*, 1473. [CrossRef]

105. Tayeh, B.A.; Zeyad, A.M.; Agwa, I.S.; Amin, M. Effect of elevated temperatures on mechanical properties of lightweight geopolymer concrete. *Case Stud. Constr. Mater.* **2021**, *15*, e00673. [CrossRef]

106. Vogt, O.; Ukrainczyk, N.; Ballschmiede, C.; Koenders, E. Reactivity and microstructure of metakaolin based geopolymers: Effect of fly Ash and liquid/solid contents. *Materials* **2019**, *12*, 3485. [CrossRef]

107. Jamil, N.H.; Abdullah, M.M.A.B.; Pa, F.C.; Mohamad, H.; Ibrahim, W.M.A.W.; Amonpattaratkit, P.; Gondro, J.; Sochacki, W.; Ibrahim, N. Self-fluxing mechanism in geopolymerization for low-sintering temperature of ceramic. *Materials* **2021**, *14*, 1325. [CrossRef]

108. Haruna, S.; Mohammed, B.S.; Wahab, M.M.A.; Kankia, M.U.; Amran, M.; Gora, A.U.M. Long-Term Strength Development of Fly Ash-Based One-Part Alkali-Activated Binders. *Materials* **2021**, *14*, 4160. [CrossRef]

109. Zhang, H.; Li, L.; Long, T.; Sarker, P.K.; Shi, X.; Cai, G.; Wang, Q. The effect of ordinary portland cement substitution on the thermal stability of geopolymer concrete. *Materials* **2019**, *12*, 2501. [CrossRef]

110. Burduhos Nergis, D.D.; Vizureanu, P.; Sandu, A.V.; Burduhos Nergis, D.P.; Bejinariu, C. XRD and TG-DTA Study of New Phosphate-Based Geopolymers with Coal Ash or Metakaolin as Aluminosilicate Source and Mine Tailings Addition. *Materials* **2021**, *15*, 202. [CrossRef] [PubMed]

111. Irshidat, M.R.; Al-Nuaimi, N.; Rabie, M. Sustainable utilisation of waste carbon black in alkali-activated mortar production. *Case Stud. Constr. Mater.* **2021**, *15*, e00743.

112. Khan, M.; Cao, M.; Ai, H.; Hussain, A. Basalt fibers in modified whisker reinforced cementitious composites. *Period. Polytech. Civ. Eng.* **2022**, *66*, 344–354. [CrossRef]

113. Xie, C.; Cao, M.; Guan, J.; Liu, Z.; Khan, M. Improvement of boundary effect model in multi-scale hybrid fibers reinforced cementitious composite and prediction of its structural failure behavior. *Compos. Part B Eng.* **2021**, *224*, 109219. [CrossRef]

114. Khan, M.; Cao, M.; Xie, C.; Ali, M. Effectiveness of hybrid steel-basalt fiber reinforced concrete under compression. *Case Stud. Constr. Mater.* **2022**, *16*, e00941. [CrossRef]

115. Cao, M.; Khan, M. Effectiveness of multiscale hybrid fiber reinforced cementitious composites under single degree of freedom hydraulic shaking table. *Struct. Concr.* **2021**, *22*, 535–549. [CrossRef]

116. Cao, M.; Khan, M.; Ahmed, S. Effectiveness of Calcium Carbonate Whisker in Cementitious Composites. *Period. Polytechnica. Civ. Eng.* **2022**, *64*, 265. [CrossRef]

117. Zhang, N.; Yan, C.; Li, L.; Khan, M. Assessment of fiber factor for the fracture toughness of polyethylene fiber reinforced geopolymer. *Constr. Build. Mater.* **2022**, *319*, 126130. [CrossRef]

118. Öz, H.Ö.; Doğan-Sağlamtimur, N.; Bilgil, A.; Tamer, A.; Günaydin, K. Process Development of Fly Ash-Based Geopolymer Mortars in View of the Mechanical Characteristics. *Materials* **2021**, *14*, 2935. [CrossRef]

119. Kljajević, L.; Nenadović, M.; Ivanović, M.; Bučevac, D.; Mirković, M.; Mladenović Nikolić, N.; Nenadović, S. Heat Treatment of Geopolymer Samples Obtained by Varying Concentration of Sodium Hydroxide as Constituent of Alkali Activator. *Gels* **2022**, *8*, 333. [CrossRef]

120. Najm, H.M.; Ahmad, S.; Khan, R.A. Mechanical and Microstructural Analysis of Waste Ceramic Optimal Concrete Reinforced by Hybrid Fibers Materials: A Comprehensive Study. *J. Archit. Environ. Struct. Eng. Res.* **2022**, *5*, 11–33. [CrossRef]

121. Najm, H.M.; Nanayakkara, O.; Ahmad, M.; Sabri Sabri, M.M. Mechanical Properties, Crack Width, and Propagation of Waste Ceramic Concrete Subjected to Elevated Temperatures: A Comprehensive Study. *Materials* **2022**, *15*, 2371. [CrossRef]

122. Najm, H.M.; Nanayakkara, O.; Ahmad, M.; Sabri Sabri, M.M. Colour Change of Sustainable Concrete Containing Waste Ceramic and Hybrid Fibre: Effect of Temperature. *Materials* **2022**, *15*, 2174. [CrossRef]

123. Çelik, A.İ.; Özkılıç, Y.O.; Zeybek, Ö.; Özdöner, N.; Tayeh, B.A. Performance Assessment of Fiber-Reinforced Concrete Produced with Waste Lathe Fibers. *Sustainability* **2022**, *14*, 11817. [CrossRef]

124. Najm, H.M.; Ahmad, S. Effect of Elevated Temperatures Exposure on the Mechanical Properties of Waste Ceramic Concrete Reinforced with Hybrid Fibers Materials. *Sigma J. Eng. Nat. Sci.* **2021**, *in press*.

125. Aksoylu, C.; Özkılıç, Y.O.; Hadzima-Nyarko, M.; Işık, E.; Arslan, M.H. Investigation improvement in shear performance of reinforced concrete beams produced with recycled steel wires from waste tyre. *Sustainability* **2022**, *14*, 13360. [CrossRef]

126. Najm, H.M.; Ahmad, S. The Use of Waste Ceramic Optimal Concrete for A Cleaner and Sustainable Environment—A Case Study of Mechanical Properties. *Civ. Environ. Eng. Rep.* **2022**, *32*, 85–102. [CrossRef]

127. Karalar, M.; Özkılıç, Y.O.; Deifalla, A.; Aksoylu, C.; Arslan, M.H.; Ahmad, M.; Sabri, M.M.S. Improvement in Bending Performance of Reinforced Concrete Beams Produced with Waste Lathe Scraps. *Sustainability* **2022**, *14*, 12660. [CrossRef]

128. Najm, H.M.; Ahmad, S.; Submitter, Y. Artificial Neural Networks for Evaluation & Prediction of the Mechanical Properties of Waste Ceramic Optimal Concrete Exposed to Elevated Temperature. *Available SSRN* **2021**, 4032028. [CrossRef]

129. Hussein, O.H.; Ibrahim, A.M.; Abd, S.M.; Najm, H.M.; Shamim, S.; Sabri, M.M.S. Hybrid Effect of Steel Bars and PAN Textile Reinforcement on Ductility of One-Way Slab Subjected to Bending. *Molecules* **2022**, *27*, 5208. [CrossRef]

130. Najm, H.M.; Ahmad, S. The effect of metallic and non-metallic fiber on the mechanical properties of waste ceramic concrete. *Innov. Infrastruct. Solut.* **2021**, *6*, 204. [CrossRef]

131. Qaidi, S.; Najm, H.M.; Abed, S.M.; Özkılıç, Y.O.; Al Dughaishi, H.; Alosta, M.; Sabri, M.M.S.; Alkhatib, F.; Milad, A. Concrete Containing Waste Glass as an Environmentally Friendly Aggregate: A Review on Fresh and Mechanical Characteristics. *Materials* **2022**, *15*, 6222. [CrossRef] [PubMed]

132. Nanayakkara, O.; Najm, H.M.; Sabri, M.M.S. Effect of Using Steel Bar Reinforcement on Concrete Quality by Ultrasonic Pulse Velocity Measurements. *Materials* **2022**, *15*, 4565. [CrossRef] [PubMed]

Article

Experimental Evaluation of Industrial Mushroom Waste Substrate Using Hybrid Mechanism of Vermicomposting and Effective Microorganisms

Khalid Ansari [1,*], Shantanu Khandeshwar [1], Charuta Waghmare [1], Hassan Mehboob [2], Tripti Gupta [3], Avinash N. Shrikhande [4] and Mohamed Abbas [5,6]

1   Department of Civil Engineering, Yeshwantrao Chavan College of Engineering, Nagpur 441110, India; khandeshwar333@gmail.com (S.K.); charutawaghmare@gmail.com (C.W.)
2   Department of Engineering Management, College of Engineering, Prince Sultan University, Riyadh 11586, Saudi Arabia; hmehboob@psu.edu.sa
3   Department of Civil Engineering, Shri Ramdeobaba College of Engineering and Management, Nagpur 440013, India; guptatb@rknec.edu
4   Department of Civil Engineering, Kavikulguru Institute of Technology and Science, Ramtek 441106, India; dranskitsr@gmail.com
5   Electrical Engineering Department, College of Engineering, King Khalid University, Abha 61421, Saudi Arabia; mabas@kku.edu.sa
6   Computers and Communications Department, College of Engineering, Delta University for Science and Technology, Gamasa 35712, Egypt
*   Correspondence: ksansari@ycce.edu

Abstract: Mushroom waste substrates are highly resistant lignocellulosic wastes that are commercially produced by industries after harvesting. These wastes produce large environmental challenges regarding disposal and, thus, require treatment facilities. In the present article, the effect of *Eisenia-fetida*-based vermicomposting and an effective microorganism solution on the mushroom waste substrate were investigated using four different composting mixtures: mushroom waste [MW] substrate composting with effective microorganisms [MW+EM], raw mushroom waste [RWM] substrate composting with effective microorganisms [RMW+EM], mushroom waste substrate composting with vermicomposting and effective microorganisms [MW+V+EM], and raw mushroom waste substrate composting with vermicomposting and effective microorganisms [RWM+V+EM]. This article discusses the structural and physiochemical changes at four samples for 45 days (almost six weeks) of composting. The physical and chemical parameters were monitored during composting and provided information on the duration of the process. The results indicated pH (7.2~8), NPK value (0.9~1.8), and C:N ratio < 14, and heavy metals exhibited a decreasing trend in later stages for all sets of compost materials and showed the maturity level. FTIR spectra revealed that all four samples included peaks for the -OH (hydroxy group) ranging from 3780 to 3500 cm^{-1} and a ridge indicating the C=C (alkenyl bond) ranging from 1650 to 1620 cm^{-1} in compost. The X-ray diffraction spectrum clearly shows how earthworms and microbes break down molecules into cellulose compounds, and the average crystallinity size using Scherrer's equation was found to be between 69.82 and 93.13 nm. Based on the experimental analysis, [RWM+V+EM] accelerated the breakdown of organic matter and showed improvement compared with other composts in compostable materials, thus, emphasizing the critical nature of long-term mushroom waste management and treatment.

Keywords: mushroom waste; vermicomposting; effective microorganisms; XRD method; FTIR method

1. Introduction

Mushroom farming is a green enterprise since it recycles the waste from farms, animals, breweries, and other sources while producing fruit bodies with unique nutritional and medicinal properties [1] Every year, 6–7% more global mushroom production is grown in

over 100 countries with high-tech mechanization and automation, particularly in wealthy China (36%) as well as European (18%) and North American countries (7%). Currently, mushroom farming in India is growing 30–40% annually [2]. Wheat straw, soybean straw or paddy, and other agricultural wastes are valuable residues of edible mushroom production described in Table 1. Mushroom substrates generate almost 1–2 tonnes of waste for every tonne of mushrooms collected [3] and are generally disposed of in landfills, which causes eutrophication of the surface water basins through nutrient leaching or composted after mushroom harvest [4] as well as commonly disposed of through open burning, producing airborne hazards [5–14].

Table 1. Various crop residues used in mushroom production.

Strains	Residues	References
Agaricus bisporus	wheat straw residues and rice straw and hulls.	[15,16]
Pleurotus sp.	soybean straw, coffee pulp, corn fibre, cottonseed hulls, groundnut shells, and maize straw.	[17]
Volvallella	paddy straw; coconut fibre, coir, and husks; cotton waste; and barley straw.	[18,19]
Ganoderma	sawdust, jowar leaves, sugar cane bagasse, and cottonseed hulls.	[20]

As a result, mushroom waste contains high concentrations of salts and organics, which cause numerous environmental issues and are difficult to handle and dispose of using traditional disposal and burning methods, which is again improper and unsupervised. In recent years, ecological restrictions have increased the pressure on mushroom producers, underlining the essential need for a more suitable means of disposing of waste, which includes direct application to the soil as a bioremediation agent and animal and fish feed [3,4]. On the other hand, composting can be a suitable technology that is a cost-effective and environmentally friendly option for disposing of mushroom waste [6]. It is a biological process (agricultural waste disinfectant turned into a corresponding and usable flora matter) that occurs in the presence of sufficient oxygen, humidity, and temperature [7].

In composting, microorganisms generate heat, and a solid substrate is converted into less carbon and nitrogen. This method is time-consuming. For different quality organic wastes, frequently aeration is required, which depends on the ingredients [4–8]. Earthworm-based composting (vermicomposting) can decompose organic waste to produce odourless humus-like substances that are beneficial to the environment, according to the scientific literature in recent years [7–10]. Vermicomposting is a key biotechnological composting technology in which various earthworms are adapted to improve the waste conversion process [11–14], combining an advanced microbe technology with a vermicomposting approach, such as effective microorganism technology, can reduce the time required and shows the stability and maturity of the product.

Effective microorganism (EM) technology is a method for the natural agricultural protection of live microorganism communities isolated from naturally rich soils and used as a by-product to improve the earth's biodiversity, resulting in increased agricultural yields. The most crucial effective microorganisms are *Lactobacillus plantarum*, *Lactobacillus casei*, *Streptococcus lactis*, *Rhodopseudomonas palustris*, *Rhodobacter spaeroides*, *Streptomyces albur*, *Mucorhiemalis*, and *Aspergillus oryzae* [6]. These include lactic acid bacteria, which is a powerful sterilizing ingredient that suppresses pathogenic germs and accelerates the degradation of organic material [9,10].

With the rapid generation of mushroom waste, it can be valorized for agricultural applications in terms of compost, which in turn increases the soil mineral nitrogen, specifically nitrate (NO_3^-) and ammonia (NH_3), making it an excellent soil conditioner and natural soil insecticide [21–39]. Researchers have focused on new and alternative energy resources derived from the mushroom waste substrate, which includes vast amounts of lignocellulosic components, such as cellulose, hemicellulose, and lignin that can be converted to bio-oils using modern heating technologies [39].

Thus, the objective of this research is to evaluate the composting process by examining the transformation of mushroom waste and raw mushroom waste substrates into mature and stable compost by using the effective microorganism alone and hybrid mechanism of vermicomposting and effective microorganisms concerning temporal and physicochemical characteristics associated with the structural behaviour during compost development.

2. Materials and Methods

2.1. Mushroom Waste Substrates Collection

Mushroom waste (MW) substrates are the waste materials collected from the mushroom industry at nearly two months after harvesting, and they are dried and stored for ten days. In contrast, raw mushroom waste substrates (RMW) are the materials harvested at one to two days that are dried and stored for ten days. For the partial decomposition, both wastes were kept at an ambient temperature of (25~30 °C) with relative humidity (60~90%), consisting of a mixture of wheat straw (*Agaricus bisporus*) and soybean straw (*Pleurotus* sp.) ranging from 1.0 to 5.0 cm, which was brought in a plastic container from Balaji Farms Pvt. Ltd. in Khond Hali, Wardha, Nagpur, India. Prior to the experimental trial, both waste products were sliced and sieved to a particle size of 0.6~0.9 mm to increase the material's homogeneity and digestion by earthworms. The initial chemical characteristics of the materials are presented in Table 2.

Table 2. Initial characteristics of the materials used for the experiment.

Parameter	Mushroom Waste (MW)	Raw Mushroom Waste (RMW)	Cow Manure
pH	7.3	7.9	9.3
TOC%	40.02	38.23	34.60
C:N ratio	39.80	38.05	45.62
MC%	55.80	54.90	58.6
N%	0.71	0.64	2.88
P%	0.19	0.22	0.32
K%	1.35	1.18	1.91

TOC: Total Organic Carbon, C:N ratio: Carbon/Nitrogen ratio, MC: Moisture Content, N: Nitrogen, P: Phosphorous, and K: Potassium.

2.2. Activation of Effective Microorganisms (EM)

The EM solution is activated using the Bokashi method (EM-1® solution, jaggery, and water). Jaggery is a lump of non-centrifugal cane sugar that has been consumed in India and Southeast Asia for centuries, containing up to 50% sucrose, 20% invert sugar, and 20% moisture, and the remainder consisting of different insoluble substances, such as wood ash, proteins, and bagasse fibres [4–6]. To activate the EM solution before usage, a dormant EM-1® solution, roughly 1000 mL, was mixed in an airtight container with 2 kg jaggery and 20 Liters of distilled water. It was then stored at room temperature for 8 to 10 days, away from direct sunlight, and absorbed actinomycetes during activation at the top of the surface with a pleasant smell and a pH below 3.3~3.5. [15].

2.3. Earthworms Culture

Eisenia-fetida (earthworms' species) were obtained from Sath Company, Narendra Nagar, Nagpur, India. Earthworms were brought in with a quantity of 1.5 kg; weight between 0.5 and 1 g, their length between 2 and 4 cm, and their breadth between 1 and 2 mm. They were maintained using 3 kg cow manure and 1 kg of soil as a culture medium for 15 days in a container with mechanical aeration, with a moisture content of 55% to 65%, and a pH for earthworm survival ranging between 7.0 and 7.6. The C:N ratio was maintained at less than 20, to provide favourable environmental conditions for earthworms.

2.4. Experimental Set Up

Four experiments were conducted under aerobic conditions, using rectangle glass jars (with dimensions of 300 × 450 × 560 mm) and a top opening with a 1 cm small orifice opening on each side of the jar for drainage as shown in Figure 1.
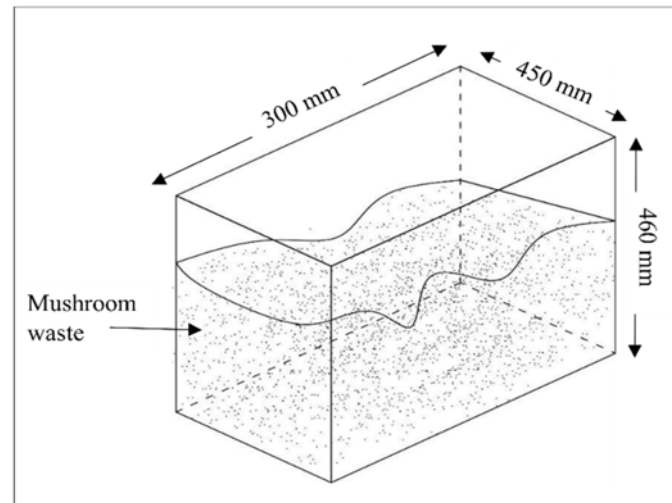

Figure 1. Illustrated diagram of a rectangular glass jar.

2.4.1. Effective Microorganism Design

Figure 2 shows set-up 1, which consisted of 10 kg of mushroom waste [MW] substrate on a dry weight basis in a glass jar and was served in four layers at a depth of 100 mm, with 240 mL (60 mL on each layer) of activated EM solution and 4000 mL (1000 mL on each layer) of water spread over the layers. After every three days, the container of waste substrates was opened for aeration and to maintain its moisture content of approximately 50–60% by periodically sprinkling an adequate quantity of water [6]. The same replicates were prepared with raw mushroom waste in set-up 2, as shown in Figure 3.
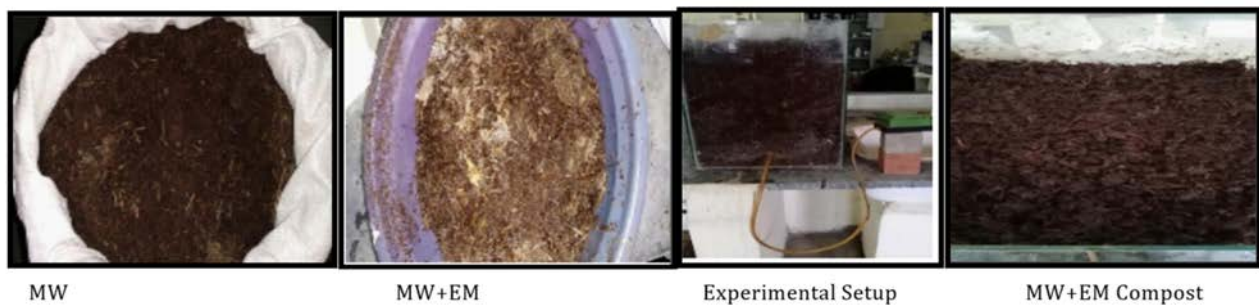
Figure 2. Set up 1 shows the images of mushroom waste with EM [MW+EM].
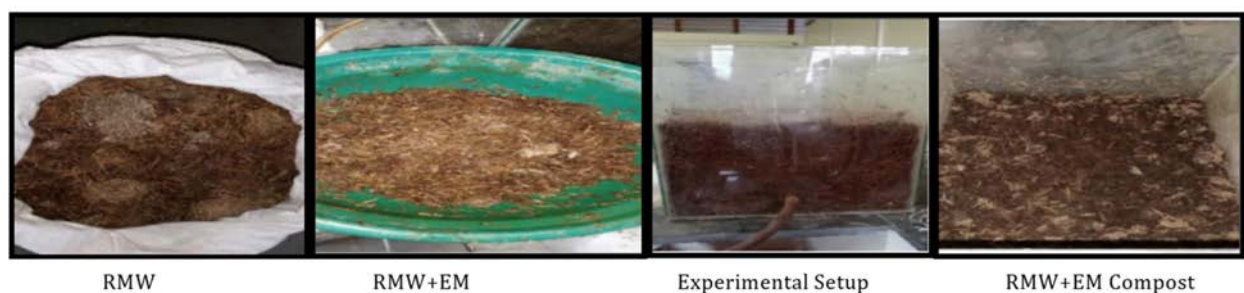
Figure 3. Set up 2 shows the images of raw mushroom waste with EM [RWM+EM].

2.4.2. Vermibed Design

Figure 4 shows set-up 3, which consisted of 10 kg of mushroom waste [MW] substrate on a dry weight basis in a glass jar and was served in four layers at a depth of 100 mm, with 240 mL (60 mL on each layer) of activated EM solution and 4000 mL (1000 mL on each layer) of water spread over the layers. 40 healthy earthworms (10 in each layer), approximately 4–6 cm in length and (1.5–3) g in weight, were introduced after 15 days of partial decomposition of wastes substrates, and 3 kg of cow dung was mixed in a container. The container of waste substrates was aerated every three days, and its moisture content was maintained at around 50 to 60% by spraying a suitable amount of water regularly [6]. The same replicates were created in set-up 4 with raw mushroom waste, as indicated in Figure 5.

MW+EM+ Eisenia-fetida   MW+EM+ Earthworms+ Cow dung   Experimental Setup   MW+V+EM Final Compost
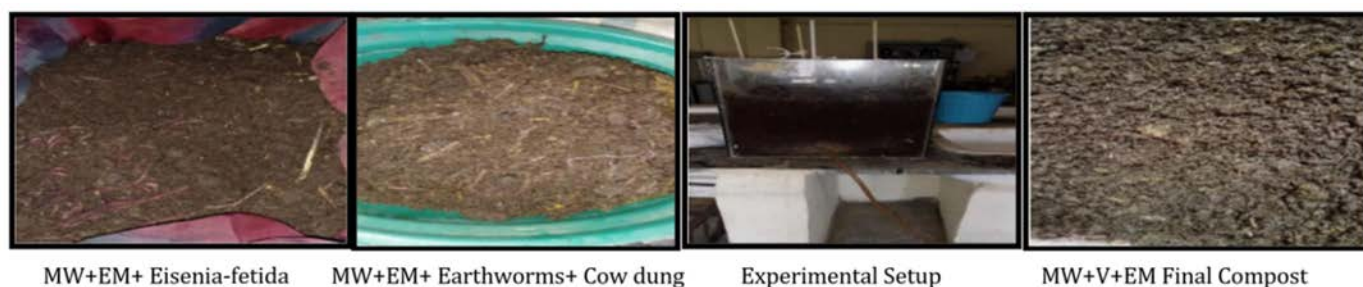
Figure 4. Set up 3 shows the images of mushroom waste with vermicomposting and EM [MW+V+EM].

RWM +EM+ Eisenia-fetida   MW+EM+ Earthworms+ Cowdung   Experimental Setup   RMW+V+EM Final Compost
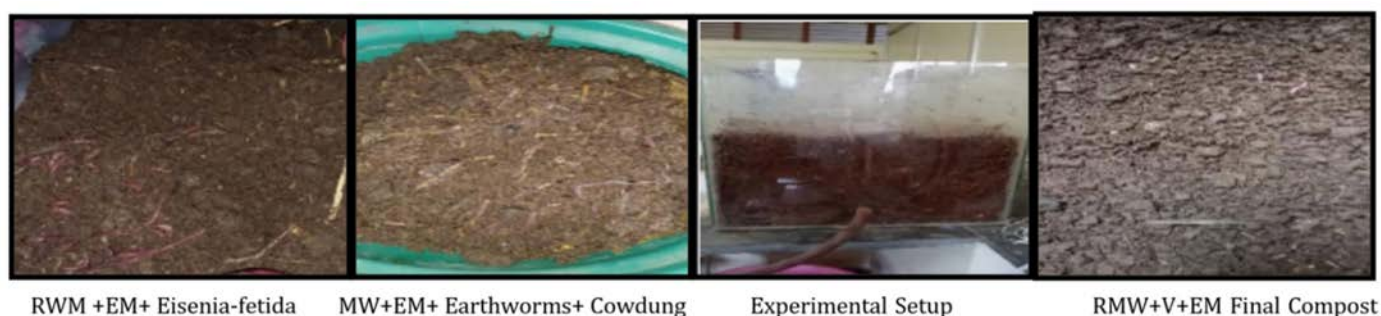
Figure 5. Set up 4 shows the images of raw mushroom waste with vermicomposting EM [RMW+V+EM].

The experiments lasted for 6 weeks with the completion of compost of each set of an experimental container, and the examined samples were dried in an oven at 60° C for 48 h, pulverized in a stainless-steel mixer, and stored in sterilized plastic containers [7]. The glass jar was covered with jute cotton cloths to prevent moisture loss and direct sunlight. The details of each set (1 to 4) from raw waste to compost are shown in Figures 2–5, respectively.

2.5. Physico-Chemical Analysis

It is critical to assess mixed and homogeneous compost's quality, maturity, and nutrient content before deciding on its potential uses. Based on the experimental analysis, each compost (50 g) sample was taken every week and was homogenously mixed for analyses of pH, temperature, odour, colour, C:N ratio, and changes in humic acid. The preparation of pH was done with 1 g of compost and 5 mL of distilled water and checked in pH digital electrode meter after every three days [11]; the temperature was checked regularly at an interval of three days with the thermometer at a depth of 60% from the top at three different zones of the jar, colour and odour were observed every three days interval visually and smelling [4].

The Hach TOC Bio-Tector B3500 C (HACH, Loveland, CO, USA) was used to assess The Total Organic Carbon (TOC) concentrations in pulverized dry materials. The micro-kjeldahl technique was used to determine The Total Nitrogen (TN). The C:N ratio was calculated as TOC/TN. The concentration of NPK was determined using Spectroquant test kits using soluble potassium (K_2O), and soluble phosphate (P_2O_5) were analysed photometrically. Solution reagents were put in test kits [11], and heavy metals like Fe, Cu, and Zn were determined using standard procedures using atomic absorption spectroscopy (SYSTRONICS, Ahmedabad, India) [3,11].

The structure of humic acids and structural changes induced in a crystalline composting material was characterized by FTIR and XRD analysis performed at the Chemistry Department of Nagpur University (Nagpur, India). Samples from each set of composting after 6 weeks were oven-dried and coarsely pulverized for X-ray diffraction analysis using an X-ray diffractometer (Philips PRO model) (Philips, U.K) equipped with a copper length anticathode and operated with radiations (λ = 1.5406 A°) with data capturing angles of (2θ) [16].

The Crystallinity size (D in nm) was calculated by Scherrar Equation [22].

$$D = [(K\,\lambda)/(\beta.\cos\theta)] \tag{1}$$

where D = crystallites average size (nm),
    K = Scherrer's constant (0.94 for spherical crystals shape),
    λ = wavelength of radiation (0.1546 nm),
    β = FWHM (in radian) full width at half maximum intensity,
    θ = Bragg angle at peak position = 2θ (in radian)

FTIR spectra were identified using a (Bruker Vertex 70 spectrometer model) (Bruker, UK) with OPUS 6.5 software for data manipulation and statistical analysis equipped with attenuated total reflection (ATR). A 5 mg of each sets samples were oven-dried and grounded with a spectroscopic grade of KBr in (1:100) ratio with scanning range of 4000–400 cm^{-1} at a rate of 0.5 cm/s [3] to ascertain the behavior of humic acids and visualize both their infinitesimal structure and their microscopic environment.

2.6. Statistical Analysis

The significant difference between the initial and final compost results for the parameters was investigated using one-way ANOVA. A Tukey's *t*-test was used to analyse the data, and all values are reported as the mean ± SE. For the tests, the probability thresholds utilized for statistical significance were $p \leq 0.05$.

3. Results and Discussion

3.1. Temperature

Temperature is a very important environmental factor that specifies the metabolic intensity and organic waste changes during microorganism activity [17,22]. Each set increased rapidly and gradually over the first few days, i.e., during the first and second weeks of the composting process, peaking between 42 and 55 °C, indicating the development and metabolic activity of the microbial community within the compost quantity, and then decreasing to an ambient temperature of (25–33) °C.

This demonstrates that the [MW+V+EM] (56.2 °C) and [RMW+V+EM] (58.3 °C) samples reached the thermophilic stage (>45 °C) and lasted for 12–14 days, in comparison to the [MW+EM] (50 °C) and [RMW+EM] (52 °C) samples, which reached the thermophilic stage (>45 °C) and lasted for 8–10 days, as shown in Figure 6a, which shows that the EM maintained the minimum requirement of thermophilic stages in all the sets and due to aeration effects, higher biodegradation activity is possible during the loading period [8] in the feedstock via the heat generated by the microorganism population's respites, and substrate breakdown is possible [1–3]. Again, it was seen that the temperatures of all the sets began to drop at the beginning of the third week, suggesting the maturity of the organic

matter as demonstrated by the mass reduction in compost volume and odour emission as well [15].
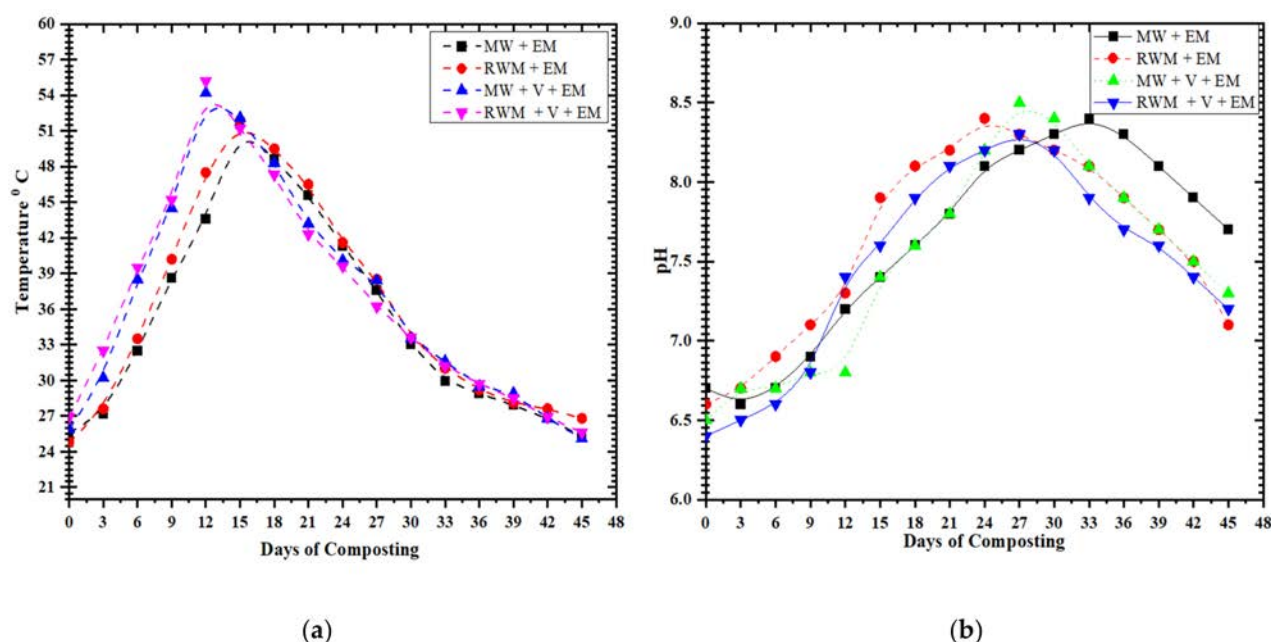

Figure 6. Variation of temperature (**a**) and pH (**b**) changes during composting days.

3.2. pH and Odour

As seen in Figure 6b, the pH increase in all four sets of samples from the acidic original compost during the initial days and turned to neutral and alkaline (pH > 8), which results in the microbial activity converting organic acid to CO_2, suggesting that the organic matter was stable [10,26], and this had an unusual odour. According to researchers, the appropriate scale for high-quality compost is between pH 6 and 8.5 [25]. Composts made from vermibed waste, such as [MW+V+EM] and [RMW+V+EM], gradually lost pH in comparison to [MW+EM] and [RMW+EM], owing to CO_2 and the loss of organic acids due to ammonia volatilization during composting [23]. Additionally, it was observed that the pH values of all substrates decreased after the fourth week of composting, which could be due to the biochemical properties of organic acids resulting in an increase in the microbial population, which results in increased manure development, and the pH slightly approaches neutrality [38].

Composting generated odour in all four sets, which indicates the presence of organic waste and other metabolic products produced entirely aerobically and anaerobically [1,31], thereby, increasing and upgrading the bacterial population responsible for decomposition in organic matter during composting, as well as providing a beneficial environment [24–28]. In addition, we observed that the unpleasant smell associated with the composting decreased over time due to the degradation of the material [27,29]. In addition, [MW+V+EM] and [RMW+V+EM] produced an earthy smell in a shorter time due to the capability of earthworms for bioconversions of the substrate to compost compared with [MW+EM] and [RMW+EM].

3.3. C:N Ratio

As illustrated in Figure 7, the carbon to nitrogen ratio had the most significant effect on the composting maturity efficiency [30,31]. According to present research, the carbon-to-nitrogen ratio final reductions in each set of composters with 77% in RMW+V+EM were slightly greater than 69% in MW+V+EM, which is significantly more than in the composters

consisting of 59% RWM+EM and 55% MW+EM, which may be due to organic conditions composed of inorganic metabolizable components [7].
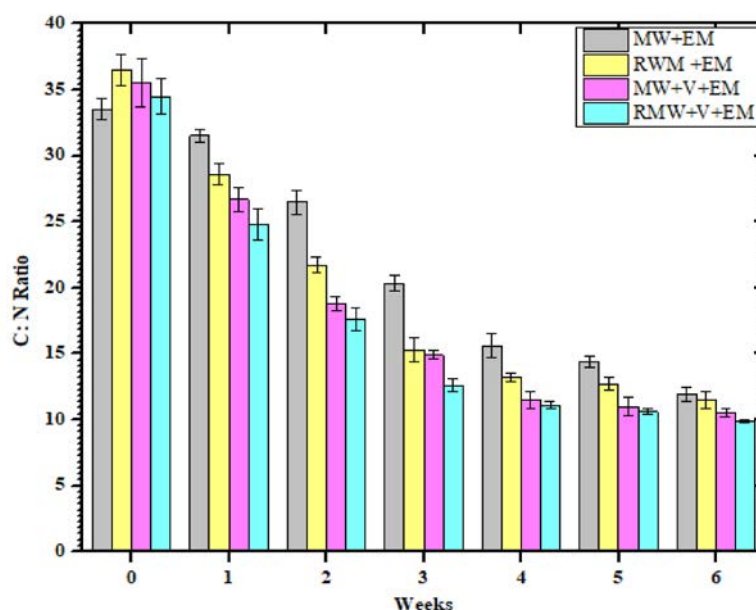
Figure 7. Variation of the C:N ratio within different weeks of [MW+EM], [RMW+EM] [MW+V+EM] and [RMW+V+EM]. Error bars represent standard errors for six samples.

Within the first four weeks, the carbon-to-nitrogen ratio of all EM-treated samples decreased significantly as carbon was primarily evaluated as carbon dioxide, while nitrogen was lost via volatilization [35] and showed maturity and phytotoxic by the competition of 6 weeks. According to experts [32], the C:N balance should be at least 20 for optimal quality and mature compost. The C:N ratio did not differ more between composts with and without earthworms (*Eisenia-fetida*), indicating that the degradation rate was similar in all situations.

3.4. Heavy Metals

After the end of the composting process, the vermicomposting sets of containers showed a significant ($p < 0.05$) increase in the metal content, as shown in Figure 8a–c. The accumulation of heavy metals, such as iron (Fe) and manganese (Zn), in [RWM+V+EM] and [MW+V+EM] ($p < 0.05$) was due to metal bioaccumulation in earthworm tissues, which accelerates the decomposition rate due to a higher temperature of 54 °C. The additionally effective microorganisms were responsible for the breakdown of organic waste and enhanced humification process indicating that the compost had matured [6,37]. The same was observed for [MW+EM] and [RWM+EM] with a slow pace of increase, whereas copper (Cu) ($p < 0.05$) decreased proportionately with time for all sets of samples displaying that the available waste particles were converted into useless small particles as a result of earthworm and microorganism activity [37].

Indirectly, these findings support that heavy metal removals, such as (Cu and Zn) use of show a maturity limit of compost sets for in EU countries {for Cu (mg/kg), the limit range is 70~600 and for Zn (mg/kg), the limit range is 210~4000} and for the USA (for Cu (mg/kg), the limit range is 1500 and for Zn (mg/kg), the limit range is 2800) [39]. Heavy metals, such as Fe, Zn, and Cu are micronutrients that are critical for plant growth and rapidly rise and fall during the composting process, thus, indicating the compost's development.
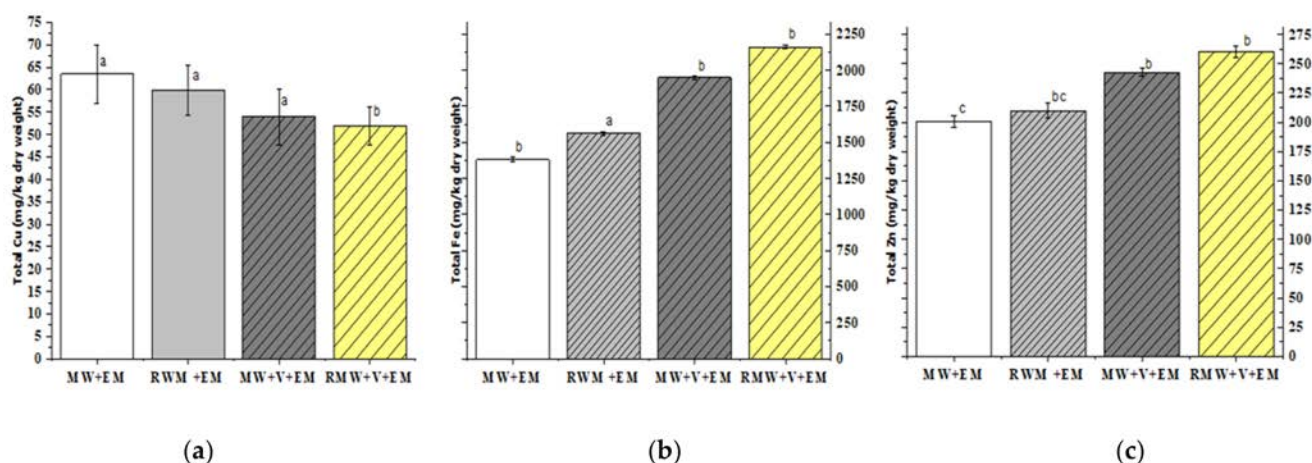
Figure 8. The total concentrations of Cu (**a**), Fe (**b**), and Zn (**c**) of [MW+EM], [RMW+EM], [MW+V+EM], and [RMW+V+EM]. Error bars represent the standard errors for six samples. Columns followed by the same letter do not differ significantly (ANOVA; Tukey's test, $p < 0.05$).

3.5. Evaluation of NPK

Other key components, nitrogen, phosphorus, and potassium (NPK), as illustrated in Figure 9, revealed that adding EM solution to the compost samples boosted their value. The nitrogen contents of [MW+EM] and [RMW+EM] were significantly higher in this study than in [MW+V+EM] and [RMW+V+EM], owing to the usage of nitrogen by microbes to create cells that operate as nitrogen-fixing biological organisms throughout the compost growth process. The total nitrogen concentrations should generally range between 1% and 3% by dry weight [4]. The statistics ($p < 0.05$) indicate that EM and vermicomposting had a good effect, with desired values ranging from 0.9% to 1.8%for each of the four samples.
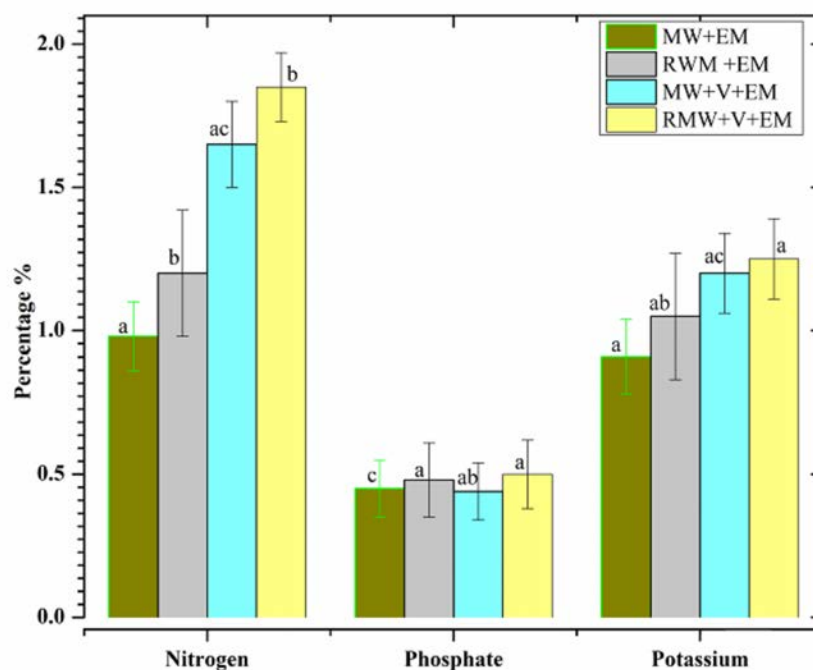
Figure 9. The total concentrations of the NPK values of [MW+EM], [RMW+EM], [MW+V+EM], and [RMW+V+EM]. Error bars represent standard errors for six samples. Columns followed by the same letter do not differ significantly (ANOVA; Tukey's test, $p < 0.05$).

Phosphorus is a vital nutrient, and the available phosphate is fine-tuned by Fe^{3+} and Al^{3+} ions in an acidic environment. The results suggest that the phosphorous nutrient statistic ($p < 0.05$) decreased somewhat with or without the input of earthworms, with a range of around 0.43% to 0.5%. Potassium is required to form proteins and carbohydrates and to regulate di-hydrogen monoxide levels during culture. The findings of potassium levels in [MW+EM] and [RWM+EM] indicate that the compost was substantially more potent than [MW+V+EM] and [RWM+V+EM], as earthworms added microbial-mediated nutrient mineralization to the final product. Overall, the NPK values suggest that earthworms and efficient microbial activities are necessary for optimal nutrient absorption.

3.6. FTIR

The FTIR analysis of the mushroom waste substrate compost samples was used to examine the existence or absence of a functional group, as well as the degradation or stabilization process. The FTIR study indicated changes in the material characteristics for [MW+EM], [RWM+EM], [MW+V+EM], and [RWM+V+EM] to demonstrate the variance in the IR spectroscopic bands, as seen in Figure 10. The ranges [MW+EM] at 3392.56 cm^{-1}, [RMW+EM] at 3320.27 cm^{-1}, [MW+V+EM] at 3361.52 cm^{-1}, and [RMW+V+EM] at 3326.98 cm^{-1} reflect the hydroxy group, H-bonded OH stretch, and robust, wide absorption intensity, respectively.

Due to the inadequate absorption intensity of band 2397.54 cm^{-1} in [MW+EM] and 2349.12 cm^{-1} in [MW+V+EM], the existence of a terminal alkyne (monosubstituted) molecule was detected. The alkenyl C=C stretch resulted in a medium absorption rate (C=C in the aromatic region) at 1633.62 cm^{-1}, 1629.89 cm^{-1}, 1640.33 cm^{-1}, and 1633.62 cm^{-1} in [MW+EM], [MW+V+EM], [RMW+EM], and [RMW+V+EM], respectively. The bands at 1090.74 cm^{-1} in [MW+EM], 1099.97 cm^{-1} in [RMW+EM], and 1089.54 cm^{-1} in [MW+V+EM] and 1089.64 cm^{-1} in [RMW+V+EM] correspond to a secondary alcohol—a C-O stretch molecule with a dynamic molecular structure.

The bands at 541.73 cm^{-1}, 549.19 cm^{-1}, 552.17 cm^{-1}, and 545.46 cm^{-1} in [MW+EM], [MW+V+EM], [RMW+EM], and [RMW+V+EM], respectively, indicate Aliphatic Bromo compounds—a C-Br stretch with a high absorption intensity [15,28]. The presence of an aromatic region indicates that stable compounds are being formed. Ultimately, these results reveal that the increasing lowering of peaks over the composting days reflects the modifications presented in the structural components via the activity of effective microorganisms [28].
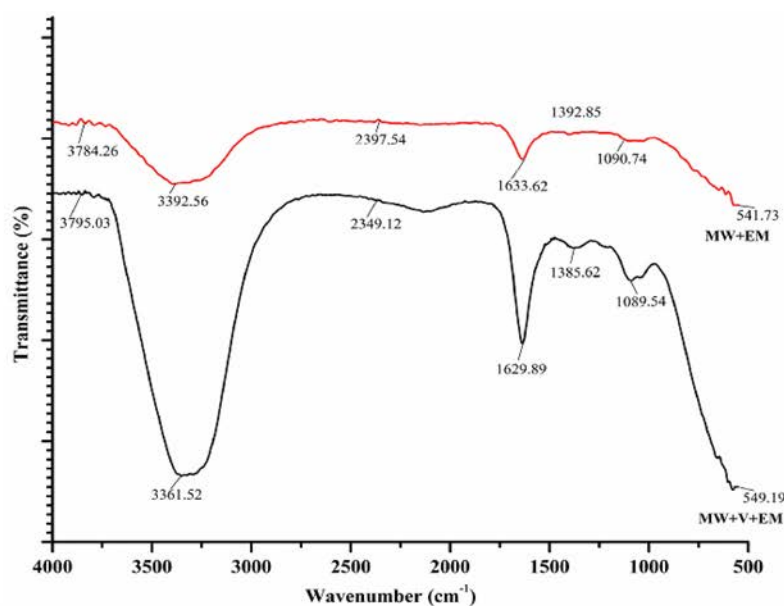
Figure 10. *Cont.*
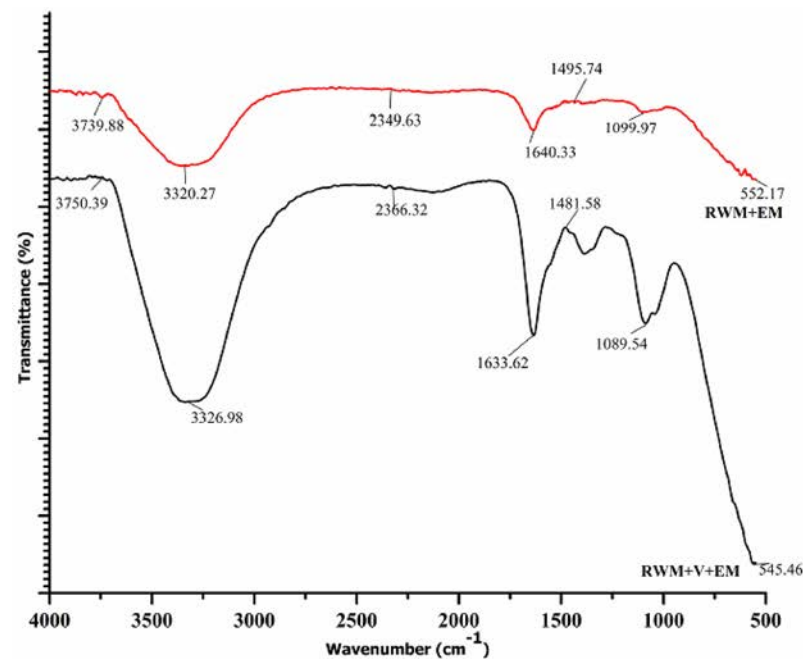
Figure 10. Variation of FTIR of the samples: [RWM +EM], [MW+EM], [MW+ V+EM], and [RWM+V+EM].

3.7. X-ray Diffraction Analysis

X-ray diffraction is a supplementary approach for deciphering a compound's structural features. Figure 11 shows changes in the peak heights for all XRD signals representing crystal planes from 10 to 70 diffraction angles, which illustrates the spectroscopy of various mushroom waste substrates composting samples, such as (a), (b), (c), and (d) collected after completion of six weeks, indicating a decrease in the number of peaks levels due to an increase in decomposition processes and indicating the formation of ready manure.
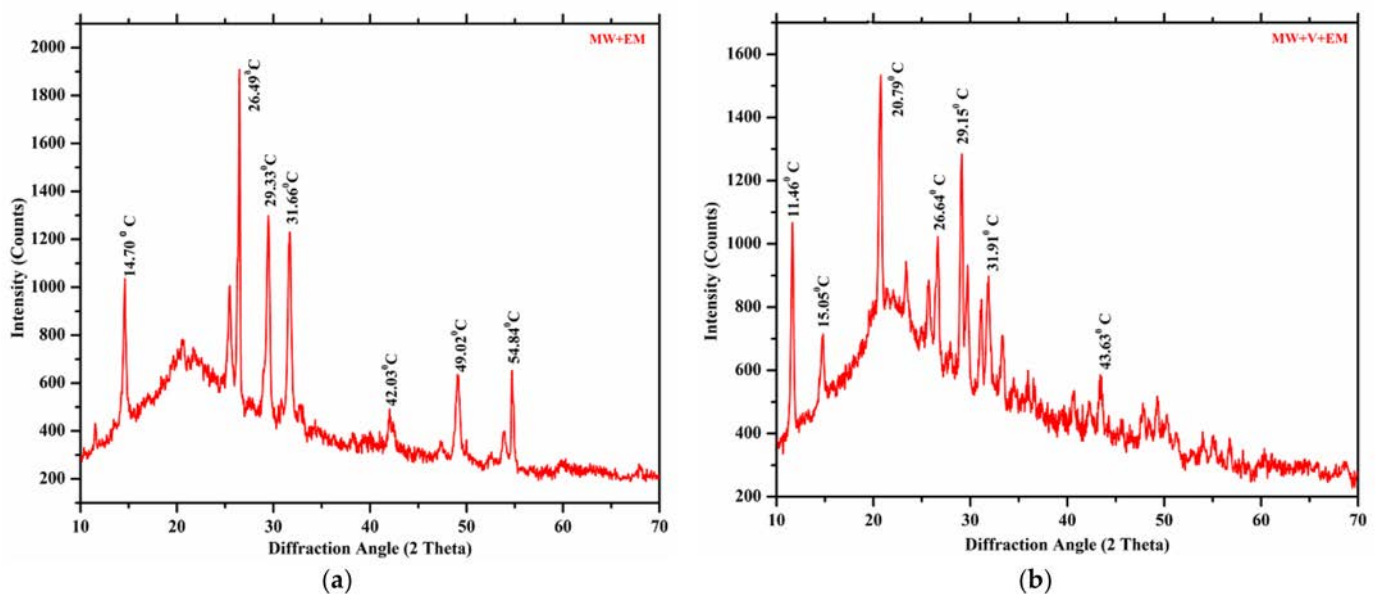
Figure 11. *Cont.*
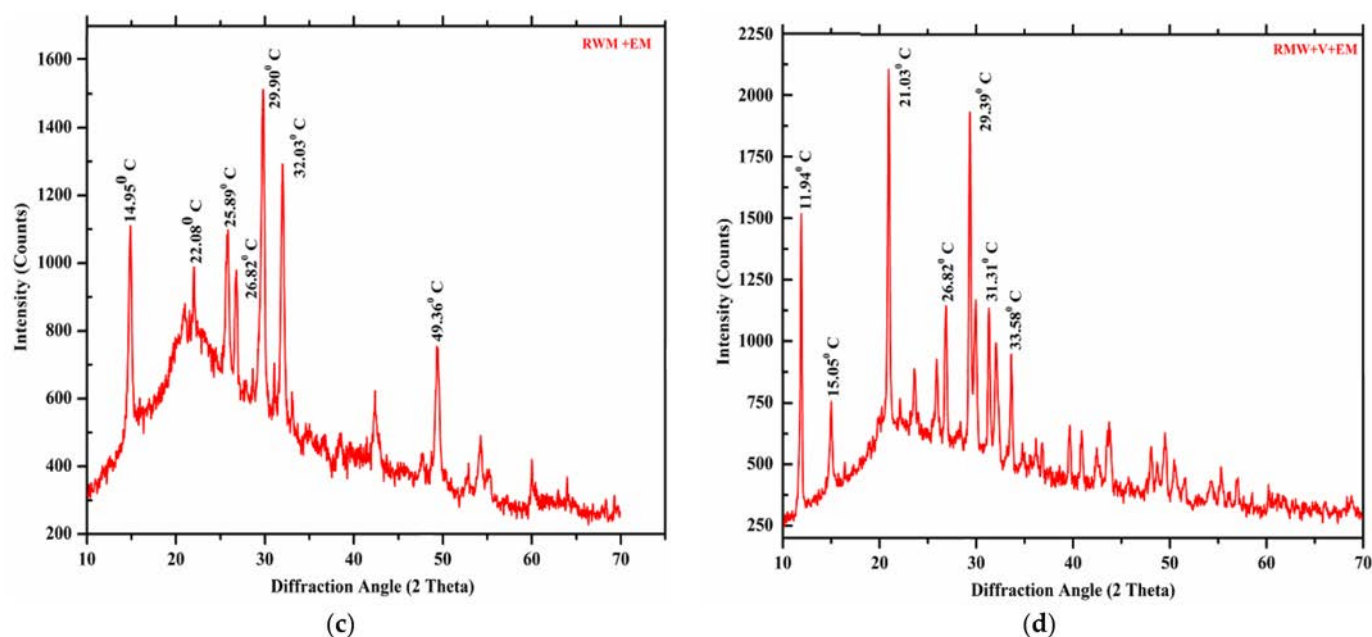
Figure 11. XRD analysis of the sample (**a**) [MW+EM], (**b**) [MW+V + EM], (**c**) [RWM+EM], and (**d**) [RMW+V+ EM].

The findings showed that [RWM+V+EM] and [MW+V+EM] have acute peaks appearing at 2θ of 21.03 and 20.79, respectively, in the early stages, indicating a decrease in the C:N ratio and thus a reduction of cellulose compounds, which results in the destruction of hydrogen bonds and is easily destroyed [28], whereas [RMW+EM] and [MW+EM] had sharp peaks appearing at 2θ of 29.90 and 26.49, respectively, related to the crystalline nature of cellulose. The X-ray diffraction technique used in Equation (1), to calculate the cross-sectional dimension of cellulose crystallites, and Scherrer's equation is useful for approximating the crystallite size.

The data in Table 3 demonstrate that, according to the results of the FWHM measurement, the crystallite size of [MW+EM], [RWM+EM], [MW+V+EM], and [RWM+V+EM] are 93.13, 86.52, 72.43, and 69.82 nm, respectively. It has been found that crystallinity plays a significant role in the mechanical and physical properties, which results in the strength and stiffness of the cellulose fibres [35–39]. Lastly, the XRD spectrum indicates that the particle size of mushroom waste substrates reduced during the decay phase of the compost material. In a nutshell, the XRD data showed that all composting samples generated cellulose, which was attributed to the presence of earthworms and microbiological activity [40–50].

Table 3. Seven averages of the cellulose peaks used to calculate the crystallinity size.

Samples	Average β = FWHM (in Radian)	Average 2θ (in Radian)	Average Crystallinity Size (nm)
MW+EM	0.4269	30.38	93.13
RWM+EM	0.4861	28.71	86.52
MW+V+EM	0.5194	25.51	72.43
RWM+V+EM	0.5376	24.16	69.82

3.8. Duration and C:N Ratio: Comparison with Other Studies

Table 4 shows the results of the previous and present study's treatment of mushroom waste substrate compared to other vermicomposting using earthworm species. The present study demonstrates the effectiveness of duration, the C:N ratio, and the rapid development of mature and stable compost, which opens a new method that can reduce the volume of cumulative waste in the environment [51–57].

Table 4. Comparative results of the mushroom waste compost.

Treatment of Mushroom Waste	Earthworm Species	Manure	Duration (Time)	C: N Ratio	References
Vermicomposting	*Lumbricus rubellus*	Cow Dung	10 Weeks	8.9 *	[1]
Vermicomposting	*Eisenia-fetida*	Cow Dung	12 Weeks	6.67 *	[11]
Vermicomposting	*Lumbricus rubellus*	Goat Manure	20 Weeks	6.39 *	[30]
Vermicomposting	*Eisenia-fetida*	Cow Dung	75 Days	11.97	[35]
Vermicomposting	*Eisenia-fetida*	Pig Dung	Four Month	10.43 *	[37]
Effective Microorganism + Vermicomposting	*Eisenia-fetida*	Cow Dung	6 Weeks	10.2 *	[PS]

* Highlight the best quality of compost with Statistically (ANOVA $p < 0.05$), [PS] Present Study.

4. Conclusions

A composting experiment was conducted on mushroom waste substrate and raw mushroom waste substrate with the application of effective microorganisms and a hybrid method of vermicomposting and effective microorganisms over 6 weeks. The final four experimental set-ups resulted in nutrient-rich compost that improved in odour and colour and showed maturity and stability.

The compost with effective microorganisms and vermibed demonstrated an accelerated increase in N, P, and K values as well as a decrease in the C:N ratio that was slightly higher than the effective microorganisms alone with [MW] and [RMW] during the composting duration. Furthermore, infrared spectra analysis revealed that samples from compost [EM+V] included more biodegradable components than compost with [EM]. The findings of ANOVA analysis (p value < 0.05) showed that the physical and chemical parameters of both [EM+V] and [EM] composts differed significantly.

The XRD technique demonstrated the breakdown of complicated compounds into simpler components indicating cellulose degradation, and hence, based on an average crystallinity size of 69.82 nm, [RWM+EM+V] proved the accelerated maturity level of compost compared with others. Overall, the study approach suggested that a rapid composting mechanism is possible through vermi-technology-microorganisms and could be a viable option for transforming industrial raw mushroom waste into sustainable value products.

References

1. Na, N.N.I.; Adi, A.J.; Noor, Z.M. Potential of spent mushroom substrate in vermicomposting. *Vermitechnol. I. Dyn. Soil Dyn. Plant* **2009**, *3*, 87–90.
2. Sadler, M. Nutritional properties of edible fungi. *Nutr. Bull.* **2003**, *28*, 305–308. [CrossRef]
3. Allen, D.T.; Palen, E.J.; Haimov, M.I.; Hering, S.V.; Young, J.R. Fourier Transform Infrared Spectroscopy of Aerosol Col-lected in a Low-Pressure Impactor (LPI/FTIR): Method Development and Field Calibration. *Aerosol Sci. Technol.* **1994**, *21*, 325–342. [CrossRef]
4. Van Fan, Y.; Lee, C.T.; Klemeš, J.J.; Chua, L.S.; Sarmidi, M.R.; Leow, C.W. Evaluation of Effective Microorganisms on home scale organic waste composting. *J. Environ. Manag.* **2018**, *216*, 41–48. [CrossRef]
5. Sangwan, P.S.; Swami, S.; Singh, J.P.; Kuhad, M.S.; Dhaiya, S.S. The effect of spent mushroom compost and inorganic fertilizer on yield and nutrient uptake by wheat. *J. Indian Soc. Soil Sci.* **2002**, *50*, 186–189.
6. Jusoh, M.L.C.; Manaf, L.A.; Latiff, P.A. Composting of rice straw with effective microorganisms (EM) and its influence on compost quality. *Iran. J. Environ. Health Sci. Eng.* **2013**, *10*, 17. [CrossRef]
7. Suthar, S. Vermicomposting of vegetable-market solid waste using Eisenia fetida: Impact of bulking material on earthworm growth and decomposition rate. *Ecol. Eng.* **2009**, *35*, 914–920. [CrossRef]
8. Karnchanawong, S.; Nissaikla, S. Effects of microbial inoculation on composting of household organic waste using passive aeration bin. *Int. J. Recycl. Org. Waste Agric.* **2014**, *3*, 113–119. [CrossRef]
9. Deepashree, C.; Lingegowda, J.; Kumar, A.G.; Shubha, D.P.M. FTIR Spectroscopic Studies on Cleome Gynandra Comparative Analysis of Functional Group Before and After Extraction. *Rom. J. Biophys.* **2012**, *22*, 137–143.
10. Mehmet, C.; Ergun, B.; Hakan, S.; Hilmi, T.; Ferah, Y.; Colak, M.; Baysal, E.; Simsek, H.; Toker, H.; Yilmaz, F. Cultivation of Agaricus bisporus on wheat straw and waste tea leaves based composts and locally available casing materials Part III: Dry matter, protein, and carbohydrate contents of Agaricus bisporus. *Afr. J. Biotechnol.* **2007**, *6*, 2855–2859. [CrossRef]
11. Tajbakhsh, J.; Abdoli, M.A.; Mohammadi Goltapeh, E.; Alahdadi, I.; Malakouti, M.J. Trend of physico-chemical properties change in recycling spent mushroom compost through vermicomposting by epigeic earthworms Eisenia foetida and E. andrei. *J. Agric. Technol.* **2008**, *4*, 185–198.
12. Guo, F.L.; Yang, W.J.; Wan, Z. Yield and size of oyster mushroom grown on rice/wheat straw basal substrate supplemented with cottonseed hull. *Saudi J. Biol. Sci.* **2013**, *20*, 333–341.
13. Cortina-Escribano, M.; Pihlava, J.M.; Miina, J.; Veteli, P.; Linnakoski, R.; Vanhanen, H. Effect of Strain, Wood Substrate and Cold Treatment on the Yield and β-Glucan Content of *Ganoderma lucidum* Fruiting Bodies. *Molecules* **2020**, *25*, 4732. [CrossRef] [PubMed]
14. Sharma, A.; Ganguly, R.; Gupta, A.K. Spectral characterization and quality assessment of organic compost for agricultural purposes. *Int. J. Recycl. Org. Waste Agric.* **2018**, *8*, 197–213. [CrossRef]
15. Lee, C.T. Physico-chemical and biological changes during co-composting of model kitchen waste, rice bran and dried leaves with different microbial inoculants. *Malays. J. Anal. Sci.* **2016**, *20*, 1447–1457. [CrossRef]
16. Belewu, M.A.; Belewu, K.Y. Evaluation of feeding graded levels aspergillus treated rice husk on milk yield and composition of goat. *Bull. Pure Appl. Sci.* **2005**, *24*, 29–35.
17. Berthomieu, C.; Hienerwadel, R. Fourier transform infrared (FTIR) spectroscopy. *Photosynth. Res.* **2009**, *101*, 157–170. [CrossRef]
18. Chang, Y.; Hudson, H.J. The fungi of wheat straw compost. *Trans. Br. Mycol. Soc.* **1967**, *50*, 649–666. [CrossRef]
19. Olle, M.; Williams, I.H. Effective microorganisms and their influence on vegetable production—A review. *J. Hortic. Sci. Biotechnol.* **2013**, *88*, 380–386. [CrossRef]
20. Coury, C.; Dillner, A.M. A method to quantify organic functional groups and inorganic compounds in ambient aerosols using attenuated total reflectance FTIR spectroscopy and multivariate chemometric techniques. *Atmos. Environ.* **2008**, *42*, 5923–5932. [CrossRef]
21. Rinker, D.L. *Spent Mushroom Substrate Uses. Medicinal Mushrooms: Technology and Applications*; John Wiley & Sons: Hoboken, NJ, USA, 2017; pp. 427–454.
22. Monshi, A.; Foroughi, M.R.; Monshi, M.R. Modified Scherrer Equation to Estimate More Accurately Nano-Crystallite Size Using XRD. *World J. Nano Sci. Eng.* **2012**, *2*, 154–160. [CrossRef]
23. Fogarty, A.; Tuovinen, O. Microbiological Degradation of Pesticides in Yard Waste Composting. *Microbiol. Rev.* **1991**, *55*, 225–233. [CrossRef] [PubMed]
24. Manohara, B.; Belagali, S.L.; Ragothama, S. studied decomposition pattern during aerobic composting of municipal solid waste by physicochemical and spectroscopic method. *Int. J. Chem. Tech. Res.* **2017**, *10*, 27–34.
25. Venkatesan, S.; Pugazhendy, K.; Sangeetha, D.; Vasantharaja, C.; Prabakaran, M. Fourier Transform Infrared (FT-IR) Spec-troscopic Analysis of Spirulina. *Int. J. Pharm. Biol. Arch.* **2012**, *3*, 969–972.
26. Benito, M.; Masaguer, A.; Moliner, A.; Arrigo, N.; Palma, R.M. Chemical and microbiological parameters for the character-isation of the stability and maturity of pruning waste compost. *Biol. Fertil. Soils* **2003**, *37*, 184–189. [CrossRef]
27. Hitman, A.; Bos, K.; Bosch, M.; Arjan, K. Fermentation versus Composting. Feed Innovation Services: Wageningen, The Netherlands; p. 2013.
28. Jiménez, E.I.; Garcia, V.P. Evaluation of city refuse compost maturity: A review. *Biol. Wastes* **1989**, *27*, 115–142. [CrossRef]
29. Bidlingaier, W.; Grauenhorst, V.; Schlosser, M. Chapter 11 Odor emissions from composting plants. *Waste Manag. Ser.* **2017**, *8*, 215.

30. Jamaludin, A.A.; Mahmood, N.Z.; Abdullah, N. Waste recycling: Feasibility of saw dust based spent mushroom substrate and goat manure in vermicomposting. *Sains Malays.* **2012**, *41*, 1445–1450.

31. Haug, R.T. *Compost Engineering Principles and Practice*; Technomic Publishing: Lancaster, PA, USA, 1980; Volume 655.

32. Biyada, S.; Merzouki, M.; Elkarrach, K.; Benlemlih, M. Spectroscopic characterization of organic matter transformation during composting of textile solid waste using UV–Visible spectroscopy, Infrared spectroscopy and X-ray diffraction (XRD). *Microchem. J.* **2020**, *159*, 105314. [CrossRef]

33. Martín-Olmedo, P.; Rees, R.M. Short-term N availability in response to dissolved-organic-carbon from poultry manure, alone or in combination with cellulose. *Biol. Fertil. Soils* **1999**, *29*, 386–393. [CrossRef]

34. Kumar, M.; Ou, Y.-L.; Lin, J.-G. Co-composting of green waste and food waste at low C/N ratio. *Waste Manag.* **2010**, *30*, 602–609. [CrossRef] [PubMed]

35. Purnawanto, A.M.; Ahadiyat, Y.R.; Iqbal, A. Tamad the Utilization of Mushroom Waste Substrate in Producing Vermicompost: The Decomposer Capacity of *Lumbricus rubellus*, *Eisenia fetida* and *Eudrilus eugeniae*. *Acta Technol. Agric.* **2020**, *23*, 99–104. [CrossRef]

36. Roosmalen, G.R.V.; Langerijt, J.C.V.D. Green was composting in the Netherlands. *Biocycle* **1989**, *30*, 32–35.

37. Song, X.; Liu, M.; Wu, D.; Qi, L.; Ye, C.; Jiao, J.; Hu, F. Heavy metal and nutrient changes during vermicomposting animal manure spiked with mushroom residues. *Waste Manag.* **2014**, *34*, 1977–1983. [CrossRef] [PubMed]

38. Bakari, S.S.; Moh'd, L.M.; Maalim, M.K.; Aboubakari, Z.M.; Salim, L.A.; Ali, H.R. *Characterization of Household Solid Waste Compost Inoculated with Effective Microorganisms*; Modern Environmental Science and Engineering; Academic Star Publishing: New York, NY, USA, 2016; ISSN 2333-2581. [CrossRef]

39. Mahari, W.A.W.; Peng, W.; Nam, W.L.; Yang, H.; Lee, X.Y.; Lee, Y.K.; Liew, R.K.; Ma, N.L.; Mohammad, A.; Sonne, C.; et al. A review on valorization of oyster mushroom and waste generated in the mushroom cultivation industry. *J. Hazard. Mater.* **2020**, *400*, 123156. [CrossRef]

40. Afzal, A.; AD, M.S.; Javad, A. Heat transfer analysis of plain and dimpled tubes with different spacings. *Heat Transf.—Asian Res.* **2017**, *47*, 556–568. [CrossRef]

41. Soudagar, M.E.M.; Afzal, A.; Safaei, M.R.; Manokar, A.M.; El-Seesy, A.I.; Mujtaba, M.A.; Samuel, O.D.; Badruddin, I.A.; Ahmed, W.; Shahapurkar, K.; et al. Investigation on the effect of cottonseed oil blended with different percentages of octanol and suspended MWCNT nanoparticles on diesel engine characteristics. *J. Therm. Anal.* **2020**, *147*, 525–542. [CrossRef]

42. Soudagar, M.E.M.; Afzal, A.; Kareemullah, M. Waste coconut oil methyl ester with and without additives as an alternative fuel in diesel engine at two different injection pressures. *Energy Sources Part A Recover. Util. Environ. Eff.* **2020**, 1–19. [CrossRef]

43. Labeckas, G.; Slavinskas, S.; Mažeika, M. The effect of ethanol–diesel–biodiesel blends on combustion, performance and emissions of a direct injection diesel engine. *Energy Convers. Manag.* **2014**, *79*, 698–720. [CrossRef]

44. Afzal, A.; Aabid, A.; Khan, A.; Khan, S.A.; Rajak, U.; Verma, T.N.; Kumar, R. Response surface analysis, clustering, and random forest regression of pressure in suddenly expanded high-speed aerodynamic flows. *Aerosp. Sci. Technol.* **2020**, *107*, 106318. [CrossRef]

45. Afzal, A.; Saleel, C.A.; Badruddin, I.A.; Khan, T.Y.; Kamangar, S.; Mallick, Z.; Samuel, O.D.; Soudagar, M.E. Human thermal comfort in passenger vehicles using an organic phase change material– an experimental investigation, neural network modelling, and optimization. *Build. Environ.* **2020**, *180*, 107012. [CrossRef]

46. Aneeque, M.; Alshahrani, S.; Kareemullah, M.; Afzal, A.; Saleel, C.; Soudagar, M.; Hossain, N.; Subbiah, R.; Ahmed, M. The Combined Effect of Alcohols and *Calophyllum inophyllum* Biodiesel Using Response Surface Methodology Optimization. *Sustainability* **2021**, *13*, 7345. [CrossRef]

47. Afzal, A.; Mokashi, I.; Khan, S.A.; Abdullah, N.A.; Bin Azami, M.H. Optimization and analysis of maximum temperature in a battery pack affected by low to high Prandtl number coolants using response surface methodology and particle swarm optimization algorithm. *Numer. Heat Transf. Part A Appl.* **2020**, *79*, 406–435. [CrossRef]

48. Chaluvaraju, B.V.; Afzal, A.; Vinnik, D.A.; Kaladgi, A.R.; Alamri, S.; Tirth, V. Mechanical and Corrosion Studies of Friction Stir Welded Nano Al$_2$O$_3$ Reinforced Al-Mg Matrix Composites: RSM-ANN Modelling Approach. *Symmetry* **2021**, *13*, 537. [CrossRef]

49. Nagaraja, S.; Kodandappa, R.; Ansari, K.; Kuruniyan, M.S.; Afzal, A.; Kaladgi, A.R.; Aslfattahi, N.; Saleel, C.A.; Gowda, A.C.; Anand, P.B. Influence of Heat Treatment and Reinforcements on Tensile Characteristics of Aluminium AA 5083/Silicon Carbide/Fly Ash Composites. *Materials* **2021**, *14*, 5261. [CrossRef] [PubMed]

50. Chairman, C.A.; Ravichandran, M.; Mohanavel, V.; Sathish, T.; Rashedi, A.; Alarifi, I.M.; Badruddin, I.A.; Anqi, A.E.; Afzal, A. Mechanical and Abrasive Wear Performance of Titanium Di-Oxide Filled Woven Glass Fibre Reinforced Polymer Composites by Using Taguchi and EDAS Approach. *Materials* **2021**, *14*, 5257. [CrossRef]

51. Akhtar, M.; Khan, M.; Khan, S.; Afzal, A.; Subbiah, R.; Ahmad, S.; Husain, M.; Butt, M.; Othman, A.; Bakar, E. Determination of Non-Recrystallization Temperature for Niobium Microalloyed Steel. *Materials* **2021**, *14*, 2639. [CrossRef]

52. Sharath, B.; Venkatesh, C.; Afzal, A.; Aslfattahi, N.; Aabid, A.; Baig, M.; Saleh, B. Multi Ceramic Particles Inclusion in the Aluminium Matrix and Wear Characterization through Experimental and Response Surface-Artificial Neural Networks. *Materials* **2021**, *14*, 2895. [CrossRef]

53. Sathish, T.; Mohanavel, V.; Arunkumar, T.; Raja, T.; Rashedi, A.; Alarifi, I.M.; Badruddin, I.A.; Algahtani, A.; Afzal, A. Investigation of Mechanical Properties and Salt Spray Corrosion Test Parameters Optimization for AA8079 with Reinforcement of TiN + ZrO$_2$. *Materials* **2021**, *14*, 5260. [CrossRef]

54. Nagaraja, S.; Nagegowda, K.U.; Kumar, V.A.; Alamri, S.; Afzal, A.; Thakur, D.; Kaladgi, A.R.; Panchal, S.; Saleel, C.A. Influence of the Fly Ash Material Inoculants on the Tensile and Impact Characteristics of the Aluminum AA 5083/7.5SiC Composites. *Materials* **2021**, *14*, 2452. [CrossRef]

55. Rethnam, G.S.; Manivel, S.; Sharma, V.K.; Srinivas, C.; Afzal, A.; Razak RK, A.; Alamri, S.; Saleel, C.A. Parameter Study on Friction Surfacing of AISI316Ti Stainless Steel over EN8 Carbon Steel and Its Effect on Coating Dimensions and Bond Strength. *Materials* **2021**, *14*, 4967. [CrossRef] [PubMed]

56. Jeevan, T.P.; Jayaram, S.R.; Afzal, A.; Ashrith, H.S.; Soudagar, M.E.M.; Mujtaba, M.A. Machinability of AA6061 aluminum alloy and AISI 304L stainless steel using nonedible vegetable oils applied as minimum quantity lubrication. *J. Braz. Soc. Mech. Sci. Eng.* **2021**, *43*, 1–18. [CrossRef]

57. Sathish, T.; Mohanavel, V.; Ansari, K.; Saravanan, R.; Karthick, A.; Afzal, A.; Alamri, S.; Saleel, C. Synthesis and Characterization of Mechanical Properties and Wire Cut EDM Process Parameters Analysis in AZ61 Magnesium Alloy + B_4C + SiC. *Materials* **2021**, *14*, 3689. [CrossRef] [PubMed]

Review Article

A Review on Association between Electronic Health Record use and Quality of Patient Care

Deoyani V. Pure, Ranjit Ambad[1], Meghali Kaple[2], R. R. Dighade[3]

Hospital Management, Datta Meghe Medical College, Wanadogri, [3]Civil Engineering Associate Professor, Yeshwantrao Chavan College of Engineering, Nagpur, [1]Department of Biochemistry, Datta Meghe Medical College, Shalinitai Meghe Hospital and Research Centre, Wanadongri, Hingna, [2]Department of Biochemistry, Jawaharlal Nehru Medical College, Datta Meghe Institute of Medical Sciences, Sawangi, Meghe, Wardha, Maharashtra, India

Abstract

Health-care systems have been under increasing pressure to transition from manual to electronic systems as information technology has advanced. The electronic health record is a cutting-edge information technology system that has attracted a lot of attention. An electronic medical record (EMR) is a computerized legal medical record created in a health-care organization such as a hospital or a doctor's office. Health-care systems have been under increasing pressure to transition from manual to electronic systems as information technology has advanced. The electronic health record is a cutting-edge information technology system that has attracted a lot of attention. To increase the quality of care in the health-care context, EMRs were deployed. I looked into the link between EMRs and patient care quality. EMR aids in the storage and management of information on a patient's status, as well as medical and surgical procedures and treatments. EMRs are also beneficial to health providers since they save time by eliminating the need for paper documentation and accurately storing past health histories and treatments. I have compiled a list of publications about EMRs and patient care quality. The aim of the study was to find the association between EMR use and quality of patient care. After reviewing all of the preceding research and papers on the relationship between EMR use and patient care quality, I have come to the conclusion that EMR use improves patient care quality. Because it records and manages patient data, medical history, and treatment, it enables health-care providers to streamline their work and paperwork processes, allowing them to focus on the quality of patient care they provide. In the ambulatory environment, primary care clinicians who used a single EHR found that intense use of specific EHR features was linked to improved adherence to advised care as shown by results on electronically reported "meaningful use" quality metrics. This study is pertinent to current policy because it employs quantitative EHR usage measurements rather than self-reported use and quality indicators developed by modern certified EHR technology. The use of particular EHR features was linked early on in the "meaningful use" initiative to better results on metrics for the health-care system. Apart from this, there were some limitations which were found in some articles such as limited patients' information because the administrative data were collected from the billing details. Furthermore, non-EHR variables that cannot be completely accounted for in some analyses may contribute to changes in care quality following the introduction of EHRs.

Keywords: Electronic medical records, quality of patient care, health care system

Introduction

Health-care systems have been under increasing pressure to transition from manual to electronic systems as information technology has advanced. The electronic health record is a cutting-edge information technology system that has attracted a lot of attention.

An electronic medical record (EMR) is a computerized legal medical record created in a health-care organization such as a

hospital or a doctor's office. EMR stands for "EMR," which is an electronic version of a patient's medical file. An electronic health record collects, creates, and stores information on a patient's health in a digital format. The use of EMR has been hailed as a vital to improving care quality. EMR's health information technology methods boost health-care efficiency

Address for correspondence: Dr. Ranjit Ambad,
Department of Biochemistry, Datta Meghe Medical College, Shalinitai Meghe Hospital and Research Centre, Hingna, Wanadongri, Maharashtra, India.
E-mail: ambad.sawan@gmail.com

Access this article online

Quick Response Code:

Website:
www.journaldmims.com

DOI:
10.4103/jdmimsu.jdmimsu_280_22

How to cite this article: Pure DV, Ambad R, Kaple M, Dighade RR. A Review on Association between Electronic Health Record use and Quality of Patient Care. J Datta Meghe Inst Med Sci Univ 2022;17:457-60.

while also ensuring patient safety. Health information systems, particularly EMRs, are expected to increase the quality and expertise of health-care organizations of all sizes, from small offices to major corporations.

The EMR is a systematized collection of patient and population health information in a digital format. An EMR keeps track of a patient's medical history, including diagnoses, medications, investigations, allergies, immunizations, and treatment plans. All health-care practitioners who are caring for the patient can access the EMR, which can be utilized to assist and make recommendations concerning the patient's care and condition. Today, doctors are integrating data from patient records to improve quality outcomes through their care management program rather than only documenting for patients.

An EMR is a software database application designed to organize and improve workflow in a medical office. The EMR system can replicate each stage of patient integration, increasing efficiency, productivity, and revenue. Increasing incomes, reducing costs, reducing the cost of malpractice, reducing medical errors, improving treatment quality, improving documentation and accuracy, improving safety, and saving time for health-care workers are just a few of the benefits of EMR.

Digital digitization of patient records opens up a world of medical professionals' opportunities, including rapid access and processing of patient data, automatic reminders to avoid medication errors, sharing advanced information across the medical team, and growing transparency by ensuring complete and legible documentation. Quality improvement is one of the widely publicized benefits of EMR. EMR improves patient safety and clinical outcome through a variety of methods. EMR improves clinical communication.

The decision support system is an EMR feature that provides the latest medical information, reminders, or other activities to help health professionals make decisions. EHRs can also help with data management, especially for critically ill patients or those who need more monitoring and evaluation. These problems require a large amount of clinical information to diagnose and monitor. EHRs can assist in collecting and organizing this information, speeding up, and improving treatment decisions.

EMR has application in the various departments of the hospital such as administrative department, computerized physician order entry, laboratory system, radiologist system, pharmacy system, and clinical documentation. As we can explain the use of EMR in administrative application, it deals with the patient admission process which includes the patient demographic data, contact information, and insurance information. Computerized physician order entry helps the physician to record their orders laboratory, radiology, and treatment in the computer rather than on the paper. EMR helps in laboratory system as it makes available laboratory reports and interpreted

results in online mode only. Radiology department is another system of the hospital where we can use EMR and it will initiate picture archiving and communication system which stores the digital radiography images. Pharmacy department has the major use of EMR deals with prescription and dispatch of medicines as per doctor's order. Pharmacy they used a bar-coding system as per the patient's ID will help to minimize the medication error and patient's harm.

MATERIALS AND METHODS

Datta Meghe Medical College in Wanadongri, Nagpur, was the site of the investigation. There were 65 publications in the study, it was discovered. I found 46 relevant articles and 19 irrelevant ones out of those 65 articles, which I disregarded. In addition to those 46 articles, 10 articles did not connect to the topic of my essay while 36 articles did. Thirteen of the 36 were pertinent to my topic.[1-7]

DISCUSSION

Lin *et al.* conducted an observational study using discharge data from Tri-Service General Hospital and discussed that there were three levels of EMR usage: no EMRs, partial EMRs, and full EMRs. Inpatient mortality, readmission within 14 days, and 48-h postoperative mortality were the key health-care quality measures. To assess the association between EMR utilization and health-care quality, they used a Cox proportional hazards regression analysis. They believed that different levels of EMR adoption contribute to the quality of health care.

Yanamadala *et al.* conducted an observational study and discussed that patients who receive medical and surgical care in hospital without an EMR system have similar results as patients who seek care in hospital with a full EMR system after 1 year. On inpatient setting's patient outcomes, EMRs may have a minor role to play. In terms of patient outcomes and overall care quality, it plays a larger effect than expected.

Campanella *et al.* conducted a review and reported in accord with PRISMA guidelines for meta-analyses and systematic reviews. They concluded that when effectively implemented, an EHR system can improve health-care quality by boosting time efficiency and adherence to guidelines, as well as minimizing prescription errors and adverse events. As a result, EHR implementation strategies should be encouraged and pushed.

Zhou *et al.* discovered that between 2000 and 2005, the percentage of doctors reporting EHR adoption and the availability of core EHR functions more than doubled. In 2005, the average time spent using an EHR was 4.8 years. There was no distinction in performance between EHR users and nonusers for any of the six clinical conditions. Furthermore, in both bivariate and multivariate analyses for these six clinical situations, there was no discernible relationship between the duration of EHR use and physician performance on quality indicators. Despite the weak power of their cross-sectional

analysis, they discovered no correlation between the length of time an EHR was used and performance in terms of service quality. To achieve quality improvement from EHRs, increasing the usage of essential EHR features such as clinical decision assistance may be required. Future research should look at the link between how often physicians utilize important EHR features and how they perform over time in terms of quality indicators.

Keyhani *et al*., with the exception of inhaled steroids among asthmatics, observed no correlation between electronic doctor notes and blood pressure management or receipt of suitable medications (adjusted odds ratio, 2.86; 95% confidence interval, 1.12–7.32). Aside from angiotensin-converting enzyme inhibitors or angiotensin receptor blockers in individuals with diabetes and hypertension, they also observed no correlation between electronic reminder devices and proper treatment or blood pressure management (odds ratio, 2.58; 95% confidence interval, 1.22–5.42). They discovered no connection between digital medical records and any sort of quality metric. They discovered no connection between having a whole EHR and any of the quality indicators looked into. As a result, they came to the conclusion that there was no consistent relationship between managing chronic illnesses and blood pressure and certain EHR components. Our comprehension of the effect of EHRs on the quality of care will be improved by future study that focuses on how an EHR is installed and used and how care is integrated through an EHR.

Selvaraj *et al*., using varying levels of EHR adoption, looked at individuals from the Get With The Guidelines-Heart Failure (HF) registry who were hospitalized with HF in 2008 (n = 21 222) (no EHR, partial EHR, and full EHR). To ascertain the relationship between EHR status and several inhospital quality measures and outcomes, we used multivariable logistic regression. They examined the association between EHR status and rates of 30-day death, readmission, and a composite outcome in a substudy of Medicare enrollees (n = 8421). The cohort's median age was 71 and 15 years, and 64% of its members were white. Ejection fraction on average was 39.17%. In hospitals with no EHR (n = 1484), limited EHR (n = 13 473), and complete EHR (n = 6265), participants were admitted. On multivariable-adjusted logistic regression, there was no correlation between EHR status and any quality parameter (except than blocker at discharge) or inhospital outcomes (P > 0.05 for all comparisons). There was no connection between EHR status and 30-day mortality, readmission, or the combined outcome in the Medicare population. They came to the conclusion that there was no correlation between levels of EHR deployment and a number of quality measures and 30-day postdischarge mortality or readmission in a large registry of hospitalized patients with HF. Their findings indicated that EHR might not be enough to enhance HF quality or associated outcomes.[8-12]

Davlyatov *et al*. their analysis made use of both primary and secondary data from the 2017–2018 Medicare Cost Reports as well as the long-term Care Focus, Nursing Home Compare, Area Health Resource File, and long-term Care Focus at Brown University. The main survey information was gathered by sending a nationwide mailer to Directors of Nursing (DONs) in nursing facilities with a large Medicaid enrollment. The Nursing Home Compare Five-Star Quality Rating System was used to construct the dependent variable, nursing home quality, where a higher score denotes higher quality (1–5). EHR score, the independent variable, was a composite measurement created from 23 components. The correlation between the average EHR score and the quality star rating in nursing facilities with high Medicaid reimbursement rates was modeled using ordered logistic regression. They discovered a significant positive correlation between the five-star quality rating and the average EHR score. The likelihood of being in a higher star rating category improves by 50% for every unit increase in the average EHR score. Being a nonprofit, having a greater occupancy rate, and being situated in a county with a higher per capita income were additional criteria that were significantly linked to higher quality. They came to the conclusion that quality enhancements were positively correlated with EHR use in nursing facilities with substantial Medicaid enrollment. Their findings provide more proof of the HER's potential to enhance treatment quality in nursing homes with limited resources. The adoption and use of EHRs may help to enhance care quality in these under-resourced nursing homes, which have issues with regard to quality.

Buntin *et al*. examined recent research on the impact of health information technology on outcomes, such as quality, effectiveness, and provider satisfaction. They discovered that 92% of the most recent papers on health information technology came to generally uplifting findings. They also discovered that, in addition to major enterprises who were early adopters, the advantages of the technology are starting to be felt by smaller practices and organizations. However, a challenge that prevents some health-care practitioners from fully using the promise of health information technology is their discontent with electronic health records. These facts underline the requirement for research that detail the difficult elements of integrating health information technology especially and how these difficulties may be overcome.

Conclusion

After reviewing all of the preceding research and papers on the relationship between EMR use and patient care quality, I have come to the conclusion that EMR use improves patient care quality. Because it records and manages patient data, medical history, and treatment, it enables health-care providers to streamline their work and paperwork processes, allowing them to focus on the quality of patient care they provide. As a result, I have come to the conclusion that EMRs have a substantial role in the quality of patient treatment, either directly or indirectly.

In the ambulatory environment, primary care clinicians who used a single EHR found that intense use of specific EHR features was linked to improved adherence to advised care as shown by results on electronically reported "meaningful use" quality metrics. This study is pertinent to current policy because it employs quantitative EHR usage measurements rather than self-reported use and quality indicators developed by modern certified EHR technology. The use of particular EHR features was linked early on in the "meaningful use" initiative to better results on metrics for the health-care system.

Apart from this, there were some limitations which were found in some articles such as limited patients' information because the administrative data were collected from the billing details. Furthermore, non-EHR variables that cannot be completely accounted for in some analyses may contribute to changes in care quality following the introduction of EHRs.[12-15]

Financial support and sponsorship

Conflicts of interest

There are no conflicts of interest.

REFERENCES

1. Gatiti P, Ndirangu E, Mwangi J, Mwanzu A, Ramadhani T. Enhancing healthcare quality in hospitals through electronic health records: A systematic review. J Health Inf Dev Ctries 2021;15:1-25.
2. Seymour T, Frantsvog D, Graeber T. Electronic health records (EHR). Am J Health Sci (AJHS) 2012;3:201-10.
3. Kimble C. Electronic health records: Cure-All or chronic condition? Global Bus Org Excell 2014;33:63-74.
4. Gunter TD, Terry NP. The emergence of national electronic health record architectures in the United States and Australia: Models, costs, and questions. J Med Internet Res 2005;7:e3.
5. Atasoy H, Greenwood BN, McCullough JS. The digitization of patient care: A review of the effects of electronic health records on health care quality and utilization. Annu Rev Public Health 2019;40:487-500.
6. Campanella P, Lovato E, Marone C, Fallacara L, Mancuso A, Ricciardi W, *et al*. The impact of electronic health records on healthcare quality: A systematic review and meta-analysis. Eur J Public Health 2016;26:60-4.
7. Available from: https://www.healthhit.gov/faq/whatare-advantges-electronic-health-records. [Last accessed on 2021 Oct 18].
8. Lin HL, Wu DC, Cheng SM, Chen CJ, Wang MC, Cheng CA. Association between electronic medical records and healthcare quality. Medicine (Baltimore) 2020;99:e21182.
9. Yanamadala S, Morrison D, Curtin C, McDonald K, Hernandez-Boussard T. Electronic health records and quality of care: An observational study modeling impact on mortality, readmissions, and complications. Medicine (Baltimore) 2016;95:e3332.
10. Zhou L, Soran CS, Jenter CA, Volk LA, Orav EJ, Bates DW, *et al*. The relationship between electronic health record use and quality of care over time. J Am Med Inform Assoc 2009;16:457-64.
11. Keyhani S, Hebert PL, Ross JS, Federman A, Zhu CW, Siu AL. Electronic health record components and the quality of care. Med Care 2008;46:1267-72.
12. Selvaraj S, Fonarow GC, Sheng S, Matsouaka RA, DeVore AD, Heidenreich PA, *et al*. Association of electronic health record use with quality of care and outcomes in heart failure: An analysis of get with the guidelines-heart failure. J Am Heart Assoc 2018;7:e008158.
13. Davlyatov G, Lord J, Ghiasi A, Weech-Maldonado R. Association between electronic health record use and quality of care in high Medicaid nursing homes. J Hosp Manage Health Policy 2021;5:20-64.
14. Buntin MB, Burke MF, Hoaglin MC, Blumenthal D. The benefits of health information technology: A review of the recent literature shows predominantly positive results. Health Aff (Millwood) 2011;30:464-71.
15. Ancker JS, Kern LM, Edwards A, Nosal S, Stein DM, Hauser D, *et al*. Associations between healthcare quality and use of electronic health record functions in ambulatory care. J Am Med Inform Assoc 2015;22:864-71.

ICE Publishing

Performance evaluation of microbial fuel cell using novel anode design and with low-cost components

Sudhir V. Ambekar PhD
Professor, Department of Civil Engineering, Yeshwantrao Chavan College of
Engineering, Nagpur, India (corresponding author: sv_ambekar@rediffmail.com)

Makarand M. Ghangrekar PhD
Professor, Department of Civil Engineering, Indian Institute of Technology
Kharagpur, Kharagpur, India

Microbial fuel cells (MFCs) have proven to be an effective technology for treatment of waste water with the additional advantage of electricity generation. Although the power density obtained has increased manyfold over the past decade, the cost of treatment and cost of electricity generation need to be brought down to make the process feasible. In the present research, an attempt was made to use locally available, low-cost and effective materials for the construction of an MFC using novel anode architecture. The MFC was made using multiple membranes in a single cell. The special design of the anode proved to be very effective in obtaining a higher power density. A volumetric power density of $2002 \, mW/m^3$ could be achieved without the use of any chemical catholyte. The corresponding coulombic efficiency obtained was 13.17%. When a chemical catholyte was used, the power density increased to $5201 \, mW/m^3$, an increase by more than 2.5 times. The corresponding coulombic efficiency of the MFC also increased to 29.16%. Such novel anode architecture could take this technology a step forward for practical implementation to harvest carbon dioxide neutral electricity from waste water. The performance of the MFC in the removal of chemical oxygen demand (COD) from waste water was found to be 93.9–97.75%, which is highly satisfactory. The removal efficiency was found to be independent of the initial COD of the substrate.

Keywords: energy/microbial fuel cell/power density

Notation

K_s half-velocity constant (mg/l)
k maximum specific substrate utilisation rate (day^{-1})
r_{su} rate of substrate utilisation (mg/(l day))
S substrate concentration (mg/l)
X biomass concentration (mg/l)

Introduction

The changing nature of industrial waste water characteristics and their impact on human health and environment are the most important concerns in waste water treatment. In aerobic treatment of waste water, the costs of treatment of sludge, nutrients and energy are prohibitive and, hence, pose challenges to the engineers. Anaerobic treatment of waste water is an alternative strategy, the main advantage being the low volume of sludge generated and low electricity consumption along with simultaneous generation of methane (biogas). However, anaerobic treatment of domestic waste water, many times, is considered not feasible due to low strength or biochemical oxygen (O_2) demand concentrations. Simultaneously, the increasing demand for energy with the increase in population has forced mankind to look for alternative sources of energy, which need to be environmentally sustainable (Hozenuzzaman et al., 2015; Sonell, 2015).

Conversion of organic matter to biofuels is another option for simultaneous treatment of waste water and energy recovery. A whole range of biofuels and related bioproducts can be produced by means of microbiological fermentation. Bioethanol, biogas and hydrogen gas

are the major biofuels. Bioethanol has emerged as the most promising fuel to replace fossil fuel in recent years (Stafford et al., 2018).

Microbial fuel cells (MFCs) represent relatively a new approach for waste water treatment along with the advantage of recovering energy in the form of direct electricity. An MFC uses biomass through bacteria and generates electricity. Compared with other biofuel options, an MFC has the scope to convert 1 kg of organic matter into 3 kWh of electrical energy, that too in a single step, unlike two or more steps for all other biofuels, implying that the highest efficiency of conversion of biomass to electricity can be achieved in MFCs (Cheng and Logan, 2011). Another important advantage of an MFC is the lower sludge yield compared with that of aerobic processes, which is caused by the reduced energy available for biomass growth as a significant part of the substrate energy is converted to electrical power. In MFCs, the sludge yield range from 0.07 to 0.22 g biomass chemical oxygen demand (COD) per gram of substrate COD, compared with 0.4 g biomass COD per gram of substrate COD removed for aerobic treatment (Rabaey and Verstraete, 2005).

An MFC is a type of hybrid system and is very different from traditional aerobic or anaerobic waste-water-treatment systems. At the microbial level, this is an anaerobic treatment technology. The bacteria must be grown in an anaerobic environment to produce electricity. However, since oxygen is used at the cathode end, it is also an aerobic system, although oxygen is not directly used for microbial respiration; rather, it is required only for reduction or proton, or other cations, to support cathodic reaction.

1

Journal of Environmental Engineering
and Science

Performance evaluation of microbial fuel
cell using novel anode design and with
low-cost components
Ambekar and Ghangrekar

In its simplest form, an MFC consists of two chambers, separated by a membrane that allows the flow of protons across it (proton-exchange membrane (PEM)). The two chambers consist of electrodes, which are made of a non-corrosive material.

The anodic chamber consists of an anode, waste water and fermentative as well as electrogenic bacteria and is sealed to prevent oxygen diffusion in the anodic chamber. The cathode chamber consists of a cathode immersed in water, and the water is bubbled with air. A schematic diagram of an MFC is shown in Figure 1.

An MFC converts energy, available in a biodegradable substrate, directly into electricity. This can be achieved when bacteria, instead of using a natural electron acceptor such as oxygen, use an insoluble acceptor such as an anode (Rabaey and Verstraete, 2005). This transfer can occur through membrane-associated components or soluble electron shuttles. The electrons then flow through a resister to the cathode, at which the electron acceptor is reduced. In this state, they are used to fuel the reactions that provide the living cell with energy for their growth. The ultimate 'electron sink' is generally molecular oxygen.

In an MFC, electrons are diverted from the respiratory chain and the 'stolen' electrons are then carried to the electrode, reducing the anode, which appears as an electric current driven around the external circuit. To complete this circuit, a second positive oxidising electrode is required that is external to this biological system. The oxidising material can be oxygen (Benneto, 1990). It is necessary that all complex organic compounds present in the substrate must be oxidised to carbon dioxide (CO_2) in order to extract most of available electrons and convert them to current (Lovely, 2008). This may become possible due to the presence of complex communities of microorganisms with greater phylogenetic diversity. Substantial research work has been carried out in about past 15 years on different aspects of MFCs, and focus has been given on maximising electricity generation.

Researchers are successful in achieving higher power production. Chae et al. (2009) used a two-chamber rectangular shaped MFC
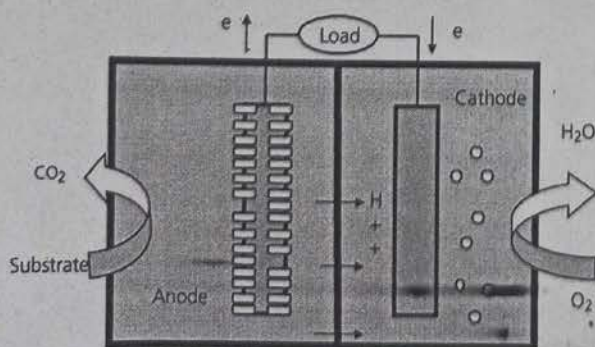
with a Nafion 117 PEM and a carbon felt anode and a perforated titanium (Ti) plate as the cathode. They compared the performance of four different substrates in terms of coulombic efficiency and power density. The study showed that glucose-fed cells gave the maximum power density ($156.0 \, mW/m^2$), followed by cells fed with acetate ($64.3 \, mW/m^2$), propionate ($58.0 \, mW/m^2$) and butyrate ($51.4 \, mW/m^2$). Rabaey et al. (2003) reported that a maximum power density of $3.6 \, W/m^2$ was obtained using glucose as a substrate and ferric cyanide as a catholyte. They used a block MFC consisting of four cells in which plain graphite electrodes were used at the cathode as well as the anode with an Ultrex PEM. Ahn and Logan (2010) examined the performance of MFCs using domestic waste water as a substrate at two different temperatures, 23 and 30°C, in batch and continuous flow modes in single-chamber air cathode MFCs. The highest power density of $422 \, mW/m^2$ was achieved under continuous flow and mesophilic conditions, at an organic loading rate (OLR) of 54 g COD/(l day). COD removal of 25.8% was achieved.

It can be concluded from the various research papers reviewed by the authors that parameters such as the cost and durability of the materials used for construction of the MFC, hydraulic retention time (HRT) and energy cost of pumping have not been given due importance. These parameters are important in view of feasibility studies for MFCs to be used as a treatment system in sewage or industrial waste water treatment.

The factors that contribute to a higher cost of treatment using MFCs are the separators and the electrodes. The material used for the anode is important because the oxidation process occurs at the anode surface. Improvement in the anode is more essential for better performance of an MFC (ElMekawy et al., 2017). The properties of the anode the influence the performance of an MFC are (a) material surface area, (b) biocompatibility of the material, (c) electrical conductivity, (d) material stability and durability and (e) cost of material (Gajda et al., 2020; Saadi et al., 2020). The electrodes used in most of the research studies were either of costly material such as titanium or were given special treatments such as platinum (Pt) coating. These measures have resulted in increased power production, but the cost of the treatment along with the cost of electricity generated has also increased. The durability of such electrodes also needs to be studied. It has therefore become essential to look at alternative materials and design so that the cost of treatment and electricity generated can be reduced. In the present research, an attempt was made to study the performance of an MFC constructed using universally available, low-cost effective materials for its efficacy in treating waste water of varying strength and electricity generation.

Materials and methods

MFC fabrication

The MFC was constructed using plexiglass material. The anodic chamber was made using a 100 mm internal dia. cylinder. The height of the cylinder was kept at 128 mm so as to obtain a total

Figure 1. Schematic diagram of an MFC

Journal of Environmental Engineering
and Science

Performance evaluation of microbial fuel
cell using novel anode design and with
low-cost components
Ambekar and Ghangrekar

volume of the anodic chamber of 1.0 l. The cathodic chamber was made square in shape with a size that can accommodate the anodic chamber concentrically. Electrodes were made of stainless steel. The anode consisted of four rods made of stainless steel wires and was designed such that it gave the appearance of a brush. This was made to increase the surface area of the electrode. The electrodes were fabricated using a 0.8 mm dia. stainless steel wire as shown in Figure 2.

The cathode was made of stainless steel mesh (150 gsi). Four cathode meshes were attached to the reactor. Openings were provided to the anodic chamber to enable collecting a sample of the substrate for measurement of COD. The anodic chamber was covered from the top to ensure that anaerobic conditions prevail inside the chamber. A tiny opening (1 mm dia. hole) was made at the top for exit of gases from the anodic chamber. All anodes and cathodes were connected with aluminium (Al) wire with sufficient care. Four separators were kept between the anodic and cathodic chambers. The cathodes were kept very near to the separators. The separators used were lead (Pb) acid battery separators made of poly(vinyl chloride) (PVC). Before using them as separators, the sheets were pressed at a pressure of 5 kg/cm^2 for 30 min and soaked in hydrogen peroxide (H_2O_2) for 48 h.

MFC operation

The synthetic waste water substrate used in the experiment was prepared using lactose (Merck, India). The pH of solution was

Figure 2. Brushlike design of the anode

kept between 7.0 and 7.5 at the start of the cycle. A phosphate (PO_4^{3-}) buffer (50 mM) was used to maintain the pH of the substrate solution, whenever required. A mixed culture was used as the inoculum in the anodic chamber throughout the experiment. It was preferred over a pure culture for greater proximity to field conditions. The substrate was inoculated with sludge collected from an upflow anaerobic sludge blanket reactor treating dairy waste water. The pH of the catholyte water was kept in the range 7.0–7.5.

The MFC was operated in batch mode throughout the experiment. The experiment was conducted using substrates of different strengths in terms of COD values. Considering the range of COD values generally observed in domestic waste waters and dairy effluent, the experiments were performed on waste water with COD values of 200, 500, 1250, 2000, 3000 and 4000 mg/l. The cathode chamber was aerated continuously using a diffuser aerator. It was ensured that the dissolved oxygen (DO) in catholyte water would remain sufficient to support cathodic reactions. Additional batch studies were conducted at substrate COD of 1250 mg/l using potassium permanganate ($KMnO_4$) (500 mg/l) in tap water as a catholyte to study its effect on power generation.

Analysis

The circuit of the MFC was always kept closed except at the time of measurement of open-circuit voltages (OCVs). The reference electrode used for the measurement was a silver (Ag)/silver chloride (AgCl) electrode. The voltages measured were between the cathode and the anode and voltages at the anode and cathode with respect to the reference electrode. As the voltage approached the peak value, the voltage between the cathode and the anode was also measured for series of different loads, starting from 250 to 10 Ω. The COD value of the substrate was measured regularly using the closed reflux method, following the procedure prescribed in the standard methods by the American Public Health Association (APHA et al., 2005). The DO present in the catholyte was measured regularly following the titrimetric method prescribed in APHA standard methods (APHA et al., 2005).

Results and discussion

Substrate degradation in the MFC

The MFC is an attached growth, anaerobic treatment unit process. Therefore, it is important to evaluate its performance in terms of COD removal. The performance of the MFC in the removal of COD from waste water was found to be 93.9–97.75%, which is highly satisfactory. The removal efficiency was found to be independent of the initial COD of the substrate (Table 1).

Aelterman et al. (2008) studied the effect of increasing the loading rate on continuous electricity generation at different external loads. They found that at external load of 10.5 Ω the power increased significantly when the OLR was increased from 1.6 to 3.3 kg/(m^3 day). Min and Logan (2004) could achieve 58% COD removal in an
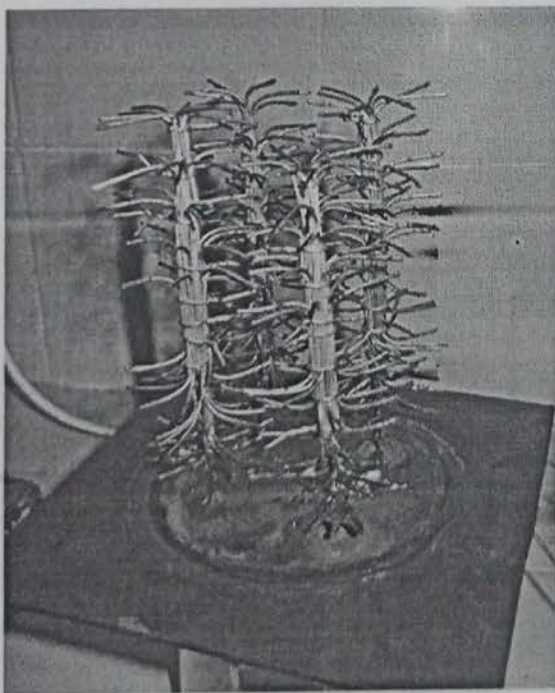
Journal of Environmental Engineering
and Science

Performance evaluation of microbial fuel
cell using novel anode design and with
low-cost components
Ambekar and Ghangrekar

Table 1. Treatment efficiency obtained computed for different
initial substrate COD values

Number	Initial substrate COD: mg/l	COD removal: %
1	200	95.67
2	500	93.90
3	1250	94.65
4	2000	96.83
5	3000	97.75
6	4000	96.77

MFC operated at an HRT of 2 h, and COD removal of 79% was
reported at an HRT of 4 h using domestic waste water with COD of
246 mg/l as feed and continuous mode of operation. Jana et al.
(2010) obtained COD removal of more than 90% in their experiment
at an HRT of 20 h using synthetic waste water with a COD value of
500 mg/l. They further reported that the COD removal efficiency
decreased with a decrease in HRT. Jadhav et al. (2009) obtained
COD removal efficiency of about 90% when the MFC was operated
at a higher temperature of 20–35°C in continuous mode with an
HRT of 24.55 h using synthetic waste water with COD in the range
470–510 mg/l. Ahn and Logan (2010) studied the working of an
MFC at a mesophilic temperature, providing an HRT of 4–20 h with
a corresponding OLR of 0.35–1.75 kg/(m^3 day) in a fed batch
reactor. They obtained a maximum power density of 177 mW/m^2
(5.4 mW/m^3) and COD removal of 33%. Rabaey et al. (2005) used
maple syrup (a plant extract) as a substrate in their study on an MFC
operated under continuous mode at an OLR of 1 kg COD/(m^3 day)
(corresponding HRT 2.7–7.3 h) and obtained COD removal of 70%.
The COD reduction obtained in the present work is highly
satisfactory and comparable with that of any good-performing MFC.
More accuracy in the results can be expected if the same system is
run in continuous mode.

The kinetics of microbial growth controls the degradation of the
substrate and the production of the biomass. In a batch reactor,
limiting substrate is available to the microorganisms. The
substrate utilisation rate in a batch reactor can be expressed as
follows (Baily and Ollis, 1986):

$$1. \quad r_{su} = -\frac{kXS}{K_s + S}$$

In the preceding expression, r_{su} is the rate of substrate utilisation
(mg/(l day)), k is the maximum specific substrate utilisation rate
(day^{-1}), X is the biomass concentration (mg/l), S is the substrate
concentration (mg/l) and K_s is the half-velocity constant (mg/l). The
half-velocity constant is the substrate concentration at one-half the
maximum specific substrate utilisation rate. A plot of r_{su} against
the substrate concentration is shown in Figure 3. The graph is drawn
from the beginning of the cycle to the time of that the maximum cell
voltage was obtained. The graph clearly follows microbial growth
under limiting substrate conditions. From the graph, the half-velocity
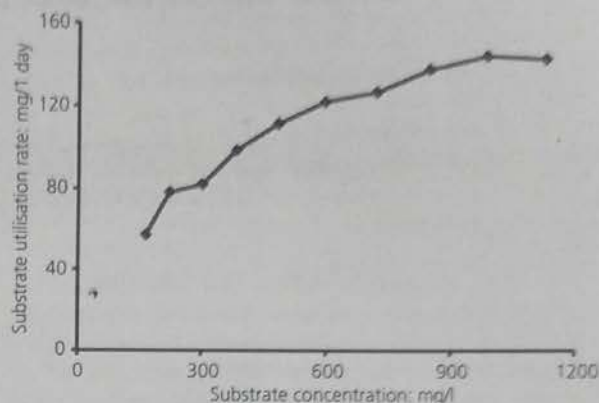constant obtained is 590.78 mg/l.

Figure 3. Graph showing the rate of change of substrate
utilisation against COD concentration (initial COD concentration =
1250 mg/l)

Electricity production

The performance of the MFC was also evaluated using parameters
related to the power recovered by it. The parameters are the
maximum voltage generated, the maximum volumetric power
produced and the resistance offered by the configuration of the
cell. A maximum anode potential of −494 mV was obtained,
whereas the anode potential variation for different substrate COD
values was between −455 and −494 mV. Figure 4 shows the
variation of the maximum anode potential with the initial
substrate COD. This suggests that the strength (COD) of the
substrate affects the anode potential, although the effect is not
substantial. As the voltage produced follows substrate-limiting
growth kinetics, beyond certain substrate concentration, there is a
very small increment in the anode voltage produced. The
maximum cathode potential obtained was 78 mV, which is
substantially less than the theoretical value of 0.805 V (Bard
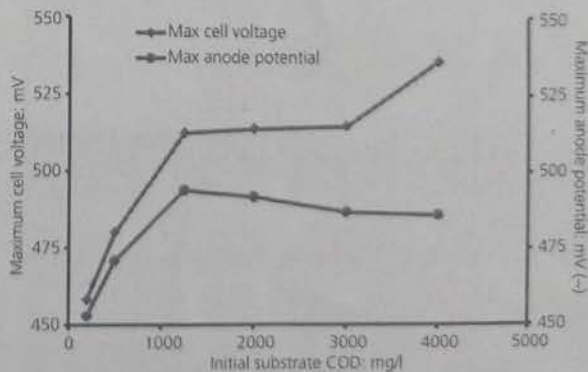et al., 1985), indicating a high amount of energy losses at

Figure 4. Graph showing variation of the maximum anode
potential and maximum cell voltage for different initial substrate
COD values

Journal of Environmental Engineering
and Science

Performance evaluation of microbial fuel
cell using novel anode design and with
low-cost components
Ambekar and Ghangrekar

cathode. With an increase in initial substrate COD, the performance of the cathode showed improvement (Figure 4).

The maximum value of OCV obtained in the study was 556 mV. The maximum cell voltage increased with the initial COD of the substrate, but the increase is not substantial (Figure 4). The OCV produced by an MFC is always less than that predicted by maximum potential calculations for the cell based on redox potential. So far, the maximum OCV obtained using oxygen at a cathode is 830 mV (Cheng and Logan, 2007); however, to obtain such a high voltage, phosphate buffer was used as the catholyte along with ammonia treatment to the cathode.

The maximum volumetric power density obtained in the MFC was 2002.23 mW/m^3 for a substrate COD concentration of 1250 mg/l (Figure 5). Power density curves for different substrate COD values are shown in Figure 5. It was also found that the performance of the MFC in terms of power generation is the function of the COD of the substrate. Figure 6 shows the variation of the maximum power density generated for different COD values of the substrate. The figure clearly indicates that the power density obtained is maximum at a COD value of 1250 mg/l; and it decreases if the COD of the substrate is higher or lower than 1250 mg/l. Similar results were reported by Jana et al. (2010) and Mohan et al. (2007). Studies by Raad et al. (2020) indicated the effect of COD as well as mixed liquor suspended solids concentration on sludge stabilisation and power generation.
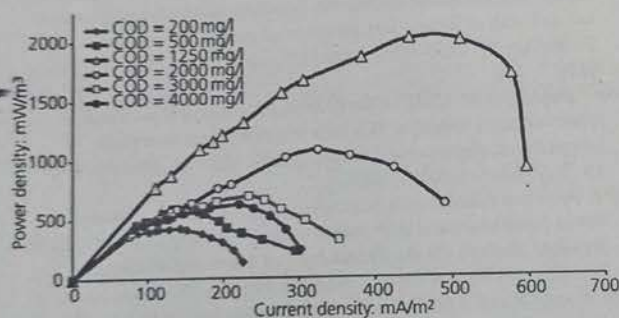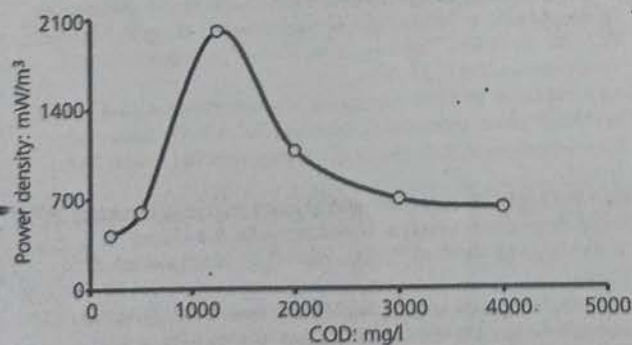
The internal resistance of an MFC has a direct impact on the power generated by the cell. In the present study, it was found that the internal resistance of the cell was the least at a COD value of 1250 mg/l (40 Ω), at which the power production was maximum (2002.23 mW/m^3). The polarisation curve is shown in Figure 7. It shows that overpotential losses are quite low; therefore, the slope of the polarisation curve is not higher at low current values.

The coulombic efficiency obtained in the experiment varied between 34.35 and 4.1%. The reduced efficiency at higher substrate strength was probably due to the use of mixed anaerobic culture as inoculum. Some species must have converted the substrate to organic acids and to methane (CH_4) and carbon dioxide under anaerobic conditions. This affects the process of conversion of the substrate to electricity. The coulombic efficiency for a substrate COD of 1250 mg/l was 13.17%. Figure 8 shows the variation of coulombic efficiency with substrate COD.

Rabaey et al. (2003) performed their experiments using an MFC assembly containing four cells and using plain graphite electrodes. They used glucose as a substrate, and inoculation was done with a mixed culture. The cells were operated with continuous flow with the OLR varying from 0.5 to 5.0 kg COD/(m^3 day). They obtained maximum power of 3.6 W/m^2. They also found that as the loading rate increased, the coulombic efficiency steadily decreased from 89 to 10%.

The effect of the use of potassium permanganate as a catholyte was also studied for a substrate COD concentration of 1250 mg/l. A minimum anode potential of −505 mV and a maximum cathode potential of 558 mV were observed with potassium permanganate as a catholyte. The variation in cathode potential was remarkably
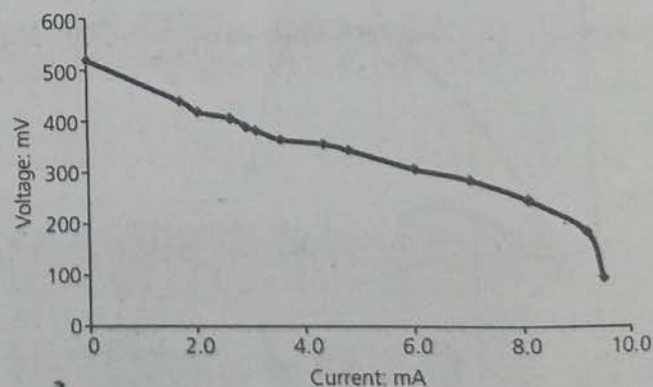

Figure 5. Power density curves for different initial substrate COD concentrations

Figure 6. Effect of the initial substrate COD on the maximum power density generated by the MFC

Figure 7. Polarisation curve for waste water with an initial COD of 1250 mg/l

Journal of Environmental Engineering
and Science

Performance evaluation of microbial fuel
cell using novel anode design and with
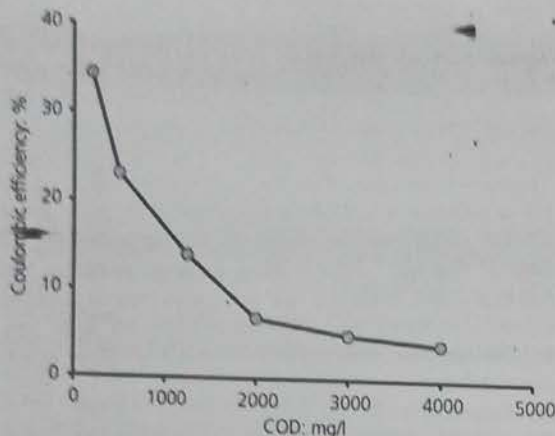low-cost components
Ambekar and Ghangrekar

Figure 8. Variation of coulombic efficiency with initial substrate COD

negligible over the whole cycle. While the anode potential obtained was satisfactory, the cathode potential again was below the expected value, indicating scope for improvement in cathode design for better performance of the cell.

A maximum cell potential of 1.101 V was produced with potassium permanganate as a catholyte, which is more than a twofold increase. Similarly, a maximum power density of 5200.83 mW/m³ was produced, which is a more than 2.5 times increase compared with that using oxygen as a cathodic electron acceptor (Figure 9). The internal resistance of the cell calculated from the polarisation curve was found to be 29.49 Ω which is substantially lower than the previously obtained value of 40 Ω using oxygen as a catholyte at the same substrate concentration in feed. The coulombic efficiency also showed a remarkable increase to 29.16%, an increase by 2.2 times.
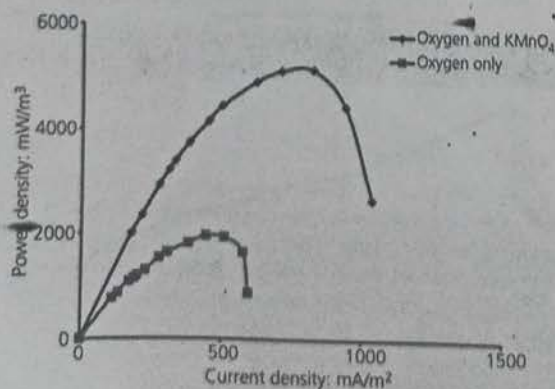
Figure 9. Variation in power density with and without using potassium permanganate as a catholyte

Conclusions

The special, brushlike anode design of the MFC using stainless steel wires helped in improving the contact between the anode biofilm and the substrate and demonstrated about 95% COD removal. Also, proper transfer of electrons from the microbes to the electrode seems to have taken place, effectively demonstrating coulombic efficiency of 34.35–4.1% using oxygen and 29.16% using potassium permanganate as a cathodic electron acceptor (at COD of waste water of 1250 mg/l). This coulombic efficiency observed is far superior considering the fact that mixed anaerobic sludge was used as inoculum. This low-cost MFC made with a PVC battery separator produced a power density of 2 W/m³ using oxygen and 5.2 W/m³ using potassium permanganate as the cathodic electron acceptor, which is really a satisfactory performance for the materials used for MFC construction without involving a costly catalyst. The internal resistance of this MFC was found to be around 30 Ω showing that the separator used is efficient. This internal resistance value is very low, indicating the good design and architecture of the cell. The maximum cathode potential at the cathode was quite low (89 mV), and there is further scope for improvement in the performance of the cathode. The performance can be improved by changing the cathode material and its design for further increasing the power production of this system.

REFERENCES

Aelterman P, Vessichele M, Marzorati M and Boon N (2008) Loading rate and external resistance control the electricity generation of microbial fuel cell with different three dimensional anodes. *Bioresource Technology* 99: 8895–8902, https://doi.org/10.1016/j.biortech.2008.04. 061.

Ahn Y and Logan BE (2010) Effectiveness of domestic wastewater treatment using microbial fuel cells at ambient and mesophilic temperatures. *Bioresource Technology* 101: 469–475, https://doi.org/ 10.1016/j.biortech.2009.07.039.

APHA (American Public Health Association), AWWA (American Water Works Association) and WEF (Water Environmental Federation) (2005) *Standard Methods for the Examination of Water and Wastewater*, 21st edn. APHA, AWWA and WEF Washington, DC, USA.

Baily JE and Ollis DF (1986) *Biochemical Engineering Fundamentals*, 2nd edn. McGraw-Hill, New York, NY, USA.

Bard AJ, Parson R and Jorden J (1985) *Standard Potentials in Aqueous Solutions*. Marcel Dekker, New York, NY, USA.

Benneto HP (1990) Electricity generation by microorganisms. *Biotechnology Education* 1(4): 163–168.

Chae K, Choi M, Lee J, Kim K and Kim I (2009) Effect of different substrates on the performance, bacterial diversity and bacterial viability in microbial fuel cells. *Bioresource Technology* 100: 3515–3525, https://doi.org/10. 1016/j.biortech.2009.02.065.

Cheng S and Logan BE (2007) Ammonia treatment of carbon cloth anodes to enhance power generation of microbial fuel cell. *Electrochemistry Communications* 9: 492–496, https://doi.org/10.1016/j.elecom.2006. 10.023.

Cheng S and Logan BE (2011) Increasing power generation for scaling up single chamber air cathode microbial fuel cells. *Bioresource Technology* 102: 4468–4473, https://doi.org/10.1016/j.biortech.2010. 12.104.

ElMekawy A, Hegab HM, Losic D, Saint CP and Pant D (2017) Application of graphene in microbial fuel cells: a gap between promise and reality. *Renewable & Sustainable Energy Reviews* 72: 1389–1403, https://doi.org/10.1016/j.rser.2016.10.044.

Gajda I, Greenman J and Leropoulis I (2020) Microbial fuel cell stack performance enhancement through carbon veil anode modification

Scanned with OKEN Scanner

Journal of Environmental Engineering
and Science

Performance evaluation of microbial fuel
cell using novel anode design and with
low-cost components
Ambekar and Ghangrekar

with activated carbon powder. *Applied Energy* 262: article 114475, https://doi.org/10.1016/j.apenergy.2019.114475.

Hozenuzzaman M, Rahim NA, Selvaraj J, Malek ABMA and Nahar A (2015) Global prospects, programs, policies and environmental impact of solar photovoltaic power generation. *Renewable & Sustainable Energy Reviews* 41: 284–297, http://doi.org/10.1016/j.rser.2014.08.046.

Jadhav GS and Ghangrekar MM (2009) Performance of microbial fuel cell subjected to variation in pH, temperature, external load and substrate concentration. *Bioresource Technology* 100: 717–723, https://doi.org/10.1016/j.biortech.2008.07.041.

Jana PS, Behera M and Ghangrekar MM (2010) Performance comparison of upflow microbial fuel cells fabricated using proton exchange membrane and earthen cylinder. *International Journal of Hydrogen Energy* 35: 5681–5686, https://doi.org/10.1016/j.ijhydene.2010.03.048.

Lovely DR (2008) The microbe electric: conversion of organic matter to electricity. *Current Opinion in Biotechnology* 19: 1–8, https://doi.org/10.1016/j.copbio.2008.10.005.

Min B and Logan BE (2004) Continuous electricity generation from domestic wastewater and organic substrates in a flat plate microbial fuel cell. *Environmental Science and Technology* 38: 5809–5814, https://doi.org/10.1021/es0491026.

Mohan SV, Raghavulu SV, Srikanth S and Sarma PN (2007) Bioelectricity production by mediatorless microbial fuel cell under acidophilic condition using wastewater as substrate: influence of substrate loading rate. *Current Science* 92: 1720–1725.

Raad NK, Farrokhi F, Mousavi SA, Darvishi P and Mahmoudi A (2020) Simultaneous power generation and sewage sludge stabilization using an air cathode-MFCs. *Biomass and Bioenergy* 140: article 105642, https://doi.org/10.1016/j.biombioe.2020.105642.

Rabaey K and Verstraete W (2005) Microbial fuel cells: novel biotechnology for energy generation. *Trends in Biotechnology* 23(6): 291–298, https://doi.org/10.1016/j.tibtech.2005.04.008.

Rabaey K, Lissens G, Siciliano SD and Verstraete W (2003) A microbial fuel cell capable of converting glucose to electricity at high rate and efficiency. *Biotechnology Letters* 25: 1531–1535, https://doi.org/10.1023/A:1025484009367.

Rabaey K, Boon N, Hofte M and Verstraete W (2005) Microbial phenazine production enhances electron transfer biofuels cells. *Environmental Science and Technology* 39(9): 1–8, https://doi.org/10.1023/A:1025484009367.

Saadi M, Pezard I, Haddour N et al. (2020) Stainless steel coated with carbon nanofibre/PDMS composite as anodes in microbial fuel cells. *Material Research Express* 7(2): article 025504, https://doi.org/10.1088/2053-1591/ab6c99.

Sonell S (2015b) Reducing energy demand: a review of issues, challenges and approaches. *Renewable & Sustainable Energy Reviews* 47: 74–82, https://doi.org/10.1016/j.rser.2015.03.002.

Stafford WHL, Lotter GA, Malfitz GPV and Brent AC (2018) Biofuels technology development in southern Africa. *Development Southern Africa* 36(2): 155–174, https://doi.org/10.1080/0376835X.2018.1481732.
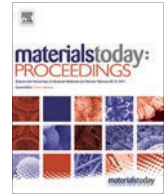
How can you contribute?

To discuss this paper, please submit up to 500 words to the editor at journals@ice.org.uk. Your contribution will be forwarded to the author(s) for a reply and, if considered appropriate by the editorial board, it will be published as a discussion in a future issue of the journal.

Utilization of phosphogypsum and rice husk to develop sustainable bricks

Sanjay P. Raut [a], Uday Singh Patil [b,*], Mangesh V. Madurwar [c]

[a] Department of Civil Engineering, Yeshwantrao Chavan College of Engineering, Nagpur 441110, India
[b] Department of Civil Engineering, Yeshwantrao Chavan College of Engineering, Nagpur 441110, India
[c] Department of Civil Engineering, Visvesvaraya National Institute of Technology, Nagpur 440010, India

ABSTRACT

Rapid industrialization and advancement in technology have led to the creation of bulk loads of waste material. Subsequently, the management of these waste materials has been a topic of major concern due to their complex treatment processes. As a result, utilizing these wastes with new ideas has presented viable solutions to global concerns in recent years. One of them is the utilization of waste materials in manufacturing sustainable brick. In the present study, phosphogypsum (PG), rice husk ash (RHA), and cement are used in different proportions [PG-65% to 82.5%, RHA-2.5% to 15%, cement-15% to 20%] to develop sustainable bricks. The developed sustainable bricks were tested as per the Indian and ASTM Standards. Findings revealed that the compressive strength and water absorption value of composition 'H' [PG(77.5%). RHA(7.5%). CEMENT(15%)] meet the requirement of IS 3495:1992. The designed sustainable brick of composition 'H' is shown to have a higher specific heat capacity than commercially available fly ash bricks (FAB) and burnt clay bricks (BCB); hence the developed sustainable brick (composition H) is found to be thermally insulated. Present research can be used by various resource persons who are active in developing sustainable construction materials or bricks from industrial wastes.
Copyright © 2022 Elsevier Ltd. All rights reserved.
Selection and peer-review under responsibility of the scientific committee of the Sustainable Materials and Practices for Built Environment.

1. Introduction

Bricks contain the majority of the embodied energy in a unit of a wall. They are the fundamental building unit of any structure. The interest in developing bricks from diverse industrial or agricultural wastes has increased because population expansion outpaces available housing. The production of building materials has an irreversible impact on the environment. The construction industry's growth is reliant on finite natural resources, thus forcing manufacturers to seek alternative solutions. Due to the increased demand for construction materials, several academics or researchers are attempting to turn industrial wastes into sustainable construction materials. Recycling and reusing these wastes in developing sustainable construction materials may help to reduce reliance on natural resources, conserve non-renewable resources, improve population health and security, and reduce waste disposal costs.

The most efficient use of waste materials in the creation of sustainable bricks is a great approach to solve the problem of waste storage while also cutting the cost of construction materials. Globally, different waste materials are produced in industries viz. chemical solvents, paints, agricultural wastes, paper products, industrial by-products, metals, construction wastes, and radioactive wastes. A variety of these wastes has been used for manufacturing sustainable materials like agro-industrial wastes [1], granulated blast-furnace slag, waste paper pulp, waste steel slag, rice husk ash, expanded polystyrene [2], etc. Some of them have become prime waste materials for brick production, and others are still undergoing research works. In this study, statistics about phosphogypsum (PG) and rice husk ash (RHA) have been described to get a general idea of the potentiality of these waste materials. The PG comes from phosphoric acid factories' filtration process [3,4]. Approximately 4–6 Tonnes [5] of PG is generated per ton of P_2O_5 recovered. If PG is dumped in an open area, it could endanger the ecosystem. The handling and control of PG is also a critical challenge in plants owing to their massive volumes, as well as the likelihood of dust, and heavy metals emissions. [6] There are 11 phosphoric acid pro-

S.P. Raut, Uday Singh Patil and M.V. Madurwar
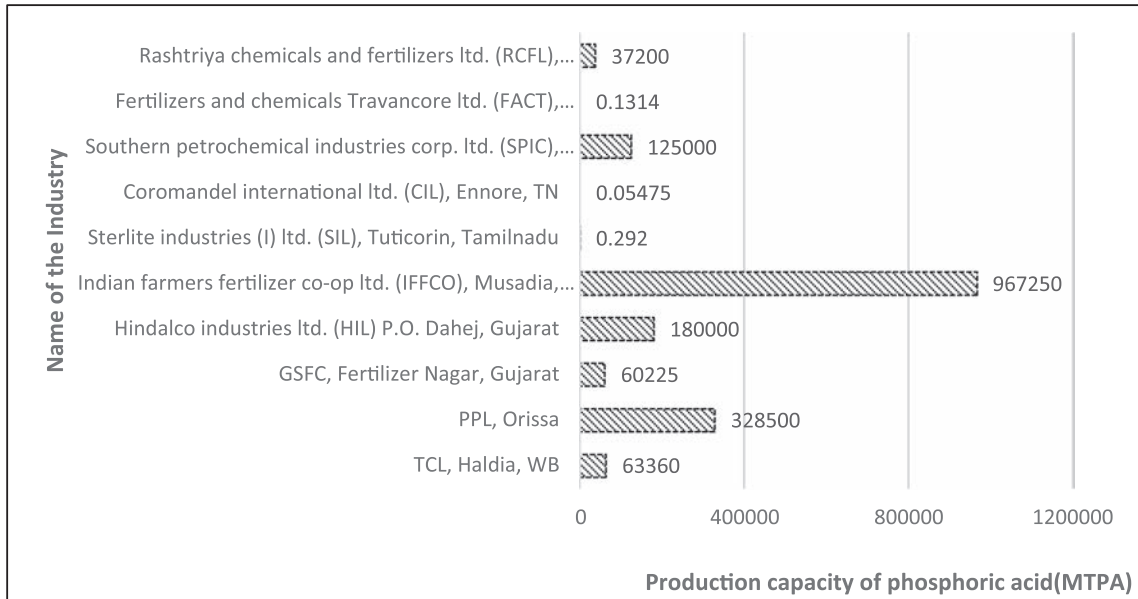
Fig. 1. Details about phosphoric acid manufacturing in India [6].

duction units in India, which are spread over 7 states as shown in Fig. 1. PG is currently stored, and some of it is exported to other businesses for usage as a raw material in cement manufacturing, for alkali soil additives, and reconditioning. The Hazardous Waste Rules [7], exempted PG from the Schedule-I hazardous waste category and mandated that PG from phosphoric acid fertilizer plants be managed according to the CPCB guidelines. PG production in the country is estimated to be over 11 million tonnes per year (based on the assumption that 5 tonnes of PG are produced for every tonne of phosphoric acid). Fig. 1 depicts the country's phosphoric acid production scenario by industry [6].

RHA is a rice milling waste product [8]. It is formed from burned rice paddy husks. Non-crystalline amorphous RHA is created by burning rice husks at temperatures between 500 and 800 °C. RHA contains 90% amorphous silica [9]. Because of its high surface area and high silica concentration, it has good pozzolanic activity. India produces roughly 24 million tonnes of rice husk each year [10]. It is used as fuel in boilers and to generate electricity in the industrial sector. Rice husk has a high ash percentage, ranging from 15 to 20% when compared to other forms of biomass utilized for gasification [11]. RHA is mostly made up of silica. With such a high silica content in the ash, extracting silica from it becomes cost-effective, which has a large market and reduces the need for ash disposal. Rice husk is used for a variety of purposes, including as a fuel in brick kilns, furnaces [12], for parboiling (Rice mills), as a cleaning agent in the machine sector, and in the manufacture of construction materials. Although rice husk has a variety of well-known uses, only a small fraction of it is actually used; the rest is thrown away or used as cattle feed. Because there is so much rice husk produced, the issues associated with its exploitation must be addressed not only in terms of quality but also in terms of quantity. However, efficient brick production is the most promising and profitable use of this ash. Thus, the objective of this study is to develop sustainable bricks using wastes viz. PG, and RHA along with cement as a binding material. Numerous compositions have been explored and tested as per various standards to produce brick with enhanced properties.

2. Material and methodology

2.1. Material

In this study, the PG is procured from Samudrapur Dist. Wardha (Fig. 2). RHA is procured from Ellora Industries, Tumsar, Dist. Bhandara (Fig. 3). Ordinary Portland Cement of grade 43, is employed as a binder for the development of sustainable bricks. The chemical composition was determined by the XRF (Xray-Fluorescence) test at the Indian Bureau of Mines, Nagpur.

2.2. Development of sustainable bricks

To prepare sustainable bricks possible proportions of raw materials were made as shown in Table 1. After that, the raw materials were hand-mixed until they were homogeneous [13]. (Fig. 4) The

Fig. 2. Production of PG from the fertilizer industry.

S.P. Raut, Uday Singh Patil and M.V. Madurwar

Fig. 3. Rice Husk Ash.

Table 1
Proportioning of raw materials for sustainable bricks.

Composition name	Phosphogypsum (%)	Cement (%)	Rice husk ash (%)
A	65	20	15
B	70	17	13
C	80	19	1.0
D	80	15	5.0
E	80	17	3.0
F	72.5	15	12.5
G	75	15	10
H	77.5	15	7.5
I	80	15	5.0
J	82.5	15	2.5

Fig. 4. Brick casting work.

mixture is then molded at various proportions in a mould of size 190 × 75 × 100 mm. After that, the developed bricks are dried in the open air for 15 to 20 days as shown in Fig. 5. The dried bricks are subsequently put through a series of testing in compliance with various standards (Table 2).

The initial five compositions namely A to E and the bricks developed using 0–50% PG was not effective as the bricks produced resulted in poor structural formation and also developed shrinkage cracks resulting in a strength low enough to be broken by hand. Hence, it was not possible to carry out tests on them. The next five compositions i.e F to J had constant cement content with increasing PG and decreasing RHA content. The resulting bricks were firm and strong. Therefore, the study is conducted on these five compositions to develop a sustainable brick.

Fig. 5. Manufactured bricks kept for sun drying.

Table 2
Various tests performed on sustainable bricks.

Sr. No.	Tests Performed	IS Codes/References
1	Density and Dimension Test	IS 1077.1992 [14]
2	Compressive Strength Test	IS 3495 Part I.1992 [15]
3	Water Absorption Test	IS 3495 Part II.1992 [15]
4	Voidage Test	IS 3495 Part II.1992 [15]
5	Efflorescence Test	IS 3495 Part III.1992 [15]
6	Specific Heat Capacity	–
7	Shear Bond Test	Source - [16]
8	Flexure Bond Test	ASTM C1072 [17]

3. Results and discussion

3.1. Chemical characterization of PG and RHA

Table 3 shows the findings of the XRF study of PG and RHA. According to the results, the principal ingredients in the PG sample are CaO, F, P_2O_5, SO_3, and SiO_2. The specific gravity of PG is found to range from 2.3 to 2.6, and a maximum dry bulk density varies between 1470 kg/m^3 to 1670 kg/m^3. PG sample is found to have a pH of 2.9, indicating their acidic nature. The major oxides that are found in the RHA samples are iron oxide, silicon dioxide, and aluminium oxide. The specific gravity of RHA is found to be 2.13 and the density of 2216.5 kg/m^3. The specific gravity of cement used is found to be 3.15 and its density is 1440 kg/m^3. From the

Table 3
Chemical composition of phosphogypsum and rice husk ash elements (%).

Chemical composition	Phosphogypsum (PG)%	Rice Husk Ash (RHA)%
Na_2O	0.11	0.12
MgO	0.02	0.44
Al_2O_3	0.13	0.46
SiO_2	1.74	88.32
P_2O_5	1.04	–
SO_3	52.94	–
CaO	38.87	0.67
TiO_2	0.05	–
Fe_2O_3	0.16	0.67
SrO	0.04	–
Y_2O_3	0.008	–
F	0.32	–
K_2O	–	2.91
L.O.I	3.97	5.81

S.P. Raut, Uday Singh Patil and M.V. Madurwar

sieve analysis of PG and RHA samples, the majority of particles were found to be retained on a 0.075 mm sieve i.e (31% and 80% respectively).

3.2. Test on sustainable bricks

The results are tabulated for the five compositions namely F, G, H, I, and J, and a comparative study amongst them with commercially available common burnt clay bricks (BCB) and fly ash bricks (FAB) was carried out for each test.

3.2.1. Dimension test
The size of bricks was kept similar to the conventional BCB and FAB bricks (Table 4). The dimensions of bricks are found to slightly differ from standard modular dimension size with a fluctuation margin of ±5 mm.

3.2.2. Density test
As can be seen from Fig. 6, The density of the bricks is observed to increase as the quantity of PG increases, but the RHA decreases. The lowest density was obtained as 1282.05 Kg/m^3 and a maximum of 1695 Kg/m^3 was observed. The density of BCB is around 1700 Kg/m^3. Thus, in comparison, it can be inferred that the PG-RHA bricks are light-weighted and hence have a lower density than BCB and FAB. This suggests that using the RHA and PG in the right amounts can significantly reduce the unit weight of bricks.

3.2.3. Water absorption test
From Fig. 7, It is observed that as the content of PG increases, the water absorption capacity decreases. However, water absorption values of PG and RHA incorporated bricks were higher than BCB and FAB bricks. But, from the obtained results, it is evident that all the composition has a water absorption capacity of less than 20% which agrees with the Indian standard [11]. The water absorption capacity of bricks I and J also satisfied the Chinese standards (JC/T422-2007) [18] wherein the top limit is given as 18%.

3.2.4. Voidage test
The volume of voids in brick should be minimum. Therefore, composition 'H' filters out to be better than any other composition in achieving the voidage criteria (Fig. 8). The fine texture of RHA and PG provides improved particle packing density due to the filler effect, as a result, the void percentage between particles decreases.

3.2.5. Efflorescence test
The bricks were tested in accordance with IS 3495. Part 3 [15]. Fig. 9, It is observed that there was no perceptible deposit of efflorescence after the conduction of the test on any of the tested sample compositions. Therefore, the liability of efflorescence is nil.

3.2.6. Specific heat capacity test
The specific heat of brick is calculated by using a temperature gun (Fig. 11) to measure the average temperatures on all surfaces of the brick before and after an hour in the oven. The specific heat
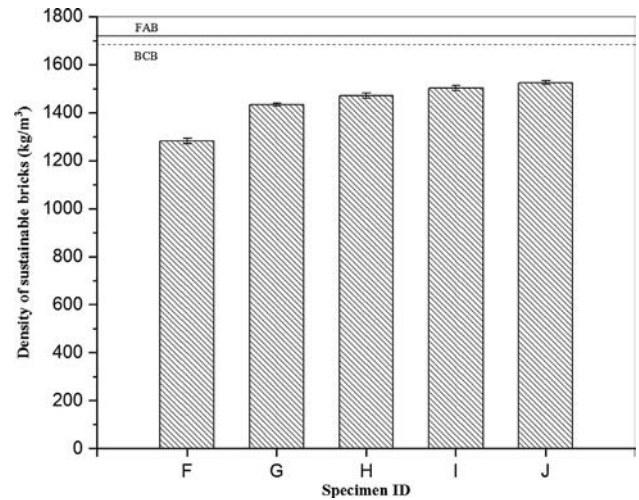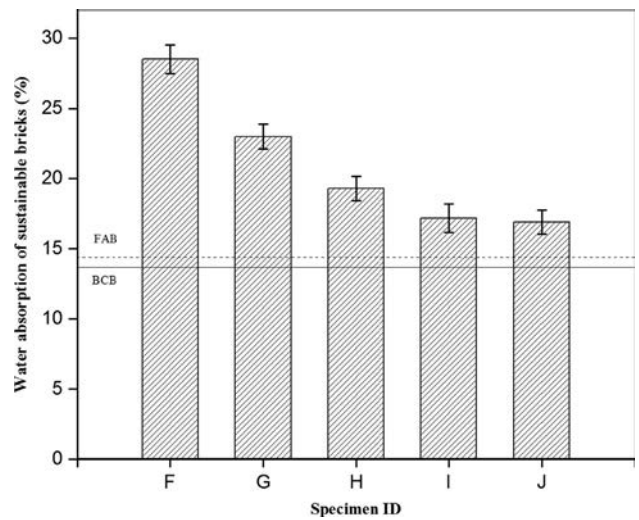
Table 4
Result of dimension test.

Composition	Length (mm)	Width (mm)	Height (mm)
BCB	195	100	70
FAB	195	100	70
F	195	100	70
G	195	100	70
H	195	100	70
I	195	100	70
J	195	100	70

Fig. 6. Density of specimens.

Fig. 7. Water absorption values of specimens.

Fig. 8. Voidage test.

S.P. Raut, Uday Singh Patil and M.V. Madurwar

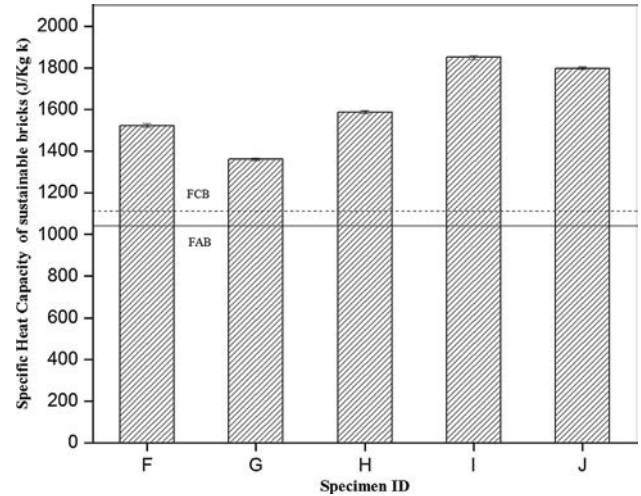**Fig. 9.** Efflorescence test.

Fig. 10. Specific heat capacity test.

capacity is computed using the energy consumed (q) per brick to generate this temperature difference (t) by the known mass (m) of brick, as shown in Table 5. From Table 5 and Fig. 10, it is evident that PG incorporated bricks require more amount of heat than a common BCB to have their temperature increased by one degree Celsius. Therefore, all sample compositions are more effective in temperature control than BCB.

3.2.7. Compressive strength

Fig. 12 shows the results obtained as an average of measurements taken on three specimens of various compositions. It can be seen that as the percentage of PG increases, the brick's compressive strength increases. i.e up to 77.5%, thereafter slightly decreases but the change observed is very small. Similar results were reported in the past study [19] i.e PG incorporated clay brick showed an increase in strength up to 75%, after which a decrease in strength was observed. Sample composition 'H' clearly has the highest failure load and has a compressive strength of 3.7 N/mm^2 which is more than 3.5 N/mm^2 prescribed by Indian Standard for common brick [14] (see Fig. 13).

3.2.8. Load compression curve

From Fig. 14, it is evident that the line for composition H shows lesser compression as compared to other compositions as the load gradually increases. Also, the area under the curve for composition H is more compared to other compositions. Thus it can be inferred that the energy absorption capacity for bricks made with H composition is higher when compared with the other compositions.

3.2.9. Shear bond strength test

The experimental setup for determining shear bond strength is shown in Fig. 15. This strength is related to the mortar/brick bond. It usually falls in the range of 0.10 to 0.30 Mpa. Fig. 16, The test carried out on sample compositions indicates that sample 'H' has the

Fig. 11. Measurement of temperature by temperature gun.

highest shear strength i.e 0.125 Mpa when compared with other compositions and conventional BCB bricks.

3.2.10. Flexure bond strength test

Fig. 17 shows the experimental setup of the flexural bond strength test. Masonry performs well in compression but not so well in tension. Its flexure bond strength is thus determined and it depends on the mortar/brick bond. From Fig. 18, It can be seen that the flexure strength of sample 'H' is 0.09 Mpa whereas sample 'J' has the lowest strength.

Table 5
Result of specific heat capacity test.

Composition	Before avg temp. (k)	After avg temp. (k)	Change in temperature Δt (k)	Mass	Specific heat capacity (J/Kg k)
BCB	7375	10378.83	3003.83	0.236	1143.18
FAB	7376	10590.74	3214.74	0.236	1065.42
F	7374	10355.76	2981.76	0.178	1522.80
G	7374.2	10360.87	2986.67	0.199	1360.88
H	7376	10437.22	3061.22	0.167	1587.60
I	7375	10442.10	3067.10	0.143	1850.54
J	7374	10370.48	2996.48	0.150	1797.84

S.P. Raut, Uday Singh Patil and M.V. Madurwar
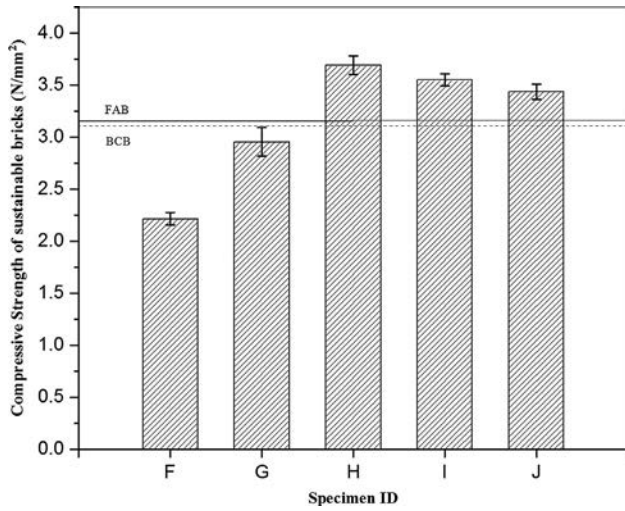
Fig. 12. Compressive strength test.

Fig. 15. Test setup for shear bond strength.

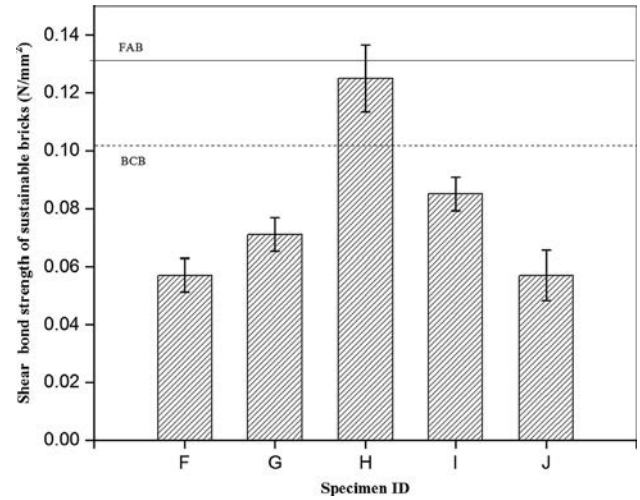**Fig. 13.** Test setup for compressive strength.

Fig. 16. shear bond strength of specimens.
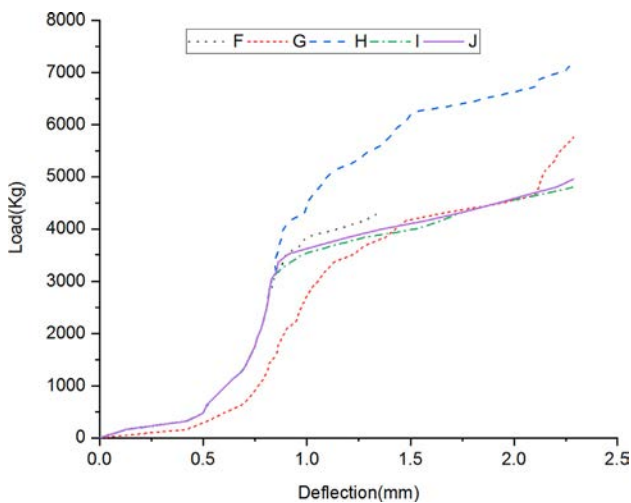

Fig. 14. Combined load-deformation curve of all bricks.

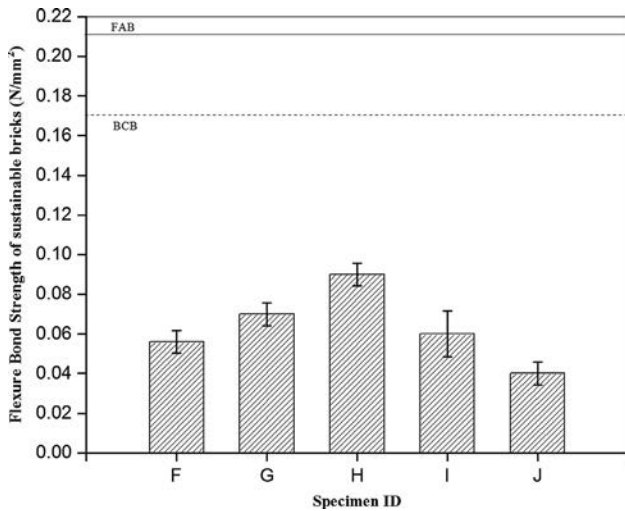**Fig. 17.** Test setup for flexure bond strength.

Fig. 18. Flexure bond strength test.

4. Conclusion

the following conclusions can be drawn from this exhaustive study.

1. The brick composition 'H' has better brick properties than other compositions. It has a compressive strength of 3.7 N/mm², water absorption of 19.3%, voidage of 23.07%, flexure bond strength of 0.09 N/mm², and shear bond strength of 0.125 N/mm².
2. The developed sustainable bricks exhibit better thermal insulation than commercially available BCB and FAB.
3. The optimum percentages of PG in the brick increases the mechanical strength of bricks.
4. The value of water absorption of bricks decreases with a percentage increase of PG.
5. As the RHA percentage increases, the water absorption of brick increases, and the compressive strength of brick reduces. Thus the optimum range of RHA is suggested.
6. The results also show that the PG-RHA bricks with proper composition have higher strength compared to conventional BCB and FAB.

As a result, it can be stated that the use of PG and RHA in the brick manufacturing process can be made environmentally friendly if it is done properly and in the right optimum proportion. Bricks created from these wastes might be considered a better alternative to traditional BCB and FAB. This characteristic can be used to turn waste into wealth.

CRediT authorship contribution statement

Sanjay P. Raut: Conceptualization, Methodology, Formal analysis. **Uday Singh Patil:** Methodology, Writing - original draft, Writing - review & editing. **Mangesh V. Madurwar:** Conceptualization, Methodology, Formal analysis.

Declaration of Competing Interest

The authors declare that they have no known competing financial interests or personal relationships that could have appeared to influence the work reported in this paper.

References

[1] V.D. Katare, M.V. Madurwar, S. Raut, Agro-Industrial Waste as a Cementitious Binder for Sustainable Concrete: An Overview, Sustainable Waste Management: Policies and Case Studies, 2020, pp. 683-702.
[2] V.V. Sakhare, S.P. Raut1, S.A. Mandavgane, R.V. Ralegaonkar, Development of sustainable retrofitting material for energy conservation of existing buildings, Int. J. Civil Eng., 13(4A) (2015) 411-418.
[3] T.P. Mashifana, Chemical treatment of phosphogypsum and its potential application for building and construction, Procedia Manuf. 35 (2019) 641–648.
[4] R. Pérez-López, A.M. Álvarez-Valero, J.M. Nieto, Changes in mobility of toxic elements during the production of phosphoric acid in the fertilizer industry of Huelva (SW Spain) and environmentalimpact of phosphogypsum wastes, J. Hazard. Mater. 148 (3) (2007) 745–750.
[5] A.M. Rashad, Phosphogypsum as a construction material, J. Cleaner Prod. 166 (2017) 732–743.
[6] M. o. E. F. &. C. C. CPCB, Guidelines for Management, Handling, Utilisation and Disposal of Phosphogypsum Generated from Phosphoric Acid Plants, Delhi, India: Central Pollution Control Board, 2014-15.
[7] M. o. E. a. Forest, The Hazardous Wastes (Management, Handling And Transboundary Movement) Rules, 2008, Ministry of Environment and Forest, New Delhi, India, 2008.
[8] SK.S. Hossain, L. Mathur, P.K. Roy, Rice husk/rice husk ash as an alternative source of silica in ceramics: a review, J. Asian Ceram. Soc. 6 (4) (2018) 299–313.
[9] B. Singh, in: Waste and Supplementary Cementitious Materials in Concrete, Woodhead Publishing, 2018, pp. 417–460, https://doi.org/10.1016/B978-0-08-102156-9.00013-4.
[10] P.N. Babaso, H. Sharanagouda, Rice Husk and Its Applications: Review, Int. J. Curr. Microbiol. Appl. Sci. 6 (10) (2017) 1144–1156.
[11] A. Nuamah, A. Malmgren, G. Riley, E. Lester, in: Comprehensive Renewable Energy, Elsevier, 2012, pp. 55–73, https://doi.org/10.1016/B978-0-08-087872-0.00506-0.
[12] B. Mistry, Properties and Industrial Applications of Rice Husk, Int. J. Eng. Sci. Computing 6 (10) (2016) 2677–2679.
[13] Patil Udaysingh, Raut Sanjay Padmakar, Ralegaonkar Rahul V, Madurwar Mangesh V, Sustainable building materials using textile effluent treatment plant sludge: a review, Green Materials, 2021, pp. 1-15, 10.1680/jgrma.21.00027.
[14] IS 1077:1992, Common Burnt Clay Building Bricks- Specification, India: Bureau Of Indian Standards, 1992.
[15] IS 3495 (Parts 1 to 4): 1992 Methods of Tests of Burnt Clay, India: Bureau of Indian Standards.
[16] G. Sarangapani, B.V. Venkatarama Reddy, K.S. Jagadish, Brick-Mortar Bond and Masonry Compressive Strength, J. Mater. Civ. Eng. 17 (2) (2005) 229–237.
[17] ASTM C1072, - Standard Test Methods for Measurement of Masonry Flexural Bond Strength,2019 Edition, December 1, 2019.
[18] Non-fired rubbish gangue brick. JC/T422-2007. Bureau of Building Materials Industry of China, Beijing, 2007 [in Chinese with English abstract].
[19] J. Zhou, H. Gao, Z. Shu, Y. Wang, C. Yan, Utilization of waste phosphogypsum to prepare non-fired bricks by a novel Hydration-Recrystallization process, Constr. Build. Mater. 34 (2012) 114–119.

Development of self-compacting concrete blended with sugarcane bagasse ash

Monali Wagh [*], U.P. Waghe [b]

[a] Research Scholar & Assistant Professor ,Department of Civil Engineering, Yeshwantrao Chavan College of Engineering, Nagpur, India
[b] Professor, Department of Civil Engineering, Yeshwantrao Chavan College of Engineering, Nagpur, India

ARTICLE INFO

ABSTRACT

Self-compacting concrete (SCC) can be flows in crowded reinforcement without segregation and it flows under its own weight without vibration. Sugarcane Bagasse ash (SCBA) (agricultural waste) is present in massive amounts in India. The use of SCBA in SCC is described in this paper as a feasible solution to environmental concerns. The usage of bagasse ash is important for sustainable development since it decreases carbon emissions and structural costs. The goal of this study is to discover and compare the fresh and strength properties of SCC made using SCBA as replacement of cement in 0, 10, 15 and 20%. The fresh characteristics of SCC are marginally lowered when the proportion of SCBA increases due to partial cement replacement, but they remain within the EFNARC range. It has been discovered that using it in SCC improves its strength properties.

Copyright © 2022 Elsevier Ltd. All rights reserved.
Selection and peer-review under responsibility of the scientific committee of the International Conference on Latest Developments in Materials & Manufacturing.

1. Introduction

Sugar cane is one of the most widely farmed crops in the world, with a total production of over 1500 million tonnes in over 110 nations [1]. Every year, India produces around 10 million tonnes of SCBA and 300 million tonnes of sugarcane [2]. The sugar processing industry produces SCBA as a by-product. Many researchers proposed that bagasse ash is pozzolanic in nature and it improves properties of concrete [3]. SCBA's pozzolanic reactivity is fundamental to the reported results [4]. SCBA contains amorphous silica, which produces pozzolanic action [5]. As a result, scientists have looked at the utilization of SCBA as a pozzolanic supplementary cementitious materials in order to limit CO_2 emissions into the environment [6,7]. Adding up to 15% SCBA reduced porosity and sorptivity while increasing strength and durability properties [8].

SCC is a rising concrete with new properties like filling, passing through congested reinforcement, and resistance to segregation. A higher binder concentration (400–600 kg/m^3), a low water- powder ratio, a smaller coarse aggregate quantity, and a superplasticizer admixture are all required for SCC mixtures [9]. Add a viscosity modifying admixture (VMA) to the SCC mixture to accomplish the viscosity property . In SCC, the addition of alternate cement-based materials saves material costs while improving self-compaction. SCC research has recently focused on the incorporation of extra cementitious materials with the goal of alleviating solid waste disposal issues. When agricultural by-products like SCBA are employed in concrete manufacturing, significant energy and cost reductions is attainable [10]. For achieving self-consolidation is to substantially surge the volume of fine materials such as SCBA without raising the pricing [11]. Because SCBA has a larger percentage of amorphous silica, it is an outstanding pozzolanic material and may be utilised as an advantages cementitious material [12]. The strength properties of specimens formed from a combination of 30% SCBA and 30% BFS in place of OPC was equivalent to that of the control.

In SCC, significantly enhanced sulphate resistance, particularly in mixtures with the greatest SCBA ratio . Ingredients for a particular SCC including bagasse ash are 35.63 percent less expensive than those for a control concrete . GGBFS, SCBA, and fly ash have enhanced the strength, and durability because of silica rich content [13]. With the accumulation of SCBA to SCC, the resistance to sulphate assault is reduced [14]. SCC slump flow improves with more bagasse ash, and filling and passing ability improves . Low permeability, decreased ion penetration, and strong resistance to heat assault were seen in concrete replaced with SCBA, resulting

* Corresponding author.
E-mail address: wagh.monali04@gmail.com (M. Wagh).

proved durability [16]. When cement is substituted in the concrete with 10% SCBA and 10% micro silica by weight proportion, the concrete has the best tolerance to sulphate and chloride attack [17]. With the accumulation of SCBA in concrete, decreases weight loss by sulfuric acid attack [18].

The goal of this study is to use SCBA as an advantageous cementitious material in the formation of SCC that is environmentally friendly. An exploratory approach is used to examine the fresh and strength characteristics of the proposed SCC. This research would add to a growing body of information about the use of agricultural wastes in the production of environmentally friendly concrete.

2. Materials Used:

2.1. Cement (OPC)

The OPC cement of grade 43 was used to make self-compacting concrete. The cement conformed through IS 8112–2013. For all concrete mixtures, Ultra Tech cement was utilised to cast cubes, beams and cylinders.

2.2. Aggregate

The fine and coarse aggregate used in the studies conformed to IS 383 provisions. The fine aggregate was sieved using a 4.75 mm sieve, while the coarse aggregates were 10 mm and 20 mm in size. The specific gravity of fine aggregate, 10 mm and 20 mm coarse aggregate are 2.68, 2.86 and 2.90 respectively.

2.3. Sugarcane bagasse ash (SCBA)

The SCBA utilised in this investigation was collected from sugarcane industry Devhala district, Tumsar, India. Chemical composition of sugarcane bagasse ash by X-ray fluorescence (XRF) was investigated and shown in Table. 1. At IBM Nagpur, XRF tests were performed. Furthermore, the findings of the X-ray fluorescence study on SCBA reveal that this material has a high silica content of 54.93 percent SiO_2, followed by Al_2O_3 37.14%, TiO_2 2.53% and Fe_2O_3 1.15%. The colour of SCBA is grey (Fig. 1). The specific gravity of sugarcane bagasse ash is 1.9. SCBA is irregular in shape, as demonstrated by SEM examination. (Fig. 2). Fig. 3 shows the result EDS analysis for SCBA. From EDS analysis, it is observed that the silica content is higher than other elements (see Figs. 4–9).

2.4. Superplasticizer

Visco-Flux 5507 was used as superplasticizer in SCC. The relative density is 1.11 at 27 °C with pH is greater than 6. This product confirmed with ASTMC-494 Type A and F and IS 9103–1999.
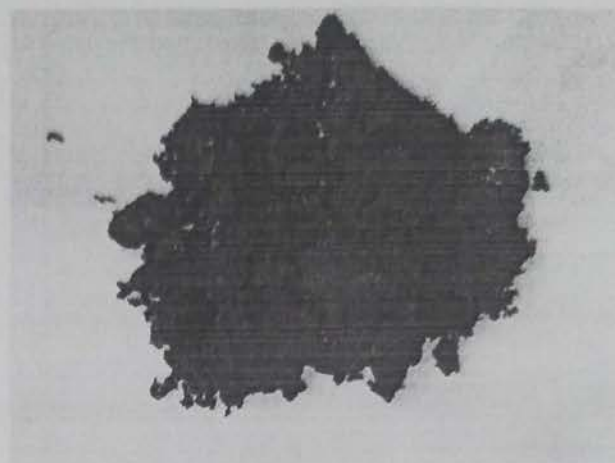

Fig. 1. Photos of SCBA sample utilised in this research.

Fig. 2. Scanning electron micrographs for SCBA.

2.5. Viscosity modifying admixture (VMA)

AC-Gel-Build was used as VMA in SCC. The relative density is 1.0 with pH value in between 5 and 8. This product confirmed with IS 9103–1999.

3. Experimental Programme:

Table 2 shows mix proportioning data of the SCBA integrated self-compacting concrete along with their specified designation. The SCC mixes contains 0%, 10%, 15% and 20% of SCBA as a supplementary to the cement designated as SCCB0, SCCB10, SCCB15 and SCCB20 respectively. For this study, total 4 trial mixes are produced by incorporating various percentage of SCBA. Total 9 cube
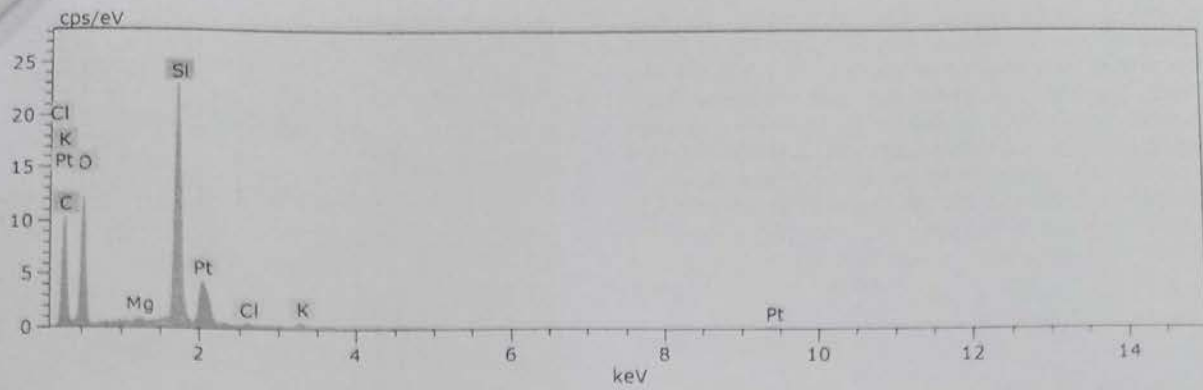
Table 1
Chemical compositions of cement and SCBA using X-ray fluorescence.

Materials	Chemical composition (%)								
	Na_2O	MgO	Al_2O_3	SiO_2	SO_3	K_2O	P_2O_5	SrO	BaO
Bagasse Ash	0.18	0.19	37.14	54.93	0.15	0.15	0.11	0.02	0.02
Cement	0.7	1.92	4.29	22.93	0.35	0.9	–	–	–
	CeO_2	TiO_2	Cr_2O_3	Fe_2O_3	MnO_2	CaO	Cl	ZrO_2	Bi_2O_3
	0.05	2.53	0.03	1.15	0.02	1.3	0.02	0.04	0.03
	–	–	–	2.89	–	66.2	–	–	–

Fig. 3. Energy Dispersive X-ray Spectroscopy for SCBA.
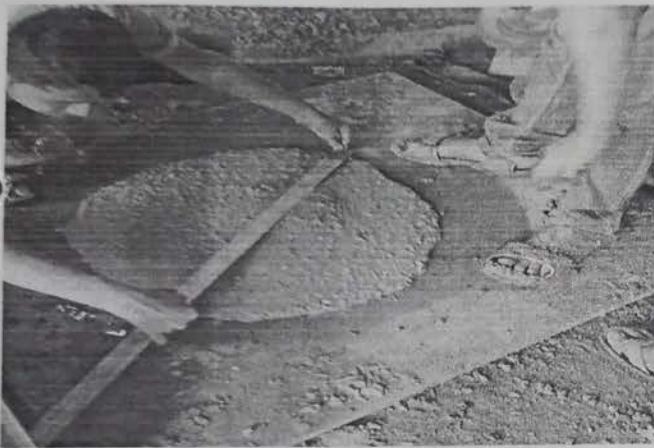

Fig. 4. The photo shows Slump Flow test.

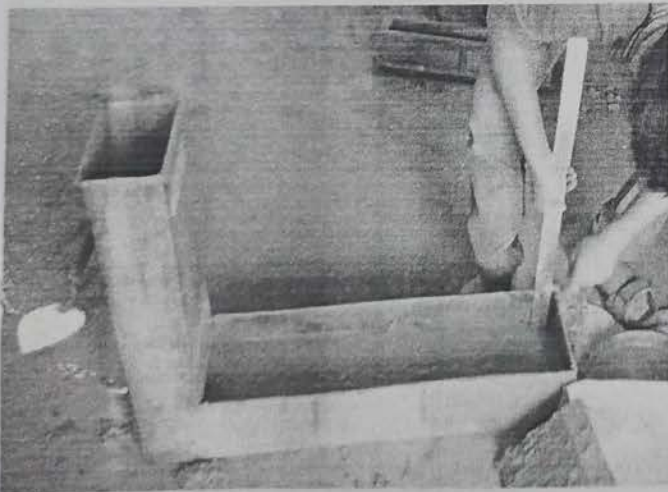
Fig. 6. The photo shows V-Funnel test.

Fig. 5. The photo shows L-Box test.

Fig. 7. The photo Cube, Beam and Cylinder prepared.

of size 150mmx150mmx150mm and 9 beams of size 100 mm x100mm x500mm are prepared for each mix proportion. Viscoflux 5507, a high range water lowering concrete additive, was employed to create excellent workability and flowability. The amount of superplasticizer was used constant as 1.2% by weight of the binder ingredient. The VMA dosage of 0.3% by total weight of the binder ingredient is incorporated in the work. Slump-flow, V-funnel test, T500 slump and L-box test were all assessed in the fresh test. Compressive strength (CS) and the flexural strength

(FS) was all tested at various ages in the hardened condition. Table 3.

4. Result and Discussion:

4.1. Slump flow test

Values of slump were measured on all SCC mixtures and completely fell within the limits of 650 mm to 800 mm for slump flow

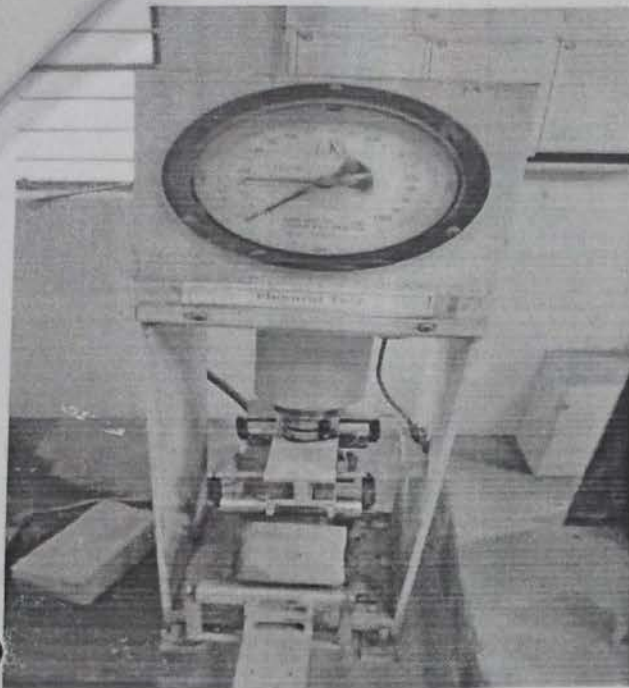(see Fig. 10), which are adequate for several situations and suggested by EFNARC. When compared to the control sample (SCCB0), which had the most slump and slump flow, substituting SCBA in mixes leads to lower flowability [ ]. In a newly developed SCC, the larger the quantity of supplementary cementitious materials, the slump flow shows the lower value than the control sample. In comparison to the control group, the slump flow values of fresh SCC mixtures containing 10%, 15%, and 20% SCBA was reduced from 693 mm to 689 mm, 671 mm, 667 mm respectively. The above finding was in line with earlier observations [ ] and it might be due to various of factors.

4.2. T 500 slump flow test

The average diameter of slump flow of the SCC mixes was in between 650 and 700 mm which indicating reasonable flowability. The easiest method for determining the flowability of SCC is T-500 slump flow testing. According to EFNARC recommendations (EFNARC, 2002), the time necessary for the SCC combinations to spread 50 cm ranged from 2 to 5 s [ ]. The slump flow time surges with the amount of SCBA in self-compacting concrete. The slump flow time increases with the use of SCBA in SCC because of high surface area. Maximum slump flow time is recorded for SCCB20.

4.3. V-Funnel Test

The EFNARC specified that V-funnel flow times should be between the time period of 6 to 12 s [ ]. The V-funnel timings in mixes SCCB0, SCCB10, SCCB15 and SCCB20 were all within the required range. Because the particles soaked water, the flow time rose as the amount of SCBA grew, resulting in extraordinarily viscous mixtures [10]. As shown in Fig. 11, the V funnel timing were recorded in between 7 and 11 sec. When SCBA were replaced with OPC, the flow duration of fresh concrete was consistently increased, as shown in Fig. 11. The flow time recorded is largest for SCCB20 which is 36% superior than the control mix.

4.4. L-Box test

The L-Box test determines the capability to pass through densely congested reinforcing by its own weight. The higher values of H_2/H_1 ratio shows the higher passing capability, and vice versa. Fig. 11 shows that, with the addition of SCBA in SCC resulted in the lower values of H_2/H_1 ratio as compare to the control SCC mix. The values of H_2/H_1 ratio were in the range of 0.86 to 0.91 as shown in Fig. 11.

4.5. Compressive strength (CS)

The CS was performed for the all mixes of SCC at of 7 days, 14 days and 28 days. The CS for the control mix of SCC were 35.04, 42.89 and 48.81 N/mm^2 at 7, 14 and 28 days respectively. The CS of the SCC made with the use of SCBA as a partial substitution to the cement, were comparable to the control mix. The CS of control mix of SCC at 7, 14 and 28 days were 35.04, 42.89 and 48.81Mpa respectively. The SCC blended with SCBA performed

Fig. 8. The photo shows Flexural strength test.

Fig. 9. The photo shows Compressive strength test.

Table 2
Mix Proportion of developed SCC.

No.	Type	Mix I.D.	Cement %	SCBA %	Aggregates(kg/m³)		Fly Ash(kg/m³)	Superplasticizer (%)
					Coarse	Fine		
1	Single	SCCB0	100	0	796.6	928.38	110	1.2
2	Binary	SCCB10	90	10	796.7	888.06	110	1.2
3	Binary	SCCB15	85	15	796.7	874.61	110	1.2
4	Binary	SCCB20	80	20	796.8	861.17	110	1.2

Properties of developed SCC.

Sr. No.	Type	Mix I.D.	Slump flow Dia. in (mm)	T-500 in (sec)	V-funnel Time (sec)	L box Test (H₂/H₁)
1	Single	SCCB00	693	3.6	7.56	0.91
2	Binary	SCCB10	689	3.91	9.01	0.89
3	Binary	SCCB15	671	4.1	9.54	0.87
4	Binary	SCCB20	667	4.3	10.3	0.86
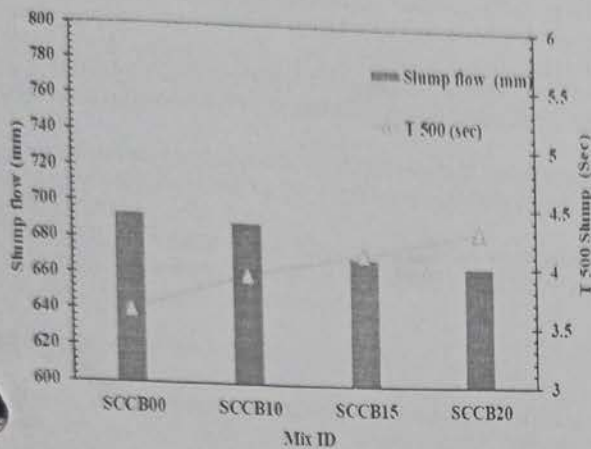
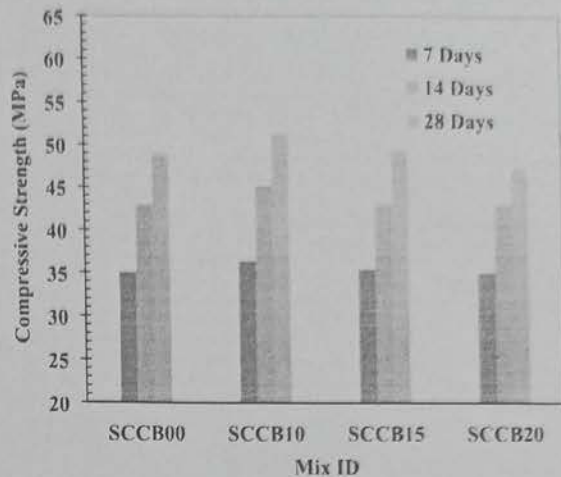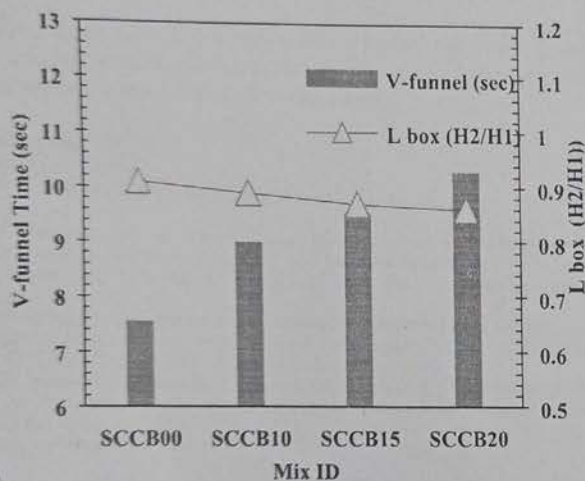Fig. 10. Slump Flow and T-500 Slump Time of newly prepared SCC with respect control mix.

Fig. 11. V-funnel Time & L-Box (H2/H1) of newly prepared SCC with respect control mix.

Fig. 12. CS of developed SCC blended with SCBA at 7, 14 and 28 days.

14 days and 28 days respectively. The FS of developed SCC with 10% substitution of cement with SCBA were 10.46% greater than that of control mix. The maximum strength occurred for SCCB10 mixes. At the age of 7 days, the FS of SCC blended with 10% and 15% SCBA were 11.22% and 5.44% superior than that of SCCB0. At 28 days, the FS of SCC blended with 10% and 15% SCBA were 10.46% and 3.43% higher than that of SCCB0. Furthermore, when the SCBA replacing level grew, the strength of the mixture improved, indicating that the pozzolanic hydration of SCBA progressed with time [9].

Further increase of SCBA up to 20% in SCC, reduces the FS little bit. The optimum percentage of SCBA in SCC was observed to be 15% as a replacement by cement. Boukendakdji et al. observed that the pattern of strength variation induced by slag substitution was comparable in SCC with 10% to 15% slag substitution [21].
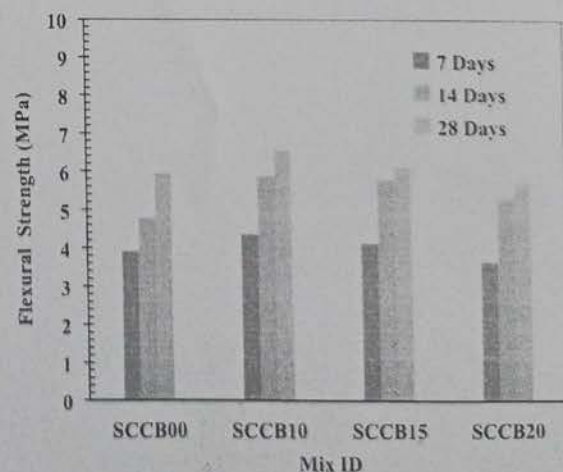
3.8%, 1.26% greater strength for SCCB10 and SCCB15 respectively as equated to control mix at 7 days. The strength of SCBA blended SCC were comparable or even superior than that of control mix of SCC. For SCCB10, the strength of SCC was 5.02% greater than that of SCCB0 at 28 days as shown in Fig. 12. When compared to a control mix, SCC combined with 10% bagasse ash increases CS, split tensile strength, and FS by 8.5, 35, and 33% respectively [14]. Improved the strength properties as well as impact resistance if SCC containing 5% of bagasse ash [15]. The CS of SCC with 20% SCBA as replacement of cement was nearer to control mix [20].

4.6. Flexural strength (FS)

Fig. 13 exhibited the FS of all developed SCC mixes blended with SCBA. The FS of SCCB0 were 3.92, 4.80, and 5.93 MPa at 7 days,

Fig. 13. FS of developed SCC blended with SCBA at 7, 14 and 28 days.

Conclusion:

1. In the development of SCC, the use of SCBA as a cement substitute may be advantageous.
2. Fresh properties of SCC are slightly reduced as percentage of bagasse ash as partial substitution of cement increases, but are within the range of EFNARC.
3. Slump flow and L-box results are marginally reduced when SCBA is used as a substitution of the cement in developed SCC.
4. V-funnel time and T-500 slump increases with the increase of SCBA as a substitution of the cement in developed self-compacting concrete but within the range of EFNARC.
5. Optimum percentage of SCBA as a substitution of cement in SCC is 15%.
6. The compressive strength (CS) of developed SCC blended with SCBA were 5.02% greater for SCCB10 and comparable to control mix for SCCB15 at 28 days.
7. The flexural strength of SCC blended with SCBA were 10.46% and 3.43% enhanced for SCCB10 and SCCB15 respectively at 28 days as compare to control mix.

CRediT authorship contribution statement

Monali Wagh: Conceptualization, Data curation, Writing – review & editing. **U.P. Waghe:** Methodology, Validation, Investigation.

Declaration of Competing Interest

The authors declare that they have no known competing financial interests or personal relationships that could have appeared to influence the work reported in this paper.

References

[1] J. A. Patel and D. B. Raijiwala, "Use of Sugar Cane Bagasse Ash as Partial," vol. 15, no. 5, 2015.
[2] S. Dhengare et al., "Utilization of Sugarcane Bagasse Ash As a Supplementary Cementitious Material in Concrete and Mortar-a Review," Int. J. Civ. Eng. Technol., vol. 0976, no. 4, pp. 94–106, 2015, [Online]. Available: www.jifactor.com.
[3] N. Chusilp, C. Jaturapitakkul, K. Kiattikomol, Utilization of bagasse ash as a pozzolanic material in concrete, Constr. Build. Mater. 23 (11) (2009) 3352–3358, https://doi.org/10.1016/j.conbuildmat.2009.06.030.
[4] J.T. Kolawole, A.J. Babafemi, E. Fanijo, S. Chandra Paul, R. Combrinck, State-of-the-art review on the use of sugarcane bagasse ash in cementitious materials, Cem. Concr. Compos. 118 (2021) 103975, https://doi.org/10.1016/j.cemconcomp.2021.103975.
[5] S.A. Khawaja, U. Javed, T. Zafar, M. Riaz, M.S. Zafar, M.K. Khan, Eco-friendly incorporation of sugarcane bagasse ash as partial replacement of sand in foam concrete, Clean. Eng. Technol. 4 (2021) 100164, https://doi.org/10.1016/j.clet.2021.100164.
[6] E.M.R. Fairbairn, B.B. Americano, G.C. Cordeiro, T.P. Paula, R.D. Toledo Filho, M. M. Silvoso, Cement replacement by sugar cane bagasse ash: CO2 emissions reduction and potential for carbon credits. J. Environ. Manage. 91 (9) (2010) 1864–1871, https://doi.org/10.1016/j.jenvman.2010.04.008.
[7] J.P. Moretti, S. Nunes, A. Sales, Self-compacting concrete incorporating sugarcane bagasse ash, Constr. Build. Mater. 172 (2018) 635–649, https://doi.org/10.1016/j.conbuildmat.2018.03.243.
[8] J.d.S. Andrade Neto, M.J.S. de França, N.S.d. Amorim Júnior, D.V. Ribeiro, Effects of adding sugarcane bagasse ash on the properties and durability of concrete, Constr. Build. Mater. 266 (2021) 120959, https://doi.org/10.1016/j.conbuildmat.2020.120959.
[9] D.H. Le, Y.N. Sheen, M.N.T. Lam, Fresh and hardened properties of self-compacting concrete with sugarcane bagasse ash–slag blended cement, Constr. Build. Mater. 185 (2018) 138–147, https://doi.org/10.1016/j.conbuildmat.2018.07.029.
[10] G. Sua-iam, N. Makul, Use of increasing amounts of bagasse ash waste to produce self-compacting concrete by adding limestone powder waste, J. Clean. Prod. 57 (2013) 308–319, https://doi.org/10.1016/j.jclepro.2013.06.009.
[11] T. Akram, S.A. Memon, H. Obaid, Production of low cost self compacting concrete using bagasse ash, Constr. Build. Mater. 23 (2) (2009) 703–712, https://doi.org/10.1016/j.conbuildmat.2008.02.012.
[12] W. Ahmad, A. Ahmad, K.A. Ostrowski, F. Aslam, P. Joyklad, P. Zajdel, "Sustainable approach of using sugarcane bagasse ash in cement-based composites: A systematic review", Case Stud. Constr. Mater. 15 (2021) e00698, https://doi.org/10.1016/j.cscm.2021.e00698.
[13] A.S. Suprakash, S. Karthiyaini, M. Shanmugasundaram, Future and scope for development of calcium and silica rich supplementary blends on properties of self-compacting concrete - A comparative review, J. Mater. Res. Technol. 15 (2021) 5662–5681, https://doi.org/10.1016/j.jmrt.2021.11.029.
[14] A. Khatun, K. Singh, R. Sharma, Utilization of bagasse ash as a partial replacement of cement in self-compacting concrete, Int. J. Civ. Eng. Technol. 9 (7) (2018) 1078–1088.
[15] S.A. Zareei, F. Ameri, N. Bahrami, Microstructure, strength, and durability of eco-friendly concretes containing sugarcane bagasse ash, Constr. Build. Mater. 184 (2018) 258–268, https://doi.org/10.1016/j.conbuildmat.2018.06.153.
[16] B. Yogitha, M. Karthikeyan, M.G. Muni Reddy, Progress of sugarcane bagasse ash applications in production of Eco-Friendly concrete - Review, Mater. Today Proc. 33 (xxxx) (2020) 695–699.
[17] M.I. Khan, M.A.A. Sayyed, M.M.A. Ali, Examination of cement concrete containing micro silica and sugarcane bagasse ash subjected to sulphate and chloride attack, Mater. Today Proc. 39 (xxxx) (2020) 558–562, https://doi.org/10.1016/j.matpr.2020.08.468.
[18] P. Chindaprasirt, P. Sujumnongtokul, P. Posi, ScienceDirect Durability and Mechanical Properties of Pavement Concrete Containing Bagasse Ash, Mater. Today Proc. 17 (2019) 1612–1626, https://doi.org/10.1016/j.matpr.2019.06.191.
[19] P. Dinakar, Design of self-compacting concrete with fly ash, Mag. Concr. Res. 64 (5) (2012) 401–409, https://doi.org/10.1680/macr.10.00167.
[20] A.G. Abdel-Rahman, Mechanical Properties of Self Compacting Concrete, ERJ. Eng. Res. J. 25 (2) (2002) 1–11, https://doi.org/10.21608/erjm.2002.70617.
[21] O. Boukendakdji, S. Kenai, E.H. Kadri, F. Rouis, Effect of slag on the rheology of fresh self-compacted concrete, Constr. Build. Mater. 23 (7) (2009) 2593–2598, https://doi.org/10.1016/j.conbuildmat.2009.02.029.

Use of industrial waste burnt residue to develop sustainable brick

S.S. Meshram [a,*], S.P. Raut [b], M.V. Madurwar [c]

[a] Department of Civil Engineering, YCCE, Nagpur 44110, India
[b] Department of Civil Engineering, YCCE, Nagpur 441110, India
[c] Department of Civil Engineering, VNIT, Nagpur 440012, India

ARTICLE INFO

ABSTRACT

An increase in environmental concern has occurred from the accumulation of mismanaged industrial burned residue, particularly in developing countries. Recycling these wastes as a sustainable building material seems to be a potential solution not only to the pollution problem, but also to the cost of green building design. In order to develop sustainable construction materials, industrial and incinerated left-over materials are being used. The goal of this research is to find out more about the probability of replacing natural soil in brick production with burned industrial waste, such as Cupola Slag and fly ash. This study is based on various mix proportions for making bricks keeping constant cement by 10 %. Brick mixture was prepared with cupola slag and fly ash for various proportions. From the five distinct mixes with variable CS from 80% to 60%, the M1 mix with 80 % CS, 10% FA, 10% Cement had the highest compressive strength 4.5 N/mm^2. Compressive strength for burnt clay bricks is 3.5 N/mm^2 which is less than cupola slag bricks, while the brick mix M5 (60 CS: 30 FA: 10 cement) had the lowest water absorption and density 6.53 % and 1350.57 kg/m^3. This study reveals that used of cupola slag and fly ah in combination gives satisfactory results to be used in making sustainable bricks. This study also reflects the use of burnt residue to developed sustainable building blocks.
Copyright © 2022 Elsevier Ltd. All rights reserved.
Selection and peer-review under responsibility of the scientific committee of the Sustainable Materials and Practices for Built Environment.

1. Introduction

As a result of urbanization, a large quantity of solid waste was produced, and disposal of this waste became a big issue. Dumping and land-filling of solid waste causes environmental deterioration such as ground water contamination due to leaching, soil pollution, and human health concerns. In recent years, solid waste utilization has grown in potential to recycle valuable materials while reducing solid waste volume, other pollutants, and disposal costs. Brick is a widely utilized building material all over the world. Brick plays an essential part in the construction sector due to its exceptional qualities like as low cost, high strength, and long durability [1]. Because of the high demand for building materials, particularly in the previous decade as a result of rising population, there is a gap in demand–supply management of these resources. As a result, experts are working to create and develop sustainable alternative building material options to suit the ever-increasing demand. Lightweight construction materials low-cost and environmentally friendly are becoming increasingly popular in the construction sector has demanded research on ways to do so while still following the standards material criteria. [2]. Approximately 960 million tonnes of solid waste are created per annum in India as waste material of industrial, mining, and mining operations [3]. Various industrial and agricultural wastes are now being used to create building blocks that provide a long-term answer for the construction sector [4]. Cupola slag is a waste product produced by the cast iron industry when molten steel is alienated from impurities in cupola furnaces [5]. During the cast iron production process in cupola furnaces, roughly 57 percent of the waste is produced. Industry produces between 50 and 3000 tonnes of C.I [6]. In concrete, cupola slag has been used as a partial cement substitute [7]. Cupola slag was also employed in concrete to evaluate its behavior as a partial replacement for both coarse and fine aggregate combinations [8]. For increasing various thermo-mechanical properties, several types of bricks such as burnt clay bricks, fly ash bricks, stone masonry, refractory bricks, solid sand lime bricks, blocks, and thermos acoustic bricks can be employed [9]. Different waste materials were used to make sustainable bricks, including co-fired blended ash, spent mushrooms compost, electric arc furnace

* Corresponding author.
 E-mail address: sangitameshram3@gmail.com (S.S. Meshram).

S.S. Meshram, S.P. Raut and M.V. Madurwar

dust, recycle paper mills waste, ground granulated blast furnace Slag, Sugarcane Bagasse ash, waste glass sludge, waste tyre rubber, construction waste, and residues made from recycled paper. The use of waste glass sludge improved the thermal performance of bricks [10].

Several studies have employed cupola slag as a substitute for cement, fine and coarse aggregate in concrete, pavement, and mortar. Furthermore, there is no research on cupola slag utilized in bricks. This can be put to good use in the manufacture of building blocks. Using this cupola slag as a raw material for making sustainable building materials will not only address the issue of environmental pollution, but it will also improve construction efficiency makes the construction materials sustainable and cost-effective. Cupola slag (CS) was used as the principal raw material in this investigation, along with fly ash as an industrial waste and a consistent cement percentage. Cupola slag and fly ash were physically and chemically characterised in order to determine their suitability as a raw material for developing sustainable building blocks. The physico-mechanical properties of the developed bricks were tested. This research focuses on the efficient use of cupola slag to generate cost-effective, long-lasting, and high-performance building blocks, providing another option for industrial waste management and pollution prevention.

2. Materials And Test Methods

2.1. Raw materials and preparation of brick specimen

Cupola slag and fly Ash (FA) was utilized as an industrial waste in this paper. As a binding material, cement was used. Though the cement percentage was kept constant, variable proportions of fly ash and cupola slag were utilized to provide a wide range of results. Fly ash is a finely distributed residue formed by the burning of pulverized coal that is conveyed away from the combustion chamber by exhaust gases. Coal-fired power plants and steam plants produce fly ash. Coal is commonly pulverized and mixed with air in a boiler's combustion chamber, where it quickly burns, producing molten mineral residue and the heat. Fly ash was gathered from the thermal power plant in Khaperkheda, Nagpur, Maharashtra as shown in Fig. 1. Cupola slag is a type of industrial waste that comes from the steel industry Neco Heavy Engineering and casting limited, MIDC Hingna, Nagpur, Maharashtra. This can only be used for land filling purposes. Cupola slag is a thick substance with a lot of iron filling shown in Fig. 2 (a). Before employing slag

Fig 1. Fly ash dumped at Thermal Power plant.

in bricks, it must be sieved. It was sieved using a 1.18 mm IS sieve as per Fig. 2 (b). As a binding material, OPC grade 53 cement was used. It was utilized in all proportions with a minimum percentage and a constant proportion.

The quantity of raw materials necessary was first determined using various combinations of cupola slag, fly ash, and cement, as well as the dimensions of the mould ($190 \times 90 \times 90$ mm) and densities of all raw materials. Cupola slag was dry mixed with fly ash and cement in the quantities listed in Table 1. The water was then added into the dry mixture by hand mixing, and blending was resumed until a homogenous consistency was reached. A frog with dimensions of $140 \times 60 \times 10$ mm was cast using the same dimensioned hardwood piece as the brick. Bricks (Fig. 3) were made with the proper moulds. The bricks are next dried for seven days in the sun in a rain-protected shed.

2.2. Test methodology

The chemical constituents of raw materials were analyzed out using X-ray fluorescence (XRF). Using an XRF spectrometer, the elemental composition of cupola slag was examined (Indian bureau of Mines, Nagpur). IS 2386 (Part III):1963 was used to calculate the specific gravity of raw materials [12]. The cupola's particle size distribution was also examined. Block densities are calculated according to IS 2185 (Part 1): 2005 [13]. IS 3495 (Part 1): 1992 was used to conduct compressive strength tests on cupola slag brick specimens (Fig. 3) [14]. All generated bricks were exposed to compressive load at a constant rate of 14 N/mm² per minute until failure happened. The weight of bricks soaked in water for 24 h and oven dried brick specimens were used to determine water absorption for bricks. A total of 100 brick specimens were made of various concentrations.

3. Results and discussion

3.1. Properties of raw materials

3.1.1. Chemical composition

The chemical composition of cupola slag and fly ash is shown in Table 2. Cupola slag has substantial amounts of silica and alumina, making it ideal for brick production. The cupola slag also contained trace levels of calcium oxide, magnesium oxide, and iron oxides. The presence of a large amount of silica in the cupola slag improves the binding properties of the brick specimen. Fly ash also has a higher concentration of silica. Cupola slag has more calcium oxide than fly ash, which may contribute to pozzolanic activity. The majority of the chemical composition is made up of SiO_2 and CaO. When Al_2O_3 and MgO were present, more cementitious hydration products were produced. The presence of large quantities of silicon, calcium, and aluminium oxides in the cupola slag indicates that the material has a high reactivity potential. If the content of silica (SiO_2) is greater than 25 %, Sum of Silica (SiO_2), Alumina (Al_2O_3) and iron oxide (Fe_2O_3) is greater than or nearly Equal to 70% and Sulphur (SO_3) is less than 5%, the material can be utilized as a supplementary cementitious material. Cupola slag also has a larger percentage of lime, which aids in the improvement of binding properties.

3.1.2. Specific gravity and unit weight

CS and FA had specific gravities of 2.917 and 1.87, respectively. The water absorption of CS and FA was 0.37 percent and 11 percent, respectively, with CS having much lower water absorption than FA. CS and FA had a density of 1477. 71 kg/m³ and 1310 kg/m³ could help reduce the weight of a single brick, resulting in a

S.S. Meshram, S.P. Raut and M.V. Madurwar

Fig. 2. (a) Cupola Slag before sieving (b) Cupola Slag after sieving.

Table 1
Mix proportions of raw materials for bricks.

Mix	No of Specimen	Cupola Slag (%)	Fly Ash (%)	Cement (%)
M1	20	80	10	10
M2	20	75	15	10
M3	20	70	20	10
M4	20	65	25	10
M5	20	60	30	10

Fig. 3. Brick Specimen.

Table 2
Chemical Properties of the raw materials.

Chemical composition	Cupola Slag (CS)	Fly ash (FA) [11]
Lime, CaO (%)	24.27	1.49
Silica, SiO_2	36.86	58.69
Alumina, AL_2O_3	7.5	25.1
Iron oxide, Fe_2O_3	21.79	5.8
Magnesia, MgO	1.22	2.22
Sulphur trioxide, SO_3	0.11	0.12
Sodium Oxide, Na_2O	0.15	0.59
Potassium oxide, K_2O	0.9	4.04
Titanium Oxide, Tio_2	0.97	–
Pentium Oxide, P_2O_5	0.23	–
Sodium Oxide, NaO	0.15	–
Strontium Oxide, SrO	0.03	–
Barium Oxide, BaO	0.04	–
Magnesium dioxide, MnO_2	1.76	–
Chromium trioxide, CrO3	0.11	–
Zirconium dioxide, ZrO2	0.3	–
Tin oxide, SnO2	0.02	–
Free Cl	–	1.28

lighter, more cost-effective construction. The physical parameters of cement are also shown in Table 3.

3.1.3. Particle size distribution

Fig. 4 depicts the particle size distribution of cupola slag. It was discovered that 95% of the cupola slag particles were classified as sand (Table 4). This suggests that the slag particles from the cupola can be used to make bricks. Only 5% of the particles were classified as silt. There are no particles in the gravel and clay categories, as shown in the table. Fig. 5 indicated the particle size distribution for fly ash. It was discovered that 96% of the fly ash particles were classified as sand.

3.2. Mechanical properties

3.2.1. Density

Hollow (open and closed cavity) concrete blocks bearing units must have a minimum block density of 1500 kg/m^3 according to IS 2185 (Part 1):2005. After 28 days, minimum compressive strengths of 3.5, 5.5, 7.0, 8.5, 10.0, 12.5 and 15.0 N/mm^2 are required. As the percentage of CS in the mix increases, the density of the bricks dropped (Fig. 6). When the amount of CS increased from 80 % to 60 %, the dry density reduced by 20%, from 1670.45 kg/m^3 to 1350.57 kg/m^3, as indicated in Table 5. Because of the lower density of fly ash and cupola slag in the brick mix, this trend in density was noticed. This came in handy for making light-weight bricks. As a result, lighter bricks were more cost-effective, economical, and convenient to carry. For all mix proportions, the density of cupola slag bricks is comparable to commercially available fly ash bricks and burnt clay bricks shown in Table 8.

3.2.2. Water absorption

Water absorption has a substantial impact on the quality and strength of bricks. Fig. 7 shows that after introducing cupola slag into the brick mix, water absorption drops from 11.7 to 6.53 % as the proportion of cupola slag lowers according to Table 6. As long as water absorption is less than 15%, as indicated by IS 1077:1992,

S.S. Meshram, S.P. Raut and M.V. Madurwar

Table 3
Physical Properties of the cement, fly ash and cupola slag.

S.N	Tests Performed	Test Results		
		Cement	Fly Ash	Cupola Slag
1	Specific Gravity	3.15	1.87	2.917
2	Density	1440 kg/m³	1310 kg/m³	1477.71 kg/m³
3	Standard Consistency	32 %	–	–
4	Fineness	5 %	15.03	–
5	Water Absorption	–	11 %	0.37 %
6	Initial Setting Time	75 min	–	–
7	Final Setting time	130 min	–	–
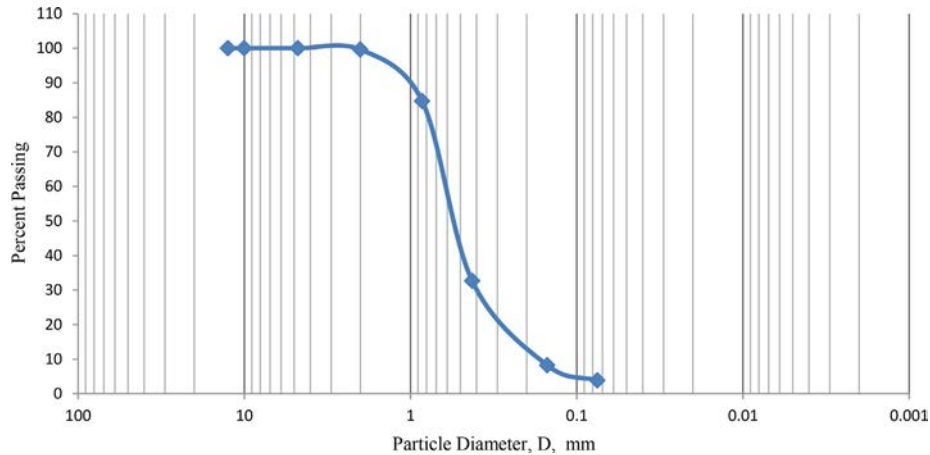
Fig. 4. Particle size distribution for Cupola Slag.

Table 4
Cupola Slag Particle size distribution.

Percentage Distribution	Size Specifications (in mm)	Cupola Slag	Fly ash
Clay	<0.002	0	0
Silt	0.002–0.075	5	4
Sand	0.075–2	95	96
Gravel	>2	0	0

higher brick classes can be utilised, and values less than 20% can be used for brick classes up to 12.5. The addition of CS can thus aid in the production of more durable, cost-effective, and environmentally friendly masonry bricks. Water absorption values of cupola slag bricks for all the mix proportion are less as compared to commercially available fly ash bricks and burnt clay bricks (Table 8).

3.2.3. Compressive strength

Compressive strength is the main characteristic since it indicates the brick's strength and quality. Fig. 8 indicates the results for all of the bricks that were tested. Table 7 shows that the compressive strength of M1 to M5 mixes drops from 4.5 N/mm² to 3.6 N/mm², a reduction of 12.5 % (Fig. 9). The M1 percentage mix (80 CS: 10 FA: 10 cement) yielded the highest strength. This is because of the chemical makeup of the basic components. Higher compressive strength of bricks mixes with cupola slag due to lower CaO content in the chemical composition. The minimum compres-
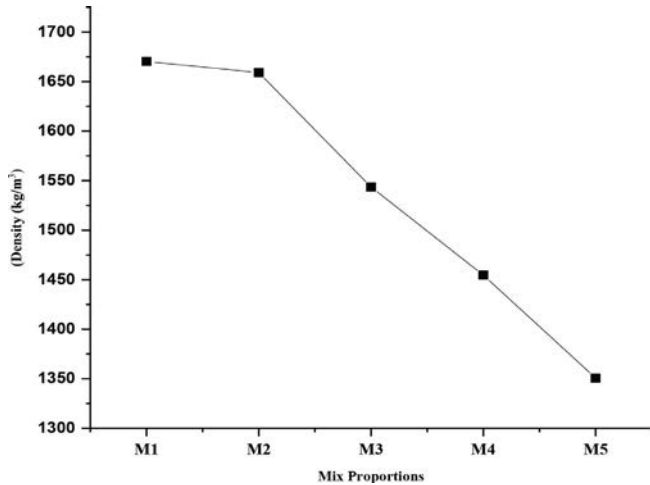

Fig. 5. Particle size distribution for Fly Ash.

S.S. Meshram, S.P. Raut and M.V. Madurwar
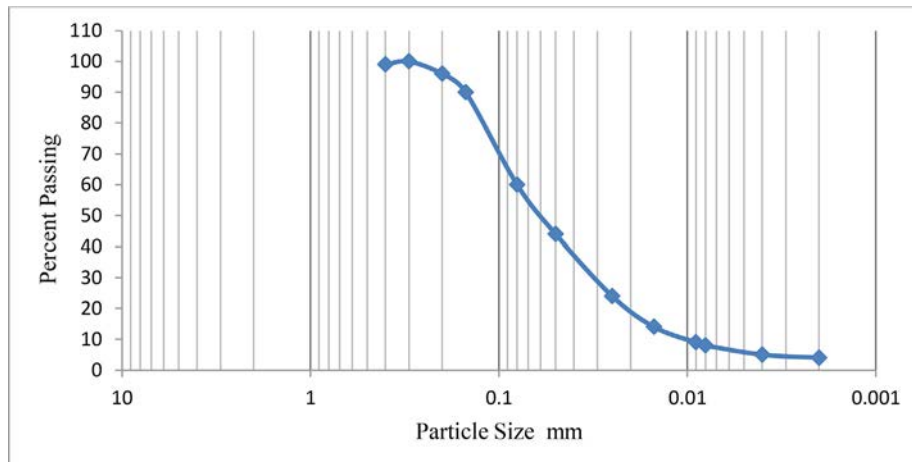
Fig. 6. Density for brick specimens.

Table 5
Density for brick specimens.

Mix Proportion	Density (kg/m^3)
M1	1670.45
M2	1659.1
M3	1543.56
M4	1454.64
M5	1350.57

Fig. 8. Compression Test on brick Specimen.

Table 7
Compressive strength of brick specimens incorporating CS.

Mix Proportion	Compressive Strength (N/mm^2)
M1	4.5
M2	4.2
M3	4
M4	3.7
M5	3.6
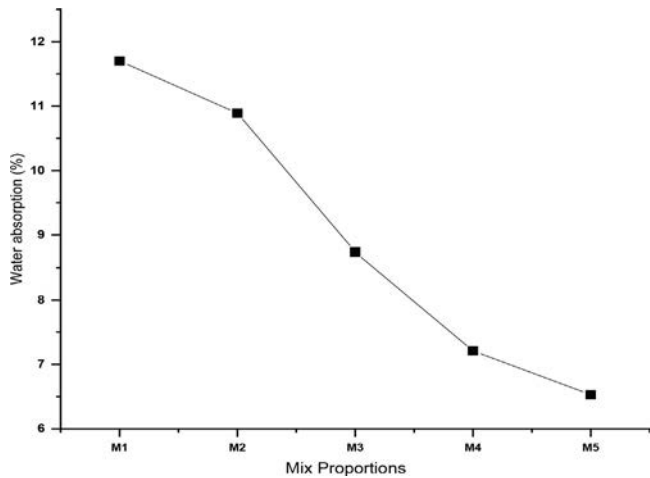
Fig. 7. Effect of CS on water absorption.

Table 6
Water Absorption for brick specimens.

Mix Proportion	Water Absorption (%)
M1	11.7
M2	10.89
M3	8.74
M4	7.21
M5	6.53

Fig. 9. Compressive strength of brick specimens incorporating CS.

can be employed in environmentally friendly building. Fly ash bricks have a minimum compressive strength of 5.4 N/mm^2, while burnt clay ricks have a minimum compressive strength of 3.5 N/mm^2. When compared to regular burnt clay bricks, cupola slag has higher compressive strengths in all proportions, and when compared to commercially available fly ash bricks, the maximum value is about 4.5 N/mm^2 as per Table 8.

3.2.4. Thermal conductivity

Thermal comfort of human being is based on the amount of heat conduction through the building components, which can be

sive strength requirements are 3.5 N/mm^2 according to Indian standard code 1077:1992 [15]. All cupola slag brick specimens passed the IS criteria for compressive strength. It also complies with the I Class brick 4 N/mm^2 criteria. As a result, created blocks

Table 8
Comparison between Cupola slag bricks, burnt clay bricks, fly ash bricks.

Types of Bricks	Density(kg/m^3)	Compressive Strength (N/mm^2)	Water Absorption(%)	Thermal Conductivity (W/mK)
Burnt Clay Bricks	1650	3.5	27.11	1.24
Fly ash bricks	1700	5.8	18.43	1.1
Cupola Slag bricks	1670.45	4.5	11.7	0.8

reduced by means of thermal protection in building external walls and roofs. The proper use of thermally insulated sustainable construction material in building reduces the cooling/heating load. For good thermally efficient building blocks the requirement is low thermal conductivity. Thermal conductivity is estimated for best combination of brick mix. Thermal conductivity for M1 mix is 0.8 W/mK as per Table 8 which is less than fly ash brick and burnt clay bricks.

4. Conclusion

Dumping on land and disposing of cupola slag results in contamination of the soil, which has a direct influence on the ecosystem. As a result, its productive usage in the construction of bricks provides an alternative remedy for such issues to some extent. Cupola slag as a by-product of the cast iron industry was combined with fly ash as an industrial waste in the construction of bricks with a constant cement ratio. The presence of silica and alumina in the cupola slag indicates that it could be used to make sustainable building blocks. From the five distinct mixes with variable CS from 80% to 60%, the M1 mix with 80 percent CS, 10% FA, 10% Cement had the highest compressive strength 4.5 N/mm^2. Compressive strength for burnt clay bricks is 3.5 N/mm^2 which is less than cupola slag bricks, while the brick mix M5 (60 CS: 30 FA: 10 cement) had the lowest water absorption and density 6.53 percent and 1350.57 kg/m^3 when compared with fly ash bricks and burnt clay bricks it has higher water absorption and density as 18.43 % and 27.11 %, 1700 kg/m^3 and 1650 kg/m^3. Thermal conductivity for M1 mix is 0.8 W/mK which is less than fly ash brick and burnt clay bricks as 1.1 and 1.24. The water absorption value for all of the mixes was determined to be less than 20%, indicating that they meet the specifications. As a result, cupola slag can be used to create long-lasting construction blocks. Cupola slag is a discarded product from the iron industry which can be utilised to make bricks, as well as reducing its disposal and land filling issues, which helps to reduce land pollution. Based on the findings of the tests, it is suggested that CS will be utilised in the production of large-scale building bricks to improve the physico-mechanical properties of bricks, thereby contributing to cost-effective, ecologically friendly, and sustainable building construction.

CRediT authorship contribution statement

S.S. Meshram: Conceptualization, Methodology, Formal analysis. **S.P. Raut:** Methodology, Writing – review & editing. **M.V. Madurwar:** Visualization, Investigation.

Declaration of Competing Interest

The authors declare that they have no known competing financial interests or personal relationships that could have appeared to influence the work reported in this paper.

References

[1] Z. Zhang, Y.C. Wong, A. Arulrajah, S. Horpibulsuk, Review of studies on bricks using alternative materials and approaches, Constr. Build. Mater. 188 (2018) 1101–1118.
[2] S.P. Raut, R.V. Ralegaonkar, S.A. Mandavgane, Development of sustainable construction material using industrial and agricultural solid waste: A review of waste-create bricks, Constr. Build. Mater. 25 (10) (2011) 4037–4042.
[3] C. Bories, M.-E. Borredon, E. Vedrenne, G. Vilarem, Development of eco-friendly porous fired clay bricks using pore-forming agents: A review, J. Environ. Manage. 143 (2014) 186–196.
[4] A. Pappu, M. Saxena, S.R. Asolekar, Solid wastes generation in India and their recycling potential in building materials, J. Building Environ. 42 (6) (2007) 2311–2320.
[5] R. Balaraman, S. Anne Ligoria, Utilization of Cupola Slag in Concrete as Fine and Coarse Aggregate, Int. J. Civil Eng. Technol. (IJCIET) 6 (8) (2015) 06–14.
[6] Vishwash K. Mistry, B.R. Patel, D.J. Varia, Suitability of Concrete Using Cupola Slag as Replacement of Coarse Aggregate, Int. J. Scientific Eng. Res. 7 (2) (2016).
[7] J.O. Afolayan, S.A. Alabi, Investigation on the Potentials of Cupola Furnace Slag in Concrete, Int. J. Integrated Eng. 5 (2013) 59–62.
[8] R. Balaraman, Dr. N.S. Elangovan. "Behaviour of Cupola Slag in Concrete as Partial Replacement with a Combination of Fine and Coarse Aggregates". (2018).
[9] D.S. Vijayan, A. Mohan, J. Revathy, D. Parthiban, R. Varatharajan, Evaluation of the impact of thermal performance on various building bricks and blocks: A review, Environ. Technol. Innovation 23 (2021), https://doi.org/10.1016/j.eti.2021.101577 101577.
[10] S.M.S. Kazmi, M.J. Munir, Y.-F. Wu, A. Hanif, I. Patnaikuni, Thermal performance evaluation of eco-friendly bricks incorporating waste glass sludge, J. Cleaner Prod. 172 (2018) 1867–1880.
[11] T. Bilir, O. Gencel, Ilker Bekir Topcu, Properties of mortars with fly ash as fine aggregate, Constr. Build. Mater. 93 (2015) 782–789.
[12] IS 2386 (Part III):1963 – Methods of tests for aggregate of concrete.
[13] IS 2185(Part 1): 2005 – Concrete Masonry Units- Specification.
[14] IS 3495 (Part 1): 1992 – Methods of tests of Burnt Clay Building bricks.
[15] IS 1077:1992 - Common Burnt Clay Building Bricks - Specification

A case report on 6-yr old female child patient with a known case of lower lip Hemangioma.

Bhagyashri Pohane*, Priya Dhanksar, Aniket Pathade

Department of Nursing, Datta Meghe Institute of Medical Sciences, Sawangi (M), Wardha, Maharashtra, India

Abstract

Hemangioma is an endothelial tumor that primarily affects children and babies. Hemangiomas usually appear during or shortly after birth, proliferate for the first 18 months, and then fade away between the ages of 5 and 10. The most prevalent complaints of patients with hemangiomas are psychosocial issues, which can affect the appearance and invite attestation. Hemangioma is one of the most common benign vascular tumors in children, affecting 10%–12% of them. By the age of five, half of the haemangiomas have dissipated, and ninety percent have dissipated by the age of nine. Haemangiomas can sometimes recur, requiring systemic or surgical intervention. Hemangioma is one of the most prevalent vascular benign tumors, affecting about 12% of neonates. Hemangioma of infancy is most common in the head and neck region, accounting for about 60% of cases, with the lips, tongue, and palate being the most common sites. Within 9 years of age, about 90% of lesions had vanished. Hemangiomas can sometimes persist and require treatment. Depending on the size, location, and stage of the hemangioma, systemic or surgical treatment may be used. Surgical procedures such as simple excision or combinations with plastic surgery are rarely suggested. We discuss a case of lower lip haemangioma in an 8-year-old female who was diagnosed and treated at our facility.

Conclusion: More research on hemangiomas and their growth patterns is needed to develop tailored treatments to treat and alleviate the patient's social embarrassment. Despite the many treatment options for lip hemangiomas, surgery may be the best option in the case of big abnormalities, as long as critical care measures are performed.

Keywords: Lip, Tumour, Haemangioma, Vascular Malformation

Introduction

Haemangiomas are blood vessel tumors that are benign (noncancerous). Hemangiomas come in a variety of forms and can appear anywhere on the body [1], including the skin, muscle, bone, and other internal organs. The majority of hemangiomas appear on the skin's surface or immediately under it [2]. They commonly appear on the face and neck, and their color, shape, and size can vary widely. Most hemangiomas do not require medical treatment since they seldom turn malignant [3]. Some haemangiomas, on the other hand, might be unsightly, and many people seek medical help for cosmetic reasons. Surgery is not required in the majority of haemangioma patients [4]. Tumors deep in muscle or bone, as well as tumors on the skin that cause eyesight, breathing, or eating problems, are examples of situations when surgery may be required [5]. Hemangiomas are benign vascular tumors that commonly emerge in childhood and adolescence; a small percentage of them may be present during birth or develop later in life. Hemangiomas are three times as common in women than in men [6].

Haemangiomas on the lips are particularly vulnerable to problems, which can have substantial functional and aesthetic consequences. Early ulceration of these lesions can result in pain and bleeding, making it difficult for small infants to eat [7]. Lips are prominent features of the face, and big hemangiomas can alter the intricate lip architecture. Surgical intervention may be indicated if lip shape and symmetry are disturbed despite involution. The lip, tongue, and palate are the most prevalent sites for lesions in the head and neck area, accounting for 60% of all cases. Hemangioma is a smooth or lobulated soft tissue tumor that causes physical deformity and functional disturbance It can be a few millimetres long or several centimetres long. The majority of the lesion involutes on its own, thus no additional treatment is required. The patient's age, size, location, extension, and pace of advancement all influence treatment for a persistent lesion. This is a common occurrence in babies and youngsters. Hemangiomas usually appear during or shortly after birth, proliferate for the first 18 months, and then fade away between the ages of 5 and 10.

The most prevalent complaints of individuals with hemangiomas are psychosocial issues, which are situations that may affect their appearance and attract the attention of others around them. Hemangiomas come in a wide range of

sizes and shapes [8]. Endothelial cell proliferation causes mouth hemangiomas (OHs), which are benign tumors that form in and around the oral cavity. OHs are uncommon and mostly affect the lips, tongue, buccal mucosa, and palate. OHs are relatively rare and most commonly include the lips, tongue, buccal mucosa, and palate. While 60 to 70% of hemangiomas originate in the head and neck region, OHs are very rare and most commonly involve the lips, tongue, buccal mucosa, and palate.

Patient information

Patient-specific information: A 6-year-old female child visited AVBR Hospital on 20/07/2021 with the chief Complaint of abdominal bloating, Nausea and Loss of appetite for further management. Present case Visit AVBR Hospital on the old basis with the chief Complaint of abdominal bloating, Nausea, and Loss of appetite patient has No past medical & Surgical history she was mentally stable. she an oriented person. She has maintained a good personal relationship with family members.

The primary concern and Symptoms of the patient: A patient was admitted to AVBR Hospital on date 20-09-2021 with a chief Complaint abdominal of blotting, Nausea, and Loss of appetite further investigation patient was diagnosed with lower lip hemangioma.

Medical family & psychological history: The patient has no past medical history like asthma, tuberculosis, diabetic Mellitus, etc. patient belongs to the nuclear family. There are 5members alive included in the patient. All family members are healthy. All family members maintain a good relationship with doctors and nurses.

Clinical Findings: On general examination patient status is unhealthy. Conscious of the patient is conscious. Body build is thin. Patient hygiene maintains. The vital parameter of the patient is blood pressure 120/80MMHG. Respiration is normal no sound was found at auscultation.

On systematic examination respiration system bilateral breath sound is decreased. Cardiac system normal S1 and S2 sound is hearing with no abnormality. There is no localized neurological deficit, and the central nervous system is cognizant and directed.

Significant physical examination and important clinical findings: Abnormalities of lower lip hemangioma.

Present complaint and investigation

A 6 year old female child patient was admitted to AVBR Hospital with the chief complaint of abdominal discomfort and bloating. Nausea, loss of appetite pain. a sense of fullness after eating a small.

Main symptoms: Abdominal discomfort of blotting, Nausea, Loss of appetite.

Main diagnosis: A 6year old female child patient was admitted to AVBR Hospital. The patient was abdominal discomfort of blotting, Nausea, Loss of appetite. The doctor identified the case of lover lip hemangioma.

Therapeutic Interventions: on the therapeutic intervention patient had taken Tab. Cymoralfort, Tab. Augmentin, Tab. Pantop, Tab. Omen.

Outcome: After the medication chief completed abdominal discomfort of blotting, Nausea, Loss of appetite was diminished.

Conclusion: She responded to the medicine antibiotics, analgesic, and physical counseling.

Timeline: Present case has a history of abdominal blotting Nausea and Loss of appetite and she visited the Sewagram hospital in June 2020 for further management. MRI, CT scan was done diagnosed as a lower lip hemangioma. And then follow up AVBR Hospital for further treatment patient was visited in AVBR Hospital on the old basis with the chief Complaint of abdominal bloating, Nausea, and Loss of appetite further management.

Diagnostic assessment

Based on patient history, physical examination, systemic examination, and other investigations reveal a different outcome. After investigation Report shows that a client with abnormalities of lower lip hemangioma is present all routine blood test is done. CT scan and MRI were done.

Diagnostic challenge: No diagnostic challenge

Diagnosis: After physical examination of this investigation CT scan MRI was done, and the doctor found outpatient was diagnosed of lower lip hemangioma.

Prognosis: The case of prognosis was satisfied.

Therapeutic intervention: Medical management was provided to the patient. IV. Fluid DNS, NS, 500ml Tab. Pantop 40mg Tab. Cyaremalfort, 1Rute is oral. Antibiotic.

Blood investigation: Hemoglobin- 12.1, RBS count-5.24million/MMC, WBC count-9200/MMC, platelet count-2.56/MMC

Discussion

Haemangiomas and vascular malformations are two different types of vascular lesions that are frequently confused, and the terms are commonly used interchangeably. Anatomical, structural, and biological characteristics are used to classify vascular lesions [9]. Hemangiomas and other vascular abnormalities were the most common lesions found. Hemangioma is a broad term that refers to a variety of vascular diseases defined by abnormal endothelial cell development and proliferation. Vascular malformations, on the other hand, are structural abnormalities of blood vessels that do not involve endothelial cell growth [10]. Haemangiomas and vascular malformations are two forms of vascular lesions that are frequently mistaken, and the names are frequently interchanged. Anatomical, structural, and biological characteristics are used to classify vascular lesions. Hemangiomas and other vascular abnormalities were the most common lesions found. Hemangioma is a broad

term that refers to a variety of vascular diseases defined by abnormal endothelial cell development and proliferation. Vascular malformations, on the other hand, are structural abnormalities of blood vessels that do not involve endothelial cell growth [11]. The distinctions between hemangiomas and vascular malformations are Shown. The beginning of swelling immediately after birth, as well as the persistence of swelling after ten years, led us to consider both vascular malformation and hemangiomas as possibilities in our case. The majority of hemangiomas involute on their own by the age of 10, however, this was not the case in our situation. However, the lack of bruit or thrill on auscultation, as well as the MRI report and histological view, led us to the conclusion that the patient had a hemangioma [12].

Large, persistent hemangiomas can cause physical disfigurement and. functional disruption, necessitating treatment. Compound hemangioma involving the deeper tissues of the lower lip persisted in this case, and early surgical excision was not performed due to the patient's poor financial situation. A hemangioma can be treated with systemic corticosteroids, intraregional sclerosing agent injections, electrocoagulation, cryosurgery, laser therapy, embolization, and surgical excision. In this example, the lesion was treated with a pressure-induced intraregional injection of triamcinolone, followed by full excision [13], Enlargement of endothelial tissues into surrounding tissues, which thereafter become canalized and vascularized in some circumstances. Central hemangioma is a congenital condition that most typically affects the jaw. Panoramic radiography rule Patten KB, Pearl M, Takes A, Mitchell SE. Update on the pediatric extracranial vascular anomalies of the head and neck. Other types of hemangiomata should be ruled out, as should central hemangioma. The cause and pathophysiology of hemangioma remain unknown [14].

Childbearing age, gestational hypertension, and infant birth weight are all common features. Physical deformity and functional disruption can result from large chronic hemangiomas, needing treatment. Systemic corticosteroids, intraregional sclerosing medication injections, electrocoagulation, cryosurgery, and laser therapy are all possible treatments [15].

Conclusion

Finally, sclerosis of a large lip hemangioma combined with surgical excision is a therapy option worth considering because it offers good aesthetic and functional results.

References

1. Rao BV, Bharathi MS. Vascular malformations-Treatment modalities. IAIM, 2019; 6(9): 58-65.

2. Ghasemi H, Owlia P, Jalali-Nadoushan MR, et al. A clinicopathological approach to sulfur mustard-induced organ complications: a major review. Cutan Ocular Toxicol. 2013;32(4):304-24.

3. Buckley D. Congenital Nevi, Melanocytic Naevi (Moles) and Vascular Tumors in Newborns and Children. Prim Care Dermatol 2021;225-231.

4. Wagner RS, Gold R, Langer P. Management of capillary hemangiomas. J Pedia Ophthalmol Strabis. 2006;43(6):326.

5. Stengler M. Outside the Box Cancer Therapies: Alternative Therapies that Treat and Prevent Cancer. Hay House 2019.

6. Mahady K, Thust S, Berkeley R, et al. Vascular anomalies of the head and neck in children. Quant Imag Med Surg. 2015;5(6):886.

7. Tyagi I, Syal R, Goyal A. Management of low-flow vascular malformations of upper aero digestive system—role of N-butyl cyanoacrylate in peroperative devascularization. Br J Oral Maxillofac Surg. 2006;44(2):152-6.

8. Cooke Macgregor F. Facial disfigurement: problems and management of social interaction and implications for mental health. Aesth Plastic Surg. 1990;14(1):249-57.

9. Ianniello A, Laredo J, Loose DA, et al. ISVI-IUA consensus document diagnostic guidelines of vascular anomalies: vascular malformations and hemangiomas. Int Angiol 2015;34:1-2.

10. Dhole P, Lohe VK, Sayyad A, et al., A case report on capillary hemangioma and Leukoplakia on Tongue. Med Sci. 2020;24(106):4211-6.

11. Pote PG, Banode P, Rawekar S. Lifesaving successful embolization of aggressive vertebral body hemangioma and a large pulmonary arteriovenous malformation. In J Vasc Endovasc Surg. 2021;8(3):269.

12. Haile LM, Kamenov K, Briant PS, et al. Hearing loss prevalence and years lived with disability, 1990–2019: findings from the Global Burden of Disease Study 2019. Lancet. 2021;397(10278):996-1009.

13. Vos T, Lim SS, Abbafati C, et al. Global burden of 369 diseases and injuries in 204 countries and territories, 1990–2019: a systematic analysis for the Global Burden of Disease Study 2019. Lancet. 2020 ;396(10258):1204-22.

*Correspondence to:

Department of Nursing, Datta Meghe Institute of Medical Sciences, Sawangi (M), Wardha, Maharashtra, India

E-mail: Pohaneb1989@gmail.com

‹   **Back**

ORIGINAL PAPER

Sensorless voltage balancing method for modular multilevel converter

Hari Babu Gobburi ✉, Vijay B. Borghate, Prafullachandra M. Meshram

Abstract

Modular multilevel converters (MMCs) have become prominent for high and medium power applications. The phase-disposition pulse width modulation (PDPWM) technique is a carrier-based method that generates good quality output. However, it has the inherent problem of uneven power distribution. Conventionally, this is solved by expensive voltage and current measurements. In this paper, a capacitor voltage balancing method is presented for MMC, which eliminates the need for voltage and current sensors. It also ensures uniform power distribution among the submodules (SMs). In addition, it needs only one carrier per phase, and one PWM reference, for either upper arm or lower arm to produce $N+1$ level with N SMs per arm. The capacitor voltage balancing method is analyzed mathematically and verified for the MMC with two-level half-bridge SMs. The same method is also extended to the MMC with three-level flying capacitor SMs. MATLAB/SIMULINK simulations and experimental results on a laboratory prototype are presented to verify the theoretical concepts.

Open Research ⌃

DATA AVAILABILITY STATEMENT

Data sharing is not applicable to this article as no datasets were generated or analyzed during the current study.

REFERENCES ⌃

1   Meshram PM, Borghate VB. A Simplified Nearest Level Control (NLC) voltage balancing method for Modular Multilevel Converter (MMC). In: *IEEE Trans Power Electron*. Jan. 2015; **30**(1): 450-462.

10/21/23, 11:13 AM   Sensorless voltage balancing method for modular multilevel converter - Gobburi - 2022 - International Journal of Circuit Th…

< Back

2   Karasani RR, Borghate VB, Meshram PM, Suryawanshi HM, Sabyasachi S. A three-phase hybrid cascaded modular multilevel inverter for renewable energy environment. In: *IEEE Trans Power Electron*. Feb. 2017; **32**(2): 1070-1087. doi:10.1109/TPEL.2016.2542519

View | **Web of Science®** | **Google Scholar**

3   Kumar YS, Poddar G. Balanced submodule operation of modular multilevel converter-based induction motor drive for wide-speed range," in. *IEEE Trans Power Electron*. April 2020; **35**(4): 3918-3927. doi:10.1109/TPEL.2019.2938096

View | **Web of Science®** | **Google Scholar**

4   Park J, Yeo S, Choi J. Development of ±400Mvar World Largest MMC STATCOM. In: *2018 21st International Conference on Electrical Machines and Systems (ICEMS)*; 2018: 2060-2063.

View | **Google Scholar**

5   Lesnicar A. and Marquardt R., " An innovative modular multilevel converter topology suitable for a wide power range," presented at the IEEE Bologna Tech COnf., Bologna, Italy, vol.3, 2003, p. 6.

Google Scholar

6   Debnath S, Qin J, Bahrani B, Saeedifard M, Barbosa P. Operation, control, and applications of the modular multilevel converter: a review. In: *IEEE Trans Power Electron*. Jan. 2015; **30**(1): 37-53. doi:10.1109/TPEL.2014.2309937

View | **Web of Science®** | **Google Scholar**

7   Yadav A, Singh SN, Das SP. Modular multi-level converter topologies: Present status and key challenges. In: *2017 4th IEEE Uttar Pradesh Section International Conference on Electrical, Computer and Electronics (UPCON)*; 2017: 280-288.

View | **Google Scholar**

8   Hu P, Jiang D. A level-increased nearest level modulation method for modular multilevel converters. In: *IEEE Trans Power Electron*. April 2015; **30**(4): 1836-1842. doi:10.1109/TPEL.2014.2325875

View | **Web of Science®** | **Google Scholar**

9   Sheikh M, Meshram PM, Borghate VB. SHE technique for MMC based on modified flying capacitor multicell converter. In: *IEEE Power Communication and Information Technology Conference (PCITC) Siksha 'O'*. Anusandhan University; 2015.

View | **Google Scholar**

‹ **Back**

converter. In: *IEEE Trans Power Delivery*. Jan. 2014; (1): 298-306. doi:10.1109/TPWRD.2013.2279263

View | **Web of Science®** | **Google Scholar**

11   Ilves K, Norrga S, Harnefors L, Nee H. On energy storage requirements in modular multilevel converters. In: *IEEE Trans Power Electron*. Jan. 2014; **29**(1): 77-88. doi:10.1109/TPEL.2013.2254129

View | **Web of Science®** | **Google Scholar**

12   Grigoletto FB, Stefanello M, da Silva GS, Pinheiro H. Space vector pulse width modulation for Modular Multilevel Converters. In: *IECON 2016-42nd Annual Conference of the IEEE Industrial Electronics Society*; 2016: 2575-2581.

View | **Google Scholar**

13   Hagiwara M, Akagi H. Control and experiment of pulsewidth-modulated modular multilevel converters. In: *IEEE Trans Power Electron*. July 2009; **24**(7): 1737-1746. doi:10.1109/TPEL.2009.2014236

View | **Web of Science®** | **Google Scholar**

14   Li Z, Wang P, Zhu H, Chu Z, Li Y. An improved pulse width modulation method for chopper-cell-based modular multilevel converters. In: *IEEE Trans Power Electron*. Aug. 2012; **27**(8): 3472-3481. doi:10.1109/TPEL.2012.2187800

View | **Web of Science®** | **Google Scholar**

15   Mei J, Shen K, Xiao B, Tolbert LM, Zheng J. A new selective loop bias mapping phase disposition PWM with dynamic voltage balance capability for modular multilevel converter. In: *IEEE Trans. Ind. Electron.* Feb. 2014; **61**(2): 798-807. doi:10.1109/TIE.2013.2253069

View | **Web of Science®** | **Google Scholar**

16   Dekka A, Wu B, Zargari NR, Fuentes RL. Dynamic voltage balancing algorithm for modular multilevel converter: a unique solution. In: *IEEE Trans Power Electron*. Feb. 2016; **31**(2): 952-963. doi:10.1109/TPEL.2015.2419881

View | **Web of Science®** | **Google Scholar**

17   Kumar LVS, Kumar GVN. A logic sort algorithm based voltage balancing of modular multilevel converters in back HVDC Systems. *Int J Control Theory Appl*. December 2016; **No.9, Issue No.32**: 11-22.

Google Scholar

18   Wang Y, Hu C, Ding R, Xu L, Fu C, Yang E. A nearest level PWM method for the MMC in DC distribution grids. In: *IEEE Trans Power Electron.* Nov. 2018; **33**(11): 9209-9218. doi:10.1109/TPEL.2018.2792148

View | **Web of Science®** | **Google Scholar**

‹ Back

Converters. In: 2016 IEEE Transportation Electrification Conference and Expo (ITEC); 2016.

View │ **Google Scholar**

20   Saeedifard M, Iravani R. Dynamic performance of a modular multilevel back-to-back HVDC System. In: *IEEE Trans. On Power Del.* Oct. 2010; **25**(4): 2903-2912. doi:10.1109/TPWRD.2010.2050787

View │ │ **Web of Science®** │ **Google Scholar**

21   Shi X, Wang Z, Tolbert LM, Wang F. A comparison of phase disposition and phase shift PWM strategies for modular multilevel converters. *IEEE Energy Conver Congr Expo*. 2013; **2013**: 4089-4096.

Google Scholar

22   Zhou F, Luo A, Xiong Q, Xu Q, Xie N. Research of single-carrier modulation strategy for modular multilevel converter. *International Power Electronics and Application Conference and Exposition*. 2014; **2014**: 1462-1466.

View │ **Google Scholar**

23   Ronanki D, Williamson SS. Single carrier-based pulse width modulator for modular multilevel converters. In: *2018 IEEE International Conference on Power Electronics, Drives and Energy Systems (PEDES)*; 2018: 1-6.

View │ **Google Scholar**

24   Fan S, Zhang K, Xiong J, Xue Y. An improved control system for modular multilevel converters with new modulation strategy and voltage balancing control. In: *IEEE Trans Power Electron*. Jan. 2015; **30**(1): 358-371. doi:10.1109/TPEL.2014.2304969

View │ │ **Web of Science®** │ **Google Scholar**

25   Ronanki D, Williamson SS. A novel 2N + 1 carrier-based pulse width modulation scheme for modular multilevel converters with reduced control complexity. In: *IEEE Trans Ind Appl*. Sept.-Oct. 2020; **56**(5): 5593-5602. doi:10.1109/TIA.2020.3009078

View │ │ **Web of Science®** │ **Google Scholar**

26   Dekka A, Wu B, Zargari NR, Fuentes RL. A space-vector PWM-based voltage-balancing approach with reduced current sensors for modular multilevel converter. In: *IEEE Trans Ind Electron*. May 2016; **63**(5): 2734-2745. doi:10.1109/TIE.2016.2514346

View │ │ **Web of Science®** │ **Google Scholar**

27   Deng F, Chen Z. A control method for voltage balancing in modular multilevel converters. In: *IEEE Trans. On Power Electron.* Jan. 2014; **29**(1): 66-76. doi:10.1109/TPEL.2013.2251426

View │ │ **Web of Science®** │ **Google Scholar**

‹ Back

of modular multilevel converters. In: *IEEE Trans on Power Del*. April 2020; 35(2): 1057-1067. doi:10.1109/TPWRD.2019.2931287

View | **Web of Science®** | **Google Scholar**

29   Abushafa OSM, Gadoue SM, Dahidah MSA, Atkinson DJ, Missailidis P. Capacitor voltage estimation scheme with reduced number of sensors for modular multilevel converters. *IEEE J Emerg Sel Topics Power Electron*. Dec. 2018; **6**(4): 2086-2097. doi:10.1109/JESTPE.2018.2797245

View | **Web of Science®** | **Google Scholar**

30   Li Z, Lizana R, Sha S, Yu Z, Peterchev AV, Goetz SM. Module implementation and modulation strategy for sensorless balancing in modular multilevel converters. In: *IEEE Trans Power Electron.* Sept. 2019; **34**(9): 8405-8416.

View | **Web of Science®** | **Google Scholar**

31   Liu X, Lv J, Gao C, et al. A novel diode-clamped modular multilevel converter with simplified capacitor voltage-balancing control. In: *IEEE Trans on Ind Electron*. Nov. 2017; **64**(11): 8843-8854. doi:10.1109/TIE.2017.2682013

View | **Web of Science®** | **Google Scholar**

32   Shu H, Lei S, Tian X. A New Topology of Modular Multilevel Converter With Voltage Self-Balancing Ability. *IEEE Access*. 2019; **7**: 184786-184796. doi:10.1109/ACCESS.2019.2958857

View | **Web of Science®** | **Google Scholar**

33   Yin T, Wang Y, Wang X, Yin S, Sun S, Li G. Modular multilevel converter with capacitor voltage self-balancing using reduced number of voltage sensors. In: *2018 International Power Electronics Conference (IPEC-Niigata 2018 -ECCE Asia)*; 2018: 1455-1459.

View | **Google Scholar**

34   Tashakor N, Kilictas M, Bagheri E, Goetz S. Modular multilevel converter with sensorless diode-clamped balancing through level-adjusted phase-shifted modulation. In: *IEEE Trans Power Electron*. July 2021; **36**(7): 7725-7735. doi:10.1109/TPEL.2020.3041599

View | **Web of Science®** | **Google Scholar**

35   Deng F, Liu C, Wang Q, Zhu R, Cai X, Chen Z. A currentless submodule individual voltage balancing control for modular multilevel converters. In: *IEEE Trans Ind Electron.* Nov. 2020; **67**(11): 9370-9382. doi:10.1109/TIE.2019.2952808

View | **Web of Science®** | **Google Scholar**

36   Gobburi HB, Borghate VB, Meshram PM. Generalized Sensorless Capacitor Voltage Balancing technique for Modular Multilevel Converter with increased output voltage levels. In: *2020 IEEE*

‹ **Back**

View │ **Google Scholar**

---

37   Elserougi A, Daoud MI, Massoud AM, Abdel-Khalik AS, Ahmed S. Investigation of sensorless capacitor voltage balancing technique for modular multilevel converters. In: *IECON 2014-40th Annual Conference of the IEEE Industrial Electronics Society*. Dallas: TX; 2014: 1569-1574.

View │ **Google Scholar**

---

38   Ghazanfari A, Mohamed YAI. A hierarchical permutation cyclic coding strategy for sensorless capacitor voltage balancing in modular multilevel converters. In: *IEEE J Emerg Sel Topics Power Electron*. June 2016; **4**(2): 576-588. doi:10.1109/JESTPE.2015.2460672

View │ **Web of Science®** │ **Google Scholar**

---

39   Liu Y, Peng FZ. A modular multilevel converter with self-voltage balancing part ii: y-matrix modulation. In: *IEEE J Emerg Sel Topics Power Electron*. June 2020; **8**(2): 1126-1133. doi:10.1109/JESTPE.2019.2923576

View │ **Web of Science®** │ **Google Scholar**

---

40   Bai Z, Xia H, Ma H, Wang J. MMC capacitor voltage balancing strategy based on carrier rotation. *IEEE Int Power Electron Appl Conf Expo (PEAC)*. 2018; **2018**: 1-5.

Google Scholar

---

41   Abarzadeh M, Javadi A, Al-Haddad K. Novel simplified single carrier PWM method for 5L ANPC converter with capacitor voltage self-balancing and improved output voltage spectrum. In: *2019 IEEE 28th International Symposium on Industrial Electronics (ISIE)*; 2019: 2021-2026.

View │ **Google Scholar**

---

42   Shukla A, Ghosh A, Joshi A. Natural balancing of flying capacitor voltages in multicell inverter under pd carrier-based PWM. In: *IEEE Trans Power Electron*. June 2011; **26**(6): 1682-1693. doi:10.1109/TPEL.2010.2089807

View │ **Web of Science®** │ **Google Scholar**

---

43   Lee W-K, Kim T-J, Kang D-W, Hyun D-S. A carrier-rotation strategy for voltage balancing of flying capacitors in flying capacitor multi-level inverter. In: *IECON'03. 29th Annual Conference of the IEEE Industrial Electronics Society (IEEE Cat. No.03CH37468)*; 2003: 2173-2178 Vol.3.

Google Scholar

---

44   Song Q, Liu W, Li X, Rao H, Xu S, Li L. A steady-state analysis method for a modular multilevel converter. In: *IEEE Trans Power Electron*. Aug. 2013; **28**(8): 3702-3713. doi:10.1109/TPEL.2012.2227818

View │ **Web of Science®** │ **Google Scholar**

‹ Back

analysis of MMC based VSC-HVDC system. *IEEE International Symposium on Industrial Electronics.*
2013; **2013**: 1-6.
Google Scholar

Citing Literature   ⌃

Number of times cited according to CrossRef: 4

Mohammad Bagheri Hashkavayi, S. Masoud Barakati, S. Hamed Torabi, Vahid Barahouei, An
improved method to sub-module voltage balancing in modular multilevel converters with two
voltage sensors, International Journal of Circuit Theory and Applications, 10.1002/cta.3588, **51**, 7,
(3263-3287), (2023).

View

Amish A. Shirsat, Hari Babu Gobburi, Vijay B. Borghate, P. M. Meshram, undefined, 2022 IEEE
International Conference on Power Electronics, Drives and Energy Systems (PEDES),
10.1109/PEDES56012.2022.10080185, (1-6), (2022).

View

Hari Babu Gobburi, V. B. Borghate, P. M. Meshram, undefined, 2022 IEEE IAS Global Conference
on Emerging Technologies (GlobConET), 10.1109/GlobConET53749.2022.9872328, (828-833),
(2022).

View

Hari Babu Gobburi, Vijay B. Borghate, Prafullachandra M. Meshram, A level enhanced voltage
balancing method for modular multilevel converter without using sensors, International Journal of
Circuit Theory and Applications, 10.1002/cta.3522, **51**, 5, (2266-2288), (2022).

View

Download PDF

Back

Training and Support
DMCA & Reporting Piracy

OPPORTUNITIES

Subscription Agents
Advertisers & Corporate Partners

CONNECT WITH WILEY

The Wiley Network
Wiley Press Room

Design and Implementation of a Quadratic Converter for the Grid-Tied System Using Symmetrical Shoot-Through PWM

Sumant G. Kadwane, Shilpa P. Ashtankar (Sarode), Nitesh Y. Funde & Ritesh K. Keshri

Published online: 11 Nov 2022.

Submit your article to this journal ⬈

View related articles ⬈

View Crossmark data ⬈

Design and Implementation of a Quadratic Converter for the Grid-Tied System Using Symmetrical Shoot-Through PWM

Sumant G. Kadwane[1], Shilpa P. Ashtankar (Sarode)[1], Nitesh Y. Funde[2] and Ritesh K. Keshri[3]

[1]Department of Electrical Engineering, Yeshwantrao Chavan College of Engineering, Nagpur, India; [2]Hardware Design Engineer-II (Product Development), TE Connectivity India Pvt. Ltd, Bangalore, India; [3]Department of Electrical Engineering, Visvesvaraya National Institute of Technology, Nagpur, India

ABSTRACT

A quadratic converter is now a days being investigated for high boost topologies. This paper presents the quadratic converter-based single-phase grid-connected system. For this system, the DC side control loop is regulated using a symmetrical shoot-through (SST)-based PWM. AC side current controller is implemented by the variation of modulation index in a nearly decoupled manner. The advantage of the suggested system is in terms of several controls particularly for input variations and load changes which are most beneficial in the case of grid application. The experimental results are presented to support the simulation results. The simulation results are achieved using MATLAB/SIMULINK.

1. INTRODUCTION

With the increased use of renewable energy sources across the world, power electronic converters are investigated for some specific applications. The input to such converters may come from the solar cell, wind turbine, fuel cell or any other DC source [1–3]. In most of these cases, a proper control strategy has to be investigated for the specific purpose. Most of the DC-to-DC converters used in renewable energy applications require boosting the voltage level from 12, 24 V or 48 V to a suitably higher DC voltage for providing power to the load. For these applications, a conventional DC-to-DC boost converter is used for increased voltage gains. However, the conventional boost converter is not an energy-efficient option. The voltage stress across the switches in such a converter also has a higher amplitude. This increases the volume of the switches that makes the system less efficient and more expensive. The most viable option for battery efficiency and reliability is the impedance source network [4,5].

In the last decade many researchers have gained an interest in Z-source converter-based applications [6,7]. Nowadays, the improved version of the Z-source inverter (ZSI) is being popularly investigated for an application like the grid-fed inverters for solar-based generation [8]. Such applications are based on transformerless operation and use various types of control such as PI and sliding mode control (SMC) [9]. The limitation of Z-source topology is the difficulty in controlling the boost on the DC side. It also faces the problem of controlling the power being fed

to the AC grid independently [10,11]. In our earlier publication, symmetrical shoot-through-based control was investigated to obtain nearly decoupled control [12]. This control was investigated in Z-source converter topology. Nowadays quadratic boost converters are being investigated with a duty cycle control [13–15]. The converter can operate at a very high switching frequency. In this converter, the capacitor is charged in parallel and discharged in series using a coupled inductor, a voltage stress across the switches is lesser with a much higher voltage gain without an increase in turn ratio and larger duty cycle [16–23].

The specific contribution of this paper is the investigation of the quadratic converter-based grid-connected system. This control strategy is not proposed in any of the papers yet. Another unique contribution is the decoupled control implemented in a quadratic converter using a symmetrical shoot-through PWM control.

The paper is organised as follows. A quadratic converter is proposed for the single-phase grid system in section 2. The mathematical analysis for the quadratic converter is given in section 3. The shoot-through pulses are generated using a symmetrical shoot-through PWM control in section 4. The passive component size reduction is available in section 5. Section 6 gives the simulation results of a quadratic converter-based single-phase grid-tied inverter system using SST PWM control for steady-state and dynamic state. Section 7 provides a hardware
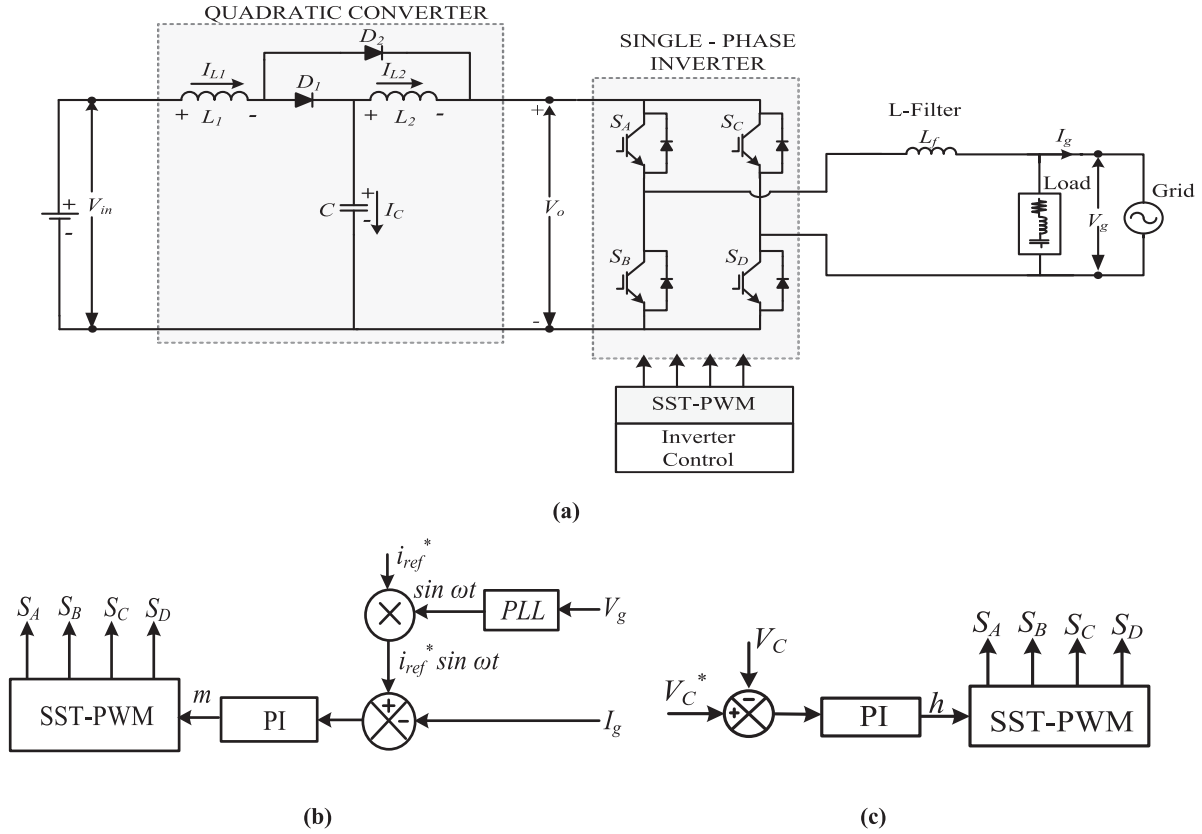
Figure 1: (a) Equivalent circuit configuration of the proposed quadratic converter (b) AC side controller (c) DC side controller

prototype of the proposed grid-tied system and its experimental results. Section 8 provides the conclusion and future scope.

2. THE PROPOSED QUADRATIC CONVERTER-BASED GRID-TIED INVERTER SYSTEM

Figure 1(a) depicts the methodology for the proposed grid-tied inverter using a quadratic converter. This converter is installed between the DC source and grid-tied inverter. The load is connected on the AC side in parallel to the grid. In this system, two control loops are acting simultaneously. One loop is on the DC side for regulating the capacitor voltage of the quadratic converter, as shown in Figure 1(b). This loop will take care of disturbances from the input side and the second loop will take care of fluctuations in the load AC side for controlling the grid current. It controls the flow of power from the inverter to the grid, as depicted in Figure 1(c).

The power balance and power flow from DC to AC using an inverter are ensured by the control scheme applied on the AC side, as shown in Figure 1(b). The reference current waveform that ensures grid current is in phase

with grid voltage indicates that power is fed into the grid. Therefore, the flow of power is from DC to AC. We can also reverse this power flow by adding a phase of 180° but as we are not using a bidirectional converter, it is not used in this case.

Figure 1(b) shows the AC side current control that controls the modulation index, while Figure 1(c) shows only the DC side controller which controls the shoot-through duty ratio. The output of both is the unique controller that controls both AC side current and DC side capacitor voltage. As shown in the SST-PWM waveform of Figure 6, the reference sinusoidal wave gives the modulation index, which is controlled as shown in Figure 1(b), while the shoot-through duty cycle is controlled as shown in Figure 1(c). These two figuresdemonstrate decoupled control.

SST-PWM is an effective technique for nearly decoupled control [12]. The proof of the control algorithm is shown in terms of decoupled control between modulation index M and h, which is verified through the equation shown in reference [12]. The switching logic of SST-PWM is shown in the upcoming sections. The next section deals with the mathematical modelling of the quadratic converter.
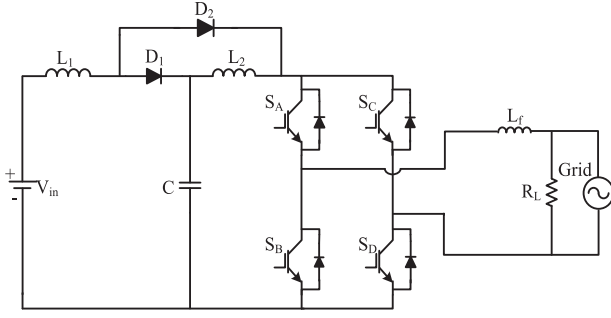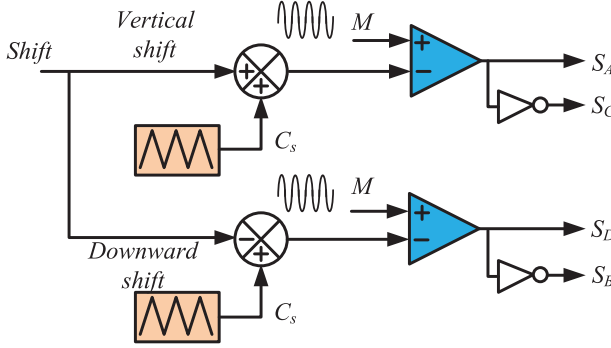
Figure 2: The single-phase grid-tied quadratic converter

Figure 3: The logic diagram of SST PWM generation

3. MATHEMATICAL N OF A QUADRATIC CONVERTER-BASED SINGLE-PHASE INVERTER

Figure 2 shows the quadratic converter connected to the grid. The input-output relation of this converter gives a quadratic form of an equation for the duty cycle.

Figure 3 shows the SST PWM logic diagram. Here, the carrier signal is shifted by a magnitude upward and downward which is added in a triangular wave. The two shifted carrier signals are compared with the modulation index M, as shown in Figure 1(b). The upper comparator produces an SST pulse for S_A and its inverted pulse for S_C. Similarly, the lower comparator produces SST pulses for S_D and inverted pulses for S_B, as shown in Figure 3.

The nature of current waveforms across diodes D_1 and D_2 is shown in Figure 3. During the shoot-through state if switches S_A and S_B of the same leg are triggered, then the current flows through diode D_2 as diode D1 becomes reverse biased and gets open. Similarly, in a non-shoot-through state, the current passes through diode D_1, while diode D_2 remains off. The corresponding waveform of all the switches and two diode currents is shown in Figure 3.

Assuming that the inductors L_1 and L_2 have the same inductance, Figure 4 shows the equivalent circuit for shoot-through via one leg or both legs for T_0 duration
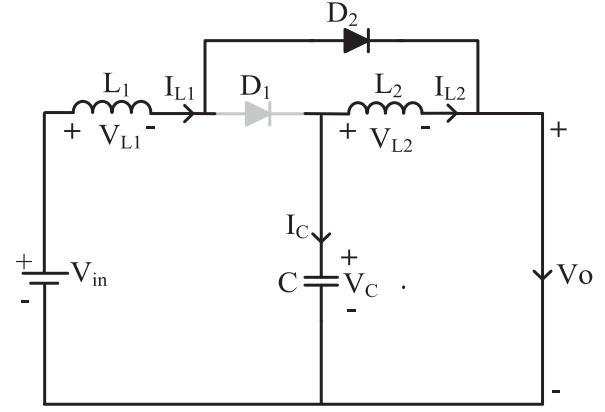

Figure 4: Equivalent circuit of single-phase grid-tied quadratic converter in the shoot-through state
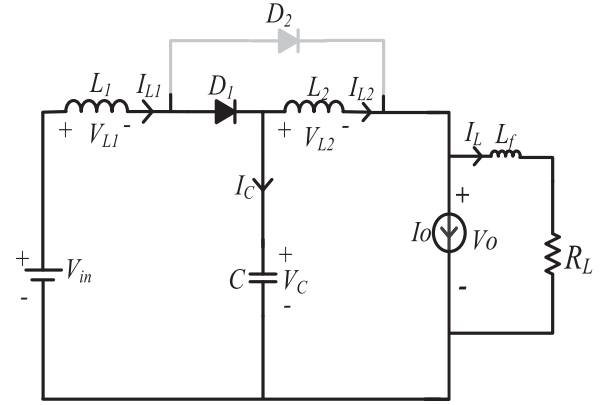

Figure 5: Equivalent circuit of single-phase grid-tied quadratic converter in the non-shoot-through state

of a switching cycle tperiod T. From the above equivalent circuit diagram, the following equations are written from (1) to (3).

$$V_{in} = V_{L_1} - V_{L_2} + V_C \tag{1}$$

$$V_C = V_{L_2} \tag{2}$$

$$V_{in} = V_{L_1} \tag{3}$$

Now consider that the inverter is in non-shoot-through states for T_1 duration of a switching cycle period T. Figure 5 shows the equivalent circuit for non-shoot-through switching state. The modelling of quadratic converters is referred to in [22], and [23] in the text in this section.

From the equivalent circuit diagram shown in Figure 5, equations can be derived as follows.

$$V_{in} = V_{L_1} + V_C \tag{4}$$

$$V_C = V_{L_2} + V_0 \tag{5}$$

$$V_{L_2} = V_C - V_0 \tag{6}$$

where, the period of one complete cycle is given by
$T = T_0 + T_1$

Duty cycle, $D = \frac{T_0}{T}$

In the steady-state, the average voltage of the inductor is zero for one switching period T.

The average voltage in inductor L_1 is zero, then

From (3) and (4)

$$V_{L_1} = \frac{T_0 * V_{in} + T_1 * (V_{in} - V_C)}{T} = 0 \qquad (7)$$

$$T_1 * V_C = V_{in} * (T_0 + T_1) = 0$$

$$\frac{V_C}{V_{in}} = \frac{T_0 + T_1}{T_1} = \frac{T}{T - T_0}$$

$$\frac{V_C}{V_{in}} = \frac{1}{(1 - D)} \qquad (8)$$

Similarly, the average voltage in inductor L_2 is

From (2) and (5)

$$V_{L_2} = \frac{T_0 * V_C + T_1 * (V_C - V_0)}{T} = 0 \qquad (9)$$

$$T_1 * V_0 = V_C * (T_0 + T_1)$$

$$\frac{V_0}{V_{in}} = \frac{T_0 + T_1}{T_1} = \frac{T}{T - T_0}$$

$$\frac{V_0}{V_C} = \frac{1}{1 - D} \qquad (10)$$

From Equations (8) and (10)

$$\frac{V_C}{V_{in}} * \frac{V_0}{V_C} = \frac{1}{1 - D} * \frac{1}{1 - D}$$

$$\frac{V_0}{V_{in}} = B = \frac{1}{(1 - D)^2} \qquad (11)$$

where $B =$ Boost Factor $= \frac{1}{(1-D)^2}$

4. SST PWM CONTROL

The concept of SST was introduced in our previous publication [12]. In this paper, the same concept of SST is now applied to the quadratic inverter. The SST PWM waveform is shown in Figure 6 for all four switches of the inverter leg i.e. S_A, S_B, S_C and S_D. The figure shows that the sinusoidal form is conserved in the upper and lower switching pattern for each leg of the H-bridge inverter.
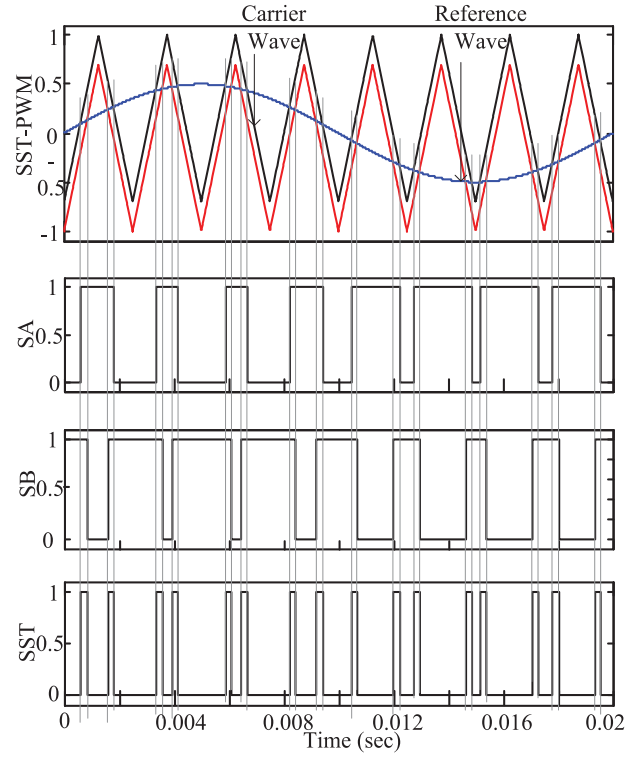

Figure 6: The waveform of symmetrical shoot-through-based PWM

The sensitivity of the boost factor B and modulation index M for duty ratio D is given in (12) for ZSI, as mentioned in [12].

$$S_h^B = \frac{\partial B/B}{\partial h/h} = \frac{h}{(1 - h)} \qquad (12)$$

For a quadratic converter, the sensitivity can be derived as

$$S_h^B = \frac{\partial B/B}{\partial h/h} = \frac{h}{\left(1 - \frac{h}{2}\right)} \qquad (13)$$

$$S_h^M = \frac{\partial M/M}{\partial h/h} = \frac{h^2}{2\left(1 - \frac{h^2}{4}\right)} \qquad (14)$$

From Equations (12) and (13) it is clear that SST sensitivity for h of the quadratic converter-based inverter is less than that of ZSI. Equation (14) shows that the modulation index m is also insensitive to h. Hence the proposed decoupled strategy is successfully justified. The maximum value of h for the simulation purpose is assumed to be 0.4.

5. SIZING OF COMPONENTS

Component size reduction is an important aspect of the designer for the design of any system. At shoot-through

state the inductor will limit the current ripple R_C through the devices during boost conversion mode. The maximum power P_{max} operation of the inductor value is given by

$$L = \frac{(1-D)\, V_{in}{}^2\, Ts\, D}{(1-2D)\, P_{max}\, Rc\%} \tag{15}$$

The capacitor absorbs the current ripple and limits the voltage ripple R_V in the inverter bridge to keep the output voltage sinusoidal, which can be calculated as

$$C = \frac{(1-D)\, P_{max}\, Ts\, D}{V_{in}{}^2\, Rv\%} \tag{16}$$

For a quadratic converter the inductor value is lower but the capacitor value is higher owing to the reduced number as compared to quasi-ZSI or ZSI topology.

Power flow from DC to AC using inverter control is shown by equations.

As shown in Figure 1(a), the DC to AC inverter controls the power flow into the grid by controlling its input current that balances the power in the system.

The equation of AC side power is given by

$$P_{AC} = V_{g\,rms} * I_{g\,rms} * Cos\varphi \tag{17}$$

From the simulation result shown in Figure 7(c), the grid current is in phase with grid voltage which is also verified by the experimental result shown in Figure 12. It shows that the power factor Cos φ is obtained as unity.

Now Equation (17) can be rewritten by keeping Cos $\varphi = 1$ as

$$P_{AC} = V_{g\,rms} * I_{g\,rms} \tag{18}$$

where V_{grms} and I_{grms} are the RMS value of grid voltage and grid current, respectively.

At the input DC side, the average power equation can be given as

$$P_{DC} = V_{in} * I_{in} \tag{19}$$

where V_{in} and I_{in} are the input DC voltage and input DC, respectively. Hence by controlling the input DC I_{in}, the power flow can be controlled.

In an ideal condition, the input DC power is equal to the output AC power. But practically both the input and output power cannot be the same due to the losses in the converter and grid.
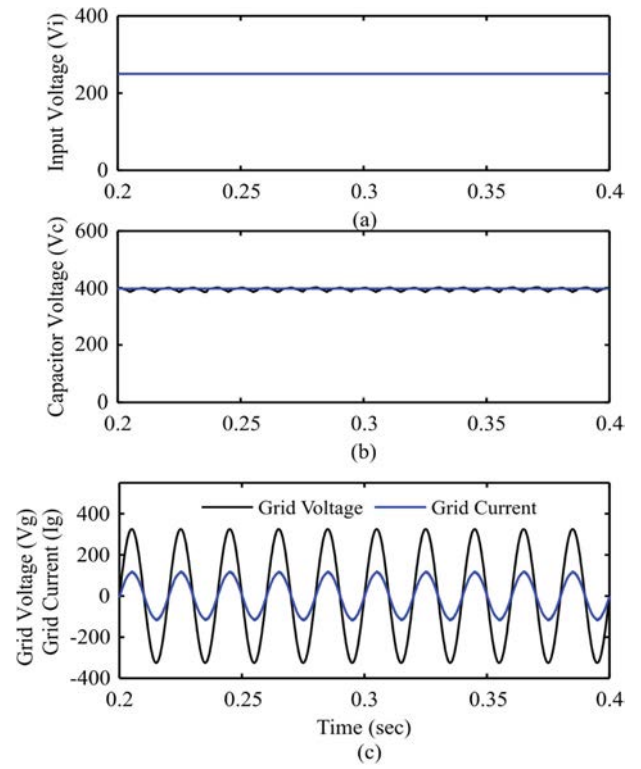

Figure 7: Simulation result for steady-state condition (a) Input voltage (b) Capacitor voltage (c) Grid voltage and current

Table 1: Specification of the quadratic converter-based grid-tied system

Sr. No.	Parameters	Values
01	Grid Voltage (RMS)	230 V
02	Supply Frequency	50 Hz
03	Switching Frequency	10 kHz
04	AC filter inductor	10 mH
05	Quadratic Capacitor (C_1)	1200 µF
06	Quadratic converter inductor (L_1, L_2)	70 µH
07	Local Load	3 KW

6. SIMULATION RESULT

The simulation is done in MATLAB Simulink software. The specifications of the simulated system are specified in Table 1.

Figure 7 shows the steady-state waveform of input voltage, capacitor voltage, grid voltage and grid current. To verify the transient behaviour of the DC side controller, a sudden change in input voltage and a capacitor reference voltage is noticed.

Figure 8 shows the step change in input voltage at 0.5 sec from an amplitude of 250 V to 200 V. The capacitor voltage and grid side voltage and current remain regulated. The duty ratio is controlled by the PI controller with $K_p = 1$ and $K_I = 1$ and sampling time $T_s = 5$nsec.
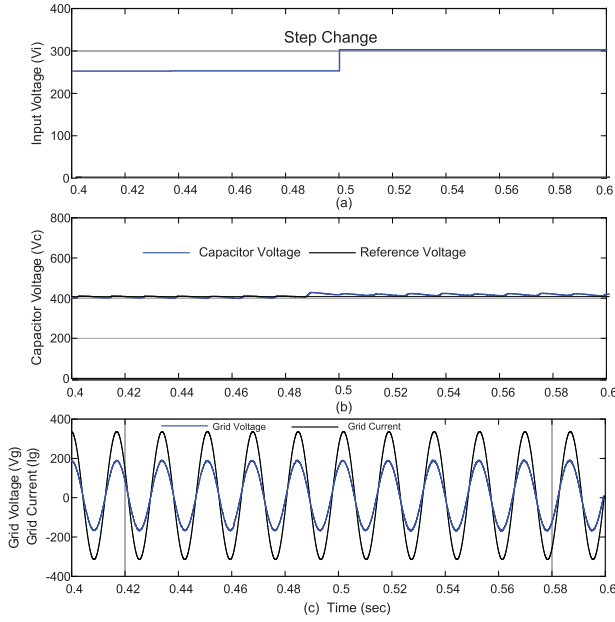
Figure 8: Simulation result for a step change in voltage from 250 V to 200 V (a) Input voltage (b) Capacitor voltage (c) Grid voltage and current

Figure 9 shows that the step change in capacitor reference voltage at 0.5 sec is carried out from 450 V to 400 V. This signifies the effectiveness of SST- PWM controlled by the PI controller. It shows the response time of the DC side controller is given in milliseconds which is fast enough to regulate the capacitor voltage.

Figure 10 displays the step change in the grid-connected load from 15 A to 10 A at 0.5 sec showing the effectiveness of the AC side controller.

In simulation results shown in Figures 7–10, the voltage amplitude is 325 V and the current is between 10 and 15 A. To make the current waveform more visible in the combined waveform of current and voltage, the current waveform is scaled by 10 times i.e. 10x.

7. EXPERIMENTAL INVESTIGATION

The proposed scheme of the grid-connected quadratic converter-based inverter is validated by hardware setup, as shown in Figure 11. This experimental setup is divided into four parts, namely, quadratic converter, controller card using dsPIC33EP256MC202, driver circuit board and H-bridge inverter. The sensing circuit senses the current and voltage across the point of common coupling between load and inverter output and feeds them to the ADC of the DSP controller card.
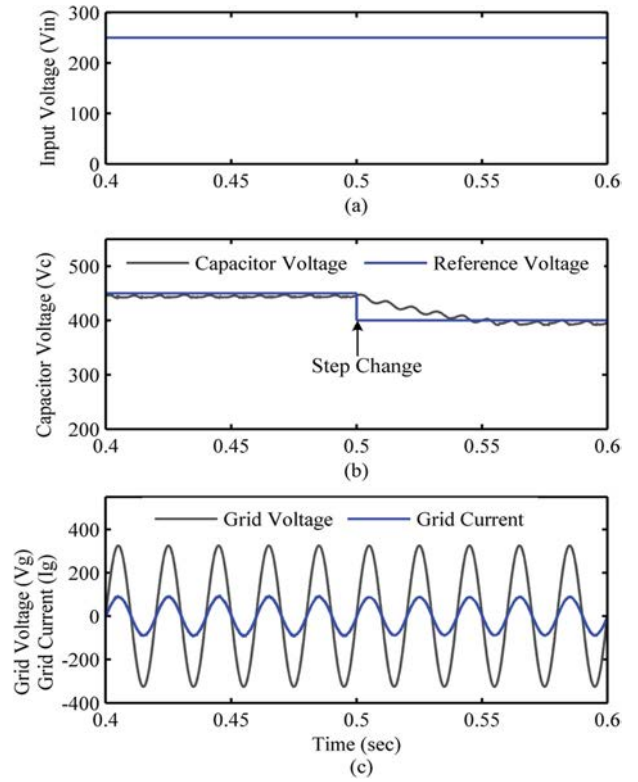

Figure 9: Simulation result for a step change in capacitor voltage from 450 V to 400 V (a) Input voltage (b) Capacitor voltage (c) Grid voltage and current
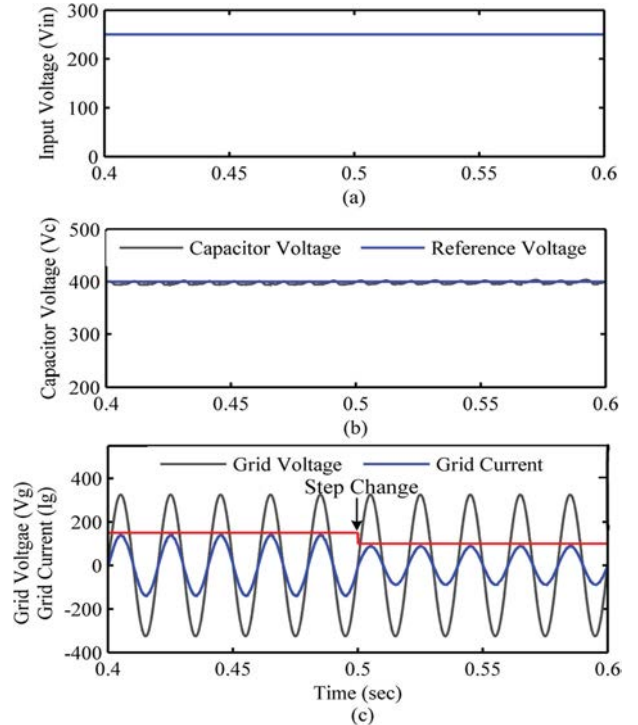

Figure 10: Simulation result for a step change in load from 15 A to 10 A (a) Input voltage (b) Capacitor voltage (c) Grid voltage and current
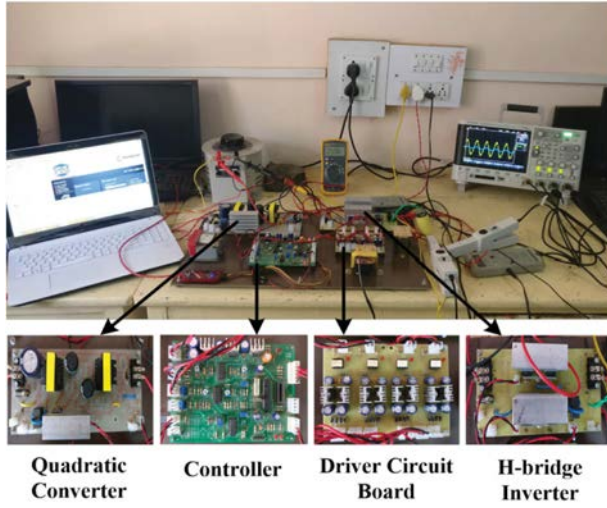
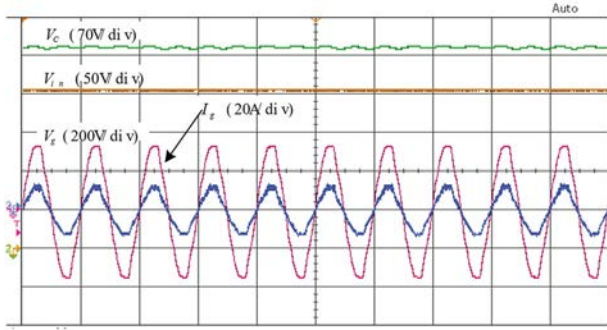**Figure 11:** Experimental setup of the proposed converter for the grid-tied system

Figure 12: Hardware result for the steady-state condition

Figure 13: Experimental result for a step change in input voltage

Figure 14: Experimental result for a step change in capacitor voltage

Figure 15: Experimental result for a step change in grid current

The experimental results are evaluated for various conditions like a step change in capacitor reference voltage and a step change in AC side current.

In Figure 12, the steady-state waveforms for the proposed system of grid-connected quadratic converter are shown. The results are obtained using SST PWM with the reference capacitor voltage $V_C = 350$ V as a reference peak value of grid current $I_g = 10$ A and input voltage of 210 V. To analyse the effect of input variations, the step change across input voltage is demonstrated in Figure 13 from 200 V to 160 V. Here V_C is regulated at 350 V and AC side waveforms are also regulated at its prescribed values.

The DC side control is investigated by reducing the capacitor voltage from 370 V to 320 V with $V_{in} = 250$ V, as shown in Figure 14. Irrespective of the change in capacitor reference voltage, AC side quantities like grid current remain unaffected. A further step change in load
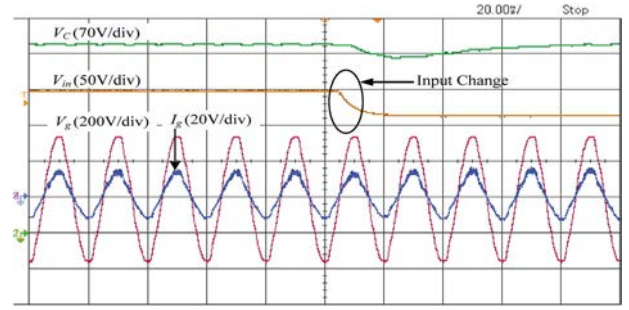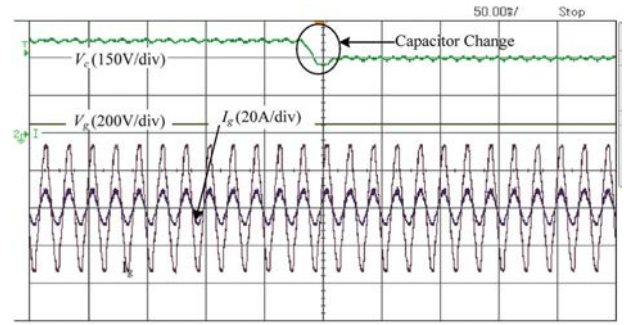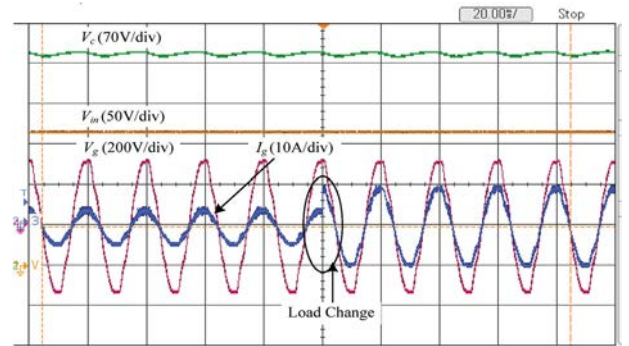
from 5 A to 10 A peak is shown in Figure 15, which indicates the stable operation of the AC control circuit. The overall experimental results are in agreement with the simulation result which is provided in an earlier section.

The grid current THD is obtained using simulation and experimental in three different cases shown in Table 2. The capacitor voltage, input voltage and load current are regulated in the first, second and third case, respectively. It is clear from Table 2 that the current THD is obtained less than 5% which satisfies IEEE-519 norms. It is within acceptable limits.

Table 2: **Study of harmonic under different conditions with a local load of R = 100 Ω, L = 100 mH.**

| Sr.no.	Input voltage	Capacitor voltage	Load current	Simulated grid current		Experimental grid current	
				THD%	Fundamental	THD%	Fundamental
1	$V_{in} = 250\,V$	$V_c = 350\,V$	$I_g = 10\,A$	4.20	8.40	4.10	8.30
		$V_c = 400\,V$		2.36	8.978	2.61	9.07
		$V_c = 450\,V$		2.63	9.026	2.72	9.05
2	$V_{in} = 220\,V$	$V_c = 400\,V$	$I_g = 10\,A$	2.49	8.96	2.48	8.98
	$V_{in} = 250\,V$			2.36	8.978	2.38	8.95
	$V_{in} = 300\,V$			1.91	8.827	1.91	8.92
3	$V_{in} = 250\,V$	$V_c = 400\,V$	$I_g = 05\,A$	3.97	3.70	4.23	3.30
			$I_g = 10\,A$	2.36	8.978	2.86	8.34
			$I_g = 15\,A$	1.77	13.94	1.89	13.45
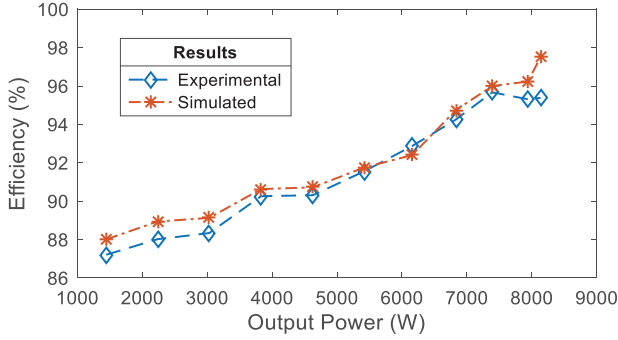
Figure 16: Efficiency versus output power graph at R-L load

Figure 16 shows the graph of efficiency vs. output power for input voltage $V_{in} = 250\,V$ and grid voltage $Vg_{(rms)} = 230\,V$. Experimental loading efficiency analysis is performed with a constant local load of R = 100 Ω, L = 100 mH and varying grid load Ig from rated power to nominal power. As seen from the graph, the efficiency is higher for higher output power. With an increase in load current, the THD contents are reduced owing to the reduction of ripples. Therefore, the loading efficiency is getting improved with a higher load. After 2.5 KW it is observed that the efficiency is almost constant at around 95%. Both simulated and experimental results are compared.

8. CONCLUSION AND FUTURE SCOPE

This paper presents a quadratic converter for a single-phase grid-connected system. SST-based PWM is used as a modulator for the design of the controller on both the AC side and the DC side to obtain nearly independent control. The simulation and experimental results are presented showing the efficacy of the proposed scheme. The controller is stable and suitable for higher load currents. The dynamic response of the system is efficient and works well like the other conventionally used impedance source networks like quasi Z-source. This particular controller can be useful for applications like PV-based generation in smart grid and microgrid for distributed generation.

DISCLOSURE STATEMENT

No potential conflict of interest was reported by the author(s).

REFERENCES

1. R. D. Middlebrook, "Transformerless dc-to-dc converters with large conversion ratios," *Tele. Energy Conf., INTELEC'84*, 455–460, 1984.

2. M. Hoshino, G. Kimura, and M. Shioya, "Dc to-dc converters and inverter for photovoltaic modules," *Ind. Electron. Soc., IECON'88, 14 Annual Conf.*, Vol. 3, pp. 569–574, 1988.

3. E. Van Dijk, J. N. Spruijt, D. M. O'sullivan, and J. B. Klaassens, "PWM-switch modelling of dc-dc converters," *IEEE Trans. Power Electron.*, Vol. 10, no. 6, pp. 659–665, 1995. doi:10.1109/63.471285

4. F. Z. Peng, "Z-source inverter," *IEEE Trans. Ind. Appl.*, Vol. 39, no. 2, pp. 504–510, 2003. doi:10.1109/TIA.2003.808920

5. P. C. Loh, D. M. Vilathgamuwa, Y. S. Lai, G. T. Chua, and Y. Li. "Pulse-width modulation of Z source inverters," *IEEE*, 2004.

6. F. Z. Peng, M. Shen, and Z. Qian, "Maximum boost control of the Z-source inverter," *IEEE Trans. Power Electron.*, Vol. 20, no. 4, pp. 833–838, 2005. doi:10.1109/TPEL.2005.850927

7. M. Shen, A. Joseph, Y. Huang, F. Z. Peng, and Z. Qian, "Design and development of a 50 kW Z-source inverter for fuel cell vehicles," *CES/IEEE, IPEMC*, Vol. 2, pp. 1–5, 2006.

8. R. Badin, Y. Huang, F. Z. Peng, and H. G. Kim. "Grid interconnected Z-source pv system," *IEEE*, pp. 2328–2333, 2007.

9. V. P. Galigekere, and M. K. Kazimierczuk, "Analysis of pwm Z-source dc-dc converter in ccm for steady state," *IEEE Trans. Circuits Syst. i: Reg. Papers*, Vol. 59, no. 4, pp. 854–863, 2012. doi:10.1109/TCSI.2011.2169742

10. Y. Liu, B. Ge, H. Abu-Rub, and D. Sun, "Comprehensive modeling of single-phase quasi-Z-source photovoltaic inverter to investigate low- frequency voltage and current ripple," *IEEE Trans. Ind. Electron.*, Vol. 62, no. 7, pp. 4194–4202, Jul. 2015. doi:10.1109/TIE.2014.2384472

11. Q. Tran, T. Chun, J. Ahn, and H. Lee, "Algorithms for controlling both the dc boost and ac output voltage of Z-source inverter," *IEEE Trans. Ind. Electron.*, Vol. 54, no. 5, pp. 2745–2750, Oct. 2007. doi:10.1109/TIE.2007.895146

12. S. G. Kadwane, U. K. Shinde, S. P. Gawande, and R. K. Keshri, "Symmetrical shoot-through based decoupled control of Z-source inverter," *IEEE. Access.*, Vol. 5, pp. 11298–11306, 2017. doi:10.1109/ACCESS.2017.2715065

13. E. E. Carbajal-Gutierrez, J. A. Morales-Saldaña, and J. Leyya-Ramos, "Modeling of a single-switch quadratic buck converter," *IEEE Trans. Aerospace Electron. Sys.*, Vol. 41, no. 4, pp. 1451–1457, 2005. doi:10.1109/TAES.2005.1561895

14. S. Zerouali, A. Allag, S. M. Mimoune, M. Y. Ayad, M. Becherif, A. Miraoui, and S. Khanniche, "An adaptive optimal linear quadratic regulator applied to three phases pwm ac-dc converter," *IEEE Ind. Electron.*, 371–376, 2006.

15. J. A. Morales-Saldana, R. Galarza-Quirino, J. Leyva-Ramos, E. E. Carbajal-Gutierrez, and M. G. Ortiz-Lopez, "Multiloop controller design for a quadratic boost converter," *IET Electric Power Appl.*, Vol. 1, no. 3, pp. 362–367, 2007. doi:10.1049/iet-epa:20060426

16. J. P. Gaubert, and G. Chanedeau. "Evaluation of dc-to-dc converters topologies with quadratic conversion ratios for photovoltaic power systems," *Power Electron. Appl., EPE'09*, pp. 1–10, 2009.

17. O. Lopez-Santos, L. Martinez-Salamero, G. Garcia, H. Valderrama-Blavi, and T. Sierra Polanco, "Robust sliding-mode control design for a voltage regulated quadratic boost converter," *IEEE Trans. Power Electron.*, Vol. 30, no. 4, pp. 2313–2327, 2015. doi:10.1109/TPEL.2014.2325066

18. P. Saadat, and K. Abbaszadeh, "A single-switch high step-up dc–dc converter based on quadratic boost," *IEEE Trans Ind. Electron.*, Vol. 63, no. 12, pp. 7733–7742, 2016. doi:10.1109/TIE.2016.2590991

19. S. H. Chincholkar, and C. Y. Chan, "Design of fixed-frequency pulsewidth-modulation-based sliding-mode controllers for the quadratic boost converter," *IEEE Trans. Circuits Syst. II: Exp. Briefs*, Vol. 64, no. 1, pp. 51–55, 2017. doi:10.1109/TCSII.2016.2546902

20. S.-W. Lee, and H.-L. Do, "Quadratic boost dc–dc converter with high voltage gain and reduced voltage stresses," *IEEE Trans. Power Electron.*, Vol. 34, pp. 1–8, 2018.

21. C.-Y. Chan, S. Chincholkar, and W. Jiang, "A modified fixed current-mode controller for improved performance in quadratic boost converters," *IEEE Trans. Circuits Syst.*, Vol. 67, pp. 1–5, Sept. 2019.

22. R. Hu, J. Zeng, J. Liu, Z. Guo, and N. Yang, "An ultra-high step-up quadratic boost converter base on coupled-inductor," *IEEE Trans. Power Electron.*, Vol. 35, pp. 1–9, Dec. 2020. doi:10.1109/TPWRD.2020.3038118

23. O. L. Santos, J. C. Mayo-Maldonado, J. C. R. Caro, J. E. Valdez-Resendiz, D. A. Zambrano-Prada1, and O. F. Ruiz-Martinez, "Quadratic boost converter with low-output voltage ripple," *IET Power Electron.*, 1605–1612, May 2020. doi:10.1049/iet-pel.2019.0472

AUTHORS

Sumant G Kadwane obtained his BE in electrical engineering from Yeshwantrao Chavan College of Engineering (YCCE), Nagpur, India in the year 1999. He obtained his ME in control systems from Govt College of Engineering, Pune in 2002 and his PhD in electrical engineering from Birla Institute of Technology, Mesra, India in January 2010. He is currently working as a professor in the Department of Electrical Engineering at YCCE Nagpur from the year 2015. He has published in various international journals including IEEE, IET, Elsevier, Taylor and Francis and IEEE conferences. He is a member of ISTE, a Fellow IE (I) and a senior member of IEEE. He is the Editor-in-Chief for Journal for Research in Engineering and Applied Sciences Published in central India. He has published 3 Indian patents. His areas of interest are control system design, power electronic converters and renewable energy.

Email: sgkadwane@gmail.com

S P Ashtankar (Sarode) received a BE degree in electrical engineering from Nagpur University and an MTech degree in the department of electrical engineering from YCCE, Autonomous Institute Nagpur, Maharashtra, India. Since 2008, she has been working as assistant prof in the Electrical department at KITS, Ramtek, Nagpur University, Nagpur. Currently, she is pursuing her PhD in the department of Electrical Engineering from YCCE, Autonomous Institute Nagpur, Maharashtra India. Her research interests include power converter design and renewable energy and control system design.

Corresponding author. Email: shilpabhauraosarode@gmail.com

Nitesh Y Funde is working as electronics design engineer in the automotive and energy industry. He has more than 3 years of experience in the circuit design of power supplies, motor control drives, power system protection and IoT devices. His fields of interest are power electronics, power system analysis and protection, network analysis and control system.

Email: nitesh151193@gmail.com

Ritesh K Keshri is working as asst professor in Electrical Engineering department at VNIT, Nagpur, India. He received the award of Visvesvaraya Young faculty, MIETY, India. He also received the 2016 Best paper award from IEEE Transactions on industrial electronics. He also received the Young Researcher Award, MIUR. His areas of interest are power electronics and drives for electric vehicle propulsion and electric vehicle charging.

Email: riteshkeshri@eee.vnit.ac.in

An Overview of the Second Harmonic (2ω) Passive Power Decoupling Technique of 1-Phase ZSI/QZSI to Eliminate/Minimize Low-Frequency Power Ripple

Shilpa P. Ashtankar (Sarode) & Sumant G. Kadwane

Published online: 05 Oct 2022.

Submit your article to this journal ↗

View related articles ↗

View Crossmark data ↗

Check for updates

REVIEW ARTICLE

An Overview of the Second Harmonic (2ω) Passive Power Decoupling Technique of 1-Phase ZSI/QZSI to Eliminate/Minimize Low-Frequency Power Ripple

Shilpa P. Ashtankar (Sarode)[1] and Sumant G. Kadwane[2]

[1]Kavikulguru Institute of Technology and Science, Ramtek, India; [2]Electrical Engineering Department, Yeshwantrao Chavan College of Engineering, Nagpur, India

ABSTRACT

1ϕ Z/quasi-Z source (ZSI/qZSI) inverters are nowadays increasingly used in a variety of power applications like renewable energy. During the rectification process of AC to DC side, the low-frequency ripples (2ω) are present in the DC side inductor current, capacitor voltage and also in DC-link voltage. These low-frequency ripples are the double line frequency power ripples that occur at two times the fundamental frequency i.e. at 100 Hz. In the case of renewable energy applications such as PV and fuel cells, these ripples are most hazardous. Due to current and voltage (2ω) ripples, the extraction of power from PV/fuel cell reduces. It also decreases its lifetime. These low-frequency ripples also increase the output current and voltage distortion. Ultimately it affects the performance of a system and degrades its power quality. Passive power decoupling techniques are used to eliminate/reduce low-frequency power ripples (2ω). The primary contribution of this article is to show a comprehensive overview of the passive power decoupling technique for the second harmonic (2ω) power elimination over two decades. This article also provides a proposed modified control strategy that achieves the elimination/reduction of (2ω) ripple in inductor current and capacitor voltage at the lowest values of qZS inductor and capacitor. The simulation and experimental results are also obtained for the proposed model.

1. INTRODUCTION

In recent years, voltage-fed ZSI and qZSI have primarily been considered for for 1-phase/3-phase applications. . ZSI/qZSI can be applied to all conversions of power such as AC-AC, AC-DC, DC-DC and DC -AC [1]. ZSI/qZSI is most popular due to the single one-level buck–boost feature and more reliable due to shoot-through feature [2–4]. qZSI has more deserving qualities than ZSI such as uninterrupted input current and cutting down the passive component count [5,6]. The ZS/qZS network is applied for 3ϕ AC to 3ϕ AC applications [7–9]. It is also applied for 1ϕ AC to 1ϕ AC applications [10–13]. The application for the ZS/qZS network for AC to DC power conversion is given [14]. The literature review gives that there are various applications of the ZS/qZS network for DC-DC [15–19], DC to 3ϕ AC [20–30] and DC to1ϕ AC [31–36]. Most of the literature [37–39] shows that the popular application of the ZS/qZS network is electric vehicles, motor drive, fuel cells, PVs, grids, UPS, and EV DC charger application. It has also wide PV applications using cascaded multilevel inverters [40–43]. The second harmonic (2ω) or double line frequency power exists in DC to AC and AC to DC single-phase inverter. These 2ω power ripples transferred from AC to DCside which occurs at two times

the electrical grid voltage fundamental frequency. . Due to the second harmonic (2ω) component of the current and voltage drawn by the inverter, DC side qZS inductor current and capacitor voltage as well as DC link voltage still suffer from the double-line frequency power ripple also known as low-frequency power (100 Hz) ripples. (2ω) power flows through both the inverter input (DC side) and inverter output (AC side). This second harmonic power ripple degrades system power quality and its performance. Low-frequency ripple elimination techniques are mentioned for 1ϕ traditional inverters [44–59]. Similar to the single-phase inverters [60], single-phase ZSI/qZSI inverters also suffer from the second harmonic power ripples. This results in higher voltage and current stress of power devices. The output and the input side of ZSI/qZSI are affected due to 2ω ripple. The fluctuating nature of ripples in the input DC side shortens the lifespan of the DC source. It is mostly affected in PV applications as these ripples reduce the energy extraction from PV panels. To buffer these ripples, bulky capacitors and inductors are used which makes the system more bulky and expensive too. Hence to lower down/remove these 2ω ripples, the passive and active power decoupling techniques are reviewed for ZSI/qZSI [61–63]. The passive power decoupling is used to reduce the
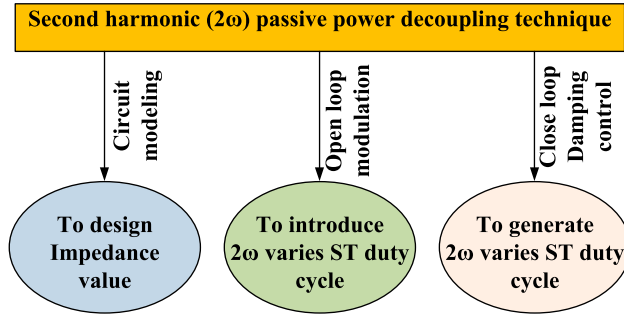
Figure 1: Block diagram of the passive power decoupling technique of 1ϕ ZSI/qZSI

low-frequency (2ω) ripple by (1) circuit impedance design control (2) open-loop/modified modulation control and (3) closed-loop damping control. The passive technique reduces low-frequency power ripple at a lower volume and achieves minimum cost due to non-requirement of any extra hardware circuit [64–87].

Figure 1 interprets the second harmonic (2ω) power decoupling technique which is common to single-phase traditional inverters and single-phase ZSI /qZSI inverters but comparatively single-phase ZSI/ qZSI inverters face more dispute due to their unique ZS/qZS network. In the present situation, no such literature is available which provides a systematic survey and future development of such type of inverter. Passive power decoupling techniques include the first technique which consists of designing of the ZS/qZS inductor and capacitor to limit/reduce 2ω ripple [64–72]. To reduce these low-frequency ripples generally, bulky inductors and capacitors are used. An electrolytic capacitor is suitable to reduce these ripples which carry large capacitors and less volume but not a good option due to its short lifespan. The second passive decoupling technique is open-loop modulation. This is the technique in which shoot through duty cycle is varied by adding 2ω ripple into this duty cycle [73–80]. The third technique is the closed-loop damping control which reduces low-frequency power (2ω) ripple at a minimum value of qZS impedance [81–87]. So it creates an interest in researchers to solve this issue.

The active power decoupling techniques remove/reduce 2ω power ripple by an extra ripple port consisting of additional power switches, diodes and compensator capacitors [88–97]. This technique increases the price and volume of a system due to excessive hardware circuits.

The paper is organized as follows: Section 2 provides an overview of single-phase qZSI and double-line frequency power ripple (2ω). Section 3 provides the summary of the passive decoupling technique of 1ϕ ZSI/QZSI as well

as proposed the modified control strategy to eliminate or reduce 2ω power ripple at minimum component volume . Finally, Section 4 represents the conclusion.

2. AN OVERVIEW OF 1-PHASE QZSI AND LOW-FREQUENCY POWER (2ω) RIPPLE

Figure 2 shows 1ϕ qZSI which is the modified topology of ZSI with the pair of inductors (L$_1$ and L$_2$) and capacitors (C$_1$,C$_2$) [61,62]. There are two operating ways of qZSI i.e. shoot-through and non-shoot-through modes.

Assuming T is the period of one switching cycle, which includes the interval of shoot through a period given by T_{sh} and for non-shoot through the time period given by T_{nsh}. Hence the shoot-through duty cycle, D is given by

$$D = \frac{T_{sh}}{T} \text{ while } T = T_{sh} + T_{nsh} \tag{1}$$

The qZS capacitor voltage (Vc_1 and Vc_2) and the peak-to-peak DC link voltage (V_{dcl}) are shown by the formula in Table 1.

Figure 2 shows that low-frequency power ripples are transferred during the rectification process from AC to DC side input (PV), qZS inductor current, qZS capacitor voltage and DC link voltage. The input PV current consists of a DC component along with a double-line
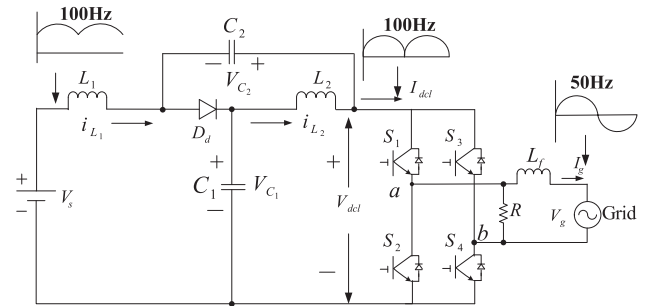

Figure 2: The circuit diagram of 1-phase quasi-ZSI with low-frequency power ripples transferred to the DC side

Table 1: Formulae of capacitor voltage and DC-link voltage

Voltage	Formula in terms of shoot-through time	Formula in terms of shoot-through duty cycle
V_{C_1}	$\left(\dfrac{1 - \frac{T_{sh}}{T}}{1 - \frac{2T_{sh}}{T}}\right) * V_s$	$\left(\dfrac{1 - D}{1 - 2D}\right) * V_s$
V_{C_2}	$\left(\dfrac{\frac{T_{sh}}{T}}{1 - \frac{2T_{sh}}{T}}\right) * V_s$	$\left(\dfrac{D}{1 - 2D}\right) * V_s$
V_{dcl}	$\left(\dfrac{1}{1 - 2\left(\frac{T_{sh}}{T}\right)}\right) * V_s$	$\left(\dfrac{1}{1 - 2D}\right) * V_s$

frequency component. Ripple current causes hysteresis losses which increase losses of MPPT resulting in poor efficiency in the case of PV application.

The inverter output voltage V_{ac} can be given as

$$V_{ac} = V_M \sin(\omega * t) = \sqrt{2}V_R \sin(\omega * t)$$
$$I_{ac} = I_M \sin((\omega * t) - \varphi) = \sqrt{2}I_R \sin((\omega * t) - \varphi)$$
$$P_{ac} = V_R I_R \cos\varphi - V_R I_R \cos(2(\omega * t) - \varphi) \qquad (2)$$

where V_M and V_R are the maximum and RMS value of output voltage, respectively. Similarly, I_M and I_R are the maximum and RMS value of output current, respectively.

The output power in Equation (2) shows that it consists of double-line frequency power (2ω) ripples. Due to DC side low-frequency ripples, it results in large THD in output voltage and current. Hence to reduce THD, generally, large sizes of inductors and capacitors are required.

3. SUMMARY OF PASSIVE DECOUPLING TECHNIQUES OF 1Φ ZSI/QZSI

3.1 Modeling Analysis of the Second Harmonic Power Component Circuit for Impedance Design

To reduce the second harmonic (2ω)/low-frequency power ripples from the input DC side generally qZS network inductor (L_1 and L_2) and capacitor (C_1 and C_2) are helpful. The impedance design is one of the passive decoupling technique in which the analysis of the circuit is built in correlation with 2ω to reduce the low-frequency power ripples that occur on the DC side (L_1, L_2 and C_1, C_2). Table 2 shows the review of circuit modeling for designing the impedance parameter. (In this table the abbreviations used for low-frequency (2ω) power ripple are K_{VC}, K_{IL}, K_{Vdcl}, K_{Vs} where K_{VC} is the low-frequency capacitor voltage ripple, K_{IL} is the low-frequency inductor current ripple, K_{Vdcl} is the low-frequency DC link voltage ripple and K_{Vs} is the low-frequency input voltage ripple. The internal capacitance across the PV panel is shown by C_{in}.

In reference [64], six possible states of operation are divided equally into static state and dynamic state. But in order to lower the values of L and C of the impedance network, the design methods are provided for the case where the inverter operates only in dynamic states such as active and shoot-through the state. Static states are involved only when there is a large variation in inductor current and capacitor voltage. In reference [65]

among three dynamic states, the open state is considered an active state and based on this state, the values of low-frequency L and C are designed [66] gives the designed formula of L1, L2 and C2. Where Df is the shoot-through duty cycle. Tf is the shoot through time period. ri% and rv% are the high-frequency percentage constants of DC link voltage in inductor current and capacitor voltage, respectively. In ref. [67], the exact models of double-line frequency ripples are provided. In the design of L and C, a and b c are considered as the ripple voltage constant of DC link voltage and inductor current ripple constant. In reference [68], the impedance design of the high-power qZS-HBI module is given for PV input. The internal resistance of the PV panels is also considered. The detailed impedance design for qZS-CMI is mentioned in ref. [69] where a* and b* are the desired ripple ratio of DC link voltage and inductor current, respectively. In reference [70], while calculating the impedance value of qZS, the voltage across the PV terminal capacitor is considered, while battery energy storage is also accounted for in refs [71,72]. Now the principle behind the different approaches is mentioned for an individual article in terms of the equation of L and C (design of L and C) which is mentioned in Table 2.

3.2 Open-Loop Modulation Control

In open-loop modulation control the PWM control technique is modified by adding low-frequency power ripple time period into a shoot-through time period to reduce the 2ω ripples of qZS inductor, qZS capacitor and DC-link voltage within the desired range, as shown in Figure 3(a–e) given in Table 3. In reference [69], the traditional PWM control is used where two DC vectors Vp^* and Vn^* of opposite polarity having the desired magnitude are helpful to generate the shoot-through duty cycle, as shown in Figure 3(a). The shoot-through duty cycle is given by

$$D_s = 1 - MO_i \qquad (3)$$

where D_s and MO_i are the shoot-through duty cycle and modulation index, respectively.

$$MO_i = \frac{A_r}{A_c} \leq 1 \qquad (4)$$

where Ar is the magnitude of the reference wave and Ac is the magnitude of the carrier wave. The modulation index should be always less than 1, whereas for shoot-through boost application, D_s should lie between 0 and –0.5.

Figure 3(b–e) are the modified PWM control scheme obtained by adding low-frequency ripple variation in

Table 2: The brief review of the impedance design technique

Ref. no.	Parameter specification	Design of L and C	Magnitude of low frequency (2ω) ripple	Advantage	Disadvantage
[64]	For nonlinear waveform $L = L_1 = L_2 = 2.1$ mH, $C = C_1 = C_2 = 0.094$ mF Critical values $L_1 = L_2 = 0.148$ mH, $C_1 = C_2 = 0.0067$ mF	$L = \dfrac{3D_s MO_i ImCos\phi}{8fs\ K_{VC}\ Vs\ (1-D_s)}$ $C = \dfrac{2D_s\ Vs(1-D_s)}{3fs\ K_{IL}\ ImCos\phi}$	$K_{VC} = 0.05$ $K_{IL} = 0.05$ $K_{VC} = 0.89$ $K_{IL} = 0.89$	1. The impedance values are accurately designed for non-linearity. 2. Lower size of inductor and capacitor required for low ripples. 3. Obtained the critical values of inductor and capacitor at any ripple factor	1. Allowed large (2ω) power ripples. 2. Increase in voltage and current rating of the component. 3. An increase in low-frequency power ripple increases the rating of the inductor and capacitor.
[65]	$L_1 = L_2 = 2.29$ mH, $C_1 = C_2 = 7.679$ mF $L_1 = L_2 = 2.29$ mH, $C_1 = C_2 = 5.355$ mF $L_1 = L_2 = 2.29$ mH, $C_1 = C_2 = 4.192$ mF $L_1 = L_2 = 2.29$ mH $C_1 = C_2 = 3.029$ mF	$L = \dfrac{0.5\ Vc(t)\ (1-2D_s)}{\Delta Il_1(t)\ fs}$ $C = \dfrac{il(t)\ (1-2D_s) - id(t)(1-D_s)}{2\Delta Vc_1(t)\ fs}$ $Vc(t)$ are corresponding to low-frequency oscillations	$K_{VC} = 0.01$ $K_{IL} = 0.1$ $K_{Vdcl} = 0.018$ $K_{VC} = 0.015$ $K_{IL} = 0.1$ $K_{Vdcl} = 0.027$ $K_{VC} = 0.02$ $K_{IL} = 0.1$ $K_{Vdcl} = 0.036$ $K_{VC} = 0.03$ $K_{IL} = 0.1$ $K_{Vdcl} = 0.054$	1. The accuracy of the proposed model is more satisfactory for small (2ω) power ripple 2. Limit DC link voltage ripple in the acceptable range.	1. The accuracy of the proposed model reduces with large ripples 2. Inductor and capacitor size increases to reduce (2ω) power ripple on the DC side.
[66]	$L_1 = 0.030$ mH, $L_2 = 0.021$ mH, $C_1 = 6.5$ mF $C_2 = 0.175$ mF	$L_1 = \dfrac{Vs\ (1-D_s)\ Tf}{(1-2D_s)\ ri\%\ IL_{1\,max}}$ $L_2 = \dfrac{Vs\ (1-D_s)\ Tf}{(1-2D_s)\ ri\%\ IL_{1\,max}}$ $C_2 = \dfrac{IL_1 T_s}{rv\%\ VC_{2\,max}}$	$KVs = 0.05$	1. The low-frequency input voltage ripples are within the tolerance range 2. The inductor current 2ω ripples are also reduced 3. Achieve high power density and high efficiency	1. High-frequency ripples also exist 2. The modeling analysis is quite complicated. 3. A large value of capacitor C_1 is required.
[67]	$L_1 = L_2 = 1$ mH, $C_1 = C_2 = 4.4$ mF	$L \geq \dfrac{a\ Vdcl\ (1-2D_s)}{2\ \omega\ b\ Mo_i\ Ia\ Cos\phi}$ $C \geq \dfrac{(1-2D_s)\ (1+b\ \cos\phi)\ Mo_i\ Ia}{2\ \omega\ a\ V_{dcl}}$	$K_{IL} = 0.18$ $K_{Vdcl} = 0.03$	1. The precise equation is derived to calculate low- frequency inductor and capacitor ripple component	1. A large value of the capacitor is required to reduce inductor and capacitor 2ω ripples within the desired range

(*continued*)

Table 2: Continued.

| Ref. no.	Parameter specification	Design of L and C	Magnitude of low frequency (2ω) ripple	Advantage	Disadvantage
[68]	$L_1 = L_2 = 3.3$ mH, $C_1 = C_2 = 4.7$ mF $C_{pv} = 1.1$ mF	$L \geq \dfrac{(1-2D_{max})d\,V_{dcl}^*\,\hat{V}_{dcl}}{4\,\omega\,d\,iL^*\,IL_{min}}$ $C \geq \dfrac{(1-2D_{max})\Delta iL_{max}+(1-D_{max})M_{min}\,I_m}{\omega\,d\,V_{dcl}^*\,\hat{V}_{dcl}}$	$K_{IL} = 0.25$ $KV_s = 0.0133$ $K_{Vdcl} = 0.057$	1. PV internal resistance is considered while designing the high-power qZS-HBI module 2. Due to PV's internal resistance, 2ω ripples in inductor current IL_1 are lower	1. The large 2ω ripples are present in inductor current IL_2 2. The small signal model built is quite complicated
[69]	$L_1 = L_2 = 0.5$ mH, $C_1 = C_2 = 4.4$ mF	$L \geq \dfrac{a^*\,Vs\,(1-2D_s)}{4\,\omega\,b^*\,Mo_i\,I_a\,\cos\phi}$ $C \geq \dfrac{(1-2D_s)(1+b^*\cos\phi)Mo_i\,I_a}{a^*\,\omega\,Vs}$	$K_{IL} = 0.18$ $K_{Vdcl} = 0.06$	1. The more accurate model is built with conduction and switching loss of the H bridge device including qZS diode, inductor and capacitor power loss	1. Symmetric configuration in the impedance parameter limits the optimization of the parameter. 2. Large inductor and capacitor value required 3. Assumes only ideal DC source as ignores PV panel dynamics
[70]	$L_1 = L_2 = 0.5$ mH, $C_1 = C_2 = 4.4$ mF $C_{in} = 0.023$ mF	———-	$K_{IL} = 0.25$ $K_{Vdcl} = 0.0969$ $KV_s = 0.0245$	1. The model considers PV panel dynamic, terminal capacitor and qZS network parameter 2. The terminal capacitance reduces 2ω voltage ripple in the PV panel and completely current I_{L1}.	1. THD increases with PV panel dynamics and terminal capacitance. 2. Requires larger capacitance and inductance
[71]	$L_1 = 0.85$ mH, $L_2 = 0.25$ mH, $C_1 = 3.7$ mF $C_2 = 0.41$ mF $C_{in} = 0.1$ mF	$L_1 = \dfrac{VC_{in}\,D_s\,(1-D_s)}{fs\,(1-2D_s)\,ri\%\,IL_1}$ $L_2 = \dfrac{VC_{in}\,D_s\,(1-D_s)}{fs\,(1-2D_s)\,ri\%\,IL_2}$ $C_1 = \dfrac{IL_2\,D_s}{fs\,rv\%\,Vc_1}$ $C_2 = \dfrac{(IL_1-I_b)\,D_s}{fs\,rv\%\,Vc_2}$	$K_{VC2} = 0.02$ $K_{Vdcl} = 0.05$ $KV_s = 0.02$	1. The proposed model includes a 2ω ripple model including the design of the battery and with no restriction on impedance parameter. 2. Buffer the fluctuation in PV power	1. Even though C_1 is large enough VC_1 carries a large low-frequency ripple compared to VC_2. 2. Carry small ripples in the DC-link voltage, PV panel voltage
[72]	$L_1 = 0.95$ mH, $L_2 = 0.35$ mH, $C_1 = 2$ mF $C_2 = 0.4$ mF $C_{in} = 0.040$ mF	————	$K_{VC2} = 0.02$ $K_{Vdcl} = 0.05$ $KV_s = 0.02$	1. Broad fluctuation in the PV panel voltage does not affect the 2ω voltage ripple ratio. 2. Asymmetric configuration of parameters ($L_1 \neq L_2$, $C_1 \neq C_2$) provides the optimized value of the inductor and capacitor	1. The dynamic change in load power affects 2ω power ripple at the DC side. 2. The analysis includes complicated equations.
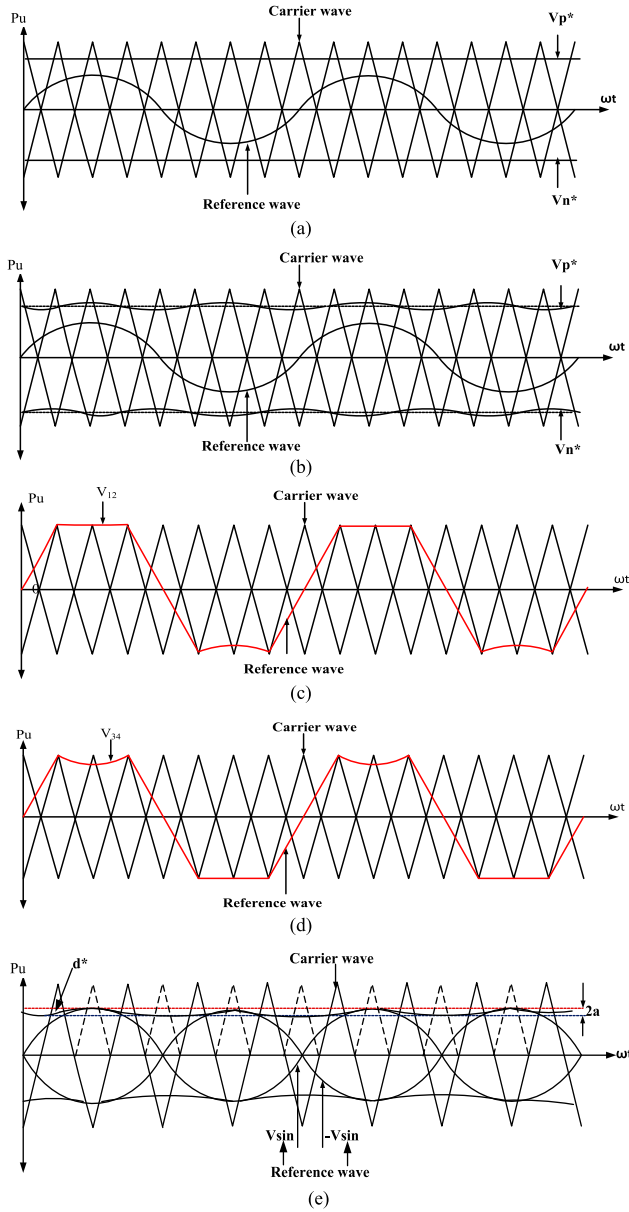
Figure 3: (a) Control waveform of traditional PWM, (b) Control waveform of modified PWM, (c) Control waveform of hybrid PWM for switch 1 and 2, (d) Control waveform of hybrid PWM for switch 3 and 4, (e) Control waveform of maximum boost PWM.

shoot-through duty cycle. In reference [73] the sinusoidal wave with a small magnitude in low frequency is added to Vp* and Vn* to obtain the final varying duty cycle D_f shown in Figure 3(b). In references [74,75], the reference signals are modified V_{12} and V_{34} to obtain the desired modulation index, as shown in Figure 3(c) and (d), respectively. This modified control strategy is used for various applications like PV [76] and drive applications [77].

In Figure 3(e), the maximum boost control PWM is provided for quasi-switched boost inverter [78]. In this
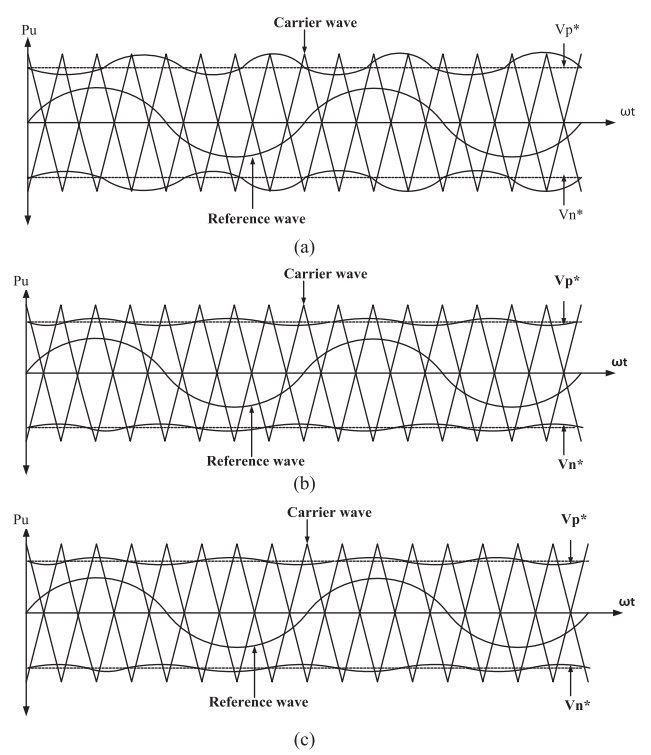

Figure 4: (a) Control waveform of non sinusoidal PWM, (b) Control waveform of current ripple damping PWM, (c) Control waveform of ripple vector cancellation PWM.

inverter, the additional switch S_5 is provided to control 2ω ripple. In this PWM control, two sine reference waves i.e. Vsin and –Vsin having the magnitude MO_i are compared to a triangular signal to generate pulses for switches S_1 and S_4. 2ω sine waveform of voltage $d*$ is compared with the dotted triangular wave to generate the pulse for switch S_5. This S_5 pulse is fed as an input to switch S1 and S_4 through the OR logic gate to get shoot-through duty cycle D_f. The term "a" is 1/2 of the peak-to-peak value of $d*$ where $\bar{d}$ is the average duty cycle.

The maximum boost control concept is applied for the extended topology of ZSI/qZSI [79,80] to achieve large voltage gain and lower voltage stress across the capacitor.

3.3 Close-Loop Modulation Control

To reduce the low-frequency ripples of the inductor current, capacitor and DC-link voltage of qZSI completely or to the minimum value, the damping control scheme is used in a close loop known as close-loop damping control. In this damping control, 2ω ripple duty cycle $\Delta d(t)$ is merged into a shoot-through duty cycle d_0 and the final duty cycle is provided as opposite vector Vp* and Vn,* as shown in Figure 4(a–c) shown in Table 4. In ref.

Table 3: The review of open-loop modulation control

Ref. No.	Open-loop modulation control	Figure	Control Waveform	Equation of final duty cycle (D_f), Design of the inductor (L) and capacitor (C)
[69]	Traditional PWM	3(a)		$d_0 = \dfrac{1 - \frac{V_s}{V_{dcl}}}{2}$ $Vp^*(t) = 1 - d_0$ $Vn^*(t) = d_0 - 1$
[73]	Modified PWM	3(b)		$D_f(t) = d_0 + \dfrac{\omega MO_i^2 L}{Z(1-2d_0)}\sin(2\omega t - \phi)$ $Vp^*(t) = 1 - D_f(t)$ $Vn^*(t) = D_f(t) - 1$ No theoretical design of L and C
[74][75]	Hybrid PWM	3(c)		$D_f(t) = \begin{cases} 0 & |MO_i Sin\omega t| < 1 \\ \dfrac{|MO_i Sin\omega t|}{1 - 2|MO_i Sin\omega t|} & |MO_i Sin\omega t| \geq 1 \end{cases}$
		3(d)		$L = \dfrac{2Vc_1\max * D_f\max}{0.02 * IL * fs}$ $C = \dfrac{IL * D_f\max}{0.35 * V_{pn}\max * fs}$ $D_f\max = \dfrac{(1 - MO_i)}{(1 - 2MO_i)}$
[78]	Maximum boost control	3(e)		$\bar{d} = MO_i - a$ $D_f = 1 - \bar{d} = 1 - (MO_i - a) = 1 - MO_i + a$ The equations of L and C are not provided

Table 4: The review of close-loop modulation control

Ref. No.	Close-loop modulation control	Figure	Control Waveform	Equation of final duty cycle (D_f), Design of the inductor (L) and capacitor (C) Advantage
[81]	Non-sinusoidal PWM	4(a)		$D_f(t) = d_0 + \Delta d(t) = \dfrac{Vc_1 - Vs}{2Vc_1 - Vs}$ $L_1 = \dfrac{D_{f\max} * (1 - D_{f\max}) * Vs}{0.022 * I_{L1\max} * fs * (1 - 2D_{f\max})}$ $L_2 = \dfrac{D_{f\max} * (1 - D_{f\max}) * Vs}{0.022 * I_{L2\max} * fs * (1 - 2D_{f\max})}$ $C_1 = \dfrac{Vm * Im}{1 * \omega * V_{dcl}^2}$ $C_2 = \dfrac{I_L}{0.021 * Vc_{2\max} * fs}$
[82]	Current ripple damping control	4(b)		$D_f(t) = d_0 + \Delta d(t) = \dfrac{Vc_1 - Vs}{2Vc_1 - Vs}$ $L = \dfrac{D_{f\max} * (1 - D_{f\max}) * Vs}{0.022 * I_L * fs * (1 - 2D_{f\max})}$ $C = \dfrac{Vm * Im}{0.05 * \omega * V_{dcl}^2}$
[83]	Ripple vector cancellation control	4(c)		$D_f(t) = d_0 + \Delta d(t)$ The equations of L and C are not provided

[81], 2ω variation in frequency ripple will be added to D_f, Vp* and Vn* to obtain time-varying final duty cycle as $D_f(t)$. $D_{f\max}$ is the maximum value of the final duty cycle. $\Delta d(t)$ is the 2ω ripple shoot duty cycle, as shown in Figure 4(a). The current ripple close-loop modulation control shown in Figure 4(b) is given in reference [82].

In this close-loop damping control, the variation in 2ω ripple in shoot-through duty cycle is implemented in a feedback loop.

In ripple vector cancelation control [83] also the variation in double line frequency ripple shoot through duty cycle $\Delta d(t)$ is added in original duty cycle d_0 to control low-frequency inductor current and capacitor voltage ripple, as shown in Figure 4(c). The double line frequency ripple of L and C depends on the switching frequency (fs) and duty cycle (D).

Table 4 shows the survey of the close-loop modulation technique along with different PWM waveforms. All the waveforms in Table 4 look the same but their vectors Vp and Vn have different frequencies for all waveforms.

In Table 5, the selection of qZS impedance parameters and magnitude of low-frequency ripple are reviewed for open- and close-loop modulation.

The parameters in Tables 2 and 5 are shown for the same rating of the power converter as per the literature review. Advantages and disadvantages are discussed based on the ripples.

It shows that compared to open-loop modulation control, the close-loop technique reduces low-frequency ripple in a good manner at a lower value of qZS inductor and capacitor. The same PWM control of [83] is used in reference [84] for grid-tied PV applications. The control strategy is used to obtain the lower capacitance along with lower input voltage low-frequency ripple. Reference [85–87] shows the different model control to achieve the minimum power ripples in input voltage [86] and zero inductor current ripple [87].

3.3.1 Modified Ripple Damping Control
Figure 5 shows the modified ripple damping control method to cut down the passive component count. The novelty of this control is the elimination/reduction in low-frequency inductor current ripple and capacitor voltage ripple at the lowest rating of inductor and capacitor.

The modified ripple damping control includes mainly two important controls. Firstly, DC side control includes current ripple damping and DC component control. Secondly, AC side control includes grid current control. DC side control mainly focuses on the control of shoot-through duty cycle D which achieves approximately zero low-frequency ripple in inductor current. While AC side control focuses on modulation index control that

achieves grid current control. Simple boost carrier control is used in this article as an SPWM technique to generate the shoot-through pulses. This technique is very simple and easy to apply.

1. DC control

In this DC side control, the shoot-through duty cycle D is modified using current ripple and DC component control. Current ripple control [82] is used to obtain the fluctuation in duty cycle d to eliminate the low-frequency (100 Hz) ripple of the inductor current. In this control, the final shoot-through duty cycle D is given by

De is the duty cycle obtained at the equilibrium point. De is used to control the DC component of inductor current and capacitor voltage [82]. In this reference paper , De is calculated using the formula as

$$D_e = \frac{V_{C_1} - V_s}{2V_{C_1} - V_s} \tag{5}$$

D_e is obtained using the above mathematical formulae [82].[]. But in this article, De is regulating the DC component value using the capacitor voltage control method. In this control actual capacitor voltage V_{C_1} compared with the reference capacitor voltage $V_{C_{1ref}}$. The error is fed to the PI controller. It minimizes the error and obtains the output in terms of the duty cycle De. De is added with a small duty cycle d which obtains the final duty cycle D. The purpose of this DC component control is to obtain the exact duty cycle D_e by regulated capacitor voltage. Also, this proposed control strategy achieves another benefit of the regulated value of V_{C_1} which is forbidden in ref. [82].

2. AC control

In AC side control the grid is synchronized with inverter output using phase-locked loop (PLL). The synchronized output of PLL multiplied with reference grid current $i_{g_{ref}}$ produces the sinusoidal reference grid current as $i_{g_{ref}} \times \sin \omega\, t$. Finally, this sinusoidal reference grid current is compared with the original grid current, producing an error tfed to the PI controller. The PI controller helps to reduce the error and generate the output in terms of modulation signal M which can send to the simple boost carrier control the PWM technique.

3.3.1.1 Simulation Results.
The Simulink diagram of the circuit shown in Figure 5 is built in MATLAB/SIMULINK and the simulation is performed using the following specification shown in Table 6. In this article,

Table 5: The review of parameter selection and low-frequency ripple magnitude in open-loop/close-loop modulation

Ref. No.	Open-/Close-loop modulation control	Parameter specification	Magnitude of low-frequency (2ω) ripple	Advantage	Disadvantage
[69]	Traditional PWM	$L_1 = L_2 = 2.29\,\text{mH}$, $C_1 = C_2 = 2.7\,\text{mF}$ $L_1 = L_2 = 2.29\,\text{mH}$ $C_1 = C_2 = 5.4\,\text{mF}$	$K_{VC} = 2.97$ $K_{VC} = 1.44$	1. Easy to carry out 2. Most simplified PWM control	1. Only constant shoot-through pulses are obtained. 2. Required large values of qZS inductor and qZS capacitor to limit the low-frequency ripples
[73]	Modified PWM (LFHEC)	$L_1 = L_2 = 2.29\,\text{mH}$, $C_1 = C_2 = 2.7\,\text{mF}$ $L_1 = L_2 = 2.29\,\text{mH}$ $C_1 = C_2 = 5.4\,\text{mF}$	$K_{VC} = 0.47$ $K_{VC} = 0.21$	1. The DC link voltage and capacitor voltage ripples are effectively reduced	1. But still, large values of the qZS inductor and capacitor are essential 2. Increases the current rating of the inductor
[74,75]	Hybrid PWM	$L_1 = L_2 = 0.25\,\text{mH}$, $C_1 = C_2 = 0.01\,\text{mF}$	–	1. Smaller values of qZS inductor and qZS capacitor required 2. The efficiency of the system is enhanced	1. More fluctuations are obtained qZS inductor and qZS capacitor in low frequency 2. A large terminal capacitor is required across the input DC source
[78]	Maximum boost control	For qZSI $L_1 = L_2 = 3\,\text{mH}$, $C_1 = C_2 = 4\,\text{mF}$ For qSBI $L_1 = L_2 = 6\,\text{mH}$, $C_1 = C_2 = 2\,\text{mF}$	–	1. The inductor current and capacitor voltage low-frequency ripple are reduced.	1. A large value of inductor and capacitor is required
[79]	Maximum boost control	$L_1 = L_2 = L_3 = L_4 = 1\,\text{mH}$, $C_1 = C_2 = 1\,\text{mF}$	–	1. Lower voltage stress along with higher voltage gain	1. Inductor current consists of large ripples.
[80]	Maximum boost control	$L_1 = L_2 = L_3 = L_4 = 1\,\text{mH}$, $C_1 = C_2 = 1\,\text{mF}$	–	1. Reduces voltage across DC link 2. Lower capacitor voltage and inductor current stress	1. Additional component increases the complexity and cost of the system
[81]	Non- sinusoidal PWM	$L_1 = 0.33\,\text{mH}$, $L_2 = 0.22\,\text{mH}$ $C_1 = 0.2\,\text{mF}$ $C_2 = 0.02\,\text{mF}$	$K_{Vs} = 0.05$	1. The input DC voltage became constant 2. Lower the size of qZS inductor and qZS capacitor	1. There is complexity in close loop control design 2. The low-frequency ripples exist in the inductor, capacitor and DC link voltage of qZSI.
[82]	Modified PWM	$L_1 = L_2 = 0.52\,\text{mH}$, $C_1 = C_2 = 1.9\,\text{mF}$	$K_{IL} = 0$ $K_{Vdcl} = 0.05$	1. Effectively the DC link voltage ripples are reduced 2. Inductor current ripples are eliminated	1. But still, large values of qZS capacitor are essential
[83]	Ripple vector cancellation PWM	$L_1 = L_2 = 1\,\text{mH}$, $C_1 = C_2 = 1\,\text{mF}$	$K_{IL} = 0.0169$ $K_{VC1} = 0.0253$ $K_{VC2} = 0.0775$	1. Inductor current ripples are effectively reduced 2. Decrease in the value of capacitor and inductor compared to traditional PWM	1. This method has a small effect on output power quality 2. There is not much effect on capacitor voltage ripple.
[84]	Modified shoot-through PWM	$L_1 = 0.330\,\text{mH}$ $L_2 = 0.215\,\text{mH}$, $C_1 = 0.2\,\text{mF}$ $C_2 = 0.02\,\text{mF}$	$K_{Vs} = 0.05$	1. The input capacitance value is reduced by a large value	1. The system efficiency is reduced 2. Observed low-frequency ripples in input voltage and capacitor voltage
[85]	Simple PWM	$L_1 = L_2 = 0.220\,\text{mH}$ $C_1 = C_2 = 0.100\,\text{mF}$	$K_{Vs} = 0.05$	1. Reduction in inductor current ripple with the reduction in capacitance value	1. Still carry low-frequency ripples in capacitor voltage.
[86]	Sine PWM	$L_1 = L_2 = 0.7\,\text{mH}$ $C_1 = C_2 = 0.240\,\text{mF}$	$K_{pin} = 0.03$	1. Input power fluctuation is reduced	1. QZS capacitors carry large ripples
[87]	Simple boost control	$L_1 = L_2 = 2.5\,\text{mH}$ $C_1 = C_2 = 1\,\text{mF}$	$K_{IL} = 0$	1. Inductor current ripples eliminated	1. Still, a large value of the inductor is required

the switching frequency is kept at 10KHz. As the switching frequency increases above 10 KHz, the switching losses became more dominant which slows the performance of the system .

The simulation results without and with a modified control strategy are shown in the table 7. In Figure 6(a$_1$),

2ω ripples exist in the inductor current (IL1). Here the peak-to-peak value of 2ω i.e. (100 Hz) ripple in inductor current is about 5A. After applying the modified control strategy (100 Hz) ripple in the inductor current (IL1) is eliminated, as shown in Figure 6(a$_2$). It is also found that the peak-to-peak value of (100 Hz) ripple in capacitor voltage (Vc$_1$) is about 14 V in Figure 6(b$_1$) but with
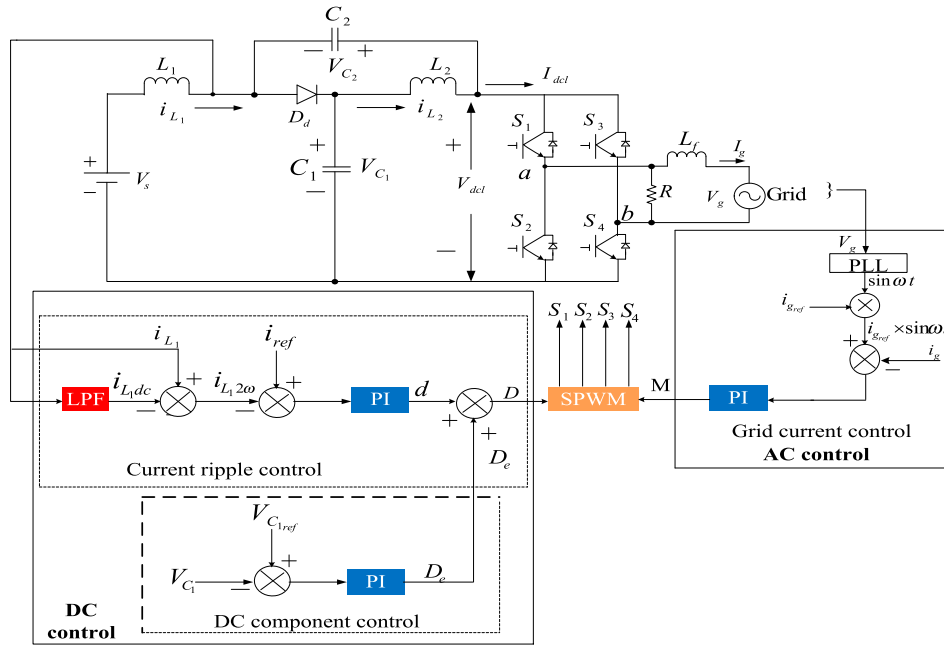
Figure 5: Block Diagram of Modified control strategy

a control strategy that value is also reduced to 10 V, as shown in Figure 6(b$_2$). 2ω ripples are observed in DC link voltage (Vdcl) in Figure 6(c$_1$) and (c$_2$), but with control strategy, the peak-to-peak value of (100 Hz) ripple in DC link voltage is 14 V, shown in Figure 6(c$_2$) while without modified control it is 21 V, as shown in Figure 6(c$_1$). Actually, DC-link voltage, as shown in Figure 6 (c$_1$) and (c$_2$), is the voltage obtained across switches S1 and S4 similarly for S2 and S3, as shown in Figure 2. ZSC/QZSC works on two modes of operation i.e. shoot-through and non-shoot-through modes. In the non-shoot-through mode, the power flows from the supply side to the load side through diagonal switches S1 and S2 and similarly through S3 and S4. So as the DC link voltage is obtained between S1 and S4 similarly for S2 and S3, at a time only one switch will operate from the upper leg or lower leg i.e. either S1 or S4 and from the second link either S2 or S3. Hence the maximum DC link voltage is obtained

during the period of the non-shoot-through mode. During the shoot-through state the switches S1 and S4 similarly S2 and S3 turn on simultaneously. Due to these, switches get short-circuited and zero DC link voltage will appear across the input terminal of the inverter. Because of the shoot-through and non-shoot-through modes of operation, the DC-link voltage varies from zero to maximum.

As in Figure 6(d$_1$), it observed that a constant steady shoot-through duty cycle is obtained at 0.22, whereas it found that the nature of the same duty cycle is fluctuating in nature due to the modified control strategy shown in Figure 6(d$_2$). As the mentioned control strategy is a closed loop , the duty cycle varies. But at a steady state, the value of the duty cycle is kept at 0.22. The reason is that as the duty cycle increases, the 100 Hz ripple content in the inductor and capacitor increases.

As compared to Figure 6(e$_1$), a smoother waveform is obtained for grid current using the control strategy, as observed in Figure 6(e$_2$). Figure 6(f$_2$) shows that with a modified control strategy, grid current THD is reduced to 2.63% from 4.81% as shown in Figure 6(f$_1$).

Table 6: The simulation specification of the circuit mentioned in Figure 5
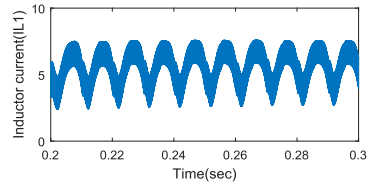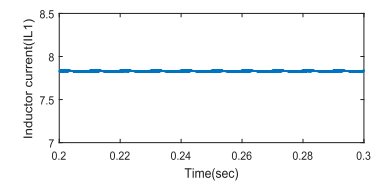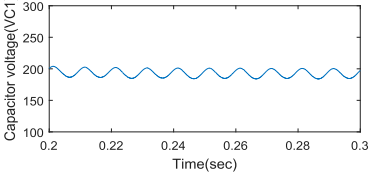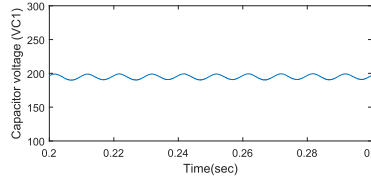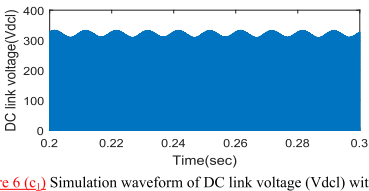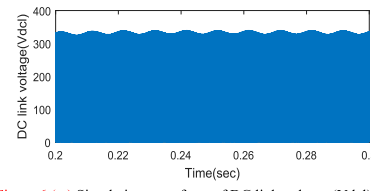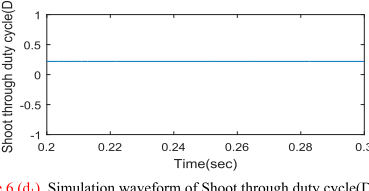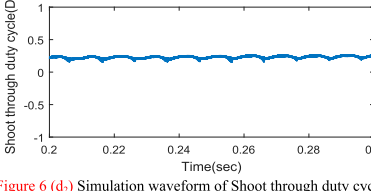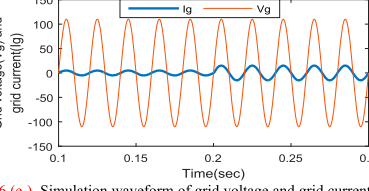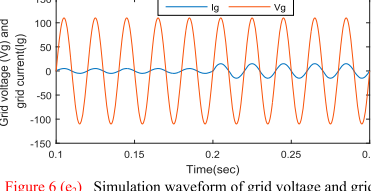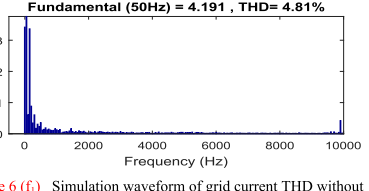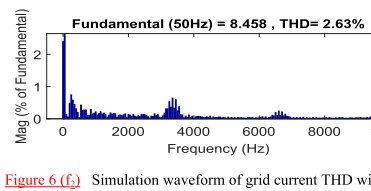
Circuit parameters	Specifications
Output power	990 W
Input Voltage	164 V
Output Voltage (Peak))	110 V
QZS inductance (L$_1$ = L$_2$)	160 uH
QZS Capacitance (C$_1$ = C$_2$)	1200 uF
Switching frequency (fs)	10 KHz
Modulation index (M)	0.6
Load Resistance	30 Ω
Output L filter	20 mH
Proportional constant (Kp)	1.15
Integral constant (Ki)	0.5

As per [82], the inductance and capacitance of the qZS network will be calculated with the desirable 100 Hz magnitude of inductor current ripple $I_L{}^*$ and capacitor voltage ripple $V_C{}^*$.

$$L = \frac{V_C{}^*(1 - 2D)}{2\omega I_L{}^*} \tag{6}$$

Table 7: **The simulation result of single-phase qZSI with and without a modified control strategy**

Without modified control strategy	With modified control strategy

Figure 6 (a₁) Simulation waveform of inductor current (I_{L1}) without modified control strategy

Figure 6 (a₂) Simulation waveform of inductor current (IL_1) with modified control strategy

Figure 6 (b₁) Simulation waveform of Capacitor voltage (Vc_1) without modified control strategy

Figure 6 (b₂) Simulation waveform of Capacitor voltage (Vc_1) with modified control strategy

Figure 6 (c₁) Simulation waveform of DC link voltage (Vdcl) without modified control strategy

Figure 6 (c₂) Simulation waveform of DC link voltage (Vdcl) with modified control strategy

Figure 6 (d₁) Simulation waveform of Shoot through duty cycle(D) without modified control strategy

Figure 6 (d₂) Simulation waveform of Shoot through duty cycle(D) with modified control strategy

Figure 6 (e₁) Simulation waveform of grid voltage and grid current for change in grid current from 5A to 18A without modified control strategy

Figure 6 (e₂)   Simulation waveform of grid voltage and grid current for change in grid current from 5A to 18A with modified control strategy

Figure 6 (f₁) Simulation waveform of grid current THD without modified control strategy

Figure 6 (f₂)   Simulation waveform of grid current THD with modified control strategy

$$C = \frac{(1-2D)^2 + \sqrt{(1-2D)^2\left(\frac{V_iI_i}{V_{dcl}*I_L^*}\right)^2 - \left(\frac{4\omega L*I_{dcl}(D-1)}{V_{dcl}}\right)^2}}{4\omega^2 L} \quad (7)$$

V_i is the inverter output voltage and I_i is the inverter output current.

In Figure 5, $L_1 = L_2 = L$, similarly $C_1 = C_2 = C$ and hence an analytical value of L and C for modified control strategy will be calculated using the following formula [79].

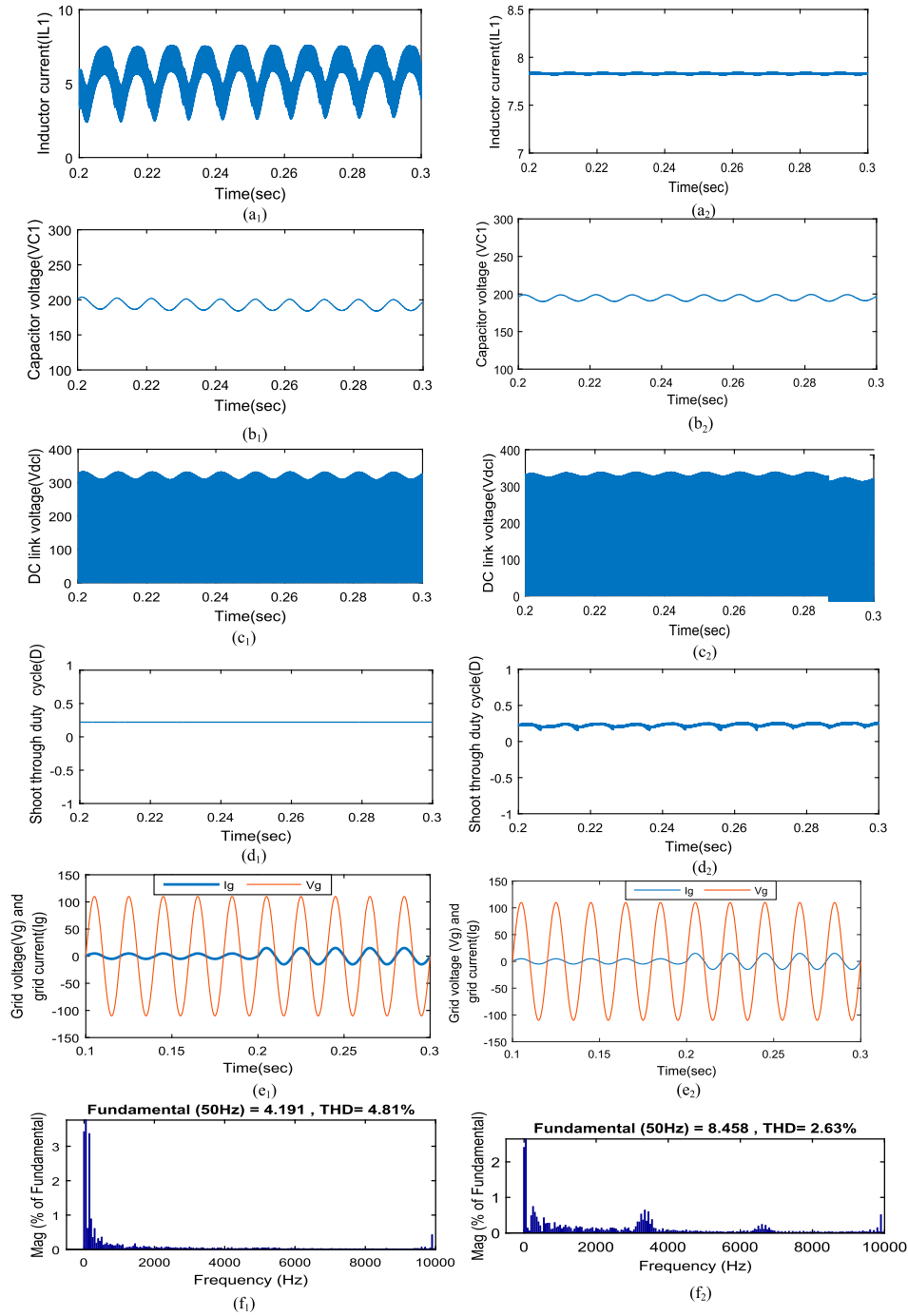$$L = \frac{D*(1-D)*Vs}{0.022*I_{L_s}*fs*(1-2D)} \quad (8)$$

Figure 6: (a₁) Simulation waveform of inductor current (I_L1) without modified control strategy, (a₂) Simulation waveform of inductor current (IL₁) with modified control strategy, (b₁) Simulation waveform of Capacitor voltage (Vc1) without modified control strategy, (b₂) Simulation waveform of Capacitor voltage (Vc1) with modified control strategy, (c₁) Simulation waveform of DC link voltage (Vdcl) without modified control strategy, (c₂) Simulation waveform of DC link voltage (Vdcl) with modified control strategy, (d₁) Simulation waveform of Shoot through duty cycle(D) without modified control strategy, (d₂) Simulation waveform of Shoot through duty cycle(D) with modified control strategy, (e₁) Simulation waveform of grid voltage and grid current for change in grid current from 5A to 18A without modified control strategy, (e₂) Simulation waveform of grid voltage and grid current for change in grid current from 5A to 18A with modified control strategy, (f₁) Simulation waveform of grid current THD without modified control strategy, (f₂) Simulation waveform of grid current THD with modified control strategy.

Table 8: The comparison of qZS impedance values for existing techniques and the proposed close-loop technique

100 Hz inductor current ripple	100 Hz capacitor voltage ripple	General calculations (6) and (7)	The method given in ref. [68]	The optimum design given in ref. [79]	Proposed modified control strategy (8) and (9)
2%2%2%	5%2.5%0.25%	$L = 10.28\,mH$ $C = 1.89\,mF$ $L = 5.15\,mH$ $C = 3.82\,mF$ $L = 0.515\,mH$ $C = 38.52\,mF$	$L = 10.27\,mH$ $C = 1.9\,mF$ $L = 5.13\,mH$ $C = 3.83\,mF$ $L = 0.514\,mH$ $C = 2.32\,mF$	None None None	None None None
40%	5%	$L = 0.515\,mH$ $C = 2.31\,mF$	$L = 0.514\,mH$ $C = 2.32\,mF$	None	None
0	5%	Practically impossible due to infinite inductance	Practically impossible due to infinite inductance	$L = 0.517\,mH$ $C = 1.9\,mF$	$L = 0.160\,mH$ $C = 1.2\,mF$
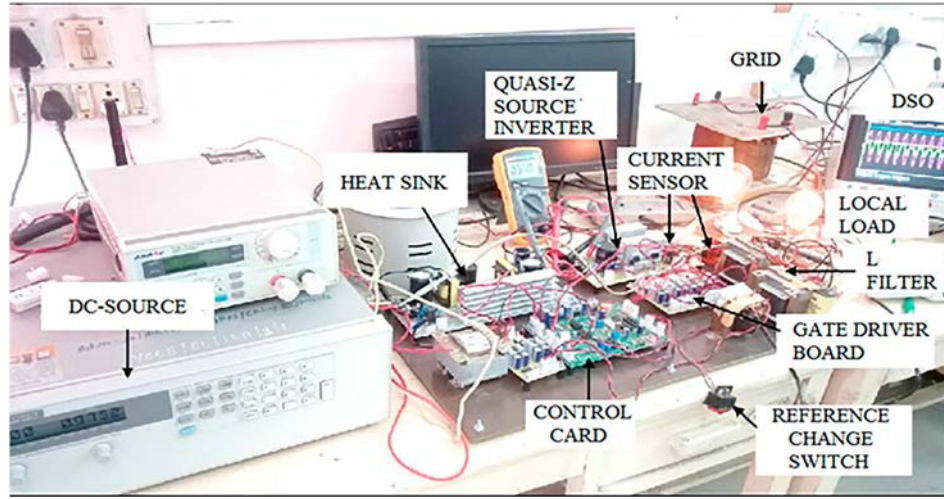
Figure 7: Experimental set-up of the proposed modified control strategy

where I_{L_s} is the switching frequency ripples in inductor current. The inductor current switching frequency ripple is 40% in Equation (8).

$$C = \frac{V_i * I_i}{0.05 * \omega * V_{dcl}^2} \tag{9}$$

Table 8 shows the comparison between the existing close-loop and the proposed modified control technique and it shows that with the proposed technique, the impedance values of the quasi-Z source network are reduced than all other existing techniques.

3.3.1.2 Experimental Results.
The main important hardware parts of Figure 7 are the DC power supply, qZS inverter, gate driver circuit, and grid. Input DC voltage is provided to single-phase quasi-Z source inverter and a gate driver circuit is used to drive the switches of qZSI. A single-phase transformer is treated as a grid and the bulb is considered a resistive load. A reference switch is provided to change the capacitor voltage.

Additional benefits of the proposed strategy are a reduction in grid current THD, no need for additional ripple port to minimize for a reduction of low-frequency power ripple, a reduction in circuit volume, and a reduction in overall circuit cost.

The sluggish dynamic response of capacitor voltage Vc1 is the major weakness of the proposed control strategy and it can be overcome by sliding mode control.

The experimental results are obtained for the dynamic change in grid current and capacitor voltage reference, as per the specifications given in Table 6.

Figure 8 shows a step change in grid current from 5 A to 10 A. The input DC voltage is provided at 164 V. It was observed that the capacitor voltage and grid voltage remains constant for change in grid current. It was also observed that nearby 10 V peak to peak 2ω ripple are observed in capacitor voltage (Vc_1).

Figure 9 shows the experimental result for a step change in capacitor voltage from 200 V to 250 V. It was observed
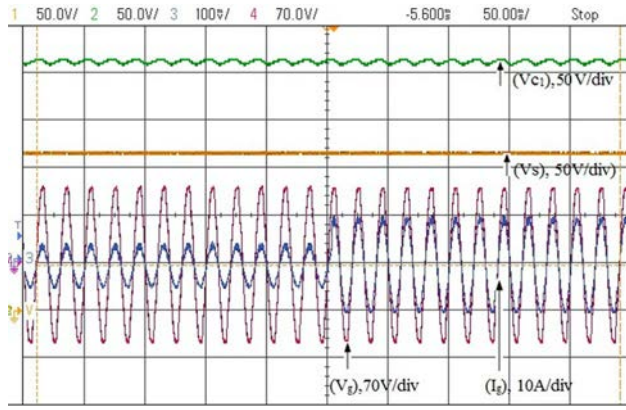
Figure 8: Experimental result for capacitor voltage, input DC voltage and grid voltage for a change in grid current.
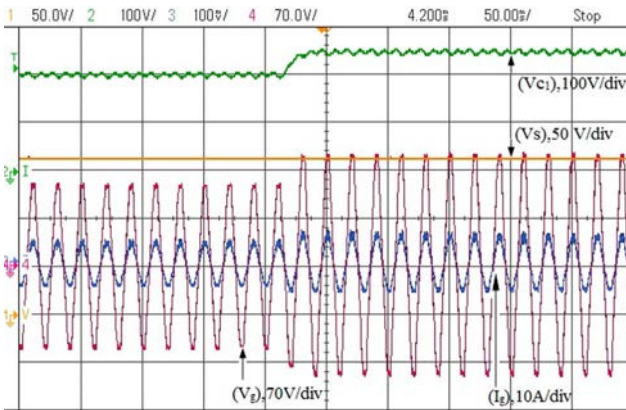

Figure 9: Experimental result for input DC voltage, grid current, and grid voltage for a change in capacitor reference voltage from 200 V to 250 V.

that grid current and grid voltage increased by a small value.

Table 9 shows the comparison between three passive power decoupling techniques.

4. CONCLUSION

The second harmonic (2ω) passive power decoupling technique for single-phase ZSI/qZSI has been reviewed in this paper. The survey shows that the passive power decoupling technique is more economical and reliable than the active power decoupling technique. The review shows that the passive decoupling technique includes different 2ω minimization techniques such as impedance design, open-loop modulation and close-loop modulation. In the impedance design technique, the inductor and capacitor values are designed in relation to double-line frequency power ripple. In this technique,

Table 9: Differentiation between three different passive power decoupling techniques

Passive power decoupling Method	Advantage	Disadvantage
Impedance design	1. Minimize low-frequency qZS inductor current and capacitor voltage ripple	1. Require complex design 2. Large values of qZS inductor and capacitor
Open loop modulation	1. Very easy to apply 2. Reduce 2ω power ripples in qZS impedance parameter using modified control	1. Large values of qZS passive parameter are required
Close loop modulation	1. Lower the value of qZS inductor and capacitor 2. Minimize the low-frequency ripple as desired	1. Requires complex control

the designing part is complicated, and still, large values of qZS inductor and capacitor are required to reduce 2ω ripples. Open-loop modulation is a very simple technique. The modified control technique reduces the low-frequency power ripple in a better way but requires large impedance values.

The close-loop modulation is a better option to reduce 2ω inductor current and capacitor voltage ripples at its desired range. This control also requires a minimum value of impedance but it demands somewhat complicated control.

The proposed modified control technique is compared with other existing close-loop techniques. It was found that the proposed technique achieves zero 2ω ripples in inductor current and 5% ripple in capacitor voltage at the lowest values of inductor and capacitor, as shown in Table 8. It also observed that the proposed control is simple to implement. The experimental results were also obtained for dynamic variation in capacitor voltage (Vc_1) and grid current. It shows that the experimental result matches with simulation results. There are many options to reduce 100 Hz ripple such as capacitor multiplexer and chock filter but a low-pass filter is an effective and easy technique for eliminating 100 Hz inductor current ripple.

DISCLOSURE STATEMENT

No potential conflict of interest was reported by the author(s).

REFERENCES

1. F. Z. Peng, "Z-source inverter," *IEEE Tran. Ind. Appl.*, Vol. 39, no. 2, pp. 504–10, Mar./Apr. 2003.

2. Y. P. Siwakoti, F. Z. Peng, F. Blaabjerg, P. Chiang Loh, and G. E. Town, "Impedance-source networks for electric power conversion part I: A topological review," *IEEE Trans. Power Electron*, Vol. 30, no. 2, pp. 699–716, Feb. 2015.

3. Y. P. Siwakoti, F. Z. Peng, and P. Loh, "Impedance-source networks for electric power conversion part ii: Review of control and modulation techniques," *IEEE Trans. Power Electron*, Vol. 30, no. 4, pp. 1887–1905, Apr. 2015.

4. Y. Liu, H. Abu-Rub, B. Ge, F. Blaabjerg, O. Ellabban, and P. C. Loh. *Impedance Source Power Electronic Converters*. Hoboken, NJ: Wiley, 2016.

5. J. Anderson, and F. Z. Peng, "Four quasi-Z-source inverters," *IEEE*, 2743–9, 2008.

6. J. Anderson, and F. Z. Peng, "A class of quasi-Z-source inverters," *IEEE Ind. Appl. Soc. Annu. Meeting*, 1–7, 2008.

7. F. Z. Peng, X. Yuan, X. Fang, and Z. Qian, "Z-source inverter for adjustable speed drives," *IEEE Power Electron. Letters*, Vol. 1, no. 2, pp. 33–5, Jun. 2003.

8. F. Z. Peng, A. Joseph, J. Wang, M. Shen, L. Chen, E. Ortiz-Rivera, and Y. Huang, "Z-source inverter for motor drives," *IEEE Tran. Power Electron*, Vol. 20, no. 4, pp. 857–63, Jul. 2005.

9. B. Ge, Q. Lei, W. Qian, and F. Z. Peng, "A family of Z-source matrix converters," *IEEE Tran. Ind. Electron*, Vol. 59, no. 1, pp. 35–46, Jan.2012.

10. X. P. Fang, Z. M. Qian, and F. Z. Peng, "Single-phase Z-source PWM AC-AC converters," *IEEE Power Electron. Letters*, Vol. 3, no. 4, pp. 121–4, Dec.2005.

11. Z. Aleem, and M. Hanif, "Single-phase transformer based Z-source AC-AC converters," *IEEE*, 1–6, 2016.

12. M. Nguyen, Y. Jung, and Y. Lim, "Single-phase AC–AC converter based on quasi-Z-source topology," *IEEE Trans. Power Electron*, Vol. 25, no. 8, pp. 2200–10, Aug. 2010.

13. M. K. Nguyen, Y. C. Lim, and Y. J. Kim, "A modified single-phase quasi-Z-source AC-AC converter," *IEEE Trans. Power Electron*, Vol. 27, no. 1, pp. 201–10, Jan. 2012.

14. K. You, and M. F. Rahman, "A matrix–Z-source converter with AC–DC bidirectional power flow for an integrated starter alternator system," *IEEE Trans. Ind. Appl*, Vol. 45, no. 1, pp. 239–48, Jan./Feb. 2009.

15. D. Cao, and F. Z. Peng. "A family of Z-source and quasi-Z-source DC-DC converters," in *Proc. 24th Annu. IEEE Appl. Power Electron. Conf. Expo.*, pp. 1097–101, 2009.

16. B. Zhao, Q. Yu, Z. Leng, and X. Chen, "Switched Z-source isolated bidirectional DC–DC converter and its

phase-shifting shoot-through bivariate coordinated control strategy," *IEEE Tran. Ind. Electron*, Vol. 59, no. 12, pp. 4657–70, Dec.2012.

17. D. Vinnikov, and I. Roasto, "Quasi-Z-source based isolated DC/DC converters for distributed power generation," *IEEE Trans. Ind. Electron*, Vol. 58, pp. 192–201, 2011.

18. I. Roasto, D. Vinnikov, J. Zakis, and O. Husev, "New shoot-through control methods for qZSI-based DC/DC converters," *IEEE Trans. Ind. Inform*, Vol. 9, no. 2, pp. 640–7, May 2013.

19. H. Shen, B. Zhang, and D. Qiu, "Hybrid Z-source boost DC-DC converters," *IEEE Tran. Ind. Electron,* Vol.64, pp.310_319, 2016.

20. F. Z. Peng, M. Shen, and K. Holland, "Application of Z-source inverter for traction drive of fuel cell—battery hybrid electric vehicles," *IEEE Trans. Power Electron*, Vol. 22, no. 3, pp. 1054–61, May 2007.

21. C. Gajanayake, D. Vilathgamuwa, and P. Loh, "Development of a comprehensive model and a multiloop controller for *Z*- source inverter DG systems," *IEEE Trans. Ind. Electron*, Vol. 54, no. 4, pp. 2352–9, Aug. 2007.

22. C. Gajanayake, D. Vilathgamuwa, P. Loh, R. Teodorescu, and F. Blaabjerg, "Z-source-inverter-based flexible distributed generation system solution for grid power quality improvement," *IEEE Trans. Energy Con*, Vol. 24, no. 3, pp. 695–704, Sep. 2009.

23. S. Dehghan, M. Mohamadian, and A. Yazdian, "Hybrid electric vehicle based on bidirectional Z-source nine-switch inverter," *IEEE Trans. Vehic. Tech*, Vol. 59, no. 6, pp. 2641–53, Jul. 2010.

24. B. Ge, et al., "An energy-stored quasi-Z-source inverter for application to photovoltaic power system," *IEEE Trans. Ind. Electron*, Vol. 60, no. 10, pp. 4468–81, Oct. 2013.

25. Y. Liu, B. Ge, H. Abu-Rub, and F. Z. Peng, "Control system design of battery-assisted quasi- Z source inverter for grid-tie photovoltaic power generation," *IEEE Trans. Sustain. Energy*, Vol. 4, no. 4, pp. 994–1001, Oct. 2013.

26. F. Guo, L. Fu, C. H. Lin, C. Li, W. Choi, and J. Wang, "Development of an 85-kW bidirectional quasi-Z-source inverter with DC-link feedforward compensation for electric vehicle applications," *IEEE Trans. Power Electron*, Vol. 28, no. 12, pp. 5477–88, Dec. 2013.

27. S. Hu, Z. Liang, D. Fan, and X. He, "Hybrid ultra capacitor-battery energy storage system based on quasi-Z-source topology and enhanced frequency dividing coordinated control for EV," *IEEE Trans. Power Electron*, Vol. 31, no. 11, pp. 7598–610, Nov. 2016.

28. Y. Li, J. Anderson, F. Z. Peng, and D. Liu. "Quasi-Z-source inverter for photovoltaic power generation systems," in

Proc. IEEE 24th Annu. Appl.Power Electron. Conf. Expo., pp. 918–24, Feb.2009.

29. U. Supatti, and F. Z. Peng, "Z-source inverter with grid connected for wind power system," *IEEE Energy Convers. Congr. Expo*, 398–403, Sep. 2009.

30. J. H. Park, H. G. Kim, E. C. Nho, and T. W. Chun, "Power conditioning system for a grid connected PV power generation using a quasi-Z-source inverter," *J. Power Electron*, Vol. 10, no. 1, pp. 79–84, Jan. 2010.

31. Y. Huang, M. Shen, F. Z. Peng, and J. Wang, "Z-source inverter for residential photovoltaic systems," *IEEE Trans. Power Electron*, Vol. 21, no. 6, pp. 1776–82, Nov. 2006.

32. Z. J. Zhou, X. Zhang, P. Xu, and W. X. Shen, "Single-phase uninterruptible power supply based on Z-source inverter," *IEEE Trans. Ind. Electron*, Vol. 55, no. 8, pp. 2997–3004, Aug. 2008.

33. J. C. Rosas-Caro, F. Z. Peng, H. Cha, and C. Rogers, "Z-source-converter- based energy-recycling zero-voltage electronic loads," *IEEE Tran. Ind. Electron*, Vol. 56, no. 12, pp. 4894–902, Dec. 2009.

34. M. Shahparasti, A. Sadeghi Larijani, A. Fatemi, A. YaZdian Varjani, and M. Mohammadian. "Quasi Z-source inverter for photovoltaic system connected to single phase AC grid," in *Proc.1st Power Electron. Drive Syst. Technologies Conf.*, pp. 456–60, 2010.

35. D. Cao, S. Jiang, X. Yu, and F. Z. Peng, "Low-cost semi-Z-source inverter for single-phase photovoltaic systems," *IEEE Trans. Power Electron*, Vol. 26, no. 12, pp. 3514–22, Dec.2011.

36. S. A. Singh, G. Carli, N. A. Azeez, and S. S. Williamson, "Modelling, design, control, and implementation of a modified z-source integrated PV/grid/EV DC charger/inverter," *IEEE Tran. Ind. Electron*, Vol.65, pp. 5213_5220,2017.

37. U. K. Shinde, S. G. Kadwane, S. P. Gawande, and M. J. Reddy, "Sliding mode control of single-phase grid connected quasi-Z- source inverter," *IEEE Access, Vol.5, pp.10232_10240*, 2017.

38. Y. Rekha, I. W. Christopher, and V. Jamuna, "Fuel cell based SL quasi z-source inverter for motor drive," *IEEE*, pp. 1-6, 2019.

39. Y. Liu, H. Abu-Rub, and B. Ge, "Z-source/quasi- Z-source inverters: Derived networks, modulations, controls, and emerging applications to photovoltaic conversion," *IEEE Ind. Electron. Mag*, Vol. 8, no. 4, pp. 32–44, Dec. 2014.

40. L. Liu, H. Li, Y. Zhao, X. He, and Z. J. Shen, "1MHz cascaded Z-source inverters for scalable grid-interactive photovoltaic (PV) applications using GaN device," *in Proc. IEEE Energy Conversion Congr. and Exposition (ECCE)*, 2738–45, 2011.

41. D. Sun, B. Ge, F. Z. Peng, A. R. Haitham, D. Bi, and Y. Liu. "A new grid-connected PV system based on cascaded H-bridge quasi-Z source inverter," *IEEE Int. Symp. Ind. Electron.*, May 28–31, pp. 951–6, 2012.

42. Y. Liu, B. Ge, H. Abu-Rub, and F. Z. Peng, "An effective control method for quasi-Z-source cascade multilevel inverter-based grid-tie single-phase photovoltaic power system," *IEEE Trans. Ind. Inform*, Vol. 10, no. 1, pp. 399–407, Feb. 2014.

43. L. Yi, Q. Gui, and Z. Wang, "A novel phase-shifted pulse width amplitude modulation for extended –boost quasi-Z source cascaded multilevel inverter based on photovoltaic power system," *J. Renew. Sustain. Energy*, Vol.11,pp.1–16, Jan. 2019.

44. T. ShimiZu, K. Wada, and N. Nakamura, "A flyback-type single phase utility interactive inverter with low-frequency ripple current reduction on the DC input for an AC photovoltaic module system," *IEEE 33rd Annu. Power Electron. Spec. Conf.*, Vol. 3, pp. 1483–8, 2002.

45. S. B. Kjaer, and F. Blaabjerg. "A novel single-stage inverter for the AC module with reduced low-frequency ripple penetration," Presented at the *Eur. Conf. Power Electron. and Application,* 2003.

46. J. I. Itoh, and F. Hayashi, "Ripple current reduction of a fuel cell for a single-phase isolated converter using a DC active a center tap," *IEEE Trans. Power Electron*, Vol. 25, no. 3, pp. 550–6, Mar.2010.

47. H. Hu, S. Harb, N. Kutkut, I. Batarseh, and Z. J. Shen, "A review of power decoupling techniques for micro inverters with three different decoupling capacitor locations in PV systems," *IEEE Trans. Ind. Electron*, Vol. 28, no. 6, pp. 2711–26, Jun.2013.

48. G. Zhu, H. Wang, B. Liang, S. Tan, and J. Jiang, "Enhanced single-phase full-bridge inverter with minimal low-frequency current ripple," *IEEE Trans. Ind. Electron*, Vol. 63, no. 2, pp. 937–43, Feb. 2016.

49. Y. Sun, Y. Liu, M. Su, W. Xiong, and J. Yang, "Review of active power decoupling topologies in single-phase systems," *IEEE Trans. Power Electron*, Vol. 31, pp. 4778–94, Jul.2016.

50. X. Zhao, L. Zhang, R. Born, and J. S. Lai, "Solution of input double-line frequency ripple rejection for high-efficiency high-power density string inverter in photovoltaic application," *IEEE*, 1148–54, 2016.

51. M. Mellincovsky, V. Yuhimenko, M. M. Peretz, and A. Kuperman, "Low-frequency DC link ripple elimination in power converters with reduced capacitance by multi resonant direct voltage regulation," *IEEE Trans. Ind. Electron*, Vol.64, pp.2015-2023, Nov.2016.

52. M. A. Vitorino, L. F. S. Alves, R. Wang, and M. B. de Rossiter Corrêa, "Low-frequency power decoupling in single-phase

applications: A comprehensive overview," *IEEE Trans. Power Electron*, Vol. 32, no. 4, pp. 2892–912, Apr. 2017.

53. S. Qin, Y. Lei, C. Barth, W. C. Liu, and R. C. N. Pilawa-Podgurski, "A high power density series-stacked energy buffer for power pulsation decoupling in single-phase converters," *IEEE Trans.Power Electron*, Vol. 32, no. 6, pp. 4905–24, Jun. 2017.

54. H. Watanabe, J. Itoh, and Q. Roudier, "Single-phase power decoupling technique utilizing hybrid method with passive and active power decoupling," *IEEE*, pp.1-6,2018.

55. Y. Huang, Y. Zhang, C. Rui, and J. Liu, "An automatic power decoupling control method on three level DC-AC converter to suppress the double-line-frequency ripple," *IEEE*, , pp. 888–92, 2019.

56. S. Luo, K. Yang, F. An, and W. Song, "The double line ripple voltage reduction with feed forward control for boost SRC converter," *IEEE*, , pp. 1861–66, 2019.

57. G. Zarei, E. Babaei, and M. B. Bannae Sharifian, "Elimination of double line frequency in single- phase interface converters in renewable energy sources by designing proportional controller," *IEEE*, pp.1-6,Sept. 2019.

58. S. Shi, Y. Sun, H. Dan, D. Song, M. Su, B. Guo, and H. Tang. "A general closed–loop power–decoupling control for reduced–switch converter–fed IM drives," *Springer*, Jun.2020.

59. S. Amin, H. Lee, and W. Choi, "A novel power decoupling control method to eliminate the double line frequency ripple of two stage single phase DC-AC power conversion system," *Electronics*, Vol. 9, pp. 1–17, 2020.

60. M. Ghodsi, and S. M. Barakati. "A new switched boost inverter using transformer suitable for the microgrid-connected PV with high boost ability," *7th Power Electron., and Drive Systems Technologies Conference (PEDSTC)*, pp. 123–128, 2016.

61. Y. Liu, H. Abu-Rub, Y. Wu, B. Ge, and M. Trabelsi. Overview of double-line-frequency power decoupling techniques for single-phase Z-source/Quasi-Z-source inverter," in *Proc.43rd IEEE Ind. Electron. Society Annu.Conf. (IECON)*, pp. 7704–9, 2017.

62. Y. Liu, B. Ge, H. Abu-Rub, and F. Blaabjerg, "Single-phase Z-source/quasi-Z-source inverter and converters: An overview of double-line-frequency power decoupling method and perspective," *IEEE Ind. Electron. Magazine*, Vol. 12, pp. 6–23, Jun.2018.

63. S. Vadi, R. Bayindir, and E. Hossain, "A review of control methods on suppression of 2ω ripple for single-phase quasi-z-source inverter," *IEEE. Access.*, Vol. 8, pp. 42055–70, Feb.2020.

64. R. L. Jayawickrama, "Steady-state analysis and designing impedance network of Z-source inverters," *IEEE Trans. Ind. Electron*, Vol. 57, no. 7, pp. 2480–90, Jul. 2010.

65. Y. Yu, Q. Zhang, X. Liu, and S. Cui. "DC-link voltage ripple analysis and impedance network design of single-phase Z-source inverter," *Proceedings of the 2011-14th Eur. Conf. Power Electron. and Appl.*, pp. 1–10, 2011.

66. Y. Zhou, L. Liu, and H. Li, "A high performance photovoltaic module integrated converter (MIC) based on cascaded quasi-Z-source inverters (qZSI) using eGaN FETs," *IEEE Trans. Power Electron*, Vol. 28, no. 6, pp. 2727–38, Jun. 2013.

67. D. Sun, B. Ge, X. Yan, D. Bi, H. Abu-Rub, and F. Peng, "Impedance design of quasi-Z source network to limit double fundamental frequency voltage and current ripples in single-phase quasi-Z source inverter," *IEEE Energy Con. Congress and Expos*, 2745–50, 15-19 Sept. 2013.

68. Y. Liu, H. Abu-Rub, B. Ge, and F. Peng, "Impedance design of 21-kW quasi-Z-source H-bridge module for MW-scale medium-voltage cascaded multilevel photovoltaic inverter," *Int. Sympo. Ind. Electron*, 2490–95, 1-4 June 2014.

69. D. Sun, et al., "Modeling, impedance design, and efficiency analysis of quasi-Z source module in cascade multilevel photovoltaic power system," *IEEE Trans. Ind. Electron*, Vol. 61, no. 11, pp. 6108–17, Nov.2014.

70. Y. Liu, B. Ge, and D. Sun, "Comprehensive modeling of single-phase quasi-z-source photovoltaic inverter to investigate low-frequency voltage and current ripple," *IEEE Tran. Ind. Electron*, Vol. 62, no. 7, pp. 4194–02, Jul. 2015.

71. W. Liang, B. Ge, Y. Liu, H. Abu-Rub, R. S. Balog, and Y. Xue, "Modeling, analysis, and impedance design of battery energy stored single phase quasi-z-source photovoltaic inverter system," *in Proc. IEEE Energy Conv. Congr. and Expo. (ECCE)*, pp. 1–6, 2016.

72. W. Liang, Y. Liu, B. Ge, H. Abu-Rub, R. S. Balog, and Y. Xue, "Double-line -frequency ripple model, analysis and impedance design for energy stored single- phase quasi-z source photovoltaic system," *IEEE Trans. Ind. Electron*, Vol. 65, pp. 3198–3209, 2017.

73. Y. Yu, B. Liang, and S. Cui, "Single phase Z-source inverter: Analysis and low frequency harmonics elimination pulse width modulation," *IEEE Energy Conversion Congress and Exposition (ECCE)*, 2260–7, 17–22 Sep.2011.

74. H. Zhang, B. Ge, Y. Liu, and D. Sun, "A hybrid modulation method for single-phase quasi-Z source inverter," *IEEE Energy Conv. Congr. and Expo.(ECCE)*, Vol. 12, pp. 4444–9, 2014.

75. Y. Liu, B. Ge, H. Abu-Rub, and H. Sun, "Hybrid pulse width modulated single-phase quasi-Z source grid-tie photovoltaic power system," *IEEE Trans. Ind. Informat*, Vol. 12, no. 2, pp. 621–32, Apr.2016.

76. W. Liang, Y. Liu, B. Ge, and H. Abu-Rub, "Investigation on pulse- width amplitude modulation based single-phase quasi-Z-source photovoltaic inverter," *IET Power Electron.*, Vol. 10, no. 14, pp. 1810–8, 2017.

77. Y. Li, Y. Liu, and H. Abu-Rub. "PWAM controlled quasi-Z source motor drive," in *Proc. IEEE Int. Symp. Ind. Electron. (ISIE)*, pp. 1669–75, 2017.

78. M. K. Nguyen, and Y. O. Choi, "Maximum boost control method for single-phase quasi-switched-boost and quasi-Z-source inverters," *Energies*, Vol. 10, no. 4, pp. 553, Apr. 2017.

79. M. Ghodsi, and S. M. Barakati. "A new switched-inductor quasi-Z-source inverter," *7th Power Electron., and Drive Sys. Technologies Conference* (PEDSTC), pp. 177–84, 2016.

80. M. Ghodsi, S. M. Barakati, and B. Wu, "Extended switched-inductor quasi-Z-source inverter: Modeling and prototype realization," *Int. Trans. Electron., Energy Syst*, Vol. 29, 2018.

81. Y. Zhou, H. Li, H. Li, and X. Lin. "A capacitance minimization control strategy for single-phase PV quasi-Z-source inverter," in *Proc. 13th. IEEE Applied Power Electron. Annu. Conf. (APEC)*, pp. 1730–5, 2015.

82. B. Ge, Y. Liu, H. Abu-Rub, and F. Z. Peng, "Current ripple damping control to minimize impedance network for single- phase quasi-Z source inverter system," *IEEE Trans. Ind. Inorm*, Vol. 12, pp. 1043–54, 2016.

83. Y. Tang, Z. Li, Y. Chen, and R. We, "Ripple vector cancellation modulation strategy for single-phase quasi-z-source inverter," *Energies*, Vol. 12, pp. 1–12, 2019.

84. Y. Zhou, and H. Li, "A single- phase quasi-z-source inverter with reduced capacitance using modified modulation and double-frequency ripple suppression control," *IEEE Trans. Power Electron*, Vol. 31, no. 3, pp. 2166–73, Mar. 2016.

85. D. He, W. Cai, and F. Yi. "A power decoupling method with small capacitance requirement based on single-phase quasi-Z-source inverter for DC microgrid applications," in *Proc. 14th IEEE Applied Power Electron. Annu. Conf. (APEC)*, pp. 2599–606, 2016.

86. E. Makovenko, O. Husev, J. Zakis, C. Roncero- Clemente, E. Romero-Cadaval, and D. Vinnikov. "Passive power decoupling approach for three-level single-phase impedance source inverter based on resonant and PID controllers," *IEEE Int. Conf. Compatibility, Power Electron. and Power Eng.(CPEPOWERENG)*, pp. 516–21, 2017.

87. H. Komurcugil, S. Bayhan, F. Bagheri, O. Kukrer, and H. Abu-Rub, "Model-based current control for single-phase grid-tied quasi-Z-source inverters with virtual time constant," *IEEE Trans. Ind. Electron*, Vol. 65, no. 10, pp. 8277–86, Oct. 2018.

88. B. Ge, Y. Liu, H. Abu-Rub, R. S. Balog, F. Z. Peng, H. Sun, and X. Li, "An active filter method to eliminate DC-side low-frequency power for a single-phase quasi-Z-source inverter," *IEEE Trans. Ind. Electron*, Vol. 63, no. 8, pp. 4838–48, Aug. 2016.

89. T. Na, Q. Zhang, J. Tang, and J. Wang, "Active power filter for single-phase quasi-Z-source integrated on-board charger," *CPSS Trans. Power Electron. Appl*, Vol. 3, no. 3, pp. 197–201, Sep. 2018.

90. R. Y. Wei, Y. F. Tang, S. J. Wang, and Z. Y. Li, "A ripple suppression strategy based on virtual self-injection APF for quasi-Z source inverter," *IOP Conf. Earth Environ. Sci*, Vol. 188, pp. 1–10, Oct. 2018.

91. Y. Liu, B. Ge, H. Abu-Rub, H. Sun, F. Z. Peng, and Y. Xue, "Model predictive direct power control for active power decoupled single-phase quasi-Z-source inverter," *IEEE Trans. Ind. Informat*, Vol. 12, no. 4, pp. 1550–9, Aug. 2016.

92. Y. Liu, B. Ge, and H. Abu-Rub. "An active power decoupling quasi-Z-source cascaded multilevel inverter," in *Proc. 42nd IEEE Ind. Electron., Society Annu. Conf. (IECON)*, pp. 6453–8, 2016.

93. Y. Li, W. Gao, J. Li, R. Zhang, and F. Fang. "Double line frequency ripple cancelling for single-phase quasi-Z-source inverter," in *Proc. IEEE Energy Con. Congr. and Expo. (ECCE)*, pp. 1–6, 2016.

94. Y. Liu, B. Ge, and H. Abu-Rub, "A model predictive control for low-frequency ripple power elimination of active power filter integrated single-phase quasi-Z-source inverter," *in Proc. IEEE Int. Conf. Ind. Tech.(ICIT)*, pp. 1540–45, 2017.

95. S. Stepenko, O. Husev, S. P. Pimentel, D. Vinnikov, C. Roncero-Clemente, and E. Makovenko, "Digital control strategy for interleaved quasi-Z source inverter with active power decoupling," *IEEE*, pp. 3725–30, 2018.

96. S. A. Singh, N. A. Azeez, and S. S. Williamson. "Capacitance reduction in a single phase quasi Z-source inverter using a hysteresis current controlled active power filter," in *Proc. IEEE 25th Int. Symp. Ind. Electron.(ISIE)*, pp. 805–10, 2016.

97. Y. Liu, W. Liang, B. Ge, H. Abu-Rub, and N. Nie, "Quasi-Z-source three-to-single-phase matrix converter and ripple power compensation based on model predictive control," *IEEE Tran. Ind. Electron*, Vol. 65, pp. 5146–56, Jun. 2018.

AUTHORS

Shilpa P Ashtankar (Sarode) received a BE degree in electrical engineering from Nagpur University and an MTech degree in the department of Electrical Engineering from YCCE, Nagpur, Maharashtra, India. Currently, she is pursuing her PhD at the department of Electrical Engineering from Yeshwantrao Chavan College of Engineering (YCCE),Nagpur, and Maharashtra, India in power converter design for grid application and its control strategy.

Corresponding author. Email:ashtankar.shilpa@ymail.com

Sumant G Kadwane obtained his BE in electrical engineering from Yeshwantrao Chavan College of Engineering (YCCE), Nagpur, India in 1999. He obtained his ME in control systems from Govt College of Engineering, Pune in 2002 and a PhD in electrical engineering from Birla Institute of Technology, Mesra, India in 2010. His areas of interest are control system design, power electronic converters and renewable energy.

Email: sgkadwane@gmail.com

Article

Performance Investigation Based on Vital Factors of Agricultural Feeder Supported by Solar Photovoltaic Power Plant [†]

Nivedita Padole * [ID]**, Ravindra Moharil** [ID] **and Anuradha Munshi**

Department of Electrical Engineering, Yeshwantrao Chavan College of Engineering, Nagpur 441110, India; rmm_ycce_ep@yahoo.com (R.M.); aam.nyss@gmail.com (A.M.)
* Correspondence: niveditapande1@gmail.com
[†] This paper is an extended version of our paper published in 2021 IEEE International Conference on Electrical, Computer, Communications and Mechatronics Engineering (ICECCME 2021), Mauritius, 7–8 October 2021; pp. 1–7.

Abstract: Solar photovoltaic (SPV) installations are growing in the distribution network due to the continuously decreasing prices of solar photovoltaic panels. Installing the SPV Plant on the distribution feeder supplying to the agricultural pumps is a challenging task due to the varying agricultural load pattern of the Agricultural Feeder (AG Feeder). Supply of power and demand creates potential challenges in the low voltage (LV) distribution system. This paper presents a case study of a 2 MW SPV connected to an agricultural feeder in India. Performance analysis has been carried out using field measurement data. The key parameters such as PV Penetration and Capacity Utilization Factor (CUF) are calculated for analysis. Parameters such as Grid Dependency of the load and PV Contribution have been introduced in this paper, which relates to the SPV system behavior more aptly. It is recommended that the Time of Day (ToD) metering with the lowest cost during the solar generation hours will make agricultural consumers shift their demand matching with solar generation hours. Extensive analysis of agricultural feeder connected SPV power plant indicates that the power supply has improved for the feeder during winter and summer months.

Keywords: agricultural feeder; low voltage distribution system; PV contribution; PV penetration; renewable energy system (RES); solar photovoltaic plant

1. Introduction

The main economic activity in India is agriculture, and there is a significant area covered by fertile land. In addition, it is a densely populated country and needs large-scale production of food grains. India also receives clear solar radiation for around 300 days. Hence, solar energy and farming are a winning combination. The SPV systems are preferred in powering agricultural load [1], and it has been an essential driver for the 'Green Revolution' to increase the productivity of the farm.

In India, in order to promote the agricultural sector, the Ministry of New and Renewable Energy Sources (MNRE) has started the Pradhan Mantri Kisan Urja Suraksha evam Utthan Mahabhiyam (PM-KUSUM) for the development of farmers and for strengthening the rural distribution network. The scheme aims to promote the usage of solar pumps and grid-connected solar power in the agricultural sector. Through PM-KUSUM policy, the Gujarat state in India has announced the Suryashakti Kisan Yojna (SKY) scheme. Under SKY, farmers can install a net–metering SPV powered irrigation pump sets on the fields. This scheme offers several benefits to the farmers, such as well-planned use of water, increased crop cultivation due to the availability of power during the daytime, an additional source of income for the farmers, which results in an improved economy in rural areas [2].

It is very well known that the RES penetration in the LV distribution network has a positive impact, such as reducing the energy losses of distribution feeders, feeding peak

energy demands, and providing voltage support to distribution feeders. However, the exponential increase in RES installations over a widespread area of LV distribution may have a negative impact in the form of power quality issues, stability, and protection challenges.

Government of India (GoI) policy initiatives has significantly improved the number of grid-connected SPV systems in LV distribution systems in India. Thus it is of vital importance to realize the technical influence of high penetration levels of SPV systems on the operating performance of these networks. A significant number of research papers that have already been published recognize the possible challenges and effects of integration of distributed generation in LV distribution systems. The researchers have analyzed the power quality impact on LV distribution networks with high penetration levels of SPV by considering real-time case studies.

This paper mainly focuses on, SPV connected AG feeder performance analysis based on the selected site credentials. Feeders are separated to supply electricity to agricultural and non-agricultural consumers at the site. This feeder separation makes a provision to offer a planned power supply to the AG feeder. AG feeder being connected to SPV plant reduces the dependency of AG feeder on Grid supply during the daytime as most of the power is provided by the SPV plant. Therefore, it is decided to analyze the performance of a 2 MW SPV plant. For appropriate analysis, new terms such as 'Grid Dependency' and 'PV Contribution' have been introduced in this paper. System performance has also been checked via PV Penetration and CUF factors.

The performance analysis of the solar photovoltaic (SPV) system installed at Sagardeep Island in the West Bengal state of India is reported in [3]. The technical and commercial factors of the system were analyzed in this literature, focusing on the effects of SPV installations on social life.

The significance of a grid-connected PV system concerning the erratic nature of renewable generation and the categorization of PV generation pertaining to grid code compliance is investigated and highlighted in [4].

A case study of a distribution feeder is presented in [5], which provides a traditional capacity penetration level of 47% and perhaps more. In addition, it defines PV penetration as "the rated power output of the aggregate PV systems on a distribution circuit segment divided by the peak load of that circuit segment".

In [6], the significant factors obstructing the growth of renewable energy in India are reported. This study shows that though the status of renewable energy sources, particularly solar and wind systems, is acceptable in India, further attention for enhancing renewable energy sources is necessary.

The methodology for determining the maximum photovoltaic penetration level in the grid is mentioned in [7]. The authors have analyzed the different scenarios of PV penetration levels and extracted the reasons responsible for limiting the PV penetration. It has been mentioned that PV generation is maximum in summer due to irradiation, and selected a summer day to obtain peak PV penetration for the grid.

The voltage quality issues caused due to PV systems integration and their operating characteristics have been analyzed in the paper [8]. The study has been carried out on the real grid-connected PV system located at the University of Queensland (UQ), St. Lucia campus. The collected data has been analyzed for voltage rise, fluctuations, and flickers.

A study that assesses the ability of grid-connected wind and solar resources for the regional power grid of India is presented in [9]. This study concluded that the southern grid has the most potential for renewable energy, followed by the western, eastern, and northeastern grids.

A broad overview of significant problems affecting the distribution system due to PV penetration is illustrated in [10,11]. These papers also discuss relevant issues such as voltage fluctuation, voltage rise, voltage balance, and harmonics and their effect on the system in detail.

The case study and performance comparison of two different solar power plants of 1 MW based on one crucial parameter, Performance Ratio, are explained in [12]. The

plants are located at Fatehgarh and Bap (Rajasthan). The authors have discussed a vital performance parameter, 'Performance Ratio (P.R.)'. The authors have inferred that an uncertain rise of the performance ratio to 95% may be possible by detailed analysis.

The effects of connecting a PV system to the grid through simulation of the system in RSCSD software are depicted in [13]. The monthly Performance Ratio was estimated for a PV system connected to a grid at a specific location in India.

The literature review focused on limits of PV penetration due to the voltage variations in LV networks, and Medium Voltage (MV) networks is explained in [14]. The review further revealed that in contrast to the MV level network, voltage violations in the LV network can be avoided even at high penetration levels in certain conditions. High PV integration in the LV distribution network is acceptable without significant changes in the system parameters.

An agricultural system with integrated renewable energy sources for adequate irrigation to improve the overall efficiency of crops is presented in [15]. The paper contributes to verifying and analyzing the technical and economic viability of an agricultural setup consisting of renewable energy sources integrated with an effective irrigation system to strengthen crop cultivation.

Assessment of solar power potential of Silchar (Assam, India) and to perform a feasibility study for the installation of a solar-based power plant is carried out by using an anisotropic sky model in [16]. This radiation data has been used to evaluate the PV power output.

An investigation of power quality characteristics of an urban LV distribution network with high PV penetration levels in Sri Lanka is presented in [17]. The authors also have validated the effects on power flows and voltages of the LV network using field measurements.

A case study based on the analysis of the low-voltage, rural distribution system of Santana da Vargem is discussed in [18].

The solar PV plant of 10 KWp for Shree Samarth Agro-Tech Foundation located in Solapur District of Maharashtra State, India, is presented in [19]. Detailed performance analysis of the proposed system has been carried out using the PVsyst simulation tool.

The survey of the impact of rooftop PV panels on the distribution system is discussed in [20]. The paper incorporates rooftop PV's effect on voltage quality, power losses, and the working of other voltage regulating devices.

In this paper, Section 2 represents the role of RES, particularly PV, in the agricultural sector in India, giving an insight into the PM-KUSUM policy. A detailed case study of a 2 MW SPV power plant connected to an 11 kV LV Distribution network at Manjarda in Yavatmal district in the Maharashtra state of India is presented in Section 3, and the comprehensive analysis of the collected data has been carried out in Section 4. In addition, two performance parameters, Grid Dependency and PV Contribution are proposed, and the system behavior is analyzed using two existing factors, CUF and PV penetration. Conclusions have been drawn in Section 5.

2. Role of PV in the Agricultural Sector of India

By replacing traditional water pumps with solar water pumps, India can attain 100 GW solar energy by 2022. Grid-connected, net-metred solar pumps are essential in providing secondary income to farmers by giving them access to quality power for irrigation. In India, till now, there have been many success stories of solar powered systems such as solar powered drip irrigation. Solar powered drip irrigation technology has been introduced in the Gosaba Island situated in the Sunderbans region of West Bengal in India under the 'Cropping System Intensification in the Salt-affected Coastal Zones' CSISCZ project [21,22]. This solar-powered drip irrigation technology was more beneficial for farmers. There was 20–30% extra yield, 40–60% irrigation water, 40% saving of labor, and growth in the cropping intensity up to 300% than the old practices.

PM-KUSUM policy was launched on 8 March 2019 [23], with a target to install 25,750 MW solar capacities by 2022 with the financial support of Rs. 34,422 crore from the central government. For the financial year of 2020–2021, the ministry of finance has sanctioned 20 lakh farmers to set up standalone solar pumps and permitted 15 lakh farmers to solarize grid-connected agricultural pumps. An addition of 10–15 GW installed capacity is expected if this scheme is successful. It is proposed that farmers use dry/uncultivable land for 25 years for this project. To use cultivable land, a developer must ensure that farmers continue growing crops by installing the plant above minimum height. These installations may supply the daytime load. It is a win-win situation for farmers and the Distribution Company (DISCOM) by achieving a reduction in diesel cost for farmers. Reduction in rural load and achieving Renewable Procurement Obligations (RPO) targets benefit DISCOM.

3. A Detailed Case Study

The 2 MW SPV Power plant in Manjarda, Yavatmal, Maharashtra, India, has been identified for analysis. The plant was commissioned on 24 August 2018 and has been installed according to the guidelines given by the Central Electricity Authority (CEA) of India. Two separate feeders are set as per the feeder separation scheme under Demand Side Management (DSM) schemes by [24]. One feeder is for Gaothan (village lighting and other purposes with 24 × 7 power supply to all consumers) and another for AG feeder to provide 8–10 h of power supply. The primary purpose of installing this SPV power plant is to supply power during the daytime to agricultural pumps during the winter and summer seasons to fulfill the necessity for a high-quality day-time power supply. SPV power plant decreases agricultural power consumption from the grid and increases electrical energy access to farmers. Moreover, due to feeder separation, there is a provision of electricity to agricultural pumps at off-peak hours when electricity demand from other consumers is low, which helps in load management.

3.1. Need for Feeder Separation

Feeder separation becomes the most popular solution to supply electricity to agricultural and non-agricultural consumers (domestic and non-domestic) separately through dedicated feeders. Feeder separation offers planned supply to farming consumers and continuous supply to non-agricultural consumers in rural areas. It helps better load control and improved power supply to farm and non-farm consumers. According to a study conducted by the World Bank in 2014, before feeder separation, more than 80% of consumers in Rajasthan and Gujarat, India suffered from low voltage problems; this reduced to 6% after feeder separation. The rise in electricity supply via feeder separation has also led to socio-economic welfare, including job creation and improved quality of life.

Based on the collected data from the plant, Table 1 represents the site credentials; Table 2 mentions the technical description of the plant. According to the Central Electricity Authority (Technical Standards for Connectivity to the Grid) [25], in the Solar Photovoltaic generating station, each inverter and associated modules will be reckoned as a separate generating unit.

Figure 1 depicts a single line diagram of 33 kV/11 kV Kolambi Substation and a 2 MW Solar Plant at Village Manjarda. The 33 kV Kolambi substation feeds power to three 11 kV feeders; two Gaothan feeders, namely Akola Bazar, and Kolambi and one AG feeder for Akola Bazar through 5 MVA Power Transformer. The generated SPV power is supplied to an 11 kV Akola Bazar AG feeder, and surplus solar energy is then exported to two 11 kV Gaothan feeders.

Table 1. Site Credentials.

Project	2 MW (2.23 MWp) Grid Connected SPV Power Plant
Location	Village: Manjarda District: Yavatmal
State, Country	Maharashtra, India
Geographical Location	20°15′38″ N, 78°15′21″ E
Capacity (AC/DC)	2 MW/2.23 MWp
The technology of PV Modules	Poly Crystalline

Table 2. Technical Description.

PV-Modules	270 Wp
Inverters	Tmeic 1000 KW, PVL-L1000E-1 N
Inverter Transformer	2.1 MVA 11 kV/2 × 380 V
Auxiliary Transformer	Melcon, 40 kVA, 380/415 V
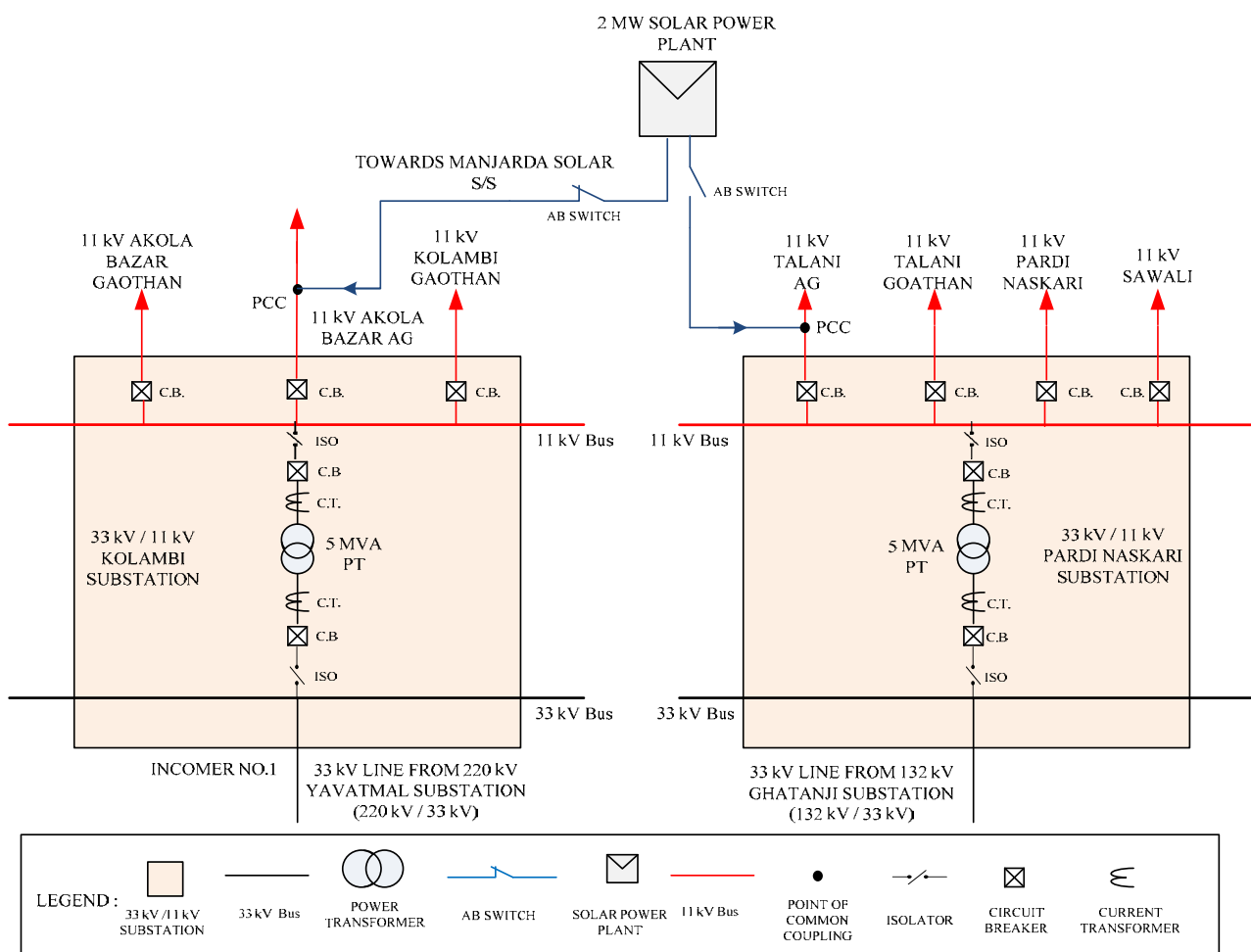
Figure 1. Single line diagram of 33 kV/11 kV Kolambi Substation and Solar Power Plant at village Manjarda.

In case of electricity failure, breakdown, or fault in the feeder, the back-feed arrangement is provided in Figure 1. It depicts that the feeder line is disconnected via AB switch

during the defect, breakdown, or supply failure. It detaches a portion of the AG feeder from the 2 MW solar power plant. In such cases, a 2 MW SPV plant will supply the generated solar power to 11 kV Talani AG Feeder to avoid the wastage of generated energy. As soon as the fault clears, solar power is fed back to the AG feeder by closing the AB switch and disconnecting the 11 kV Talani AG Feeder from the 2 MW solar power plant, as depicted in Figure 1.

Feeder details of the Akola Bazar AG feeder and two Gaothan feeders are presented in Table 3.

Table 3. Feeder Details.

11 kV Akola Bazar AG	
Sub-Station	33 kV Kolambi
Feeder	11 kV Akola AG (205)
Length of Feeder	95.8 km
No of Consumer	1277
Peak Load	189 AMP
Akola Bazar Gaothan	
Sub-Station	33 kV Kolambi
Feeder	11 kV Akola AG (202)
Length of Feeder	61.2 km
No of Consumer	2902
Peak Load	90 AMP
11 kV Kolambi Gaothan	
Sub-Station	33 kV Kolambi
Feeder	11 kV Kolambi Gaothan (201)
Length of Feeder	17.5 km
No of Consumer	985
Peak Load	38 AMP

3.2. Load Details

The Solar power generation point and injection point is Manjarda (Kolambi Substation). The distance between the generation point and injection point is approximately 1.5 km. A 5 MVA transformer has been used to which three outgoing feeders are connected; one AG feeder and two Gaothan feeders. Total 1277 consumers, approximately 3.87 KW, all related to 11 kV Akola Bazar AG feeder. Among them, 1250 are only agricultural pumps of 4935 KW (6616 HP), and the remaining 27 are based on agricultural processes (15.7 KW) having some additional load. The total load connected to the 11 kV Akola Bazar AG feeder is 4.95 MW.

4. Performance Analysis of the Plant

2 MW SPV power plant generation data and AG feeder load side data for seven months (September 2018 to March 2019) were collected for analysis. Indian Metrological department has published the statistical data with the observations over 25 years on an hourly basis. The DISCOM Company has provided the generation data on a daily basis in place of an hourly basis. Considering this, the expected power in a day is calculated using the Hourly Mean Solar Radiation (HMSR) method [26]. February month's desired solar power is computed using the HMSR method and compared with actual generation values. The detailed analysis of the data collected is presented below.

The comparison of expected solar power generation on days with clear skies versus actual solar power generation for the two months of February 2019 and December 2018 is

made. From Figure 2a, it is to be noted that there are fewer variations between actual and expected generations. Due to no interruption and clear sky, the actual generation crosses the expected value on 9, 18, and 26 February 2019. Comparatively, on 3, 7, and 22 February 2019, generation is less than expected due to multiple breakdowns and electricity failures.
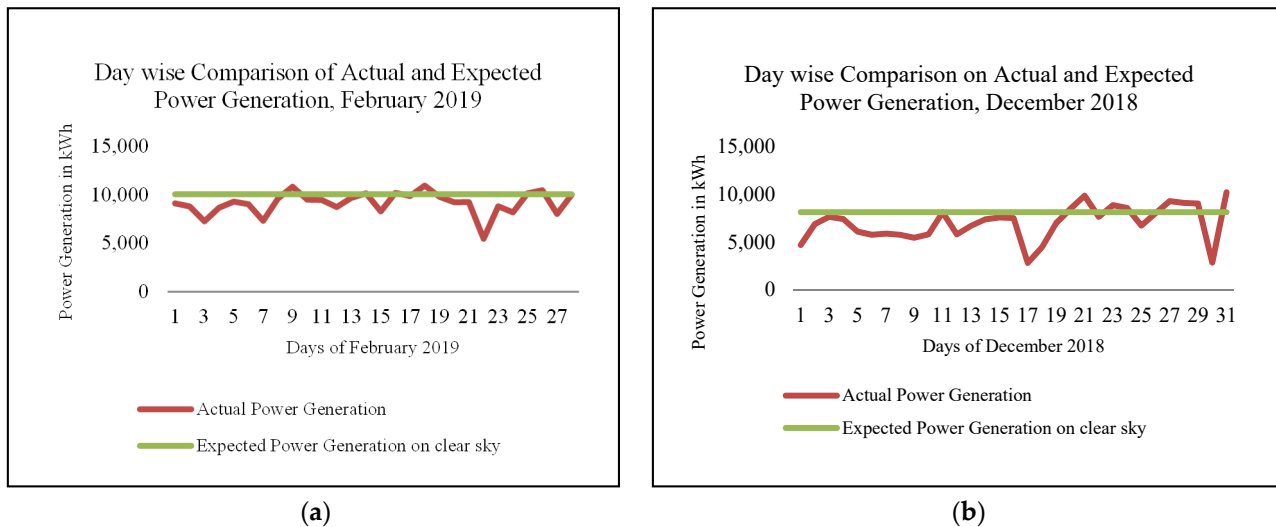

(a)   (b)

Figure 2. (**a**) Actual versus Expected Solar power generation of February 2019. (**b**) Actual versus Expected Solar power generation of December 2018.

In contrast, Figure 2b shows more variations between actual and expected solar power generation of December 2018 than February 2019. Here, it is clear that on 1, 17, 18, and 30 December 2018, the generation dropped down to a lower value because of the following reasons:

1. 1 December 2018: The plant was under shutdown for the duration of 01:44 h due to a technical issue observed in the Vacuum Circuit Breaker (VCB) spring charging AC motor connected to the incomer side of the substation.
2. 17 December 2018: Cloudy weather throughout the day and 33 kV supply failure from 220 kV Yavatmal substation for the duration of 00:08 h.
3. 18 December 2018: Cloudy weather and electricity failure for the duration of 00:25 h.
4. 30 December 2018: Electricity failure for the duration of 00:20 h and breakdown for the time of 05:45 h.

However, 21, 27, 28, 29, and 31 December 2018 reported the higher solar power generation in kWh than expected as a result of clear skies.

For each month, maximum power generation was observed in the afternoon between 12:00 p.m. to 01:00 p.m.

Figure 3 shows month-wise (from September 2018 to March 2019) generated cumulative solar power and cumulative AG consumption with the number of cumulative exported units in kWh. The cumulative solar generation is maximum in the March 2019 owing to more sunshine hours. The AG consumption is more in February 2019 and less in September 2018.

From month-wise exported units, it can be seen that the maximum units are exported to Gaothan feeder in March 2019 because of less AG consumption, and fewer units were exported in December 2018 due to more AG consumption. The excess power exported as depicted in Figure 3 is supplied to the two Gaothan feeders.
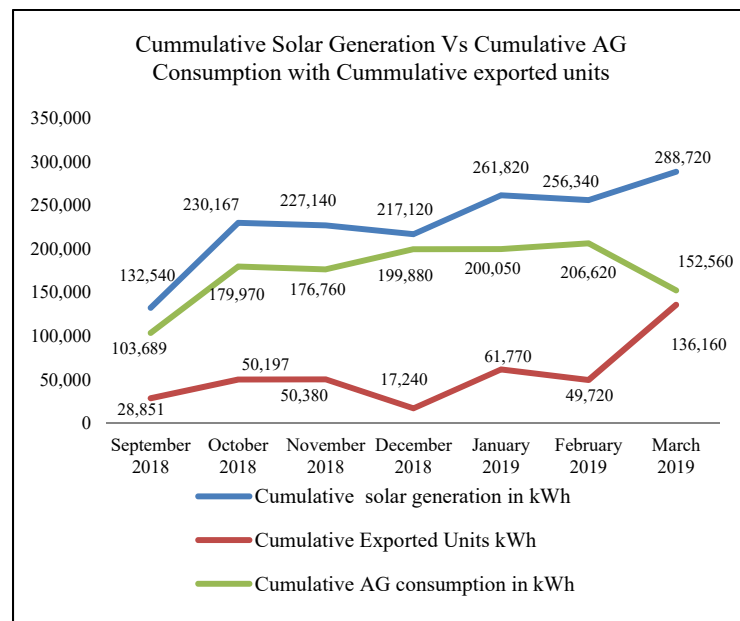
Figure 3. Comparison of cumulative solar generation versus cumulative AG consumption with cumulative units exported (kWh).

Figure 4 represents the hourly maximum active power generated in a day over a month. Here, the variations in a maximum hourly generation are due to cloudy weather, breakdowns of feeder, and the non-availability of grid supply. In September 2018, the average maximum active power was recorded the least of the remaining months because of a higher number of feeder breakdowns. In addition to that, on 2, 8, and 9 September 2018, weather was cloudy throughout the day. The other discrepancies affecting the plant's performance were grid undervoltage and grid overvoltage.
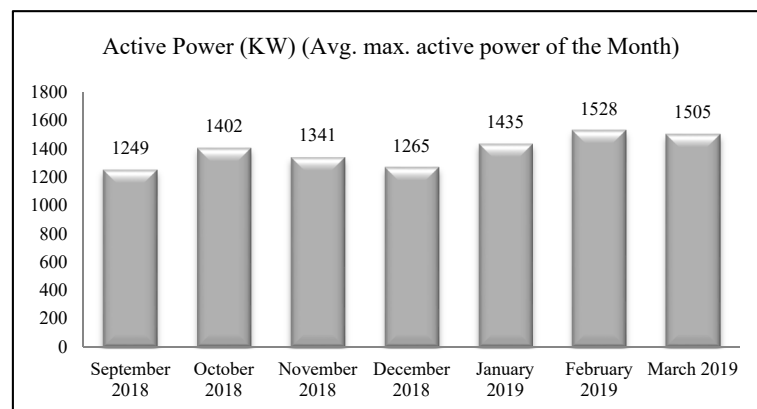
Figure 4. Hourly maximum active power averaged over the month.

Table 4 presents discrepancies affecting all seven months' average maximum active power. These include the number of breakdowns and their duration, duration of load shedding hours, and a total generation lost hours due to non-availability of supply. In February 2019, the average active power was maximum due to fewer breakdowns, load shedding hours, and generation lost hours.

Table 4. Breakdown, load shedding, and a generation lost hours of seven months.

| Months	Discrepancies			
	Total No. of Breakdown of Feeder	Total Duration of Breakdowns (h)	Total Duration of Load Shedding (h)	Total Generation Lost Hours due to Non-Availability of Supply (h)
September 2018	126	31:10:00	146:50:00	200:10:00
October 2018	189	37:13:00	124:00:00	161:13:00
November 2018	114	26:53:00	26:50:00	53:43:00
December 2018	86	21:26:00	63:37:00	85:03:00
January 2019	90	13:45:00	50:26:00	64:11:00
February 2019	93	17:06:00	26:04:00	43:10:00
March 2019	143	31:29:00	0:00:00	31:29:00

Other discrepancies that affected the plant's performance were grid undervoltage and grid overvoltage. The month of November 2018 faced non-availability of power supply for two days due to 11 kV line R-phase LA burst.

Feeder breakdown occurred due to malfunction operation of protective relays, which are needed to detect the phase fault of the feeder. In addition, weather and equipment failure cause faults, trips, and interruptions resulting in feeder breakdown.

The cloudy weather and technical issues such as faults, equipment failure, and protection challenges cause insufficient power generation from conventional generators to meet the electricity demand. Hence, load shedding is required.

To avoid the loss of power generation in the grid connected SPV plant, an effective battery storage system can be an alternative solution. This solution can provide the extra energy needed during the peak energy consumption periods and fulfill the consumers' demands during grid failure and when renewable energy (RE) sources go offline.

Figure 5 represents the maximum and minimum voltage per unit (pu) of the 11 kV line for the months' September 2018 to March 2019 with the permissible limit of voltage variations for the distribution system, i.e., (11 kV ± 10%).
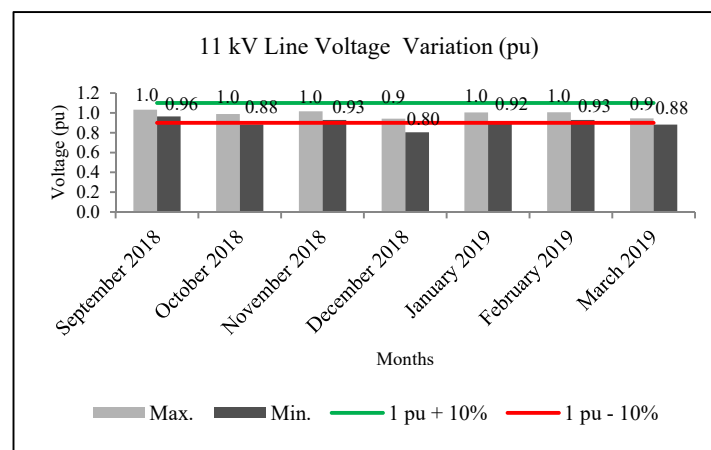
Figure 5. 11 kV Line voltage variation (pu) for different months at Manjarda.

From Figure 5, it is observed that the voltage never crosses the upper voltage limit, but for three months, the lower voltage limit constraint was violated. The lower voltage constraint violation is due to the agricultural pumps, three-phase induction motor drives drawing a lagging reactive power resulting in a lower power factor. This can be avoided by penetrating more reactive power into the grid with the help of capacitors.

It is suggested that introducing time-of-day metering for the farmers with the maximum incentive during solar power generation hours helps shift the agricultural water

pump demand during the solar generation hours. It also reduces the burden of distribution substation during evening hours (5:00 p.m. to 7 p.m.).

Figure 6 shows solar generation and AG consumption on 24 December 2018 for 24 h. Here, during peak hours of Solar PV generation, the AG feeder is not dependent on the grid power supply. However, the AG feeder is taking power from the grid during off-peak hours, as depicted in Figure 6.
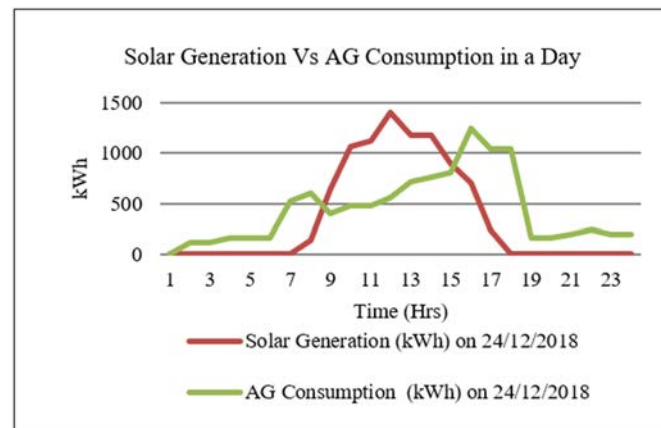

Figure 6. Solar Generation and AG Consumption in a day.

The excess PV power is fed back to the grid. When there is no PV generation and before the evening peak starts (5 p.m. to 7 p.m.), AG feeders are supplied by grid, and during peak evening and at night (7 p.m. to 12 midnight), the demand of AG feeder is deficient.

This paper suggests four essential performance parameters of solar power plants; PV Penetration, CUF, and two proposed terms, PV Contribution and Grid Dependency. To supply reliable daytime electricity to farmers via a separate feeder that is the AG feeder, it is now essential to understand the 'Grid dependency' of Agricultural Consumers.

- **Grid Dependency**: Grid Dependency is the ratio of power taken from grid by AG load to the total power consumed by AG load.
- **PV Penetration**: PV Penetration is the ratio of peak PV capacity to the peak load on the feeder.
- **PV Contribution:** PV Contribution is the ratio of total PV power supplied to the feeder to the total load demand on the feeder.
- **CUF**: Capacity Utilization Factor (CUF) is the ratio of total export to the installed capacity of the plant.

Figure 7 represents the Power Flow of AG feeder from the Grid distribution system and solar panel.
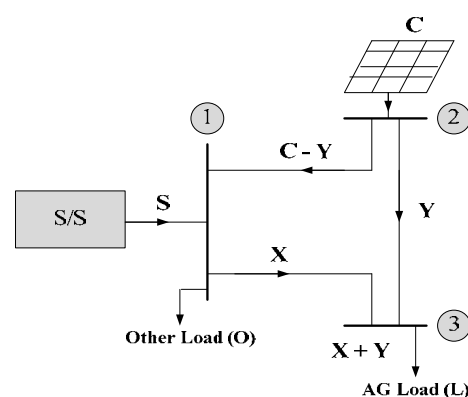

Figure 7. Power Flow for AG Feeder from Grid Distribution System and Solar Panel.

As depicted in Figure 7, consider a solar generated power as 'C' supplied to the AG load (L). The AG load's power received from the SPV power plant is 'Y'. During off-peak hours power provided to the AG load by the grid is 'X'. Hence, the total power received by the AG load throughout the day will become 'X + Y'. Surplus power fed back to the grid becomes 'C–Y'. Considering this power flow for the AG feeder from the grid and the SPV power plant, the following terms have been presented.

As per the proposed term Grid dependency;

$$\text{Grid Dependency in a Day} = \left(\frac{\text{Power taken from Grid by AG Load in a Day}}{\text{Total Power Consumed by AG Load in a Day}} \right) \tag{1}$$

From Figure 7, Grid Dependency can be expressed as;

$$\text{Grid Dependency} = \frac{X}{X+Y} = \frac{X}{L} \tag{2}$$

As per the proposed term PV Contribution;

$$\text{PV Contribution} = \frac{\text{Total PV power supplied to the feeder}}{\text{Total load demand on the feeder}} \tag{3}$$

From Figure 7, PV Contribution can be written as;

$$\text{PV Contribution} = \frac{Y}{X+Y} = \frac{Y}{L} \tag{4}$$

Therefore, from (2) and (4),

Grid Dependency + PV Contribution = Power supplied to the AG load.

That is, $\frac{X}{X+Y} + \frac{Y}{X+Y} = 1$.

Hence, it is inferred that the proposed terms Grid Dependency and PV Contribution are interdependent. Correlation cannot be exhibited for other performance parameters, PV penetration and CUF.

On 24 December 2018, the amount of power given to the grid and taken from the grid is shown in Figure 8. It is noted that no power is taken from the grid during day hours (PV generation hours) as the demand of AG consumers is completely fulfilled by the Solar PV plant.

4.1. Grid Dependency

It is essential to know about the AG feeder dependency on the grid if the solar PV plant supplies power to the AG Feeder for 10 h per day. This will reveal the AG feeder independence from the Grid power supply. Hence, this new term has been introduced here, which exposes the Grid dependency of the AG feeder.

Grid Dependency is defined as the ratio of power taken from the grid in a day/month/ year to the total energy consumed by the load in a day/month/year.

$$\text{Grid Dependency in a Day} = \left(\frac{\text{Power taken from Grid by AG Load in a Day}}{\text{Total Power Consumed by AG Load in a Day}} \right) \tag{5}$$

As of 24 December 2018, the Grid Dependency was;

$$\text{Grid Dependency (\%)} = (2400 \text{ kWh}/10{,}520 \text{ kWh}) \times 100$$

$$\text{Grid Dependency (\%)} = 22.81\%$$

where, 2400 kWh is the power taken from the grid by AG consumers, and 10,520 kWh is the total power consumed by AG feeder throughout the day.

Therefore, on 24 December 2018, it can be concluded that the load was almost 77% independent of the Grid power supply.

Table 5 shows the Grid Dependency for the months November 2018 to March 2019 as per the data availability. By observing the Grid Dependency of the five months from Table 5, it can be noted that almost every month AG feeders' Grid dependency is below 50%, which happens because of the maximum power supplied by the Solar Power Plant to the load.
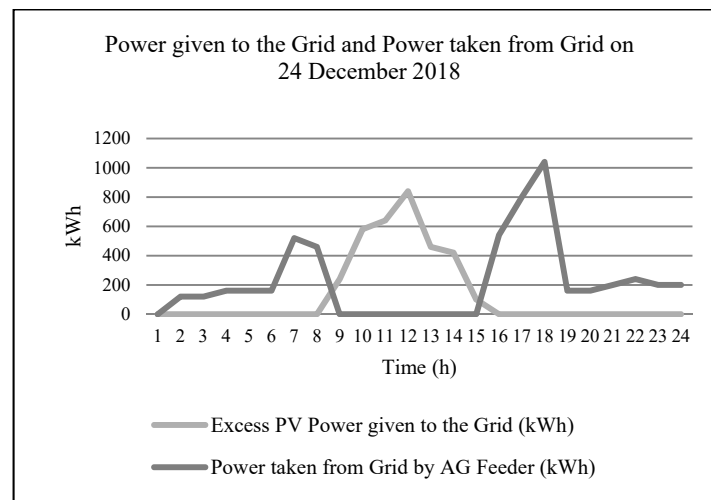
Figure 8. Power fed to the grid and power taken from grid.

4.2. PV Penetration

The available literature has suggested several definitions of Photovoltaic Distributed Generators (PVDG) penetration limits. It differs broadly among researchers; some have considered it the ratio of houses with PV systems to the total houses in the area under study [27]. Some researchers have tried to outline it with the transformer capacity [14], while others have evaluated it as the ratio of installed PV peak capacity to the maximum load on the feeder [5,28].

From Figure 9, it is clear that the 65% penetration was recorded in October 2018 owing to the maximum load on the transformer where three feeders are connected (one AG Feeder and two Gaothan Feeders).

After October 2018, PV penetration increased as summer approached (till March 2019). The highest penetration was recorded in March 2019, which was 110%. Some of the literature stated that the penetration level can be achieved up to 110% if photovoltaic distributed generators (PVDGs) are uniformly distributed over shorter lengths [14,29].

Table 5. Grid Dependency (%) of AG Feeder in a Month.

Date	November 2018	December 2018	January 2019	February 2019	March 2019
1	29.31	7.99	19.47	30.53	25.68
2	18.28	7.45	21.57	28.35	31.49
3	15.98	6.68	24.64	30.74	28.57
4	4.54	8.84	26.44	22.36	13.04
5	9.21	9.28	25.35	24.72	24.74
6	17.74	9.00	16.13	26.39	31.02
7	17.60	13.97	26.48	21.72	32.80
8	22.45	14.14	32.83	13.29	32.81
9	23.33	7.79	28.95	26.87	29.67
10	14.46	1.47	33.96	18.75	32.37
11	15.45	6.67	21.83	29.32	31.02
12	15.70	8.33	25.78	31.10	32.49
13	14.02	4.85	31.97	31.05	29.67
14	15.89	10.75	16.89	31.84	32.81
15	10.78	7.73	30.29	35.87	29.11
16	13.46	0	22.58	33.96	40.00
17	15.22	21.53	39.33	31.11	18.33
18	16.28	39.59	31.21	34.56	23.03
19	18.03	48.09	48.60	34.05	27.71
20	6.45	40.94	25.18	28.69	17.33
21	14.13	36.67	27.07	26.70	19.39
22	0	34.93	26.07	24.51	23.57
23	2.74	22.13	27.78	16.63	13.85
24	15.14	22.81	29.54	46.07	20.53
25	8.76	24.15	33.33	42.60	26.23
26	12.80	21.07	30.69	47.36	21.31
27	8.93	25.42	30.26	48.67	18.61
28	8.12	29.39	32.02	45.42	18.31
29	6.62	21.84	24.55		21.21
30	11.46	37.82	32.58		21.43
31		27.45	31.64		27.42

The maximum load on the feeder against peak PV capacity is the best-suited definition used for the current study because it has more decisive significance for both the power flows and the voltage profiles of the network. Therefore, PV penetration can be defined concerning peak PV capacity and Peak load on the feeder as (6);

$$\text{PV Penetration} = \left(\frac{\text{Peak PV Capacity}}{\text{Peak Load on the Feeder}} \right) \tag{6}$$

4.3. PV Contribution

PV penetration explained in the previous subsection 'B' may mislead readers while analyzing the collected data from the solar power plant. To clarify this, compare the bar chart of the PV penetration shown in Figure 7 and cumulative month-wise solar generation is illustrated in Figure 2. On comparing, it is observed that the solar generation was less in December 2018 than November 2018; however, for the same month (December 2018) PV penetration is more than November 2018. This is because the load consumption was also more in December 2018 than November 2018, even though the solar generation was more in November 2018 than December 2018. Therefore, a new term, 'PV Contribution' is suggested to avoid this misconception and analyze the data more aptly [30], which is more relevant for the data analysis.
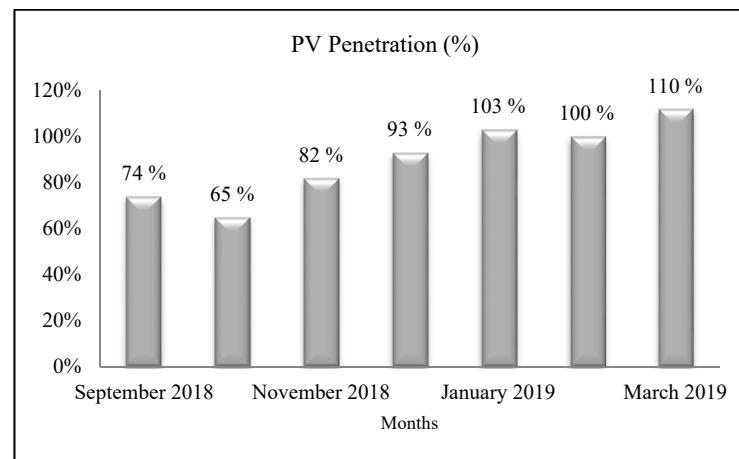
Figure 9. PV Penetration (%) of the months from September 2018 to March 2019.

The term PV Contribution is defined as;

$$\text{PV Contribution} = \frac{\text{Total PV power supplied to the feeder}}{\text{Total load demand on the feeder}} \tag{7}$$

The plot of PV Contribution shown in Figure 10 relates the plot of solar power generation in Figure 3 and the average maximum active power in Figure 4 based on solar power generation and AG consumption in December 2018.
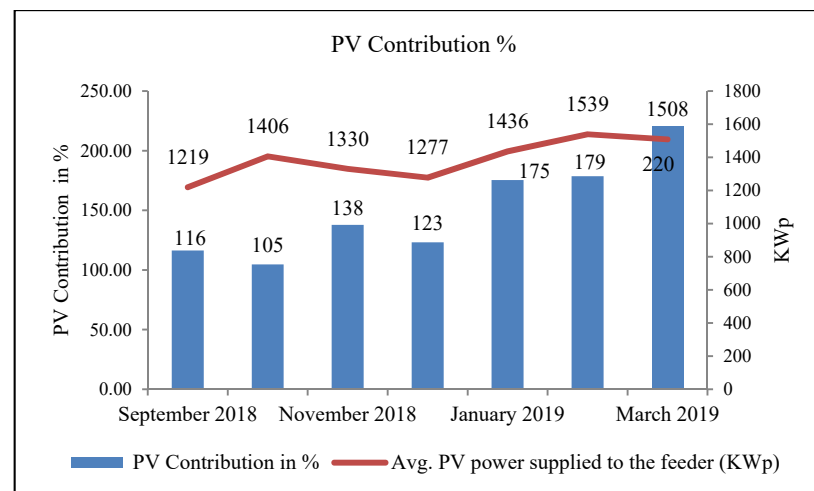

Figure 10. PV Contribution of the Months.

In September 2018, the average PV power supplied to the feeder was the lowest 1219 KWp, and in December 2018 it was 1277 KWp; however, the average load demand on the feeder was more in September 2018 which was 1048 KW, and it was less in December 2018 that is 1037 KW than September 2018.

Hence, this variation can be seen in terms of the PV contribution of the respective months in Figure 10. Furthermore, in October 2018 average PV power supplied to the feeder was more, 1406 KWp. On the other hand, the average load demand on the feeder was also more, 1344 KW. Thus, leading towards the lowest PV Contribution as depicted in Figure 10.

If the contribution factor is less than 100%, then grid power is taken during the daytime for feeding the agricultural pumps.

However, suppose the contribution factor is more than 100%. In that case, it represents that the total agricultural load is supplied by solar PV, and excess PV power generated is supplied to the Gaothan feeder.

4.4. Capacity Utilization Factor

The worldwide standard for measuring a solar plant's performance is the performance ratio (P.R.). However, most project developers, investors in India use the CUF as the standard for measuring the performance of a plant.

It is the ratio of actual output from a solar plant over the year/month/day to the maximum possible output for a year/month/day under ideal conditions [31]. CUF is usually referred to in percentage, as mentioned in (8).

$$CUF = \left(\frac{Total\ Export\ in\ a\ Day}{24 \times Installed\ Capacity\ of\ the\ Plant} \right) \tag{8}$$

Usually, 15% to 25% CUF is expected from various SPV power plants using thin film or crystalline PV modules and up to 35% CUF is expected based on concentrated PV (CPV) [32].

The plant's CUF for September 2018 to March 2019 is depicted in Figure 11. From the plot, it can be inferred that the plant was better utilized in March 2019 (20%), and less utilization can be observed in September 2018 (10%). CUF represents solar power generation concerning the capacity of the plant. CUF has no relation with the load on the feeder, whereas PV penetration shows the relationship between load and installed capacity (Peak PV Capacity) of the plant.
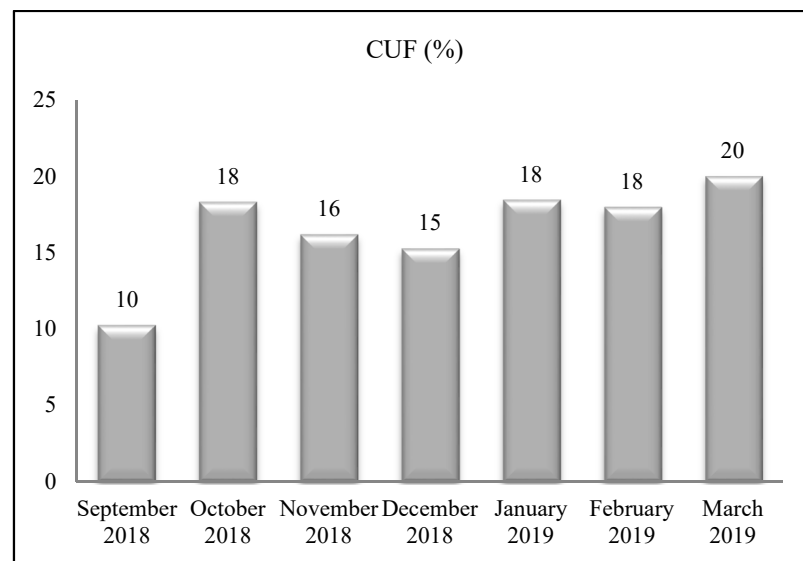
Figure 11. Month wise CUF.

PV Contribution term signifies the load shared by the solar PV system following the actual load. Hence, it is not unfair to say that the term PV contribution reveals the direct contribution of PV generation to the current load on the feeder. In December 2018, generation and the load were lower than November 2018, as depicted in Figure 3. Therefore, CUF is less in December 2018 than November 2018, as CUF is based on solar power exported considering the peak PV capacity of the plant.

5. Conclusions

To explore the performance of solar energy in the agricultural sector, a case study of an AG feeder connected 2 MW SPV system installed at Manjarda, Yavatmal, Maharashtra, India, has been presented. Graphical analysis by considering the expected and actual solar power generation, month wise cumulative solar energy generation and consumption, the power given to the grid and taken from the grid has been carried out to examine the plant behavior. Such analysis is essential to take necessary actions while supplying power to the agricultural feeder during the winter and summer. Furthermore, two vital factors are verified: PV penetration and CUF to validate the SPV system performance. CUF of the 2 MW SPV Manjarda power plant is calculated which is within the range of 10% to 20%. From the parameters mentioned above, the PV penetration and CUF depict the plant's overall performance and are higher during the months January 2019 to March 2019. The New terms Grid Dependency and PV Contribution are proposed in this paper and are found to be more relevant and convenient while analyzing the data collected from the SPV power plant. The suggested parameter Grid Dependency has disclosed the AG feeder independence from the Grid power supply. It is inferred from the analysis that the AG feeder dependency on the Grid power supply is below 50%, which is a good indication of superior SPV plant performance.

The proposed term PV Contribution clarifies the SPV system behavior more precisely. This term directly relates to the day-wise or month-wise collected solar power generation and load demand data. To increase the SPV penetration to the grid, grid availability needs to be enhanced, and capacitors should be connected at the agricultural pumps (load points) to provide the reactive power support locally, so the lower voltage constraint will not be violated. In conclusion, the SPV power plant connected AG feeder in the LV network has been found to be capable of providing power supply to agricultural consumers during the daytime, which may lead to proper load management by making AG feeder nearly Grid independent.

References

1. Anas, R.; Agrawal, S.; Jain, A. *Powering Agriculture in India: Strategies to Boost Components A & C under PM-KUSUM Scheme*; Council on Energy, Environment and Water (CEEW): New Delhi, India, 2021.
2. Patel, R.B.; Patel, R.D. *Smart Energy Management for the Grid Connected Solar Agricultural Prosumers and Consumers*; Metering India—Leema: New Delhi, India, 2019.
3. Moharil, R.M.; Kulkarni, P.S. A case study of solar photovoltaic power system at Sagardeep Island India. *Renew. Sustain. Energy Rev.* **2009**, *13*, 673–681. [CrossRef]
4. Eltawil, M.A.; Zhao, Z. Grid-connected photovoltaic power systems: Technical and potential problems—A review. *Renew. Sustain. Energy Rev.* **2010**, *14*, 112–129. [CrossRef]

5.   Coddington, M.H.; Baca, D.; Kroposki, B.D.; Basso, T. Deploying high penetration photovoltaic systems–A case study. In Proceedings of the 2011 37th IEEE Photovoltaic Specialists Conference, Seattle, WA, USA, 19–24 June 2011; pp. 002594–002599.

6.   Khare, V.; Nema, S.; Baredar, P. Status of solar wind renewable energy in India. *Renew. Sustain. Energy Rev.* **2013**, *27*, 1–10. [CrossRef]

7.   Kordkheili, R.; Bak-Jensen, B.; Pillai, J.R.; Mahat, P. Determining maximum photovoltaic penetration in a distribution grid considering grid operation limits. In Proceedings of the 2014 IEEE PES General Meeting|Conference & Exposition, National Harbor, MD, USA, 27–31 July 2014.

8.   Chidurala, A.; Saha, T.; Mithulananthan, N. Field investigation of voltage quality issues in distribution network with PV penetration. In Proceedings of the 2015 IEEE PES Asia-Pacific Power and Energy Engineering Conference (APPEEC), Brisbane, Australia, 15–18 November 2015.

9.   Lolla, S.; Roy, S.; Chowdhury, S. Wind and Solar Energy Resources in India. *Energy Procedia* **2015**, *76*, 187–192. [CrossRef]

10.   Karimi, M.; Mokhlis, H.; Naidu, K.; Uddin, S.; Bakar, A.H. Photovoltaic penetration issues and impacts in distribution network–A review. *Renew. Sustain. Energy Rev.* **2016**, *53*, 594–605. [CrossRef]

11.   Uzum, B.; Onen, A.; Hasanien, H.M.; Muyeen, S.M. Rooftop Solar PV Penetration Impacts on Distribution Network and Further Growth Factors—A Comprehensive Review. *Electronics* **2021**, *10*, 55. [CrossRef]

12.   Sarraf, A.; Agarwal, S.; Sharma, D. Performance of 1 MW photovoltaic system in Rajasthan: A case study. In Proceedings of the 2016 IEEE 7th Power India International Conference (PIICON), Bikaner, India, 25–27 November 2016.

13.   Sreedevi, J.; Ashwin, N.; Naini Raju, M. A study on grid connected PV system. In Proceedings of the 2016 National Power Systems Conference (NPSC), Bhubaneswar, India, 19–21 December 2016.

14.   Aziz, T.; Ketjoy, N. PV penetration limits in low voltage networks and voltage variations. *IEEE Access* **2017**, *5*, 16784–16792. [CrossRef]

15.   Badulescu, N.; Triștiu, I. Integration of photovoltaics in a sustainable irrigation system for agricultural purposes. In Proceedings of the 2017 International Conference on ENERGY and ENVIRONMENT (CIEM), Bucharest, Romania, 19–20 October 2017; pp. 36–40.

16.   Maisanam, A.; Biswas, A.; Sharma, K. Solar power potential of North-east India–A case study for Silchar. *AIP Conf. Proc.* **2018**, *1952*, 020002.

17.   Chathurangi, D.; Jayatunga, U.; Rathnayake, M.; Perera, S. Potential power quality impacts on LV distribution networks with high penetration levels of solar PV. In Proceedings of the 2018 18th International Conference on Harmonics and Quality of Power (ICHQP), Ljubljana, Slovenia, 13–16 May 2018.

18.   Oliveira, R.; Amaral, F.; Oliveira, F. Solar generation impact on voltage of rural power distribution networks: A case study. In Proceedings of the 2018 Simposio Brasileiro de Sistemas Eletricos (SBSE), Niteroi, Brazil, 12–16 May 2018.

19.   Hasarmani, T.; Holmukhe, R.; Tamke, S. Performance analysis of grid interfaced photovoltaic systems for reliable agri-microgrids using PVsyst. In Proceedings of the 2019 International Conference on Information and Communications Technology (ICOIACT), Yogyakarta, Indonesia, 24–25 July 2019; pp. 894–898.

20.   Alboaouh, K.A.; Salman Mohagheghi, S. Impact of rooftop Photovoltaics on the distribution system. *J. Renew. Energy* **2020**, *2020*, 4831434. [CrossRef]

21.   Akshay Urja, A. Bi-Monthly Newsletter of the Ministry of New and Renewable Energy, Government of India. August 2018; Volume 12, pp. 1–52. Available online: https://mnre.gov.in/img/documents/uploads/670406a017f54c9386fcde911ee5abe6.pdf (accessed on 4 December 2021).

22.   Mahanta, K.; Burman1, D.; Sarangi1, S.; Mandal1, U.; Maji1, B.; Mandal, S.; Digar, S.; Mainuddin, M. Drip Irrigation for Reducing Soil Salinity and Increasing Cropping Intensity: Case Studies in Indian Sundarbans. *J. Indian Soc. Coast. Agric. Res.* **2019**, *37*, 64–71.

23.   Ministry of New and Renewable Energy. *'Vikaspedia' Online Information Guide Launched by the Government of India. PM KUSUM Scheme*; MNRE: New Delhi, India, 2019. Available online: https://vikaspedia.in/energy/policy-support/renewable-energy-1/solar-energy/pm-kusum-scheme (accessed on 10 May 2021).

24.   *Best Practices on e-Platform of CEA*; MSEDCL: Mumbai, India, 2012; Available online: https://cea.nic.in/wp-content/uploads/2020/04/mah.pdf (accessed on 18 May 2021).

25.   Central Electricity Authority (Technical Standards for Connectivity to the Grid) Amendment Regulations. 2013. Available online: https://cea.nic.in/wp-content/uploads/2020/02/grid_connectivity_12112013.pdf (accessed on 10 May 2021).

26.   Moharil, R.; Kulkarni, P. Reliability analysis of solar photovoltaic system using hourly mean solar radiation data. *Sol. Energy* **2010**, *84*, 691–702. [CrossRef]

27.   Verschueren, T.; Mets, K.; Meersman, B.; Strobbe, M.; Evelder, C.; Vandevelde, L. Assessment and mitigation of voltage violations by solar panels in a residential distribution grid. In Proceedings of the 2011 IEEE International Conference on Smart Grid Communications (SmartGridComm), Brussels, Belgium, 17–20 October 2011.

28.   Ellis, A. *Grid Operations and High Penetration PV*; National Renewable Energy Laboratory (NREL): Golden, CO, USA; U.S. Department of Energy: Washington, DC, USA, 2010. Available online: https://www1.eere.energy.gov/solar/pdfs/2010ulw_ellis.pdf (accessed on 30 November 2021).

29.   Impact of Photovoltaic Generation on Power Quality in Urban Areas with High PV Population (Results from Monitoring Campaigns). 2008. Available online: http://www.pvupscale.org/IMG/pdf/WP4_D4-3_public_v1c.pdf (accessed on 5 December 2021).

30. Padole, N.; Moharil, R.; Munshi, A. Solar Photovoltaic (SPV) Power Plant Connected Agricultural Feeder Performance Analysis. In Proceedings of the 2021 International Conference on Electrical, Computer, Communications and Mechatronics Engineering (ICECCME), Mauritius, Mauritius, 7–8 October 2021; pp. 1–7.

31. Shiva Kumar, B.; Sudhakar, K. Performance evaluation of 10 MW grid connected solar photovoltaic power plant in India. *Energy Rep.* **2015**, *1*, 184–192. [CrossRef]

32. Central Electricity Regulatory Commission. *Performance of Solar Power Plants in India*; Central Electricity Regulatory Commission: New Delhi, India, 2011. Available online: https://cercind.gov.in/2011/Whats-New/PERFORMANCE%20OF%20SOLAR%20POWER%20PLANTS.pdf (accessed on 30 November 2021).

Carcinoma of the penis withTesticular Involvement

Mr.Sangam R. Dhorwagh[1], Mrs. LinaFating[2], Roshan Umate[3], S. G. Kadwane[4],Samruddhi Gujar[5]

1] Florence Nightingale Training College of Nursing, Datta Meghe Institute of Medical Sciences (DU), Wardha.
2] Nursing Tutor, Florence Nightingale Training College of Nursing, Datta Meghe Institute of Medical Sciences (DU), Wardha.
3] Research Scientist, Jawaharlal Nehru Medical College, Datta Meghe Institute of Medical Sciences, Sawangi (M), Wardha, Maharashtra, India.
4] Dept. of Electrical Engineering, Yeshwantrao Chavan College of Engineering, Nagpur. Email: psp4india16@gmail.com
5] Dept. of Medical Surgical Nursing, Shrimati Radhikabai Meghe Memorial College of Nursing, Datta Meghe Institute of Medical Sciences, Sawangi (M), Wardha, Maharashtra, India.

Abstract:
Introduction: In wealthy countries, around two in per 100,00 males has penile cancer per year. Penile cancer is a disease that affects men classified"Genito-urinary, nonspecific, and other"in every year Cancer Statistics, accounting for approximately There are 200 new instances and 30 old one'sfatalities. Similarly, the American Cancer Society projected 1370 new cases and 330 fatalities from penile cancer in 2011. The new EAU and NCCN recommendations recommend radiation therapies as an option for organ preservation. It is most typically utilised as either external beam radiation or brachytherapyboth for T1 or T2 illness with a diameter of less than 4 cm. McLean and colleagues studied After the primary external beam, penile preservation is radiation. Penis cancers are unusual tumours that are generally fatal for the patient and difficult to diagnose and treat for the urologist.Despite the fact that it is uncommon in North America and Europe. In many England, Countries in South America and Asia, penile malignant neoplasms are a major health concern. In the United States and Europe,England penile carcinoma accounts for 0.5 percent to 0.7 percent of all malignant neoplasms in men.Testicular cancer occurswhen abnormal cells I the testicles divide and growing uncontrolled. It is highly treatable and usually curable from of cancer the cure rate is more than 90% all ages. Testicular cancer is relatively rare, accounting for less than 2 percent of all cancer found in males between 15 to 34 years of age.
Patient History: patient admitted in AVBRHospital with chief complaint of fever, fatigue, nausea vomiting, bleeding, pain over penile lesion, painless enlargement of the testes, abdominalpain, weightloss.
Clinical finding: A history and physical examination, x-ray, palpation penis area. A visible Pain, bleeding, or discharge accompany a visible or palpable lesion. is a common symptom of penile cancer. Monthly "TESTICULAR SELF EXAMINATION", CT scan PET.
Medical management: Medical management was provided to the patient inj.ceftriaxone 1gm dose frequency is BD second inj.amikacin dose is 5oomg and frequency is OD and tablets form pan,Dolo also provided.
Nursing management: Administered fluid replacement i, e NS, DNS and RL,monitored all vital signs hourly.
Conclusion: Timely treatment of CA penis and improving the outcome of patient

Key word: Approximately, Genito,statistics, amikacin, penile.

Introduction:
Penile cancer in wealthy countries, around two in per 100,00 males has penile cancer per year. Penile cancer is disease that affect men classified as "Genito-urinary, unspecified and other" in the annual CA Statistics, accounting for about there are 210 new instance and 40 deaths.2 In the state of United, the American Cancer Society reported 1370 increase cases and 330 deaths related to penile cancer in 2011. [1,2,3]
Men between the ages of 65 and 74 are most typically affected by penile cancer, which manifests as a well-or moderately differentiated illness. Penile cancer is a numberof type cancer that originates in the penis' skin and tissues. Abnormal growth, an ulcer or sore on the penile skin, and bleeding or foul-smelling discharge are all possible symptoms. [4,5,6]

People with carcinoma in situ get a 6-year survival rate of over90%, but this lowers to 61% with nodal involvement and 20percent in cancer patients. Condom use is thought to protect against HPV-related penile cancer. Balanitis and penile cancer can be avoided by practising good genital hygiene, which includes washing the penis, scrotum, and foreskin with water on a daily basis. Soaps with harsh substances, on the other hand, should be avoided. [7,8,9]

The role of vaccination in the prevention of HPV and related diseases is still debated. HPV4 (Gardasil, Merck & Co.) is a vaccine that protects against four different diseases. HPV7, 12, 17, &19. The Cervix bivalent HPV2 vaccination (GlaxoSmithKline) protects against HPV17 &19. Both vaccinations have been recommended for use in females by Health Canada. Our goal was to create based on available information, existing rules, as well as expert advice from Canada, For Canadian oncologists treating genitourinary cancers, the first Canadian Consensus Statement on the management of penile cancer was released, in order to better meet the needs of penile cancer patients in Canada. [10,11,12]

Penile cancer is eight times more common in HIV patients. The cause of this observation is unknown, however it could be related to an increase in HPV infection. [12]

Erectile and ejaculatory function may be preserved by residual penile shaft lengths of 4 cm or greater. One of numerous outcomes in recent clinical research was the effect of immunisation on early penile cancer lesions. HPV4,18 In a phase III randomised,there was no statistically significant effect against grade 1 to grade 3 penile intraepithelial neoplasia in a placebo-controlled experiment. The trial's flaws include the participants' narrow age range and the current short follow-up period. [12]

Penis cancers are unusual tumours that are generally fatal for the patient and difficult to diagnose and treat for the urologist. [12]

Despite the fact that it is uncommon in North America and Europe A large number of African, South American, and Asian nations experiencing economic hardship. penile malignant neoplasms are major health concern penile in the UniStates and England, carcinomas account for 0.5 percent to 0.7 percent of all malignant in men neoplasms. Some African, South American, South Asian it may account for up to 10% of malignant neoplasms. Panil carcinoma is a disease that affects older men and is more common in their sixth decade of life.[13,14,15]

Patient information: - Patient admitted in AVBRHospital with chief complaint of fever, fatigue, nausea vomiting, bleeding, pain over penile lesion, painless enlargement of the testes, abdominalpain, weight loss.

Patient specificinformation: - A36 year .old male patient had previous present case has a of multiple warty lesions over glands penis in the last 2 year and hi visited in AVBR hospital.

Primary concerns symptoms of the patient: -visited/reported in AVBR hospital in OPD base on dated with complaint of fever, weakness, fatigue, nausea vomiting, bleeding, pain over penile lesion, painless enlargement of the testes, abdominalpain, weight loss. Penile carcinoma is a form of cancer that affects men. that originates in the penis' skin and tissues. Abnormal growth, an ulcer or sore on the penile skin, and bleeding or foul-smelling discharge are all possible symptoms.

Medical family and psychosocial history: - Presentcase had multiple warty lesions over glands penis for 2 years. In family history is belongs to nuclear family and her wife his medical history I,e DM. Her mentally stable, oriented and conscious was maintaining the good relationships with doctors and nurses as well as other patients also.

Relevant past intervention with outcomes: -Patient has a history a penile lesion swelling and they visited to AVBR hospital biopsy was done and detected a case of CA penis. Under aap painting & dropping done, wedge shape biopsy.

Clinical findings: Present case was unhealthy, her was conscious and oriented to place, time, date. Her body built was moderate and her was maintained good personal hygiene. A physical examination, x-ray, palpation penis area. The presence of a visible or palpable lesion that is accompanied by discomfort, bleeding, or dischargeis a common symptom of penile cancer.

Diagnostic assessment: physical examination, on the basis of patient History, patient past history is multiple warty lesions over glands penis and other investigation revels different outcomes, a thought clinical finding and after USG report and x-ray report. No any challenges during diagnostic evaluation.

Prognosis:

Therapeutic intervention: -Present case took the medical management medical management was provided to the patient inj.ceftriaxone 1gm dose frequency is BD second inj.amikacin dose is 5oomg and frequency is OD and tablets form pan,Dolo also provided.

Nursing perspectives: - IV fluids were providing to maintain the fluid and electrolytes. Monitored Vital signs per hourly.

Discussion:

Primroses, chronic inflammatory disorders of the UV, psoralen, and the penis of several sexual partners, and a young age upon first contact are now the major penile cancer risk factors with just a probability. Video endoscopic inguinal lymphadenectomy is an alternative to radical inguinal lymph node dissection that can result in fewer complications and a shorter hospital stay than normal dissection of the lymph nodes in the groyne. The numbers, on other hand, aren't accurate yet complete, and more time is needed to assess the false-negative and survival rates. At present time, the method isn't regarded as standard of care. [16,17,18]

Circumcision is a contentious subject that pits individual freedom of choice and preventing disease and reducing the likelihood of complications a population-based approach's cost-effectiveness programme. Circumcision during childhood or adolescence may offer some anti-cancer protection for the penile area. severalauthors have contributed to this work. Suggested circumcision as a possible penile cancer prevention strategy; however, the American Cancer Society emphasises the disease's rarity and points that neither the American Academy of Pediatrics nor the Canadian Academy of Pediatrics suggest routine neonatalcircumcision. [19,20,21]

In a recent big systematic review, HPV prevalence in penile cancer was estimated to be around50%, with a suspected causative relationship. A in the case of palpable adenopathy, abdominal and pelvic imaging can detect are location and extend of afflicted nodes, pelvic and retroperitoneallymphadenopathy, and distant disease. [22]

In the absence of distant cancer, the most common complication is lymph node involvement. powerful prognostic predictor in penile cancer.Carbon dioxideor neodymium, local excision (circumcision or not), photodynamic therapy with yttrium aluminum garnet laser therapy are all alternatives for treatment. Mohs micrographic surgery can be used to treat verrucous carcinoma, and topical 5-fluorouracil or 5-percent imiquimod cream can be used to treat recurrent superficial lesions. [15]

The use of Prior to decisive local therapy, systemic therapy (chemotherapy) is used. is known as neoadjuvant chemotherapy. To make local treatment easier, neoadjuvant treatment seeks too downstages or lessen the size or scope of the tumour. Furthermore, neoadjuvant chemotherapy has the potential to remove micro metastatic illness. For example, in the therapy of breastscancers, pathologically full response has been linked to. [22]

The major purpose of follow-up is to discover and possible treat recurrences in the local and/or regional areas. (Table 6). In the case of distant metastases, the therapeutic goals are palliative. The initial therapy should be used to determine the surveillance schedule. 92.2 percent of all recurrences occurred during the first 6 yrs, according to one big study. [11]

With the increased use of penile-sparing techniques, early diagnosis of recurrence is very critical. Penile cancer treatment will differ based on the clinical stage of the tumour at the time of diagnosis. [24] Depending on the stage of the malignancy, there are many therapy choices. Surgical procedures, radiation therapy, chemotherapy, and biological therapy are among them. One of five types of surgery is the most prevalent treatment: The tumour and some surrounding healthy tissues are removed in a large local excision. [12]

Penile cancer is eight times more common in HIV patients. The cause of this finding is unknown, but it could be related to an increase in HPV infection. as much good tissue as possible Laser surgery is the use of laser light to burning cut away malignant cells. Circumcision is the removal of the malignant foreskin. Amputation (penectomy)—removal of the penis and possibly accompanying lymph nodes in part or in whole. At specialised centres, radiation treatment is used to treat early-stage penile cancer in an organ-sparing manner. In addition, adjuvant therapy is used. [18]

In A strong in the case a history of bleeding or discharge from a non-retractile foreskin or a penile lesion, a high index of suspicion is required. The staging of the primary lesion comprises a physical assessmentthat pays particular attention to the morphologic appearance, extent, and position of the lesion. One of the mostsensitive tests is an MRI of the penis with a prostaglandin E1-induced erection was performed.[22]

Reference:

1. Barnholtz-Sloan JS, Maldonado JL, Pow-Sang J, et al. Incidence trends in primary malignant penile cancer. Urol Oncol. 2007;25:361–7. .urolonc.2006.08.029.
2. Canadian Cancer Society's Steering Committee on Cancer Statistics . Canadian Cancer Statistics. Toronto, ON: Canadian Cancer Society; 2011. 2011.
3. American Cancer Society . Cancer Facts and Figures 2011. Atlanta, Ga: American Cancer Society; 2011.
4. Giuliano AR, Palefsky JM, Goldstone S, et al. Efficacy of Quadrivalent HPV Vaccine against HPV Infection and Disease in Males. N Engl J Med. 2011;364:401–11. doi: 10.1056/NEJMoa0909537.
5. Frisch M, Biggar RJ, Engels EA, et al. AIDS-Cancer Match Registry Study Group Association of cancer with AIDS-related immunosuppression in adults. JAMA. 2001; 285:1736–45. doi: 10.1001/jama.285.13.1736.
6. Romero FR, Romero KR, Mattos MA, et al. Sexual function after partial penectomy for penile cancer. Urology. 2005;66:1292–5. doi: 10.1016/j.urology.2005.06.081.

7. Engel JD, Kuzel TM, Moceanu MC, Oefelein MG, Schaeffer AJ. Angiosarcoma of the bladder: a review. Urology. 1998 Nov 1;52(5):778-84.
8. Vatanasapt V, Martin N, Sriplung H, Chindavijak K, Sontipong S, Sriamporn H, Parkin DM, Ferlay J. Cancer incidence in Thailand, 1988-1991. Cancer Epidemiology and Prevention Biomarkers. 1995 Jul 1;4(5):475-83.
9. Maden C, Sherman KJ, Beckmann AM, et al. History of circumcision, medical conditions, and sexual activity and risk of penile cancer. J Natl Cancer Inst. 1993;85:19–24. doi: 10.1093/jnci/85.1.19.
10. Schoen EJ. The relationship between circumcision and cancer of the penis. CA Cancer J Clin. 1991;41:306–9. doi: 10.3322/canjclin.41.5.306.
11. Miralles-Guri C, Bruni L, Cubilla AL, et al. Human papillomavius prevalence and type distribution in penile carcinoma. J Clin Pathol. 2008;62:870–8. doi: 10.1136/jcp.2008.063149.
12. Leijte JAP, Valdes Olmos RA, Neiweg OE, et al. Anatomical mapping of lymphatic drainage in penile carcinoma with SPECT-CT implications for the extent of inguinal lymph node dissection. Eur Urol. 2008;54:885–992. doi: 10.1016/j.eururo.2008.04.094.
13. von Minckwitz G, Untch M, Blohmer J-U, et al. Definition and impact of pathologic complete response on prognosis after neoadjuvant chemotherapy in various intrinsic breast cancer subtypes. J Clin Oncol. 2012;30:1796–804. doi: 10.1200/JCO.2011.38.8595.
14. Leijte JA, Kirrander P, Antonini N, et al. Recurrence patterns of squamous cell carcinoma of the penis: recommendations for follow-up based on a two-centre analysis of 700 patients. Eur Urol. 2008;54:161–8. doi: 10.1016/j.eururo.2008.04.016.
15. Mobilio G, Ficarra V. Genital treatment of penile carcinoma. Curr Opin Urol. 2001;11:299. doi: 10.1097/00042307-200105000-00010.
16. Frisch M, Biggar RJ, Engels EA, et al. AIDS-Cancer Match Registry Study Group Association of cancer with AIDS-related immunosuppression in adults. JAMA. 2001;285:1736–45. doi: 10.1001/jama.285.13.1736.
17. Kayes O, Minhas S, Allen C, et al. The role of MRI in the local staging of penile cancer. Eur Urol. 2007;51:1313–9. doi: 10.1016/j.eururo.2006.11.014.
18. Goje, K., Phatak, S., 2018. Testicular torsion causing infarction of testis, ultrasonography and color Doppler imaging. Journal of Datta Meghe Institute of Medical Sciences University 13, 215–216. https://doi.org/10.4103/jdmimsu.jdmimsu_60_18
19. Jain, Soumya, Suresh Phatak V, Amruta Varma, and Gaurav Mishra. "Testicular Torsion - USG and Color Doppler Correlation: A Case Report." MEDICAL SCIENCE 24, no. 103 (June 2020): 1553–57.
20. Sawale, Shantanu, Meenakshi Yeola, Samarth Shukla, and Sourya Acharya. "Self-Examination of Scrotum-Need of the Hour to Create Awareness Regarding Testicular Pathologies- A Cross Sectional Study." JOURNAL OF EVOLUTION OF MEDICAL AND DENTAL SCIENCES-JEMDS 9, no. 19 (May 11, 2020): 1528–32. https://doi.org/10.14260/jemds/2020/334.
21. Bhansali PJ, Phatak SV, Bishnoi L, Raj N. Intratesticular Simple Cyst - Ultrasound and Elastography Appearance. JOURNAL OF EVOLUTION OF MEDICAL AND DENTAL SCIENCES-JEMDS. 2021 May 17;10(20):1561–2.
22. Lohchab, B., Phatak, S., Gulve, S., Tapadia, S., 2020. Intratesticular and extratesticular varicocele: Ultrasound and doppler appearance. Journal of Datta Meghe Institute of Medical Sciences University 15, 669–671. https://doi.org/10.4103/jdmimsu.jdmimsu_138_19

Moderately Differentiated Early-Stage Buccal Squamous Cell Carcinoma

Ms. Shraddha U lokhande[1], Ms. Priyanka S. Meshram[2], Roshan Umate[3]S. P. Adhau[4],Samruddhi Gujar[5]

1] Florence Nightingale Training College of Nursing, Datta Meghe Institute of Medical Sciences (DU), Wardha.
2] Nursing Tutor, Florence Nightingale Training College of Nursing, Datta Meghe Institute of Medical Sciences (DU), Wardha.
3] Research Scientist, Jawaharlal Nehru Medical College, Datta Meghe Institute of Medical Sciences, Sawangi (M), Wardha, Maharashtra, India.
4] Dept. of Electrical Engineering, Yeshwantrao Chavan College of Engineering, Nagpur. Email: aniketmunshi@gmail.com
5] Dept. of Medical Surgical Nursing, ShrimatiRadhikabaiMeghe Memorial College of Nursing,Datta Meghe Institute of Medical Sciences, Sawangi (M), Wardha, Maharashtra, India.

Abstract:
Introduction- Buccal mucosal cancer is an uncommon but fatal oral cavity cancer that has a high rate of locoregional recurrence and a poor prognosis.We looked at our experience with 119 patients who had never been treated for buccal SCC.In Southeast Asia, buccal mucosal squamous cell carcinoma (SCC) is a prevalent cancer. Our 7-year clinical experience with buccal SCC was the motivation for our study.
Main symptoms and/or important clinical findings: A 63-year-oldfemale was admitted in AVBRH in medicine ward sawangimeghewardha with chief complaint of pain in mouth and swelling in face upper part of the mouth, anorexia.
The main diagnoses, therapeutic interventions, and outcomes: This instance was diagnosed after inspecting the buccal area and the gingivolabial sulcus, as well as the lateral, superior, and inferior walls. Direct and indirect vision, as well as bi-digital palpation of the entire area, are used to examine moderately differentiated buccal Squamous cell carcinoma with a chief complaint of the buccal mucosa. Chemotherapy and radiotherapy were used to treat his moderately differentiated squamous cell carcinoma.Case was stable but blood pressure revealed sign of Hypertension.
Nursing perspective: Radiotherapy, Fluid replacement i.e., DNS and RL, monitoring of vital signs per hourly.
Conclusion: Present case wasadmitted in hospital with chief complaint of pain in mouth and swelling on upper part of the mouth, anorexia, difficulty in swallowing, stiffness, fever since 1month. After physical examination and investigation, doctor diagnosed this case as Moderate differentiated early-stage buccal Squamous cell carcinoma. He took treatment of antimicrobial drug. Patient condition was stable.

Keywords: Moderate differentiated buccal Squamous cell carcinoma, Radiotherapy

Introduction:

The most frequent oral cavity cancer in the Indian sub - continent is buccal mucosa carcinoma.The researchers wanted to see how patients who had their buccal mucosa squamous cell carcinoma (BMSCC) surgically removed fared and what prognostic factors they had. In the Indian sub - continent, oral cancer is one of the deadliest public health issues. Oral cavity cancer is the second most prevalent cancer in India, and it is the thirteenth most common cancer worldwide.India alone is responsible for a quarter (77,000 cases) of all mouth cancer cases worldwide. [1,2]
In India, oral mucosa carcinoma is the most common type of oral cancer. Ahmedabad urban males, followed by Bhopal, had the highest age-adjusted incidence of mouth cancer, according to the Cancer Registry Program (Inhabitants Cancer Registries). [2,3,4]
Cancer of the mouth was likewise identified as the most common location in Mumbai for men in the Hospital-Based Cancer Registry analysis, and it was among the top five most common sites in all registries for men. When compared to the Indian subcontinent, cancer buccal mucosa is quite infrequent in Western countries.The extensive use of gutkha, a tobacco product, and chewing betel sticks (with or without tobacco) puts India's population,

especially its youth, at danger of acquiring oral fibro, a pre-malignant illness that raises the risk of oral cancer in young people. [5,6]

Buccal cancer is usually treated with surgery, with postoperative radiation reserved for those with high-risk histopathologic characteristics such perineural invasion, lymph node invasion, bone invasion, extramedullary dissemination, or close margins.Our hospital has previously published a study on the treatment of buccal cancer during a 20-year period. According to the findings, intensive surgical treatment of buccal cancer may improve survival rates.Our goals in this study are to build on our 40 years of experience with this serious condition, to focus our analysis on a homogeneous patient population by including only unresectable buccal SCCA patients whose disease is isolated to or originates from the buccal mucosa, and to see if complete cheek resection is ontologically necessary. When detected early, squamous cell carcinoma has a good survival rate, with a five-year survival rate of 99 percent. Even if cancer has spread to nearby lymph nodes, squamous cell carcinoma can be effectively treated with a combination of surgery and radiation therapy. [7,8,9]

Regional lymph node metastases in buccal cancer were found to be less prevalent than in other mouth cavity subsites in previous research. Coppen et al found a rate of 25.0 percent for neck lymph node metastasis, while Diaz et al estimated a prevalence of 27.8 percent. The prevalence was 23.4 percent in our study. In research published by DeConde et al, however, 54 percent of the patient sample tested positive for lymph node metastases in the neck. The changes in distribution according to tumour differentiation could explain these findings. [10]

Buccal SCC is a malignant tumour that is aggressive, with the degree of differentiation affecting prognosis and survival the most. A proper systemic treatment is required in the event of poorly differentiated malignancies. Buccal SCC is a malignant tumour that is aggressive, with the degree of differentiation affecting prognosis and survival the most. A proper systemic treatment is required in the event of poorly differentiated malignancies. [11]

Patient information:

Patient specific information: A 50-year-old male was admitted in AVBRH in oral surgery wardsawangimeghewardha with chief complaint ofpain in mouth and swelling on upper part of the mouth, anorexia, difficulty in swallowing, stiffness, feversince 1month. After physical examination and investigation, doctor diagnosed this case asModeralty differentiated early-stage buccal Squamous cell carcinoma.

Primary concerns and symptoms of the patient: Present case visited AVBR hospital at Dental OPD on date 14/07/2021 with chief complaint of pain in mouth and swelling on upper part of the mouth, anorexia, difficulty in swallowing, stiffness, fever since 1monthand hypertension at the time of reporting.

Medical, family, and psycho-social history: Present case had no history of any medical problems. She having bad habits like tobacco chewing for20 years. She belonged to nuclear family and her husband had medical history of Diabetes mellitus. She was mentally stable, conscious and oriented to date, time and place. He had maintained good relationship with doctors and nurses as well as other patients also.

Relevant past intervention with outcomes: Present case had no any bad medical history.

Clinical findings: The patient was conscious and well oriented to date, time and place. Her body built was moderate and she had maintained good personal hygiene. Her haemoglobin was low i.e., 9gm, pulse rate was slightly increased. Blood pressure was 130/90 mmhg.

Timeline: Present case had no any bad medical history. The patient was admitted in private hospital with chief complaint of pain in mouth and swelling on upper part of the mouth, anorexia, difficulty in swallowing, stiffness, fever since 1month.

Because the patient's general health was deteriorating at the time, he was referred to AVBRH Sawangi Wardha for additional treatment.

Diagnostic assessment: On the basis of patient history, physical examination, blood investigation and other investigations the patient is having Moderalty differentiated early-stage buccal Squamous cell carcinoma. The blood test sample report as Hb % 9 gm and total RBC is 4.41 and WBC count 20200 and total platelet count 2.74. Fine needle aspiration was done.

Blood sugar was normal but Hemoglobin level was decrease. Urea serumwas slightly decreased. Total WBC count wasincreased. Blood pressure was 130/90 mmhg, No challenges experienced during diagnostic evaluation.

Prognosis: Blood investigations show that the Hemoglobin level slightly low, WBC level is increased.

Therapeutic intervention:

Present case took the medical management with the patient antimicrobial agents in the treatment of moderately differentiated buccal squamous cell carcinoma. For the first three weeks, methotrexate (50 mg) was administered intravenously at weekly intervals. Bleomycin and methotrexate were used in the second regimen. Bleomycin 30 mg was given twice weekly intravenously, while methotrexate 25 mg was given twice weekly intravenous infusion. Radiation therapy and chemotherapy given to the patient.The patient was kept under antibiotic and anti-

2392

inflammatory therapy for one week.Changes in therapeutic intervention (with rationale). No challenges were reported in therapeutic intervention.

Nursing perspectives: IVfluid was provided to maintain the fluid and electrolyte. Monitored vital sign per hourly.

Follow- up and outcome

Clinical and patient assessed outcome: - In spite of the all care of patient progress in active health of the patient care of the present regular medication, healthy diet they will be recover and health status are improved more than before condition.

Important follow up diagnostic and other test result - Change occur in all sign and symptoms such as muscle pain, fever, weakness, numbness.

Discussion:

Present case wasadmitted in hospital with chief complaint of pain in mouth and swelling on upper part of the mouth, anorexia, difficulty in swallowing, stiffness, fever since 1month. After physical examination and investigation, doctor diagnosed this case as Moderalty differentiated early-stage buccal Squamous cell carcinoma. He took treatment of antimicrobial drug. Patient condition was stable, Haemoglobin was slightly normal i.e., 11gm %. And blood pressure was normal that is 120/80 mmhg. [12,13]

Chewing tobacco, drinking alcohol, and chewing betel quid are all known risk factors for the development of buccal SCC. Buccal SCC was more common in older males, ethnic minority groups, and poorer socioeconomic categories, according to Markopoulos.Bacall SCC is more frequent in adults between the ages of 50 and 80. Diaz et al 8 In a prior study, the average age of the patients was 66.0 years. The patients in this study were on average 65.0 years old, but one patient was diagnosed at the age of 25. We discovered that 38.8% of the patients had drunk alcohol, 61.3 percent had consumed tobacco products, and that all of the patients were from low socioeconomic backgrounds in this study. One probable reason is that betel quid chewing, which is more widespread among men in Taiwan, is the main cause of the condition. It's worth noting that the number of smokers among China's female population is on the rise. [14,15]

Regional lymph node metastases in buccal cancer were found to be less prevalent than in other mouth cavity subsites in previous research. Coppen et al found a rate of 25.0 percent for neck lymph node metastasis, while Diaz et al estimated a prevalence of 27.8 percent. Regional lymph node metastases in buccal cancer were found to be less prevalent than in other mouth cavity subsites in previous research. Coppen et al found a rate of 25.0 percent for neck lymph node metastasis, while Diaz et al estimated a prevalence of 27.8 percent. [16,17,18,19]

Conclusion: In Southeast Asia, squamous cell carcinoma (SCC) of the buccal mucosa is a prevalent cancer. The purpose of this research was to provide our seven years of clinical experience with buccal SCCand assess the parameters that influenced surgical outcome. We looked at 67 buccal SCC patients who had malignancies that were limited to or originated from the buccal mucosa between September 2005 and May 2011. In Southeast Asia, buccal mucosal squamous cell carcinoma (SCC) is a prevalent cancer. Our 7-year clinical experience with buccal SCC was the motivation for our study. In a survival study, recurrence, nodal stage, and degree of differentiation were all considered relevant factors.

Bibliography

1. Ferlay J, Soerjomataram I, Ervik MB. GLOBOCAN 2012: Cancer Incidence, Mortality and Prevalence Worldwide. International Agency for Research on Cancer. 2012. [Last accessed on 2016 Aug 17].
2. Torre LA, Bray F, Siegel RL, Ferlay J, Lortet-Tieulent J, Jemal A, et al. Global cancer statistics, 2012. CA Cancer J Clin. 2015;65:87–108.
3. Incidence, Distribution, Trends in Incidence Rates and Projections of Burden of Cancer. Three-Year Report of Population Based Cancer Registries 2012-2014.
4. An Assessment of the Burden and Care of Cancer Patients. Consolidated Report of Hospital Based Cancer Registries 2012-2014.
5. Srivastava V, Kaur T, Sucharita V. Consences Document for Managment of Buccal Mucosa Cancer. New Delhi: Indian Council of Medical Reserch; 2014.
6. Agrawal M, Pandey S, Jain S, Maitin S. Oral cancer awareness of the general public in Gorakhpur city, India. Asian Pac J Cancer Prev. 2012; 13:5195–9.
7. Chhetri DK, Rawnsley JD, Calcaterra TC. Carcinoma of the buccal mucosa. Otolaryngol Head Neck Surg2000;123:566-71.
8. Dixit S, Vyas RK, Toparani RB, et al. Surgery versus surgery and postoperative radiotherapy in squamous cell carcinoma of the buccal mucosa: a comparative study. Ann Surg Oncol 1998;5: 502-10
9. Markopoulos AK. Current aspects on oral squamous cell carcinoma. Open Dent *J*. 2012; 6:126–130.

10. Diaz EM, Jr, Holsinger FC, Zuniga ER, Roberts DB, Sorensen DM. Squamous cell carcinoma of the buccal mucosa: one institution's experience with 119 previously untreated patients. Head Neck. 2003; 25:267–273.
11. Fang FM, Leung SW, Huang CC, et al. Combined-modality therapy for squamous carcinoma of the buccal mucosa: treatment results and prognostic factors. 1997; 19:506–512.
12. Ambad, Ranjit S., Priya Koundal, Akansha Singh, and Roshan Kumar Jha. "Association between Glutathione-S-Transferase and Gastric Carcinoma: A Case Control Study." JOURNAL OF EVOLUTION OF MEDICAL AND DENTAL SCIENCES-JEMDS 9, no. 38 (September 21, 2020): 2783–86. https://doi.org/10.14260/jemds/2020/606.
13. Anand, Anupam Surya, and Raju Kamlakarrao Shinde. "To Compare the Effects of Adjuvant and Neoadjuvant Chemotherapy on Outcome of Stage III Carcinoma Breast." JOURNAL OF EVOLUTION OF MEDICAL AND DENTAL SCIENCES-JEMDS 9, no. 8 (February 24, 2020): 496–501. https://doi.org/10.14260/jemds/2020/112.
14. Dighe, Sajika Pramod, Raju K. Shinde, Sangita Jogdand Shinde, and Anupam Anand. "Review on Assessment of Response of Neo-Adjuvant Chemotherapy in Patients of Carcinoma Breast by High Frequency Ultrasound." JOURNAL OF EVOLUTION OF MEDICAL AND DENTAL SCIENCES-JEMDS 9, no. 51 (December 21, 2020): 3873–80. https://doi.org/10.14260/jemds/2020/849.
15. Ganapathi, Keerthan, Saood Ali, Ulhas Jadhav, and Babaji Ghewade. "A Case of Small Cell Carcinoma of Lung Presenting as Opaque Hemithorax." JOURNAL OF CLINICAL AND DIAGNOSTIC RESEARCH 14, no. 10 (October 2020). https://doi.org/10.7860/JCDR/2020/45825.14120.
16. Jaggi, Ria, Samarth Shukla, Sourya Acharya, and Sunita Vagha. "Utility of TP53 in Breast Carcinoma Immunophenotypes." JOURNAL OF CLINICAL AND DIAGNOSTIC RESEARCH 14, no. 9 (September 2020). https://doi.org/10.7860/JCDR/2020/44743.14049.
17. Laddha, Ankita Gajanan, Samarth Shukla, Ravindra P. Kadu, Arvind S. Bhake, Sunita Vagha, and Miheer Jagtap. "Histopathological Types of Benign Proliferative Lesions in Peritumoural Vicinity of Carcinoma Breast." JOURNAL OF CLINICAL AND DIAGNOSTIC RESEARCH 14, no. 5 (May 2020): EC21–26. https://doi.org/10.7860/JCDR/2020/43291.13701.
18. Mishra, Preeti, Sunita Vagha, Samarth Shukla, Sourya Acharya, and Aditi Goyal. "Assessment of Cytokeratin Expression in Carcinoma Breast." JOURNAL OF EVOLUTION OF MEDICAL AND DENTAL SCIENCES-JEMDS 9, no. 35 (August 31, 2020): 2545–49. https://doi.org/10.14260/jemds/2020/553.
19. Mounika, Pottala, Deepit Sandeep Shrivastava, and Deepika Diwani. "Umbilical Metastasis Secondary to Ovarian Carcinoma - A Rare Case of Sister Mary Joseph Nodule." JOURNAL OF EVOLUTION OF MEDICAL AND DENTAL SCIENCES-JEMDS 9, no. 44 (November 2, 2020): 3343–44. https://doi.org/10.14260/jemds/2020/734.

Performance enrichment of hybrid photovoltaic thermal collector with different nano-fluids

Sourav Diwania[1,2], Rajeev Kumar[1,2] [iD] **,
Maneesh Kumar[3], Varun Gupta[2] and Theyab
R Alsenani[4]**

Abstract

This work manifests the influence of different nanoparticles on the photovoltaic-thermal (PVT) system. The hybrid PVT (hPVT) systems provide thermo-electric energy by utilizing the module heat. The module heat is recovered for controlling the cell temperature using coolant in the channel. This work examines the impact of the type and volume concentration of different nano-fluids on the cell temperature, outlet temperature, thermo-electric efficiency of hPVT collectors. Copper (Cu), titanium dioxide (TiO_2), and silicon dioxide (SiO_2) dispersed in pure water are considered nano-fluids in this study. The investigation reveals that the outcomes of the PVT collector with copper-water as nano-fluid are superior to the other nano-fluids considered in the study. At 0.012 kg/s mass flow rate (MFR), the thermo-electric efficiency of the hPVT collector is 1.645% and 6.239% higher than the thermo-electric efficiency of the PVT at an MFR of 0.002 kg/s. It is also observed that with a 4% vol. concentration of Cu in the base fluid, the thermo-electric efficiency is considerably better than the efficiency at 2% and base fluid.

Keywords

Nano-fluid, hybrid PVT (hPVT) collector, thermal efficiency, electrical efficiency, outlet temperature

[1]Department of Electrical Engineering, Jamia Millia Islamia, New Delhi, India
[2]Deparment of Electrical & Electronics Engineering, KIET Group of Institutions, Ghaziabad, India
[3]Department of Electrical Engineering, YCCE, Nagpur, India
[4]Electrical Engineering Department, Prince Sattam Bin Abdulaziz University, Al-Kharj, Saudi Arabia

Corresponding author:
Rajeev Kumar, Department of Electrical Engineering, Jamia Millia Islamia, Jamia Nagar, New Delhi-110025, India.
Email: rajeev.rakshit@gmail.com

Introduction

Climate change, air pollution, and population explosion are the factors that are responsible for the replacement of fossils or conventional fuels with renewable energy sources. Energy sources such as wind, solar, geothermal, biomass, hydro, tidal, etc., are considered under the renewable energy sources (RESs) category. Among various available RESs, solar has the potential to meet the global energy demand prominently. Solar energy is the cleanest form of energy and doesn't require importation from other countries. As a result, it improves energy-security for the countries that utilize it and lowers air pollution. Solar radiations can be easily transformed into thermo-electric energy with solar collectors and photovoltaic (PV) modules, respectively. Still, solar energy has a major drawback. Only 15–20% of the available sunlight can be transformed into electrical energy with solar PV modules, wasting 80% of solar energy as heat. This results in a rise in the cell temperature and has an adverse effect on its effectiveness and lifetime.[1] The electrical efficiency and output power of a PV module vary linearly with cell temperature. The role of cell temperature is very important in PV applications. The solar cell is tested at 25°C (STC) and depending upon the installed location, the output power is affected 10–25% by heat. With an increase in temperature above STC, the output current increases exponentially while the output power reduces linearly. Therefore, the cell temperature affects the output power and efficiency. From the last few decades, the focus has shifted from the use of PV alone to photovoltaic-thermal (PVT) systems.[2] The PVT system is capable of generating electricity as well as thermal energy by utilizing waste heat. For incorporating the wasted heat, a thermal energy management system (TEMS) is provided below the PV module. This system recovers the wasted heat using coolants viz. air, water, refrigerant, nano-fluids, etc.[3] Figure 1 portrays a typical hPVT system. This recovered heat using coolant is described as functional or useful thermal energy which can be utilized under many households, as well as agricultural activities. According to the literature, air as a coolant in a PVT system guarantees more safety and simplicity in design, but it comes with a number of drawbacks when compared to coolants like water and glycols. Because of its low specific heat and thermal conductivity, it has a poorer thermal efficiency than liquid cooling fluids. Therefore, enhancing the fluid thermal conductivity is an area of concern to the researchers. Extensive research is undergoing around the globe for thermophysical property enhancement of fluids by adding nanoparticles in the base fluid (nano-fluid).[4]

Literature survey

Most of the researchers either worked on mathematical modeling, experimental setup, simulation software, or a combination of these methods to improve the thermo-electrical effectiveness, reduce cost and improve the life cycle conversion efficiency. Diwania et al.[5] examined the thermo-electric outcomes of PVT with several nano-fluids. The impact of MFR and nanoparticle volume fraction in the base fluid is also investigated. A reduction in PV cell temperature is observed with higher MFR values and the nano-particles vol. fraction. With this, the overall performance of the PVT collector. Radwan et al.[6] worked upon the application of Al_2O_3 and SiC nanoparticles to PVT as coolant. From the observations, a considerable deduction in cell temperature is observed at a higher volume fraction of nano-fluids. Further, the electrical power output increases with an increase in vol. fractions of the nanoparticle in the base fluid.

Yousefi et al.[7] analyzed the impact of distinct fractions (0.2% and 0.4% wt) of Al_2O_3 nanoparticles in the base fluid (water). Adding 0.2% wt. of Al_2O_3 in water leads to enhances the overall efficiency 28.3% as compared to the water cooling case. Khanjari et al.[8] proposed a precise and
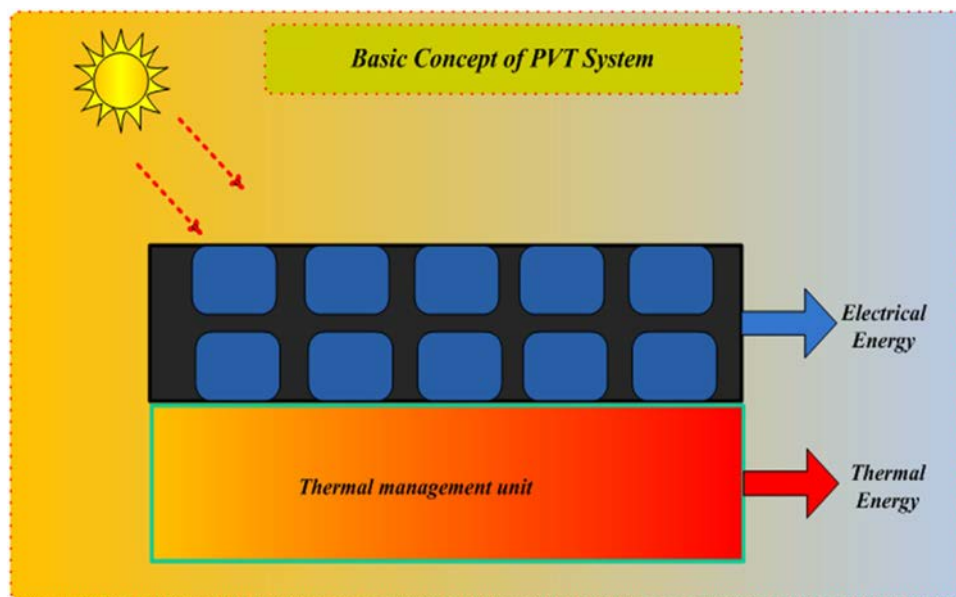
Figure 1. Basic concept of a PVT system.

comprehensive numerical simulation on PVT collectors using Ag-water, Al_2O_3-water, and pure water as coolant. The impact of volume concentration of nanoparticles (1% to 10% vol. concentration) and inlet fluid velocity (0.04 to 0.23 m/s) have been investigated on the outcomes of the PVT system. A considerable rise in the PVT outcomes is observed at higher vol. the concentration of nanoparticles in the base fluid. Hissouf et al.[9] numerically investigate the thermo-electric outcome of hPVT with Cu-water and Al_2O_3-water nano-fluids. The outcomes indicate that using (2 vol%) of Cu nanoparticles in water, the thermo-electric outcome of an hPVT enhances by 4.1% and 1.9%, respectively, and using Al_2O_3 nanoparticles in water, the thermo-electric outcome enhances by 2.7% and 1.2%, respectively. Michael et. al.[10] examined the impact of CuO nanoparticles on the flat plate solar collector's (FPSC) performance. By adding a vol. fraction of 0.05% in the water, the thermo-electrical efficiency enhances by 9% and 1.44%, respectively. Further, the author found that the kind of nanoparticles in the base fluid impacts thermo-electrical performance. Ghadari et al.[11] worked upon Fe_3O_4 nanoparticles (3 wt%) as a coolant in hPVT and observed improvement of 46.29% and 4.93% in thermal and electrical efficiency. Sint et al.[12] developed a mathematical model in MATLAB for calculating the performance of FPSC. The effect of vol. fraction and size of nanoparticles on the performance of FPSC is investigated. The outcomes of the study show that the collector's efficiency significantly enhances with the increase in vol. fraction of nanoparticles in the base fluid while the size of nanoparticles shows a marginal increase in collector's performance. The influence of silica/water nano-fluids on the PV/T was examined by Sardarabadi et al.[13] The nanoparticle wt. fractions in the base fluid were chosen between 1% and 3%. The aggregate outcomes of the collectors using 1% and 3% silica-water nano-fluid enhance by 3.6% and 7.9% concerning the PV/T water collector.

The impact of mass flow rate, nanoparticles concentration, fluid velocity, etc., were investigated by various authors. Fudholi et al.[14] investigated the output of a PVT collector with TiO_2 water-based nano-fluid (at 0.5 wt% and 01 wt% TiO_2) under changing solar radiation intensity. The outcomes

show that at a higher solar emission, the thermal efficiency improves, and electrical efficiency falls because of rising cell temperature. The overall efficiency improves by 20% using 1 wt% of TiO_2-water nano-fluid concerning the traditional PVT water collectors. Al-Shamani et al.[15] investigated the effect of various critical parameters such as module temperature and the temperature on the output of the PVT collectors using various nano-fluids (SiO_2, TiO_2, and SiC). It has been concluded the thermo-electric and overall performance of the PVT was improved up to a value of 13.52%, 68.21%, and 81.73%, with SiC nano-fluid. The PVT outcome is improved with SiC nano-fluid as compared to other nano-fluids considered for the investigation. The working of two-phase closed thermosyphons, which is coupled with a PV module, has been investigated by Moradgholi et al.[16] In this study, methanol and Al_2O_3/methanol are used to elaborate the effect of filling ratio and nano-fluid concentration over the system output. The optimal result of the proposed system is achieved with a 50% filling ratio and 1.5 wt% of nano-fluid concentration. Nasrin et al.[17] examine MWCNT-water nano-fluid by using a 1% wt fraction of MWCNT, an enhancement of 3.67% and 0.14% has been observed in thermo-electric efficiency, respectively. It is observed that current and solar irradiation significantly affects the power production of the PVT collector than voltage and temperature.

For enhancing heat and thermal conductivity, researchers around the globe are attracted to the application of hybrid nano-fluids. In this direction, Wole-Osho et al.[18] investigate the thermo-electrical outcome of PVT systems at several volume fractions of hybrid ($Al_2O_3 + ZnO$)-water nano-fluid. The outcomes show that the PVT thermo-electric performance improves with an increment in MFR. Mirzaei et al.[19] examined the PVT outcome under the influence of CuO-water, Al_2O_3-water, and hybrid nano-fluid. The PVT system shows better performance with hybrid nano-fluids as compared to mono nano-fluids. Verma et al.[20] prepared the hybrid nano-fluid by mixing multi-walled carbon nanotubes (MWCNT) with CuO-MgO nanoparticles. The PVT outcome is investigated at various concentrations of nanoparticles and distinct MFR's. The outcomes reveal the energy and exergy efficiency obtained using hybrid nano-fluid is 70.55% and 71.54%, respectively, which is significantly better than the outcomes obtained using mono nano-fluid.

Nowadays, the utility of phase change material (PCM) has increased significantly in energy storage systems due to its energy storage abilities. Many researchers emphasized the use of PCM with nano-fluids to further improve the effectiveness of hPVT systems. The inclusion of PCM to PVT collectors reduces the heat loss to the surroundings more effectively. Salem et al.[21] examined the PVT outcomes using Al_2O_3-PCM as nano-fluid. The outcomes of the investigation show that the PVT outcomes using nano-fluid are considerably better concerning water cooling. Yang et al.[22] developed the PVT-PCM and hPVT collector setup for experimentation and compared the outcome of both systems based on power output. The investigation reveals that the output power of the PVT-PCM is 14% more concerning the PVT system alone. Hosseinzadeh et al.[23] experimentally analyzed the PV system performance under three categories viz. PV system (traditional), hPVT with nano-fluid, and PVT-PCM system with nano-fluid. A 0.2 wt% of ZnO in water and paraffin wax is used as a nano-fluid and PCM, respectively, for the PVT-PCM system. It is observed that the nano-fluid-based PVT-PCM have higher outcomes as compared to the other systems under consideration. Kandilli[24] proposed the use of zeolites in their natural form to be utilized as thermal or heat energy storage in an hPVT collector. In the proposed work, the performance of zeolite has been compared with paraffin-wax and the stearic acid-based PVT. Experimental analysis shows that energy efficiency is 40.0%, 33.0%, and 37.0% for PVT with zeolites, paraffin-wax, and stearic acid, respectively. Manigandan et. al.[25] experimentally investigates the outcome of PVT with the help of nano-fluids such as (ZnO & CuO) and PCM. In this work, five different types of nano-fluids are considered and compared. Ali Salari et al.[26] worked upon the numerical simulation and thermodynamic analysis of a 3-D PVT system integrated with PCM material. The nano-fluid considered for the study were nano-magnesium oxide, multiwall carbon nanotube,

and hybrid nano-fluid (mixture of nano-MgO and carbon nanotube). The outcomes show that the surface temperature reduces with an increase in thickness of the PCM layer and MFR. By using multiwall carbon nano-fluid as a cooling medium, better performance was achieved as compared to other combinations of fluids. Nano-fluids help in enhancing thermal conductivity as compared to water cooling. Also, it offers several benefits such as reduced particle clogging, higher stability of a colloidal suspension, lower pumping power, and higher specific surface area. Figure 2 indicates the salient features of nano-fluid.[27]

The different findings summarizing the enhancement in the thermo-electric outcomes of the PVT with nano-fluids are outlined in Table 1.

Main contribution

As mentioned in the literature, the utilization of nano-fluids for the efficiency up-gradation of PVT systems develops interest among researchers. The present study elucidates the impact of different nanofluids (Cu-water, SiO_2-water, and TiO_2-water) on the thermo-electrical performance of the hPVT collector. The comprehensive effect of varying MFR and particles volume concentration upon the hPVT outcomes is also tested. For this purpose, the energy balance equation (EBE) of PVT with nano-fluid is obtained through the analysis of various operating- parameters.

The rest of the paper is arranged as, In the second section, mathematical modeling of PVT collector with nano-fluid and equation describing thermophysical properties of nano-fluid as well as
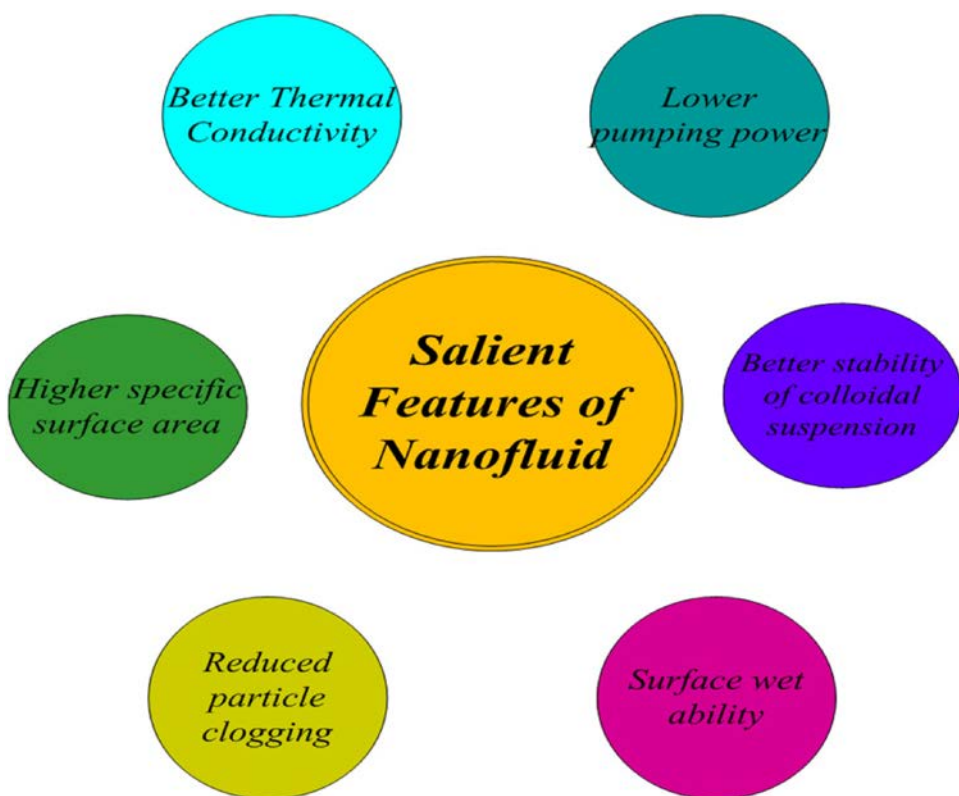
Figure 2. Salient features of nano-fluid..[27]

Table 1. Summary of findings showing improvement in thermo-electrical efficiency using nano-fluids.

Author	Nanofluid	Concentration	Findings
Yousefi et al.[7]	Al_2O_3-water	0.2% and 0.4% wt	Overall efficiency improved by 28.3% using nanofluid as compared to basefluid.
Khanjari et al.[8]	Ag-water Al_2O_3-water	10 vol % 10 vol %	The thermal and electrical efficiency enhances by 12.43% and 3.9% using Ag-water nanofluid and 4.54% and 1.83% respectively using Al_2O_3-water nanofluid.
Hissouf et al.[9]	Cu-water Al_2O_3-water	2 vol % 2 vol%	Maximum enhancement in the thermo-electric outcome of hybrid PVT is observed with Cu-water nanofluid. Thermo-electric efficiency enhances by 4.1% and 1.9% respectively using Cu-water nanofluid.
Michael and Iniyan[10]	CuO-water	5 vol%	Under the same operating condition, the thermo-electrical efficiency enhances by 9% and 1.44% using CuO nanofluid as compared to pure water as basefluid.
Ghadari et al.[11]	Fe_3O_4-water	3 wt%	Thermo-electric outcome enhances by 46.29% and 4.93%.
Sint et al.[12]	CuO-water	2 vol%	The impact of the size of nanoparticles is minimal on the performance of FPSC while the efficiency improves significantly with an increase in vol% of nanoparticles in the base fluid.
Sardarabadi et al.[13]	Silica-water	1 wt % and 3 wt %	The overall efficiency improved by 7.9% and 3.6% using 3% and 1% silica nanoparticles in water respectively.
Nasrin et al.[17]	MWCNT-water	1 wt %	1 wt % of MWCNT nanoparticles in water results in Thermo-electric efficiency enhancement of 0.14% and 3.67% respectively.
Al-Shamani et al.[18]	TiO_2-water SiO_2-water SiC-water	1 wt % 1 wt % 1 wt %	The highest enhancement in the thermo-electrical performance was observed using SiC-water nanofluid. The thermo-electric, and overall performance of the PVT collector were enhanced up to a value of 13.52%, 68.21%, and 81.73%, using SiC nanofluid.
Current Study	Cu-water SiO_2-water TiO_2-water	2 vol% and 4 vol %	The performance of a hybrid PVT collector was investigated considering different nanofluid and at different MFR. The thermo-electrical efficiency enhances by 1.645% and 6.239% respectively using Cu-water nanofluid at 4 vol% as compared to other nanofluids.

base fluid are established, the third section presents the detailed performance analysis of PVT collector with nano-fluid. The final section, 4 concludes the study.

Adopted methodology

System configuration

Figure 3 portrays the schematics of sheet-tube type hPVT collectors. An hPVT collector consists of a PV-module, glaze (glass-cover), an absorber associated with the module with adhesives, a water tube over the absorber, and a layer of insulation over the bottom. The glass cover is used to absorb more

thermal energy from the sun. This is mentioned in the literature that glazing above the PV module enabled getting an improved thermal outcome concerning the unglazed system. A mixture of nanoparticles with water is used as a coolant in water tubes for heat transfer from PV modules.

Energy balance equations of nano-fluid based PVT collector

The EBE is used to describe the various components of an hPVT collector. Feasible mathematical modeling allows evaluating the thermal characteristics such as heat transfer and temperature variation across the hPVT collector elements. To formulate the EBE across the different layers of the collector, a thermal circuit model of PVT collector with nano-fluid is considered and portrayed in Figure 4.

The EBE is solved with the following assumptions:

- Heat transmission is supposed to be a unidirectional and quasi-statical process.
- Since solar radiations and ambient temperature are allowed to vary hence the components of the hPVT are supposed to be in the quasi-state.
- A fixed temperature is assumed to maintain across the layers of the hybrid collector.
- The impact of sunlight and radiant heat transfer on the system performance is neglected.
- PVT components bear a constant heat or thermal conductivity.
- The optic losses associated with the PV module are considered to be negligible. The transmittance (τ) and absorbance (α) coefficient product are considered as 1.

With the above assumptions, the EBE across the various PVT collector components can be formulated and represented as:

EBE For glass cover. A part of the solar irradiance strikes over the glass cover is reflected back in the atmosphere. In contrast, the PV module consumes the remaining part of solar energy through the
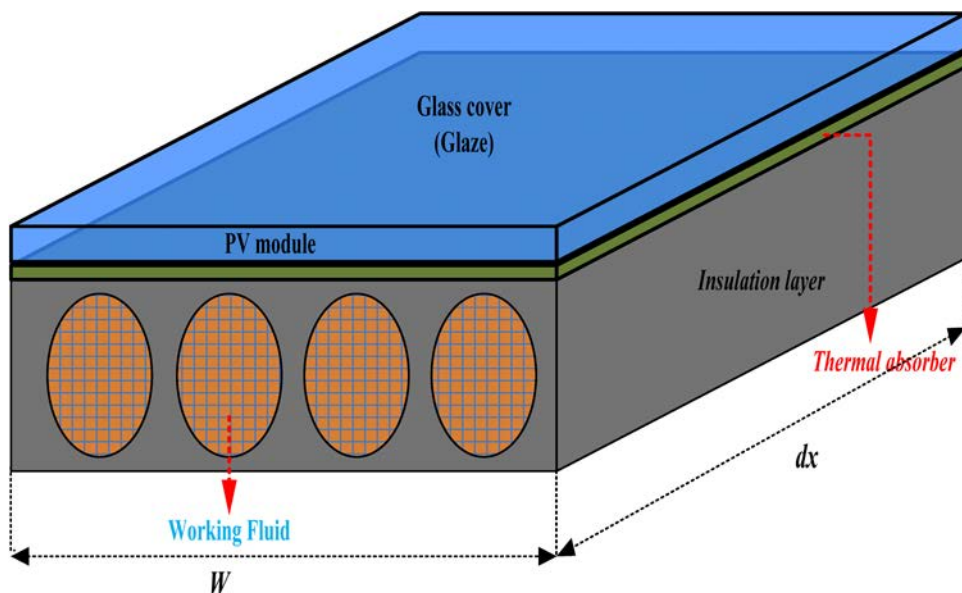

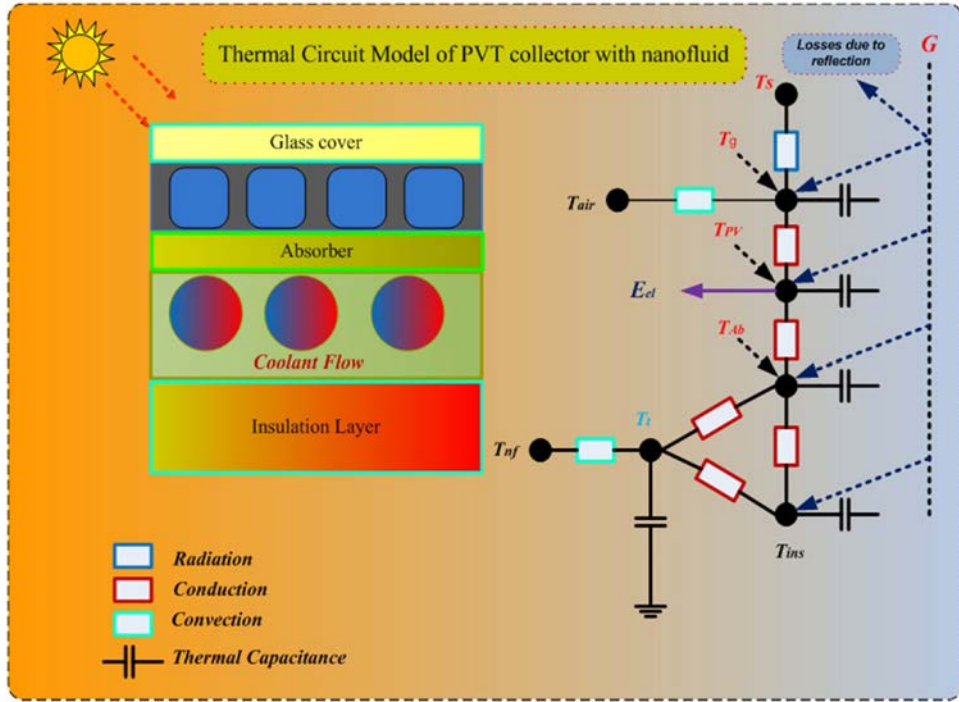**Figure 3.** Schematic of an hPVT-collector.

Figure 4. Thermal circuit model of PVT collector with nano-fluid.

heat-transfer process.

$$G\alpha_g = h_{g.a}(T_g - T_{air}) + H_{pv.g}(T_g - T_{PV}) = (3v_w + 2.8)(T_g - T_{air}) + H_{pv.g}(T_g - T_{PV}) \quad (1)$$

Where G stands for the solar radiation (W/m^2) and $h_{g.a}$ is the convection heat loss coefficient.

The PV module-glass conductive HTC (heat transfer coefficient; $H_{pv.g}$) is expressed as:

$$H_{pv.g} = \frac{1}{(\delta_{pv} / \lambda_{pv}) + (\delta_g / \lambda_g)} \quad (2)$$

For the Pv module. The major part of the incoming radiation is diverted to the absorber and the rest part is converted into electrical energy.

$$G\tau_g\alpha_{pv}[1 - \eta_{el}] = H_{pv.g}(T_{PV} - T_g) + H_{pv.Ab}(T_{PV} - T_{Ab}) + H_{pv.t}(T_{PV} - T_t) \quad (3)$$

Where τ_g and α_{pv} are the transmission and absorption coefficients of the PV module.

The HTC between PV module- absorber ($H_{pv.Ab}$) and PV module-tube ($H_{pv.t}$) can be defined as.[28]

$$H_{pv.Ab} = \frac{\lambda_{ad}}{\delta_{ad}}\left(1 - \frac{D_{out}}{W}\right) \quad (4)$$

$$H_{pv.t} = \frac{\delta_{pv}}{(W^2 / 8\lambda_{pv}) + (\delta_{ad} / \lambda_{ad}).(\delta_{pv} W / D_{out})} \tag{5}$$

here δ, λ represents the thickness of the layer and heat conductivity. D_{out} is the outer diameter of the tube.

For the absorber and tube assembly. The heat from the PV-module is absorbed by the thermal absorber. This heat is exchanged among the absorber, tube, and insulation layers. The EBE for the absorber could be defined as:

$$H_{pv.Ab}(T_{cell} - T_{Ab}) = H_{Ab.t}(T_{Ab} - T_t) + H_{Ab.ins}(T_{Ab} - T_{ins}) \tag{6}$$

Where $H_{Ab.t}$ and $H_{Ab.ins}$ represent the HTC's of the absorber sheet-tube and sheet-insulation layer respectively.[28]

$$H_{Ab.t} = \frac{8\lambda_{Ab}}{W - D_{out}} \cdot \frac{\delta_{Ab}}{W} \tag{7}$$

$$H_{Ab.ins} = \frac{1}{(\delta_{Ab} / \lambda_{Ab}) + (\delta_{ins} / \lambda_{ins})} \tag{8}$$

The EBE for the tube is represented as:

$$H_{Ab.t}(T_{Ab} - T_t) + H_{pv.t}(T_{cell} - T_t) = H_{t.nf}\left(T_t - \bar{T}_{nf}\right) + H_{t.ins}(T_t - T_{ins}) \tag{9}$$

The heat transfer between the absorber, insulation layer, and the fluid is shown in equation (9).

   Where $H_{t.nf}$ and $H_{t.ins}$ stands for the conductive heat transfer coefficients between tube-nano-fluid and insulation layer.

$$H_{t.ins} = \frac{2\lambda_{ins}}{\delta_{ins}}\left(\frac{\Pi}{2} + 1\right)\frac{D_{out}}{W} \tag{10}$$

$$H_{t.nf} = \frac{1}{(W / h_{nf}\Pi D_{in}) + (W / \lambda_{ad})} \tag{11}$$

Where h_{nf} is the convective HTC and presents the forced flow of nano-fluids in the tubes.

$$h_{nf} = \frac{Nu_{nf}\lambda_{nf}}{D_{in}} \tag{12}$$

For the insulation layer. In the insulation layer, the exchange of heat takes place among the absorber, tube, and environment.

$$H_{Ab.ins}(T_{Ab} - T_{ins}) + H_{t.ins}(T_t - T_{ins}) = H_{ins.air}(T_{ins} - T_{air}) \tag{13}$$

The conductive HTC between the insulation layer and atmosphere is defined as:

$$H_{ins.air} = \frac{1}{(\delta_{ins} / 2\lambda_{ins}) + (1 / h_{g.air})} \tag{14}$$

For working fluid. The EBE for the working fluid is a function of the heat exchange among the working fluids and the tube.[29]

$$H_{t.nf}.d.A_c\left(T_t - \bar{T}_{nf}\right) = m_{nf}.c_p.dT_{nf} \tag{15}$$

T_{nf} is expressed as:

$$T_{nf}(x) = (T_{nf.i} - T_t)e^{-Cx} + T_t \tag{16}$$

Where C is the constant used to simplify the above equation.

$$C = \frac{H_{t.nf}.W_d}{m_{nf}.c_p} \tag{17}$$

Where m_{nf} stands for the MFR of nano-fluid, c_p represents the specific heat.

The temperature of the nano-fluid at the outlet of the tube can be calculated as:

$$T_{nf.o} = T_{nf}(L_c) = T_{nf.i}A + T_t(1 - A) \tag{18}$$

By solving the equations (16) and (18), the temperature of nano-fluids circulating in the tube is mathematically expressed as:

$$\bar{T}_{nf} = \frac{1}{L_c}\int_0^{L_c} T_{nf}(x).dx = T_{nf.i}.B + T_t.(1 - B) \tag{19}$$

A and B are the constants used to simply the equation and can be defined as:

$$A = e^{-CL_c} \tag{20}$$

$$B = \frac{1 - A}{C.L_c} \tag{21}$$

Performance of nano-fluid based PVT system

The performance of a hPVT is accessed by its thermo-electric, and overall efficiencies. The heat efficiency depends upon the tubes inlet/outlet temperature difference.[30]

$$\eta_{Th} = \frac{Q_{th}}{G.A_c} \tag{22}$$

$$\eta_{Th} = \frac{mc_p(T_{nf.o} - T_{nf.i})}{G.A_c} \tag{23}$$

The η_{el} of the PVT is a function of the cell temperature and is calculated by the relation.[31]

$$\eta_{el} = P\eta_0[1 - \beta_0(T_{PV} - T_{air})] \tag{24}$$

Where P signifies the module packing factor.

Equation (25) computes the electric power output of the PVT (E_{el}).

$$E_{el} = \tau_g G\eta_{el} \tag{25}$$

The overall efficiency (η_{PVT}) consists of thermal and electrical efficiencies.

$$\eta_{PVT} = \eta_{Th} + \eta_{el} \tag{26}$$

Nusselt number

Nusselt number (Nu) mostly depends upon the base fluid under study. This characterizes the rate of heat transmission between the circulating fluid and the tube surface in fluid contact. For pure water, Nu is determined for the streamline and turbulent flow with the following relation.[32]

Laminar/streamline flow (Re < 2300)

$$Nu_{water} = \begin{cases} 1.953(x*) - 1/3, \, x* \leq 0.03 \\ 4.364 + 0.0722/x*, \, x* > 0.03 \end{cases} \tag{27}$$

Turbulent flow (Re > 2300)

$$Nu_{water} = \frac{(f/8)(\text{Re} - 1000)\text{Pr}}{1 + 12.7(f/8)^{1/2}(\text{Pr}^{2/3} - 1)} \tag{28}$$

Where

$$x* = \frac{L_c}{\text{Re}\,\text{Pr}\,D} \tag{29}$$

Xuan & Li[32] mathematically formulated the Nusselt number for various nano-fluids.

$$Nu_{nf} = c_1(1 + c_2\phi^{m1}Pe^{m2})\text{Re}_{nf}^{m3}\,\text{Pr}_{nf}^{0.4} \tag{30}$$

Where $c_1, c_2, m1, m2,$ and $m3$ are the constants whose values depend on the type of nano-fluid used.

Thermophysical properties

The thermophysical properties of nano-fluids and base fluid, play a vital role in solving the EBE mentioned above.

Density. The density of nano-fluid (ρ_{nf}) is mathematically formulated by Pak & Cho[33] and represented as:

$$\rho_{nf} = \varphi.\rho_{np} + (1 - \phi)\rho_{bf} \tag{31}$$

Heat or thermal capacity. The heat capacity (c_{pnf}) is calculated according to the mathematical expression.[8,33]

$$c_{p.nf} = \frac{\phi(\rho.c_p)_{np} + (1 - \phi)(\rho.c_p)_{bf}}{\rho_{nf}} \tag{32}$$

$$c_{p.nf} = \phi c_{p.np} + (1 - \phi)c_{p.bf} \tag{33}$$

Where ϕ stands for the nanoparticles volume concentration mixed with the base fluid.

Viscosity. Jia et al.[34] mathematically formulated the dynamic viscosity of nano-fluid (v_{nf}) as:

$$\begin{cases} v_{nf} = (1 + 2.5\phi)v_{bf}, \, \phi < 0.05 \\ v_{nf} = (1 + 2.5\phi + 6.5\phi^2)v_{bf}, \, 0.05 < \phi < 0.1 \end{cases} \tag{34}$$

Thermal conductivity. The the thermal conductivity of nano-fluid (λ_{nf}) is mathematically formulated by Xuan & Li[32] and expressed as:

$$\lambda_{nf} = \frac{\lambda_{np} + 2\lambda_{bf} - 2\varphi(\lambda_{bf} - \lambda_{np})}{\lambda_{np} + 2\lambda_{bf} + \varphi(\lambda_{bf} - \lambda_{np})} \cdot \lambda_{bf} + \frac{\rho_{np}\varphi c_{pbf}}{2}\sqrt{\frac{2\kappa T_{nf}}{3\Pi d_{np}v_{bf}}} \tag{35}$$

In the present work, water is considered as a basefluid. Its thermophysical charecterstics used for mathematical models are temperature-dependent as determined by equations (36)–(39).

$$\rho_{water} = -0.03XT^2 + 1.505XT + 816.781 \tag{36}$$

$$c_{p,water} = -0.0000463XT^3 + 0.0552XT^2 - 20.86XT + 6719.637 \tag{37}$$

$$v_{water} = 0.00002414X10^{\frac{247.8}{T-140}} \tag{38}$$

$$\lambda_{water} = -0.000007843XT^2 + 0.0062XT - 0.54 \tag{39}$$

The thermophysical characteristics of copper, TiO_2, and SiO_2 nanoparticles and water as a basefluid at 25°C are shown in Table 2. The thermophysical and heat transfer properties of nanoparticles and basefluid play a vital role in formulating the EBE.

Analytical results

The present study examines the outcomes of a glazed PVT collector for the climatic conditions of Ghaziabad city, India (28.66856°N, 77.4538°E) with copper (Cu), Titanium oxide (TiO_2), and silicon dioxide (SiO_2) as nanoparticles dispersed in pure water as base fluid. Figure 5 shows the data for the sunlight intensity and ambient temperature for a typical summer day.

It has been observed that the sunlight intensity first increases, reaches its optimum value between 12:00 p.m. and 13:00, and falls to a minimum as the time increases. The variation in ambient temperature and intensity is recorded at half-hour intervals from 07:00 a.m. to 17:30 afternoon. The numerical simulation obtained using mathematical modeling was performed using Matlab software. The design parameters used are reported in Table 3. In this section, the performance is analyzed with different nanoparticles type, particle volume concentrations, and MFR.

The temperature variations of the PV module with Copper-water, SiO_2-water, and TiO_2-water nano-fluid are shown in Figure 6. These data sets are recorded when the nanoparticles vol. fraction (ϕ) is 2%, the nano-fluid MFR is 0.012 kg/s, and the dimensions of the coolant tube are fixed. It has been observed that the PV module temperature rises with a rise in the solar intensity and ambient temperature. The optimal value of the PV module temperature with Copper-water, SiO_2-water, and TiO_2-water nano-fluid is 35.14°C, 35.41°C, and 35.67°C, respectively. As given earlier in Table 2,

Table 2. Thermophysical charecterstics of nanoparticles and basefluid.[35]

Nano-fluid/ base fluid	ρ (kg/m3)	c_p (J/kg/K)	λ (W/m-K)
Cu	8932	386	392
TiO_2	4230	692	8.4
SiO_2	2200	765	40
Water	997.1	4179	0.6130

the copper has higher heat conductivity as compared to the other two considered nanoparticles considered. The PV module temperature is lower using copper-water nano-fluid while comparing SiO_2-water and TiO_2-water nano-fluids.

Figure 7 illustrates the variation in electrical efficiency (η_{el}) of PVT collectors with time for different nano-fluids. The η_{el} shows an inverse variation with the PV module temperature, as given in equation (24). As indicated in Figure 6, the PV module temperature using Copper-water nano-fluid is lower than other nano-fluids. Therefore, the η_{el} of Copper-water nano-fluid is higher in contrast to SiO_2-water and TiO_2-water nano-fluids. The average η_{el} reported for Copper-water, SiO_2-water, and TiO_2-water nano-fluid is 14.763%, 14.59%, and 14.51%, respectively.

As mentioned in equation (23), η_{Th} is a function of the inlet/outlet temperature difference of the tube. At a constant MFR of 0.012 kg/s, the η_{Th} calculated for PVT with distinct nano-fluids is shown in Figure 8. As seen from the curve, the η_{Th} increases up to 12:30, and then a constant decrement is observed throughout the observation. The average value of η_{Th} recorded for Copper-water, SiO_2-water, and TiO_2-water nano-fluid was 41.70%, 41.54%, and 41.39%, respectively. Hence, the η_{Th} of PVT collector is higher while utilizing the copper-water as a coolant as compared to SiO_2-water and TiO_2-water as nano-fluid.

It is observed for the aforementioned analysis that the thermoelectric outcome of the photovoltaic collectors with Copper-water as nano-fluid is superior as compared to the SiO_2-water and TiO_2-water nano-fluids. Even though the difference in the thermo-electric efficiency is significantly small, it is very interesting to see that Cu as a nano-fluid exhibited superior performance. Thus, the copper-water is considered as a coolant to further check the changing MFR effect and the concentration of particle vol. on the thermo-electric outcomes of the hPVT collector.

Impact of MFR variations

In this section, an analysis is done to investigate the impact of variations in MFR on the temperature of the PV module, thermo-electric outcomes of PVT collectors have been investigated with Copper-water as a nano-fluid. The variation of photovoltaic cell temperature versus the time at various MFR of Copper-water as a nano-fluid is illustrated in Figure 9. The MFR is varied from 0.012 to 0.002 kg/s. As observed from the curve, the photovoltaic cell temperature decreases with an increase in the MFR of nano-fluid. This is observed that, at the higher MFR, extra
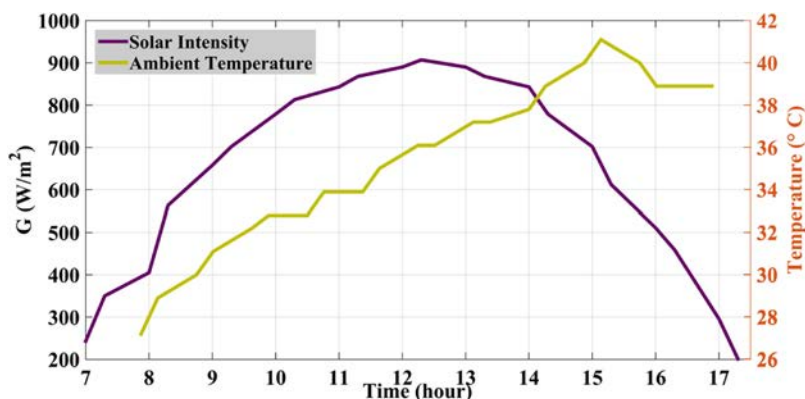

Figure 5. The intensity of sunlight and ambient temperature variation with time.

Table 3. Design parameter considered for simulation.

Component	Parameter	Value
Glass cover	Thickness	0.004 m
	Transmittance	0.92
	Absorptance	0.04
	Thermal conductivity	0.7 W/m-K
PV module	Temperature coefficient	0.0045 K^{-1}
	Reference PV cell efficiency	0.18
	Absorptance	0.9
	Thermal conductivity	100 W/m-K
	Reference cell temperature	298 K
Absorber	Thickness	0.0005 m
	Thermal conductivity	310 W/m-K
Tube	Number of tubes	10
	Space between tubes	0.1 m
	Length	2 m
	Outer diameter	0.010 m
	Inner diameter	0.006 m
	Thickness of tube	0.00012 m
Insulation layer	Thickness	0.05 m
	Thermal conductivity	0.034 W/m-K
Others	Collector slope	30°
	Packing factor	0.9
	Ambient temperature	298 K
	Wind speed	1 m/s
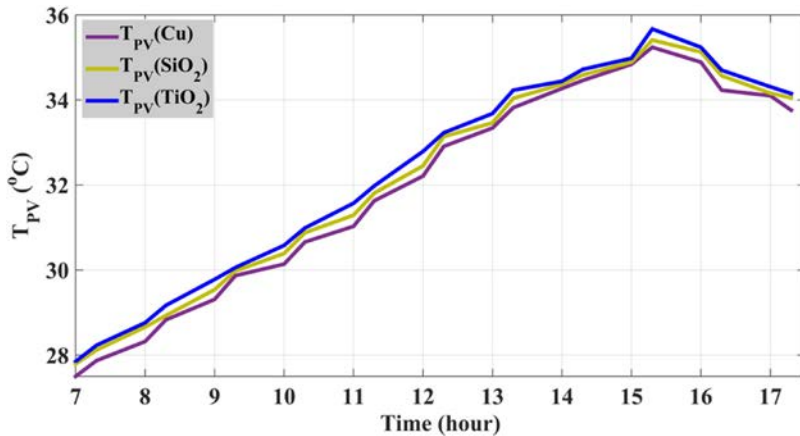
Figure 6. Comparison of PV module temperature with different nano-fluids.

thermal energy can be extracted from the PVT collector, which helps in the reduction of photovoltaic module temperature. At 0.012 kg/s MFR, the peak temperature of the PV module is 34.5°C, while at 0.002 kg/s, the peak temperature of the PV module is 40.23°C.
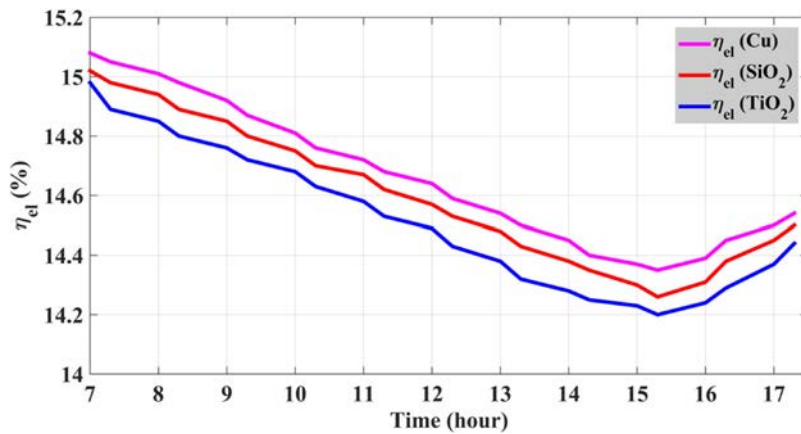
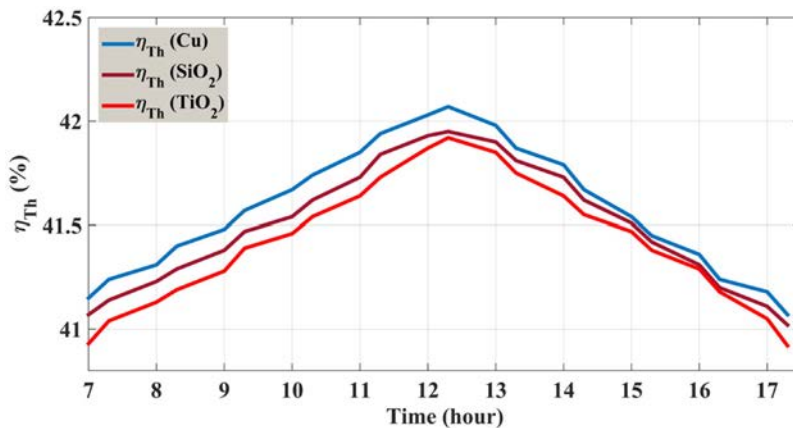**Figure 7.** Electrical efficiency comparison using different nano-fluid.

Figure 8. Thermal efficiency comparison using different nano-fluid.

Figure 10 portrays the effect of varying MFR on the η_{el} of PVT with copper-water nano-fluid. The η_{el} of the PVT collector increases with rising MFR. The figure shows more the MFR; more is the amount of heat evacuated from the bottom of the PV module. Thus the operating cell temperature decreases, as explained in Figure 9. Hence, the MFR has a positive effect over η_{el} of the hPVT collector.

The impact of MFR on the outlet temperature of the PVT collector with copper-water as nano-fluid is presented in Figure 11.

At a greater MFR, the output temperature decreases, and the inlet/outlet temperature difference is small and simultaneously, more heat is evacuated from the PV module. Hence, the PVT collector thermal output η_{Th} is improved at a greater MFR, as depicted in Figure 12.

With an MFR of 0.012 kg/s, the maximum value of η_{Th} for the PVT collector is 42.13%, 0.002 kg/s, MFR the peak value of η_{Th} of PVT collector is 41.70%. The η_{Th} depends upon the MFR and the inlet/outlet temperature difference of the tube, as mentioned in equation (23). The
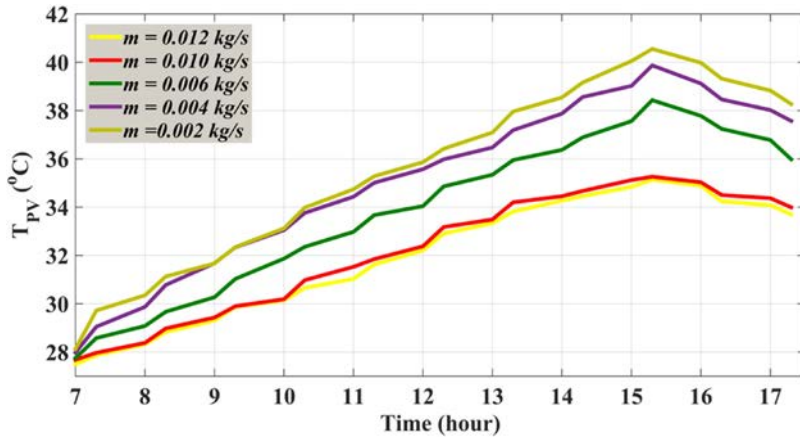
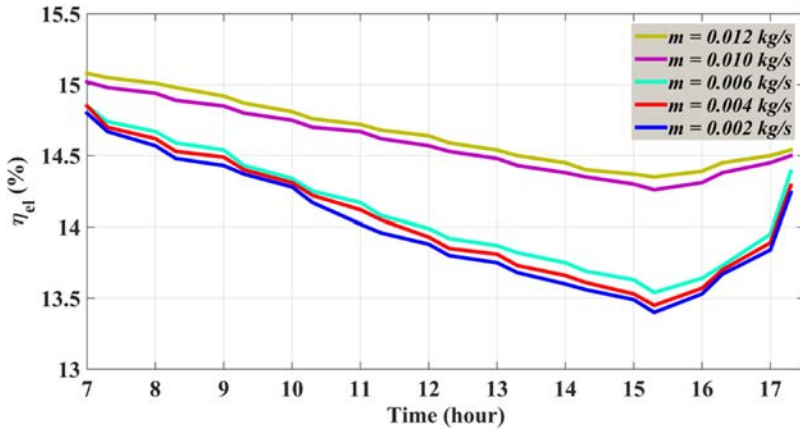**Figure 9.** Variation in PV module temperature at a distinct MFR.

Figure 10. Variation in electrical efficiency with time at a distinct MFR.

effect of MFR on the η_{Th} of PVT collector is more dominating over the temperature difference. Hence, at the greater mass flow rate, higher η_{Th} is obtained.

Table 4 presents the mean value of η_{el} and η_{Th} at distinct mass flow rates. A considerable rise in the thermo-electric outcome of the PVT is observed at a higher MFR using Copper-water as a nano-fluid. With an MFR of 0.012 kg/s, an enhancement in η_{el} and η_{Th} of approximately 6.239% and 1.645% is observed in comparison to the efficiencies at MFR of 0.002 kg/s.

Effects of volume concentration of nano-fluids

This section examines the impact of different volume fractions, i.e., 0%, 2%, and 4% of nano-fluid on the PVT module temperature. The thermo-electric output of the PVT collector is also tested. The other parameter is kept fixed at its reference values. The deviations of PV module temperature concerning the time of a particular day at distinct volume concentrations of nano-fluid are
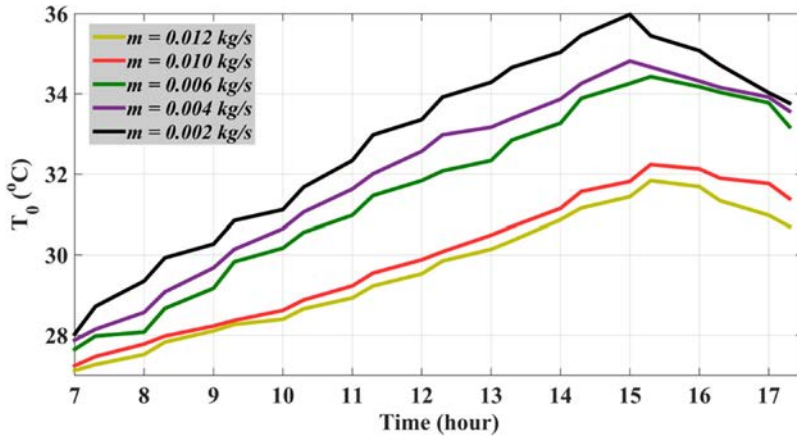
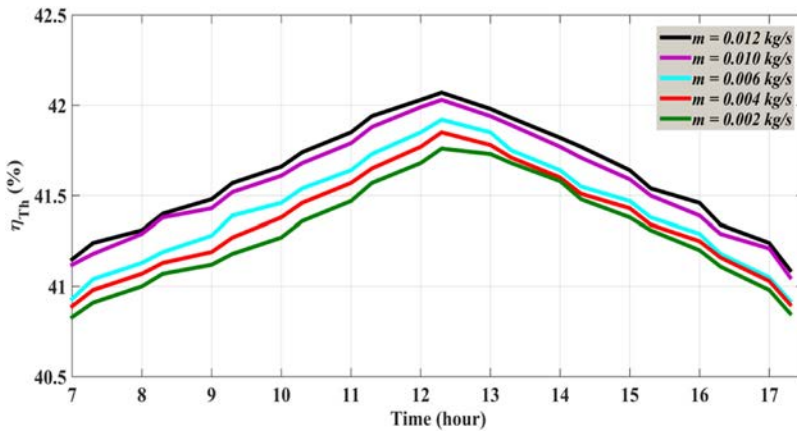**Figure 11.** Variation in outlet temperature with time at distinct MFR.

Figure 12. Thermal efficiency variation with time at a different MFR.

portrayed in Figure 13. The module temperature rises until 15:00 with the rise in the ambient temperature. It has been concluded that the module temperature decays with the increase in vol. fraction of nanoparticles in the base fluid. The crest of PV module temperature is 34.89°C, 35.24°C, and 35.38°C at 4%, 2%, and 0% vol. fraction of copper in the base fluid, respectively. At a higher volume fraction of nanoparticles, additional heat may be evacuated from the backside of the PV module; hence the heat transfer coefficient of nano-fluid rises accordingly.

The volume fraction impact of Cu on the η_{el} of the PVT collector is presented in Figure 13. As explained in equation (24) The η_{el} decays with an increase in the cell temperature. At 0% vol. fraction of nanoparticles, the η_{el} is appeared to be minimum while at 4% vol. fraction; the η_{el} is the highest The average value of η_{el} with a 4% vol. fraction of copper in water is 14.73% while deploying pure water as a coolant, and the average η_{el} is 14.48%. Hence, η_{el} of PVT collector can be enhanced at higher volume fractions of nanoparticles in the basefluid. (Figure 14)

Table 4. Average thermo-electric efficiencies at a different MFR.

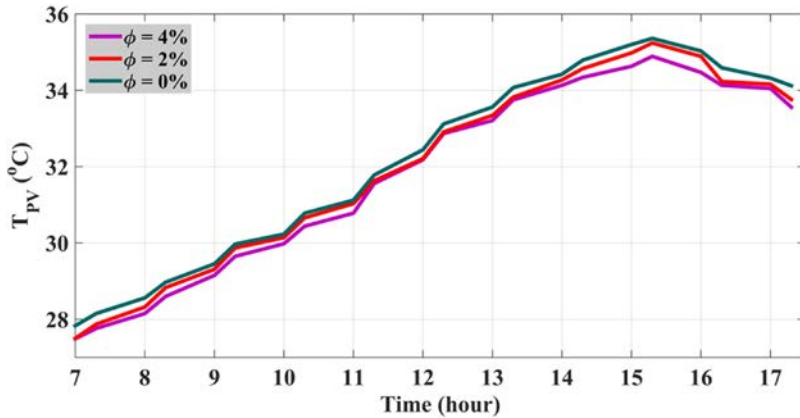| Efficiency (%)	MFR (kg/s)				
	$m = 0.012$	$m = 0.010$	$m = 0.006$	$m = 0.004$	$m = 0.002$
Avg. electrical efficiency	14.763	14.598	14.103	14.0435	13.896
Avg. thermal efficiency	41.702	41.555	41.417	41.305	41.027

Figure 13. Pv module temperature variation at a distinct volume concentration of nanoparticles.

Figure 15 portrays the PVT collector outlet temperature wrt. time at various vol. concentrations of copper in the basefluid. It is concluded that the outlet temperature of the fluid grows with an increase in the vol. fraction of nanoparticles.

This effect is summarized as: at a higher volume fraction of the nanoparticle in water, the heat transfer capacity of fluid increases. Hence, the outlet temperature of the tube is slightly higher at a higher vol. fraction of nanoparticles.

The η_{Th} variations of PVT collector at various vol. concentrations of copper are shown in Figure 16. The η_{Th} increases until 12:30 and then decreases till 17:30. The η_{Th} of PVT collectors depends upon various factors such as specific heat capacity, solar intensity, and temperature difference at the inlet/outlet of the tube. With an increase in the concentration of nanoparticles in the base fluid, the specific heat capacity increases while the temperature at the outlet of the tube decreases, and hence the temperature difference at the inlet/outlet of the tube increases. This increase in temperature difference mostly affects the η_{Th} concerning the specific heat capacity. Hence η_{Th} rises with increasing nanoparticle concentration in the base fluid.

Table 5 shows the average thermo-electric efficiencies at 0%, 2%, and 4% vol. fractions of Cu in the basefluid.

Conclusion

This study numerically investigates, the thermo-electric outcome of an hPVT using Copper-water, TiO$_2$-water, and SiO$_2$-water nano-fluid for the climatic conditions of Ghaziabad city, India.
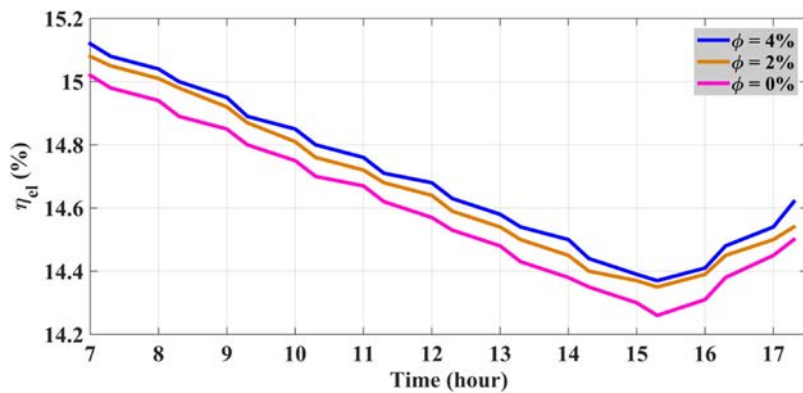
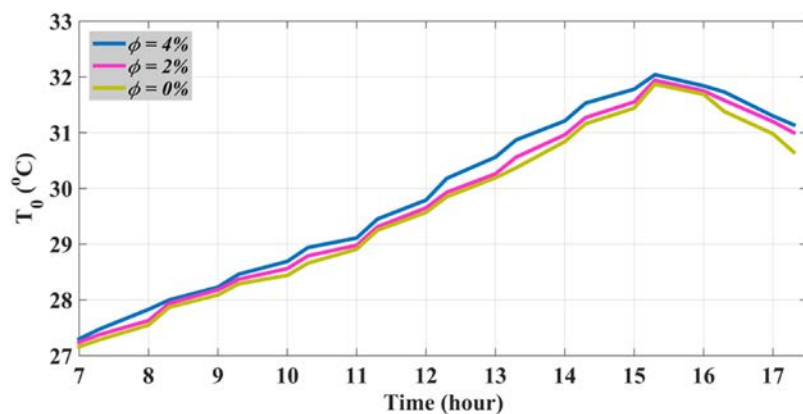**Figure 14.** Electrical efficiency with the various vol. concentrations of nanoparticle.

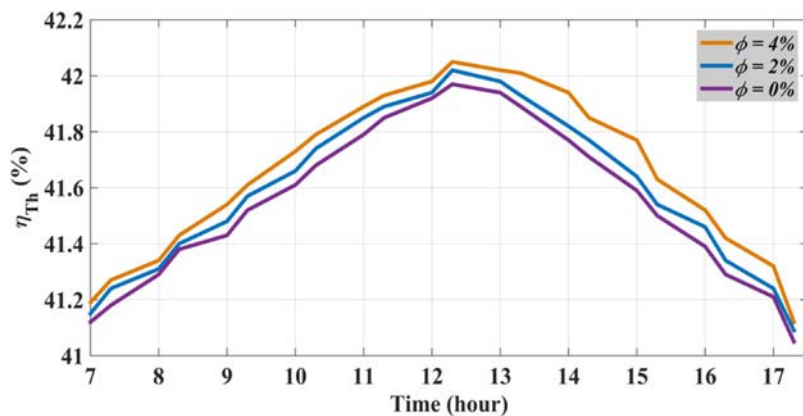**Figure 15.** Outlet temperature with different volume concentrations.

Figure 16. Thermal efficiency variations with time at distinct volume concentrations.

Table 5. Average electrical and thermal efficiencies with distinct volume concentrations.

The volume concentration of nanoparticle (ϕ)	Avg. thermal efficiency (%)	Avg. electrical efficiency (%)
$\Phi = 0\%$	41.509	14.482
$\Phi = 2\%$	41.653	14.567
$\Phi = 4\%$	41.720	14.731

Detailed mathematical modeling is presented on the basis of energy balance equations. According to the numerical analysis, the entire work is summarized as:

- The PVT collector outcomes using Copper-water as nano-fluid is significantly better in comparison to the other two nano-fluids considered in the study. Hence, Copper-water is considered as a working nano-fluid for the rest of the analysis.
- The thermo-electric outcome of the hybrid collector is grown over a higher MFR. At 0.012 kg/s MFR, enhancement of approximately 6.239% and 1.645% is observed in thermo-electric efficiencies concerning the efficiencies at the MFR of 0.002 kg/s.
- The impact of the vol. fraction of copper as a nanoparticle on the PVT collectors output is also investigated. At a 4% vol. fraction of copper in the base fluid, the average value of thermo-electric efficiency of hPVT is obtained as 41.720% and 14.731%. When pure water is deployed as a coolant, the thermo-electric efficiencies are 41.509% and 14.482%, respectively.

Declaration of conflicting interests

Funding

ORCID iD

Rajeev Kumar https://orcid.org/0000-0003-3705-2667

References

1. Al-Waeli AHA, Sopian K, Chaichan MT, et al. An experimental investigation on using of nano-SiC-water as base-fluid for photovoltaic thermal system. *Energy Conserv Manage* 2017; 142: 547–558.
2. Diwania S, Siddiqui AS, Agrawal S, et al. Performance assessment of PVT-air collector with V-Groove absorber: a theoretical and experimental analysis. *Heat Mass Transfer* 2020; 57: 665–679.
3. Al-Waeli AHA, Sopian K, Kazem HA, et al. PV/T (photovoltaic/ thermal): status and future prospects. *Renew Sustain Energy Rev* 2017; 77: 109–130.
4. Bellos E, Tzivanidis C, Antonopoulos KA, et al. Thermal enhancement of solar parabolic trough collectors by using nano-fluids and converging-diverging absorber tube. *Renew Energy* 2016; 94: 213–222.
5. Diwania S, Siddiqui AS, Agrawal S, et al. Modeling and assessment of the thermo-electrical performance of a photovoltaic-thermal (PVT) system using different nano-fluids. *J Braz Soc Mech Sci Eng* 2021; 43: 190.
6. Radwan A, Ahmed M and Ookawara S. Performance enhancement of concentrated photovoltaic systems using a microchannel heat sink with nano-fluids. *Energy Convers Manage* 2016; 119: 289–303.
7. Yousefi T, Veysi F, Shojaeizadeh E, et al. An experimental investigation on the effect of Al2O3–H2O nano-fluid on the efficiency of flat-plate solar collectors. *Renew Energy* 2012; 39: 293–301.

8. Khanjari Y, Pourfayaz F and Kasaeian AB. Numerical investigation on using of nano-fluid in a water-cooled photovoltaic thermal system. *Energy Convers Manage* 2016; 122: 263–278.

9. Hissouf M, Feddaoui M, Najim M, et al. Numerical study of a covered photovoltaic-thermal collector (PVT) enhancement using nano-fluids. *Sol Energy* 2020; 199: 115–127.

10. Michael JJ and Iniyan S. Performance analysis of copper sheet laminated photovoltaic thermal collector using copper oxide water nano-fluid. *Sol Energy* 2015; 119: 439–451.

11. Ghadiri M, Sardarabadi M, Pasandideh-fard M, et al. Experimental investigation of a PV/T system performance using nano ferrofluids. *Energy Convers Manag* 2015; 103: 468–476.

12. Sint NKC, Choudhary I, Masjuki HH, et al. Theoritical analysis to determine the efficiency of a CuO-water nano-fluid based flat-plate solar collector for domestic solar water heating system in Myanmar. *Sol Energy* 2017; 155: 608–619.

13. Sardarabadi M, Passandideh-Fard M and Heris SZ. Experimental investigation of the effects of silica/water nano-fluid on PV/T (photovoltaic thermal units). *Energy* 2014; 66: 264–272.

14. Fudholi A, Razali NFM, Yazdi MH, et al. TiO$_2$-water-based photovoltaic thermal (PVT) collector: novel theoretical approach. *Energy* 2019; 183: 305-314. doi:10.1016/j.energy.2019.06.143.

15. Al-Shamani, Sopian K, Mat S, et al. Experimental studies of rectangular tube absorber photovoltaic thermal collector with various types of nano-fluids under the tropical climate conditions. *Energy Convers Manage* 2014; 124: 528–542.

16. Moradgholi M, Nowee SM and Farzaneh A. Experimental study of using Al$_2$O$_3$/methanol nano-fluid in a two phase closed thermosyphons (TPCT) array as a novel photovoltaic/ thermal system. *Sol Energy* 2018; 164: 243–250.

17. Nasrin R, Rahim NA, Fayaz H, et al. Water/MWCNT nano-fluid based cooling system of PVT: experimental and numerical research. *Renew Energy* 2018; 121: 286–300.

18. Wole-Osho I, Adun H, Adedeji M, et al. Effect of hybrid nano-fluids mixture ratio on the performance of a photovoltaic thermal collector. *Int J Energy Res* 2020; 44: 1–18.

19. Mirzaei M and Kim KC. Effects of a mixture of Cuo and Al$_2$O$_3$ nanoparticles on the thermal efficiency of a flat plate solar collector at different mass flow rates. *Heat Transf Res* 2019; 50: 945–965.

20. Verma SK, Tiwari AK, Tiwari S, et al. Performance analysis of hybrid nano-fluids in flat plate solar collector as an advanced working fluid. *Sol Energy* 2018; 167: 231–241.

21. Salem NR, Elsayed MM, Abd-Elaziz AA, et al. Performance enhancement of the photovoltaic cells using Al2O3/PCM mixture and/or water cooling-techniques. *Renew Energy* 2019; 138: 876–890.

22. Yang X, Sun L, Yuan Y, et al. Experimental investigation on performance comparison of PV/T-PCM system and PV/T system. *Renew Energy* 2018; 119: 152–159.

23. Hosseinzadeh M, Sardarabadi M and Passandidehfard M. Energy and exergy analysis of nano-fluid based photovoltaic thermal system integrated with phase change material. *Energy* 2018; 147: 636-647. DOI: 10.1016/j.energy.2018.01.073.

24. Kandilli C. Energy, exergy and economic analysis of a photovoltaic thermal system integrated with the natural zeolites for heat management. *Int J Energy Res* 2019; 43(9): 4670-4685.

25. Manigandan S and Kumar V. Comparative study to use nano-fluid ZnO and CuO with phase change material in photovoltaic thermal systems. *Int J Energy Res* 2019; 43(5): 1882-1891.

26. Salari A, Kazemian A, Ma T, et al. Nano-fluid based photovoltaic thermal systems integrated with phase change materials. Numerical simulation and thermodynamic analysis. *Energy Convers Manage* 2020; 205: 112384.

27. Bakthavatchalam B, Habib K, Saidur R, et al. Comprehensive study on nano-fluid and ionano-fluid for heat transfer enhancement: a review on current and future perspective. *J Mol Liq* 2020; 305: 112787.

28. Chow T. Performance analysis of photovoltaic-thermal collector by explicit dynamic model. *Sol Energy* 2003; 75: 143–152.

29. Yazdanifard F, Ameri M and Ebrahimnia-Bajestan E. Performance of nano-fluid-based photovoltaic/thermal systems: a review. *Renewable Sustainable Energy Rev* 2017; 76: 323–352.

30. Guarracino I, Freeman J, Ramos A, et al. Systematic testing of hybrid PV-thermal (PVT) solar collectors in steady-state and dynamic outdoor conditions. *Appl Energy* 2019; 240: 1014–1030.

31. Diwania S, Agrawal S, Siddiqui AS, et al. Photovoltaicthermal (PV/T) technology: a comprehensive review on application and its advancement. *Int J Energy Environ Eng* 2019; 11: 33–54.

32. Xuan Y and Li Q. Investigation on convective heat transfer and flow features of nano-fluids. *J Heat Transfer* 2003; 125: 151–155.

33. Pak BC and Cho YI. Hydrodynamic and heat transfer study of dispersed fluids with submicron metallic oxide particles. *Exp Heat Transf Int J* 1998; 11: 151–170.

34. Jia Y, Ran F, Zhu C, et al. Numerical analysis of photovoltaic-thermal collector using nano-fluid as a coolant. *Sol Energy* 2020; 196: 625–636.

35. Bellos E, Said J and Tzivanidis C. The use of nano-fluids in solar concentrating technologies: a comprehensive review. *J Cleaner Prod* 2018; 196: 84-99. DOI: 10.1016/j.jclepro.2018.06.048.

Appendix

Notation

A_c	area of collector [m^2]
c_p	heat capacity of fluid [J/kg^{-1}.K^{-1}]
d	nanoparticle diameter [m]
D_{in}	inner tube diameter [m]
D_{out}	outer tube diameter [m]
f	coefficient of friction, dimensionless
G	incident solar radiation [W/m^2]
h	air heat transfer coefficient [W/m^{-2}.K^{-1}]
H	conductive heat transfer coefficient [W/m^{-2}.K^{-1}]
L_c	tube length [m]
m	mass flow rate of fluid [kgs^{-1}]
N_u	nusselt number, dimensionless
P	packing factor of the cell
Pe	peclet number, dimensionless
Pr	prandtl number, dimensionless
Re	reynolds number, dimensionless
T	temperature [K]
V_f	volume flow rate [m^{3}sec^{-1}]
v_w	wind speed [msec^{-1}]
W	distance from tube to tube [m]

Subscript

air	layer of air
Ab	absorber layer
bf	base fluid
cell	photovoltaic cell
g	glass cover
ins	insulation layer
nf	nanofluid

pv   photovoltaic module
t   tube
th   thermal

Greek symbols

α absorptance
ρ density [kg.m^{-3}]
η_0 efficiency at STC [%]
η_{el} electrical efficiency [%]
η_{PVT} overall efficiency [%]
β_0 temperature coefficient of efficiency
λ thermal conductivity [Wm^{-1}K^{-1}]
η_{Th} thermal efficiency [%]
δ thickness [m]
υ viscosity of fluid [Pa.s]
ϕ volume fraction of nanoparticles

Abbreviations

HTC   heat tansfer coefficient
hPVT   hybrid Photovoltaic-thermal
PCM   phase change material
PV   photovoltaic
MWCNT   multi-walled carbon nanofluid
HTF   heat transfer fluid

Case Report on Antiphospholipid Antibody: Asherson Syndrome

**Ms. Rohini Moon[1], Ms. PriyaRewatkar[2], Aniket Pathade[3],S. G. Kadwane[4]
, Miss. Kanchan Bokade[5]**

1] GNM 2nd year Florence Nightingale Training college of Nursing, Datta Meghe Institute of medical science (DU) Sawangi (M) Wardha
Email: rohinimoon23@gmail.com, Mob. No. 7774917239
2] Nursing Tutor, Florence Nightingale training college of nursing, Datta Meghe Institute of medical science (DU) Sawangi (M) Wardha
Email: priyarewatkar92@gmail.com, Mob. No. 90491215402
3] Research Scientist, Jawaharlal Nehru Medical College, Datta Meghe Institute of Medical Sciences, Sawangi (M), Wardha, Maharashtra, India.
4] Dept. of Electrical Engineering, Yeshwantrao Chavan College of Engineering, Nagpur. Email: psp4india16@gmail.com
5] Clinical Instructor, ShrimatiRadhikabaiMeghe Memorial College of Nursing, Email:kanchanbokade31@gmail.com

Abstract
Introduction: Thromboses in the arterial and venous systems characterize the antiphospholipid syndrome (APS).in the arterial, venous, or minor artery. as well as pregnancy morbidity, when antiphospholipid antibody titers are chronically increased. Since virtually any organ can be involved, the clinical presentation of APS is very varied. Abdominal manifestations are rare but may be life-threatening, and include Budd-Chiari Syndrome.We discuss a 26-year-old lady with primary APS brought toIn March 2017, the Bangabandhu Sheikh Mujib Medical University (BSMMU) in Dhaka, Bangladesh, was established., on aspirin medicationwith ascites for which she had been receiving treatment for abdominal tuberculosis. Following clinical and laboratory evaluation, she was diagnosed as a case of Budd-Chiari Syndrome with portal hypertension and initiated treatment with warfarin.
Main Symptom and/ or important clinical finding:25-year-old female admitted in Acharya vinobaBhave Rural hospital on date 7-07-21 with the chief complaint of excessive breathing, weakness, fatigue, high blood pressure, headache blood clot etc. After physical examination & investigation doctor diagnose a case of Antiphospholipid antibody syndrome.
The main diagnoses, therapeutic interventions, and outcome: After physical examination and investigation doctor diagnose a case antiphospholipid antibody syndrome medical management was provided to the patient calcium &multivitaminsupplementary was given for 7 days to enhance immune function. Tab. Valproate 1.5 mg. Anticoagulant.Tab. Atenolol 50mg.beta blocker. Tab. Vit. B12 for supplementary he was taking all treatment and outcome was good.
Conclusion: She was response to all medication as well as doctor treatment and her recovery was good.

Keyword: Aortic Thrombosis, Cerebral Infarcts, β2 Glycoprotein 1 antibodies, Ascherson's syndrome.

Introduction:
Antiphospholipid antibody syndrome (APLA) is a complicated illness that affects both men and women. that is rarely seen in everyday practice. APLA is a fairly varied disease with a wide range of clinical manifestations. [1,2,3]
The prevalence Antiphospholipid antibody syndrome is defined as thromboembolic issues in the presence of regularly increased antiphospholipid antibody titers, and/or pregnancy morbidity. It can manifest in a variety of ways and affect any organ, and it is currently affecting most surgical and medical professions. [4,5,6]
Antiphospholipid syndrome causes microangiopathy, which affects small blood arteries throughout the body. The majority of individuals develops thrombocytopenia, with hemolytic Anaemia and disseminated intravascular coagulation occurring less commonly. Antibodies against the most prevalent antibodies linked to CAPS have been found as lupus anticoagulant and anticardiolipin. [7,8]

2346

Clinical signs of APS are generally non-specific in the if there hasn't been a thrombotic incident,we recently saw a young man who had recently been diagnosed with hypertension and kidney disease. who had primary APS. His kidney biopsy findings, which revealed chronic microangiopathy features under electron microscopy, Multiple organ involvement and a triple-positive antiphospholipid antibody profile later validated the diagnosis of APS. [9,10] Anti-beta-2-glycoprotein 1 The most commonly implicated antibodies include antibodies, lupus anticoagulant, and anti-beta-2-glycoprotein 1 antibodies. and anticardiolipinantibody.1 and anticardiolipin antibody are the most often implicated antibodies. Anticoagulant activity is the primary function of these antibodies. These antibodies, contrary to their name, are linked to a Rather than a bleeding diathesis, this is a procoagulant disorder. Antiphospholipid (APL) bind to membrane plasma proteins. causes them to be activated chain reaction involving A prothrombotic state is caused by a combination of molecules are all involved in the healing process. While the popular belief is that thrombosis is the primary cause of APS, the importance of atherosclerosis should not be overlooked. [11,12]

Discovery of antibodies and our understanding of the syndrome's pathobiology We suggest a method to explain how anti-beta2-glycoprotein I antibodies have been associated to a number of different diseases of clinical conditions. The occurrence of thrombo-embolic problems and Anti-phospholipid antibody (APLA) syndrome is defined as Pregnancy morbidity in the presence of anti-phospholipid antibody (APLA) syndrome titers that are constantly growing. It can affect any organ and has a wide range of clinical symptoms. making it a contemporary concern. in a wide range of surgical and medical specialties. The example of a 34-year-old woman with APLA syndrome who was diagnosed with the cerebral venous thrombosis and deep vein thrombosis of the left leg veins are discussed in this article. Three types of APLAs were found to be increased (IgG, IgM, and activated protein C). Other autoimmune or systemic disorders were not found in clinical or laboratory tests. R is being used to treat the patient. Antiphospholipid syndrome (APS) is an autoimmune disorder marked by hypercoagulability and the risk of thrombosis of all arterial bed segments of arterial and venous circulations, as well as pregnancy morbidity. Multiple organs are affected by this illness, which manifests itself in a variety of clinical symptoms. The most severe type, known as catastrophic antiphospholipid syndrome (CAPS), affects less than 1% of patients and is linked to multiple organ thrombosis. The most common signs areDVT, PE, and stroke are all examples of deep venous thrombosis. Anti-beta-2-glycoprotein 1 antibodies, lupus anticoagulant, and anticardiolipin antibody are all examples of anti-beta-2-glycoprotein 1 antibodies the most typically implicated antibodies. [12,13]

Recurrent thromboembolic events in the veins and/or the arteries, as well as pregnancy morbidity are all factors to consider. are clinical features of the syndrome. Aside from these clinical signs, the existence of a distinct set of autoantibodies directed against certain phospholipid-binding proteins is a need for the illness. The three laboratory tests evaluated in the updated version are antibodies against2-glycoprotein I (a2GPI) and cardiolipin (aCL), as well as the lupus anticoagulant functional assay (LAC). [14,15]

Patient specific information:a 25-year-old female admitted in Acharya vinobaBhave Rural hospital on date 7-07-21 with the chief complaint of excessive breathing, weakness, fatigue, high blood pressure, headache, blood clot etc. After physical examination &investigation doctor diagnose a case of Antiphospholipid antibody syndrome.

Primary concern and symptoms of the patient: chief complaint of patient excessive breathing, weakness, fatigue, high blood pressure headache bloodclots. After physical examination&investigationsdoctor diagnosea caseof antiphospholipid antibody syndrome asherson syndrome.

Relevant past interventions with outcome: History of antiphospholipid antibody syndrome   6 month back for which she was hospitalized. After CBC test, LFT test & other in Asherson syndrome was observed he took all support to treatment & his outcome was good.

Clinical finding: The patient was conscious &well oriented to time, place, date his body build was moderate &he had maintained good personal hygiene. Her weight 45 kg his in-milestone development the patient is anemic.

Timeline: 6 monthsago, he was admitted in the hospital Antiphospholipid antibody syndrome is treated with this drug. He is currently being treated for antiphospholipid antibody syndrome. currently he was admitted for the treatment of antiphospholipid antibody syndrome calcium and multivitaminsupplementary was given for 7 days. To enhancement function.

Diagnostic assessment: On the basis of the of patient's history collection, physical examination, CBS blood test investigation was also done WBC count (20,000/cumm) less than normal platelets count was less 1.57 lacs commandhemoglobin was less 7.5 and other investigation was also done.

Diagnostic challenges: No any challenging during the diagnostic evaluation.

Diagnosis: After physical examination &Investigation doctor diagnosed a case of antiphospholipid antibody Asherson syndrome.

Prognosis: was good.

Therapeutic interventions: Medical management was provided to the patient calcium &multivitaminsupplementary was given for 7 days to enhance immune function. Tab.Valproate1. 5mg.Anticoagulant. Tab. Atenolol 50mg.beta blocker. Tab. Vit. B12 for supplementary she was taking all treatment and outcome was good. No any change in restorative.

Follow-Up &Outcome:

Clinical &patient assessment Outcome:

Patient conditions was improved important check out investigation and other test results to preventing to progression of disease &trying to reserve any sign & symptoms doctor advice to follow up blood investigation & other examination to know the disease progression.

Interventions Adherence&Tolerability: patient took all prescribed medications regular. But sometimes he was refused to take medication. He also followed the dietician advised. Dietician was advised healthy food &rich in calcium &multivitaminsupplementation. Her interventional adherence was satisfactory.

Nursing perspective:Monitor the vital signs of patient person hourly. Multifluid and electrolytes balance.

Discussion:

APS is a type of autoimmune disease that causes thrombosis in the arteries and veins, as well as recurrent foetal loss and thrombocytopenia. It was first discovered It was first discovered in people with SLE (systemic lupus erythematosus), which was later connected to other autoimmune disorders Primary APS is another name for this condition. which is a syndrome that can arise without any underlying disease. CAPS, a deadly variation of APS that affects about 1% of the population, was initially identified in 1992. (7) APS is a thrombotic autoimmune disease that manifests itself in a variety of ways. For the diagnosis of definite APS, at least one clinical and one laboratory criterion is required. [16]

Based on HIRA data, which is a statewide required insurance programme offered by the Korean government, this is the first nationwide population-based investigation of the incidence, prevalence, and related consequences of APS. In contrast to a prior population-based investigation, our findings revealed that the incidence rate of APS varied by gender and age group.Anionic phospholipids are antigenic bilaminar phospholipids that are found on the inner sides of membranes. Accessory proteins like beta-2 glycoprotein I, on the other hand, may help to speed up and stabilize the shift to hexagonal antigenic forms. Antiphospholipid antibodies are thought to be made up of a variety of proteins. of antiphospholipid I combination of antibodies and anti-beta-2 glycoprotein antibodies, Or I complex, or antibodiesand anti-beta-2 glycoprotein antibodies against phospholipids exclusively. [16]

The phrase APLA syndrome refers to the clinical link between APLAs and a hypercoagulability syndrome. It's an autoimmune condition marked by thromboembolic issues and pregnant morbidity. Antibodies to are the most often identified subgroups of APLAs. Rather than clinical bleeding, Thromboembolic events have been associated to lupus anticoagulant antibodies. Both pro- and anti-coagulant pathways can be disrupted by APL. [15]

Sarcoidosis Expression Antiphospholipid antibody syndrome (APS), sarcoidosis, and systemic lupus erythematosus (SLE) are chronic immunological dysregulation illnesses. causes are unknown in the previous 60 years, only a few incidences of Individuals have been diagnosed with sarcoidosis and SLE. In this investigation, we present two cases with sarcoidosis and SLE that coexisted, with problems linked to Anticardiolipin antibodies were found in both cases. Clinical, serological, and pathological information are all available in each case confirmed the diagnoses, and both patients responded well to treatment. The relationship between sarcoidosis, SLE, and APS is unusual, and it can make treatment challenging. Thrombosis manifests itselfDVT, pulmonary thromboembolism, and stroke are all examples of thromboembolism in people with APS. Valvular illness and intracardiac thrombus development are the most common cardiac symptoms of APS. Only 4% of the time does a myocardial infarction occur Autoimmune illnesses, such asChronic inflammation is recognized to promote early atherosclerosis in Systemic lupus erythematosus, rheumatoid arthritis, systemic sclerosis, and other autoimmune illnesses and APS. While the role of APL antibodies in an etiology of thrombosis in APS is well understood, the existence of certain cardiovascular risk factors or medical conditions in these patients increases the risk of thrombosis. [17]

Conclusion: -Traditional cardiovascular risk factors have been shown to substantially enhance the risk of thrombosis and atherosclerosis time and time again. Due to the existence of Antibodies against APL and chronic inflammation, both of which lead to early atherosclerosis Thrombotic loadis already high in APS patients. To prevent future endothelial and vascular damage, primary care physicians must be vigilant in identifying and actively managing conventional risk factors. To treat diabetes, hypertension, and obesity, Strict dietary and physical activity modifications are required. Furthermore, In the elderly, women, and diabetics, silent myocardial infarction is

prevalent Further more silent in the elderly, women, and diabetics. A common concern is myocardial infarction. Quitting smoking is another way to reduce the progression of atherosclerotic disease. To achieve improved patient outcomes, a multidisciplinary strategy combining primary care doctors, for coordinated management of these patients, hematologists and cardiologists are essential.

Reference:

1. Naik SN, Raghavendra Y. Antiphospholipid antibody syndrome-A case report. Ayu. 2017 Jan;38(1-2):62.
2. Luma HN, Doualla MS, Temfack E, Bagnaka SA, Mankaa EW, Fofung D. The antiphospholipid antibody syndrome: a case report. International medical case reports journal.
3. Strakhan M, Hurtado-Sbordoni M, Galeas N, Bakirhan K, Alexis K, Elrafei T. 36-year-old female with catastrophic antiphospholipid syndrome treated with eculizumab: a case report and review of literature. Case reports in hematology. 2014 Oct 15;2014.
4. Tsiakas S, Skalioti C, Kotsi P, Boletis I, Marinaki S. Case of an unusual diagnosis of primary antiphospholipid syndrome with multiple clinical complications. Oxford medical case reports. 2020 Dec;2020(12): omaa117.Parsi M, Rai M, Swaab R. A
5. Rare Case of Catastrophic Antiphospholipid Antibody Syndrome: A Case Report and Review of Traditional Cardiovascular Risk Factors Implicated in Disease Occurrence. Cureus. 2020 Mar;12(3).
6. Durrani, O. M., Gordon, C., & Murray, P. I. (2002). Primary anti-phospholipid antibody syndrome (APS): current concepts. Survey of ophthalmology, 47(3), 215-238.
7. M. Hurtado-Sbordoni, N. Galeas, K. Bakirhan, K. Alexis, T. Elrafei, M. Hurtado-Sbordoni, N. Galeas, K. Bakirhan, K. Alexis, T. Elrafei, M. Hurtado-Sbordoni, N. Galeas, K. Bakirhan, K. Alexis, T. A case report and literature review of a 36-year-old woman who was treated with eculizumab for catastrophic antiphospholipid syndrome. Hematology Case Reports, published online October 15, 2014, is a journal that publishes case reports in the field of haematology.
8. Tsiakas S, Skalioti C, Kotsi P, Boletis I, Marinaki S. Case of an unusual diagnosis of primary antiphospholipid syndrome with multiple clinical complications. Oxford medical case reports. 2020 Dec;2020(12): omaa117.
9. CastañedaOspina SA, Cardona Maya WD, Bueno Sánchez JC, Cadavid Jaramillo ÁP. Pregnancy outcome in women with antiphospholipid syndrome and alloimmunity: a case report. Sao Paulo Medical Journal. 2003; 121:248-50.
10. Naik SN, Raghavendra Y. Antiphospholipid antibody syndrome-A case report. Ayu. 2017 Jan;38(1-2):62.
11. Pashnina, I. A., Krivolapova, I. M., Fedotkina, T. V., Ryabkova, V. A., Chereshneva, M. V., Churilov, L. P., &Chereshnev, V. A. (2021). Antinuclear autoantibodies in health: autoimmunity is not a synonym of autoimmune disease. Antibodies, 10(1), 9.
12. Mohammad, S., Bhute, A., Acharya, N., Acharya, S., 2020b. Moschcowitz syndrome or thrombotic thrombocytopenic purpura and antiphospholipid antibody syndrome as a rare cause of thrombocytopenia in pregnancy mimicking hemolysis, elevated liver enzymes, and low platelets syndrome in a patient with bad obstetric history: A diagnostic dilemma. Journal of SAFOG 12, 250–253. https://doi.org/10.5005/jp-journals-10006-1791
13. Abbafati, Cristiana, Kaja M. Abbas, Mohammad Abbasi, Mitra Abbasifard, Mohsen Abbasi-Kangevari, HedayatAbbastabar, Foad Abd-Allah, et al. "Five Insights from the Global Burden of Disease Study 2019." LANCET 396, no. 10258 (October 17, 2020): 1135–59.
14. Abbafati, Cristiana, Kaja M. Abbas, Mohammad Abbasi, Mitra Abbasifard, Mohsen Abbasi-Kangevari, HedayatAbbastabar, Foad Abd-Allah, et al. "Global Burden of 369 Diseases and Injuries in 204 Countries and Territories, 1990-2019: A Systematic Analysis for the Global Burden of Disease Study 2019." LANCET 396, no. 10258 (October 17, 2020): 1204–22.
15. Franklin, Richard Charles, Amy E. Peden, Erin B. Hamilton, Catherine Bisignano, Chris D. Castle, Zachary Dingels V, Simon Hay I, et al. "The Burden of Unintentional Drowning: Global, Regional and National Estimates of Mortality from the Global Burden of Disease 2017 Study." INJURY PREVENTION 26, no. SUPP_1, 1 (October 2020): 83–95. https://doi.org/10.1136/injuryprev-2019-043484.
16. James, Spencer L., Chris D. Castle, Zachary Dingels V, Jack T. Fox, Erin B. Hamilton, Zichen Liu, Nicholas L. S. Roberts, et al. "Estimating Global Injuries Morbidity and Mortality: Methods and Data Used in the Global Burden of Disease 2017 Study." INJURY PREVENTION 26, no. SUPP_1, 1 (October 2020): 125–53. https://doi.org/10.1136/injuryprev-2019-043531.

17. James, Spencer L., Chris D. Castle, Zachary Dingels V, Jack T. Fox, Erin B. Hamilton, Zichen Liu, Nicholas L. S. Roberts, et al. "Global Injury Morbidity and Mortality from 1990 to 2017: Results from the Global Burden of Disease Study 2017." INJURY PREVENTION 26, no. SUPP_1, 1 (October 2020): 96–114. https://doi.org/10.1136/injuryprev-2019-043494.

Case Report on Vesicoureteral Reflux

Ms. Rishita Maheshgavali1, Mis. PriyaRewatkar[2], Roshan Umate[3],S. P. Adhau[4]
, Miss. Kanchan Bokade[5]
1] G.N.M 2ndyear, Florence Nightingale Training College of Nursing, Datta Meghe Institute of Medical Science [DU] Sawangi [M], Wardha
E-mail: -rishitamhaisagavali@gmail.comMob: - 9049827348
2] NursingTutor,Florence Nightingale Training College of Nursing, Datta Meghe Institute of Medical Science [DU] Sawangi [M], Wardha
Email: -priyarewatkar92@gmail.com, Mob: - 9049125402
3] Research Scientist, Jawaharlal Nehru Medical College, Datta Meghe Institute of Medical Sciences, Sawangi (M), Wardha, Maharashtra, India.
4] Dept. of Electrical Engineering, Yeshwantrao Chavan College of Engineering, Nagpur. Email: aniketmunshi@gmail.com
5] Clinical Instructor, ShrimatiRadhikabaiMeghe Memorial College of Nursing, Email:kanchanbokade31@gmail.com

ABSTRACT
Introduction: -Infants and children are the most often usedvictims of vesicoureteral reflux. Infections of a urinary tract are more likely as a result of the illness, if left untreated, this condition might lead to kidney damage. In children, primary vesicoureteral It can lead to kidney damage. Primary vesicoureteral reflux affects children. Can be outgrown. The goal of treatment, which may involve medication or surgery, is to avoid kidney damage. Primary vesicoureteral reflux can be outgrown in children. The goal of treatment, which may involve medication or surgery, is to avoid kidney damage. In children, the most common congenital urological anomaly areas primary vesicoureteral reflux (VUR), It's been related to a higher Urinary tract infection (UTI) and kidney scarring both are risk, commonly known as nephropathy caused by acid reflux (RN)The most prevalent cause of RN n children is a urinary tract infection (acquired RN) or at a later stage for hydronephrosis diagnosed antenatally but without a prior UTI (congenital RN).Female children are more likely to get acquired RN, whereas male children are more likely to develop congenital RN. This finding in children could explain why males are more likely than Hypertension, proteinuria, and renal failure are all symptoms of renal failure. Females, on the other hand, are more likely to get and had a better prognosis for recurring UTI eternal reflux-Urge to urinate that is strong and Persistent when urinating, there is a burning feeling. The need to pass tiny amounts of pee frequently, cloudy urine, fever, or side pain are all indications of kidney failure (flank) or abdomen.
Main symptoms and/or important clinical findings: A patient of 1 year male admitted registration to the pediatric ward on dated 05 /07/21 with the chief complaint. Wetting the bed or losing control of bowel movements are both signs of a problem.constipation for 2 months and he developed pain abdomen and right kidney diagnosed from general physical examination and blood investigation.
The main diagnose therapeutic intervention and outcomes: The doctor identified a case of Vesicoureteral reflux after physical examination and investigation A patient of 1 year male admitted registration to the pediatric ward on dated 05 /07/21 with the chief complaint. vomiting the bed or losing control of bowel motions, constipation for 2 months and he developed pain abdomen and right kidney diagnosed from general physical examination and blood investigation.

Keywords: Vesicoureteral Reflux [VUR],pain abdomen,right kidney, ultrasound, Reflux Nephropathy.

Introduction
In young children, Urine is filtered as it travels backwards from the bladder to the kidney. called vesicoureteral reflux (VUR). VUR is a voiding cystourethrogram that also is done after a voiding cystourethrogram.be diagnosed in roughly Urinary tract infections affects 30% of children. The majority of VUR cases recover on their own; Between 20% and 30% of men have new Although only a tiny fraction of infections leads to longer renal damage,complications.VUR is caused by the breakdown Cellular differentiation and complex signaling pathways throughout development. These systems are most likely They are genetically programmed, but environmental

2334

factors may influence them.VUR manifests itself in a variety of ways, illnesses ranging from mild renal parenchymal disease to end-stage renal disease and severe renal parenchymal disease. [1,2,3]

In the general population, Vesicoureteral reflux (VUR) affects less than 1% of people. 2 In children, the prevalence of urinary tract infection (UTI) ranges from 29% to 50%.11 The kidneys are at risk of scarring when reflux is paired with a urinary tract infection (UTI) and a urinary tract infection (UTI) intrarenal reflux, Renal failure is a disease in which the kidney has come to the end of [ESRD]. Is a disease in which the renal were damaged [ESRD]. [4,5,6]

Primary VUR (vesicoureteral reflux) is a prevalent condition.urinary system defect. that is the problem usually found after an Infection of the urinary tract in children (UTI). The voiding cystourethrogram (VCUG) is a treatment that is classified from I to V, with V being the most severe, is the gold standard for identifying how acute a disease is. In patients who suffer from VUR a condition known as reflux nephropathy (RN) develops. And is often accompanied with an infection in the urinary tract (UTI)Renal scarring, on the other hand, can happen if you have a UTI without a VUR or if you have a VUR without a UTI. The evidence for the for a long time, the former has been documented in the literature, Whereas The latter has more recent evidence, especially from children with hydronephrosis diagnosed during birth who are discovered to be sick from VUR and renal scarring on post-natal evaluation. The RN is now classified as either congenital (also known as primary) or acquired (also known as modified) caused by irregular renal development, resulting in focal renal dysplasia, or acquired, resulting in focal renal dysplasia. induced by renal harm caused by pyelonephritis. [7,8,9]

Vesicoureteral reflux (VUR) may be suspected when the upper urinary tract is a tube connected the urethra to temporarily dilated Observed synced with the emptying of the bladder during pregnancy.Approximately 10% of the newborns with prenatally identified the effect of dilatation of the upper urinary tract will be felt. a urinary tract infection. Experience reflux after birth. It is important to highlight that VUR cannot be detected during pregnancy. Unless complicated by a urinary tract infection, there are no specific signs or symptoms associated with VUR (UTI). To put it another way, unless VUR has caused a kidney infection, it is almost always asymptomatic (febrile UTI). Irritability, a high fever that persists, and a feeling of being bored are among the A neonate's clinical manifestations ofa febrile UTI. could display in cases of VUR and febrile UTI caused by a serious underlying urinary tract abnormality, antibiotic should be used, symptoms include Respiratory distress, failure to thrive, renal failure, flank masses, and urinary ascites are all signs that you should be aware. [10,11,12]

Symptoms of Vesicoureteral reflux

Urge to urinate it is strong & persistent.The need to pass small amounts of urine frequently.

Urine that is cloudy.Fever, pain in your side (flank) or abdomen.

Patient Specificinformation: -A patient of 1 year male admitted registration to the pediatric ward on dated 05 /07/21 with the chief complaint. Wetting the bed or losing control of bowel motions, constipationfor 2 months and he developed pain abdomen and right kidney. All diagnosis like ultrasound-ray, CT scan, blood examination a voiding cysto -urethrogram (VCUG) and all other investigation are done. His blood pressure is normal 87/105mmhg, pulse 130bpm, patient was conscious and disoriented

Primary concern and Symptoms ofthe patient: Patient visited in A.V.B.R.H hospital on dated 05/07/21 with chief complaint of pain in abdominal for 2 month then He developed pain in his right kidney.

Medical, family and psycho-social history: A case of Vesicoureteral reflux (VUR) was diagnosed by the general physical examination and investigation.Patient belonged to a middle class, nuclear family .He was not mentally stable ,he was Disoriented to date, time and place Patient has a good relationship with his family members.

Relevant past intervention with outcomes: History of Vesicoureteral reflux since at the birth back for which he was hospitalized for 15 days after investigation was observed he took treatment for that and his outcomes was good.

Clinical findings: -bowel and bladder movement is not proper, swelling over kidney, urinary tract infection. State of health was unhealthy, thin body build, the height 77 cm and weight7.5kg vital signs normal, heart sound abnormal, breathing difficulty.

Timeline: Patient was visited in AVBRH hospital on OPD base with chief complaint of Wetting the bed or losing control of bowel motions, constipation for 2 months and he developed pain abdomen and right kidney diagnosed.

Diagnostic assessment: On the basis of patient history, physical examination, CT scan, ultrasound, x-ray, blood examination a voiding cysto -urethrogram.

Diagnostic challenging: No any challenges during diagnostic evaluation.

Diagnosis: After physical examination and this investigation CT scan, ultrasound, x-ray blood examination a voiding cysto -urethrogram doctor diagnoses the patient having Vesicoureteral reflux.

Prognosis: Case of prognosis was satisfied

Therapeutic intervention:
Medical management was provided to the patient injection Emset 1mg, injection pan top 7mg syp.paracetamol 4 ml.He was took all the treatment and the outcomes was good. His sign symptoms were reduced, he was able to him own activities.No change in therapeutic interventions.

Follow up and outcomes: -
Clinical and patient assessmentoutcomes: Patient had a history pain in abdominal for 2 months pain in abdomen and swelling over right kidney.

Adverse and unanticipated event: No adverse event was noted

Discussion: -In early children, VUR, a congenital defect defined by unilateral or bilateral urine reflux from the bladder to the kidneys, is prevalent. After a UTI, a routine voiding cystourethrogram found 30 percent of children under the age of 5 to have VUR, Prenatal mortality varies from 9% to 20%. hydronephrosis with VUR is discovered postnatally. VUR, for the most part, resolves it. Only about 20% to 30% of people is becoming sick again, and only about 20% to 30% of those who are already infected will become infected again. a small proportion will have long-term kidney consequences. discovered of renal scarring is widely established to be linked to the severity of VUR. According to Chen et al., renal scarring was linked to an VUR diagnosis at an older age (five years), a greater VUR grade, anda greater incidence of UTIs. Swirlersson et al. discovered a link between Renal dysplasia, high-grade VUR, and male sex in a similar study. As a result, early detection and treatment of VUR should be preferred in efforts to prevent renal scarring. At the age of ten, our kid was diagnosed with ASB without a history of febrile UTI. Among other things, he had bladder and bowel problems, as well as high-grade VUR and CKD This unusual example of can explain the relation between VUR and CKD, which should not be avoided until later in life. Finally, in male patients with ASB, a thorough radiological imaging study It's probably a good idea to look into it. [13,14,15]

A malfunction of the ureterovesical valve mechanism develops VUR.VUR is classified into five groups based on the international VCUG grading criteria.The kidneys were affected to mild VUR.According to Kamil's research, 80 percent of people who have primary VUR don't need surgery. Only severe VUR has clinical relevance. since it increases risk severe kidney damage if a urinary tract infection occurs. Unless VUR is combined with a urinary tract infection, it may not present with any clinical symptoms or cause any specific symptoms. As a result, asymptomatic VUR can cause long-term kidney damage. After our prenatal observation of grade IV VUR, we performed frequent. Urinary tract infection (UTI) and VURfollow-up examinations after the birth. It indicates that a severe VUR diagnosis by prenatal ultrasound can provide useful information. Earlyadvice for treating and preventing kidney damage after birth. [16]

Hypertension has been associated with VUR stands for ureteropelvic Obstruction at the junction, multicystic dysplastic kidney, and posterior urethral valves are all possible reasons.In children, one of the most common causes of severe hypertension is bulging veins.VUR was found with between 29% to 50% of children with UTIs.And it was generally first sign . Hypertension was found to be more common primary vesicoureteral reflux in children as they became older: 1.7 % in children 1.8 % in children aged 1 to 9.9 years, 4.7 % between the ages of 10- and 14.9-years children between the ages of 15 and 19, 9 years and children aged >20 years. At 30 and 22 As according estimations, 50% of patients with unilateral and bilateral renal There would be harm be hypertensive by the age of 50. Hypertension has been linked to Renal scarring is frequent, and VUR makes it even worse. [17]

Conclusion:
The patient was admitted in AVBR hospital with chief complain of Wetting the bed or losing control of bowel motions, constipation for 2 months and he developed pain abdomen and right kidney diagnosed

After all investigation patient was diagnosed a case of Vesicoureteral reflux In our case stresses the need for good clinical assessment, good nursing care by trained nurses and the use of effective forensic studies is compulsory to secure patient form such a vital health conditions.

Reference:
1. Alexander SI, Craig JC. Vesicoureteral reflux. Journal of the American Society of Nephrology. 2008 May 1;19(5):8847-62
2. Moorthy I, Easty M, McHugh K, RidoutD, L, Gordon I. The presence of vesicoureteric reflux does not identify a population at risk for renal scarring following a first urinary tract infection. Archives of disease in childhood. 2005 Jul 1;90(7):733-
3. Mattoo TK. Vesicoureteral reflux and reflux nephropathy. Advances in chronic kidney disease. 2011 Sep 1;18(5):348-54.

4. MATTOO, Tej K. Vesicoureteral reflux and reflux nephropathy. Advances in chronic kidney disease, 2011, 18.5: 348-354.
5. Choi YD, Lee JH, Lee JW. Unusual Case of Vesicoureteral Reflux and Chronic Kidney Disease in a 10-Year-old Boy with Asymptomatic Bacteriuria. The Ewha Medical Journal. 2021 Apr 30;44(2):46-9
6. Zhang T, Wu S. Prenatal ultrasound diagnosis of 1 case of vesicoureteral reflux. Quantitative imaging in medicine and surgery. 2016 Jun;6(3):320.
7. SANDAL, Shaifali; KHANNA, Apurv. Vesicoureteral reflux, a scarred kidney, and minimal proteinuria: an unusual cause of adult secondary hypertension. Case reports in medicine, 2011, 2011.
8. Bhokardankar, Prashant S., and Bharat Rathir. "Indigenous Wisdom of Ayurvedic Drugs to Treat Urinary Tract Infections." INTERNATIONAL JOURNAL OF AYURVEDIC MEDICINE 11, no. 3 (September 2020): 370–77.
9. Jankar, Jayshri Sadashiv, KumudNamdeorao Harley, Kanchan ManoharraoMohod, and Vijay Yashwantrao Babar. "Association of Urinary Albumin with HbA1c Levels in Subjects of Type 2 Diabetes Mellitus in Central India." JOURNAL OF EVOLUTION OF MEDICAL AND DENTAL SCIENCES-JEMDS 9, no. 52 (December 28, 2020): 3921–25. https://doi.org/10.14260/jemds/2020/859.
10. Wadekar, Abhijit, Yash Gupte, ParthGodhiwala, Swapnil Lahole, Sachin Agrawal, and Sunil Kumar. "Emphysematous Cystitis an Unusual Case of Urinary Tract Infection in Long Standing Rheumatoid Arthritis: A Case Report." MEDICAL SCIENCE 24, no. 105 (October 2020): 2993–96.
11. Palkrit S, Naqvi WM, Burhani T. Physiotherapeutic Approach in Stress Urinary Incontinence with Prolapsed Uterus: A Case Report. JOURNAL OF PHARMACEUTICAL RESEARCH INTERNATIONAL. 2021;33(34A):54–9.
12. Bele AW, Qureshi MI. Impact of Electrotherapy or Muscle Training on Quality of Life in Urinary Incontinence of Male Geriatric Population-A Protocol. JOURNAL OF CLINICAL AND DIAGNOSTIC RESEARCH. 2021 Mar;15(3).
13. Bhayani, P., Rawekar, R., Bawankule, S., Kumar, S., Acharya, S., Gaidhane, A., Khatib, M., 2019. Profile of urinary tract infection in a rural tertiary care hospital: Two-year cross-sectional study. Journal of Datta Meghe Institute of Medical Sciences University 14, 22–26. https://doi.org/10.4103/jdmimsu.jdmimsu_87_18
14. Chadha, A., Salve, M., Bapat, A.V., 2020. Evaluation of the correlation between spot urinary protein/creatinine ratio and serum uric acid and its association with feto-maternal outcome in hypertensive pregnancy. International Journal of Current Research and Review 12, S-35-S-37. https://doi.org/10.31782/IJCRR.2020.SP77
15. Chandi, D.H., Bankar, N., Ambad, R.S., Singh, B.R., 2020b. Urinary tract infection by esherichia coli in patients attending tertiary care hospital of central India. Journal of Critical Reviews 7, 1089–1092. https://doi.org/10.31838/jcr.07.08.228
16. Kasatwar, P., Bele, A., Dhankar, S., Naqvi, W., 2020. Comparative study of effect of vaginal cones as a biofeedback device and pelvic floor exercises in rural females with urinary incontinence. Journal of Datta Meghe Institute of Medical Sciences University 15, 36–39. https://doi.org/10.4103/jdmimsu.jdmimsu_181_19
17. 549.	Khandelwal, S., Tayade, S., Gode, C., 2020. Prediction of pre-eclampsia by urinary calcium and creatinine ratio. International Journal of Current Research and Review 12, 19–22. https://doi.org/10.31782/IJCRR.2020.SP69

Management and outcome of Cystocele with Rectocele

[1]Ms. Bhawana Dhanvij,
Nursing Tutor,Florence Nightingale Training college of nursing ,Sawangi (M) ,Wardha; Email id: dhanvijbhawna@gmail.com, Ph. No: 8378025836

[2] Roshan Umate,
Research Scientist, Jawaharlal Nehru Medical College, Datta Meghe Institute of Medical Sciences, Wardha.

[3]Bharat S. Sudame,
Dept. of Electrical Engineering, Yeshwantrao Chavan College of Engineering, Nagpur. Email: bharat_sudame@rediffmail.com

[4]KavitaGomase, Assistant Professor, Dept of Obstetrics and Gynecology Nursing,Smt. RadhikabaiMeghe Memorial College of Nursing, kavitapravin3@gmail.com

ABSTRACT:

INTRODUCTION:A cystocele is a condition in which a portion of the bladder wall protrudes the vaginal canal is a tube that connects the uterus to the vaginal. The bulge is caused by a hole in the wall between the bladder and the vaginal canal. Cystocele. Nucleus Medical Media, Inc. is a company that specialises in medical publishing. A rectocele occurs when a portion of the rectum wall bulges into the vaginal canal. The pelvic organs are separated by connective tissue. Fascia is a connective tissue that connects neighbouring muscles. The bladder, vagina, and rectum are all supported by fascia and muscles. Cystocele and Rectocele are both caused by defects in the fascia. A cystocele is a malformation of the fascia connecting the bladder and the vaginal canal. A portion of the bladder wall bulges the uterine canal is a tube that connects the uterus to the vaginalas a result of this. Cystocele is divided into three categories: mild, moderate, and severe cystocele. Grade 1—the mildest kind, in which the bladder merely protrudes partially into the vaginal canal. Grade 2: The bladder has descended far enough to reach the vaginal entrance in the moderate type. Grade 3—the most severe version, in which the bladder protrudes through the vaginal opening.

Present Complaints and Investigation: Something coming out of vaginanot feeling bladder relief immediately,frequent urinary tract infection,heaviness in vagina.

Past History: No history of medical and surgical illness, no history previous hospitalization.

The main diagnosis, therapeutic intervention and outcome: A case was diagnosed after a physical examination and investigation Cystocele and rectocele with procedentia with cervical elongation for further management included inj.c-tax,inj.pan,inj.metro,t-bact ointment,tab-iron,tab-calcium,inj.pause, She was took all treatment and outcomes was good.

Conclusion: In order to treat cystoceles successfully, both lateral and central flaws must be evaluated, as poor treatment of either defect will result in recurrence. Rectocele is a more difficult condition to treat.

Keywords: Cystocele, Rectocele,Vagina,prolapse

Introduction:

The pelvic floor's muscles and connective tissues keep the pelvic organs in place, including the bladder, uterus, and intestines. Anterior prolapsedWhen the pelvic floor gets weak or overused, this happens. This might occur over time, for example, following vaginal childbirth, long-term constipation, a hard cough, or heavy lifting. Anterior prolapsed can be treated. Nonsurgical treatment is generally helpful for mild or moderate prolapsed. Surgery may be required in more severe situations to retain the vaginal and other pelvic organs in their normal locations.

Pain is the most prevalent and unavoidable complication of surgery, and it might suggest cardiac (tachycardia, hypertension), respiratory (atelectasis, pulmonary infections, and arterial hypoxia), and gastrointestinal (decreased stomach uptake, decreased stomach uptake, and decreased stomach uptake, decreased stomach uptake, decreased stomach uptake, decreased stomach uptake, decreased stomach uptake, decreased stomach uptake, decreased stomach uptake, decreased stomach uptake, decreased paralysed intestine) issues movement, and ileus), and finally urinary incontinence. Identifying and controlling the source of pain after surgery is one of the most difficult challenges.[1]Thelevatorani muscle and the apical descent abnormalities have been linked to Prolapse of the anterior

and posterior vaginal walls. The proportional roles of these factors to descending pathophysiology in distinct vaginal compartments, however, are unknown. In addition, the symptoms of prolapse in these compartments are not well understood.[2]Rectocele and cystocele surgery is typically performed in a hospital setting under a regional (spinal or epidural) or general anaesthetic, with patients spending one or two days. It's enticing to undertake the operation as an outpatient treatment with less bleeding and pain, no surgical support, quick discharge, and, most significantly, no compromise in postoperative results. There have been no research that we are aware of looked into the relationship between rectocele and cystocele. Cystoceles, rectoceles, and enteroceles (all other cystoceles, rectoceles, and enteroceles), uterine and vaginal cysts, and Rectoceles, enteroceles, and uterine and vaginal rectoceles are all examples of rectoceles cysts were also excluded. Cystocele and rectocele recur in the mid-vaginal plane were the most important outcome factors.[4]Female patients over the age of 30 who were having cystocele and rectocele repair surgery, treatment, or oral contraceptive pills were included in the study. Chronic diseases include diabetes, hypertension, hepatic or renal failure, and cancer. [5] Different alternatives Depending on the topography of the access route, helical needles, curved needles, plastic sheets, and sheaths are available for situating the mesh arms to assure tissue-sparing insertion.There is currently little long-term evidence on whether the theoretical assumptions that support mesh interposition transfer to successful prolapse repair. Short-term findings, on the other hand, show that the concept is workable, but that 5.3 percent of women, despite permanent tissue replacement, develop recurrent prolapse within three months following surgery.Based on previous experience with ultrasound evaluation of the polypropylene tape in women after tension-free vaginal tape (TVT) repair, we conducted the current study to determine sonographically the postoperative size of the mesh implant, compare it to the size of the implanted mesh, and evaluate whether full support of the anterior or posterior compartment is achieved.[6]Pelvic organ prolapse results in a slew of symptoms that get worse with time. Despite efforts to standardise clinical examinations, a variety of imaging modalities are employed. The purpose of this study was to see if dynamic pelvic magnetic resonance imaging and dynamic cystocolpoproctography could help surgeons treat patients with severe pelvic floor disorders.[7]
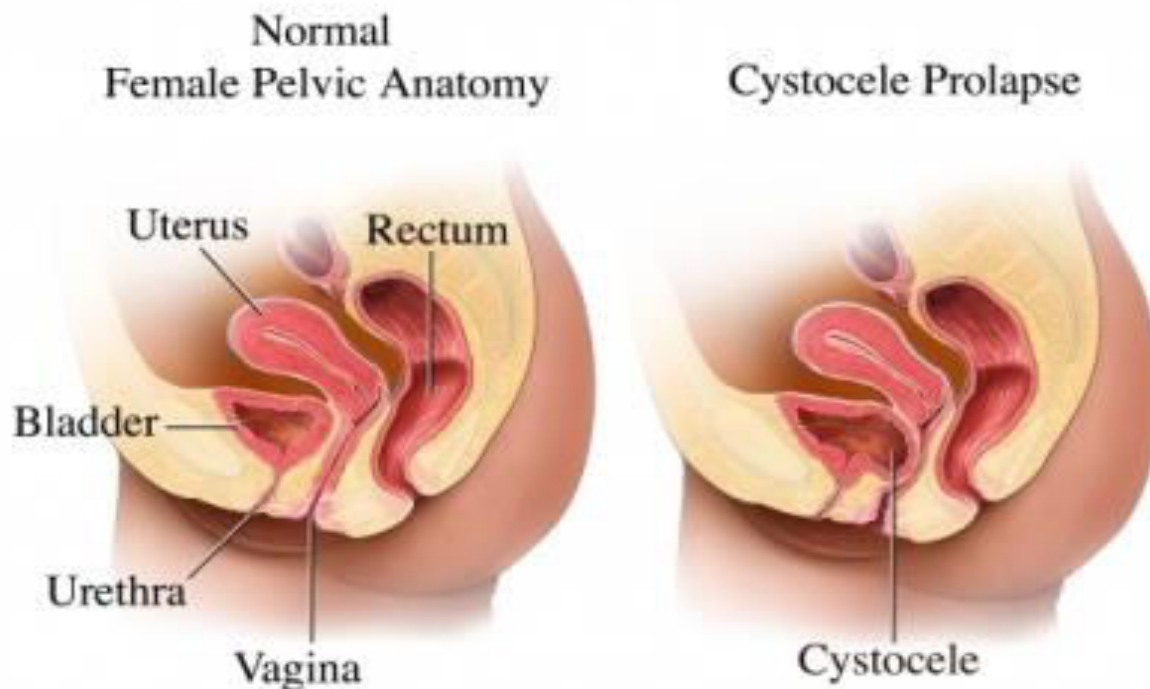
Patient Information:A 30 years old married female admitted in AVBR Hospital on date 28/09/2021 with chief complaints of Something coming out of vagina not feeling bladder relief immediately, frequent urinary tract infection, heaviness in vagina.

Primary Concern And Symptoms of Patient: Present case visited in AVBR Hospital in OPD base on dated 28/09/2021 with chief complaints of Something coming out of vagina not feeling bladder relief immediately, frequent urinary tract infection, heaviness in vagina.

Medical And Family And Psychosocial History: Patient suffering from Cystocele and rectocele with procedentia with cervical elongation for further managementPresent case belong nuclear family in her family belongs to middle

class family. She was mentally stable, she was oriented date, time and place and she maintained good relationship with family members.

Habits:
Watching TV, reading newspaper and sleeping and patient don't have any bad habit like chewing tobacco and smoking.

Relevant Past Intervention with Outcomes: Cystocele and rectocele with procedentia with cervical elongation for further managementfor few days before admitted in AVBRH After investigation patients diagnosis is conformed, was observed she took treatment for that and her outcomes was good.

Physical Examination clinical findings:

General Examination:
30 years female patient have unhealthy, she was conscious and oriented to date ,time and place patient body build was moderate and she was not maintain good personal hygiene, her haemoglobin was 9.7gm,pulserate is 68,blood pressure-120/90mmhg.,platlate-8lac/cumm

The patient was consciousand well oriented to date imeplace. his body built was moderate and he maintained good personal hygiene.

General Examination:state of health was unhealthy,

thin body built, but distension of necrosis the height of patient is 168 cm

weight is 50kg. her vital parameters are normal.

Timeline:
The patient was admitted for few weeks, that time patient general condition was poor, she took treatment in A.V.B.R.Hospital and she got the proper treatment. Taking proper medication and now she has been seen the improvement of condition**.**

Diagnostic assessment:
After physical Examination and investigation (such as CBC, Per Vaginal examination, Ultrasonography, Paps Smear,) Hemoglobin-9.7gm,cytopathology-smear shows and groupof benign epithelium cells and flue clattle inflammatory cell.

Diagnosis:
After all physical examination and investigation patient diagnosis is Cystocele and rectocele with procedentia with cervical elongation.

Therapeutic Intervention:
Medical intervention: included inj.c-tax,inj.pan,inj.metro,t-bactointment,tab-iron,tab-calcium,inj.pause, She was took all treatment and outcomes was good.

Nusingperspective:IV fluid was provided to maintan the fluid and electrolyte monitored heart rate and vital sign per hourly.

Follow up and outcomes:

Follow up:
Patient advice to daily exercise, and avoid high cholesterol diet, salt diet, given healthy diet. Regular checked up , maintained the personal hygiene as well as take it properly medication by Dr order.

Outcomes:
In-spite all care patient progress good, he was advised to strictly avoid heavy work, advised to take complete bed rest

Intervention adherence and tolerability: Patients took all prescribed medication regularly, he follow diet, No, any intervention adherence. Patient tolerated treatment properly

Discussion:
The levatorani muscle and the apical descent abnormalities have been linked to Prolapse of the anterior and posterior vaginal walls. The proportional these individuals' contributions variables to the pathophysiology of descent in various compartments vaginal, however, are unknown remain uncertain. In addition, the symptoms of prolapse in these compartments are not well understood.

Because of the elegance of transobturator or transischioanal access, the ease of application using the manufacturers' needles, the variable mesh sizes that can be cut to size intraoperatively, the lack of a laparotomy, the option of permanent tissue replacement after fascial reconstruction failure, and Ulmsten's excellent experience with similar materials.[8]The simultaneous treatment of cistocele and rectocele with protesic polypropylene multifilament macropore mesh via the The tension-free transvaginal method It appears to be a secure and successful method surgery procedure. There are a variety of approaches that can be taken, and In the literature, there is currently no

significant agreement.If the rectocele is isolated or affects the low or mid rectum, a transabdominal rectopexy is more appropriate, but if the rectocele is high and/or connected to other conditions of If you have pelvic stasis, a transabdominal rectopexy is a better option appropriate.[9]

The Pelvic organ prolapse is defined as a downward descent of the pelvic organs that results in a protrusion of the vagina (POP), is a frequent disease in the United States, accounting for 300,000 surgeries each year. After cystocele, rectocele, or rectum prolapse through the POP is the second most prevalent type of POP is posterior vaginal wall (PVW). Rectocele is typically seen in multicompartment pelvic floor disorders alongside other types of prolapse. Rectocele development mechanisms are still understood, making early detection and progression prediction difficult. Thanks to advances in imaging and computer modelling tools, a range Vaginal prolapse has been studied using a variety of finite element (FE) models, providing for a better understanding of the dynamic interactions between pelvic organs and their supporting structures systems. The majority of research has so far concentrated Little is known about anterior vaginal prolapse (or cystocele), and involvement of pelvic muscles and ligaments in rectocele's onset and progression. Based on full-scale magnetic resonance imaging, this research generated a three-dimensional (3D) computer model of the female pelvis (MRI).[10]Studies on different aspects of rectal lesions were reviewed[11-16].

Conclusion:

The laparoscopic pelvic floor repair treatment combines the benefits of a with the decreased morbidity of a vaginal laparotomy operation. Although Suspension of the uterosacral ligament is the most natural anatomic restoration of abnormalities and thus the ones who are least likely to result in future deformities in Vaginal function may be hampered by the anterior or posterior vaginal wall, sacrocolpopexy was more popular in Europe. To assess the technique's utility, more research on its long-term efficiency and reliability is required. Sacrocolpopexy with mesh interposition is a method for vault prolapse that is both safe and effective. and rectocele repair. To uncover any late issues, aIt is necessary to conduct long-term follow-up. Contrary to popular opinion, pelvic organ prolapse is not always chronic and progressive, as our findings show. Patients with grade 1 prolapse frequently have spontaneous regression.

References:

1. Vahabi S, Karimi A, Beiranvand S, Moradkhani M, Hassanvand K. Comparison of the effect of different dosages of celecoxib on reducing pain after cystocele and rectocele repair surgery. The Open Anesthesia Journal. 2020 Jun 15;14(1).
2. Berger MB, Kolenic GE, Fenner DE, Morgan DM, DeLancey JO. Structural, functional, and symptomatic differences between women with rectocele versus cystocele and normal support. American journal of obstetrics and gynecology. 2018 May 1;218(5):510-e1.
3. Durnea CM, Khashan AS, Kenny LC, Durnea UA, Smyth MM, O'Reilly BA. Prevalence, etiology and risk factors of pelvic organ prolapse in premenopausal primiparous women. International urogynecology journal. 2014 Nov;25(11):1463-70.
4. Sand PK, Koduri S, Lobel RW, Winkler HA, Tomezsko J, Culligan PJ, Goldberg R. Prospective randomized trial of polyglactin 910 mesh to prevent recurrence of cystoceles and rectoceles. American journal of obstetrics and gynecology. 2001 Jun 1;184(7):1357-64.
5. Vahabi S, Abaszadeh A, Yari F, Yousefi N. Postoperative pain, nausea and vomiting among pre-and postmenopausal women undergoing cystocele and rectocele repair surgery. Korean journal of anesthesiology. 2015 Dec;68(6):581.
6. Tunn R, Picot A, Marschke J, Gauruder-Burmester A. Sonomorphological evaluation of polypropylene mesh implants after vaginal mesh repair in women with cystocele or rectocele. Ultrasound in Obstetrics and Gynecology: The Official Journal of the International Society of Ultrasound in Obstetrics and Gynecology. 2007 Apr;29(4):449-52.
7. Kaufman HS, Buller JL, Thompson JR, Pannu HK, DeMeester SL, Genadry RR, Bluemke DA, Jones B, Rychcik JL, Cundiff GW. Dynamic pelvic magnetic resonance imaging and cystocolpoproctography alter surgical management of pelvic floor disorders. Diseases of the colon & rectum. 2001 Nov 1;44(11):1575-83.
8. Tunn R, Picot A, Marschke J, Gauruder-Burmester A. Sonomorphological evaluation of polypropylene mesh implants after vaginal mesh repair in women with cystocele or rectocele. Ultrasound in Obstetrics and Gynecology: The Official Journal of the International Society of Ultrasound in Obstetrics and Gynecology. 2007 Apr;29(4):449-52.
9. Aubert M, Mege D, Nho RL, Meurette G, Sielezneff I. Surgical management of the rectocele–An update. Journal of Visceral Surgery. 2021 Jan 22.

10. Chanda A, Meyer I, Richter HE, Lockhart ME, Moraes FR, Unnikrishnan V. Vaginal changes due to varying degrees of rectocele prolapse: A computational study. Journal of biomechanical engineering. 2017 Oct 1;139(10).
11. Bhojraj, Nandini, and Gaurav Sawarkar. "The Effect of Panchagavya Formulations in the Case of CA Rectum." INTERNATIONAL JOURNAL OF AYURVEDIC MEDICINE 11, no. 3 (September 2020): 572–74.
12. Khandare, Kiran, and PradnyaGhormode. "Prolapsed Rectal Submucosal Hematoma in Pediatric Case." PAN AFRICAN MEDICAL JOURNAL 37 (October 13, 2020). https://doi.org/10.11604/pamj.2020.37.154.26149.
13. Sreedhar, Rashmi, SuhasJajoo, MeenakshiYeola, YashwantLamture, and Darshana Tote. "Role of Tumour Markers CEA and CA19-9 in Colorectal Cancer." JOURNAL OF EVOLUTION OF MEDICAL AND DENTAL SCIENCES-JEMDS 9, no. 46 (November 16, 2020): 3483–88. https://doi.org/10.14260/jemds/2020/762.
14. Thomas, Sophia, and Arvind Bhake. "Expression of K-Ras, P53 and Ki-67 in Precancerous and Cancerous Lesions of Colorectum." JOURNAL OF EVOLUTION OF MEDICAL AND DENTAL SCIENCES-JEMDS 9, no. 32 (August 10, 2020): 2261–65. https://doi.org/10.14260/jemds/2020/490.
15. Tote, Darshana, Rajesh Domakunti, and Sachin Tote. "Scenario of Rectal Carcinoma Cases in a Rural Setting of Central India." JOURNAL OF EVOLUTION OF MEDICAL AND DENTAL SCIENCES-JEMDS 9, no. 46 (November 16, 2020): 3434–38. https://doi.org/10.14260/jemds/2020/753.
16. Yeola, MeenakshiEknath, and Aditya PrabhalkarraoBorgaonkar. "Passage of Gangrenous Small Bowel Per Rectum Following Superior Mesenteric Vessel Thrombosis." JOURNAL OF CLINICAL AND DIAGNOSTIC RESEARCH 13, no. 12 (December 2019). https://doi.org/10.7860/JCDR/2019/42828.13381.

Review Article

Artificial Intelligence for Diabetic Care

Ankita Kapse, Marina Semin, Rakesh Kumar Jha[1], Bhushan Bawankar[2], Praful Patil[3]

Departments of Medicine and [1]Biochemistry, Datta Meghe Medical Science, [2]Department of Medicine, Yeshwantrao Chavan College of Engineering, Nagpur, [3]Department of Microbiology, Datta Meghe Institute of Medical Sciences, Jawaharlal Nehru Medical College, Wardha, Maharashtra, India

Abstract

Artificial intelligence (AI) has the potential to enhance results in the future, diabetes care. The goal of this article was to help people with diabetes, their clinicians, families, and caregivers better understand what AI breakthroughs are important now. AI medical applications include diagnosis, categorization, therapy, and robotics, among others. We are no longer confined to descriptive data analysis because we may acquire a larger by recognizing and anticipating patterns coming from inductive reasoning, owing to medical learning. AI applications have the potential to revolutionize diabetic care by assisting millions of people with diabetes in achieving better blood glucose management, reducing hyperglycemic episodes, and lowering diabetic morbidity and complications. We can see the evolution of closed-loop insulin delivery systems with inbuilt AI algorithms to safeguard both hypoglycemia and hyperglycemia in Type 1 diabetes, which have been relatively few attempts in management techniques for diabetes excursions. The medication you choose and how much you take depend on a variety of factors, including your body mass index, which influences beta-cell activity and insulin resistance, among other things. There are great assessments of research that have employed an AI approach to treat diabetes. The only way to deal with vast, diverse datasets is to rely solely on quantitative data. At this point, there are numerous issues with absolute reliance on quantitative data, depending on the frequently poor quality of this sort of information, as well as the necessity to complement combining a quantitative and qualitative approach. Attempting toward the transformation of unstructured data into digitally processed information data is a domain of cognitive computing that is predicted to grow in importance. To make a substantial contribution to AI aside from the purpose, there are 48 other factors to consider.

Keywords: Artificial intelligence, diabetes care, diabetes, hypoglycemia and hype glycemia

INTRODUCTION

Diabetes is a worldwide epidemic. Diabetes affects an estimated 425 million people globally, accounting for 12% of global health expenditures, while 1 in every 2 people is still undiagnosed and untreated.[1] AI methodology and approaches have been used to medicine and health in general throughout the previous few decades. Diagnosis, categorization, therapy, and robotics are all topics covered in this book. Common AI medical applications include, among others. Among neural networks and a variety of other AI technologies to date, fuzzy logic has been the most widely employed. Other strategies and methodologies, on the other hand, are available. They have also been chosen for inclusion in this review due to their importance.[2]

Most people have now become part of a vibrant, changing ecosystem, in which their social, biological, and other factors are available to anyone who is interested. While third-party access to these data will undoubtedly be regulated, if an agreement is reached, if an individual agrees to provide his or her data, AI will result in more confident recommendations.[3] The data used to develop AI/ML intelligence are only as good as the data used to generate it. Our country is sometimes referred as "the land of no records," which may or may not be accurate, but it does highlight the need of keeping documents.[4]

The discipline of artificial intelligence (AI), which is rapidly expanding, has applications that might revolutionize how this chronic ailment is diagnosed and managed. Diabetes is a global pandemic. Digital therapies have established itself as an established intervention for diabetic lifestyle treatment. Patients are more empowered to manage their diabetes on their

Access this article online

Quick Response Code:

Website:
www.journaldmims.com

DOI:
10.4103/jdmimsu.jdmimsu_275_22

Address for correspondence: Dr. Marina Semin,
Datta Meghe Medical Science, Wanadongri, Nagpur, Maharashtra, India.
E-mail: jhaarakesh1993@gmail.com

How to cite this article: Kapse A, Semin M, Jha RK, Bawankar B, Patil P. Artificial intelligence for diabetic care. J Datta Meghe Inst Med Sci Univ 2022;17:487-90.

own, and clinical decision support benefits both patients and health-care providers. These astute technical modifi ations have resulted in improved glycemic management, including decreases in fasting and postprandial glucose levels, glucose excursions, and glycosylated hemoglobin.[5]

Digitalization

From electronic medical records to imaging, almost every daily function of a dialectologist involves digitalization. Diagnostics ranges from laboratory references to software. Administrative practices and certifications programs, and sensor data derived from glucose level data obtained from glucometer's insulin pumps and continuous glucose monitoring (CGM) through dialectologists make therapeutic decisions based on the study of these data.[6] AI uses vast volumes of important data to satisfy customer demand in every industry, including health care. According to a 2017 survey, 68% of mobile health app developers and publishers believe diabetes will remain the single most important health-care fi ld with the greatest market potential for digital health solutions in the near future, and 61% believe AI will be the most disruptive technology shaping the digital health sector.[7]

Individualized care and artificial intelligence

In this context, the use of AI, namely machine learning, allows for a significant advancement compared to traditional methods. With typical data analysis approaches (graphics, for example) representing a realistic image, which is incredibly valuable and exact, but they're out of date. By way of the automatic the discovery of specific patterns in the data, as well as through Machine learning, inductive reasoning. Can draw attention to correlations that lead to "predictions" without causing alarm.[6]

Risk stratification and personalized medicine

The ability to extract knowledge and exponentially make predictive assessments on individual behavior, as well as, more broadly, assume decisions for the entire community, is enabled by the ability to elaborate a large and heterogeneous amount of data, even in real time, through increasingly powerful algorithms. This means that using AI will allow you to translate raw data (descriptive) into the knowledge of the factors that "condition" behavior and correlations (predictive), all the way to identify the important factors that can help you improve your predicted results.[6]

Connectivity and data management

The collection and management of individual patient data were done in person at the hospital initially to literally connect the local cable network or software/wireless network. Currently, due to technological advances, these data can be automatically transferred from the device as it changes. Glucometers connected to the "cloud" or data collection platforms collect data on various devices and present the report in the same format. This huge amount of data can be dangerous, if not handled properly. Both the patient and the health-care system may be frustrated by the data. The expert, as well as

expert knowledge, in reading these reports is undoubtedly an additional value that enhances their capabilities.

Advanced informatics technologies can make data processing and interpretation easier. Make recommendations to help the doctor make better clinical decisions a physician.[6]

To avoid acute problems (e.g., ketoacidosis) and reduce long-term implications, patients must receive timely diagnosis, self-management education, and ongoing medical care for each type of diabetes. Long-term complications (e.g., nephropathy) are a possibility. Retinopathy, diabetic foot, cardiovascular disease, and stroke are examples of these conditions. Diabetes management involves more than just medication. Devotion to a variety of self-care habits that is often very difficul to achieve.

Patients find it difficult

Meal planning and counting are essential, carbohydrates, exercise, blood sugar monitoring, and modifying on a daily basis, he pursues his goals. The consequences of not adhering to the rules and recommendations for treatment are not always obvious, and long-term effects can take a long time to manifest. As a result, diabetes treatment is difficul and time consuming. Various medical factors must be considered when making judgments. Actions connected to one's way of life that must be optimized to increase the quality of life of diabetes patients.[8]

Diet is currently one of the key risk factors for a wide range of disorders, including diabetes. The quantity and kind of food consumed is a major predictor of human health. Diet is an important component of diabetes care, which can include diet alone, diet plus oral hypoglycemic medications, or diet with insulin.[9]

Social networking

The rising usage of social networks and applications has significant consequences for diabetes care. The new technologies might be utilized to supplement traditional educational activities with motivating and coaching tools, as well as an alternative data source. As a result, to obtain a more precise picture of the general population's or specific subgroups' health status, we cannot limit ourselves in collecting and analyzing only health data but must also consider what comes from the world of social networking and smartphone apps, despite all of the known limitations and criticalities.[10]

Materials and Methods

The information was obtained from several articles. I identifie 22 articles, however 12 of them were irrelevant to the topic; therefore, they were eliminated. The remaining 12 were picked, with six carrying the same content that was required to assess the article.

Discussion

Dankwa-Mullan *et al*., in their review article, concluded that applications of AI aiming to improve a wide range of diabetes care, including from diabetes screening and detection

to treatment and monitoring, It featured patient-assistance applications, gadgets, and systems, as well as clinicians and health-care systems. The pieces in this collection have been published. This search had a strong clinical impact, because it aimed to develop and test AI technologies that may have an influence on diabetes care. Notably, in terms of accessibility, accuracy, efficiency, and affordability, quickness, and patient, clinician, and staff satisfaction caretakers.[1] Diabetic retinopathy (DR) is the leading cause of secondary blindness, wreaking havoc on individuals, families, and the health-care system. The annual diabetic retinal examination is used to check for diabetes patients with early treatable retinopathy and to discover them early. Improved prediction, early identification, and treatment procedures are projected to prevent 98% of vision loss due to DR and macular edema, and their cost-effectiveness is well proven. However, the limited number of eye-care practitioners educated in interpreting retinal pictures, as well as access to care, are key impediments in establishing more widespread screenings. Deep learning-based AI grading of DR from retinal pictures now has a sensitivity and specifi ity of above 90%, according to study.[11]

DR is the leading cause of secondary blindness, wreaking havoc on individuals, families, and the health-care system. The diabetic retinal examination is done once a year to screen and detect diabetes patients who are at risk of developing complications. Approximately 98% of vision is thought to be impaired. It is possible to avert vision loss due to DR and macular edema by taking preventative measures. Proven approach for early detection, prognosis, and treatment. It is also well known for its cost-effectiveness

Seventeen Nonetheless, there are some significant differences Obstacles in conducting more broad testing in the workplace, including the small number of ophthalmologists and optometrists who are with access to and training in analyzing retinal images barriers to care deep learning-based, AI-based DR grading from retinal images, have been linked to sensitivity and specificity more than 90% [11]

Rigla *et al*. intended for their post to illustrate in a simple and straightforward manner how most AI approaches are utilized to increase the involvement of health-care providers, doctors, and nurses, in this subject. From this, they concluded that to incorporate new tools for diabetes management, dialectology must undergo an adaptation process. Sensors and computer applications, in particular, have benefi ed from technological advancements, become important tool in diabetes management situations. Insulin pumps, among other things, are covered.[12]

Sriram and Reddy concluded in this review article that AI can aid in the creation of artificial pancreas (closed-loop systems) and the understanding of the interaction between social variables and physiological biomarkers of health. Diabetes also creates a large amount of data in the retina, kidneys, vascular system, and other areas.[13]

Singla *et al*. concluded that the data used to develop AI/ML intelligence are only as good as the data used to generate it.

Our country is sometimes referred as "the land of no records," which may or may not be accurate, but it does highlight the need of keeping documents. In general, there is a lack of recordkeeping as an important aspect of the process. India's medical practice disease may wreak havoc on a life. If all data are harnessed, it can be transformed into an opportunity.[14]

Musacchio *et al*. concluded from their review article that changes brought about by technology advancements have resulted in an unprecedented quantity of data collecting and processing, which is set to grow even more with the introduction of new technologies. Robotics and augmented reality applications, a new frontier. We have crossed the threshold into the era of big data and intelligent systems.

A new category of technologies has emerged, one that makes use of natural resources. It has the ability to boost language processing and machine learning.[15]

Contreras and Vehi concluded that a great number of research on the application of AI to diabetes in a variety of management domains have previously been published. Our investigation of PubMed reveals a significant increase in speed in the rate of research into AI-powered tools that can predict the future and to avoid the difficultie that come with diabetes. Even though there are technologies and approaches for diabetes management available, in terms of quantity, management is expanding dramatically. Regarding quality, AI's potential to improve efficiency and accura .[16]

CONCLUSION

The only way to deal with vast, diverse datasets is to rely solely on quantitative data. At this point, there are numerous issues with absolute reliance on quantitative data, depending on the frequently poor quality of this sort of information, as well as the necessity to complement combining a quantitative and qualitative approach. Attempting toward the transformation of unstructured data into digitally processed information data is a domain of cognitive computing that is predicted to grow in importance. To make a substantial contribution to AI aside from the purpose, there are 48 other factors to consider. Sentiment, for example, is used in clinical decision-making intuition and a physician's experience, both of which have been used in the past referred described as "gut feeling" or "judgment." Computer-assisted cognitive processing is now unprepared to mimic this subjective component in the process of arriving medical conclusions. The goal of enhanced glycemic control has not yet been fully realized as a result of the expansion of technology to assist patients in T1D management. AI principles used to patients on multiple daily injections therapy in the alkyl-diol-silica (ADS) in its early stages have showed promise in bridging this gap and to strengthen the population's management. There are numerous systems and platforms in

the works, and as a bonus, as new tools become available, suppliers will be expected to use them. Patients should be educated and trained on how to use this equipment; improved CGM technology reduces the load even further.

Despite of obstacles, medical AI applications are evolving at a breakneck pace, and the potential and research worth of these applications cannot be overstated. The future usage of integrated and complete applications of individual AI technologies in diabetes education can provide full-course, tailored, and intelligent instruction, providing patients with advice and protection for a lifetime.[17]

Financial support and sponsorship
Nil.

Conflicts of interest
There are no conflicts of interest

REFERENCES

1. Bergenstal RM, Garg S, Weinzimer SA, Buckingham BA, Bode BW, Tamborlane WV, *et al.* Safety of a hybrid closed-loop insulin delivery system in patients with type 1 diabetes. JAMA 2016;316:1407-8.
2. Miller KM, Foster NC, Beck RW, Bergenstal RM, DuBose SN, DiMeglio LA, *et al.* Current state of type 1 diabetes treatment in the U.S. Updated data from the T1D exchange clinic registry. Diabetes Care 2015;38:971-8.
3. Cavanaugh K, Huizinga MM, Wallston KA, Gebretsadik T, Shintani A, Davis D, *et al.* Association of numeracy and diabetes control. Ann Intern Med 2008;148:737-46.
4. Ahola AJ, Makimattila S, Saraheimo M, Mikkila V, Forsblom C, Freese R, *et al*. Many patients with type 1 diabetes estimate their prandial insulin need inappropriately. J Diabetes 2010;2:194-202.
5. Ellahham S. Artificial intelligence: The future for diabetes care. Am J Med 2020;133:895-900.
6. Foster NC, Beck RW, Miller KM, Clements MA, Rickels MR, DiMeglio LA, *et al.* State of type 1 diabetes management and outcomes from the T1D exchange in 2016-2018. Diabetes Technol Ther 2019;21:66-72.
7. Research 2 Guidance. Top 3 Therapy Fields with the Best Market Potential for Digital Health Apps. Available from: https://research2guidance.com/top-3-therapy-fields-with-the-best-market-potential-for-digital-health-apps/. [Last accessed on 2018 Jul 18].
8. Reddy M, Pesl P, Xenou M, Toumazou C, Johnston D, Georgiou P, *et al.* Clinical safety and feasibility of the advanced bolus calculator for type 1 diabetes based on case-based reasoning: A 6-week nonrandomized single-arm pilot study. Diabetes Technol Ther 2016;18:487-93.
9. Sofi F, Innocenti G, Dini C, Masi L, Battistini NC, Brandi ML, *et al.* Low adherence of a clinically healthy Italian population to nutritional recommendations for primary prevention of chronic diseases. Nutr Metab Cardiovasc Dis 2006;16:436-44.
10. Aggarwal M, Bozkurt B, Panjrath G, Aggarwal B, Ostfeld RJ, Barnard ND, *et al*., American college of cardiology's nutritionlifestyle committee of the prevention of cardiovascular disease council lifestyle modifications for preventing and treating heart failure. J Am Coll Cardiol 2018;72:2391-405.
11. Dankwa-Mullan I, Rivo M, Sepulveda M, Park Y, Snowdon J, Rhee K. Transforming diabetes care through artificial intelligence: The future is here. Popul Health Manag 2019;22:229-42.
12. Rigla M, García-Sáez G, Pons B, Hernando ME. Artificial intelligence methodologies and their application to diabetes. J Diabetes Sci Technol 2018;12:303-10.
13. Sriram RD, Reddy SS. Artificial intelligence and digital tools: Future of diabetes care. Clin Geriatr Med 2020;36:513-25.
14. Singla R, Singla A, Gupta Y, Kalra S. Artificial intelligence/machine learning in diabetes care. Indian J Endocrinol Metab 2019;23:495-7.
15. Musacchio N, Giancaterini A, Guaita G, Ozzello A, Pellegrini MA, Ponzani P, *et al.* Artificial intelligence and big data in diabetes care: A position statement of the Italian association of medical Diabetologists. J Med Internet Res 2020;22:e16922.
16. Contreras I, Vehi J. Artificial intelligence for diabetes management and decision support: Literature review. J Med Internet Res 2018;20:e10775.
17. Li J, Huang J, Zheng L, Li X. Application of artificial intelligence in diabetes education and management: Present status and promising prospect. Front Public Health 2020;8:173.

DEEP LEARNING BASED MISSING OBJECT DETECTION AND PERSON IDENTIFICATION AND APPLICATION FOR SMART CCTV

R. C. Dharmik

Assistant Professor, Department of Information Technology Yeshwantrao Chavan College of Engineering, Nagpur, Maharashtra, (India).

Sushilkumar Chavhan

Assistant Professor, Department of Information Technology Yeshwantrao Chavan College of Engineering, Nagpur, Maharashtra, (India).

S. R. Sathe

Professor, Department of CSE, VNIT Nagpur, (India).

https://doi.org/10.17993/3ctecno.2022.v11n2e42.51-57

ABSTRACT

Security and protection are the most crucial concerns in today's quickly developing world. Deep Learning methods and computer vision assist in resolving both problems. One of the computer vision subtasks that allows us to recognise things is object detection. Videos are a source that is taken into account for detection, and image processing technology helps to increase the effectiveness of state-of-the-art techniques. With all of these technologies, CCTV is recognised as a key element. Using a deep convolutional neural network, we accept CCTV data in real time in this article. The main objective is to make content the centre of things. Using the YOLO technique, we were able to detect the missing item with an improvement of 10% sparsity over the current state-of-the-art algorithm in the context of surveillance systems, where object detection is a crucial step. It can be utilised to take immediate additional action.

KEYWORDS

Deep Learning, Object Detection, Computer vision

1. INTRODUCTION

The method of object detection involves comprehending the entire image, concentrating on proper categorization while focusing on the item in the image. This process is a subtask of computer vision, which also covers face detection and skeleton identification by Zhao, Zheng, Xu, and Wu (2019) ,Felzenszwalb, Girshick, Mcallester, and Ramanan (2010),Sung and Poggio (1998),Doll´ar, Wojek, Schiele, and Perona (2011)and Sampat and Bovik (2003). The development of computational models that offer the most fundamental data required by computer vision applications is the aim of object detection. An industrial revolution changes the face of the computer vision task where identification, surveillance, medical, robotics, self-driving cars can be part of it. In recent era advancement in deep leaning accelerated the object detection task. A specific form of machine learning called "deep learning" (DL) uses neural networks to learn in phases. It can therefore mimic human thought. Video analytics is closely related with the deep learning which provides application in different fields. Traditional Object detection is complex in complexity and low level features are also leads to saturation to increased complexities (Zhao et al., 2019).

Image classification and detection are the steps for the detection of object for surveillance. Primary task for both the operation to receive the relevant features. Deep Learning is the better solution for it. It learns from previous stages and extracts new features. Deep Network may conventio al neural network or Multilayer Perceptron networks which consist of activation functions and various hidden layers. Image is extracted from the video with fixed size as neural network required for model (Sung and Poggio, 1998). If fully integrated networks are necessary. However, size reduction results in information loss inside the image, reducing accuracy, precision, and sparsity as well as applicability for surveillance system (Zhao et al., 2019). Viola-Jones Detector (Viola and Jones, 2001) and HOG Detector (Dalal and Triggs, 2005) are two examples of conventional object detection algorithms. One-stage and two-stage algorithms based on deep learning are the two main categories. The two-stage algorithms RCNN and SPPNet(Girshick, Donahue, Darrell, and Malik, 2013),(Liu, Anguelov, Erhan, Szegedy, Reed, Fu, and Berg, 2016), Fast RCNN and Faster RCNN(He, Zhang, Ren, and Sun, 2014), Mask R–CNN, Pyramid Networks/FPN(Girshick, 2015), and G–RCNN(Ren, He, Girshick, and Sun, 2015) propose object region utilising deep feature before classification. Without the region suggestion, one-stage algorithms like YOLO (Redmon, Divvala, Girshick, and Farhadi, 2016), SSD (Liu et al., 2016), RetinaNet (Girshick, 2015), YOLOv3, YOLOv4, etc. anticipate bounding boxes over the pictures.

In this paper we created application using CCTV will be helpful to understand whether any object is stolen from the area (room, cabin, etc.) and recognition of the person, thus helping to form the better security infrastructure. This system can be used at official workspaces where there is a crucial need for more secure surveillance than earlier. Analyses frames and find stolen objects by using structural similarities. A deep learning-based object recognition system coupled with YOLO for remote surveillance that can accurately and quickly identify the target inside video frames has been suggested. proposed system has the ability to send data to a localised remote server after automatically detecting a person or item. To detect and transmit the information, a thin coating of YOLO was utilised. We applied filters to the data to keep it clean.

2. LITERATURE REVIEW

Viola and Jones (2001) proposed a machine Learning based object detection which is populary know as Viola-Jones Detector where they calculate new feature, learn by using AdaBoost and able to clasify more complex features. Dalal and Triggs (2005) proposed HOG (Histograms of Oriented Gradient) object detection algorithm which uses dense overlapping grid gives which provides betteer results for person identification, reducing false positive rates with resppect to Haar wavelet based detector. Forsyth (2014) Exnded the above work and proposed the DPM model for object Detection. They

modify the SVM algorithm of data mining for the purpose object detection. It uses divide and conqure technology with the root filter and various part filters which make it Multi instance Leaning algorithm. All above traditional methods have far surpassed many algorithm in term of accuracy.

Girshick et al. (2013) proposed RCNN object detection algorithm with mean average precision. As local Search combine with CNN it said to be RCNN. They Combine the CV and Deep Learning for better results as comparre to traditional Methods. He et al. (2014) proposed SPPNet model for object detection. It Detect the object by variriyng the image size. For that they changes the image size as most of object detection algorithms are used the strandard size of 255*255.Girshick (2015) proposed Fast RCNN detector, advanced verison of R-CNN and SPPNet. They suggested Dense boxex and and Parse preposal to acceleate process as it is costly process.

Ren et al. (2015) proposed Faster RCNN detector and target is too reduce the time of RCNN. Which is mostly presented as RPN as it uses more deep learning network.Redmon et al. (2016) proposed Feature Selection framewok inside convonet popurarly know as FPN (Feature Pyramid Network) which is based on Faster RCNN with framework. They suggest multi scale problems with deep learning. Redmon et al. (2016) proposed most popolar and widely used algoritrhm you only looks one (YOLO) one stage detector using deep learning. Instead of consideration of whole image, it convert image in to region and simulteniously predict the bounding boxes and probability of each region. Also they train the loss function which helps model to detect the images. Further they improved to YOLOv3, YOLOv4.

3. METHODOLOGY

By observing the various literature, we apply the CNN with two layer architecture and different activation function and Filter. Identified Process is as follows.
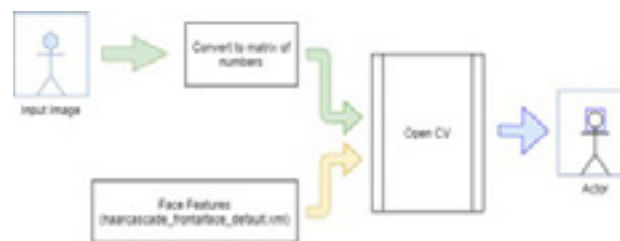
Fig 1: Feature Selection.

Fig 2: Flow of Process.

In this process we used real time data capture from CCTV and camera. The images which received which are filter using LBPS parameters. This helps process simpler. Then 2 layer deep neural network with Relu activation functions.

4. RESULTS

Step1: Collection of images: We accept the images from CTTV camera and then we create the slices as shown in bellow figure. Which store in specific folder with less size.
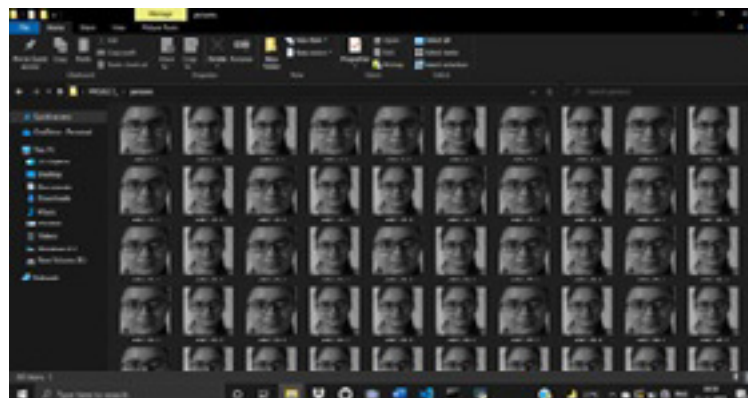

Fig 3: Extraction of images of one frame.

Step2: Extraction of features using specific one layer deep neural Network. The Features are selected as core point of the real time flowing image.
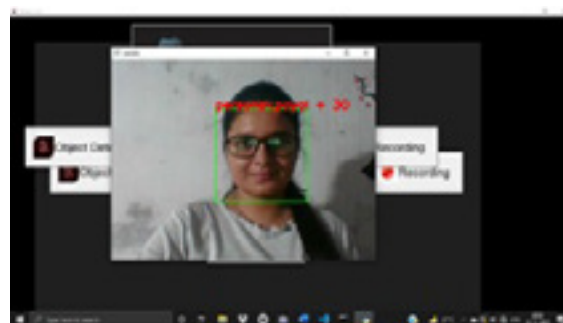
Fig 4: Feature Selection

Step3: identification of images using second deep layer where we can identified the images. Following figure demonstrate the detection of images.
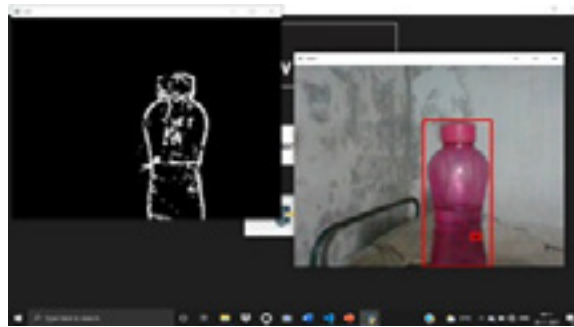
Fig 5: Detection of images.

5. DISCUSSION

The System Developed is shown below:

Fig 6: System GUI.

It is application which having Portable CCTV with some in-built night vision capability. In That by using CNN we adding deep learning if having high power device. It consist of feature such as Deadly weapon detection, Accident detection,Fire Detection,much more.. Working of standalone device. As shown in following figure
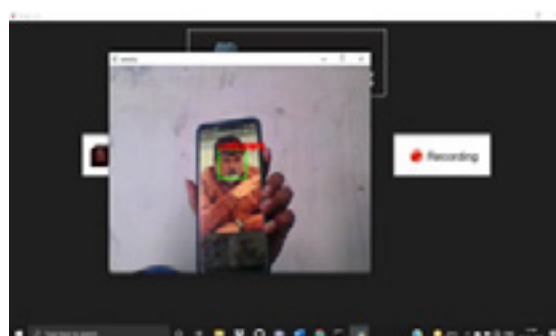
Fig 7: Object Detection.

6. CONCLUSION AND FUTURE SCOPE

In this paper we used two layer deep networks for the object Detection. Using architecture we are able to chive accuracy up to 90%. CNN level are provided the features which helps to make the fast detection of object. In This study it is observed that reduction of image sizes helps to train the networks more faster and deep network can also provide the essentials features. As we implement this

study for security purposed we able to detect object and provide suitable alarm messages.as a Future scope we can used high end camera and test the accuracy and speed.

REFERENCES

[1] Dalal, N. and Triggs, B. 2005. Histograms of oriented gradients for human detection. Comput. Vision Pattern Recognit. 1, 886–893.

[2] DollaÅLr, P., Wojek, C., Schiele, B., and Perona, P. 2011. Pedestrian detection: An evaluation of the state of the art. IEEE transactions on pattern analysis and machine intelligence 34, 743–61.

[3] Felzenszwalb, P., Girshick, R., Mcallester, D., and Ramanan, D. 2010. Object detection with discriminatively trained part-based models. IEEE transactions on pattern análisis and machine intelligence 32, 1627–45.

[4] Forsyth, D. 2014. Object detection with discriminatively trained part-based models. Computer 47, 6–7.

[5] Girshick, R. 2015. Fast r-cnn.

[6] Girshick, R., Donahue, J., Darrell, T., and Malik, J. 2013. Rich feature hierarchies for accurate object detection and semantic segmentation. Proceedings of the IEEE Computer Society Conference on Computer Vision and Pattern Recognition.

[7] He, K., Zhang, X., Ren, S., and Sun, J. 2014. Spatial pyramid pooling in deep convolutional networks for visual recognition. IEEE Transactions on Pattern Analysis and Machine Intelligence 37.

[8] Liu, W., Anguelov, D., Erhan, D., Szegedy, C., Reed, S., Fu, C.-Y., and Berg, A. 2016. Ssd: Single shot multibox detector. Vol. 9905. 21–37.

[9] Redmon, J., Divvala, S., Girshick, R., and Farhadi, A. 2016. You only look once: Unified, real-time object detection. 779–788.

[10] Ren, S., He, K., Girshick, R., and Sun, J. 2015. Faster r-cnn: Towards real-time object detection with region proposal networks. IEEE Transactions on Pattern Analysis and Machine Intelligence 39.

[11] Sampat, M. and Bovik, A. 2003. Detection of spiculated lesions in mammograms. Annual International Conference of the IEEE Engineering in Medicine and Biology - Proceedings 1.

[12] Sung, K. and Poggio, T. 1998. Example based learning for view-based human face detection. Pattern Analysis and Machine Intelligence, IEEE Transactions on 20, 39 – 51.

[13] Viola, P. and Jones, M. 2001. Rapid object detection using a boosted cascade of simple features. IEEE Conf Comput Vis Pattern Recognit 1, I–511.

[14] Zhao, Z.-Q., Zheng, P., Xu, S.-T., and Wu, X. 2019. Object detection with deep learning: A review. IEEE Transactions on Neural Networks and Learning Systems PP, 1–21.

Review Article

Artificial Intelligence in Reproductive Medicine

Anistha Rajendra Bansod, Rakesh Kumar Jha[1], Akash More[2], Rupa A. Fadnavis[3]

Clinical Embryology, Datta Meghe Medical College, [1]Tutor, Department of Biochemistry, Datta Meghe Medical Collage, [2]Department of Clinical Embryology, Jawaharlal Nehru Medical College, Datta Meghe Institute of Medical Sciences Sawangi (Meghe) Wardha, [3]Computer Science and Engineering Assistant Professor, Yeshwantrao Chavan College of Engineering, Nagpur, Maharashtra, India

Abstract

Artificial intelligence (AI) refers to a computer-controlled system or device's ability to interpret and judge human tasks. AI has advanced significantly in a range of disciplines in recent years, from medical to experimental. With the assistance of someone who knows what they are doing, you can learn concepts and algorithms. The success of current efforts has contributed to learning because of the availability of huge datasets, accessibility, and computing capacity. Machine learning is the process of a computer extracting information from patterns and using those patterns to make predictions. Technology for assisted reproduction, many mechanical learning technologies have been employed to improve assisted reproductive technology performance, and they are now being used more frequently in health care. Despite the numerous hurdles, the integration of AI therapy will undoubtedly provide an important direction for the future development of medicine. We cover the work done on machine learning and AI in this overview, as well as how to keep the industries ahead of the curve, and, in terms of fertility therapists, the tests conducted on these industries and experiments address the issues as well as give light on the future direction and potential. We have accounted for all of these things in this post, keeping machine learning and AI expertise and concepts in mind. A review of the above-mentioned reproductive medicine experiments, as well as a review of AI future issues and trends, are thoroughly examined. AI trials in the medical industry will continue to rise as precision medicine develops and large data becomes more widely available. Despite its limits, present AI technology is ideally suited to addressing well-defined difficultie in a variety of therapeutic settings. Women who do not have children, such as infertility patients, could benefit from such a system, which could improve pregnancy outcomes and treatment. Similarly, to a married woman who, despite her best attempts, has been unable to conceive for many years, that type of woman can assist in conceiving. We realize that AI technology capabilities are expected to grow over time and that solutions can benefit by delivering high-quality health care more precisely and effectively in practice

Keywords: Artificial intelligence, embryo, machine learning, oocytes, reproductive medicine, sper

INTRODUCTION

The efficienc of robots to teach and evidence across the desert dividing line between animal and human natural intelligence is characterized as assisted reproductive technology (ART). Keeping all of this in mind, AI has swiftly advanced and has gradually crept into our personal and social lives. In just a few years, computers have gained significant computing power, data storage, and memory, and the ability to manage massive amounts of data. With this incredible accomplishment, I have been able to handle comprehensive learning work in a gradual manner.[1] Speech identification is an example of an AI application that is used in everyday life.[2] There is little doubt that these coverings will get faster, smarter, and more accessible, despite the fact that the current location of AI studies still has a long way to go.[3]

DISCUSSION

AI is widely used in a number of areas, such as sperm cell selection and precision imaging to increase treatment success rates, assess fetal and oocyte quality, and develop a viable and effective ART anticipation model. Further research is being done to identify positive symptoms of resistance to increase the rate of elimination and improve the ART

Address for correspondence: Dr. Rakesh Kumar Jha,
Tutor, Department of Biochemistry, Datta Meghe Medical Collage
Wanadongri, Hingna, Nagpur, Maharashtra, India.
E-mail: vaishali.ten@gmail.com

Access this article online	
Quick Response Code:	**Website:** www.journaldmims.com
	DOI: 10.4103/jdmimsu.jdmimsu_279_22

How to cite this article: Bansod AR, Jha RK, More A, Fadnavis RA. Artificial intelligence in reproductive medicine. J Datta Meghe Inst Med Sci Univ 2022;17:499-503.
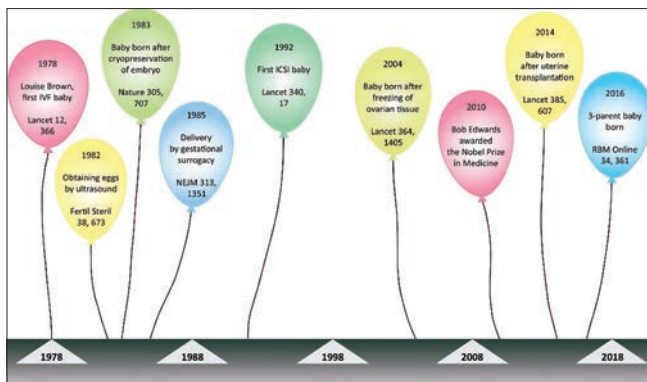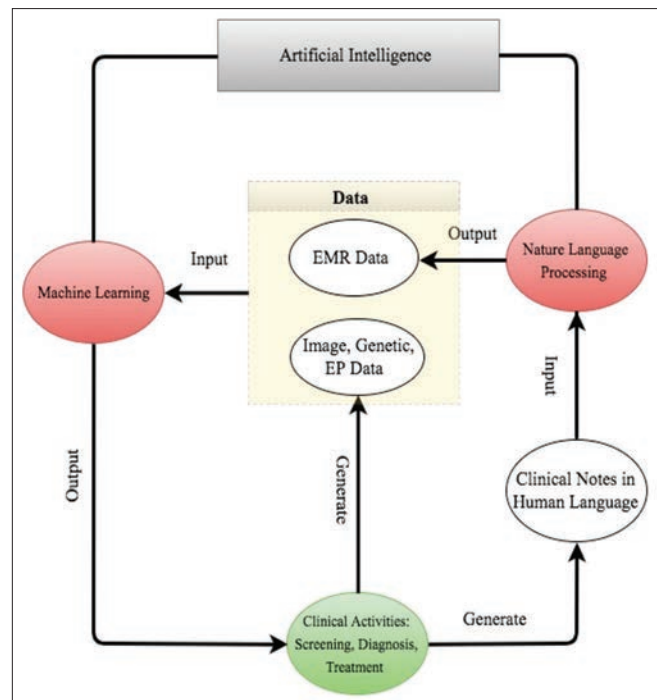
Figure 1: Very important part of human reproductive medicine, in the last 40 years

treatment environment. By allowing flexible separation of sperm, embryos, and oocytes, a well-structured AI component with image analysis can improve detection efficien , reduce errors, and gain less manual classification. However, the main limitations of current studies range from the breadth and quality of data, which has a significant impact on the use of a trained model, application, and standard practice. Data used in most studies are limited, from a single source, and are lagging behind. Major clinical studies are still lacking to evaluate the external validity of algorithms and make extensive use of inadequate scientific resources to classify and predict, rather than to combine findings and conclusions. Anthical techniques, artificial intelligence (AI) in the treatment of infertility, are often limited and are usually spontaneous. He can see the need to improve on his or her testing and treatment, remote specialist medical systems, or the reproductive capacity of intelligence. In reproductive medicine, AI has a role [Figure 1].

Medications such as oocyte and embryo cryopreservation, assisted fertilization, prenatal testing, and embryonic stem cell technology have significantly improved clinical pregnancy rates in the 40 years since the birth of the first child *in vitro* fertilization (IVF), despite many complications. Stay.[4] The most important part of the success of IVF is the level of embryos, however, there are still gaps in methods for accurately determining the quality of eggs, sperm, and embryos. There are no embryo selection methods using one parameter or algorithm. As a result, predicting the chances of a successful pregnancy for each patient and understanding the cause of each failure is difficult In reproductive medicine, AI-based methods may provide a solution to current problems. The goal of improving the treatment and prognosis of infertile patients using large amounts of data generated by complex diagnostic and therapeutic methods is the driving force behind the development of these applications. AI has the potential to improve clinical efficac and efficien , ultimately improving the ART treatment cycle.

An Overview of Genetic Engineering

Mechanical learning (ML), natural language processing (NLP), and robotic surgery are now the three most important types of

AI methods commonly used in medical systems. Features and predictions of disease outcomes.[5] In addition to structured data, the NLP method obtains and processes relevant information from randomized clinical data, such as electronic medical records (EMRs).[6,7] NLP converts informal data into structured data that a machine can understand and analyze using machine learning techniques.

Artificial Intelligence in Health Care

Reproductive medicine applications of artificial intelligence

Choosing sperm and analyzing sperm

The study of sperm is the initial stage in determining whether or not a couple is infertile. Anomalies in human sperm samples are reflected in sperm morphology. To assess a sample's prospective fertility, the ability to distinguish sperm cell morphology and track changes in sperm motility is critical. Computer-assisted sperm analysis (CASA) equipment is currently being used in human and animal studies as well as conventional analysis. Technology can detect the fullness of sperm cells and report moving percentages and kinematic data.[8] Due to the inherent lack of consideration and difficul in assessing sperm formation in person, as well as a wide range of results obtained by different laboratories, automated image-based methods should be developed to provide meaningful and accurate results. In addition, idiopathic male factor infertility accounts for one-third of male infertility. [9] (this shows that existing sperm testing procedures cannot diagnose many of the causes of infertility. Using 2043 sperm tracks from the CASA system, researchers designed a random and quantitative way to differentiate mouse sperm movement patterns. 2017 was a year of change.[8] Human

sperm was treated in the same way. The total accuracy of this model is 89.92%, and it was enhanced using data from 425 human sperm. The researchers used dosage, total testicular volume, follicle-stimulating hormone, luteinizing hormone, complete testosterone, and ejaculate. The capacity to predict chromosomal irregularities with more than 95% accuracy. Deug drilling algorithms can also be used to improve predictions about seminal quality based on lifestyle data and environmental factors.[10] Using a list of questions and environmental parameters, two different sensory networks are designed to predict the fullness of human sperm and its flo . Despite the fact that this procedure appears to be less expensive than the more expensive laboratory tests, it can work in early detection.[11] Five AI algorithms were used to predict human reproductive ratings, and eight trait variants were used to determine acceptable traits that could more accurately predict male reproductive rates. properly remove noise. Finally, feature selection methods improved AI accuracy, as well as vector support and improved particle swarm optimizations, fit, and area under curve (AUC) level (94 and 0.932).

Oocytes are assessed and chosen

Oocyte levels play a major role in complete reproductive success, whether naturally or on ART. Pregnancy rates per oocyte currently detected are believed to be 4.5%.[12] Further knowledge of oocyte development skills will allow for the development of new IVF procedures and indicators for oocyte quality prediction and selection of the best IVF egg.[13] Most methods are designed to test and select an oocyte with the potential to develop, however, barriers such as a normal oocyte or embryo may obscure the aneuploidy and make further research needed to improve the precision and methods. As a result, applying AI selection methods for oocytes in IVF systems may open up new opportunities.[14] Photographs were taken of mouse oocytes as they grew *in vitro* from the germinal vesicle to the metaphase II phase for end-stage analysis. They used the particle image velocimetry method to calculate the cytoplasm motion velocity profil , and then analyzed data on the artifi ial neural network of differentiation to distinguish oocytes that are capable or inappropriate with 91.03% accuracy. In addition, a few studies have used noninvasive methods to quantify the developmental capacity of human oocytes. In addition, using AI to test human oocytes using end-of-life or to test genetic expression by transcriptomics or genomics may have a promising future and benefit from ART.[15]

Choosing an embryo

Fetal selection methods based on morphokinetic signals have recently been described. In addition, embryonic testing using a flexible monitoring system (Time lapse [TL]) provides continuous information on the embryonic growth stage and morphokinetics, although over time algorithms are still debated, and some researchers do not consider the evidence of fetal selection benefit (evidence).[16] In an incubator using the TL system, 800 human embryos with known implant data

have been tested repeatedly. They developed a model based on an examination of morphokinetic traits and an examination of embryo morphology in D3. Low-intensity artificial embryos can be eliminated using morphokinetics.

THE PROGNOSIS OF *IN VITRO* FERTILIZATION SUCCESS

Many infertile couples use ART to try to conceive a child. However, many infertile couples are under a lot of pressure because of the low rate of clinical pregnancy and the high cost per cycle. Physicians can streamline complementary therapies for infertile couples and enhance the effect of ART pregnancy by incorporating an effective IVF and AI predictive model[17] of the clinic. They used previous IVF/intracytoplasmic sperm injection records to predict the outcome with more than 80% AUC, indicating that more research is needed. The best predictions were the age of the woman, the number of mature embryos, and the level of serum estradiol/day of human chorionic gonadotropin treatment. The quality and size of the input database where the trained model limits even the best model in terms of performance. In a future study, efforts should be made to address these issues. The recognition of natural language.

NLP is a branch of AI that deals with the understanding and translation of a person's speech or text using the software. Combining machine learning, in-depth learning, and mathematical models allows the computer to capture the natural way people communicate. Indigenous language processing (NLP) is the subject of computer science — in particular, the branch of AI-computer computers' ability to understand the text and spoken words in a way that people can understand. NLP is an AI program that attempts to interpret human speech and extract useful insights into things like EMR data to aid in clinical decisions. Text processing and splitting are both parts of the NLP process.[18] However, instead of entering health information into a precise structure so that the computer can see the data, NLP allows doctors to write automatically.

Big data in the reproductive system involves studying a large number of patients and combining different types of data. Using AI to analyze this type of data has a lot of power to detect patterns that people do not see. EMRs are commonly used to store and share medical data. In reproductive medicine research, the use of EMRs is a good solution for data collection. Patient statistics, medical history, adverse events, physical examination, clinical laboratory findings and tracking data are all digitally recorded in EMRs. By extracting important information from EMRs through NLP, we can obtain sufficien data for the following machine learning process.

LIMITATIONS AND DIFFICULTIES OF AI RESEARCH

Some AI barriers include developmental delays, which may vary depending on what you are trying to achieve. Influence performance and lack of knowledge about high technology.

Compatibility with various systems and platforms, as well as usability. The most prevalent problems that most businesses experience when attempting to implement AI

- Identifying the correct data set
- Data security and storage
- Infrastructure
- Integration of
- AI into existing systems
- AI model training and complex algorithms.

Image analysis of sperm cells and embryos, as well as predicting ART success, are two important areas for AI research. Early diagnosis, treatment, and forecasting technology are very poor. To encourage the use of AI in reproductive medicine, further research is needed. In some cases, AI technology has evaluated or performed more than skilled physicians, raising concerns that machine learning models will eventually replace physicians. We should think of AI as a tool to help doctors grow and improve their work. Simple and repetitive tasks can be handled by machine learning, saving time, and doctors effort [19] In the meantime, clinicians should harmonize the results of machine learning models in clinical practice rather than following systemic recommendations thoughtlessly. Physicians should always check whether the model is structured in a logical way and whether it is in line with the actual clinical situation.[19] AI's role in reproductive medicine in the future.

An important guide to development in reproductive medicine is a data-based decision-making process. Through motivating programs and strengthening learning methods, it can be developed in real-time, supporting physicians in making better clinical decisions based on the patient's clinical information. Read, test, and summarize medical data using NLP to create large databases, and then use in-depth reading to read these data volumes to build models. Models are constantly being developed by comparing expert diagnoses and eventually used in AI-assisted diagnostics. The most important and important application is an AI-based medical diagnostic program, which can support physicians in resolving complex medical problems and serve as a useful medical tool. IBM's Watson is a well-known machine learning machine in health care.[18] It reveals cancer screening and treatment options. The method can help physicians make informed decisions and anticipate patient outcomes. The more information a patient provides, the more likely it is that an accurate result will be obtained.

The mechanization of IVF laboratories is also a promising area for development. Combining the technological advances in selective embryonic and embryonic stem cells, oocyte extraction by the mechanical removal of cumulus cells, oocyte formation, fertilization, embryonic culture, and monitoring embryonic development in a self-replicating machine can greatly enhance ART efficienc and effectiveness. As a result, the development of AI will benefit a large number of infertile couples.

CONCLUSION

We have accounted for all of these things in this post, keeping machine learning and AI expertise and concepts in mind. A review of the above-mentioned reproductive medicine experiments, as well as a review of AI future issues and trends, are thoroughly examined. AI trials in the medical industry will continue to rise as precision medicine develops and large data becomes more widely available. Despite its limits, present AI technology is ideally suited to addressing well-defined difficultie in a variety of therapeutic settings. Women who do not have children, such as infertility patients, could benefit from such a system, which could improve pregnancy outcomes and treatment. Similarly to a married woman who, despite her best attempts, has been unable to conceive for many years, that type of woman can assist in conceiving. We realize that AI technology capabilities are expected to grow over time and that solutions can benefi by delivering high-quality health care more precisely and effectively in practice

Financial support and sponsorship
Nil.

Conflicts of interest
There are no conflicts of interest

REFERENCES

1. Diana M, Marescaux J. Robotic surgery. Br J Surg 2015;102:e15-28.
2. Abdel-Hamid O, Mohamed AR, Jiang H, Deng L, Penn G, Yu D. Convolutional neural networks for speech recognition. IEEE/ACM Trans Audio Speech Lang Process 2014:22;1533-45.
3. LeCun Y, Bengio Y, Hinton G. Deep learning. Nature 2015;521:436-44.
4. Esteva A, Kuprel B, Novoa RA, Ko J, Swetter SM, Blau HM, *et al.* Corrigendum: Dermatologist-level classification of skin cancer with deep neural networks. Nature 2017;546:686.
5. Darcy AM, Louie AK, Roberts LW. Machine learning and the profession of medicine. JAMA 2016;315:551-2.
6. Nadkarni PM, Ohno-Machado L, Chapman WW. Natural language processing: An introduction. J Am Med Inform Assoc 2011;18:544-51.
7. Mehta N, Devarakonda MV. Machine learning, natural language programming, and electronic health records: The next step in the artificial intelligence journey? J Allergy Clin Immunol 2018;141:2019-21.e1.
8. Goodson SG, White S, Stevans AM, Bhat S, Kao CY, Jaworski S, *et al.* CASAnova: A multiclass support vector machine model for the classificatio of human sperm motility patterns. Biol Reprod 2017;97:698-708.
9. Gudeloglu A, Brahmbhatt JV, Parekattil SJ. Medical management of male infertility in the absence of a specific etiology. Semin Reprod Med 2014;32:313-8.
10. Girela JL, Gil D, Johnsson M, Gomez-Torres MJ, De Juan J. Semen parameters can be predicted from environmental factors and lifestyle using artificial intelligence methods. Biol Reprod 2013;88:99
11. Sahoo AJ, Kumar Y. Seminal quality prediction using data mining methods. Technol Health Care 2014;22:531-45.
12. Santos Filho E, Noble JA, Poli M, Griffit T, Emerson G, Wells D. A method for semi-automatic grading of human blastocyst microscope images. Hum Reprod 2012;27:2641-8.
13. Kaser DJ, Racowsky C. Clinical outcomes following selection of human preimplantation embryos with time-lapse monitoring: A systematic review. Hum Reprod Update 2014;20:617-31.
14. Armstrong S, Bhide P, Jordan V, Pacey A, Farquhar C. Time-lapse systems for embryo incubation and assessment in assisted reproduction. Cochrane Database Syst Rev 2018;5:CD011320.
15. De Geyter C, Calhaz-Jorge C, Kupka MS, Wyns C, Mocanu E, Motrenko T, *et al.* ART in Europe, 2014: Results generated from

European registries by ESHRE: The European IVF-monitoring consortium (EIM) for the European society of human reproduction and embryology (ESHRE). Hum Reprod 2018;33:1586-601.

16. Hashimoto DA, Rosman G, Rus D, Meireles OR. Artificial intelligence in surgery: Promises and perils. Ann Surg 2018;268:70-6.

17. Kohli M, Prevedello LM, Filice RW, Geis JR. Implementing machine learning in radiology practice and research. AJR Am J Roentgenol 2017;208:754-60.

18. Danilov GV, Shifrin MA, Kotik KV, Ishankulov TA, Orlov YN, Kulikov AS, *et al.* Artificial intelligence in neurosurgery: A systematic review using topic modeling. Part I: Major research areas. Sovrem Tekhnologii Med 2021;12:106-12.

19. Gyawali B. Does global oncology need artificial intelligence? Lancet Oncol 2018;19:599-600.

RFM ANALYSIS FOR CUSTOMER SEGMENTATION USING MACHINE LEARNING: A SURVEY OF A DECADE OF RESEARCH

Sushilkumar Chavhan

Assistant Professor, Department of Information Technology Yeshwantrao Chavan College of Engineering, Nagpur, Maharashtra, (India).

R. C. Dharmik

Assistant Professor, Department of Information Technology Yeshwantrao Chavan College of Engineering, Nagpur, Maharashtra, (India).

Sachin Jain

Assistant Professor, Department of Computer Science Oklahoma State University Stillwater, (United States).

Ketan Kamble

Student, Department of Information Technology YCCE, Nagpur, Maharashtra, (India).

https://doi.org/10.17993/3ctic.2022.112.166-173

ABSTRACT

Customer segmentation is a method of categorizing corporate clients into groups based on shared characteristics. In this study, we looked at the different customer segmentation methods and execute RFM analysis by using various clustering algorithms. Based on RFM values (Recent, Frequency, and Cost) of customers, the successful classification of company customers is divided into groups with comparable behaviors. Customer retention is thought to be more significant than acquiring new clients are analyzed on two different databases. Results show the significance of each method. Comparison is helps for selection of better customer segmentation.

KEYWORDS

Clustering, Classification, RFM, Customer segmentation.

1. INTRODUCTION

Customer Segmentation is way of organization of customers with respect to the various features. In recent years there has been a huge boom in opposition between companies to stay in the field. The income of the organization may be stepped forward through a patron segmentation model. According to the Pareto principle (Srivastava, 2016), 20% of the clients make a contribution greater to the sales of the organization than the relaxation Customer segmentation is the exercise of dividing an organization's clients into agencies that mirror similarity amongst clients in every group. The intention of segmenting clients is to determine how to narrate to clients in every section that allows you to maximize the fee of every patron to the business. Customer segmentation has the ability to permit entrepreneurs to cope with every patron withinside the simplest way. Using the massive quantity of statistics to be had on clients (and ability clients), a patron segmentation evaluation lets in entrepreneurs to identify discrete agencies of clients with an excessive diploma of accuracy primarily based totally on demographic, behavioral and different indicators.

Evaluation of RFM (Recency, Frequency, and Monetary) is a famend approach is worn for comparing the clients primarily based totally on their shopping for behavior. Scoring method was developed to test Recent, Frequency, and Finance ratings. Finally, ratings of all three variables are strengthened as RFM ratings from different ranges (Haiying and Yu, 2010) which are compiled to anticipate recants trends for studying existing and higher sponsor transactions history. Next step is defined as the remaining time the consumer buys. The latest currency is the type of days the sponsor takes between purchases. The latest small payment means that the sponsor visits the organization frequently in a timely manner. Similarly, extra money means that the sponsor is less likely to go to the organization soon. Frequency is described because the variety of transaction a patron makes in a selected period. The better the fee of frequency the greater unswerving are the clients of the organization.

Cash is defined as the amount spent by the investor over a period of time in a favorable period. The improvement in the amount of money spent by the large sales they provide to the organization. Each sponsor is given 3 different ratings of the latest, frequency, and economic volatility. Score points are used within a range from five to 1. The core quintile is given a five-point scale, while the others are given 4, 3, 2 and 1.

In recent years, there has been a significant increase in the number of opposition groups among companies in care within the arena. Customer retention is more important than purchasing the latest customers. Customer segregation allows people's messages to speak more to target audiences.

2. LITERATURE REVIEW

Segmentation is middle of the advertising and marketing approach due to the fact exclusive consumer organizations mean the want for exclusive advertising and marketing mixes primarily based totally on consumer conduct and its needs. Many authors give the segamentaion methods to increase the profit and sustain the company position. (Jiang and Tuzhilin, 2009) proposed K-Classifiers Segmentation algorithm which recognized that each client segmentation and consumer focused on are important to enhance the marketing performances. K-Classifiers Works as optimizer who have two tasks. Above method more resources to the ones clients who supply greater returns to the company. (He and Li, 2016) proposed a 3-dimensional approach to improving consumer health (CLV), customer pride and customer behavior. The authors conclude about the customers and the requirements for a better service. A segment used to meet customer expectations and suggest better service. (Sheshasaayee and Logeshwari, 2017) used RFM Analysis which provides the usage of CRM (Customer Relationship Management). Authors analyzed the customers by segmenting them which helps to increase company profits. Further they enhanced the segmentation by using Fuzzy Clustering Method which classified them into the appropriate scoring strategies based on their needs.

(Shah and Singh, 2012) provides the K-means algorithm and K-medoids algorithms for clustering. The presented techniques do not always yield the best answer, but they do minimise the cluster error criterion. They came to the conclusion that when the number of clusters grows, the new method takes

less time to run than existing methods. (Sheshasaayee and Logeshwari, 2017) developed hybrid method which combine RFM and LTV methods. Authors used K-means and Neural Network algorithms for segmentation with two phase models. They suggested having better optimizer for customer categorization. Using logistic regression, (Liu, Chu, Chan, and Yu, 2014) proposed predicting customer attrition. Individual marketing methods can be used to identify customers with similar churn value and to keep them. Benefit customer segmentation using various methodologies allows customers to be classified based on their relationships, allowing marketers to focus their marketing efforts on their strengths and target benefit categories accordingly.

3. TYPES OF CUSTOMER SEGMENTATION

Customer segmentation models come in a range of shapes and sizes, ranging from simple to complex, and they can be used for a variety of purposes. Demographic, Recency, Frequency Monetary (RFM), High-Value Customers, Customer Status, Behavioral, and Psychographic models are some of the most common models.

3.1 DEMOGRAPHIC

It is a method of segmenting customers based on characteristics such as age, gender, ethnicity, income, education, religion, and career (Lu, Lin, Lu, and Zhang, 2014).

3.2 RFM

It is a direct segmentation strategy whose main goal is to categories clients based on the time since their previous purchase, the total number of purchases they've made (frequency), and the amount they've spent (monetary) (Sheshasaayee and Logeshwari, 2017).

3.3 HVCS (HIGH-VALUE CUSTOMER)

It's an extended RFM segmentation for any firm, focusing on what traits they have in common so you can get more of them.

3.4 CUSTOMER STATUS

It is a mechanism which check the status of customer which categories as active and lapsed. The focus of this method is to how the customer engaged by the company on the time period as a status.

3.5 BEHAVIORAL SEGMENTATION

It is a mechanism which check the status of customer which categories as active and lapsed. The focus of this method is to how the customer engaged by the company on the time period as a status.

3.6 PSYCHOGRAPHIC SEGMENTATION

It is allows grouping the customers based on attitudes, beliefs, or even personality traits. For this we require good data analysis method. Analysis done on all above attributes.

3.7 GEOGRAPHIC SEGMENTATION

It is allows grouping the customers based on geographical location i.e region, city, country etc. It is used when target area is location wise improvement of services and increased the profit.

4. MAJOR CLUSTERING TECHNOLOGIES FOR CUSTOMER SEGMENTATION

4.1 K –MEANS

It is a popular unsupervised method that accepts parameters and k value as number of clusters as inserting and separating data into clusters with high intra-cluster similarities. K-Means is a method that repeats itself, adding the number of centroids before each multiplication. Depending on the inches calculated for each multiplication, data points are allocated among distinct sets. Using min max normalization, the RFM values are normalized (Lee and Memon, 2016).

4.2 FUZZY C-MEANS

It is a Method (?, ?) that allows a specific piece of data to appear to numerous clusters. It no longer determines a cluster's club records for a given information factor. Rather, the probabilities of a specific information factor with similarities are determined. The advantage of this method over previously discussed K-Means is that the final result obtained of a large and comparable database is most suitable than a set of K-method rules, because in the KMeans method, as cluster formation of based on data element. The normalization in this approach is done using min max normalization. Cluster RFM value is based on cluster (Zahrotun, 2017) value.

4.3 REPETITIVE MEDIAN K-MEANS

It's a novel approach to determining the initial centroids for the K-Means method. The traditional K–Means algorithm's range of iterations and computational time is reduced by choosing preliminary centroids with it's proposed distribution. RFM values will be combined and sorted into three vectors, R', F', and M ', respectively. The initial centroids are calculated using the median value of each vector. The median values are derived k times iteratively from the R', F', and M' values, depending on the value of k. (number of segments).

5. RFM ANALYSIS USING ON ONLINE SHOPPING DATA

RFM: according to following definitions. The RFM method divides clients into segments. It categorises clients based on their previous purchase transactions, taking into account criteria like as Recency (R): Last purchase date in specified session. Frequency (F):Purchase count in the specified session. Monetary (M):Value of Purchase in the specified session Based on forms needs, we define a season with different intervals for this model and we calculate RFM values for each customer. Working with a set of customer activity data in an online retail store year-round from the University of California Irwin (UCI) repository was used to evaluate system performance.

The following is a sample customer separation process. STEP 1: Sort the customer by recency.

STEP 2 AND 3: Sort the customer from most to least frequent customer and summarized the F, M score. STEP 4: Rank customers by combining R,F, and M ranking

Fig1: Sample Data.

Fig2: Calculation of Recency.

Fig3: Calculation of F and M Score.

CUSTOMER ID	RFM CELL	RFM SCORE
1	5,4,4	4.3
2	4,5,4	4.3
3	1,1,1	1.0
4	2,2,2	2.0
5	3,3,3	3.0
6	2,2,2	2.0
7	4,3,3	3.3
8	1,1,5	2.3
9	1,5,5	3.7
10	3,4,3	3.3
11	5,4,4	4.3
12	5,5,5	5.0
13	2,3,2	2.3
14	3,2,1	2.0
15	4,1,1	2.0

Fig4: Customer Segmentation.

6. ANALYSIS OF VARIOUS ALGORITHMS

For evaluation of commonly used clustering algorithm was done on two different open source databases like the transactional data set of the customers of an online retail store available at UCI repository and on e-commerce datasets which is available at UCI Machine Learning Repository.

Fig5: Result Analysis of various Algorithms on online retail.

From above analysis it is observed that Fuzzy C means perform well on the basis of average Silhouette width but the time taken is more and number of iterations are also more as compared to others algorithms.
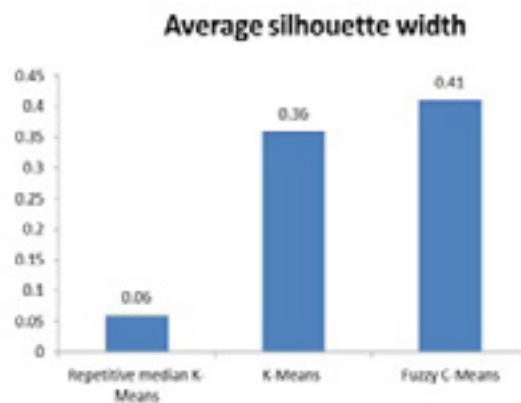

Fig6: Result Analysis of various Algorithms on E- commerce data.

7. CONCLUSION AND FUTURE SCOPE

This paper provides the overview of customer Segmentation and its different type's with types. RFM segmentation allows to group based on the requirements and target the different marketing strategies. In future more complex methods would be designed to target specific customers and the methods would also be more flexible if the company wants to target a different audience for a particular time or wants to permanently change their customers based on the needs of the company or priorities of the customer. The RFM should be made more flexible according to the needs of the different companies.

REFERENCES

[1] Haiying, M. and Yu, G. 2010. Customer segmentation study of college students based on the rfm. 3860–3863.

[2] He, X. and Li, C. 2016. The research and application of customer segmentation on e-commerce websites. 203–208.

[3] Jiang, T. and Tuzhilin, A. 2009. Improving personalization solutions through optimal segmentation of customer bases. IEEE Trans. Knowl. Data Eng. 21, 305–320.

[4] Lee, D.-H. and Memon, K. 2016. Generalised fuzzy c-means clustering algorithm with local information. IET Image Processing 11.

[5] Liu, C., Chu, S.-W., Chan, Y.-K., and Yu, S. 2014. A modified k-means algorithm - two-layer k-means algorithm. 447–450.

[6] Lu, N., Lin, H., Lu, J., and Zhang, G. 2014. A customer churn prediction model in telecom industry using boosting. Industrial Informatics, IEEE Transactions on 10, 1659–1665.

[7] Shah, S. and Singh, M. 2012. Comparison of a time efficient modified k-mean algorithm with k-mean and k-medoid algorithm.

[8] Sheshasaayee, A. and Logeshwari, L. 2017. An efficiency analysis on the tpa clustering methods for intelligent customer segmentation. 784–788.

[9] Srivastava, R. 2016. Identification of customer clusters using rfm model: A case of diverse purchaser classification.

[10] Zahrotun, L. 2017. Implementation of data mining technique for customer relationship management (crm) on online shop tokodiapers.com with fuzzy c-means clustering. 299–303.

About Journal

The International Journal of Next-Generation Computing (IJNGC) is a peer-reviewed journal aimed at providing a platform for researchers to showcase and disseminate high-quality research in the domain of next-generation computing. With the introduction of new computing paradigms such as cloud computing, IJNGC promises to be a high-quality and highly competitive dissemination forum for new ideas, technology focus, research results and sicussions in these areas.

Feature Selection for Ranking using Heuristics based Learning to Rank using Machine Learning

Published Nov 26, 2022

Download

🔒 PDF (https://ijngc.perpetualinnovation.net/index.php/ijngc/article/view/958/386)

Statistic

Volume 13, Special Issue 5, November 2022 (https://ijngc.perpetualinnovation.net/index.php/ijngc/issue/view/45)

Sushilkumar Chavhan
Yeshwantrao Chavan College of Engineering, Nagpur

Dr. R. C. Dharmik
Yeshwantrao Chavan College of Engineering, Nagpur

Abstract

Machine Learning based ranking is done every filed. Ranking is also solved by using (LTR i. e. learning to Rank) techniques. In this work, we propose a Heuristics LTR based models for information retrieval. Different new algorithms are tackling the problem feature selection in ranking. In this proposed model try to makes use of the simulated annealing and Principal Component analysis for document retrieval using learning to rank. A use of simulated annealing heuristics method used for the feature Selection to test the results improvement. The feature extraction technique helps to find the minimal subsets of features for better results. The core idea of the proposed framework is to make use of k-fold cross validation of training queries in the SA as well as the training queries in the any feature selection method to extract features and only using training quires make use of validation and test quires to create a learning model with LTR. The standard evaluation measures are used to verify the significant improvement in the proposed model. Performance of proposed model are measured based on prediction on some selected benchmark datasets, Improvement in the results are compare on recent high performed pairwise algorithms.

How to Cite

Sushilkumar Chavhan, & Dr. R. C. Dharmik. (2022). Feature Selection for Ranking using Heuristics based Learning to Rank using Machine Learning. *International Journal of Next-Generation Computing*, *13*(5). https://doi.org/10.47164/ijngc.v13i5.958

More Citation Formats ▾

References

1. Aljarah, I., Al-Zoubi, A., Faris, H., Hassonah, M., Mirjalili, S., and Saadeh, H. 2018. Simultaneous feature selection and support vector machine optimization using the grasshopper optimization algorithm. Cognitive Computation 10. DOI: https://doi.org/10.1007/s12559-017-9542-9 (https://doi.org/10.1007/s12559-017-9542-9)

2. Bai, B., Weston, J., Grangier, D., Collobert, R., Sadamasa, K., Qi, Y., Chapelle, O., and Weinberger, K. 2010. Learning to rank with (a lot of) word features. Information Retrieval 13, 291–314. DOI: https://doi.org/10.1007/s10791-009-9117-9 (https://doi.org/10.1007/s10791-009-9117-9)

3. Burges, C., Ragno, R., and Le, Q. 2006. Learning to rank with nonsmooth cost functions.193–200.

4. Chavhan, S., Raghuwanshi, M., and Dharmik, R. 2021. Information retrieval using machine learning for ranking: A review. Journal of Physics: Conference Series 1913, 012150. DOI: https://doi.org/10.1088/1742-6596/1913/1/012150 (https://doi.org/10.1088/1742-6596/1913/1/012150)

5. Chelaru, S., Orellana-Rodriguez, C., and Altingo¨vde, I. 2012. Can social features help learning to rank youtube videos? DOI: https://doi.org/10.1007/978-3-642-35063-4_40 (https://doi.org/10.1007/978-3-642-35063-4_40)

6. Cheng, F., Guo, W., and Zhang, X. 2018. Mofsrank: A multiobjective evolutionary algorithm for feature selection in learning to rank. Complex. 2018, 7837696:1–7837696:14. DOI: https://doi.org/10.1155/2018/7837696 (https://doi.org/10.1155/2018/7837696)

7. Duan, Y., Jiang, L., Qin, T., Zhou, M., and Shum, H.-Y. 2010. An empirical study on learning to rank of tweets 1. Vol. 2. 295–303.

8. Freund, Y., Iyer, R., Schapire, R., and Singer, Y. 2003. An efficient boosting algorithm for combining preferences. Journal of Machine Learning Research 4, 933–969.

9. Johnson, D., Aragon, C., McGeoch, L., and Schevon, C. 1989. Optimization by simulated annealing: An experimental evaluation. part i, graph partitioning. Operations Research 37, 865–892. DOI: https://doi.org/10.1287/opre.37.6.865 (https://doi.org/10.1287/opre.37.6.865)

10. Kang, C., Wang, X., Chen, J., Liao, C., Chang, Y., Tseng, B., and Zheng, Z. 2011. Learning to re-rank web search results with multiple pairwise features. 735–744. DOI: https://doi.org/10.1145/1935826.1935924 (https://doi.org/10.1145/1935826.1935924)

11. Lai, H., Pan, Y., and Tang, Y. 2013. Fsmrank: Feature selection algorithm for learning to rank. Neural Networks and Learning Systems, IEEE Transactions on 24, 940–952. DOI: https://doi.org/10.1109/TNNLS.2013.2247628 (https://doi.org/10.1109/TNNLS.2013.2247628)

12. Macdonald, C., Santos, R., and Ounis, I. 2012. On the usefulness of query features for learning to rank. 2559–2562. DOI: https://doi.org/10.1145/2396761.2398691 (https://doi.org/10.1145/2396761.2398691)

13. Purpura, A., Buchner, K., Silvello, G., and Susto, G. A. 2021. Neural Feature Selection for Learning to Rank. 342–349. DOI: https://doi.org/10.1007/978-3-030-72240-1_34 (https://doi.org/10.1007/978-3-030-72240-1_34)

14. Rahangdale, A. and Raut, S. 2019. Deep neural network regularization for feature selection in learning-to-rank. IEEE Access 7, 53988–54006. DOI: https://doi.org/10.1109/ACCESS.2019.2902640 (https://doi.org/10.1109/ACCESS.2019.2902640)

15. Rajpurohit, J., Sharma, D. T., and Abraham, A. 2017. Glossary of metaheuristic algo- rithms. 181–205.

16. Sousa, D., Canuto, S., Gonc¸alves, M., Couto, T., and Martins, W. 2019. Risk-sensitive learning to rank with evolutionary multi-objective feature selection. ACM Transactions on Information Systems 37, 1–34. DOI: https://doi.org/10.1145/3300196 (https://doi.org/10.1145/3300196)

17. Xu, J. and Li, H. 2007. Adarank: a boosting algorithm for information retrieval. In SIGIR. DOI: https://doi.org/10.1145/1277741.1277809 (https://doi.org/10.1145/1277741.1277809)

18. Yang, Y. and Gopal, S. 2012. Multilabel classification with meta-level features in a learning- to-rank framework. Machine Learning 88. DOI: https://doi.org/10.1007/s10994-011-5270-7 (https://doi.org/10.1007/s10994-011-5270-7)

19. Yeh, J.-Y. and Tsai, C.-J. 2021. A graph-based feature selection method for learning to rank using spectral clustering for redundancy minimization and biased pagerank for relevance analysis. Computer Science and Information Systems 19, 42–42. DOI: https://doi.org/10.2298/CSIS201220042Y (https://doi.org/10.2298/CSIS201220042Y)

20. Zheng, H.-T., Li, Q., Jiang, Y., Xia, S.-T., and Zhang, L. 2013. Exploiting multiple features for learning to rank in expert finding. In Advanced Data Mining and Applica- tions, H. Motoda, Z. Wu, L. Cao, O. Zaiane, M. Yao, and W. Wang, Eds. Springer Berlin Heidelberg, Berlin, Heidelberg, 219–230. DOI: https://doi.org/10.1007/978-3-642-53917-6_20 (https://doi.org/10.1007/978-3-642-53917-6_20)

Address

Perpetual Innovation Media
Pvt Ltd.
5006, Hauz Qazi,
Near Canara Bank,
Delhi-6
Phone: 095604044488,
09990893093
info@perpetualinnovation.net

Home (https://ijngc.perpetualinnovation.net/index.php/ijngc)
Current Issue (https://ijngc.perpetualinnovation.net/index.php/ijngc/issue/view/35)
Archives (https://ijngc.perpetualinnovation.net/index.php/ijngc/issue/archive)
About the Journal (https://ijngc.perpetualinnovation.net/index.php/ijngc/about)
Announcement (https://ijngc.perpetualinnovation.net/index.php/ijngc/announcement)
Editorial Team (https://ijngc.perpetualinnovation.net/index.php/ijngc/about/editorialTeam)

Academic Free Theme
by openjournaltheme.com (https://openjournaltheme.com)

Motion Pattern Based Anomalous Pedestrian Activity Detection

Kamal Omprakash Hajari*
Yeshwantrao Chavan College of Engineering, Rashtrasant Tukadoji Maharaj Nagpur University, Department of Information Technology, Maharashtra, India – 441110
E-mail: kamalhajari123@gmail.com
ORCID iD: https://orcid.org/0000-0002-4959-8117
*Corresponding Author

Ujwalla Haridas Gawande
Yeshwantrao Chavan College of Engineering, Rashtrasant Tukadoji Maharaj Nagpur University, Department of Information Technology, Maharashtra, India - 441110
E-mail: ujwallgawande@yahoo.co.in
ORCID iD: https://orcid.org/0000-0002-7059-0937

Yogesh Golhar
St. Vincent Palloti College of Engineering and Technology, Rashtrasant Tukadoji Maharaj Nagpur University, Department of Computer Engineering, Maharashtra, India - 441110
E-mail: yogesh.golhar28@gmail.com
ORCID iD: https://orcid.org/0000-0002-6817-3552

Abstract: In this paper, an efficient technique for anomalous pedestrian activity detection in the academic institution is proposed. At the pixel and block levels, the proposed method elicits motion components that accurately represent pedestrian action, velocity, and direction, as well as along a frame. We also adopted these motion features to detect anomalous actions. The detection of anomalous behavior in academic environments is not available at the moment. Similarly, the existing method produces a high number of false positives. An anomaly detection dataset and a newly designed proposed student behavior database were used to validate the proposed framework. A significant improvement in anomalous activity recognition has been demonstrated in experimental results. Based on motion features, the proposed method reduces false positives by 3% and increases true positives by 5%. A discussion of future research directions concludes the paper.

Index Terms: Artificial Intelligence, Computer vision, Pedestrian dataset, Tracking, Detection, Motion Pattern, Anomalous activity.

1. Introduction

Surveillance cameras are now used to keep an eye on both public and private notable areas. Monitoring the conduct of pedestrians under human supervision is a challenging undertaking. It is difficult and time-consuming to identify and separate anomalous behavior patterns from video in real-time with the conventional approach. We need a system that can identify anomalous actions in real-time due to system restrictions. Recognizing human movement and activity in video frames has drawn the attention of numerous academics and experts in this field in recent years [1, 2, 3]. In recent years, expert's attention has shifted towards spotting anomalous activities in densely populated areas. Pedestrians cannot be detected and tracked in high-density areas due to factors like partial or total occlusion of objects, changes in object size, and variations in ambient lighting. The use of texture-based information for identifying unusual behaviors in crowded situations has been attempted by numerous authors. Example techniques include temporal gradients [4], dynamic texture characteristics [5], and spatio-temporal frequency features [6, 7]. Optical flows have also been studied, which can be used in video frames to identify motion features directly. Examples include motion pattern clusters [8, 9, 10], force map generation for congested area behavior prediction [12], heat map generation for motion pattern map generation [8], spatial motion feature [11], trajectory-based object motion analysis [14], motion of

individual object detection using an optical flow of motion directions [13], and isolated object motion pattern intensity based histography [13]. The motion flow pattern strategy has been shown to be useful in prior research, and we think there is still an opportunity for development in the current approaches. It is crucial to include information on objects of various sizes, their motions, speeds, and interactions between frames. By carefully examining the information related to this motion, we can improve our performance. The information concerning this movement can help us perform better if we take it into account. Regardless of the size and orientation of the object, the proposed methodology extracts the movement of the moving pedestrian.
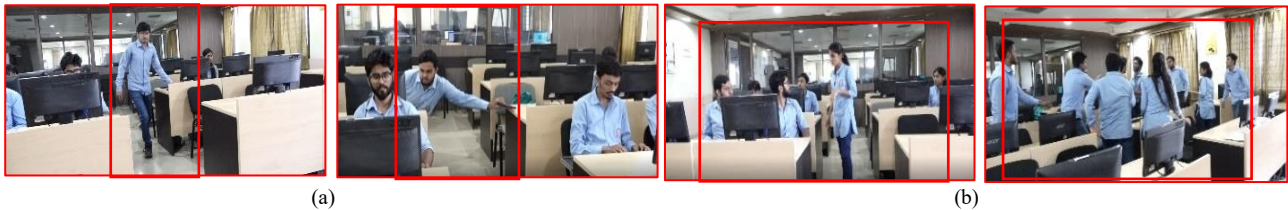

(a)   (b)

Fig. 1. Example of academic activity student anomalous behavior. (a) Mobile phone stealing (Local region). (b) Dispute in the lab. (Global region).

We outline a brand-new motion component that effectively captures the motion patterns of objects in a congested space. In this method, distinct activity areas in video frames into two groups: local and global. Both the region of extraordinary activity and the zone of regular activity are shown in Fig.1. A local area is a discrete active area inside an abnormal area. A global region, on the other hand, denotes the area where odd behaviors are seen. Different methods of determining the region's extraordinary activity have been introduced in the literature. In [15] the author proposed a social force map-based method for spotting global aberrant behavior. A particle grid was used to map the optical flow field, and the forces exerted by the particles were determined. In [11] the author described a method for spotting fake local motions in a scene. In order to locate abnormalities close by, they created a subspace feature map employing optical flow features of various sizes. A real-time monitoring system needs a comprehensive framework that can identify odd student's behavior. We put forth a special method for spotting localized and widespread aberrant student conduct in a crowded setting. We evaluated the proposed approach using our own student behavior dataset as well as other benchmark datasets, such as the University of Minnesota anomaly detection datasets. The proposed contribution has the following objectives:

1. The main objective of the motion-based unusual activity recognition systems is to make surveillance systems smarter and more intelligent.
2. To develop the active video surveillance system that can work efficiently in the real-time environment and it can be used as active and real-time automated medium of security.
3. To detect anomalous or abnormal activities in videos to avoid future happening or to alert whenever any type of mis- happening occur.
4. To detect intruders around the perimeter of the main building.

The proposed contributions are as follows:

1. To solve existing state-of-the-art database concerns such as size and illumination variance in pedestrian images, we present the motion pattern based unusual activity detection framework.
2. We propose a student activity dataset. In which we have recorded the student's normal and anomalous activities.
3. Within the framework of the proposed pedestrian dataset for academic settings, we conduct a comprehensive review of previous work and compare existing techniques.

The remainder of the contribution is structured as follows: In Section 2, the current contribution in this field is described. In Section 3, we suggest a motion feature-based anomalous activity detection system. A novel pedestrian, a database of common behaviors created in an academic environment, and experimental findings are covered in Section 4. A research direction is given in the final section.

2. Literature Survey

The most recent and pertinent datasets on pedestrians are described in this section. We also go through the limitations of advanced deep learning algorithms for detecting, following, and identifying anomalous conduct in pedestrians.

2.1. Anomalous activity detection recent methodology

The detection of unexpected activity has recently attracted the attention of researchers in smart video surveillance systems. The authors of [17] discuss how challenging it is to interpret and model behavior from surveillance footage.

Violations were found utilizing likelihood ratio analysis and categories of pedestrian legal action in an unsupervised learning framework. The author of [18] offered a method for locating anomalies in a spatial and temporal context. They showed an immediate event for a specific object in a scene that includes the object's position, movement, direction, and velocity. They combine three partitioned atomic events to describe legitimate occurrences. The aforementioned strategies are not appropriate for situations when it is difficult to detect and monitor a single pedestrian in high-density locations, under various lighting conditions, and at various scales. Other more recent studies use motion flow and directional data to track and recognize pedestrians. The authors in [19] use the Kanade Lucas-Tomasi (KLT) technique, in which things are represented utilizing the motion of the objects. It employs two distinct categories of historical and self-history descriptors, as well as the histories of surrounding objects, to detect anomalies in a scene [10]. The author of [20] described a method for manually counting the number of persons in a photograph. Along with foreground relationships, they also used an optical-flow motion pattern. They calculated the crowd's exponential distribution patterns as well as the dynamic energy of using optical flow to distinguish between running and walking motions. Understanding and simulating densely populated people behavior has been the focus of several academics [21, 22, 23, 24]. By modelling the behavior of the crowd, several techniques were employed to find abnormal activity around the world. The social force model was employed by the author in [22] to describe crowd behavior. This technique locates and detects the object in a scene by utilizing the optical flow of moving objects [25].

The social force, which was calculated via latent Dirichlet allocation, is used to distribute normal activities. The authors of [26] examine social behavior and its behavioral using interactive energy potentials. The moving objects in a scene are represented as spatiotemporal interest points [27], and a KLT tracker is used to keep track of each object in a frame [19] [33]. On the other hand, other research teams have focused on identifying regional aberrant activity. The phrase "quantifiable" is used by the author to describe how uncommon it is to choose uncorrelated motions from a geographical environment in [11]. They identified the index in numerous channels that were travelling in diverse directions and at various rates. Nearly all the anomalous behavior in the area could be detected using the linear map that was provided. The author of [8] used motion intensities to build a motion heat map and compared it to local motion fluctuations. The authors of [5] use atypical behaviors that are localized in crowded settings utilizing spatial cues. Once more, crowd behavior analysis has been done using spatio-temporal cuboids that were recovered from optical flow or gradient pattern characteristics [29, 34, 35, 36, 37]. The aforementioned techniques have been found to be effective in research, although they are often only capable of spotting odd activity in a local or global setting. In present state-of-the-art view, depicting pedestrian activity in a high-density scene can be accomplished by considering the motion flows pattern, changing item sizes, and interactions between close-by objects in a frame [38, 39, 40]. This can improve performance in detecting anomalous activity. In this study, we offer a powerful technique for capturing motion data and employing a motion feature to identify both local and global aberrant behaviors [40, 41, 42].

2.2. Pedestrian Dataset

We outline pedestrian datasets used by scientists to identify anomalous activities and detect and track pedestrians. First, there are 350 000 annotated bounding boxes in the Caltech dataset that represent 2,300 distinct pedestrians. Using the camera installed on the car and a city road, this dataset was produced [3]. The second dataset is the well-known pedestrian dataset from MIT, which includes examples of high-quality pedestrian images. There are 709 different pedestrians present. The variety of posture images captured on city streets [4], whether in front view or back view, is somewhat constrained. Third, Daimler, this dataset documents pedestrian activity in an urban setting during daylight hours using cameras mounted on moving vehicles. The dataset consists of ground truth images, floating disparity map files, annotated labeled bounding boxes, and pedestrian tracking features. 15560 pedestrian images and 6744 annotated pedestrian images make up the training set. 56,492 annotated images and 21,790 images of pedestrians make up the test set [5]. The ATCI dataset, a database of pedestrians collected by a typical car's rear-view camera, is used to evaluate pedestrian detection in parking lots, metropolitan settings, city streets, and private as well as public lanes. The data collection consists of 200,000 indicated pedestrian bounding boxes and 250 video clips, each lasting 76 minutes and taken under daylight conditions with contrast weather conditions [6]. The traffic scene is observed from the inside of the car using the ETH dataset. Over the car, the actions of pedestrians are seen. The dataset can be used in an urban environment for mobile platform-based pedestrian tracking and recognition. The dataset includes both on-road vehicles and pedestrians [7]. The TUD-Brussels dataset was produced in an urban setting on a mobile device. The vehicle's front side was equipped with a camera that was used to capture the activity of crowded metropolitan streets. It can be used in urban driving safety scenarios [8]. The INRIA dataset is one of the most ethereal pedestrian detection datasets. It includes human activity along with a moving camera and intricate background scenes with different variations in posture, appearance, clothing, background, lighting, contrast, etc. [9]. Static objects with varying angles and positions can be found in an urban scene in the PASCAL Visual Object Classes (VOC) 2017 and 2007 collection. The objective of this dataset was to identify visual item types in practical situations. There are 20 distinct categories in this collection, including those for people, cars, trees, and road signs [10]. The MS COCO 2018 dataset was used to create the Common Object in Context [11].

Recently, the 2018 dataset was used with an emphasis on stimulus item detection to identify various things in the context. The annotations provide instances of various items related to 91 distinct human segmentation categories and 80 distinct object categories. There are five picture labels per sample image and key point annotations for pedestrian examples. The COCO 2018 dataset tasks include (1) real-scene item recognition with a segmentation mask, (2) panoptic

segmentation, (3) pedestrian key point evaluation, and (4) Dense Pose estimation in a congested scene [12]. The Mapillary Vistas Research dataset is used to segment street pictures [13]. With the use of panoramic segmentation, which successfully combines the ideas of semantic and instance segmentation, pedestrians and other non-living categories are solved. Table 1 compares pedestrian databases and the reasons for their video surveillance. We've also added our suggested dataset, which is described in the section after this one. The usage, size, environment, label, and annotation of the dataset all play a role in the link. These specifics are needed to confirm that the object detection and tracking algorithms are accurate.

Table 1. Comparison of benchmark pedestrian dataset.

Dataset	Dataset size	Annotation	Environment	Year	Ref.	Issues and Challenges
Caltech	250000 frames	2300 unique pedestrian	City street	2012	[3]	Only urban roads are captured.
MIT	709 unique pedestrians	No annotated pedestrian	Day light scenario	2000, 2005	[4]	Missing annotation not allow user to verify different techniques.
Daimler	15,560 unique pedestrians	Ground truth with bounding boxes.	City street	2016	[5]	Only urban roads are captured.
GM-ATCI	Video clips:250	Annotated pedestrian bounding boxes: 200K	Day and complex Weather and lighting	2015	[6]	Only urban roads are captured. Side view of road not captured.
ETH	Videos	Annotated cars and pedestrians	City street	2010	[7]	Small size dataset. Limited scenarios cover.
TUD Brussels	1092 frames	Pedestrian Annotation 1776	City street	2009	[8]	Only urban roads are captured.
INRIA	498 images	Manual Annotations	City street	2005	[9]	Only urban roads are captured.
PASCAL VOC 2012	11,530 images, 20 objects classes	ROI Annotated 27,450	City street	2012	[10]	Only urban roads are captured.
MS COCO 2017	328,124 images	Segmented people object	City street	2017	[11]	Only urban roads are captured.
MS COCO 2015	328,124 images	Segmented people object	City street	2015	[12]	Only urban roads are captured.
Mapillary Vistas	152 objects , 25,000 images	Pixel accurate instance Pedestrian	City street	2017	[13]	Only urban roads are captured. Side view of road not captured.

3. Proposed Methodology

The proposed method accurately depicts the moving object features in dense locations by exploiting data on pedestrian motion. We noticed the quick and deliberate movement of an unusual pedestrian activity in both the local and global parts of the image. The general design of the proposed method is depicted in Fig.2. Each frame is split into blocks, from which motion data is then extracted to create motion characteristics at the pixel and block levels.

Input Video   **Pixel level Optical flow**   **Local and Global region identification**

Motion Feature Vector   **K-Means cluttering**   **Motion Estimation**
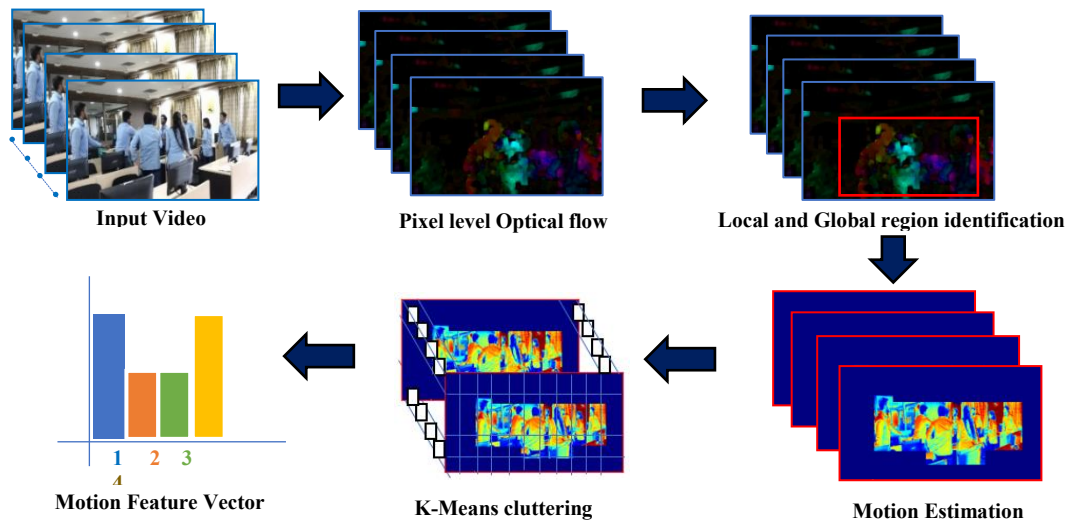
Fig. 2. Proposed framework architecture for motion feature extraction using Pixel-level Optical Flow.

The following steps comprise the motion feature extraction process:

1. The activities of moving objects are segmented at the pixel and block levels and computed progressively throughout a set of frames.
2. First, the motion information is extracted at pixel level using the optical flow method. The motion feature represented by (u, v) that encodes the displacement in x and y direction between pixels in an 8-neighborhood. i.e. (left, right, up-left, up-right, down, down-left, and down-right). The optical flow is computed for each pixel $I(x, y, t)$. It changes its location by (dx, dy) at time dt. It is represented by Eq. 1.

$$I(x, y, t) = I(x + dx, y + dy, t + dt) \tag{1}$$

3. Next, the following equation is obtained by taking the Taylor series approximation of the right-hand side, eliminating common phrases, and dividing by dt:

$$f_x u + f_y v + f_t = 0 \tag{2}$$

Were,

$$f_x = \frac{\partial f}{\partial x} \text{ and } f_y = \frac{\partial f}{\partial y}$$

$$u = \frac{\partial x}{\partial t} \text{ and } v = \frac{\partial y}{\partial t}$$

Here, f_x and f_y are the gradient and f_t is the gradient over time. (u, v) are the unknown term computed using the Lucas-Kanade method and it is represented by Eq. 3.

$$\begin{bmatrix} u \\ v \end{bmatrix} = \begin{bmatrix} \sum_i fx_i^2 & \sum_i fx_i\, fy_i \\ \sum_i fx_i\, fy_i & \sum_i fy_i^2 \end{bmatrix} \begin{bmatrix} -\sum_i fx_i\, ft_i \\ -\sum_i fy_i\, ft_i \end{bmatrix}$$

4. Different orientations of the motion characteristics are retrieved. A single feature matrix that embodies both spatial and temporal properties is produced after the integration of motion information.
5. To categorise the activity, k-means clustering is done for each zone to pinpoint the global and local region.
6. Frame-level clustering produces different clustered motion sequence that is represented as features. Extracted features contain the motion of an item in each frame.
7. Using pixel-level localization, we may pinpoint the precise position of the unexpected behaviour after classifying a frame as unusual. The procedure will go on until the entire video sequence has been produced.

A technique that involves going through each frame of a video stream and looking for anomalous human activity. Each pixel's optical flow in Eq. 3 is first extracted using the proposed method.

$$Block_i = \frac{1}{J} \sum_{j=0}^{n} f(x, y)_i^j \tag{3}$$

Where, $Block_i$ represented by the ith position in block of optical flow, each pixel in a frame size is denoted by J, i^{th} block j^{th} pixel of each individual frame of optical flow is denoted by $f(x, y)_i^j$.

Furthermore, each block threshold is computed, which is represented by Th_d using optical flow motion pattern denoted by $Block_i$ and it is having the width Wd computed using the Eq. 4.

$$Th_d \leftarrow Block_i \; x \; Wd \tag{4}$$

If the $EucliD_{(i,j)}$ less than the threshold then the output is 1 and in other condition it is set to 0. The angle between the motion feature vector represented by Θ_{ij}.

$$\Theta_{ij} \begin{cases} 1 & EucliD_{(i,j)} < Th_d \\ 0 & \text{Otherwise} \end{cases}$$

The motion feature vector is computed using $MotF\,(\Theta B_i)$, $EucliD_{(i,j)}$, and $Block_i$ represented by Eq. 5.

$$MotF = \frac{MotF\,(\Theta B_i) + EucliD_{(i,j)}}{Block_i} \tag{5}$$

wherein MF is the motion vector of the block. The Euclidean distance between ith and jth block is represented by $EucliD_{(i,j)}$. The algorithm that follows provides a basic description of motion feature extraction. Additionally, the motion region in a frame was clustered at the frame level, with each cluster's optical pixel flow in a distinct direction being considered the feature vector. The likelihood of unexpected behavior in the matching block decreases as the distance between them grows closer together. The classification of anomalous activities in additional frames is possible if a higher value of distance is found. So, the current scene is identified as an uncommon activity frame if the distance exceeds a certain limit of the constant threshold value. Next, we will go over the findings of the experiment.

Algorithm: Motion information retrieval algorithm for spotting anomalous human activities in video.

	Inputs:	*Vi, the surveillance video input*
		N, No. of frames in video
		W, Width of the block
		S, Size of block for each frame
		f, the sequence of frame
		Blk, the individual block within the frame
	Output:	*Mof, the motion feature vector*

3   [Read sequence of frame from video]
  for f = 1 to *N* **do**
   [Compute for each block Blk]
   for i = 1 to *S* **do**
    [Compute optical flow at the pixel level]
    $(u, v) \leftarrow OpticalFlow (Blk_i)$
    [Compute each block threshold]
    $Th_d \leftarrow Blk_i \; x \; W$
4   [Process neighbor frames in video sequence]
    for j = 1 to *K* **do**
5   [Compare the dissimilar frame in video sequence]
     If i ≠ j **then**
     [Compute the neighbor block Euclidean distance]
     $EuD_{(i,j)} \leftarrow EuD(Blk_i, Blk_j)$
6   [Compute distance matrix and compare with threshold]
     if $| EuD_{(i,j)} < \; Th_d|$ **then**
7   *Compute Angle Θ_{ij} across adjacent block Blk_i and Blk_j*
8   *if* $-\Theta Blk_i < \Theta_{ij} < \Theta Blk_j$ **then**
9        $MoF \leftarrow MoF(\Theta Blk_i) + EuD_{(i,j)}/Blk_i$
10   *end if*
11   *end if*
12   *end if*
13   *end for*
14   *end for*
15   *end for*

---

4. Experimental Results

In the experiment, datasets for proposed student behaviour, anomaly detection datasets from the University of Minnesota, and public databases were all used. Two different factors were taken into account: 1) In the proposed and University of Minnesota datasets for anomaly identification, identifying global unusual activity at the frame level; and 2) identifying local odd activity at the and pixel levels. In this case, the pixel level detection accuracy was assessed using the fact that the localized area's - which is regarded as exceptional - overlapping size is greater than 40% of the ground truth. Similarly to earlier studies [31, 32, 33], we used the parameters of the receiver operating characteristics (ROC) curve, the area under the ROC curve (AUC), and the equal error rate (EER).

4.1. University of Minnesota Pedestrian Dataset

The University of Minnesota dataset includes 11 video clips of crowded escape situations from three separate indoor and outdoor environments. There are 7,740 frames total, each measuring 320x240 pixels. A person walks around the scene at the beginning of each video segment. In this instance, walking was regarded as a typical activity (Fig.3a). Everyone in each clip makes an abrupt, quick-moving movement away from the scene (Fig.3b), which was considered unique in this collection. Walking along a walkway was expected to be a typical activity for this dataset. Ground truths at the pixel and frame levels are provided by the dataset, allowing for the localization of the unexpected activity-rich

areas. 34 practice clips and 36 exam segments make up single pedestrian. It has a 238x158 frame size. There are 16 training video and 12 test clips in multiple pedestrian. The frame is 360x240 in size. The training videos only show regular pedestrians moving along a walkway. Unusual activities including bicycling, skating, and cart-driving are being done for the test clips.
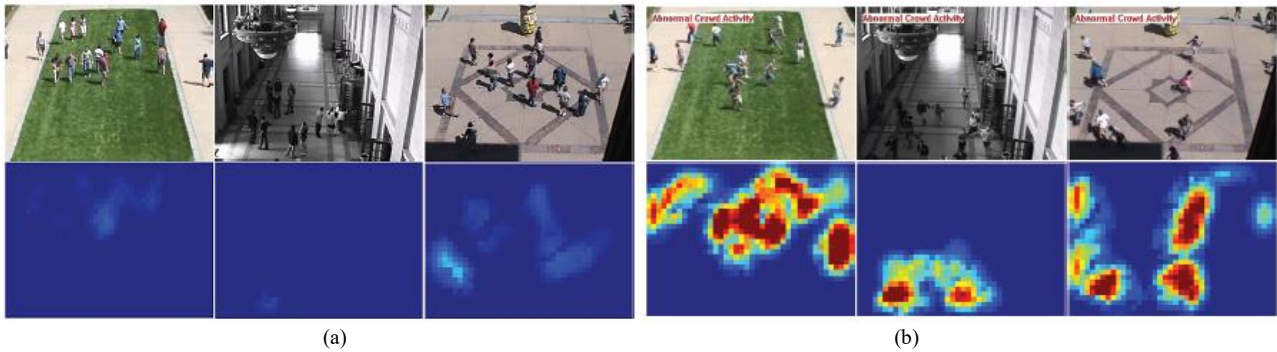

Fig. 3. Sample frames of University of Minnesota dataset and corresponding motion based Optical flow (a) For normal activity. (b) For unusual activity.

4.2. Proposed Pedestrian Dataset

The student's behavior on college property was observed using a top-notch DSLR camera from a different vantage point for the proposed dataset. We used a resolution of 3840x2160 and H.264 compression for shooting video at 30 frames per second. Around 100 sample videos are present in the database. Each example video lasts 20 to 30 minutes. In the dataset, there is a video series with an example frame shown in Fig.4. The camera tilts from 45 to 90 degrees. Over 90% of Yeshwantrao Chavan College of Engineering students in Nagpur are pedestrians. They are primarily of Indian origin, aged 22 to 27, and 65% of them are male. The proposed pedestrian database includes a variety of student actions in academic activities under various circumstances, such as students studying in practical laboratories, test hall scenarios, the classroom, a student cheating in the exam hall, a student removing the answer key outside the exam hall, a student stealing the mobile phone or other electronic devices like the mouse or keyboard, a student stealing the lab equipment, a student quarrel on the college grounds, etc. The proposed dataset includes expert human annotations for each video frame. For every video sequence, we produce a csv file with the exact same file naming convention as videofilename.csv. There are three phases to the labelling process: 1) Human detection; 2) tracking; 3) identifying unusual activities; and 4) soft biometric features Prior to manually validating and correcting the data, the Mask R-CNN [12] approach is used to produce a first estimate of each pedestrian's position in the scene. The preliminary tracking information was then provided using the deep sort method [14] and was once again rectified manually. We get a rectangular bounding box that represents the region of interest (ROI) for each pedestrian in each frame as a result of these first two stages. In the manual last stage of the annotation process, a human expert who is familiar with the college's students creates ID information and assigns soft labels to the samples. We also give a list of potential values for each label.

Fig. 4. Proposed pedestrian dataset. The first row shows the original sample images in the proposed pedestrian database. The second row shows the pedestrian annotation.

4.3. Performance Evaluation

Each video frame is split into eight 8x8-pixel blocks, and the threshold is set to the motion feature's maximum feature value in the training frames of the input video sequence. Receiving Operating Curves (ROC) for the proposed and current approaches are shown in Fig. 5 and are taken from [31, 32, 33]. We analyze the proposed method's ROC

curve with the ROC curves of three cutting-edge approaches: sparse reconstruction [31], a social force model [32], and a mixture of dynamic textures [33].
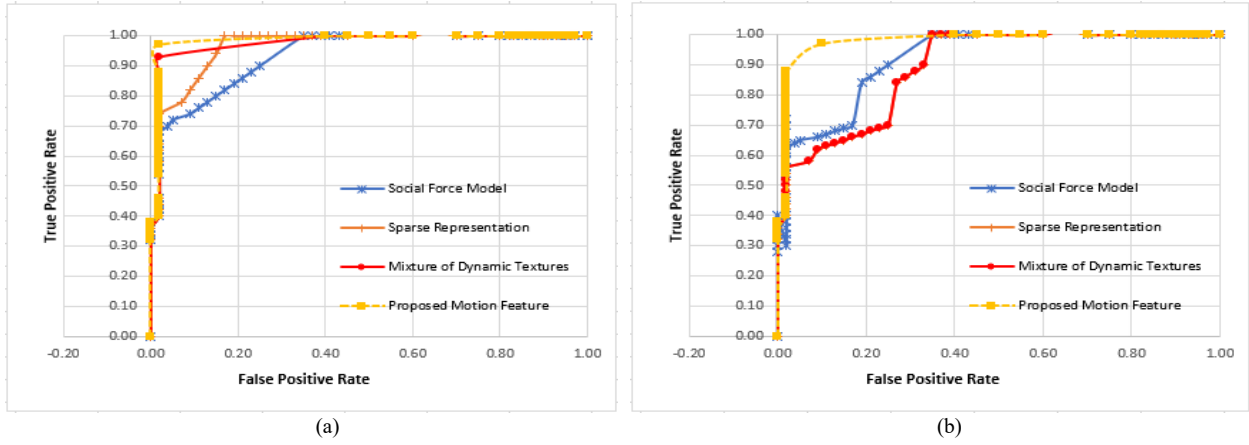

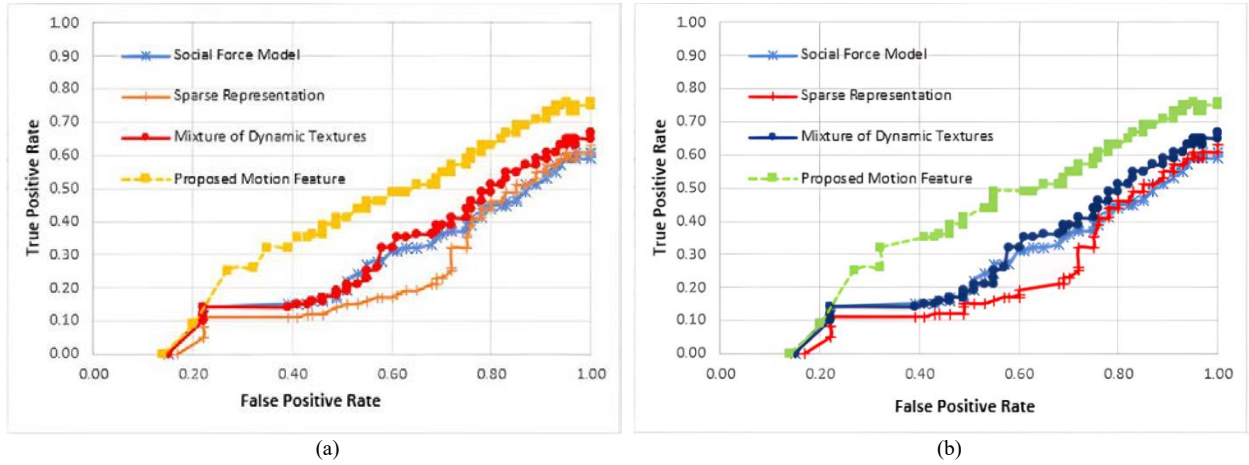Fig. 5. ROC curve for the comparative analysis (a) For USD dataset. (b) Proposed Dataset.

Fig. 6. (a) Frame Level local anomalous activity detection (a) For USD dataset. (b) For proposed dataset.
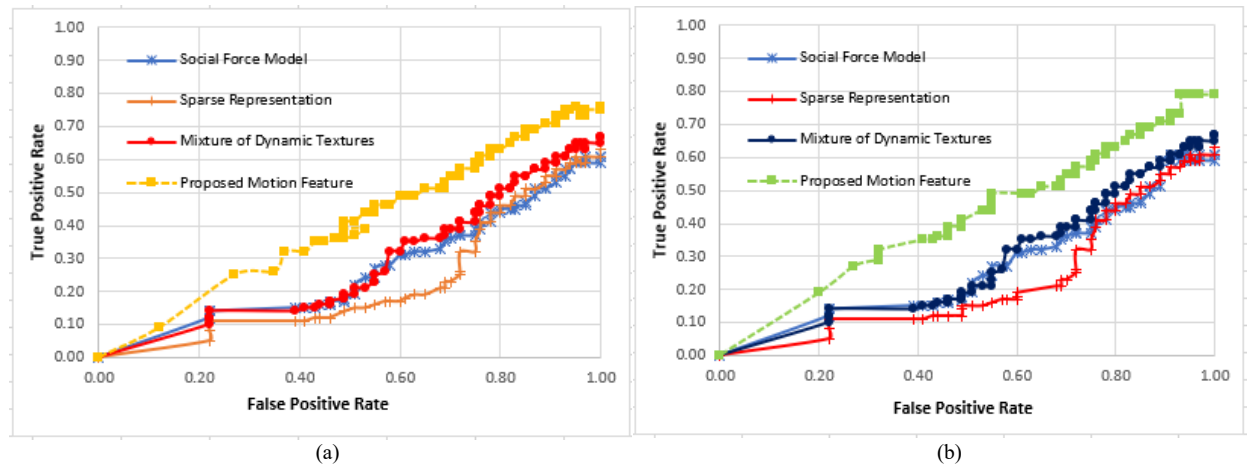

Fig. 7. (a) Pixel level local anomalous activity detection (a) For USD dataset. (b) For proposed dataset.

The proposed and current approaches given in [31, 32, 33] are represented by the Receiving Operating Curve (ROC) in Fig. 6 at the frame-level and pixel-level in Fig.7. In Tables 2 and 3, which provide quantitative comparisons, we also provided the ERRs and AUCs of the competing approaches, which were derived from the corresponding studies. On both datasets, with respective error rates of 16.1% and 18.1%, we found that the proposed technique performs comparably well compare to the conventional methods.

Table 2. Comparison of the proposed methodology with the state-of-the-art method on University of Minnesota anomaly detection dataset (ERR) frame level.

Technique or Methodology	Single Pedestrian	Multiple Pedestrian	Average
Dynamic Texture Mixture [32]	22.9%	22.9%	22.9%
Social Force Model [32]	36.5%	35.0%	35.7%
Sparce Matrix Representation [31]	35.6%	35.8%	35.7%
Motion-based method (Proposed)	21.1%	18.1%	16.1%

Table 3. Comparison of the proposed methodology with the state-of-the-art method on proposed dataset (AUC) at frame-level.

Technique or Methodology	Single Pedestrian	Multiple Pedestrian	Average
Dynamic Texture Mixture [32]	24.9%	23.9%	23.5%
Social Force Model [32]	37.5%	34.0%	36.7%
Sparce Matrix Representation [31]	32.6%	35.8%	33.7%
Motion-based method (Proposed)	22.1%	19.2%	18.1%

As demonstrated in Tables IV and V for both datasets, Area Under the Curve (AUC) for the current approach and the proposed method, respectively. The AUC for the proposed approach is 73.2% and 72.1%. It demonstrates that the suggested framework is more reliable and accurate when applied to the dataset and is, in comparison, superior to other methods of addressing anomalous behavior. Using a straightforward distance threshold-based classification algorithm, our method produced results on par with cutting-edge techniques.

Table 4. Comparison of the proposed methodology with the state-of-the-art method on University of Minnesota anomaly detection dataset (AUC).

Technique or Methodology	Single Pedestrian	Multiple Pedestrian	Average
Dynamic Texture Mixture [32]	59.3%	56.8%	58.0%
Social Force Model [32]	40.9%	27.6%	34.2%
Sparce Matrix Representation [31]	32.6%	22.4%	27.5%
Motion-based method (Proposed)	64.9%	81.5%	73.2%

Table 5. Comparison of the proposed methodology with the state-of-the-art method on proposed dataset (AUC).

Technique or Methodology	Single Pedestrian	Multiple Pedestrian	Average
Dynamic Texture Mixture [32]	35.6%	35.8%	35.7%
Social Force Model [32]	50.8%	63.4%	57.1%
Sparce Matrix Representation [31]	74.5%	70.1%	72.3%
Motion-based method (Proposed)	63.4%	80.2%	72.1%

5. Conclusion

In order to identify students engaging in aberrant behavior in a classroom setting, this paper offers a practical and original methodology. We can characterize pedestrian activity in a frame as normal or abnormal, and we can also pinpoint specific portions of abnormal activity as local or global regions, according to the spatial and temporal characteristics of motion-based features. We conducted tests using proposed student behavior datasets and anomaly detection datasets from the University of Minnesota. In comparison to state-of-the-art techniques, the experimental results demonstrate that the suggested framework lowers the false acceptance rate to 3% and raises the True positive rate to 5%. The primary objective of this effort is, however, to effectively identify aberrant behavior in a classroom setting. The similar approach can be utilized in the future for a variety of scenarios involving student conduct, including situations when students are caught cheating on exams or getting into arguments on campus. Again, if the proposed approach is improved by the inclusion of further features like scale, rotation, and lighting invariant features, scale, rotation, and illumination changes can also be addressed.

References

[1] Wanli Ouyang, Xingyu Zeng, Xiaogang Wang, Single-Pedestrian Detection Aided by Two-Pedestrian Detection, *TPAMI*, vol. 37, no. 9, pp. 1875-1889, September 2015.

[2] Weihang Kong, He Li, Guanglong Xing, Fengda Zhao, "An Automatic Scale-Adaptive Approach With Attention Mechanism-Based Crowd Spatial Information for Crowd Counting," in *IEEE Access*, vol. 7, pp. 66215-66225, 2019.

[3] Khosro Rezaee, Mohammad R. Khosravi, Maryam Saberi Anari, "Deep-Transfer-Learning-Based Abnormal Behavior Recognition Using Internet of Drones for Crowded Scenes," in *IEEE Internet of Things Magazine*, vol. 5, no. 2, pp. 41-44, June 2022.

[4] Lei Cao and Lin Wang, "Analysis and intervention in pedestrian evacuation via a modified social force model," *The 27th Chinese Control and Decision Conference (2015 CCDC),* 2015, pp. 5924-5929, doi: 10.1109/CCDC.2015.7161870.

[5] Fanchao Xu, Yunbo Rao, Qifei Wang, "An unsupervised abnormal crowd behavior detection algorithm," *2017 International Conference on Security, Pattern Analysis, and Cybernetics (SPAC)*, 2017, pp. 219-223, doi: 10.1109/SPAC.2017.8304279.

[6]   Fabian Flohr, Madalin Dumitru-Guzu, Julian F. P. Kooij, Dariu M. Gavrila, "A Probabilistic Framework for Joint Pedestrian Head and Body Orientation Estimation," in *IEEE Transactions on Intelligent Transportation Systems*, vol. 16, no. 4, pp. 1872-1882, Aug. 2015, doi: 10.1109/TITS.2014.2379441.

[7]   Amir Rasouli, Iuliia Kotseruba, John K. Tsotsos, "Understanding Pedestrian Behavior in Complex Traffic Scenes," in *IEEE Transactions on Intelligent Vehicles*, vol. 3, no. 1, pp. 61-70, March 2018, doi: 10.1109/TIV.2017.2788193.

[8]   Liang-qun Li, Chun-lan Li, Jun-bin Liu, Wei-xin Xie, "A novel occlusion handling method based on particle filtering for visual tracking," 2016 *IEEE 13th International Conference on Signal Processing (ICSP)*, 2016, pp. 934-937, doi: 10.1109/ICSP.2016.7877967.

[9]   Bing Wang, Kap Luk Chan, Gang Wang, Haijian Zhang, "Pedestrian detection in highly crowded scenes using "online" dictionary learning for occlusion handling," *2014 IEEE International Conference on Image Processing (ICIP)*, 2014, pp. 2418-2422, doi: 10.1109/ICIP.2014.7025489.

[10]   Ho-chul Shin, "Abnormal Detection based on User Feedback for Abstracted Pedestrian Video," *2019 International Conference on Information and Communication Technology Convergence (ICTC),* 2019, pp. 1036-1038, doi: 10.1109/ICTC46691.2019.8939600.

[11]   Md Maruf Hossain Shuvo, Nafis Ahmed, Koundinya Nouduri, Kannappan Palaniappan, "A Hybrid Approach for Human Activity Recognition with Support Vector Machine and 1D Convolutional Neural Network," *2020 IEEE Applied Imagery Pattern Recognition Workshop (AIPR)*, 2020, pp. 1-5, doi: 10.1109/AIPR50011.2020.9425332.

[12]   Arundhati Chattoadhyay, Aruna Tripathy, "Anomalous Crowd Behavior Detection Using Raspberri PI," *2020 IEEE 5th International Conference on Computing Communication and Automation (ICCCA),* 2020, pp. 462-466, doi: 10.1109/ICCCA49541.2020.9250824.

[13]   Kazunari Takasaki, Ryoichi Kida, Nozomu Togawa, "An Anomalous Behavior Detection Method Based on Power Analysis Utilizing Steady State Power Waveform Predicted by LSTM," *2021 IEEE 27th International Symposium on On-Line Testing and Robust System Design (IOLTS)*, 2021, pp. 1-7, doi: 10.1109/IOLTS52814.2021.9486706.

[14]   Feng Zheng, Quanyun Liu, "Anomalous Telecom Customer Behavior Detection and Clustering Analysis Based on ISP's Operating Data," in *IEEE Access*, vol. 8, pp. 42734-42748, 2020, doi: 10.1109/ACCESS.2020.2976898.

[15]   Shuoyan LIU, Hao XUE, Chunjie XU, Kai FANG, "Abnormal behavior detection based on the motion-changed rules," *2020 15th IEEE International Conference on Signal Processing (ICSP)*, 2020, pp. 146-149, doi: 10.1109/ICSP48669.2020.9321012.

[16]   Wei Fang, Lin Wang, Peiming Ren, "Tinier-YOLO: A Real-Time Object Detection Method for Constrained Environments," in *IEEE Access*, vol. 8, pp. 1935-1944, 2020, doi: 10.1109/ACCESS.2019.2961959.

[17]   Zhihong Sun, Jun Chen, Liang Chao, Weijian Ruan, Mithun Mukherjee, "A Survey of Multiple Pedestrian Tracking Based on Tracking-by-Detection Framework," in *IEEE Transactions on Circuits and Systems for Video Technology*, vol. 31, no. 5, pp. 1819-1833, May 2021, doi: 10.1109/TCSVT.2020.3009717.

[18]   Yang Li, Jinshen Wang, Xiang Liu, Ning Xian, Changsheng Xie, "DIM Moving Target Detection using Spatio-Temporal Anomaly Detection for Hyperspectral Image Sequences," *IGARSS 2018 - 2018 IEEE International Geoscience and Remote Sensing Symposium*, 2018, pp. 7086-7089, doi: 10.1109/IGARSS.2018.8517601.

[19]   Yunpeng Jiang, Ningning Le, Yufeng Zhang, Yinger Zheng, Yang Jiao, "Research on the Flight Anomaly Detection During Take-off Phase Based on FOQA Data," *2019 CAA Symposium on Fault Detection, Supervision and Safety for Technical Processes (SAFEPROCESS),* 2019, pp. 756-760, doi: 10.1109/SAFEPROCESS45799.2019.9213422.

[20]   Chaoqin Huang, Qinwei Xu, Yanfeng Wang, Yu Wang, Ya Zhang, "Self-Supervised Masking for Unsupervised Anomaly Detection and Localization," in *IEEE Transactions on Multimedia*, doi: 10.1109/TMM.2022.3175611.

[21]   Gal Mishne, Israel Cohen, "Multiscale Anomaly Detection Using Diffusion Maps," in *IEEE Journal of Selected Topics in Signal Processing*, vol. 7, no. 1, pp. 111-123, Feb. 2013, doi: 10.1109/JSTSP.2012.2232279.

[22]   Kursat Rasim Mestav, Xinyi Wang, Lang Tong, "A Deep Learning Approach to Anomaly Sequence Detection for High-Resolution Monitoring of Power Systems," in *IEEE Transactions on Power Systems*, doi: 10.1109/TPWRS.2022.3168529.

[23]   Huawen Liu, Xiaodan Xu, Enhui Li, Shichao Zhang, Xuelong Li, "Anomaly Detection With Representative Neighbors," in *IEEE Transactions on Neural Networks and Learning Systems*, doi: 10.1109/TNNLS.2021.3109898.

[24]   Chunde Yang, Tongyao Xu, Minghong Lv, Yi Yu, Xiaoming Jiang, "Pedestrian Angle Recognition Based on JDE Multi-object Tracking Algorithm," *2022 7th International Conference on Intelligent Computing and Signal Processing (ICSP)*, 2022, pp. 647-651, doi: 10.1109/ICSP54964.2022.9778590.

[25]   Chuangxin He, Xu Zhang, Zhonghua Miao, Teng Sun, "Intelligent vehicle pedestrian tracking based on YOLOv3 and DASiamRPN," *2021 40th Chinese Control Conference (CCC)*, 2021, pp. 4181-4186, doi: 10.23919/CCC52363.2021.9549997.

[26]   Zhihong Sun, Jun Chen, Liang Chao, Weijian Ruan, Mithun Mukherjee, "A Survey of Multiple Pedestrian Tracking Based on Tracking-by-Detection Framework," in *IEEE Transactions on Circuits and Systems for Video Technology,* vol. 31, no. 5, pp. 1819-1833, May 2021, doi: 10.1109/TCSVT.2020.3009717.

[27]   Kai Chen, Xiao Song, Xiang Zhai, Baochang Zhang, Baocun Hou, Yi Wang, "An Integrated Deep Learning Framework for Occluded Pedestrian Tracking," in *IEEE Access*, vol. 7, pp. 26060-26072, 2019, doi: 10.1109/ACCESS.2019.2900296.

[28]   Shan Gao, Zhenjun Han, Ce Li, Qixiang Ye, Jianbin Jiao, "Real-Time Multipedestrian Tracking in Traffic Scenes via an RGB-D-Based Layered Graph Model," in *IEEE Transactions on Intelligent Transportation Systems*, vol. 16, no. 5, pp. 2814-2825, Oct. 2015, doi: 10.1109/TITS.2015.2423709.

[29]   Ying Liu, Weiwei Zhang, Guohua Cui, Yong Zhang, "Multipedestrian Online Tracking Based on Social Force-Predicted Deformable Key-Points Mapping via Compressive Sensing," in *IEEE Systems Journal*, vol. 15, no. 2, pp. 1905-1916, June 2021, doi: 10.1109/JSYST.2020.3003024.

[30]   Qinglin Tian, Zoran Salcic, Kevin I-Kai Wang, Yun Pan, "A Multi-Mode Dead Reckoning System for Pedestrian Tracking Using Smartphones," in *IEEE Sensors Journal*, vol. 16, no. 7, pp. 2079-2093, April1, 2016, doi: 10.1109/JSEN.2015.2510364.

[31]   Zhengqiang Jiang, Du Q. Huynh, "Multiple Pedestrian Tracking From Monocular Videos in an Interacting Multiple Model Framework," in *IEEE Transactions on Image Processing*, vol. 27, no. 3, pp. 1361-1375, March 2018, doi: 10.1109/TIP.2017.2779856.

[32]   M. Zaharin, N. Ibrahim, T. Tuan Dir,. "Comparison of human detection using background subtraction and frame difference". *Bulletin of Electrical Engineering and Informatics*, vol. 9, no. 1, pp. 345-353, 2020 , doi: 10.11591/eei.v9i1.1458.

[33] M. Gheisari, Z. Safari, M. Almasi, A. Najafabadi, A. Sridharan, R. G K, Y. Liu, A. Abbasi,. "A novel enhanced algorithm for efficient human tracking". *International Journal of Informatics and Communication Technology (IJ-ICT)*, vol. 11, no. 1, pp. 1-7, 2022 , doi: 10.11591/ijict.v11i1.pp1-7.

[34] S. V. Aruna Kumar, Ehsan Yaghoubi, Abhijit Das, B. S. Harish, Hugo Proença, "The P-DESTRE: A Fully Annotated Dataset for Pedestrian Detection, Tracking, and Short/Long-Term Re-Identification From Aerial Devices," in *IEEE Transactions on Information Forensics and Security*, vol. 16, pp. 1696-1708, 2021, doi: 10.1109/TIFS.2020.3040881.

[35] L. Knoedler, C. Salmi, H. Zhu, B. Brito and J. Alonso-Mora, "Improving Pedestrian Prediction Models With Self-Supervised Continual Learning," in *IEEE Robotics and Automation Letters*, vol. 7, no. 2, pp. 4781-4788, April 2022, doi: 10.1109/LRA.2022.3148475.

[36] G. Shen, L. Zhu, J. Lou, S. Shen, Z. Liu, L. Tang, "Infrared Multi-Pedestrian Tracking in Vertical View via Siamese Convolution Network," in *IEEE Access*, vol. 7, pp. 42718-42725, 2019, doi: 10.1109/ACCESS.2019.2892469.

[37] W. Ge, R. Collins, R. Ruback, "Vision-Based Analysis of Small Groups in Pedestrian Crowds," in *IEEE Transactions on Pattern Analysis and Machine Intelligence*, vol. 34, no. 5, pp. 1003-1016, May 2012, doi: 10.1109/TPAMI.2011.176.

[38] M. Rai, R. Yadav, A. Husain, T. Maity, D. Yadav,"Extraction of Facial Features for Detection of Human Emotions under Noisy Condition", *International Journal of Engineering and Manufacturing(IJEM)*, Vol.8, No.5, pp.49-62, 2018.DOI: 10.5815/ijem.2018.05.05.

[39] F. Chamasemani, L. Affendey, "Systematic Review and Classification on Video Surveillance Systems", *I.J. Information Technology and Computer Science*, Vol. 2013, No.7, pp.87-102, June 2013. DOI: 10.5815/ijitcs.2013.07.11.

[40] A. Dey, F. Mohammad, S. Ahmed, R. Sharif, A. Saif, "Anomaly Detection in Crowded Scene by Pedestrians Behaviour Extraction using Long Short Term Method: A Comprehensive Study", *International Journal of Education and Management Engineering(IJEME)*, Vol.9, No.1, pp.51-63, 2019.DOI: 10.5815/ijeme.2019.01.05.

[41] Y. Imamverdiyev, L. Sukhostat, "An Anomaly Detection Based on Optimization", *International Journal of Intelligent Systems and Applications(IJISA),* Vol.9, No.12, pp.87-96 2017. DOI: 10.5815/ijisa.2017.12.08.

[42] H. Salami, R. Ibrahim, M. Yahaya, "Detecting Anomalies in Students' Results Using Decision Trees", *International Journal of Modern Education and Computer Science(IJMECS)*, Vol.8, No.7, pp.31-40, 2016.DOI: 10.5815/ijmecs.2016.07.04.

Authors' Profiles

Kamal O. Hajari is pursuing a Ph.D. degree from the IT Department, YCCE. He completed his bachelor and master degree from YCCE College. It is an Autonomous institution affiliated to Rashtrasant Tukadoji Maharaj Nagpur University, Nagpur. His research interests of areas are video surveillance, video processing and analysis, pattern recognition, machine learning, neural network and fuzzy logic, and computer vision. He is a life time member of Institute of Engineers (IE), ACM, and ISTE.

Ujwalla H. Gawande is an Associate Professor and Dean R & D, IT Department, YCCE. She got her B.E. from KITS, Ramtek and M.Tech. Degree from Raisoni college of Engineering, RTMNU University, Nagpur in 2001 and 2007, and a Ph.D. degree from SVNIT, Surat in 2014. Her research interests of areas are video surveillance, video processing and analysis, pattern recognition, machine learning, neural network and fuzzy logic, and computer vision. She is a reviewer of peer review journal such as AI, IEEE Transaction of Multimedia, and IEEE Access. She is having life time membership of IE, ACM, and ISTE.

Yogesh Golhar is an Assistant Professor, CSE Department, St. Vincent Palloti College of Engineering and Technology, Nagpur. He got his BE and M.Tech. Degree from Raisoni College in 2008 and 2012. His research area includes AI, Big Data Analytics, ML, CN, and CV. He is having membership of IE, ACM, and ISTE.

Novel approach for pedestrian unusual activity detection in academic environment

Kamal Omprakash Hajari[1], Ujwalla Haridas Gawande[1], Yogesh Golhar[2]

[1]Department of Information Technology, Yeshwantrao Chavan College of Engineering, Nagpur, India
[2]Department of Computer Engineering, St. Vincent Palloti College of Engineering and Technology, Nagpur, India

Article Info	ABSTRACT
	In this paper, we propose an efficient method for the detection of student unusual activity in the academic environment. The proposed method extracts motion features that accurately describe the motion characteristics of the pedestrian's movement, velocity, and direction, as well as their intercommunication within a frame. We also use these motion features to detect both global and local anomalous behaviors within the frame. The proposed approach is validated on a newly built proposed student behavior database and three additional publicly available benchmark datasets. When compared to state-of-the-art techniques, the experimental results reveal a considerable performance improvement in anomalous activity recognition. Finally, we summarize and discuss future research directions.

Corresponding Author:

Kamal Hajari
Department of Information Technology, Yeshwantrao Chavan College of Engineering (YCCE)
Hingna Road, Wanadongri, Nagpur, Maharashtra-441110, India
Email: kamalhajari123@gmail.com

1. INTRODUCTION

Today, public and private prominent areas are monitored with surveillance cameras due to increased security concerns. It is a difficult task to monitor pedestrian behavior by human supervision. The current problem with the traditional approach is that it is difficult to detect and separate suspicious activities from real-time video, and this procedure is extensive and time-consuming. Due to the current limitations of the system, we need an intelligent video surveillance system that can automatically recognize suspicious behavior in real time. Many researchers and practitioners in the fields of computer vision and video analysis have dedicated their efforts in recent years to recognizing human movement and behavior in video frames [1]–[3]. In recent years, researchers have concentrated increasingly on the detection of suspicious activity in high-density areas. Traditional systems cannot detect and track pedestrians in high density areas due to full or partial occlusion of objects, changes in item size, changes in ambient lighting, and other factors. Many authors have attempted to detect abnormal behaviour in overcrowded environments using texture-based information, such as time gradients [4], dynamic texture characteristics [5] and the spatiotemporal frequency properties [6], [7]. Other groups concentrate on optical flows, which recognize motion features in video frames directly, such as multi-scale pedestrian features [8], fuzzy clustering based features [9], behavioural model for pedestrian detection [10], convolutional neural networks (CNN) features [11], weighted autoencoder based features [12], trajectory based features [13], student object behavioral features [14], multi-target association based features [15], [16]. Previous research has shown that the technique of motion is beneficial, and we believe that the present methods can still be improved. It is essential to provide data on objects of different sizes, motion direction, speed, and inter-frame interactions. We can increase

proposed method performance if we analyze the facts concerning this movement. In the proposed motion pattern-based method, we distinguish moving pedestrian using motion information, orientation, pedestrian size, and interaction within the video sequence, specifically in highly dense regions. Figure 1 illustrate the student suspicious behavior examples. Figure 1(a) depicts the unusual activity of student in which student stealing the mobile phone of another student. Figure 1(b) depicts the student dispute behavior in the lab. A small active segment of an anomalous area is classified as a local area. Meanwhile, a global region refers to the area where strange behavior is observed. In the literature, various ways to identify the region's unusual activity have been introduced.
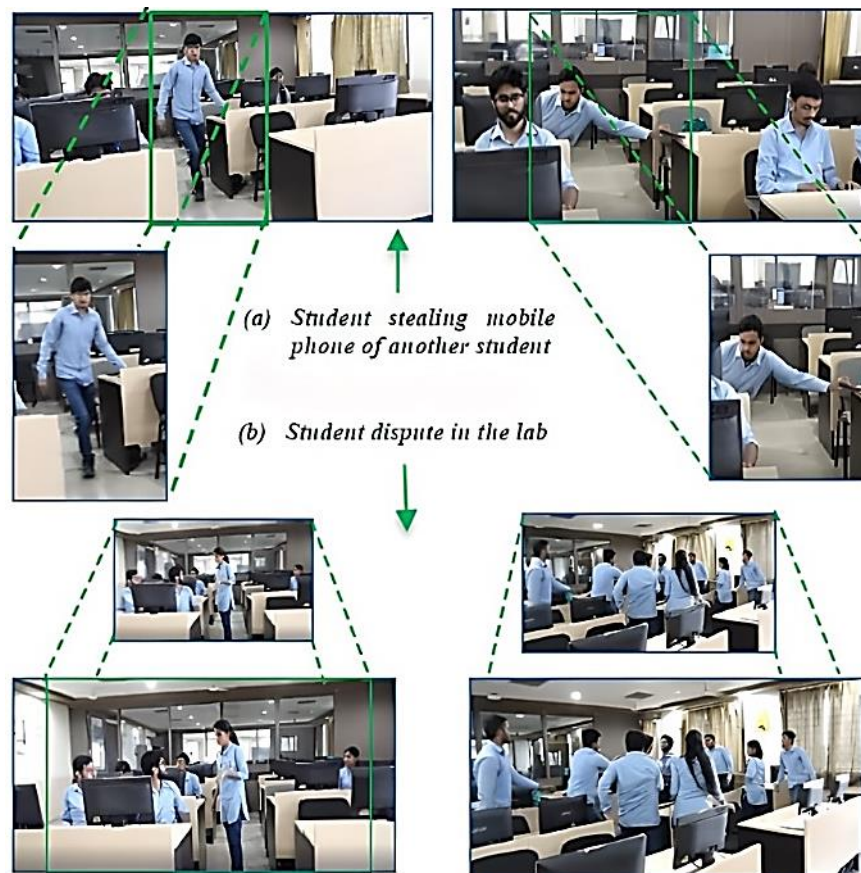

Figure 1. Student suspicious behavior examples (a) student steal the mobile phone of another student (specific area) and (b) student dispute in the lab. (full frame)

Li *et.al.* [15] presented a social force map-based strategy for detecting worldwide anomalous activity. They placed a particle grid across the optical flow field and computed the interaction force between each particle. Tufek and Ozkaya [11] described a method for detecting erroneous local motions in a scene. To detect anomalies in the immediate area, they created a saliency feature map employing optical flow features at various sizes. A comprehensive framework for detecting abnormal activity is required for a real-time monitoring system. The proposed contribution is outlined: i) at the pixel level, we proposed a unique approach for detecting behavioral patterns in academic environment; and ii) on our proposed database as well as other benchmark datasets, such as the University of Minnesota anomaly detection datasets, we assessed the effectiveness of the proposed motion-based method. The following is how the rest of the contribution is organized: The existing contribution in this area is outlined in section 2. We propose a motion feature-based suspicious activity detection in section 3. Section 4 covers a new pedestrian behavior database developed in an academic setting, as well as results and performance comparison with other relevant methodologies. The last section concludes with a research direction.

2.   LITERATURE SURVEY

Researchers in a smart video surveillance system have recently become interested in the unusual activity detection. Gaddigoudar *et al.* [17] describe the difficulty of understanding and modelling behavior in surveillance video. In an unsupervised learning framework, violations are discovered using likelihood ratio analysis and pedestrian legal action categories. Mehmood [18] presented a method for detecting anomalies in a spatiotemporal environment. They showed an atomic event for a single object in a scene that includes the object's position, movement, direction, and velocity. To characterize valid occurrences, they use an aggregation of three partitioned atomic events. In crowded scenes, it's hard to comprehend moving pedestrians. Therefore, the aforementioned strategies aren't appropriate.

The multi-scale pedestrian detected using a deep learning architecture. The CNN features are used for classification of pedestrians in highly dense regions. The different issues and challenges addressed using author approaches are scale and illumination variation. Other recent research groups have concentrated on moving pedestrian motion orientation and speed information. The Kanade Lucas-Tomasi (KLT) approach [9] is employed by Zhang *et al.* [19], in which corner points are used to display pedestrians that are moving and cluster the motion information features in the controlled environment. The author used two types of historical and self-history descriptors, as well as neighbouring object histories, to detect abnormalities in a scene [10]. Chebli and Khalifa [20] presented a method for identifying the number of humans in an image without the use of a camera. They exploited foreground relationships as well as an optical-flow motion pattern. They calculated the dynamic energy of using optical flow to distinguish between walking and running activities, as well as crowd exponential distribution patterns.

Other academics have focused on understanding and modelling crowd behavior [21]–[24]. Several strategies were used to detect worldwide anomalous activity by modelling the crowd's behavior. Wang and Hou [22] author used the social force model to characterize crowd behavior [22]. The moving object optical flow pattern is computed for pedestrian detection in the crowded environment [14], [25]. The behavior classification of pedestrians performed by social force was also determined using latent Dirichlet allocation (LDA). Minguez *et al.* [26] use interactive energy potentials to study social behavior and its behavior. Zhang *et al.* [19] used the KLT feature-based pedestrian tracker. In this motion, characteristics are computed using temporal distinct points. It calculates interaction energy potentials based on the velocities of spatiotemporal interest points to see if they will collide soon [27]. Other research groups, on the other hand, have concentrated on detecting local aberrant activity. Quantifiable is a term used in [11] to describe the global rarity of picking uncorrelated motions from a spatial context. They calculated the index across numerous channels with varying velocities and directions.

Using the associated saliency map, they were almost able to detect local aberrant behavior. Zaki and Sayed [28] the author used motion intensities for creating a motion heat map and compared it to local motion fluctuations. Direkoglu [5] the author proposed a texture feature-based abnormal activity recognition in highly dense areas. Finally, crowd behavior analysis was performed using moving objects, optical flow patterns and directional information. Papathanasopoulou *et al.* [29] the author proposed an approach for highly dense areas for extracting the moving objects within the cluster of frames. Although the aforementioned strategies have been shown to be useful in studies, they are usually limited to detecting unusual activity in a local or global location. We contend that joint contemplation of the motion flows pattern, variable item sizes, and interactions between neighboring objects in a frame can reflect pedestrian activities in a high-density scene, resulting in improved performance in detecting unusual activity. We proposed an effective technique for dealing with the aforementioned issues and challenges with clustering of motion patterns in consecutive frames. We begin by extracting motion features at different scales and directions with sequences of frames. Furthermore, we also used motion analysis to identify abnormal activities within a scene.

3.   PROPOSED METHODOLOGY

We describe a strategy for identifying and localizing abnormal activity in high-density zones in this section, which incorporates the motion component. We detected fast and slow movement of a pedestrian's unusual activities in the local and global regions of the scene. Figure 2 depicts the general architecture of the suggested technique. Each frame is broken down into blocks, and motion data is retrieved to generate motion characteristics at the pixel and block levels. The motion feature extraction process is divided into following stages:
- First, within a series of frames, the motion characteristics of moving pedestrians are extracted at spatial plane coordinates and block by block incrementally in different orientation and scale.
- After integrating the motion information single feature matrix is generated that represents both spatial and temporal characteristics.
- To classify the activity k-means clustering for each zone applied to identify the global and local region.

- The euclidean distances computed across the frames. Again, the directional motion pattern are the distinct feature values for the detection of abnormal behavior in academic environments.
- Once a frame has been categorized as unusual, we use pixel-level localization to determine the specific location of the unexpected behavior. The process will continue until the video sequence is complete.
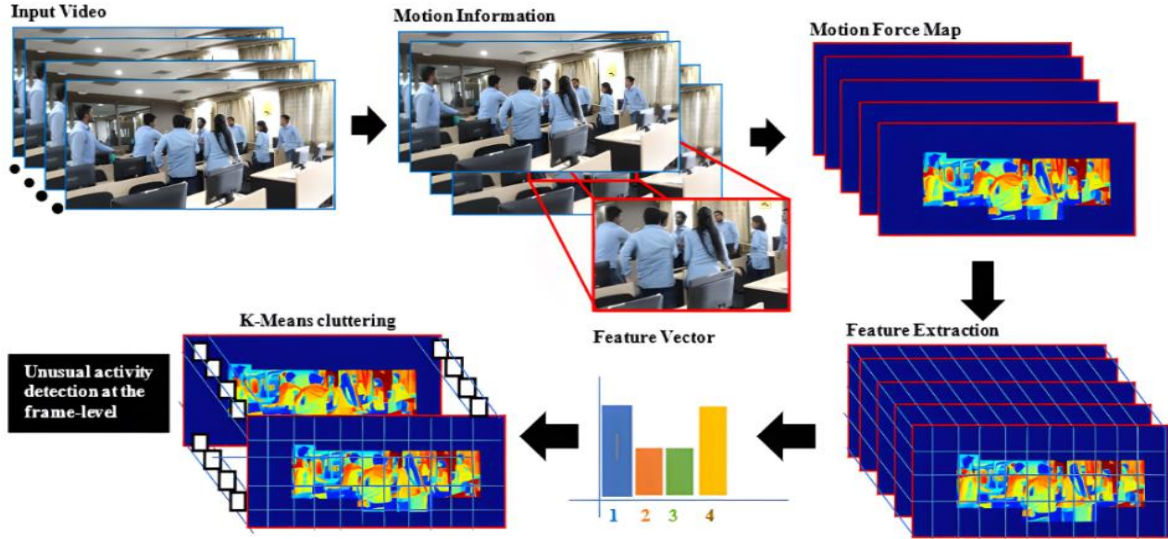

Figure 2. Proposed framework architecture to represent moving object behavior in academic environment

A method for detects an unusual human activity by processing each frame of the video sequence, the proposed method first extracts the optical flows of the pixels within each block of frame represented in (1).

$$B_i = \frac{1}{J} \sum_{j=0}^{n} f(x,y)_i^j \tag{1}$$

Where, B_i denotes the ith block optical flow, pixel size is represented by J, i^{th} block j^{th} pixel optical flow represented by $f(x,y)_i^j$. Next, the threshold T_d for the block computed using the motion vector B_i and block width S represented in (2).

$$T_d \leftarrow B_i \ x \ S \tag{2}$$

The angle between the feature vector θ_{ij} computed using $ED_{(i,j)}$

$$\theta_{ij} \begin{cases} 1 & ED_{(i,j)} < T_d \\ 0 & Otherwise \end{cases}$$

The motion feature extraction process defined by (3).

$$MF = \frac{MF \ (\theta B_i) + ED_{(i,j)}}{B_i} \tag{3}$$

Where in MF is the motion feature map, $ED_{(i,j)}$ Euclidean distance between object i and j. Next, we have described motion feature extraction briefly in the algorithm.

In addition, clustered at frame level defined the motion region in a frame, each cluster optical flow of a pixel in a different direction being considered as the feature vector. Whenever distance between blocks decreases, the probability of unexpected behavior in the corresponding block decreases. If a larger value distance is determined, then we can classify anomalous actions in consecutive frames. As a result, if the distance is over a set limit of the constant threshold value, the current scene is recognized as an unusual activity frame. Next, we describe the experimental results.

Algorithm: Motion information extraction for detection of unusual human activity from video.	
Inputs:	V, the input video sequence
	n, Last frame of video
	S, Block width
	K, Each frame block size
	f, the frame of the input video sequence
	B, Motion vector
Output:	MF, the motion Features

3 *Read each frame of video*
 for $f = 1$ **to** N **do**
  Process each block of frame
  for $i = 1$ **to** K **do**
   Compute the threshold for each block
   $T_d \leftarrow B_i \times S$
4   *Process adjacent block in a frame*
    for $j = 1$ **to** K **do**
5   *Compute the centroid from the bounding box points. represented by: (cX; cY)*
     Append centroid in centroid dictionary
     If i *not equal* j **then**
      Compute the distance across the consecutive block
      $ED_{(i,j)} \leftarrow EucliDist(B_i, B_j)$
6   *Compute distance and compare against threshold*
      if $|ED_{(i,j)} < T_d|$ **then**
7   *Compute Angle* Θ_{ij} *between* B_i *and* B_j
8   **if** $-\Theta B_i < \Theta_{ij} < \Theta B_j$ **then**
9        $MF \leftarrow MF(\Theta B_i) + ED_{(i,j)}/B_i$
10   **end if**
11   **end if**
12   **end if**
13   **end for**
14   **end for**
15 **end for**

4. RESULTS AND DISCUSSION

We validated the proposed approach accuracy on public datasets, as well as the suggested student behavior dataset and the University of Minnesota anomaly detection datasets. The experiments and proposed deep learning framework were carried out using a single NVIDIA graphics processing unit (GPU) and an Intel Core i7 3.4GHz processor with 32GB random-access memory (RAM) and a 32GB NVIDIA graphics card, all of which were configured using CUDA-optimized architecture and the open source computer vision library (OpenCV) deep learning framework. The suggested method is compared to the state-of-the-art unusual activity detection methods [29], [30], social force models [31], sparse representation-based method [32], and mixture of dynamic textures-based method [32]. True positive (TP), true negative (TN), false positive (FP), false negative (FN), equal error rate (ERR), true positive rate (TPR), true negative rate (TNR), and area under curve (AUC) are some common performance measuring metrics. We have computed these metrics using (4), (5), (6), and (7). These metrics are computed for the performance comparison.

$$TPR = \frac{TP}{TP+TN} \tag{4}$$

$$TNR = \frac{TN}{FP+FN} \tag{5}$$

$$AUC = \frac{1}{2} * (TPR + TNR) \tag{6}$$

$$ERR = 1 - \frac{1}{2} * (TPR + TNR) \tag{7}$$

First, we have performed experiments on University of Minnesota anomaly detection dataset. Figure 3 shows the receiving operating curve (ROC) for the proposed and existing approach presented in [31], [32]. Similarly, we have computed the ROC for the proposed student behavior dataset in Figure 4. After analysing the ROC curve, the proposed framework is efficient and outperformed the method available in the literature. For quantitative comparative analysis, we have computed ERR for the existing and proposed method as

shown in Table 1 and Table 2 for both the datasets. We observed that the proposed method gives less error rate, comparatively, on both the datasets, i.e., 16.1% and 18.1% respectively. Again, AUC for the existing and proposed method as shown in Table 3 and Table 4 for both the dataset. As illustrated in the table AUC for the proposed method is 73.2% and 72.1%. It shows that the proposed motion pattern-based approach is more efficient, robust, and accurate on both the dataset and is comparatively better than existing approaches of the suspicious behavior.
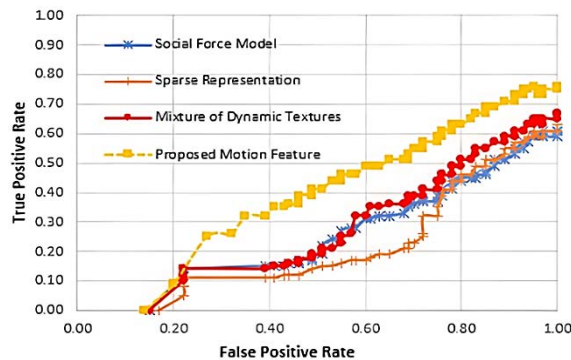

Figure 3. FPR and TPR for the existing and proposed motion feature map-based method for University of Minnesota anomaly detection dataset
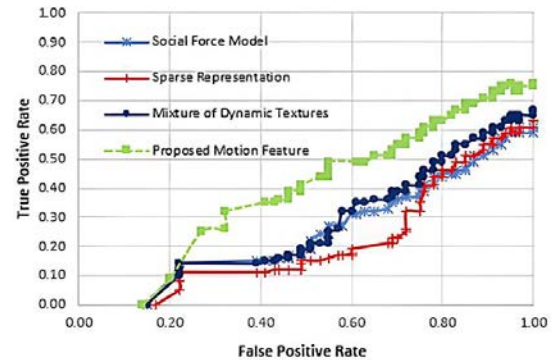
Figure 4. FPR and TPR for the existing and proposed motion feature map-based method for proposed student behavior dataset

Table 1. ERR for the existing and proposed motion feature map-based method on University of Minnesota anomaly detection dataset

Methodology	Ped. 1	Ped. 2	Avg.
Social Force Model [32]	36.5%	35.0%	35.7%
Sparce Representation [31]	35.6%	35.8%	35.7%
Mixture of Dynamic Texture [32]	22.9%	22.9%	22.9%
Proposed Motion Feature based method	21.1%	18.1%	16.1%

Table 2. ERR for the existing and proposed motion feature map-based method on student behavior dataset

Methodology	Ped. 1	Ped. 2	Avg.
Social Force Model [32]	37.5%	34.0%	36.7%
Sparce Representation [31]	32.6%	35.8%	33.7%
Mixture of Dynamic Texture [32]	24.9%	23.9%	23.5%
Proposed Motion Feature based method	22.1%	19.2%	18.1%

Table 3. AUC for the existing and proposed motion feature map-based method on University of Minnesota anomaly detection dataset

Methodology	Ped. 1	Ped. 2	Avg.
Social Force Model [32]	40.9%	27.6%	34.2%
Sparce Representation [31]	32.6%	22.4%	27.5%
Mixture of Dynamic Texture [32]	59.3%	56.8%	58.0%
Proposed Motion Feature based method	64.9%	81.5%	73.2%

Table 4. AUC for the existing and proposed motion feature map-based method on proposed student behavior dataset

Methodology	Ped. 1	Ped. 2	Avg.
Social Force Model [32]	50.8%	63.4%	57.1%
Sparce Representation [31]	74.5%	70.1%	72.3%
Mixture of Dynamic Texture [32]	35.6%	35.8%	35.7%
Proposed Motion Feature based method	63.4%	80.2%	72.1%

5.   CONCLUSION

In this paper, we have proposed a novel method to detect the unusual human activities in an academic environment. Due to the spatial and temporal features of motion features, we can classify frames as

normal or abnormal activity of the pedestrian and also able to locate regions of abnormal activity within the frame as local or global region. We conducted experiments on the University of Minnesota anomaly detection datasets and the proposed student behavioural dataset. The proposed method was confirmed to be effective, surpassing other competing methods in the literature. However, the purpose of this research is to detect abnormal actions in an academic environment, for which cameras generally cover a large area. In future, same method can be used for the different scenarios of student behaviour such as the student examination cheating scenarios, student dispute in the campus, etc. Again, scale, rotation, and illumination changes can also be address if the proposed approach enhance with the additional features such as scale, rotation, and illumination invariant feature.

ACKNOWLEDGEMENTS

REFERENCES

[1] W. Ouyang, X. Zeng, and X. Wang, "Single-pedestrian detection aided by two-pedestrian detection," *IEEE Transactions on Pattern Analysis and Machine Intelligence*, vol. 37, no. 9, pp. 1875–1889, Sep. 2015, doi: 10.1109/TPAMI.2014.2377734.
[2] B. Song and R. Sheng, "Crowd counting and abnormal behavior detection via multiscale gan network combined with deep optical flow," *Mathematical Problems in Engineering*, vol. 2020, no. 6692257, pp. 1–11, Dec. 2020, doi: 10.1155/2020/6692257.
[3] S. Elbishlawi, M. H. Abdelpakey, A. Eltantawy, M. S. Shehata, and M. M. Mohamed, "Deep learning-based crowd scene analysis survey," *Journal of Imaging*, vol. 6, no. 9, p. 95, Sep. 2020, doi: 10.3390/jimaging6090095.
[4] E. Bassoli and L. Vincenzi, "Parameter calibration of a social force model for the crowd-induced vibrations of footbridges," *Frontiers in Built Environment*, vol. 7, no. 1, May 2021, doi: 10.3389/fbuil.2021.656799.
[5] C. Direkoglu, "Abnormal crowd behavior detection using motion information images and convolutional neural networks," *IEEE Access*, vol. 8, pp. 80408–80416, Apr. 2020, doi: 10.1109/ACCESS.2020.2990355.
[6] R. Sundararaman, C. de Almeida Braga, E. Marchand, and J. Pettré, "Tracking pedestrian heads in dense crowd," in *Proceedings of the IEEE Computer Society Conference on Computer Vision and Pattern Recognition*, Jun. 2021, pp. 3864–3874, doi: 10.1109/CVPR46437.2021.00386.
[7] Y. Qu, Y. Xiao, J. Wu, T. Tang, and Z. Gao, "Modeling detour behavior of pedestrian dynamics under different conditions," *Physica A: Statistical Mechanics and its Applications*, vol. 492, pp. 1153–1167, Feb. 2018, doi: 10.1016/j.physa.2017.11.044.
[8] F. Li, X. Li, Q. Liu, and Z. Li, "Occlusion handling and multi-scale pedestrian detection based on deep learning: a review," *IEEE Access*, vol. 10, pp. 19937–19957, Feb. 2022, doi: 10.1109/ACCESS.2022.3150988.
[9] D. Jin, X. Bai, and Y. Wang, "Integrating structural symmetry and local homoplasy information in intuitionistic fuzzy clustering for infrared pedestrian segmentation," *IEEE Transactions on Systems, Man, and Cybernetics: Systems*, vol. 51, no. 7, pp. 4365–4378, Jul. 2021, doi: 10.1109/TSMC.2019.2931699.
[10] J. Qianyin, L. Guoming, Y. Jinwei, and L. Xiying, "A model based method of pedestrian abnormal behavior detection in traffic scene," in *2015 IEEE 1st International Smart Cities Conference, ISC2 2015*, Oct. 2015, pp. 1–6, doi: 10.1109/ISC2.2015.7366164.
[11] N. Tufek and O. Ozkaya, "A comparative research on human activity recognition using deep learning," in *27th Signal Processing and Communications Applications Conference, SIU 2019*, Apr. 2019, pp. 1–4, doi: 10.1109/SIU.2019.8806395.
[12] B. Yang, J. Cao, N. Wang, and X. Liu, "Anomalous behaviors detection in moving crowds based on a weighted convolutional autoencoder-long short-term memory network," *IEEE Transactions on Cognitive and Developmental Systems*, vol. 11, no. 4, pp. 473–482, Dec. 2019, doi: 10.1109/TCDS.2018.2866838.
[13] A. M. Kanu-Asiegbu, R. Vasudevan, and X. Du, "Leveraging trajectory prediction for pedestrian video anomaly detection," in *2021 IEEE Symposium Series on Computational Intelligence, SSCI 2021 - Proceedings*, Dec. 2021, pp. 01–08, doi: 10.1109/SSCI50451.2021.9660004.
[14] A. Fekry, G. Dafoulas, and M. Ismail, "The relation between individual student behaviours in video presentation and their modalities using VARK and PAEI results," in *2019 2nd International Conference on New Trends in Computing Sciences, ICTCS 2019 - Proceedings*, Oct. 2019, pp. 1–7, doi: 10.1109/ICTCS.2019.8923094.
[15] Y. J. Li, X. Weng, Y. Xu, and K. Kitani, "Visio-temporal attention for multi-camera multi-target association," in *Proceedings of the IEEE International Conference on Computer Vision*, Oct. 2021, pp. 9814–9824, doi: 10.1109/ICCV48922.2021.00969.
[16] C. He, X. Zhang, Z. Miao, and T. Sun, "Intelligent vehicle pedestrian tracking based on YOLOv3 and DASiamRPN," in *Chinese Control Conference, CCC*, Jul. 2021, vol. 2021-July, pp. 4181–4186, doi: 10.23919/CCC52363.2021.9549997.
[17] P. K. Gaddigoudar, T. R. Balihalli, S. S. Ijantkar, N. C. Iyer, and S. Maralappanavar, "Pedestrian detection and tracking using particle filtering," in *Proceeding - IEEE International Conference on Computing, Communication and Automation, ICCCA 2017*, May 2017, vol. 2017-January, pp. 110–115, doi: 10.1109/CCAA.2017.8229782.
[18] A. Mehmood, "Efficient anomaly detection in crowd videos using pre-trained 2D convolutional neural networks," *IEEE Access*, vol. 9, pp. 138283–138295, Oct. 2021, doi: 10.1109/ACCESS.2021.3118009.
[19] W. Zhang, X. Dong, H. Li, J. Xu, and D. Wang, "Unsupervised detection of abnormal electricity consumption behavior based on feature engineering," *IEEE Access*, vol. 8, pp. 55483–55500, Mar. 2020, doi: 10.1109/ACCESS.2020.2980079.
[20] K. Chebli and A. Ben Khalifa, "Pedestrian detection based on background compensation with block-matching algorithm," in *2018 15th International Multi-Conference on Systems, Signals and Devices, SSD 2018*, Mar. 2018, pp. 497–501, doi: 10.1109/SSD.2018.8570499.
[21] P. Vasishta, D. Vaufreydaz, and A. Spalanzani, "Building prior knowledge: a markov based pedestrian prediction model using urban environmental data," in *2018 15th International Conference on Control, Automation, Robotics and Vision, ICARCV 2018*, Nov. 2018, pp. 247–253, doi: 10.1109/ICARCV.2018.8581368.
[22] J. X. Wang and Y. R. Hou, "Pedestrian fall action detection and alarm in video surveillance," in *Proceedings - 2016 3rd International Conference on Information Science and Control Engineering, ICISCE 2016*, Jul. 2016, pp. 502–505, doi:

10.1109/ICISCE.2016.114.

[23]   L. Mao, Y. Xu, F. Cheng, and R. Zhang, "Multi-part pedestrian tracking algorithm with fuzzy decision for partial occlusion," in *Proceedings of the 30th Chinese Control and Decision Conference, CCDC 2018*, Jun. 2018, pp. 937–940, doi: 10.1109/CCDC.2018.8407264.

[24]   Z. Sun, J. Chen, L. Chao, W. Ruan, and M. Mukherjee, "A survey of multiple pedestrian tracking based on tracking-by-detection framework," *IEEE Transactions on Circuits and Systems for Video Technology*, vol. 31, no. 5, pp. 1819–1833, May 2021, doi: 10.1109/TCSVT.2020.3009717.

[25]   S. J. Kim, J. Y. Nam, and B. C. Ko, "Online tracker optimization for multi-pedestrian tracking using a moving vehicle camera," *IEEE Access*, vol. 6, pp. 48675–48687, 2018, doi: 10.1109/ACCESS.2018.2867621.

[26]   R. Q. Minguez, I. P. Alonso, D. Fernandez-Llorca, and M. A. Sotelo, "Pedestrian path, pose, and intention prediction through gaussian process dynamical models and pedestrian activity recognition," *IEEE Transactions on Intelligent Transportation Systems*, vol. 20, no. 5, pp. 1803–1814, May 2019, doi: 10.1109/TITS.2018.2836305.

[27]   R. Zhu *et al.*, "Efficient human activity recognition solving the confusing activities via deep ensemble learning," *IEEE Access*, vol. 7, pp. 75490–75499, Jun. 2019, doi: 10.1109/ACCESS.2019.2922104.

[28]   M. H. Zaki and T. Sayed, "Automated analysis of pedestrian group behavior in urban settings," *IEEE Transactions on Intelligent Transportation Systems*, vol. 19, no. 6, pp. 1880–1889, Jun. 2018, doi: 10.1109/TITS.2017.2747516.

[29]   V. Papathanasopoulou, I. Spyropoulou, H. Perakis, V. Gikas, and E. Andrikopoulou, "Classification of pedestrian behavior using real trajectory data," in *2021 7th International Conference on Models and Technologies for Intelligent Transportation Systems, MT-ITS 2021*, Jun. 2021, pp. 1–6, doi: 10.1109/MT-ITS49943.2021.9529266.

[30]   L. Knoedler, C. Salmi, H. Zhu, B. Brito, and J. Alonso-Mora, "Improving pedestrian prediction models with self-supervised continual learning," *IEEE Robotics and Automation Letters*, vol. 7, no. 2, pp. 4781–4788, Apr. 2022, doi: 10.1109/LRA.2022.3148475.

[31]   X. Zhou, Y. Chen, and Q. Zhang, "Trajectory analysis method based on video surveillance anomaly detection," in *Proceeding - 2021 China Automation Congress, CAC 2021*, Oct. 2021, pp. 1141–1145, doi: 10.1109/CAC53003.2021.9727735.

[32]   A. K. Jhapate, S. Malviya, and M. Jhapate, "Unusual crowd activity detection using OpenCV and motion influence map," in *2nd International Conference on Data, Engineering and Applications, IDEA 2020*, Feb. 2020, pp. 1–6, doi: 10.1109/IDEA49133.2020.9170704.

BIOGRAPHIES OF AUTHORS

Kamal Omprakash Hajari (ID) (g) SC P holds a is currently pursuing a Ph.D. degree from the Department of Information technology, Yeshwantrao Chavan College of Engineering, Hingna Road, Wanadongri, Nagpur, Maharashtra, India. He got his Bachlor of Engineering in Computer Technology and Master of Technology in Information Technology degree from Rashtrasant Tukadoji Maharaj Nagpur University, Nagpur in 2013 and 2015. His research interests mainly include computer vision, deep learning, machine learning, pattern recognition, artificial intelligence, real-time image/video processing, and video surveillance. He is affiliated with IEEE as student member and having membership of Institute of Engineers (IE), ACM, ISTE. He can be contacted at email: kamalhajari123@gmail.com.

Ujwalla Haridas Gawande (ID) (g) SC P is currently working as Dean Research and Development and Associate Professor at the Department of Information technology, Yeshwantrao Chavan College of Engineering, Nagpur. She got her B.E. and M.Tech. degree from RTMNU University, Nagpur in 2001 and 2007, and a Ph.D. degree from SVNIT, Surat in 2014. Her current research interest focuses on machine learning and computer vision, artificial intelligence, pattern recognition techniques for large video and image data analysis. Specifically, she works in object recognition, deep learning, machine learning, etc. Reviewer of artificial intelligence, IEEE Transaction of Multimedia, and IEEE Access reviewer. She is having membership of Institute of Engineers (IE), ACM, ISTE. She can be contacted at email: ujwallgawande@yahoo.co.in.

Yogesh Golhar (ID) (g) SC P is currently working as Assistant Professor, Computer Engineering Department, St. Vincent Palloti College of Engineering and Technology, Nagpur, Maharashtra, India. He got his Bachlor of Engineering and Master of Technology degree from Rashtrasant Tukadoji Maharaj Nagpur University, Nagpur in 2008 and 2012. His current research interest focuses on big data analytics, machine learning and computer vision, artificial intelligence, pattern recognition techniques, and computer networks. He is having membership of Institute of Engineers (IE), ACM, ISTE. He can be contacted at email: yj999@ymail.com.

Multi Oral Disease Classification from Panoramic Radiograph using Transfer Learning and XGBoost

3 authors, including:

Priyanka Jaiswal
Veermata Jijabai Technological Institute
5 PUBLICATIONS   **14** CITATIONS

SEE PROFILE

Multi Oral Disease Classification from Panoramic Radiograph using Transfer Learning and XGBoost

Priyanka Jaiswal[1], Dr. Vijay Katkar[2], Dr. S.G. Bhirud[3]

Professor[3]

Department of CE & IT, Veermata Jijabai Technical Institute, Mumbai-400019, India[1, 3]

Department of IT, YCCE, Nagpur[1]

Associate Professor, Department of Computer Engineering, Marwadi University, Rajkot, India[2]

Abstract—The subject of oral healthcare is a crucial research field with significant technological development. This research examines the field of oral health care known as dentistry, a branch of medicine concerned with the anatomy, development, and disorders of the teeth. Good oral health is essential for speaking, smiling, testing, touching, digesting food, swallowing, and many other aspects, such as expressing a variety of emotions through facial expressions. Comfort in doing all these activities contributes to a person's self-confidence. For diagnosing multiple oral diseases at a time panoramic radiograph is used. Oral healthcare experts are important to appropriately detect and classify disorders. This automated approach was developed to eliminate the overhead of experts and the time required for diagnosis. This research is based on a self-created dataset of 500 images representing six distinct diseases in 46 possible combinations. Tooth wear, periapical, periodontitis, tooth decay, missing tooth, and impacted tooth are all examples of diseases. This system is developed using the concept of transfer learning with the use of a different pre-trained network such as "ResNet50V2", "ResNet101V2", "MobileNetV3Large", "MobileNetV3Small", "MobileNet", "EfficientNetB0", "EfficientNetB1", and "EfficientNetB2" with XGBoost and to get the final prediction The images in the dataset were divided into 80% training and 20% images for testing. To assess the performance of this system, various measuring metrics are used. Experiments revealed that the proposed model detected Tooth wear, periapical, periodontitis, tooth decay, missing tooth, and impacted tooth with an accuracy of 91.8%, 92.2%, 92.4%, 93.2%, 91.6%, and 90.8%, respectively.

Keywords—*Panoramic radiograph; dentistry; deep learning; ensemble classifier; multi-disease classification and prediction; oral diseases; weighted ensemble module; XGBoost*

I. INTRODUCTION

According to the WHO survey, the population of seniors aged 65 and more has surpassed 150 million, and the population of patients with chronic conditions has surpassed 400 million. Due to the increase in periodontal diseases in the 35-44 age group, the percentage of infection is higher in the 65-74 age group. Additionally, proper oral health is essential for maintaining a healthy heart and digestive system. Aging and mouth problems have a long history of interdependence; a lack of attention to oral health might predispose older individuals to other health conditions, such as malnutrition, heart-related issues, Digestion related problems, etc. [2] This has increased the demand for automated medical and healthcare solutions that are secure and of superior quality.

Which must be useful for the early detection and classification of the present disorders of an individual. To perform diagnosis of present tooth-related diseases in the mouth, Currently, dental radiography plays a crucial role in diagnosing the condition of oral health. Due to its accurate confirmation of clinical findings, dental panoramic radiography (DPR) images are attracting a rising amount of attention in the diagnostic process. Typically, three types of dental X-ray radiographs are used for diagnosis in dental imaging. Dental radiographs consist of bitewing, periapical, and panoramic types. Bitewing focuses mostly on the coronal half of teeth, periapical encompasses the apical region of teeth, and panoramic X-ray scans consider the entire upper and lower jaw, including teeth and supporting bones. For disease localization diagnosis, periapical radiography is suggested. But when the disease is widespread, panoramic X-rays are used to obtain a thorough perspective for diagnosis and therapy planning. They are easily standardizable and reproducible.

Fig. 1. Different types of dental radiography

Due to the unspecified quality of x-ray images, varying tooth sizes, and other factors, numerous challenges are associated with automatically separating teeth from dental radiograph images. Fig. 1 depicts the three main types of x-ray images of teeth: bitewing, periapical, and panoramic teeth. The dentist manually clarifies radiographs by identifying each tooth and the corresponding issue. But if the x-ray radiography is unclear, it can lead to misinterpretation during analysis [1]. Conventionally, a dentist uses dental radiographs and a clinical evaluation of the patient to make a diagnosis, based on the available infrastructure and expertise. These numerous methods encourage researchers to use and build new machine learning, deep learning, and dental image comprehension techniques more effectively [2][3]. This approach will help to classify multiple oral diseases automatically.

Image processing is currently the most prominent field in digital healthcare applications; it is also utilized well in the medical environment to analyze illness more precisely [4]. As

a result of these developments, medical image processing has become prevalent in both medical and health sectors in analyzing diseases with precise sensitivity and measurement [5]. Similarly, medical image processing is applied to dental information to identify and classify disease types and severity [6]. To identify dental problems, all factors must be considered [7]; this is the predominant trend in the detection of dental diseases. The kind and severity of the condition differed between patients [8] due to inconsistencies in the data. Several mathematical models have been created to predict, identify, assess, and monitor the early oral health of teeth [9]. However, the issues are not addressed because of the complexity of the images [10]. Furthermore, dental images differ depending on the patient's genes and body condition. Predicting dental disease is thus a difficult task. Furthermore, a mathematical model has carried out the different cavity analysis processes practically. The cavity severity analysis procedure has varied depending on the patient's body and tooth conditions [11]. Finally, the current tooth diseases and their causes were identified. Nonetheless, those model features are insufficient for real-time data. Because actual time tooth X-ray data contains whiter spaces, and some tooth X-rays have tooth clips [12] disease identification becomes more difficult. Furthermore, those types of images have required more additional features to identify the affected tooth [13]. As a result, those approaches failed to identify the diseased tooth. Furthermore, a standard filtering process was used to remove the noisy features in the trained data, which increased the cost of the resource [29]. Furthermore, when the dataset images were complex, the filtering results were poor. In other domain concepts, deep learning is used to efficiently estimate remote heart rates and to classify breast lesions in mammography using a conventional neural network, which helped us understand the running complexity of different machine intelligence techniques [14]. These issues prompted the current study to develop optimized deep networks with filtering parameters to obtain more precise disease classification results [17].

The current article has descended into a new solution for maximizing disease classification by utilizing the different pre-trained deep learning models. The proposed study has a step-down in the multi-disease classification model, which is defined as multiple parameters in the proposed framework being upgraded to classify multi-disease features. The following section goes over the specifics and importance of detecting tooth wear, tooth decay(cavity), impacted tooth, missing tooth, periapical, and periodontitis at an early stage. The image of a patient suffering from tooth wear is shown in Fig. 2.

A. The Necessity of Detecting Tooth Wear in Dentistry

Teeth have specific anatomy consisting of several cusps and fissures to serve the function of chewing food like a mortar and pestle where the approximating cusps work as a pestle and fissures work as mortar crushing the food coming in between. If these anatomical landmarks are worn-out due to wear, this crushing mechanism gets disturbed and food slips from between the teeth causing a decrease in chewing efficiency ultimately leading to nutritional deficiency and decreased quality of life. Hence teeth wear if diagnosed early can be

treated conservatively and a patient can be counseled to prevent further damage. Dental wear has several types which include dental attrition, erosion, abrasion, and abreaction. Dental attrition, abrasion, and erosion are commonly found in the Indian population. All these have specific patterns and causative factors following which they can be diagnosed.

Fig. 2.   Tooth wear (erosive)

All these wear patterns can cause irreparable harm to a tooth's structure without creating any noticeable pain in the early stages. When wear and tear reached a severe stage, treatment can be quite costly for the patient. It is possible to avoid getting them by getting checked for them early and making some changes to one's way of living. [15]

B. The Necessity of Detecting Periodontitis

The following section describes the details of gingivitis, periodontitis, and the process of diagnosing these diseases using radiographs and clinical examination. Gingivitis is an inflammatory disease limited to gums adjoining the teeth in which the primary signs are redness and bleeding from the gums along with their swelling. Whereas periodontitis is when the inflammation of the gums extends to the adjoining tooth-supporting bone it is derived as periodontitis. Primary signs of periodontitis are loss of tooth-supporting bone and tooth mobility. Methods are different to diagnose periodontitis and Gingivitis as gingivitis can be diagnosed with the help of clinical examination, observing for the signs and symptoms of the disease. Like red, swollen, and bleeding gums. Periodontitis can be diagnosed with the help of clinical and radiographic examinations. Clinically Doctors can measure the loss of supporting bone with the help of a periodontal probe measuring the sulcus depth, and radio graphically the amount of horizontal and vertical bone loss can be identified to gauge the severity and prognosis of periodontitis. The reason for not considering Gingivitis in this implementation is as it is an early stage that can be diagnosed only on clinical examination and here in our research, we had considered OPGs as a sturdy base which is the most preferred diagnostic tool to diagnose periodontitis. By considering all mentioned parameters early diagnosis is needed to prevent the further loss of teeth-supporting tissues and plan for the repair. Fig. 3 represents an image with periapical and periodontitis.

Fig. 3.   Periodontitis and periapical

C. The Necessity of Detecting Tooth Caries (Dental Cavity)

Dental caries is a disease that can be diagnosed easily on clinical and radiographic examination. Treatment of decayed teeth depends upon the extent of decay which can be viewed only radiographically. Orthopantomograms are used to diagnose caries between the teeth and over the teeth and Intraoral periapical radiographs and bitewing radiographs are the specific radiographs to detect the extent of the decay. A representation of a tooth with a cavity is shown in Fig. 4.

Fig. 4.   Tooth caries/dental cavity

D. The Necessity of Detecting Periapical

periapical infections can only be diagnosed radiographically as clinical symptoms often appear in the delayed stage. In OPG the extent and the size of the periapical lesion can be exactly gauged. It is shown in Fig. 2 and Fig. 7.

E. The Necessity of Identification of Missing Teeth

Often one or more missing teeth do make complex changes in patients' quality of life. One missing tooth can lead to decay and periodontal disease to seven teeth as the teeth approximating the edentulous space and opposing arch teeth drift from their natural definite position. These all changes can be diagnosed only through an OPG. Fig. 5 shows missing teeth. it is observed that two teeth are missing and the last is affected by decay.

Fig. 5.   Missing tooth

F. The Necessity of Identification of Impacted Tooth

Impacted wisdom teeth or any other tooth can't be seen clinically. OPG gives the exact two-dimensional view of the impacted tooth. A representation of an Impacted tooth is shown in Fig. 6
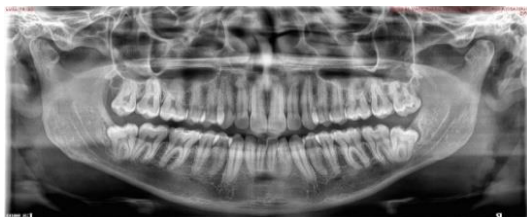

Fig. 6.   Impacted tooth

Fig. 7.   Wear, decay periapical, and impact

This research work is conceived as a collaborative effort between technical expertise and a dentistry stream in an area of significant interest to the medical community. Literature review reveals that extensive research on tooth extraction or diagnostic purposes used in cybercrimes such as estimation of age, identification of a person based on tooth anatomy, etc, but regrettably, there has been very little work combining the oral health care and engineering fields for continuous engineering and clinical problem-solving. This research began with an emphasis on the various stages of oral illnesses [16]. Such as tooth wear, periapical, periodontitis, tooth decay, tooth loss, and tooth fractures, impacted tooth.

The remaining sections are organized as follows. Section II offers a concise assessment of pertinent literature. It discusses the current state of the art in the use of image processing, machine learning, and deep learning techniques in the domain of dentistry. Understanding different types of radiographs and their importance in evaluating models is discussed using various methods and networks. Section III describes the data collection, radiograph selection, and disease identification processes. The importance of various diseases that can be identified using panoramic radiographs has already been discussed in the introduction section. This section focuses on dataset labeling as well as expert validation of labels. Section IV elaborates on the concept of transfer learning with XGBoost and ensemble learning concerning medical image processing. The proposed methodology is illustrated in Section V, which is followed by the results and discussion and future scope sections.

II.   RELATED WORKS

A comparative analysis of the deep learning model for dental segmentation in panoramic radiographs is reported in [18]. The comparison is made between U-Net, DCU-Net, Double U-Net, and NanoNet. On the 1500-image dataset provided by Silva and Olivia. There is also a teeth mask available for this. Their system is designed to identify 32 teeth, fillings, braces, and dental implants. Data enhancement is achieved through random rotation and horizontal inversion. Using a dataset with data augmentation and segmentation without data augmentation based on the segmentation model, the experiment results are shown. The outcome is then compared to the current state of the art.

In this biomedical study [19], the U-Net approach to apical lesion segmentation on panoramic radiographs is discussed. The objective of this study was to extract apical lesions from 470 dental panoramic radiographs. This dataset included 380 images for training, 43 for validation, and 47 for testing. 1140 images were generated after augmentation was applied at the second stage of implementation. For augmentation, horizontal

and vertical flips are used. Cropping (pre-processing) is used after augmentation to divide images into four parts: upper right, upper left, lower right, and lower left with size=1000x530. They then multiplied 1140 by 4 for the training group. This dataset is not available to the public.

For apical lesion segmentation from panoramic radiographs, [20] adopts a deep learning technique. There were a total of 1691 images utilized for segmentation. For the training set, all radiographs were manually tagged in red using a polygon labeling tool to construct lesions' contours. The name of the software is "deep stack." The image's original resolution of 1976x976 was reduced to 960x480. Various augmentation techniques, including flip, blur, shift, scale, rotation, sharpness, emboss, contrast, brightness, grid distortion, and elastic transform, are utilized to increase the dataset via online augmentation. Utilizing a pre-trained U-Net CNN for pre-processing and training.

In [21]: Work on a multimodal panoramic x-ray dataset for diagnostic system benchmarking was presented. There are a total of one thousand photos about the labeling of anomalies and teeth. This study was carried out on five levels: anatomical location, peripheral characteristics, radiodensity, surrounding structure effects, and anomaly category. Using eye tracking and a think-aloud methodology, this is the first-time radiologist skill has been captured. This study includes a publicly accessible dataset as well as benchmark performance analyses for a variety of cutting-edge devices. In addition, picture enhancement and image segmentation are carried out. The maxillomandibular region of interest is delineated using x-ray images, gaze maps, and multimodal audio text files. A thousand radiographs and a ground truth mask make up the dataset. 15% is utilized for validation, whereas 85% is used for training. Adam was trained on GPUs with 32 GB of RAM that was NVIDIA Tesla V100 devices. However, in terms of image quality, CLAHE outperforms well with AME Score=24.32 and Log AME=0.3702. Ground truth images were used for segmentation, and the results were compared using UNET, UNET++, PSPNet, DeepLabV3, and DeepLabV3+. VGG19, ResNet18, and ResNet 50 were used to train each of the given networks. The module learning rate is 1x10-3, the weight decay is 1x10-4, the epoch is 150, and the batch size is 16. Pixel accuracy, intersection over union, and dice coefficient are all evaluated. To achieve the desired result, CNN for periodontal bone loss and Squeeze Net for implant fixtures were used. To detect and classify periodontal bone loss, a hybrid framework with Mask RCNN and ResNet101 was used. For intraoral radiographs covering caries, a back propagation neural network is used.

Work on dental caries is being conducted by [c1concepts.]'s (cavity). Utilizing a multi-input deep convolutional neural network ensemble known as MI DCNNE, they were able to obtain accurate results and overcome negative perceptions of panoramic radiography. This system is based on computer-based intelligent vision systems supported by techniques for machine learning and image processing. This new approach accepts both raw periapical images and an improved version of them as inputs. In total, 340 photos were considered for this study. The model has a 99.13% accuracy rate when diagnosing dental caries from periapical pictures.

The primary goal of this work [25] is to extract the area of interest (ROI). Because of background noise, the original image may contain useless information. We occasionally come across images that are of poor quality. Because of this, separation is critical. U-Net was used in three phases to accomplish this: one feature encoder, corresponding decoder, and multipath feature extractor.

The author of [26] proposed an automatic teeth recognition model based on residual network-based faster R-CNN techniques. This model is implemented in two stages. The results obtained in step one, i.e., using R-CNN, are refined further using candidate optimization techniques. These improvements improve the results by about 1%. Ten-fold cross-validation is used in this system to test the model's feasibility and robustness. This model is used to describe the various tooth categories in a panoramic radiograph.

The implementation in [27] is based on the use of u-net architecture to perform panoramic radiograph segmentation. They used CNN to achieve accurate panorama image segmentation. With a 94% accuracy and a 94% dice score. The performance of the u-net is compared with various segmentation techniques in this work. This fuzzy c-means (FCM) is developed using a hybrid of FCM and a neutrophilic approach to segment the jaw and lesion present in the jaw using a panoramic radiogram. This paper investigates the comparison of global thresholding, fuzzy c-means, watershed, canny edge detection algorithms, and the U-NET model. When compared to the other techniques, n-net performed the best. Ivison lab provided the dataset for this study.

In [28], researchers offered an innovative approach to segmenting and classifying data. They have covered 15 various disorders including healthy teeth, missing teeth, dental restoration implants, fixed prostheses, mobile prostheses, etc. To depict all 15 diseases, a total of 2,000 images are made. All these images were taken at separate dental clinics. A convolutional neural network (CNN) was trained to perform semantic segmentation on images from the dataset, and many techniques were employed to enhance the annotated data. Images are segmented and then binarized with multiple thresholds. The detection of teeth is a two-stage algorithmic process. When discrepancies are uncovered during semantic segmentation, refinement techniques are employed to rectify the situation. In this study, the Nobel approach to teeth detection and dental problem classification using deep learning and image processing was introduced.

The paper [22] compares ten different segmentation methods for use with dental imaging. The offered solutions were evaluated and classified using five different metrics: accuracy, specificity, precision, recall, and F1-score. Because of the shattered bones in the buccal cavity, not one of the ten segmentation methods tried was successful in isolating the teeth.

With the help of a mask region-based convolution neural network, the authors of [23] suggested a method for instance segmentation of teeth in panoramic photos. In the wake of Resnet-101-driven feature extraction, a feature pyramid network (FPN) is built with predetermined anchors and extracted regions of interest.

Each region's proposal network consists of the FPN and its anchors (RPN). The regions of interest are then repositioned so that they are all the same size. Additionally, the bounding box coordinates are used to classify each feature as either a tooth or a background and to pinpoint its exact location. Finally, a bounding box is formed around the tooth once it has been segmented.

DeNTNet, described in [24], is a deep neural transfer network trained to identify panoramic dental radiographic evidence of periodontal bone loss (PBL). During detection, several convolutional neural networks are trained. A segmentation network is then trained to extract teeth from the ROI, and a second network is trained to predict areas of periodontal bone loss. Using the encoder portion of the lesion segmentation network as a pre-trained model, a classification network is constructed to predict the presence of PBL in each tooth.

Table I provides a complete overview of the various datasets available, the work done in dental image processing, and the disorders linked with it. It has been observed that work is being done in various disciplines of dentistry employing artificial intelligence techniques. To begin, a private dataset is produced and not made public. Another observation is that most systems are designed to segment teeth. Furthermore, the minimum one and maximum four diseases covered for classification and detection are one. One method is used, in which 14 diseases are investigated, but just the highlighting of diseases is done, rather than classification or detection.

TABLE I.   ANALYSIS OF AN AVAILABLE DATASET AND METHODOLOGY USED

Papers	Variable detected	Total Images	Publicly available	Labeled Teeth	Labeled abnormalities	Methodology Used
[36]	Teeth	100	No	Yes	No	CNN
[37]	Teeth	100	No	Yes	No	CNN
[38]	Teeth	1500	Yes	Yes	No	Mask R-CNN
[39]	Teeth	1352	No	Yes	No	CNN
[40]	Endodontic	85	No	No	Yes	CNN
[41]	Endodontic	300	No	Yes	No	CNN
[42]	Teeth	1000[116]	Yes (Kaggle)	No	No	CNN
[32]	Teeth	1200	No	Yes	No	Yolov3
[43]	Teeth	1000	No	Yes	No	Deep Learning and Image Processing Techniques
Own Dataset	Teeth	500	No	No	Yes	Transfer Learning and XGBoost

III. DATASET DESCRIPTION

Researching any specific domain data availability is the primary step, but in the field of dental informatics dataset availability is a major concern. After analyzing all the related work in Dental Image Processing (DIP), we discovered that obtaining a suitable dataset for the early stages of research is challenging. As a result, we collaborated with many dental healthcare sections to acquire data. Rather than waiting for new patients for each ailment, we chose to screen panoramic dental X-rays from electronic medical records to collect data efficiently. There is no ethical issue because these images do not contain any personally identifiable information. The dataset consists of images and a questionnaire, which was supplementary at the initial level of research. Collecting symptoms and images for every patient is a time-consuming task so we focused on a collection of radiographs. Principally there are many types of radiographs available in dental radiography, such as Bitewing X-ray, Periapical X-ray, Occlusion X-ray, Panoramic X-ray, Cephalometric Projection, and Cone Beam X-ray. Among these categories, Panoramic OPG (Orthopantomogram) is considered as is two-dimensional radiograph that covers maximum all diseases with complete coverage. Dental radiographic images in OPG format were collected.

A. Panoramic (OPG) X-Ray and its Benefits

The maxillary and mandibular teeth, as well as the surrounding periodontium and certain anatomical landmarks like the maxillary sinus and the temporomandibular joints, are all visible on an OPG, a two-dimensional radiograph. Oral disorders such as periapical abscess, cysts, osteitis, and various tumors and cysts of mandibular and maxillary origin can be diagnosed using OPG X-ray. OPG is useful for determining how much bone has been lost due to periodontal disease and how severe it is. OPG X-ray is useful for diagnosing a wide variety of dental conditions, including cavities, root fractures, and periodontal inflammation. OPG X-rays can help identify and evaluate dental cusp fracture and enamel deterioration, but their two-dimensional nature has its limitations.

The data was collected from Government Dental College and several private dental clinics and laboratories in Nagpur and cities across India. Here image collection work is focused on the wear of the tooth to find erosion, attrition, and abrasion of the tooth and other oral diseases, including impacted tooth, periapical lesion, fractured tooth, missing teeth, etc.,

B. Process of Collecting, Preparing and Labeling the Data

This section describes the process of collecting, preparing, and labeling the dataset. The main contribution while

collecting images and preparing the dataset are expressed with the help of the diagram given below:

a) From 2019 to 2021, we collected approximately 2,000 OPG radiographs from multiple sources.

b) All images were then checked for contrast and illumination quality.

c) Images of poor quality and nonrelevant, such as images with prostheses, multiple caps, braces, etc were removed from the dataset.

d) Diseases that can be seen through OPG are identified and discussed with clinicians.

e) OPG radiographs can be used to diagnose diseases such as caries, periodontitis, periapical infection, impacted teeth, tooth wear, bone fracture, missing teeth, and anatomy of the maxillary sinus and temporomandibular joint.

f) Following disease identification, images are labeled with the assistance of various dental experts (such as Oral and Maxillofacial Radiologists, Prosthodontists, Oral and Maxillofacial Surgeons, Periodontics, and endodontists,).

g) Image labeling is done in two ways: radiograph with multiple diseases and radiograph with a single disease.

h) After the image sorting process, it is discovered that the approximate probability of receiving a relevant radiograph is 50/500. Finally, we can filter 500 useful radiographs from available images.

i) Before developing any module, various pre-processing steps are performed to create the extension of the data set, In this automatic cropping of the image is done to extract the relevant portion by using an automatic cropping algorithm.

j) Our dataset is cross-validated and tested with the help of three different domain experts to make it more consistent, reliable, authentic, and useful.

k) The final label matrix is generated for different six diseases if the disease is present in that image so marked as 1 otherwise 0 which is shown in Table II: Labelled dataset. For example, in image id 92 wear, decay, missing, and impacted tooth diseases are present.

TABLE II.   SAMPLE LABELLED DATASET

Image Id	Wear	Decay	Peri-Apical	Periodontitis	Missing	Impacted
1	0	1	0	0	0	0
92	1	1	0	0	1	1
104	1	0	0	0	0	1
238	1	1	0	0	1	0
347	1	1	1	0	0	0
457	1	0	1	1	0	0

To check the validity and authentication of dataset creation complete supplementary material is available. The panoramic dental images were obtained from a variety of sources, including dental laboratories. The image properties due to

different acquisition systems vary in terms of contrast and brightness. The pre-processing challenge was to adjust the contrast and illumination levels of all the collected images so that subsequent stages produced the same set of features corresponding to each class or group. We gathered images that were prone to six major issues: dental decay, dental wear, periapical, periodontitis, missing teeth, impacts, and a combination of all six diseases. An experienced medical practitioner in the respective field. While creating the LABEL matrix great care was taken to avoid any false labeling in the LABEL matrix. Images with low contrast and illumination were discarded after being manually sorted one by one. Duplicated images were identified using image comparison and separate codes. Finally, 500 images were taken for this research project, while the remaining unclear images were discarded. Fig. 8 shows the analysis of the total number of images available in the dataset.
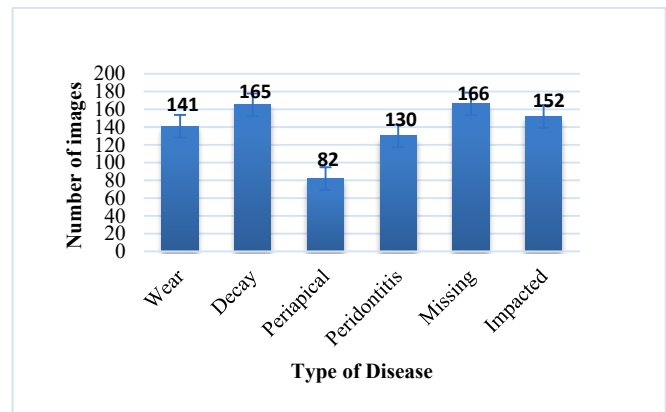

Fig. 8.   Analysis of images available in the dataset

IV. TRANSFER LEARNING, XGBOOST, AND ENSEMBLE APPROACH

A. Transfer Learning

Deep feature extraction (DFE) and Transfer learning (TL) are two of the most effective alternatives to employing a small number of images as training samples. When a small sample size of images is present. TL refers to the process of applying previously taught models to unexpected challenges. TL is not a distinct classification of Machine learning algorithms; rather, it is a technique that can be used to create a new Machine learning model. The model will be able to use the knowledge and skills acquired from earlier training in new scenarios. In a manner like the preceding task, data will need to be organized based on the type of data. A further application of TL is the extraction of deep feature data.

Rather than manually modifying the activation layers of the CNN, it is possible to extract feature vectors by utilizing pre-trained CNN models. The deeper layers, which are activated by the activation of the lower-level layers, include the picture classification-critical higher-level features.

Transfer Learning is a technique in which we reuse a previously trained model as the foundation for a new model on a new challenge. In this case, a model trained on one task is repurposed for another. Transfer learning tries to improve target learners' performance on the target domain by

transferring knowledge from distinct but related source domains. ResNet50V2, ResNet101V2', 'MobileNetV3Large', 'MobileNetV3Small', 'MobileNet', 'EfficientNetB0', 'EfficientNetB1', and 'EfficientNetB2' are examples of pre-trained networks. [33].

ResNet50V2 [34] is a changed version of ResNet50. It does better on the ImageNet dataset than ResNet50 and ResNet101. ResNet-101 is a 101-layer convolutional neural network.

MobileNetV3 [35] is a convolutional neural network that is tuned to mobile phone CPUs using a combination of hardware-aware network architecture search (NAS) and the NetAdapt algorithm. It was then improved by making new architectural advances.

EfficientNet-B0 is a convolutional neural network that has been trained on more than a million images from the ImageNet database [30]. The network can divide images into 1000 different kinds of objects, like a keyboard, mouse, pencil, and many animals.

B. XGBoost

Extreme Gradient Boosting, which is what XGBoost stands for, is a distributed gradient-boosted decision tree (GBDT) machine learning library that can be used on a large scale. It is the best machine learning library for regression, classification, and ranking problems, and it has parallel tree boosting. It's like Random Forest in that it builds a group of decision trees, but instead of training the models at the same time, XGBoost trains them one at a time. Each new decision tree learns from the mistakes made by the one before it. Boosting is the process of training models one after the other. A gradient in XGBoost stands for a type of boosting that uses weak learners. Weak learners are simple models that only do better than random chance. The algorithm starts with a weak learner at the

beginning. Each new model tries to fix the mistakes that the previous decision tree made. This keeps happening until there are no more ways to make the model better. The result is a strong learner model. [31]

C. Ensemble Modeling

Ensemble modeling is a way to predict what will happen based on several different base models. The goal of using a group of models is to reduce the prediction's generalization error. When the ensemble approach is used, the prediction error goes down if the base models are different and can be used on their own. The method tries to figure out what will happen by asking a variety of individuals. Even though the ensemble model is made up of several base models, it works like a single model. [32]

D. Weighted Average or Weighted Sum Ensemble

Weighted average or weighted sum ensemble is a type of machine learning that uses a group of models to make a prediction. The contribution of each model is weighted according to how good it is. The voting ensemble has something to do with the weighted average ensemble. In this method, we didn't tune it; instead, we used the weights that were already there. In other words, a weight tells how much the input affects the output. Biases, which are always the same, are an extra input for the next layer that will always be 1[33][34].

V. PROPOSED METHODOLOGY

We have created a database of 500 images of panoramic radiographs which are explained in section III. Dataset is divided into a training set and a testing set. The training set goes to eight different pre-trained models.
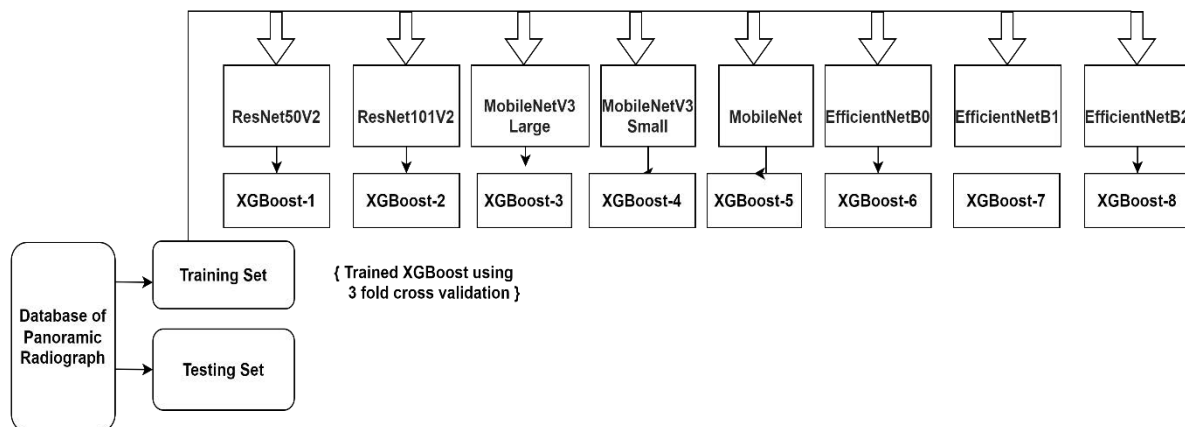

Fig. 9. Proposed methodology (training phase)

Different pre-trained models used for this phase are „ResNet50V2', 'ResNet101V2', 'MobileNetV3Large', 'MobileNetV3Small', 'MobileNet', 'EfficientNetB0', 'EfficientNetB1', and 'EfficientNetB2'. Out of 500 samples 80% samples used for training. The detailed process of the training and evaluation phase is given in Fig. 9 and Fig. 10. While training we used 3-fold cross-validation. Cross-validation is a technique for testing models that involves

training them on distinct subsets of the available input data and then testing them on the other. Dataset D is divided into three identically sized subsets. The process of fitting and evaluating the model is done three times, and each time a different subset is used as a training sample. At last, in the testing phase given in Fig. 10, we get eight tuned XGBoost. pre-trained networks are used to extract the features and then extracted features are given as input to the XGBoost model for training.

In comparison to other gradient-boosting approaches, XGBoost is nearly ten times faster and has a strong predictive power. Additionally, it contains a range of regularizations that minimize overfitting and enhance overall performance. These eight trained XGBoost will generate eight different classifier

prediction outputs. To get the final prediction weighted ensemble module which is an extension of a model averaging ensemble where the contribution of each member to the final prediction is weighted by the performance of the model.
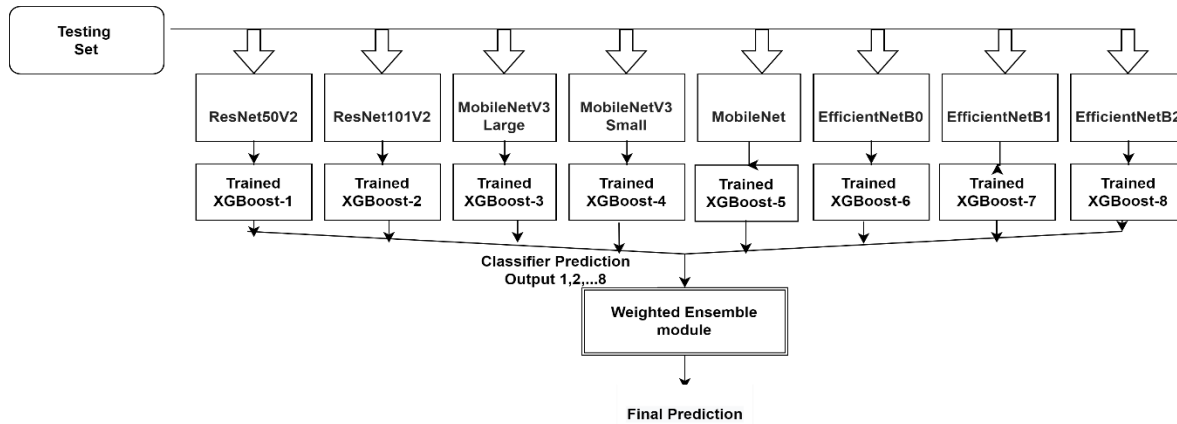

Fig. 10. Proposed methodology (evaluation phase)

VI. RESULTS AND DISCUSSION

The developed methodology employing transfer learning is processed using Python; the predicted model's success rate is evaluated utilizing existing mechanisms in terms of accuracy, sensitivity, F-measure, precision, and recall. In this approach, 500 X-ray dental images are utilized by considering 80% for training and 20% for testing. The proposed system can classify multiple diseases which cover six different categories with 46 possible combinations. the dataset covers all types of images like one image with one disease and one image with multiple diseases. For example, this system can identify images where only wear or decay is present, apart from this it is also able to identify and classify images where different diseases are present such as wear, and decay as shown in image id.347. Thus, to prove the sustainability of the proposed work ablation study is performed which is expressed in Tables III, IV, V, and VI by considering different 8 pre-trained networks. Table III shows the performance of the model by considering seven different networks with 91% accuracy. Similarly, Table IV shows the performance of the classification of six different diseases by considering six different networks with 90% accuracy on average.

TABLE III. 7-PRE TRAINED MODELS [MOBILENETSMALL, MOBILENET, MOBILENETLARGE, EFFICIENTNETB0 EFFICIENTNETB1 EFFICIENTNETB2 RESNET50V2]

Performance Measure	Wear	Decay	Periapical	Periodontics	Missing	Impacted
Precision	0.776	0.843	0.717	0.799	0.826	0.773
Recall	0.957	0.912	0.855	0.925	0.91	0.944
F1-Score	0.857	0.876	0.78	0.857	0.866	0.85
Specificity	0.895	0.921	0.933	0.926	0.913	0.888
Accuracy	0.912	0.918	0.92	0.926	0.912	0.904

TABLE IV. 6-PRE TRAINED MODELS[MOBILENETSMALL, MOBILENET, MOBILENETLARGE, EFFICIENTNETB0 EFFICIENTNETB1 EFFICIENTNETB2]

Performance Measure	Wear	Decay	Periapical	Periodontics	Missing	Impacted
Precision	0.767	0.841	0.703	0.793	0.825	0.764
Recall	0.957	0.899	0.855	0.925	0.904	0.944
F1-Score	0.852	0.869	0.772	0.854	0.862	0.845
Specificity	0.89	0.921	0.928	0.924	0.913	0.882
Accuracy	0.908	0.914	0.916	0.924	0.91	0.9

TABLE V. 5-PRE TRAINED MODELS [MOBILENETSMALL, MOBILENET, MOBILENETLARGE, EFFICIENTNETB0 EFFICIENTNETB1]

Performance Measure	Wear	Decay	Periapical	Periodontics	Missing	Impacted
Precision	0.765	0.831	0.689	0.786	0.815	0.756
Recall	0.942	0.899	0.855	0.917	0.904	0.944
F1-Score	0.844	0.864	0.763	0.846	0.857	0.84
Specificity	0.89	0.915	0.923	0.921	0.907	0.876
Accuracy	0.904	0.91	0.912	0.92	0.906	0.896

TABLE VI. 4-PRE TRAINED MODELS[MOBILENETSMALL, MOBILENET, MOBILENETLARGE, EFFICIENTNETB0]

Performance Measure	Wear	Decay	Periapical	Periodontics	Missing	Impacted
Precision	0.765	0.826	0.67	0.786	0.815	0.756
Recall	0.929	0.893	0.852	0.902	0.892	0.932
F1-Score	0.83	0.858	0.75	0.84	0.852	0.834

	9					
Specificity	0.889	0.912	0.919	0.921	0.906	0.876
Accuracy	0.9	0.906	0.908	0.916	0.902	0.892

A. Precision

Precision is the proportion of precise teeth affected region computed using Eqn. (1).

$$P = \frac{T_p}{T_p + F_p}$$

(1)

Fig. 11 shows the evaluation of precision for different diseases. it is observed that the precision of wear, decay, periapical, periodontitis, missing tooth, and impacted tooth is 79%, 85%, 73%, 82%, 84%, and 78% respectively.
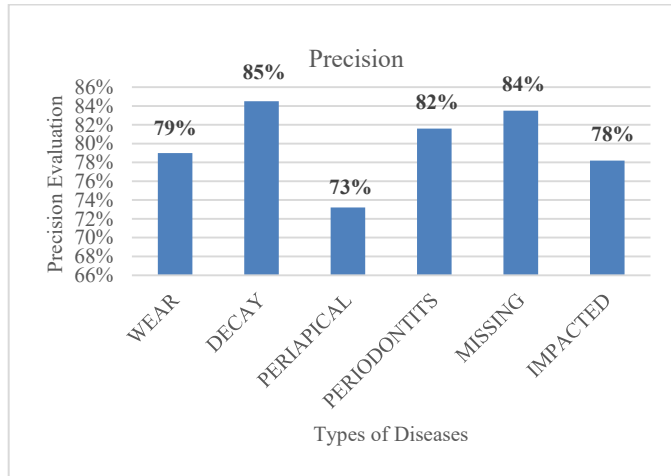

Fig. 11. Comparison of precision for different diseases

B. Recall

It expresses the proportion of predictions that have been correctly diagnosed as expected outcomes and is calculated using Eqn. (2).

$$R = \frac{T_p}{T_p + F_n}$$

(2)

It is observed from Fig. 12 that the Recall value for wear, decay, periapical, periodontitis, missing tooth, and impacted tooth is acceptable in the healthcare domain as it is above 95%,93%,86%,93%,91%, and 94% respectively.

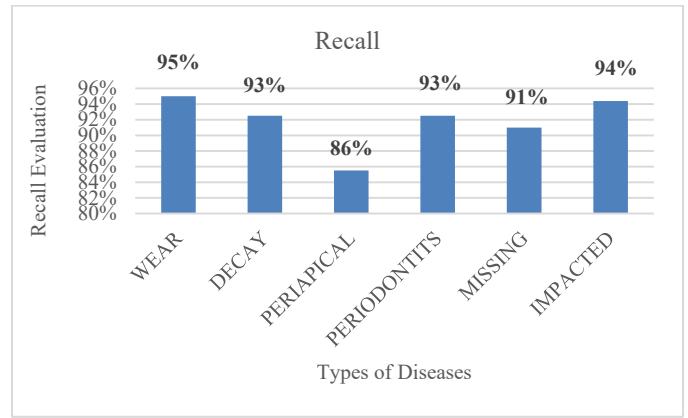
Fig. 12. Comparison of recall for different diseases

C. F-measure

F1-score is measured using Eqn. (3).

$$F1 - score = 2\left(\frac{P*R}{P+R}\right)$$

(3)

As per statistics shown in Fig. 13, it is observed that the F1-score for the detection of wear, decay, periapical, periodontitis, missing tooth, and impacted tooth is 86%, 88%, 79%, 87%, 87%, and 86% respectively.
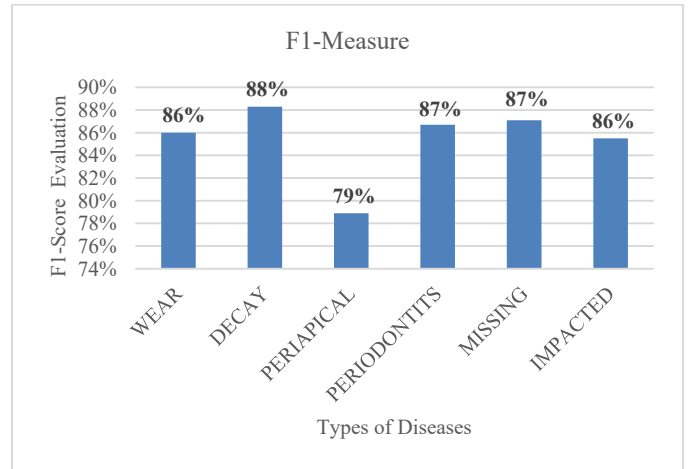

Fig. 13. Comparison of F1-measure for different diseases

D. Specificity

A recall is the probability of a negative diagnosis such as the patient being free from that disease. It is measured using eq. (4).

$$S = \frac{Tn}{(Tn + Fp)}$$

(4)

As per the statistical data presented in Fig. 14 specificity for all the diseases covering wear, decay, periapical, periodontitis, missing, and impacted teeth are found to be 90%,92%,94%,93%,92%, and 89% respectively.
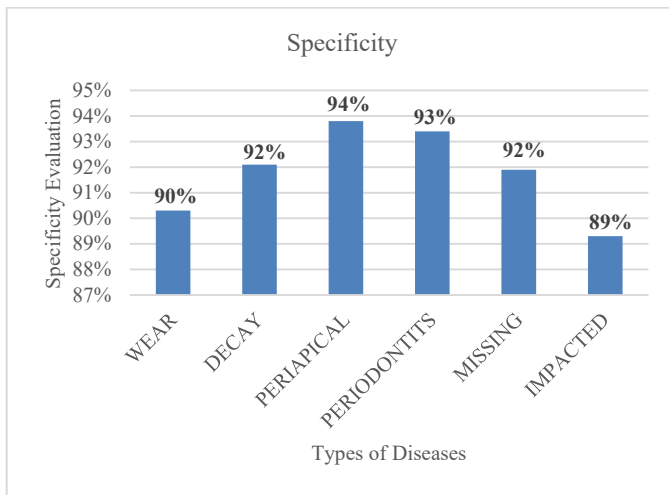
Fig. 14. Comparison of specificity for different diseases

E. Accuracy

Accuracy to the entire observations that are expressed in Eqn. (5),

$$A = \frac{T_p + T_n}{T_p + T_n + F_p + F_n} \quad (5)$$

As per statistics shown in Fig. 15, it is examined that accuracy for classification of wear, decay, periapical, periodontitis, missing tooth, and impacted tooth is 92%, 92%, 92%, 93%, 92%, and 91% respectively.
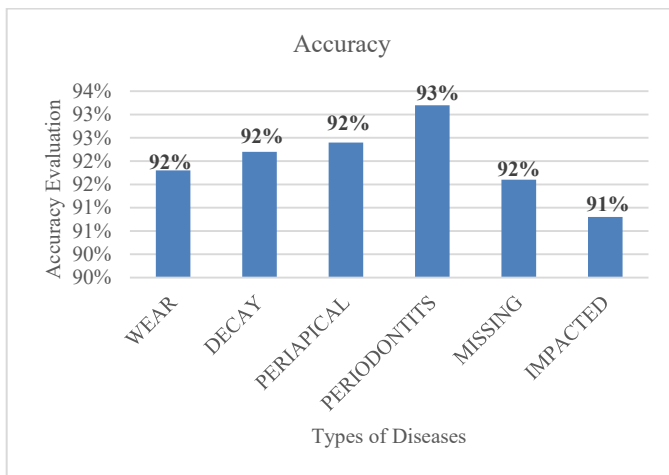

Fig. 15. Comparison of accuracy for different diseases

VII. CONCLUSION AND FUTURE WORK

This system is implemented using the idea of transfer learning and different pre-trained networks, such as 'ResNet50V2', 'ResNet101V2', 'MobileNetV3Large', 'MobileNetV3Small', 'MobileNet', 'EfficientNetB0', 'EfficientNetB1', and 'EfficientNetB2', with XGBoost. To get the final prediction, a weighted ensemble module is used. Additionally, the developed technique has achieved better outcomes in terms of accuracy, precision, F-measure, recall, and sensitivity. Thus, it achieved 92-93% of accuracy in classifying multiple dental diseases including tooth wear, periapical, periodontitis, tooth decay, missing tooth, and

impacted tooth. This approach is implemented on new diseases and compared the measuring parameters against different diseases. For some measuring parameters, values are less compared which can be improved in future work by using the extension of this dataset. In this present study, the given model is tested by classifying six diseases and their 46 possible combinations. this system can identify one disease present in an image as well as a combination of multiple diseases present in one image. The proposed method performs better in terms of accuracy and different measuring parameters than current state-of-the-art methods and has a variety of uses in computer-assisted multiple tooth disease identification and classification.

DATA AVAILABILITY

On request, the corresponding author will provide the data used to generate the study's findings.

REFERENCES

[1] Gu, Zaiwang, et al. "Ce-net: Context encoder network for 2d medical image segmentation." IEEE transactions on medical imaging 38.10 (2019): 2281-2292.

[2] Shiraisi, Ai, et al. "Improvement in Oral Health Enhances the Recovery of Activities of Daily Living and Dysphagia after Stroke." Journal of Stroke and Cerebrovascular Diseases 30.9 (2021): 105961.

[3] Lakshmi, M. Muthu, and P. Chitra. "Tooth Decay Prediction and Classification from X-Ray Images using Deep CNN." 2020 International Conference on Communication and Signal Processing (ICCSP). IEEE, 2020.

[4] Schwendicke, Falk, et al. "Convolutional neural networks for dental image diagnostics: A scoping review." Journal of dentistry 91 (2019): 103226.

[5] Hashem, Mohamed, and Ahmed E. Youssef. "Teeth infection and fatigue prediction using optimized neural networks and big data analytic tool." Cluster Computing 23.3 (2020): 1669-1682.

[6] Angst, Patrícia Daniela Melchiors, et al. "Oral health status of patients with leukemia: a systematic review with meta-analysis." Archives of Oral Biology (2020): 104948.

[7] Banu, Ancuta, et al. "Dental health between self-perception, clinical evaluation and body image dissatisfaction–a cross-sectional study in mixed dentition pre-pubertal children." BMC Oral Health 18.1 (2018): 1-9.

[8] Liu, Lizheng, et al. "A smart dental health-IoT platform based on intelligent hardware, deep learning, and mobile terminal." IEEE journal of biomedical and health informatics 24.3 (2019): 898-906.

[9] Glurich, Ingrid, et al. "Interdisciplinary care model: pneumonia and oral health." Integration of Medical and Dental Care and Patient Data. Springer, Cham, 2019. 123-139.

[10] Abdalla-Aslan, Ragda, et al. "An artificial intelligence system using machine-learning for automatic detection and classification of dental restorations in panoramic radiography." Oral Surgery, Oral Medicine, Oral Pathology and Oral Radiology 130.5 (2020): 593-602.

[11] Grischke, Jasmin, et al. "Dentronics: Towards robotics and artificial intelligence in dentistry." Dental Materials 36.6 (2020): 765-778.

[12] Mahmoud, Nourelhoda M., et al. "Detecting dental problem-related brain disease using intelligent bacterial optimized associative deep neural network." Cluster Computing 23.3 (2020): 1647-1657.

[13] Lee, Jeong-Hoon, et al. "Automated cephalometric landmark detection with confidence regions using Bayesian convolutional neural networks." BMC oral health 20.1 (2020): 1-10.

[14] Sonavane, Apurva, RohitYadav, and AdityaKhamparia. "Dental cavity Classification using Convolutional Neural Network." IOP Conference Series: Materials Science and Engineering. Vol. 1022. No. 1. IOP Publishing, 2021.

[15] Tandon, Divya, JyotikaRajawat, and Monisha Banerjee. "Present and future of artificial intelligence in dentistry." Journal of Oral Biology and Craniofacial Research 10.4 (2020): 391-396.

[16] P. Jaiswal and S. Bhirud, "Study and Analysis of an Approach Towards the Classification of Tooth Wear in Dentistry Using Machine Learning Technique," 2021 IEEE International Conference on Technology, Research, and Innovation for Betterment of Society (TRIBES), 2021, pp. 1-6, DOI: 10.1109/TRIBES52498.2021.9751650.

[17] Nripendra Kumar Singh, Khalid Raza, Progress in deep learning-based dental and maxillofacial image analysis: A systematic review, Expert Systems with Applications, Volume 199,2022,116968, ISSN 0957-4174,

[18] https://doi.org/10.1016/j.eswa.2022.116968. da Silva Rocha, É.; Endo, P.T. A Comparative Study of Deep Learning Models for Dental Segmentation in Panoramic Radiograph. Appl. Sci. 2022, 12, 3103. https://doi.org/10.3390/app12063103

[19] Ibrahim S. Bayrakdar, Kaan Orhan, Özer Çelik, Elif Bilgir, Hande Sağlam, Fatma Akkoca Kaplan, Sinem Atay Görür, Alper Odabaş, Ahmet Faruk Aslan, Ingrid Różyło-Kalinowska, "A U-Net Approach to Apical Lesion Segmentation on Panoramic Radiographs", BioMed Research International, vol. 2022, Article ID 7035367, 7 pages, 2022. https://doi.org/10.1155/2022/7035367

[20] Il-Seok Song, Imaging Science in Dentistry 2022, Deep learning-based apical lesion segmentation from panoramic radiographs.

[21] K. Panetta, R. Rajendran, A. Ramesh, S. P. Rao, and S. Agaian, "Tufts Dental Database: A Multimodal Panoramic X-Ray Dataset for Benchmarking Diagnostic Systems," in IEEE Journal of Biomedical and Health Informatics, vol. 26, no. 4, pp. 1650-1659, April 2022, DOI: 10.1109/JBHI.2021.3117575.

[22] G. Silva, L. Oliveira, M. Pithon, "Automatic segmenting teeth in X-ray images: Trends, a novel data set, benchmarking and future perspectives", Expert Systems with Applications, 107, pp. 15-31, 2018.

[23] G. Jader, J. Fontineli, M. Ruiz, K. Abdalla, M. Pithon, L. Oliveira, "Deep instance segmentation of teeth in panoramic X-ray images" 31 st SIBGRAPI Conference on Graphics, Patterns and Images, October 2018.

[24] J. Kim, H. S. Lee, I. S. Song & K. H. Jung, "DeNTNet: Deep Neural Transfer Network for the detection of periodontal bone loss using panoramic dental radiographs", in Scientific reports, vol.9(1), pp. 1-9, Nov. 2019.

[25] K. Zhang, J. Wu, H. Chen, and P. Lyu, "An effective teeth recognition method using label tree with cascade network structure", Computerized Medical Imaging and Graphics, vol. 68, pp. 61-70, 2018.

[26] D. Abdelhafiz, C. Yang, R. Ammar, S. Nabavi, "Deep convolutional neural networks for mammography: advances, challenges, and applications", BMC Bioinformatics, 20(S11), 2019.

[27] [8] M.A. Kadampur, S. Al Riyaee, "Skin cancer detection: Applying a deep learning based model driven architecture in the cloud for classifying dermal cell images", Informatics in Medicine Unlocked, 18, 100282, 2020

[28] D.V. Tuzoff, L.N. Tuzova, M.M. Bornstein, A.S. Krasnov, M.A. Kharchenko, S.I. Nikolenko, M.M. Sveshnikov, G.B. Bednenko, "Tooth detection and numbering in panoramic radiographs using convolutional neural networks", Dentomaxillofacial Radiol, 48, 20180051, 2019.

[29] Saleh A. Albelwi, "Deep Architecture based on DenseNet-121 Model for Weather Image Recognition" International Journal of Advanced Computer Science and Applications(IJACSA), 13(10), 2022. http://dx.doi.org/10.14569/IJACSA.2022.0131065

[30] Krois, J., Cantu, A. G., Chaurasia, A., Patil, R., Chaudhari, P. K., Gaudin, R., Gehrung, S., & Schwendicke, F. (2021). Generalizability of deep learning models for dental image analysis. Scientific Reports, 11. https://doi.org/10.1038/s41598-021-85454-5

[31] Xin Yu Liew, Nazia Hameed, Jeremie Clos, An investigation of XGBoost-based algorithm for breast cancer classification, Machine Learning with Applications, Volume 6,2021,100154, ISSN 2666-8270,https://doi.org/10.1016/j.mlwa.2021.100154.

[32] Almalki, Y.E.; Din, A.I.; Ramzan, M.; Irfan, M.; Aamir, K.M.; Almalki, A.; Alotaibi, S.; Alaglan, G.; Alshamrani, H.A.; Rahman, S. Deep Learning Models for Classification of Dental Diseases Using Orthopantomography X-ray OPG Images. Sensors 2022, 22, 7370. https://doi.org/10.3390/s22197370

[33] Guo, Y., Ge, Y., Yang, C., Al-Garadi, M. A., & Sarker, A. (2022). Comparison of Pretraining Models and Strategies for Health-Related Social Media Text Classification. Healthcare, 10(8). https://doi.org/10.3390/healthcare10081478

[34] Raeho Lee and Haewon Byeon, "Application of Stacking Ensemble Machine in Big Data: Analyze the Determinants for Vitalization of the Multicultural Support Center" International Journal of Advanced Computer Science and Applications(IJACSA), 13(10), 2022. http://dx.doi.org/10.14569/IJACSA.2022.0131007

[35] Munindra Lunagaria, Vijay Katkar, and Krunal Vaghela, "Covid-19 and Pneumonia Infection Detection from Chest X-Ray Images using U-Net, EfficientNetB1, XGBoost and Recursive Feature Elimination" International Journal of Advanced Computer Science and Applications(IJACSA), 13(9), 2022. http://dx.doi.org/10.14569/IJACSA.2022.0130954

[36] A. B. Oktay, "Tooth detection with convolutional neural networks," in Proc. IEEE Med. Technol. Nat. Congr., 2017, pp. 1–4.

[37] C. Muramatsu et al., "Tooth detection and classification on panoramic radiographs for automatic dental chart filing: Improved classification by multi-sized input data," Oral Radiol., vol. 37, no. 1, pp. 13–19, 2021.

[38] G. Jader, J. Fontineli, M. Ruiz, K. Abdalla, M. Pithon, and L. Oliveira, "Deep instance segmentation of teeth in panoramic X-ray images," in Proc. IEEE 31st SIBGRAPI Conf. Graph., Patterns Images, 2018, pp. 400–407.

[39] D. V. Tuzoff et al., "Tooth detection and numbering in panoramic radiographs using convolutional neural networks," Dentomaxillofacial Radiol., vol. 48, no. 4, 2019, Art. no. 20180051

[40] T. Ekert et al., "Deep learning for the radiographic detection of apical lesions," J. Endodontics, vol. 45, no. 7, pp. 917–922.e5, 2019

[41] M. Fukuda et al., "Evaluation of an artificial intelligence system for detecting vertical root fracture on panoramic radiography," Oral Radiol., pp. 1–7, 2019

[42] K. Panetta, R. Rajendran, A. Ramesh, S. P. Rao, and S. Agaian, "Tufts Dental Database: A Multimodal Panoramic X-Ray Dataset for Benchmarking Diagnostic Systems," in IEEE Journal of Biomedical and Health Informatics, vol. 26, no. 4, pp. 1650-1659, April 2022, DOI: 10.1109/JBHI.2021.3117575.

[43] M. P. Muresan, A. R. Barbara, and S. Nedevschi, "Teeth Detection and Dental Problem Classification in Panoramic X-Ray Images using Deep Learning and Image Processing Techniques," 2020 IEEE 16th International Conference on Intelligent Computer Communication and Processing (ICCP), 2020, pp. 457-463, DOI: 10.1109/ICCP51029.2020.9266244.
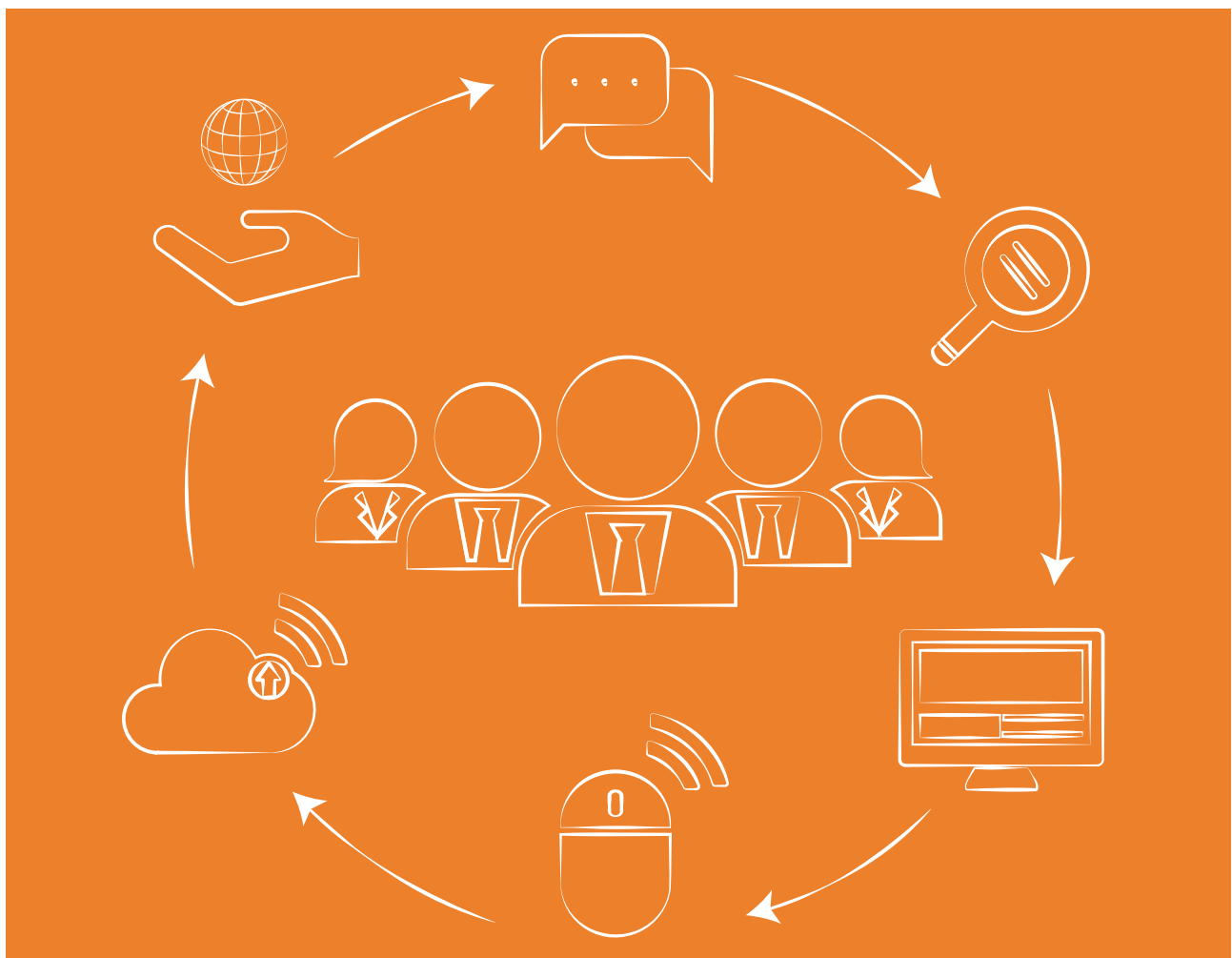
Cuadernos de desarrollo aplicados a las TIC

3C TIC. Cuadernos de desarrollo aplicadoso a las TIC.

EDITORIAL BOARD

AIMS AND SCOPE

PUBLISHING GOAL

3Ciencias wants to transmit to society innovative projects and ideas. This goal is reached thought the publication of original articles which are subdue to peer review or thorough the publication of scientific books.

TEMATIC COVERAGE

3C Empresa is a scientific - social journal, where original works are spread, written in English, for dissemination with empirical and theoretical analyzes on financial markets, leadership, human resources, market microestructure, public accounting and bussines management.

OUR TARGET

- Research staff.
- PhD students.
- Professors.
- Research Results Transfer Office.
- Companies that develop research and want to publish some of their works.

SUBMISSION GUIDELINES

3C Empresa is an arbitrated journal that uses the double-blind peer review system, where external experts in the field on which a paper deals evaluate it, always maintaining the anonymity of both the authors and of the reviewers. The journal follows the standards of publication of the APA (American Psychological Association) for indexing in the main international databases.

Each issue of the journal is published in electronic version (e-ISSN: 2254-3376), each work being identified with its respective DOI (Digital Object Identifier System) code.

STRUCTURE

The original works will tend to respect the following structure: introduction, methods, results, discussion/conclusions, notes, acknowledgments and bibliographical references.
The inclusion of references is mandatory, while notes and acknowledgments are optional. The correct citation will be assessed according to the 7th edition of the APA standards.

PRESENTATION WORK

All the information, as well as the templates to which the works must adhere, can be found at:

https://www.3ciencias.com/en/journals/infromation-for-authors/

https://www.3ciencias.com/en/regulations/templates/

ETHICAL RESPONSIBILITIES

Previously published material is not accepted (they must be unpublished works). The list of signatory authors should include only and exclusively those who have contributed intellectually (authorship), with a maximum of 4 authors per work. Articles that do not strictly comply with the standards are not accepted.

STATISTICAL INFORMATION ON ACCEPTANCE AND INTERNATIONALIZATION FEES

- Number of accepted papers published: 19.
- Level of acceptance of manuscripts in this number: 66,7%.
- Level of rejection of manuscripts: 33,3%.
- Internationalization of authors: 3 countries (India, Spain, China).

Guidelines for authors: https://www.3ciencias.com/en/regulations/instructions/

INDEXATIONS

INDEXATIONS

/SUMMARY/

/01/

FIXED POINT THEOREMS FOR SUZUKI NONEXPANSIVE MAPPINGS IN BANACH SPACES

John Sebastian

Department of Mathematics, Central University of Kerala, Kasaragod, India.

E-mail: john.sebastian@cukerala.ac.in

ORCID: 0000-0002-6759-9228

Shaini Pulickakunnel

Department of Mathematics, Central University of Kerala, Kasaragod, India.

E-mail: shainipv@cukerala.ac.in

ORCID: 0000-0001-9958-9211

ABSTRACT

In this paper, we investigate the existence of fixed points for Suzuki nonexpansive mappings in the setting of Banach spaces using the asymptotic center technique. We also establish the convergence of regular approximate fixed point sequence to the fixed points of Suzuki nonexpansive mappings. Examples are also given to illustrate the results. Our theorems generalize several results in the literature.

KEYWORDS

Banach space, Nonexpansive mapping, Suzuki nonexpansive mapping, Fixed point, Approximate fixed point.

1   INTRODUCTION

Fixed point results for nonexpansive mappings in Banach spaces are of great importance in the development of fixed point theory and are widely used to solve problems in diverse fields such as differential equations, game theory, engineering, medicine and many more (see [3, 14, 16]. The possibility of using the theory in a wide range of applications has attracted many researchers and has consequently resulted in a rapid growth of research in this field. Several authors have introduced extensions of nonexpansive mappings such as generalized nonexpansive mappings, relatively nonexpansive mappings, α- nonexpansive mappings, etc. (see [1, 6, 15]) and proved fixed point results in Banach spaces and various other spaces as well. In 2008, Suzuki introduced a new condition called condition (C) [17]. The mapping which satisfies condition (C) is now known as Suzuki nonexpansive mapping. Suzuki proved that all nonexpansive mappings satisfy the condition (C). Unlike nonexpansive mappings, the Suzuki nonexpansive mappings need not be always continuous. We can find a couple of examples for mappings which are not continuous but satisfying condition (C) in [17].

There are several techniques for finding the fixed points of nonexpansive mappings. One of the most widely used techniques, introduced by Edelstein in 1972 [5], uses the concept of asymptotic radius and asymptotic center of a sequence relative to a set K. Many researchers have used the properties and geometric behavior of the asymptotic center of sequences under consideration, to prove several fixed point results for nonexpansive mappings (see [5, 9]). For any sequence, asymptotic center can be considered as the intersection of some closed balls [7]. Therefore, the asymptotic center is always closed. But it need not be nonempty. Researchers proved that if a set K is nonempty, weakly compact and convex, then the asymptotic center of any sequence in K has the same properties as K [7]. These results boosted the usefulness of asymptotic center technique as a tool to find fixed points for Suzuki nonexpansive mapping. Dhompongsa [4] used this technique in Suzuki nonexpansive mapping and proved that if K is a Banach space and T is a self mapping of K satisfying condition (C), then for any bounded approximate fixed point sequence in K, the asymptotic center relative to K is invariant under T. Another equally important method to find fixed points in Banach spaces is the Chebyshev center technique, which uses the concept of Chebyshev radius and Chebyshev center to analyze the geometric structure of a set. A good amount of research work is reported in literature which makes use of these two techniques to find fixed points (see [4, 5, 7–10, 13].

In this paper, we primarily focus on the asymptotic center technique and show that it is possible to derive an interesting relation between the asymptotic radius and Chebyshev radius under certain conditions. In [8], Kirk proved a fixed point result for nonexpansive mapping in reflexive Banach spaces having normal structure. We extended this result for Suzuki nonexpansive mapping in weakly compact Banach spaces. Also, we investigated some sufficient conditions for the existence of fixed points for Suzuki nonexpansive mapping in a closed, bounded and convex subset of a Banach space. Apart from these, we also developed certain sufficient conditions for the convergence of regular approximate fixed point sequences to the fixed points of Suzuki nonexpansive mappings.

1.1   PRELIMINARIES

Definition 1.   [7] *A mapping T on a subset K of a Banach space X is called a nonexpansive mapping if $||Tx - Ty|| \leq ||x - y||$ for all $x, y \in K$.*

Definition 2.   [17] *Let T be a mapping on a subset K of a Banach space X. Then T is said to satisfy condition (C) if for all $x, y \in K$,*

$$\frac{1}{2}||x - Tx|| \leq ||x - y|| \implies ||Tx - Ty|| \leq ||x - y||.$$

The mapping satisfying condition (C) is called Suzuki nonexpansive mapping.

Definition 3.   [10] *Let $T : K \to K$ be any mapping. A sequence $\{x_n\}$ in K is called approximate fixed point sequence if $||Tx_n - x_n|| \to 0$ as $n \to \infty$.*

Definition 4. [4] *Let K be a nonempty closed and convex subset of a Banach space X and $\{x_n\}$, a bounded sequence in X. For $x \in X$, the asymptotic radius of $\{x_n\}$ at x is defined as*

$$r(x, \{x_n\}) = \limsup\{||x_n - x||\}.$$

The asymptotic radius and asymptotic center of $\{x_n\}$ relative to K are defined as follows:

$$r \equiv r(K, \{x_n\}) = \inf\{r(x, \{x_n\}) : x \in K\}$$

$$A \equiv A(K, \{x_n\}) = \{x \in K : r(x, \{x_n\}) = r\}.$$

Definition 5. [9] *A bounded sequence is said to be regular if each of its subsequence has the same asymptotic radius.*

Definition 6. [9] *A bounded sequence is said to be uniform if each of its subsequence has the same asymptotic center.*

Definition 7. [7] *For any subset K of X, the radius of K relative to x, Chebyshev radius of K, Chebyshev center of K and the diameter of K are defined as follows:*
For any $x \in X$, $r_x(K) = \sup\{||x - y|| : y \in K\}$

$$r(K) = \inf\{r_x(K) : x \in K\}$$

$$C(K) = \{x \in K : r_x(K) = r(K)\}$$

$$diam(K) = \sup\{r_x(K) : x \in K\}.$$

Definition 8. *A nonempty, closed, convex subset D of a given set K is said to be a minimal invariant set for a mapping $T : K \to K$ if $T(D) \subseteq D$ and D has no nonempty, closed and convex proper subsets which are T-invariant.*

Definition 9. [7,8] *A convex subset K of X is said to have normal structure if each bounded, convex subset S of K with $diam S > 0$ contains a nondiametral point.*

Definition 10. [2] *A convex set K of X is said to have asymptotic normal structure if, given any bounded convex subset S of K which contains more than one point and given any decreasing net of nonempty subsets $\{s_\alpha; \alpha \in A\}$ of S, the asymptotic center of $\{s_\alpha; \alpha \in A\}$ in S is a proper subset of S.*

Definition 11. [11] *Let X be a Banach space. X is said to have Opial property if for each weakly convergent sequence $\{x_n\}$ in X with weak limit z and for all $x \in X$ with $x \neq z$,*

$$\limsup ||x_n - z|| < \limsup ||x_n - x||.$$

Lemma 1. [17, Lemma 6] *Let T be a mapping on a bounded convex subset K of a Banach space X. Assume that T satisfies condition (C). Define a sequence $\{x_n\}$ in K by $x_1 \in K$ and*

$$x_{n+1} = \lambda T x_n + (1 - \lambda) x_n$$

for $n \in \mathbb{N}$, where λ is a real number belonging to $[\frac{1}{2}, 1)$. Then

$$\lim_{n \to \infty} ||T x_n - x_n|| = 0$$

holds.

Lemma 2. [7, Lemma 9.1] *Let $\{x_n\}$ be a sequence in a Banach space X and K a nonempty subset of X.*
(a) If K is weakly compact, then $A(K, \{x_n\}) \neq \phi$.
(b) If K is convex, then $A(K, \{x_n\})$ is convex.

Lemma 3. [4, Lemma 3.1] *Let K be a subset of a Banach space X, and $T : K \to K$ be a mapping satisfying condition (C). Suppose $\{x_n\}$ is a bounded approximate fixed point sequence for T. Then $A(K, \{x_n\})$ is invariant under T.*

Proposition 1. [9, Preposition 1] *Every bounded sequence has a regular subsequence.*

Theorem 1. [7, Theorem 3.2] *Suppose K is a nonempty, weakly compact, convex subset of a Banach space. Then for any mapping $T : K \to K$ there exists a closed convex subset of K which is minimal T-invariant.*

Theorem 2. [12, Theorem 1] *A convex subset K of X has normal structure if and only if K has asymptotic normal structure.*

Remark 1. [7] *It is clear that if for any sequence $\{x_n\}$ in K and $x \in X$, $r(x, \{x_n\}) = 0$ if and only if $\lim_{n \to \infty} x_n = x$.*

Remark 2. [9] *If $\{x_{n_k}\}$ is a subset of $\{x_n\}$, then $r(K, \{x_{n_k}\}) \leq r(K, \{x_n\})$ and if $r(K, \{x_{n_k}\}) = r(K, \{x_n\})$, then $A(K, \{x_n\}) \subseteq A(K, \{x_{n_k}\})$.*

2   RESULTS

Theorem 3. *Let K be a weakly compact convex subset of a Banach space X and $T : K \to K$ satisfies condition (C). Assume that K is minimal T-invariant and $\{x_n\}$ is an approximate fixed point sequence in K. Then*
(i) $A(K, \{x_n\}) = K$
(ii) $r(K, \{x_n\}) = r(K)$.

Proof. Let K be a weakly compact and convex subset of a Banach space X.
Suppose $diam(K) = 0$. Then there is nothing to prove.
Now, suppose $diam(K) > 0$.
Let $\{x_n\}$ be any bounded approximate fixed point sequence in K. Then $A(K, \{x_n\})$ is closed.
Also by Lemma 2, $A(K, \{x_n\})$ is nonempty and convex. Thus $A(K, \{x_n\})$ is weakly compact.
By Lemma 3, $A(K, \{x_n\})$ is T-invariant and by the minimality of K, we have $A(K, \{x_n\}) = K$.
Since K is weakly compact, there exist a subsequence $\{x_{n_k}\}$ of $\{x_n\}$ and $z \in K$ such that $x_{n_k} \to z$ weakly.
Clearly $\{x_{n_k}\}$ is an approximate fixed point sequence in K.
Since $A(K, \{x_{n_k}\}) = K$, $\limsup \|x_{n_k} - x\| = r(K, \{x_{n_k}\})$ for all $x \in K$.
Also, we have for any $x \in K$, $\limsup \|x_{n_k} - x\| \leq \sup\{\|x - y\| : y \in K\}$.
Therefore,

$$r(K, \{x_{n_k}\}) \leq r_x(K) \implies r(K, \{x_{n_k}\}) \leq r(K). \tag{1}$$

Now, for any $y \in K$, $x_{n_k} - y \to z - y$ weakly and hence we have

$$\|z - y\| \leq \limsup \|x_{n_k} - y\| = r(K, \{x_{n_k}\}).$$

Hence for all $y \in K$,

$$\|z - y\| \leq r(K, \{x_{n_k}\}) \implies r_z(K) \leq r(K, \{x_{n_k}\})$$
$$\implies r(K) \leq r(K, \{x_{n_k}\}). \tag{2}$$

Thus from (1) and (2) we get

$$r(K, \{x_{n_k}\}) = r(K). \tag{3}$$

We know that for any subsequence $\{x_{n_k}\}$ of $\{x_n\}$,

$$r(K, \{x_{n_k}\}) \leq r(K, \{x_n\}). \tag{4}$$

Since $r(K, \{x_{n_k}\}) = r(K)$, if $x \in C(K)$, then for all $y \in K$, $\|x - y\| \leq r(K, \{x_{n_k}\})$.
Therefore, for all x_n,

$$\|x_n - x\| \leq r(K, \{x_{n_k}\}) \implies r(K, \{x_n\}) \leq r(K, \{x_{n_k}\}). \tag{5}$$

Hence from (4) and (5), $r(K, \{x_n\}) = r(K, \{x_{n_k}\})$. Thus from (3) we get
$r(K, \{x_n\}) = r(K)$.

Corollary 1. *Let K be a weakly compact convex subset of a Banach space X and $T : K \to K$ satisfies condition (C). If K is minimal T-invariant, then every approximate fixed point sequence in K are regular and uniform.*

Proof. Let $\{x_n\}$ be an approximate fixed point sequence in K. Then every subsequence $\{x_{n_k}\}$ of $\{x_n\}$ is also an approximate fixed point sequence.
Hence by (ii) in Theorem 3, $r(K, \{x_n\}) = r(K, \{x_{n_k}\})$.
Therefore, $\{x_n\}$ is regular.
By (i) in Theorem 3, $A(K, \{x_n\}) = A(K, \{x_{n_k}\}) = K$.
Hence $\{x_n\}$ is uniform.

Corollary 2. [10, Preposition 6.3] *Let K be a weakly compact convex subset of a Banach space X, and $T : K \to K$ be a nonexpansive mapping. Assume that K is minimal for T, that is, no closed convex bounded proper subset of K is invariant for T. If $\{x_n\}$ is an approximate fixed point sequence in K, then $A(K, \{x_n\}) = K$.*

Proof. Since every nonexpansive mapping satisfies condition (C), by above theorem, $A(K, \{x_n\}) = K$.

Theorem 4. *Let K be a nonempty, weakly compact and convex subset of a Banach space X and suppose K has normal structure. Then every mapping $T : K \to K$ satisfying condition (C) has a fixed point.*

Proof. By Theorem 1, we can consider K as closed, convex minimal T- invariant subset.
Suppose $diam K > 0$.
Consider an approximate fixed point sequence $\{x_n\} \subseteq K$.
By (i) in Theorem 3, $A(K, \{x_n\}) = K$.
Now, define $W_n := \{x_m : m \geq n\}, \ n \in \mathbb{N}$.
Clearly, $\{W_n, n \in \mathbb{N}\}$ is a decreasing chain of nonempty bounded subsets of K.
We can easily prove that Asymptotic center of $\{W_n, n \in \mathbb{N}\} = A(K, \{x_n\}) = K$.
Since K has normal structure, by Theorem 2, K has asymptotic normal structure.
Thus $A(K, \{x_n\}) = K$, which is a contradiction.
Therefore, $diam K = 0$ and hence K has only one element x (say).
Thus $T(x) = x$.

We obtain the result of Kirk [8] and Theorem 4.1 in [7] as corollaries of our result.

Corollary 3. [8, Theorem] *Let K be a nonempty, bounded, closed and convex subset of a reflexive Banach space X, and suppose that K has normal structure. If $T : K \to K$ is nonexpansive, then T has a fixed point.*

Proof. Since a bounded, closed and convex subset of a reflexive Banach space is weakly compact and every nonexpansive mapping is Suzuki nonexpansive, by the above theorem, T has a fixed point.

Corollary 4. [7, Theorem 4.1] *Let K be a nonempty, weakly compact, convex subset of a Banach space, and suppose K has normal structure. Then every nonexpansive mapping $T : K \to K$ has a fixed point.*

Proof. Since every nonexpansive mapping is Suzuki nonexpansive, by the above theorem, T has a fixed point.

The following theorem gives sufficient conditions for the existence of fixed points for Suzuki nonexpansive mapping in Banach spaces.

Theorem 5. *Let K be a closed, bounded and convex subset of a Banach space X and $T : K \to K$ satisfies condition (C). If $T(K)$ is contained in a compact subset of K, then T has a fixed point in K.*

Proof. Let $\{x_n\}$ be an approximate fixed point sequence in K.

Therefore, $||Tx_n - x_n|| \to 0$.

Consider the sequence $\{Tx_n\}$ in $T(K)$.

Since $T(K)$ is a subset of a compact set of K, there exist a subsequence $\{Tx_{n_k}\}$ of $\{Tx_n\}$ and $z \in K$ such that $Tx_{n_k} \to z$.

Therefore, $\lim\limits_{k\to\infty} ||x_{n_k} - z|| = \lim\limits_{k\to\infty} ||x_{n_k} - Tx_{n_k}|| = 0$.

Hence $x_{n_k} \to z$.

Clearly, $\{x_{n_k}\}$ is a bounded approximate fixed point sequence and $A(K, \{x_{n_k}\}) = \{z\}$.

Also by Lemma 3, $A(K, \{x_{n_k}\})$ is T-invariant and hence $T(z) = z$.

The following is an example to illustrate this theorem.

Example 1. *In the space l_2 consider the closed unit ball*

$K = \{x = (x_1, x_2, ...) \in l_2 : ||x||_2 \leq 1\}$.

Define $T : K \to K$ as

$$T(x) = \begin{cases} (\frac{1}{3}, 0, 0, ..), & if \ x = (1, 0, 0, ...) \\ 0, & otherwise. \end{cases}$$

For all $x, y \neq (1, 0, 0, ...)$ in K, $||Tx - Ty||_2 = 0 \leq ||x - y||_2$.

If $x = (1, 0, 0, ...)$ then $\frac{1}{2}||x - Tx||_2 = \frac{1}{2}||(\frac{2}{3}, 0, 0, ...)||_2 = \frac{1}{3}$.

Therefore, if $\frac{1}{2}||x - Tx||_2 \leq ||x - y||_2$ for any $y \in K$, then $\frac{1}{3} \leq ||x - y||_2$.

Thus $||Tx - Ty||_2 = \frac{1}{3} \leq ||x - y||_2$.

Hence T satisfies condition (C).

$T(K) = \left\{(0, 0, 0, ...), (\frac{1}{3}, 0, 0, ...)\right\}$ is a subset of a compact set of K.

Thus all conditions in the above theorem are satisfied.

Since $T(0) = 0$, T has a fixed point.

Theorem 6. *Let X be a Banach space with Opial property and K be a closed, bounded and convex subset of X. Let $T : K \to K$ satisfies condition (C) and if $T(K)$ is contained in a weakly compact subset of K, then T has a fixed point in K.*

Proof. Let $\{x_n\}$ be an approximate fixed point sequence in K. Then we have, $||Tx_n - x_n|| \to 0$.

Since $\frac{1}{2}||Tx_n - x_n|| \leq ||Tx_n - x_n||$ and T satisfies condition (C), we have $||T^2x_n - Tx_n|| \leq ||Tx_n - x_n||$ for all $n \in \mathbb{N}$.

Therefore, $\lim\limits_{n\to\infty} ||T^2x_n - Tx_n|| \leq \lim\limits_{n\to\infty} ||Tx_n - x_n|| = 0$.

Hence $\{T(x_n)\}$ is an approximate fixed point sequence.

Since $T(K)$ is a subset of a weakly compact set of K, there exist a subsequence $\{Tx_{n_k}\}$ of $\{Tx_n\}$ and $z \in K$ such that $Tx_{n_k} \to z$ weakly as $k \to \infty$.

By Opial property, for any $x \neq z$, $\limsup ||Tx_{n_k} - z|| < \limsup ||Tx_{n_k} - x||$.

Therefore, for any $x \neq z, r(z, \{Tx_{n_k}\}) < r(x, \{Tx_{n_k}\}) \implies r(K, \{Tx_{n_k}\}) = r(z, \{Tx_{n_k}\})$ and $A(K, \{Tx_{n_k}\}) = \{z\}$.

By Lemma 3, $A(K, \{x_{n_k}\})$ is T-invariant and hence $T(z) = z$.

Corollary 5. [17, Theorem 4] *Let T be a mapping on a convex subset K of a Banach space X. Assume that T satisfies condition (C). Assume also that either of the following holds:*

(i) K is compact;

(ii) K is weakly compact and X has the Opial property.

Then T has a fixed point.

Proof. Suppose K is compact and convex. Therefore, K is closed, bounded and convex.

Also, since $T : K \to K$, we have $T(K) \subseteq K$. Thus $T(K)$ is a subset of a compact set.

Hence by Theorem 5, T has a fixed point.

Now suppose K is weakly compact, convex and X has the Opial property.

Therefore, K is closed, bounded and convex. Also, since $T : K \to K$, we have $T(K) \subseteq K$.

Thus $T(K)$ is a subset of a weakly compact set.

Hence by Theorem 6, T has a fixed point.

Theorem 7. *Let K be a compact subset of a Banach space X. Let $T : K \to K$ satisfies condition (C). Let $\{x_n\}$ be a regular approximate fixed point sequence in K. Then $\{x_n\}$ converge strongly to a fixed point of T.*

Proof. Let $\{x_n\}$ be a regular approximate fixed point sequence in K.

Since K is compact, there exist a subsequence $\{x_{n_k}\}$ of $\{x_n\}$ and $z \in K$ such that $x_{n_k} \to z$.

Therefore, $A(K, \{x_{n_k}\}) = \{z\}$.

Since $\{x_{n_k}\}$ is an approximate fixed point sequence, by Lemma 3, $A(K, \{x_{n_k}\})$ is T-invariant. Hence $T(z) = z$.

Since $\{x_n\}$ is regular, $r(K, \{x_n\}) = r(K, \{x_{n_k}\}) = 0$.

Since K is compact and $\{x_n\}$ is an approximate fixed point sequence, $A(K, \{x_n\})$ is nonempty.

We know that if $\{x_n\}$ is regular, then for any subsequence $\{x_{n_k}\}$,

$A(K, \{x_n\}) \subseteq A(K, \{x_{n_k}\})$.

Therefore, $A(K, \{x_n\}) = \{z\}$. Hence $x_n \to z$.

The following example shows that even if T has fixed points, if $\{x_n\}$ is not regular, then $\{x_n\}$ need not converge to a fixed point.

Example 2. *Consider the compact set $K = [-1, 1]$ in $\mathbb{R}$ and define $T : K \to K$ as $T(x) = x$.*

Clearly T is a nonexpansive mapping and hence satisfies condition (C).

Consider $x_n = (-1)^n$ for all $n \in \mathbb{N}$

For all $n \in \mathbb{N}$, $||x_n - Tx_n|| = 0$. Thus $\{x_n\}$ is an approximate fixed point sequence.

But $\{x_n\}$ does not converge to a fixed point.

This will not contradict the above theorem because $\{x_n\}$ is not regular.

Asymptotic radius of $\{x_n\}$ $= r(K, \{x_n\}) = 1$ and $A(K, \{x_n\}) = \{0\}$.

Consider the subsequence $\{x_{2n}\} = \{1, 1, 1, ...\}$. Clearly $x_{2n} \to 1$.

Therefore, $A(K, \{x_{2n}\}) = \{1\}$ and $r(K, \{x_{2n}\}) = 0$.

Hence $\{x_n\}$ is not regular.

Theorem 8. *Let K be a subset of a Banach space X and $T : K \to K$ satisfies condition (C). Suppose $T(K)$ is contained in a compact subset of K and let $\{x_n\}$ be a regular approximate fixed point sequence in K with nonempty asymptotic center. Then $\{x_n\}$ converge strongly to a fixed point of T.*

Proof. Let $\{x_n\}$ be a regular approximate fixed point sequence in K with nonempty asymptotic center.

Consider the sequence $\{Tx_n\}$ in $T(K)$. Since $T(K)$ is compact, there exist a subsequence $\{Tx_{n_k}\}$ of $\{Tx_n\}$ and $z \in T(K)$ such that $Tx_{n_k} \to z$.

Therefore, $\lim_{n \to \infty} ||x_{n_k} - z|| \le \lim_{n \to \infty} ||x_{n_k} - Tx_{n_k}|| = 0$.

Thus $x_{n_k} \to z$ and hence $A(K, \{x_{n_k}\}) = \{z\}$.

Since $\{x_{n_k}\}$ is an approximate fixed point sequence, by Lemma 3, $A(K, \{x_{n_k}\})$ is T-invariant.

Hence $T(z) = z$.

Since $\{x_n\}$ is regular, $r(K, \{x_n\}) = r(K, \{x_{n_k}\}) = 0$.

Also if $\{x_n\}$ is regular, then for any subsequence $\{x_{n_k}\}$, we have $A(K, \{x_n\}) \subseteq A(K, \{x_{n_k}\})$.

Thus we have $A(K, \{x_n\}) = \{z\}$, which implies that $x_n \to z$.

3   CONCLUSIONS

In this paper, we have used the asymptotic center technique to establish the existence of fixed points for Suzuki nonexpansive mappings in Banach spaces. We have shown that under certain condition, the asymptotic radius and Chebyshev radius are equal. Using this result, we have established that every

approximate fixed point sequence is regular as well as uniform. The convergence of regular approximate fixed point sequences to a fixed points of the Suzuki nonexpansive mapping is also established. A couple of examples are given to illustrate the results.

ACKNOWLEDGMENT

REFERENCES

[1] **Aoyama, K.**, and **Kohsaka, F.** (2011). Fixed point theorem for α-nonexpansive mappings in Banach spaces. *Nonlinear Analysis: Theory, Methods & Applications, 74(13)*, 4387-4391.

[2] **Bogin, J.** (1976). A generalization of a fixed point theorem of Goebel, Kirk and Shimi. *Canadian Mathematical Bulletin, 19(1)*, 7–12.

[3] **Byrne, C.** (2003). A unified treatment of some iterative algorithms in signal processing and image reconstruction. *Inverse problems, 20(1)*, 103.

[4] **Dhompongsa, S.**, **Inthakon, W.** and **Kaewkhao, A.** (2009). Edelstein's method and fixed point theorems for some generalized nonexpansive mappings. *Journal of Mathematical Analysis and Applications, 350(1)*, 12–17.

[5] **Edelstein, M.** (1972). The construction of an asymptotic center with a fixed point property. *Bulletin of the American Mathematical Society, 78(2)*, 206–208.

[6] **Eldred, A.**, **Kirk, W.**, and **Veeramani, P.** (2005). Proximal normal structure and relatively nonexpansive mappings. *Studia Mathematica, 3(171)*, 283-293.

[7] **Goebel, K.** and **Kirk, W. A.** (1990). Topics in metric fixed point theory. *Cambridge university press.*

[8] **Kirk, W.A.** (1965). A fixed point theorem for mappings which do not increase distances. *The American Mathematical Monthly, 72(9)*, 1004–1006.

[9] **Kirk, W.A.** and **Massa, S.** (1990). Remarks on asymptotic and Chebyshev centers. *Houston Journal of Mathematics, 16*, 364–375.

[10] **Kirk, W. A.**, and **Sims, B.** (2002). Handbook of metric fixed point theory. *Australian Mathematical Society GAZETTE*, 29(2).

[11] **Lami Dozo, E.** (1973). Multivalued nonexpansive mappings and Opial's condition. *Proceedings of the American Mathematical Society, 38(2)*, 286-92.

[12] **Lim, T.C.** (1974). Characterization of normal structure. *Proceedings of the American Mathematical Society, 43(2)*, 313-319.

[13] **Lim, T.C.** (1980). On asymptotic centers and fixed points of nonexpansive mappings. *Canadian Journal of Mathematics, 32(2)*, 421-430.

[14] **Lopez, G.**, **Martin, V.**, and **Xu, H. K.** (2009). Perturbation techniques for nonexpansive mappings with applications. *Nonlinear Analysis: Real World Applications, 10(4)*, 2369-2383.

[15] **Park, J. Y.**, and **Jeong, J. U.** (1994). Weak convergence to a fixed point of the sequence of Mann type iterates. *Journal of Mathematical Analysis and Applications, 184(1)*, 75-81.

[16] **Shimoji, K.**, and **Takahashi, W.** (2001). Strong convergence to common fixed points of infinite nonexpansive mappings and applications. *Taiwanese Journal of Mathematics, 5(2)*, 387-404.

[17] **Suzuki, T.** (2008). Fixed point theorems and convergence theorems for some generalized nonexpansive mappings. *Journal of mathematical analysis and applications, 340(2)*, 1088-1095.

/02/

A SURVEY ON THE FIXED POINT THEOREMS VIA ADMISSIBLE MAPPING

Erdal Karapınar

Department of Medical Research, China Medical University Hospital, China Medical University, 40402, Taichung, Taiwan

Department of Mathematics, Çankaya University, 06790, Etimesgut, Ankara, Turkey

E-mail:erdalkarapinar@yahoo.com, karapinar@mail.cmuh.org.tw

ORCID:0000-0002-6798-3254

https://doi.org/10.17993/3ctic.2022.112.26-50

ABSTRACT

In this survey, we discuss the crucial role of the notion of admissible mapping in the metric fixed point theory. Adding admissibility conditions to the statements leads not only to generalizing the existing results but also unifying several corresponding results in different settings. In particular, a contraction via admissible mapping involves and covers contractions defined on partially ordered sets, and contractions forming cyclic structure.

KEYWORDS

Admissible mapping, fixed point

1 INTRODUCTION

The metric fixed point theory is one of the most attractive research topics that lies in the intersection of three disciplines of the mathematics; topology, applied mathematics and nonlinear functional analysis. In the literature, it was assumed that the first metric fixed point theorem was proved by Banach [18] in 1922. On the other hand, it was noted that the idea of the fixed point theorem was used before Banach's paper. Indeed, the fixed point results were used to prove the existence and uniqueness solution of the initial value problems in the some research papers of Liouville, Picard, Poincaré and so on. Despite this fact, the sole purpose of Banach's theorem is the indicate the existence and uniqueness of the fixed point.

The Banach's fixed point theorem stated perfectly and its proof is also awesome: Every contraction in a complete metric space guarantee not only the existence but also uniqueness of a fixed point. In the proof, Banach indicates how the desired fixed point should be found. Regarding that it is a core tool in the solution of the certain differential equation, the existence and uniqueness of the solution of the differential equations are induced to the existence and uniqueness of a fixed point. Indeed, this observation can be the main reason why the metric fixed point theory has been investigated heavily.

In the last three decades, thousands of new results have been announced in the framework of the metric fixed point theory. Most of them claimed that it was the generalization of the existing results. Mainly, these announced results are slight generalizations or extensions of the existing ones. Indeed, predominantly, most of the proofs are the mimic of the proof of the pioneer fixed point theorem of Banach: Construct a sequence (usually, by using the Picard operator); indicate that this sequence is convergent and finally prove that the limit of this recursive sequence is the required fixed point of the considered operator. The fact that existing so many publications on this topic has encouraged researchers to organize and unify this scattered literature. One of the best examples of this trend was given by Samet *et al.* [61] in 2012 by involving the notion of admissible mappings.

Now, we shall explain why the new notion of Samet *et al.* [61], an admissible mapping, is important. First of all, we need to underline that Banach's famous fixed point theorem has been generalized and extended in many different ways in the literature. The most classic approach for generalization and extension is to change the definitions of contraction. The other approach and method are that a given contraction function is in cyclic form. One of the other methods for generalization and extension is to add a partial order on the structure where contraction is defined. Admissible mappings make it possible to put together these three approaches in a single statement. For the clarification of the fixed point theory literature, admissible mapping plays one of the key roles.

In this manuscript, we shall revisit the literature by using the auxiliary function: admissible mapping. We shall provide examples and put several consequences to illustrate how this approach works successfully.

2 Preliminaries

In this section, we collect some necessary tools (notions, notations) that are essential to express the results.

First of all, we shall fixed some basic notations: Hereafter, $\mathbb{N}$ and $\mathbb{N}_0$ denote the set of positive integers and the set of nonnegative integers. Furthermore, the symbols $\mathbb{R}$, $\mathbb{R}^+$ and $\mathbb{R}_0^+$ represent the set of reals, positive reals and the set of nonnegative reals, respectively. Throughout the manuscript, all considered sets are non-empty.

We shall first recall the admissible mapping defined by Samet *et al.* [61]. Let $\alpha : X \times X \to [0, \infty)$ be a function. Then, the mapping $T : X \to X$ is said to be α-admissible [61] if, for all $x, y \in X$,

$$\alpha(x, y) \geq 1 \implies \alpha(Tx, Ty) \geq 1.$$

Next, we recollect the notion of triangular α-admissible that plays crucial rules in usage of triangle inequality axiom of the metric.

Definition 1. *[41] A self-mapping $T : X \to X$ is called triangular α-admissible if*

$$(T_1) \quad T \text{ is } \alpha - \text{admissible},$$
$$(T_2) \quad \alpha(x, z) \geq 1, \quad \alpha(z, y) \geq 1 \Longrightarrow \alpha(x, y) \geq 1, \quad x, y, z \in X.$$

Example 1. *Suppose that $M = (0, +\infty)$. Define $T : M \to M$ and $\alpha : M \times M \to [0, \infty)$ by*

(1) $T(x) = \ln(x + 1)$, for all $x \in M$ and $\alpha(x, y) = \begin{cases} 1, & \text{if } x \geq y; \\ 0, & \text{if } x < y. \end{cases}$
Then T is α-admissible.

(2) $T(x) = \sqrt[3]{x}$, for all $x \in M$ and $\alpha(x, y) = \begin{cases} e^{x-y}, & \text{if } x \geq y; \\ 0, & \text{if } x < y. \end{cases}$
Then T is α-admissible.

For more examples of such mappings are presented in $[30, 40, 41, 46\text{--}48, 61]$ and references therein.

In 2014, Popescu [54] conclude that the notion of triangular α-admissible can be refined slightly, as follows:

Definition 2. *[54] Let $T : X \to X$ be a self-mapping and $\alpha : X \times X \to [0, \infty)$ be a function. Then T is said to be α-orbital admissible if*

$$(T3) \quad \alpha(x, Tx) \geq 1 \Rightarrow \alpha(Tx, T^2 x) \geq 1.$$

Definition 3. *[54] Let $T : X \to X$ be a self-mapping and $\alpha : X \times X \to [0, \infty)$ be a function. Then T is said to be triangular α-orbital admissible if T is α-orbital admissible and*

$$(T4) \quad \alpha(x, y) \geq 1 \text{ and } \alpha(y, Ty) \geq 1 \Rightarrow \alpha(x, Ty) \geq 1.$$

As it is expected, each α-admissible mapping is an α-orbital admissible mapping and each triangular α-admissible mapping is a triangular α-orbital admissible mapping. Notice also that the converse is false, see e.g. ([54] Example 7).

A metric space (X, d) is said α-regular [54], if for every sequence $\{x_n\}$ in X such that $\alpha(x_n, x_{n+1}) \geq 1$ for all n and $x_n \to x \in X$ as $n \to \infty$, then there exists a subsequence $\{x_{n(k)}\}$ of $\{x_n\}$ such that $\alpha(x_{n(k)}, x) \geq 1$ for all k.

Lemma 1. *[54] Let $T : X \to X$ be a triangular α-orbital admissible mapping. Assume that there exists $x_0 \in X$ such that $\alpha(x_0, Tx_0) \geq 1$. Define a sequence $\{x_n\}$ by $x_{n+1} = Tx_n$ for each $n \in \mathbb{N}_0$. Then we have $\alpha(x_n, x_m) \geq 1$ for all $m, n \in \mathbb{N}$ with $n < m$.*

In what follows, we recall the following auxiliary family of the functions, namely, comparison and c-comparison functions. A mapping $\psi : [0, \infty) \to [0, \infty)$ is called a *comparison function* if it is increasing and $\psi^n(t) \to 0$, $n \to \infty$, for any $t \in [0, \infty)$. We denote by Φ, the class of the corporation function $\psi : [0, \infty) \to [0, \infty)$. For more details and examples , see e.g. [21, 58]. Among them, we recall the following essential result.

Lemma 2. *(Berinde [21], Rus [58]) If $\psi : [0, \infty) \to [0, \infty)$ is a comparison function, then:*

(1) each iterate ψ^k of ψ, $k \geq 1$, is also a comparison function;

(2) ψ is continuous at 0;

(3) $\psi(t) < t$, for any $t > 0$.

Later, Berinde [21] introduced the concept of (c)-*comparison function* in the following way.

Definition 4. *(Berinde [21]) A function $\psi : [0, \infty) \to [0, \infty)$ is said to be a (c)-comparison function if*

(c_1) *ψ is increasing,*

(c_2) *there exists $k_0 \in \mathbb{N}$, $a \in (0, 1)$ and a convergent series of nonnegative terms $\sum_{k=1}^{\infty} v_k$ such that*

$$\psi^{k+1}(t) \leq a\psi^k(t) + v_k, \text{ for } k \geq k_0 \text{ and any } t \in [0, \infty).$$

From now on, the letter Ψ is reserved to indicate the family of functions (c)-comparison function. It is evident that Lemma 2 is valid for $\psi \in \Psi$. Further, (c_2) yields

$$\sum_{n=1}^{+\infty} \psi^n(t) < \infty,$$

for all $t > 0$, where ψ^n is the nth iterate of ψ.

Samet *et al.* [61] prove the first fixed point result via admissible mapping by introducing the following concepts.

Definition 5. *Let (X, d) be a metric space and $T : X \to X$ be a given mapping. We say that T is an $\alpha - \psi$ contractive mapping if there exist two functions $\alpha : X \times X \to [0, \infty)$ and $\psi \in \Psi$ such that*

$$\alpha(x, y)d(Tx, Ty) \leq \psi(d(x, y)), \text{ for all } x, y \in X.$$

It is obvious that, any contractive mapping forms an $\alpha - \psi$ contractive mapping with $\alpha(x, y) = 1$ for all $x, y \in X$ and $\psi(t) = kt$, $k \in (0, 1)$.

The following is the interesting fixed point theorem of Samet et al. [61]

Theorem 1. *Let (X, d) be a complete metric space and $T : X \to X$ be an $\alpha - \psi$ contractive mapping. Suppose that*

(i) *T is $\alpha-$admissible;*

(ii) *there exists $x_0 \in X$ such that $\alpha(x_0, Tx_0) \geq 1$;*

(iii) *T is continuous, or*

(iii) *if $\{x_n\}$ is a sequence in X such that $\alpha(x_n, x_{n+1}) \geq 1$ for all n and $x_n \to x \in X$ as $n \to \infty$, then $\alpha(x_n, x) \geq 1$ for all n.*

Then there exists $u \in X$ such that $Tu = u$.

Note that in this setting, for the uniqueness additional condition is considered.

Theorem 2. *Adding to the hypotheses of Theorem 1 (resp. Theorem 1) the condition: For all $x, y \in X$, there exists $z \in X$ such that $\alpha(x, z) \geq 1$ and $\alpha(y, z) \geq 1$, we obtain uniqueness of the fixed point.*

Another successful attempt to simplify and clarify the literature of the metric fixed point theory was done by Khojasteh *et al.* [44] in 2015. In this paper, the authors introduced the notion of the simulation functions to combine the several existing results. In what follows, we recall the definition of this auxiliary function.

Definition 6. *(See [44]) A function $\zeta : [0, \infty) \times [0, \infty) \to \mathbb{R}$ is said to be* simulation *if it satisfies the following conditions:*

(ζ_1) $\zeta(0,0) = 0$;

(ζ_2) $\zeta(t,s) < s - t$ for all $t, s > 0$;

(ζ_3) if $\{t_n\}, \{s_n\}$ are sequences in $(0, \infty)$ such that $\lim\limits_{n \to \infty} t_n = \lim\limits_{n \to \infty} s_n > 0$, then

$$\limsup_{n \to \infty} \zeta(t_n, s_n) < 0. \tag{1}$$

The family of all simulation functions $\zeta : [0, \infty) \times [0, \infty) \to \mathbb{R}$ will be denoted by $\mathcal{Z}$. On account of (ζ_2), we observe that

$$\zeta(t,t) < 0 \text{ for all } t > 0, \zeta \in \mathcal{Z}. \tag{2}$$

Notice also that the condition (ζ_1) is superfluous due to (ζ_2).

Example 2. *(See e.g. [12, 15, 42–44, 56]) Let $\zeta_i : [0, \infty) \times [0, \infty) \to \mathbb{R}$, $i \in \{1, 2, 3\}$, be mappings defined by*

(i) *$\zeta_1(t,s) = \psi(s) - \phi(t)$ for all $t, s \in [0, \infty)$, where $\phi, \psi : [0, \infty) \to [0, \infty)$ are two continuous functions such that $\psi(t) = \phi(t) = 0$ if, and only if, $t = 0$, and $\psi(t) < t \leq \phi(t)$ for all $t > 0$.*

(ii) *$\zeta_2(t,s) = s - \dfrac{f(t,s)}{g(t,s)} t$ for all $t, s \in [0, \infty)$, where $f, g : [0, \infty) \to (0, \infty)$ are two continuous functions with respect to each variable such that $f(t,s) > g(t,s)$ for all $t, s > 0$.*

(iii) *$\zeta_3(t,s) = s - \varphi(s) - t$ for all $t, s \in [0, \infty)$, where $\varphi : [0, \infty) \to [0, \infty)$ is a continuous function such that $\varphi(t) = 0$ if, and only if, $t = 0$.*

(iv) *If $\varphi : [0, \infty) \to [0, 1)$ is a function such that $\limsup\limits_{t \to r^+} \varphi(t) < 1$ for all $r > 0$, and we define*

$$\zeta_T(t,s) = s\,\varphi(s) - t \qquad \text{for all } s, t \in [0, \infty),$$

then ζ_T is a simulation function.

(v) *If $\eta : [0, \infty) \to [0, \infty)$ is an upper semi-continuous mapping such that $\eta(t) < t$ for all $t > 0$ and $\eta(0) = 0$, and we define*

$$\zeta_{BW}(t,s) = \eta(s) - t \qquad \text{for all } s, t \in [0, \infty),$$

then ζ_{BW} is a simulation function.

(vi) *If $\phi : [0, \infty) \to [0, \infty)$ is a function such that $\int_0^\varepsilon \phi(u)du$ exists and $\int_0^\varepsilon \phi(u)du > \varepsilon$, for each $\varepsilon > 0$, and we define*

$$\zeta_K(t,s) = s - \int_0^t \phi(u)du \qquad \text{for all } s, t \in [0, \infty),$$

then ζ_K is a simulation function.

Suppose (X, d) is a metric space, T is a self-mapping on X and $\zeta \in \mathcal{Z}$. We say that T is a $\mathcal{Z}$-contraction with respect to ζ [44], if

$$\zeta(d(T(x), T(y)), d(x,y)) \geq 0, \text{ for all } x, y \in X.$$

It is evident that renowned Banach contraction forms $\mathcal{Z}$-contraction with respect to ζ where $\zeta(t,s) = ks - t$ with $k \in [0, 1)$ and $s, t \in [0, \infty)$.

Theorem 3. *On the complete metric space, every $\mathcal{Z}$-contraction possesses a unique fixed point.*

3   A theorem with many consequences

In this section, we shall consider a theorem that generalizes and hence unifies a number of existing results. Consequently, we list many corollaries.

Definition 7. *Let (X, d) be a metric space and $T : X \to X$ be a given mapping. We say that T is a generalized Suzuki type $(\alpha - \psi) - \mathcal{Z}$-contraction mapping if there exist two functions $\alpha : X \times X \to [0, \infty)$, $\zeta \in \mathcal{Z}$ and $\psi \in \Psi$ such that for all $x, y \in X$, we have*

$$\frac{1}{2}d(x, Tx) \leq d(x, y) \text{ implies } \zeta(\psi(M(x, y)), \alpha(x, y)d(Tx, Ty)) \geq 0, \tag{3}$$

where $M(x, y) = \max \left\{ d(x, y), \dfrac{d(x, Tx) + d(y, Ty)}{2}, \dfrac{d(x, Ty) + d(y, Tx)}{2} \right\}$.

Theorem 4. *Let (X, d) be a complete metric space. Suppose that $T : X \to X$ is a generalized Suzuki type $(\alpha - \psi) - \mathcal{Z}$-contraction mapping and satisfies the following conditions:*

(i) T is triangular α-orbital admissible;

(ii) there exists $x_0 \in X$ such that $\alpha(x_0, Tx_0) \geq 1$;

(iii) T is continuous.

Then there exists $u \in X$ such that $Tu = u$.

Proof. On account of the assumption (ii) of the theorem, there is a point $x_0 \in X$ such that $\alpha(x_0, Tx_0) \geq 1$.

Starting with this initial point, we shall built-up a recursive sequence $\{x_n\}$ in X by $x_{n+1} = Tx_n$ for all $n \in \mathbb{N}_0$. We, first, observe that incase of $x_{n_0} = x_{n_0+1}$ for some n_0, we conclude that $u = x_{n_0}$ is a fixed point of T. Accordingly, we presume that $x_n \neq x_{n+1}$ for all n. Hence, we find that

$$0 < \frac{1}{2}d(x_n, x_{n+1}) = \frac{1}{2}d(x_n, Tx_n) \leq d(x_n, x_{n+1}),$$

for all n.

On the other hand, employing that T is $\alpha-$admissible, we derive that

$$\alpha(x_0, x_1) = \alpha(x_0, Tx_0) \geq 1 \Rightarrow \alpha(Tx_0, Tx_1) = \alpha(x_1, x_2) \geq 1.$$

Inductively, we have

$$\alpha(x_n, x_{n+1}) \geq 1, \text{ for all } n = 0, 1, \ldots \tag{4}$$

From (3) and (4), it follows that for all $n \geq 1$, we have

$$\frac{1}{2}d(x_n, Tx_n) \leq d(x_n, x_{n+1}),$$

implies that

$$\zeta(\psi(M(x_n, x_{n+1})), \alpha(x_n, x_{n+1})d(Tx_n, Tx_{n+1}))) \geq 0,$$

which is equivalent to

$$d(x_{n+1}, x_n) = d(Tx_n, Tx_{n-1}) \leq \alpha(x_n, x_{n-1})d(Tx_n, Tx_{n-1}) \leq \psi(M(x_n, x_{n-1})). \tag{5}$$

Now, we shall simplify the right hand side of the inequality above, as follows

$$
\begin{aligned}
M(x_n, x_{n-1}) &= \max \left\{ d(x_n, x_{n-1}), \frac{d(x_n, Tx_n) + d(x_{n-1}, Tx_{n-1})}{2}, \frac{d(x_n, Tx_{n-1}) + d(x_{n-1}, Tx_n)}{2} \right\} \\
&= \max \left\{ d(x_n, x_{n-1}), \frac{d(x_n, x_{n+1}) + d(x_{n-1}, x_n)}{2}, \frac{d(x_{n-1}, x_{n+1})}{2} \right\} \\
&\leq \max \left\{ d(x_n, x_{n-1}), \frac{d(x_n, x_{n+1}) + d(x_{n-1}, x_n)}{2} \right\} \\
&\leq \max\{d(x_n, x_{n-1}), d(x_n, x_{n+1})\}.
\end{aligned}
$$

Consequently, regarding (5) together with the fact that ψ is a nondecreasing function, we derive

$$d(x_{n+1}, x_n) \leq \psi \left(\max\{d(x_n, x_{n-1}), d(x_n, x_{n+1})\} \right),\tag{6}$$

for all $n \geq 1$. If for some $n \geq 1$, we have $d(x_n, x_{n-1}) \leq d(x_n, x_{n+1})$, from (6), we obtain that

$$d(x_{n+1}, x_n) \leq \psi(d(x_n, x_{n+1})) < d(x_n, x_{n+1}),$$

a contradiction. Thus, for all $n \geq 1$, we have

$$\max\{d(x_n, x_{n-1}), d(x_n, x_{n+1})\} = d(x_n, x_{n-1}).\tag{7}$$

Using (6) and (7), we get that

$$d(x_{n+1}, x_n) \leq \psi(d(x_n, x_{n-1})) < d(x_n, x_{n-1}),\tag{8}$$

for all $n \geq 1$. By induction, we get

$$d(x_{n+1}, x_n) \leq \psi^n(d(x_1, x_0)), \text{ for all } n \geq 1.\tag{9}$$

From (9) and using the triangular inequality, for all $k \geq 1$, we have

$$\begin{aligned}
d(x_n, x_{n+k}) &\leq d(x_n, x_{n+1}) + \ldots + d(x_{n+k-1}, x_{n+k}) \\
&\leq \sum_{p=n}^{n+k-1} \psi^n(d(x_1, x_0)) \\
&\leq \sum_{p=n}^{+\infty} \psi^n(d(x_1, x_0)) \to 0 \text{ as } n \to \infty.
\end{aligned}$$

This implies that $\{x_n\}$ is a Cauchy sequence in (X, d). Since (X, d) is complete, there exists $u \in X$ such that

$$\lim_{n \to \infty} d(x_n, u) = 0.\tag{10}$$

Since T is continuous, we obtain from (10) that

$$\lim_{n \to \infty} d(x_{n+1}, Tu) = \lim_{n \to \infty} d(Tx_n, Tu) = 0.\tag{11}$$

From (10), (11) and the uniqueness of the limit, we get immediately that u is a fixed point of T, that is, $Tu = u$.

In what follows, the continuity of the contraction in Theorem 4 is refined.

Theorem 5. *Let (X, d) be a complete metric space. Suppose that $T : X \to X$ is a generalized Suzuki type $(\alpha - \psi) - \mathcal{Z}$-contraction mapping and satisfies the following conditions:*

(i) T is triangular α-orbital admissible;

(ii) there exists $x_0 \in X$ such that $\alpha(x_0, Tx_0) \geq 1$;

(iii) if $\{x_n\}$ is a sequence in X such that $\alpha(x_n, x_{n+1}) \geq 1$ for all n and $x_n \to x \in X$ as $n \to \infty$, then there exists a subsequence $\{x_{n(k)}\}$ of $\{x_n\}$ such that $\alpha(x_{n(k)}, x) \geq 1$ for all k.

Then there exists $u \in X$ such that $Tu = u$.

Proof. Following the proof of Theorem 4 line by line, we deduce that the recursive sequence $\{x_n\}$ defined by $x_{n+1} = Tx_n$ for all $n \geq 0$, converges for some $u \in X$. From (4) and condition (iii), there exists a subsequence $\{x_{n(k)}\}$ of $\{x_n\}$ such that $\alpha(x_{n(k)}, u) \geq 1$ for all k.

Now, we use (3) to deduce $u \in X$ is the required fixed point. For this purpose, we need to show that $\frac{1}{2}d(x_{n(k)}, x_{n(k)+1}) = \frac{1}{2}d(x_{n(k)}, Tx_{n(k)}) \leq d(x_{n(k)}, u)$ or $\frac{1}{2}d(x_{n(k)+1}, x_{n(k)+2}) = \frac{1}{2}d(x_{n(k)+1}, Tx_{n(k)+1}) \leq d(x_{n(k)+1}, u)$. Suppose, on the contrary, that $\frac{1}{2}d(x_{n(k)}, x_{n(k)+1}) > d(x_{n(k)}, u)$ and $\frac{1}{2}d(x_{n(k)+1}, x_{n(k)+2}) > d(x_{n(k)+1}, u)$. On account of the triangle inequality, we have

$$
\begin{aligned}
d(x_{n(k)}, x_{n(k)+1}) \quad &\leq d(x_{n(k)}, u) + d(u, x_{n(k)+1}) \\
&< \tfrac{1}{2}d(x_{n(k)}, x_{n(k)+1}) + \tfrac{1}{2}d(x_{n(k)+1}, x_{n(k)+2}) \\
\text{on account of (8)} \quad &< \tfrac{1}{2}d(x_{n(k)}, x_{n(k)+1}) + \tfrac{1}{2}d(x_{n(k)}, x_{n(k)+1}) = d(x_{n(k)}, x_{n(k)+1}),
\end{aligned}
\tag{12}
$$

a contradiction. Thus, we have

$$
\frac{1}{2}d(x_{n(k)}, Tx_{n(k)}) \leq d(x_{n(k)}, u) \text{ or } \frac{1}{2}d(x_{n(k)+1}, Tx_{n(k)+1}) \leq d(x_{n(k)+1}, u).
$$

After this observation, by applying (3), for all k, we find

$\frac{1}{2}d(x_{n(k)}, Tx_{n(k)}) \leq d(x_{n(k)}, u)$ implies $\zeta(\psi(M(x_{n(k)}, u)), \alpha(x_{n(k)}, u)d(Tx_{n(k)}, Tu)) \geq 0$ which yields that

$$
d(x_{n(k)+1}, Tu) = d(Tx_{n(k)}, Tu) \leq \alpha(x_{n(k)}, u)d(Tx_{n(k)}, Tu) \leq \psi(M(x_{n(k)}, u)).
\tag{13}
$$

On the other hand, we have

$$
M(x_{n(k)}, u) = \max\left\{d(x_{n(k)}, u), \frac{d(x_{n(k)}, x_{n(k)+1}) + d(u, Tu)}{2}, \frac{d(x_{n(k)}, Tu) + d(u, x_{n(k)+1})}{2}\right\}.
$$

Letting $k \to \infty$ in the above equality, we obtain that

$$
\lim_{k\to\infty} M(x_{n(k)}, u) = \frac{d(u, Tu)}{2}.
\tag{14}
$$

Suppose that $d(u, Tu) > 0$. From (14), for k large enough, we have $M(x_{n(k)}, u) > 0$, which yields that $\psi(M(x_{n(k)}, u)) < M(x_{n(k)}, u)$. Hence, from (13), we find

$$
d(x_{n(k)+1}, Tu) < M(x_{n(k)}, u).
$$

Letting $k \to \infty$ in the above inequality, using (14), we obtain that

$$
d(u, Tu) \leq \frac{d(u, Tu)}{2},
$$

which is a contradiction. Thus we have $d(u, Tu) = 0$, that is, $u = Tu$.

Notice that the proved theorems above are valid when we replace Instead of $M(x, y)$ with $N(x, y)$, where

$$
N(x, y) = \max\left\{d(x, y), \frac{d(x, Tx) + d(y, Ty)}{2}\right\}.
$$

The following example indicate that the hypotheses in Theorem 4 and Theorem 5 do not guarantee uniqueness of the fixed point.

Example 3. *Consider the set $X = \{(2, 1), (1, 2)\} \subset \mathbb{R}^2$ endowed with the standard Euclidean distance*

$$
d((x, y), (u, v)) = |x - u| + |y - v|,
$$

for all $(x, y), (u, v) \in X$. It is evident that (X, d) is a complete metric space. It is clear that $T(x, y) = (x, y)$ that is trivially continuous. On account of the inequality $0 = d(T(x, y), T(u, v)) \leq d((x, y), (u, v))$ we have

$$\zeta(\psi(M((x, y), (u, v))), \alpha((x, y), (u, v))d(T(x, y), T(u, v))) \geq 0,$$

for any $\psi \in \Psi$. Consequently, we have

$$\alpha((x, y), (u, v))d(T(x, y), T(u, v)) \leq \psi(M((x, y), (u, v))),$$

for all $(x, y), (u, v) \in X$, where

$$\alpha((x, y), (u, v)) = \begin{cases} 1 & if \quad (x, y) = (u, v), \\ 0 & if \quad (x, y) \neq (u, v). \end{cases}$$

Consequently, T is a generalized Suzuki type $(\alpha - \psi) - \mathcal{Z}$-contraction mapping. On the other hand, for all $(x, y), (u, v) \in X$, we have

$$\alpha((x, y), (u, v)) \geq 1 \rightarrow (x, y) = (u, v) \rightarrow T(x, y) = T(u, v) \rightarrow \alpha(T(x, y), T(u, v)) \geq 1.$$

Thus, the mapping T is $\alpha-$admissible. Furthermore, for all $(x, y) \in X$, we have $\alpha((x, y), T(x, y)) \geq 1$. Hence, the assumptions of Theorem 4 are fulfilled. Note that the assumptions of Theorem 5 are also satisfied, indeed if $\{(x_n, y_n)\}$ is a sequence in X that converges to some point $(x, y) \in X$ with $\alpha((x_n, y_n), (x_{n+1}, y_{n+1})) \geq 1$ for all n, from the definition of α, we have $(x_n, y_n) = (x, y)$ for all n, that yields $\alpha((x_n, y_n), (x, y)) = 1$ for all n. Notice that, in this case, T has two fixed points in X.

For the uniqueness of a fixed point of such mappings, we need to the following additional condition:

(H) For all $x, y \in \text{Fix}(T)$, there exists $z \in X$ such that $\alpha(x, z) \geq 1$ and $\alpha(y, z) \geq 1$.

Here, $\text{Fix}(T)$ denotes the set of fixed points of T.

Theorem 6. *Adding condition (H) to the hypotheses of Theorem 4 (resp. Theorem 5), we obtain that u is the unique fixed point of T.*

Proof. Suppose, on the contrary, that v is another fixed point of T. From (H), there exists $z \in X$ such that

$$\alpha(u, z) \geq 1 \text{ and } \alpha(v, z) \geq 1. \tag{15}$$

Due to the fact that T is $\alpha-$admissible together with (15), we find

$$\alpha(u, T^n z) \geq 1 \text{ and } \alpha(v, T^n z) \geq 1, \text{ for all } n. \tag{16}$$

Construct a sequence $\{z_n\}$ in X by $z_{n+1} = T z_n$ for all $n \geq 0$ and $z_0 = z$.

Taking (16) into account, for all n, we have

$$0 = \frac{1}{2}d(u, Tu) \leq d(u, z_n) \text{ implies } \zeta(\psi(M(u, z_n)), \alpha(u, z_n)d(Tu, Tz_n)) \geq 0, \tag{17}$$

which is equivalent to

$$d(u, z_{n+1}) = d(Tu, Tz_n) \leq \alpha(u, z_n)d(Tu, Tz_n) \leq \psi(M(u, z_n)). \tag{18}$$

On the other hand, we find

$$\begin{aligned} M(u, z_n) &= \max\left\{d(u, z_n), \frac{d(z_n, z_{n+1})}{2}, \frac{d(u, z_{n+1}) + d(z_n, u)}{2}\right\} \\ &\leq \max\left\{d(u, z_n), \frac{d(z_n, u) + d(u, z_{n+1})}{2}\right\} \\ &\leq \max\{d(u, z_n), d(u, z_{n+1})\}. \end{aligned}$$

On account of the inequality above, the expression (18) and the monotone property of ψ, we derive that

$$d(u, z_{n+1}) \leq \psi\left(\max\{d(u, z_n), d(u, z_{n+1})\}\right), \tag{19}$$

for all n. Without restriction to the generality, we can suppose that $d(u, z_n) > 0$ for all n. If $\max\{d(u, z_n), d(u, z_{n+1})\} = d(u, z_{n+1})$, we get from (19) that

$$d(u, z_{n+1}) \leq \psi(d(u, z_{n+1})) < d(u, z_{n+1}),$$

which is a contradiction. Thus we have $\max\{d(u, z_n), d(u, z_{n+1})\} = d(u, z_n)$, and

$$d(u, z_{n+1}) \leq \psi(d(u, z_n)),$$

for all n. This implies that

$$d(u, z_n) \leq \psi^n(d(u, z_0)), \text{ for all } n \geq 1.$$

Letting $n \to \infty$ in the above inequality, we obtain

$$\lim_{n \to \infty} d(z_n, u) = 0. \tag{20}$$

Similarly, one can show that

$$\lim_{n \to \infty} d(z_n, v) = 0. \tag{21}$$

From (20) and (21), it follows that $u = v$. Thus we proved that u is the unique fixed point of T.

3.1   Immediate consequences

. The first immediate consequence is obtained by removing the Suzuki condition, as in the following definition.

Definition 8. *Let (X, d) be a metric space and $T : X \to X$ be a given mapping. We say that T is a generalized type $(\alpha - \psi) - \mathcal{Z}$-contraction mapping if there exist two functions $\alpha : X \times X \to [0, \infty)$, $\zeta \in \mathcal{Z}$ and $\psi \in \Psi$ such that for all $x, y \in X$, we have*

$$\zeta(\psi(M(x, y)), \alpha(x, y)d(Tx, Ty)) \geq 0, \tag{22}$$

where $M(x, y) = \max\left\{d(x, y), \dfrac{d(x, Tx) + d(y, Ty)}{2}, \dfrac{d(x, Ty) + d(y, Tx)}{2}\right\}$.

Theorem 7. *Let (X, d) be a complete metric space. Suppose that $T : X \to X$ is a generalized Suzuki type $(\alpha - \psi) - \mathcal{Z}$-contraction mapping and satisfies the following conditions:*

  (i) *T is triangular α-orbital admissible;*

  (ii) *there exists $x_0 \in X$ such that $\alpha(x_0, Tx_0) \geq 1$;*

(iii)* *T is continuous*
    or

(iii)** *if $\{x_n\}$ is a sequence in X such that $\alpha(x_n, x_{n+1}) \geq 1$ for all n and $x_n \to x \in X$ as $n \to \infty$, then there exists a subsequence $\{x_{n(k)}\}$ of $\{x_n\}$ such that $\alpha(x_{n(k)}, x) \geq 1$ for all k,*

  (iv) *the condition (H) holds.*

Then there exists $u \in X$ such that $Tu = u$.

We skipped the proof. Indeed, it is verbatim of the combinations of the proofs of Theorem 4, Theorem 5 and Theorem 6, by removing the related lines about the Suzuki condition.

Taking Example 2 into account, both Theorem 6 and Theorem 7 yields several consequences. In this direction, one of the first example, by considering the case (i) Example 2 is the following theorem

Definition 9. *Let (X, d) be a metric space and $T : X \to X$ be a given mapping. We say that T is a generalized $\alpha - \psi$ contractive mapping if there exist two functions $\alpha : X \times X \to [0, \infty)$ and $\psi \in \Psi$ such that for all $x, y \in X$, we have*

$$\alpha(x, y)d(Tx, Ty) \leq \psi(M(x, y)), \tag{23}$$

where $M(x, y) = \max \left\{ d(x, y), \dfrac{d(x, Tx) + d(y, Ty)}{2}, \dfrac{d(x, Ty) + d(y, Tx)}{2} \right\}$.

Theorem 8. *Let (X, d) be a complete metric space. Suppose that $T : X \to X$ is a generalized $\alpha - \psi$ contractive mapping and satisfies the following conditions:*

(i) *T is $\alpha-$admissible ;*

(ii) *there exists $x_0 \in X$ such that $\alpha(x_0, Tx_0) \geq 1$;*

(iii)* *T is continuous*
      or

(iii)** *if $\{x_n\}$ is a sequence in X such that $\alpha(x_n, x_{n+1}) \geq 1$ for all n and $x_n \to x \in X$ as $n \to \infty$, then there exists a subsequence $\{x_{n(k)}\}$ of $\{x_n\}$ such that $\alpha(x_{n(k)}, x) \geq 1$ for all k,*

(iv) *the condition (H) holds.*

Then there exists $u \in X$ such that $Tu = u$.

It is evident that by taking, the other cases of Example 2, into account, one can further consequences. We prefer to skip these consequences by the sake of the length of the manuscript.

4   Further Consequences

In this section, we shall indicate that several existing results in the literature can be deduced easily from our Theorem 6.

4.1   Standard fixed point theorems

Taking Theorem 6 into account, employing $\alpha(x, y) = 1$ for all $x, y \in X$, we obtain immediately the following fixed point theorem.

Corollary 1. *Let (X, d) be a complete metric space and $T : X \to X$ be a given mapping. Suppose that there exists a function $\psi \in \Psi$ such that*

$$\frac{1}{2}d(x, Tx) \leq d(x, y) \text{ implies } \zeta(\psi(M(x, y)), d(Tx, Ty)) \geq 0,$$

for all $x, y \in X$, where $M(x, y) = \max \left\{ d(x, y), \dfrac{d(x, Tx) + d(y, Ty)}{2}, \dfrac{d(x, Ty) + d(y, Tx)}{2} \right\}$. Then T has a unique fixed point.

In the same way, by letting $\alpha(x, y) = 1$, for all $x, y \in X$, in Theorem 7, we find the following result:

Corollary 2. *Let (X, d) be a complete metric space and $T : X \to X$ be a given mapping. Suppose that there exists a function $\psi \in \Psi$ such that*

$$\zeta(\psi(M(x, y)), d(Tx, Ty)) \geq 0,$$

for all $x, y \in X$, where $M(x, y) = \max \left\{ d(x, y), \dfrac{d(x, Tx) + d(y, Ty)}{2}, \dfrac{d(x, Ty) + d(y, Tx)}{2} \right\}$. Then T has a unique fixed point.

Analogously, by letting $\alpha(x, y) = 1$, for all $x, y \in X$, in Theorem 8, we find the following result:

Corollary 3. *Let (X, d) be a complete metric space and $T : X \to X$ be a given mapping. Suppose that there exists a function $\psi \in \Psi$ such that*

$$d(Tx, Ty) \leq \psi(M(x, y)),$$

for all $x, y \in X$. Then T has a unique fixed point.

The following fixed point theorems follow immediately from Corollary 3.

Corollary 4 (see Berinde [22]). *Let (X, d) be a complete metric space and $T : X \to X$ be a given mapping. Suppose that there exists a function $\psi \in \Psi$ such that*

$$d(Tx, Ty) \leq \psi(d(x, y)),$$

for all $x, y \in X$. Then T has a unique fixed point.

Corollary 5 (see Ćirić [26]). *Let (X, d) be a complete metric space and $T : X \to X$ be a given mapping. Suppose that there exists a constant $\lambda \in (0, 1)$ such that*

$$d(Tx, Ty) \leq \lambda \max \left\{ d(x, y), \frac{d(x, Tx) + d(y, Ty)}{2}, \frac{d(x, Ty) + d(y, Tx)}{2} \right\},$$

for all $x, y \in X$. Then T has a unique fixed point.

Corollary 6 (see Hardy and Rogers [33]). *Let (X, d) be a complete metric space and $T : X \to X$ be a given mapping. Suppose that there exist constants $A, B, C \geq 0$ with $(A + 2B + 2C) \in (0, 1)$ such that*

$$d(Tx, Ty) \leq Ad(x, y) + B[d(x, Tx) + d(y, Ty)] + C[d(x, Ty) + d(y, Tx)],$$

for all $x, y \in X$. Then T has a unique fixed point.

Corollary 7 (Banach Contraction Principle [18]). *Let (X, d) be a complete metric space and $T : X \to X$ be a given mapping. Suppose that there exists a constant $\lambda \in (0, 1)$ such that*

$$d(Tx, Ty) \leq \lambda \, d(x, y),$$

for all $x, y \in X$. Then T has a unique fixed point.

Corollary 8 (see Kannan [36]). *Let (X, d) be a complete metric space and $T : X \to X$ be a given mapping. Suppose that there exists a constant $\lambda \in (0, 1/2)$ such that*

$$d(Tx, Ty) \leq \lambda \, [d(x, Tx) + d(y, Ty)],$$

for all $x, y \in X$. Then T has a unique fixed point.

Corollary 9 (see Chatterjea [24]). *Let (X, d) be a complete metric space and $T : X \to X$ be a given mapping. Suppose that there exists a constant $\lambda \in (0, 1/2)$ such that*

$$d(Tx, Ty) \leq \lambda \, [d(x, Ty) + d(y, Tx)],$$

for all $x, y \in X$. Then T has a unique fixed point.

Corollary 10 (Dass-Gupta Theorem [29])**.** *Let (X, d) be a metric space and $T : X \to X$ be a given mapping. Suppose that there exist constants $\lambda, \mu \geq 0$ with $\lambda + \mu < 1$ such that*

$$d(Tx, Ty) \leq \mu d(y, Ty) \frac{1 + d(x, Tx)}{1 + d(x, y)} + \lambda d(x, y), \quad \text{for all } x, y \in X. \tag{24}$$

Then T has a unique fixed point.

*S*ketch of the Proof. Consider the functions $\psi : [0, \infty) \to [0, \infty)$ and $\alpha : X \times X \to \mathbb{R}$ defined by

$$\psi(t) = \lambda t, \ t \geq 0 \tag{25}$$

and

$$\alpha(x, y) = \begin{cases} 1 - \mu \dfrac{d(y, Ty)(1 + d(x, Tx))}{(1 + d(x, y))d(Tx, Ty)}, & \text{if } Tx \neq Ty, \\[4mm] 0, & \text{otherwise.} \end{cases} \tag{26}$$

The rest is simple evaluation. For the detailed proof, we refer to Samet [60].

Corollary 11 (Jaggi theorem [35])**.** *Let (X, d) be a metric space and $T : X \to X$ be a given mapping. Suppose there exist constants $\lambda, \mu \geq 0$ with $\lambda + \mu < 1$ such that*

$$d(Tx, Ty) \leq \mu \frac{d(x, Tx)d(y, Ty)}{d(x, y)} + \lambda d(x, y), \quad \text{for all } x, y \in X, \ x \neq y. \tag{27}$$

Then there exist $\psi \in \Psi$ and $\alpha : X \times X \to \mathbb{R}$ such that T is an α-ψ contraction. Then T has a unique fixed point.

*S*ketch of the Proof.

Consider the functions $\psi : [0, \infty) \to [0, \infty)$ and $\alpha : X \times X \to \mathbb{R}$ defined by

$$\psi(t) = \lambda t, \ t \geq 0 \tag{28}$$

and

$$\alpha(x, y) = \begin{cases} 1 - \mu \dfrac{d(x, Tx)d(y, Ty)}{d(x, y)d(Tx, Ty)}, & \text{if } Tx \neq Ty, \\[4mm] 0, & \text{otherwise.} \end{cases} \tag{29}$$

The rest is a simple evaluation. For the detailed proof, we refer to Samet [60].

Theorem 9 (Berinde Theorem [23])**.** *Let (X, d) be a metric space and $T : X \to X$ be a given mapping. Suppose that there exists $\lambda \in (0, 1)$ and $L \geq 0$ such that*

$$d(Tx, Ty) \leq \lambda d(x, y) + L d(y, Tx), \quad \text{for all } x, y \in X. \tag{30}$$

Then T has a fixed point.

*S*ketch of the Proof.

Consider the functions $\psi : [0, \infty) \to [0, \infty)$ and $\alpha : X \times X \to \mathbb{R}$ defined by

$$\psi(t) = \lambda t, \ t \geq 0$$

and

$$\alpha(x, y) = \begin{cases} 1 - L \dfrac{d(y, Tx)}{d(Tx, Ty)}, & \text{if } Tx \neq Ty, \\[4mm] 0, & \text{otherwise.} \end{cases} \tag{31}$$

The rest is straightforward. For more details for the proof, we refer to Samet [60].

Theorem 10 (Ćirić's non-unique fixed point theorem [27].). *Let (X, d) be a metric space and $T : X \to X$ be a given mapping. there exists $\lambda \in (0, 1)$ such that for all $x, y \in X$, we have*

$$\min\{d(Tx, Ty), d(x, Tx), d(y, Ty)\} - \min\{d(x, Ty), d(y, Tx)\} \leq \lambda \, d(x, y). \tag{32}$$

Then T has a fixed point.

*S*ketch of the Proof. Consider the functions $\psi : [0, \infty) \to [0, \infty)$ and $\alpha : X \times X \to \mathbb{R}$ defined by

$$\psi(t) = \lambda \, t, \ t \geq 0 \tag{33}$$

and

$$\alpha(x, y) = \begin{cases} \min\left\{1, \frac{d(x, Tx)}{d(Tx, Ty)}, \frac{d(y, Ty)}{d(Tx, Ty)}\right\} - \min\left\{\frac{d(x, Ty)}{d(Tx, Ty)}, \frac{d(y, Tx)}{d(Tx, Ty)}\right\}, \ \text{if } Tx \neq Ty, \\ \\ 0, \quad \text{otherwise.} \end{cases} \tag{34}$$

The rest is simple evaluation. For the detailed proof, we refer to Samet [60].

Theorem 11 (Suzuki Theorem [63]). *Let (X, d) be a metric space and $T : X \to X$ be a given mapping. Suppose that there exists $r \in (0, 1)$ such that*

$$(1 + r)^{-1} d(x, Tx) \leq d(x, y) \Longrightarrow d(Tx, Ty) \leq r \, d(x, y), \quad \text{for all } x, y \in X. \tag{35}$$

Then T has a unique fixed point.

*S*ketch of the Proof. Consider the functions $\psi : [0, \infty) \to [0, \infty)$ and $\alpha : X \times X \to \mathbb{R}$ defined by

$$\psi(t) = r \, t, \ t \geq 0$$

and

$$\alpha(x, y) = \begin{cases} 1, \quad \text{if } (1 + r)^{-1} d(x, Tx) \leq d(x, y), \\ \\ 0, \quad \text{otherwise.} \end{cases} \tag{36}$$

From (35), we have

$$\alpha(x, y) d(Tx, Ty) \leq \psi(d(x, y)), \quad \text{for all } x, y \in X.$$

Then T is an α-ψ contraction.

4.2   Fixed point theorems on metric spaces endowed with a partial order

In the last two decades, one of the trend in fixed point theory is the revisit the well-known fixed point theorem on metric spaces endowed with partial orders [65]. Among all, Ran and Reurings in [55] revisited the Banach contraction principle in partially ordered sets with some applications to matrix equations. Another version of the generalization of Banach contraction principle in partially ordered sets was proposed by Nieto and Rodríguez-López in [49]. Later, this trend was supported by several authors, see e.g. [2, 13, 28, 34, 53, 59] and the references cited therein . In this section, we shall show that Theorem 6 implies easily various fixed point results on a metric space endowed with a partial order. At first, we need to recall some concepts.

Definition 10. *Let $(X, \preceq)$ be a partially ordered set and $T : X \to X$ be a given mapping. We say that T is nondecreasing with respect to $\preceq$ if*

$$x, y \in X, \ x \preceq y \Longrightarrow Tx \preceq Ty.$$

Definition 11. *Let $(X, \preceq)$ be a partially ordered set. A sequence $\{x_n\} \subset X$ is said to be nondecreasing with respect to $\preceq$ if $x_n \preceq x_{n+1}$ for all n.*

Definition 12. *Let $(X, \preceq)$ be a partially ordered set and d be a metric on X. We say that $(X, \preceq, d)$ is regular if for every nondecreasing sequence $\{x_n\} \subset X$ such that $x_n \to x \in X$ as $n \to \infty$, there exists a subsequence $\{x_{n(k)}\}$ of $\{x_n\}$ such that $x_{n(k)} \preceq x$ for all k.*

We have the following result.

Corollary 12. *Let $(X, \preceq)$ be a partially ordered set and d be a metric on X such that (X, d) is complete. Let $T : X \to X$ be a nondecreasing mapping with respect to $\preceq$. Suppose that there exists a function $\psi \in \Psi$ such that*

$$\frac{1}{2}d(x, Tx) \leq d(x, y) \text{ implies } \zeta(\psi(M(x, y)), d(Tx, Ty)) \geq 0,$$

for all $x, y \in X$ with $x \succeq y$. Suppose also that the following conditions hold:

(i) there exists $x_0 \in X$ such that $x_0 \preceq Tx_0$;

(ii) T is continuous or $(X, \preceq, d)$ is regular.

Then T has a fixed point. Moreover, if for all $x, y \in X$ there exists $z \in X$ such that $x \preceq z$ and $y \preceq z$, we have uniqueness of the fixed point.

Proof. Define the mapping $\alpha : X \times X \to [0, \infty)$ by

$$\alpha(x, y) = \begin{cases} 1 \text{ if } x \preceq y \text{ or } x \succeq y, \\ 0 \text{ otherwise.} \end{cases}$$

Clearly, T is a generalized $\alpha - \psi$ contractive mapping, that is,

$$\alpha(x, y)d(Tx, Ty) \leq \psi(M(x, y)),$$

for all $x, y \in X$. From condition (i), we have $\alpha(x_0, Tx_0) \geq 1$. Moreover, for all $x, y \in X$, from the monotone property of T, we have

$$\alpha(x, y) \geq 1 \implies x \succeq y \text{ or } x \preceq y \implies Tx \succeq Ty \text{ or } Tx \preceq Ty \implies \alpha(Tx, Ty) \geq 1.$$

Thus T is $\alpha-$admissible. Now, if T is continuous, the existence of a fixed point follows from Theorem 4. Suppose now that $(X, \preceq, d)$ is regular. Let $\{x_n\}$ be a sequence in X such that $\alpha(x_n, x_{n+1}) \geq 1$ for all n and $x_n \to x \in X$ as $n \to \infty$. From the regularity hypothesis, there exists a subsequence $\{x_{n(k)}\}$ of $\{x_n\}$ such that $x_{n(k)} \preceq x$ for all k. This implies from the definition of α that $\alpha(x_{n(k)}, x) \geq 1$ for all k. In this case, the existence of a fixed point follows from Theorem 5. To show the uniqueness, let $x, y \in X$. By hypothesis, there exists $z \in X$ such that $x \preceq z$ and $y \preceq z$, which implies from the definition of α that $\alpha(x, z) \geq 1$ and $\alpha(y, z) \geq 1$. Thus we deduce the uniqueness of the fixed point by Theorem 6.

Corollary 13. *Let $(X, \preceq)$ be a partially ordered set and d be a metric on X such that (X, d) is complete. Let $T : X \to X$ be a nondecreasing mapping with respect to $\preceq$. Suppose that there exists a function $\psi \in \Psi$ such that*

$$\zeta(\psi(M(x, y)), d(Tx, Ty)) \geq 0,$$

for all $x, y \in X$ with $x \succeq y$. Suppose also that the following conditions hold:

(i) there exists $x_0 \in X$ such that $x_0 \preceq Tx_0$;

(ii) T is continuous or $(X, \preceq, d)$ is regular.

Then T has a fixed point. Moreover, if for all $x, y \in X$ there exists $z \in X$ such that $x \preceq z$ and $y \preceq z$, we have uniqueness of the fixed point.

Corollary 14. *Let $(X, \preceq)$ be a partially ordered set and d be a metric on X such that (X, d) is complete. Let $T : X \to X$ be a nondecreasing mapping with respect to $\preceq$. Suppose that there exists a function $\psi \in \Psi$ such that*

$$d(Tx, Ty) \leq \psi(M(x, y)),$$

for all $x, y \in X$ with $x \succeq y$. Suppose also that the following conditions hold:

(i) *there exists $x_0 \in X$ such that $x_0 \preceq Tx_0$;*

(ii) *T is continuous or $(X, \preceq, d)$ is regular.*

Then T has a fixed point. Moreover, if for all $x, y \in X$ there exists $z \in X$ such that $x \preceq z$ and $y \preceq z$, we have uniqueness of the fixed point.

The following results are immediate consequences of Corollary14.

Corollary 15. *Let $(X, \preceq)$ be a partially ordered set and d be a metric on X such that (X, d) is complete. Let $T : X \to X$ be a nondecreasing mapping with respect to $\preceq$. Suppose that there exists a function $\psi \in \Psi$ such that*

$$d(Tx, Ty) \leq \psi(d(x, y)),$$

for all $x, y \in X$ with $x \succeq y$. Suppose also that the following conditions hold:

(i) *there exists $x_0 \in X$ such that $x_0 \preceq Tx_0$;*

(ii) *T is continuous or $(X, \preceq, d)$ is regular.*

Then T has a fixed point. Moreover, if for all $x, y \in X$ there exists $z \in X$ such that $x \preceq z$ and $y \preceq z$, we have uniqueness of the fixed point.

Corollary 16. *Let $(X, \preceq)$ be a partially ordered set and d be a metric on X such that (X, d) is complete. Let $T : X \to X$ be a nondecreasing mapping with respect to $\preceq$. Suppose that there exists a constant $\lambda \in (0, 1)$ such that*

$$d(Tx, Ty) \leq \lambda \max \left\{ d(x, y), \frac{d(x, Tx) + d(y, Ty)}{2}, \frac{d(x, Ty) + d(y, Tx)}{2} \right\},$$

for all $x, y \in X$ with $x \succeq y$. Suppose also that the following conditions hold:

(i) *there exists $x_0 \in X$ such that $x_0 \preceq Tx_0$;*

(ii) *T is continuous or $(X, \preceq, d)$ is regular.*

Then T has a fixed point. Moreover, if for all $x, y \in X$ there exists $z \in X$ such that $x \preceq z$ and $y \preceq z$, we have uniqueness of the fixed point.

Corollary 17. *Let $(X, \preceq)$ be a partially ordered set and d be a metric on X such that (X, d) is complete. Let $T : X \to X$ be a nondecreasing mapping with respect to $\preceq$. Suppose that there exist constants $A, B, C \geq 0$ with $(A + 2B + 2C) \in (0, 1)$ such that*

$$d(Tx, Ty) \leq Ad(x, y) + B[d(x, Tx) + d(y, Ty)] + C[d(x, Ty) + d(y, Tx)],$$

for all $x, y \in X$ with $x \succeq y$. Suppose also that the following conditions hold:

(i) *there exists $x_0 \in X$ such that $x_0 \preceq Tx_0$;*

(ii) *T is continuous or $(X, \preceq, d)$ is regular.*

Then T has a fixed point. Moreover, if for all $x, y \in X$ there exists $z \in X$ such that $x \preceq z$ and $y \preceq z$, we have uniqueness of the fixed point.

Corollary 18 (see Ran and Reurings [55], Nieto and López [49])**.** *Let $(X, \preceq)$ be a partially ordered set and d be a metric on X such that (X, d) is complete. Let $T : X \to X$ be a nondecreasing mapping with respect to $\preceq$. Suppose that there exists a constant $\lambda \in (0, 1)$ such that*

$$d(Tx, Ty) \leq \lambda\, d(x, y),$$

for all $x, y \in X$ with $x \succeq y$. Suppose also that the following conditions hold:

(i) there exists $x_0 \in X$ such that $x_0 \preceq Tx_0$;

(ii) T is continuous or $(X, \preceq, d)$ is regular.

Then T has a fixed point. Moreover, if for all $x, y \in X$ there exists $z \in X$ such that $x \preceq z$ and $y \preceq z$, we have uniqueness of the fixed point.

Corollary 19. *Let $(X, \preceq)$ be a partially ordered set and d be a metric on X such that (X, d) is complete. Let $T : X \to X$ be a nondecreasing mapping with respect to $\preceq$. Suppose that there exists a constant $\lambda \in (0, 1/2)$ such that*

$$d(Tx, Ty) \leq \lambda\,[d(x, Tx) + d(y, Ty)],$$

for all $x, y \in X$ with $x \succeq y$. Suppose also that the following conditions hold:

(i) there exists $x_0 \in X$ such that $x_0 \preceq Tx_0$;

(ii) T is continuous or $(X, \preceq, d)$ is regular.

Then T has a fixed point. Moreover, if for all $x, y \in X$ there exists $z \in X$ such that $x \preceq z$ and $y \preceq z$, we have uniqueness of the fixed point.

Corollary 20. *Let $(X, \preceq)$ be a partially ordered set and d be a metric on X such that (X, d) is complete. Let $T : X \to X$ be a nondecreasing mapping with respect to $\preceq$. Suppose that there exists a constant $\lambda \in (0, 1/2)$ such that*

$$d(Tx, Ty) \leq \lambda\,[d(x, Ty) + d(y, Tx)],$$

for all $x, y \in X$ with $x \succeq y$. Suppose also that the following conditions hold:

(i) there exists $x_0 \in X$ such that $x_0 \preceq Tx_0$;

(ii) T is continuous or $(X, \preceq, d)$ is regular.

Then T has a fixed point. Moreover, if for all $x, y \in X$ there exists $z \in X$ such that $x \preceq z$ and $y \preceq z$, we have uniqueness of the fixed point.

4.3   Fixed point theorems for cyclic contractive mappings

The notion of "cyclic contraction mapping"to find a fixed point was proposed by Kirk, Srinivasan and Veeramani [45]. In this paper, they revisited the famous Banach Contraction Mapping Principle was proved by Kirk, Srinivasan and Veeramani [45] via cyclic contraction. Following this pioneer work [45], several fixed point theorems in the framework of cyclic contractive mappings have appeared (see, for instant, [1, 37, 39, 51, 52, 57]). In this section, we shall proved that Theorem 6 implies several fixed point theorems in the context of cyclic contractive mappings.

We have the following result.

Corollary 21. *Let $\{A_i\}_{i=1}^2$ be nonempty closed subsets of a complete metric space (X, d) and $T : Y \to Y$ be a given mapping, where $Y = A_1 \cup A_2$ and $\zeta \in \mathcal{Z}$. Suppose that the following conditions hold:*

(I) $T(A_1) \subseteq A_2$ and $T(A_2) \subseteq A_1$;

(II) there exists a function $\psi \in \Psi$ such that

$$\frac{1}{2}d(x, Tx) \le d(x, y) \text{ implies } \zeta(\psi(M(x, y)), d(Tx, Ty)) \ge 0;$$

Then T has a unique fixed point that belongs to $A_1 \cap A_2$.

Proof. Since A_1 and A_2 are closed subsets of the complete metric space (X, d), then (Y, d) is complete. Define the mapping $\alpha : Y \times Y \to [0, \infty)$ by

$$\alpha(x, y) = \begin{cases} 1 \text{ if } (x, y) \in (A_1 \times A_2) \cup (A_2 \times A_1), \\ 0 \text{ otherwise.} \end{cases}$$

From (II) and the definition of α, we can write

$$\alpha(x, y)d(Tx, Ty) \le \psi(M(x, y)),$$

for all $x, y \in Y$. Thus T is a generalized $\alpha - \psi$ contractive mapping.

Let $(x, y) \in Y \times Y$ such that $\alpha(x, y) \ge 1$. If $(x, y) \in A_1 \times A_2$, from (I), $(Tx, Ty) \in A_2 \times A_1$, which implies that $\alpha(Tx, Ty) \ge 1$. If $(x, y) \in A_2 \times A_1$, from (I), $(Tx, Ty) \in A_1 \times A_2$, which implies that $\alpha(Tx, Ty) \ge 1$. Thus in all cases, we have $\alpha(Tx, Ty) \ge 1$. This implies that T is $\alpha-$admissible.

Also, from (I), for any $a \in A_1$, we have $(a, Ta) \in A_1 \times A_2$, which implies that $\alpha(a, Ta) \ge 1$.

Now, let $\{x_n\}$ be a sequence in X such that $\alpha(x_n, x_{n+1}) \ge 1$ for all n and $x_n \to x \in X$ as $n \to \infty$. This implies from the definition of α that

$$(x_n, x_{n+1}) \in (A_1 \times A_2) \cup (A_2 \times A_1), \text{ for all } n.$$

Since $(A_1 \times A_2) \cup (A_2 \times A_1)$ is a closed set with respect to the Euclidean metric, we get that

$$(x, x) \in (A_1 \times A_2) \cup (A_2 \times A_1),$$

which implies that $x \in A_1 \cap A_2$. Thus we get immediately from the definition of α that $\alpha(x_n, x) \ge 1$ for all n.

Finally, let $x, y \in \text{Fix}(T)$. From (I), this implies that $x, y \in A_1 \cap A_2$. So, for any $z \in Y$, we have $\alpha(x, z) \ge 1$ and $\alpha(y, z) \ge 1$. Thus condition (H) is satisfied.

Now, all the hypotheses of Theorem 6 are satisfied, we deduce that T has a unique fixed point that belongs to $A_1 \cap A_2$ (from (I)).

Corollary 22. *Let $\{A_i\}_{i=1}^2$ be nonempty closed subsets of a complete metric space (X, d) and $T : Y \to Y$ be a given mapping, where $Y = A_1 \cup A_2$ and $\zeta \in \mathcal{Z}$. Suppose that the following conditions hold:*

(I) $T(A_1) \subseteq A_2$ and $T(A_2) \subseteq A_1$;

(II) there exists a function $\psi \in \Psi$ such that

$$\zeta(\psi(M(x, y)), d(Tx, Ty)) \ge 0;$$

Then T has a unique fixed point that belongs to $A_1 \cap A_2$.

Corollary 23. *Let $\{A_i\}_{i=1}^2$ be nonempty closed subsets of a complete metric space (X, d) and $T : Y \to Y$ be a given mapping, where $Y = A_1 \cup A_2$. Suppose that the following conditions hold:*

(I) $T(A_1) \subseteq A_2$ and $T(A_2) \subseteq A_1$;

(II) there exists a function $\psi \in \Psi$ such that

$$d(Tx, Ty) \leq \psi(M(x, y)), \ \text{for all } (x, y) \in A_1 \times A_2.$$

Then T has a unique fixed point that belongs to $A_1 \cap A_2$.

The following results are immediate consequences of Corollary 23.

Corollary 24 (see Pacurar and Rus [51]). *Let $\{A_i\}_{i=1}^2$ be nonempty closed subsets of a complete metric space (X, d) and $T : Y \to Y$ be a given mapping, where $Y = A_1 \cup A_2$. Suppose that the following conditions hold:*

(I) $T(A_1) \subseteq A_2$ and $T(A_2) \subseteq A_1$;

(II) there exists a function $\psi \in \Psi$ such that

$$d(Tx, Ty) \leq \psi(d(x, y)), \ \text{for all } (x, y) \in A_1 \times A_2.$$

Then T has a unique fixed point that belongs to $A_1 \cap A_2$.

Corollary 25. *Let $\{A_i\}_{i=1}^2$ be nonempty closed subsets of a complete metric space (X, d) and $T : Y \to Y$ be a given mapping, where $Y = A_1 \cup A_2$. Suppose that the following conditions hold:*

(I) $T(A_1) \subseteq A_2$ and $T(A_2) \subseteq A_1$;

(II) there exists a constant $\lambda \in (0, 1)$ such that

$$d(Tx, Ty) \leq \lambda \max \left\{ d(x, y), \frac{d(x, Tx) + d(y, Ty)}{2}, \frac{d(x, Ty) + d(y, Tx)}{2} \right\}, \ \text{for all } (x, y) \in A_1 \times A_2.$$

Then T has a unique fixed point that belongs to $A_1 \cap A_2$.

Corollary 26. *Let $\{A_i\}_{i=1}^2$ be nonempty closed subsets of a complete metric space (X, d) and $T : Y \to Y$ be a given mapping, where $Y = A_1 \cup A_2$. Suppose that the following conditions hold:*

(I) $T(A_1) \subseteq A_2$ and $T(A_2) \subseteq A_1$;

(II) there exist constants $A, B, C \geq 0$ with $(A + 2B + 2C) \in (0, 1)$ such that

$$d(Tx, Ty) \leq Ad(x, y) + B[d(x, Tx) + d(y, Ty)] + C[d(x, Ty) + d(y, Tx)], \ \text{for all } (x, y) \in A_1 \times A_2.$$

Then T has a unique fixed point that belongs to $A_1 \cap A_2$.

Corollary 27 (see Kirk et al. [45]). *Let $\{A_i\}_{i=1}^2$ be nonempty closed subsets of a complete metric space (X, d) and $T : Y \to Y$ be a given mapping, where $Y = A_1 \cup A_2$. Suppose that the following conditions hold:*

(I) $T(A_1) \subseteq A_2$ and $T(A_2) \subseteq A_1$;

(II) there exists a constant $\lambda \in (0, 1)$ such that

$$d(Tx, Ty) \leq \lambda d(x, y), \ \text{for all } (x, y) \in A_1 \times A_2.$$

Then T has a unique fixed point that belongs to $A_1 \cap A_2$.

Corollary 28. *Let $\{A_i\}_{i=1}^2$ be nonempty closed subsets of a complete metric space (X, d) and $T : Y \to Y$ be a given mapping, where $Y = A_1 \cup A_2$. Suppose that the following conditions hold:*

(I) *$T(A_1) \subseteq A_2$ and $T(A_2) \subseteq A_1$;*

(II) *there exists a constant $\lambda \in (0, 1/2)$ such that*

$$d(Tx, Ty) \leq \lambda \left[d(x, Tx) + d(y, Ty) \right], \ \text{for all } (x, y) \in A_1 \times A_2.$$

Then T has a unique fixed point that belongs to $A_1 \cap A_2$.

Corollary 29. *Let $\{A_i\}_{i=1}^2$ be nonempty closed subsets of a complete metric space (X, d) and $T : Y \to Y$ be a given mapping, where $Y = A_1 \cup A_2$. Suppose that the following conditions hold:*

(I) *$T(A_1) \subseteq A_2$ and $T(A_2) \subseteq A_1$;*

(II) *there exists a constant $\lambda \in (0, 1/2)$ such that*

$$d(Tx, Ty) \leq \lambda \left[d(x, Ty) + d(y, Tx) \right], \ \text{for all } (x, y) \in A_1 \times A_2.$$

Then T has a unique fixed point that belongs to $A_1 \cap A_2$.

5   Conclusion

The fixed point theorem is one of the most actively studied research fields of recent times. Naturally, there are many publications on this subject and several new results are announced. This causes the literature to become rather disorganized and dysfunctional. The more troublesome situation is that the existing theorems are rediscovered again and again due to this messiness. More accurately, the results have been repeated. It is therefore essential to organize the fixed-point theory literature, weeding out false and/or repetitive results, and, if possible, combining and unifying existing results into a more general framework. In this work, we show that using admissible mapping, many existing fixed point theorems can be written as a consequence of the main theorem we have given.

Note that the consequences of the main result of the paper, Theorem 6 is not complete. It is possible to add several corollaries. On the other hand, we prefer to skip these possible consequences, since it is clear how the possible result can be concluded from our main theorem and how can be proved. Further, we underline that the main theorem can be derived in the distinct abstract spaces, such as, partial metric space, b-metric space, quasi-metric space, and so on.

REFERENCES

[1] **Agarwal R.P.**, **Alghamdi M.A.** and **Shahzad N.** (2012). Fixed point theory for cyclic generalized contractions in partial metric spaces. *Fixed Point Theory Appl.*, 2012:40.

[2] **Agarwal R.P.**, **El-Gebeily M.A.** and **O'Regan D.** (2008). Generalized contractions in partially ordered metric spaces. *Appl. Anal. 87*, 109–116.

[3] **Aksoy U.**, **Karapinar E.** and **Erhan I. M.** (2016). Fixed points of generalized alpha-admissible contractions on b-metric spaces with an application to boundary value problems. *Journal of Nonlinear and Convex Analysis, Volume 17*, Number 6, 1095-1108

[4] **Alharbi A.S. S.**, **Alsulami H. H.**, and **Karapinar E.** (2017). On the Power of Simulation and Admissible Functions in Metric Fixed Point Theory. *Journal of Function Spaces, Volume 2017* , Article ID 2068163, 7 pages

[5] **Ali M.U.**, **Kamram T.** and **Karapinar E.** (2014). An approach to existence of fixed points of generalized contractive multivalued mappings of integral type via admissible mapping. *Abstract and Applied Analysis,* Article Id: 141489

[6] **Ali M.U.**, **Kamram T.** and **Karapinar E.** (2014). Fixed point of $\alpha-\psi$-contractive type mappings in uniform spaces. *Fixed Point Theory and Applications.*

[7] **Ali M.U.**, **Kamram T.**, **Karapinar E.** (2014). A new approach to (α, ψ)-contractive nonself multivalued mappings. *Journal of Inequalities and Applications*, 2014:71.

[8] **Ali M.U.**, **Kamram T.** and **Karapinar E.** (2014). (α, ψ, ξ)-contractive multi-valued mappings. *Fixed Point Theory and Applications*, 2014, 2014:7

[9] **Ali M.U.**, **Kamram T.**, **Karapinar E.** (2016). Discussion on ϕ-Strictly Contractive Nonself Multivalued Maps. *Vietnam Journal of Mathematics* June 2016, Volume 44, Issue 2, pp 441-447

[10] **Al-Mezel S.**, **Chen C. M.**, **Karapinar E.** and **Rakocevic V.** (2014). Fixed point results for various α-admissible contractive mappings on metric-like spaces. *Abstract and Applied Analysis Volume 2014* , Article ID 379358

[11] **Alsulami H.**, **Gulyaz S.**, **Karapinar E.** and **Erhan I.M.** (2014). Fixed point theorems for a class of alpha-admissible contractions and applications to boundary value problem. *Abstract and Applied Analysis,* Article Id: 187031

[12] **Alsulami H.**, **Karapınar E.**, **Khojasteh F.**, **Roldán-López-de-Hierro A. F.** (2014). A proposal to the study of contractions in quasi-metric spaces. *Discrete Dynamics in Nature and Society 2014,* Article ID 269286, 10 pages.

[13] **Altun I.**, **Simsek H.** (2010). Some fixed point theorems on ordered metric spaces and application. *Fixed Point Theory Appl.* 2010, Article ID 621492, 17 pages.

[14] **Arshad M.**, **Ameer E.** and **Karapinar E.** (2016). Generalized contractions with triangular alpha-orbital admissible mapping on Branciari metric spaces. *Journal of Inequalities and Applications* 2016, 2016:63 (16 February 2016).

[15] **Aydi H.**, **Felhi A.**, **Karapinar E.** and **Alojail F.A.** (2018). Fixed points on quasi-metric spaces via simulation functions and consequences. *J. Math. Anal.*, 9, 10-24

[16] **Aydi H.**, **Karapinar E.** and **Yazidi H.** (2017). Modified F-Contractions via alpha-Admissible Mappings and Application to Integral Equations. *FILOMAT Volume: 31 Issue: 5* , Pages: 1141- 148 Published: 2017.

[17] **Aydi H.**, **Karapinar E.** and **Zhang D.** (2017). A note on generalized admissible-Meir-Keeler-contractions in the context of generalized metric spaces. *Results in Mathematics,* February 2017, Volume 71, Issue 1, pp 73-92.

[18] **Banach S.** (1922). Sur les opérations dans les ensembles abstraits et leur application aux equations itegrales. *Fund. Math. 3* 133-181.

[19] **Berinde V.** (1993). Generalized contractions in quasimetric spaces. *Seminar on Fixed Point Theory,* Preprint no. 3(1993), 3-9.

[20] **Berinde V.** (1996). Sequences of operators and fixed points in quasimetric spaces. *Stud. Univ. "Babeş-Bolyai", Math.*, 16(4), 23-27.

[21] **Berinde V.** (1997). Contracţii generalizate şi aplicaţii. *Editura Club Press 22, Baia Mare,* 1997.

[22] **Berinde V.** (2002). Iterative Approximation of Fixed Points. *Editura Efemeride, Baia Mare.*

[23] **Berinde V.** (2004). Approximating fixed points of weak contractions using the Picard iteration. *Nonlinear Anal. Forum. 9* 43-53.

[24] **Chatterjea S.K.** (1972). Fixed point theorems. **C.R. Acad. Bulgare Sci.** 25, 727-730.

[25] **Chen C.-M., Abkar A., Ghods S.** and **Karapinar E.** (2017). Fixed Point Theory for the ϕ-Admissible Meir-Keeler Type Set Contractions Having KKM* Property on Almost Convex Sets. *Appl. Math. Inf. Sci. 11*, No. 1, 171-176.

[26] **Ćirić Lj.B.** (1972). Fixed points for generalized multi-valued mappings. *Mat. Vesnik.* 9 (24), 265-272.

[27] **Ćirić Lj.** (1974). On some maps with a nonunique fixed point. *Pub. Inst. Math.* 17, 52-58.

[28] **Ćirić Lj.B.**, **Cakić N.**, **Rajović M.** and **Ume J.S.** (2008). Monotone generalized nonlinear contractions in partially ordered metric spaces. *Fixed Point Theory Appl.* 2008 Article ID 131294, 11 pages.

[29] **Dass B. K.** and **Gupta S.** (1975). An extension of Banach contraction principle through rational expression. *Indian. J. Pure. Appl. Math.*, 6, 1455-1458.

[30] **Eshraghisamani M., Vaezpour S. M., Asadi M.** (2018). New fixed point results with α_{qs^p}-admissible contractions on b–Branciari metric spaces. *Journal of Inequalities and Special Functions,* 9(3):38-46, 2018.

[31] **Gulyaz S., Karapinar E.** and **Erhanand I. M.** (2017) Generalized ψ–Meir-Keeler contraction mappings on Branciari b-metric spaces. *Filomat, vol. 31*, no. 17, pp. 5445-5456, 2017.

[32] **Hammache K.**, **Karapinar E.**, **Ould-Hammouda A.** (2017). On Admissible Weak Contractions in b-Metric-Like Space. *Journal Of Mathematical Analysis Volume: 8 Issue: 3*, Pages: 167-180 Published: 2017

[33] **Hardy G.E.** and **Rogers T.D.** (1973). A generalization of a fixed point theorem of Reich. *Canad. Math. Bull. 16*, 201-206.

[34] **Harjani J.** and **Sadarangani K.** (2008). Fixed point theorems for weakly contractive mappings in partially ordered sets. *Nonlinear Anal. 71*, 3403-3410.

[35] **Jaggi D. S.** (1977). Some unique fixed point theorems. *Indian. J. Pure. Appl. Math., Vol. 8*, No 2, 223-230.

[36] **Kannan R.** (1968). Some results on fixed points. *Bull. Clacutta. Math. Soc.* 10, 71-76.

[37] **Karapınar E.** (2011). Fixed point theory for cyclic weak ϕ-contraction. *Appl. Math. Lett.* 24 (6), 822-825.

[38] **Karapinar E.** (2013). On best proximity point of ψ-Geraghty contractions. *Fixed Point Theory and Applications*, 2013:200.

[39] **Karapınar E.** and **Sadaranagni K.** (2011). Fixed point theory for cyclic $(\phi$-$\psi)$-contractions. *Fixed Point Theory Appl.* , 2011:69.

[40] **Karapınar E.** and **B. Samet**, Generalized (α, ψ) contractive type mappings and related fixed point theorems with applications, Abstr. Appl. Anal , 2012 (2012) Article id: 793486

[41] **Karapinar E., Kumam P., Salimi P.** (2013). On α-ψ-Meir-Keeler contractive mappings. *Fixed Point Theory and Applications* 2013, 94.

[42] **Karapinar E.** (2016). Fixed points results via simulation functions. *Filomat* 2016, 30, 2343–2350

[43] **Karapinar E., Khojasteh F.** (2017). An approach to best proximity points results via simulation functions. *J. Fixed Point Theory Appl.* 2017, 19, 1983-1995.

[44] **Khojasteh F., Shukla S.** and **Radenović S.** (2015). A new approach to the study of fixed point theorems via simulation functions. *Filomat 29:6* , 1189-1194.

[45] **Kirk W.A.**, **Srinivasan P.S.** and **Veeramani P.** (2003). Fixed points for mappings satisfying cyclical contractive conditions. *Fixed Point Theory.* 4(1), 79–89.

[46] **Monfared H., Asadi M., Azhini M.** $F(\psi, \varphi)$-contractions for α–admissible mappings on metric spaces and related fixed point results. *Communications in Nonlinear Analysis* (CNA), 2(1):86-94, 2.

[47] **Monfared H., Asadi M., Azhini M.**, and **O'regan D.** (2018) $F(\psi, \varphi)$-contractions for α–admissible mappings on m-metric spaces. *Fixed Point Theory and Applications,* 2018(1):22, 2018.

[48] **Monfared H., Asadi M., Farajzadeh A.** (2020). New generalization of Darbo's fixed point theorem via α-admissible simulation functions with application. *Sahand Communications in Mathematical Analysis*, 17(2):161-171, 2020.

[49] **Nieto J.J.** and **Rodríguez-López R.** (2005). Contractive Mapping Theorems in Partially Ordered Sets and Applications to Ordinary Differential Equations. *Order.* 22, 223–239.

[50] **Ozyurt S. G.** (2017). On some alpha-admissible contraction mappings on Branciari b-metric spaces. *Advances in the Theory of Nonlinear Analysis and its Applications,* vol. 1, no. 1, pp. 1–13, 2017.

[51] **Pacurar M.** and **Rus I.A.** (2010). Fixed point theory for cyclic φ-contractions. *Nonlinear Anal.*, 72, 1181–1187.

[52] **Petric M.A.** (2010). Some results concerning cyclical contractive mappings. *General Mathematics.* 18 (4), 213-226.

[53] **Petruşel A.** and **Rus I.A.** (2006). Fixed point theorems in ordered L-spaces. *Proc. Amer. Math. Soc.* 134, 411–418.

[54] **Popescu O.** (2014). Some new fixed point theorems for α-Geraghty contraction type maps in metric spaces. *Fixed Point Theory Appl.* 2014, 2014:190

[55] **Ran A.C.M.** and **Reurings M.C.B.** (2003). A fixed point theorem in partially ordered sets and some applications to matrix equations. *Proc. Amer. Math. Soc.*, 132, 1435-1443.

[56] **Roldán-López-de-Hierro A. F., Karapınar E., Roldán-López-de-Hierro C., Martínez-Moreno J.** (2015). Coincidence point theorems on metric spaces via simulation functions. *J. Comput. Appl. Math.* 275, 345–355.

[57] **Rus I.A.** (2005). Cyclic representations and fixed points. *Ann. T. Popoviciu, Seminar Funct. Eq. Approx. Convexity* 3, 171-178.

[58] **Rus, I. A.** (2001). Generalized contractions and applications. *Cluj University Press, Cluj-Napoca,* 2001.

[59] **Samet B.** (2010). Coupled fixed point theorems for a generalized Meir-Keeler contraction in partially ordered metric spaces. *Nonlinear Anal.* 72. 4508-4517.

[60] **Samet B.** (2014). Fixed Points for $\alpha - \psi$ Contractive Mappings With An Application To Quadratic Integral Equations. *Electronic Journal of Differential Equations,* Vol. 2014 , No. 152, pp. 1–18.

[61] **Samet B.**, **Vetro C.** and **Vetro P.** (2012). Fixed point theorem for $\alpha - \psi$ contractive type mappings. *Nonlinear Anal.* 75, 2154-2165.

[62] **Stephen T., Rohen Y., Saleem N., Devi M. B.** and **Singh K. A.** (2021). Fixed Points of Generalized ψ-Meir-Keeler Contraction Mappings in -Metric Spaces. *Journal of Function Spaces,* vol. 2021, Article ID 4684290, 8 pages, 2021. https://doi.org/10.1155/2021/4684290

[63] **Suzuki T.** (2008). A generalized Banach contraction principle that characterizes metric completeness. *Proc. Amer. Math. Soc. 136*, 1861-1869.

[64] **Suzuki T.** (2008). Some similarity between contractions and Kannan mappings. *Fixed Point Theory Appl.* 2008, Article ID 649749, 1-8.

[65] **Turinici M.** (1986). Abstract comparison principles and multivariable Gronwall-Bellman inequalities. *J. Math. Anal. Appl.*, 117, 100-127.

/03/

ESSENTIAL SPECTRUM OF DISCRETE LAPLACIAN – REVISITED

V. B. Kiran Kumar

Department of Mathematics, Cochin University of Science And Technology, Kochi, Kerala, (India).

E-mail:vbk@cusat.ac.in

ORCID:0000-0001-7643-4436

https://doi.org/10.17993/3ctic.2022.112.52-59

ABSTRACT

Consider the discrete Laplacian operator A acting on $l^2(\mathbb{Z})$. It is well known from the classical literature that the essential spectrum of A is a compact interval. In this article, we give an elementary proof for this result, using the finite-dimensional truncations A_n of A. We do not rely on symbol analysis or any infinite-dimensional arguments. Instead, we consider the eigenvalue-sequences of the truncations A_n and make use of the filtration techniques due to Arveson. Usage of such techniques to the discrete Schrödinger operator and to the multi-dimensional settings will be interesting future problems.

KEYWORDS

Essential Spectrum, Discrete Laplacian

1   INTRODUCTION

In this short article, we consider the discrete Laplacian operator A defined on $l^2(\mathbb{Z})$, as follows:

$$A(x(n)) = (x(n-1) + x(n+1)); x = (x(n)) \in l^2(\mathbb{Z}), n \in \mathbb{Z}.$$

This operator arises naturally in many physical situations. For example, when we approximate a partial differential equation by finite differences, such bounded operators come into the picture. This operator is widely used in image processing, particularly in edge detection problems. There are extensions of the discrete Laplacian to various settings, such as multi-dimensional operator (on $\mathbb{Z}^n$) and Laplacian on graphs, etc. An operator close to this example is the discrete Schrödinger operator. This operator can be considered as a perturbation of the discrete Laplacian, defined as follows;

$$H(x(n)) = (x(n-1) + x(n+1) + v(n)x(n)); x = (x(n)) \in l^2(\mathbb{Z}), n \in \mathbb{Z}.$$

Here the sequence $v = v(n)$ is a bounded sequence called the potential.

It is well-known from the classical theory that the spectrum of A is the compact interval $[-2, 2]$. In this article, we use the filtration techniques developed by W. B. Arveson in [1] and some elementary method to give a simple proof of this result. We plan to use such techniques in the computation of the spectrum of the discrete Schrödinger operator. However, the spectrum of the discrete Schrödinger operator can be very complicated, depending on the potential function. For example, if you choose the almost Mathieu potential, the spectrum will be a Cantor-like set (The Ten-Martini Conjecture, see [2] for, eg.).

The article is organized as follows. In the next section, we describe some essential results from [1, 3] in connection with the spectral approximation of an infinite-dimensional bounded self-adjoint operator. In the third section, we use these techniques to give an elementary proof of the connectedness of the essential spectrum of A. A possible application to the spectral computation of some special class of discrete Schrödinger operators is mentioned at the end of this article.

2   OPERATORS IN THE ARVESON'S CLASS

"How to approximate spectra of linear operators on separable Hilbert spaces?"is a fundamental question and was considered by many mathematicians. One of the successful methods is to use the finite-dimensional theory in the computation of the spectrum of bounded operators in an infinite dimensional space through an asymptotic way. In 1994, W.B. Arveson identified a class of operators for which the finite-dimensional truncations are helpful in the spectral approximation [1]. We introduce this class of operators here.

Let A be a bounded self-adjoint operator defined on a complex separable Hilbert space $\mathcal{H}$ and $\{e_1, e_2, \ldots\}$ be an orthonormal basis for $\mathcal{H}$. Consider the finite dimensional truncations of A, that is $A_n = P_n A P_n$, where P_n is the projection of $\mathcal{H}$ onto the span of first n elements $\{e_1, e_2, \ldots, e_n\}$ of the basis. We recall the notion of essential points and transient points introduced in [1].

Definition 1. *Essential point: A real number λ is an essential point of A, if for every open set U containing λ, $\lim_{n\to\infty} N_n(U) = \infty$, where $N_n(U)$ is the number of eigenvalues of A_n in U.*

Definition 2. *Transient point: A real number λ is a transient point of A if there is an open set U containing λ, such that $\sup N_n(U)$ with n varying on the set of all natural number is finite.*

Remark 3. *Note that a number can be neither transient nor essential.*

Denote $\Lambda = \{\lambda \in R; \lambda = \lim \lambda_n, \lambda_n \in \sigma(A_n)\}$ and Λ_e as the set of all essential points. The following spectral inclusion result for a bounded self-adjoint operator A is of high importance. Let $\sigma(A), \sigma_{ess}(A)$ denote the spectrum and essential spectrum of A respectively.

Theorem 4. *[1] The spectrum of a bounded self-adjoint operator is a subset of the set of all limit points of the eigenvalue sequences of its truncations. Also, the essential spectrum is a subset of the set of all essential points. That is,*

$$\sigma(A) \subseteq \Lambda \subseteq [m, M] \ \ and \ \sigma_{ess}(A) \subseteq \Lambda_e.$$

W.B Arveson, generalized the notion of band limited matrices in [1], and achieved some useful results in the case of some special class of operators. He used an arbitrary filtration H_n (an increasing subsequence of closed subspaces with the union dense in $\mathcal{H}$) and the sequence of orthogonal projections onto H_n to introduce his class of operators. Here we consider only a special case.

Definition 5. *The **degree** of a bounded operator A on $\mathbb{H}$ is defined by*

$$deg(A) = \sup_{n \geq 1} \ rank(P_n A - A P_n).$$

A Banach $*-$algebra of operators can be defined, which we call **A**rveson's class, as follows.

Definition 6. *A is an operator in the **Arveson's class** if*

$$A = \sum_{n=1}^{\infty} A_n, \ \ where \ deg(A_n) < \infty \ for \ every \ n \ and \ convergence \ is \ in \ the$$

operator norm, in such a way that

$$\sum_{n=1}^{\infty} (1 + \ deg(A_n)^{\frac{1}{2}}) \|A_n\| < \infty$$

The following gives a concrete description of operators in Arveson's class.

Theorem 7. *[1] Let $(a_{i,j})$ be the matrix representation of a bounded operator A, with respect to $\{e_n\}$, and for every $k \in \mathbb{Z}$ let*

$$d_k = \sup_{i \in \mathbb{Z}} |a_{i+k,i}|$$

be the sup norm of the kth diagonal of $(a_{i,j})$. Then A will be in Arveson's class whenever the series $\sum_k |k|^{1/2} d_k$ converges.

Remark 8. *In particular, any operator whose matrix representation $(a_{i,j})$ is band-limited, in the sense that $a_{i,j} = 0$ whenever $|i - j|$ is sufficiently large, must be in Arveson's class. Therefore, the operator under our consideration is in Arveson's class, as we see that its matrix representation is tridiagonal.*

The following result allows us to confine our attention to essential points while looking for essential spectral values for certain classes of operators.

Theorem 9. *[1] If A is a bounded self-adjoint operator in the Arveson's class, then $\sigma_{ess}(A) = \Lambda_e$ and every point in Λ is either transient or essential.*

3   SPECTRUM OF DISCRETE LAPLACIAN

Consider the discrete Laplacian operator A defined on $l^2(\mathbb{Z})$, as follows:

$$A(x(n)) = (x(n-1) + x(n+1)); x = (x(n)) \in l^2(\mathbb{Z}), n \in \mathbb{Z}.$$

If we use the standard orthonormal basis on $l^2(\mathbb{Z})$, the truncations A_n will have the following matrix representations:

$$A_n = \begin{bmatrix} 0 & 1 & 0 & 0 & & . & & & & \\ 1 & 0 & 1 & 0 & 0 & & . & & & \\ 0 & 1 & 0 & 1 & 0 & 0 & & . & & \\ 0 & 0 & 1 & 0 & 1 & 0 & 0 & & . & \\ & 0 & 0 & 1 & 0 & 1 & 0 & 0 & & . \\ . & & 0 & 0 & 1 & 0 & 1 & 0 & 0 & \\ & . & & 0 & 0 & 1 & 0 & 1 & 0 & 0 \\ & & . & & 0 & 0 & 1 & 0 & 1 & 0 \\ & & & . & & 0 & 0 & 1 & 0 & 1 \\ & & & & . & & 0 & 0 & 1 & 0 \end{bmatrix}$$

Now we recollect some properties of the discrete Laplacian operator below.

Lemma 1. $\lambda \in \sigma_{ess}(A)$ *if and only if* $-\lambda \in \sigma_{ess}(A)$.

Proof. Notice that this operator A is in Arveson's class, introduced in the last section. Therefore, we have $\lambda \in \sigma_{ess}(A)$ if and only if λ is an essential point. That is exactly when $N_n(U) \to \infty$ for every neighborhood U of λ. The characteristic polynomials of A_n are $P_n(z) = z^n - a_{n-2}z^{n-2} + \ldots \pm 1$, when n is even and $P_n(z) = -z^n + a_{n-2}z^{n-2} - \ldots \pm a_1 z$, when n is odd. Here the coefficients can be computed as follows. $a_k = \frac{(n-k+2)(n-k+4)\ldots(n+k)}{2^k.k!}$

Therefore the eigenvalues of A_n are distributed symmetrically on both sides of 0 in the interval $[-2,2]$. Hence the number of truncated eigenvalues in any neighbourhood of $-\lambda$ and λ are the same if the neighbourhoods are of the same length. We can conclude that $\lambda \in \sigma_{ess}(A)$ if and only if $-\lambda \in \sigma_{ess}(A)$.

Lemma 2. *The operator norm* $\|A\| = 2$ *and* $\pm 2 \in \sigma_{ess}(A)$.

Proof. For every $x \in l^2(\mathbb{Z})$, we have

$$\|Ax\|^2 = \sum_{-\infty}^{\infty}(x(n-1) + x(n+1))^2 = \sum_{-\infty}^{\infty}\left[(x(n-1))^2 + (x(n+1))^2 + 2x(n-1)x(n+1)\right] \le 4\|x\|^2.$$

Therefore, $\|A\| \le 2$.

To prove the equality, consider the sequence $x_n = \left(\ldots 0, 0, 0, \ldots \frac{1}{n}, \frac{1}{n}, \frac{1}{n} \ldots \frac{1}{n}, 0, 0, 0 \ldots\right)$, where $\frac{1}{n}$ repeats n^2 times and all other entries are 0. Then x_n has norm 1 and $\|Ax_n\|$ increases to 2. Hence $\|A\| = 2$. Since A is a bounded self-adjoint operator, either $\|A\|$ or $-\|A\|$ is always a spectral value. That is 2 or -2 is in the spectrum, $\sigma(A)$. However, they are not eigenvalues of A, as we see below.

If ± 2 is an eigenvalue of A, then 4 is an eigenvalue of $A^2 = B + 2I$ where B is defined by $B(e_n) = e_{n-2} + e_{n+2}$. (Observe that A^2 is defined as $A^2(e_n) = e_{n-2} + 2e_n + e_{n+2}$). This will imply that 2 is eigenvalue of B. If $Bx = 2x$, for some nonzero x, then $x(n+2) + x(n-2) = 2x(n)$, for all n. Let $x(N) = p \ne 0$, for some N and $x(N-2) = q$. Then $x(n+2k) = (k+1)p - kq$ for every $k\mathbb{Z}$. Such an element x will not be in $l^2(Z)$.

Hence ± 2 is an essential spectral value. By Lemma 1, both ± 2 are in the essential spectrum, $\sigma_{ess}(A)$. Therefore both 2 and -2 are in $\sigma_{ess}(A)$.

Theorem 10. *The spectral gaps of A, if they exist, will appear symmetrically with respect to the origin. That means corresponding to each spectral gap on the positive real axis, there exists a spectral gap on the negative real axis. In particular, A cannot have an odd number of spectral gaps.*

Proof. We noticed that $A^2 = B + 2I$ where B is defined by $B(e_n) = e_{n-2} + e_{n+2}$. It is worthwhile to notice further that $\|B\| = 2$. This follows easily from the following arguments.

$$\|Bx\|^2 = \sum_{-\infty}^{\infty} (x(n-2) + x(n+2))^2 = \sum_{-\infty}^{\infty} \left[(x(n-2))^2 + (x(n+2))^2 + 2x(n-2)x(n+2) \right] \leq 4\|x\|^2.$$

Therefore we have $\|B\| \leq 2$. Now consider the sequence $x_n = \left(...0, 0, 0, ... \frac{1}{n}, \frac{1}{n}, \frac{1}{n} ... \frac{1}{n}, 0, 0, 0... \right)$ where $\frac{1}{n}$ repeats n^2 times and all other entries 0, has norm 1 and $\|Bx_n\|$ increases to 2. Hence $\|B\| = 2$. Also as in the case of A, the truncated eigenvalues are distributed symmetrically on both sides of 0, so that -2 and 2 are in the essential spectrum. Also, since $A^2 = B + 2I$, this implies that 0 is an essential spectral value of A^2, and hence of A. Hence any spectral gap of A can occur either to the right or left side of 0. By Lemma 1, each spectral gap on the right side of 0 will also give a spectral gap on the left side. Hence the proof.

Theorem 11. *The essential spectrum of A is connected. The spectrum and the essential spectrum coincide with the compact interval $[-2, 2]$.*

Proof. First, we show that A has no eigenvalues. This will imply that the spectrum and essential spectrum coincide, as the essential spectrum consists of discrete eigenvalues of finite multiplicity. If $Ax = \lambda x$, for some nonzero x, then

$$x(n+1) + x(n-1) = \lambda x(n), \text{ for all } n.$$

Let $x(N) = p \neq 0$, for some N and $x(N-1) = q$. Then a recursive argument similar to that in the proof of Lemma 2 will show that such a vector will not lie in $l^2(Z)$.

By Theorem 10, spectral gaps can occur symmetrically to the origin. Hence it suffices to show that there is no spectral gap to the right side of the origin. We consider each possible case for the existence of a spectral gap. We rule them out one by one. First consider the case when the spectral gap is of the form $(a, 2)$, with $0 \leq a \leq 1$. In this case, since the interval $(a, 2)$ contains no essential points (as the essential spectrum coincides with the set of all essential points), it will contain at most K eigenvalues of truncations for infinitely many n. Let $\lambda_{n1}, \lambda_{n2}, \lambda_{n3}, \ldots \lambda_{nK}$ be those eigenvalues. From the expression of characteristic polynomials, it is evident that the determinant of $A'_n s$ is either 0 or ± 1. Since the eigenvalues are distributed symmetrically to both sides of 0, we have the product of positive eigenvalues equal 1 for n even. Let $s_K := \prod_{i=1}^{K} \lambda_{ni}$. Then $\frac{1}{s_K} > \frac{1}{2^K}$, since $\lambda_{ni} < 2$ for $i = 1, 2, \ldots K$.

But since 0 is in the essential spectrum, it is an essential point, and we can find an N such that the interval $\left(0, \frac{1}{2}\right)$ contains at least $K+1$ eigenvalues of A_n for every $n \geq N$. For such an $n \geq N$, let $\alpha_{n1}, \alpha_{n2}, \alpha_{n3}, \ldots \alpha_{nN-K}$ be the eigenvalues of A_n, in $(0, a)$. Therefore we have,

$$\frac{1}{2^K} < \frac{1}{s_K} = \prod_{i=1}^{N-K} \alpha_{ni} < \prod_{i=1}^{K+1} \alpha_{ni} < \frac{1}{2^{K+1}} < \frac{1}{2^K}.$$

The first equality holds since the product of eigenvalues is 1, and the consequent inequality is because $a \leq 1$ (each additional α_{ni} we multiply will be a positive number below 1. Hence, the product will satisfy this inequality). This contradiction leads to the fact that $(a, 2)$, with $0 \leq a \leq 1$ is not a spectral gap.

Now we see that $(a, 2)$, with $a > 1$ cannot be a spectral gap. For if $(a, 2), a > 1$ is a gap, then it will contain at most K eigenvalues of truncations for infinitely many n. Let $\lambda_{n1}, \lambda_{n2}, \lambda_{n3}, \ldots \lambda_{nK}$ be those eigenvalues. As in the above case, let $s_K := \prod_{i=1}^{K} \lambda_{ni}$. Then $\frac{1}{s_K} > \frac{1}{2^K}$ Find an N such that the interval $\left(0, \frac{1}{2a^N}\right)$ contains at least $K+1$ eigenvalues of A_N. Now let $\alpha_{n1}, \alpha_{n2}, \alpha_{n3}, \ldots \alpha_{nN-K}$ be the eigenvalues of A_N, in $(0, a)$. Therefore we have

$$\frac{1}{s_k} = \prod_{i=1}^{N-K} \alpha_{ni} < \left(\frac{1}{2a^N}\right)^{K+1} a^{N-(2K+1)} < \left(\frac{1}{2}\right)^{K+1} < \frac{1}{2^K}.$$

The inequality is a consequence of $a > 1$. This contradiction leads to the fact that $(a, 2), a > 1$ is not a gap.

Hence we have seen that there cannot have a spectral gap of the form $(a, 2)$, with a being a non-negative real number. The number 2 does not play any role in the proof. We can easily imitate the proof techniques for intervals of the form (a, b), with $0 \leq a < b \leq 2$.

Remark 12. *We can have a different and straight forward argument to show that $(a, 2)$ cannot be a spectral gap. However, this method cannot be extended for arbitrary intervals (a, b), with $0 \leq a < b \leq 2$. For if $(a, 2)$ is a gap, then 2 will be an isolated point in the essential spectrum. Since the interval $(a, 2)$ contains at most K eigenvalues of truncations, but 2 is an essential point, we need 2 is an eigenvalue of A_n for large values of n with multiplicity increases to infinity. Nevertheless, 2 is not an eigenvalue of A_n for any n. For if*

$$
\begin{bmatrix}
0 & 1 & & & & & & & & \\
1 & 0 & 1 & & & & & & & \\
& 1 & 0 & 1 & & & & & & \\
& & 1 & 0 & 1 & & & & & \\
& & & 1 & 0 & 1 & & & & \\
& & & & . & . & . & & & \\
& & & & & . & . & . & & \\
& & & & & & . & . & . & \\
& & & & & & & 1 & 0 & 1 \\
& & & & & & & & 1 & 0
\end{bmatrix}
\begin{bmatrix}
x_1 \\ x_2 \\ x_3 \\ x_4 \\ . \\ . \\ . \\ . \\ x_n
\end{bmatrix}
= 2
\begin{bmatrix}
x_1 \\ x_2 \\ x_3 \\ x_4 \\ . \\ . \\ . \\ . \\ x_n
\end{bmatrix}
$$

then
$x_2 = 2x_1$
$x_3 = 3x_1$
$x_4 = 4x_1, \ldots x_{n-1} = (n-1)x_1, x_n = nx_1$
Also $x_{n-1} = 2x_n = 2nx_1$
But this will hold only when $x_1 = 0$ which makes $x = 0$ and hence 2 is not an eigenvalue. Hence we conclude that $(a, 2)$ is not a gap.

Remark 13. *The eigenvalues of the matrices A_n are explicitly calculated to be $2\cos(\pi k/n + 1), k = 1, 2, 3...n$. We may arrive at some conclusions from that information also.*

Remark 14. *An important question is whether we can approximate the eigenvalues of A using the eigenvalues of truncation. Since the operator we considered has no eigenvalues, it is interesting to see from the truncations itself whether the operator has an eigenvalue or not. In general, we observe the following; If $\lambda = \lim \lambda_n, \lambda_n \in \sigma(A_n)$ and if the sequence of eigenvectors x_n corresponding to λ_n, is Cauchy in $\mathcal{H}$, then λ is an eigenvalue of A. This can easily be seen as follows.*

Let x_n converges to some x in $\mathcal{H}$. $\lambda = \lim \lambda_n, x = \lim x_n$ together imply $\lambda x = \lim \lambda_n x_n$ Also $\lim A_n x_n = Ax$. Hence for any $\epsilon > 0$, there is an N such that $\|\lambda - \lambda_N x_N\| < \frac{\varepsilon}{2}, \|Ax - A_N x_N\| < \frac{\varepsilon}{2}$ Hence for any $\epsilon > 0, \|Ax - \lambda x\| < \varepsilon$. That is λ is an eigenvalue of A.

4 CONCLUDING REMARKS

We used only elementary tools and the filtration techniques due to Arveson to prove the connectedness of the essential spectrum. When we consider the Discrete Schrödinger operator H defined by

$$H(x(n)) = (x(n-1) + x(n+1) + v(n)x(n)); x = (x(n)) \in l^2(\mathbb{Z}), n \in \mathbb{Z},$$

with the potential sequence $v = v(n)$ being periodic, there will be spectral gaps unless when v is constant (see [4,5] for example). However, if we write the matrix representation with respect to the standard orthonormal basis, it is tridiagonal; hence, Arveson's techniques are available. Here the spectral analysis depends on the nature of the potential. The spectral gap issues of such operators were studied with the linear algebraic techniques in [6]. The spectral gap issues of arbitrary bounded self-adjoint operators can be found in the literature (see [7,8] for example).

Another interesting point is to carry over such techniques to the multi-dimensional case by replacing $\mathbb{Z}$ by $\mathbb{Z}^n$.

ACKNOWLEDGMENT

REFERENCES

[1] **W.B. Arveson**, (1994). C^*- algebras and numerical linear algebra. *J. Funct. Anal.* **122** *, no.2*, pp. 333–360.

[2] **A. Avila**, and **S. Jitomirskaya** (2009). The Ten Martini Problem *Ann. of Math.* **170** *, no.1*, pp. 303–342.

[3] **A. Böttcher**, **A.V. Chithra**, and **M.N.N. Namboodiri** (2001). Approximation of approximation numbers by truncation *Integral Equations Operator Theory* **39** *,* pp. 387–395.

[4] **L. Golinskii**,**V. B. Kiran Kumar**, **M.N.N. Namboodiri**, and **S. Serra-Capizzano**, (2013). A note on a discrete version of Borg's Theorem via Toeplitz-Laurent operators with matrix-valued symbols *Boll. Unione Mat. Ital.* **39**, *no.1* , pp. 205–218.

[5] **V. B. Kiran Kumar**, **M.N.N. Namboodiri**, and **S. Serra-Capizzano**, (2014). Perturbation of operators and approximation of spectrum *Proc. Indian Acad. Sci. Math. Sci.* **124** *(2014), no. 2,* , pp. 205–224.

[6] **V. B. Kiran Kumar**(2015). Truncation Method for Random Bounded Self-adjoint Operators *Banach J. Math. Anal. 9 no.3*, pp. 98–113.

[7] **M.N.N. Namboodiri**(2002). Truncation method for Operators with disconnected essential spectrum *Proc.Indian Acad.Sci.(MathSci) 112* , pp. 189–193.

[8] **M.N.N. Namboodiri**(2005). Theory of spectral gaps- A short survey *J.Analysis 12* , pp. 1–8.

/04/

REIDEMEISTER NUMBER IN LEFSCHETZ FIXED POINT THEORY

T. Mubeena

Assistant Professor, Department of Mathematics, University of Calicut. Malappuram (India).

E-mail: mubeenatc@uoc.ac.in, mubeenatc@gmail.com

ORCID:https://orcid.org/0000-0002-2493-5893

https://doi.org/10.17993/3ctic.2022.112.61-70

ABSTRACT

Several interesting numbers such as the homotopy invariant numbers the Lefschets number $L(f)$, the Nielsen number $N(f)$, fixed point index $i(X, f, U)$ and the Reidemeister number $R(f)$ play important roles in the study of fixed point theorems. The Nielsen number gives more geometric information about fixed points than other numbers. However the Nielsen number is hard to compute in general. To compute the Nielsen number, Jiang related it to the Reidemeister number $R(f_\pi)$ of the induced homomorphism $f_\pi : \pi_1(X) \to \pi_1(X)$ when X is a lens space or an H-space (Jian type space). For such spaces, either $N(f) = 0$ or $N(f) = R(f)$ the Reidemeister number of f_π and if $R(f) = \infty$ then $N(f) = 0$ which implies that f is homotopic to a fixed point free map. This is a review article to discuss how these numbers are related in fixed point theory.

KEYWORDS

Twisted conjugacy, Reidemiester number, Lefschetz number, Nielsen number, Jiang space

1 INTRODUCTION

Let $\phi : G \to G$ be an endomorphism of an infinite group G. One has an equivalence relation $\sim_\phi$ on G defined as $x \sim_\phi y$ if there exists a $g \in G$ such that $y = gx\phi(g)^{-1}$. The equivalence classes are called the Reidemeister classes of ϕ or ϕ-conjugacy classes. When ϕ is the identity, the Reidemeister classes of ϕ are the usual conjugacy classes. The Reidemeister classes of ϕ are the orbits of the action of G on itself defined as $g.x = gx\phi(g^{-1})$. The Reidemeister classes of ϕ containing $x \in G$ is denoted $[x]_\phi$ or simply $[x]$ when ϕ is clear from the context. The set of all Reidemeister classes of ϕ is denoted by $\mathcal{R}(\phi)$. We denote by $R(\phi)$ the cardinality of $\mathcal{R}(\phi)$ if it is finite and if it is infinite we set $R(\phi) := \infty$ and $R(\phi)$ is called the Reidemeister number of ϕ on G. We say that G has the R_∞-property if the Reidemeister number of ϕ is infinite for every automorphism ϕ of G. If G has the R_∞-property, we call G an R_∞-group.

The notion of Reidemeister number originated in the Nielsen–Reidemeister fixed point theory. See [?] and the references therein. The problem of determining which classes of groups have R_∞-property is an area of active research. Many mathematicians have been trying to determine which class of groups have the R_∞-property using the internal structure of the class, such as Lie group structure, C^*-algebra structure or purely algebraic properties of the class. There is no particular way to solve this problem, which makes it more difficult and interesting. If X is an H-space or a lens space, their fundamental groups are abelian. The Reidemeister number of an endomorphism of an abelian group is easily computable in many cases. In fact, if G is an abelian group, $\mathcal{R}(\phi)$ is an abelian group under the well defined operation $[x][y] := [xy], x, y \in G$.

The R_∞-property does not behave well with respect to finite index subgroups and quotients as the D_∞ and any free group of rank $n > 1$ has the R_∞-property although the infinite cyclic group and finitely generated free abelian groups, which are quotients of free groups, do not (ref. [5], [4]). Thus the R_∞-property is not invariant under quasi isometry, that is it is not *geometric* among the class of all finitely generated groups. The works of Levitt and Lustig [5] and Felshtyn [2] show that this property is geometric in the class of non-elementary hyperbolic groups. It is been proved in [7] that the R_∞-property is geometric for the class of all finitely generated groups that are quasi-isometric to irreducible lattices in real semisimple Lie groups with finite centre and finitely many connected components. The R_∞-property for irreducible lattices was proved in [6].

We have stated some results without proofs. For proofs and further readings, we refer the reader [1].

2 THE LEFSCHETZ NUMBER

Let X be a connected compact ANR and $f : X \to X$ a continuous map. We have seen fixed point theorems like Brouwer fixed point theorem that states "Any map $f : \mathbb{D}^n \to \mathbb{D}^n$ has a fixed point" where $\mathbb{D}^n$ is the closed disk in $\mathbb{R}^n$ and the traditional Lefschetz fixed point theorem that states "If $L(f) \neq 0$ then f has a fixed point", where $L(f)$ is the Lefschetz number with respect to the rational homology. Our statement of the Lefschetz fixed point theorem differs from the traditional one. We will prove the theorem for $L(f, \mathbb{F})$, where $\mathbb{F}$ is any field, because it is often easier to compute $L(f, \mathbb{F})$ if the field is chosen properly than it is to compute $L(f)$, and the conclusion is for all maps homotopic to f rather than just for the map f. An important reason, however, was that the converse of the traditional statement is -"If $L(f) = 0$, then f is fixed point free"- and this is trivially false (we will see an example). On the other hand, the converse of our statement is -"If $L(f, \mathbb{F}) = 0$ for all fields $\mathbb{F}$, then there is a fixed point free map g homotopic to f". This is true. A proof can be seen in [1].

To define the Lefschetz number we need the following definitions. A subset A of a space X is called a *neighbourhood retract* of X if there exists an open subset U of X containing A and a retraction of U onto A, i.e., a map $r : U \to A$ such that the restriction of r to A is the identity map. A space X is an *absolute neighbourhood retract* (**ANR**) if it has the following property: If X imbeds into a separable metric space Y, then X is a neighbourhood retract of Y. The ANR property is a topological invariant. A compact space X is a *compact **A**NR* if and only if there exists an imbedding $i : X \to I^\infty$ such that

$i(X)$ is a neighbourhood retract of I^∞, where

$$I^\infty = \bigsqcup_{n \in \mathbb{N}} [\frac{-1}{n}, \frac{1}{n}]$$

is the infinite Hilbert cube with the metric $d(x_n, y_n) = (\sum |x_n{}^2 - y_n{}^2|)^{1/2}$. I^∞ itself is an ANR by definition. Since $i : \mathbb{D}^n \to I^\infty$ defined by $(x_1, ...x_n) \mapsto (x_1, x_2/2, ...x_n/n, 0, 0....)$ is an imbedding such that $i(\mathbb{D}^n)$ is a retraction of I^∞, the n-cell $\mathbb{D}^n$ is an ANR. Any locally finite polyhedron is an ANR. Open subsets of an ANR and a neighbourhood retract of an ANR are also an ANR.

Throughout this note we will assume X is a connected compact ANR. Note that any compact ANR has only countably many connected components with each is open and an ANR. For a compact ANR, the homology $H_*(X, \mathbb{F})$ is a finitary graded $\mathbb{F}$-vector space and any map $f : X \to X$ induces a morphism $f_* : H_*(X, \mathbb{F}) \to H_*(X, \mathbb{F})$ between the homology groups which is a morphism of finitary graded vector space over $\mathbb{F}$.

Definition 1. *Let $f : X \to X$ be a map on X, $\mathbb{F}$ be a field. The Lefschetz number of f over $\mathbb{F}$ is defined to be the number:*

$$L(f, \mathbb{F}) := \sum (-1)^q Tr(f_q)$$

We denote $L(f) = L(f, \mathbb{Q})$.

We state the Lefschets fixed point theorem without proof.

Theorem 1 (Lefschetz Fixed Point Theorem ([1])). *If X is a compact ANR and $f : X \to X$ is a map such that $L(f, \mathbb{F}) \neq 0$ for some field $\mathbb{F}$, then every map homotopic to f has a fixed point.*

For any field $\mathbb{F}$ the homology and cohomology are isomorphic and the induced morphism is the transpose of f_* so we can define the Lefschetz number using the cohomolgy too.

Observe that: (1) for the identity map 1_X of X, the Lefschetz number

$$L(1_X) = \sum_q (-1)^q Tr(1_q) = \sum (-1)^q dim(H_q(X, \mathbf{q})) = \sum (-1)^q b_q = \chi(X)$$

where $\chi(X)$ is the Euler characteristic and b_q is the qth Betti number of X. (2) Since homotopic maps induce the same homomorphism on the homology groups, if $f : X \to X$ any continuous map and if g is homotopic to f then $L(g, \mathbb{F}) = L(f, \mathbb{F})$ for all field $\mathbb{F}$.

A space X is said to have the *fixed point property* if every continuous self map on X has a fixed point. Thus a contractible compact ANR X has fixed point property since $H_q(X, \mathbb{Q}) = 0, \forall q \neq 0$ and $H_0 = \mathbb{Q}$, thus $L(f) = 1$ (since every map on a path connected space induces the identity morphism on H_0) implies f has a fixed point by the Lefschetz fixed point theorem. For $X = \mathbb{S}^n$, the $n-$sphere, $\chi(X) = 0$ whenever n is odd. Thus the converse of the traditional fixed point theorem is false. Brouwer Fixed point theorem is an immediate consequence of the Lefschetz fixed point theorme, for; let $f : \mathbb{D}^n \to \mathbb{D}^n$ is any map. Since I^∞ is a contractible compact ANR and since retract of a space with fixed point property has the fixed point property, f has a fixed point.

3   Index for ANRs

For X, a compact ANR, a map $f : X \to X$, and an open set U of X without fixed points of f on its boundary it is possible to associate a number $i(X, f, U)$, the index of f on U. We define the index for such triples.

3.1   The axioms for an index

Let $\mathcal{C}_A$ denote the collection of all connected compact ANR spaces X where the Lefschetz number is defined since $H_*(X, \mathbf{q})$ is finitary. We define index for triples $i(X, f, U)$ with the following propeties:

1. $X \in \mathcal{C}_A$,

2. $f : X \to X$ is a map,

3. U is open in X,

4. there are no fixed points of f on the boundary of U.

The collection of such triples (X, f, U) is denoted by $\mathcal{C}$. Observe that $(X, f, X), (X, f, \phi)$ satisfy these properties.

A (*fixed point*) *index* on $\mathcal{C}_A$ is a function $i : \mathcal{C} \to \mathbb{Q}$ which satisfies the following axioms:

1. (Localization). If $(X, f, U) \in \mathcal{C}$ and $g : X \to X$ is a map such that $g(x) = f(x)$ for all $x \in \bar{U}$ (the closure of U), then
$$i(X, f, U) = i(X, g, U).$$

2. (Homotopy). For $X \in \mathcal{C}_A$ and $H : X \times I \to X$ a homotopy, define $f_t : X \to X$ by $f_t(x) = H(x, t)$. If $(X, f_t, U) \in \mathcal{C}$ for all $t \in I$, then
$$i(X, f_0, U) = i(X, f_1, U).$$

3. (Additivity). If $(X, f, U) \in \mathcal{C}$ and $U_1, ... U_n$ is a set of mutually disjoint open subsets of U such that $f(x) \neq x$ for all
$$x \in U - \bigcup_{j=1}^{n} U_j,$$
then
$$i(X, f, U) = \sum_{j=1}^{n} i(X, f, U_j).$$

4. (Normalization). If $X \in \mathcal{C}_A$ and $f : X \to X$ is a map, then
$$i(X, f, X) = L(f).$$

5. (Commutativity) If $X, Y \in \mathcal{C}_A$ and $f : X \to Y, g : Y \to X$ are maps such that $(X, gf, U) \in \mathcal{C}$, then
$$i(X, gf, U) = i(Y, fg, g^{-1}(U)).$$

The localization axiom 1 obviously makes the definition of the index "local" in the sense that $i(X, f, U)$ is not affected by the behaviuor of f outside of $\bar{U}$. The normalization axiom 4 connects the index to Lefschetz theory. The homotopy and commutativity axioms are generalizations of properties of the Lefschetz number.

Lemma 1. *If there is an index i on $\mathcal{C}_A$ and if $(X, f, U) \in \mathcal{C}$, such that $i(X, f, U) \neq 0$, then f has a fixed point in U.*

Proof. Note that $i(X, f, \phi) = i(X, f, \phi) + i(X, f, \phi)$ by additivity 3 $(U = U_1 = U_2 = \phi)$. Thus $i(X, f, \phi) = 0$ since it is rational. Suppose $f(x) \neq x$ on U. Then we can apply additivity 3 for the given open set U and $U_1 = \phi$, and we get $i(X, f, U) = i(X, f, \phi) = 0$. Which is a contradiction. Hence f has a fixed point in U.

Lemma 2. *Assume there is an index on $\mathcal{C}$ and if $X \in \mathcal{C}_A, f : X \to X$ a map such that $L(f) \neq 0$ then every map homotopic to f has a fixed point.*

Proof. Let g be any map homotopic to f; then $L(g) = L(f) \neq 0$. By the normalization axiom, $i(X, g, X) = L(g) \neq 0$, so g has a fixed point in X by 1.

The last Lemma 1 makes the important point that Index Theory is more powerful than Lefschetz Theory in the sense that the existance of a function on $\mathcal{C}_A$ satisfying just two of the axioms of an index, namely additivity 3 and normalization 4, is enough to imply that the Lefschetz Fixed Point Theorem 1 is true for all maps on spaces in a collection $\mathcal{C}'$ on which an index is defined.

Example 1. *Let X be a compact connected ANR and $(X, f, U) \in \mathcal{C}$ where f is a constant map say $f(x) = x_0, \ \forall x \in X$. Then*

$$i(X, f, U) = \begin{cases} 0 & \text{if } x_0 \notin U \\ 1 & \text{if } x_0 \in U \end{cases}$$

For, if $x_0 \notin U$. Then by additivity 3 for the given U and $U_1 = \phi$, $i(X, f, U) = i(X, f, \phi) = 0$. Now suppose $x_0 \in U$. Let $Y = \{x_0\}$ the singleton space and $g : X \to Y, h : Y \to X$ be the maps $x \mapsto x_0, h = 1_Y$ respectively. Then $i(X, f, U) = i(X, hg, U) = i(Y, gh, Y) = L(gh) = L(1_Y)$ by the commutativity 5 and normalization 4 axioms. Since any map f on a path connected space induces the identity on the homology group H_0 and since Y is path connected and higher homology groups are trivial, $L(1_Y) = 1$. Hence $i(X, f, U) = 1$ in this case. The following theorem tells us that such an index exists on $\mathcal{C}_A$. Details can be seen in chapters IV and V of [1].

Theorem 2. *For the collection $\mathcal{C}_A$ of all connected compact ANR, there is a unique index defined on it satisfying all the five axioms.*

Now we are ready to define an index on the Nielsen classes of a map $f : X \to X$.

4   The Nielsen Number

For X, a compact ANR, and a map $f : X \to X$, we shall define a non-negative integer $N(f)$, called the *Nielsen number* of f. The Nielsen number is a lower bound for the number of fixed points of f.

4.1   Nielsen Classes

Assume that the set $Fixf$ of all fixed points of f is non-empty. Two points $x_0, x_1 \in Fixf$ are f-equivalent if there is a path $c : I \to X$ from x_0 to x_1 such that c and $f \circ c$ are homotopic with respect to the end points. This relation defines an equivalence relation on $Fixf$. The equivalence classes are called *Nielsen classes* or *fixed point classes* of f. It is known that the set of Nielsen classes of a map f on a connected, compact, ANR X is finite.

Theorem 3. *A map $f : X \to X$ on a compact ANR has only finitely many Nielsen classes.*

Hence we will denote the set of fixed point classes by $\mathcal{N}(f) := \{F_1, F_2, ..., F_n\}$.

4.2   Nielsen Number

Let $f : X \to X$ be a map with fixed point classes $F_1, ..., F_n$. Then for each $j = 1, .., n$, there is an open set $U_j \subset X$ such that $F_j \subset U_j$ and $\bar{U}_j \cap Fixf = F_j$. Let i be the index on $\mathcal{C}_A$. Note that $(X, f, U_j) \in \mathcal{C}$. Define the *index $i(F_j)$* of the fixed point class F_j by $i(F_j) = i(X, f, U_j)$. This definition is independent of the choice of the open set $U_j \subseteq X$ such that $F_j \subseteq U_j$ and $\bar{U}_j \cap Fixf = F_j$ because, suppose U, V are two such open sets. If $x \in U - U \cap V$ then since x belongs to $U, x \notin F_k$ for $k \neq j$, while $x \notin V$, so $x \notin F_j$. Thus $x \notin Fixf$. By the additivity axiom, $i(X, f, U) = i(X, f, U \cap V)$. The same reasoning implies $i(X, f, V) = i(X, f, U \cap V)$. A fixed point class F of f is said to be *essential* if $i(F) \neq 0$ and *inessential* otherwise. The *Nielsen number $N(f)$* of the map f is defined to be the number of fixed point classes of f that are essential.

A fixed point theorem with this number is that:

Theorem 4. *Any continuous map f on a connected compact ANR has at least $N(f)$ fixed points.*

Theorem 5. *Let $f, g : X \to X$ be homotopic maps; then $N(f) = N(g)$.*

Thus any continuous function g homotopic to f has at least $N(f)$ fixed points.
The example 1 is an example with only one fixed point class and it is essential, i.e, $N(f) = 1$.

Computing $N(f)$ is difficult in general, in some cases it can be computed via the Reidemeister number $R(f)$ by knowing $L(f)$ and f_π, the induced homomorphism on the fundamental group of X. The main tool to compute the Nielsen number is the Jiang subgroup of the fundamental group. Before going to the computation method of Nielsen number we will see how it is related to the Reidemeister number $R(f)$.

5   The Reidemeister Number

Let $f : X \to X$ be a map on a connected compact ANR and let $Fix f = \{x \in X : f(x) = x\}$. Let $p : \widetilde{X} \to X$ be the universal covering of X and $\tilde{f} : \widetilde{X} \to \widetilde{X}$ be a lifting of f, ie. $p \circ \tilde{f} = f \circ p$. Two liftings $\tilde{f}$ and $\tilde{f}'$ are called conjugate if there is a $\gamma \in \Gamma = \pi_1(X)$ such that $\tilde{f}' = \gamma \tilde{f} \gamma^{-1}$. Note that if $\tilde{f}$ is a lift of f and $\gamma \in \Gamma$, then $p(Fix\tilde{f}) = p(Fix\gamma\tilde{f}\gamma^{-1})$ and $p(Fix\tilde{f}) = p(Fix\tilde{f}')$, then $\tilde{f}' = \gamma\tilde{f}\gamma^{-1}$ for some $\gamma \in \Gamma$. This is an equivalence relation on the set $Fix f = \bigsqcup_{[\tilde{f}]} p(Fix\tilde{f})$, ie. $Fix f$ is a disjoint union of projections of fixed points of lifts from distinct lifting classes. The subset $p(Fix\tilde{f}) \subseteq Fix f$ is called the *fixed point class* of f determined by the lifting class $[\tilde{f}]$. Note that for any point $y \in \widetilde{X}$, since $(f \circ p)_\pi(\pi_1(\widetilde{X})) \subset p_\pi(\pi_1(X))$, there is a unique map $\tilde{f}$ such that $p \circ \tilde{f} = f \circ p$ and $\tilde{f}(y) = y$. In particular, any fixed point of f is a projection of a fixed point of some lift $\tilde{f}$ of f.

Now we define the Reidemeister number of a group homomorphism $\varphi : G \to G$. Let $\varphi : G \to G$ be a group homomorphism on a group G. One has an action of G on itself given by $g.x = gx\varphi(g)^{-1}$. Two elements $x, y \in G$ are said to be $\varphi-$ twisted conjugate, $x \sim_\varphi y$, if they are in the same orbit of this action. The orbits are called the φ-twisted conjugacy classes or the *Reidemeister classes* and $R(\varphi)$, the number of Reidemeister classes is called the *Reidemeister number* of φ. If $\varphi = Id$ then $R(\varphi)$ coincides with the number of conjugacy classes of G.

By fixing a lift $\tilde{f}$ of f and $\alpha \in \Gamma \simeq \pi_1(X)$, $\tilde{x} \in \widetilde{X}$, we obtain a unique element $\tilde{\alpha} \in \Gamma$ such that $\tilde{\alpha}\tilde{f}(\tilde{x}) = \tilde{f}(\alpha(\tilde{x}))$. Thus we obtain a homomorphism $\phi : \pi_1(X) \to \pi_1(X)$ such that $\tilde{f}\alpha = \phi(\alpha)\tilde{f}, \forall \alpha \in \Gamma$. Also once we fix a lift $\tilde{f}$ of f, then every lift is of the form $\alpha\tilde{f}$ for some $\alpha \in \Gamma$. Let $\alpha, \beta \in \Gamma$. Then

$$[\alpha\tilde{f}] = [\beta\tilde{f}] \iff \beta\tilde{f} = \gamma\alpha\tilde{f}\gamma^{-1}$$

for some $\gamma \in \Gamma$. ie.

$$\iff \beta\tilde{f} = \gamma\alpha\phi(\gamma^{-1})\tilde{f}$$

By the uniqueness of lifts, we have $[\alpha\tilde{f}] = [\beta\tilde{f}] \iff \beta = \gamma\alpha\phi(\gamma^{-1})$ for some $\gamma \in \Gamma$. Furthermore, by choosing appropriate base point, ϕ can be identified with the induced homomorphism f_π on Γ. From now on, we write $R(f)$ for $R(f_\pi)$. It follows from the above definition that there is a one-one correspondence between the lifting classes of f and the Reidemeister classes of f_π.

Remark 1. *If we choose a different lifting $\tilde{f}'$ and thus a different homomorphism ϕ', we get a bijection between the ϕ-Reidemeister classes and the ϕ'-Reidemeister classes so that the cardianality of such sets is a constant.*

5.1   Relationship with Nielsen number

Suppose $x_1, x_2 \in Fix f$ are in the same Nielsen class, ie. there exists a path $c : I \to X$ from x_1 to x_2 such that $f \circ c$ and c are homotopic relative to the end points. Let $\tilde{f}$ be a lift of f and $\tilde{x}_1 \in Fix\tilde{f}$ such that $p(\tilde{x}_1) = x_1$. Lift c to a path $\tilde{c}$ starting from $\tilde{x}_1$ and ending at some $\tilde{x}_2$ in $\tilde{X}$. Then $\tilde{f} \circ \tilde{c}$ projects onto $f \circ c$ which is homotopic to c. Thus $\tilde{f} \circ \tilde{c}$ also ends at $\tilde{x}_2$. Hence $\tilde{f}(\tilde{x}_2) = \tilde{x}_2$. In otherwords, they belong to the same lifting class. Conversely, let $\tilde{x}_1, \tilde{x}_2 \in Fix\tilde{f}$ such that $p(\tilde{x}_1) = x_1 \neq x_2 = p(\tilde{x}_2)$. Let $\tilde{c} : I \to \widetilde{X}$ be a path from $\tilde{x}_1$ to $\tilde{x}_2$. Then $c = p \circ \tilde{c}$ is a path from x_1 to x_2 in X and $p(\tilde{f} \circ \tilde{c}) = f \circ p \circ \tilde{c} = f \circ c$, ie. $\tilde{f} \circ \tilde{c}$ projects onto $f \circ c$. In fact, the loop $\tilde{c}(\tilde{f} \circ \tilde{c})^{-1}$ projects to the loop $c(f \circ c)^{-1}$. Since $\widetilde{X}$ is simply-connected, the former loop is trivial in $\pi_1(\widetilde{X})$ and thus the later loop is homotopic to the trivial loop, ie. $c \sim f \circ c$. That is x_1 and x_2 are in the same Nielsen class. This shows that there is a one-to-one

map, say ψ, from the set of Nielsen classes to the set of Reidemeister classes and which implies that $N(f) \leq R(f)$. Note that a lifting class $p(Fix\tilde{f})$ might be empty, but Nielsen classes are non-empty. Also $R(f)$ need not be finite while $N(f)$ is always finite. For example, if $f = 1_X$ then any two points are Nielsen equivalent, thus $N(f) \leq 1$ while $R(f)$ is the number of conjugacy classes in $\pi_1(X)$. In particular, if $\pi_1(X)$ is abelian then $R(f) = |\pi_1(X)|$.

6 Computing Nielsen Number

First, let us consider a simple example: For a simply connected space X, there is only one Nielsen class for any self map f of X, so $N(f) \leq 1$. In this case $L(f) = 0 \Rightarrow N(f) = 0$ or $L(f) \neq 0 \Rightarrow N(f) = 1$. $N(f)$ does not give more information than $L(f)$.

The main tool to calculate $N(f)$ is the Jiang subgroup $T(f) \leq \pi_1(X)$ introduced by B. Jiang(1963).

6.1 The Jiang Subgroup

Fix a point x_0 in a compact connected ANR X and a self map f on X. We denote by $Map(X)$ the set of all maps from X to itself with the supremum metric $d(f, g) = sup\{d(f(x), g(x)) \mid x \in X\}$, then it is a complete metric space. Let $p : Map(X) \to X$ be the map given by $p(g) = g(x_0)$. Then p induces a homomorphism $p_\pi : \pi_1(Map(X), f) \to \pi_1(X, f(x_0))$. The Jiang subgroup $T(f, x_0)$ is the image of the homomorphism p_π. Equivalently, an element $\alpha \in \pi_1(X, f(x_0))$ is said to be in the Jiang subgroup $T(f, x_0)$ of f if there is a loop H in $Map(X)$ based at f such that the loop c in X defined by $c(t) = H(t)(x_0)$ is homotopic to α.

Lemma 3. *The Jiang subgroup is independent of the base point, ie. $T(f, x_0) \simeq T(f, x_1)$ for any $x_0, x_1 \in X$.*

Theorem 6. *If f is such that $T(f, x_0) \simeq \pi_1(X, x_0)$. Then all the fixed point classes have the same index. If $f : X \to X$ is such that $T(f, x_0) = \pi_1(X, x_0)$, then $L(f) = 0$ implies $N(f) = 0$. Proof.If $Fix f = \phi$, then certainly $N(f) = 0$. Otherwise, let $\{F_1, F_2, ..., F_n\}$ be the different fixed point classes of f, and assume $x_0 \in F_1$ (Lemma 3). By Theorem 6 $i(F_j) = i(F_1)$ for every j; so, by additivity (3) and normalization (4) axioms,*

$$0 = L(f) = \sum_j i(F_j) = n \ i(F_1)$$

Thus $i(F_1) = 0 \Rightarrow i(F_j) = 0$ for every j, which implies $N(f) = 0$. $\square$

Lemma 4. *If f and g are homotopic, then $T(f, x_0) \simeq T(g, x_0)$.*

Lemma 5. *$f : X \to X, x_0, x_1 \in X$. Then there exists a map $g : X \to X$ such that both $f^{-1}(x_0), x_1 \in g^{-1}(x_0)$.*

This lemma implies that, given f, x_0 as above, there is a map $g \sim f$ such that $g(x_0) = x_0$. Hence we can choose $x_0 \in Fix f$ (Lemmas 3, 4, 5). We will drop the base point from the fundamental group and the Jiang subgroup. The Jiang subgroup of the identity map on X is denoted by $T(X)$ and $T(f) = T(f, x_0)$.

Theorem 7. *For any map $f : X \to X$, $T(X) \subseteq T(f)$. Proof.Let $\alpha \in T(X) \leq \pi_1(X)$. Then there is a loop $[H] \in \pi_1(Map(X), 1_X)$ based at the identity map such that $[pH] = \alpha$. Define a loop H' in $Map(X)$ (based at f) by $H'(t)(x) = H(t)(f(x))$. Then, since $f(x_0) = x_0$, it follows that $H'(t)(x_0) = H(t)(x_0)$, which proves that $\alpha = [pH] = [pH'] \in T(f)$.* $\square$ *An ANR is an H-space if there is an element $e \in X$ and a map $\mu : X \times X \to X$ such that $\mu(x, e) = \mu(e, x) = x, \forall x \in X$. (The fundamental group of an H-spaces is abelian), $(\mathbb{S}^0, \mathbb{S}^1, \mathbb{S}^3, \mathbb{S}^7$ are the only spheres which are H-spaces). An important property of an H-space is:*

Theorem 8. *If X is a H-space, then $T(X) = \pi_1(X)$. Proof.We use e as the base point. Let c be any loop in X at e and define $H : [0, 1]^a Map(X) by H(t)(x)=\mu(c(t), x)$. Thus $[c] \in T(X)$.* $\square$

Note that for any H-space, $L(f) = 0$ implies $N(f) = 0$.

Now on we will work with X a connected polyhedron and will fix a triangulation (K, τ) on X. A space X is aspherical *if $\pi_n(X) = 1$, for all $n \geq 2$.*

Theorem 9. *Let X be a connected aspherical polyhedron and $f : X^a X. Then Z(f_\pi(\pi_1(X))) \subseteq T(f)$.*

Note that, if $f_\pi(\pi_1(X)) \subseteq Z(\pi_1(X))$, then $Z(f_\pi(\pi_1(X))) \subseteq \pi_1(X)$. If $f_\pi(\pi_1(X)) \subseteq Z(\pi_1(X))$, then $T(f) = \pi_1(X)$. Proof. $f_\pi(\pi_1(X)) \subseteq Z(\pi_1(X)) Z(f_\pi(\pi_1(X))) \subseteq T(f) T(f) = \pi_1(X)$. $\square$ *Now on we assume $L(f) \neq 0$ (then there is at least one essential fixed point class, ie. $L(f) \neq 0 N(f) \geq 1$ (by additivity 3), and X a compact ANR. If we apply the equivalence relation of f_π-equivalence (twisted action) to the Jiang subgroup $T(f) \subseteq \pi_1(X)$, then the set of equivalence classes is denoted by $T'(f)$. Let $J(f)$ be the cardinality of $T'(f)$. In other words, $J(f)$ is the number of f_π- twisted classes in $\pi_1(X)$ which contain elements of $T(f)$.*

Theorem 10. *If $\alpha \in T(f)$, then there is an essential fixed point class F of f such that $\psi(F) = [\alpha]$, the Reidemeister class containing α, where ψ is the map from the set of all Nielsen classes to the set of all Reidemeister classes of f discussed in section 5.1. It follows that $J(f) \leq N(f)$. If $T(f) = \pi_1(X)$, then $N(f) = R(f)$. Proof. $T(f) = \pi_1(X)$ implies that $J(f) = R(f)$ by definition. We know that $N(f) \leq R(f)$. Now the result follows from theorem 10, it states $J(f) \leq N(f)$.* $\square$

Example 2. *Let $X = \mathbb{S}^1$, the circle, an aspherical H-space with $\pi_1(X) =$. Then $T(X) = T(1_X) = \pi_1(\mathbb{S}^1) =$. If $f : \mathbb{S}^1{}^a S^1$ be any map, then $T(X) \subseteq T(f) T(f) = \pi_1(\mathbb{S}^1)$. Now $L(f) = 0 \iff f_\pi$ is the identity isomorphism (since $H_0(\mathbb{S}^1) == H_1$). Thus $L(f) = 0 N(f) = 0$. If f_π is not the identity isomorphism, say $f_\pi(1) = q \neq 1$, then $T(f) = \pi_1(\mathbb{S}^1) N(f) = R(f) = \#Coker(1 - f_\pi) = |1 - q|$ since for an abelan group G and a given homomorphism $\phi : G^a G, the Reidemeister number R(\phi) = \#Coker(1 - \phi)$.*

Example 3. *Let $f : \mathbb{S}^2{}^a S^2$ be a rotation by an angle θ. Let $p, n \in \mathbb{S}^2$ be the south and north poles and are the only fixed points of f. Since $\mathbb{S}^2$ is simply connected, there is exactly one Nielsen class F and hence $N(f) \leq 1$. Note that f is homotopic to the identity map. Thus $L(f) = L(1) = \chi(\mathbb{S}^2) = 2 \neq 0 N(f) \geq 1$. Hence $N(f) = 1$ and $i(F) = 1$.*

Example 4. *Let $f : \mathbb{S}^n{}^a S^n$ be the map $f(x) = -x$ for all $x \in \mathbb{S}^n$. Then $L(f) = 1 - deg(f)$, where degree of f is $deg(f) = (-1)^{n+1}$.*

ACKNOWLEDGMENT

REFERENCES

[1] **R.F. Brown**, (1971). The Lefschetz Fixed Point Theorem. *Scott. Foresman.*

[2] **A.L. Fel'shtyn**, (2001). The Reidemeister number of any automorphism of a Gromov hyperbolic group is infinite. *Zap. Nauchn. Sem. S.-Peterburg. Otdel. Mat. Inst. Steklov. (POMI), 279(Geom. i Topol.6), 250*, pp. 229–240.

[3] **A.L. Fel'shtyn**, (2010). New directions in Nielsen-Reidemeister theory. *Topology Appl., 157(10-11)*, pp. 1724-1735.

[4] **Daciberg Gonçalves** and **Peter Wong** (year). Twisted conjugacy classes in nilpotent groups. *J. Reine Angew. Math., 633*, pp. 11-27.

[5] **Gilbert Levitt** and **Martin Lustig** (2000). Most automorphisms of a hyperbolic group have very simple dynamics. *Ann. Sci. École Norm. Sup.(4), 33, 4*, pp.507–517.

[6] **T. Mubeena** and **P. Sankaran** (2014). Twisted conjugacy in lattices in semisimple lie groups. *Transformation Groups, 19*, pp. 159-169.

[7] **T. Mubeena** and **P. Sankaran** (2019). Twisted conjugacy and quasi-isometric rigidity of irreducible lattices in semisimple lie groups. *Indian Journal of Pure and Applied Mathematics, 50, 2*, pp. 403-412.

/05/

APPLICATIONS OF FIXED POINT THEOREMS TO SOLUTIONS OF OPERATOR EQUATIONS IN BANACH SPACES

Neeta Singh

Department of Mathematics, University of Allahabad, Allahabad (India).

E-mail:n_s32132@yahoo.com

ORCID:

ABSTRACT

In this paper we use Browder's and Gohde's fixed point theorem, Kirk's fixed point theorem and the Sadovskii fixed point theorem to obtain solutions of operator equations in Banach spaces.

73 |

KEYWORDS

fixed point, Banach spaces

1   INTRODUCTION

Perhaps the most famous fixed-point theorem is the Banach's contraction principle which has several applications. Motivated by this we have considered in this review article, applications of other well-known fixed-point theorems in various kinds of Banach spaces. This article should be of interest to mathematicians working in the fields of fixed-point theory and functional analysis.

In Section 1 we apply the Browder's and Göhde's fixed point theorem for the existence of solutions of operator equations involving asymptotically nonexpansive mappings in uniformly convex Banach spaces. In Section 2 we apply Kirk's fixed point theorem for the existence of solutions of the operator equation $x - T\,x = f$ in reflexive Banach spaces and in Section 3 we apply the Sadovskii fixed point theorem for existence of solutions of the operator equation $x - T\,x = f$ in arbitrary Banach spaces.

2   Application of Browder's and Göhde's fixed point theorem

Definition 1.   *[1] A mapping T from a metric space (X, d) into another metric space (Y, ρ) is said to satisfy Lipschitz condition on X if there exists a constant $L > 0$ such that*

$$\rho(Tx, Ty) \leq Ld(x, y)$$

for all $x, y \in X$. If L is the least number for which Lipschitz condition holds, then L is called Lipschitz constant. If $L = 1$, the mapping is said to be nonexpansive.

Definition 2.   *[2] Let K be a nonempty subset of a Banach space X. A mapping $T : K \to K$ is said to be asymptotically nonexpansive if for each $n \in \mathbb{N}$ there exists a positive constant $k_n \geq 1$ with $\lim_{n \to \infty} k_n = 1$ such that*

$$||T^n x - T^n y|| \leq k_n ||x - y||$$

for all $x, y \in K$.

The Browder's and Göhde's fixed point theorem is as follows:

Theorem 1.   *[3] Let X be a uniformly convex Banach space and C a nonempty, closed, convex and bounded subset of X. Then every nonexpansive mapping $T : C \to C$ has a fixed point in C.*

We now state the main theorem of Section 1.

Theorem 2.   *Let X be a uniformly convex Banach space and K a nonempty subset of X. Let $T : K \to K$ be an asymptotically nonexpansive mapping and $f_n \in K$, then the operator equation*

$$k_n x = T^n x + f_n$$

where $n \in \mathbb{N}$ and k_n is the Lipschitz constant of the iterates T^n, has a solution if and only if, for any $x_1 \in K$, the sequence of iterates $\{x_n\}$ in K defined by

$$k_n x_{n+1} = T^n x_n + f_n$$

$n \in \mathbb{N}$ is bounded.

Proof. For every $n \in \mathbb{N}$, let T_{f_n} be defined to be a mapping from K into K by

$$T_{f_n}(u) = \frac{1}{k_n}[T^n u + f_n].$$

Then $u_n \in K$ is a solution of

$$x = \frac{1}{k_n}[T^n x + f_n]$$

if and only if u_n is a fixed point of T_{f_n}. Since T is asymptotically nonexpansive it follows that T_{f_n} is nonexpansive for all $n \in \mathbb{N}$.

$$||T_{f_n}(x) - T_{f_n}(y)|| = \frac{1}{k_n}||T^n(x) - T^n(y)|| \leq ||x - y||.$$

Suppose T_{f_n} has a fixed point $u_n \in K$. Then

$$||x_{n+1} - u_n|| = ||\frac{1}{k_n}[T^n x_n + f_n] - u_n|| = ||T_{f_n}(x_n) - T_{f_n}(u_n)|| \leq ||x_n - u_n||,$$

T_{f_n} being nonexpasive. Since $\{||x_n - u_n||\}$ is non-increasing, hence $\{x_n\}$ is bounded. Conversely, suppose that $\{x_n\}$ is bounded. Let $d = diam(\{x_n\})$ and

$$B_d[x] = \{y \in K : ||x - y|| \leq d\}$$

for each $x \in K$. Set

$$C_n = \bigcap_{i \geq n} B_d[x_i] \subset K.$$

Hence C_n is a nonempty, convex set for each $n \in \mathbb{N}$. Now we claim that $T_{f_n}(C_n) \subset C_{n+1}$. Let $y \in B_d[x_n]$ which implies $||y - x_n|| \leq d$. Since T_{f_n} is nonexpansive, we get

$$||T_{f_n}(y) - T_{f_n}(x_n)|| \leq d$$

$$||\frac{1}{k_n}[T^n(y) + f_n] - \frac{1}{k_n}[T^n(x_n) + f_n]|| \leq d$$

or

$$||\frac{1}{k_n}[T^n(y) + f_n] - x_{n+1}|| \leq d$$

or

$$\frac{1}{k_n}[T^n(y) + f_n] \in B_d[x_{n+1}]$$

giving

$$T_{f_n}(y) \in B_d[x_{n+1}]$$

proving that $T_{f_n}(C_n) \subset C_{n+1}$.

Let $C = \overline{\bigcup_{n \in \mathbb{N}} C_n}$. Since C_n increases with n, C is a closed, convex and bounded subset of K. We can easily see that T_{f_n} maps C into C.

$$T_{f_n}(C) = T_{f_n}(\overline{\bigcup_{n \in \mathbb{N}} C_n}) \subseteq \overline{T_{f_n}(\bigcup_{n \in \mathbb{N}} C_n)} = \overline{\bigcup_{n \in \mathbb{N}} T_{f_n}(C_n)} \subseteq \overline{\bigcup_{n \in \mathbb{N}} C_{n+1}} = C.$$

Applying the Browder's and Göhde's theorem to T_{f_n} and C we get a fixed point of T_{f_n} in C. Since $C \subset K$, we obtain a fixed point of T_{f_n} in K.

3   Application of Kirk's Fixed Point Theorem

Let us recall some definitions and results that we shall require for the proof of the Main Theorem of Section 2.

Definition 3.   *[2] Let (X, ρ) and (M, d) be metric spaces. A mapping $f : X \to M$ is said to be nonexpansive if for each $x, y \in X$,*

$$d(f(x), f(y)) \leq \rho(x, y).$$

Definition 4.   *[1] A convex subset K of a Banach space X is said to have normal structure if each bounded, convex subset S of K with diam $S > 0$ contains a nondiametral point.*

The following theorem gives application of the Browder-Göhde-Kirk's theorem for the existence of solutions of the operator equation

$$x - Tx = f.$$

It is known that every uniformly convex Banach space is reflexive. We generalize the theorem below to reflexive Banach spaces using Kirk's fixed point theorem

Theorem 3. *[3] Let X be a uniformly convex Banach space, f an element in X and $T : X \to X$ a nonexpansive mapping, then the operator equation*

$$x - Tx = f$$

has a solution x if and only if for any $x_0 \in X$, the sequence of Picard iterates $\{x_n\}$ in X defined by $x_{n+1} = Tx_n + f$, $n \in \mathbb{N}_0$ is bounded.

Definition 5. *[1] A Banach space X is said to satisfy the Opial condition if whenever a sequence $\{x_n\}$ in X converges weakly to $x_0 \in X$, then*

$$\liminf_{n \to \infty} \|x_n - x_0\| < \liminf_{n \to \infty} \|x_n - x\|$$

for all $x \in X$, $x \neq x_0$.

Lemma 1. *[3] Let X be a reflexive Banach space with the Opial condition. Then X has normal structure.*

Lemma 2. *[3] A closed subspace of a reflexive Banach space is reflexive.*

Now we state the Kirk's fixed point theorem.

Theorem 4. *[3] Let X be a Banach space and C a nonempty weakly compact, convex subset of X with normal structure, then every nonexpansive mapping $T : C \to C$ has a fixed point.*

We state the main theorem of Section 2.

Theorem 5. *Let X be a reflexive Banach space satisfying Opial condition. Let $f \in X$ and $T : X \to X$ be a nonexpansive mapping. Then the operator equation*

$$x - Tx = f$$

has a solution x if and only if for any $x_0 \in X$, the sequence of Picard iterates $\{x_n\}$ in X defined by $x_{n+1} = Tx_n + f$, $n \in \mathbb{N}_0$ is bounded.

Proof. Let T_f be the mapping from X into X given by

$$T_f(u) = Tu + f.$$

Then u is a solution of

$$x - Tx = f$$

if and only if u is a fixed point of T_f. Clearly T_f is nonexpansive. Suppose T_f has a fixed point $u \in X$. Then for all $n \in \mathbb{N}$,

$$\|x_{n+1} - u\| \leq \|x_n - u\|.$$

Hence $\{x_n\}$ is bounded.

Conversely, suppose that $\{x_n\}$ is bounded. Let $d = diam(\{x_n\})$ and

$$B_d[x] = \{y \in X : \|x - y\| \leq d\}$$

for each $x \in X$. Set $C_n = \bigcap_{i \geq n} B_d[x_i]$. Then C_n is a nonempty convex set for each n, and

$$T_f(C_n) \subset C_{n+1}.$$

Let C be the closure of the union of C_n for $n \in \mathbb{N}$,

$$C = \overline{\bigcup_{n \in \mathbb{N}} C_n}.$$

Since C_n increases with n, C is a closed, convex and bounded subset of X. It is known that [1] bounded, closed and convex subsets of reflexive Banach spaces are weakly compact, hence we get that C is weakly compact.

Now since

$$T_f(C) = T_f(\overline{\bigcup C_n}) \subseteq \overline{T_f(\bigcup C_n)} = \overline{\bigcup T_f(C_n)} \subseteq \overline{\bigcup C_{n+1}} = C,$$

we get that T_f maps C into itself. By Lemma 1.3.6, C is a reflexive Banach space. Now X satisfies Opial condition and C being a closed subset of X, will also satisfy Opial condition. Hence by Lemma 1.3.5, C has normal structure. Finally, applying Kirk's fixed point theorem we get that T_f has a fixed point in C which proves the theorem.

4   Application of Sadovskii Fixed Point Theorem

We recall some definitions

Definition 6.   *[1] Let (M, ρ) denote a complete metric space and let $\mathfrak{B}$ denote the collection of nonempty and bounded subsets of M. Define the Kuratowski measure of noncompactness $\alpha : \mathfrak{B} \to \mathbb{R}^+$ by taking for $A \in \mathfrak{B}$,*
$\alpha(A) = \inf\{\epsilon > 0$ A is contained in the union of a finite number of sets in $\mathfrak{B}$ each having diameter less than $\epsilon\}$.
If M is a Banach space the function α has the following properties for $A, B \in \mathfrak{B}$
1. $\alpha(A) = 0 \Leftrightarrow \overline{A}$ is compact,
2. $\alpha(A + B) \leq \alpha(A) + \alpha(B)$.

Definition 7.   *[2] Let K be a subset of a metric space M. A mapping $T : K \to M$ is said to be condensing if T is bounded and continuous and if*

$$\alpha(T(D)) < \alpha(D)$$

for all bounded subsets D of M for which $\alpha(D) > 0$.

We state the Sadovskii fixed point theorem.

Theorem 6.   *[2] Let K be a nonempty, bounded closed and convex subset of a Banach space and let $T : K \to K$ be a condensing mapping, then T has a fixed point.*

The main result of section 3 is the following:

Theorem 7. *Let X be an arbitrary Banach space, let $f \in X$ and $T : X \to X$ be a condensing mapping, then the operator equation*
$$x - Tx = f$$
has a solution if and only if for any $x_0 \in X$, the sequence of Picard iterates $\{x_n\}$ in X, defined by $x_{n+1} = Tx_n + f$, $n \in \mathbb{N}_0$ is bounded.

Proof. Let the mapping $T_f : X \to X$ be defined by

$$T_f(u) = Tu + f.$$

Then u is a solution of the operator equation

$$x - Tx = f$$

if and only if u is a fixed point of T_f.

Since T is bounded and continuous, T_f is also bounded and continuous. Using the properties of the Kuratowski measure of noncompactness, for all bounded subsets D of X, we have

$$\alpha(T_f(D)) = \alpha(T(D) + \{f\}) \leq \alpha(T(D)) + \alpha(\{f\}).$$

Since $\{f\}$ is compact, $\overline{\{f\}}$ is compact, implying $\alpha(\{f\}) = 0$, giving

$$\alpha(T_f(D)) \leq \alpha(T(D)) < \alpha(T(D)).$$

Since T is condensing mapping and it follows that T_f is a condensing mapping.

Suppose T_f has a fixed point u in X. Then for all $n \in \mathbb{N}$, since T_f is a continuous mapping being condensing, we get

$$\|x_{n+1} - u\| = \|Tx_n + f - u\| = \|T_f(x_n) - T_f(u)\| \leq \|x_n - u\|.$$

Hence $\{x_n\}$ is bounded.

Conversely, suppose that $\{x_n\}$ is bounded. Let $d = diam(\{x_n\})$ and for each $x \in X$

$$B_d[x] = \{y \in X : \ \|x - y\| \leq d\}.$$

Set $C_n = \bigcap_{i \geq n} B_d[x_i]$, then C_n is a nonempty convex set for each n. Using that T is a continuous mapping and the given Picard iteration, we have

$$y \in B_d[x_n] \Rightarrow \|y - x_n\| \leq d$$
$$\Rightarrow \|Ty - Tx_n\| \leq d$$
$$\Rightarrow \|Ty - [x_{n+1} - f]\| \leq d$$
$$\Rightarrow \|(Ty + f) - x_{n+1}\| \leq d$$
$$\Rightarrow (Ty + f) \in B_d[x_{n+1}].$$

Applying this, we get the following

$$T_f(C_n) = T_f(\bigcap_{i \geq n} B_d[x_i])$$

$$\subseteq \bigcap_{i \geq n} T_f(B_d[x_i])$$

$$= \bigcap_{i \geq n} \{T_f(y) : \ \|y - x_i\| \leq d\}$$

$$= \bigcap_{i \geq n} \{(Ty + f) : \ \|y - x_i\| \leq d\}$$

$$\subseteq \bigcap_{i \geq n+1} B_d[x_i] = C_{n+1}.$$

Let us define

$$C = \overline{\bigcup_{n \in \mathbb{N}} C_n}.$$

Since C_n increases with n,

$$C_n \subset C_{n+1} \subset C_{n+2} \subset ....,$$

it follows that C is a closed, convex and bounded subset of X. Now we have

$$T_f(C) = T_f\left(\overline{\bigcup_{n \in \mathbb{N}} C_n}\right) \subseteq \overline{T_f\left(\bigcup_{n \in \mathbb{N}} C_n\right)} = \overline{\bigcup_{n \in \mathbb{N}} T_f(C_n)} \subseteq \overline{\bigcup_{n \in \mathbb{N}} C_{n+1}} = C$$

giving $T_f : C \to C$ since T_f is continuous mapping.

Finally, applying the Sadovskii fixed point theorem to T_f and C, we obtain that T_f has a fixed point in C which proves the theorem.

REFERENCES

[1] **Goebel K.** and **Kirk W. A.** (1990). *Topics in metric fixed point theory. Cambridge Studies in Advanced Mathematics, volume 28, Cambridge University Press.*

[2] **Khamsi M. A.** and **Kirk W. A.** (2001). An Introduction to Metric Spaces and Fixed Point Theory. *Pure and Applied Mathematics. John Wiley & Sons, Inc.*

[3] **Agarwal R. P.** , **O'Regan R. P.** , and **Sahu D. R.** (2009). Fixed point theory for Lipschitzian-type mappings with applications. *Topological fixed point theory and its Applications, volume 6. Springer.*

/06/

FG- COUPLED FIXED POINT THEOREMS IN PARTIALLY ORDERED S^* METRIC SPACES

Prajisha E.

Assistant Professor, Department of Mathematics, Amrita Vishwa Vidyapeetham, Amritapuri (India).

E-mail:prajisha1991@gmail.com, prajishae@am.amrita.edu

ORCID:0000-0001-6677-3135

Shaini P.

Professor, Department of Mathematics,Central University of Kerala (India).

E-mail:shainipv@gmail.com

ORCID:0000-0001-9958-9211

ABSTRACT

This is a review paper based on a recent article on FG- coupled fixed points [17], in which the authors established FG- coupled fixed point theorems in partially ordered complete S^* metric space. The results were illustrated by suitable examples, too. An S^* metric is an n-tuple metric from n-product of a set to the non negative reals. The theorems in [17] generalizes the main results of Gnana Bhaskar and Lakshmikantham [5].

KEYWORDS

FG- Coupled Fixed Point, Mixed Monotone Property, Partially Ordered Set, S^* Metric

1 INTRODUCTION

In 1906, Maurice Frechet introduced the concept of metric as a generalization of distance. He defined a metric on a set as a function from the bi-product of the set to the non-negative reals that satisfy certain axioms. Later, several authors generalized the concept of metrics by either changing the domain or co-domain of the metric function or by varying the properties of the metric function [3, 4, 8, 11, 15, 16]. An n-tuple metric called S^* metric is the latest development in this direction. Since the existence of fixed points is depending on the function as well as on its domain, studies started on fixed point theory by considering those generalized metric spaces. Now a lot of fixed point and coupled fixed point results are available under different types of metric spaces [2, 6, 7, 9, 13, 14]. In [1] Abdellaoui, M.A. and Dahmani, Z. introduced S^* metric and they have proved fixed point results in S^* metric spaces. But the same concept can be seen in [10], under a different name. In [10] Mujahid Abbas, Bashir Ali, and Yusuf I Suleiman coined the name A- metric for this concept, and they have proved common coupled fixed point theorems with an illustrative example.

Recently, the concept of FG- coupled fixed points was introduced as a generalization of the concept of coupled fixed points in [12]. Some of the famous coupled fixed point theorems are generalized to FG- coupled fixed point theorems in [12, 18, 19].

In [17], the authors established FG- coupled fixed point theorems in the setting of partially ordered complete S^* metric spaces. This is a review paper of [17].

Some useful definitions and results are as follows:

Definition 1. *[1, 10] An S^* metric on a nonempty set X is a function $S^* : X^n \to [0, \infty)$ satisfying:*

(i) $S^*(x_1, x_2, \cdots, x_n) \geq 0$,

(ii) $S^*(x_1, x_2, \cdots, x_n) = 0$ if and only if $x_1 = x_2 = \cdots = x_n$,

(iii) $S^*(x_1, x_2, \cdots, x_n) \leq S^*(x_1, \cdots, x_1, a) + S^*(x_2, \cdots, x_2, a) + \cdots + S^*(x_n, \cdots, x_n, a)$

for any $x_1, x_2, \cdots, x_n, a \in X$. The pair (X, S^*) is called S^* metric space.

Lemma 1. *[1, 10] Suppose that (X, S^*) is an S^* metric space. Then for all $x_1, x_2 \in X$, we have $S^*(x_1, x_1, \cdots, x_1, x_2) = S^*(x_2, x_2, \cdots, x_2, x_1)$*

Definition 2. *[1, 10] We say that the sequence $\{x_p\}_{p \in \mathbb{N}}$ of the space X is convergent to x if $S^*(x_p, x_p, \cdots, x_p, x) \to 0$ as $p \to \infty$. We write $\lim_{p \to \infty} x_p = x$*

Definition 3. *[1, 10] We say that the sequence $\{x_p\}_{p \in \mathbb{N}}$ of the space X is of Cauchy if for each $\epsilon > 0$, there exist $p_0 \in \mathbb{N}$ such that for any $p, q \geq p_0$, $S^*(x_p, \cdots, x_p, x_q) < \epsilon$*

The space (X, S^*) is **complete** if all its Cauchy sequences are convergent.

Lemma 2. *[1, 10] Let (X, S^*) be an S^* metric space. If $\{x_p\}_{p \in \mathbb{N}}$ in X converges to x, then x is unique.*

Definition 4. *[12] Let X and Y be any two non-empty sets and $F : X \times Y \to X$ and $G : Y \times X \to Y$ be two mappings. An element $(x, y) \in X \times Y$ is said to be an FG- coupled fixed point if $F(x, y) = x$ and $G(y, x) = y$.*

Definition 5. *[12] Let $(X, \preceq_{P_1})$ and $(Y, \preceq_{P_2})$ be two partially ordered sets and $F : X \times Y \to X$ and $G : Y \times X \to Y$ be two mappings. We say that F and G have mixed monotone property if F and G are increasing in first variable and monotone decreasing second variable, i.e., if for all $(x, y) \in X \times Y$, $x_1, x_2 \in X, x_1 \preceq_{P_1} x_2$ implies $F(x_1, y) \preceq_{P_1} F(x_2, y)$ and $G(y, x_2) \preceq_{P_2} G(y, x_1)$ and $y_1, y_2 \in Y, y_1 \preceq_{P_2} y_2$ implies $F(x, y_2) \preceq_{P_1} F(x, y_1)$ and $G(y_1, x) \preceq_{P_2} G(y_2, x)$.*

Note 1. [12] Let $F : X \times Y \to X$ and $G : Y \times X \to Y$ be two mappings, then for $n \geq 1$, $F^n(x, y) = F(F^{n-1}(x, y), G^{n-1}(y, x))$ and $G^n(y, x) = G(G^{n-1}(y, x), F^{n-1}(x, y))$, and $F^0(x, y) = x$ and $G^0(y, x) = y$ for all $x \in X$ and $y \in Y$.

Note 2. Let $(X, \preceq_{P_1})$ and $(Y, \preceq_{P_2})$ be two partially ordered sets, then we define the partial order $\leq_{12}$ on $X \times Y$ and the partial order $\leq_{21}$ on $Y \times X$ as follows:
For all $x, u \in X$ and $y, v \in Y$

$$(x, y) \leq_{12} (u, v) \quad \Leftrightarrow \quad x \preceq_{P_1} u \ and \ v \preceq_{P_2} y$$
$$(y, x) \leq_{21} (v, u) \quad \Leftrightarrow \quad y \preceq_{P_2} v \ and \ u \preceq_{P_1} x$$

2   Main Results in [17]

Mainly two FG-coupled fixed point theorems are discussed in [17], first one deals with the existence of FG-coupled fixed point and the second deals with both the existence and uniqueness of FG-coupled fixed point. They are as follow:

Theorem 1. *[17] Let $(X, S_x^*, \preceq_{P_1})$ and $(Y, S_y^*, \preceq_{P_2})$ be two partially ordered complete S^* metric spaces and $F : X \times Y \to X$ and $G : Y \times X \to Y$ be two mappings with mixed monotone property and satisfy the following:*

$$
\begin{aligned}
S_x^* & \big(F(x, y), \cdots, F(x, y), F(u, v)\big) \\
& \leq a_1 S_x^*(x, \cdots, x, u) + a_2 S_x^*\big(x, \cdots, x, F(x, y)\big) + a_3 S_x^*\big(x, \cdots, x, F(u, v)\big) \\
& \quad + a_4 S_x^*\big(u, \cdots, u, F(x, y)\big) + a_5 S_x^*\big(u, \cdots, u, F(u, v)\big), \ \forall (x, y) \leq_{12} (u, v)
\end{aligned}
\tag{1}
$$

and

$$
\begin{aligned}
S_y^* & \big(G(y, x), \cdots, G(y, x), G(v, u)\big) \\
& \leq b_1 S_y^*(y, \cdots, y, v) + b_2 S_y^*\big(y, \cdots, y, G(y, x)\big) + b_3 S_y^*\big(y, \cdots, y, G(v, u)\big) \\
& \quad + b_4 S_y^*\big(v, \cdots, v, G(y, x)\big) + b_5 S_y^*\big(v, \cdots, v, G(v, u)\big), \ \forall (y, x) \leq_{21} (v, u)
\end{aligned}
\tag{2}
$$

for the non negative $a_i, b_i, i = 1, 2, 3, 4, 5$ with
$a_1 + a_2 + na_3 + a_5 < 1, \ b_1 + b_2 + nb_4 + b_5 < 1, \ a_3 + a_5 < 1, \ b_2 + b_4 < 1.$
Also suppose that either

(I) F and G are continuous or

(II) X and Y have the following properties:

(i) if $\{z_k\}$ is an increasing sequence in X with $z_k \to z$, then $z_k \preceq_{P_1} z$ for all $k \in \mathbb{N}$

(ii) if $\{w_k\}$ is a decreasing sequence in Y with $w_k \to w$, then $w \preceq_{P_2} w_k$ for all $k \in \mathbb{N}$.

If there exist $x_0 \in X$ and $y_0 \in Y$ with $(x_0, y_0) \leq_{12} \big(F(x_0, y_0), G(y_0, x_0)\big)$, then there exist an FG-coupled fixed point.

Proof. Given $x_0 \in X$ and $y_0 \in Y$ such that $(x_0, y_0) \leq_{12} \big(F(x_0, y_0), G(y_0, x_0)\big)$. If $(x_0, y_0) = \big(F(x_0, y_0), G(y_0, x_0)\big)$ then (x_0, y_0) is an FG- coupled fixed point.
Otherwise we have

$$(x_0, y_0) <_{12} \big(F(x_0, y_0), G(y_0, x_0)\big)$$

Then by the definition of the partial order on $X \times Y$ we have either
$x_0 \preceq_{P_1} F(x_0, y_0)$ and $G(y_0, x_0) \prec_{P_2} y_0$ **or** $x_0 \prec_{P_1} F(x_0, y_0)$ and $G(y_0, x_0) \preceq_{P_2} y_0$.
Without loss of generality we assume that

$$x_0 \preceq_{P_1} F(x_0, y_0) \quad \text{and} \quad G(y_0, x_0) \prec_{P_2} y_0 \tag{3}$$

Let $x_1 = F(x_0, y_0)$ and $y_1 = G(y_0, x_0)$.

By (3) we have,

$$x_0 \preceq_{P_1} x_1 \text{ and } y_1 \prec_{P_2} y_0$$

By the mixed monotone property of F and G we have

$$
\begin{aligned}
F(x_0, y_0) \quad &\preceq_{P_1} \quad F(x_1, y_0) \\
&\preceq_{P_1} \quad F(x_1, y_1)
\end{aligned}
\tag{4}
$$

and

$$
\begin{aligned}
G(y_1, x_1) \quad &\preceq_{P_2} \quad G(y_0, x_1) \\
&\preceq_{P_2} \quad G(y_0, x_0)
\end{aligned}
\tag{5}
$$

Let $x_2 = F(x_1, y_1)$ and $y_2 = G(y_1, x_1)$.

By (4) and (5) we have,

$$x_1 \preceq_{P_1} x_2 \text{ and } y_2 \preceq_{P_2} y_1$$

Continuing this process by using the mixed monotone property of F and G and by using the definition of partial order on $X \times Y$ we get sequences $\{x_m\}$ and $\{y_m\}$ in X and Y respectively as: for all $m \in \mathbb{N} \cup \{0\}$

$$x_{m+1} = F(x_m, y_m) \text{ and } y_{m+1} = G(y_m, x_m) \tag{6}$$

with the property that for all $m \in \mathbb{N} \cup \{0\}$

$$x_m \preceq_{P_1} x_{m+1} \text{ and } y_{m+1} \preceq_{P_2} y_m \tag{7}$$

That is by the definition of partial order on $X \times Y$ and $Y \times X$ we have,

$$(x_m, y_m) \leq_{12} (x_{m+1}, y_{m+1})$$

and

$$(y_m, x_m) \geq_{21} (y_{m+1}, x_{m+1})$$

Claim: For all $k \in \mathbb{N}$

$$S_x^*(x_k, \cdots, x_k, x_{k+1}) \leq \alpha^k \ S_x^*(x_0, \cdots, x_0, x_1) \tag{8}$$

and

$$S_y^*(y_k, \cdots, y_k, y_{k+1}) \leq \beta^k \ S_y^*(y_0, \cdots, y_0, y_1) \tag{9}$$

where

$$\alpha = \frac{a_1 + a_2 + (n-1)a_3}{1 - a_3 - a_5} < 1 \text{ and } \beta = \frac{b_1 + b_5 + (n-1)b_4}{1 - b_2 - b_4} < 1 \tag{10}$$

Now, we prove the claim by the method of mathematical induction.

When $k = 1$ we have,

$$
\begin{aligned}
S_x^*&(x_1, \cdots, x_1, x_2) \\
&= S_x^*\big(F(x_0, y_0), \cdots, F(x_0, y_0), F(x_1, y_1)\big) \\
&\leq a_1 S_x^*(x_0, \cdots, x_0, x_1) + a_2 S_x^*\big(x_0, \cdots, x_0, F(x_0, y_0)\big) + a_3 S_x^*\big(x_0, \cdots, x_0, F(x_1, y_1)\big) \\
&\qquad + a_4 S_x^*\big(x_1, \cdots, x_1, F(x_0, y_0)\big) + a_5 S_x^*\big(x_1, \cdots, x_1, F(x_1, y_1)\big) \\
&= a_1 S_x^*(x_0, \cdots, x_0, x_1) + a_2 S_x^*(x_0, \cdots, x_0, x_1) + a_3 S_x^*(x_0, \cdots, x_0, x_2) \\
&\qquad\qquad\qquad + a_5 S_x^*(x_1, \cdots, x_1, x_2) \\
&= (a_1 + a_2) S_x^*(x_0, \cdots, x_0, x_1) + a_3 S_x^*(x_0, \cdots, x_0, x_2) + a_5 S_x^*(x_1, \cdots, x_1, x_2) \\
&\leq (a_1 + a_2) S_x^*(x_0, \cdots, x_0, x_1) + a_3 \big[(n-1) S_x^*(x_0, \cdots, x_0, x_1) \\
&\qquad\qquad + S_x^*(x_2, \cdots, x_2, x_1)\big] + a_5 S_x^*(x_1, \cdots, x_1, x_2) \\
&= (a_1 + a_2) S_x^*(x_0, \cdots, x_0, x_1) + a_3 \big[(n-1) S_x^*(x_0, \cdots, x_0, x_1) \\
&\qquad\qquad + S_x^*(x_1, \cdots, x_1, x_2)\big] + a_5 S_x^*(x_1, \cdots, x_1, x_2) \\
&= (a_1 + a_2 + (n-1)a_3) \ S_x^*(x_0, \cdots, x_0, x_1) + (a_3 + a_5) S_x^*(x_1, \cdots, x_1, x_2)
\end{aligned}
$$

which implies that

$$(1 - a_3 - a_5)S_x^*(x_1,\cdots,x_1,x_2) \leq (a_1 + a_2 + (n-1)a_3)\, S_x^*(x_0,\cdots,x_0,x_1)$$

That is,

$$S_x^*(x_1,\cdots,x_1,x_2) \leq \frac{a_1 + a_2 + (n-1)a_3}{1 - a_3 - a_5}\, S_x^*(x_0,\cdots,x_0,x_1)$$

Similarly we have,

$$S_y^*(y_1,\cdots,y_1,y_2) \leq (b_1 + b_5 + (n-1)b_4)\, S_y^*(y_0,\cdots,y_0,y_1) + (b_2 + b_4)S_y^*(y_1,\cdots,y_1,y_2)$$

which implies that

$$(1 - b_2 - b_4)\, S_y^*(y_1,\cdots,y_1,y_2) \leq (b_1 + b_5 + (n-1)b_4)\, S_y^*(y_0,\cdots,y_0,y_1)$$

That is,

$$S_y^*(y_1,\cdots,y_1,y_2) \leq \frac{b_1 + b_5 + (n-1)b_4}{1 - b_2 - b_4}\, S_y^*(y_0,\cdots,y_0,y_1)$$

Thus the claim is true for $k = 1$.

Now assume the claim for $k \leq m$ and check for $k = m + 1$.

Consider,

$$
\begin{aligned}
&S_x^*(x_{m+1},\cdots,x_{m+1},x_{m+2})\\
&= S_x^*\big(F(x_m,y_m),\cdots,F(x_m,y_m),F(x_{m+1},y_{m+1})\big)\\
&\leq a_1 S_x^*(x_m,\cdots,x_m,x_{m+1}) + a_2 S_x^*\big(x_m,\cdots,x_m,F(x_m,y_m)\big)\\
&\qquad + a_3 S_x^*\big(x_m,\cdots,x_m,F(x_{m+1},y_{m+1})\big) + a_4 S_x^*\big(x_{m+1},\cdots,x_{m+1},F(x_m,y_m)\big)\\
&\qquad\qquad + a_5 S_x^*\big(x_{m+1},\cdots,x_{m+1},F(x_{m+1},y_{m+1})\big)\\
&= a_1 S_x^*(x_m,\cdots,x_m,x_{m+1}) + a_2 S_x^*(x_m,\cdots,x_m,x_{m+1})\\
&\qquad + a_3 S_x^*(x_m,\cdots,x_m,x_{m+2}) + a_5 S_x^*(x_{m+1},\cdots,x_{m+1},x_{m+2})\\
&= (a_1 + a_2)S_x^*(x_m,\cdots,x_m,x_{m+1}) + a_3 S_x^*(x_m,\cdots,x_m,x_{m+2}) + a_5 S_x^*(x_{m+1},\cdots,x_{m+1},x_{m+2})\\
&\leq (a_1 + a_2)S_x^*(x_m,\cdots,x_m,x_{m+1}) + a_3\big[(n-1)S_x^*(x_m,\cdots,x_m,x_{m+1})\\
&\qquad + S_x^*(x_{m+2},\cdots,x_{m+2},x_{m+1})\big] + a_5 S_x^*(x_{m+1},\cdots,x_{m+1},x_{m+2})\\
&= (a_1 + a_2)S_x^*(x_m,\cdots,x_m,x_{m+1}) + a_3\big[(n-1)S_x^*(x_m,\cdots,x_m,x_{m+1})\\
&\qquad + S_x^*(x_{m+1},\cdots,x_{m+1},x_{m+2})\big] + a_5 S_x^*(x_{m+1},\cdots,x_{m+1},x_{m+2})\\
&= (a_1 + a_2 + (n-1)a_3)\, S_x^*(x_m,\cdots,x_m,x_{m+1}) + (a_3 + a_5)S_x^*(x_{m+1},\cdots,x_{m+1},x_{m+2})
\end{aligned}
$$

which implies that

$$
\begin{aligned}
&(1 - a_3 - a_5)S_x^*(x_{m+1},\cdots,x_{m+1},x_{m+2})\\
&\leq (a_1 + a_2 + (n-1)a_3)\, S_x^*(x_m,\cdots,x_m,x_{m+1})\\
&\leq (a_1 + a_2 + (n-1)a_3)\Big[\frac{a_1 + a_2 + (n-1)a_3}{1 - a_3 - a_5}\Big]^m S_x^*(x_0,\cdots,x_0,x_1)
\end{aligned}
$$

Therefore,

$$S_x^*(x_{m+1},\cdots,x_{m+1},x_{m+2}) \leq \Big[\frac{a_1 + a_2 + (n-1)a_3}{1 - a_3 - a_5}\Big]^{m+1} S_x^*(x_0,\cdots,x_0,x_1)$$

Similarly we have,

$$
\begin{aligned}
S_y^*(y_{m+1},\cdots,y_{m+1},y_{m+2}) \leq\ & (b_1 + b_5 + b_4(n-1))S_y^*(y_m,\cdots,y_m,y_{m+1})\\
& + (b_2 + b_4)S_y^*(y_{m+1},\cdots,y_{m+1},y_{m+2})
\end{aligned}
$$

which implies that

$$(1 - b_2 - b_4)S_y^*(y_{m+1}, \cdots, y_{m+1}, y_{m+2})$$
$$\leq (b_1 + b_5 + b_4(n-1))S_y^*(y_m, \cdots, y_m, y_{m+1})$$
$$\leq (b_1 + b_5 + b_4(n-1))\left[\frac{b_1 + b_5 + (n-1)b_4}{1 - b_2 - b_4}\right]^m S_y^*(y_0, \cdots, y_0, y_1)$$

Therefore,

$$S_y^*(y_{m+1}, \cdots, y_{m+1}, y_{m+2}) \leq \left[\frac{b_1 + b_5 + (n-1)b_4}{1 - b_2 - b_4}\right]^{m+1} S_y^*(y_0, \cdots, y_0, y_1)$$

Thus the claim is true for all $k \in \mathbb{N}$.

Next we prove that $\{x_m\}$ is a Cauchy sequence in X and $\{y_m\}$ is a Cauchy sequence in Y.

Let $p, q \in \mathbb{N}$ with $p < q$.

Consider,

$$S_x^*(x_p, \cdots, x_p, x_q)$$
$$\leq (n-1)S_x^*(x_p, \cdots, x_p, x_{p+1}) + S_x^*(x_q, \cdots, x_q, x_{p+1})$$
$$= (n-1)S_x^*(x_p, \cdots, x_p, x_{p+1}) + S_x^*(x_{p+1}, \cdots, x_{p+1}, x_q)$$
$$\leq (n-1)S_x^*(x_p, \cdots, x_p, x_{p+1}) + (n-1)S_x^*(x_{p+1}, \cdots, x_{p+1}, x_{p+2})$$
$$+ S_x^*(x_q, \cdots, x_q, x_{p+2})$$
$$= (n-1)\left[S_x^*(x_p, \cdots, x_p, x_{p+1}) + S_x^*(x_{p+1}, \cdots, x_{p+1}, x_{p+2})\right]$$
$$+ S_x^*(x_{p+2}, \cdots, x_{p+2}, x_q)$$
$$\cdots$$
$$\cdots$$
$$\cdots$$
$$\leq (n-1)\left[S_x^*(x_p, \cdots, x_p, x_{p+1}) + S_x^*(x_{p+1}, \cdots, x_{p+1}, x_{p+2})\right.$$
$$\left. + \cdots + S_x^*(x_{q-2}, \cdots, x_{q-2}, x_{q-1})\right] + S_x^*(x_q, \cdots, x_q, x_{q-1})$$
$$= (n-1)\sum_{i=p}^{q-2} S_x^*(x_i, \cdots, x_i, x_{i+1}) + S_x^*(x_{q-1}, \cdots, x_{q-1}, x_q)$$
$$\leq (n-1)\sum_{i=p}^{q-2} \alpha^i S_x^*(x_0, \cdots, x_0, x_1) + \alpha^{q-1} S_x^*(x_0, \cdots, x_0, x_1)$$

$$= (n-1)S_x^*(x_0, \cdots, x_0, x_1)\sum_{i=p}^{q-2} \alpha^i + \alpha^{q-1} S_x^*(x_0, \cdots, x_0, x_1)$$

$$\leq (n-1)\frac{\alpha^p}{1-\alpha}S_x^*(x_0, \cdots, x_0, x_1) + \alpha^{q-1} S_x^*(x_0, \cdots, x_0, x_1)$$
$$\to 0 \; as \; p, \; q \to \infty \; since \; \alpha < 1$$

Thus, $\{x_m\}$ is a Cauchy sequence in X.

Similarly we have,

$$S_y^*(y_p, \cdots, y_p, y_q) \le (n-1) \sum_{i=p}^{q-2} S_y^*(y_i, \cdots, y_i, y_{i+1}) + S_y^*(y_{q-1}, \cdots, y_{q-1}, y_q)$$

$$\le (n-1) \sum_{i=p}^{q-2} \beta^i \, S_y^*(y_0, \cdots, y_0, y_1) + \beta^{q-1} S_y^*(y_0, \cdots, y_0, y_1)$$

$$= (n-1) \, S_y^*(y_0, \cdots, y_0, y_1) \sum_{i=p}^{q-2} \beta^i + \beta^{q-1} S_y^*(y_0, \cdots, y_0, y_1)$$

$$\le (n-1) \frac{\beta^p}{1-\beta} S_y^*(y_0, \cdots, y_0, y_1) + \beta^{q-1} S_y^*(y_0, \cdots, y_0, y_1)$$

$$\to 0 \ as \ p, \ q \to \infty \ \text{since} \ \beta < 1$$

Thus, $\{y_m\}$ is a Cauchy sequence in Y.

Since X and Y are complete S^* metric spaces, there exist $x \in X$ and $y \in Y$ such that

$$\lim_{p \to \infty} x_p = x \quad \text{and} \quad \lim_{p \to \infty} y_p = y \tag{11}$$

Case (I): First assume that F and G are continuous.

Therefore by (6) and (11) we have,

$$x = \lim_{p \to \infty} x_{p+1} = \lim_{p \to \infty} F(x_p, y_p) = F(x, y)$$

and

$$y = \lim_{p \to \infty} y_{p+1} = \lim_{p \to \infty} G(y_p, x_p) = G(y, x)$$

That is $F(x, y) = x$ and $G(y, x) = y$.

Thus (x, y) is an FG- coupled fixed point.

Case (II): Suppose that X and Y have the properties (i) and (ii) respectively.

By (7) we have, $\{x_m\}$ is an increasing sequence in X and $\{y_m\}$ is a decreasing sequence in Y and by (11) we have $\lim_{m \to \infty} x_m = x$ and $\lim_{m \to \infty} y_m = y$

Therefore by the hypothesis we have for all $m \in \mathbb{N}$

$$x_m \preceq_{P_1} x \quad \text{and} \quad y \preceq_{P_2} y_m$$

Therefore by the definition of partial order on $X \times Y$ and $Y \times X$ we have

$$(x_m, y_m) \le_{12} (x, y) \quad \text{and} \quad (y, x) \le_{21} (y_m, x_m)$$

Consider,

$$S_x^*\big(x, \cdots, x, F(x, y)\big)$$
$$\le (n-1) S_x^*(x, \cdots, x, x_{m+1}) + S_x^*(F(x, y), \cdots, F(x, y), x_{m+1})$$
$$= (n-1) S_x^*(x, \cdots, x, x_{m+1}) + S_x^*\big(F(x, y), \cdots, F(x, y), F(x_m, y_m)\big)$$
$$= (n-1) S_x^*(x, \cdots, x, x_{m+1}) + S_x^*\big(F(x_m, y_m), \cdots, F(x_m, y_m), F(x, y)\big)$$
$$\le (n-1) S_x^*(x, \cdots, x, x_{m+1}) + a_1 S_x^*(x_m, \cdots, x_m, x) + a_2 S_x^*(x_m, \cdots, x_m, F(x_m, y_m))$$
$$\quad + a_3 S_x^*\big(x_m, \cdots, x_m, F(x, y)\big) + a_4 S_x^*\big(x, \cdots, x, F(x_m, y_m)\big) + a_5 S_x^*\big(x, \cdots, x, F(x, y)\big)$$
$$= (n-1) S_x^*(x, \cdots, x, x_{m+1}) + a_1 S_x^*(x_m, \cdots, x_m, x) + a_2 S_x^*(x_m, \cdots, x_m, x_{m+1})$$
$$\quad + a_3 S_x^*\big(x_m, \cdots, x_m, F(x, y)\big) + a_4 S_x^*(x, \cdots, x, x_{m+1}) + a_5 S_x^*\big(x, \cdots, x, F(x, y)\big)$$
$$\le (n-1) S_x^*(x, \cdots, x, x_{m+1}) + a_1 S_x^*(x_m, \cdots, x_m, x) + a_2 S_x^*(x_m, \cdots, x_m, x_{m+1})$$
$$\quad + a_3 \big[(n-1) S_x^*(x_m, \cdots, x_m, x) + S_x^*(F(x, y), \cdots, F(x, y), x)\big]$$
$$\quad + a_4 S_x^*(x, \cdots, x, x_{m+1}) + a_5 S_x^*\big(x, \cdots, x, F(x, y)\big)$$

By taking the limit as $m \to \infty$ on both sides, and by using (11) and Lemma 1 we get

$$S_x^*\big(x, \cdots, x, F(x,y)\big) \leq (a_3 + a_5)\, S_x^*\big(x, \cdots, x, F(x,y)\big)$$

since $a_3 + a_5 < 1$ we get $S_x^*\big(x, \cdots, x, F(x,y)\big) = 0$
Thus we get

$$F(x,y) = x \tag{12}$$

Similarly,

$$
\begin{aligned}
&S_y^*\big(y, \cdots, y, G(y,x)\big) \\
&\leq (n-1)S_y^*(y, \cdots, y, y_{m+1}) + S_y^*(G(y,x), \cdots, G(y,x), y_{m+1}) \\
&\leq (n-1)S_y^*(y, \cdots, y, y_{m+1}) + S_y^*\big(G(y,x), \cdots, G(y,x), G(y_m, x_m)\big) \\
&\leq (n-1)S_y^*(y, \cdots, y, y_{m+1}) + b_1 S_y^*(y, \cdots, y, y_m) + b_2 S_y^*\big(y, \cdots, y, G(y,x)\big) \\
&\qquad + b_3 S_y^*\big(y, \cdots, y, G(y_m, x_m)\big) + b_4 S_y^*\big(y_m, \cdots, y_m, G(y,x)\big) \\
&\qquad\qquad\qquad\qquad\qquad + b_5 S_y^*\big(y_m, \cdots, y_m, G(y_m, x_m)\big) \\
&\leq (n-1)S_y^*(y, \cdots, y, y_{m+1}) + b_1 S_y^*(y, \cdots, y, y_m) + b_2 S_y^*\big(y, \cdots, y, G(y,x)\big) \\
&\qquad + b_3 S_y^*(y, \cdots, y, y_{m+1}) + b_4 S_y^*\big(y_m, \cdots, y_m, G(y,x)\big) + b_5 S_y^*(y_m, \cdots, y_m, y_{m+1}) \\
&\leq (n-1)S_y^*(y, \cdots, y, y_{m+1}) + b_1 S_y^*(y, \cdots, y, y_m) + b_2 S_y^*\big(y, \cdots, y, G(y,x)\big) \\
&\qquad + b_3 S_y^*(y, \cdots, y, y_{m+1}) + b_4\big[(n-1)S_y^*(y_m, \cdots, y_m, y) + S^*(G(y,x), \cdots, G(y,x), y)\big] \\
&\qquad\qquad\qquad\qquad\qquad + b_5 S_y^*(y_m, \cdots, y_m, y_{m+1})
\end{aligned}
$$

By taking the limit as $m \to \infty$ on both sides, using (11) and Lemma 1 we get

$$S_y^*\big(y, \cdots, y, G(y,x)\big) \leq (b_2 + b_4)\, S_y^*\big(y, \cdots, y, G(y,x)\big)$$

since $b_2 + b_4 < 1$ we get $S_y^*\big(y, \cdots, y, G(y,x)\big) = 0$
Thus we get

$$G(y,x) = y \tag{13}$$

Therefore by (12) and (13), (x,y) is an FG- coupled fixed point.
Hence the proof.

By taking $n = 2$, $X = Y$, $F = G$, $a_2 = b_2 = k$, $a_5 = b_5 = l$ and the remaining $a_i, b_i = 0$, we get a coupled fixed fixed point theorem for Kannan type mapping. We give the result as a corollary as follows:

Corollary 1. *Let $(X, d, \preceq)$ be a partially ordered complete metric space and $F : X \times X \to X$ be a mapping having the mixed monotone property on X satisfying:*

$$d\big(F(x,y), F(u,v)\big) \leq k\, d\big(x, F(x,y)\big) + l\, d\big(u, F(u,v)\big) \ \forall\ (x,y) \geq (u,v)$$

for non negative k, l with $k + l < 1$
Suppose that either

(I) F is continuous or

(II) X satisfy the following:

    (i) if $\{x_k\}$ is an increasing sequence in X with $x_k \to x$, then $x_k \preceq x$ for all $k \in \mathbb{N}$

    (ii) if $\{y_k\}$ is a decreasing sequence in X with $y_k \to y$, then $y \preceq y_k$ for all $k \in \mathbb{N}$.

If there exist $x_0, y_0 \in X$ such that $(x_0, y_0) \leq \big(F(x_0, y_0), F(y_0, x_0)\big)$ then F has a coupled fixed point.

By taking $n = 2$, $X = Y$, $F = G$, $a_3 = b_3 = k$, $a_4 = b_4 = l$ and the remaining $a_i, b_i = 0$, we get a coupled fixed point theorem for Chatterjea type mapping. We give the result as a corollary as follows:

Corollary 2. *Let $(X, d, \preceq)$ be a partially ordered complete metric space and $F : X \times X \to X$ be a mapping having the mixed monotone property on X satisfying:*

$$d\big(F(x,y), F(u,v)\big) \leq k \; d\big(x, F(u,v)\big) + l \; d\big(u, F(x,y)\big) \; \forall \; (x,y) \geq (u,v)$$

for $k, l \in [0, \frac{1}{2})$
Suppose that either

   (I) F is continuous or

  (II) X satisfy the following:

     (i) if $\{x_k\}$ is an increasing sequence in X with $x_k \to x$, then $x_k \preceq x$ for all $k \in \mathbb{N}$

     (ii) if $\{y_k\}$ is a decreasing sequence in X with $y_k \to y$, then $y \preceq y_k$ for all $k \in \mathbb{N}$.

If there exist $x_0, y_0 \in X$ such that $(x_0, y_0) \leq \big(F(x_0, y_0), F(y_0, x_0)\big)$ then F has a coupled fixed point.

Remark 1. *By putting different values to the constants a_i, b_i; $i = 1, 2, 3, 4, 5$ which satisfy the conditions mentioned in Theorem 1 we get various FG- coupled fixed point theorems.*

Remark 2. *By varying the constants a_i, b_i; $i = 1, 2, 3, 4, 5$ which satisfy the conditions mentioned in Theorem 1 and by taking $X = Y$ and $F = G$ we get different coupled fixed point theorems.*

Example 1. *Let $X = [0, 1]$ and $Y = [-1, 0]$*
Consider the metric S^* defined on both X and Y as

$$S^*(a_1, \cdots, a_n) = \sum_{i=1}^{n} \sum_{i < j} |a_i - a_j|$$

For $x, u \in X$, consider the partial order $\leq$ as $x \leq u \iff x = u$
and for $y, v \in Y$, define partial order $\leq$ as $y \leq v \iff y = v$.
Let $F : X \times Y \to X$ and $G : Y \times X \to Y$ be defined as

$$F(x, y) = \frac{x - y}{2} \quad and \quad G(y, x) = \frac{2y - x}{3}$$

As per the partial order defined on X and Y it can be easily verified that F and G are mixed monotone mappings and satisfy the conditions (1) and (2).
Here $\{(x, -x) : x \in [0, 1]\}$ is the set of all FG- coupled fixed points.

Theorem 2. *[17] Let $(X, S_x^*, \preceq_{P_1})$ and $(Y, S_y^*, \preceq_{P_2})$ be two partially ordered complete S^* metric spaces and $F : X \times Y \to X$ and $G : Y \times X \to Y$ be two mappings with mixed monotone property satisfying:*

$$S_x^*\big(F(x,y), \cdots, F(x,y), F(u,v)\big) \leq a S_x^*(x, \cdots, x, u) + b S_y^*(y, \cdots, y, v), \; \forall (x,y) \leq_{12} (u,v) \quad (14)$$

and

$$S_y^*\big(G(y,x), \cdots, G(y,x), G(v,u)\big) \leq a S_y^*(y, \cdots, y, v) + b S_x^*(x, \cdots, x, u), \; \forall (y,x) \leq_{21} (v,u) \quad (15)$$

for non negative a, b with $a + b < 1$. Also suppose that either

   (I) F and G are continuous or

  (II) X and Y have the following properties:

     (i) if $\{z_k\}$ is an increasing sequence in X with $z_k \to z$, then $z_k \preceq_{P_1} z$ for all $k \in \mathbb{N}$

     (ii) if $\{w_k\}$ is a decreasing sequence in Y with $w_k \to w$, then $w \preceq_{P_2} w_k$ for all $k \in \mathbb{N}$.

If there exist $x_0 \in X$ and $y_0 \in Y$ with $(x_0, y_0) \leq_{12} \big(F(x_0, y_0), G(y_0, x_0)\big)$, then there exist an FG-coupled fixed point in $X \times Y$.

Moreover unique FG- coupled fixed point exists if

(III) for every $(x, y), (x_1, y_1) \in X \times Y$ there exist a $(u, v) \in X \times Y$ that is comparable to both (x, y) and (x_1, y_1).

Proof. Following as in the prof of Theorem 1 we can construct an increasing sequence $\{x_m\}_{m \in \mathbb{N}}$ in X and a decreasing sequence $\{y_m\}_{m \in \mathbb{N}}$ in Y defined as:

$$x_{m+1} = F(x_m, y_m) \ \text{ and } \ y_{m+1} = G(y_m, x_m) \tag{16}$$

with the property that

$$(x_m, y_m) \leq_{12} (x_{m+1}, y_{m+1})$$

and

$$(y_m, x_m) \leq_{21} (y_{m+1}, x_{m+1})$$

By (16) we have

$$x_{m+1} = F(x_m, y_m) = F^{m+1}(x_0, y_0) \ \text{ and } \ y_{m+1} = G(y_m, x_m) = G^m(y_0, x_0) \tag{17}$$

Claim: For $p \in \mathbb{N}$,

$$S_x^*(x_p, \cdots, x_p, x_{p+1}) \leq (a+b)^p \left[S_x^*(x_0, \cdots, x_0, x_1) + S_y^*(y_0, \cdots, y_0, y_1) \right] \tag{18}$$

and

$$S_y^*(y_p, \cdots, y_p, y_{p+1}) \leq (a+b)^p \left[S_x^*(x_0, \cdots, x_0, x_1) + S_y^*(y_0, \cdots, y_0, y_1) \right] \tag{19}$$

Now we prove the claim by the method of mathematical induction.

When $p = 1$ we have,

$$
\begin{aligned}
S_x^*(x_1, \cdots, x_1, x_2) &= S_x^*\big(F(x_0, y_0), \cdots, F(x_0, y_0), F(x_1, y_1)\big) \\
&\leq a\, S_x^*(x_0, \cdots, x_0, x_1) + b\, S_y^*(y_0, \cdots, y_0, y_1) \\
&\leq (a+b)\, [S_x^*(x_0, \cdots, x_0, x_1) + S_y^*(y_0, \cdots, y_0, y_1)]
\end{aligned}
$$

and

$$
\begin{aligned}
S_y^*(y_1, \cdots, y_1, y_2) &= S_y^*(y_2, \cdots, y_2, y_1) \\
&= S_y^*\big(G(y_1, x_1), \cdots, G(y_1, x_1), G(y_0, x_0)\big) \\
&\leq a\, S_y^*(y_1, \cdots, y_1, y_0) + b\, S_x^*(x_1, \cdots, x_1, x_0) \\
&= a\, S_y^*(y_0, \cdots, y_0, y_1) + b\, S_x^*(x_0, \cdots, x_0, x_1) \\
&\leq (a+b)\, \left[S_x^*(x_0, \cdots, x_0, x_1) + S_y^*(y_0, \cdots, y_0, y_1) \right]
\end{aligned}
$$

Therefore the claim is true for $p = 1$.

Now assume the claim for $p \leq m$ and check for $p = m + 1$.

Consider,

$$
\begin{aligned}
S_x^*(x_{m+1}, \cdots, x_{m+1}, x_{m+2}) &= S_x^*\big(F(x_m, y_m), \cdots, F(x_m, y_m), F(x_{m+1}, y_{m+1})\big) \\
&\leq a\, S_x^*(x_m, \cdots, x_m, x_{m+1}) + b\, S_y^*(y_m, \cdots, y_m, y_{m+1}) \\
&\leq a\,(a+b)^m\, [S_x^*(x_0, \cdots, x_0, x_1) + S_y^*(y_0, \cdots, y_0, y_1)] \\
&\quad + b\,(a+b)^m\, [S_x^*(x_0, \cdots, x_0, x_1) + S_y^*(y_0, \cdots, y_0, y_1)] \\
&= (a+b)^{m+1}\, [S_x^*(x_0, \cdots, x_0, x_1) + S_y^*(y_0, \cdots, y_0, y_1)]
\end{aligned}
$$

Similarly,

$$S_y^*(y_{m+1}, \cdots, y_{m+1}, y_{m+2}) \leq (a+b)^{m+1}\, [S_x^*(x_0, \cdots, x_0, x_1) + S_y^*(y_0, \cdots, y_0, y_1)]$$

Thus the claim is true for all $p \in \mathbb{N}$.

Next we prove that $\{x_p\}_{p \in \mathbb{N}}$ and $\{y_p\}_{p \in \mathbb{N}}$ are Cauchy sequences in X and Y respectively.

Consider for $p, q \in \mathbb{N}$ with $p < q$,

$$
\begin{aligned}
S_x^*&(x_p, \cdots, x_p, x_q) \\
&\leq (n-1)S_x^*(x_p, \cdots, x_p, x_{p+1}) + S_x^*(x_q, \cdots, x_q, x_{p+1}) \\
&= (n-1)S_x^*(x_p, \cdots, x_p, x_{p+1}) + S_x^*(x_{p+1}, \cdots, x_{p+1}, x_q) \\
&\leq (n-1)S_x^*(x_p, \cdots, x_p, x_{p+1}) + (n-1)S_x^*(x_{p+1}, \cdots, x_{p+1}, x_{p+2}) \\
&\qquad\qquad\qquad\qquad\qquad\qquad + S_x^*(x_q, \cdots, x_q, x_{p+2}) \\
&= (n-1)\Big[S_x^*(x_p, \cdots, x_p, x_{p+1}) + S_x^*(x_{p+1}, \cdots, x_{p+1}, x_{p+2}) \Big] \\
&\qquad\qquad\qquad\qquad\qquad\qquad + S_x^*(x_{p+2}, \cdots, x_{p+2}, x_q) \\
&\qquad\qquad\qquad\qquad \cdot\ \cdot\ \cdot \\
&\qquad\qquad\qquad\qquad\quad \cdot\ \cdot\ \cdot \\
&\qquad\qquad\qquad\qquad\qquad \cdot\ \cdot\ \cdot \\
&\leq (n-1)\Big[S_x^*(x_p, \cdots, x_p, x_{p+1}) + S_x^*(x_{p+1}, \cdots, x_{p+1}, x_{p+2}) \\
&\qquad + \cdots + S_x^*(x_{q-2}, \cdots, x_{q-2}, x_{q-1}) \Big] + S_x^*(x_q, \cdots, x_q, x_{q-1}) \\
&= (n-1)\sum_{i=p}^{q-2} S_x^*(x_i, \cdots, x_i, x_{i+1}) + S_x^*(x_{q-1}, \cdots, x_{q-1}, x_q) \\
&\leq (n-1)\sum_{i=p}^{q-2} (a+b)^i \left[S_x^*(x_0, \cdots, x_0, x_1) + S_y^*(y_0, \cdots, y_0, y_1) \right] \\
&\qquad + (a+b)^{q-1} \left[S_x^*(x_0, \cdots, x_0, x_1) + S_y^*(y_0, \cdots, y_0, y_1) \right] \\
\\
&= (n-1) \left[S_x^*(x_0, \cdots, x_0, x_1) + S_y^*(y_0, \cdots, y_0, y_1) \right] \sum_{i=p}^{q-2}(a+b)^i \\
&\qquad + (a+b)^{q-1} \left[S_x^*(x_0, \cdots, x_0, x_1) + S_y^*(y_0, \cdots, y_0, y_1) \right] \\
&\leq (n-1) \frac{(a+b)^p}{1-a-b} \left[S_x^*(x_0, \cdots, x_0, x_1) + S_y^*(y_0, \cdots, y_0, y_1) \right] \\
&\qquad + (a+b)^{q-1} \left[S_x^*(x_0, \cdots, x_0, x_1) + S_y^*(y_0, \cdots, y_0, y_1) \right] \\
&\to 0 \ as \ p, q \to \infty, \quad \text{since } a+b < 1.
\end{aligned}
$$

Thus, $\{x_m\}_{m \in \mathbb{N}}$ is a Cauchy sequence in X.

Similarly we have,

$$
\begin{aligned}
S_y^*(y_p, \cdots, y_p, y_q) \ \leq \ & (n-1) \frac{(a+b)^p}{1-a-b} \left[S_x^*(x_0, \cdots, x_0, x_1) + S_y^*(y_0, \cdots, y_0, y_1) \right] \\
& + (a+b)^{q-1} \left[S_x^*(x_0, \cdots, x_0, x_1) + S_y^*(y_0, \cdots, y_0, y_1) \right] \\
& \to 0 \ as \ p, q \to \infty, \quad \text{since } a+b < 1.
\end{aligned}
$$

Thus, $\{y_m\}_{m \in \mathbb{N}}$ is a Cauchy sequence in Y.

Since X and Y are complete S^* metric spaces, there exist $x \in X$ and $y \in Y$ such that

$$
\lim_{p \to \infty} x_p = x \quad \text{and} \quad \lim_{p \to \infty} y_p = y \tag{20}
$$

As in the Theorem 1, by assuming the continuity of F and G we can prove that $(x, y) \in X \times Y$ is an FG- coupled fixed point.

Now, suppose that X and Y have the properties (i) and (ii) respectively.

Since $\{x_m\}$ is increasing in X and $\{y_m\}$ is decreasing in Y and by using (20) we have $\forall\, m \in \mathbb{N}$ $x_m \preceq_{P_1} x$

and $y_m \succeq_{P_2} y$

That is by the definition of partial order on $X \times Y$ and $Y \times X$ we have

$$(x_m, y_m) \leq_{12} (x, y) \quad \text{and} \quad (y_m, x_m) \geq_{21} (y, x)$$

Now consider,

$$
\begin{aligned}
& S_x^*\big(x, \cdots, x, F(x, y)\big) \\
& \leq (n-1)\, S_x^*\big(x, \cdots, x, F(x_p, y_p)\big) + S_x^*\big(F(x, y), \cdots, F(x, y), F(x_p, y_p)\big) \\
& = (n-1)\, S_x^*\big(x, \cdots, x, F(x_p, y_p)\big) + S_x^*\big(F(x_p, y_p), \cdots, F(x_p, y_p), F(x, y)\big) \\
& \leq (n-1)\, S_x^*(x, \cdots, x, x_{p+1}) + a\, S_x^*(x_p, \cdots, x_p, x) + b\, S_y^*(y_p, \cdots, y_p, y) \\
& \to 0 \ as \ p \to \infty
\end{aligned}
$$

Thus, $F(x, y) = x$.

Similarly,

$$
\begin{aligned}
& S_y^*\big(y, \cdots, y, G(y, x)\big) \\
& \leq (n-1)\, S_y^*\big(y, \cdots, y, G(y_p, x_p)\big) + S_y^*\big(G(y, x), \cdots, G(y, x), G(y_p, x_p)\big) \\
& = (n-1)\, S_y^*(y, \cdots, y, y_{p+1}) + S_y^*\big(G(y, x), \cdots, G(y, x), G(y_p, x_p)\big) \\
& \leq (n-1)\, S_y^*(y, \cdots, y, y_{p+1}) + a\, S_y^*(y, \cdots, y, y_p) + b\, S_x^*(x, \cdots, x, x_p) \\
& \to 0 \ as \ p \to \infty
\end{aligned}
$$

Thus, $G(y, x) = y$.

That is, $F(x, y) = x$ and $G(y, x) = y$.

Hence (x, y) is an FG- coupled fixed point.

Next we prove the uniqueness of FG- coupled fixed point.

Claim: for any two points (x_1, y_1), $(x_2, y_2) \in X \times Y$ which are comparable and for all $k \in \mathbb{N}$

$$S_x^*\big(F^k(x_1, y_1), \cdots, F^k(x_1, y_1), F^k(x_2, y_2)\big) \leq (a+b)^k \big[S_x^*(x_1, \cdots, x_1, x_2) + S_y^*(y_1, \cdots, y_1, y_2)\big] \qquad (21)$$

and

$$S_y^*\big(G^k(y_1, x_1), \cdots, G^k(y_1, x_1), G^k(y_2, x_2)\big) \leq (a+b)^k \big[S_x^*(x_1, \cdots, x_1, x_2) + S_y^*(y_1, \cdots, y_1, y_2)\big] \qquad (22)$$

Without loss of generality assume that $(x_1, y_1) \leq_{12} (x_2, y_2)$.

That is by the definition of partial order we have $x_1 \preceq_{P_1} x_2$ and $y_2 \preceq_{P_2} y_1$

By the mixed monotone property of F and G we have

$$
\begin{aligned}
F(x_1, y_1) \quad & \preceq_{P_1} \quad F(x_2, y_1) \\
& \preceq_{P_1} \quad F(x_2, y_2)
\end{aligned}
$$

and

$$
\begin{aligned}
G(y_1, x_1) \quad & \succeq_{p_2} \quad G(y_2, x_1) \\
& \succeq_{p_2} \quad G(y_2, x_2)
\end{aligned}
$$

Again by the mixed monotone property of F and G we have

$$
\begin{aligned}
F^2(x_1, y_1) \quad & = \quad F\big(F(x_1, y_1), G(y_1, x_1)\big) \\
& \preceq_{P_1} \quad F\big(F(x_2, y_2), G(y_1, x_1)\big) \\
& \preceq_{P_1} \quad F\big(F(x_2, y_2), G(y_2, x_2)\big) \\
& = \quad F^2(x_2, y_2)
\end{aligned}
$$

and

$$
\begin{aligned}
G^2(y_1, x_1) &= G\big(G(y_1, x_1), F(x_1, y_1)\big) \\
&\succeq_{P_2} G\big(G(y_2, x_2), F(x_1, y_1)\big) \\
&\succeq_{P_2} G\big(G(y_2, x_2), F(x_2, y_2)\big) \\
&= G^2(y_2, x_2)
\end{aligned}
$$

Continuing like this we get $\forall\, m \in \mathbb{N} \cup \{0\}$,

$$
F^m(x_1, y_1) \preceq_{P_1} F^m(x_2, y_2) \ \text{ and } \ G^m(y_1, x_1) \succeq_{P_2} G^m(y_2, x_2)
$$

That is by the definition of partial order on $X \times Y$ and $Y \times X$ we have $\forall\, m \in \mathbb{N} \cup \{0\}$

$$
\big(F^m(x_1, y_1), G^m(y_1, x_1)\big) \leq_{12} \big(F^m(x_2, y_2), G^m(y_2, x_2)\big)
$$

and

$$
\big(G^m(y_1, x_1), F^m(x_1, y_1)\big) \geq_{21} \big(G^m(y_2, x_2), F^m(x_2, y_2)\big)
$$

Now, we prove the claim by the method of mathematical induction.
When $k = 1$ we have,

$$
\begin{aligned}
&S_x^*\big(F(x_1, y_1), \cdots, F(x_1, y_1), F(x_2, y_2)\big) \\
&\leq\ a\, S_x^*(x_1, \cdots, x_1, x_2) + b\, S_y^*(y_1, \cdots, y_1, y_2) \\
&\leq\ (a + b)[S_x^*(x_1, \cdots, x_1, x_2) + S_y^*(y_1, \cdots, y_1, y_2)]
\end{aligned}
$$

and

$$
\begin{aligned}
&S_y^*\big(G(y_1, x_1), \cdots, G(y_1, x_1), G(y_2, x_2)\big) \\
&=\ S_y^*\big(G(y_2, x_2), \cdots, G(y_2, x_2), G(y_1, x_1)\big) \\
&\leq\ a\, S_y^*(y_2, \cdots, y_2, y_1) + b\, S_x^*(x_2, \cdots, x_2, x_1) \\
&\leq\ a\, S_y^*(y_1, \cdots, y_1, y_2) + b\, S_x^*(x_1, \cdots, x_1, x_2) \\
&\leq\ (a + b)[S_x^*(x_1, \cdots, x_1, x_2) + S_y^*(y_1, \cdots, y_1, y_2)]
\end{aligned}
$$

Therefore claim is true for $k = 1$.
Now assume the claim for $k \leq m$ and check for $k = m + 1$.
Consider,

$$
\begin{aligned}
&S_x^*\big(F^{m+1}(x_1, y_1), \cdots, F^{m+1}(x_1, y_1), F^{m+1}(x_2, y_2)\big) \\
&= S_x^*\Big(F\big(F^m(x_1, y_1), G^m(y_1, x_1)\big), \cdots, F\big(F^m(x_1, y_1), G^m(y_1, x_1)\big), F\big(F^m(x_2, y_2), G^m(y_2, x_2)\big)\Big) \\
&\leq a S_x^*\big(F^m(x_1, y_1), \cdots, F^m(x_1, y_1), F^m(x_2, y_2)\big) + b S_y^*\big(G^m(y_1, x_1), \cdots, G^m(y_1, x_1), G^m(y_2, x_2)\big) \\
&\leq a\,(a + b)^m[S_x^*(x_1, \cdots, x_1, x_2) + S_y^*(y_1, \cdots, y_1, y_2)] \\
&\quad + b\,(a + b)^m[S_x^*(x_1, \cdots, x_1, x_2) + S_y^*(y_1, \cdots, y_1, y_2)] \\
&= (a + b)^{m+1}[S_x^*(x_1, \cdots, x_1, x_2) + S_y^*(y_1, \cdots, y_1, y_2)]
\end{aligned}
$$

Similarly we get,

$$
\begin{aligned}
S_y^*\big(G^{m+1}(y_1, x_1), \cdots, G^{m+1}(y_1, x_1), G^{m+1}(y_2, x_2)\big) &\leq\ (a + b)^{m+1}[S_x^*(x_1, \cdots, x_1, x_2) \\
&\quad + S_y^*(y_1, \cdots, y_1, y_2)]
\end{aligned}
$$

Thus the claim is true for all $k \in \mathbb{N}$.
Suppose that $(x, y), (x^*, y^*)$ be any two FG- coupled fixed points.
That is

$$
F(x, y) = x \ \text{ and } \ G(y, x) = y \tag{23}
$$

and

$$F(x^*, y^*) = x^* \quad \text{and} \quad G(y^*, x^*) = y^* \tag{24}$$

Case 1: If (x, y) and (x^*, y^*) are comparable, then

$$S_x^*(x, \cdots, x, x^*) = S_x^*\big(F(x,y), \cdots, F(x,y), F(x^*, y^*)\big)$$
$$\leq a\ S_x^*(x, \cdots, x, x^*) + b\ S_y^*(y, \cdots, y, y^*) \tag{25}$$

and

$$S_y^*(y, \cdots, y, y^*) = S_y^*\big(G(y,x), \cdots, G(y,x), G(y^*, x^*)\big)$$
$$\leq a\ S_y^*(y, \cdots, y, y^*) + b\ S_x^*(x, \cdots, x, x^*) \tag{26}$$

Adding (25) and (26) we get

$$S_x^*(x, \cdots, x, x^*) + S_y^*(y, \cdots, y, y^*) \leq (a + b)\ [S_x^*(x, \cdots, x, x^*) + S_y^*(y, \cdots, y, y^*)]$$

which implies that $S_x^*(x, \cdots, x, x^*) + S_y^*(y, \cdots, y, y^*) = 0$ since $a + b < 1$.
Therefore we have, $x = x^*$ and $y = y^*$.
Case 2: Suppose (x, y) and (x^*, y^*) are not comparable.
Then by the hypothesis there exist $(u, v) \in X \times Y$ which is comparable to both (x, y) and (x^*, y^*).
Consider,

$$S_x^*(x, \cdots, x, x^*) = S_x^*\big(F^k(x,y), \cdots, F^k(x,y), F^k(x^*, y^*)\big)$$

$$\leq (n-1)\ S_x^*\big(F^k(x,y), \cdots, F^k(x,y), F^k(u,v)\big) + S_x^*\big(F^k(x^*,y^*), \cdots, F^k(x^*,y^*), F^k(u,v)\big)$$
$$\leq (n-1)\ (a+b)^k [S_x^*(x, \cdots, x, u) + S_y^*(y, \cdots, y, v)]$$
$$+ (a+b)^k [S_x^*(x^*, \cdots, x^*, u) + S_y^*(y^*, \cdots, y^*, v)]$$
$$\to 0\ as\ k \to \infty \text{ since } a + b < 1$$

Thus we have $x = x^*$.
Consider,

$$S_y^*(y, \cdots, y, y^*)$$
$$= S_y^*\big(G^k(y,x), \cdots, G^k(y,x), G^k(y^*, x^*)\big)$$
$$\leq (n-1)\ S_y^*\big(G^k(y,x), \cdots, G^k(y,x), G^k(v,u)\big) + S_y^*\big(G^k(y^*,x^*), \cdots, G^k(y^*,x^*), G^k(v,u)\big)$$
$$\leq (n-1)\ (a+b)^k [S_x^*(x, \cdots, x, u) + S_y^*(y, ..., y, v)]$$
$$+ (a+b)^k [S_x^*(x^*, \cdots, x^*, u) + S_y^*(y^*, \cdots, y^*, v)]$$
$$\to 0\ as\ k \to \infty \text{ since } a + b < 1$$

Thus by Definition 1 (ii) we have $y = y^*$.
Therefore, $x = x^*$ and $y = y^*$
Hence the proof.

Remark 3. *By taking $n = 2$, $a = b = \frac{k}{2}$, $X = Y$ and $F = G$ and assuming condition (I) and (II) of the above theorem we get the Theorems 2.1 and 2.2 of Bhaskar and Lakshmikantham [?] respectively as corollaries to our results.*

Remark 4. *By taking $n = 2$, $a = b = \frac{k}{2}$, $X = Y$ and $F = G$ and assuming condition (I) and (III) of the above theorem we get the Theorems 2.4 of Bhaskar and Lakshmikantham [?] as a corollary to our results.*

We illustrate the above theorem with the following example.

Example 2. *Let $X = [0, \infty)$ and $Y = (-\infty, 0]$ with the usual order in $\mathbb{R}$*
Consider the S^* metric on both X and Y as

$$S^*(a_1, \cdots, a_n) = \sum_{i=1}^{n} \sum_{i<j} |a_i - a_j|$$

Define $F : X \times Y \to X$ and $G : Y \times X \to Y$ by

$$F(x, y) = \frac{2x - 3y}{7n} \quad and \quad G(y, x) = \frac{2y - 3x}{7n}$$

For $x, u \in X$ and $y, v \in Y$ with $x \leq u$ and $y \geq v$ we have

$$\frac{2x - 3y}{7n} \leq \frac{2u - 3y}{7n}, \ \frac{2y - 3x}{7n} \geq \frac{2y - 3u}{7n}$$

and

$$\frac{2x - 3y}{7n} \leq \frac{2x - 3v}{7n}, \ \frac{2y - 3x}{7n} \geq \frac{2v - 3x}{7n}$$

That is,

$$F(x, y) \leq F(u, y), \ G(y, x) \geq G(y, u) \quad and \quad F(x, y) \leq F(x, v), \ G(y, x) \geq G(v, x)$$

Therefore F and G are mixed monotone mappings.
Next we show that F and G satisfy the contractive type conditions (14) and (15)

$$
\begin{aligned}
S^*(F(x, y), \cdots, F(x, y), F(u, v)) &= (n - 1) \left| \frac{2x - 3y}{7n} - \frac{2u - 3v}{7n} \right| \\
&\leq \frac{2}{7n} (n - 1)|x - u| + \frac{3}{7n} (n - 1)|y - v| \\
&= \frac{2}{7n} S^*(x, \cdots, x, u) + \frac{3}{7n} S^*(y, \cdots, y, v)
\end{aligned}
$$

and

$$
\begin{aligned}
S^*(G(y, x), \cdots, G(y, x), G(v, u)) &= (n - 1) \left| \frac{2y - 3x}{7n} - \frac{2v - 3u}{7n} \right| \\
&\leq \frac{2}{7n} (n - 1)|y - v| + \frac{3}{7n} (n - 1)|x - u| \\
&= \frac{2}{7n} S^*(y, \cdots, y, v) + \frac{3}{7n} S^*(x, \cdots, x, u)
\end{aligned}
$$

Therefore F and G satisfy the contractive type conditions (14) and (15) for $a = \frac{2}{7n}$ and $b = \frac{3}{7n}$.
Here $(0, 0)$ is the unique FG- coupled fixed point.

REFERENCES

[1] **Abdellaoui, M.A.** and **Dahmani, Z.** (2016). New Results on Generalized Metric Spaces, *Malaysian Journal of Mathematical Sciences* 10(1): 69 - 81.

[2] **Ajay Singh** and **Nawneet Hooda** (2014). Coupled Fixed Point Theorems in S-metric Spaces. *International Journal of Mathematics and Statistics Invention*, 2 (4), 33 − 39.

[3] **Dhage B. C.** (1992). Generalized metric spaces mappings with fixed point. *Bull. Calcutta Math. Soc.* 84, 329 - 336.

[4] **Gahler, S** (1963). 2-metriche raume und ihre topologische struktur. *Math. Nachr.* 26,115 - 148.

[5] **Gnana Bhaskar T.**, **Lakshmikantham V.** (2006). Fixed point theorems in partially ordered metric spaces and applications. *Nonlinear Analysis* 65, 1379 - 1393.

[6] **Hans Raj** and **Nawneet Hooda** (2014). Coupled fixed point theorems in S- metric spaces with mixed g- monotone property. *International Journal of Emerging Trends in Engineering and Development*, 4 (4), 68 – 81.

[7] **Hemant Kumar Nashine** (2012). Coupled common fixed point results in ordered G-metric spaces. *J. Nonlinear Sci. Appl.* 1, 1 – 13.

[8] **Huang Long- Guang**, **Zhang Xian** (2007). Cone metric spaces and fixed point theorems of contractive mappings. *Journal of Mathematical Analysis and Applications* 332, 1468 – 1476.

[9] **Erdal Karapnar**, **Poom Kumam** and **Inci M Erhan** (2012). Coupled fixed point theorems on partially ordered G-metric spaces. *Fixed Point Theory and Applications*, 2012:174.

[10] **Mujahid Abbas**, **Bashir Ali** and **Yusuf I Suleiman** (2015). Generalized coupled common fixed point results in partially ordered A-metric spaces. *Fixed Point Theory and Applications*,64 DOI 10.1186/s13663- 015-0309-2.

[11] **Mustafa, Z.** and **Sims B.**(2006). A new approach to generalized metric spaces. *J. Nonlinear Convex Anal.,* 7(2), 289 - 297.

[12] **Prajisha E.** and **Shaini P.** (2019). FG- coupled fixed point theorems for various contractions in partially ordered metric spaces. *Sarajevo Journal of Mathematics, vol.15* (28), No.2, 291 – 307

[13] **K. Prudhvi** (2016). Some Fixed Point Results in S-Metric Spaces. *Journal of Mathematical Sciences and Applications,* Vol. 4, No. 1, 1-3.

[14] **Sabetghadam F.**, **Masiha H.P.** and **Sanatpour A.H.** (2009). Some coupled fixed point theorems in cone metric spaces. *Fixed Point Theory and Applications*, 8 doi:10.1155/2009/125426. Article ID 125426.

[15] **Sedghi S.**, **Shobe N.** and **Aliouche A.**(2012). A generalization of fixed point theorem in S-metric spaces. *Mat. Vesnik*, 64, 258 – 266.

[16] **Sedghi S.**, **Shobe N.** and **Zhou H.** (20007). A common fixed point theorem in D^* metric space. *Fixed Point Theory Appl.*,1 - 13.

[17] **Prajisha E.** and **Shaini P.** (2017). FG- coupled fixed point theorems in generalized metric spaces. *Mathematical Sciences International Research Journal, Volume 6 (Spl Issue)*, 24-29.

[18] **Karichery Deepa**, and **Shaini Pulickakunnel** (2018). FG-coupled fixed point theorems for contractive type mappings in partially ordered metric spaces. *Journal of Mathematics and Applications* 41.

[19] **Prajisha E.** and **Shaini P.** (2017). FG- coupled fixed point theorems in cone metric spaces. *Carpathian Math. Publ.,* 9 (2), 163–170.

/07/

THE LERAY-SCHAUDER PRINCIPLE IN GEODESIC SPACES

Sreya Valiya Valappil

Department of Mathematics, Central University of kerala, Kasaragod, India.

E-mail:sreya.v.v@cukerala.ac.in

ORCID:0000-0003-1089-3036

Shaini Pulickakunnel

Department of Mathematics, Central University of kerala, Kasaragod, India.

E-mail:shainipv@cukerala.ac.in

ORCID:0000-0001-9958-9211

ABSTRACT

The essential maps introduced by Granas in 1976 is a best tool for proving continuation results for compact maps. Several authors modified this idea to different scenarios. This is a review article, here, we consider the continuation results based on essential maps and the Leray-Schauder principle in the setting of uniquely geodesic spaces [20].

KEYWORDS

$\Gamma-$*uniquely geodesic spaces, Essential maps, Fixed point, Leray Schauder principle.*

1 INTRODUCTION

This paper is based on the notion of essential maps defined by Granas [9] in 1976. Many studies and extensions of this concept in variety of settings have been done by several authors [2, 8, 16–18]. Essential map techniques are one of the best tools to prove continuation results for compact maps [1].

Compact maps play a vital role in proving the existence and uniqueness of solutions of differential and integral equations. The classical Schauder fixed point theorem proved by Juliusz Schauder in 1930 in the setting of Banach spaces as a generalization of the celebrated Brouwer's fixed point theorem and the famous Leray-Schauder principle are milestones in the theory of fixed points and both of these incredible results are based on compact maps. For many years, researchers were trying to extend the concepts in normed spaces to more general spaces. In that direction, several authors have extended very many important fixed point theorems to various general spaces [3, 15]. Most importantly, the geodesic spaces grasped the attention of many fixed point theorists after the publication of the papers [11, 12] due to Kirk. A version of Schauder fixed point theorem has been proved by Niculescu and Roventa in $CAT(0)$ spaces [15] by assuming the compactness of convex hull of finite number of elements. Followed by this, in [3], Ariza, Li and Lopez have proved the Schauder Fixed point theorem in the setting of $\Gamma-$uniquely geodesic spaces, which includes Busemann spaces, Linear spaces, $CAT(\kappa)$ spaces with diameter less than $D_k/2$, Hyperbolic spaces [19] etc.

Granas introduced essential maps in order to prove continuation results for compact maps in Banach spaces [9]. In his paper, he has proved topological transversality principle and the Leray Schauder principle, using essential maps techniques. The Leray Schauder principle was first proved for compact mappings in Banach spaces and this has been broadly used to obtain fixed points of variety of mappings under different settings and many interesting contributions can be found in the literature [4, 6, 7, 13, 14]. In [9], Granas has also proved several fixed point results for compact maps using essential mappings and homotopical methods. Followed by the results established by Granas, Agarwal and O'Regan [2] have extended the concept of essential maps to a large class of mappings and established several fixed point theorems in 2000. The concept of essential maps has been further extended to $d-$essential maps, and $d-L$-essential maps [18].

In this review article, we consider the continuation results based on essential maps, and the Leray-Schauder principle in the setting of uniquely geodesic spaces.

2 Preliminaries

We recall some basic definitions and results used in this paper.

Definition 1. [5] *Let (X, ρ) be a metric space. A geodesic segment (or geodesic)from $x \in X$ to $y \in X$ is a map γ from a closed interval $[0, l] \subseteq \mathbb{R}$ to X such that $\gamma(0) = u$, $\gamma(l) = v$ and $\rho(\gamma(t_1), \gamma(t_2)) = |t_1 - t_2|$ for all t_1, t_2 in $[0, l]$.*
(X, ρ) is said to be a geodesic space if every two points in X are joined by a geodesic and (X, ρ) is uniquely geodesic if there is exactly one geodesic joining u to v, for all $u, v \in X$.

We denote the set of all geodesic segments in X by Ω. For $A \subseteq X$, closure and boundary of A in X is denoted by $\overline{A}$ and ∂A respectively.

Definition 2. [3] *Let (X, ρ) be a metric space and $\Gamma \subseteq \Omega$ be a family of geodesic segments. We say that (X, ρ) is a $\Gamma-$uniquely geodesic space if for every $x, y \in X$, there exists a unique geodesic in Γ passes through x and y. We denote a unique geodesic segment in Γ joining x and y by $\gamma_{x,y}$.*

Remark 1. [3] *Let (X, ρ) be a $\Gamma-$uniquely geodesic space. Then, the family Γ induces a unique mapping $\bigoplus_\Gamma : X^2 \times [0, 1] \to X$ such that $\bigoplus_\Gamma(x, y, \tau) \in \gamma_{x,y}$ and the following properties hold for each $u, v \in X$:*

1. $\rho(\bigoplus_\Gamma(x,y,\tau), \bigoplus_\Gamma(u,v,s)) = |\tau - s|\rho(u,v)$ for all $\tau, s \in [0,1]$

2. $\bigoplus_\Gamma(u,v,0) = u$ and $\bigoplus_\Gamma(u,v,1) = v$

Also, it is enough to consider $\bigoplus_\Gamma(u,v,\tau) = \gamma_{u,v}(\tau\rho(u,v))$, i.e., it is a point on γ at a distance $\tau\rho(u,v)$ from u and we denote it by $(1-\tau)u \oplus \tau v$.

Definition 3. [1] *Let X and Y be two metric spaces. A map $\zeta : X \to Y$ is called compact if $\zeta(X)$ is contained in a compact subset of Y.*

Definition 4. [1] *Let T be a closed convex subset of a Banach space X and S be a closed subset of T. Denote set of all continuous, compact maps $\zeta : S \to T$ by $\mathscr{K}(S,T)$ and set of all maps $\zeta \in \mathscr{K}(S,T)$ with $x \neq \zeta(x)$ by $\mathscr{K}_{\partial S}(S,T)$ for $x \in \partial S$.*
A map $\zeta \in \mathscr{K}_{\partial S}(S,T)$ is essential in $\mathscr{K}_{\partial S}(S,T)$ if for every map $\xi \in \mathscr{K}_{\partial S}(S,T)$ with $\zeta|_{\partial S} = \xi|_{\partial S}$ there exists $x \in \text{int} S$ with $x = \xi(x)$. Otherwise ζ is inessential in $\mathscr{K}_{\partial S}(S,T)$, that is, there exists a fixed point free $\xi \in \mathscr{K}_{\partial S}(S,T)$ with $\zeta|_{\partial S} = \xi|_{\partial S}$.

Definition 5. [1] *Two maps $\zeta, \xi \in \mathscr{K}_{\partial S}(S,T)$ are homotopic in $\mathscr{K}_{\partial S}(S,T)$, written $\zeta \simeq \xi$ in $\mathscr{K}_{\partial S}(S,T)$, if there exists a continuous, compact mapping $H : S \times [0,1] \to T$ such that $H_t(x) := H(\cdot, \tau) : S \to T$ belongs to $\mathscr{K}_{\partial S}(S,T)$ for each $\tau \in [0,1]$ with $H_0 = \zeta$ and $H_1 = \xi$.*

Definition 6. [3] *A $\Gamma-$uniquely geodesic space is said to have property (Q) if*

$$\lim_{\varepsilon \to 0} \sup\{\rho((1-\tau)x \oplus \tau y, (1-\tau)x \oplus \tau z) : \tau \in [0,1], \quad x,y,z \in X, \quad \rho(y,z) \leq \varepsilon\} = 0.$$

Definition 7. [3] *Let S be a nonempty subset of a $\Gamma-$uniquely geodesic space. We say that S is $\Gamma-$convex if $\gamma_{x,y} \subseteq S$ for all $x,y \in S$*

Remark 2. [3] *Let $(X, \|.\|)$ be a normed linear space, Γ_L the family of linear segments and let ρ denote the metric induced by the norm $\|.\|$. Then (X, ρ) is a Γ_L-uniquely geodesic space with property (Q).*

Definition 8. [3] *A metric space (X, ρ) is a hyperbolic space (in the sense of Reich-Shafir [19]) if X is $\Gamma-$ uniquely geodesic and the following inequality holds*

$$\rho(\frac{1}{2}x \oplus \frac{1}{2}y, \frac{1}{2}x \oplus \frac{1}{2}z) \leq \frac{1}{2}\rho(y,z).$$

Many authors have developed various extensions, and modifications to Schauder's fixed point theorem [10, 15]. In [3], Schauder-type fixed point theorem in the setting of geodesic spaces with the property (Q) is proved as follows:

Theorem 1. [3] *Let (X, ρ) be a $\Gamma-$ uniquely geodesic space with property (Q), and all balls are Γ-convex. Let K be a nonempty, closed, $\Gamma-$convex subset of (X, ρ). Then, any continuous mapping $T : K \to K$ with compact range $\overline{T(K)}$ has at least one fixed point in K.*

Throughout this paper, we denote a closed $\Gamma-$convex subset of the geodesic space X by T and interior of S by int S, where S is a closed subset of T. We denote the set of all continuous, compact maps $\zeta : S \to T$ by $\mathscr{K}(S,T)$ and set of all maps $\zeta \in \mathscr{K}(S,T)$ with $x \neq \zeta(x)$ by $\mathscr{K}_{\partial S}(S,T)$ for $x \in \partial S$.

3 RESULTS

Theorem 2. [20] *Let (X, ρ) be a Γ-uniquely geodesic space satisfying property (Q) and $\zeta, \xi \in \mathscr{K}_{\partial S}(S,T)$. Suppose that for all $(u, \tau) \in \partial S \times [0,1]$,*

$$u \neq (1-\tau)\zeta(u) \oplus \tau\xi(u)$$

i.e., geodesic segment joining $\zeta(u)$ and $\xi(u)$ does not contain u. Then $\zeta \simeq \xi$ in $\mathscr{K}_{\partial S}(S,T)$.

Proof. Let $H(u,\tau) = H_t(u) = \bigoplus_\Gamma (\zeta(u), \xi(u), \tau) = (1-\tau)u \oplus \tau \xi u$. Clearly, H is continuous. We show that $H : S \times [0,1] \to T$ is a compact map.

Let $\{x_i\}$ be a sequence in S. Since $\zeta, \xi : S \to T$ are compact maps, $\zeta(x_i) \to u$ and $\xi(x_i) \to v$ as $i \to \infty$ for some subsequence $\mathbb{S}$ of natural numbers and $u, v \in T$. Let $\tau \in [0,1]$ be such that τ is the limit of some sequence $\tau_i \in [0,1]$. Now using Remark 1,

$$
\begin{aligned}
\rho\big(H(x_i, \tau_i), (1-\tau)u \oplus \tau v\big) &= \rho\big(\bigoplus_\Gamma (\zeta(x_i), \xi(x_i), \tau_i), (1-\tau)u \oplus \tau v\big) \\
&\leq \rho\big((1-\tau_i)\zeta(x_i) \oplus \tau_i \xi(x_i), (1-\tau)\zeta(x_i) \oplus \tau \xi(x_i)\big) \\
&\quad + \rho\big((1-\tau)\zeta(x_i) \oplus \tau \xi(x_i), (1-\tau)u \oplus \tau v\big) \\
&\leq |\tau_i - \tau|\rho(\zeta(x_i), \xi(x_i)) \\
&\quad + \rho\big((1-\tau)\zeta(x_i) \oplus \tau \xi(x_i), (1-\tau)\zeta(x_i) \oplus \tau v\big) \\
&\quad + \rho\big((1-\tau)\zeta(x_i) \oplus \tau v, (1-\tau)u \oplus \tau v\big).
\end{aligned}
\tag{1}
$$

Since $\tau_i \to \tau$, we get

$$
|\tau_i - \tau|\rho(\zeta(x_i), \xi(x_i)) \to 0.
\tag{2}
$$

Since $\xi(x_i) \to v$, we have $\rho(\xi(x_i), v) \leq \epsilon$ for every $\epsilon > 0$. Thus using property (Q), we get,

$$
\rho\big((1-\tau)\zeta(x_i) \oplus \tau \xi(x_i), (1-\tau)\zeta(x_i) \oplus \tau v\big) \to 0.
\tag{3}
$$

Similarly,

$$
\rho\big((1-\tau)\zeta(x_i) \oplus \tau v, (1-\tau)u \oplus \tau v\big) \to 0.
\tag{4}
$$

Using (2), (3) and (4) in (1), we have

$$
\{H(x_i, \tau_i)\} \to (1-\tau)u \oplus \tau v, \quad \text{for } t_i \in [0,1].
\tag{5}
$$

Since T is $\Gamma-$convex, $(1-\tau)u \oplus \tau v \in T$. Hence H is compact.

But it is given that $u \neq (1-\tau)\zeta(u) \oplus \tau \xi(u)$ for $(u,\tau) \in \partial S \times [0,1]$. Hence $H_\tau(u) \in \mathscr{K}_{\partial S}(S,T)$, $H(u,0) = \zeta(u)$ and $H(u,1) = \xi(u)$. Therefore $\zeta \simeq \xi$ in $\mathscr{K}_{\partial S}(S,T)$.

Following result in [1] is a corollary to our theorem.

Corollary 1. [1, Theorem 6.1] *Let X be a Banach space, T a closed, convex subset of X, S a closed subset of T and $\zeta, \xi \in \mathscr{K}_{\partial S}(S,T)$. Suppose that for all $(u, \lambda) \in \partial S \times [0,1]$,*

$$
u \neq (1-\lambda)\zeta(u) + \lambda \xi(u).
$$

Then $\zeta \simeq \xi$ in $\mathscr{K}_{\partial S}(S,T)$.

Proof. Using Remark 2, X is a Γ_L-uniquely geodesic space. Hence by Theorem 2, the result follows.

Next result is a characterization of inessential maps in $\mathscr{K}_{\partial S}(S,T)$ in $\Gamma-$uniquely geodesic spaces.

Theorem 3. [20] *Let (X, ρ) be a Γ-uniquely geodesic space satisfying property (Q) and let $\zeta \in \mathscr{K}_{\partial S}(S,T)$. Then ζ is inessential in $\mathscr{K}_{\partial S}(S,T)$ if and only if there exists $\xi \in \mathscr{K}_{\partial S}(S,T)$ with $\xi(u) \neq u$ for all $u \in S$ and $\zeta \simeq \xi$ in $\mathscr{K}_{\partial S}(S,T)$.*

Proof. Assume that ζ is inessential in $\mathscr{K}_{\partial S}(S,T)$. Hence there exists a map $\xi \in \mathscr{K}_{\partial S}(S,T)$ such that $\xi(u) \neq u$ for all $u \in S$ and $\zeta|_{\partial S} = \xi|_{\partial S}$ by definition. Suppose there exists $(u,\tau) \in \partial S \times [0,1]$ such that $u = (1-\tau)\zeta(u) \oplus \tau \xi(u)$. Since $\zeta|_{\partial S} = \xi|_{\partial S}$, it follows that $u = \xi(u)$, which is a contradiction to the fact that $\xi \in \mathscr{K}_{\partial S}(S,T)$. Hence $u \neq (1-\tau)\zeta(u) \oplus \tau \xi(u)$, for each $(u,\tau) \in \partial S \times [0,1]$. Hence by using Theorem 2, we have $\zeta \simeq \xi$. Thus we have $\xi u \neq u$ and $\zeta \simeq \xi$.

Conversely assume that there exists $\xi \in \mathscr{K}_{\partial S}(S,T)$ with $\xi(u) \neq u$ for all $u \in S$ and $\zeta \simeq \xi$ in $\mathscr{K}_{\partial S}(S,T)$. Let $H : S \times [0,1] \to T$ with $H_t \in \mathscr{K}_{\partial S}(S,T)$ for all $\tau \in [0,1]$ be a continuous compact map with $H_0 = \zeta$ and $H_1 = \xi$. Consider

$$
M = \Big\{ u \in S : u = H(u, \tau) \text{ for some } \tau \in [0,1] \Big\}.
$$

There arise two cases.

Case-1: $M = \emptyset$.
If $M = \emptyset$ then $H_t(u) \neq u$ for all $u \in S$ and $\tau \in [0,1]$. In particular, $\zeta(u) = H_0(u) \neq u$ for all $u \in S$. Hence the inessentiality of ζ in $\mathscr{K}_{\partial S}(S,T)$ follows.

Case-2: $M \neq \emptyset$.
Let $\{x_i\} \in M$ such that $\{x_i\} \to u$. Then $x_i = H(x_i, \tau_i)$. Using the continuity of H, we get $u = H(u, \tau)$. Thus M is a closed subset of S.
Now, suppose $M \bigcap \partial S \neq \emptyset$. If $u \in M \bigcap \partial S$, then $u \in M$ and $u \in \partial S$, which implies $u = H_t(u)$ for $u \in \partial S$, a contradiction since $H_t \in \mathscr{K}_{\partial S}(S,T)$. Hence by the Urysohn's lemma, there exist $\xi : S \to [0,1]$ continuous, with $\xi(M) = 1$ and $\xi(\partial S) = 0$.
Define $f : S \to T$ by $f(u) = H(u, \xi(u))$. Clearly, f is a continuous compact map. If $u \in \partial S$, $f(u) = H(u,0) = \zeta(u)$. Thus $f|_{\partial S} = \zeta|_{\partial S}$.
If $u = f(u)$ for some $u \in S$ then, $u = f(u) = H(u, \xi(u))$. Thus $u \in M$ and hence $\xi(u) = 1$. Hence $u = f(u) = H(u, \xi(u)) = H(u,1) = \xi(u)$. Thus $f \in \mathscr{K}_{\partial S}(S,T)$ with $u = f(u)$ with $f|_{\partial S} = \zeta|_{\partial S}$. Therefore ξ has a fixed point, which is a contradiction to our assumption. Thus $u \neq f(u)$. Hence ζ is inessential in $\mathscr{K}_{\partial S}(S,T)$, by Definition 4. Hence the proof.

As a consequence of Theorem 3, we obtain the following corollary.

Corollary 2. *Let X be a Hyperbolic space (in the sense of [19]), T a closed, convex subset of X, S a closed subset of T and $\zeta \in \mathscr{K}_{\partial S}(S,T)$. Then the following are equivalent:*

(i) *ζ is inessential in $\mathscr{K}_{\partial S}(S,T)$.*

(ii) *There exists $\xi \in \mathscr{K}_{\partial S}(S,T)$ with $\xi(u) \neq u$ for all $u \in S$ and $\zeta \simeq \xi$ in $\mathscr{K}_{\partial S}(S,T)$.*

Proof. Every Hyperbolic space is a Γ-uniquely geodesic space with property (Q). Hence the result follows from Theorem 3.

Theorem 4. *[20] Let (X, ρ) be a Γ-uniquely geodesic space satisfying property (Q). Suppose that $\zeta, \xi \in \mathscr{K}_{\partial S}(S,T)$ with $\zeta \simeq \xi$ in $\mathscr{K}_{\partial S}(S,T)$. Then ζ is essential in $\mathscr{K}_{\partial S}(S,T)$ if and only if ξ is essential in $\mathscr{K}_{\partial S}(S,T)$.*

Proof. Suppose ζ is inessential in $\mathscr{K}_{\partial S}(S,T)$. Then from Theorem 3, there exists $T \in \mathscr{K}_{\partial S}(S,T)$ with $\zeta \simeq T$ in $\mathscr{K}_{\partial S}(S,T)$ such that $T(u) \neq u$ for all $u \in S$. Hence, $\xi \simeq T$ in $\mathscr{K}_{\partial S}(S,T)$. Thus $\zeta \simeq \xi$ and $\xi \simeq T$ implies $\xi \simeq T$ in $\mathscr{K}_{\partial S}(S,T)$. Therefore by Theorem 3, ξ is inessential in $\mathscr{K}_{\partial S}(S,T)$. Hence the proof.

Corollary 3. *[20] Let X be a Hyperbolic space (in the sense of [19]), S be a closed, convex subset of X, S be a closed subset of T and $\zeta, \xi \in \mathscr{K}_{\partial S}(S,T)$ with $\zeta \simeq \xi$ in $\mathscr{K}_{\partial S}(S,T)$. Then ζ is essential in $\mathscr{K}_{\partial S}(S,T)$ if and only if ξ is essential in $\mathscr{K}_{\partial S}(S,T)$.*

The above corollary is a special case of Theorem 4.

Theorem 5. *[20] Let (X, ρ) be a Γ-uniquely geodesic space with all balls are $\Gamma-$convex and satisfies property (Q). Let $w \in \text{int } S$. Then the map $\zeta(S) = w$ is essential in $\mathscr{K}_{\partial S}(S,T)$.*

Proof. Consider the continuous compact map $\xi : S \to T$ which agrees with ζ on ∂S. It is enough to show that $\xi(u) = u$ for some $u \in \text{int } S$. Let $\zeta : T \to T$ be given by

$$\zeta(u) = \begin{cases} \xi(u), & u \in S; \\ w, & u \in T \setminus S. \end{cases}$$

Then ζ is continuous and compact (since ξ and w are continuous and compact and on ∂S, $\zeta(u) = \xi(u) = w$). Thus by Theorem 1, $\zeta(u) = u$ for some $u \in S$. If $u \in T \setminus S$, we get $\zeta(u) = w$. Hence

$\zeta(w) = w$, which is a contradiction, since $w \in \text{int} S$. Clearly $u \in \text{int } S$. Hence x is a fixed point of ξ. Therefore ζ is essential in $\mathscr{K}_{\partial S}(S, S)$.

The following result in [1] is a corollary to our theorem.

Corollary 4. [1, Theorem 6.5] *Let X be a Banach space, T a closed, convex subset of X, S a closed subset of T and $u \in \text{int } S$. Then the constant map $\zeta(S) = w$ is essential in $\mathscr{K}_{\partial S}(S, T)$.*

Proof. We know that all balls in Banach spaces are convex. Hence the result follows from theorem 5.

As a consequence of the above theorems, authors proved the Leray Schauder principle in $\Gamma-$uniquely geodesic spaces in [20], which generalizes the Leray Schauder principle in Hyperbolic spaces proved in [3].

Theorem 6. [20] *Let (X, ρ) be a Γ-uniquely geodesic space satisfying property (Q), and all balls are $\Gamma-$convex. Suppose that $\zeta : S \to T$ is a continuous compact map. Then either*

(i) ζ has a fixed point in S, or

(ii) There exists $(x_0, \tau) \in \partial S \times [0, 1]$ such that $x_0 = (1 - \tau)u \oplus \tau\zeta(x_0)$.

Proof. Suppose that (ii) does not hold and $\zeta(u) \neq u$ for all $u \in \partial S$. Define $\xi : S \to T$ by $\xi(u) = w$ for all $u \in S$. Consider the map $H : S \times [0, 1] \to T$ defined by

$$H(u, \tau) := (1 - \tau)w \oplus \tau\zeta(u),$$

which is continuous and compact. Also, for all $u \in \partial S$, $H_t(u) = (1 - \tau)w \oplus \tau\zeta(u) \neq u$ for a fixed τ (since we assumed that condition (ii) does not hold). Hence by Theorem 2, $\zeta \simeq w$ in $\mathscr{K}_{\partial S}(S, T)$. But we know that w is essential in $\mathscr{K}_{\partial S}(S, T)$ by theorem 5. Hence ζ is essential in $\mathscr{K}_{\partial S}(S, T)$ by Theorem 4. Now using Definition 4, $\zeta(u) = u$ for some $u \in \text{int } S$.

The following Theorem is a consequence of Theorem 6.

Corollary 5. [3, Theorem 23] *Let X be a Hyperbolic space(in the sense of [19]), $x_0 \in X$ and $r > 0$. Suppose that $T : B[x_0, r] \to X$ be a continuous mapping with $\overline{T(B[x_0, r])}$ compact. Then either*

(i) T has at least one fixed point in $B[x_0, r]$, or

(ii) There exists $(u, \lambda) \in \partial B[x_0, r] \times [0, 1]$ with $u = (1 - \lambda)x_0 \oplus \lambda T(u)$.

Proof. Hyperbolic spaces are geodesic spaces with property (Q), and balls are Γ-convex. Hence the result follows from the above theorem.

4 CONCLUSIONS

In this review article, we considered continuation results in Γ-uniquely geodesic spaces and the Leray-Schauder principle in $\Gamma-$uniquely geodesic spaces proved in [20]. Geodesic spaces having the property (Q) include Busemann spaces, linear spaces, $CAT(\kappa)$ spaces with diameters smaller than $D_k/2$, hyperbolic spaces (in the sense of [19], etc., and balls are Γ-convex in these spaces. All the results in this paper are thus applicable to these spaces as well. One can attempt to develop similar results for multivalued mappings in geodesic spaces and establish similar results for d-essential maps, d-L essential maps, and other general classes of maps [2, 18].

ACKNOWLEDGMENT

REFERENCES

[1] **Agarwal, R. P.**, **Meehan, M.**, and **O'regan, D**. (2001). *Fixed point theory and applications* (Vol. 141). Cambridge university press.

[2] **Agarwal, R. P.**, and **O Regan, D.** (2000). Essential and inessential maps and continuation theorems. *Applied Mathematics Letters,* 13(2), 83-90.

[3] **Ariza-Ruiz, D.**, **Li, C.**, and **López-Acedo, G.** (2014). The Schauder fixed point theorem in geodesic spaces. *Journal of Mathematical Analysis and Applications*, 417(1), 345-360.

[4] **Borisovich, Y. G.**, Zvyagin, V. G., and **Sapronov, Y. I.** (1977). Non-linear Fredholm maps and the Leray-Schauder theory. *Russian Mathematical Surveys,* 32(4), 1.

[5] **Bridson, M. R.**, and **Haefliger, A.** (2013). *Metric spaces of non-positive curvature* (Vol. 319). Springer Science & Business Media.

[6] **Cronin, J.** (1995). *Fixed points and topological degree in nonlinear analysis* (Vol. 11). American Mathematical Soc..

[7] **Fucík, S.** (1981). *Solvability of nonlinear equations and boundary value problems* (Vol. 4). Springer Science & Business Media.

[8] **Gabor, G.**, **Górniewicz, L.**, and **Ślosarski, M**. (2009). Generalized topological essentiality and coincidence points of multivalued maps. *Set-Valued and Variational Analysis,* 17(1), 1-19.

[9] **Granas, A.** (1976). Sur la mhode de continuitb de PoincarB. *CR Acad. Sci., Paris*, 282, 983-985.

[10] **Granas, A.**, and **Dugundji, J.** (2003). *Fixed point theory* (Vol. 14, pp. 15-16). New York: Springer.

[11] **Kirk W. A.** (2003). Geodesic geometry and fixed point theory. *Seminar of Math. Analy., Proc.*

[12] **Kirk, W. A.** (2004). Geodesic geometry and fixed point theory II. *Fixed Point Theory and Applications.*

[13] **Ladyzhenskaya O. A.**, **Uraltseva N. N.** Linear and Quasilinear Elliptic Equations. *Moscow Academic Press, New York,* 2008.

[14] **Mawhin J.** (2008). Leray-Schauder degree: A half century of extensions and applications. *Topol. Methods Nonlinear Anal.*

[15] **Niculescu, C. P.**, and **Rovenţa**, I. (2009). Schauder fixed point theorem in spaces with global nonpositive curvature. *Fixed Point Theory and Applications*, 2009, 1-8.

[16] **Precup, R.** (1993). On the topological transversality principle. *Nonlinear Analysis: Theory, Methods & Applications*, 20(1), 1-9.

[17] **O'Regan, D.** (2015). Coincidence points for multivalued maps based on ϕ-epi and ϕ-essential maps. *Dynamic Systems and Applications*, 24(1-2), 143-155.

[18] **O'Regan, D.** (1999). Continuation principles and d-essential maps. *Mathematical and computer modelling,* 30(11-12), 1-6.

[19] **Reich, S.**, and **Shafrir, I.** (1990). Nonexpansive iterations in hyperbolic spaces. *Nonlinear analysis: theory, methods & applications,* 15(6), 537-558.

[20] **Sreya, V. V.**, and **Shaini, P.** (2021, May). Some Continuation results in Uniquely Geodesic Spaces. In *Journal of Physics: Conference Series (Vol. 1850, No. 1, p. 012046). IOP Publishing.*

/08/

P-BIHARMONIC PSEUDO-PARABOLIC EQUATION WITH LOGARITHMIC NON LINEARITY

Sushmitha Jayachandran

Research Scholar, Department of Mathematics,Central University of Kerala, Kerala - 671 320, India.

E-mail:sushmithaakhilesh@gmail.com

ORCID:

Gnanavel Soundararajan

Assistant Professor, Department of Mathematics,Central University of Kerala, Kerala - 671 320, India.

E-mail:gnanavel.math.bu@gmail.com

ORCID:

ABSTRACT

This paper deals with the existence of solutions of a p-biharmonic pseudo parabolic partial differential equation with logarithmic nonlinearity in a bounded domain. We prove the global existence of the weak solutions using the Faedo-Galerkin method and applying the concavity approach, that the solutions blow up at a finite time. Further, we provide a maximal limit for the blow-up time.

KEYWORDS

p-Biharmonic, pseudo-parabolic, global existence, blow up

1   INTRODUCTION

Here we examine the following problem for a p-biharmonic pseudo-parabolic equation with logarithmic nonlinearity.

$$\begin{cases} u_t - \Delta u_t + \Delta(|\Delta u|^{p-2}\Delta u) - \text{div}(|\nabla u|^{q-2}\nabla u) = -\text{div}(|\nabla u|^{q-2}\nabla u \log|\nabla u|) & \text{if } (x,t) \in \Omega \times (0,T), \\ u = \frac{\partial u}{\partial \nu} = 0 & \text{if } (x,t) \in \partial\Omega \times (0,T), \\ u(x,0) = u_0(x) & \text{if } x \in \Omega. \end{cases}$$

(1)

where $\Omega \subset \mathbb{R}^N (N \geq 1)$ represents a bounded domain whose boundary $\partial\Omega$ is smooth enough, $T \in (0,\infty)$, ν indicates the normal vector on $\partial\Omega$ pointing outward, $u_0 \in W_0^{2,p}(\Omega)\backslash\{0\}$ and the condition $2 < p < q < p(1 + \frac{2}{N+2})$ holds for p and q.

Pseudo-parabolic equations address several significant physical processes, like the evolution of two components of intergalactic material, the leakage of homogeneous fluids through a rock surface, the biomathematical modeling of a bacterial film, some thin film problems, the straight transmission of nonlinear, dispersive, long waves, the heat transfer containing two temperatures, a grouping of populations, etc. Shawalter and Ting [18], [22] first examined the pseudo parabolic equations in 1969. After their precursory results, there are many papers studied the nonlinear pseudo-parabolic equations, like semilinear pseudo-parabolic equations, quasilinear pseudo-parabolic equations, and even singular and degenerate pseudo-parabolic equations (see [1], [28], [4], [6], [15], [24], [25]). A pseudo-parabolic equation with p-Laplacian $\Delta_p u = div(|\nabla u|^{p-2}\nabla u)$ and logarithmic nonlinearity were studied by Nahn, and Truong [13] in 2017. Considering the equation,

$$u_t - \Delta u_t - \Delta_p u = |u|^{p-2} u \log|u|$$

and by using the potential well method proposed by Sattinger [17] and a logarithmic Sobolev inequality, they proved the existence or nonexistence of global weak solutions. Additionally, they provided requirements for both the large time decay of weak global solutions and the finite time blow-up of weak solutions. Later, many authors [26], [27], [23] considered pseudo-parabolic equations with logarithmic nonlinearity and established results for local and global existence, uniqueness, decay estimate and asymptotic behaviour of solutions, blow-up results. Logarithmic nonlinearities in parabolic and pseudo-parabolic equations were studied by Lakshmipriya et.al [11], [10] and other researchers [29], [9], [5] and they proved the existence of weak solutions and their blow up in finite time. Lower bound of Blow-up time to a fourth order parabolic equation modelling epitaxial thin film growth

Recently, higher-order equations have gained much importance in studies. Lower bound of Blow-up time to a fourth order parabolic equation modelling epitaxial thin film growth studied by Liu et.al [3]. The p-biharmonic equation

$$u_t + \Delta(|\Delta u|^{p-2}\Delta u) + \lambda|u|^{p-2}u = 0$$

were studied by Liu and Guo [14], and by using the discrete-time method and uniform estimates, they established the existence and uniqueness of weak solutions. Hao and Zhou [7] obtained results for blow up, extinction and non-extinction of solutions for the equation

$$u_t + \Delta(|\Delta u|^{p-2}\Delta u) = |u|^q - \frac{1}{|\Omega|}\int_\Omega |u|dx.$$

Wang and Liu [8] studied the p-biharmonic parabolic equation with logarithmic nonlinearity,

$$u_t + \Delta(|\Delta u|^{p-2}\Delta u) = |u|^{q-1}u \log|u|$$

for $2 < p < q < p(1 + \frac{4}{n})$ and proved the global existence, blow up, extinction and no extinction of solutions. Then Liu and Li [2] studied,

$$u_t + \Delta(|\Delta u|^{p-2}\Delta u) = \lambda|u|^{q-1}u \log|u|.$$

Based on the difference and variation methods, they showed the existence of weak solutions and observed large-time behaviour and the transmission of solution perturbations for $\lambda > 0, p > q > \frac{p}{2} + 1, p > \frac{n}{2}$.

Comert and Piskin [?] studied a p-biharmonic pseudo-parabolic equation with logarithmic nonlinearity and used the potential well method and logarithmic Sobolev inequality obtained the existence of the unique global weak solution. In addition, they also exhibited polynomial decay of solutions. Motivated by these works, we have formulated our problem (1) for a p-biharmonic pseudo-parabolic equation with logarithmic nonlinearity and studied their existence and non-existence. The problem (1) for the case $p = 2$ is already investigated and proved the existence, uniqueness and blow up of solutions (see [19], [20], [21]).

The rest of this paper is arranged to the two sections below. The preliminary notations, definitions, and results we need to support our main findings are described in Section 2. Section 3 contains the major findings of this paper explained in five theorems.

2   PRELIMINARIES

In this section, we provide some fundamental ideas and facts that are necessary for us to explain our findings. In this article, we follow the notations listed below throughout. $\|.\|_r$ denotes the $L^r(\Omega)$ norm for $1 \leq r \leq \infty$, $\|.\|_{H_0^1}$ denotes the norm in $H_0^1(\Omega)$, $(.,.)_1$ denotes the $H_0^1(\Omega)$-inner product.=, r' denotes the Holder conjugate exponent of $r > 1$ (that is, $r' = \frac{r}{r-1}$).
We define the energy functional J and the Nehari functional I as follows:
$I, J : W_0^{2,p}(\Omega) \to \mathbb{R}$ by

$$J(u) \quad = \quad \frac{1}{p}\|\Delta u\|_p^p + \frac{q+1}{q^2}\|\nabla u\|_q^q - \frac{1}{q}\int_\Omega |\nabla u|^q \log|\nabla u| dx \tag{2}$$

$$I(u) \quad = \quad \|\Delta u\|_p^p + \|\nabla u\|_q^q - \int_\Omega |\nabla u|^q \log|\nabla u| dx \tag{3}$$

Then we have,

$$J(u) = \frac{1}{q}I(u) + \left(\frac{1}{p} - \frac{1}{q}\right)\|\Delta u\|_p^p + \frac{1}{q^2}\|\nabla u\|_q^q \tag{4}$$

We introduce the Nehari manifold as

$$\mathcal{N} = \{u \in W_0^{2,p}(\Omega)\backslash\{0\} : I(u) = 0\}$$

also define the potential well as

$$\mathcal{W} = \{u \in W_0^{2,p}(\Omega)\backslash\{0\} : J(u) < d, I(u) > 0\}$$

where $d = \inf_{u \in \mathcal{N}} J(u)$ is referred to as the depth of the potential well.

Definition 1. *A function $u = u(x,t)$ is considered to be a weak solution of problem (1) if $u \in L^\infty(0,T; W_0^{2,p}(\Omega))$, $u_t \in L^2(0,T; H_0^1(\Omega))$ and validates*

$$(u_t, \phi) + (\nabla u_t, \nabla \phi) + (|\Delta u|^{p-2}\Delta u, \Delta \phi) + (|\nabla u|^{q-2}\nabla u, \nabla \phi) = (|\nabla u|^{q-2}\nabla u \log|\nabla u|, \nabla \phi) \tag{5}$$

for all $\phi \in W_0^{2,p}(\Omega)$ and a.e $0 \leq t \leq T$ along with $u(x,0) = u_0(x)$ in $W_0^{2,p}(\Omega)\backslash\{0\}$. Furthermore, it also agrees the energy inequality

$$\int_0^t \|u_\tau\|_{H_0^1}^2 d\tau + J(u) \leq J(u_0) \quad , 0 < t \leq T. \tag{6}$$

Lemma 1. *[12] Let ρ be a positive number. Then we have the following inequalities:*

$$x^p \log x \leq (e\rho)^{-1} \text{ for all } x \geq 1$$

and

$$|x^p \log x| \leq (ep)^{-1} \text{ for all } 0 < x < 1.$$

The following lemma is similar to one in [8], [16]. However, we explain the proof with some changes due to the occurrence of the non-linear logarithmic term $-\text{div}(|\nabla u|^{q-2}\nabla u \log|\nabla u|)$ and the q-Laplacian $\text{div}(|\nabla u|^{q-2}\nabla u)$.

Lemma 2. *For any* $u \in W_0^{2,p}(\Omega)\backslash\{0\}$, *we have the following:*

(i) $\lim_{\gamma \to 0^+} J(\gamma u) = 0$ *and* $\lim_{\gamma \to \infty} J(\gamma u) = -\infty$;

(ii) $\frac{d}{d\gamma} J(\gamma u) = \frac{1}{\gamma} I(\gamma u)$ *for* $\gamma > 0$;

(iii) there exists a unique $\gamma^* = \gamma^*(u) > 0$ *such that* $\frac{d}{d\gamma} J(\gamma u)|_{\gamma=\gamma^*} = 0$. *Also* $J(\gamma u)$ *is increasing on* $0 < \gamma \le \gamma^*$, *decreasing on* $\gamma^* \le \gamma < \infty$ *and takes the maximum at* $\gamma = \gamma^*$;

(iv) $I(\gamma u) > 0$ *for* $0 < \gamma < \gamma^*$, $I(\gamma u) < 0$ *for* $\gamma^* < \gamma < \infty$ *and* $I(\gamma^* u) = 0$.

Proof.

(i) Applying the definition of J we have

$$J(\gamma u) = \frac{\gamma^p}{p}\|\Delta u\|_p^p + \frac{\gamma^q(q+1)}{q^2}\|\nabla u\|_q^q - \frac{\gamma^q \log \gamma}{q}\|\nabla u\|_q^q - \frac{\gamma^q}{q}\int_\Omega |\nabla u|^q \log|\nabla u| dx$$

so it is evident that $\lim_{\gamma \to 0^+} J(\gamma u) = 0$ and $\lim_{\gamma \to \infty} J(\gamma u) = -\infty$ since $2 < p < q$.

(ii) Direct computation yields,

$$\frac{d}{d\gamma} J(\gamma u) = \gamma^{p-1}\|\Delta u\|_p^p + \gamma^{q-1}\|\nabla u\|_q^q - \gamma^{q-1}\int_\Omega |\nabla u|^q \log|\gamma \nabla u| dx = \frac{1}{\gamma} I(\gamma u)$$

(iii) We have,

$$\frac{d}{d\gamma} J(\gamma u) = \gamma^{q-1}\left(\gamma^{p-q}\|\Delta u\|_p^p + \|\nabla u\|_q^q - \log \gamma \|\nabla u\|_q^q - \int_\Omega |\nabla u|^q \log|\nabla u| dx\right)$$

Now define,

$$g(\gamma) = \gamma^{p-q}\|\Delta u\|_p^p + \|\nabla u\|_q^q - \log \gamma \|\nabla u\|_q^q - \int_\Omega |\nabla u|^q \log|\nabla u| dx$$

Then we can observe that g is decreasing since

$$g'(\gamma) = (p-q)\gamma^{p-q-1}\|\Delta u\|_p^p - \frac{1}{\gamma}\|\nabla u\|_q^q < 0$$

Also, $\lim_{\gamma \to 0^+} g(\gamma) = \infty$ and $\lim_{\gamma \to \infty} g(\gamma) = -\infty$.
Hence, a unique γ^* with $g(\gamma^*) = 0$ is guaranteed.
Also, $g(\gamma) > 0$ for $0 < \gamma < \gamma^*$ and $g(\gamma) < 0$ for $\gamma^* < \gamma < \infty$.
Now, since $\frac{d}{d\gamma} J(\gamma u) = \gamma^{q-1} g(\gamma)$ we obtain $\frac{d}{d\gamma} J(\gamma u)|_{\gamma=\gamma^*} = 0$ and also $J(\gamma u)$ is increasing on $0 < \gamma \le \gamma^*$, decreasing on $\gamma^* \le \gamma < \infty$ and takes the maximum at $\gamma = \gamma^*$.

(iv) *(iv)* is obvious since $I(\gamma u) = \gamma \frac{d}{d\gamma} J(\gamma u)$.

The above lemmas are useful to prove the main results in the following section.

3   MAIN RESULTS

In this section, we prove the existence of weak local solutions to the problem (1). Further, we show that the weak solution exists globally using the potential well method when the initial energy of the system is subcritical and critical. We show that the solution becomes unbounded in finite time and specifies an upper limit for the blow-up time.

Theorem 1. *(The Local existence)*
Let $u_0 \in W_0^{2,p}(\Omega)\backslash\{0\}$ and $2 < p < q < p(1 + \frac{2}{N+2})$. Then a $T > 0$ and a unique weak solution $u(t)$ of problem(1) agreeing the energy inequality

$$\int_0^t \|u_\tau\|_{H_0^1}^2 d\tau + J(u(t)) \leq J(u_0) \quad , 0 \leq t \leq T \tag{7}$$

and $u(0) = u_0$ exists.

*Proof.***Existence**
Let $\{w_i\}_{i \in \mathbb{N}}$ be an orthonormal basis for $W_0^{2,p}(\Omega)$. We use the approximation,

$$u_k(x,t) = \sum_{i=1}^k a_{k,i}(t)w_i(x), \quad k = 1, 2, \ldots$$

where $a_{k,i}(t) : [0,T] \to \mathbb{R}$ accepts the below ODE.

$$(u_{kt}, w_i) + (\nabla u_{kt}, \nabla w_i) + (|\Delta u_k|^{p-2}\Delta u_k, \Delta w_i) + (|\nabla u_k|^{q-2}\nabla u_k, \nabla w_i)$$
$$= (|\nabla u_k|^{q-2}\nabla u_k \log |\nabla u_k|, \nabla w_i) \tag{8}$$

$i = 1, 2, \ldots, k$ and

$$u_k(x,0) = \sum_{i=1}^k a_{k,i}(0)w_i(x) \to u_0(x) \text{ in } W_0^{2,p}(\Omega)\backslash\{0\}$$

By Peano's theorem, the above ODE has a solution $a_{k,i}$ and we can find a $T_k > 0$ with $a_{k,i} \in C^1([0,T_k])$, which implies $u_k \in C^1([0,T_k]; W_0^{2,p}(\Omega))$.
Now by multiplying (8) by $a_{k,i}(t)$, summing it for $i = 1, 2, \ldots, k$ and integrating with respect to t from 0 to t we obtain,

$$\frac{1}{2}\|u_k\|_{H_0^1}^2 + \int_0^t (\|\Delta u_k\|_p^p + \|\nabla u_k\|_q^q)dt = \frac{1}{2}\|u_k(0)\|_{H_0^1}^2 + \int_0^t \int_\Omega |\nabla u_k|^q \log |\nabla u_k| dx dt$$

That is,

$$\psi_k(t) = \psi_k(0) + \int_0^t \int_\Omega |\nabla u_k|^q \log |\nabla u_k| dx dt \tag{9}$$

where

$$\psi_k(t) = \frac{1}{2}\|u_k\|_{H_0^1}^2 + \int_0^t (\|\Delta u_k\|_p^p + \|\nabla u_k\|_q^q)dt \tag{10}$$

We obtain the following by employing lemma(1), Gagliardo-Nirenberg interpolation inequality and Young's inequality.

$$
\begin{aligned}
\int_\Omega |\nabla u_k|^q \log |\nabla u_k| dx &\leq \int_{\{x \in \Omega: |\nabla u_k| \geq 1\}} |\nabla u_k|^q \log |\nabla u_k| dx \\
&\leq (e\rho)^{-1}\|\nabla u_k\|_{q+\rho}^{q+\rho} \\
&\leq (e\rho)^{-1}C_1^{q+\rho}\|\Delta u_k\|_p^{\theta(q+\rho)}\|u_k\|_2^{(1-\theta)(q+\rho)} \\
&\leq \epsilon\|\Delta u_k\|_p^p + C(\epsilon)\|u_k\|_2^{\frac{p(1-\theta)(q+\rho)}{p-\theta(q+\rho)}} \tag{11}
\end{aligned}
$$

where $\theta = \left(\frac{1}{n} + \frac{1}{2} - \frac{1}{q+\rho}\right)\left(\frac{2}{n} + \frac{1}{2} - \frac{1}{p}\right)^{-1}, \epsilon \in (0,1)$,

$C(\epsilon) = \left(\frac{p\epsilon}{\theta(q+\rho)}\right)^{\frac{\theta(q+\rho)}{\theta(q+\rho)-p}}\left(\frac{p-\theta(q+\rho)}{p}\right)\left((e\rho)^{-1}C_1^{q+\rho}\right)^{\frac{p}{p-\theta(q+\rho)}}$ and,

ρ is chosen so that $2 < q + \rho < p(1 + \frac{2}{n+2})$.

Let $\beta = \frac{p(1-\theta)(q+\rho)}{2(p-\theta(q+\rho))} = \frac{np+(p-n)(q+\rho)}{p(4+n)-(n+2)(q+\rho)}$. Then $\beta > 1$ and

$$\int_\Omega |\nabla u_k|^q \log |\nabla u_k| dx \leq \epsilon \|\Delta u_k\|_p^p + C(\epsilon)\|u_k\|_2^{2\beta} \tag{12}$$

Then (9) implies that,

$$
\begin{aligned}
\psi_k(t) &\leq \psi_k(0) + \epsilon \int_0^t \|\Delta u_k\|_p^p dt + C(\epsilon)\int_0^t \|u_k\|_2^{2\beta} dt \\
&\leq C_2 + \epsilon\psi_k(t) + C(\epsilon)2^\beta \int_0^t \left(\left(\frac{1}{2}\|u_k\|_{H_0^1}^2\right)^\beta + \left(\int_0^s (\|\Delta u_k\|_p^p + \|\nabla u_k\|_q^q)ds\right)^\beta\right)dt \\
&\leq C_2 + \epsilon\psi_k(t) + C_3\int_0^t \psi_k(t)^\beta dt
\end{aligned}
$$

Hence we get,

$$\psi_k(t) \leq C_4 + C_5 \int_0^t \psi_k(t)^\beta dt$$

Then the Gronwall-Bellman-Bihari type integral inequality gives a T such that $0 < T < \frac{C_4^{1-\beta}}{C_5(1-\beta)}$ and

$$\psi_k(t) \leq C_T \text{ for all } t \in [0,T]. \tag{13}$$

Hence the solution of (8) exists in $[0,T]$ for all k.

Now multiplying (8) by $a'_{k,i}(t)$ and summing for $i = 1,2,\ldots,k$ we get,

$$(u_{kt}, u_{kt}) + (\nabla u_{kt}, \nabla u_{kt}) + (|\Delta u_k|^{p-2}\Delta u_k, \Delta u_{kt}) + (|\nabla u_k|^{q-2}\nabla u_k, \nabla u_{kt})$$
$$= (|\nabla u_k|^{q-2}\nabla u_k \log |\nabla u_k|, \nabla u_{kt})$$

integrating with respect to t,

$$\int_0^t \|u_{kt}\|_{H_0^1}^2 dt + J(u_k(t)) = J(u_k(0)) \text{ for all } t \in [0,T]. \tag{14}$$

As contrast to that, a constant $C_6 > 0$ satisfying

$$J(u_k(0)) \leq C_6 \text{ for all } k. \tag{15}$$

exists since $u_k(0) \to u_0$ and by the continuity of J. Then from (12),(13),(14) and (15) we can see that

$$
\begin{aligned}
C_6 &\geq \int_0^t \|u_{kt}\|_{H_0^1}^2 dt + \frac{1}{p}\|\Delta u_k\|_p^p + \frac{q+1}{q^2}\|\nabla u_k\|_q^q - \frac{1}{q}\int_\Omega |\nabla u_k|^q \log|\nabla u_k| dx \\
&\geq \int_0^t \|u_{kt}\|_{H_0^1}^2 dt + \left(\frac{1}{p} - \frac{\epsilon}{q}\right)\|\Delta u_k\|_p^p + \frac{q+1}{q^2}\|\nabla u_k\|_q^q - \frac{C(\epsilon)}{q}\|u_k\|_{H_0^1}^{2\beta} \\
&\geq \int_0^t \|u_{kt}\|_{H_0^1}^2 dt + \left(\frac{1}{p} - \frac{\epsilon}{q}\right)\|\Delta u_k\|_p^p + \frac{q+1}{q^2}\|\nabla u_k\|_q^q - \frac{C(\epsilon)}{q}2^\beta C_T^\beta
\end{aligned}
$$

Let $\tilde{C} = C_6 + \frac{C(\epsilon)2^\beta}{q}C_T^\beta$. Then we gain that

$$\int_0^t \|u_{kt}\|_2^2 dt \leq \tilde{C}$$

$$\int_0^t \|\nabla u_{kt}\|_2^2 dt \leq \tilde{C}$$

$$\|\Delta u_k\|_p^p < \tilde{C}\left(\frac{1}{p} - \frac{\epsilon}{q}\right)^{-1}$$

$$\|\nabla u_k\|_q^q < \tilde{C}\frac{q^2}{q+1}$$

Thus we have $\{u_k\}_{k\in\mathbb{N}}$ is bounded in $L^\infty(0,T;W_0^{2,p}(\Omega))$ and $\{u_{kt}\}_{k\in\mathbb{N}}$ is bounded in $L^2(0,T;H_0^1(\Omega))$. Hence there exists a subsequence, however indicated by $\{u_k\}_{k\in\mathbb{N}}$ which agrees,

$$u_k \to u \qquad \text{weakly* in } L^\infty(0,T;W_0^{2,p}(\Omega))$$
$$u_{kt} \to u_t \qquad \text{weakly in } L^2(0,T;H_0^1(\Omega))$$
$$u_k \to u \qquad \text{weakly* in } L^\infty(0,T;W_0^{1,q}(\Omega))$$

since

$$u_{kt} \to u_t \qquad \text{weakly in } L^2(0,T;L^2(\Omega))$$

by Aubin-Lions lemma we get,

$$u_k \quad \to \quad u \text{ strongly in } C(0,T;L^2(\Omega))$$

Therefore,

$$|\Delta u_k|^{p-2}\Delta u_k \quad \to \quad \xi_1 \text{ weakly* in } L^\infty(0,T;W_0^{-2,p'}(\Omega))$$

and,

$$|\nabla u_k|^{q-2}\nabla u_k \quad \to \quad \xi_2 \text{ weakly* in } L^\infty(0,T;W_0^{-1,q'}(\Omega))$$

where $W_0^{-2,p'}(\Omega)$ is the dual space of $W_0^{2,p}(\Omega)$ and $W_0^{-1,q'}(\Omega)$ is the dual space of $W_0^{1,q}(\Omega)$. Now from the theory of monotone operators, it concludes,

$$\xi_1 = |\Delta u|^{p-2}\Delta u \qquad \text{and} \qquad \xi_2 = |\nabla u|^{q-2}\nabla u.$$

Now let $\Phi(u) = |u|^{q-2}u\log|u|$. We have

$$\nabla u_k \to \nabla u \qquad \text{weakly* in } L^\infty(0,T;L^2(\Omega))$$
$$\nabla u_{kt} \to \nabla u_t \qquad \text{weakly in } L^2(0,T;L^2(\Omega))$$

Therefore,

$$\nabla u_k \to \nabla u \text{ strongly in } C(0,T;L^2(\Omega))$$

and

$$\Phi(\nabla u_k) \to \Phi(\nabla u) \qquad a.e \text{ in } \Omega \times (0,T)$$

We again use Lemma(1) and Gagliardo-Nirenberg interpolation inequality to emerge the below.

$$
\begin{aligned}
\int_\Omega (\Phi(\nabla u_k))^{q'} dx &\leq \int_{\{x\in\Omega:|\nabla u_k|\leq 1\}} \left(|\nabla u_k|^{q-1}|\log|\nabla u_k||\right)^{q'} dx \\
&\quad + \int_{\{x\in\Omega:|\nabla u_k|\geq 1\}} \left(|\nabla u_k|^{q-1}|\log|\nabla u_k||\right)^{q'} dx \\
&\leq (e(q-1))^{-q'}|\Omega| + (e\mu)^{-q'}\|\nabla u_k\|_r^r \\
&\leq (e(q-1))^{-q'}|\Omega| + (e\mu)^{-q'}C_7^r\|\Delta u_k\|_p^{r\alpha}\|u_k\|_2^{r(1-\alpha)} \\
&< C_8
\end{aligned}
$$

where $r = (q-1+\mu)q'$, $q' = \frac{q}{q-1}$ and $\alpha = \left(\frac{1}{n}+\frac{1}{2}-\frac{1}{r}\right)\left(\frac{2}{n}+\frac{1}{2}-\frac{1}{p}\right)^{-1}$. Hence,

$$\Phi(\nabla u_k) \to \Phi(\nabla u) \text{ weakly* in } L^\infty(0,T;L^{q'}(\Omega))$$

Now for a fixed i in (8) letting k tends to ∞ we get,

$$(u_t, w_i) + (\nabla u_t, \nabla w_i) + (|\Delta u|^{p-2}\Delta u, \Delta w_i) + (|\nabla u|^{q-2}\nabla u, \nabla w_i) = (|\nabla u|^{q-2}\nabla u \log|\nabla u|, \nabla w_i)$$

for all $i = 1, 2, \ldots, k$. Then for all $\phi \in W_0^{2,p}(\Omega)$ and for a.e. $t \in [0, T]$,

$$(u_t, \phi) + (\nabla u_t, \nabla \phi) + (|\Delta u|^{p-2} \Delta u, \Delta \phi) + (|\nabla u|^{q-2} \nabla u, \nabla \phi) = (|\nabla u|^{q-2} \nabla u \log |\nabla u|, \nabla \phi)$$

and $u(x, 0) = u_0(x)$ in $W_0 2, p^2(\Omega) \backslash \{0\}$.

Uniqueness

Let u and $\tilde{u}$ be two weak solutions of problem (1). For any $\phi \in H_0^2(\Omega)$, it is noted that,

$$(u_t, \phi) + (\nabla u_t, \nabla \phi) + (|\Delta u|^{p-2} \Delta u, \Delta \phi) + (|\nabla u|^{q-2} \nabla u, \nabla \phi) = (|\nabla u|^{q-2} \nabla u \log |\nabla u|, \nabla \phi)$$

$$(\tilde{u}_t, \phi) + (\nabla \tilde{u}_t, \nabla \phi) + (|\Delta \tilde{u}|^{p-2} \Delta \tilde{u}, \Delta \phi) + (|\nabla \tilde{u}|^{q-2} \nabla \tilde{u}, \nabla \phi) = (|\nabla \tilde{u}|^{q-2} \nabla \tilde{u} \log |\nabla \tilde{u}|, \nabla \phi)$$

On subtraction of one equation from the other and taking $\phi = u - \tilde{u}$, the above yields that

$$(\phi_t, \phi) + (\nabla \phi_t, \nabla \phi) + \int_\Omega (|\Delta u|^{p-2} \Delta u - |\Delta \tilde{u}|^{p-2} \Delta \tilde{u})(\Delta u - \Delta \tilde{u}) dx$$

$$+ \int_\Omega (|\nabla u|^{q-2} \nabla u - |\nabla \tilde{u}|^{q-2} \nabla \tilde{u})(\nabla u - \nabla \tilde{u}) dx$$

$$= \int_\Omega (|\nabla u|^{q-2} \nabla u \log |\nabla u| - |\nabla \tilde{u}|^{q-2} \nabla \tilde{u} \log |\nabla \tilde{u}|)(\nabla u - \nabla \tilde{u}) dx$$

Then by the monotonicity of q-Laplacian $\text{div}(|\nabla u|^{q-2} \nabla u)$ and the p-Biharmonic operator $\Delta(|\Delta u|^{p-2} \Delta u)$ and by the Lipschitz continuity of $|x|^{q-2} x \log |x|$ we get,

$$(\phi_t, \phi)_1 \leq L \int_\Omega (\nabla u - \nabla \tilde{u})^2 dx$$

where $L > 0$ is the Lipschitz constant. Thus we obtain,

$$(\phi_t, \phi)_1 \leq L \|\nabla \phi\|_2^2 \leq L \|\phi\|_{H_0^1}^2$$

By the integration from 0 to t with respect to t we obtain that,

$$\|\phi\|_{H_0^1}^2 - \|\phi(0)\|_{H_0^1}^2 \leq L \int_0^t \|\phi\|_{H_0^1}^2 dt.$$

Since $\phi(0) = u(0) - \tilde{u}(0) = 0$, apply Gronwall's inequality to gain,

$$\|\phi\|_{H_0^1}^2 = 0$$

Therefore, $\phi = 0$ a.e. in $\Omega \times (0, T)$. That is, $u = \tilde{u}$ a.e. in $\Omega \times (0, T)$.

Energy inequality

Let $\chi \in C[0, T]$ be a non-negative function. Then (14) implies

$$\int_0^T \chi(t) \int_0^t \|u_{kt}\|_{H_0^1}^2 ds dt + \int_0^T J(u_k(t)) \chi(t) dt = \int_0^T J(u_k(0)) \chi(t) dt$$

Since, we have the lower semi-continuity $\int_0^T J(u_k(t)) \chi(t) dt$ with respect to the weak topology of $L^2(0, T; W_0^{2,p}(\Omega))$.

$$\int_0^T J(u(t)) \chi(t) dt \leq \liminf_{k \to \infty} \int_0^T J(u_k(t)) \chi(t) dt$$

also $\int_0^T J(u_k(0)) \chi(t) dt \to \int_0^T J(u_0) \chi(t) dt$ as $k \to \infty$. Thus we get,

$$\int_0^T \chi(t) \int_0^t \|u_t\|_{H_0^1}^2 ds dt + \int_0^T J(u(t)) \chi(t) dt \leq \int_0^T J(u_0) \chi(t) dt$$

Since $\chi(t)$ is arbitrary,

$$\int_0^t \|u_\tau\|_{H_0^1}^2 d\tau + J(u(t)) \leq J(u_0) \quad \text{for } 0 \leq t \leq T.$$

Hence the proof is complete.

Next theorem address the case of the initial energy of the system is sub-critical, i.e, $J(u_0) < d$. We will demonstrate the existence of weak global solutions.

Theorem 2. *(Global Existence for $J(u_0) < d$)*
A unique global weak solution u satisfying the energy estimate,

$$\int_0^t \|u_\tau\|_{H_0^1}^2 d\tau + J(u(t)) \le J(u_0) \quad \text{for } 0 \le t < \infty \tag{16}$$

exists for problem(1) if the conditions $J(u_0) < d$ and $I(u_0) > 0$ holds for the initial value $u_0 \in W_0^{2,p}(\Omega)\backslash\{0\}$.

Proof. Define $\{w_i\}_{i\in\mathbb{N}}$ and $\{u_k\}_{k\in\mathbb{N}}$ as in the proof of Theorem(1). Multiplying (8) by $a'_{k,i}(t)$ and summing over i and integrating with respect to t from 0 to t we identify,

$$\int_0^t \|u_{kt}\|_{H_0^1}^2 dt + J(u_k(t)) = J(u_k(0)) \text{ for all } t \in [0, T_{max}) \tag{17}$$

where T_{max} is the maximum time for solution $u_k(x,t)$ to exist.
We have $J(u_k(0)) \to J(u_0)$ as $k \to \infty$ and $J(u_0) < d$. Therefore,

$$\int_0^t \|u_{kt}\|_{H_0^1}^2 dt + J(u_k(t)) < d, \quad t \in [0, T_{max}) \tag{18}$$

Since $I(u_0) > 0$ we have $I(u_k(0)) > 0$ for sufficiently large k. We claim that $I(u_k) > 0$ for sufficiently large k. Otherwise we can locate a t_0 such that $I(u_k(t_0)) = 0$, $u_k(t_0) \ne 0$. Then $u_k(t_0) \in \mathcal{N}$ and $J(u_k(t_0)) \ge d$, which is a contradiction to (18).
Therefore $I(u_k) > 0$ for appropriately large k.
Then we get,

$$J(u_k) = \frac{1}{q}I(u_k) + \left(\frac{1}{p} - \frac{1}{q}\right)\|\Delta u_k\|_p^p + \frac{1}{q^2}\|\nabla u_k\|_q^q > 0$$

Therefore,

$$\int_0^t \|u_{kt}\|_{H_0^1}^2 dt < d$$

also

$$\left(\frac{1}{p} - \frac{1}{q}\right)\|\Delta u_k\|_p^p + \frac{1}{q^2}\|\nabla u_k\|_q^q < J(u_k) < d$$

Let $K_0 = \min\{\frac{1}{p} - \frac{1}{q}, \frac{1}{q^2}\}$ and $K = d + \frac{d}{K_0}$ then

$$\|\Delta u_k\|_p^p + \|\nabla u_k\|_q^q < d/K_0$$

and

$$\int_0^t \|u_{kt}\|_{H_0^1}^2 dt + \|\Delta u_k\|_p^p + \|\nabla u_k\|_q^q < K \tag{19}$$

where $K > 0$. Hence we take $T_{max} = \infty$. Now it is noticeable that problem (1) has a weak global solution by applying identical ideas used to prove the Theorem(1), and the solution u also agrees with the energy inequality

$$\int_0^t \|u_\tau\|_{H_0^1}^2 d\tau + J(u(t)) \le J(u_0), \quad 0 \le t < \infty.$$

We will explain the global existence of weak solutions in the following theorem for the critical initial energy. That is when $J(u_0) = d$.

Theorem 3. *(Global existence for $J(u_0) = d$)*
Observe the conditions $J(u_0) = d$ and $I(u_0) > 0$ holds for the initial value $u_0 \in W_0^{2,p}(\Omega)\backslash\{0\}$. Subsequently problem(1) possesses a unique global weak solution $u \in L^\infty(0, T; W_0^{2,p}(\Omega))$ with $u_t \in L^2(0, T; L^2(\Omega))$ for $0 \le t \le T$ and it also accepts the energy estimate (16).

Proof. Let $\eta_j = 1 - \frac{1}{j}$, $j = 1, 2, \ldots$ then $\eta_j \to 1$ when $j \to \infty$. Take into account the below problem:

$$\begin{cases} u_t - \Delta u_t + \Delta(|\Delta u|^{p-2}\Delta u) - \text{div}(|\nabla u|^{q-2}\nabla u) = -\text{div}(|\nabla u|^{q-2}\nabla u \log |\nabla u|) & \text{if } (x,t) \in \Omega \times (0,T), \\ u = \frac{\partial u}{\partial \nu} = 0 & \text{if } (x,t) \in \partial\Omega \times (0,T), \\ u(x,0) = \eta_j u_0(x) = u_0^j & \text{if } x \in \Omega. \end{cases}$$

$$(20)$$

Since $I(u_0) > 0$, lemma (2)(iv) gives a $\gamma^* > 1$ with $I(\gamma^* u_0) = 0$.

Again from lemma (2)(iii) and (iv) we gain $I(\eta_j u_0) > 0$ and $J(\eta_j u_0) < J(u_0)$ since $\eta_j < 1 < \gamma^*$.

Thus we have $J(u_0^j) < d$ and $I(u_0^j) > 0$.

Then by Theorem(2), for each j problem (20) has a global weak solution $u^j \in L^\infty(0,T;W_0^{p-2}(\Omega))$ with $u_t^j \in L^2(0,T;L^2(\Omega))$ which satisfies the energy inequality,

$$\int_0^t \|u_\tau^j\|_{H_0^1}^2 d\tau + J(u^j(t)) \leq J(u_0^j) \quad \text{for } 0 \leq t < \infty.$$

Thus we have

$$\int_0^t \|u_\tau^j\|_{H_0^1}^2 d\tau + J(u^j) < d \quad \text{for } 0 \leq t < \infty.$$

Now by applying ideas similar to the one used to prove Theorem(1), we obtain a subsequence of $\{u^j\}_{j\in\mathbb{N}}$ converging to a function u, which is a weak solution of problem (1). It also fulfils the energy inequality (16). The solution's uniqueness can also be proved as in Theorem(1).

Hence the proof is over.

The following theorem gives the blow-up of solutions for the subcritical initial energy and an upper bound for blow up time.

Theorem 4. *(Blow up for $J(u_0) < d$)*
Let $u_0 \in H_0^2(\Omega)\backslash\{0\}$, $J(u_0) < d$ and $I(u_0) < 0$. Then the weak solution u of problem (1) blows up in a finite time T_* in the notion, $\lim_{t \to T_*^-} \|u\|_{H_0^1}^2 = \infty$. Furthermore, the upper bound of blow-up time T_* is given by

$$T_* \leq \frac{4(q-1)\|u_0\|_{H_0^1}^2}{q(q-2)^2(d - J(u_0))}.$$

Proof. First we prove $J(u(t)) < d$ and $I(u(t)) < 0$ for $t \in [0,T]$, where T indicates the maximum time for which $u(x,t)$ exists.

We have $J(u(t)) < J(u_0) < d$ by (6).

If we can choose a $t_0 \in (0,T)$ with $I(u(t_0)) = 0$ or $J(u(t_0)) = d$, since $J(u(t_0)) < d$, we must have $I(u(t_0)) = 0$.

Which implies $u(t_0) \in \mathcal{N}$ and thus $d \leq J(u(t_0))$, a contradiction.

Hence, $J(u(t)) < d$ and $I(u(t)) < 0$ for $t \in [0,T]$. Now define

$$\mathcal{P}(t) = \int_0^t \|u\|_{H_0^1}^2 dt$$

Then,

$$\mathcal{P}'(t) = \|u\|_{H_0^1}^2$$

and

$$\mathcal{P}''(t) = 2(u, u_t)_1 = -2I(u) > 0$$

Hence for $t > 0$, $\mathcal{P}'(t) \geq \mathcal{P}'(0) = \|u_0\|_{H_0^1}^2 > 0$.

Now fix $t_1 > 0$. Then for $t_1 \leq t < \infty$,

$$\mathcal{P}(t) \geq \mathcal{P}(t_1) \geq t_1 \|u_0\|_{H_0^1}^2 > 0$$

By Holder's inequality, we have,

$$\frac{1}{4}(\mathcal{P}'(t) - \mathcal{P}'(0))^2 \leq \int_0^t \|u\|_{H_0^1}^2 dt \int_0^t \|u_t\|_{H_0^1}^2 dt \tag{21}$$

Since $I(u(t)) < 0$, Lemma 2 *(iv)*, gives a γ^* with $0 < \gamma^* < 1$ and $I(\gamma^* u) = 0$. Therefore,

$$
\begin{aligned}
d &\leq \left(\frac{1}{p} - \frac{1}{q}\right)(\gamma^*)^p \|\Delta u\|_p^p + \frac{1}{q^2}(\gamma^*)^q \|\nabla u\|_q^q \\
&\leq \left(\frac{1}{p} - \frac{1}{q}\right)\|\Delta u\|_p^p + \frac{1}{q^2}\|\nabla u\|_q^q
\end{aligned}
\tag{22}
$$

Now by using $(4),(6)$ and (22) we see that,

$$
\mathcal{P}''(t) \geq 2q(d - J(u_0)) + 2q\int_0^t \|u_t\|_{H_0^1}^2 dt
\tag{23}
$$

Then from (21) and (23) it follows that

$$
\mathcal{P}''(t)\mathcal{P}(t) - \frac{q}{2}(\mathcal{P}'(t) - \mathcal{P}'(0))^2 \geq \mathcal{P}(t)2q(d - J(u_0)) > 0 \text{ for } t \in [t_1, \infty)
\tag{24}
$$

Now choose $\tilde{T} > 0$ large enough to introduce,

$$
\mathcal{Q}(t) = \mathcal{P}(t) + (\tilde{T} - t)\|u_0\|_{H_0^1}^2 \text{ for } t \in [t_1, \tilde{T}]
$$

Then $\mathcal{Q}(t) \geq \mathcal{P}(t) > 0$ for $t \in [t_1, \tilde{T}]$, $\mathcal{Q}'(t) = \mathcal{P}'(t) - \mathcal{P}'(0) > 0$ and $\mathcal{Q}''(t) = \mathcal{P}''(t) > 0$. Hence from (24) we observe,

$$
\mathcal{Q}(t)\mathcal{Q}''(t) - \frac{q}{2}(\mathcal{Q}'(t))^2 \geq \mathcal{P}(t)2q(d - J(u_0)) + \mathcal{P}''(t)(\tilde{T} - t)\|u_0\|_{H_0^1}^2 > 0
\tag{25}
$$

Now define

$$
\mathcal{R}(t) = \mathcal{Q}(t)^{-\frac{q-2}{2}}
$$

Then,

$$
\mathcal{R}'(t) = -\frac{q-2}{2}\mathcal{Q}(t)^{-\frac{q}{2}}\mathcal{Q}'(t)
$$

and

$$
\mathcal{R}''(t) = \frac{q-2}{2}\mathcal{Q}(t)^{-\frac{q+2}{2}}\left(\frac{q}{2}(\mathcal{Q}'(t))^2 - \mathcal{Q}(t)\mathcal{Q}''(t)\right) < 0
$$

Hence $\mathcal{R}(t)$ is a concave function in $[t_1, \tilde{T}]$ for any sufficiently large $\tilde{T} > t_1$. Also since $\mathcal{R}(t_1) > 0$ and $\mathcal{R}''(t_1) < 0$, there appears a finite time $T_* > t_1 > 0$ having $\lim_{t \to T_*^-}\mathcal{R}(t) = 0$. That yields $\lim_{t \to T_*^-}\mathcal{Q}(t) = +\infty$, which in turn gives $\lim_{t \to T_*^-}\mathcal{P}(t) = +\infty$. Hence we get

$$
\lim_{t \to T_*^-}\|u\|_{H_0^1}^2 = +\infty.
$$

To obtain an upper limit for blow-up time we define,

$$
\mathcal{S}(t) = \mathcal{P}(t) + (T_* - t)\|u_0\|_{H_0^1}^2 + \sigma(t + \varphi)^2 \text{ for } t \in [0, T_*]
$$

where the constants $\sigma, \varphi > 0$ will be given later.
Then,

$$
\mathcal{S}'(t) = \|u\|_{H_0^1}^2 - \|u_0\|_{H_0^1}^2 + 2\sigma(t + \varphi) > 2\sigma(t + \varphi) > 0
\tag{26}
$$

also by (23) we get,

$$
\mathcal{S}''(t) \geq 2q(d - J(u_0)) + 2q\int_0^t \|u_t\|_{H_0^1}^2 dt + 2\sigma
\tag{27}
$$

By Schwartz's inequality, we have,

$$
\int_0^t \frac{d}{dt}\|u\|_{H_0^1}^2 dt \leq 2\int_0^t \|u\|_{H_0^1}^2 dt \int_0^t \|u_t\|_{H_0^1}^2 dt
\tag{28}
$$

Therefore,

$$
\begin{aligned}
(\mathcal{S}'(t))^2 &= 4\left(\frac{1}{2}\int_0^t \frac{d}{dt}\|u\|_{H_0^1}^2 dt + \sigma(t+\varphi)\right)^2 \\
&\leq 4\left(\int_0^t \frac{d}{dt}\|u\|_{H_0^1}^2 dt + \sigma(t+\varphi)^2\right)\left(\int_0^t \frac{d}{dt}\|u_t\|_{H_0^1}^2 dt + \sigma\right) \\
&= 4\left(\mathcal{S}(t) - (T_* - t)\|u_0\|_{H_0^1}^2\right)\left(\int_0^t \frac{d}{dt}\|u_t\|_{H_0^1}^2 dt + \sigma\right) \\
&\leq 4\mathcal{S}(t)\left(\int_0^t \frac{d}{dt}\|u_t\|_{H_0^1}^2 dt + \sigma\right)
\end{aligned}
\tag{29}
$$

Now by applying (27) and (29) we can see that,

$$
\mathcal{S}(t)\mathcal{S}''(t) - \frac{q}{2}(\mathcal{S}'(t))^2 \geq \mathcal{S}(t)(2q(d - J(u_0)) - 2\sigma(q-1))
$$

If $\sigma \in \left(0, \frac{q(d-J(u_0))}{q-1}\right)$, then

$$
\mathcal{S}(t)\mathcal{S}''(t) - \frac{q}{2}(\mathcal{S}'(t))^2 > 0.
$$

Also we have $\mathcal{S}(0) = T_*\|u_0\|_{H_0^1}^2 + \sigma\varphi^2 > 0$ and $\mathcal{S}'(0) = 2\sigma\varphi > 0$. Then by Levine's Concavity approach, we obtain the upper bound for blow-up as,

$$
T_* \leq \frac{\mathcal{S}(0)}{(\frac{q}{2}-1)\mathcal{S}'(0)} = \frac{T_*\|u_0\|_{H_0^1}^2}{(q-2)\sigma\varphi} + \frac{\varphi}{q-2}
$$

Therefore,

$$
T_* \leq \frac{\sigma\varphi^2}{(q-2)\sigma\varphi - \|u_0\|_{H_0^1}^2}
$$

thus we must have

$$
\varphi \in \left(\frac{(q-1)\|u_0\|_{H_0^1}^2}{q(q-2)(d-J(u_0))}, \infty\right)
$$

Let $\upsilon = \sigma\varphi \in \left(0, \frac{q(d-J(u_0))\varphi}{q-1}\right)$, then $T_* \leq \frac{\varphi\upsilon}{(q-2)\upsilon - \|u_0\|_{H_0^1}}$.

Now let $h(\varphi, \upsilon) = \frac{\varphi\upsilon}{(q-2)\upsilon - \|u_0\|_{H_0^1}}$. Since h is monotonically decreasing concerning υ, we have

$$
\begin{aligned}
\inf_{\{(\varphi,\upsilon)\}} h(\varphi, \upsilon) &= \inf_{\{\varphi\}} h\left(\varphi, \frac{q(d-J(u_0))\varphi}{q-1}\right) \\
&= \inf_{\{b\}} k(\varphi)
\end{aligned}
$$

where,

$$
k(\varphi) = h\left(\varphi, \frac{q(d-J(u_0))\varphi}{q-1}\right) = \frac{\varphi^2 q(d-J(u_0))}{q(q-2)(d-J(u_0))\varphi - (q-1)\|u_0\|_{H_0^1}}
$$

now since $k(\varphi)$ takes the minimum at $\varphi^* = \frac{2(q-1)\|u_0\|_{H_0^1}}{q(q-2)(d-J(u_0))}$ we can conclude that,

$$
T_* \leq k(\varphi^*) = \frac{4(q-1)\|u_0\|_{H_0^1}^2}{q(q-2)^2(d-J(u_0))}. \qquad \square
$$

The following theorem show that the weak solution of the system blow-up when the initial energy of the system is critical.

Theorem 5. *(Blow up for $J(u_0) = d$)*
Let $u_0 \in W_0^{2,p}(\Omega)\backslash\{0\}$, $J(u_0) = d$ and $I(u_0) < 0$, then the weak solution $u(t)$ of problem (1) blows up in the sense, there appears a $T_* < \infty$ such that $\lim_{t \to T_*^-} \|u\|_{H_0^1}^2 = \infty$.

*Proof.*Since $J(u_0) = d > 0$ and $J(u)$ is continuous with respect to t, there appears a t_0 with $J(u(x,t)) > 0$ for $0 < t \leq t_0$. Also, it is easy to see $I(u(t)) < 0$ for every t. Therefore from the energy inequality, $\int_0^{t_0} \|u_\tau\|_{H_0^1}^2 d\tau + J(u(t_0)) < J(u_0) = d$, it follows that $J(u(t_0)) < d$.

Now choose $t = t_0$ as initial time, we have $J(u(t_0)) < d$ and $I(u(t_0)) < 0$. Now define

$$\mathcal{P}(t) = \int_{t_0}^t \|u\|_{H_0^1}^2 \quad \text{for } t > t_0$$

and the rest of proof resembles the proof of Theorem (4). □

ACKNOWLEDGMENT

REFERENCES

[1] **Brill, H.** (1977), A semilinear Sobolev evolution equation in a Banach space. *J. Differential Equations, 24, 412-425.*

[2] **Changchun Liu,** and **Pingping Li,**(2019). A parabolic p-biharmonic equation with logarithmic non linearity, *U.P.B. Sci. Bull., Series A, 81.*

[3] **Changchun Liu, Yitong Ma,** and **Hui Tang,**(2020). Lower bound of Blow-up time to a fourth order parabolic equation modelling epitaxial thin film growth, *Applied Mathematics Letters.*

[4] **David, C.,** and **Jet, W.**(1979). Asymptotic behaviour of the fundamental solution to the equation of heat conduction in two temperatures, *J. Math. Anal. Appl., 69, 411-418.*

[5] **Fugeng Zeng, Qigang Deng,** an **Dongxiu Wang,**(2022). Global Existence and Blow-Up for the Pseudo-parabolic p(x)-Laplacian Equation with Logarithmic Nonlinearity, *Journal of Nonlinear Mathematical Physics, 29, 41-57.*

[6] **Gopala Rao, V.R.,** and **Ting, T. W.,**(1972). Solutions of pseudo-heat equations in the whole space, *Arch. Ration. Mech. Anal., 49.*

[7] **Hao, A. J.,** and **Zhou, J.,**(2017). Blow up, extinction and non extinction for a non local p-biharmonic parabolic equation, *Appl. Math. Lett., 64, 198-204.*

[8] **Jiaojiao Wang,** and **Changchun Liu,**(2019). p-Biharmonic parabolic equations with logarithmic nonlinearity, *Electronic J. of Differential Equations, 08, 1-18.*

[9] **Lakshmipriya Narayanan,** and **Gnanavel Soundararajan,**(2022). Nonexistence of global solutions of a viscoelastic p(x)-Laplacian equation with logarithmic nonlinearity, *AIP Conference proceedings 2451.*

[10] **Lakshmipriya Narayanan,** and **Gnanavel Soundarararajan,** Existence of solutions of a viscoelastic p(x)-Laplacian equation with logarithmic, nonlinearity *Discontinuity, Nonlinearity, and Complexity, Accepted.*

[11] **Lakshmipriya, N., Gnanavel, S., Balachandran, K.,** and **Yong-Ki Ma,**(2022) Existence and blow-up of weak solutions of a pseudo-parabolic equation with logarithmic nonlinearity, *Boundary Value Problems.*

[12] **Le, C. N.,** and **Le, X. T.,**(2017). Global solution and blow up for a class of p-Laplacian evolution equations with logarithmic non linearity. *Acta. Appl. Math., 151, 149-169.*

[13] **Le Cong Nhan,** and **Le Xuan Truong,**(2017). Global solution and blow-up for a class of pseudo p-Laplacian evolution equations with logarithmic nonlinearity. *Computers and Mathematics with Applications.*

[14] **Liu, C.,** and **Guo, J.,**(2006). Weak solutions for a fourth-order degenerate parabolic equation, Bulletin of the Polish Academy of Sciences, *Mathematics, 54, 27-39.*

[15] **Liu, W. J., Yu,** and **J. Y.,**(2018). A note on blow-up of solution for a class of semilinear pseudo parabolic equations, *J. Funct. Anal., 274 , 1276-1283.*

[16] **Menglan Liao,** and **Qingwei Li,**(2020). A Class of Fourth-order Parabolic Equations with Logarithmic Nonlinearity, *Taiwanese J. of Math., 24, 975-1003.*

[17] **Sattinger, D. H.,**(1968). On global solution of nonlinear hyperbolic equations. *Arch. Rational Mech. Anal., 30, 148-172.*

[18] **Showalter, R. E.,** and **Ting, T. W.,**(1970). Pseudoparabolic partial differential equations, *SIAM J. Math. Anal., 1, 1-26.*

[19] **Sushmitha Jayachandran,** and **Gnanavel Soundararajan,**(2022). A fourth order pseudo parabolic equation with logarithmic non linearity, *Communicated.*

[20] **Sushmitha Jayachandran,** and **Gnanavel Soundararajan,**(2022). An upper and lower bound for blow up of pseudo parabolic equation with logarithmic non linearity, *Communicated.*

[21] **Sushmitha Jayachandran,** and **Gnanavel Soundararajan,**(2022). A pseudo-parabolic equation modeling thin film growth with Logarithmic nonlinearity, *Communicated in conference proceedings ICDSCA 2022.*

[22] **Tsuan Wu Ting,**(1969). Parabolic and Pseudo parabolic partial differential equations, *J. Math. Soc. Japan, 21.*

[23] **Wen-Shuo Yuan,** and **Bin Ge,**(2022). Global well-posedness for pseudo-parabolic p-Laplacian equation with singular potential and logarithmic nonlinearity, *J. Math. Phys. 63, 061503.*

[24] **Xu, R. Z.,** and **Su, J.,**(2013). Global existence and finite time blow-up for a class of semilinear pseudo-parabolic equations, *J. Funct. Anal. ,264, 2732-2763.*

[25] **Xu, R. Z., Wang, X. C.,** and **Yang, Y. B.,**(2018). Blowup and blow up time for a class of semilinear pseudo-parabolic equations with high initial energy, *Appl. Math. Lett., 83, 176-181.*

[26] **Yijun He, Huaihong Gao,** and **Hua Wang,**(2017) Blow-up and decay for a class of pseudo-parabolic p-Laplacian equation with logarithmic nonlinearity, *Computers and Mathematics with Applications.*

[27] **Yang Cao,** and **Congui Liu,**(2018). Initial boundary value problem for a mixed pseudo-parabolic p-laplacian type equation with logarithmic non linearity, *Electronic Journal of Differential Equations, 116, 1-19.*

[28] **Yang Cao, Jingxue Yin,** and **Chunpeng Wang,**(2009). Cauchy problems of semilinear pseudo-parabolic equations. *J. Differential Equations, 246, 4568-4590.*

[29] **Yunzhu Gao, Bin Guo,** and **Wenjie Gao,**(2014) Weak solutions for a high-order pseudo-parabolic equation with variable exponents, *Applicable Analysis, 93, 322-338*

/09/

EXTREME STATES, OPERATOR SPACES AND TERNARY RINGS OF OPERATORS

A. K. Vijayarajan

Kerala School of Mathematics, Kozhikode 673 571 (India).

E-mail:vijay@ksom.res.in

ORCID:0000-0001-5084-0567

ABSTRACT

In this survey article on extreme states of operator spaces in C^i-algebras and related ternary ring of operators an extension result for rectangular operator extreme states on operator spaces in ternary rings of operators is discussed. We also observe that in the spacial case of operator spaces in rectangular matrix spaces, rectangular extreme states are conjugates of inclusion or identity maps implemented by isometries or unitaries. A characterization result for operator spaces of matrices for which the inclusion map is an extreme state is deduced using the above mentioned results.

KEYWORDS

keyword 1, Keyword 2,...

1   INTRODUCTION

Arveson's extension theorem [3, Theorem1.2.3] for completely positive(CP) maps in the context of operator systems in C^i-algebras is a remarkable result in the study of boundary representations of C^i-algebras for operator systems. The theorem asserts that any CP map on an operator system $\mathcal{S}$ in a C^i-algebra $\mathcal{A}$ to $B.\mathcal{H}/$ can be extended to a CP map from $\mathcal{A}$ to $B.\mathcal{H}/$. A natural non-self-adjoint counterpart of the set up Arveson worked with can be considered to be consisting of operator spaces in ternary rings of operators(TROs) and completely contractive maps on them. An important recent work in this scenario is [10] where rectangular matrix convex sets and boundary representations of operator spaces were introduced. An operator space version of Arveson's conjecture, namely, every operator space is completely normed by it's boundary representations is also established in [10].

Apart from Arveson's fundamental work [3–5], we refer to the work of Douglas Farenick on extremal theory of matrix states on operator systems [8,9] and Kleski's work on pure completely positive maps and boundary representations for operator systems [12].

In this article we study an extension result for rectangular extreme states on operator spaces in TROs. A characterization result for rectangular extreme state on operator spaces of matrices with trivial commutants is deduced.

2   Preliminaries

In this section we recall the fundamental notions that we require for the discussions later on in this article.

Let $\mathcal{H}$ and $\mathcal{K}$ be Hilbert spaces and $B.\mathcal{H},\mathcal{K}/$ be the space of all bounded operators from $\mathcal{H}$ to $\mathcal{K}$. When $\mathcal{K} = \mathcal{H}$, we denote $B.\mathcal{H},\mathcal{H}/$ by $B.\mathcal{H}/$. A (concrete) *operator space* is a closed subspace of the (concrete) C^i-algebra $B.\mathcal{H}/$. The space $B.\mathcal{H},\mathcal{K}/$ can be viewed as a subspace of $B.\mathcal{K} \ \mathcal{H}/$, and hence it is always an operator space which we study more in later parts of this article.

An abstract characterisation of operator spaces was established by Ruan [16]. A subclass of operator spaces called ternary rings of operators referred to as TROs is of special interest to us here. These were shown to be the injective objects in the category of operator spaces and completely contractive linear maps by Ruan [17].

Definition 1. *A ternary ring of operators (TRO) T is a subspace of the C^i-algebra $B.\mathcal{H}/$ of all bounded operators on a Hilbert space $\mathcal{H}$ that is closed under the triple product $.x,y,z/ \rightarrow xy^iz$ for all x, y, z Ë T.*

A triple morphism between TROs is a linear map that preserves the triple product.

A triple morphism between TROs can be seen as the top-right corner of a *-homomorphism between the corresponding linking algebras [11]; see also [6, Corollary 8.3.5].

Clearly, an obvious, but important example of a TRO is the space $B.\mathcal{H},\mathcal{K}/$, where $\mathcal{H}$ and $\mathcal{K}$ are Hilbert spaces.

Definition 2. *Let X and Y be operator spaces. A linear map $\phi : X \rightarrow Y$ is called completely contractive (CC) if the linear map $\mathbb{1}_n \ \phi : \mathbb{M}_n \ X \rightarrow \mathbb{M}_n \ Y$ is contractive for all n.*

We denote the set of all CC maps from X to $B.\mathcal{H},\mathcal{K}/$ by $CC.X,B.\mathcal{H},\mathcal{K}//$.

Definition 3. *A representation of a TRO T is a triple morphism $\phi : T \rightarrow B.\mathcal{H},\mathcal{K}/$ for some Hilbert spaces $\mathcal{H}$ and $\mathcal{K}$.*

A representation $\phi : T \rightarrow B.\mathcal{H},\mathcal{K}/$ is *irreducible* if, whenever p, q are projections in $B.\mathcal{H}/$ and $B.\mathcal{K}/$ respectively, such that $q\phi.x/ = \phi.x/p$ for every x Ë T, one has $p = 0$ and $q = 0$, or $p = 1$ and $q = 1$.

A linear map $\phi : \mathbf{T} \to B.\mathcal{H}, \mathcal{K}/$ is *nondegenerate* if, whenever p, q are projections in $B.\mathcal{H}/$ and $B.\mathcal{K}/$, respectively, such that $q\phi.x/ = \phi.x/p = 0$ for every $x \ddot{E} \mathbf{T}$, one has $p = 0$ and $q = 0$.

Definition 4. *A rectangular operator state on an operator space X is a non degenerate linear map $\phi : X \to B.\mathcal{H}, \mathcal{K}/$ such that $\phi_{cb} = 1$ where the norm here is the completely bounded norm.*

Several characterizations of nondegenerate and irreducible representations of TROs are obtained in [7, Lemma 3.1.4 and Lemma 3.1.5].

A concrete TRO $\mathbf{T}$ $B.\mathcal{H}, \mathcal{K}/$ is said to act irreducibly if the corresponding inclusion representation is irreducible.

3   systems and spaces

An operator system in a $C^{\dot{\imath}}$-algebra is a unital selfadjoint closed linear subspace. Let $\mathcal{S}$ be an operator system in a $C^{\dot{\imath}}$-algebra $\mathcal{A}$, and $\mathcal{B}$ be any other $C^{\dot{\imath}}$-algebra.

A linear map $\phi : \mathcal{S} \to \mathcal{B}$ is called completely positive (CP) if the linear map $\mathbb{1}_n$ $\phi : \mathbb{M}_n$ $\mathcal{S} \to \mathbb{M}_n$ $\mathcal{B}$ is positive for all natural numbers n.

We denote the set of all unital CP maps from $\mathcal{S}$ to $B.\mathcal{H}/$ by $UCP.\mathcal{S}, B.\mathcal{H}//$.

One of the crucial theorems in this context is Arveson's extension theorem [3, Theorem1.2.3]. Arveson's extension theorem asserts that any CP map on an operator system $\mathcal{S}$ to $B.\mathcal{H}/$ can be extended to a CP map from the $C^{\dot{\imath}}$-algebra $\mathcal{A}$ to $B.\mathcal{H}/$.

Given an operator space X $B.\mathcal{H}, \mathcal{K}/$, we can assign an operator system $S.X/$ $B.\mathcal{K}$ $\mathcal{H}/$, called the *Paulsen system* [15, Chapter 8] which is defined to be the space of operators

$$\left\| \begin{bmatrix} \lambda I_{\mathcal{K}} & x \\ y^{\dot{\imath}} & \mu I_{\mathcal{H}} \end{bmatrix} : x, y \ \ddot{E} \ X, \lambda, \mu \ \ddot{E} \ \mathbb{C} \right\|$$

where $I_{\mathcal{H}}$, $I_{\mathcal{K}}$ denote the identity operators on $\mathcal{H}$, $\mathcal{K}$ respectively. It is well known that [15, Lemma 8.1] any completely contractive map $\phi : X \to B.\mathcal{H}, \mathcal{K}/$ on the operator space X extends canonically to a unital completely positive (UCP) map $S.\phi/ : S.X/ \to B.\mathcal{K}$ $\mathcal{H}/$ defined by

$$S.\phi/(\begin{bmatrix} \lambda I_{\mathcal{K}_0} & x \\ y^{\dot{\imath}} & \mu I_{\mathcal{H}_0} \end{bmatrix} / = \begin{bmatrix} \lambda I_{\mathcal{K}} & \phi.x/ \\ \phi.y/^{\dot{\imath}} & \mu I_{\mathcal{H}} \end{bmatrix} .$$

4   Extreme states and boundary theorems

4.1   Commutant of a TRO and boundary theorem

We introduce the notion of commutant of a rectangular operator set X $B.\mathcal{H}, \mathcal{K}/$ for Hilbert spaces $\mathcal{H}$ and $\mathcal{K}$. In the context of Hilbert $C^{\dot{\imath}}$-module by Aramba*sić* [1] introduced a similar notion. We can now define commutants of operator spaces in general and TROs in particular. We will prove that in the case of TROs, the commutants satisfy the usual properties with respect to the relevant notions of invariant subspaces and irreducibility of representations and thereby justifying the term. We observe that commutant behaves well with respect to the Paulsen map which is crucial for us. Throughout the artilce unless mentioned otherwise T represents a TRO.

Definition 5. *For X $B.H, K/$, the commutant of X is the set in $B.K$ $H/$ denoted by $X^{\acute{\imath}}$ and defined by*

$$X^{\acute{\imath}} = \hat{\ } A_1 \ A_2 \ \ddot{E} \ B.\mathcal{K} \ \mathcal{H}/ : A_1 \ \ddot{E} \ B.\mathcal{K}/ \ and \ A_2 \ \ddot{E} \ B.\mathcal{H}/, A_1 x = x A_2 \ and$$

$$A_2 x^{\dot{\imath}} = x^{\dot{\imath}} A_1, \ \mathring{A} x \ \ddot{E} \ X^{\,\prime}$$

where $.A_1 \ A_2/.\eta_1 \ \eta_2/ = A_1 \eta_1 \ A_2 \eta_2$, $\eta_1 \ \ddot{E} \ K$ and $\eta_2 \ \ddot{E} \ H$.

Remark 1. *For any non-empty set $X \subseteq B(\mathcal{H}, \mathcal{K})$, the commutant $X^{\prime}$ is a von Neumann subalgebra of $B(\mathcal{K} \oplus \mathcal{H})$.*

Definition 6. *Let $\phi : T \to B(\mathcal{H}, \mathcal{K})$ be a non-zero representation and $\mathcal{H}_1 \subseteq \mathcal{H}$ and $\mathcal{K}_1 \subseteq \mathcal{K}$ be closed subspaces. We say that the pair $(\mathcal{H}_1, \mathcal{K}_1)$ of subspaces is ϕ-invariant if $\phi(T)\mathcal{H}_1 \subseteq \mathcal{K}_1$ and $\phi(T)^{*}\mathcal{K}_1 \subseteq \mathcal{H}_1$.*

The following two results follow easily from the definitions above.

Lemma 1. *Let $\phi : T \to B(H, K)$ be a non-zero representation. Let p and q be the orthogonal projections on closed subspaces $H_1 \subseteq H$ and $K_1 \subseteq K$ respectively. Then (H_1, K_1) is a ϕ-invariant pair of subspaces if and only if $q \oplus p \in \phi(T)^{\prime}$.*

Corollary 1. *Let $\phi : T \to B(H, K)$ be a representation. Then ϕ is irreducible if and only if ϕ has no ϕ-invariant pair of subspaces other than $(0, 0)$ and (H, K).*

The following result illustrate that the term *commutant* used above is an appropriate one.

Proposition 1. *Let $\phi : T \to B(H, K)$ be a non zero representation of a TRO T. Then ϕ is irreducible if and only if $\phi(T)^{\prime} = \mathbb{C}(I_K \oplus I_H)$.*

Proof. Assume ϕ is irreducible. Let $q \oplus p$ be a projection in $\phi(T)^{\prime}$. From the definition of commutant we have $\phi(x)p = q\phi(x)$. By irreducibility of ϕ we have either $p = 0$ and $q = 0$, or $p = 1$ and $q = 1$. Hence $\phi(T)^{\prime} = \mathbb{C}(I_K \oplus I_H)$.

Conversely let $\phi(T)^{\prime} = \mathbb{C}(I_K \oplus I_H)$ and p, q be projections such that $\phi(x)p = q\phi(x)$. Applying adjoint we have $p\phi(x)^{*} = \phi(x)^{*}q$. Thus $q \oplus p \in \phi(T)^{\prime}$. By assumption, either $p = 0$ and $q = 0$, or $p = 1$ and $q = 1$. Hence ϕ is irreducible.

The following result shows that commutant behaves well with respect to the Paulsen map.

Lemma 2. *For a rectangular matrix state $\phi : X \to \mathbb{M}_{n,m}(\mathbb{C})$ we have*

$$\phi(X)^{\prime} = [S(\phi)(S(X))]^{\prime}.$$

Proof. To show $\phi(X)^{\prime} \subseteq [S(\phi)(S(X))]^{\prime}$, consider $A_1 \oplus A_2 \in \phi(X)^{\prime}$, then we have

$$
\begin{bmatrix} \lambda & \phi(x) \\ \phi(y)^{*} & \mu \end{bmatrix}
\begin{bmatrix} A_1 & 0 \\ 0 & A_2 \end{bmatrix}
= \begin{bmatrix} \lambda A_1 & \phi(x)A_2 \\ \phi(y)^{*}A_1 & \mu A_2 \end{bmatrix}
$$

$$
= \begin{bmatrix} \lambda A_1 & A_1\phi(x) \\ A_2\phi(y)^{*} & \mu A_2 \end{bmatrix}
$$

$$
= \begin{bmatrix} A_1 & 0 \\ 0 & A_2 \end{bmatrix}
\begin{bmatrix} \lambda & \phi(x) \\ \phi(y)^{*} & \mu \end{bmatrix}
$$

Hence $A_1 \oplus A_2 \in [S(\phi)(S(X))]^{\prime}$.

Conversely, since the Paulsen system contains a copy of scalar matrices, if $A \in [S(\phi)(S(X))]^{\prime}$, then $A = A_1 \oplus A_2$, where $A_1 \in B(K)$ and $A_2 \in B(H)$. Using the commutativity relation of the Paulsen map on the matrices

$$
\begin{bmatrix} 0 & \phi(x) \\ 0 & 0 \end{bmatrix} \text{ and }
\begin{bmatrix} 0 & 0 \\ \phi(x)^{*} & 0 \end{bmatrix}
$$

we can conclude that $A_1\phi(x) = \phi(x)A_2$ and $A_2\phi(x)^{*} = \phi(x)^{*}A_1$, $\forall x \in X$. Hence $A = A_1 \oplus A_2 \in \phi(X)^{\prime}$. Thus $[S(\phi)(S(X))]^{\prime} \subseteq \phi(X)^{\prime}$.

We prove a version of the rectangular boundary theorem proved in [10, Theorem 2.17] which is an analogue of boundary theorem of Arveson in the context of operator systems. Arveson's boundary theorem [4, Theorem 2.1.1] states that if $\mathcal{S} \subset B.\mathcal{H}/$ is an operator system which acts irreducibly on $\mathcal{H}$ such that the C^i-algebra $C^i.\mathcal{S}/$ contains the algebra of compact operators $\mathcal{K}.\mathcal{H}/$, then the identity representation of $C^i.\mathcal{S}/$ is a boundary representation for $\mathcal{S}$ if and only if the quotient map $B.\mathcal{H}/ \to B.\mathcal{H}/ \cdot \mathcal{K}.\mathcal{H}/$ is not completely isometric on $\mathcal{S}$. Our context here is that of an operator space and the generated TRO.

Throughout we assume that X is an operator space, and T is a TRO containing X as a generating set. We say that a rectangular operator state $\phi : X \to B.\mathcal{H}, \mathcal{K}/$ has *unique extension property* if any rectangular operator state ϕ on T whose restriction to X coincides with ϕ is automatically a triple morphism. Boundary representations for operator spaces were introduced in [10]. For our purposes we consider the following definition which is slightly different from the definition given in [10, Definition 2.7] but we remark that both are the same.

Definition 7. *An irreducible representation $\theta : T \to B.\mathcal{H}, \mathcal{K}/$ is a boundary representation for X if θ_X is a rectangular operator state on X and θ_X has unique extension property.*

An exact sequence of TROs induces an exact sequence of the corresponding linking algebras, which is actually an exact sequence of C^i-algebras. The decomposition result for representations of C^i-algebras is well known [5, section 7] and the result for TROs follows from it.

If $0 \to T^0 \to T \to T^Í \to 0$ is an exact sequence of TRO's, then every non degenerate representation

$$\pi : T \to B.\mathcal{H}, \mathcal{K}/$$

of T decomposes uniquely into a direct sum of representations $\pi = \pi_T^0 \ \pi_T^Í$ where π_T^0 is the unique extension to T of a nondegenerate representation of the TRO-ideal [7, Definition 2.2.7] T^0, and where $\pi_T^Í$ is a nondegenerate representation of T that annihilates T^0. When $\pi = \pi_T^0$ we say that π *lives on* T^0.

With X and T as above let $\mathcal{K}.\mathcal{H}, \mathcal{K}/$ denotes the set of compact operators from $\mathcal{H}$ to $\mathcal{K}$. Then $\mathcal{K}_T = T \tilde{} \mathcal{K}.\mathcal{H}, \mathcal{K}/$ is a TRO-ideal and we have an obvious exact sequence of TRO's. Denote $\mathcal{K}_T$ to be the set of all irreducible triple morphisms $\theta : T \to B.\mathcal{H}, \mathcal{K}/$ such that θ lives on $\mathcal{K}_T$ and θ_X is a rectangular operator state on X. The following is a boundary theorem in this context.

Theorem 1. *Let $X \subset B.\mathcal{H}, \mathcal{K}/$ be an operator space such that TRO T generated by X acts irreducibly and $\mathcal{K}_T \neq {}^{\wedge}0{}^{\prime}$. Then $\mathcal{K}_T$ contains a boundary representation for X if and only if the quotient map $q : T \to T \cdot \mathcal{K}_T$ is not completely isometric on X.*

Proof. Assume that the quotient map q is not completely isometric on X. If $\mathcal{K}_T$ contains no boundary representations for X, then every boundary representation must annihilate $\mathcal{K}_T$ and consequently it factors through q. By [10, Theorem 2.9], there are sufficiently many boundary representations π_l, $l \ddot{E} I$, for X so that

$$.q.x_{ij}/ \leq .x_{ij}/ = \sup_{l \ddot{E} I} \pi_l.x_{ij}/ \leq .q.x_{ij}/$$

for every $n \dot{I} n$ matrix $.x_{ij}/$ over X and every $n \geq 1$. This is a contradiction.

Conversely, if the quotient map is completely isometric on X, then we show that no $\pi \ddot{E} \mathcal{K}_T$ can be a boundary representation for X. Let $\pi : T \to B.\mathcal{H}, \mathcal{K}/$ be an irreducible representation that lives on $\mathcal{K}_T$ and consider the map $Q : q.T/ \to B.\mathcal{K} \ \mathcal{H}/$ defined by $Q.q.a// = \pi.a/$. Then Q is well defined and

$$Q.q.a// = \pi.a/ \leq a = q.a/.$$

Similarly $Q_n.q.a_{ij}// \leq .q.a_{ij}//$ and hence Q is completely contractive. Then the Paulsen's map $S.Q/ : S.q.T// \to B.\mathcal{K} \ \mathcal{H}/$ is unital and completely positive. By Arveson's extension theorem $S.Q/$

extends to a completely positive map $S.Q/ : C^{\rceil}.S.q.T/// \to B.\mathcal{K}\ \mathcal{H}/$. Define $\psi : T \to B.\mathcal{H},\mathcal{K}/$ via

$$S.Q/ \left(\begin{vmatrix} 0 & q.a/ \\ 0 & 0 \end{vmatrix} \right) = \begin{vmatrix} \dashv & \psi.a/ \\ \dashv & \dashv \end{vmatrix}$$

Then clearly ψ is linear. Also for all $a \ \ddot{\mathrm{E}}\ T$,

$$\psi.a/ = \begin{vmatrix} 0 & \psi.a/ \\ 0 & 0 \end{vmatrix} \leq S.Q/ \left(\begin{vmatrix} 0 & q.a/ \\ 0 & 0 \end{vmatrix} \right) \leq S.Q/q.a/ \leq a.$$

Since $\pi\ \ddot{\mathrm{E}}\ \mathcal{K}_T$ and $\psi_X = \pi_X$ we have $\psi_{cb} = 1$. Also we have $\psi.\mathcal{K}_T/ = 0$ and hence $\pi.\mathcal{K}_T/ = 0$ which is a contradiction to the fact that π lives in $\mathcal{K}_T$.

Remark 2. *The following result is a specific form of rectangular boundary theorem given above. Here we give an independent proof which directly uses the corresponding version of Arveson's boundary theorem and Lemma 2.*

Theorem 2. *Assume that X is an operator space in $\mathbb{M}_{n,m}.\mathbb{C}/$ such that $\dim.X^{\acute{\mathrm{I}}}/ = 1$. If $\phi : X \to \mathbb{M}_{n,m}.\mathbb{C}/$ is a rectangular matrix state on $\mathbb{M}_{n,m}.\mathbb{C}/$ for which $\phi.x/ = x$, $\mathring{\mathrm{A}}x\ \ddot{\mathrm{E}}\ X$, then $\phi.a/ = a$, $\mathring{\mathrm{A}}\ a\ \ddot{\mathrm{E}}\ \mathbb{M}_{n,m}.\mathbb{C}/.$*

Proof. By Lemma 2, $\phi.X/^{\acute{\mathrm{I}}} = [S.\phi/.S.X//]^{\acute{\mathrm{I}}}$. Hence $\dim[S.\phi/.S.X//]^{\acute{\mathrm{I}}} = 1$. Since $\phi.x/ = x$, $\mathring{\mathrm{A}}x\ \ddot{\mathrm{E}}\ X$, we have $S.\phi/.y/ = y$, $\mathring{\mathrm{A}}\ y\ \ddot{\mathrm{E}}\ S.X/$. Then by [9, Thoerem 4.2] , $S.\phi/.z/ = z$, $\mathring{\mathrm{A}}\ z\ \ddot{\mathrm{E}}\ \mathbb{M}_{n+m}$. In particular,

$$\begin{vmatrix} 0 & \phi.a/ \\ 0 & 0 \end{vmatrix} = S.\phi/(\begin{vmatrix} 0 & a \\ 0 & 0 \end{vmatrix} / = \begin{vmatrix} 0 & a \\ 0 & 0 \end{vmatrix},$$

and hence $\phi.a/ = a$, $\mathring{\mathrm{A}}\ a\ \ddot{\mathrm{E}}\ \mathbb{M}_{n,m}.\mathbb{C}/.$

4.2   Rectangular operator extreme states

We prove an important extension result in this section. In this section we prove that any rectangular operator extreme state on an operator space in a TRO can be extended to a rectangular operator extreme state on the TRO. Extension results in the same spirit concerning operator systems and UCP maps were proved by Kleski [12]. The following definition which appeared in [10, Definition 2.9] is important for our further discussion.
We begin by defining rectangular operator convex combination, and rectangular operator extreme states.

Definition 8. *Suppose that X is an operator space, and $\phi : X \to B.\mathcal{H},\mathcal{K}/$ is a completely contractive linear map. A rectangular operator convex combination is an expression $\phi = \alpha_1^{\dashv}\phi_1\beta_1 + \triangledown + \alpha_n^{\dashv}\phi_n\beta_n$, where $\beta_i : \mathcal{H} \to \mathcal{H}_\rangle$ and $\alpha_i : \mathcal{K} \to \mathcal{K}_\rangle$ are linear maps, and $\phi_i : X \to B.\mathcal{H}_\rangle,\mathcal{K}_\rangle/$ are completely contractive linear maps for $i = 1, 2, \triangledown n$ such that $\alpha_1^{\dashv}\alpha_1 + \triangledown + \alpha_n^{\dashv}\alpha_n = 1$ and $\beta_1^{\dashv}\beta_1 + \triangledown + \beta_n^{\dashv}\beta_n = 1$. Such a rectangular convex combination is proper if α_i, β_i are surjective, and trivial if $\alpha_i^{\dashv}\alpha_i = \lambda_i 1$, $\beta_i^{\dashv}\beta_i = \lambda_i 1$, and $\alpha_i^{\dashv}\phi_i\beta_i = \lambda_i\phi_i$ for some $\lambda_i\ \ddot{\mathrm{E}}\ [0, 1]$.*

A completely contractive map $\phi : X \to B.\mathcal{H},\mathcal{K}/$ is a rectangular operator extreme state if any proper rectangular operator convex combination $\phi = \alpha_1^{\dashv}\phi_1\beta_1 + \triangledown + \alpha_n^{\dashv}\phi_n\beta_n$ is trivial.

Rectangular operator states will be referred to as *rectangular matrix states* if the underlying Hilbert spaces are finite dimensional. The following theorem illustrates a relation between linear extreme states and and rectangular operator extreme states.

Theorem 3. *Let $X_1\ X_2$ be operator spaces. If a completely contractive map $\phi : X_2 \to B.\mathcal{H},\mathcal{K}/$ is linear extreme in the set $CC.X_2, B.\mathcal{H},\mathcal{K}//$ of all completely contractive maps from X_2 to $B.\mathcal{H},\mathcal{K}/$, and ϕ_{X_1} is rectangular operator extreme, then ϕ is a rectangular operator extreme state.*

Proof. Let $\phi : X_2 \to B.\mathcal{H}, \mathcal{K}/$ be linear extreme and ϕ_{X_1} be rectangular operator extreme. Then $S.\phi/ : S.X_2/ \to B.\mathcal{K} \ \mathcal{H}/$ is linear extreme in $UCP.S.X_2/, B.\mathcal{K} \ \mathcal{H}//$. For, let $\psi_1, \psi_2 \ \text{Ë} \ UCP.S.X_2/, B.\mathcal{K} \ \mathcal{H}//$ and $0 < t < 1$ be such that

$$S.\phi/ = t\Psi_1 + .1 * t/\Psi_2.$$

Then $S.\phi/ * t\Psi_1$ is UCP, so by ([10], Lemma 1.11) there exists a completely contractive map $\phi_1 : X_2 \to B.\mathcal{H}, \mathcal{K}/$ such that

$$t\Psi_1 \left(\begin{vmatrix} \lambda & x \\ y^{\text{i}} & \mu \end{vmatrix} \right) = w^{1 \cdot 2} \begin{vmatrix} \lambda I_\mathcal{K} & \phi_1.x/ \\ \phi_1.y/^{\text{i}} & \mu I_\mathcal{H} \end{vmatrix} w^{1 \cdot 2},$$

where

$$w = t\Psi_1 \left(\begin{vmatrix} 1 & 0 \\ 0 & 1 \end{vmatrix} \right) = t \begin{vmatrix} I_\mathcal{K} & 0 \\ 0 & I_\mathcal{H} \end{vmatrix}.$$

So

$$t\Psi_1 \left(\begin{vmatrix} \lambda & x \\ y^{\text{i}} & \mu \end{vmatrix} \right) = tS.\phi_1/ \left(\begin{vmatrix} \lambda & x \\ y^{\text{i}} & \mu \end{vmatrix} \right).$$

Thus $\Psi_1 = S.\phi_1/$. Similarly $\Psi_2 = S.\phi_2/$ for some cc map $\phi_2 : X_2 \to B.\mathcal{H}, \mathcal{K}/$. Hence

$$\begin{aligned} S.\phi/ &= tS.\phi_1/ + .1 * t/S.\phi_2/ \text{ and therefore} \\ \phi &= t\phi_1 + .1 * t/\phi_2. \end{aligned}$$

Since ϕ is a linear extreme point, we have $\phi = \phi_1 = \phi_2$. Thus

$$\begin{aligned} S.\phi/ &= S.\phi_1/ = S.\phi_2/ \\ S.\phi/ &= \Psi_1 = \Psi_2. \end{aligned}$$

Thus $S.\phi/ : S.X_2/ \to B.\mathcal{K} \ \mathcal{H}/$ is a linear extreme point. Since $S.\phi/_{S.X_1/}$ is pure [10, Proposition 1.12], by [12, Proposition 2.2] $S.\phi/$ is a pure UCP map on $S.X_2/$. Hence ϕ is a rectangular operator extreme state on X_2.

Here we consider the set of bounded operators from X to $B.\mathcal{H}, \mathcal{K}/$ with the weak$^{\text{i}}$ topology called the bounded weak topology or BW-topology, identifying this set with a dual Banach space. In its relative BW-topology, $CC.X, B.\mathcal{H}, \mathcal{K}//$ is compact (see [3, Section 1.1] or [15, Chapter 7] for details).

Theorem 4. *Let $X_1 \ X_2$ be operator spaces. Then every rectangular operator extreme state on X_1 has an extension to a rectangular operator extreme state on X_2.*

Proof. Let $\phi \ \text{Ë} \ CC.X_1, B.\mathcal{H}, \mathcal{K}//$ be a rectangular operator extreme state and let

$$\mathcal{F} = \hat{\ } \psi \ \text{Ë} \ CC.X_2, B.\mathcal{H}, \mathcal{K}// : \psi_{X_1} = \phi\text{'}.$$

Then clearly $\mathcal{F}$ is linear convex, and BW-compact. We claim that it is a face. For let $\psi_1, \psi_2 \ \text{Ë} \ CC.X_1, B.\mathcal{H}, \mathcal{K}//$ and $0 < t < 1$ be such that $t\psi_1 + .1 * t/\psi_2 \ \text{Ë} \ \mathcal{F}$. Then

$$t\psi_{1_{X_1}} + .1 * t/\psi_{2_{X_1}} = \phi$$

$$tS.\psi_1/_{.S.X_1/} + .1 * t/S.\psi_2/_{S.X_1/} = S.\phi/.$$

Since $S.\phi/$ is pure,

$$S.\psi_1/_{S.X_1/} = S.\psi_2/_{S.X_2/} = S.\phi/.$$

$$\psi_{1_{X_1}} = \psi_{2_{X_2}} = \phi.$$

$\Rightarrow \psi_1, \psi_2 \ \text{Ë} \ \mathcal{F}$ and hence $\mathcal{F}$ is a face. Thus $\mathcal{F}$ has a linear extreme point say $\phi^{\text{í}}$ which is a linear extreme point of $CC.X_2, B.\mathcal{H}, \mathcal{K}//$. By Theorem 3, it follows that $\phi^{\text{í}} : X_2 \to B.\mathcal{H}, \mathcal{K}/$ is a rectangular operator extreme state.

Now, in view of the above results, extension of rectangular operator extreme state from an operator space to the generated TRO is immediate.

Corollary 2. *If X is an operator space and T is the TRO generated by X and containing X, then any rectangular operator extreme state on the operator space X can be extended to a rectangular operator extreme state on the TRO T.*

Proof. Follows directly from the Theorem 4 by taking $X_1 = X$ and $X_2 = T$.

4.3 Rectangular matrix extreme states

Here we take up the special case of finite dimensional rectangular operator states and show that they are isometric or unitary 'conjugates' of the identity map. Here we investigate the relation between matrix extreme states on operator spaces and commutants of images of operator spaces under rectangular matrix extreme states. For operator spaces in rectangular matrix algebras with trivial commutants, we deduce that rectangular matrix extreme states are certain 'conjugates' of the identity state.

Proposition 2. *If $\phi : X \to \mathbb{M}_{n,m}(\mathbb{C})$ is a rectangular matrix extreme state on the operator space X, then $\dim(\phi(X)') = 1$.*

Proof. The commutant $\phi(X)'$ is a unital $*$-subalgebra of $\mathbb{M}_{n+m}(\mathbb{C})$ and is therefore the linear span of its projections. Choose any nonzero projection $p \oplus q \in \phi(X)'$. Then $\phi = q\phi p + (I * q)\phi(I * p)$. Since ϕ is a rectangular matrix extreme point, we have $p^i p = \lambda_1 I$, $q^i q = \lambda_1 I$ and $(I * p)^i(I * p) = \lambda_2 I$, $(I * q)^i(I * q) = \lambda_2 I$ and $q\phi p = \lambda_1 \phi$, $(I * q)\phi(I * p) = \lambda_2 \phi$, for some $\lambda_1, \lambda_2 \in [0,1]$. Thus $\lambda_1^2 = \lambda_1$ and $\lambda_2^2 = \lambda_2$. This gives $p = I$ and $q = I$. Therefore $\phi(X)' = \mathbb{C}I$. Hence $\dim(\phi(X)') = 1$.

Theorem 5. *Assume that X is an operator space in $\mathbb{M}_{n,m}(\mathbb{C})$ and that $\dim(X') = 1$.*

1. *If $\phi : X \to \mathbb{M}_{r,s}(\mathbb{C})$ is a rectangular matrix extreme state on X, then $r \leq n$, $s \leq m$ and there are isometries $w : \mathbb{C}^r \to \mathbb{C}^n$ and $v : \mathbb{C}^s \to \mathbb{C}^m$ such that $\phi(x) = w^i x v$, $\forall\, x \in X$.*

2. *A rectangular matrix state ϕ on X with values in $\mathbb{M}_{n,m}(\mathbb{C})$ is rectangular matrix extreme if and only if there exist unitaries $v \in \mathbb{M}_n(\mathbb{C})$ and $u \in \mathbb{M}_m(\mathbb{C})$ such that $\phi(x) = v^i x u$, $\forall\, x \in X$.*

Proof. (1): Let $X \subseteq \mathbb{M}_{n,m}(\mathbb{C})$, and $\dim(X') = 1$. Let $\phi : X \to \mathbb{M}_{r,s}(\mathbb{C})$ be a rectangular matrix extreme state. By Corollary 2, ϕ can be extended to a rectangular extreme state $\Phi : \mathbb{M}_{n,m}(\mathbb{C}) \to \mathbb{M}_{r,s}(\mathbb{C})$. Then $S(\Phi) : S(\mathbb{M}_{n,m}(\mathbb{C})) \to B(\mathbb{C}^r \oplus \mathbb{C}^s)$ is pure. So by [12, Theorem 3.3] there exists a boundary representation $w : \mathbb{M}_{n+m}(\mathbb{C}) \to B(\mathcal{L})$ for $S(\mathbb{M}_{n,m}(\mathbb{C}))$ and an isometry $u : \mathbb{C}^r \oplus \mathbb{C}^s \to \mathcal{L}$ such that

$$S(\phi)(y) = u^i w(y) u, \text{ for all } y \in S(\mathbb{M}_{n,m}(\mathbb{C})).$$

By [10, Proposition 2.8] we can decompose $\mathcal{L}$ as an orthogonal direct sum $\mathcal{L} = K_w \oplus H_w$ in such a way that $w = S(\pi)$ for some irreducible representation $\pi : \mathbb{M}_{n,m}(\mathbb{C}) \to B(\mathcal{H}_w, \mathcal{K}_w)$.

From the construction of $\mathcal{H}_w$ and $\mathcal{K}_w$, it follows that u maps $\mathbb{C}^r \oplus 0$ to $\mathcal{K}_w$ and $0 \oplus \mathbb{C}^s$ to $\mathcal{H}_w$. By defining the maps u_1 and u_2 as $u_1(x) = u(x \oplus 0)$, $x \in \mathbb{C}^r$ and $u_1(y) = u(0 \oplus y)$, $y \in \mathbb{C}^s$ we see that $u_1 : \mathbb{C}^r \to \mathcal{K}_w$ and $u_2 : \mathbb{C}^s \to \mathcal{H}_w$ are isometries such that $u = u_1 \oplus u_2$. Then $\Phi(x) = u_1^i \pi(x) u_2$, $\forall x \in \mathbb{M}_{n,m}(\mathbb{C})$ and thus Φ is a compression of an irreducible representation of $\mathbb{M}_{n,m}(\mathbb{C})$. Since every irreducible representation of $\mathbb{M}_{n,m}(\mathbb{C})$ is unitarily equivalent to the identity representation [7, Lemma 3.2.3] we have that ϕ is a compression of the identity representation. That is, there are isometries $w : \mathbb{C}^r \to \mathbb{C}^n$ and $v : \mathbb{C}^s \to \mathbb{C}^m$ such that

$$\phi(x) = w^i x v, \quad \forall\, x \in X.$$

Since v and w are isometries, we conclude that $r \leq n$ and $s \leq m$.

(2) Let $\phi : X \to \mathbb{M}_{n,m}.\mathbb{C}/$ be a rectangular matrix extreme state. Then by part $.a/$, there are isometries (unitaries in this case) u Ë $\mathbb{M}_n.\mathbb{C}/$, v Ë $\mathbb{M}_m.\mathbb{C}/$ such that

$$\phi.x/ = v^{\text{i}}xu, \; \text{Å}x \text{ Ë } X.$$

Conversely let $\phi.x/ = v^{\text{i}}xu$, Åx Ë X for unitaries u and v then

$$S.\phi/ \left(\begin{vmatrix} \lambda & x \\ y^{\text{i}} & \mu \end{vmatrix} \right) = \begin{vmatrix} u^{\text{i}} & 0 \\ 0 & v^{\text{i}} \end{vmatrix} \begin{vmatrix} \lambda & x \\ y^{\text{i}} & \mu \end{vmatrix} \begin{vmatrix} u & 0 \\ 0 & v \end{vmatrix}, \; \text{Å} \; x,y \; \text{ Ë } \; X.$$

Then by [9, Theorem 4.3] $S.\phi/$ is pure. Hence ϕ is a rectangular matrix extreme state by ([10, Proposition2.12]).

The following result is now an immediate consequence of Proposition 2 and Theorem 5.

Theorem 6. *Let X $\mathbb{M}_{n,m}.\mathbb{C}/$ be an operator space. Then the inclusion map $i.x/ = x$, Åx Ë X, is a rectangular matrix extreme state if and only if $dim.X^{\hat{\text{i}}}/ = 1$.*

REFERENCES

[1] **Aramba*sić* L.**(2005). Irreducible representations of Hilbert C*-modules. *Math. Proc. Roy. Irish Acad.*, 105 A, 11-14; MR2162903.

[2] **Arunkumar C.S.**, **Shabna A. M.**, **Syamkrishnan M. S.** and **Vijayarajan A. K.** (2021). Extreme states on operator spaces in ternary rings of operators. *Proc. Ind. Acad. Sci.***131**, 44, MR 4338047.

[3] **Arveson W. B.** (1969). Subalgebras of C^{i}-algebras. *Acta Math.* **123**, 141-224; MR0253059.

[4] **Arveson W. B.**(1972). Subalgebras of C^{i}-algebras II. *Acta Math.* **128**(1972) no. 3-4 , 271-308; MR0394232.

[5] **Arveson W. B.**(2011). The noncommutative Choquet boundary II: Hyperrigidity. *Israel J. Math.* **184** (2011), 349-385; MR2823981.

[6] **Blecher D. P.** and **Christian Le Merdy** (2004). Operator algebras and their modules-an operator space approach. *London Mathematical Society Monographs, New Series, vol. 30, Oxford University Press, Oxford.*

[7] **Bohle D.** (2011). *K-Theory for ternary structures*, Ph.D Thesis, Welstfälishe Wilhelms-Universität Münster.

[8] **Farenick D. R.** (2000). Extremal Matrix states on operator Systems. *Journal of London Mathematical Society* **61**, no. 3, 885-892; MR1766112.

[9] **Farenick D. R.**(2004). Pure matrix states on operator systems. *Linear Algebra and its Applications* **393**, 149-173; MR2098611.

[10] **Fuller A. H.**, **Hartz M.** and **Lupini M.** (2018). Boundary representations of operator spaces, and compact rectangular matrix convex sets. *Journal of Operator Theory*, Vol.79, No.1, 139-172; MR3764146.

[11] **Hamana M.** (1999). Triple envelopes and Shilov boundaries of operator spaces. *Mathematical Journal of Toyama University* **22**, 77-93; MR1744498.

[12] **Kleski C.** (2014). Boundary representations and pure completely positive maps. *Journal of Operator Theory*, pages 45-62; MR3173052.

[13] **Lobel R.** and **Paulsen V. I.** (1981). Some remarks on C^i-convexity. *Linear Algebra Appl.* **78**, 63-78, 1981; MR0599846.

[14] **Magajna B.** (2001). On C^i-extreme points. *Proceedings of the American Mathematical Society* **129**, 771-780; MR1802000.

[15] **Paulsen V. I.** (2002). Completely bounded maps and operator algebras. *Cambridge Studies in Advanced Mathematics Vol. 78, Cambridge University Press, Cambridge.*

[16] **Ruan Z. J.** (1988). Subspaces of C^i-algebras. *Journal of Functional Analysis* **76**, 217-230, MR0923053.

[17] **Ruan Z. J.** (1989). Injectivity and operator spaces. *Transactions of the American Mathematical Society,* **315**, 89-104; MR0929239.

[18] **Webster C.** and **Winkler S.** (1999). The Krein-Milman theorem in operator convexity. *Transactions of the American Mathematical Society,* Vol.351, no 1, 307-322; MR1615970.

[19] **Wittstock G.** (1984). On Matrix Order and Convexity. *Functional Analysis: survey and recent results, III, Math Studies* **90**, 175-188, MR0761380.

/10/

SHAPLEY VALUES TO EXPLAIN MACHINE LEARNING MODELS OF SCHOOL STUDENT'S ACADEMIC PERFORMANCE DURING COVID-19

Yunusov Valentin

Kazan Federal University, Kazan, (Russian Federation).

E-mail: valentin.yunusov@gmail.com

Gafarov Fail

Kazan Federal University, Kazan, (Russian Federation).

Ustin Pavel

Kazan Federal University, Kazan, (Russian Federation).

https://doi.org/10.17993/3ctic.2022.112.136-144

ABSTRACT

In this work we perform an analysis of distance learning format influence, caused by COVID-19 pandemic on school students' academic performance. This study is based on a large dataset consisting of school students grades for 2020 academic year taken from "Electronic education in Tatarstan Republic" system. The analysis is based on the use of machine learning methods and feature importance technique realized by using Python programming language. One of the priorities of this work is to identify the academic factors causing the most sensitive impact on school students' performance. In this work we used the Shapley values method for solving this task. This method is widely used for the feature importance estimation task and can evaluate impact of every studied feature on the output of machine learning models. The study-related conditional factors include characteristics of teachers, types and kinds of educational organization, area of their location and subjects for which marks were obtained.

KEYWORDS

Data Science, Python, education, Machine Learning, Feature Importance.

1. INTRODUCTION

Failure to achieve educational goals negatively affects society as a whole and is a serious problem. This problem can manifest itself most significantly during periods of drastic changes, one of which was the introduction of distance learning during the COVID-19 pandemic. To quantify the influence of this event on educational system, a variety of quantitative models based on modern statistical methods in combination with Big Data approaches can be used, as has shown in Li et al. [2021].

Machine learning (ML) is one of the new and actively developing methods of analysis, combining approaches that can "learn" based on the received data, which allows to perform a wide range of different tasks. ML can be used to solve problems of detection, recognition, prediction, prediction, diagnostics, and optimization.

A large number of huge datasets has been accumulated recently in educational system, which can be used to analyze and then improve educational process, as was demonstrated by Park [2020]. For example, Livieris et al. [2019] analyze a dataset consisting of performance of 3716 students in course of Mathematics of the first 5 years of secondary school. They develop two semisupervised machine learning algorithms to predict students' performance in the final examinations and then evaluate methods' accuracy. Authors compare these two methods with supervised machine learning method and as a result, these approaches outperform it, and the final accuracy exceeds 80%.

Jeslet et al. [2021] used well-known algorithms of machine learning Logistic Regression and Support Vector Machine to predict whether student is eligible to acquire a degree or not. Authors analyzed dataset of 1460 students' final year's results and obtained a model trained to 99.27% and 99.72% accuracy. Also, Nuanmeeseri et al. [2022] analyzed dataset of 1650 university students' academic performance. As a result, after adjusting model's parameters, authors achieved accuracy of 96.98%, so their model outperformed other considered machine learning methods and can be effectively used to evaluate significant academic performance factors in drastically changing period.

In our work, we study changes of academic performance of whole school grades in the framework of a variety of machine learning methods with the following feature importance analysis to identify significant parameters that affect academic performance the most after the introduction of distance learning format due to the COVID-19 pandemic.

2. MACHINE LEARNING METHODS AND FEATURE IMPORTANCE

2.1 MACHINE LEARNING TECHNIQUES

Hastie et al. [2009] introduce Machine learning as a set of mathematical techniques that give computer algorithms an ability to learn. This methodology is based on the input and required output of the algorithms and can automate the way how humans are able to carry out the task, as stated by Mnih et al. [2015].

Ensemble methods are groups of algorithms that use several machine learning methods at once and makes correction of each other's errors. Bostanabad et al. [2016] define supervised learning as a type of algorithms where the method is supplied with example inputs along with the required output, which then allows it to learn a rule that maps inputs to outputs. Bengio et al. [2013] state that in unsupervised learning, on the contrary, only the inputs are supplied, and the learning algorithm is required to determine the structure of the input and perform according to unknown characteristics [10].

In this work we use supervised machine learning methods: Decision Tree, Gradient Boosting, K-nearest neighbors (KNN) Regressor, Lasso Regression, Linear Regression and MultiLayer Perceptron neural networks, Support Vector Regressor; and ensemble method: Random Forest.

In our study, we solved the regression task to predict Cohen's effect size, defined by Cohen [1988], based on subsets of school grades' marks in February and March, and April and May. Cohen's effect size measures the difference between mean values of two variables Cohen [1988].

2.2 SHAP FEATURE IMPORTANCE IMPLEMENTATION

Usually, machine learning models are difficult to interpret and it's hard to identify which features affect the output of the models the most. SHAP method (Shapley additive explanations) is one of the techniques used to solve this problem. This method is based on cooperative game theory, explained by Shapley [1953], and is used to increase transparency and interpretability of machine learning models. Absolute SHAP value shows us how much a single feature affected the prediction. SHAP values can represent the local importance of features and how it changes with lower and higher values, as shown by Sahakyan et al. [2021].

3. EXPERIMENTAL DATA DESCRIPTION

In this work, we study the influence of COVID-19 pandemic on school students' academic performance by analyzing a large dataset consisting of data from all schools in Tatarstan Republic, introduced by Ustin et al. [2022]. The dataset includes marks of entire grades of school students for main subjects for grades from 2 to 11.

During the preprocessing of original data, for the following analysis by machine learning methods, the initial dataset was modified into a new dataset consisting of features describing different parameters. These parameters included teachers' characteristics (age, sex, and educational category), mean mark of grade for February and March of 2020, school characteristics (location in or out of town, region of location, organization kind and type, subject). Data was filtered to consider school grades with at least 60 school grades in certain time periods (February and March, April and May 2020). For every row in dataset, Cohen's effect size   was calculated. Figure 1 shows histograms for certain grades that represent whole dataset. It should be noted that most parameter values are positive, i.e., after the introduction of distance learning format, grades have generally increased.
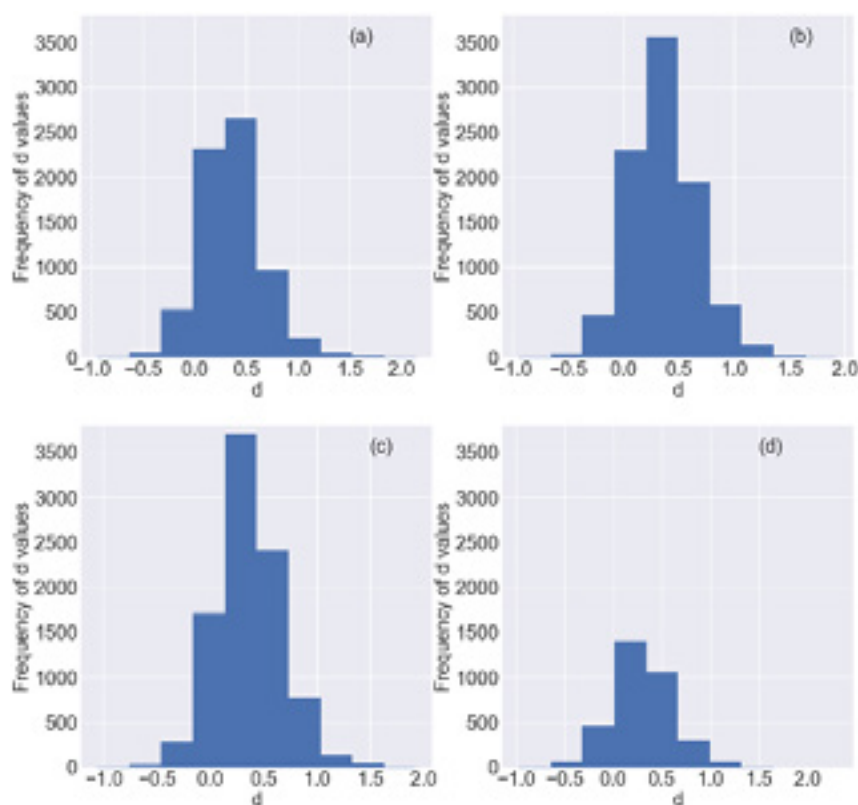
Fig. 1. Histograms of parameter d for: (a) 5th grade; (b) 7th grade; (c) 8th grade; (d) 11th grade.

4. APPLICATION OF MACHINE LEARNING METHODS IN THE ANALYSIS OF THE SCHOOL STUDENTS' ACADEMIC PERFORMANCE

The analysis was performed in two stages. At the first stage, we implemented a variety of machine learning methods for a comparative analysis of machine learning methods in the regression problem of predicting the values of the Cohen's effect size   based on a large set of features. At the second stage, we performed evaluation of the importance of explanatory variables in the predictive model.

4.1 MACHINE LEARNING METHODS IMPLEMENTATION

In our work we applied machine learning techniques realized in PyTorch and scikit-learn frameworks in Python. Among the applied methods: one-layer Linear regression and MultiLayer Perceptron realized in Pytorch; Decision Tree, Gradient Boosting, K-nearest neighbors algorithm, Lasso regression, Random Forest and Support Vector Regression realized in scikit-learn framework.

MultiLayer Perceptron consisted of the input layer, two hidden layers with 64 neurons and output layer with 1 neuron. We used ReLU as activation function, Adam as optimizer with learning rate equal to 0.00005 and Mean Squared Error (MSE) as loss function. Figure 2 shows the learning curve of one-layer Linear regression and MultiLayer Perceptron.
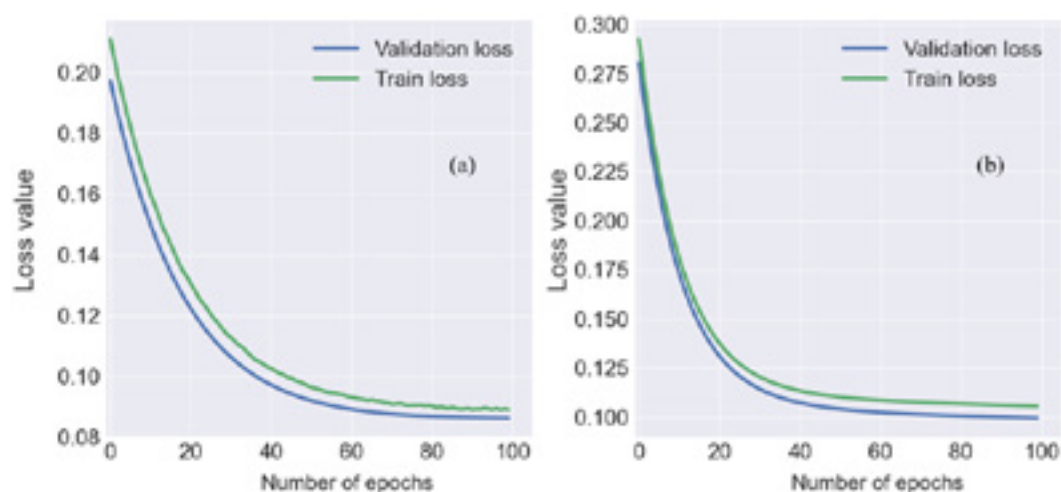
Fig. 2. Learning curve of: (a) MultiLayer Perceptron for 6th grade; (b) one-layer Linear regression for 6th grade.

Figure 3 shows the resulting plot of minimal MSE values for each method of machine learning for every studied school grade. It should be noted that the most precise algorithms are Random Forest, Lasso Regression, K-nearest neighbors and Support Vector Regression. Decision Tree and Gradient Boosting, on the other hand, have high values of error function. Also we obtained that for 8th and 10th grade values of MSE are increased significantly of the methods, and hence the Cohen's effect size values are more difficult to predict, while for 4th and 9th these values are decreased. Therefore, marks of students in 8th and 10th grade after the introduction of distant learning format due to the COVID-19 pandemic changed more randomly than the marks of students in other grades, especially in 4th and 9th grades.
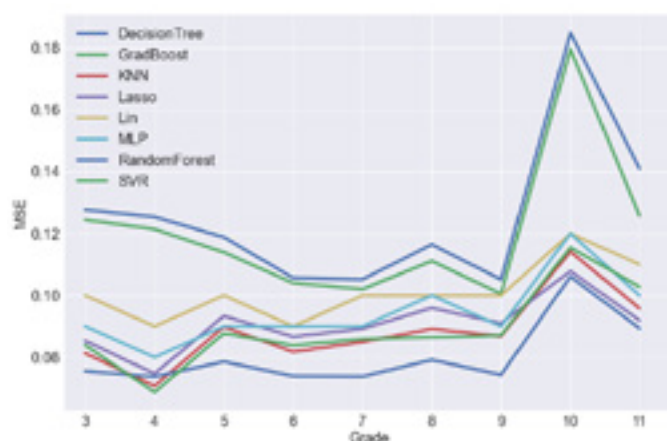
Fig. 3. The values of MSE for machine learning algorithms for each studied school grade.

4.2 EVALUATION OF THE IMPORTANCE OF EXPLANATORY VARIABLES

At the second stage of our analysis, we evaluated importance of our explanatory features for predicting values of Cohen's effect size. Figure 4 shows the distribution of Shapley values, i.e., influence on the value of parameter   exerted by the studied explanatory features. Analysis was performed for Gradient Boosting, Random Forest and MultiLayer Perceptron models with primary Explainer and Tree Explainer.
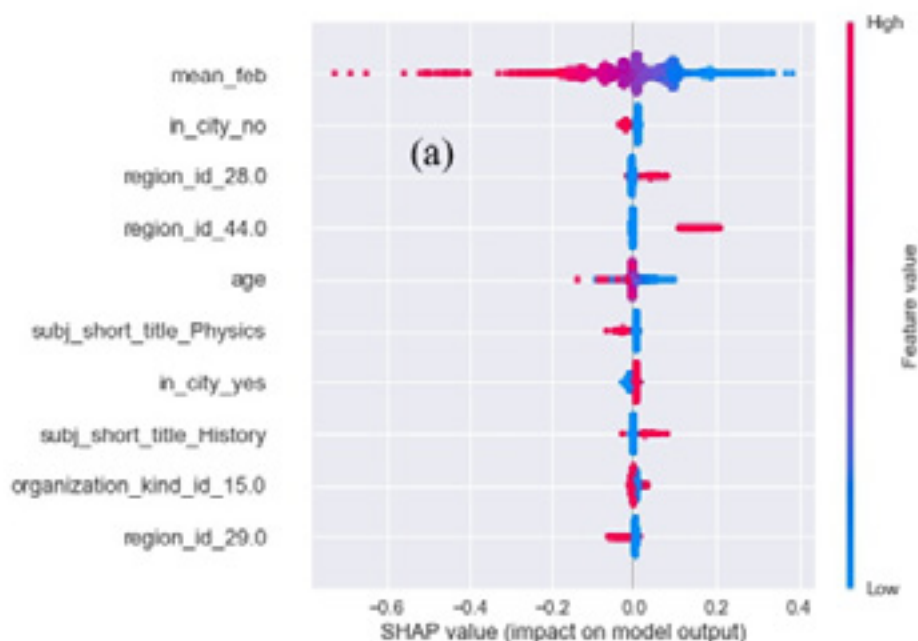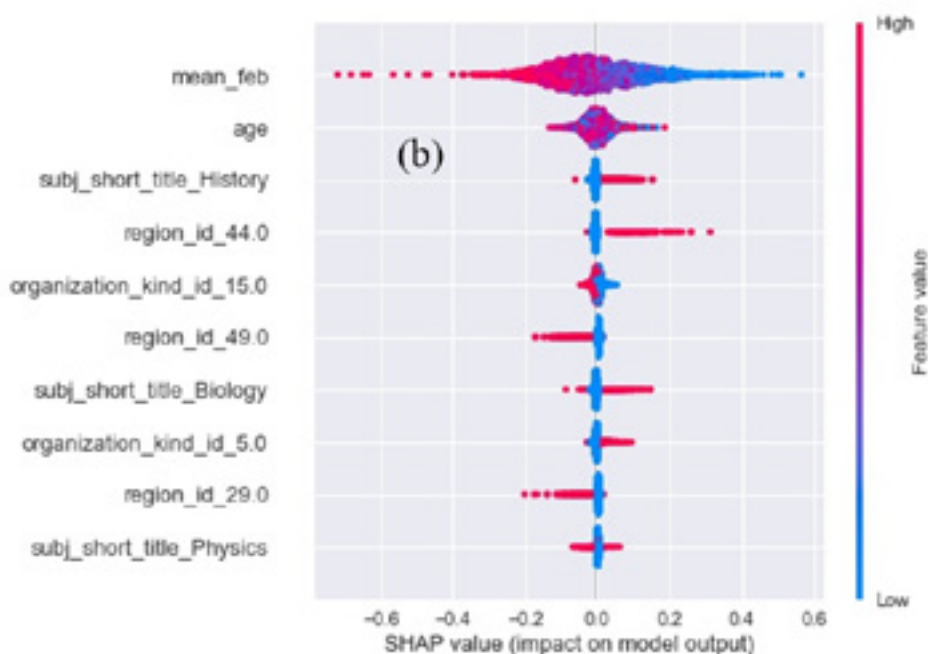
Fig. 4. The distribution of SHAP values (impact on parameter d) of explanatory features for predictive models: (a) for Gradient Boosting model with primary Explainer; (b) for Random Forest model with Tree Explainer. Cases with high values are shown in red, and those with low values are shown in blue. The variables are ranked in descending order. The horizontal location indicates whether the effect of that value is associated with a higher or lower prediction.

The main influence on the prediction of the Cohen's effect size value is exerted by the mean value of school grade in February and March, which obviously follows from the formula for the parameter . Also, significant contribution to the prediction of the parameter Cohen's effect size value is also made by the age of teachers: usually it is either not defined, or also negative (with an increase of age value, the value of the parameter decreases), which means that young teachers were more likely to give higher grades after introduction of distance learning format.

There exists also a significant improvement in school marks for the lessons of history, biology, while for such important subjects as physics, mathematics and Russian language, grades decreased after the introduction of distance learning. Besides that, location in certain regions: Naberezhnye Chelny, Kazan's Vakhitovsky, Novo-Savinovsky and Privolzhsky districts, also made significant positive contribution to the value of effect size . And in opposite, for schools located in Nizhnekamsk and Sovetsky district of Kazan, mean marks decreased significantly. Location of schools in the town also made positive contribution to the value of parameter d, while location outside of the town had a negative impact.

Besides that, different kinds of schools also played a special role as the used models features. The most significant influence was due to whether the educational organizations were secondary schools, lyceums, gymnasiums, or boarding schools. In case of lyceums, gymnasiums and boarding schools, the influence was strictly positive and increased the value of the Cohen's effect size , which means that after the introduction of distance learning into them, the marks of school grades increased. A different situation has developed in secondary schools: on average, the impact of the introduction of the distance learning format was mixed and did not affect academic performance in a certain way.

The influence of all the above factors may be explained by the fact that, depending on the characteristics of teachers, subjects taught and geographical location, the approach and time of transition to a new, previously practically unused format of education varied in different schools.

5. CONCLUSIONS

In this paper, we performed analysis of variation of academic performance in a large set of schools in Tatarstan Republic in the period before and during distance learning caused by COVID-19 pandemic.

We used eight different machine learning methods to solve the regression task of forecasting value of Cohen's effect size . We determined the values of the error function corresponding to all applied algorithms and established school classes for which prediction is easier and the ones for which prediction is more difficult.

We discovered impact of age of teachers to the forecasting of parameter; lessons for which marks were more significant in the studied task and areas of Tatarstan Republic, location of school in which increased or decreased Cohen's effect size. Moreover, we discovered that the kind of educational organization also plays a special role in the forecasting task and identified the ones which had a significant impact on the value of Cohen's effect size. The impact of these study-related factors may indicate that different schools, school types and teacher had different periods of adaptation to a rapidly changing learning format, and these changes can be evaluated using feature importance method in combination with machine learning algorithms.

The results obtained during the research, after appropriate verification, may be used to evaluate the influence on academic performance of school students after introduction of distance learning.

ACKNOWLEDGMENTS

REFERENCES

[1] BENGIO, Y., COURVILLE, A., AND VINCENT, P. 2013. Representation Learning: A Review and New Perspectives. *IEEE Trans Pattern Anal Mach Intell 35*, 1798–1828.

[2] BOSTANABAD, R., BUI, A., XIE, W., APLEY, D.W., AND CHEN, W. 2016. Stochastic microstructure characterization and reconstruction via supervised learning. *Acta Materialia 103*, 89–102.

[3] COHEN, J. 1988. *Statistical Power Analysis for the Behavioral Sciences (2nd ed.)*. Lawrence Erlbaum Associates, Hillsdale, NJ.

[4] HASTIE, T., TIBSHIRANI, R., AND FRIEDMAN, J. 2009. *The Elements of Statistical Learning*. Springer, New York.

[5] JESLET, D.S., KOMARASAMY, D., AND HERMINA, J.J. 2021. Student Result Prediction in Covid-19 Lockdown using Machine Learning Techniques. *JPCS 1911*, 012008.

[6] LI, J., AND JIANG, Y. 2021. The Research Trend of Big Data in Education and the Impact of Teacher Psychology on Educational Development During COVID-19: A Systematic Review and Future Perspective. *Front. Psychol. 12*, 753388.

[7] LIVIERIS, I.E., DRAKOPOULOU, K., TAMPAKAS, V.T., MIKROPOULOS, T.A.M AND PINTELAS, P. 2019. Predicting Secondary School Students' Performance Utilizing a Semi-supervised Learning Approach. *J. Educ. Comput. Res. 57*, 448–470.

[8] MNIH, V., KAVUKCUOGLU, K., SILVER, D., RUSU, A.A., VENESS, J., BELLEMARE, M.G., GRAVES, A., RIEDMILLER, M., FIDJELAND, A.K., OSTROVSKI, G., PETERSON, S., BEATTIE, C., SADIK, A., ANTONOGLOU, I., KING H., KUMARAN, D., WIERSTRA, D., LEGG, S., AND HASSABIS, D. 2015. Human-level control through deep reinforcement learning. *Nature 518*. 529–533.

[9] NUANMEESERI, S., POOMHIRAN, L., CHOPYITAYAKUN, S., AND KADMATEEKARUN, P. 2022. Improving Dropout Forecasting during the COVID-19 Pandemic through Feature Selection and Multilayer Perceptron Neural Network. *Int. J. Inf. Educ. Technol. 12*, 851–857.

[10] PARK, Y-E. 2020. Uncovering trend-based research insights on teaching and learning in big data. *J. Big Data 7*, 1–17.

[11] SAHAKYAN, M., AUNG, Z., AND RAHWAN, T. 2021. Explainable Artificial Intelligence for Tabular Data: A Survey. *IEEE Access 9*, 135392.

[12] SHAPLEY, L.S. 1953. *Contributions to the Theory of Games vol 2*. Princeton University Press, Princeton.

[13] USTIN, P., SABIROVA, E., ALISHEV, T., AND GAFAROV, F. 2022. Key Factors of Teacher's Professional Success in the Digital Educational Environment. *ARPHA Proceedings 5*, 1747–1761.

/11/

BENCHMARKING FOR RECOMMENDER SYSTEM (MFRISE)

Mahesh Mali

Computer Engineering Department, SVKMs NMIMS, Mukesh Patel School of Technology Management and Engineering, Mumbai, (India).

E-mail: maheshmalisir@gmail.com

Dhirendra Mishra

Computer Engineering Department, SVKMs NMIMS, Mukesh Patel School of Technology Management and Engineering, Mumbai, (India).

M. Vijayalaxmi

Computer Engineering Department, V.E.S. College of Engineering, Mumbai University, (India).

https://doi.org/10.17993/3ctic.2022.112.146-156

ABSTRACT

The advent of the internet age offers overwhelming choices of movies and shows to viewers which create need of comprehensive Recommendation Systems (RS). Recommendation System will suggest best content to viewers based on their choice using the methods of Information Retrieval, Data Mining and Machine Learning algorithms. The novel Multifaceted Recommendation System Engine (MF-RISE) algorithm proposed in this paper will help the users to get personalized movie recommendations based on multi-clustering approach using user cluster and Movie cluster along with their interaction effect. This will add value to our existing parameters like user ratings and reviews.

In real-world scenarios, recommenders have many non-functional requirements of technical nature. Evaluation of Multifaceted Recommendation System Engine must take these issues into account in order to produce good recommendations. The paper will show various technical evaluation parameters like RMSE, MAE and timings, which can be used to measure accuracy and speed of Recommender system. The benchmarking results also helpful for new recommendation algorithms.

The paper has used MovieLens dataset for purpose of experimentation. The studied evaluation methods consider both quantitative and qualitative aspects of algorithm with many evaluation parameters like mean squared error (MSE), root mean squared error (RMSE), Test Time and Fit Time are calculated for each popular recommender algorithm (NMF, SVD, SVD++, SlopeOne, Co-Clustering) implementation. The study identifies the gaps and challenges faced by each above recommender algorithm. This study will also help researchers to propose new recommendation algorithms by overcoming identified research gaps and challenges of existing algorithms.

KEYWORDS

Comparing recommender system, bench-marking recommendation system algorithms, comparing recommendation algorithms, challenges of various recommendation algorithms, Performance evaluation of Recommendation algorithms.

1. INTRODUCTION

Availability of internet and global resources has increased number of availability of movies and shows which can be viewed by users. Recommendation Systems are tools used to give movie recommendations to the end-users based on their likes or likes of the similar users [1]. Recommender systems are good for both service providers as well as users. They reduce the time to find and selecting correct item on internet. A recommender system is an information filtering system which recommends the best movies to the user by considering some similarity between users or movies or user ratings for movies. The existing types of recommendation systems algorithms are Collaborative Filtering (CF) and Content-Based Filtering (CB).

Multiple well-known recommendation algorithms based on above categories are already proposed, KDD algorithm, SVD algorithms, SlopeOne and Co-Clustering algorithm. In this paper we have implemented and analyzed their comparative performance, as it can be used for benchmarking performance of our proposed multifaceted recommender system (MFRISE). This paper also explained the challenges and limitations of each algorithm. Such, challenges can be used to improve performance quality recommendations by modifying algorithm.

2. ARCHITECTURE OF MULTIFACETED RECOMMENDER SYSTEM (MFRISE)

The general recommendation system algorithm will use the mathematical function to suggest recommendations based on past similarity between users and movies [3]. The algorithm must be able to measure the usefulness of movie to user. In order to get good recommendations, we need lot of implicit and explicit data. Data coming from user ratings is acts as explicit data. Implicit data fetched from social data and watch history. The MFRISE is hybrid recommender system introduced by our paper which is used for Improvement Recommendations with help of identifying similar movies using content based (CB) filtering and perform multi-clustering and find the community impact on recommendations using text analytics,

Step 1 : Data Prepossessing

Step 2 : Similarity based recommendations

Step 3 : Clustering using Items similarity

Step 4 : Clustering using User similarity

Step 5 : Find Social impact on items

Step 6 : Multi-cluster & interactions

Step 7 : Ranking recommendations to user
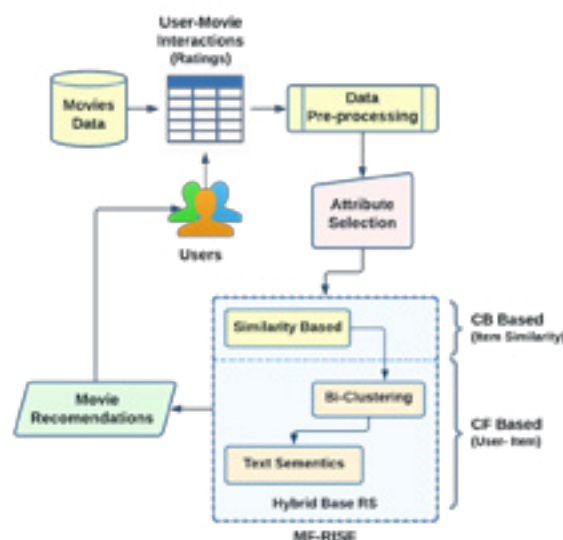
Step 8 : Validation and testing

Fig. 2. MS-RISE Proposed Architecture.

The detailed Implementation of Multifaceted Recommendation System Engine (MF-RISE) is included in upcoming paper on our proposed work. The proposal of method and

experimentation on benchmarking algorithms is proposed in this paper.

2.1 RECOMMENDER SYSTEM (RS) EVALUATION METHODS

The evaluation of recommendation system algorithm is not as easy as evaluation of any other machine learning algorithms, as the recommendation output for each user is different than other user [3]. This is main reason for which we cannot simply divide dataset into training and testing data. The methods used for evaluation RSs are,

a) Train - Test Split [6]: In RS algorithms it is not possible to take separate Training data set and testing data set, since the training data used to fit algorithm and test data set is used for evaluating RS algorithm. But, the user in training data may not be available in test data so, it is difficult to use separate test data. We have used masking method, rating values for some users are masked and then rating are predicted using algorithm then we can compare these ratings for checking accuracy.
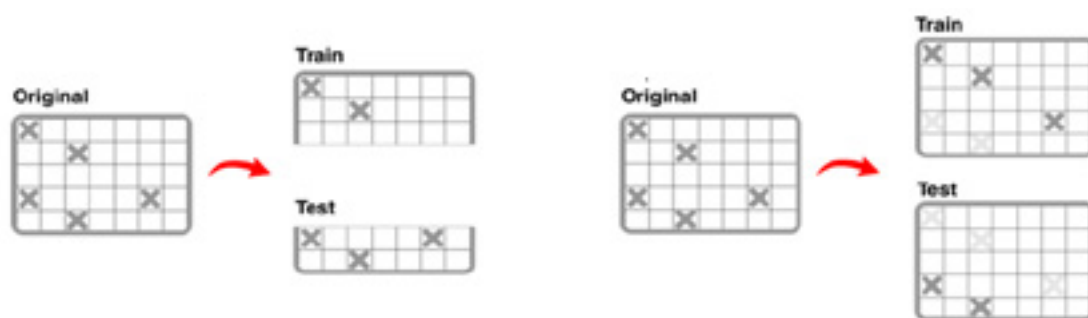
Fig. 3. Train-Test Split (masking).

b) K-Fold Cross Validation Method [7]: Cross-validation is a statistical method used to estimate the performance of RS algorithms or any machine learning algorithm.

- Dataset divided in k Groups

- Accept that group as Test Data

- Take remaining groups as Training Data

- Fit Model on Training Data

- Evaluate on Test Data

- Calculate Evaluation Score
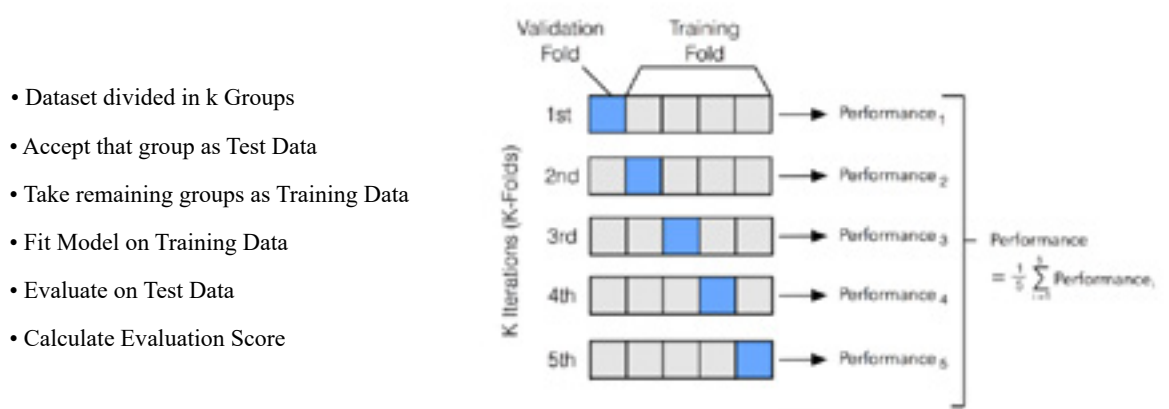
Fig. 4. K-Fold Cross Validation Concept.

3. BENCHMARKING RECOMMENDER SYSTEM (RS) ALGORITHMS

We usually categorize recommendation engine algorithms as collaborative filtering models and content-based models. In this paper, we are going to study and discuss few advantages and drawbacks of some popular recommender algorithms to compare their performances based on various evaluation

metrics. This paper will set a benchmark for our proposed implementation of MF-RISE with below popular RS algorithms,

a) Similarity Based Algorithm

- Baseline algorithm

b) Neighborhood Algorithm

- K-Nearest Neighbors Algorithm (KNN)

c) Hybrid Methods

- Co-Clustering

- Slope-One

d) Matrix Factorization Method

- Single value Decomposition (SVD)

- Advanced SVD (SVD++)

- Negative Matrix Factorization (NMF)

4. EVALUATION METRICS FOR RECOMMENDER SYSTEMS

The most important thing for RS is to evaluate the performance of algorithm. The traditional algorithm evaluation metrics used to measure errors may not be effective for recommendation algorithms, as there are different recommendations for each user and no recommendations can be same for even same user. We need to take help of various traditional and modern methods for validating recommendation results.

A. Accuracy Metrics

Recommendation accuracy will measure difference between recommender's estimated ratings and actual user ratings.

a) Mean Absolute Error(MAE): [5] Absolute Error is the amount of error in prediction and actual rating.

$$AbsoluteError = |r_{ui} - \hat{r}_{ui}|$$

r_{ui} = Rating from the proposed algorithm
$\hat{r}_{ui}$ = Actual user Rating

The mean value of absolute errors can be given as Mean Absolute Error(MAE),

$$MAE = \frac{1}{|\hat{R}|} \sum_{r_{ui} \in \hat{R}} |r_{ui} - \hat{r}_{ui}|$$

b) Mean Square Error(MSE): [5] The measure of the average of the squares of the errors is called as Mean Square Error(MSE). MSE is not as small as MAE. MSE can be calculated as,

$$MSE = \frac{1}{|\hat{R}|} \sum_{r_{ui} \in \hat{R}} (r_{ui} - \hat{r}_{ui})^2$$

c) Root Mean Square Error(RMSE): [5] The Root Mean Squared Error(RMSE) is better in terms of performance when dealing with larger error values. RMSE is more useful when lower residual values

are preferred. MSE is highly biased for higher values. Therefore, RMSE is more preferred accuracy measure.

B. Classification Metrics: Recommendation accuracy can also be measured by traditional precision and recall metrics. Recommended items has a high interaction value i.e. number of ratings, can be considered as most accurate predictions.

i)   Precision: Precision is the ratio of true positives (number of relevant results) and total positives recommended items.

ii) Recall: A Recall is essentially the ratio of number of relevant items that are recommended to all relevant items.

C. Ranking Metrics [4]: Recommendation accuracy can also measure by Top-N results given by RS algorithm.

i)   Hit Rate: The Hit occurs, if a user rated one of the top-10 recommended movie. So,

first we find the Top 10 movie recommendations. then, we find movies rated by

user. If user rates a movie which is already recommended, we consider that as one

hit. Finally, ratio of Number of hits and total recommended movies is Hit Ratio.

ii) Miss Ratio: The Miss occurs, if a user rated movie not present in the top-10 recommended movie. If user rates a movie which is not recommended, we consider that as Miss. Finally, ratio of Number of Misses and total recommended movies is Miss Ratio.

D. Execution Time Metrics

Recommendation algorithm speed can be one of the important metrics, as we are dealing with very large set of data. The time required for algorithm to calculate the recommendation from input dataset is used as execution time. The time required for fitting algorithm is Fit Time and the time taken to run it on test data is Test time.

5. EXPERIMENTAL SETUP

We build experiments based on MovieLens datasets provided by Group Lens [11]. MovieLens datasets contain user ratings for multiple movies. The dataset contains 2113 users, 10197 movies and 855598 user ratings including tag assignments. The datasets contain only users that have rated at least 20 movies. They have conventional ratings which is preferred when predicting ratings. Since the Root Mean Squared Error(RMSE) and Mean Squared Error(MAE) values are depended on the rating scale, the results will be more comparable. We have used 5-Fold cross validation method for selecting training and testing dataset more effectively. The performance after each fold is analyzed and decided to work on 5 Folds for memory and time optimization. After 5-Folds, the performance is not improved considerably hence, decided to work with 5-Fold method [7]. The comparison of MovieLens datasets,

Table I. Comparisons of Datasets.

Dataset	HetRec [6]	ml latest [6]	100k [6]
Movies	10197	9742	1682
Users	2113	610	943
Ratings	855598	100836	1000000

6. PERFORMANCE EVALUATION

A. Baseline Algorithms [12]

The similarity based algorithms are content based algorithms used for predicting a random rating based on the distribution, this algorithm assumes user ratings are normally distributed. The prediction is generated from a normal distribution N (μ, σ^2) where μ and σ are estimated from the training data using Maximum Likelihood Estimation [3], If user u is unknown, then the bias b_u is assumed to be zero. The same applies for item i with b_i.

$$\hat{\mu} = \frac{1}{|R_{train}|} \sum_{r_{ui} \in R_{train}} r_{ui}$$

$$\hat{\sigma} = \sqrt{\sum_{r_{ui} \in R_{train}} \frac{(r_{ui} - \hat{\mu})^2}{|R_{train}|}}$$

Predicted Rating is,

$$\hat{r}_{ui} = b_{ui} = \mu + b_u + b_i$$

The best part of algorithm is simple implementation and useful for comparing algorithm accuracy. The points to improve is need more personalized predictions and less execution time for complex predictions. This algorithm also faces the problem of cold start for novice system users.

B. Matrix factorization Algorithm [16]

The Single Value Decomposition (SVD) is a Matrix factorization algorithm popularized by Simon Funk during the Netflix Prize. This is equivalent to Probabilistic Matrix Factorization algorithm. It Constructs a matrix with the row of users and columns of items and the elements are given by the users' ratings The singular value decomposition [15] is a method of decomposing a matrix into three other matrices.

A=U S V^T

Where A= m x n utility matrix

U= m x r rating singular matrix

The prediction r_{ui} is set as,

$$\hat{r}_{ui} = \mu + b_u + b_i + q_i^T p_u$$

If user u is unknown, then the bias b_u and the factors p_u are assumed to be zero.

The SVD is good for with few datasets and it can improve performance on many algorithms. It majorly uses the Principal component analysis(PCA) which is useful for dimensional reduction.

C. SVD++ Algorithm [20]

The Single Value Decomposition (SVD++) is extension of SVD algorithm, with considering implicit ratings This is equivalent to Probabilistic Matrix Factorization algorithm. It Constructs a matrix with the row of users and columns of items and the elements are given by the users' ratings.

The prediction r_{ui} is set as,

$$\hat{r}_{ui} = \mu + b_u + b_i + q_i^T \left(p_u + |I_u|^{-\frac{1}{2}} \sum_{j \in I_u} y_j \right)$$

Where, the y_j terms are a new set of item factors that capture implicit ratings. Here, an implicit rating describes the fact that a user u rated an item j, regardless of the rating value. If user u is unknown, then the bias b_u and the factors p_u are assumed to be zero.

D. Non-Negative Matrix Factorization(NMF) [22]

The Non-Negative Matrix Factorization(NMF) is equivalent to Non negative Matrix Factorization algorithm. It Constructs a matrix with the row of users and columns of items and the elements are given by the users' ratings.

The NMF algorithm can improves performance on many algorithms. NMF based methods used in for solving problems in computer vision. The computational complexity of CF based algorithm is very high and it results in many missing ratings. Some major improvements are required to achieve high computational efficiency and prediction accuracy.

E. Co-Clustering Algorithm [25]

A Co-Clustering is based on collaborative filtering algorithm. This approach is based on simultaneous clustering of users and movies (items) for efficient CF based algorithm.

In Co-clustering method, every users and movies are assigned some clusters C_u, C_i, and some co-clusters C_{ui} The prediction r_{ui} is set as,

$$r_{ui} = C_{ui} + (\mu_u - C_u) + (\mu_i - C_i)$$

Where, If the user is unknown, the prediction is $r_{ui} = \mu_i$, If the item is unknown, the prediction is $r_{ui} = \mu_u$, If both are unknown, the prediction is $r_{ui} = \mu$

The co-clustering algorithm has good control over learning and can consider multiple dimensions of data. but, needs more execution time in few cases for some critical recommendation. The cold start issue become major issue in this algorithm.

F. Slope One Algorithms [27]

Slope One algorithm is based on the movie-user rating matrix based on the linear model y=xb+c. Where, parameter y is the rating of the predicted target user on the target movie, parameter x is the rating of the target user on the reference movie, and parameter b is the deviation value of the user's score of different movies. Slope One algorithm calculates enter of the evaluation of excessive user ratings mean the score difference between the movies, and then at the time of target users recommend, uses the linear relationship, estimate the prediction score of the movies y according to the target user's score of project x and the deviation value b , that is, generate the prediction by using the deviation value of all users among different movies. Slope One algorithm is simple in calculation and having good performance. It can handle cold start issue well by predicting ratings. But, the fit time will be higher as compare to other algorithms.

7. RESULTS

All experiments are run on a Desktop with Intel Core i5 8th gen (CPU@2.30GHz) and 8GB RAM, all data stored on solid state Memory (SSD) for faster access and optimum performance. In this paper, we present the various evaluation parameter like average RMSE, MAE and total execution time of various algorithms (used in study) with a 5-fold cross-validation procedure.

Table II. Evaluation Metrics for Benchmark Algorithms.

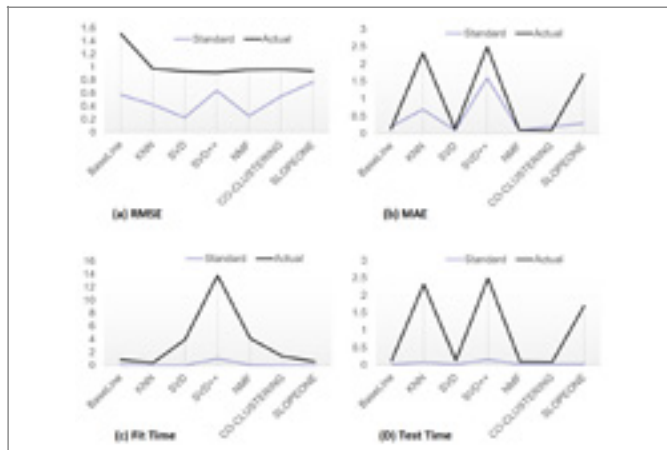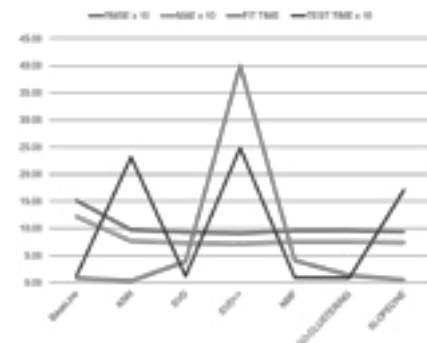| Parameter	RMSE	MAE	FIT TIME	TEST TIME
BaseLine	1.52	1.2224	0.9	0.13
KNN	0.9793	0.7736	0.41	2.32
SVD	0.9379	0.7394	3.97	0.13
CO-CLUSTERING	0.9654	0.7555	1.41	0.09
SLOPEONE	0.9434	0.74527	0.55	1.71

Fig. 15. Benchmark Algorithms Performance Analysis.

Fig. 17. Comparative Performance Analysis.

8. CONCLUSION AND FUTURE WORK

In this paper, we present a real-world benchmark for our new recommendation system algorithm. The prediction accuracy of a recommender system is dependent on various parameters. In study, we have seen all algorithms are optimized for the MovieLens dataset. SVD, NMF and co-clustering algorithm performs better on the larger dataset than the other collaborative filtering algorithm. To obtain more detailed results, testing algorithms on datasets with more similar properties can be performed.

We have deployed many important RS algorithms to study their performance comparisons, which was ubiquitous and crucial in recommendation scenarios. After comparing all algorithms, we found that SVD++ algorithm need highest Fit Time due to complexity of calculations. There is lower RMSE calculations in all algorithms except Baseline algorithm. Overall execution time of SVD algorithm and co-clustering algorithm is very lower. So, we are planning to can plan to use SVD, NMF and Co-Clustering algorithms for efficient implementation of movies recommendation process.

We can conclude that the SVD, NMF and Co-Clustering algorithm is seemingly more accurate than other the Item-based collaborative filtering algorithm for larger datasets.

REFERENCES

[1] MALI, MAHESH, DHIRENDRA S. MISHRA, AND M. VIJAYALAXMI. "Multifaceted recommender systems methods: A review." Journal of Statistics and Management Systems 23.2 (2020): 349-361.

[2] MEHTA Y., SINGHANIA A., TYAGI A., SHRIVASTAVA P., MALI M. (2020) A Comparative Study of Recommender Systems. In: Kumar A., Paprzycki M., Gunjan V. (eds) ICDSMLA 2019. Lecture Notes in Electrical Engineering, vol 601. Springer, Singapore.

[3] F.O. ISINKAYE, Y.O. FOLAJIMI, B.A. OJOKOH, Recommendation systems: Principles, methods and evaluation, Egyptian Informatics Journal, Volume 16, Issue 3, 2015, Pages 261-273, ISSN 1110-8665,

https://doi.org/10.1016/j.eij.2015.06.005.

[4] PU, PEARL, LI CHEN, AND RONG HU. "Evaluating recommender systems from the user's perspective: survey of the state of the art." User Modeling and User-Adapted Interaction 22.4 (2012): 317-355.

[5] CREMONESI, PAOLO, ET AL. "An evaluation methodology for collaborative recommender systems." 2008 International Conference on Automated Solutions for Cross Media Content and Multi-Channel Distribution. IEEE, 2008.

[6] CANAMARES, ROCIO, PABLO CASTELLS, AND ALISTAIR MOFFAT. "Offline evaluation options for recommender systems." Information Retrieval Journal 23.4 (2020): 387-410.

[7] MORENO-TORRES, JOSE GARCIA, JOSE A. SAEZ, AND FRANCISCO HERRERA. "Study on the impact of partition-induced dataset shift on k-fold cross validation." IEEE Transactions on Neural Networks and Learning Systems 23.8 (2012): 1304-1312.

[8] FAYYAZ, ZESHAN, ET AL. "Recommendation systems: Algorithms, challenges, metrics, and business opportunities." applied sciences 10.21 (2020): 7748.

[9] SHARMA, RITU, DINESH GOPALANI, AND YOGESH MEENA. "Collaborative filtering-based recommender system: Approaches and research challenges." 2017 3rd international conference on computational intelligence and communication technology (CICT). IEEE, 2017.

[10] HUG, NICOLAS. "Surprise: A Python library for recommender systems." Journal of Open Source Software 5.52 (2020): 2174.

[11] F. MAXWELL HARPER AND JOSEPH A. KONSTAN. 2015. The MovieLens Datasets: History and Context. ACM Trans. Interact. Intell. Syst. 5, 4, Article 19 (January 2016), 19 pages. https://doi.org/10.1145/2827872

[12] RENDLE, STEFFEN, LI ZHANG, AND YEHUDA KOREN. "On the difficulty of evaluating baselines: A study on recommender systems." arXiv preprintarXiv:1905.01395 (2019).

[13] WANG, KAI, ET AL. "Rl4rs: A real-world benchmark for reinforcement learning based recommender system." arXiv preprint arXiv:2110.11073 (2021).

[14] AHUJA, RISHABH, ARUN SOLANKI, AND ANAND NAYYAR. "Movie recommender system using k-means clustering and k-nearest neighbor." 2019 9th International Conference on Cloud Computing, Data Science and Engineering (Confluence). IEEE, 2019.

[15] WANG, JIANFANG, ET AL. "A collaborative filtering algorithm based on svd and trust factor." 2019 international conference on computer, network, communication and information systems (CNCI 2019). Atlantis Press, 2019.

[16] MEHTA, RACHANA, AND KEYUR RANA. "A review on matrix factorization techniques in recommender systems." 2017 2nd International Conference on Communication Systems, Computing and IT Applications (CSCITA).

IEEE, 2017.

[17] RICCI, FRANCESCO, LIOR ROKACH, AND BRACHA SHAPIRA. "Recommender systems: introduction and challenges." Recommender systems handbook. Springer, Boston, MA, 2015. 1-34.

[18] ZHANG, WEIWEI, ET AL. "Recommendation system in social networks with topical attention and probabilistic matrix factorization." PloS one 14.10 (2019): e0223967.

[19] VOZALIS, MANOLIS G., AND KONSTANTINOS G. MARGARITIS. "A recommender system using principal component analysis." Published in 11th panhellenic conference in informatics. 2007.

[20] AL SABAAWI, A., KARACAN, H. AND YENICE, Y. (2021). Two Models Based on Social Relations and SVD++ Method for Recommendation System. International Association of Online Engineering. Retrieved May 9, 2022

from https://www.learntechlib.org/p/218689/.

[21] GUAN, XIN, CHANG-TSUN LI, AND YU GUAN. "Matrix factorization with rating completion: An enhanced SVD model for collaborative filtering recommender systems." IEEE access 5 (2017): 27668-27678.

[22] LUO, XIN, ET AL. "An efficient non-negative matrix-factorization-based approach to collaborative filtering for recommender systems." IEEE Transactions on Industrial Informatics 10.2 (2014): 1273-1284.

[23] ZHANG, SHENG, ET AL. "Learning from incomplete ratings using nonnegative matrix factorization." Proceedings of the 2006 SIAM international conference on data mining. Society for Industrial and Applied

Mathematics, 2006.

[24] KUMAR, RAJEEV, B. K. VERMA, AND SHYAM SUNDER RASTOGI. "Social popularity based SVD++ recommender system." International Journal of Computer Applications 87.14 (2014).

[25] FENG, LIANG, QIANCHUAN ZHAO, AND CANGQI ZHOU. "Improving performances of Top-N recommendations with co-clustering method." Expert Systems with Applications 143 (2020): 113078.

[26] LI, MAN, LUOSHENG WEN, AND FEIYU CHEN. "A novel Collaborative Filtering recommendation approach based on Soft Co-Clustering." Physica A: Statistical Mechanics and its Applications 561 (2021): 125140.

[27] WANG, QING-XIAN, ET AL. "Incremental Slope-one recommenders." Neuro-computing 272 (2018): 606-618.

[28] SONG, YUE TING, AND SHENG WU. "Slope one recommendation algorithm based on user clustering and scoring preferences." Procedia Computer Science 166 (2020): 539-545.

[29] SALAM PATROUS, ZIAD, AND SAFIR NAJAFI. "Evaluating prediction accuracy for collaborative filtering algorithms in recommender systems." (2016).

/12/

RICE QUALITY ANALYSIS USING IMAGE PROCESSING AND MACHINE LEARNING

R. C. Dharmik

Assistant Professor, Department of Information Technology Yeshwantrao Chavan College of Engineering, Nagpur, Maharashtra, (India).

Sushilkumar Chavhan

Assistant Professor, Department of Information Technology Yeshwantrao Chavan College of Engineering, Nagpur, Maharashtra, (India).

Shashank Gotarkar

Asst. Professor, Dept. of Community Medicine, Jawaharlal Nehru Medical College, Datta Meghe Institute of Medical Sciences, Sawangi (M), Wardha, (India).

Arjun Pasoriya

Software Test Team Lead,Amdocs, (Cyprus).

https://doi.org/10.17993/3ctic.2022.112.158-164

ABSTRACT

Object Detection and its analysis are used in various fields. Rice quality evaluation subtask in Agricultural industries is not exception for object Detection. Manual identification using image processing techniques, Machine Learning Techniques and Deep Learning is also used for the rice quality analysis. Due to Feature identification challenge machine Learning and Deep Learning are in the demand. As rice is mostly used agricultural product so it is important to have the proper analysis of the crops. In this study we proposed the used of image processing method with the help of Machine Learning model. Rice grain morphological characteristics are what define a grain's quality analysis. The suggested method can operate efficiently with little expense.

KEYWORDS

Object Detection, Machine Learning, Morphological characteristics, Deep Learning.

1. INTRODUCTION

The oldest and largest sector of the global economy is agriculture. Traditionally, a human sensory panel uses physical and chemical features of food products to determine their quality (Mahale and Korde, 2014)(Shah, Jain, and Maheshwari, 2013). In Asian nations, rice is a popular and widely eaten cereal grain. It is widely accessible anywhere in the world. When rice is used for human consumption, several items with value added are created. Quality is a major factor in the milled rice business. With the growth of the import and export industries, quality assessment becomes increasingly crucial. The dispensable items found in rice samples include paddy, chaff, broken grains, weed seeds, stones, etc. These impurity levels affect the quality of the rice. As a complex problem it is solved by using image processing techniques. There have been major advancements in the essential and cutting-edge technology field of image processing such as canny edge detection algorithm (Mahale and Korde, 2014), Artificial Neural Network(Hamzah and Mohamed, 2020).

The approach of image processing is intended to preserve the integrity of the specifications. Image manipulation involves applying certain procedures to a target image in order to produce a better and more appealing image. And extract some useful data from the supplied image. Genetic algorithm based LS-SVM(Chen, Ke, Wang, Xu, and Chen, 2012) was used which provides good result but required lots of processing and complex operation. Later machine Learning based algorithms are used for this classification and Analysis. ANN(Chen et al., 2012), SVM(Philip and Anita, 2017) is mostly used algorithm which provides the good quality of results.

The main purpose of the proposed method is, to offer an alternative way for quality control and analysis which reduce the required effort, cost and time by using other Machine Learning algorithms and with object Detection. As rice quality analysis is control the diet and business of agriculture industry, proper analysis is required. Image Processing Techniques and Machine Learning are tested for the analysis. In this work we apply the object detection machine learning algorithm Region-based Convolutional Neural Networks (R-CNN) with dimension reduction techniques. Results depict that the results are less difference in the above methods.

This paper is organized as follows, and Section II describes the work of various researchers on Rice quality analysis or detection. Section III gives a detailed overview of the technology used to select good Rice and analyse it. Section IV uses this method to elaborate on the results. Section V provides an overview of the results description, better performance than other results, and shortcomings.

2. LITERATURE REVIEW

Philip and Anita (2017), proposed new characteristics for rice grain categorization. For the categorization of nine types of commercially accessible grains in the South Indian area, both spatial and frequency-based criteria were applied. The classification is carried out in two phases, with the first stage utilising the NB Tree classifier and the second stage utilising the SMO classifier.

Authors archives remarkable accuracy to the spatial features and suggested two work on real time. Images. Parveen, Alam, and Shakir (2017) proposed image processing algorithm based some characteristics with colour images. Characteristics wised results are obtained to user. Author suggested applying the same with large data with more feature or characteristics. Kuchekar and Yerigeri (2018) attempted to grade rice grains using image processing and morphological methods. Segmenting the individual grains comes first, followed by pre-processing of the picture.

The grain's geometrical characteristics, such as its area and the lengths of its main and minor axes, are extracted and classified. The results have been determined to be positive. Rice is graded according to the length of the grain. As a future scope it can be expanded in the future by focusing on moving images and identifying additional qualities of rice grains. Kong, Fang, Wu, Gong, Zhu, Liu, and Peng (2019) suggested to use an automated approach for extracting rice thickness based on edge properties.

The solution addressed the issue brought on by the structural similarity of edges by matching the appropriate edge points based on the form of the edge rather than its texture. As a future scope authors suggested to go with edge features extraction, with epipolar geometry to match the corresponding points on the rice edge.

Avudaiappan and Sangamithra () analyse the visual features with image processing and MLP.

Authors used the SVM and Na¨ıve bays algorithm with 90% accuracy. As a future scope authors focused on Non-Uniform Illumination with Transformation using top-hat so that rice can be classify in long, normal or small category. Using a k-NN classifier, Wah, San, and Hlaing (2018) suggested an image processing method and assessed three classes (30 images for each class).

Other studies Xiaopeng and Yong (2011), Yao, Chen, Guan, Sun, and Zhu (2009), Tahir, Hussin, Htike, and Naing (2015) put more focus on identifying the grain's apparent chalkiness. A grain with a partly opaque or milky white kernel is said to be chalky. One of the key markers in the evaluation process is the level of chalkiness. High levels of chalkiness in rice grains make them more likely to shatter during milling, which will alter how they taste. An automated system for grading milled rice is suggested by Wyawahare, Kulkarni, Dixit, and Marathe (2020).

Broken rice is an essential factor in rice grading. This technique may be used to determine the percentage of broken rice from a sample's picture. The relevant characteristics are retrieved from the coloured pictures of the samples using particular preprogrammed processing procedures, and the regression model is created. Estimating the percentage of broken rice requires less runtime than other approaches since basic regression models are used. Lin, Li, Chen, and He (2018) offered a comparison of two approaches—CNN and conventional methods—to identify rice grains with three distinct forms (medium, round, and long grain). 5,554 photos were examined for calibration, and 1,845 images were examined for validation. In the CNN approach, the experiments changed training parameters like batch size and epochs. In a separate trial, they used conventional statistical techniques, and the categorization accuracy they obtained ranged from 89 to 92%. As opposed to the conventional approaches, the experiment employing the CNN method obtained a classification accuracy of 95.5%. Benefits from the interplay between CNN and hyperspectral imaging were employed by Chatnuntawech, Tantisantisom, Khanchaitit, Boonkoom, Bilgi¸c, and Chuangsuwanich (2018). Their research used two sets of data, 414 samples from paddy rice and 232 samples from six different types of milled rice. The accuracy of the suggested approach was 86.3%. In contrast, the SVM method on the paddy seed dataset produced a result of 79.8%, whilst the accuracy of the other set was somewhat off. By combining three machine learning techniques—kNN, SVM, and CNN—with hyper spectral imagery, Qiu, Chen, Zhao, Zhu, He, and Zhang (2018) were able to identify four different types of rice seeds. Two distinct spectral ranges were used in the experiment, and there were various numbers of training samples.

In various studies, a hyperspectral camera was used to address the issue of classifying rice types. The gadget, however, was expensive and complicated. Additionally, a quick computer, sensitive detectors, and ample data storage were needed.

3. PROPOSED FRAMEWORK

By observing the various literature we Identified architecture. Process is as follows.

Fig 1: Architecture of the proposed system.

1. Training the data: To train the data Rice seeds image scanning needed then it Seed area segmentation is done then Seed orientation was performed then proper data frame of images is form for training of data.
2. Training of data Training is done for both RCNN and statistical classical model.
3. Feature Extraction: For better accuracy we have to find the Features of the data frames. We used Greedy Filter method to get the proper features.
4. Again training was performing and tests the accuracy on both RCNN and statistical classical model.
5. Dimension Reduction: to speed the process at each epoch we reduce the dimension by using PCA.

4. RESULTS

The below table gives average aspect ratio and classification which is based on kind of rice grain used. It will show the exact value of parameters for the rice grain used in a bar graph where x-axis belongs to particles and y-axis is average aspect ratio of parameters. Following Figure shows the ranges which generally known as classification of rice grains that have been identified and training was done.

Table 1: classification of rice grains.

Long Slender(LS)	Length >= 6mm, L/B Ratio>=3mm
Short slender(SS)	Length< 6mm, L/B Ratio>=3mm
Medium Slender (MS)	Length >= 6mm, 2.5< L/B Ratio <3mm
Long Bold (LB)	Length >= 6mm, L/B Ratio<3mm
Short Bold (SB)	Length < 6mm, L/B Ratio<3mm

As per Architecture we have applied RCCN object detection method for identification of edges of the rice so that classification can be done by training machine learning model. Here we train it using Recurrent neural network (RNN) with activation function as Relu in hidden layers which can be helpful for RCNN. The Rice quality analysis of application b uisng this application is shown below.
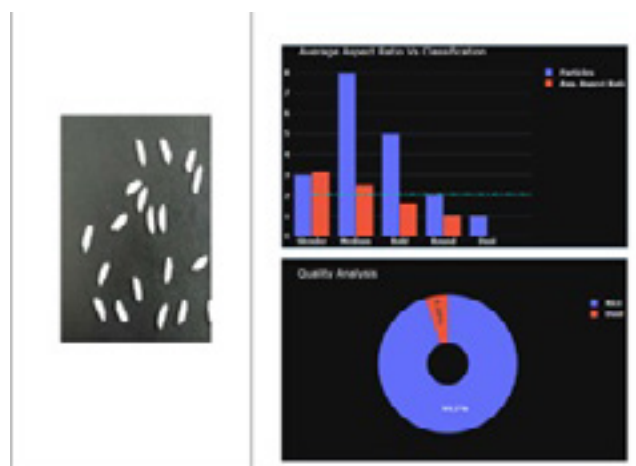
Fig 2: Quality Analysis Avg. Aspect Ratio VS Classification with single proper image.

5. CONCLUSION AND FUTURE SCOPE

In this work we applied machine learning and image processing techniques for identification and rice quality analysis of work. In the process we used RNN model as machine: earning model for classification. To detect the edge and identify its type RCNN object detect ion method where used. Accuracy of the model is 92.36% and analysis was done on the rice grace classification. We have successfully executed all the steps proposed. Last two steps include calculating the size of the grains and then classifying them according to the Table provided. As a future challenge we can try with another edge Detection algorithm which detect in less time so that above accuracy will be increased and reduced the time of analysis.

REFERENCES

[1] Avudaiappan, T. and Sangamithra, S. Analysing rice seed quality using machine learning algorithms.

[2] Chatnuntawech, I., Tantisantisom, K., Khanchaitit, P., Boonkoom, T., Bilgic., B., and Chuangsuwanich, E. 2018. Rice classification using spatio-spectral deep convolutional neural network. ArXiv abs/ 1805.11491.

[3] Chen, X., Ke, S., Wang, L., Xu, H., and Chen, W. 2012. Classification of rice appearance quality based on ls-svm using machine vision. Communications in Computer and Information Science 307, 104–109.

[4] Hamzah, A. and Mohamed, A. 2020. Classification of white rice grain quality using ann: a review. IAES International Journal of Artificial Intelligence (IJ-AI) 9, 600.

[5] Kong, Y., Fang, S., Wu, X., Gong, Y., Zhu, R., Liu, J., and Peng, Y. 2019. Novel and automatic rice thickness extraction based on photogrammetry using rice edge features. Sensors 19, 24.

[6] Kuchekar, N. and Yerigeri, V. 2018. Rice grain quality grading using digital image processing techniques. IOSR J Electronics Communication Eng 13, 3, 84–88.

[7] Lin, P., Li, X., Chen, Y., and He, Y. 2018. A deep convolutional neural network architecture for boosting image discrimination accuracy of rice species. Food and Bioprocess Technology 11, 1–9.

[8] Mahale, B. and Korde, S. 2014. Rice quality analysis using image processing techniques. 1–5.

[9] Parveen, Z., Alam, M. A., and Shakir, H. 2017. Assessment of quality of rice grain using optical and image processing technique. In 2017 International Conference on Communication, Computing and Digital Systems (C-CODE). 265–270.

[10] Philip, T. M. and Anita, H. 2017. Rice grain classification using fourier transform and morphological features. Indian Journal of Science and Technology 10, 14, 1–6.

[11] Qiu, Z., Chen, J., Zhao, Y., Zhu, S., He, Y., and Zhang, C. 2018. Variety identification of single rice seed using hyperspectral imaging combined with convolutional neural network. Applied Sciences 8, 212.

[12] Shah, V., Jain, K., and Maheshwari, C. 2013. Non-destructive quality analysis of Gujarat 17 oryza sativa ssp indica (indian rice) using artificial neural network. 2321–0613.

[13] Tahir, W. P. N., Hussin, N., Htike, Z. Z., and Naing, W. Y. N. 2015. Rice grading using image processing. ARPN Journal of Engineering and Applied Sciences 10, 21, 10131–10137.

[14] Wah, T., San, P., and Hlaing, T. 2018. Analysis on feature extraction and classification of rice kernels for myanmar rice using image processing techniques. International Journal of Scientific and Research Publications (IJSRP) 8.

[15] Wyawahare, M., Kulkarni, P. A., Dixit, A., and Marathe, P. 2020. Statistical Model for Qualitative Grading of Milled Rice. 234–246.

[16] Xiaopeng, D. and Yong, L. 2011. Research on the rice chalkiness measurement based on the image processing technique. In 2011 3rd International Conference on Computer Research and Development. Vol. 2. 448–451.

[17] Yao, Q., Chen, J., Guan, Z., Sun, C., and Zhu, Z. 2009. Inspection of rice appearance quality using machine vision. 2010 Second WRI Global Congress on Intelligent Systems 4, 274–279.

/13/

RFM ANALYSIS FOR CUSTOMER SEGMENTATION USING MACHINE LEARNING: A SURVEY OF A DECADE OF RESEARCH

Sushilkumar Chavhan

Assistant Professor, Department of Information Technology Yeshwantrao Chavan College of Engineering, Nagpur, Maharashtra, (India).

R. C. Dharmik

Assistant Professor, Department of Information Technology Yeshwantrao Chavan College of Engineering, Nagpur, Maharashtra, (India).

Sachin Jain

Assistant Professor, Department of Computer Science Oklahoma State University Stillwater, (United States).

Ketan Kamble

Student, Department of Information Technology YCCE, Nagpur, Maharashtra, (India).

https://doi.org/10.17993/3ctic.2022.112.166-173

ABSTRACT

Customer segmentation is a method of categorizing corporate clients into groups based on shared characteristics. In this study, we looked at the different customer segmentation methods and execute RFM analysis by using various clustering algorithms. Based on RFM values (Recent, Frequency, and Cost) of customers, the successful classification of company customers is divided into groups with comparable behaviors. Customer retention is thought to be more significant than acquiring new clients are analyzed on two different databases. Results show the significance of each method. Comparison is helps for selection of better customer segmentation.

KEYWORDS

Clustering, Classification, RFM, Customer segmentation.

1. INTRODUCTION

Customer Segmentation is way of organization of customers with respect to the various features. In recent years there has been a huge boom in opposition between companies to stay in the field. The income of the organization may be stepped forward through a patron segmentation model. According to the Pareto principle (Srivastava, 2016), 20% of the clients make a contribution greater to the sales of the organization than the relaxation Customer segmentation is the exercise of dividing an organization's clients into agencies that mirror similarity amongst clients in every group. The intention of segmenting clients is to determine how to narrate to clients in every section that allows you to maximize the fee of every patron to the business. Customer segmentation has the ability to permit entrepreneurs to cope with every patron withinside the simplest way. Using the massive quantity of statistics to be had on clients (and ability clients), a patron segmentation evaluation lets in entrepreneurs to identify discrete agencies of clients with an excessive diploma of accuracy primarily based totally on demographic, behavioral and different indicators.

Evaluation of RFM (Recency, Frequency, and Monetary) is a famend approach is worn for comparing the clients primarily based totally on their shopping for behavior. Scoring method was developed to test Recent, Frequency, and Finance ratings. Finally, ratings of all three variables are strengthened as RFM ratings from different ranges (Haiying and Yu, 2010) which are compiled to anticipate recants trends for studying existing and higher sponsor transactions history. Next step is defined as the remaining time the consumer buys. The latest currency is the type of days the sponsor takes between purchases. The latest small payment means that the sponsor visits the organization frequently in a timely manner. Similarly, extra money means that the sponsor is less likely to go to the organization soon. Frequency is described because the variety of transaction a patron makes in a selected period. The better the fee of frequency the greater unswerving are the clients of the organization.

Cash is defined as the amount spent by the investor over a period of time in a favorable period. The improvement in the amount of money spent by the large sales they provide to the organization. Each sponsor is given 3 different ratings of the latest, frequency, and economic volatility. Score points are used within a range from five to 1. The core quintile is given a five-point scale, while the others are given 4, 3, 2 and 1.

In recent years, there has been a significant increase in the number of opposition groups among companies in care within the arena. Customer retention is more important than purchasing the latest customers. Customer segregation allows people's messages to speak more to target audiences.

2. LITERATURE REVIEW

Segmentation is middle of the advertising and marketing approach due to the fact exclusive consumer organizations mean the want for exclusive advertising and marketing mixes primarily based totally on consumer conduct and its needs. Many authors give the segamentaion methods to increase the profit and sustain the company position. (Jiang and Tuzhilin, 2009) proposed K-Classifiers Segmentation algorithm which recognized that each client segmentation and consumer focused on are important to enhance the marketing performances. K-Classifiers Works as optimizer who have two tasks. Above method more resources to the ones clients who supply greater returns to the company. (He and Li, 2016) proposed a 3-dimensional approach to improving consumer health (CLV), customer pride and customer behavior. The authors conclude about the customers and the requirements for a better service. A segment used to meet customer expectations and suggest better service. (Sheshasaayee and Logeshwari, 2017) used RFM Analysis which provides the usage of CRM (Customer Relationship Management). Authors analyzed the customers by segmenting them which helps to increase company profits. Further they enhanced the segmentation by using Fuzzy Clustering Method which classified them into the appropriate scoring strategies based on their needs.

(Shah and Singh, 2012) provides the K-means algorithm and K-medoids algorithms for clustering. The presented techniques do not always yield the best answer, but they do minimise the cluster error criterion. They came to the conclusion that when the number of clusters grows, the new method takes

less time to run than existing methods. (Sheshasaayee and Logeshwari, 2017) developed hybrid method which combine RFM and LTV methods. Authors used K-means and Neural Network algorithms for segmentation with two phase models. They suggested having better optimizer for customer categorization. Using logistic regression, (Liu, Chu, Chan, and Yu, 2014) proposed predicting customer attrition. Individual marketing methods can be used to identify customers with similar churn value and to keep them. Benefit customer segmentation using various methodologies allows customers to be classified based on their relationships, allowing marketers to focus their marketing efforts on their strengths and target benefit categories accordingly.

3. TYPES OF CUSTOMER SEGMENTATION

Customer segmentation models come in a range of shapes and sizes, ranging from simple to complex, and they can be used for a variety of purposes. Demographic, Recency, Frequency Monetary (RFM), High-Value Customers, Customer Status, Behavioral, and Psychographic models are some of the most common models.

3.1 DEMOGRAPHIC

It is a method of segmenting customers based on characteristics such as age, gender, ethnicity, income, education, religion, and career (Lu, Lin, Lu, and Zhang, 2014).

3.2 RFM

It is a direct segmentation strategy whose main goal is to categories clients based on the time since their previous purchase, the total number of purchases they've made (frequency), and the amount they've spent (monetary) (Sheshasaayee and Logeshwari, 2017).

3.3 HVCS (HIGH-VALUE CUSTOMER)

It's an extended RFM segmentation for any firm, focusing on what traits they have in common so you can get more of them.

3.4 CUSTOMER STATUS

It is a mechanism which check the status of customer which categories as active and lapsed. The focus of this method is to how the customer engaged by the company on the time period as a status.

3.5 BEHAVIORAL SEGMENTATION

It is a mechanism which check the status of customer which categories as active and lapsed. The focus of this method is to how the customer engaged by the company on the time period as a status.

3.6 PSYCHOGRAPHIC SEGMENTATION

It is allows grouping the customers based on attitudes, beliefs, or even personality traits. For this we require good data analysis method. Analysis done on all above attributes.

3.7 GEOGRAPHIC SEGMENTATION

It is allows grouping the customers based on geographical location i.e region, city, country etc. It is used when target area is location wise improvement of services and increased the profit.

4. MAJOR CLUSTERING TECHNOLOGIES FOR CUSTOMER SEGMENTATION

4.1 K –MEANS

https://doi.org/10.17993/3ctic.2022.112.166-173

It is a popular unsupervised method that accepts parameters and k value as number of clusters as inserting and separating data into clusters with high intra-cluster similarities. K-Means is a method that repeats itself, adding the number of centroids before each multiplication. Depending on the inches calculated for each multiplication, data points are allocated among distinct sets. Using min max normalization, the RFM values are normalized (Lee and Memon, 2016).

4.2 FUZZY C-MEANS

It is a Method (?, ?) that allows a specific piece of data to appear to numerous clusters. It no longer determines a cluster's club records for a given information factor. Rather, the probabilities of a specific information factor with similarities are determined. The advantage of this method over previously discussed K-Means is that the final result obtained of a large and comparable database is most suitable than a set of K-method rules, because in the KMeans method, as cluster formation of based on data element. The normalization in this approach is done using min max normalization. Cluster RFM value is based on cluster (Zahrotun, 2017) value.

4.3 REPETITIVE MEDIAN K-MEANS

It's a novel approach to determining the initial centroids for the K-Means method. The traditional K–Means algorithm's range of iterations and computational time is reduced by choosing preliminary centroids with it's proposed distribution. RFM values will be combined and sorted into three vectors, R', F', and M ', respectively. The initial centroids are calculated using the median value of each vector. The median values are derived k times iteratively from the R', F', and M' values, depending on the value of k. (number of segments).

5. RFM ANALYSIS USING ON ONLINE SHOPPING DATA

RFM: according to following definitions. The RFM method divides clients into segments. It categorises clients based on their previous purchase transactions, taking into account criteria like as Recency (R): Last purchase date in specified session. Frequency (F):Purchase count in the specified session. Monetary (M):Value of Purchase in the specified session Based on forms needs, we define a season with different intervals for this model and we calculate RFM values for each customer. Working with a set of customer activity data in an online retail store year-round from the University of California Irwin (UCI) repository was used to evaluate system performance.

The following is a sample customer separation process. STEP 1: Sort the customer by recency.

STEP 2 AND 3: Sort the customer from most to least frequent customer and summarized the F, M score. STEP 4: Rank customers by combining R,F, and M ranking

CUSTOMER ID	RECENCY (DAY)	FREQUENCY (NUMBER)	MONETARY (TOTAL)
1	4	6	540
2	6	11	940
3	46	1	35
4	23	3	65
5	15	4	179
6	32	2	56
7	7	3	140
8	50	1	950
9	34	15	2630
10	10	5	191
11	3	8	845
12	1	10	1610
13	27	3	54
14	18	2	40
15	6	1	25

Fig1: Sample Data.

Fig2: Calculation of Recency.

Fig3: Calculation of F and M Score.

Fig4: Customer Segmentation.

6. ANALYSIS OF VARIOUS ALGORITHMS

For evaluation of commonly used clustering algorithm was done on two different open source databases like the transactional data set of the customers of an online retail store available at UCI repository and on e-commerce datasets which is available at UCI Machine Learning Repository.
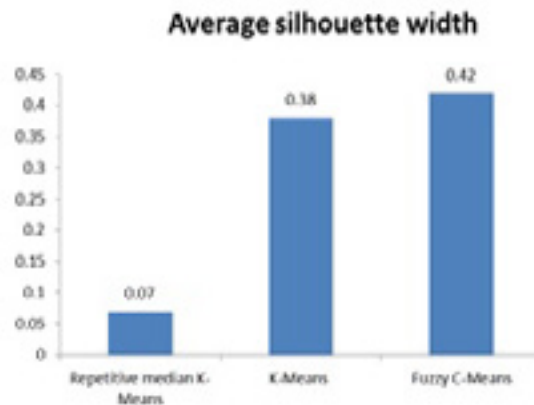
Fig5: Result Analysis of various Algorithms on online retail.

From above analysis it is observed that Fuzzy C means perform well on the basis of average Silhouette width but the time taken is more and number of iterations are also more as compared to others algorithms.

Fig6: Result Analysis of various Algorithms on E- commerce data.

7. CONCLUSION AND FUTURE SCOPE

This paper provides the overview of customer Segmentation and its different type's with types. RFM segmentation allows to group based on the requirements and target the different marketing strategies. In future more complex methods would be designed to target specific customers and the methods would also be more flexible if the company wants to target a different audience for a particular time or wants to permanently change their customers based on the needs of the company or priorities of the customer. The RFM should be made more flexible according to the needs of the different companies.

REFERENCES

[1] Haiying, M. and Yu, G. 2010. Customer segmentation study of college students based on the rfm. 3860–3863.

[2] He, X. and Li, C. 2016. The research and application of customer segmentation on e-commerce websites. 203–208.

[3] Jiang, T. and Tuzhilin, A. 2009. Improving personalization solutions through optimal segmentation of customer bases. IEEE Trans. Knowl. Data Eng. 21, 305–320.

[4] Lee, D.-H. and Memon, K. 2016. Generalised fuzzy c-means clustering algorithm with local information. IET Image Processing 11.

[5] Liu, C., Chu, S.-W., Chan, Y.-K., and Yu, S. 2014. A modified k-means algorithm - two-layer k-means algorithm. 447–450.

[6] Lu, N., Lin, H., Lu, J., and Zhang, G. 2014. A customer churn prediction model in telecom industry using boosting. Industrial Informatics, IEEE Transactions on 10, 1659–1665.

[7] Shah, S. and Singh, M. 2012. Comparison of a time efficient modified k-mean algorithm with k-mean and k-medoid algorithm.

[8] Sheshasaayee, A. and Logeshwari, L. 2017. An efficiency analysis on the tpa clustering methods for intelligent customer segmentation. 784–788.

[9] Srivastava, R. 2016. Identification of customer clusters using rfm model: A case of diverse purchaser classification.

[10] Zahrotun, L. 2017. Implementation of data mining technique for customer relationship management (crm) on online shop tokodiapers.com with fuzzy c-means clustering. 299–303.

/14/

VIRTUAL EMOTION DETECTION BY SENTIMENT ANALYSIS

Rahul Kamdi

Assistant Professor, Yeshwantrao Chavan College of Engineering, Nagpur Maharashtra, (India).

Prasheel N. Thakre

Assistant Professor, Shri Ramdeobaba College of Engineering and Management, Nagpur, Maharashtra, (India).

Ajinkya P. Nilawar

Assistant Professor, Shri Ramdeobaba College of Engineering and Management, Nagpur, Maharashtra, (India).

J. D. Kene

Assistant Professor, Shri Ramdeobaba College of Engineering and Management, Nagpur, Maharashtra, (India).
E-mail: jagdish.kene@gmail.com

https://doi.org/10.17993/3ctic.2022.112.175-181

ABSTRACT

As websites, social networks, blogs, and online portals proliferate on the internet, authors are producing reviews, opinions, ideas, ratings, and feedback. The emotional content of this writer may be about things like books, people, hotels, items, studies, events, and so on. These emotions have great value for businesses, for governments, and for people. The majority of the writer-generated material requires the usage of text mining algorithms and sentiment analysis, even if this information is meant to be instructive. Sentiment Analysis is a technique in Natural Language Processing (NLP) that tries to identify and extract assessments communicated within a given text. This paper intends to execute different content handling strategies in NLP and use of Valence Aware Dictionary for Sentiment Reasoning (VADER) Model that is sensitive to both polarity (positive/negative) and intensity (strength) of emotion.

KEYWORDS

Natural Language Processing (NLP), Polarity Intensity, Sentiment Analysis, Virtual Emotion Detection, VADER.

1. INTRODUCTION

The emotions are of primarily of six types - love, happiness, anger, sadness, surprise and fear. Sentiment analysis is used to analyze the emotions present in a text. It is a method for determining if a given piece of writing is positive, negative, or neutral. The goal of sentiment analysis is to determine the writer's attitude, sentiments, and emotions in a written text using a computational treatment of subjectivity in the text. By application of sentiment analysis one can decipher the given sentence, paragraph or a document contains a positive or negative emotions or expressions in it. In sentiment analysis we classify the polarity of given text, it results by telling about opinion whether it's positive, negative or neutral.

2. LITERATURE SURVEY

Sentiment analysis has multiple ways and Vader is one of the best way (Mozetic et al., 2016) which is being used. Vader stands for Valence Aware Dictionary and Sentiment Reasoning. It works on a ruled based sentiment analysis and it contains list of lexical features which are labeled as per semantic orientation. By analyzing the intensity of wordings in the text, the sentiment score can be obtained of that text. Vader is smart enough to extract meaning of these words or texts as positive sentiments and words like Sad, bad, awful as negative sentiments. Vader only cares about the expressions in the text. Opinions like positive negative or neutral are the expression which is concerned for Vader.

Steven Bird & Loper (2009) express when a text is changed into its canonical or standard form, then it is called as Text normalization. A few processes have to be done to standardize the content and convert it into fitting structure which would then be given to the machine learning (ML) model. This helps in reducing unnecessary information that the computer does not require, thus subsequently improving efficiency. Library utilized for this is given in. Steps associated with this cycle are shown in Figure 1 and explained briefly in the following sections.

Fig 1. Text Normalization.

2.1 REMOVING STOPWORDS

A stopword is an ordinarily utilized word that can be disregarded, both when ordering sections for looking and while recovering them (Saif et al., 2014). Using pre-compiled stopword lists or more complex algorithms for dynamic stopword recognition, removing stopwords from textual data is a popular procedure for reducing noise. The Natural Language Toolkit (NLTK) in Python includes a list of stopwords for 16 different dialects.

2.2 TOKENIZATION

The method of breaking text into smaller units called tokens is commonly known as Tokenization (Stanford NLP Group, 2015). Tokens can be words, characters, or subwords in this case. As a result, tokenization can be divided into three categories: word, character, and sub-word tokenization.

2.3 DERIVING ROOT WORD

Nicolai & Kondrak (2016) explains in the zones of Natural Language Processing we come across circumstances where a word has many offshoots Stemming and lemmatization are the two main NLP

processes for generating root words. The root type of an inflected word is produced by both stemming and lemmatization (Samir & Lahbib, 2018). Stemming computation works by removing the word's postfix. Lemmatization thinks about morphological examination of the words. It restores the lemma which is the base type of all its inflectional structures.

2.4 FEATURE EXTRACTION

Machine learning calculations are unable to work on Crude content legitimately. The procedure of component extraction requires converting content into matrix or in vector form. The module can be used to extract features from database consisting of formats such as text and images and extract features in a format supported by machine learning algorithms the most popular strategies that includes feature extraction are Bag-of-Words and TF-IDF Vectorizer. Normalize with diminishing important tokens that appears in majority samples/documents (Mahajan et al., 2020).

2.5 POLARITY AND INTENSITY SCORE IN EMOTIONAL ANALYSIS

A key element of emotional analysis is to examine the body of a text to understand the concept it expresses. Emotional analysis is appropriate for positive or negative values, known as polarity. The perfect situation usually ends up being good, neutral or bad with the help of a polarity point calculation. In general, emotional analysis works better in a submissive text than in a single context text of purpose. Emotional analysis is widely used, as part of the analysis of social media in any domain, to understand the functioning of any system, to be controlled by people and that their response is based on their opinions.

Text textual analysis data can be calculated at most levels, either at the level of each sentence, at the paragraph level, or throughout the document. There are two major theories in emotional analysis. First is Learning Prescribed machine reading or in-depth learning: In this approach, traditional machine learning techniques with a TF-IDF model using the n-gram method. These divisions are the mindless Bayes of many lands, the orderliness of things, the closest neighbor k and the uninhabited forest. In all four classes, orderliness is achieved with minimal accuracy. Second is unsupported dictionary control: This method is to use a large learning process. The accuracy we get from reading a lot is much less than how to learn by machine. After obtaining excellent performance and fragmentation, the next step is to create a final model for back-to-work using certain advanced machine learning methods.

2.6 VALENCE AWARE DICTIONARY FOR SENTIMENT REASONING (VADER)

VADER is a model used for analysis of text sentiment from which it can detect both polarity (positive/negative) and emotion intensity or strength. VADER majorly relies on a dictionary that matches the lexical features to emotion intensities also known as sentiment scores for sentimental analysis (Beri, 2020). By summing up the intensity of each word in the text we can get the sentiment score of a text. Sentiment analysis statistically detects whether the polarity of a piece of text is negative or positive. Sentimental analysis is based on two approaches: polarity-based analysis, in which texts are classed as either negative or positive, and valence-based analysis, in which the intensity of the emotion or sentiment is considered.

2.7 WORKING OF VADER

VADER is a sentiment or emotion analysis method that uses lexicons of sentiment-related words. Each word in the lexicon is classed as positive or negative, and the strength of positivity or negativity is also examined using this method. Table 1 depicts the sentiment rating of an excerpt from VADER's lexicon, with higher positive ratings for more positive words and lower negative ratings for more negative terms.

Table I. Sentiment rating of the various words in a text.

Word	Sentiment rating
tragedy	-3.3
rejoiced	2.0
insane	-1.6
disaster	-3.2
great	3.3

According to Hutto & Gilbert in 2014, to determine if these terms are favorable or negative, a group of individuals must personally rate them, which is both time-consuming and costly (Hutto & Gilbert, 2014). The lexicon must contain a good coverage of the words of interest in your text; otherwise, accuracy will be poor. When the lexicon and the text are well-matched, this method is quite precise, and it even produces speedy results on vast volumes of text. VADER not only matches the words in the text with its lexicon, but it also takes into account certain aspects of the way the words are written as well as their context meaning.

3. EXPERIMENTATION AND PERFORMANCE ANALYSIS

In this paper, sentiment analysis by the utilization of VADER is performed. Firstly, utilize standardization methods in Natural Language Processing (NLP) for converting the test text into its vector form. The implementation of emotion analysis evaluated in Python using Natural Language Toolkit (NLTK) library. Figure 2 shows the virtual emotion analysis of the text where the emotional content is adjudged as 75% positive. Figure 3 shows the virtual emotion analysis of the text where the emotion is adjudged as 26% positive which is shown in red color depicting 26% negative. Figure 4 shows the sentiment analysis of long text where the sentiment is adjudged as 92% positive. By adding
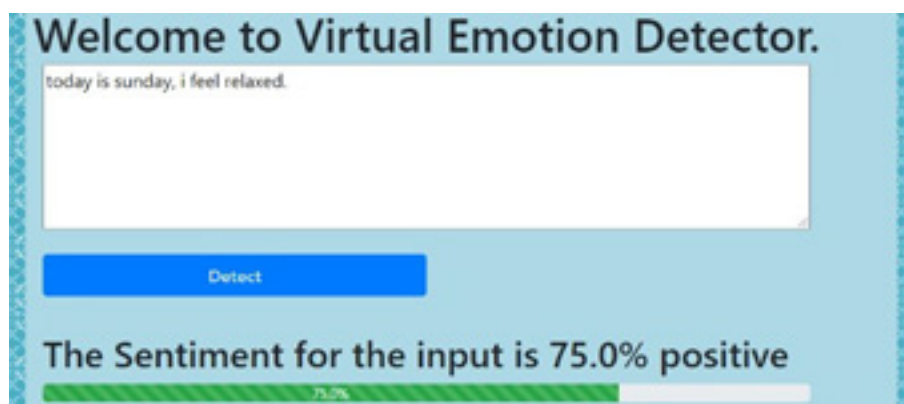
this feature of detecting gibberish, we are able to detect gibberish text where the algorithm returns 50% as can be seen in Figure 5.

Fig 2. Virtual emotion detection of text showing 75% positive polarity.
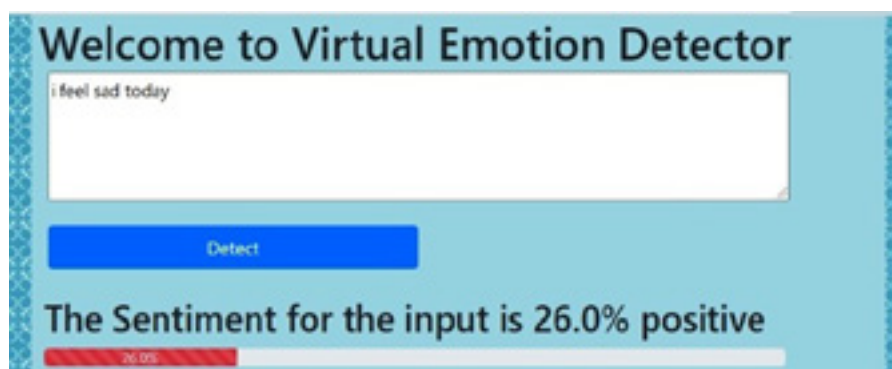
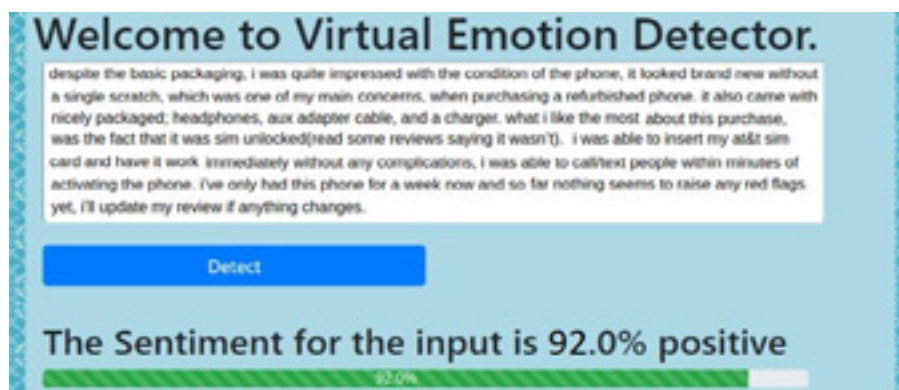Fig 3. Virtual emotion detection of text showing 26% negative polarity.

Fig 4. Virtual emotion detection of long text showing 92% positive polarity.
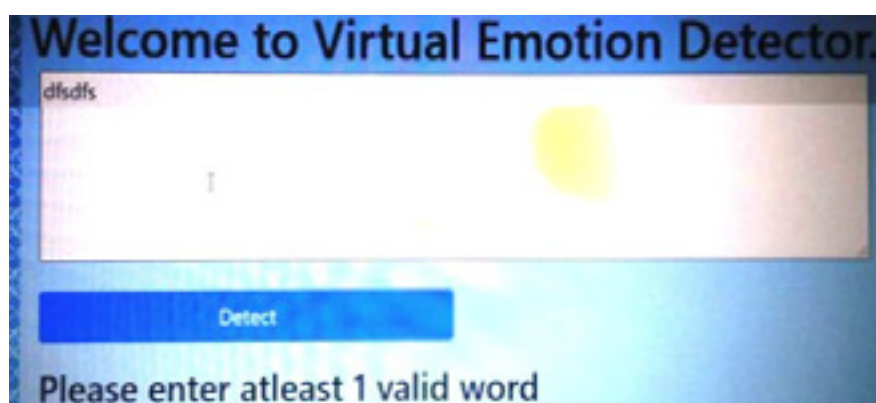

Fig 5. Emotion detection of gibberish text.

4. CONCLUSION

The main focus of this paper is to calculate two scores of text: polarity and its intensity by using machine learning. The polarity range is between -1 to 1(negative to positive) and which help us to find whether the text is positive or negative. In this paper we have tested different emotions of a text by using natural language processing toolkit in python and quantified this emotion as positive or negative. Also we were able to identify a gibberish text i.e. words which does not make any sense or are rubbish.

REFERENCES

[1] Mozetic, I., Grcar, M. & Smailovic, J. (2016), 'Multilingual twitter sentiment classification: The role of human annotators', PLoS One 11(5), 1–26.

[2] Steven Bird, E. K. & Loper, E. (2009), Natural Language Processing with Python – Analyz- ing Text with the Natural Language Toolkit, O'Reilly Media.

[3] Saif, H., Fernandez, M., He, Y. & Alani, H. (2014), On stopwords, filtering and data sparsity for sentiment analysis of Twitter, in 'Proceedings of the Ninth International Conference on Language Resources and Evaluation (LREC'14)'.

[4] Stanford NLP Group (2015), CoreNLP, Stanford University, Stanford USA. https:// stanfordnlp.github.io/CoreNLP/index.html.

[5] Nicolai, G. & Kondrak, G. (2016), Leveraging inflection tables for stemming and lemmati- zation, in 'Proceedings of the 54th Annual Meeting of the Association for Computational Linguistics', Vol. 1, Association for Computational Linguistics, Berlin, pp. 1138–1147.

[6] Samir, A. & Lahbib, Z. (2018), Stemming and lemmatization for information retrieval sys- tems in amazigh language, in M. A. A. N. E. Y. Tabii, M. Lazaar, ed., 'Big Data, Cloud and Applications. BDCA 2018', Vol. 872 of Communications in Computer and Informa- tion Science, Springer, Cham, Kenitra, Morocco, pp. 222–233.

[7] Mahajan, A., Ray, A., Verma, A., Kohad, S. & Thakare, P. N. (2020), 'Sentiment analy- sis using supervised machine learning', International Journal of Advance Research and Innovative Ideas in Education 6(6), 103–109.

[8] Beri, A. (2020), 'Sentimental analysis using VADER', Available online https://towardsdatascience.com/sentimental-analysis-using-vader-a3415fef7664.

[9] Hutto, C. & Gilbert, E. (2014), VADER: A parsimonious rule-based model for sentiment analysis of social media text, in 'Proceedings of the Eighth International AAAI Con- ference on Weblogs and Social Media', Association for the Advancement of Artificial Intelligence, Ann Arbor, MI, pp. 216–225.

/15/

PERFORMANCE ANALYSIS OF NOMA IN RAYLEIGH AND NAKAGAMI FADING CHANNEL

Prasheel N. Thakre

Assistant Professor, Department of Electronics and Communication Shri Ramdeobaba College of Engineering and Management Nagpur, (India).

E-mail: thakrepn2@rknec.edu

Sanjay Pokle

Professor, Department of Electronics and Communication Shri Ramdeobaba College of Engineering and Management Nagpur, (India).

E-mail: poklesb@rknec.edu

Radhika Deshpande

B.Tech Student, Department of Electronics and Communication Shri Ramdeobaba College of Engineering and Management Nagpur, (India).

E-mail: deshpandera@rknec.edu

Samruddhi Paraskar

B.Tech Student, Department of Electronics and Communication Shri Ramdeobaba College of Engineering and Management Nagpur, (India).

E-mail: paraskarsp@rknec.edu

Shashwat Sinha

B.Tech Student, Department of Electronics and Communication Shri Ramdeobaba College of Engineering and Management Nagpur, (India).

E-mail: sinhasr@rknec.edu

Yash Lalwani

B.Tech Student, Department of Electronics and Communication Shri Ramdeobaba College of Engineering and Management Nagpur, (India).

E-mail: lalwaniys@rknec.edu

ABSTRACT

Cellular connectivity is expanding rapidly in the modern world. The multiple access strategy is one of the highly used methods for allocating the range of users in cellular network. Spectrum allocation is a crucial element to take into account since cellular communication is becoming more and more popular. NOMA is a channel access mechanism used in 5G mobile communication. It is also known as non-orthogonal multiple access. NOMA is a potential strategy for enhancing spectral efficiency and sum rate. Using the NOMA method, we evaluated the BER versus transmitted power of two users in rayleigh and nakagami fading channels. In this NOMA setup, a single antenna is shared by two users. Two users can accept the same frequency using 5G NOMA technology, but at different power levels. The results of the MATLAB simulation show that the two user NOMA in the Nakagami channel performs better than the Rayleigh channel in terms of Bit Error Rate vs. Transmitted Power.

KEYWORDS

NOMA, Rayleigh, Nakagami Fading, BER, Transmitted Power and Probability Density Function.

1. INTRODUCTION

One of the crucial requirements for 5th generation mobile systems is expanded data networks. The development in this field aims to boost system throughput and capacity. This is a must-have requirement given the rapid increase in mobile traffic that has just occurred. The network's increasing traffic should be able to be handled by the multiple access strategy that is suggested Aditi Agrawal et al. [2022] M. W. Baidas et al. [2018]. Early versions of multiple access strategies distributed users and resources in an orthogonal way. But, in 5G, NOMA has been the centre of study. A mechanism called as NOMA is used to make sure that there is equity in the deployment of forthcoming radio access resources. The fifth generation must offer high connectivity, dependability, and low latency, therefore this is necessary. In this type of design, NOMA surpasses OMA by roughly 30% B. Kim et al. [2019. Superposition coding is used by the base station (BS) to broadcast in NOMA, while SIC is used to decode the signals. Combining this SIC with an interference cancellation combining receiver will boost capacity A. Benjebbour et al.[2013]. Non-orthogonal multiple access may be divided into 2 categories which are the domains of code and power C. Hsiung et al. [2019]. In NOMA domain, users having poor channel conditions receive high power, while users having acceptable channel conditions receive low power. While the less powerful user performs SIC, the more powerful user directly decodes their own signal in the receiver. Because users may communicate in both good and bad channel conditions, NOMA is more democratic than OMA P. N. Thakre et al. [2022]. In comparison to other orthogonal users, the throughput of cell edge users improves owing to the intra beam SIC's removal of interference D. K. Hendraningrat et al. [2020].

When fifth-generation systems connect large devices, improving spectrum allocation is essential. NOMA helps to improve spectrum utilization. In this study, the simulation results of BER vs transmitted power in two different fading channels are shown. This article has the advantage of illustrating the BER of a system employing NOMA in two fading channels. To enhance the spectral efficiency in 5-G communications, NOMA has been proposed. Spectrum distribution becomes significant in a number of methods as user numbers increase A. Benjebbour et al. [2013]. In order to improve a network's overall rate, outage probability, and ergodic capacity, multiple access approaches are deployed. The importance of power allocation in network performance also increases along with the number of users K. Wang et al. [2019] K. Higuchi et al. [2015] Y. Kishiyama et al. [2012] Harada et al. [2014] Prasheel Thakre et al. [2022] Y. Saito et al. [2013]. Performance is assessed using the users' BER calculations. Since the performance is usually acceptable, power domain NOMA is properly assessed. Performance will be better with the distribution to NOMA users than with regular OMA. Applications, like visible light communications, are also where NOMA is most commonly employed. The most frequent issue with VLC is blockages; the dynamic user pairing strategy helps with distribution of resource, which right away enhances the performance of the system Z. Xiao et al. [2019] Y. Yin at al. [2019] . Combining user pairing with power allocation, the fractional transmit power that results in low performance is used for resource allocation Y. Yin at al. [2019]. BER vs SNR of two users was compared for various fading channels using NOMA approach and it was found that Nakagami channel performs considerably better when compared to the Rayleigh and Rician channel in BER vs SNR but transmit power isn't considered for the different channels K. Higuchi et al. [2015]. Moreover, comparison of NOMA against OMA networks conveys that NOMA outperforms OMA and provide better spectral efficiency and user fairness (C. Hsiung et al. [2019]. Closed-form expressions of BER at near and far users of the considered downlink NOMA are calculated in the presence of SIC over Nakagami fading channel A. Benjebbour et al. [2013]. The equations for average SNR, achievable rate, and outage probability show that network users' ordered channel gains are equal to their diversity orders M. W. Baidas et al. [2018]. NOMA has developed independently in every aspect of wireless communication. Whenever there is a rise in users, the allocation of resources is also considered to account for the effectiveness of the system.

2. NOMA SYSTEM MODEL

We consider Non-Orthogonal Multiple Access Scheme. Here, the BS superimposes the information waveforms for its serviced users. Each user equipment employs Successive Interference Cancellation to detect their own signals.

In a NOMA system with two users , suppose User 1 is a faraway user with a weak signal and User 2 is a close user with a good signal.

The BS serves both users on the same frequency spectrum. h_1 and h_2 be the channels of far user and near user respectively. The base station's signal can be described as follows:

$$x = \sqrt{P}(\sqrt{\alpha_1}\, x_1 + \sqrt{\alpha_2}\, x_2)$$

where, P is the transmitted power, α is fractional coefficient of total power such that $\alpha_1 > \alpha_2, \alpha_1 + \alpha_2 = 1$

At the User 1, the received vector is expressed as:

$$y_1 = h_1\sqrt{P}(\sqrt{\alpha_1}\, x_1 + \sqrt{\alpha_2}\, x_2) + w_1 \tag{2}$$

or,

$$y_1 = \underbrace{h_1\sqrt{P}\sqrt{\alpha_1}\, x_1} + \underbrace{h_2\sqrt{P}\sqrt{\alpha_2}\, x_2} + \underbrace{w_1} \tag{3}$$

<div style="text-align:right; color:red">

Desired   Interference   Noise
dominating   low power

</div>

Now, direct decoding is performed to estimate x_1

The SINR for decoding the 1st (far) user signal is given by:

$$\gamma_1 = \frac{\alpha_1 P\,|h_1|^2}{\alpha_2 P\,|h_1|^2 + \sigma^2} \tag{4}$$

The achievable rate(bps/Hz) of the User 1 is given as:

$$R_1 = \log_2\left(1 + \frac{\alpha_1 P\,|h_1|^2}{\alpha_2 P\,|h_1|^2 + \sigma^2}\right) \tag{5}$$

For User 2, the received vector is given as:

$$y_2 = \underbrace{h_2\sqrt{P}\sqrt{\alpha_1}\, x_1} + h_2\sqrt{P}\sqrt{\alpha_2}\, x_2 + \underbrace{w_2} \tag{6}$$

<div style="text-align:right; color:red">

Interference   Desired   Noise
dominating   low power

</div>

Firstly, direct decoding for the x1 signal, then the concept of the SIC is applied as:

$$y_2' = h_2\sqrt{P}\sqrt{\alpha_1}\,x_1 + h_2\sqrt{P}\sqrt{\alpha_2}\,x_2 + w_2 - h_2\sqrt{P}\sqrt{\alpha_1}\,\hat{x}_1 \tag{7}$$

Now, direct decoding for the near user signal x2.

The SINR for decoding far user's signal at near user is given by:

$$\gamma_{1,2} = \frac{\alpha_1 P\left|h_2\right|^2}{\alpha_2 P\left|h_2\right|^2 + \sigma^2} \tag{8}$$

Hence the achievable rate(bps/Hz) will be:

$$R_{1,2} = \log_2\left(1 + \frac{\alpha_1 P\left|h_2\right|^2}{\alpha_2 P\left|h_2\right|^2 + \sigma^2}\right) \tag{9}$$

After the far user's signal has been cancelled, the near user's SINR for decoding its own signal is:

$$\gamma_2 = \frac{\alpha_2 P\left|h_2\right|^2}{\sigma^2} \tag{10}$$

The corresponding achievable rate(bps/Hz) is given as:

$$R_2 = \log_2\left(1 + \frac{\alpha_2 P\left|h_2\right|^2}{\sigma^2}\right) \tag{11}$$

The three types of NOMA schemes that are now being employed in the broad spectrum are PD-NOMA, waveform domain NOMA, and CD-NOMA, according to the survey and resources that are currently accessible. The focus of most NOMA research is PD-NOMA, which necessitates a substantial power differential between the signals allocated to various users. At the transmitter's side of a PD-NOMA system, superposition coding (SC) is used to create the signals of numerous users on each subcarrier, which are dispersed over several users (In SC, although sharing the same time-frequency-code resources, each user has their own power level. Each user's power level is determined by the channel gain value; those with lower channel gain values receive greater power levels, and vice versa. At the receiver side, the SIC approach is used to filter out extra user signals that interfere with that band.

In terms of spectrum efficiency, NOMA's SIC method outperforms OMA. Between users 1 and 2, the power is split. The power distribution to users has a considerable impact on the throughput of users in the NOMA domain. The fairness of the users' Power allocation largely determines throughput.

3. FADING CHANNELS

During wireless propagation, fading refers to the degradation of the transmitted signal power caused by a variety of factors. These variables include geographic location, time, radio frequency, and atmospheric conditions like rainfall and lightning. There are different types of fading channels and they are Rayleigh, Rician, Nakagami, Weibull fading channel, etc.

In this paper two fading channels Rayleigh and Nakagami are considered. Only NLOS components between the transmitter and receiver are modelled in the Rayleigh. It is assumed that there is an absence of Line-Of-Sight route between the transmitter and receiver. When multipath scattering occurs with relatively high delay time spans and various groups of reflected waves, Nakagami fading takes place. Table 1 shows a comparative study of Rayleigh and Nakagami fading channels taking few key parameters into consideration.

Table I. Comparison between rayleigh and nakagami fading channel.

Parameters	Rayleigh fading channel	Nakagami fading channel
SNR	For 1000 samples, SNR=0.9	For 1000 samples, SNR=0.35
Power Consumption	More power consumption	Less power consumption
BER vs SNR	BER vs SNR values for Rayleigh are lower as compared to Nakagami	BER vs SNR values for Nakagami are higher as compared to Rayleigh

4. PERFORMANCE OF NOMA IN RAYLEIGH AND NAKAGAMI FADING CHANNEL

From Fig. 1, we can infer that for a two user NOMA to maintain user fairness, the system has given the distant user more power and the close user less. Secondly, we conclude that as power increases, the BER for both users decreases. Also, at a particular value of transmit power, BER value for user who is located distantly from the base station is more compared to user nearer.
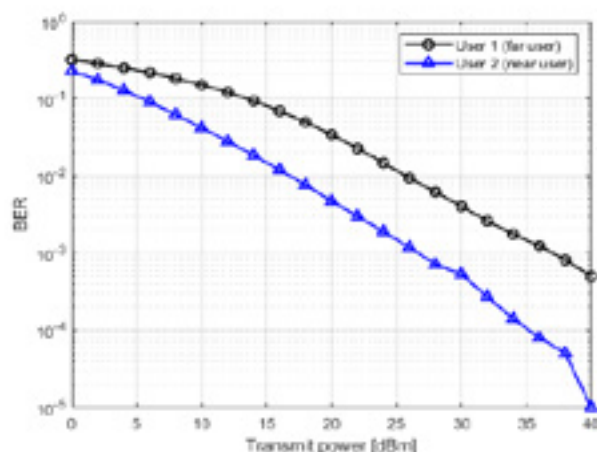
Fig. 1. BER vs Transmitted power graph for rayleigh channel.

Fig. 2 shows the Probability Density Function for Nakagami channel for different m values. From the literature survey, we infer that mu should be greater than 1 so that it corresponds to lesser fading than Rayleigh fading and omega is mostly taken 1.

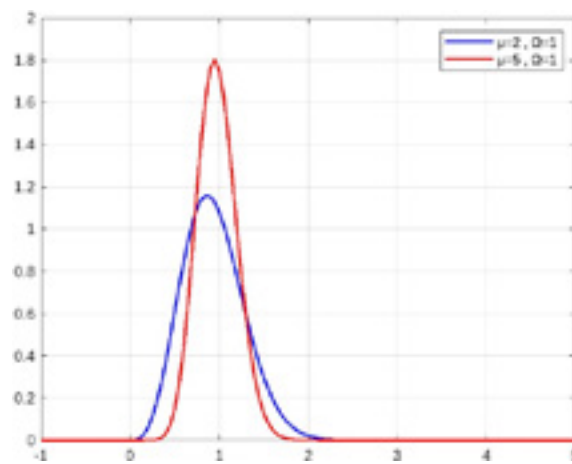mu=2 , w=1 and mu=5 and w=1 might be considered as the best values.

Fig. 2. PDF curve for nakagami-m channel for different values of mu and omega.

In Fig. 3, BER vs Transmit power has been plotted for Nakagami fading channel using different values of mu and omega as shown.
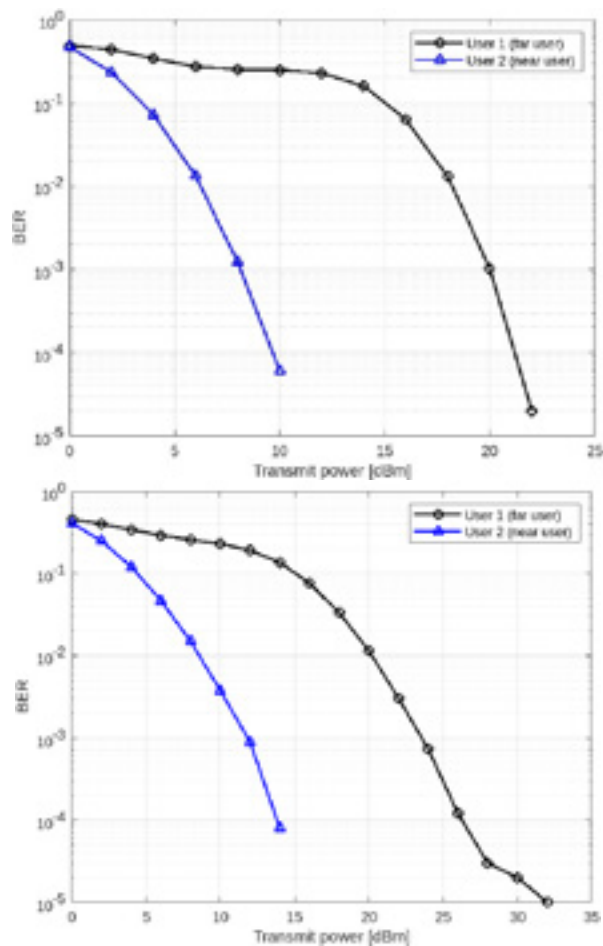

Fig. 3. BER vs Transmitted power graphs for nakagami channel (mu=5, omega=1) and (mu=2, omega=1).

5. CONCLUSION

NOMA is favored for 5G communications because it offers a strong connection, stability, and minimal latency. Large-scale networking is facilitated by this NOMA's improved spectrum efficiency. In this study, the performance analysis of two different fading channels—Rayleigh and Nakagami—for wireless NOMA communication is assessed. According to our research,

when power increases in a Rayleigh fading channel, the bit error rate drops, greater power is distributed to far users while low power is distributed to nearby users, ensuring user fairness. Similar findings are obtained with Nakagami fading, although the BER performance is superior to that of Rayleigh fading. The Nakagami channel performs better than the Rayleigh channel in terms of Bit Error Rate. A rise in BER might be reduced by the employment of several coding techniques or differentiation strategies.

REFERENCES

[1] A. Benjebbour, Y. Saito, Y. Kishiyama, A. Li, A. Harada and T. Nakamura. (2013). Concept and practical considerations of nonorthogonal multiple access. International Symposium on Intelligent Signal Processing and Communication Systems, pp.770-774. doi:10.1109/ISPACS.2013.6704653

[2] Aditi Agrawal, Ishant Kohad, Mrunmayi Kinhikar, Dolly Tiwari, Prasheel Thakre, & Sanjay Pokle. (2022). Outage Probability and Capacity Analysis for NOMA based 5G and B5G Cellular Communication. International Journal of Next-Generation Computing, 13(5). doi:https://doi.org/10.47164/ijngc.v13i5.912

[3] B. Kim, Y. Park and D. Hong (2019, Oct.). Partial Non-Orthogonal Multiple Access (P-NOMA). IEEE Wireless Communications Letters, 8(5), 1377-1380. doi:10.1109/LWC.2019.2918780

[4] C. Hsiung, R. Huang, Y. Zhou and V. W. S. Wong (2019). Dynamic User Pairing and Power Allocation for Throughput Maximization in NOMA Systems. IEEE International Conference on Communications Workshops (ICC Workshops), (pp. 1-6). doi:10.1109/ICCW.2019.8756777

[5] Denny Kusuma Hendraningrat, Muhammad Basit Shahab , Soo Young Shin (2020). Virtual user pairing based non-orthogonal multiple access in downlink coordinated multipoint transmissions. IET Communications, 14(12), 1910-1917.

[6] Higuchi, K., & Benjebbour, A. (2015). Non-orthogonal multiple access (NOMA) with successive interference cancellation for future radio access. IEICE Transactions on Communications, 98(3), 403-414. doi:10.1587/transcom.E98.B.403

[7] Wang, K., Liang, W., Yuan, Y., Liu, Y., Ma, Z., & Ding, Z. (2019). User Clustering and Power Allocation for Hybrid Non-Orthogonal Multiple Access Systems. IEEE Transactions on Vehicular Technology, 68(12), 12052-12065. doi:10.1109/TVT.2019.2948105.

[8] Li, A., Harada, A., & Kayama, H. (2014). Investigation on low complexity power assignment method and performance gain of nonorthogonal multiple access systems. IEICE Transactions on Fundametals of Electronics Communications and Computer Sciences, 97(1), 57-68. doi:10.1587/transfun.E97.A.57

[9] Baidas, M. W., Alsusa, E., & Hamdi, K. A. (2018). Performance analysis of downlink NOMA networks over Rayleigh fading channels. IEEE Wireless Communications and Networking Conference (WCNC), (pp. 1-6). doi: 10.1109/WCNC.2018.8377014

[10] Thakre, P. N., & Pokle, S. B. (2022). A survey on Power Allocation in PD-NOMA for 5G Wireless Communication Systems. 10th International Conference on Emerging Trends in Engineering and Technology - Signal and Information Processing (ICETET-SIP-22) (pp. 1-5). Nagpur: IEEE. doi:10.1109/ICETET-SIP-2254415.2022.9791576

[11] Thakre, P. N., & Pokle, S. B. (2022). Optimal power allocation for NOMA-based Internet of things over OFDM sub bands. International Journal of Next-Generation Computing, 13(5). doi:https://doi.org/10.47164/ijngc.v13i5.909

[12] Kishiyama, Y., Benjebbour, A., Ishii, H., & Nakamura, T. (2012). Evolution concept and candidate technologies for future steps of LTEA. IEEE International Conference on Communication Systems (ICCS), (pp. 473-477). doi:10.1109/ICCS.2012.6406193

[13] Saito, Y., Kishiyama, Y., Benjebbour, A., Nakamura, T., Li, A., & Higuchi, K. (2013). Non-Orthogonal Multiple Access (NOMA) for Cellular Future Radio Access.

IEEE 77th Vehicular Technology Conference (VTC Spring), (pp. 1-5). doi:10.1109/VTCSpring.2013.6692652

[14] YIN, Y., PENG, Y., LIU, M., YANG, J., & GUI, G. (2019). Dynamic User Grouping-Based NOMA Over Rayleigh Fading Channels. IEEE Access, 7, 110964-110971. doi:10.1109/ACCESS.2019.2934111

[15] Z. XIAO, ZHU, L., GAO, Z., WU, D. O., & XIA, X. G. (2019). User Fairness Non-Orthogonal Multiple Access (NOMA) for MillimeterWave Communications With Analog Beamforming. IEEE Transactions on Wireless Communications, 18(7), 3411-3423. doi:10.1109/TWC.2019.2913844

AUTORS BIOGRAPHY

P. N. Thakre has received Bachelor's degree in Electronics Engineering from RTM Nagpur University in 2010. He has done M.Tech. in Electronics Engineering from Shri Guru Gobind Singhji Institute of Engineering and Technology, Nanded University in 2013. Presently he is pursuing Ph. D. from Shri Ramdeobaba College of Engineering and Management, RTM Nagpur University, under the fellowship of Visvesvaraya PhD Scheme for Electronics & IT. His research area includes Non-Orthogonal Multiple Access (NOMA) for 5G Wireless Communication Systems and Wireless channel Estimation Algorithms. Presently he is working as Assistant Professor in Electronics & Communication Engineering Department, Shri Ramdeobaba College of Engineering and Management, Nagpur.

D r. S. B. Pokle has received Bachelor's degree in Electronics and Telecommunication Engineering from Govt. College of Engineering Pune, Pune University in 1993. He has done M.Tech. in Electronics Engineering and Ph. D. in Electronics from Visvesvaraya National Institute of Technology Nagpur. His research area includes designing aspects of MIMO-OFDM Wireless Communication Systems and Wireless channel Estimation Algorithms. He has published 74 research papers in the reputed national and international Journals and presented papers in the reputed national and international conferences. This includes 06 SCI indexed and 04 Scopus indexed publications. He has guided several projects in the area of signal processing, Digital image processing, Artificial intelligence etc. at post-graduation level and graduate level. He has delivered many Expert lectures in reputed Engineering institutions and also worked as judge in many national level technical competitions. He is approved supervisor for Ph. D. under R.T.M. Nagpur University, Nagpur. 07 candidates has been awarded Ph.D., and 01is pursuing Ph.D. under his guidance. He is member of technical societies like ISTE and IEEE. He has total 26 years of experience which includes 3 years industry and 23 years of teaching experience. He worked as Head of department for 10 years. Presently he is working as Professor in Electronics & Communication Engineering Department, Shri Ramdeobaba College of Engineering and Management, Nagpur. Also, he is appointed as Chairman, Board of Studies Electronics Engineering by RTM Nagpur University, Nagpur.

Ms. Radhika Deshpande is pursuing 4th year B.E. in the department of Electronics and Communication Engineering, at Shri Ramdeobaba College of Engineering and Management, Nagpur.
E-mail: deshpandera@rknec.edu

Ms. Samruddhi Paraskar is pursuing 4th year B.E. in the department of Electronics and Communication Engineering, at Shri Ramdeobaba College of Engineering and Management, Nagpur.
E-mail: paraskarsp@rknec.edu

Mr. Shashwat Sinha is pursuing 4th year B.E. in the department of Electronics and Communication Engineering, at Shri Ramdeobaba College of Engineering and Management, Nagpur.
E-mail: sinhasr@rknec.edu

Mr. Yash Lalwani is pursuing 4th year B.E. in the department of Electronics and Communication Engineering, at Shri Ramdeobaba College of Engineering and Management, Nagpur.

E-mail: lalwaniys@rknec.edu

/16/

BACKGROUND REMOVAL OF VIDEO IN REALTIME

Arya Khanorkar

Yeshwantrao Chavan College of Engineering, Nagpur, Maharashtra, (India).

Bhavika Pawar

Yeshwantrao Chavan College of Engineering, Nagpur, Maharashtra, (India).

Diksha Singh

Yeshwantrao Chavan College of Engineering, Nagpur, Maharashtra, (India).

Kritika Dhanbhar

Yeshwantrao Chavan College of Engineering, Nagpur, Maharashtra, (India).

Nikhil Mangrulkar

Yeshwantrao Chavan College of Engineering, Nagpur, Maharashtra, (India).
E-mail: mangrulkar.nikhil@gmail.com

https://doi.org/10.17993/3ctic.2022.112.195-206

ABSTRACT

Background removal for video is a computer-vision based system to remove the background from a video with ease. Creating a professional background when at home, i.e., not in a very professional environment, can be a tedious task. Not everyone has time to learn editing and the technicalities involved in having an entire setup for creating a sophisticated background and it is not practical that normal people buy green screens or blue screens just for their everyday formal meets. Our goal is to create a quick and easy solution to that by removing background in real time while also maintaining the quality of the call, having the additional benefit of adding custom backgrounds and enabling users to add effects like adjust lighting, contrast etc., we are combining all 4-5 steps in 1 single step. SelfieSegmentation module of Mediapipe helps us achieve this. The Selfie Segmentation API creates an output mask from an input image. The mask will be the same size as the input image by default. A float integer with a range of [0.0, 1.0] is assigned to each pixel of the mask. The higher the confidence that the pixel depicts a person, and vice versa, the closer the number is to 1.0.

KEYWORDS

Categories and Subject Descriptors: G.4 [Mathematics of Computing]: Mathematical Software - User Interfaces; H5.2 [Information Interfaces and Presentation]: User Interfaces - User-centered design; Interaction styles; Theory and methods.

Background Removal, Online Meetings, Professional Background, Streaming.

1. INTRODUCTION

This pandemic has made it clear that virtual meets are here to stay. They are the new normal. But often virtual meetups from home fail to create the professional atmosphere due to backgrounds in the video. The professionalism required can be achieved by proper background in videos and minimal disturbances. Unnecessary and visually unpleasing objects need to be removed. This can be achieved by background removal, changing background color and adding virtual backgrounds. Background removal can help avoid the cumbersome task of arranging a good backdrop in some cases even eliminates the use of green screens which are used by many youtubers. It helps add to the overall aesthetics and pleasantness of video conferences or even live streams.

The technique of mimicking human intelligence in robots programmed to think and behave like humans is known as artificial intelligence (AI). Computer vision is a branch of artificial intelligence (AI) that allows computers and systems to extract useful information from digital photos, videos, and other visual inputs and act or make recommendations based on that data. A computer vision technique called object detection is used to locate and identify objects in pictures and movies. Using this type of identification and localization, object detection can be used to count the items in a scene, locate and track them precisely, and accurately label them.

Image segmentation is the technique of dividing a digital image into numerous pieces for use in digital image processing and computer vision (sets of pixels, sometimes known as image objects). Various portions of a movie can be discovered using object detection and image segmentation, and different adjustments can be performed to each of the components. We'll use these ideas to remove the backdrop from a video using AI.

Open Broadcaster Software (OBS) helps you set your scene as a virtual camera to which we will be feeding our video directly in real time using pyvirtualcam and mediapipe. We'll use Google Meet to recognize OBS as a video source and output it as a virtual camera, resulting in enhanced quality of video calls.

2.   REVIEW OF LITERATURE

2.1   PRESENT SYSTEM

The apps that currently provide such a feature for removing the background of a video in real time tends to worsen the quality of the video and do not provide us with smooth edges of the main object which is not ideal for a professional use. Also, the process to remove or change the background in these apps consists of various steps to be followed, sometimes we are even required to cut the video call and rejoin with a changed background. Through our project we have tried to overcome these problems by providing a system which removes the background while maintaining a proper quality of the video with fps greater than 30. And we also provide an easy way to change the backgrounds by just clicking a button on the keyboard.

Grzegorz Szwoch, in his paper presented, implementation of a background subtraction algorithm using the OpenCL platform. The algorithm works using a live stream of video frames from an on-line surveillance camera. A host machine and a parallel computing device are used to execute the processing. The research focuses on optimizing OpenCL algorithm implementation for GPU devices by taking into consideration specific GPU architecture aspects including memory access, data transfers, and work group structure. The technique is designed to work on any OpenCL-enabled device, including DSP and FPGA platforms. Several algorithm optimizations are presented and tested on a variety of devices with variable processing power. The work's major goal is to figure out which optimizations are required for on-line video processing in the surveillance system.

A relatively inexpensive background subtraction method is proposed by Hasup Lee et al., in their study employing background sets with im-age- and color-space reduction. Background sets are used to

recognize objects from dynamic backdrops like waves, trees, and fountains. The image space is decreased to handle jittered and unstable frames, such as those from handheld mobile devices. The color space is shrunk to account for color noise, such as the scattered RGB values from a digital camera. To reduce expenses, a combination of color-space reduction and hash-table look-up operations is used. The results, when compared to other methods, suggest that the proposed technology is feasible: it may also be used in mobile or embedded environments.

S. Joudaki, et al., in their paper, they presented a comparison of numerous existing background subtraction methods, ranging from basic background subtraction to more complicated providential techniques. The purpose of this research is to provide an overview of the advantages and disadvantages of commonly utilized approaches. The approaches are compared based on how much memory they demand, how long they take to compute, and how well they handle different types of films. Finally, other criteria such as processing time and memory needs were used to compare the existing approaches. Baoxin Li, et al., in their paper they proposed a video background replacement algorithm, this is based on adaptive background modelling and background subtraction. It can be accomplished with a pre-recorded background scene image rather of a blue screen. Identifying statistical outliers in respect to a specific background is the challenge. A two- pass approach is utilized to modify initial segmentation based on statistics about a pixel's vicinity, which lowers false positives in the background area while raising detection rates for foreground objects. Experiments with real image sequences, as well as comparisons with other existing approaches, are shown to demonstrate the benefits of the proposed methodology.

S. Brutzer, et al., in their paper, presented one of the most important approaches for automatic video analysis, particularly in the field of video surveillance, is background subtraction. Despite their usefulness, reviews of recent background removal algorithms in relation to video surveillance challenges include several flaws. To address this problem, we must first identify the major obstacles to background subtraction in video surveillance. We then evaluate the performance of nine back-ground subtraction algorithms with post-processing depending on how well they over-come those challenges. As a result, a fresh evaluation data set is presented that includes shadow masks and precise ground truth annotations. This enables us to offer a thorough evaluation of the advantages and drawbacks of various background sub-traction techniques.

In their study, R. J. Qian et al., presented an algorithm for altering video backgrounds without a blue screen physically. Pre-recording a backdrop image of the scene free of any foreground objects is required for the operation. Based on the color difference between the pixels in an input frame and their corresponding pixels in the background image, the method computes a probability map that contains the likelihood for each pixel to be classified into the foreground or background. The probability map is further improved using anisotropic diffusion, which reduces classification mistakes without adding a lot of artefacts. The foreground pixels from the input frames are then feathered onto a brand- new background video or image based on the enhanced probability map to create the output video. The method requires only a little amount of CPU resources and is designed to work in real time. Experiment findings are also reported.

A. Ilyas, et al., in their paper, presented a Modified Codebook Model-Based Real Time Foreground-Background Segmentation. The initial step in object tracking is the essential process of segmenting the scene in real time into the foreground and background. beginning with the codebook approach. Authors suggested certain changes that show notable improvements in the majority of the typical and challenging conditions. For accessing, removing, matching, and adding codewords to the codebook as well as moving cached codewords into the codebook, they included frequency options. They also suggest an evaluation procedure based on receiver operating characteristic (ROC) analysis, precision and recall methodology, to impartially compare various segmentation techniques. Authors suggested expressing the quality factor of a method as a single value based on a harmonic mean between two related features or a weighted Euclidean distance.

Rudolph C. Baron, et al., in their paper, presented a solution for managing a video conference. When establishing a video conference with a second person, a first participant can choose from among

several stored virtual backgrounds and use that background. One or more characteristics of the first and/or second participant, one or more characteristics of the video conference, and/or similar considerations may be used to choose the virtual background. The virtual backgrounds can be used, for instance, to provide people outside of a company organization a desired perception, message, and/or the like while they communicate with its employees via video conferencing. The virtual background can incorporate static image data, live or recorded video feeds, static business entity web pages, and dynamic business entity web pages.

Jian sun, et al., Effective techniques and approaches in a video sequence isolate the focus from the background, according to their paper. In one instance, a system creates an accurate real-time backdrop cut of live video by reducing the background contrast while maintaining the contrast of the segmentation boundary itself. This method enhances the border between the foreground and background images. The live video may then combine the fragmented foreground with another background. An adaptive background color mixture model can be used by the system to distinguish foreground from background more effectively when there are changes in the backdrop, such as camera movement, lighting changes, and the movement of small objects in the background.

Juana E. Santoyo-Morales, et al., in their paper presented a Background sub-traction models based on a Gaussian mixture have been widely employed in a range of computer vision applications for detecting moving objects. Background sub-traction modelling, on the other hand, remains a challenge, especially in video sequences with dramatic lighting changes and dynamic backdrops (complex backgrounds). The goal of this research is to make background subtraction models more resilient to complicated situations. The following enhancements were proposed as a result: Redefining the model distribution parameters (distribution weight, mean, and variance) involved in the detection of moving objects; enhancing pixel classification (background/foreground) and variable update mechanisms using a new time-space dependent learning rate parameter; and c) substituting a new space-time region-based model for the pixel-based model that is currently used in the literature.

According to Yiran Shen et al., background subtraction is a typical first step in many computer vision applications, including object localization and tracking. Its objective is to pick out the moving parts of a scene that match to the important things. Researchers in the field of computer vision have been working to increase the reliability and accuracy of such segmentations, but most of their techniques require a lot of computation, making them unsuitable for our target embedded camera platform, which has a much lower energy and processing capacity. In order to create a new background subtraction method that overcomes this issue while retaining an acceptable level of performance, authors added Compressive Sensing (CS) to the often-used Mixture of Gaussian. The results imply that their technique can significantly reduce the eventual time taking.

Semi-supervised video object segmentation should be considered, which is the process of creating precise and consistent pixel masks for objects in a video sequence based on ground truth annotations from the first frame, according to a suggestion made by Jonathan Luiten et al. To do this, they provided the PReMVOS algorithm (Proposal- generation, Refinement and Merging for Video Object Segmentation). The method separates the problem into two steps to specifically address the difficult issues related to segmenting multiple objects across a video sequence: first, generating a set of precise object segmentation mask proposals for each video frame; and second, choosing and merging these proposals into precise and object tracks that are pixel-wise and consistently timed inside a video sequence.

Thuc Trinh Le, et. al., demonstrated a method for removing items from videos. The technique simply requires a few input strokes on the first frame that roughly delineate the deleted objects. Authors claims that this is the first method which enables semi-automatic object removal from videos with intricate backgrounds. The following are the main phases in their system: Segmentation masks are improved after setup and then automatically distributed throughout the film. Video inpainting techniques are then used to fill in the gaps. Authors claim that their system can handle several, potentially intersecting objects, complex motions, and dynamic textures. As a result, a computational

tool that can automate time-consuming manual tasks for editing high-quality videos has been developed.

Thanarat H. Chalidabhongse, et. al., in their paper, showed how to use color pictures to detect moving items in a static background scene with shading and shadows. They created a reliable and efficient background subtraction method that can deal with both local and global lighting variations, such as shadows and highlights. The approach is based on a proposed computational color model that distinguishes between the brightness and chromaticity components. This technology has been used to create real-world image sequences of both indoor and outdoor locations. The results, which demonstrate the system's performance, are also provided, as well as several speed-up techniques used in their implementation.

Yannick Benezeth, et. al., in their paper, presented comparison of different state-of-the- art background subtraction approaches is presented. On several movies containing ground truth, there have been developed and tested methods ranging from straightforward background subtraction with global thresholding to more complex statistical algorithms. The purpose is to lay a solid analytic foundation on which to highlight the benefits and drawbacks of the most extensively used motion detection methods. The approaches are compared in terms of their ability to handle various types of videos, memory requirements, and computing effort. A Markovian prior, along with several postprocessing operators, are also considered. Most of the films are from modern benchmark collections and highlight a range of issues, including low SNR, background motion in many dimensions, and camera jitter.

Yi Murphey, et. al., in their paper, describes their work on image content-based indexing and retrieval, which is an important technique in digital image libraries. Image features used for indexing and retrieval in most extant image content-based approaches are global, meaning they are computed over the full image. Background features can readily be mistaken for object features, which is the fundamental drawback of retrieval techniques based on global picture features. Users typically refer to the color of a particular object or objects of interest in an image while searching for photos using color attributes. The technique described in this article uses color clusters to analyze image backgrounds. After being identified, the background regions are deleted from the image indexing process, so they won't interfere with it anymore. Three main calculation processes make up the algorithm: fuzzy clustering, color picture segmentation, and background.

Zhao Fei Li, et. al., in their paper, presented background noise removal is a key stage in the picture processing and analysis process. Researchers use a variety of techniques to remove background noise from images. For instance, grey threshold techniques are frequently used to eliminate noises that have a strong contrast to the object of interest. However, there are a lot of noises in the grey scale that don't change as the interesting objects do. These noises cannot be reduced using the grey level-based noise removal technique, but the contour feature is excellent at doing so. The contour feature-based image background removal approach depends on the contour model. The contour characteristic of the interest items is modelled using a revolutionary method proposed in this study. A unique background noise with the same grey level as the background noise is completely eradicated using this method.

Thuc Trinh Le, et. al., demonstrated a method for eliminating objects from videos in their study. A few strokes in at least one frame are all that are needed for the technique to roughly delimit the items to be eliminated. These undeveloped masks are then polished and automatically broadcast throughout the video. The corresponding areas are synthesized again using video inpainting methods. Authors claim that their system is capable of navigating several, perhaps crossing objects, intricate motions, and dynamic textures. As a result, a computational tool has been created for editing high-quality videos that can take the place of laborious human work.

3.   PROPOSED TECHNIQUE

The main objective of the proposed technique is to create a simpler process of removing background from a live or saved video, to simplify the process of creating an aesthetic background. Our project

allows the user to completely remove the background or put a different background and be able to switch between multiple backgrounds or colors.

The main objective of our project is to eliminate the need to physically change the arrangement of room for a better and professional background. Thus, providing users an easy way of applying or changing backgrounds while they are in some online meet or live streams while maintaining the quality of the video.
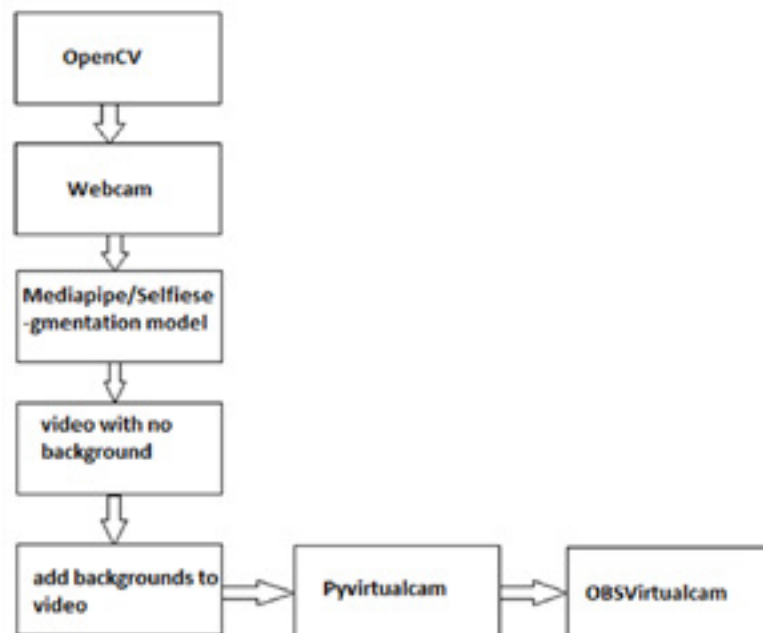
3.1   Flow of Proposed Technique

Fig. 1. Flowchart of the proposed system.

Fig. 1 shows the flow of the proposed system, starting with the accessing of the live video from webcam to the removal/changing of background and feeding the output to applications like google meet using OBS Virtual Camera.

3.2. IMPLEMENTATION

Our goal was to remove the background in real-time and with FPS more than 30.

3.2.1. STARTING THE WEBCAM

We should be able to access the webcam by simply running the code so that the video i.e., real time video can be directly taken as input. A computer vision library is called OpenCV (Open-Source Computer Vision). with a variety of image and video manipulation tools. The OpenCV library can be used to manipulate films in a variety of ways. To capture a video, you'll need a *VideoCapture* object. The index of the device or the video file's name is stored in *VideoCapture*. The device index is just a number that identifies which of the camera device is being used.

 Syntax: *capt = cv2.VideoCapture(0)*

Now a pop-up window will open if we have a webcam. We have set the frame size to 640X 480. Therefore, background-replacing images should be 640 x 480, which is the same size as the frame.

Creating a dataset for background images Make a folder called 'BackgroundImages' inside the project directory. You can download and store any image, or any number of images, in this directory.

3.2.2. BACKGROUND REMOVAL

We have used the *SelfieSegmentationModule* from *cvzone* package which uses OpenCV and *Mediapipe* libraries at its core and makes AI operations on videos and images very easy. *SelfieSegmentation* is a technique for removing the frame's background and replacing it with photos from our directory. It is based on MobileNetV3 but has been tweaked to be more efficient. It uses a 256x256x3 (HWC) tensor as input and outputs a 256x256x1 tensor as the segmentation mask. Before feeding it into the ML models, *MediaPipe SelfieSegmentation* automatically resizes the input image to the necessary tensor dimension. We use the webcam for input and frame width should be set to 640 x

480. Then we utilize the *cvzone* to execute *SelfiSegmentation*(), which carries out object identification, image segmentation, and ultimately background removal. The output frames can show the frames per second (fps) using the FPS() method.

 Syntax: seg = SelfiSegmentation() Setfps = cvzone.FPS()

 SelfieSegmentation() converts the image into RGB and sends it to the SelfieSegmentation model to process and then it checks if the image is colored; if yes it changes the color of the background and if not, it then changes the color of the image. As a result, we can see the background successfully removed.

3.2.3. STORE BACKGROUND IMAGES IN A LIST

Then, after creating a list of every image in the *BackgroundImages* folder, we iterate through it, reading each one and adding it to an empty list. At the beginning, the index is set at zero.

3.2.4. REPLACE BACKGROUND WITH DESIRED BACKGROUND

The frames are read from the camera using a while loop, and the background is then removed from the frames using the *seg.removeBG()* method and replaced with images from the directory. The camera's image *frame (img),* the directory's collection of photos, and with an index of image (*imgList[indexImg]*), are all passed to the seg.*removeBG()* function along with the threshold. To improve the edges, we additionally modify the threshold setting.

3.2.5. FUNCTIONALITY TO CHANGE BACKGROUND USING KEYBOARD SHORTCUTS

Using *cvzone.stackImages*, we stack the images and retrieve the output of the frames or background-replaced image. Then, by means of a straightforward if statement, we assign keys to change the background. The principle is to sequentially remove the indexes according to the key that was pressed to display the image for the resulting index. This lets you change the backgrounds quickly.

3.2.6. SEND THE FRAMES TO OBS VIRTUAL CAMERA

We then send the resulting frames to OBS Virtual Camera using *Pyvirtualcam().* It sends frames to a virtual camera from Python. The OBS virtual camera is detected by various platforms, and we have our very own background removal with whichever backgrounds, or no backgrounds, as required.

4. RESULTS AND DISCUSSIONS

With our proposed implementation, we successfully removed the background and add any other desired background in real time with FPS more than 30.

Fig. 2. Removal of background in real time.

Fig. 2. shows that the left half of the image has normal real-time video with backgroundand the right side has video with no background with FPS 34.
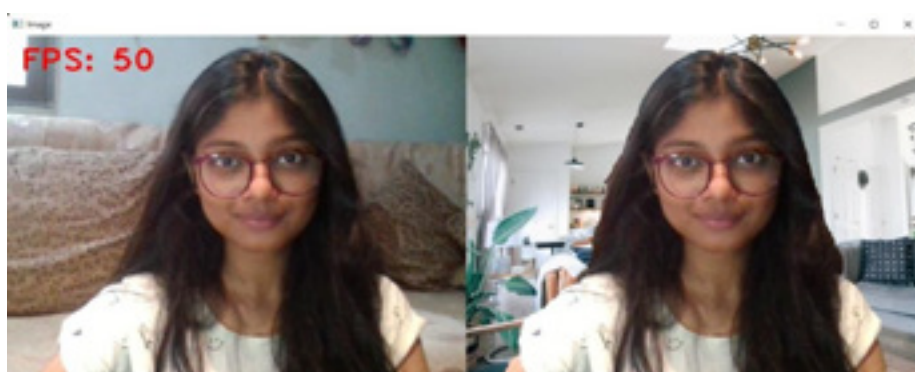

Fig. 3. Background changed in real time successfully with FPS = 50.

Fig. 3. shows that left side of the image has normal real-time video, and the right side hasvideo with desired background with FPS 50.
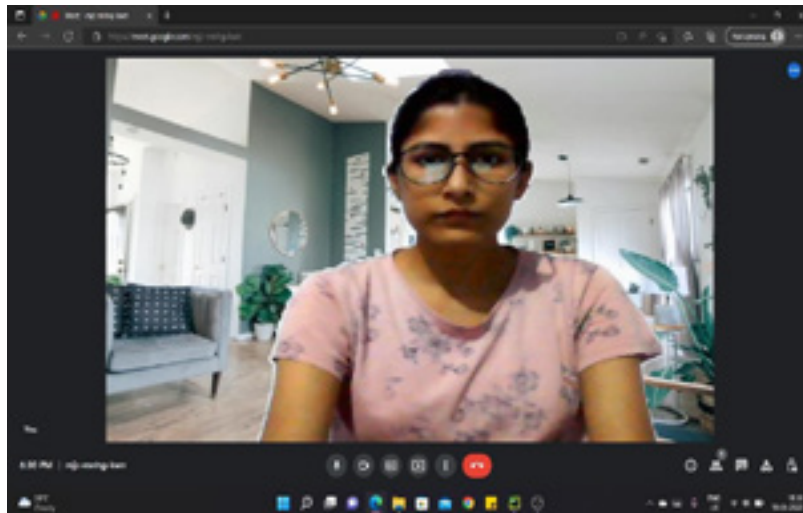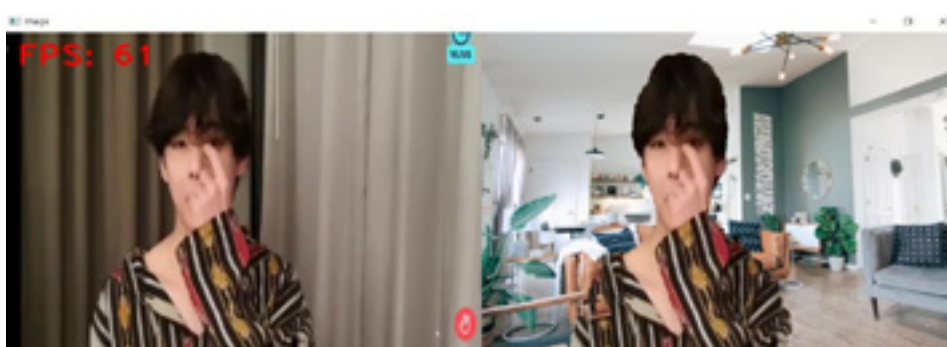

Fig. 4. Background changed of pre-recorded video successfully with FPS= 61.

Fig. 4. shows that left side of the image has normal pre-recorded video, and the right sidehas the video with desired background with FPS 61.

Fig. 5. Background changed in real time successfully on Google Meet.

Fig. 5. shows that we were able to change the background of our live video in a Google meet.

Fig. 6. Background changed in real time successfully and able to configure in Google Meet.

Fig. 6. shows that we were able to change the background of our live video as well as configure the features such as brightness, contrast, saturation, etc. of our real time videoin a Google meet.

4. CONCLUSION

We have implemented a computer-vision based system to remove the background from a video in real-time which enabled creating a professional background when not in a very professional environment. Our goal was to create solution for removing background in real time while also maintaining the quality of the call, having the additional benefit of adding custom backgrounds and enabling users to add effects like adjust lighting, contrast etc. We used *SelfieSegmentation* module of *Mediapipe* in this implementation. Our results shows that our technique successfully removed backgrounds from live videos as well as prerecorded videos at frame rate between 30 and 60. We also changed background of videos in reals time and prerecorded videos seamlessly. Our implementation also worked very well on streaming platforms like Google Meet.

REFERENCES

[1] A. ILYAS, M. SCUTURICI AND S. MIGUET, 2009, "Real Time Foreground-Background Segmentation Us - ing a Modified Codebook Model," 2009 Sixth IEEE International

Conference on Advanced Vi -deo and Signal Based Surveillance, pp. 454-459, doi: 10.1109/AVSS.2009.85.

[2] BAOXIN LI AND M. I. SEZAN, 2001, "Adaptive video background replacement," IEEE International Conference on Multimedia and Expo, 2001. ICME 2001., pp. 269-272, doi: 10.1109/IC ME.2001.1237708.

[3] G. SZWOCH, 2014, "Parallel background subtraction in video streams using OpenCL on GPU platforms," 2014 Signal Processing: Algorithms, Architectures, Arrangements, and Applications (SPA), pp. 54-59.

[4] H. LEE, H. KIM AND J. KIM, 2016, "Background Subtraction Using Background Sets With Image- and Color-Space Reduction," in IEEE Transactions on Multimedia, vol. 18, no. 10, pp.2093- 2 103 , doi: 10.1109/TMM.2016.2595262.

[5] JIAN SUN HEUNG-YEUNG, SHUM XIAOOU AND TANG WEIWEI ZHANG, 2009, "Background Removal In A Live Video," Assigned to Microsoft Technology Licensing, LLC.

[6] JONATHON LUITEN, PAUL VOIGTLAENDER AND BASTIAN LEIBE, 2019, "PReMVOS: Proposal-

[7] Generation, Refinement and Merging for Video Object Segmentation" In book: Computer Vision – ACCV 2018 (pp.565-580), DOI:10.1007/978-3-030-20870-7_35

[8] JUANA E. SANTOYO-MORALES AND ROGELIO HASIMOTO BELTRAN, 2014, "Video background

[9] Subtraction in Complex Environments" in Journal of Applied Research and Technology 12(3):527-427, DOI:10.1016/S1665-6423(14)71632-3

[10] R. J. QIAN AND M. I. SEZAN, 1999, "Video Background Replacement without a Blue Screen". Proc. of IEEE International Conference on Image Processing. Kobe, Japan.

[11] RUDOLPH C. BARON, ANDREW R. JONES, MICHEAL M. MASSIMI, KEVIN C. MCCONNELL, 2014, "Background Replacement for Video Conferencing", Application filed by International Business Machines Corp.

[12] S. BRUTZER, B. HÖFERLIN AND G. HEIDEMANN, 2011, "Evaluation of background subtraction techniques for video surveillance," CVPR 2011, pp. 1937-1944, doi: 10.1109/ CVPR.2011.59955 08.

[13] S. JOUDAKI, M. S. BIN SUNAR AND H. KOLIVAND, 2015, "Background subtraction methods in video streams: A review," 2015 4th International Conference on Interactive Digital Media (ICIDM), pp. 1-6, doi: 10.1109/IDM.2015.7516329.

[14] CHALIDABHONGSE, THANARAT & HARWOOD, DAVID & DAVIS, LARRY, 1999, "A statistical approach for real-time robust background subtraction and shadow detection", IEEE ICCV.

[15] THUC TRINH LE, ANDRÉS ALMANSA, YANN GOUSSEAU AND SIMON MASNOU, 2019, "Object removal from complex videos using a few annotations", in Computational Vidual Media 5(3) August 2019, DOI:10.1007/s41095-019-0145-0, Project: Video Inpainting

[16] THUC TRINH LE, ANDRÉS ALMANSA, YANN GOUSSEAU AND SIMON MASNOU, 2018, "Removing objects from videos with a few strokes" in Conference: SIGGRAPH Asia 2018 Technical Briefs, DOI:10.1145/3283254.3283276.

[17] YANNICK BENEZETH, PIERRE-MARC JODOIN, BRUNO EMILE, HÉLÈNE LAURENT AND CHRISTOPHE ROSENBERGER, 2010, " Comparative study of background subtraction algorithms" in Journal of Electronic Imaging 19(3):033003-033003, DOI:10.1117/1.3456695

[18] YI LU AND HONG GUO, 1999, "Background removal in image indexing and retrieval," Proceedings 10th International Conference on Image Analysis and Processing, pp. 933-938, doi: 10.1109/ICIAP.1999.797715.

[19] YIRAN SHEN,WEN HU, MINGRUI YANG AND JUNBIN LIU, 2012, "Efficient background subtraction for tracking in embedded camera networks" DOI:10.1145/2185677.2185698

[20] ZHAO FEI LIV AND JIANG QING WANG, 2014, "Image Background Removal by Contour Feature" in Advanced Materials Research 926-930:3050-3053, DOI:10.4028/ www.scientific.net/ AMR.926-930.3050

/17/

REVIEW ON DEEP LEARNING BASED TECHNIQUES FOR PERSON RE-IDENTIFICATION

Abhinav Parkhi

Reaserch Scholar, Department of Electronics & Telecommunication Engineering, YCCE, Nagpur, (India).

E-mail: abhinav.parkhi@gmail.com

Atish Khobragade

Professor, Department of Electronics Engineering, YCCE, Nagpur, (India).

E-mail: atish_khobragade@rediffmail.com

https://doi.org/10.17993/3ctic.2022.112.208-223

ABSTRACT

In-depth study has recently been concentrated on human re-identification, which is a crucial component of automated video surveillance. Re-identification is the act of identifying someone in photos or videos acquired from other cameras after they have already been recognized in an image or video from one camera. Re-identification, which involves generating consistent labelling between several cameras, or even just one camera, is required to reconnect missing or interrupted tracks. In addition to surveillance, it may be used in forensics, multimedia, and robotics.Re-identification of the person is a difficult problem since their look fluctuates across many cameras with visual ambiguity and spatiotemporal uncertainty. These issues can be largely caused by inadequate video feeds or low-resolution photos that are full of unnecessary facts and prevent re-identification. The geographical or temporal restrictions of the challenge are difficult to capture. The computer vision research community has given the problem a lot of attention because of how widely used and valuable it is. In this article, we look at the issue of human re-identification and discuss some viable approaches.

KEYWORDS

Person re-identification, Supervised Learning, Unsupervised Learning.

1. INTRODUCTION

T The process of Person Re-identification(Re-ID) has been thoroughly studied as a distinct person retrieval problem among non-overlapping cameras [1].Re-goal ID's is to determine whether a person of interest has ever been at a location at a different time that was captured by the same camera at a different time instant or even the same camera placed somewhere else [2].A photograph [3], a video clip [4], or even a written explanation [5] might be used to illustrate the subject.Person Re-ID is essential in smart surveillance technology with substantial academic effect and practical advantage due to the pressing need for community security and the growing number of security cameras.

The procedure of re-ID is difficult because of a variety of camera motions [6], poor picture resolutions [7, 8, 9, 10, 11, heterogeneous modalities [11, 12], complicated camera surroundings, background clutter [12], inaccurate bounding box creation, etc. These provide a lot of variations and uncertainty. Other elements that significantly increase the difficulties for realistic model deployment include the dynamically network of upgraded cameras [13], a massive gallery that offers effective restoration [14], group ambiguity [15], important domain change [16], unknown examining situations [17], and updating a model progressively [18], and changing clothes [19]. Re-ID still presents a problem as a result of these issues. This encourages us to carry out an extensive survey, establish a solid baseline for various Re-ID efforts,

and discuss a wide range of potential future paths. Person Although Re-ID is a difficult process, enhancing the semantic integrity of the analysis depends on it. Re-ID is crucial for programs that make use of single-camera surveillance systems. For instance, to find out if a person regularly visits the same place or if a different person or the same one picks up an abandoned box or bag. In addition to tracking, it has uses in robotics, multimedia, and more well-known technologies like automatic photo labeling and photo surfing [20].It is not difficult to comprehend the Person's Re-ID process. Being human, we always do it with ease. Our sights and minds have been conditioned to locate, identify, and then re-identify things and people in the actual world. Re-ID, which can be shown in Fig. 1, is the idea that a person who has been earlier seen would be identified as soon as they make an appearance using a specific description of the individual.

Even if hand-crafted features had some early success [21] and metric learning [22], the most advanced Re-ID algorithms currently available are constructed using convolutional neural networks (CNNs), which, when trained under supervision, need a significant amount of annotated (labelled) data to learn a stable embedding subspace. Recent deep learning approaches and detailed investigations on person Re-ID utilizing custom systemsprovided in [23], respectively. Large-scale dataset annotation for Re-ID is exceedingly labor intensive, time-consuming, and expensive, especially for techniques needing numerous bounding boxes for each individual to increase accuracy by making generalisations between two separate activities. One-shot learning and unsupervised learning are combined, for instance, in [24] and, which employ the Resnet50 [25] architecture with pre-trained networks on ImageNet [26]. Although it has been empirically demonstrated that pre-training and transfer learning significantly boost neural network performance, they are not appropriate for adjusting parameters across a wide range of domains or topologies. This article highlights the obstacles and unresolved problems in human re-identification and datasets, deep learning algorithms, and current research in these areas.

Figure 1.   Shows an example of a common DL workflow that involves following five stages (i) Data Collection (ii) Bounding Box Generation (iii)Data Annotation (iv) Model Training (v) Validation [67].

2. DEEP LEARNING MODERN RESEARCH

In today's Era, intelligent systems and tech sophisticated automation are the main focuses across a diverse range of domains, including smart cities, e-Health, enterprise intelligence, innovative treatment, cyber security intellectual ability, and many more [27].Particularly when it comes to security technologies as a wonderful approach to disclose complicated data structures in high dimensions, deep learning techniques have substantially improved in terms of effectiveness across a wide range of applications. In order to create intelligent data-driven systems that satisfy current expectations, DL techniques might be extremely important because to their exceptional learning capabilities from past data. DL has the ability to change both the world and how people live since it can automate procedures and learn from mistakes.

3. DEEP LEARNING TECHNIQUES

This section discusses the various deep neural network techniques. These strategies frequently use hierarchical structures with numerous levels of information processing to learn. Among the numerous hidden layers that are frequently observed in deep neural networks are the input and output layers. Reviewing the different training exercises available, that is (i) Supervised, an approach that is challenging and utilizes the use of tagged training data, and (ii) Unsupervised, an approach that examines unlabeled sets of data, is important before diving into the details of DL approaches.

3.1 SUPERVISED OR DISCRIMINATIVE LEARNING NETWORK

The term "supervised learning" refers to a process in which a supervisor doubles as an educator. The technique of instructing or training a computer system using labelled data is known as supervised learning. This suggests that the appropriate response has already been given to the given data. The machine is then given a new collection of examples so that the supervised learning algorithm may examine the training data (set of training examples) and provide an accurate output from labelled data.Discriminative deep architectures are frequently developed to give discriminative capability for pattern classification by modelling the posterior distributions of classes conditioned on observable data [29]. The three main categories of discriminative architectures are Multi-Layer Perceptron (MLP), Convolutional Neural Networks (CNN or ConvNet), Recurrent Neural Networks (RNN), and their variations. Here, we'll briefly discuss these techniques.
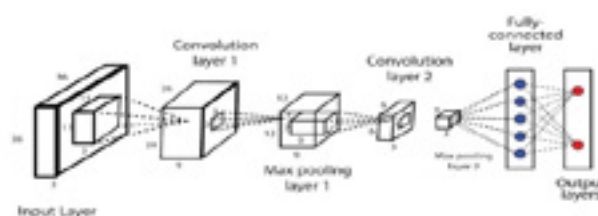
3.1.1 MULTI-LAYER PERCEPTRON (MLP)

The feed-forward artificial neural network known as the Multi-layer perceptron (MLP) [30] is a technique for supervised instruction (ANN). The deep neural network (DNN) or deep learning base architecture are other names for it. Several activation functions, often referred to as transfer functions, including ReLU (Rectified Linear Unit), Tanh, Sigmoid, and Softmax determine an MLP network's output [32].

The most popular technique for training MLP is back-propagation [31], a supervised learning method that is frequently referred to as the fundamental component of a neural network. Throughout the training phase, a variety of optimization techniques are employed liked Stochastic Gradient Descent (SGD), Limited Memory BFGS (L-BFGS), and Adaptive Moment Estimation (Adam).

3.1.2 CONVOLUTIONAL NEURAL NETWORK (CNN)

The commonly used deep learning architecture known as a convolutional neural network [33] was modelled after the visual brain of animals [34]. As seen in fig 2, Originally it had been used extensively for tasks involving object recognition, but it is currently also being investigated in areas such as object tracking [35], pose estimation [36], text detection and recognition [37], visual saliency detection [38], action recognition [39], scene labelling , and many more [40].

Since CNNs are particularly made to control the various 2D forms, they are frequently employed in visual identification, analyze clinical data, segmenting an image, processing language naturally, and many other applications [41].Several CNN versions, including visual geometry group (VGG) [42], AlexNet [43], Xception [44], Inception [45], ResNet [46], etc., may be used in various application sectors depending on their learning capacity.

1.   An illustration of Convolutional Neural Network.

3.1.3 RECURRENT NEURAL NETWORK (RNN)

Using sequential or time-series data, a different well-known neural network provides the result of one stage as input to the following step. The name for this neural network is recurrent neural network (RNN) [47]. Recurrent neural networks, like CNN and feed forward, learn from training input, but they stand out due to their "memory," which enables them to affect current input and output by consulting information from earlier inputs.While an RNN's output is reliant on what came before it in the sequence, a typical DNN assumes that inputs and outputs are independent of one another.However, because to the issue of declining gradients, standard networks with recurrence have difficulty in learning long data sequences. The popular recurrent network versions thatthe problems and perform effectively across a variety of real-life application areas are explored next.

3.1.4 LONG SHORT-TERM MEMORY (LSTM)

LSTMs are frequently used in video-based individual task re-ID and are capable of extracting temporal characteristics. Network for recurrent feature aggregation based on LSTM efficiently reduced interference brought on by background noise, shadowing, and recognition failure [48]. Among the first and shallowest LSTM nodes, it gathered cumulative discriminative characteristics. The temporal and geographical characteristics of the sections that include the probe pictures put were learned by the breakdown of a video sequence into multiple pieces [49]. The number of identical pedestrians in the sample is decreased by using this strategy, which also makes it simpler to identify similarity traits. Both of the aforementioned methods process each video frame independently.The duration of the video sequence typically has an impact on the characteristics that LSTM extracts. The RNN cannotcatch the temporalsignals of small details in the picture because it only creates temporal connections on high-level characteristics [50]. Therefore, research into a more effective technique for extracting spatial-temporal characteristics is still necessary.

3.1.5 GATED RECURRENT UNITS (GRUS)

A popular gating-based variation of the recurrent network techniques to monitor and regulate the flow of information between neural network units is the Gated Recurrent Unit (GRU) [51]. A reset gate and an update gate are all that the GRU has, as seen in Fig. 3, making it less complex than an LSTM.The primary difference between the two devices is the number of gates: an LSTM has three gates compared to a GRU's two (the reset and update gates). The GRU's characteristics allow dependencies from long data sequences to be collected adaptively without removing information from previous portions of the sequence.GRU is a little more compact approach as a consequence, often providing comparable results, and is significantly faster to compute [52].

Figure 3. A Gated Recurrent Unit's Basic Structure with a Reset and Update Gate.

3.2 UNSUPERVISED LEARNING NETWORK

DL approaches are widely used to explain the combined statistical parameters of the available data and the classes that they belong to, as well as the higher predictive properties or features for pattern recognition or synthesis [53].Since the methods under this category include frequently used to learn features or data generation and representation, they are fundamentally utilized for unsupervised learning [54]. Since generative modeling maintains the correctness of the discriminative model, it may be used as a preliminary step for supervised learning tasks as well. For generative learning or unsupervised learning, deep neural network algorithms including the Generative Adversarial Network (GAN), Autoencoder (AE), Restricted Boltzmann Machine (RBM), Self-Organizing Map (SOM), and Deep Belief Network (DBN), as well as its variations, are often utilized.

3.2.1 GENERATIVE ADVERSARIAL NETWORK (GAN)

.GANs make use of neural networks' capacity to train a function that can simulate a distribution as closely as feasible to the real thing. They are particularly capable of producing synthetic pictures with great visual fidelity and do not rely on prior assumptions about the distribution of the data. This important characteristic enables the application of GANs to any imbalance issue in computer vision tasks. GANs give a technique to alter the original picture in addition to being able to create a false image. There are several GANs with different strengths that have been published in the literature to address the imbalance issue in computer vision tasks. For example, a specific type of GANs called AttGAN [55], IcGAN [56], ResAttrGAN [57], etc., is frequently employed for tasks involving modifying face attributes.

GANs are comprised of two neural networks, as shown in Fig. 4. The discriminator D predicts the chance that a following sample will be taken from real data as opposed to data given by the generator G, which generates new data with features similar to the original data.The generator and discriminator in GAN modeling are then instructed to interact with one another.Healthcare, computer vision, data augmentation, video production, voice synthesis, epidemic prevention, traffic control, network security, and many more fields might all benefit from the utilization of GAN networks. In general, GANs have demonstrated to be a solid field of independent data expansion and a solution to problems requiring generative techniques.

2.   Generative Adversarial Networks Framework [58].

3.2.2 AUTO-ENCODER (AE)

A well-known auto-encoder (AE) unsupervised learning approach that makes use of neural networks to learn representations [59]. Data reduction describes the depiction of a set of data.High-dimensional data are often processed using auto-encoders. Three parts make up an autoencoder: an encoder, a code, and a decoder. The encoder creates the code that the decoder uses to reproduce the input by compressing it.Furthermore, generative data models have been learned using the AEs [60].Numerous unsupervised learning techniques, including dimension reduction, extraction of features, useful coding, dynamic modeling, noise removal, outlier or predictive modeling, etc., primarily rely on the auto-encoder. [59, 61]

3.2.3 KOHONEN MAP OR SELF-ORGANIZING MAP (SOM)

Another unsupervised learning method for constructing a low-dimensional (usually two-dimensional) representation of a higher-dimensional data set while preserving the topological structure of the data is the Self-Organizing Map (SOM) or Kohonen Map [62].SOM is a neural network-based method for dimension reduction in clustering [63].We can display huge datasets and identify likely clusters by using a SOM, which constantly moves a dataset's topological layout by bringing its neurons close to the data points inside the dataset.The input layer is the initial layer of a SOM, followed by the output layer, also known as the feature map, is the second layer. SOMs use competitive learning, which makes use of a neighboring function to preserve the topological properties of the input space, in contrast to other neural network models that use error-correction learning, such as Backpropagation with gradient descent [64].Sequence identification, sickness or health diagnosis, fault diagnosis, and virus or parasite attack detection are just a few of the many activities that SOM is frequently employed for [65].The main advantage of using a SOM is that it facilitates the discovery and recognition of patterns in high-dimensional data.

3.2.4 BOLTZMANN MACHINE WITH RESTRICTIONS (RBM)

A generative statistical neural network with the ability to learn a likelihood function over its inputs is the Restricted Boltzmann Machine (RBM) [66].Each node in a Boltzmann machine can be either visible or hidden and is linked to every other node.By understanding how the system functions normally, we can better comprehend anomalies. In RBMs, a subset of Boltzmann machines, there is a limit on the number of linkages between the accessible and deep layers [67].Due to this constraint, training techniques for Boltzmann machines in general can be more effective than those for Boltzmann machines, such as the gradient-based contrastive divergence algorithm [68]. Among the various uses of RBMs are data reduction, categorization, prediction, content-based- based filtering, pattern recognition, subject modelling, and many others.

3.2.5 DEEP BELIEF NETWORK (DBN)

A Deep Belief Network (DBN) [69] is a multiple-layer adaptive visuals model composed of so many unsupervised networks, such as AEs or RBMs, layered one on top of the other and using the hidden layer of each model as the input for the layer below it or connected sequentially.As a result, there are two types of DBNs: AE-DBNs, also called as stacked AE, and RBMDBNs, also known as stacked

RBMs.The AE-DBN consists of autoencoders, whereas Boltzmann machines with constraints constitute RBM-DBN, as was already indicated. The final objective is to create a descriptive divergence-based quicker unsupervised training method for every sub-network [70].The deep structure of DBN allows it to store a hierarchical representation of incoming data.Network architectures for unsupervised feed-forward are trained using unlabeled data as the basic tenet of DBN, and the networks are subsequently fine-tuned using marked input. DBN's potentially significant benefits over traditional shallow learning networks is its capacity to identify specific patterns, with strengthens logic and the ability to distinguish between true and wrong data [71].

Thus, the strategies for generative learning that were previously explored frequently allow us to use research method to build a new set of the data. Deep generative models of these kinds with supervised or discriminative learning methods may benefit from this preparation and to guarantee model correctness because improving classifier generalization through unsupervised representation learning.

4. CHALLENGES AND OPEN ISSUES

The fundamental difficulty with Re-ID is the variance in a person's appearance across multiple cameras. Re-ID is challenging to make self-operating for a variety of reasons.Re-ID networks usually consist of two essential parts:the capture of a unique individual description and the process of comparing two models to see if they match or don't match.The capacity to automatically recognize and track individuals in photos or videos is necessary in order to develop a distinctive person description.Numerous difficulties and problems are apparent, and they will guide future research in the area of person Re-ID.

4.1 RE-ID DEPENDING ON DEPTH

Depth photos capture the bones and contours of the body.Re-ID is made possible by this, which is crucial for applications involving individualized human contact in lighting and clothing variations [88]. In [72], a paradigm based on recurrent attention is put out to solve individual identification based on depth. Convolutional and recurrent neural networks are used to locate tiny, exclusionary localized parts of the body in a reinforcement learning framework.

4.2 RE-ID USING VISIBLE-INFRARED TECHNOLOGY

Visible-Infrared Re-ID handles the cross-modality matching between the noticeable and thermal pictures [88]. Because only infrared cameras can take photographs in low-light conditions, it is essential [73].Along with the cross- modality shared embedding learning [74] also looks into the classifier level discrepancy. Recent methods [75] decrease cross-modality disparity at both the picture and feature level by creating cross-modality person photographs and applying the GAN approach.[76] models the cross-modal reconstruction using a hierarchy elements. [77] presents a dual-attentive aggregate learning strategy to identify multi-level links.

4.3 CROSS-RESOLUTION RE-ID

Taking into consideration the major resolution variations [78], Cross-Resolution Re-ID [88] compares images with different resolutions.The high-resolution human pictures are produced in a cascaded fashion using a cascaded SR-GAN [79], which also incorporates the identification data. The adversarial learning method is used by Li et al. [80] to create representations of pictures that are independent of resolution.

4.4 LABEL NOISE FOR RE-ID

It is typically hard to eliminate label noise when there is an annotation issue [88]. To prevent label overfitting problems, Zheng et al. use a label smoothing algorithm [81]. To effectively learn a Re-ID model while avoiding label noise and the consequences of data with high characteristic ambiguity should be mitigated, a Distribution Net (DNet) is described in [82] that encodes the feature uncertainty.

For each identity, there aren't enough data for powerful Re-ID model training, unlike the generic classification issue [83]. It is also more challenging to learn the potent Re-ID model because of the unidentified new identities.

4.5 MULTI-CAMERA DYNAMIC NETWORK

The constantly updated multi-camera network [84], which necessitates model change for new cameras or probes, is another challenging issue. The Re-ID model may be updated and the representation can be tailored for different probing galleries employing an adaptive learning method with humans in the loop[85]. Active learning was a component of early research on continuous Re-ID in multi-camera networks [86]. [87] Introduces an approach for flexibility to adapt relying on the selective use of limited, non-redundant samples. Utilizing the ideal source camera theory and a geodesic flow kernel serve as the foundation for the development of a transitive inference strategy. An open-world person Re-ID system adds a number of contextual limitations (such Camera Topology) while dealing with large crowds and social interactions[88].

4.6 FEATURE LEARNING

High-level semantic representations of a person's traits, such their hair, gender, and age, can resist several environmental changes. For deep learning-based person Re-ID systems like those in [89], some research has used these traits to fill the gap between the photos and high-level conceptual data. Since it delivered on its predictions, feature recognition is one of the next possibilities.

4.7 ARCHITECTURE FOR AUTOMATED RE-ID

An advanced learning model's architectures must be manually created, which takes time, effort, and is prone to mistakes. The approach of automating architectural engineering, known as neural architecture search (NAS) [90], has recently been applied to address this issue. The study of NAS is currently receiving greater attention. Therefore, one of the essential aspects that must be considered in future research is the use of NAS for person Re-ID activities, as the majority of NAS techniques don't assure that there commended CNN is suitable for person Re-ID tasks.

4.8 ACCURACY VERSUS EFFICIENCY

Large models are typically employed to obtain the greatest accuracy, but they can be time and memory intensive, which reduces their usefulness, particularly when used to mimic real-time video monitoring systems. The majority of modern models did not consider CPU speed and memory capacity into account in order to increase accuracy. Authors who work in these fields must strike acompromise between processing speed and ranking accuracy.

4.9 LIGHTWEIGHT MODEL

The creation of a lightweight Re-ID model is another approach for dealing with the scalability problem. The issue of changing the network topology to create a light model is investigated [91, 92]. Another strategy is to employ model distillation. A system for multi-teacher customizable comparison reduction, for instance, is provided in [93], which in the absence of a primary data source, trains a user-specified lightweight student model from a number of teacher models.

5. DATASETS AND EVALUATION

Individuals' appearances vary greatly depending on Lighting, stances, view angles, scales, and camera resolutions may all vary while using different cameras. Visual ambiguities are further increased by elements like occlusions, a crowded background, and articulated figures. Therefore, it is crucial to gather data that successfully captures these aspects in order to create viable Re-ID approaches. In addition to good quality data that replicates actual circumstances, it is essential to compare and assess the Re-ID methodologies that are developed and find ways to enhance the methodology and databases.

5.1 DATASETS BASED ON IMAGES

Person re-ID using images, there have been a variety of datasets; the most common datasets are listed below.

VIPeR[94]: It is made up of 1,264 photos for 632 people and was taken by 2 non-overlapping cameras.

CUHK01 [95]: It is made up of 3,884 photographs for 971 individuals that were recorded by two separate cameras on a university campus.

Market-1501 [96]: It is comprised of 32,643 photos for each of the 1,501 people that make up the sample, which was taken from the front of a shop using 2 to 6 separate cameras.

DukeMTMC-ReID[97]: The dataset consists of 46,261 photos for 1852 individuals that were captured by 8 non-overlapping cameras on the Duke University campus.

Kinect-REID [98]: It has 71 person sequences that were recorded at the authors' department.

RGBD-ID [99]: There are four groups with various viewpoints, each with the same 80 people. It is produced on several days and has various aesthetic variants.

RegDB[100]: 412 people are represented by 4120 RGB photos and 4120 thermal photographs. Two types of cameras are used to capture them.

SYSU-MM01 [101]: It comprises of 491 people's 15,792 infrared photographs and 287,628 RGB photos. Six cameras, including two infrared cameras and four RGB cameras, are used to capture them from the writers' section.

5.2 DATASETS BASED ON VIDEOS

PRID2011 [102]: It is constituted of 24541 photos for 934 individuals from 600 recordings taken from two separate cameras in an airport's multi-camera network.

iLIDSVID[103]: It is made up of 600 movies shot by 2 non-overlapping airport cameras and 42495 photos for 300 people.

MARS [104]: The greatest video-based individual Re-ID dataset resides in this one. It is made up of around 1191003 photos for 1261 individuals from 200 recordings that were captured by 2 to 6 non-overlapping cameras.

RPIfield [105]: It consists of 601,581 images for 112 individuals, captured by 2 separate cameras on an open field at a college.

5.3 EVALUATION METRICS

Cumulative matching characteristics (CMC) [106] and mean average precision (mAP) are the two mostly used metrics for assessing Re-ID systems [107].

6. CONCLUSION

We have discussed the subject of human re-identification, as well as difficult problems and a summary of recent research in the discipline of person recognition, in this paper. Both closed set and open set Re-ID tasks have been taken into consideration. The approaches employed have been grouped, and their advantages and disadvantages have been covered. Additionally, we have outlined the benefits and drawbacks of the various Re-ID datasets. Popular Re-ID assessment methods are briefly discussed, along with potential expansions.In conclusion, person Re-ID is a broad and difficult field with much of space for growth and research.An effort is made in this work to give a concise overview of the Re-ID problem, its limitations, and related problems.

REFERENCES

(1)   Y.-C. Chen, X. Zhu, W.-S. Zheng, and J.-H.   Lai, "Person reidentification by camera correlation aware feature augmentation," IEEE   TPAMI, vol. 40, no. 2, 2018.

(2)   N. Gheissari, T. B. Sebastian, and R. Hartley,"Person reidentification using spatiotemporal appearance," in CVPR, 2006, pp. 1528–1535.

(3)   J. Almazan, B. Gajic, N. Murray, and D. Larlus,"Re-id done right: towards good practices for person re-identification," arXiv preprint arXiv:1801.05339, 2018.

(4)   T. Wang, S. Gong, X. Zhu, and S. Wang, "Person re-identification by video ranking," in ECCV, 2014.

(5)   M. Ye, C. Liang, Z. Wang, Q. Leng, J. Chen, and J. Liu, "Specific person retrieval via incomplete text description," in ACM ICMR, 2015, pp. 547–550.

(6)   S. Karanam, Y. Li, and R. J. Radke, "Person re-identification with discriminatively trained viewpoint invariant dictionaries," in ICCV, 2015, pp. 4516–4524.

(7)   X. Li, W.-S. Zheng, X. Wang, T. Xiang, and S. Gong, "Multi-scale learning for low-resolution person re-identification," in ICCV, 2015, pp. 3765–3773.

(8)   Y. Huang, Z.-J. Zha, X. Fu, andW. Zhang, "Illumination-invariant person re-identification," in ACM MM, 2019.

(9)   Y.-J. Cho and K.-J. Yoon, "Improving person re-identification viapose-aware multi-shot matching," in CVPR, 2016, pp. 1354–1362.

(10)   H. Huang, D. Li, Z. Zhang, X. Chen, and K. Huang, "Adversarially occluded samples for person re-identification," in CVPR, 2018, pp. 5098–5107.

(11)   A. Wu, W.-s. Zheng, H.-X. Yu, S. Gong, and J. Lai, "Rgb-infrared cross-modality person re-identification," in ICCV, 2017.

(12)   C. Song, Y. Huang, W. Ouyang, and L. Wang, "Mask-guided contrastive attention model for person re-identification," in CVPR, 2018, pp. 1179–1188.

(13)   A. Das, R. Panda, and A. K. Roy-Chowdhury, "Continuous adaptation of multi-camera person identification models through sparse non-redundant representative selection," CVIU, vol. 156, pp. 66–78, 2017.

(14)   J. Garcia, N. Martinel, A. Gardel, I. Bravo, G. L. Foresti, and C. Micheloni, "Discriminant context information analysis for post-ranking person re-identification," IEEE Transactions on ImageProcessing, vol. 26, no. 4, pp. 1650–1665, 2017.

(15)   W.-S. Zheng, S. Gong, and T. Xiang, "Towards open-world person re-identification by one-shot group-based verification," IEEE TPAMI, vol. 38, no. 3, 2015.

(16)   A. Das, R. Panda, and A. Roy-Chowdhury, "Active image pair selection for continuous person re-identification," in ICIP, 2015, pp. 4263–4267.

(17)   J. Song, Y. Yang, Y.-Z. Song, T. Xiang, and T. M. Hospedales, "Generalizable person re-identification by domain-invariant mapping network," in CVPR, 2019.

(18)   A. Das, A. Chakraborty, and A. K. Roy-Chowdhury, "Consistent re-identification in a camera network," in ECCV, 2014, pp. 330– 345.

(19)   Q. Yang, A. Wu, and W. Zheng, "Person re-identification by contour sketch under moderate clothing change." IEEE TPAMI, 2019.

(20) J. Sivic, C.L. Zitnick, R. Szeliski, Finding people in repeated shots of the same scene,Proceedings of the British Machine Vision Conference, 2006, pp. 909–918.

(21) M. Farenzena, L. Bazzani, A. Perina, V. Murino, and M. Cristani. Person re-identification by symmetry-driven accumulation of local features. In 2010 IEEE Computer Society Conference

(22) S. Liao and S. Z. Li. Efficient psd constrained asymmetric metric learning for person re-identification. In 2015 IEEE International Conference on Computer Vision (ICCV), pages 3685–3693, 2015.

(23) Liang Zheng, Yi Yang, and Alexander G. Hauptmann. Person re-identification: Past, present and future. ArXiv, abs/1610.02984, 2016.

(24) Yutian Lin, Xuanyi Dong, Liang Zheng, Yan Yan, and Yi Yang. A bottom-up clustering approach to unsupervised person re-identification. In AAAI, 2019.

(25) Kaiming He, Xiangyu Zhang, ShaoqingRen, and Jian Sun. Deep residual learning for image recognition, 2015.

(26)   J. Deng, W. Dong, R. Socher, L. Li, Kai Li, and Li Fei- Fei. Imagenet: A large-scale hierarchical image database. In 2009 IEEE Conference on Computer Vision and Pattern Recognition, pages 248–255, 2009.

(27) Sarker IH. Data science and analytics: an overview from datadrivensmart computing, decision-making and applications perspective.SN Comput Sci. 2021.

(28) Sarker IH. Machine learning: Algorithms,real-world applications and research directions. SN Computer. Science. 2021;2(3):1–21.

(29) Deng L. A tutorial survey of architectures, algorithms, and applications for deep learning. APSIPA Trans Signal Inf Process. 2014; p. 3.

(30) Pedregosa F, Varoquaux G, Gramfort A, Michel V, ThirionB,Grisel O, Blondel M, Prettenhofer P, Weiss R, Dubourg V, et al. Scikit-learn: machine learning in python. J Mach Learn Res.2011;12:2825–30.

(31) Han J, Pei J, Kamber M. Data mining: concepts and techniques. Amsterdam: Elsevier; 2011.

(32) Sarker IH. Deep cybersecurity: a comprehensive overview from neural network and deep learning perspective. SN Computer.Science. 2021;2(3):1–16.

(33) Ramachandran R, Rajeev DC, Krishnan SG, P Subathra, Deep learning an overview, IJAER, Volume 10, Issue 10, 2015, Pages 25433-25448.

(34)   D. H. Hubel and T. N. Wiesel, Receptive fields and functional architecture of monkey striate cortex, The Journal of physiology, 1968.

(35) J. Fan, W. Xu, Y. Wu, and Y. Gong, Human tracking using convolutional neural networks, Neural Networks, IEEE Transactions, 2010.

(36) A. Toshev and C. Szegedy, Deep -pose: Human pose estimation via deep neural networks, in CVPR, 2014.

(37)   M. Jaderberg, A. Vedaldi, and A. Zisserman, Deep features for text spotting, in ECCV, 2014.

(38) R. Zhao, W. Ouyang, H. Li, and X. Wang, Saliency detection by multicontext deep learning, in CVPR, 2015.

(39)   J. Donahue, Y. Jia, O. Vinyals, J. Hoffman, N. Zhang, E. Tzeng, and T. Darrell, Decaf: A deep convolutional activation feature for generic, 2014

(40) Nithin, D Kanishka and Sivakumar, P Bagavathi, Generic Feature Learning in Computer Vision, Elsevier, Vol.58, Pages202-209, 2015.

(41) LeCun Y, Bottou L, Bengio Y, Haffner P. Gradient-based learning applied to document recognition. Proc IEEE. 1998;86(11):2278–324.

(42) He K, Zhang X, Ren S, Sun J. Spatial pyramid pooling in deep convolutional networks for visual recognition. IEEE Trans PatternAnal Mach Intell. 2015;37(9):1904–16.

(43) Krizhevsky A, Sutskever I, Hinton GE. Imagenet classification with deep convolutional neural networks. In: Advances in neural information processing systems. 2012.

(44) Chollet F. Xception: Deep learning with depthwise separable convolutions. In: Proceedings of the IEEE Conference on computer vision and pattern recognition, 2017

(45) [45] He K, Zhang X, Ren S, Sun J. Deep residual learning for image recognition. In: Proceedings of the IEEE Conference on computervision and pattern recognition, 2016

(46) [46] Szegedy C, Liu W, Jia Y, Sermanet P, Reed S, Anguelov D, Erhan D, Vanhoucke V, Rabinovich A. Going deeper with convolutions.In: Proceedings of the IEEE Conference on computer vision and pattern recognition, 2015.

(47) Dupond S. A thorough review on the current advance of neural network structures. Annu Rev Control. 2019.

(48) Y. Yan, B. Ni, Z. Song, C. Ma, Y. Yan, X. Yang, Person reidentification via recurrent feature aggregation, Proceedings of the European Conference on Computer Vision, 2016.

(49) D. Chen, H. Li, T. Xiao, S. Yi, X. Wang, Video person reidentification with competitive snippet-similarity aggregation and co-attentive snippet embedding, Proceedings of the IEEE Conference on Computer Vision and Pattern Recognition, 2018, pp. 1169– 1178

(50) J. Li, S. Zhang, T. Huang, Multi-scale 3d convolution network for video based person re-identification, Proceedings of the AAAI Conference on Artificial Intelligence, volume 33, 2019, pp. 8618– 8625

(51) Chung J, Gulcehre C, Cho KH, Bengio Y. Empirical evaluation of gated recurrent neural networks on sequence modeling. arXiv preprint arXiv:1412.3555, 2014.

(52) Gruber N, Jockisch A. Are gru cells more specific and lstm cells more sensitive in motive classification of text? Front ArtifIntell. 2020;3:40.

(53) Deng L. A tutorial survey of architectures, algorithms, and applicationsfor deep learning. APSIPA Trans Signal Inf Process. 2014.

(54) Da'u A, Salim N. Recommendation system based on deep learning methods: a systematic review and new directions. Artif Intel Rev. 2020;53(4):2709–48.

(55) He Z, Zuo W, Kan M, Shan S, Chen X. AttGAN: Facial attribute editing by only changing what you want. IEEE transactions on image processing . 2019;28:5464–78.

(56) Perarnau G, van de Weijer J, Raducanu B, Álvarez JM. Invertible Conditional GANs for image editing. Conference on Neural Information Processing Systems . 2016.

(57) Tao R, Li Z, Tao R, Li B. ResAttr-GAN: Unpaired deep residual attributes learning for multi-domain face image translation. IEEE Access . 2019;7:132594–608.

(58) Moacir A. Ponti, Leonardo S. F. Ribeiro, Tiago S. Nazare,Tu Bui, John Collomosse "Everything you wanted to know about Deep Learning for Computer Vision but were afraid to ask" https://www.researchgate.net/publication/322413149

(59)   Goodfellow I, Bengio Y, Courville A, Bengio Y. Deep learning,vol. 1. Cambridge: MIT Press; 2016.

(60)   Liu W, Wang Z, Liu X, Zeng N, Liu Y, Alsaadi FE. A surveyofdeep neural network architectures and their applications. Neurocomputing.2017;234:11–26.

(61)   Zhang G, Liu Y, Jin X. A survey of autoencoder-based recommendersystems. Front Comput Sci. 2020;14(2).

(62)   Kohonen T. The self-organizing map. Proc IEEE.1990;78(9):1464–80.

(63)   [63] Sarker IH, Salah K. Appspred: predicting context-aware smartphone apps using random forest learning. Internet of Things. 2019;8:100106.

(64)   Han J, Pei J, Kamber M. Data mining: concepts and techniques. Amsterdam: Elsevier; 2011.

(65)   Kohonen T. Essentials of the self-organizing map. Neural Netw.2013;37:52–65.

(66)   [66] Marlin B, Swersky K, Chen B, Freitas N. Inductive principles for restricted boltzmann machine learning. In: Proceedings of the Thirteenth International Conference on artificial intelligence and statistics, p. 509–16. JMLR Workshop and Conference Proceedings, 2010.

(67)   Memisevic R, Hinton GE. Learning to represent spatial transformations with factored higher-order boltzmann machines. Neural Comput. 2010;22(6):1473–92.

(68)   Hinton GE, Osindero S, Teh Y-W. A fast learning algorithm for deep belief nets. Neural Comput. 2006;18(7):1527–54.

(69)   Hinton GE. Deep belief networks. Scholarpedia.2009;4(5):5947.

(70)   Hinton GE, Osindero S, Teh Y-W. A fast learning algorithm for deep belief nets. Neural Comput. 2006;18(7):1527–54.

(71)   Ren J, Green M, Huang X. From traditional to deep learning: fault diagnosis for autonomous vehicles. In: Learning control. Elsevier. 2021; p. 205–19.

(72)   A. Haque, A. Alahi, and L. Fei-Fei, "Recurrent attention models for depth-based person identification," in CVPR, 2016, pp. 1229–1238.

(73)   M. Ye, Z. Wang, X. Lan, and P. C. Yuen, "Visible thermal person re-identification via dual-constrained top-ranking," in IJCAI, 2018, pp. 1092–1099.

(74)   M. Ye, J. Shen, and L. Shao, "Visible-infrared person re-identification via homogeneous augmented tri-modal learning," IEEE TIFS, 2020.

(75)   Z. Wang, Z. Wang, Y. Zheng, Y.-Y. Chuang, and S. Satoh, "Learning to reduce dual-level discrepancy for infrared-visible person re-identification," in CVPR, 2019, pp. 618–626.

(76)   S. Choi, S. Lee, Y. Kim, T. Kim, and C. Kim, "Hi-cmd: Hierarchical cross-modalitydisentanglement for visible-infrared person reidentification," in CVPR, 2020, pp. 257–266.

(77)   M. Ye, J. Shen, D. J. Crandall, L. Shao, and J. Luo, "Dynamic dual-attentive aggregation learning for visible-infrared person reidentification," in ECCV, 2020.

(78)   X. Li, W.-S. Zheng, X. Wang, T. Xiang, and S. Gong, "Multi-scale learning for low-resolution person re-identification," in ICCV, 2015, pp. 3765–3773.

(79)   Z.Wang, M. Ye, F. Yang, X. Bai, and S. Satoh, "Cascaded sr-gan for scale-adaptive low resolution person re-identification." in IJCAI, 2018, pp. 3891–3897.

(80) Y.-J. Li, Y.-C. Chen, Y.-Y. Lin, X. Du, and Y.-C. F. Wang, "Recover and identify: A generative dual model for cross-resolution person re-identification," in ICCV, 2019, pp. 8090–8099.

(81) Z. Zheng, L. Zheng, and Y. Yang, "Unlabeled samples generated by gan improve the person re-identification baseline in vitro," in ICCV, 2017, pp. 3754–3762.

(82)   T. Yu, D. Li, Y. Yang, T. Hospedales, and T. Xiang, "Robust person re-identification by modelling feature uncertainty," in ICCV, 2019, pp. 552–561.

(83)   M. Ye and P. C. Yuen, "Purifynet: A robust person reidentification model with noisy labels," IEEE TIFS, 2020.

(84) A. Das, A. Chakraborty, and A. K. Roy-Chowdhury, "Consistent re-identification in a camera network," in ECCV, 2014.

(85) N. Martinel, A. Das, C. Micheloni, and A. K. Roy-Chowdhury, "Temporal model adaptation for person re-identification," in ECCV, 2016.

(86) A. Das, R. Panda, and A. Roy-Chowdhury, "Active image pair selection for continuous person re-identification," in ICIP, 2015.

(87)   A. Das, R. Panda, and A. K. Roy-Chowdhury, "Continuous adaptation of multi-camera person identification models through sparse non-redundant representative selection," CVIU, vol. 15.2017.

(88) Mang Ye, JianbingShen, Gaojie Lin, Tao Xiang, Ling Shao, Steven C. H. Hoi, Deep Learning for Person Re-identification:A Survey and Outlook, IEEE TRANSACTIONS ON PATTERN ANALYSIS AND MACHINE INTELLIGENCE-2021

(89) C. Su, S. Zhang, J. Xing, W. Gao, and Q. Tian, ``Multi-type attributes driven multi-camera person re-identi_cation,'' Pattern Recognit., vol. 75, pp. 77_89, Mar. 2018.

(90) T. Elsken, J. H. Metzen, and F. Hutter, ``Correction to: Neural architecture search,'' in Automated Machine Learning: Methods, Systems, Challenges, F. Hutter, L. Kotthoff, and J. Vanschoren, Eds. Cham, Switzerland: Springer, 2019.

(91) W. Li, X. Zhu, and S. Gong, "Harmonious attention network for person re-identification," in CVPR, 2018, pp. 2285–2294.

(92) K. Zhou, Y. Yang, A. Cavallaro, and T. Xiang, "Omni-scale feature learning for person re-identification," in ICCV, 2019, pp. 3702– 3712.

(93) A. Wu, W.-S. Zheng, X. Guo, and J.-H. Lai, "Distilled person reidentification: Towards a more scalable system," in CVPR, 2019,pp. 1187–1196.

(94) D. Gray, S. Brennan, and H. Tao, ``Evaluating appearance models for recognition, reacquisition, and tracking,'' in Proc. 10th Int. Workshop Perform. Eval. Tracking Surveill. (PETS), vol. 3, 2007, pp. 41_47.

(95) W. Li, R. Zhao, and X. Wang, ``Human reidenti_cation with transferred metric learning,'' in Computer Vision_ACCV (Lecture Notes in Computer Science), vol. 7724. Berlin, Germany: Springer, 2013, pp. 31_44.

(96) L. Zheng, L. Shen, L. Tian, S. Wang, J. Wang, and Q. Tian, ``Scalable person re-identi_cation:Abenchmark,'' in Proc. IEEE Int. Conf. Comput Vis. (ICCV), Dec. 2015, pp. 1116_1124.

(97) E. Ristani, F. Solera, R. Zou, R. Cucchiara, and C. Tomasi, ``Performance measures and a data set for multi-target, multi-camera tracking,'' in Computer Vision_ECCV 2016 Workshops (Lecture Notes in Computer Science), vol. 9914. Cham, Switzerland: Springer, 2016, pp. 17_35.

(98) F. Pala, R. Satta, G. Fumera, and F. Roli, ``Multimodal person re-identification using RGB-D cameras,'' IEEE Trans. Circuits Syst. Video Technol., vol. 26, no. 4, pp. 788_799, Apr. 2016.

(99) I. B. Barbosa, M. Cristani, A. Del Bue, L. Bazzani, and V. Murino,``Re-identi_cation with RGB-D sensors,'' in Compute Vision_ECCV2012. Workshops and Demonstrations, A. Fusiello, V. Murino, andR. Cucchiara, Eds. Berlin, Germany: Springer, 2012, pp. 433_442.

(100) D. T. Nguyen, H. G. Hong, K. W. Kim, and K. R. Park, ``Person recognition system based on a combination of body images from visible lightand thermal cameras,'' Sensors, vol. 17, no. 3, p. 605, 2017.

(101) A.Wu,W.-S. Zheng, H.-X. Yu, S. Gong, and J. Lai, ``RGB-infrared crossmodality person re-identi_cation,'' in Proc. IEEE Int. Conf. Comput. Vis. (ICCV), Oct. 2017.

(102) M. Hirzer, C. Beleznai, P. M. Roth, and H. Bischof, ``Person re-identification by descriptive and discriminative classification,'' in Image Analysis (Lecture Notes in Computer Science), vol. 6688. Berlin, Germany:Springer, 2011, pp. 91_102.

(103) T. Wang, S. Gong, X. Zhu, and S. Wang, ``Person re-identification by video ranking,'' in Computer Vision_ECCV, D. Fleet, T. Pajdla, B. Schiele, and T. Tuytelaars, Eds. Cham, Switzerland: Springer, 2014,pp. 688_703.

(104) L. Zheng, Z. Bie, Y. Sun, J.Wang, C. Su, S.Wang, and Q. Tian, ``MARS: A video benchmark for large-scale person re-identi_cation,'' in Computer Vision_ECCV (Lecture Notes in Computer Science), vol. 9910. Cham, Switzerland: Springer, 2016, pp. 868_884.

(105) M. Zheng, S. Karanam, and R. J. Radke, ``RPI_eld: A new dataset for temporally evaluating person re-identi_cation,'' in Proc. IEEE/CVF Conf. Comput. Vis. Pattern Recognit. Workshops (CVPRW), Jun. 2018.

(106) X. Wang, G. Doretto, T. Sebastian, J. Rittscher, and P. Tu, "Shape and appearance context modeling," in ICCV, 2007.

(107) L. Zheng, L. Shen, L. Tian, S. Wang, J. Wang, and Q. Tian,"Scalable person re-identification: A benchmark," in ICCV, 2015,pp. 1116–1124.

/18/

NEAR-LOSSLESS COMPRESSION SCHEME USING HAMMING CODES FOR NON-TEXTUAL IMPORTANT REGIONS IN DOCUMENT IMAGES

Prashant Paikrao

Research Scholar, Department of E&TC, SGGS Institute of Engineering and Technology, Nanded, (India).

E-mail: plpaikrao@gmail.com; 2019pec201@sggs.ac.in

Dharmapal Doye

Professor, SGGS Institute of Engineering and Technology, Nanded, (India).

Milind Bhalerao

Assistant Professor, SGGS Institute of Engineering and Technology, Nanded, (India).

Madhav Vaidya

Assistant Professor, SGGS Institute of Engineering and Technology, Nanded, (India).

https://doi.org/10.17993/3ctic.2022.112.225-237

ABSTRACT

Working at Bell Labs in 1950, irritated with error-prone punched card readers, R W Hamming began working on error-correcting codes, which became the most used error-detecting and correcting approach in the field of channel coding in the future. Using this parity-based coding, two-bit error detection and one-bit error correction was achievable. Channel coding was expanded further to correct burst errors in data. Depending upon the use of the number of data bits 'd' and parity bits 'k' the code is specified as (n, k) code, here 'n' is the total length of the code (d+k). It means that 'k' parity bits are required to protect 'd' data bits, which also means that parity bits are redundant if the code word contains no errors. Due to the framed relationship between data bits and parity bits of the valid codewords, the parity bits can be easily computed, and hence the information represented by 'n' bits can be represented by 'd' bits. By removing these unnecessary bits, it is possible to produce the optimal (i.e., shortest length) representation of the image data. This work proposes a digital image compression technique based on Hamming codes. Lossless and near-lossless compression depending upon need can be achieved using several code specifications as mentioned here. The achieved compression ratio, computational cost, and time complexity of the suggested approach with various specifications are evaluated and compared, along with the quality of decompressed images.

KEYWORDS

Hamming code, Parity, Lossless Compression, Near Lossless Compression, Compression Ratio.

1. INTRODUCTION

Image coding and compression is used mainly for effective data storage and transmission over a network and in some cases for encryption. Image data is also coded for achieving compression to optimize the use of these resources. In digital image compression, depending upon the quality of decompressed image the compression algorithms employed are categorised in the categories like Lossless compression, Lossy compression, and Near-lossless compression. The data redundancy is a statistically quantifiable entity, it can be defined as R_D=1-1⁄CR, where the CR is the compression ratio represents the ratio of number of bits in compressed representation to number of bits in original representation. A compression ratio of 'C' (or 'C':1) means that the original data contains 'C' information bits for every 1 bit in the compressed data. The associated redundancy of 0.5 indicates that 50% of the data in the first data set is redundant. Three primary data redundancies can be found and used in digital image compression i.e. coding redundancy, interpixel redundancy, and psychovisual redundancy. When one or more of these redundancies are considered as a key component for reduced representation of data and accordingly these redundancies are encoded with some method the compression is achieved, Sayood (2017). There is no right or wrong decision when deciding between lossless and lossy image compression techniques. Depending on what suits your application the most, you can choose. Lossy compression is a fantastic option if you don't mind sacrificing image quality in exchange for smaller image sizes. However, if you want to compress photographs without sacrificing their quality or visual appeal, you must choose lossless compression Kumar and Chandana (2009). Based on a knowledge of visual perception, the irrelevant part of the data may be neglected, a lossy compression, includes a process for averaging or eliminating this unimportant information to reduce data size. In lossy compression the image quality is compromised but a significant amount of compression is possible. When the quality of decompressed image and integrity are crucial then lossy compression shouldn't be employed Ndjiki-Nya et.al (2007). Not all images react the same way to lossy compression. Due to the constantly changing nature of photographic images, some visual elements, including slight tone variations, may result in artefacts (unintended visual effects), but these effects may largely go unnoticed. While in line graphics or text in document images will more obviously show the lossy compression artefacts than other types of images. These may build up over generations, particularly if various compression algorithms are employed, so artefacts that were undetectable in one algorithm may turn out to be significant in another. So, in this scenario one should try to bridge the consequences of lossless and lossy compression algorithms. So, the near-lossless compression algorithm should be practiced in case of document images to optimise the compression ratio and the quality of reconstruction Ansari et al. (1998). One of the very famous Error detection and correction technique used in channel coding may be used for the digital image compression Caire et.al (2004) and Hu et.al (2000). In this paper use of Hamming codes with different specifications for various compression algorithms mentioned above is done and the compression is achieved.

2. HAMMING CODES

When the channel is noisy or error-prone, the channel encoder and decoder are crucial to the overall encoding-decoding process. By adding a predetermined amount of redundancy to the source encoded data, it is possible to minimize the influence of channel noise. As the output of the source encoder is highly sensitive to transmission noise, it is based on the principle that enough controlled redundant bits must be added to the data being encoded to guarantee that a specific minimum number of bits will change during the transmission. Hamming demonstrated, showed that all single-bit errors can be detected and corrected if 3 bits of redundancy are added to a 4-bit code word, providing the Hamming distance between any two valid code words 3 bits. The 7-bit Hamming (7, 4) code word P1, P2, D3, P4, D5, D6, D7 for a 4-bit binary number b1,b2,b3,b4≅D3,D5,D6,D7 padded with parity bits p1,p2,p3≅P1,P2,P4 .
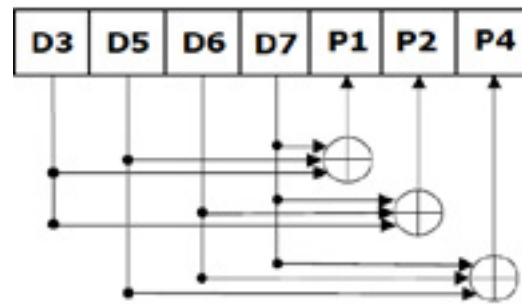
Fig. 1. Hamming Code

2.1. ERROR DETECTION

One of the most popular hamming code specifications used is (7,4); here 7 is total length of codeword and 4 is number of data bits.

Here (n-k) i.e., 7-4 =3 parity bits are used to encode 4-bit message to detect one bit error and correct one bit error.

In the following example, the first step of algorithm is to identify the position of the data bits and parity bits. All the bit positions at powers of 2 are marked as parity bits (e.g., 1, 2, 4, 8). Given below is the structure of 7-bit hamming code.

Here a data "0 1 0 1" is encoded using (7,4) even parity hamming code and an error is introduced in the fifth (D5) bit.

P1	P2	D3	P4	D5	D6	D7
1	1	0	1	1	0	1

Three parity checks and needed to be considered to determine whether there are any errors in the received hamming code.

Check 1: Here the parity of bits at position 1,3,5,7 should be verified

P1	D3	D5	D7
1	0	1	1

It is observed that the parity of above codeword is odd, it is concluded that the error is present and check1 is failed.

Check 2: Here the parity of bits at position 2,3,6,7 should be verified

P2	D3	D6	D7
1	0	0	1

It is observed that the parity of above codeword is even, then we will conclude the check2 is passed.

Check 3: Here the parity of bits at position 4,5,6,7 should be verified

P4	D5	D6	D7
1	1	0	1

It is observed that the parity of above codeword is odd, it is concluded that the error is present and check3 is failed.

So, from the above parity analysis, check1 and check3 are failed so we can clearly say that the received hamming code has errors.

2.2. ERROR CORRECTION

They must be repaired because it was discovered that the received code contains an error. Use the next few steps to fix the mistakes:

The error checks word has become:

check1	check2	check3
1	0	1

The error is in the fifth data bit, according to the decimal value of this error-checking word, which was calculated as "1 0 1" (the binary representation of 5). Simply invert the fifth data bit to make it correct.

So, the correct data will be:

P1	P2	D3	P4	D5	D6	D7
1	1	0	1	0	0	1

In the same fashion other specifications of code like (3,1), (6,3), (7,3), and so on can be implemented and error detection and error correction of messages using the parity bits can be accomplished. There has never been a way for error checking and correcting that is more effective than Hamming codes, so, it is still widely used channel encoding. It offers an effective balance between error detection and correction, in addition to that one may verify its application in data compression field, which is being discussed in the next topic.

3. PROPOSED WORK

The document image compression, if various logical regions of the document image are segmented and appropriate compression algorithm is used for those regions, then the trade-off between compression ratio and the quality of decompressed image may be resolved a bit. Lossy compression techniques for photographs, Near-lossless compression for Figures, Tables and other text-like important regions, and Lossless compression for the Text contents Shanmugasundaram *et.al* (2011).

3.1. THE EXISTING LOSSLESS ENCODING ALGORITHM

   i. Reshaping: 2D to 1D conversion of image data

   ii. Resizing: Divide the data in terms of 7-bit chunks

   iii. Checking Hamming encodability of newly formed chunks; valid and invalid hamming codes (7,4)

   iv. Lossless Encoding of data

   v. beginning with '0'+codeword (7 bit), if the chunk is invalid codeword

   vi. beginning with '1'+encoded codeword (4 bit), if the chunk is valid codeword

   vii. If the size of the coded data is smaller than the input data, then compression is achieved.

The following algorithms are the step by step modification in the existing work of Hu *et.al* (2000). Here, the near-lossless encoding algorithm based on the idea of bit plane slicing is presented as Algorithm 1. It is presumptive that the least significant bit (LSB) in an image contains the least

significant information, and that if this information is removed from a gray-level image, a little visual degradation will be caused.

3.2. ALGORITHM 1: BIT PLANE SLICING BASED LOSSY ENCODING

i.   Perform bit-plane slicing: remove LSB (assuming that LSB plane consists of least information)
ii.   Reshaping: 2D to 1D conversion of image data
iii. Resizing: Divide the data in terms of 7-bit chunks
iv.   Checking Hamming encodability of new chunks; valid and invalid hamming codes (7,4)
v.   Lossless Encoding of data
vi.   beginning with '0'+codeword (7 bit), if the chunk is invalid codeword
vii. beginning with '1'+encoded codeword (4 bit), if the chunk is valid codeword
viii. If the size of the coded data is smaller than the input data, then compression is achieved.

The second approach, which also uses (8,4) Hamming codes for lossless compression, has the additional capability of detecting and correcting error in the eighth bit, which is set or reset based on the even or odd parity of the entire 7-bit codeword in (7,4) variant. This technique offers the lossless compression in addition to the additional 1-bit detection and correction capabilities.

3.3. ALGORITHM 2: LOSSLESS ENCODING USING (8,4) HAMMING CODE SPECIFICATION

i.   Reshaping: 2D to 1D conversion of grey image data
ii.   Checking Hamming encodability of newly formed chunks; valid and invalid hamming codes (8,4)
iii. Lossless Encoding of data
iv.   beginning with '0'+codeword (8 bit), if the chunk is invalid codeword
v.   beginning with '1'+encoded codeword (4 bit), if the chunk is valid codeword
vi.   If the size of the coded data is smaller than the input data, then compression is achieved.

It is computationally expensive to scan the complete image to determine if the codewords (its grey levels) are valid or invalid hamming codewords. Therefore, a novel technique for eliminating this avoidable routine is being tested, which involves discovering the valid codewords beforehand and simply classifying image gray-levels as valid or invalid codewords by comparing with them. This process is similar to quantization but here the quantization levels are neither equidistant nor generated by some programming language function. Even though this quantization inevitably results in information loss, the compression ratio will be improved Li *et.al* (2002). These quantized gray-levels offers spectral compression at the same time the probabilities of the resultant gray-levels also get changed. The image with changed gray-level probabilities is further feed to probability-based coding like Huffman's coding and added compression is achieved Jasmi *et.al* (2015) and Huffman (1952). The algorithms 3 is subsequently modified in algorithm 4 and 5 using (8,4) code for lossless compression with 16 and 32 quantization levels respectively. After the successful compression and decompression, the quality of decompressed image using quantization approach is computed based on the parameters like Correlation of input output images Dhawan (2011), its Mean Squared Error (MSE), Signal to Noise Ratio (SNR), Structural Similarity Index Metric (SSIM) to compute the retainment of structural properties of the input images, Compression Ratio (CR) achieved and the Computational Time (CT).

3.4. ALGORITHM 3: FAST NEAR-LOSSLESS ENCODING USING (7,4) HAMMING CODE SPECIFICATION AND QUANTIZATION

i.   Reshaping: 2D to 1D conversion of image data
ii.   Perform bit-plane slicing: remove LSB (considering that it LSB plane consists of the least information) OR
      Resizing: Divide the data in terms of 7-bit chunks

iii.   Identify the '16' valid codewords and enlist them in an array valcod
iv.   valcod = [0 15 22 25 37 42 51 60 67 76 85 90 102 105 112 127]
v.   Lossy step: Quantize the entire image pixels to grey levels in valcod variables
vi.   If size of coded data is smaller than input data, then compression is achieved.

3.5. ALGORITHM 4: FAST NEAR-LOSSLESS ENCODING USING (8,4) HAMMING CODE SPECIFICATION AND 16 LEVEL QUANTIZATION

i.   Reshaping: 2D to 1D conversion of image data
ii.   Identify the '16' valid codewords and enlist them in an array valcod16
iii.   Valcod8 = [0 15 51 60 85 90 102 105 150 153 165 170 195 204 240 255]
iv.   Lossy step: Quantize the entire image pixels to grey levels in valcod16 variables
v.   If size of coded data is smaller than input data, then compression is achieved.

3.6. ALGORITHM 5: FAST NEAR-LOSSLESS ENCODING USING (8,4) HAMMING CODE SPECIFICATION AND 32 LEVEL QUANTIZATION

i.   Reshaping: 2D to 1D conversion of image data
ii.   Identify the 'total 32' valid even, odd conjugate codewords along-with its complements and enlist them in an array valcod32
iii.   valcodeoc = [0 15 23 24 36 43 51 60 66 77 85 90 102 105 119 129 136 142 150 153 165 170 178 189 195 204 212 219 231 232 240 255]
iv.   Lossy step: Quantize the entire image pixels using the 32 grey-levels in valcod32 variable
v.   If the size of the coded data is smaller than the input data, then compression is achieved.

4. RESULTS

The experimentation carried out on a dataset consisting of three classes of images like graphs, diagrams, and equations, which are the text-like regions in the document image. As discussed above the existing Hamming code-based algorithms is implemented and executed over the dataset. Performance of these algorithms is evaluated by means of the performance metrics like compression ratio and computation time. The algorithms are implemented using MATLABR2020b software on a 64-bit, 2.11 GHz processor with 8 GB RAM computer system. The algorithm offers compression generally but, in some times, (4/30) it failed to achieve the compression. The average compression ratio achieved is 1.2 : 1, which is not significant considering the computation cost of the algorithm. The regular scanned document takes computation time up to 10 min. So, the images in the dataset are resized to 512 X 512 pixel size and further computation time is observed. For this size of images, the computation time results 21.30 sec./ image. This time is also higher considering the size of image. To improve the CR and minimizing the computation cost the bit-plane slicing based lossy compression algorithm (Algorithm 1) is proposed, it has enhanced the CR a bit and the CT is also halved. Further to avoid information loss a (8,4) and need of image resizing, the Hamming code-based algorithm (Algorithm 2) is tested. It further enhanced the CR but the CT once again increased up to original algorithm. This performance of mentioned algorithms is presented using Table 1 below.

Table 1. Comparison of purely Hamming code-based algorithms based on CR and CT.

Sr. No.	Algorithm	CR (CR:1)	CT (sec/ image)
1	Algorithm 0	1.20	21.30
2	Algorithm 1	1.24	10.32
3	Algorithm 2	1.29	19.15

As both the parameters CR and CT offered by these algorithms are not attractive, the quantization-based algorithms (Algorithm 3, Algorithm 4, and Algorithm 5) are proposed, avoiding traversing throughout the image for checking the validity of codewords. These algorithms have achieved the significant CR along with 100 times less CT. The quality of decompressed image using quantization approaches is computed based on the parameters like Correlation of input output images, its Mean Squared Error, Signal to Noise Ratio, Structural Similarity Index Metric to compute the retainment of structural properties of the images, Compression Ratio achieved and the Computational Time. The results are presented in Table 2.

Table 2. Comparison of quantization-based algorithms.

	Algorithm 3	Algorithm 4	Algorithm 5
Correlation (0-1)	0.9420	0.9629	0.9658
MSE (bits/image)	11.22	37.80	12.13
PSNR (Ratio)	39.19	33.22	39.17
SSIM (0-1)	0.9295	0.9308	0.9519
CR (CR:1)	3.04	3.31	3.31
CT (sec/image)	0.2575	0.1132	0.1314

It can be observed from the above table that Algorithm 5 performs better than others considering the mentioned parameters except MSE and CT; the MSE of algorithm 3, that is less 1 bit/image lesser than Algorithm 5 and CT of Algorithm 4 is least, that is about 0.02 sec lesser than Algorithm 5. The Correlation and SSIM offered by this algorithm are highest, which is very significant while proposing the near-lossless algorithm. The performance of quantization-based approach computed over mentioned three classes using the image quality metrics discussed is presented below. The average values for these classes are shown to get overall idea about performance of algorithm.

4.1. CORRELATION

The 2D correlation between the input image and the decompressed result is calculated, it ranges from 0-1, where value '1' represent that both the images are identical. The values near to '1' signifies the near-lossless compression. The performance is displayed using Fig. 2.
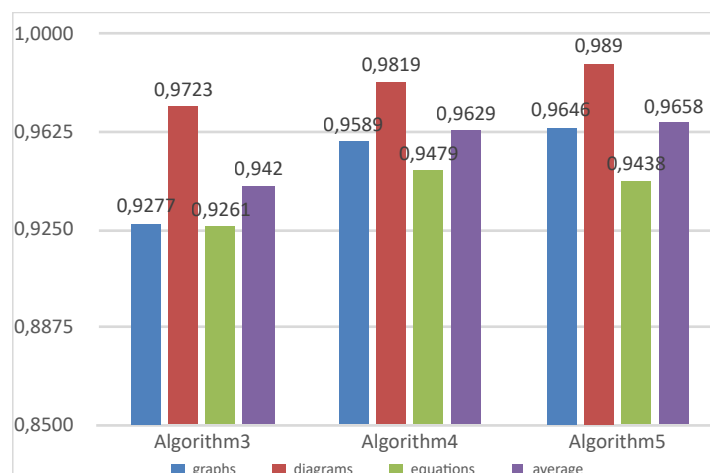
Fig. 2. Comparison of algorithms based on Correlation.

4.2. MSE

The most used estimator of image quality is MSE refers to the metric giving cumulative squared error between the original and compressed image. Near zero values are desirable. The performance is displayed using Fig. 3.
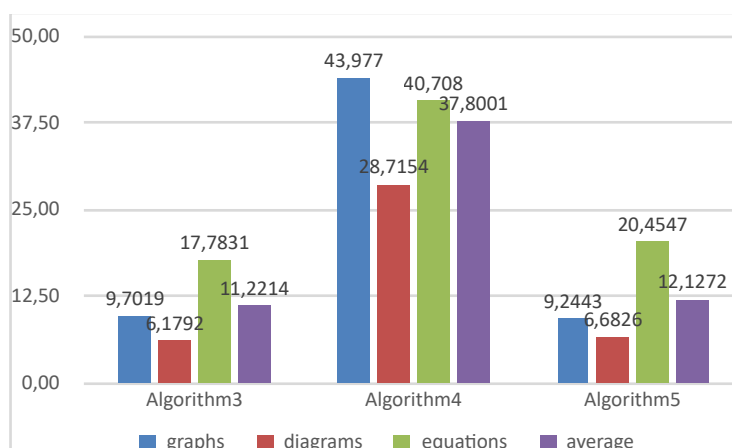

Fig. 3. Comparison of algorithms based on MSE.

4.3. PSNR

The Peak Signal to Noise Ratio is positive indicator of performance of compression algorithms. The performance is displayed using Fig. 4, here the Algorithm 5 offers the highest PSNR value, which is a good indicator of its applicability.
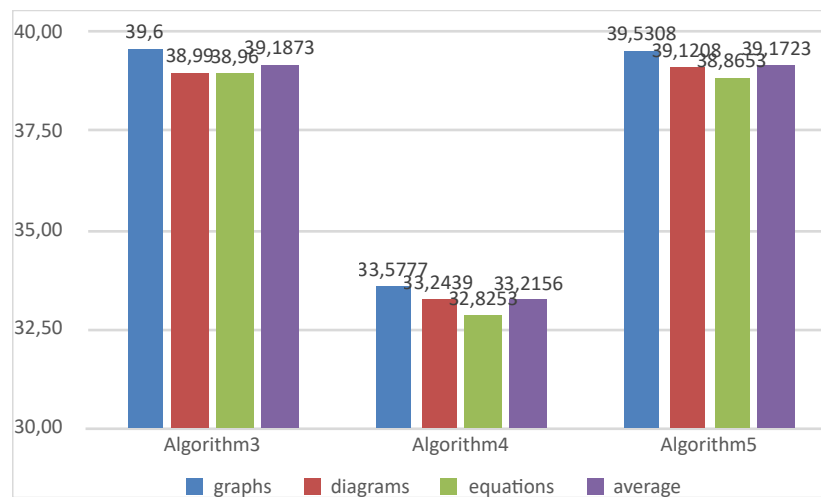
Fig. 4. Comparison of algorithms based on SNR.

4.4. SSIM

The Structural Similarity Index Measure (SSIM), a perception-based measure, considers image degradation as a perceived change in structural information. These techniques differ from others like Mean Squared Error (MSE) and Signal to Noise Ratio that include evaluate absolute errors (SNR). According to the theory behind structural information, pixels are highly interdependent, when they are spatially close to one another. These dependencies carry important details about how the elements in an image are arranged. In our experimentation Algorithm 5 has the highest SSIM, which is another good indicator of the quality of a compression algorithm. The performance is displayed using Fig. 5.
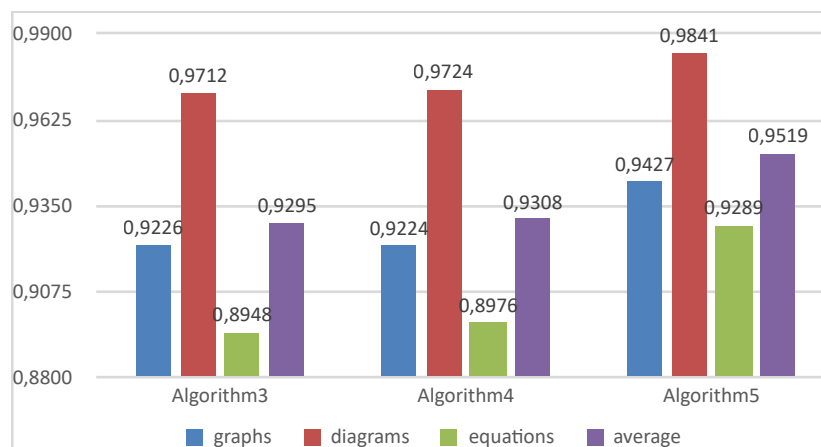
Fig. 5. Comparison of algorithms based on SSIM.

4.5. COMPRESSION RATIO

Here, the average compression ratio for the considered images, ranges from 3.04 : 1 to 3.31 : 1, algorithm 5   having the highest value and algorithm 3 having the lowest. The compression ratio is a useful indicator of decompression effectiveness, the higher value indicates a better algorithm. The performance is displayed using Fig.6.
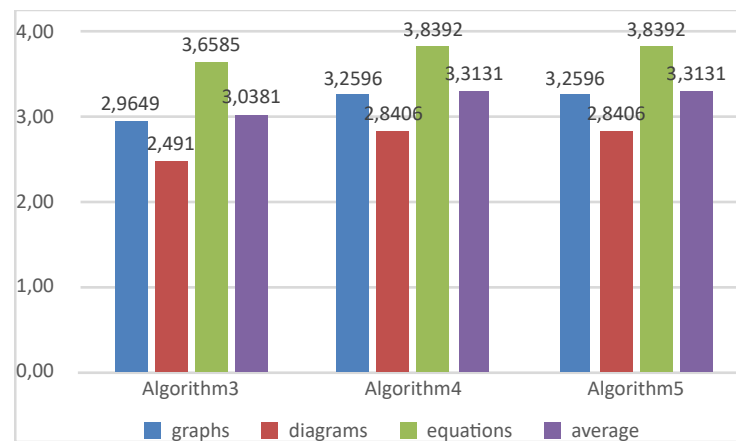
Fig. 6. Comparison based on Compression Ratio.

4.6. COMPUTATION TIME

Finally, computational time is used to study the time complexity of the algorithm; in this case, Algorithm 4 tends to be the most efficient and requires the least amount of time. The performance is displayed using Fig. 7.
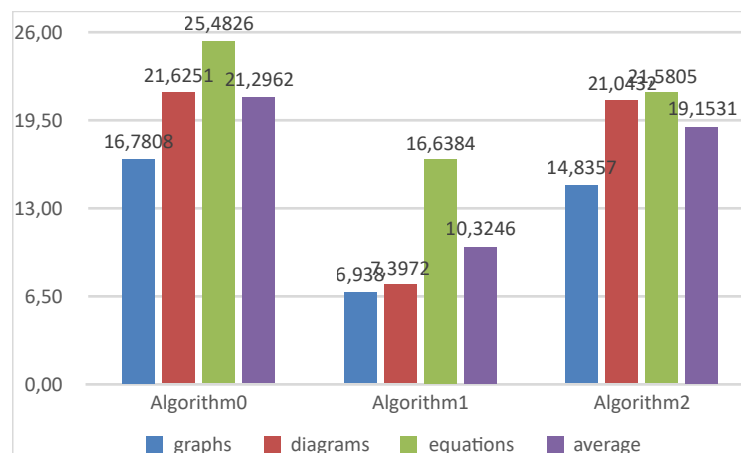
Fig. 7. Comparison based on Computation Time.

Algorithm 5 having highest CR, executes faster and performs better in terms of quality of decompressed image. So, one can conclude that the Algorithm 5 tends to the most optimized algorithm for Near-lossless compression of Document Images.

5. CONCLUSIONS

Compression offers an attractive option for efficiently storing large amounts of data. Document Images are multi-tone images, separate algorithm for different regions may improve the compression outcomes. Lossy algorithms are best for regions like photographs, lossless are necessary in case of sensitive regions like text and the non-textual but text consisting important regions like figures, plots and equations needed to be treated with near-lossless techniques. They are advantageous for maintaining the trade-off between compression ratio and quality of reconstructed image. In this work the channel coding algorithm like Huffman codes is implemented with its different specifications, the work is further optimized based on time complexity and quality of decompressed image. Considering the higher Correlation, PSNR and SSIM values obtained, one can understand that the quality of the decompressed images is really good, and the algorithms can be considered as near-lossless algorithms. It is also concluded that the (8, 4) Hamming code with even and odd conjugate complementary codes and based 32 quantization levels works best amongst the other discussed.

6. FUTURE SCOPE

After observing the performance of various hamming code-based algorithms, one may be encouraged to practice them and do some modification. So, the first thing that may be tried is to make use of (3,1) and (4,1) specifications of Hamming code. Further, after the quantization to newly achieved gray levels is done, one can implement probability-based coding scheme like Huffman or Arithmetic codes to represent the data more effectively.

REFERENCES

[1] Ansari, Rashid, Nasir D. Memon, and Ersan Ceran. "Near-lossless image compression techniques." Journal of Electronic Imaging 7, no. 3 (1998): 486-494.

[2] Caire, Giuseppe, Shlomo Shamai, and Sergio Verdú. "Noiseless data compression with low-density parity-check codes", DIMACS Series in Discrete Mathematics and Theoretical Computer Science 66, 263-284, (2004).

[3] Hu, Yu-Chen, and Chin-Chen Chang, "A new lossless compression scheme based on Huffman coding scheme for image compression", Signal Processing: Image Communication 16.4, 367-372, (2000).

[4] Sampath Kumar, Chandana, "Comparative Study of Lossless Compression Scheme Based on Huffman Coding for Medical Images", Recent Trends in Science & Technology, (2009).

[5] Shanmugasundaram, Senthil, and Robert Lourdusamy. "A comparative study of text compression algorithms." International Journal of Wisdom Based Computing, no. 3,68-76 (2011).

[6] Li, Robert Y., Jung Kim, and N. Al-Shamakhi. "Image compression using transformed vector quantization." Image and Vision Computing 20, no. 1 (2002): 37-45.

[7] Dhawan, Sachin. "A review of image compression and comparison of its algorithms." International Journal of Electronics & Communication Technology, IJECT 2, no. 1 (2011): 22-26.

[8] Jasmi, R. Praisline, B. Perumal, and M. Pallikonda Rajasekaran. "Comparison of image compression techniques using huffman coding, DWT and fractal algorithm." In 2015 International Conference on Computer Communication and Informatics (ICCCI), pp. 1-5. IEEE, 2015.

[9] Pandya, M. K. "Data compression: efficiency of varied compression techniques." Formal Report, Brunel University (2000).

[10] Huffman, David A. "A method for the construction of minimum-redundancy codes." Proceedings of the IRE 40.9, 1098-1101, (1952).

[11] P. Ndjiki-Nya, M. Barrado and T. Wiegand, "Efficient Full-Reference Assessment of Image and Video Quality," 2007 IEEE International Conference on Image Processing, 125-128, (2007).

[12] Sayood, Khalid, "Introduction to data compression", 5th edn. Morgan Kaufmann, (2017).

AUTHORS BIOGRAPHY

Mr. Prashant Laxmanrao Paikrao is Ph.D. Research Scholar in Electronics & Telecommunication Engineering department of SGGSIE&T, Nanded (M.S.), India. He is an active member of IE, ISTE and IETE. His area of interest is Image Processing, Digital Logic Design, Fuzzy Logic.

Dr. Dharmapal Dronacharya Doye is Professor in Department of Electronics & Telecommunication Engineering of SGGSIE&T, Nanded (M.S.), India. He is an active member of IE, ISTE and IETE. His area of interest is Image Processing, Video Processing, Artificial Intelligence.

Dr. Milind Vithalrao Bhalerao is Assistant Professor and Head of Electronics & Telecommunication Engineering Department of SGGSIE&T, Nanded (M.S.), India. He is an active member of ISTE and IETE. His area of interest is Image Processing, Robotics, Artificial Intelligence.

Dr. Madhav Vithalrao Vaidya is Assistant Professor in Information Technology Department of SGGSIE&T, Nanded (M.S.), India. He is an active member of IEEE, ISTE and IETE. His area of interest is Data Mining, Image Processing, Pattern Recognition, Blockchain Technology, and Internet of Things.

/19/

EFFICIENT SYSTEM FOR CPU METRIC VISUALIZATION

Kuldeep Vayadande

Professor, Department of Artificial Intelligence & Data Science, Vishwakarma Institute of Technology, Pune, (India).

Ankur Raut

Student, Department of Artificial Intelligence & Data Science, Vishwakarma Institute of Technology, Pune, (India).

Roshita Bhonsle

Student, Department of Artificial Intelligence & Data Science, Vishwakarma Institute of Technology, Pune, (India).

Vithika Pungliya

Student, Department of Artificial Intelligence & Data Science, Vishwakarma Institute of Technology, Pune, (India).

Atharva Purohit

Student, Department of Artificial Intelligence & Data Science, Vishwakarma Institute of Technology, Pune, (India).

Samruddhi Pate

Student, Department of Artificial Intelligence & Data Science, Vishwakarma Institute of Technology, Pune, (India).

https://doi.org/10.17993/3ctic.2022.112.239-250

ABSTRACT

There are multiple metrics associated with the smooth and efficient working of a computer system. Some of the crucial parts are like the CPU, memory usage and GPUs. For different Operating Systems, they have their own System Software for managing and analysing their sessions. Like Task Manager in Windows, Nmon in Linux and Activity Monitor in Mac. In addition to it, there are few applications software's which perform similar tasks with slight modifications. In this paper, a web application is proposed that will fetch these performance metrics from the user's system and display them using dynamic charts. The proposed application is a system independent tool and can be useful for all operating system. The application also can be used to determine whether or not a game is compatible with the user's system based on the system requirements.

KEYWORDS

CPU Metrics Visualization, Operating Systems, Resource Utilization, System Monitoring, Performance measures.

1. INTRODUCTION

Computer Systems have evolved by leaps and bounds in the last few decades stemming from the introduction of technology trends and improvements. This has paved the way for new architectures and systems with higher and better performance to evolve. It is always a good idea to keep an eye on how much of your resources are being used when working on various chores and projects while having a lot of files, folders, and tabs open on your local system to make sure they don't go over their allotment. Although higher-end computers or workstations rarely have these problems, it may be argued that most typical laptop and PC users must confirm the best use of their resources. The advances in new technology comes with proper analysis and evaluation of the performance metric of the processor. Understanding the performance measure is essential to comprehend the underlying computer organization and bring about modifications based on the different dependent factors. So, there are even various Hardware metrics which are essential and its detailed description helps in getting the insights of our system. Given are few metrics in accordance with Windows Task Manager. Few of them are:

- CPU: CPU's name and model number, speed, number of cores, and accessibility to hardware virtualization features. Additionally, it displays the amount of "uptime" the time since your system's last boot which is another useful statistic.

- Memory: How much RAM you have, how fast it is, and how many of the motherboard's RAM slots are occupied. You can also view the amount of cached material that is currently using your memory. For Windows, this is "standby." Although Windows will instantly clear the cached data and make room if your system requires more RAM for another job, this data will be available and waiting if your system needs it.

- Disc: Your disc driver's name, model number, size, and current read and write speeds.

- Wi-Fi: It displays the name of a network adapter along with its IP addresses (IPv4 and IPv6 addresses).

- GPU: The GPU pane displays different graphs for various activities, such as 3D vs. video encoding or decoding. Due to the GPU's own internal memory, it also displays GPU memory utilization. Here, you may also see the name, model number, and graphics driver version of your GPU.

There are various factors that may affect the system's performance. The instructions used, the memory hierarchy, handling of the input/output all contribute to the computer's performance. The most important parameter is time and is crucial to evaluate the performance of a computer. There are several time-based parameters such as the response time which can be defined as the time taken by the processor to respond after the execution of a particular task, or the throughput which is the total work done for a given time. One such parameter is CPU utilization which is commonly used to understand and evaluate the system performance. It describes the CPU usage for a given time interval as a percentage. It is also an excellent indicator of whether the system has been attacked by a virus or if the system does not have sufficient CPU power. This can be observed in a case when CPU utilization is high (indicating a heavy load) despite there being not many programs running in the background. A computer's RAM is extremely important when it comes to handling tasks and applications. The computer or device is observed to slow down in case there isn't sufficient RAM available. To get the maximum use out of a system, a tool for monitoring these performance parameters to generate logs and allow visualization in the form of graphs is absolutely necessary. Such an application provides other insights about the amount of memory used by a particular program, the availability of the computer's hardware resources and can also be used to force a frozen program. In this paper, another such application is proposed that will help the user view the system information of his device and view certain performance parameters such as CPU Utilization and availability of the RAM. While using applications such as games, the CPU usage (utilization for a given process) can go up as high as 50 or

60 % which may result in overheating of the system, decrease frame rates and even cause system crashes.

Thus, the player must be made aware if the game has system requirements not compatible with his system. A good RAM specification is needed for a smooth experience while playing games. This ensures that there are fewer lags and allows for higher frame rates. RAM usage also depends on the kind of software or game that is being run on the user's device. Hence, this paper also proposes an additional feature that will help determine if the user can run a particular game on his or her device based on his system requirements.

The paper has the following structure, the 'Literature Survey' Section provides a concise overview of the existing literature and tools available for the analysis of CPU metrics, the next section – 'Comparison Table' illustrates the different tables and diagrams used to support the ideas presented in this paper, 'Proposed Work' section discusses the methodology of implementation in detail while the results and outputs are presented in the 'Results and Discussions' section. Finally the paper discusses some aspects of improvement in the future and provides a conclusion outlining the key points of the entire paper.

2.1. LITERATURE SURVEY

Stefanov and Gradskov (2016) monitored and analysed some properties of CPU usage data provided by Linux Kernel. This work analysed CPU usage data provided by the Linux kernel and how CPU load level is calculated based on these data. For every active CPU in the system, the kernel gives the amount of time, measured in 1/100th of a second, that the system spent in different modes of execution since boot. These different modes are 'user mode' (running user processes), 'user mode with low priority' (nice), 'system mode' (running kernel), 'idle', 'iowait' (idle while waiting for IO request to complete), 'irq' (processing interrupts), 'softirq' (processing software interrupts).

Formula for calculating Load Level (L): If 'T^i_m' is the time spent in 'm-th' mode at time moment 'i' then, the CPU load level 'L_m' for the mode m is represented below using Equation (1):

$$L_m = \frac{T^i_m - T^{i-1}_m}{\sum_m (T^i_m - T^{i-1}_m)} \qquad (1)$$

Urriza and Clariño (2021) used Python to web scrape reviews written on 'Steam' website and classifies them into either Audio, Gameplay or Graphics. Further it also categorizes them into Positive, Negative and Neutral sentiments.

Gomes and Correia (2020) Cryptojacking infects the browsers and does CPU intensive computation to mine cryptocurrencies on behalf of cyber criminals. The paper introduces a new Cryptojacking detection mechanism based on monitoring CPU usage of visited web pages. They use machine learning along with monitoring and monitoring the precision and recall values to make a decision. In this Study they used CPU utilization for decking if certain games can be run or not on the computer, similarly here we are utilizing the CPU for detecting cryptojacking. It uses 'mpstat', a command line tool to monitor the CPU. It gives us several metrics such as CPU Utilization at every level, CPU Utilization at user level, CPU Utilization at system level, time that the CPU or CPUs were idle during which the system had an outstanding disk I/O request, time spent by the CPU or CPUs servicing hardware interrupts, time spent by the CPU or CPUs servicing software interrupts, time spent in involuntary wait by the virtual CPU or CPUs while the hypervisor was servicing another virtual processor, time spent by the CPU or CPUs running a virtual processor; time that the CPU or CPUs were idle and the system did not have an outstanding disk I/O request.

"Windows Task Manager" can optimize performance by terminating programmes and processes, changing processing priorities, and setting processor affinity as necessary. Task Manager shows

fundamental performance information and visual representations of CPU, swap file, and memory utilization as a monitoring tool. Disk and network information are also included in later versions of Task Manager.

"Glances - an eye on your system" Glance-Glances is a system monitoring tool for Linux computers, it is used to monitor system resources. Views can show more system information than any other conventional monitor. This comprises disc and network I/O, temperature information—which can reveal the temperatures of the CPU and other hardware—as well as fan speeds and disc utilization by logical volume and hardware device.

"What is system explorer?,System Explorer - Keep Your System Under Control." System Explorer is not only a replacement for task manager, but it is more than that. Additionally, to aiding in process management, it has a number of characteristics that can boost system security and avert disasters. Even a portable version is available for it. It provides great features like calculating the CPU metrics history, taking snapshots and more.

"Can you Run it?" System Requirements Lab is an online platform which provides information about different games and the minimum hardware and software requirements to run them in any local system. The platform also helps you to determine whether the games can run on your current system by comparing the minimum requirements and the local systems information.

2.2. COMPARISON TABLE

Various System Software's and Application Software's with the task of evaluating metrics of a system are discussed in Table 1 below:

Table 1. Comparison of various system monitoring tools.

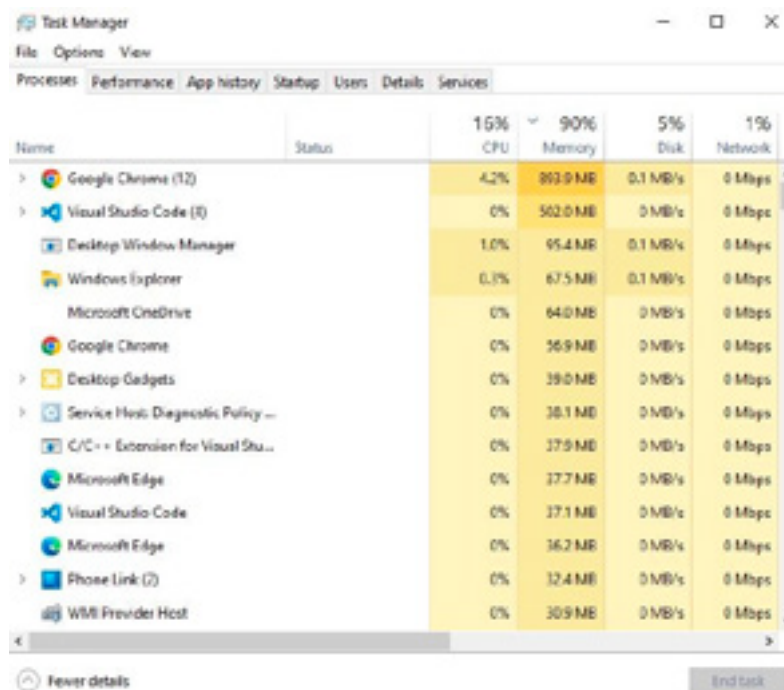| Sr No	System Monitoring Tool	Operating System	Type	Performance Metrics Monitored
1	Task Manager	Windows	System Software	CPU, Memory, Disk, Network
2	Glances	Linux	Application Software	CPU, Memory
3	Process Explorer	Windows	Application Software	Real Time – CPU, GPU, Memory, Disk, Network
4	System Explorer	Windows	Application Software	CPU, Memory

Fig. 1. Task Manager Interface.

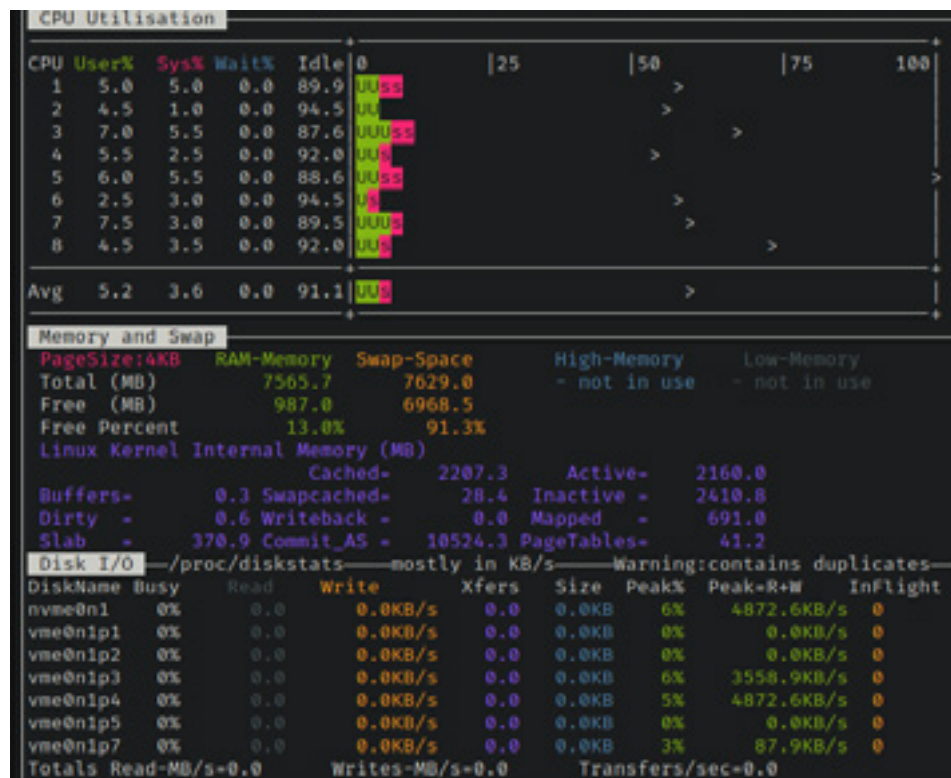Fig. 2. Activity Monitor Interface.

Fig. 3. Nmon Interface.

3. PROPOSED WORK

The need for maintaining and tracking different CPU Metrics is mentioned in this paper. Along with it, various tools which are used to monitor these metrics are described. Similarly, a web-based system for fetching system information and displaying it, has been developed which will be able to provide graphical insights to the performance parameters such as CPU usage, Memory, and GPU. It will be an effective light-weight data visualization tool, so that the history of the parameters can also be recorded.

The website fetches useful system information from the local system with the help of a '.exe' file which the user needs to download and run on the local system. The website displays different static system metrics and visualizes the dynamic information in the form of graphs. There is an additional feature added to the system where the user can check whether a particular application can work on their system or not by comparing the minimum requirements with the local systems information.

Figure 4. below illustrates the process flow diagram of the proposed system and describes the end to end working of the system.
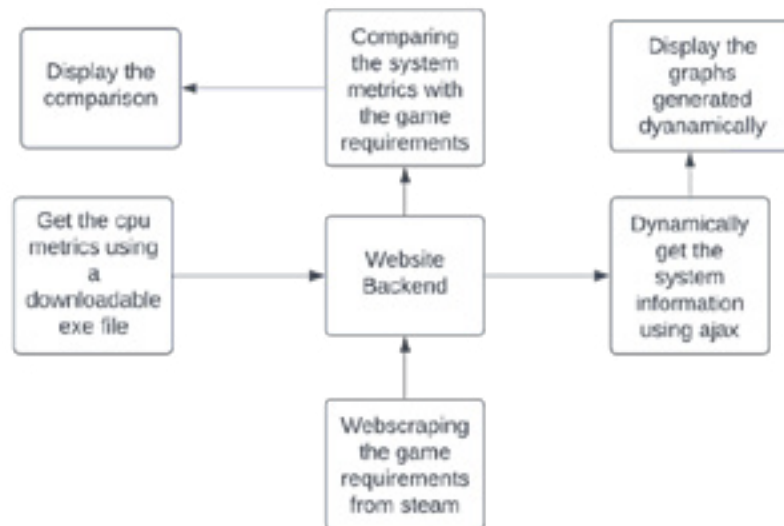
Fig. 4. Flowchart illustrating proposed work.

3.1. METRIC

There are various parameters to monitor the system performance and system resources in a computer system. Some of the most important metrics that affect the system performance are CPU utilization, Used RAM, GPU specifications, System information, etc. The website focuses on fetching the useful system information, displaying it and visualizing dynamic information that updates after every second. The metrics are fetched from the system using the 'psutil', 'wmi' and 'platform' Python libraries. The 'platform' Python library is used to fetch the operating system, node name, operating system release version and processor details. The 'psutil' library is used to retrieve the number of physical and logical cores, CPU utilization and RAM availability of the system. The 'wmi' module fetches the GPU and video RAM details. In order to get the metric from the local system, a '.exe' file is used which sends it to the web server.

3.2. VISUALIZATION

The CPU utilization and RAM availability are dynamic metrics that update after every second, so these metrics are visualized graphically as a line and pie chart. This visualization helps the user to track the systems performance and know how exactly the metrics perform. The graphs are created using the 'Chart.js' library in JavaScript and Ajax to update the graphs in real time.

3.2. SYSTEM REQUIREMENTS SATISFIED OR NOT

'Steam' is used to web-scrape minimum requirements to run games entered by the user. We compare the minimum requirements with the system metrics and warn the user if the requirements are not met by the user's system.

4.RESULTS AND DISCUSSION

Figure 5. shown below is the home page of the website of the proposed idea. It contains a navigation bar with the options – System information, Graphs and the 'Can you Run this game?' feature. The main section of the website contains the button "Download Link". A '.exe' file is downloaded on clicking the button which when executed on the user's device/computer will fetch and display the exact system information of the user's computer/laptop.
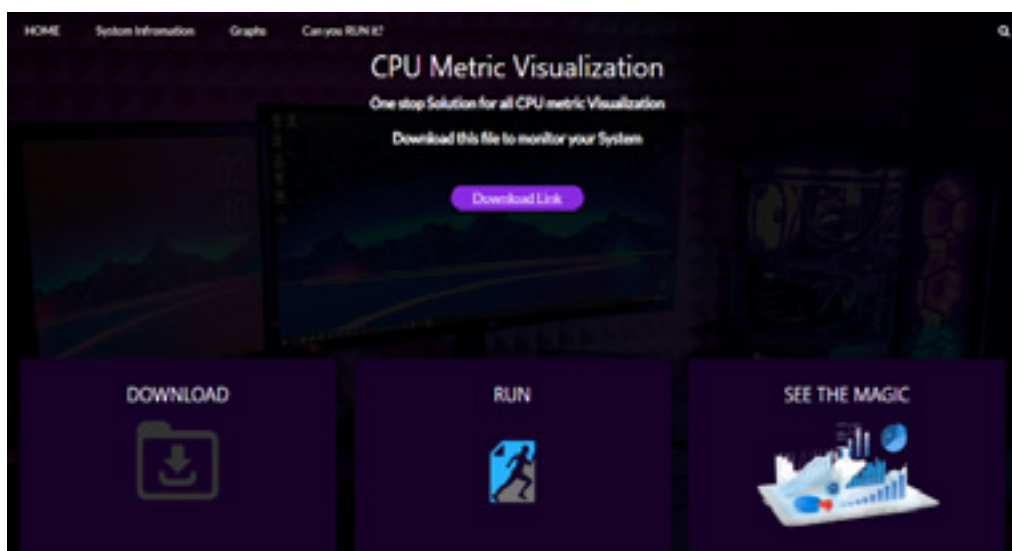
Fig. 5. Home page of the website.

Figure 6. displays the information that is fetched from the user's computer or laptop device and is displayed in a new window. The system information contains the following – NodeName, Version, Machine, Processor, LogicalCore, PhysicalCore, Operating System, Operating System Release and Version, RAM available and lastly the Total Disk Storage Space.
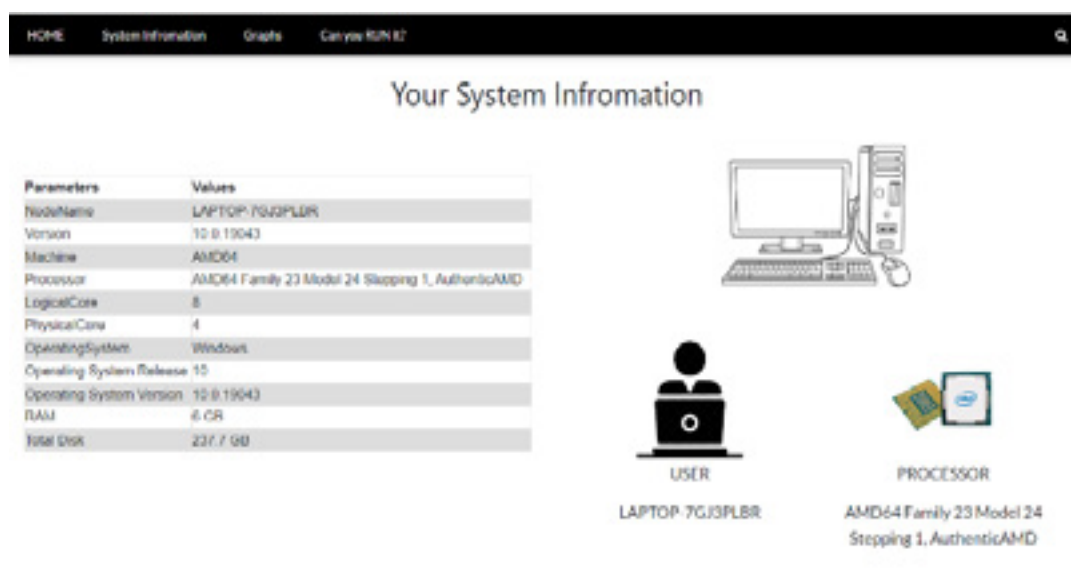

Fig. 6. System information of the user's device.

Table 2. illustrates the actual data fetched from local system in regular intervals. The table contains the CPU Utilization percentage which will be further visualized as a line chart and the RAM usage and availability which are very important in any operating system to perform well.

Table 2. CPU Metrics.

Sr No	Time (in seconds)	CPU Utilization	RAM Used	RAM Available
1	2	31.8	5.96	0.40
2	4	9.4	5.98	0.38
3	6	17.4	5.89	0.51
4	8	12.3	5.84	0.51

Figure 7 (a). and Fig 7 (b). illustrate the CPU Utilization metric and the available RAM dynamically using a line chart and a pie chart respectively. The charts are dynamic in nature and the proposed application fetches real time information about the metrics from the user's system and updates the charts with the new values every second.
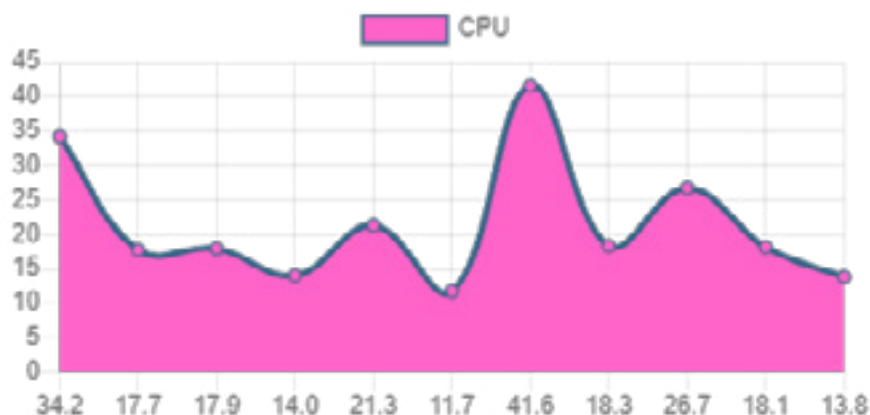
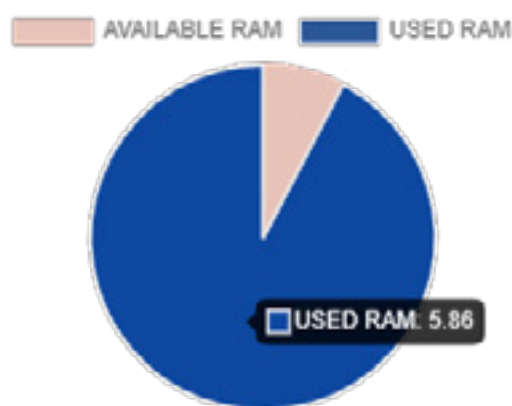**Fig. 7. (a)** CPU Utilization visualized graphically.

Fig. 7. (b) RAM availability visualized graphically.

Another essential feature of the proposed application allows the user to check if a game is compatible with his own system. This feature requires the user to enter the name of the game in the search bar and then displays the required system specification for the same. It also displays the user's system specification and based on the comparison between the two, it displays whether the game will be able to run on the user's system successfully or not.

Figure 8. Shows an example of the game "Watch Dogs" being entered by the user. Based on the comparison between the user's system specifications and the required system specifications for the game, a message "Yes you can run it!" specifies that the game is compatible with the user's system.
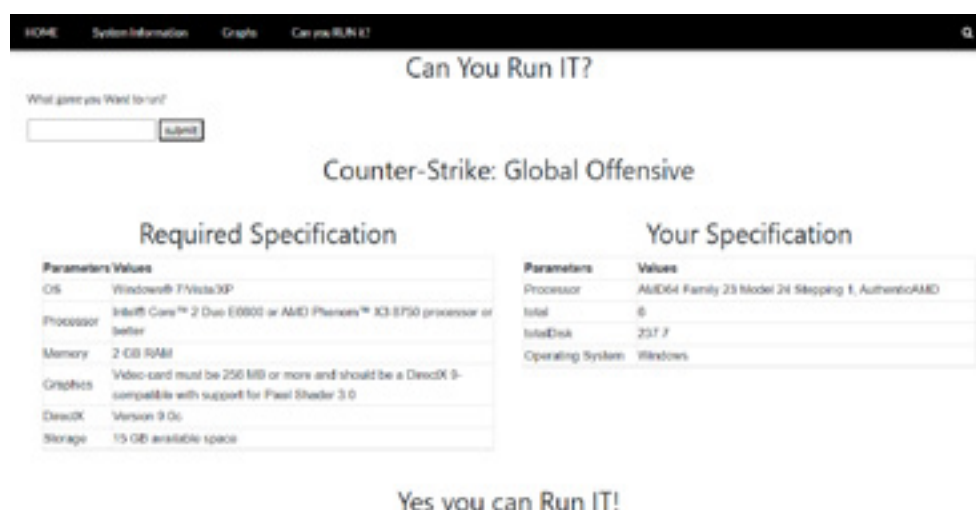
Fig. 8. Example of a game that can be run on the user's system.

Figure 9. Shows an example of the game "Red Dead Redemption 2" being entered by the user. Based on the comparison between the user's system specifications and the required system specifications for the game, a message "No you can't run it!" specifies that the game is not compatible with the user's system
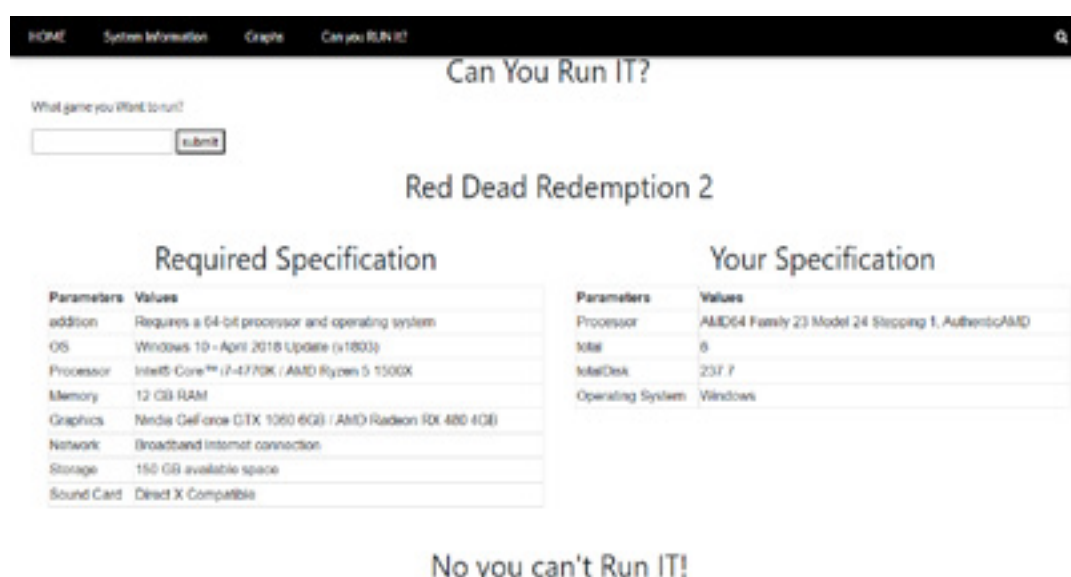

Fig. 9. Example of a game that cannot be run on the user's system.

5. FUTURE SCOPE

The proposed system provides information about whether the application will run on users' local system or not, so a recommendation system can be developed in future which will recommend necessary hardware and software to the user for better performance by analysing the system information.

6. CONCLUSION

The CPU metrics measurements are essential because they guide one's decision-making around the computer equipment which one intends to buy. It enables one to cut through the marketing spin that surrounds computer systems; without a basic understanding of how they operate, one won't be able to handle this and won't be able to make an informed decision when buying systems. Understanding performance measurements is essential for comprehending the underlying organizational motivation, or the reasons why people try to make these changes in order to increase performance for future development.

REFERENCES

[1] K. S. Stefanov, and A. A. Gradskov "Analysis of CPU Usage Data Properties and their possible impact on Performance Monitoring." in Supercomputing Frontiers and Innovations 3, no. 4 (2016): 66-73.

[2] I. M. Urriza, and M.A.A Clariño "Aspect-Based Sentiment Analysis of User Created Game Reviews." in 2021 24th Conference of the Oriental COCOSDA International Committee for the Co-ordination and Standardization of Speech Databases and Assessment Techniques (O-COCOSDA), pp. 76-81. IEEE, 2021

[3] F. Gomes, and M. Correia "Cryptojacking detection with CPU usage metrics." in 2020 IEEE 19th International Symposium on Network Computing and Applications (NCA), pp. 1-10. IEEE, 2020.

[4] "Windows Task Manager" Available at https://www.howtogeek.com/405806/windows-task-manager-the-complete-guide/

[5] Glances - an eye on your system. Available at: https://nicolargo.github.io/glances/.
"What is system explorer? System Explorer - Keep Your System Under Control." Available at: https://systemexplorer.net/.

[6] Can you Run it?" Available at https://www.systemrequirementslab.com/cyri.

[7] Kumar, S. Rajesh, and R. Aravazhi. "A Study on Ajax in Web Applications with Latest Trends." International Journal on Recent and Innovation Trends in Computing and Communication 1, no. 6 (2013): 563-568.

Robust Pedestrian Detection and Path Prediction using Improved YOLOv5

Kamal Hajari* , Ujwalla Gawande* and Yogesh Golhar[+]

* Research Scholar, IT Department, Yeshwantrao Chavan College of Engineering, Nagpur, India
* Dean R & D and Associate Professor, IT Department, Yeshwantrao Chavan College of Engineering, Nagpur, India
[+] Assistant Professor, CE Department, St. Vincent Palloti College of Engineering and Technology, Nagpur, India

Abstract

Pedestrian detection and path prediction are critical concerns in vision-based surveillance systems. Advanced computer vision applications are challenged by discrepancies in pedestrian postures, scales, backdrops, and occlusions. In the state-of-the-art approach, these challenges cannot be addressed because of limitations in postures and multiscale information missing in the features of the region of interest. In order to address these challenges, we present an improved YOLOv5-based deep learning approach. Occupied pedestrians are detected on multi-scales using the improved YOLOv5 model. We improved the YOLOv5 detection method in three ways: 1) a new feature fusion layer has been added to capture more shallow feature information of small size pedestrians, 2) features from the backbone network have been brought into the feature fusion layers to reduce feature information loss of small size pedestrians; and 3) Scale Invariant Cross-stage Partial Network (SCSP) has been added to detect the pose and scale invariant pedestrians. At last, the proposed path prediction method used to estimate the pedestrians path based on motion data. The proposed method deals with partial occlusion circumstances to reduce object occlusion-induced progression and loss, and links recognition results with motion attributes. It uses motion and directional data to estimate the movements and orientation of pedestrians. The proposed method outperforms the existing methods, according to the results of the experiments. Finally, we conclude and look into future research directions.

Key Words: CNN, Deep Learning, YOLOv5, Pedestrian detection, Tracking, Path prediction.

1 Introduction

Because of the growing concern about security, many surveillance systems are now placed in significant locations all over the world. Human resources had to monitor a lot of videos, which took a long time. As a result, one of the key shortcomings of the traditional approach is that it is difficult to detect and forecast a pedestrians path from films. It is a lengthy procedure. Because of current system constraints, an active video surveillance system that can identify and forecast pedestrian paths in real-time is required. COVID-19 viral infections are currently causing a pandemic all over the planet. In congested and densely populated places, the viruss chances

of spreading are boosted. However, in this case, an intelligent surveillance system is required to monitor the congested scene. The system should be able to detect pedestrians and routes in order to prevent people from congregating and spreading the COVID-19 virus. Pedestrian detection can also be used in computer vision applications such as homeland security, child monitoring, elder fall detection and monitoring, public and private banks, ATMs, and airports, among others. Deep learning architectures are employed in many computer vision systems because of their accuracy. In many complicated conditions, such as complex backdrop backgrounds, occlusion, object deformation, illumination, and scale fluctuation, the deep learning model surpasses conventional methods. The real-time identification of pedestrians is one of the most important study areas in computer vision. Despite the fact that deep learning models improve pedestrian identification accuracy, there is still potential for improvement in both human and machine perception [1]. The model's accuracy will be harmed by complex backdrops, low-resolution photos, lighting conditions, and obstructed and small objects in the distance. Most studies in this field have solely worked on color picture object detection so far. Pedestrian recognition in real time is still slower and less precise than human eyesight. The classic Viola-Jones detector [2], Deformable Part Model (DPM) [3], Histogram of Orientated Gradient (HOG) [4], and multiscale gradient histograms [5] technique is time-consuming and computationally difficult, and it necessitates manual intervention. Such strategies have proven quite popular in the recent evolution of deep learning methods, and deep CNN-based pedestrian detection algorithms have outperformed conventional methods [6]. R-CNN [7] is the first deep learning model for object detection. This method uses a selective search window to construct a region of interest for object detection based on deep learning, as implemented in all R-CNN series. Two-stage detectors, such as R-CNN [8], SPPNet [9], Fast-R-CNN [10], Faster R-CNN [11], and Mask-R-CNN [12], and single-stage detectors, such as SSD [13] and YOLO [14], are examples of deep learning techniques. As a result, these approaches are ineffective in real-time pedestrian detection. Deep learning-based pedestrian recognition systems have a slow processing speed, making them unsuitable for self-driving cars' real-time requirements. As a result, Joseph Redmon et al. [15] introduced the YOLO network, which is a single end-to-end object regression architecture, to increase detection speed and accuracy. Later, the researchers presented other variants of YOLO, such as YOLO (v5, v4, v3, v2, v1) [16][17], to increase both detection accuracy and speed when identifying smaller and densely distributed pedestrians.

In many cases, images of natural scenes usually vary in proportion and at different orientations. These artifacts make pedestrian detection and classification a challenging task. Several other problems include 1) uneven lighting; 2) blurry and hazy appearance; 3) changes in size with different posture changes, etc. Fig. 3 describes the key ideas for a new improved YOLOv5 framework, which is built on the Faster R-CNN pipeline [12]. There are three enhancements in the proposed improved YOLOv5 approach compared to the original YOLOv5 method. First, a new fusion layer is added, resulting in a large-scale feature map with a dimension of 152x152x255 pixels is extracted to detect the small size pedestrian efficiently. Second, additional fusion layer used to carry feature data from the backbone into the feature fusion layers. The SCSP modules are then added to feature fusion layers as the third step. It is useful for the detection of multiscale and occluded pedestrians. In comparison to the original YOLOv5 model in Fig. 2, the improved YOLOv5 model has four fusion layers. Fig. 3 shows the structure of the new fusion layer. A image pyramid-based approach designed in backbone network for detecting pedestrians based on the improved YOLOv5 detection method. The fourth step is to relocate the detection results into the original input image and eliminate duplicate ones. Once all the detection results are mapped to the original input image, the Non-maximum Suppression (NMS) algorithm is applied to eliminate duplicate detection results. Therefore, improved YOLOv5 can achieve excellent detection performance at a wide range of input scales. Since improved YOLOv5 shares the convolutional features of the entire image with different target proposals, it is very effective in terms of training and testing time. At last, proposed pedestrian direction prediction algorithm applied for efficient moment tracking of pedestrian in video. The experiment were preformed on the proposed academic environment dataset and other benchmark dataset. Small-scale unchanging pedestrians can be detected efficiently using the proposed improved YOLOv5 approach. The following are the contributions to this paper:

1. The proposed deep learning system detects and predicts pedestrian routes using improved YOLOv5 and motion information.

2. For pedestrian detection, we first employ an improved YOLOv5. It may be used to detect small, scale-invariant pedestrians in a scene.

3. For path prediction, we extract the pedestrian's motion characteristics and their intercommunication within a frame.

4. Finally, the routes prediction algorithm uses the motion pattern in the frame to estimate the pedestrian movement's direction.

5. When compared to existing state-of-the-art approaches, the experimental results reveal a significant performance improvement in pedestrian identification and path prediction.

The remainder of the research paper is organized in the following manner. In section 2, related work such as pedestrian recognition and path prediction is discussed, along with the methods drawbacks. In Section 3, a new proposed pedestrian dataset is discussed. In Section 4, a new improved YOLOv5 model and path prediction method is discussed. Section 5 contains experimental data as well as a comparison of the suggested strategy to other approaches. The final section concluded with a research direction for the future.

2   Related Work

Pedestrian detection has used a variety of technologies over the last few decades, many of which have already had a substantial influence. Some techniques try to improve the basic features employed [18, 19, 20], while others aim to improve the detection algorithm [21, 22], while some combine DPM [23] or exploit the scene context [23,24]. Many aspects and methodologies were evaluated by Benenson et al. [18]. Bensenson et al. proposed the fastest method for achieving a frame rate of 100 frames per second (FPS) for pedestrian identification once more in [20]. The deep enhanced pedestrian identification accuracy after 2012 [21][22]. However, the time it takes them to process each image is longer, lasting a few seconds. On CNNs, a variety of astonishing methodologies are presently used. P. Sakrapee et al. [25] proposed new features based on low-level vision features that included spatial pooling to improve translation invariance and the resilience of the pedestrian identification process. The author of [27] employs convolutional sparse coding to begin each layer and then fine-tunes it to perform object detection. The merging of Region Proposal Networks (RPN) and Boosted Forest Classifiers is used in the [28] technique. RPN generates candidate bounding boxes, high-resolution feature maps, and confidence scores, as proposed in Faster R-CNN [12]. The Real-boost technique is also used to design the Boosted Forest Classifier in order to leverage the information gained from the RPN. On the pedestrian test data set, this two-stage detector performs admirably. Murthy et al. [29] investigated pedestrian detection using a variety of custom-made deep learning approaches.

Zhenxue Chen [30] proposed a network for precise real-time localization of small-scale pedestrians that combines both region creation and prediction parameters. A scale-aware Fast-R-CNN approach for identifying pedestrians of various scales is proposed by Jianan et al. in [31], and the anchor frame method is used to numerous feature layers. In addition, Wanli et al. [32] suggested using a unified deep neural network to learn four components for pedestrian detection: feature extraction, deformation, occlusion, and classification. Yanwei et al. [33] proposed a mask-guided attention network for identifying occluded pedestrians, which modulates entire body attributes to emphasis just viewable portions while suppressing occluded regions. However, this strategy fails to deliver adequate results when dealing with obstructed pedestrians. A simple and compact technique is recommended by Shanshan Zhang et al. [34]. A channel-based attention network is added to the Faster R-CNN detector while detecting obstructed pedestrians. Tao et al. [35] suggested a unique method for detecting small-scale pedestrians that are far from the camera by combining somatic topological line localization

with temporal feature aggregation. By adopting a post-processing strategy based on Markov Random Fields, this method also reduces ambiguity in occluded pedestrians (MRF). For recognising small-scale and obstructed pedestrians, Yongqiang et al. [36] developed a key point-guided super-resolution network (KGSNet). They first trained the network to generate a super-resolution pedestrian image, after which a section of the estimation module encoded the semantic information of four human body parts. Chunze et al. [37] suggested a method for detecting small-scale and obstructed pedestrians using granular perception feature learning. The attention technique is utilised to build graininess-aware feature maps, and then a zoom-in-zoom-out module is used to enhance the features. To increase the identification accuracy of small-scale pedestrians, Jialian et al. [38] proposed a novel self-mimic loss learning approach. Wei-Yen et al. [39] presented a new ratio-and-scale-aware YOLO (RSA-YOLO) that detects small pedestrians more accurately.

For dealing with occlusion other research group uses an adaptive learning method. In [51] author proposed an adaptive learning system to segment an object robustly. By using the on-line adaptation of color probabilities, method presents several specific features. It handles the illumination changes even in the outdoor area in real-time. Bayes rule and Bayesian classifier is employed to calculate the probability of an object color. In [52] author proposed a methodology for motion analysis and hand tracking based on adaptive probabilistic models. In this method a deterministic clustering framework and a particle filter together in real time. The skin color of a human hand is firstly segmented. A Bayesian classifier and an adaptive process are utilized for determining skin color probabilities. The methodology can be used to deal with luminance changes. After that, author determine the probabilities of the fingertips by using semicircle models for fitting curves to fingertips. Following this, the deterministic clustering algorithm is utilized to search for regions of interest, and at last the Sequential Monte Carlo is also used to track the fingertips efficiently. Bing et al. [40] also suggested a new small-scale sensing (SSN) network that can produce some proposal regions and is effective at recognizing small-scale pedestrians. Two-stage deep learning-based object detectors, in particular, have advantages in terms of localization accuracy and precision. Despite the fact that the method necessitates a large number of resources, its computational efficiency is low. One-stage detectors are faster than two-stage detectors due to the unified network structures, even though model precision lowers. Furthermore, with deep learning-based object detectors, the amount of training data is critical. We introduce a real-time adaptive deep neural network inspired by YOLOv5 for recognising smaller and densely distributed pedestrians. YOLOv5 [15] is a feature extraction, bounding, box extraction, object classification, and detection end-to-end single deep neural network. The YOLOv5 model was used as the base model in order to obtain greater accuracy and speed when recognizing smaller and more densely scattered pedestrians. It was chosen for the accurate detection of smaller and scattered pedestrians after improvements to the YOLOv5 network structure and hyper-parameters. The suggested method improves YOLOv5 by using the YOLOv5 deep learning framework as a basis model and adjusting hyper-parameters in real time to improve detection accuracy. Additionally, the suggested model eliminates several unneeded repetitive convolution layers at the higher end, consuming less computational time than the YOLOv5 Model. As a result, the updated YOLOv5 model is the most accurate method for detecting smaller and densely distributed pedestrians in real time. The proposed model performance is compared to that of the YOLOv5 and YOLO variants on benchmark datasets. Improved YOLOv5 is additionally examined on both INRIA [37] and Caltech [38] pedestrian datasets to test the robustness of the proposed model. Next, We describe the most relevant pedestrian datasets. In addition, we discuss the state-of-the-art approaches of pedestrian detection, along with issues and challenges.

2.1 Benchmark Pedestrian Datasets and analysis

In this section, we describe the commonly used pedestrian datasets by researchers.

2.1.1 Caltech Dataset

This dataset consists of 2,300 pedestrians along with 350,000 annotated bounding boxes. It was recorded on city roads with normal traffic during the day. The video was recorded with a resolution of 640x480 from a

camera mounted on the vehicle to capture pedestrians walking on the street. Pedestrian annotation is used to verify the performance and accuracy of different pedestrian detection algorithms [38].

2.1.2 MIT Dataset

This dataset is the first pedestrian dataset; it is quite small and relatively high quality. This data set contains 709 sample pedestrian images. Whether in front view or back view, the range of pose images taken in city streets [42] is relatively limited.

2.1.3 Daimler Dataset

This dataset captures humans walking on the street through cameras installed on vehicles in an urban environment during the day. The dataset includes pedestrian tracking attributes, annotated labeled bounding boxes, ground truth images, and floating disparity map files. The training set contains 15,560 pedestrian images and 6,744 annotated images. The testing set comprises 21,790 pedestrian images with 56,492 annotated images [43].

2.1.4 ATCI Dataset

This dataset is a rear-view pedestrian database captured using a vehicle-mounted standard automotive rear-view camera for assessing rear-view pedestrian detection at different locations, such as in-house and outside parking lots, city roads, and private driveways. The data set contains 250 video clips of 76 minutes each, and 200,000 marked pedestrian bounding boxes captured in both day and night scenarios, with varying weather [44].

2.1.5 ETH Dataset

This dataset was utilized to observe traffic scenes from inside vehicles. The pedestrian behavior was captured from stereo equipment fixed on a stroller attached to a car. The dataset can be used for pedestrian detection and tracking from movable platforms in an urban scenario. The dataset includes different traffic agents such as cars and pedestrians. [40].

2.1.6 TUD-Brussels Dataset

This data set was created using a mobile platform in an urban environment. Crowded urban street behavior recorded using a camera mounted on the front side of the vehicle. It can be used in car safety scenarios in urban environments [45].

2.1.7 INRIA Dataset

This dataset is one of the popular static pedestrian detection dataset. It includes human behavior with significant changes in posture, appearance, clothing, background, lighting, contrast, etc., plus a movable camera and complex background scenes. [37].

2.1.8 PASCAL Visual Object Classes (VOC) 2017 and 2007 Dataset

This dataset consists of static objects with different views and poses in an urban environment. The aim behind the creation of this dataset was to recognize the visual object classes in real-world scenes. The 20 different categories in this dataset include animals, trees, road signs, vehicles, and pedestrians [46].

2.1.9 MS COCO Dataset

Microsoft Common Object in Context (COCO) 2018 dataset [39] created the Common Object in Context (COCO) 2018 dataset was recently used for stimulus object detection, while focusing on detecting different objects in the context. The annotations include different instances of objects related to 80 categories of objects and 91 different categories of human segmentation. There are key point annotations for pedestrian instances and five image labels per sample image. The COCO 2018 dataset challenges include (1) real-scene object detection with segmentation mask, (2) panoptic segmentation, (3) pedestrian key point evaluation, and (4) dense pose estimation in a crowded scene [39].

2.1.10 Mapillary Vistas Research Dataset

This dataset is used for real scene segmentation of street images [47]. Panoptic segmentation resolves both pedestrian and different non-living classes, consolidating the concept of semantic and instance segmentation tasks efficiently. Table 1 shows a comparative analysis of the pedestrian databases with their purposes for video surveillance. We have also included our proposed dataset, discussed later in the paper. The association is performed in terms of the use of the dataset, size of the dataset, real-world environment scenarios, type of labeling, and annotation. These details are used for validating the object detection and tracking algorithm performance.

3   Proposed Academic Environment Pedestrian Dataset

In this section, we discuss the proposed dataset development framework and its advantage over the existing state-of-the-art benchmark dataset.

3.1 Image/Video Acquisition framework

In proposed dataset the students behavior in college premises recorded using a high-quality DSLR camera from a different viewing angle. We recorded video at 30 f/s, enabled 4K recording, with a resolution of $3840x2160$, and H.264 compressed to .mp4 format. The database includes more or less 100 sample videos. The duration of each example video is 20-30 minutes. Fig. 1 shows an example frame of a video sequence available in the dataset. The camera tilt angle varies from $45°$ to $90°$. Pedestrians are students of Yeshwantrao Chavan College of Engineering in Nagpur, aged 22-27 years old, over 90%, of which 65% are male and 35% are female, mainly of Indian ethnicity. The key features of the data acquisition settings summarized in Table 2.

The proposed pedestrian database consists of different behaviors of students in academic activities under different conditions, such as students studying in practical laboratories, exam hall scenarios, classroom, a student doing the cheating in the exam hall, a student taking answer book outside the exam hall, student stealing the mobile phone or other electronic devices such as mouse, keyboard, student stealing the lab equipment, student dispute in the college premises, student disturbing another student, student threatening another student, etc.

3.2 Pedestrian Annotation

The proposed dataset completely annotated at the frame of video, by human specialists. We provide a csv file for each video sequence, using the same file naming protocol as videofilename.csv. The labeling process is divided into three stages: 1) human detection; 2) tracking, 3) suspicious activity recognition and soft biometric features. First, the Mask R-CNN [12] method is used to provide an initial estimate of the position of each pedestrian in the scene, and the data obtained are manually verified and corrected. Next, the deep sort method [14] provided the preparatory tracking information, which was again corrected manually. As a result of these two initial steps, we obtain a rectangular bounding box representing the region of interest (ROI) for each pedestrian in each frame. The final stage of the annotation process is carried out manually, where a human expert

Table 1: Comparative analysis of state-of-the-art dataset.

Dataset Title	Purpose	Source Data	Annotation	Environment	Year	Ref.
Caltech Pedestrian dataset	Pedestrian detection and tracking	Frames:250000 (137 min.)	Bounding boxes:350,000 Pedest.:2300	City Environment	2012	[38]
MIT dataset	Pedestrian segmentation, detection,	Pedestrian:709 Train: 509 Test: 200	No annotated pedestrian	Day light scenario	2000, 2005	[42]
Daimler	Detection and Tracking of pedestrian	Pedestrian: 15,560, Negative:6744	2D bounding box and a ground truth	City Environment	2016	[43]
GM-ATCI	Pedestrian segmentation, detection, and tracking	250 video sequences	200K annotated pedestrian bounding boxes	Day and complex weather and lighting	2015	[44]
ETH	Segmentation, Detection, Tracking	Videos	Traffic agents Ex. cars and pedestrians	City Environment	2010	[40]
TUD Brussels	Detection, Tracking	1092 images	Annotated Ped.:1776	City Environment	2009	[45]
INRIA	Detection, Segmentation	498 images	Manual Annotations	City Environment	2005	[37]
PASCAL VOC 2012	Detection, Classification, Segmentation	11,530 images,20 obj., classes	27,450 ROI annotated 6929 segmentation	City Environment	2012	[46]
MS COCO 2017	Recognition, Segmentation	328,124 images, 1.5 million obj.	Segmented people obj.	City Environment	2017	[39]
KITTI	Recognition, Segmentation	328,124 images, 80 obj. cat.	Segmented people obj.	City Environment	2015	[41]
Mapillary Vistas dataset 2017	Semantic understanding street scenes	25,000 images, 152 object ,categories	Pixel accurate instance specific Pedestrian annotations	City Environment	2017	[47]

Table 2: Proposed dataset video Acquisition configuration.

Parameter of Camera	Setting
Camera:DSLR High resolution camera, Effective pixels:12.4M	Video frame resolution:3840x2160
Lens FOV 94 20 mm f/2.8 focus	ISO Range: 100-3200
Camera tilt angle	45° to 90°
Video recording format	.mp4

who personally knows the students of the college sets up ID information and characterizes the samples based on soft labels. Table 3 shows the detailed information of the label annotated for each pedestrian instance in the frame, as well as the ID information, the bounding box that defines the ROI, and the frame information. For each label, we also provide a list of its possible values.

Figure 1: Sample image of the proposed database. The first row illustrates two girls dispute in the lab. The second row illustrate the scenario stealing the mobile phone in lab. The third row illustrate a scenario of a student threatening. The fourth row shows the same threatening scenario(front view). The fifth row shows the scenario of students stealing the lab equipment. The sixth row shows the scenario cheating in the exam hall.

First row illustrates two girls dispute in the lab. Second row illustrate the scenario stealing the mobile phone. Third row illustrate a scenario of a student threatening. Fourth row shows the same threatening scenario. Fifth row shows the scenario of students stealing the lab equipment. Sixth row shows scenario cheating in the exam. The proposed data set is annotated by human experts at the frame level. The labeling process is divided into three stages: 1) human detection; 2) tracking. 3) suspicious activity recognition. First, the Mask R-CNN [12] method is used to provide an initial estimate of the position of each pedestrian on the scene, and the data obtained are manually verified and corrected. Next, the deep sort method [14] provided preparatory tracking information, which was again corrected manually. Because of these two initial steps, we obtain a rectangular bounding box representing the region of interest (ROI) for each pedestrian in each frame. The final stage of the annotation process is carried out manually, where a human expert who personally knows the students of the college sets up ID information and characterizes the samples based on soft labels. The label annotated for each pedestrian instance in the frame includes pedestrian height, age, bounding box Id, feet, frame, body volume, hairstyle, hair color, head accessories, clothing, moustache beard action, and accessories. Next, the proposed improved YOLOv5 framework is detailed in depth in the next section.

4   Proposed Methodology - YOLOv5 and Improved YOLOv5

In this section, we first describe the existing YOLOv5 architecture (as shown in Fig. 2), followed by a proposed method for pedestrian detection based on the improved YOLOv5 architecture (as shown in Fig. 3). Finally, the proposed path prediction has been described. We adapt the YOLOv5 architecture for detection in order to successfully detect small-scale unchanging pedestrians in the scene. The moving pedestrian directional and motion component information is then utilized to anticipate the pedestrian's progress in subsequent frames until the pedestrian is visible in the view scope. Our method works for single individuals as well as multiple people in the scene. In YOLOv5, the compact feature corresponds to the image's greater area. It can distinguish between larger and smaller size pedestrian using the 19x19x255 and 76x76x255 features. These properties are used by YOLOv5 to detect and classify objects. In the focus module, the input image is separated into sections and then

Table 3: The proposed dataset 16 annotated attribute with other soft biometric labels.

Attributes	Values
Height	0→Children, 1→Short, 2→ Medium, 3→ Tall, 4→Not known.
Age	0→0-11, 1→12-17, 2→18-24, 3→25-34, 4→35-44, 5→45-54, 6→55-64, 7→greater than 65, 8→Not known.
Bounding Box	[x→Top Left; y→Top left row; h→Height; w→Width]
ID	1, 2, 3, 4, . Not known.
Feet	0→Sport, 1→Classic, 2→High Heels, 3→Boots, 4→Sandals, 5→Nothing, 6→Not known.
Frame	1, 2, 3, 4, . n.
Body Volume	0→Thin, 1→Medium, 2→Fat, 3→Not known.
Hairstyle	0→Bald, 1→Short, 2→Medium, 3→Long, 4→Horse Tail, 5→Unknown.
Hair Color	0→Black, 1→Brown, 2→White, 3→Red, 4→Gray, 5→Occluded, 6→Not known.
Head Accessories	0→Hat, 1→Scarf, 2→Neckless, 3→Occluded, 4→Not known.
Upper Body	0→T-shirt, 1→Blouse, 2→Sweater, 3→Coat, 4→Bikini.
Clothing	5→Naked, 6→Dress, 7→Uniform, 8→Shirt, 9→Suit, 10→Hoodie, 11→Cardigan.
Lower Body Clothing	0→Jeans, 1→Leggins, 2→Pants, 3→Shorts, 4→Skirt, 5→Bikini , 6→Dress, 7→Uniform, 8→Suit, 9→Not known.
Moustache	0→Yes, 1→No, 2→Not known.
Beard	0→Yes, 1→No, 2→Not known.
Action	0→Walk, 1→Run, 2→Standing, 3→Sit, 4→Cycle, 5→Exercise, 6→Pet, 7→Phone, 8→Leave Bag, 9→Fall, 10→Fight, 11→Date, 12→Offend, 13→Trade.
Accessories	0→Bag, 1→Backpack, 2→Rolling, 3→Umbrella, 4→Sport, 5→Market, 6→Nothing, 7→Unknown.

combined afterwards to extract the features more effectively during down-sampling. The block of convolutions Cross-stage partial network (CSP) [15] in YOLOv5 is composed of the modules for convolution, normalization, and Leaky Rectified Linear Unit (ReLU) activation functions [39]. It was utilized in the backbone network and the neck network, respectively. The front and rear layers are connected through cross-layer connection.
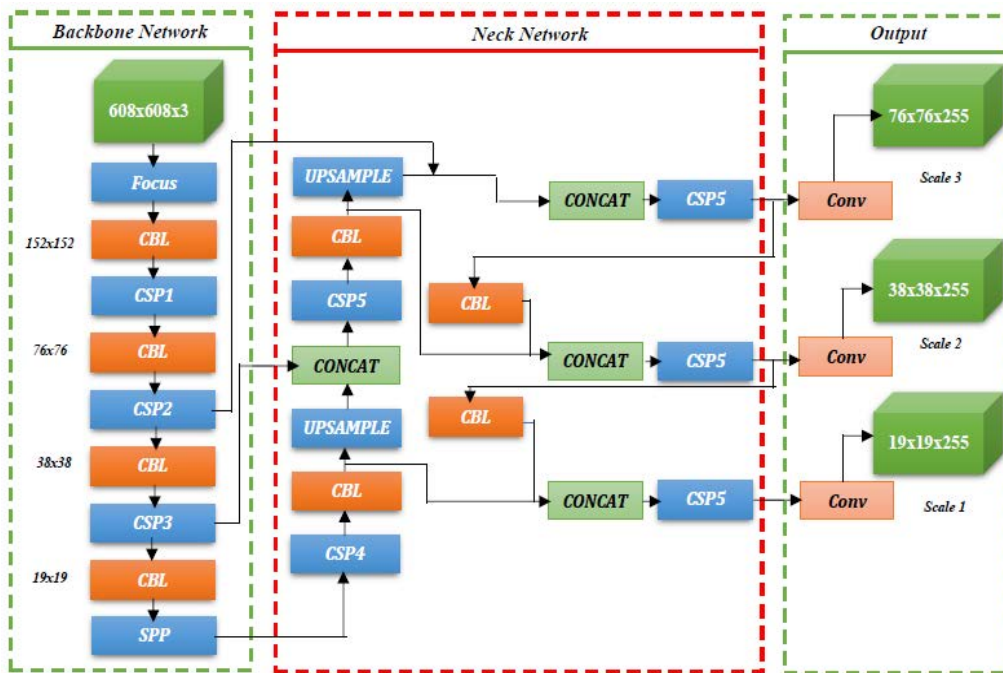
Figure 2: The architecture of the YOLOv5 model. (Backbone, Neck, and Output layers)

4.1   YOLOv5 for Pedestrian Detection

The YOLOv5 detector is a one-stage detector. The architecture of YOLOv5 is shown in Fig. 2. There are three parts to the YOLOv5 architecture: 1) A strong backbone. 2) The neck, and 3) the output. The backbone portion extracts the input picture features first. For extracting the features of the input image in varied lengths, the backbone network employs several Convolutional Neural Networks (CNN) and pooling [17]. The backbone network has four layers of feature map creation. Each layer produces a feature map with dimensions of 152x152, 76x76, 38x38, and 19x19 pixels. To gather additional contextual information and prevent information loss, the neck network combines feature maps of various levels. The Feature Pyramid Network (FPN) and Pixel Aggregation Network (PAN) feature pyramid structures are employed in the fusion process. The semantic features from the top feature maps are passed down to the lower feature maps via the FPN. Object localization features are transferred from lower feature maps to higher feature maps using the PAN structure.

We can see three feature fusion layers in the neck network, which yield three scales of new feature maps with sizes of 76x76x255, 38x38x255, and 19x19x255, where 255 is the pixel intensity range of the network. By lowering model size, the CSP network tries to enhance inference speed while retaining precision. The CSP network replaces the residual units with CBL modules in the neck. The Special Pyramid Pooling (SPP) module combines the features of the largest pooling with variable kernel sizes. The input feature map is primarily compressed. On the one hand, it reduces the size of the feature map and reduces the network's computational complexity; it compresses features and removes the most important ones. Following that, we went through the intricacies of the upgraded YOLOv5 architecture.

4.2   Improved YOLOv5 for Pedestrian Detection

To detect multiscale pedestrians, we improved the YOLOv5 detection method in three ways: 1) a new feature fusion layer with a grey background has been added to capture more shallow feature information of small pedestrians; 2) features from the backbone network have been brought into the feature fusion layers highlighted
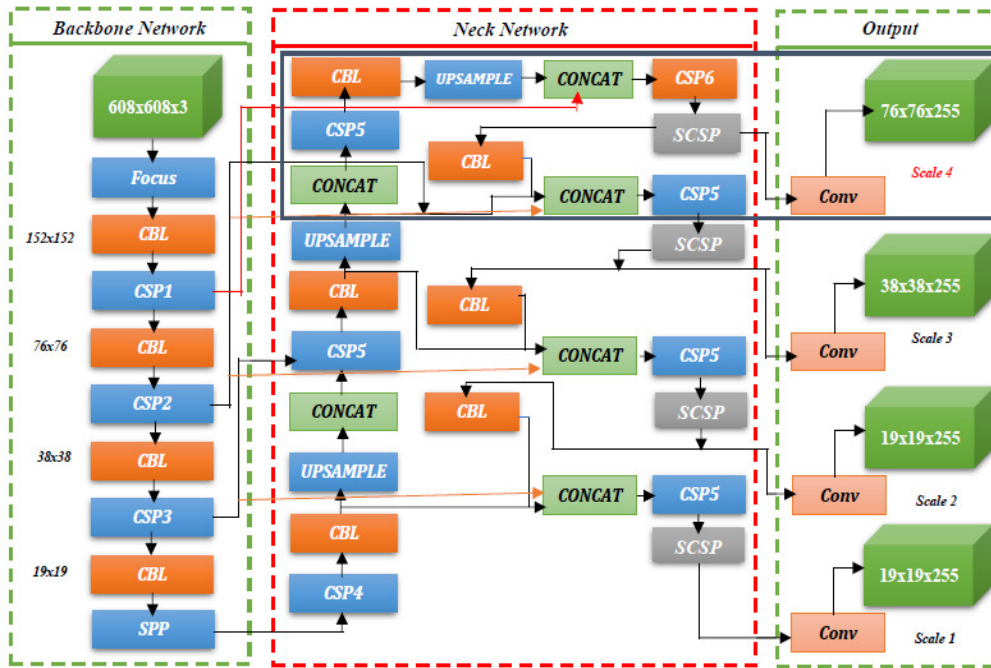
Figure 3: The architecture of the improved YOLOv5 model.

with black color to reduce feature information loss of small pedestrians; and 3) the Scale invariant Cross-stage Partial Network (SCSP) has been added to reduce feature information loss of small pedestrians. Figure 3 depicts the improved YOLOv5 architecture. There are three enhancements in the architecture of the upgraded YOLOv5 approach compared to the original YOLOv5 method. First, a new fusion layer is added, resulting in a large-scale feature map with a dimension of 152x152x255 pixels. Second, additional red-lined connections have been created to carry feature data from the backbone into the feature fusion layers. The SCSP modules are then added to feature fusion layers as the third step. To begin, we add a new fusion layer that generates a larger feature map with a size of 152x152x255 to improve the performance of YOLOv5 in recognizing little pedestrians. In comparison to the original YOLOv5 model in Figure 1, the upgraded YOLOv5 model has four fusion layers. Figure 2 shows the structure of the new fusion layer. The fused feature maps are further un-sampled and concatenated with the feature map of 152x152 pixels from the backbone network to construct an extra layer of fused feature maps as a result of the original network. The Cross Stage Partial (CSP) and Case based learning (CBL) modules are also employed in this process. CBL is used for the extraction of multiscale features of object of different size. Second, four red lines were added to bring feature information from the backbone network 152x152 pixels, 76x76 pixels, and 38x38 pixels, taking into account the large size of the images from the planets and the diverse scales of the pedestrian in the images, an image pyramid-based approach designed in this paper for detecting pedestrians based on the improved YOLOv5 detection method as shown in Fig. 4. Scale invariant Cross-stage Partial Network (SCSP) process the multiscale CNN feature paralleled to reduce the network overhead. The fourth step is to relocate the detection results into the original input image and eliminate the duplicate ones. Actually, there are two relocation steps. One is to relocate the detection results from each slice to their corresponding layer. Another is to further relocate the detection results of each layer to the original input image. Once all the detection results are mapped to the original input image, the NMS algorithm is applied to eliminate the duplicate detection results.
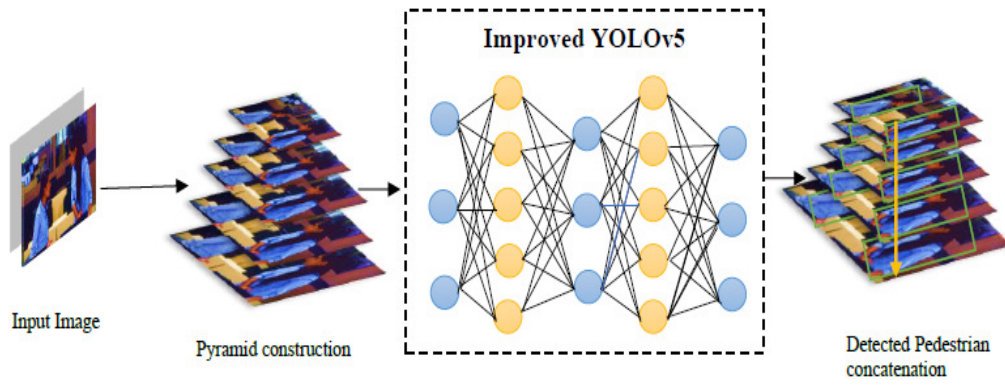
Figure 3. The architecture of Feature Pyramid Network.

Figure 4: The architecture of Feature Pyramid Network

4.3 Path Prediction

The pedestrian's path is drawn in the frame by the proposed path prediction algorithm. The fundamental concept is to track pedestrian movement. The line is drawn until the pedestrian appears in the frame. As seen in Figure 4, the bounding box parameter is represented by the $x1$, $y1$, $x2$, $y2$ created in the detection output. Eq. 1 and 2 were used to calculate the centroid of the bounding box of each identified pedestrian:

$$cX = \frac{x1 + x2}{2} \tag{1}$$

$$cY = \frac{y1 + y2}{2} \tag{2}$$

We then draw a line from the current centroid to the previous centroid to plot the position of each pedestrian
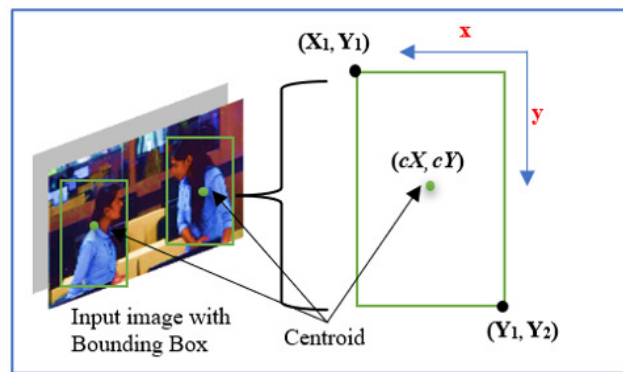
Figure 5: The Pedestrian representation with bounding box.

in the subsequent frame. We constructed two repositories: one for storing the pedestrian detection id and the other for storing the center position of each detected pedestrian object. On the initial frame, draw the start and end points afterwards. The following algorithm shows a step-by-step illustration of path prediction.

Algorithm 1: Pedestrian path prediction algorithm

Input   : $x1, x2, y1, y2$, Bonding Box parameters. $objArr$, Pedestrian detected object array.
Output   : Draw a line for path of pedestrian.

For each pedestrian in object array;
for $(objId, bboX)$ **to** $objArr$ **do**
    $bboX \leftarrow x1, x2, y1, y2$ *Compute the centroid from the bounding box points. represented by:*
    (cX, cY)
    Append centroid in centroid dictionary
    $cenDist[objId] \leftarrow (cX, cY)$
    if $objId \neq objIdList$ **then**
        $objIdList \leftarrow objId$
        start point
        $stPt \leftarrow (cX, cY)$
        end point
        $edPt \leftarrow (cX, cY)$
        Draw line on frame points $(stPt, edPt)$
    else
        for pt **to** $cenDist[objId]$ **do**
            if $objId \neq objIdList$ **then**
                $stPt \leftarrow (cenDist[pt][0], cenDist[pt][1])$
                $edPt \leftarrow (cenDist[pt + 1][0], cenDist[pt + 1][1])$
                Draw line on frame points $(stPt, edPt)$
            end
        end
    end
    Draw rectangle on frame $x1, x2, y1, y2$
end

---

5   Experiment

On benchmark pedestrian databases such as Caltech [38], INRIA [37], MS COCO [39], ETH [40], and KITTI [41], as well as our own pedestrian database, we evaluated the performance of the proposed Improved YOLOv5 framework. The tests and proposed deep learning framework were run on a single NVIDIA GPU with a CPU Intel Core i5 3.4GHz, 16GB RAM, and a 16GB NVIDIA graphics card. The limitation of these datasets are: 1) the limited range of pedestrian poses recorded on the city streets in a controlled environment, 2) these datasets contain data with short lapses of time between successive observations of each ID in a single day, which allows to use clothing appearance features in identity matching, 3) All of these pedestrian data sets are recorded in various places such as streets and parking spaces, but they do not cover student behavior in an academic environment. This paper proposes a new dataset in an academic environment. Human experts annotated student pedestrian behavior on each frame sequence of the video, providing three types of information.

1. Pedestrian positioning with bounding box. The position of each pedestrian in the video frame is represented as a bounding box, and we can use this data for pedestrian detection, tracking, instance, and semantic segmentation.

2. Physical, behavioral, or adhered to human characteristics. Each pedestrian fully characterized by labels such as Face: eyes, eyebrows, forehead, nose, ears, mouth, facial hair, moustache, glasses, beard, hairstyle, hair color, age, body volume, gender, age, height, body accessories, ethnicity, head accessories, action and clothing data.

3. Annotated class label and ID. Each pedestrian has a unique identifier that is uniform across all video frames. These characteristics of the data set make it suitable for various recognition difficulties.

5.1 Data Pre-processing

In the proposed dataset, we classified the video information namely into three directories as Train, Test and Validation". We describe the following three entities:

1. Annotations directory contains a XML file for each image. This file contains all the information about the image.

2. The frames are extracted from each video and divided into training and validation set in different directory.

3. The details about the frames are stored in the .txt file, it stores a unique identity number for each image.

However, for the classification purpose, we defined a improved YOLOv5 model, along with ReLU as an activation function. In the proposed approach, we used sparse categorical cross-entropy instead of categorical cross-entropy for the compilation of improved YOLOv5 model. The major advantage of using sparse classification cross-entropy is that it preserves time and computational effort, because it only uses a single value for a class label instead of the entire feature vector. We used simultaneous callbacks. A callback is a phenomenon that can execute processes at different stages of training phase. Each of these stages are describe as follows:

1. Early stopping stage: When the observed indicators stop improving the results, the training process stops.

2. Reduce Learning rate On Plateau:When the observed indicator stops improving the result, it is used to reduce the learning rate.

The detailed configuration of the the proposed improved YOLOv5 model illustrated in Table 4. We can see that most of the images classified by our model are correct. Also, as there is always room for improvement, this model can perform better with a larger dataset. The summary of layers with their required parameter while training and validation phase for the proposed improved YOLOv5. The model got a notable accuracy of 96% on the testing set and 95% of accuracy on the validation set. Next, we have computed the training loss and accuracy and validation loss accuracy. The $accuracy$ represented training accuracy. The $valLoss$ represented validation accuracy, and the $valAcc$ represented validation accuracy.

5.2 Experimental results and analysis

AP (Average Accuracy) is a commonly used index to measure the accuracy of object detectors (such as Faster R-CNN, Fast R-CNN SSD, etc.). Average precision calculates the average precision value of the recall value in the range of 0 to 1. We considered the following criteria in our experiments.

1. IF IoU $\geq$ 0.5, classify the object detection as True Positive (TP). We have calculated AP at IoU .50 and .75. represented as AP_{50}, AP_{75}. Also, at across scales small, medium, and large, represented as AP_S, AP_M, AP_L as shown in Table 5.

2. If IoU $<$ 0.5, then it is a wrong detection and classifies it as False Positive (FP).

3. When ground truth is present in the image and the model failed to detect the object, we classify it as False Negative (FN).

Table 4: The proposed improved YOLOv5 model summary.

Layers type	Output Shape	Params
InputLayer	(None, 224, 224, 3)	0
Conv2D	(None, 224, 224, 64)	1792
Conv2D	(None, 224, 224, 64)	36928
MaxPooling2D	(None, 112, 112, 64)	0
Conv2D	(None, 112, 112, 128)	73856
Conv2D	(None, 112, 112, 128)	147584
MaxPooling2D	(None, 56, 56, 128)	0
Conv2D	(None, 56, 56, 256)	295168
Conv2D	(None, 56, 56, 256)	590080
Conv2D	(None, 56, 56, 256)	590080
MaxPooling2D	(None, 28, 28, 256)	0
Conv2D	(None, 28, 28, 512)	2359808
Conv2D	(None, 28, 28, 512)	2359808
Conv2D	(None, 14, 14, 512)	0
MaxPooling2D	(None, 14, 14, 512)	2359808
Conv2D	(None, 14, 14, 512)	2359808
Conv2D	(None, 14, 14, 512)	2359808
Conv2D	(None, 7, 7, 512)	0
MaxPooling2D	(None, 25088)	0
Flatten	(None, 4096)	102764544
Dense	(None, 4096)	16781312
Dense	(None, 2)	8194

4. True Negative (TN) is every part of the image where we did not predict an object. This metrics is not useful for object detection, hence we ignore TN.

We have computed the precision, recall, and mean accuracy precision (mAP) using the mathematical model as:

$$Precision = \frac{TP}{TP + FP} \tag{3}$$

$$Recall = \frac{TP}{TP + FN} \tag{4}$$

$$mAP = \frac{1}{N} \sum_{i=1}^{N} \text{AP}_i \tag{5}$$

We compare improved YOLOv5 to the state-of-the-art techniques in the area of instance segmentation in Table 6. Our proposed model outperform baseline variants of previous state-of-the-art models. This involves YOLOv3[16], YOLOv4[14], and other method include MNC [48] and FCIS [49], which are the winners of the COCO 2015 and 2016 challenges, respectively. improved YOLOv5 with ResNet-101-FPN backbone is better than FCIS [47]. We achieve a benchmark AP of 79%, AP_{50} of 68%, and AP_{75} of 64%. Again, we validate our system at multiple scale and obtained the results as AP_S of 16.5%, AP_M of 39.5%, and AP_L of 54.5%.

Table 5: Evaluation metrics used for improved YOLOv5 pedestrian detector

Metric	Annotation	Description
Avg. Precision	AP	AP at IoU=.50:.05:.95
$AP_{IoU=.50}$	AP_{50}	AP at IoU=.50
$AP_{IoU=.75}$	AP_{75}	AP at IoU=.75
AP_{Small}	AP_S	AP for small objects area $< 32^2$
AP_{Medium}	AP_M	AP for medium objects $< 32^2 <$ area $< 96^2$
AP_{Large}	AP_L	Area for large objects area $> 96^2$

Table 6: Improved YOLOv5 average precision results. Comparative analysis of average precision of proposed model to the state of the art approaches available in the literature.

Methodology	Backbone	AP	AP_{50}	AP_{75}	AP_S	AP_M	AP_L
MNC [48]	ResNet-101-C4	24.6	44.3	24.8	4.7	25.9	43.6
FCIS [47]	ResNet-101-C5-dilated	29.2	49.5	-	7.1	31.3	50.0
Mask R-CNN [13]	ResNet-101-C4	33.1	54.9	34.8	12.1	35.6	51.1
Mask R-CNN [13]	ResNet-101-FPN	35.7	58.0	37.8	15.5	38.1	52.4
Mask R-CNN [13]	ResNeXt-101-FPN	37.1	60.0	39.4	16.9	39.9	53.5
R-CNN [12]	ResNeXt-101-FPN	61.61	50.13	44.79	-	-	-
pAUCEnsT [35]	ResNeXt-101-FPN	65.26	54.49	48.60	-	-	-
FilteredICF [38]	ResNeXt-101-FPN	67.65	56.75	51.12	-	-	-
DeepParts [37]	ResNeXt-101-FPN	70.49	58.67	52.78	-	-	-
CompACT-Deep [32]	ResNeXt-101-FPN	70.69	58.74	52.71	-	-	-
Regionlets [29]	ResNeXt-101-FPN	73.14	61.15	55.21	-	-	-
3DOP [30]	ResNeXt-101-FPN	77.93	65.01	60.42	-	-	-
SAF R-CNN [31]	ResNeXt-101-FPN	77.93	65.01	60.42	-	-	-
Improved YOLOv5 without SCSP	ResNeXt-101-FPN	76	63.21	61.22	14.63	35.51	47.21
Improved YOLOv5 with SCSP	ResNeXt-101-FPN	79.31	68.42	64.1	16.5	39.5	54.5

5.3 Comparison with state-of-the-Art Pedestrian Detection methods

5.3.1 Caltech

Caltech training and testing photos were used to train the suggested system. Figure 6 depicts the outcomes (a). Techniques like TA-CNN [33], Checkerboards [34], CompACT-Deep [32], and SAF R-CNN [31] are compared to the suggested method. Improved YOLOv5 surpasses the other approaches by a significant margin, and we get the lowest miss rate of 8.32%. Using Mask R-CNN, it achieves state-of-the-art performance for object detection.

5.3.2 INRIA and ETH

The INRIA and ETH database images were also used to train and test the improved YOLOv5. Figure 6(b) and Figure 6(c) illustrate the comparison results (c). First, the suggested technique has a miss rate of 7.32% for the INRIA dataset picture, which is better than the previous method [35]. Second, the suggested model has a miss rate of 32.64% for the ETH dataset, compared to 34.98% for [41] and 37.37% for [47]. In general, the

suggested strategy has a greater detection rate and a lower miss rate on the dataset.

5.3.3 KITTI

The improved YOLOv5 was also put to the test on the KITTI dataset. Figure 6 (d) shows the improved YOLOv5 pedestrian identification findings and performance comparisons with other existing techniques [48] [49] [50]. On the KITTI dataset, the proposed technique yields promising results of 76%, 64%, and 60%.

5.3.4 MS COCO and proposed pedestrian dataset

Figures 6(e) and 6(f) depict the outcomes. When compared to existing strategies [44][45][46]47], the proposed methodology outperforms them. It has an 8.57% miss rate on MS COCO and an 8.69% miss rate on the planned pedestrian dataset. The receiving operating characteristics curve was used to represent the outcome. The suggested Improved YOLOv5-based pedestrian detector is compared to current pedestrian detection techniques. Figure 6(g) shows how the proposed model compares to TA-CNN [33], Checkerboards [48], CompACT-Deep [32], and SAF R-CNN [31] in terms of recall and precision. In terms of accuracy, speed, and time required for pedestrian detection, the Improved YOLOv5 surpassed existing techniques.

6   Conclusion and Future Scope

For accurate detection and path prediction of small and distributed pedestrians, a new and enhanced YOLOv5 and an approach based on motion and direction information are proposed. While identifying smaller and more dispersed pedestrians, the proposed network structure enhances detection accuracy. The network's feature extraction capabilities were improved by removing the repetitive convolutional layer and adding a scale-invariant cross-stage partial network layer to recognize pedestrians of various sizes. In YOLOv5, we've implemented a new feature fusion layer to gather more information about little pedestrians. We additionally use the backbone network's shallow features into the feature fusion layer to further reduce feature information loss for small pedestrians. A pyramid-based approach was devised to recognise pedestrians of different scales from multiple layers of photos with different resolutions using multi-scale pedestrian examples images. According to the evaluation results, the precision of YOLOv5 has increased by 3.4%. The current object detection technology of YOLOv5 for detecting varied size pedestrians could improve the proposed methodology. On benchmark datasets such as Caltech [38], INRIA [37], MS COCO [39], ETH [40], KITTI [41], and our proposed academic environment database, the revised YOLOv5 technique produces competitive results.

On the Caltech dataset, the experimental findings indicated that the suggested technique has 1) the lowest miss rate of 8.31%. 2) the INRIA dataset has the lowest log-average miss rate of 7.31%, 3) the ETH dataset has a miss rate of 32.63%, the KITTI dataset has a pedestrian detection accuracy of 79%, and the suggested database has a miss rate of 8.68%. When compared to existing new techniques such as YOLOv4[16], Mask R-CNN [12], SAF R-CNN [31], YOLOv5[17], and SSN[40], the suggested method is superior in identifying varied sizes and varying lighted pedestrians, as well as variation in orientation. The following parts of the suggested framework can be improved in the future. Despite the fact that the model operates in real time, it still has space for improvement in terms of speed, missed detection rates on the INRIA test dataset, and missed detection of small, similar, and concealed pedestrians. The suggested model can also detect and block pedestrians by detecting human poses and trajectories of various sizes.
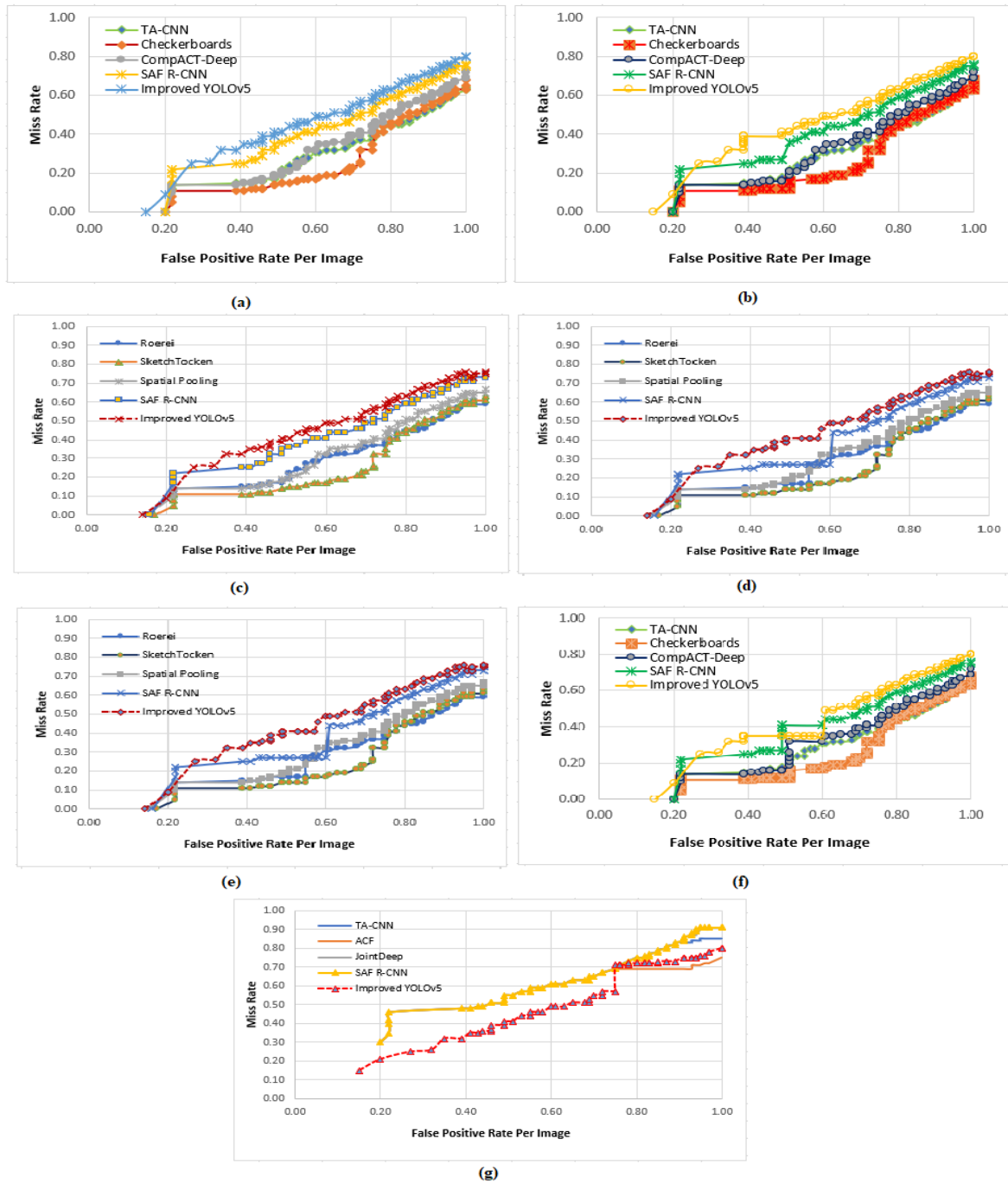
Figure 6: Improvements to the YOLOv5 pedestrian detector are compared to state-of-the-art approach and datasets. (a) Caltech: Lowest log-average miss rate of 8.32%, the improved YOLOv5 surpasses other approaches. (b) INRIA: Log-average miss rate of 7.32%, the improved YOLOv5 surpasses previous approaches. (c) ETH: The improved YOLOv5 Miss rate of 32.64% for the suggested model. (d) KITTI dataset: The upgraded YOLOv5 yields encouraging results of 76%, 64%, and 60%, respectively. (e) MS COCO: the Improved YOLOv5 outperforms other approaches, with an 8.57% miss rate. (f) Proposed pedestrian dataset: improved YOLOv5 outperforms other approaches, with an 8.69% miss rate. (g) A comparison of the Improved YOLOv5 and state-of-the-art approaches.

References

[1] Shanshan Zhang, Rodrigo Benenson, Mohamed Omran, Jan Hosang, Bernt Schiele, Towards reaching human performance in pedestrian detection, TPAMI, vol. 40, no. 4, pp. 973986, April 2018.

[2] Paul Viola. Michael Jones, "Rapid object detection using a boosted cascade of simple features," Proceedings of the 2001 IEEE Computer Society Conference on Computer Vision and Pattern Recognition. CVPR 2001, 2001, pp. I-I, DOI: 10.1109/CVPR.2001.990517.

[3] Pedro F. Felzenszwalb, Ross B. Girshick, David McAllester, Deva Ramanan, "Object Detection with Discriminatively Trained Part-Based Models," in IEEE Transactions on Pattern Analysis and Machine Intelligence, vol. 32, no. 9, pp. 1627-1645, Sept. 2010, DOI: 10.1109/TPAMI.2009.167.

[4] Navneet Dalal and Bill Triggs, "Histograms of oriented gradients for human detection," 2005 IEEE Computer Society Conference on Computer Vision and Pattern Recognition (CVPR'05), 2005, pp. 886-893 vol. 1, DOI: 10.1109/CVPR.2005.177.

[5] Najah Muhammad, Muhammad Hussain, Ghulam Muhammad, George Bebis, "Copy-Move Forgery Detection Using Dyadic Wavelet Transform," 2011 Eighth International Conference Computer Graphics, Imaging and Visualization, 2011, pp. 103-108, DOI: 10.1109/CGIV.2011.29.

[6] Ghulam Muhammad, M. Shamim Hossain, Neeraj Kumar, "EEG-Based Pathology Detection for Home Health Monitoring," in IEEE Journal on Selected Areas in Communications, vol. 39, no. 2, pp. 603-610, Feb. 2021, DOI: 10.1109/JSAC.2020.3020654.

[7] Ghulam Muhammad, Mohammed F. Alhamid, Xiaomi Long, "Computing and Processing on the Edge: Smart Pathology Detection for Connected Healthcare," in IEEE Network, vol. 33, no. 6, pp. 44-49, Nov.-Dec. 2019, DOI: 10.1109/MNET.001.1900045.

[8] Ross Girshick, Jeff Donahue, Trevor Darrell, Jitendra Malik, Rich feature hierarchies for accurate object detection and semantic segmentation, in IEEE Conference on Computer Vision and Pattern Recognition, Columbus, OH, USA, pp. 580587, 2014. DOI:10.1109/CVPR.2014.81.

[9] Kaiming He; Xiangyu Zhang; Shaoqing Ren; Jian Sun, "Spatial Pyramid Pooling in Deep Convolutional Networks for Visual Recognition," in IEEE Transactions on Pattern Analysis and Machine Intelligence, vol. 37, no. 9, pp. 1904-1916, 1 Sept. 2015, DOI: 10.1109/TPAMI.2015.2389824. 10. Ross Girshick, "Fast R-CNN," 2015 IEEE International Conference on Computer Vision (ICCV), 2015, pp. 1440-1448, DOI: 10.1109/ICCV.2015.169.

[10] Shaoqing Ren, Kaiming He, Ross Girshick, Jian Sun, "Faster R-CNN: Towards Real-Time Object Detection with Region Proposal Networks," in IEEE Transactions on Pattern Analysis and Machine Intelligence, vol. 39, no. 6, pp. 1137-1149, 1 June 2017, DOI: 10.1109/TPAMI.2016.2577031.

[11] Kaiming He, Menlo Park, Georgia Gkioxari, Piotr Dollr, Ross Girshick, "Mask R-CNN," in IEEE Transactions on Pattern Analysis and Machine Intelligence, vol. 42, no. 2, pp. 386-397, 1 Feb. 2020, DOI: 10.1109/TPAMI.2018.2844175. 13. Wei Liu, Dragomir Anguelov, Dumitru Erhan, Christian Szegedy, Scott Reed, Cheng-Yang Fu, Alexander C. Berg, SSD: Single shot multibox detector", European Conference on Computer Vision, Cham, Springer, pp. 2137, 2016.

[12] Joseph Redmon, Santosh Divvala, Ross Girshick, Ali Farhadi, "You Only Look Once: Unified, Real-Time Object Detection," 2016 IEEE Conference on Computer Vision and Pattern Recognition (CVPR), 2016, pp. 779-788, DOI: 10.1109/CVPR.2016.91.

[13] Joseph Redmon, Ali Farhadi, YOLO9000: Better, faster, stronger, IEEE Conference on Computer Vision and Pattern Recognition, Honolulu, pp. 65176525, Dec 2016.

[14] Alexey Bochkovskiy, Chien-Yao Wang, Hong-Yuan Mark Liao, YOLOv4: Optimal Speed and Accuracy of Object Detection, CVPR, 23rd April 2020.

[15] Qingqing Xu, Zhiyu Zhu, Huilin Ge, Zheqing Zhang, Xu Zang, "Effective Face Detector Based on YOLOv5 and Superresolution Reconstruction", Computational and Mathematical Methods in Medicine, vol. 2021, Article ID 7748350, 9 pages, 2021. https://doi.org/10.1155/2021/7748350.

[16] Rodrigo Benenson, Mohamed Omran, Jan Hosang, Bernt Schiele, Ten years of pedestrian detection, what have we learned, European Conference on Computer Vision, Cham, Springer, pp. 613627, Nov 2014.

[17] Arthur Daniel Costea, Sergiu Nedevschi, "Word Channel Based Multiscale Pedestrian Detection without Image Resizing and Using Only One Classifier," 2014 IEEE Conference on Computer Vision and Pattern Recognition, 2014, pp. 2393-2400, DOI: 10.1109/CVPR.2014.307.

[18] Rodrigo Benenson, Markus Mathias, Radu Timofte, Luc Van Gool, "Pedestrian detection at 100 frames per second," 2012 IEEE Conference on Computer Vision and Pattern Recognition, 2012, pp. 2903-2910, DOI: 10.1109/CVPR.2012.6248017.

[19] Ping Luo, Yonglong Tian, Xiaogang Wang, Xiaoou Tang, "Switchable Deep Network for Pedestrian Detection," 2014 IEEE Conference on Computer Vision and Pattern Recognition, 2014, pp. 899-906, DOI: 10.1109/CVPR.2014.120.

[20] Dollr, Piotr and Appel, Ron and Kienzle, Wolf (2012) Crosstalk Cascades for Frame-rate Pedestrian Detection. In: Computer Vision ECCV 2012. Vol.2. Springer, Berlin, pp. 645-659. ISBN 978-3-642-33708-6.

[21] Junjie Yan, Xucong Zhang, Zhen Lei, Shengcai Liao, Stan Z. Li, "Robust Multi-resolution Pedestrian Detection in Traffic Scenes," 2013 IEEE Conference on Computer Vision and Pattern Recognition, 2013, pp. 3033-3040, DOI: 10.1109/CVPR.2013.390.

[22] Wanli Ouyang, Xiaogang Wang, "Joint Deep Learning for Pedestrian Detection," 2013 IEEE International Conference on Computer Vision, 2013, pp. 2056-2063, doi: 10.1109/ICCV.2013.257.

[23] Sakrapee Paisitkriangkrai, Chunhua Shen, Anton van den Hengel, Strengthening the effectiveness of pedestrian detection with spatially pooled features, European Conference on Computer Vision, Cham, Springer, pp. 546561, July 2014.

[24] Xingyu Zeng, Wanli Ouyang, Xiaogang Wang, "Multi-stage Contextual Deep Learning for Pedestrian Detection," 2013 IEEE International Conference on Computer Vision, 2013, pp. 121-128, DOI: 10.1109/ICCV.2013.22.

[25] Christian Wojek, Stefan Walk, Bernt Schiele, "Multi-cue onboard pedestrian detection," 2009 IEEE Conference on Computer Vision and Pattern Recognition, 2009, pp. 794-801, DOI: 10.1109/CVPR.2009.5206638.

[26] Liliang Zhang, Liang Lin, Xiaodan Liang, Kaiming He, Is faster R-CNN doing well for pedestrian detection?, European Conference on Computer Vision, Cham, Springer, pp. 443457, July 2016.

[27] Murthy, Chinthakindi B., Mohammad F. Hashmi, Neeraj D. Bokde, and Zong W. Geem. 2020. "Investigations of Object Detection in Images/Videos Using Various Deep Learning Techniques and Embedded PlatformsA Comprehensive Review" Applied Sciences 10, no. 9: 3280. https://doi.org/10.3390/app10093280.

[28] Zhenxue Chen, Q. M. Jonathan Wu, Chengyun Liu, Real-time pedestrian detection with deep supervision in the wild, Signal Image and Video Processing, Springer, vol. 13, no. 4, pp. 761769, June 2019. DOI:10.1007/s11760-018-1406-6

[29] Jianan Li, Xiaodan Liang, Shengmei Shen, Tingfa Xu, Jiashi Feng, Shuicheng Yan, "Scale-Aware Fast R-CNN for Pedestrian Detection," in IEEE Transactions on Multimedia, vol. 20, no. 4, pp. 985-996, April 2018, DOI: 10.1109/TMM.2017.2759508.

[30] Wanli Ouyang, Hui Zhou, Hongsheng Li, Quanquan Li, Junjie Yan, Xiaogang Wang, "Jointly Learning Deep Features, Deformable Parts, Occlusion and Classification for Pedestrian Detection," in IEEE Transactions on Pattern Analysis and Machine Intelligence, vol. 40, no. 8, pp. 1874-1887, 1 Aug. 2018, DOI: 10.1109/TPAMI.2017.2738645.

[31] Yanwei Pang, Jin Xie, Muhammad Haris Khan, Rao Muhammad Anwer, Fahad Shahbaz Khan, Ling Shao, Mask-guided attention network for occluded pedestrian detection, IEEE International Conference on Computer Vision, Seoul, Korea, pp. 49664974, October 2019.

[32] Shanshan Zhang, Jian Yang, Bernt Schiele, "Occluded Pedestrian Detection Through Guided Attention in CNNs," 2018 IEEE/CVF Conference on Computer Vision and Pattern Recognition, 2018, pp. 6995-7003, DOI: 10.1109/CVPR.2018.00731. 35. Tao Song, Leiyu Sun, Di Xie, Haiming Sun, Shiliang Pu, Small-scale pedestrian detection based on somatic topology localization and temporal feature aggregation, ECCV 2018 Computer Vision and Pattern Recognition, July 2018.

[33] Yongqiang Zhang, Yancheng Bai, Mingli Ding, Shibiao Xu, Bernard Ghanem, "KGSNet: Key-Point-Guided Super-Resolution Network for Pedestrian Detection in the Wild," in IEEE Transactions on Neural Networks and Learning Systems, vol. 32, no. 5, pp. 2251-2265, May 2021, DOI: 10.1109/TNNLS.2020.3004819.

[34] Chunze Lin, Jiwen Lu, Gang Wang, Jie Zhou, "Graininess-Aware Deep Feature Learning for Robust Pedestrian Detection," in IEEE Transactions on Image Processing, vol. 29, pp. 3820-3834, 2020, DOI: 10.1109/TIP.2020.2966371. 38. Jialian Wu, Chunluan Zhou, Qian Zhang, Ming Yang, Junsong Yuan, Self-mimic learning for small-scale pedestrian detection, MM '20: Proceedings of the 28th ACM International Conference on Multimedia, pp. 20122020, October 2020. https://doi.org/10.1145/3394171.3413634

[35] Wei-Yen Hsu, Wen-Yen Lin, "Ratio-and-Scale-Aware YOLO for Pedestrian Detection," in IEEE Transactions on Image Processing, vol. 30, pp. 934-947, 2021, DOI: 10.1109/TIP.2020.3039574.

[36] Bing Han, Yunhao Wang, Zheng Yang, Xinbo Gao, "Small-Scale Pedestrian Detection Based on Deep Neural Network," in IEEE Transactions on Intelligent Transportation Systems, vol. 21, no. 7, pp. 3046-3055, July 2020, DOI: 10.1109/TITS.2019.2923752.

[37] INRIA dataset, Available at: http://pascal.inrialpes.fr/data/human/.

[38] Caltech dataset, Computer Vision Lab, http://www.vision.caltech.edu/.

[39] MS COCO (2018) dataset, Microsoft, https://cocodataset.org/download.

[40] ETH dataset, http://www.vision.ee.ethz.ch/'aess/dataset/.

[41] KITTI dataset, http://www.cvlibs.net/datasets/kitti/.

[42] MIT Dataset. http://cbcl.mit.edu/software-datasets/PedestrianData.html

[43] ATCI dataset, Computer Vision Lab, https://sites.google.com/site/rearviewpeds1/

[44] NICTA dataset, https://www.nicta.com.au/category/research/computervision/tools/ automap-datasets/

[45] TUD-Brussels dataset, Computer Vision Lab, https://www.mpiinf.mpg.de/departments/ computer-vision-and-machinelearning/publications

[46] PASCAL dataset, CV Lab, http://pascallin.ecs.soton.ac.uk/challenges/VOC/ databases.html/

[47] Nicolai W., A. Bewley, Dietrich P., Simple online and real-time tracking with a deep association metric, IEEE ICIP, pp. 36453649, March 2017.

[48] Yonglong Tian, Ping Luo, Xiaogang Wang, Xiaoou Tang, "Pedestrian detection aided by deep learning semantic tasks," 2015 IEEE Conference on Computer Vision and Pattern Recognition (CVPR), 2015, pp. 5079-5087, DOI: 10.1109/CVPR.2015.7299143.

[49] Shanshan Zhang, Rodrigo Benenson, Bernt Schiele, "Filtered channel features for pedestrian detection," 2015 IEEE Conference on Computer Vision and Pattern Recognition (CVPR), 2015, pp. 1751-1760, DOI: 10.1109/CVPR.2015.7298784.

[50] Mohammad Saberian Zhaowei Cai and Nuno Vasconcelos, "Learning complexity-aware cascades for deep pedestrian detection", IEEE Transactions on Pattern Analysis and Machine Intelligence PP(99):1-1, September 2020. DOI:10.1109/TPAMI.2019.2910514.

[51] Kerdvibulvech, Chutisant. (2011). Real-time Adaptive Learning System using Object Color Probability for Virtual Reality Applications. SIMULTECH 2011 - Proceedings of 1st International Conference on Simulation and Modeling Methodologies, Technologies and Applications, Noordwijkerhout, pp. 200-204, The Netherlands, 29 - 31 July, 2011.

[52] Chutisant Kerdvibulvech, A methodology for hand and finger motion analysis using adaptive probabilistic models. EURASIP J. Embed. Syst. 2014: 18 (2014), and Hybrid model of human hand motion for cybernetics application. SMC 2014: 2367-2372.DOI: 10.1186/s13639-014-0018-7

SIRA: Scale illumination rotation affine invariant mask R-CNN for pedestrian detection

Ujwalla Gawande[1] · Kamal Hajari[1] · Yogesh Golhar[2]

Abstract

In this paper, we resolve the challenging obstacle of detecting pedestrians with the ubiquity of irregularities in scale, rotation, and the illumination of the natural scene images natively. Pedestrian instances with such obstacles exhibit significantly unique characteristics. Thus, it strongly influences the performance of pedestrian detection techniques. We propose the new robust Scale Illumination Rotation and Affine invariant Mask R-CNN (SIRA M-RCNN) framework for overcoming the predecessor's difficulties. The first phase of the proposed system deals with illumination variation by histogram analysis. Further, we use the contourlet transformation, and the directional filter bank for the generation of the rotational invariant features. Finally, we use Affine Scale Invariant Feature Transform (ASIFT) to find points that are translation and scale-invariant. Extensive evaluation of the benchmark database will prove the effectiveness of SIRA M-RCNN. The experimental results achieve state-of-the-art performance and show a significant performance improvement in pedestrian detection.

Keywords Computer vision · Mask R-CNN · Pedestrian detection · Deep learning · CNN · Neural network

1 Introduction

In the past few decades, the world has been observing the threats to security in urban areas, which has expanded the pertinence of vision-based surveillance systems enough to detect pedestrians in high-density areas. Pedestrian detection has countless applications in computer vision. The obvious application is video surveillance [1].

Need and importance of Pedestrian detection Recently, due to the COVID-19 pandemic, surveillance systems have been used to monitor crowded places. It helps to identify hot spots (the areas where the virus infection spreads more opportunities). Owing to human interaction in highly congested areas, the chances of the spread of the COVID-19 virus increase. Therefore, the demand for pedestrian detection systems has increased. However, the current state-of-the-art installed system requires a conventional manual inspection of the video, which is in most cases time-consuming and infeasible. Pedestrian detection is an

essential and important task in any intelligent video surveillance system because it provides information for semantic understanding of video scenes. The focus of the researchers is to make it smarter and use deep learning to move from passive surveillance to active surveillance. The author proposes several promising frameworks to improve the accuracy and speed of pedestrian detection. Nevertheless, the deep learning framework still has room for improvement.

Need and importance of Pedestrian detection The detection accuracy is affected by various changes such as human body appearance, trajectory, posture, abrupt motion, scale changes, complex background, pedestrian deformation, partial or complete occlusion, shadows, etc. In this area, it is still an unresolved problem. Different factors related to the video capture method, such as low frame rate, unavailability of color information, camera sensor stability, compression technology, etc., directly affect the quality of the video sequence. It may limit the design of object detection algorithms. In addition, different cameras have different sensors, lenses, resolutions, and frame rates, resulting in different image quality. A low-quality image sequence can affect moving object detection algorithms. In some cases, different parts of a moving object might have different movements in terms of speed and orientation. When detecting moving

✉ Ujwalla Gawande

[1] IT Department, YCCE, Maharashtra, India

[2] CSE Department, GHRIET, Maharashtra, India

objects in the presence of a moving camera, the need to estimate and compensate for camera movement is inevitable. However, it is not an easy task to do because of possible camera's depth changes and its complex movements Table 1.

The development history of CNN based deep learning architecture can be summarized as follows The state-of-the-art Convolutional Neural Network (CNN) architecture used for object detection is You Only Look Once (YOLO) [2]. Compared with other CNN-based object detection frameworks, it is the most accurate and fastest.

PP-YOLO or PaddlePaddle YOLO is the most efficient and fast object detection model in real-time [3]. YOLO has different variants, such as YOLO v1, YOLO v2, YOLO v3, YOLO v4, and YOLO v5 [4]. However, YOLO-based object detection fails in multiple object detection and occlusion. Specifically, Mask R-CNN performs better in crowded environments. We can also use it for semantic, instance segmentation, and classification [5, 6]. Other architectures are Faster R-CNN [7, 8], Fast R-CNN [9], Region-based Fully Convolutional Network (R-FCN) [10], Single Shot MultiBox Detector (SSD) [11], Fully Convolutional Network (FCN) [12], Deep Convolutional Generative Adversarial Network (DCGAN) [13], Residual Neural Network (ResNet) [14], GoogLeNet [15], Visual Geometry Group (VGG Net) [16], ZFNet [17], AlexNet [18], Deep Belief Network (DBN) [19], LeNet [20], etc. used for the pedestrian detection. These frameworks are significantly better than other neural network architectures, such as Support Vector Machine (SVM) [21],

AdaBoost [22], Probabilistic Neural network (PNN) [23], Radial basis Neural Network (RBN) [24], Artificial neural network (ANN) [25].

The motivation for the proposed research work The Fig. 1 illustrates the motivation for the proposed contribution. Changes in the appearance of pedestrian instances make pedestrian detection difficult. In many cases, images of natural scenes usually vary in proportion, orientation, and lighting. These artifacts make pedestrian incident detection and classification a challenging task. Several other problems include 1) uneven lighting, 2) blurry and hazy appearance, 3) highlighting pedestrians, 4) changes in size with different posture changes, etc. Fig. 2 describes the key ideas of a new SIRA R-CNN framework, which is built on the Faster R-CNN pipeline [12]. The input image is first verified by the illumination recognition algorithm whether the input image needs illumination enhancement. The input image has low contrast, and then the histogram enhancement is performed on the input image. Afterwards, for the object proposal generation, first passes the process image through the bottom shared convolutional layers to extract its feature maps. Use these feature maps and scale rotation, affine invariant feature map for generation of to generate the final detection result, which is defined on the recommended size. We can always improve conclusive results through proposed feature maps and two-stage backbone networks, which are suitable for current input at certain scales. Therefore, SIRA R-CNN can achieve excellent detection performance in a wide range of input scales. Since SIRA R-CNN shares the convolutional
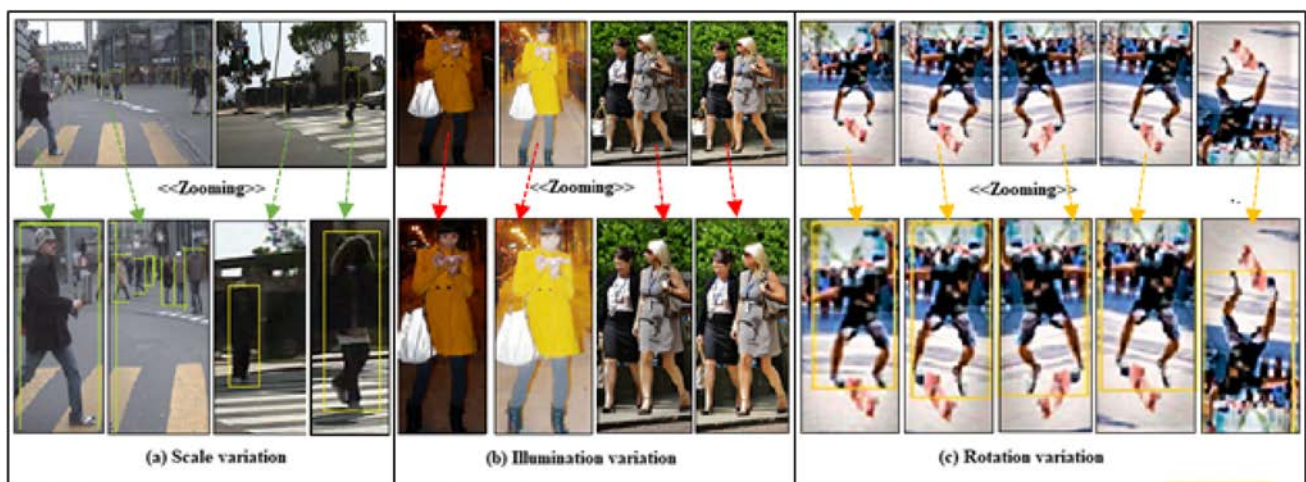
Fig. 1 Illustration of the motivation of the proposed SIRA Mask-RCNN. **(a) Scale variation:** The top row of the first column shows the pedestrian images from the California Institute of Technology [1] and the ETH [2] database. The first column and the bottom row show that the scaled visual appearance has changed significantly in proportion. **(b) Illumination variation:** The top row of the second column shows the pedestrian images from the California Institute of Tech-

nology [1] and the ETH [2] database. The bottom row of the second column shows a significant change in the visual appearance of the lighting after zooming. **(c) Rotation variation:** The top row of the third column shows the pedestrian images from the California Institute of Technology [1] and the ETH [2] database. The bottom row of the third column shows a significant change in the visual appearance when rotated after zooming
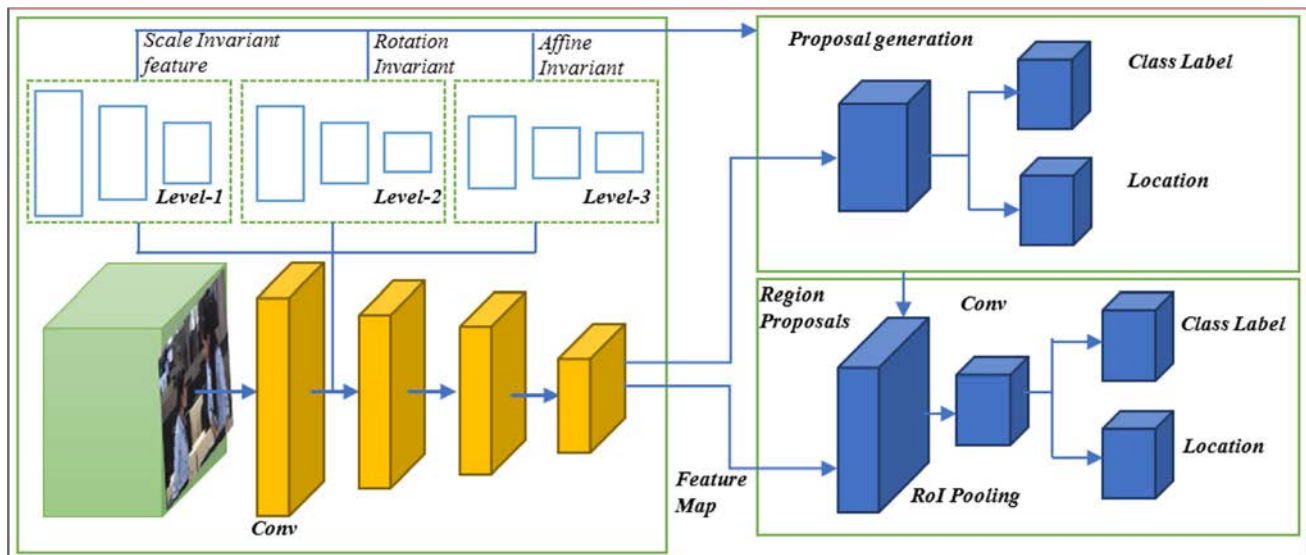
Fig. 2 Illustration of the proposed SIRA Mask R-CNN. We use multiple predefined box filters to filter multi-scale images to detect instances of different sizes. According to the proposed size of the target, the final result is obtained by fusing two-stage detectors and scale, illumination, rotation and affine invariant feature maps

Table 1 Feature extraction algorithm used in the state-of-the art pedestrian detector

Feature Extraction	Classifier	Reference
CNN	Mask R-CNN	[31]
HOG	Neural Network	[36]
LBP	SVM+CNN	[37]
Integral channel features	SVM+CNN	[38]
GLCM	SVM	[47]
Haar-wavelet transforms	SVM	[48]
Directional features	SVM	[46]
Vertical and horizontal	SVM	[47]
Edge intensities descriptors	Chamfer	[48]
Rectangular filter bank	Boosted cascade	[49]

features of the entire image with different target proposals, it is very effective in terms of training and testing time. Mask R-CNN has the advantage of predicting a binary mask for each specific detected object, while Faster-RCNN and FCN do not have this advantage. In these networks, objects are identified and classified, but no pixel-level segmentation mask is generated, and individual objects are not accurately distinguished.

The proposed region generation step generates an RoI, which may or may not contain the required objects. In the classification step, each RoI is classified as an object or background. However, despite its outstanding performance in terms of object detection accuracy, Mask RCNN is computationally costly for the new image as input to the system.

The proposal area generation process takes time to generate the RoI. Similarly, due to the unavailability of meaningful information about the object's scale and rotation-invariant features, the existing Mask R-CNN cannot effectively classify the smallest rotating object. These two drawbacks restrict the use of the Mask R-CNN in a real-world application for object detection in video surveillance.

The main objective of this research paper is to propose a method to reduce the computational cost of the pre-trained Mask-RCNN in the testing phase and to detect the small, revolved object efficiently. The key idea of this method is to modify the version of the Region Proposal Network (RPN) to generate a feature map with a scale rotation affine invariant feature map, which will provide additional object scale, orientation information. In particular, the feature map of the network can locate objects in the image. Hence, proposal regions for a new input image generated with scale and orientation aware information in the trained network, which results in the efficient small and rotated object detection in less computational cost. The detection accuracy increases because of the availability of object information on multiple scales. Joint feature maps of multiple resolutions extracted from different layers of the two networks and used for pedestrian detection, which results in a low false-positive rate. Experimental results show improvements in detection rates due to the proposed feature map.

R. Girshick et al. introduced a Fast R-CNN [9] to resolve the problem of the scale-variance issue by applying brute-force data on the image for scaling at the cost of time and computational complexity. Y. Gong et al. [29] recommended to use a multi-scale filtering model for all objects of different

sizes. However, Mask R-CNN is very popular in object detection. In this case, the recognition and generation of the object region proposal takes time to generate the ROI. Similarly, since there is no scaling factor, it will cause false detection of objects whose size changes during the object detection process. Each region proposal is convolved with a fixed-size filter mask to obtain CNN features. These features are inaccurate when the image has significant contrast, lighting, scale changes, and unclearness. These three shortcomings limit the application of Mask R-CNN in the real world.

The contributions of this paper are as follows:

1. A new SIRA Mask-RCNN is proposed to overcome scale, rotation and illumination artifacts.
2. In the proposed method. First, the illumination recognition and detection algorithms solve the problem of illumination changes. Secondly, the Contourlet transform and the direction filter bank use to solve the problem of rotation changes. Third, use ASIFT to solve the problem of translation and scale invariance.
3. The comprehensive evaluation of the proposed method on Caltech, INRIA, MS COCO, ETH, KITTI and the proposed academic environment database proves the effectiveness and robustness of the proposed SIRA Mask R-CNN.

The rest of the research paper is further organized as follows The latest architectural innovations in pedestrian detection technology and deep learning are described in Section 2. In Section 3, we describe the theoretical background of using deep neural networks for pedestrian detection. Section 4 describes the proposed approach to pedestrian detection. Section 5 presents the experimental results and comparative analysis of the proposed approach and the relevant methods. The last part ends with further research on the direction of pedestrian detection.

2 Literature survey

Researchers have proposed many pedestrian detection frameworks based on deep learning to improve the accuracy of pedestrian detection [30–35]. However, the accuracy of pedestrian detectors is affected by complex backgrounds, pedestrian scale changes, object occlusion, and illumination changes. These issues are partially addressed. The most commonly used method of pedestrian detection is the Histogram of Oriented Gradients (HOG) [36]. In this method, the directional gradient is used to detect objects in the image. It fails to detect an object in the case of occlusion and the HOG feature extraction process is time-consuming. Hence, it is not a perfect match for a real-time. In addition, In [37] proposed

a combination method of HOG and local binary mode (LBP) to deal with partial occlusion of pedestrians. In this method, LBP is used to obtain the texture features of the image. The HOG features and texture features used together to detect the pedestrian. P. Dollar et al. [38] introduce the method of combining HOG features and color features. Compared with HOG features, this method is faster because it uses integral images. In this method, the feature pyramid based on directional gradients of different scales. This leads to fast feature calculations in real time. The texture and orientated gradient feature somewhat address the issues and challenges of pedestrian detection. Therefore, researchers continue to use region-based deep learning techniques to solve the problem of detectors based on texture and directional gradient features [39, 40]. However, the region-based techniques use the pedestrian region proposals. The results of these methods are more accurate and simpler. In [41], an instance segmentation using the coverage loss method for object segmentation was proposed.

In this method, CNN features and scale-invariant feature transform (SIFT) combined together to detect objects. The limitations of this method are 1) Due to the hierarchical structure, when objects in the scene are occluded, non-adjacent areas will not merge to form a single part. A model was proposed in [42], which integrates a patch-based CNN and a global multi-receptive field (MRF) network. In this method, patches of different sizes are used to identify the ROI. CNN is used to mark each patch. MRF contains the unidirectional graph of label patches. In this graph, each vertex depicts an instance label of each pixel. The limitations of this method include: 1) It is not suitable for detecting multiple related occluded objects. In [43] exhibited a Relief R2-CNN for pedestrian detection in real-time. In this method, the main aim was on faster ROIs identification using CNN features. The weaknesses of this approach are 1) not validated and tested in real-time. 2) the classification needs more time. In [31] present, a unified joint detection model for the cyclist pedestrian detection. This approach utilizes Fast R-CNN. The limitations of this method are 1) It is not verified in real time. 2) target detection rate of cyclic pedestrians could be improved. It needs the verification of the target detection method in intelligent driven vehicles. Farther, In [30] introduced employed Mask R-CNN and an Optical flow-based method for the detection of the active football player's pedestrian. The shortcoming of this method are 1) non-active football players have been misclassified as an active player. 2) segmentation process is time-consuming and manual. Hence, not suitable for real-time. In [30], a scale-aware Fast R-CNN (SAF R-CNN) method for pedestrian detection is introduced. In this approach, two sub-networks are employed to detect varying scale pedestrians. The major disadvantage of this method is that the training and testing time increase because of the utilization of a two-sub network

and need time for computation. The proposed SIRA Mask R-CNN framework addresses the aforementioned problem by detecting the pedestrian at a different scale, orientation, and illumination. The next section describes the proposed SIRA Mask-RCNN framework (see Section 4).

3 Theoretical background

The conventional pedestrian detection system reported in the literature was classified into a Region of Interest (ROI) detection, feature extraction, and candidate classification. ROI detection is most often based on stereo vision. The most commonly used hand crafted features are HOG [36], LBP [37], Integral channel features [38], Gray level co-occurrence matrix [47], CNN features [31], HAAR-Wavelet [48], and Oriented gradients [49]. The classifier trained using these features. The different classifiers such as SVM, Mask R-CNN, Neural network, and Boosted cascade, etc. are used for the classification. The sliding windows [30] scheme and the hand-crafted feature-based method proposed, partially address the issues of pedestrian detection (1).

Hence, the researcher moves towards the region-based deep learning approaches to overcome the existing hand-crafted feature based system issues [39, 40] as shown in Table 2. LeNet is the first CNN architecture introduced by LeCun et al. [22] in 1998. It only includes two convolutional layers, a pooling layer, and a backpropagation network for training. LeNet has been trained on the revised National Institute of Standards and Technology (MNIST) database, which contains 50,000 images divided into 10 categories. At that time, it was successfully used for object detection and handwritten signature detection commercially. Its error rate is 26.2%. Next, AlexNet introduced by Krizhevsky et al. [20] in 2012. It is very similar to LeNet. AlexNet uses ReLU activation and cross-entropy loss function.

AlexNet has more convolutional layers. It is trained on the ImageNet large database and contains more than 1

million images from 1,000 categories. AlexNet has higher object detection accuracy than LeNet and is used for different types of object detection purposes. The error rate is reduced to 15.4%. Zeiler et al. [19] A modified version of AlexNet was launched in 2013. ZFNet uses 7 x 7 filters in the first convolutional layer instead of 11 x 11 as used in AlexNet. It achieves an error rate of 11.2%. Liu et al. [21] In 2009, an unsupervised deep neural network architecture was introduced. DBN consists of several layers along with multiple feature detectors or hidden units. Simonyan et al. citeref19 introduced VGGNet in 2014, which reduces the error rate to 7.2%. It expanded the number of convolutional layers to 19 layers. It limited the filter size reduced by a factor of 16 and to 3 x 3. GoogLeNet and ResNet use similar architectural patterns. Vanhoucke et al. [17, 18] The Google Inception network with VGGNet was introduced in 2014. It achieves the error rate of 6.7% marginally better than the VGGNet at the cost of complex architecture design patterns compares to VGGNet. He et al. [16] in 2015, introduced ResNet. It achieves an error rate of 3.57%. ResNet contains 152 convolutional layers. ResNet uses forward and backward instead of the initial model passes of the backpropagation algorithm. The problem with these approaches is the selection of a region before convolution. Objects in the image may have different spatial positions and aspect ratios. Need to select a huge area to get the object of interest in the image. Hence, an algorithm like YOLO, R-CNN developed to solve the problem of selection of regions that constitute an object of interest. Ross Girshick et al. [28] proposed R-CNN, in which a selective search algorithm is used to find a region of interest (RoI) in an image, which is called a region proposal. The selective search algorithm extracts 2000 regions from the image. The problem with R-CNN is that 1) it required an enormous amount of time to train the 2000 region proposals in the image. 2) We cannot use it for real-time applications. Because it takes 47 seconds for testing the image. 3) The selective search algorithm is fixed and not adaptive, so it sometimes generates bad region suggestions for complex images.

Fast R-CNN solves the shortcomings of R-CNN. Ross Girshick et al. [14] again proposed the enhanced version of R-CNN i.e. Fast R-CNN. It is similar to R-CNN, but instead of inputting regional suggestions into CNN, it inputs this architecture into CNN to generate convolutional feature maps. In this process, it max-pooled the input feature map to generate a 7 x 7 square area of fixed size. This area is inputted into the fully connected Softmax layer to predict the category of the object. Results have been represented using the bounding box. Fast R-CNN is more efficient and faster than R-CNN because it does not require 2000 region proposal training to classify objects. Both the architecture usages the selective search to find region proposals using a

Table 2 Deep learning architecture used for pedestrian detection

Architecture	Dataset	Error rate (%)
LeNet [22]	MNIST	26.2%
AlexNet [20]	ImageNet	15.4%
ZFNet [19]	ImageNet	11.2%
VGGNet [18]	MNIST	7.2%
Google Inception network with VGGNet [16]	ImageNet	6.7%
ResNet [15]	ImageNet	3.57%
Fast R-CNN [14]	MS COCO	3.1%
Faster R-CNN [13]	MS COCO	2.75%
Mask R-CNN [12]	MS COCO	2.67%

selective search algorithm. This process is slow and time-consuming that affects the performance of the network.

Shaoqing Ren et al. [12, 13] introduced a Faster R-CNN to solve the Fast R-CNN speed problem by eliminating the selective search algorithm. In this architecture, the network itself learns the region proposals instead of using a selective search algorithm to identify region proposals. It proposes to use a separate network for the recognition region in the convolutional feature map. Hence, it is faster than the Fast R-CNN but not useful in the real-time applications for object detection. In all previous versions of the R-CNN series, regions are used to locate objects in the image. Joseph Redmon et al. [8] introduced a new architecture, i.e. YOLO. Here, a single convolutional layer network predicts the bounding boxes and class labels of these boxes. The input image composed of the S x S grid and each grid, m bounding boxes generated. For each of the bounding boxes, the convolutional network generates the class probability and bounding box location values for locating the object in the image. YOLO processes 45 frames per second, which is faster than other object detection algorithms. The problem with YOLO is that it cannot detect small objects in the image due to the limitation of the spatial plane coordinate position of the algorithm. The semantic segmentation algorithms classify the object at the pixel level. Recent architecture, i.e., Mask-RCNN, has used for instance segmentation. Recognizing each instance of a single object in the image and locating each instance pixel is called instance segmentation. However, instance segmentation is difficult because it requires accurate positioning and detection of all moving and non-moving objects in the image. Hence, it combines object detection and semantic segmentation techniques. Here, object detection, object classification, and the use of bounding boxes for representation. In semantic segmentation, each pixel is classified into a meaningful group without distinguishing object instances.

4 Proposed methodology

The proposed SIRA Mask-RCNN framework includes three stages: 1) input image/video enhancement, 2) illumination, rotation, scaling and translation invariant feature extraction, and 3) classification using Mask R-CNN. We describe each of these steps in brief as follows.

4.1 Input image/video enhancement

The input to the proposed system is the image or frame of the video. If it is a video, we transform it into a frame. We have conducted experiments on the publicly obtainable standard database and on our database in an academic environment. The main steps of enhancement include the use of histogram analysis for illumination recognition and detection. These steps are essential for enhancing the input image/video quality. We describe each of the steps in the next subsection.

4.2 Illumination identification and detection

The main aim of the proposed algorithm is to identify input image/frame required illumination enhancement or not based on the histogram analysis. First, we divide the input image into three categories as 1) uneven image, 2) glare image, and 3) uniform image based on the histogram and pixel-level analysis. The input image/frame converted from RGB to HSV color space. We need the conversion because our focus is on the intensity of the image. We have plotted the histogram of a value change to identify the type of image. After several experiments on the different images, we have obtained the optimal thresholds used for distinguishing the darker and brighter intensity. We use the percentais ge of low pixel and high pixel values to classify the image into one of the three categories.

We describe the sequence of steps for lighting recognition and detection below.

The uneven intensity image composed of light that unevenly distributed in different intensity ranges. Glare images include specific areas in the image that are overexposed by light. Image specific areas comprise brighter pixels. The ideal image does not require the enhancement, it comprises the uniformly distributed intensity. if the input image has a high variance, it is the case of irregular brightness. After histogram analysis, we observed that the image background is uniform, and low variance means that the input image does not need to be enhanced. In the image below, you can view the three small peaks that process three separate illuminated areas. The highest peak in the center results from making all the dark region black pixels to the mean value. After several experiments, we found that a standard deviation above 25 can be called uneven illumination cases.

We can also identify the bright pixels easily when there is a glare on the image. Except for objects, the glare image looks like a good image. There can be a possibility that the image comprises high brightness regions, so if the mean of the input image is above 200, then it is true that there is no need to detect the object. We can eliminate those frames, as shown in Fig. 2.

Finally, by using the proposed illumination recognition and detection algorithm, it is detected whether illumination enhancement is needed. In the next section, we describe image enhancement using logarithmic transformation.

Algorithm 1: Illumination identification and detection

Input: $f(x, y)$: Read the input image or video
Output: $isEnhanReq$: Input Image require
enhancement or not
Required parameter: $T1, T2, T3, T4, T5, T6, T7$:
Threshold for comparing
pixel intensity value.

Begin:
1 Read the input image or video.
   if $readFile\ is\ video$ **then**
2 | $f(x, y) \leftarrow \sum_{n=1}^{m} vf(x, y)$ Read all the frames.
3 **else**
4 | $f(x, y) \leftarrow If(x, y)$ Read input image.
5 **end**
6 Convert input image/frame into HSV space.
   $Hf(x, y) \leftarrow rgb2hsv(f(x, y))$
   Read each pixel location by row and column index position.
   for $i \leftarrow 1$ **to** m **do**
7 | **for** $j \leftarrow 1$ **to** n **do**
8 | | Compare intensity value against threshold.
            if $f(xi, yj) \geq T1$ **then**
9 | | | Image having high pixel intensity value.
              $HPf(xi, yj) \leftarrow f(xi, yj)$
10 | | **else**
11 | | | Image having low pixel intensity value.
              $LPf(xi, yj) \leftarrow f(xi, yj)$
12 | | **end**
13 | | $j + +$ For reading next column pixel in image.
14 | **end**
15 | $i + +$ For reading next row pixel in image.
16 **end**
17 Calculate percentage of High Pixel and Low Pixel.
   PerHP $\leftarrow$ TotHPF / TotImgPixel * 100
   PerLP $\leftarrow$ TotLPF / TotImgPixel * 100
   Reshape the image to uniform the input image resolution. Plot the histogram of image pixel intensity aganist count of intensity values.
   Check weather enhancement is required or not
   isEnhanReq $\leftarrow$ False
   Check weather image having uneven illumination or not
   if $stDev \geq 25\ and\ PerLP \geq T2\ and\ PerHP \geq T3$ **then**
18 | Set **isEnhanReq** $\leftarrow$ True
19 **end**
20 Check weather image having glare
   if $mean\ f(x, y) \geq T4\ and\ PerHP \geq T5$ **then**
21 | Set **isEnhanReq** $\leftarrow$ True
22 **end**
23 Check weather image having uniform illumination
   if $stDev \leq 25\ and\ PerLP \leq T6\ and\ PerHP \leq T7$ **then**
24 | Set **isEnhanReq** $\leftarrow$ True
25 **end**

4.3 Image enhancement

Logarithmic transformation replaces all pixel values with their logarithmic values. We used it for image enhancement as it unfolds, dark pixels as compared to the bright pixel. We compute the log transformation using the following Eq. 1.

$$L(x, y) = s * \log(1 + F(x, y)) \tag{1}$$

Here, $F(x, y)$, input image and s is scaling constant and $L(x, y)$, output image. The value of s is determined such that, we get the maximum output corresponding to the bit size used. So, the s is calculated using the following Eq. 2.

$$s = 255 / \log(1 + \max(F(x, y))) \tag{2}$$

However, for the computation of constant value s any pixel intensity is 0 then its corresponding log value will be infinite. Hence, we are adding 1 to each pixel intensity value at the time of log transformation that results in any pixel intensity value is 0, then it will become 1 and its log value will be 0. Fig. 3 shows the result input image enhancement after log transformation.

In the conversion, the darker low intensity is given the brighter high value, so that the features existing in the darker or gray area of the image are more visible and obvious to the human eye. It can also reduce the brighter brightness to a lower dark value. Results in a more illuminated image in the output as shown in Fig. 4.

However, the luminous intensity not scaled down to the low-intensity region. The scaling constant represents and transforms the higher intensities. In the next subsection, we have described the rotation invariant feature extraction.

4.4 Rotation invariant feature extraction

The rotation-invariant features extracted using contourlet transformation. It converts the enhanced image into a multi-resolution part. It is a combination of the Laplacian pyramid and direction filter bank. The features obtained from the contourlet transform are scale invariants. It can provide smooth edges in any direction. We have not implemented wavelet transformation, because we see edges, but the directional information about the edges unknown. It gives edges in four directions (vertical, horizontal, +45°, -45°). We extracted the contourlet transformation edges in eight directions. In Laplace decomposition, the two main scaling operations are to perform reduction and growth. Each of the operation describe in brief as follows.

1. Reduced operation employs a low-pass filter to the transformed image and down-samples by two factors.
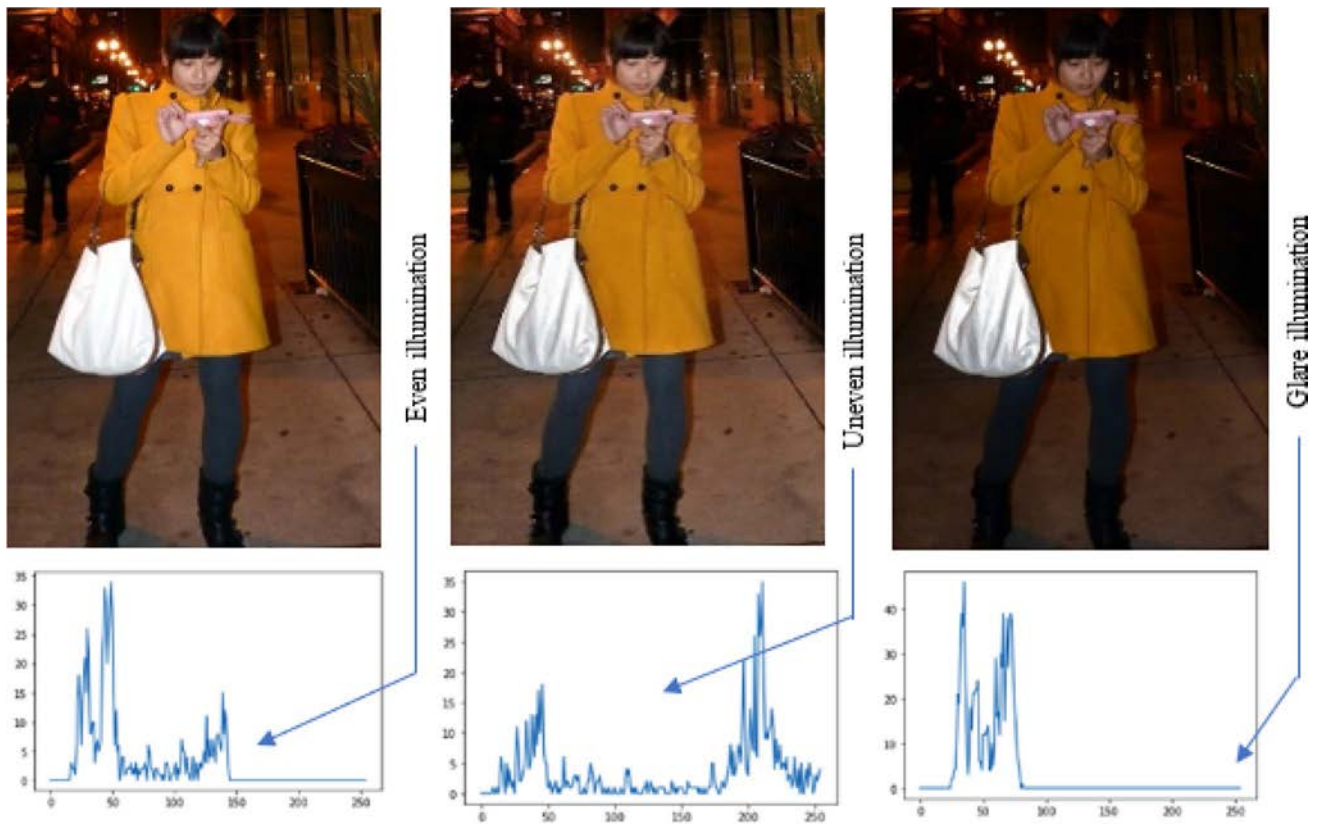
Fig. 3 First row shows even, uneven, and glare illuminated image. Second row shows the histogram of image

2. The grow operation applies a predefined interpolation technique and up-samples it by two factors.

3. Next, in the Gaussian pyramid a series of replica represented by $Gp_1, Gp_2, ..Gp_n$ of the transformed image represented by $lf(x, y)$ at different scale. It is accomplished by placing $Gp_1 = lf(x, y)$, and iteratively employing $Gp_{i+1} = reduce(Gp_i)$.

4. The Gaussian pyramid is processed to obtained Laplacian pyramids represented by $Lp_1, Lp_2, Lp_3...Lp_n$. It is accomplished by placing $Lp_n = Gp_n$, and iteratively employing $Gp_i = Lp_i$ grow Gp_{i+1}.

Later, the Laplacian pyramid feed into the directional filter bank (DFB). The input image obtained from the Laplacian pyramid of Level 1 modulated. In modulation, the constituent frequency component shifted before re-sampling the image component. In re-sampling, we have considered the frequency re-sampling matrix 2 x 2. It is used to reshape the dimand shap component to different parallelogram. At the end, down-sampled the image. It reduces the number of grid point in the original image. In down-sampling the smoothing and sharpening performed. Later We subtracted the filtered responses to obtain the contours. The obtained

edges are in 8 direction. Each of the directional filter bank steps are describe in brief as follows.

1. The first operation is a Gaussian low-pass filtering for smoothing the image. It calculates the average of pixel and replace with the original pixel repeatedly applies for every pixel with cutoff frequency D_0 as 85. It is represented by $Lo(\omega)$. The transfer function of a Gaussian lowpass filter is defined as:

$$Lo(\omega) = e^{-D^2(u,v)/2D_0^2} \tag{3}$$

2. The next operation is a high-pass. It produces the Gaussian high frequency component and reduces low frequency component with cutoff frequency D_0 is 15. It is represented by $Ho(\omega)$. The transfer function of a Gaussian highpass filter is defined as:

$$Ho(\omega) = 1 - e^{-D^2(u,v)/2D_0^2} \tag{4}$$

3. At the end both values are subtracted to obtained the contours as Eq. 3. It is represented by $Co(\omega)$.

$$Co(\omega) = Ho(\omega) - Lo(\omega) \tag{5}$$

4. The same process continuously applies up to third iteration.

5. The three levels of information are extracted from the transformation. It is eight directional information. The sub-band of 0-3 is taken as horizontal direction and sub-band of 4-7 taken as vertical direction. Later these features are combined with CNN features of Mask R-CNN to obtained the detection result.

6. The histogram equalization is applied over the transformed image to obtained the normalized image.

Next, sub-section describes the ASIFT feature extraction and architecture of improved Mask R-CNN as shown Fig. 5 used for pedestrian detection and classification.

4.5 ASIFT feature extraction and mask R-CNN

The new scale-invariant feature map generation algorithm is placed in the Regional Proposal Network (RPN) to generate multi-scale feature maps for pedestrian instances of different scales. We divide the proposed framework into three stages viz. 1) scale-invariant feature map generation. 2) region proposal generation. 3) Extract the detected pedestrian target from the image. Input to the Mask R-CNN is the transformed image, and it generates the object surrounded by a bounding box, class label, and pixel-level mask. We used Mask-RCNN for pixel-level mask generation, as shown in Fig. 5. We describe the algorithm for generation of scale and translation invariant CNN feature as follows:

Algorithm 2: ASIFT feature extraction

Input: Image u, tilt factor $\delta = \sqrt{2}$, tilt range from 1 to n where, $n = 5$, rotation sampling step factor $b = 72$

Output: ASIFT key points features computed by tilt and rotation values

Begin:

1 For each orientation compute angle. **for** $t \leftarrow 1$ **to** δm **do**

2   No need to compute the rotation points when $t = 1$, it means no tilt

    if $t = 1$ **then**

3       $\theta \leftarrow 0$

      Compute scale, rotation, and translation-invariant features on the original image

      $key(t, \theta) \leftarrow \text{SIFT}(u)$

4   **else**

5   Rotation angle **for** $\theta \leftarrow 0$ **to** Nb/t **do**

6         $u_r \leftarrow \text{rotate}(u, \theta)$

        Rotate image with bi linear interpolation

        $u_f \leftarrow \text{GaussianFilter}(u_r)$

        $u_t \leftarrow \text{tilt}(u_f, t)$

        $key(t, \theta) \leftarrow \text{SIFT}(u, u_t)$

7   **end**

8   **end**

9 **end**

As shown in Fig. 4, enhanced image is transformed by assuming all possible orientation and translation changes in the position. The tilt represented by t computed by Eq. 4.

$$t = \frac{1}{\cos\theta} \tag{6}$$

The directional transformation t on the input image $u(x, y)$ change to $u(x, y) \rightarrow u(tx, y)$. The gaussian filtering is used for reducing aliasing error. ASIFT key points, rotation invariant features, and CNN features are combined to obtained the detection result (Fig. 6).

We divided the process of pedestrian detection into three stages: 1) Region proposal generation, 2) the multi-scale, rotation, and affine invariant feature extraction. 3) Bounding box and category prediction. We convolve the different scale masks with various size anchor box filters to obtain the confidence score without omitting the low-resolution layer, which was omitted in the existing Mask R-CNN RPN network. Later, this score integrated with the rotation, scale, and affine invariant features obtained in an earlier stage. The primary purpose is to use the proposed method to improve the accuracy of regional recommendations. In RPN, we convolve the enhanced image with bottom-up and top-down methods to extract features. From the enhanced image, ResNet is used to extract high-level features.

The previous layer convolved with a $3x3$ sliding window to generate the multiple feature map. Next, apply the $1x1$ convolution filter again to the class prediction and bounding box. For the $3x3$ mask, we used a sliding window because the mask applied from the center will result in accurate information. K anchor boxes of different sizes used at the time of convolution so that different shape objects detected. We generate the output as the $2k$ score of the class layer and the $4k$ score of the bounding box regression. The scale-invariant feature map is fused with other feature maps to effectively locate objects of different scales. Next, each region's proposal aligned using the ROI align. In the end, we represent all the detected objects with the bounding box and segmentation mask at a pixel in the original image. At last, human detected class IDs separated from all detected objects.

5 Implementation

We assessed the performance of the proposed SIRA Mask R-CNN on benchmark pedestrian databases such as Caltech [1], INRIA [2], MS COCO [26], ETH [27], and KITTI [28] and our pedestrian database. The experiments and proposed deep learning framework implemented on single NVIDIA

Fig. 4 Image enhancement results. First row shows before log transformation and Second row shows after log transformation

GPU and a CPU Intel Core i5 3.4GHz processor having 16GB RAM and 16GB NVIDIA graphics card.

6 Experiment

The State-of-the-art pedestrian analysis research conducted on publicly available benchmark data sets such as Caltech [1], INRIA [2], MS COCO [26], ETH [27], and KITTI [28], etc. The limitation of these datasets are: 1) the limited range of pedestrian poses recorded on the city streets in a controlled environment, 2) these datasets contain data with short lapses of time between successive observations of each ID in a single day, which allows to use clothing appearance features in identity matching, 3) All of these pedestrian data sets are recorded in various places such as streets and parking spaces, but they do not cover student behavior in an academic environment. This paper proposes a new dataset in an academic environment. Human experts annotated student pedestrian behavior on each frame sequence of the video, providing three types of information.

1. Pedestrian positioning with bounding box. The position of each pedestrian in the video frame is represented as a bounding box, and we can use this data for pedestrian detection, tracking, instance, and semantic segmentation.
2. Physical, behavioral, or adhered to human characteristics. Each pedestrian fully characterized by labels such as 'Face': eyes, eyebrows, forehead, nose, ears, mouth, facial hair, moustache, glasses, beard, 'hairstyle', 'hair color', 'age', 'body volume', 'gender', 'age', 'height', 'body accessories', 'ethnicity', 'head accessories', 'action' and 'clothing data'.
3. Annotated class label and ID. Each pedestrian has a unique identifier that is uniform across all video frames. These characteristics of the data set make it suitable for various recognition difficulties.

6.1 Experimental setup

We propose a pedestrian database composed of different behaviors of students under different conditions in academic activities such as students studying in a practical lab, examination hall scenarios, classrooms, a student cheating in an exam hall, a student taking an answer book outside the exam hall, a student stealing a mobile phone or other electronic
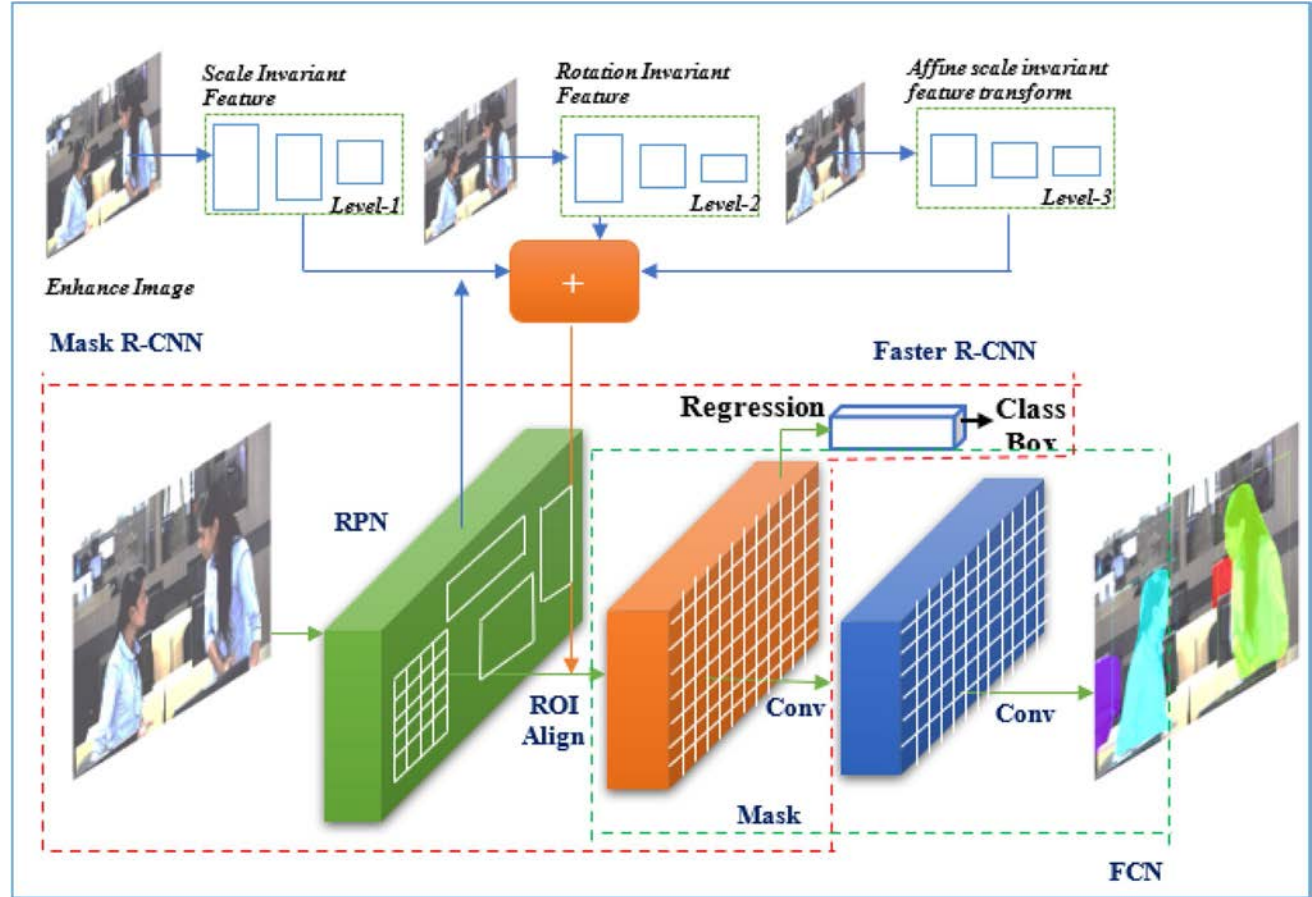
Fig. 5 SIRA Mask R-CNN: Improved Mask R-CNN Architecture

Fig. 6 Affine Scale Invariant Feature Map Generation. Point along the ray from initial point
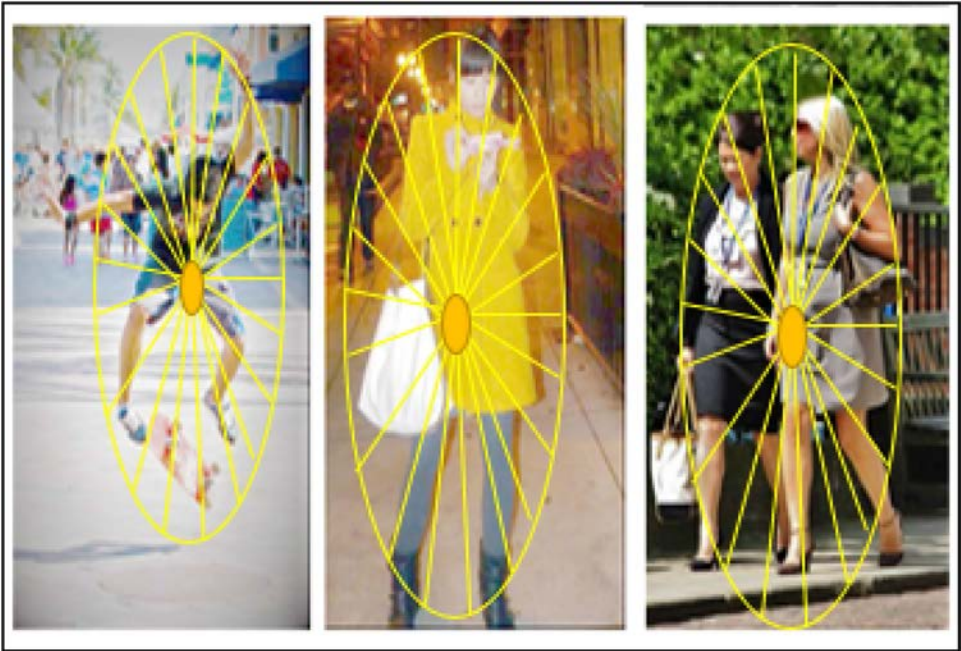
Fig. 7 Sample image of the proposed database. The first row illustrates two girls dispute in the lab. The second row illustrate the scenario stealing the mobile phone in lab. The third row illustrate a scenario of a student threatening. The fourth row shows the same threatening scenario(front view). The fifth row shows the scenario of students stealing the lab equipment. The sixth row shows the scenario cheating in the exam hall

devices such as a mouse or keyboard, a student stealing lab equipment, a student dispute on the college premises, a student disturbing another student, a student threatening another student, etc. as shown in Fig. 7. Students' behavior in college premises is recorded using a high-quality DSLR camera from different viewing angles. The video is recorded at 30 f/s. The database includes approximately 100 sample videos. 20 to 30 minute duration for each sample video.

6.1.1 Image/video acquisition framework

Student's behavior in college premises recorded using a high-quality DSLR camera from a different viewing angle. We recorded video at 30 f/s, enabled 4K recording, with a resolution of 3840×2160, and H.264 compressed to .mp4 format. The database includes more or less 100 sample videos. The duration of each example video is 20-30 minutes. The camera tilt angle varies from 45° to 90°. Pedestrians are students of Yeshwantrao Chavan College of Engineering in Nagpur, aged 22-27 years old, over 90%, of which 65% are male and 35% are female, mainly of Indian ethnicity. The key features of the data acquisition settings summarized in Table 3.

6.1.2 Data pre-processing

In the proposed dataset, we classified the video information namely into three directories as "Train", "Test" and "Validation". We describe the following three entities:

1. Annotations directory contains a XML file for each image. This file contains all the information about the image.
2. The frames are extracted from each video and divided into training and validation set in different directory.
3. The details about the frames are stored in the .txt file, it stores a unique identity number for each image.

However, for the classification purpose, we defined a SIRA Mask R-CNN model, along with "ReLU" as an activation function. In the proposed approach, we used sparse categorical cross-entropy instead of categorical cross-entropy for the compilation of SIRA Mask R-CNN model. The major advantage of using sparse classification cross-entropy is that it preserves time and computational effort, because it only uses a single value for a class label instead of the entire feature vector. We used simultaneous callbacks. A callback is a phenomenon that can execute processes at different stages of training phase. Each of these stages are describe as follows:

Table 3 The proposed dataset video Acquisition configuration

Parameter of Camera	Setting
Camera:DSLR HD:12.4M	Frame size:3840×2160
Lens FOV 94 20 mm f/2.8 focus	ISO Range: 100-3200
Camera tilt angle	45° to 90°
Video recording format	.mp4

Table 4 The proposed SIRA Mask R-CNN model configuration

Parameter	Setting
Backbone	ResNet101
Backbone Strides	[4,8,16,32,64]
Batch Size	1
BBox	[0.1 0.1 0.2 0.2]
Backbone shape	None
Max obj detection	100
Min Confidence	0.7
NMS Threshold	0.3
FPN Layer Size	1024
GPU	1
Gradient Norm	5.0
Image Per GPU	1.0
Image Channel Count	3
Image Max Dim	1024
Image Meta Size	93
Image Min Dim	800
Image Min Scale	0
Image Resize Mode	Square
Image Shape	[1024 1024 3]
Learning Momentum	0.9
Learning Rate	0.001
Loss Weight	rpnClassLoss: 1.0,
	rpnBboxLoss: 1.0,
	mrcnnClassLoss:1.0,
	mrccBboxLoss:1.0,
	mrcnnMaskLoss:1.0
Mask Pool Size	14
Mask Shape	[28 28]
Max GT Instances	100
Mean Pixel	[123.7 116.8 103.9]
Mini Mask Shape	[56 56]
Number of Class	2
Pool Size	7
Post NMS RoIs Inference	1000
Post NMS RoIs Training	2000
Pre NMS Limit	6000
RoI Positive Ratio	0.33
RPN Anchor Ratios	[0.5, 1, 2]
RPN Anchor Scales	[32, 64, 128, 256, 512]
RPN Anchor Stride	1
RPN BBox	[0.1 0.1 0.2 0.2]
RPN NMS Thresholds	0.7
RPN Train Anchors Per Image	256
RPN NMS Threshold	1000
Top Down Pyramid Size	256
Train BN	False
Train RoIs Per Image	200
USE Mini Mask	True
USE RPN RoIs	True
Validation Steps	50
Weight Decay	0.0001

1. Early stopping stage: When the observed indicators stop improving the results, the training process stops.
2. Reduce Learning rate On Plateau:When the observed indicator stops improving the result, it is used to reduce the learning rate.

The detailed configuration of the the proposed SIRA Mask R-CNN model illustrated in Table 4. We can see that most of the images classified by our model are correct. Also, as there is always room for improvement, this model can perform better with a larger dataset. The summary of layers with their required parameter while training and validation phase for the proposed SIRA Mask R-CNN shown in Table 5.

The model got a notable accuracy of 96% on the testing set and 95% of accuracy on the validation set. Next, we have computed the training loss and accuracy and validation loss accuracy. The Fig. 8(8) illustrate the accuracy and epochs plot for representing accuracy and validation accuracy and Fig. 8(8) illustrate the loss and epochs plot for representing loss and validation loss. The *loss* represented training loss. The *accuracy* represented training accuracy. The *valLoss* represented validation accuracy, and the *valAcc* represented validation accuracy.

Table 5 The proposed SIRA Mask R-CNN model summary

Layers type	Output Shape	Params
InputLayer	(None, 224, 224, 3)	0
Conv2D	(None, 224, 224, 64)	1792
Conv2D	(None, 224, 224, 64)	36928
MaxPooling2D	(None, 112, 112, 64)	0
Conv2D	(None, 112, 112, 128)	73856
Conv2D	(None, 112, 112, 128)	147584
MaxPooling2D	(None, 56, 56, 128)	0
Conv2D	(None, 56, 56, 256)	295168
Conv2D	(None, 56, 56, 256)	590080
Conv2D	(None, 56, 56, 256)	590080
MaxPooling2D	(None, 28, 28, 256)	0
Conv2D	(None, 28, 28, 512)	2359808
Conv2D	(None, 28, 28, 512)	2359808
Conv2D	(None, 14, 14, 512)	0
MaxPooling2D	(None, 14, 14, 512)	2359808
Conv2D	(None, 14, 14, 512)	2359808
Conv2D	(None, 14, 14, 512)	2359808
Conv2D	(None, 7, 7, 512)	0
MaxPooling2D	(None, 25088)	0
Flatten	(None, 4096)	102764544
Dense	(None, 4096)	16781312
Dense	(None, 2)	8194

Fig. 8 Accuracy and loss training and validation. (a) Accuracy vs Epochs for representing accuracy and validation accuracy. (b) Loss vs Epochs for representing loss and validation loss

6.1.3 Pedestrian annotation

The proposed dataset completely annotated at the frame of video, by human specialists. We provide a csv file for each video sequence, using the same file naming protocol as videofilename.csv. The labeling process is divided into three stages: 1) human detection; 2) tracking, 3) suspicious activity recognition and soft biometric features. First, the Mask R-CNN [12] method is used to provide an initial estimate of the position of each pedestrian in the scene, and the data obtained are manually verified and corrected. Next, the deep sort method [14] provided the preparatory tracking information, which was again corrected manually. As a result of these two initial steps, we obtain a rectangular bounding box representing the region of interest (ROI) for each pedestrian in each frame. The final stage of the annotation process is carried out manually, where a human expert who personally knows the students of the college sets up ID information and characterizes the samples based on soft labels. Table 6 shows the detailed information of the label annotated for each pedestrian instance in the frame, as well as the ID information, the bounding box that defines the ROI, and the frame information. For each label, we also provide a list of its possible values.

6.2 Experimental results and analysis

AP (Average Accuracy) is a commonly used index to measure the accuracy of object detectors (such as Faster R-CNN, Fast R-CNN SSD, etc.). Average precision calculates the average precision value of the recall value in the range of 0 to 1. We considered the following criteria in our experiments.

1. IF IoU $\geq$ 0.5, classify the object detection as True Positive (TP). We have calculated AP at IoU .50 and .75. represented as AP_{50}, AP_{75}. Also, at across scales small, medium, and large, represented as AP_S, AP_M, AP_L as shown in Table 7.
2. If IoU < 0.5, then it is a wrong detection and classifies it as False Positive (FP).
3. When ground truth is present in the image and the model failed to detect the object, we classify it as False Negative (FN).

Table 6 The proposed dataset 16 annotated attribute with other soft biometric Labels of the pedestrian in the frame

Attributes	Values
Height	0→'Children', 1→'Short', 2→ 'Medium', 3→ 'Tall', 4→'Not known'.
Age	0→0-11, 1→12-17, 2→18-24, 3→25-34, 4→35-44, 5→45-54, 6→55-64, 7→greater than 65, 8→'Not known'.
Bounding Box	[x→Top Left; y→Top left row; h→Height; w→Width]
ID	1, 2, 3, 4, …. 'Not known'.
Feet	0→'Sport', 1→'Classic', 2→'High Heels', 3→'Boots', 4→'Sandals', 5→'Nothing', 6→'Not known'.
Frame	1, 2, 3, 4, ... 'n'.
Body Volume	0→'Thin', 1→'Medium', 2→'Fat', 3→'Not known'.
Hairstyle	0→'Bald', 1→'Short', 2→'Medium', 3→'Long', 4→'Horse Tail', 5→'Unknown'.
Hair Color	0→'Black', 1→'Brown', 2→'White', 3→'Red', 4→'Gray', 5→'Occluded', 6→'Not known'.
Head Accessories	0→'Hat', 1→'Scarf', 2→'Neckless', 3→'Occluded', 4→'Not known'.
Upper Body Clothing	0→'T-shirt', 1→'Blouse', 2→'Sweater', 3→'Coat', 4→'Bikini'. 5→'Naked', 6→'Dress', 7→'Uniform', 8→'Shirt', 9→'Suit', 10→'Hoodie', 11→'Cardigan'.
Lower Body Clothing	0→'Jeans', 1→'Leggins', 2→'Pants', 3→'Shorts', 4→'Skirt', 5→'Bikini' , 6→'Dress', 7→'Uniform', 8→'Suit', 9→'Not known'.
Moustache	0→'Yes', 1→'No', 2→'Not known'.
Beard	0→'Yes', 1→'No', 2→'Not known'.
Action	0→'Walk', 1→'Run', 2→'Standing', 3→'Sit', 4→'Cycle', 5→'Exercise', 6→'Pet', 7→'Phone', 8→'Leave Bag', 9→'Fall', 10→'Fight', 11→'Date', 12→'Offend', 13→'Trade'.
Accessories	0→'Bag', 1→'Backpack', 2→'Rolling', 3→'Umbrella', 4→'Sport', 5→'Market', 6→'Nothing', 7→'Unknown'.

Table 7 Evaluation metrics used for SIRA Mask R-CNN pedestrian detector

Metric	Annotation	Description
Avg. Precision	AP	AP at IoU=.50:.05:.95
$AP_{IoU=.50}$	AP_{50}	AP at IoU=.50
$AP_{IoU=.75}$	AP_{75}	AP at IoU=.75
AP_{Small}	AP_S	AP for small objects area $< 32^2$
AP_{Medium}	AP_M	AP for medium objects $< 32^2 <$ area $< 96^2$
AP_{Large}	AP_L	Area for large objects area $> 96^2$

Fig. 9 Caltech dataset-SIRA Mask R-CNN gives the lowest log-average miss rate of 8.30%

4. True Negative (TN) is every part of the image where we did not predict an object. This metrics is not useful for object detection, hence we ignore TN. We have computed the precision, recall, and mean accuracy precision (mAP) using the mathematical model as:

$$Precision = \frac{TP}{TP + FP} \quad (7)$$

$$Recall = \frac{TP}{TP + FN} \quad (8)$$

$$mAP = \frac{1}{N}\sum_{i=1}^{N} AP_i \quad (9)$$

We compare SIRA Mask R-CNN to the state-of-the-art techniques in the area of instance segmentation in Table 8. Our proposed model outperform baseline variants of previous state-of-the-art models. This involves MNC [50] and FCIS [51], which are the winners of the COCO 2015 and 2016 challenges, respectively. SIRA

Mask R-CNN with ResNet-101-FPN backbone is better than FCIS [51]. We achieve a benchmark AP of 79%, AP_{50} of 68%, and AP_{75} of 64%. Again, we validate our system at multiple scale and obtained the results as AP_S of 16.5%, AP_M of 39.5%, and AP_L of 54.5%. SIRA Mask R-CNN results are illustrated in Figure 16 under challenging scenarios.

6.3 Comparison with state-of-the-art pedestrian detection methods

6.3.1 Caltech

The proposed framework trained using Caltech database images. The Fig. 9 shows the proposed method is compared with the techniques such as SAF R-CNN [30], Side

Table 8 SIRA Mask R-CNN average precision results. Comparative analysis of average precision of proposed model to the state of the art approaches available in the literature

Methodology	Backbone	AP	AP_{50}	AP_{75}	AP_S	AP_M	AP_L
MNC [50]	ResNet-101-C4	24.6	44.3	24.8	4.7	25.9	43.6
FCIS [51]	ResNet-101-C5-dilated	29.2	49.5	-	7.1	31.3	50.0
Mask R-CNN [6]	ResNet-101-C4	33.1	54.9	34.8	12.1	35.6	51.1
Mask R-CNN [6]	ResNet-101-FPN	35.7	58.0	37.8	15.5	38.1	52.4
Mask R-CNN [6]	ResNeXt-101-FPN	37.1	60.0	39.4	16.9	39.9	53.5
R-CNN [4]	ResNeXt-101-FPN	61.61	50.13	44.79	–	–	–
pAUCEnsT [45]	ResNeXt-101-FPN	65.26	54.49	48.60	–	–	–
FilteredICF [49]	ResNeXt-101-FPN	67.65	56.75	51.12	–	–	–
DeepParts [4]	ResNeXt-101-FPN	70.49	58.67	52.78	–	–	–
CompACT-Deep [48]	ResNeXt-101-FPN	70.69	58.74	52.71	–	–	–
Regionlets [47]	ResNeXt-101-FPN	73.14	61.15	55.21	–	–	–
3DOP [46]	ResNeXt-101-FPN	77.93	65.01	60.42	–	–	–
SAF R-CNN [30]	ResNeXt-101-FPN	77.93	65.01	60.42	–	–	–
SIRA Mask R-CNN	ResNeXt-101-FPN	79	68	64	16.5	39.5	54.5
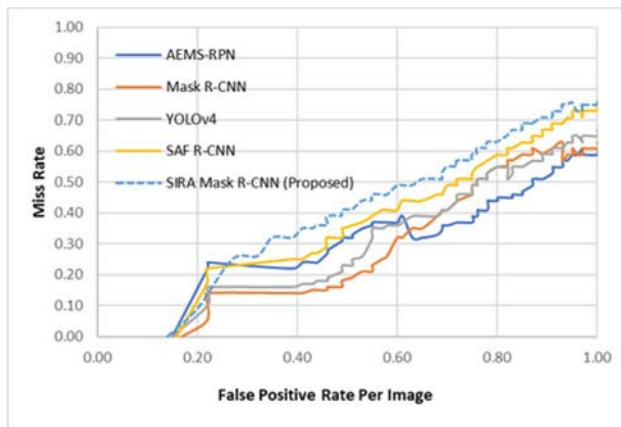
Fig. 10 INRIA dataset-SIRA Mask R-CNN gives the lowest log-average miss rate of 7.31%

Fig. 12 KITTI dataset-SIRA Mask R-CNN gives promising results 79%, 68%, and 64%

Fusion FPN (SF-FPN) [44], Small-scale sense network (SSN) [45], Attention-Enhanced Multi-Scale Region, and Proposal Network (AEMS-RPN) [46]. It can be observed that SIRA Mask R-CNN outperforms the other methods by a huge margin. We achieve the lowest miss rate of 8.31%. It is the state-of-the-art performance for object detection by utilizing Mask R-CNN as shown in Table 9.

6.3.2 INRIA and ETH

The SIRA Mask R-CNN also trained and tested with the INRIA and ETH database images. The comparative results are shown in Figs. 10 and 11. First, for the INRIA dataset image, the proposed method gives the miss rate of 7.31%, which outperforms the existing method YOLOv4

Fig. 13 MS COCO dataset-SIRA Mask R-CNN gives a miss rate of 8.56%

Fig. 11 ETH dataset-SIRA Mask R-CNN gives the miss rate of the proposed model is 32.63%
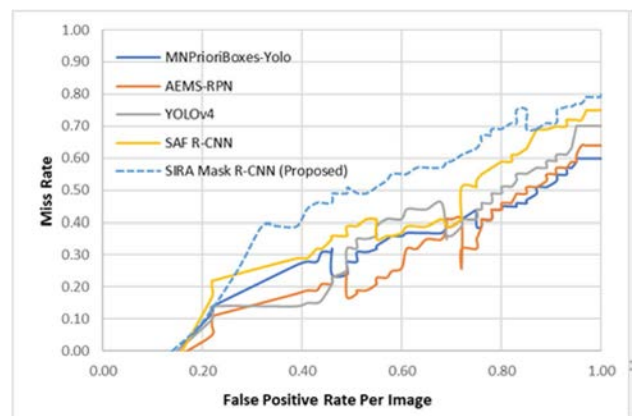
Fig. 14 Proposed pedestrian dataset-SIRA Mask R-CNN gives a miss rate of 8.68%

Fig. 15 Precision vs Recall: SIRA Mask R-CNN compare with recent state-of-the-art methods
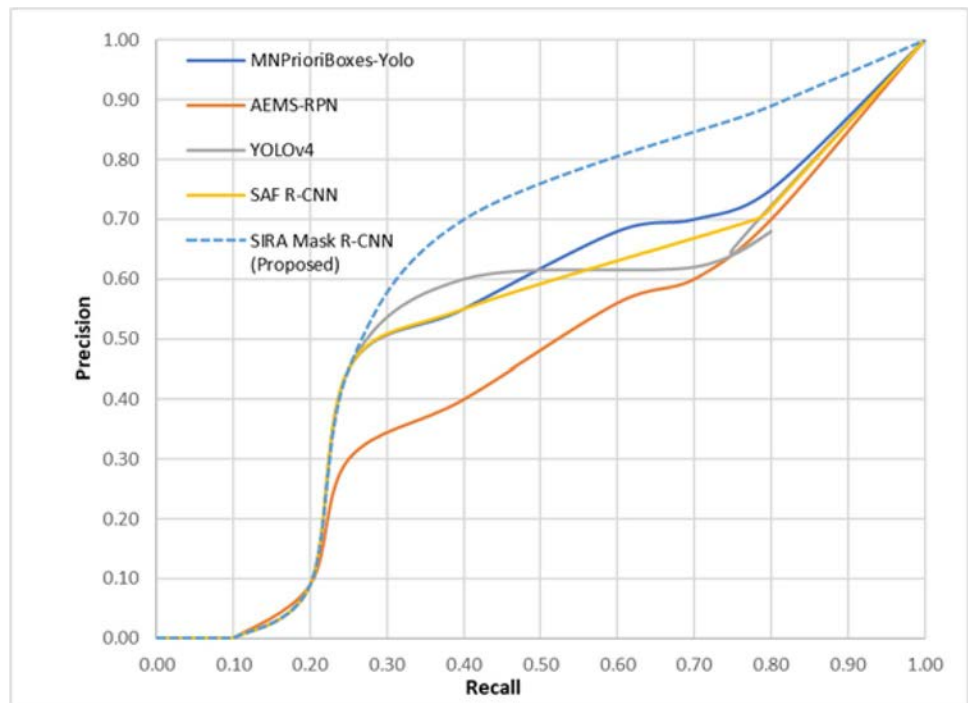
[2], Mask R-CNN [5], SAF R-CNN [30], and AEMS-RPN [46]. Second, for the ETH dataset, the miss rate of the proposed model is 32.63% compared with 33.87% of [41] and 36.46% of [46]. In general, the proposed method achieves a higher detection rate on both the dataset and lower miss rate.

6.3.3 KITTI

The SIRA Mask R-CNN also tested on challenging the KITTI dataset. The pedestrian detection performance comparisons of the SIRA R-CNN with existing methods SAF R-CNN [30], SF-FPN [44], SSN [45], AEMS-RPN [46] are

Fig. 16 SIRA Mask R-CNN result. First row - proposed database images. Second row-Results on proposed database. Third row-MS COCO dataset images [3]. Fourth row-Proposed method results on the Caltech dataset. Fifth row-Caltech dataset [1]. Sixth row-Proposed method results on the Caltech dataset

Table 9 SIRA Mask R-CNN pedestrian detector compare with the state-of-the art pedestrian detector

Framework, model	Miss rate(%)	Test Time(%)
Faster R-CNN [7]	17.60	0.22
Fast R-CNN Single scale [9]	13.70	0.34
YOLO [2]	11.67	3.04
R-CNN [9]	12.77	5.31
SAF R-CNN [31]	9.32	0.59
SIRA Mask R-CNN	8.31	0.50

shown in Fig. 12. The proposed approach gives promising results on the KITTI dataset, i.e., 79%, 68%, and 64%.

6.3.4 MS COCO and proposed pedestrian dataset

The results are shown in Figs. 13 and 14 The proposed approach compared with the existing methods in YOLOv4 [2], SAF R-CNN [30], MNPrioriBoxes-Yolo [41], and AEMS-RPN [46]. It gives a miss rate of 8.56% on MS COCO and miss rate of 8.68% on the proposed pedestrian dataset.

Figure 15 shows the results of the recall and precision of the proposed model compare with YOLOv4 [2], SAF R-CNN [30], MNPrioriBoxes-Yolo [41], and AEMS-RPN [46].

It can be observe that the SIRA Mask R-CNN outperform existing methods in terms of accuracy, speed, and time needed for pedestrian detection as shown in Fig. 15 on various pedestrian dataset. Table 9 illustrate the comparative analysis of proposed SIRA Mask RCNN with the state of the art deep learning framework such as Faster R-CNN [7], YOLO [2], Fast R-CNN [9], SAF R-CNN [30]. The proposed SIRA Mask R-CNN detect the pedestrian in presence of artifacts efficiently. The pedestrian detection accuracy is 96%, which is notable accuracy on challenging benchmark pedestrian databases.

7 Conclusion and future scope

In this paper, we proposed a scale, illumination, rotation, and affine invariant Mask-RCNN based pedestrian detector. The proposed framework detects the pedestrian in presence of scale, rotation, illumination artifacts efficiently.It delivers competitive results on the benchmark datasets such as Caltech [1], INRIA [2], MS COCO [26], ETH [27], KITTI [28], and our proposed academic environment database. The experimental results confirmed that the proposed SIRA Mask R-CNN delivers 1) the lowest miss rate of 8.31% on the Caltech dataset, 2) the lowest log-average miss rate of 7.31% INRIA, 3) miss rate of 32.63% on ETH dataset, the pedestrian detection accuracy of 79% on the KITTI dataset

and 4) miss rate of 8.68% on the proposed database. The proposed method is superior in detecting the different sizes and varying illuminated pedestrian along with variation in orientation compared with the existing state-of-the-art techniques such as YOLOv4 [2], Mask R-CNN [5], SAF R-CNN [30], MNPrioriBoxes-Yolo [41], SSN [45], and AEMS-RPN [46].

In the future, the proposed framework can be enhanced from the following aspects. First, the proposed work addresses scaling, rotation, and lighting issues. Other problems, such as motion blur, partial or complete occlusion, can be effectively solved by extracting different features of pedestrian objects that are invariant to occlusion and motion blur to improve the feature extraction process. It should improve the pedestrian detection time to meet the real-time usage. An unsupervised approach to pedestrian detection can be useful to reduce the time of detection. The proposed model can also be used to detect human poses and trajectories of different sizes and to block pedestrians.

Compliance with ethical standards

References

1. Dollar P, Wojek C, Schiele B, Perona P (2012) Pedestrian detection: An evaluation of the state of the art. TPAMI 34(4):743–761
2. Bochkovskiy A (2020) "YOLOv4: Optimal Speed and Accuracy of Object Detection", CVPR, 23 April 2020
3. Long X (2020) "PP-YOLO: An Effective and Efficient Implementation of Object Detector", CVPR, 3 August 2020
4. Redmon J, Divvala S, Girshick R, Farhadi A (2016) "YOLO", CVPR, pp. 1-10, Las Vegas, Nevada, USA, 26 June-1 July 2016
5. He K, Gkioxari G, Dollar P, Girshick R (2020) Mask R-CNN. TPAMI 42(2):386–397
6. He K, Gkioxari G, Dollar and Girshick (2017) "Mask R-CNN", ICCV, pp. 2980-2988, Italy, 22-29 October 2017
7. Ren S, He K, Girshick R, Sun J (2017) "Faster R-CNN''. IEEE Trans Pattern Ana Machine Intell (TPAMI) 39(6):1137–1149
8. Ren S, He K, Girshick R, Sun J (2015) "Faster R-CNN", NIPS, Montreal, pp. 1-9, Canada, 7-12 December 2015
9. Girshick R (2015)"Fast R-CNN", ICCV, pp 1441-1448, Santiago, Chile 7-13 December 2015
10. Dai J, Li Y, He K, Sun J (2016) "R-FCN: Object Detection via Region-based FCN", CVPR, pp 1-11, USA, July 2016
11. Liu, Anguelov D, Erhan D, Szegedy C (2016) "SSD", ECCV, pp 1-17, Netherlands, 11-14 October 2016
12. Anguelov J, Shelh E, Darrell T (2015) "FCN for Semantic Segmentation", CVPR, pp1-10, Boston, 8-10 June 2015
13. Radford A, Metz L, Chintala S (2015) Unsupervised Representation Learning with Deep Convolutional Generative Adversarial Networks, CVPR, pp 1-10, Boston, Massachusetts, 8-10 June 2015
14. He K, Zhang X, Ren S, Sun J (2015) Deep Residual Learning, CVPR, pp 1-10, Boston, 8-10 June 2015

15. Szegedy C, Ioffe S, Vanhoucke V, Alemi A (2016) Inception-v4, Inception-ResNet and the Impact of Residual Connections on Learning, CVPR, pp 1-10, LA, Nevada, USA, 26 June-1 July 2016

16. K S, Zisserman A (2015) Very Deep Convolutional Networks for Large-Scale Image Recog., CVPR, pp 1-10, Boston, 8-10 June 2015

17. Zeiler M, Fergus (2013) Visualizing and Understanding Convolutional Networks, CVPR, pp 1-11, USA, June 2013

18. Alex K, Sutskever I, Hinton G (2012) ImageNet Classification with Deep Convolutional Neural Networks, NIPS, pp 1-9, Nevada, United States, 3-6 December 2012

19. Kangming L (2016) Research on an improved pedestrian detection method based on DBN classification algorithm. RISTI 17(3):77–87

20. Lecun Y, Bottou L, Bengio Y, Haffner P (1998) Gradient-based learning applied to document recognition. Proceedings of the IEEE 86(11):2278–2324

21. Kang S, Byun H, Lee S (2002) Real-Time Pedestrian Detection Using Support Vector Machines, First International Workshop on SVM: Pattern Recog. with SVM, pp 268-277, Canada, 10 August 2002

22. Geronimo D, Sappa A, Lopez A, Ponsa D (2006) Pedestrian detection using AdaBoost learning of features and vehicle pitch estimation, International Conference on Visualization, Image and Image Processing, pp 1-8, Spain, 28-30 August 2006

23. Wu C, Yue J, Wang L, Lyu F (2019) Detection and Classification of Recessive Weakness in Superbuck Converter Based on WPD-PCA and Probabilistic Neural Network. MDPI Electronics 8(290):1–17

24. Alireza A, Mollaie, Reza, Yasser, Andi, Hosein (2011) Improved Object Tracking Using RBFNN, MVIP, Iran, pp 1-5, 16-17 November 2011

25. Emil N, Neghina, Mihai (2009) A NN approach to pedestrian detection, ICCOMP, pp 374-379, USA, 23 July 2009

26. Lin T, Maire M, Belongie S, Hays J, Perona P, Ramanan D, Piotr Dollar, Lawrence Zitnick C (2014) MS COCO:, ECCV, Springer, Switzerland, pp 1-15, 6-12 September 2014

27. Ess A, Leibe B, Gool L (2017) Depth and appearance for mobile scene analysis, ICCV, pp 1-8, Italy, 22-29 October 2017

28. Geiger A, Lenz P, Urtasun R (2012) Are we ready for autonomous driving? the KITTI vision benchmark suite, CVPR, pp 3354-3361, RI, USA, 16-21 June 2012

29. Gong Y, Wang L, Guo R, Lazebnik S (2014) Multiscale orderless pooling of deep convolutional activation features, ECCV, pp 392-407, Zurich, Switzerland, 6-12 September 2014

30. Li J, Li X (2018) Scale-aware Fast R-CNN for Pedestrian Detec. IEEE Trans Multi 20(4):985–996

31. Wang K, Zhou W (2019) Pedestrian and cyclist detection based on deep neural network fast R-CNN. Inter. Journal of Advanced Robotic Systems, SAGE 16(2):1–10

32. Pobar M, Kosm M (2018) Mask R-CNN and Optical flow-based method for detection and marking of handball actions, CISP-BMEI 2018, pp 1-6, China, 13-15 October 2018

33. Minkesh A, Worranitta K, Taizo M (2019) Human extraction and scene transition utilizing Mask R-CNN, CVPR, pp 1-6, CA, United States, 16-20 June 2019

34. Gawande, Ujwalla, Hajari, Kamal, Golhar, Yogesh (2020) Pedestrian Detection and Tracking in Video Surveillance System: Issues, Comprehensive Review, and Challenges, Recent Trends in Computational Intelligence, IntechOpen, 1-24, April 2020

35. Gawande U, Hajari K, Golhar Y (2020) Deep Learning Approach to Key Frame Detection in Human Action Videos, Recent Trends in Computational Intelligence, IntechOpen, 1-17 February 2020

36. Dalal N, Triggs B (2005) HOG for Human Detection, CVPR, pp 886-893, CA, USA, 20-25 June 2005

37. Wang X, Han TX, Yan S (2009) An HOG-LBP human detector with partial occlusion handling, ICCV, pp 32-39, Japan, 29 September-2 October 2009

38. Dollar P, Tu Z, Per P, Bel S (2009) Integral channel features, BMVC, UK, pp 1-11, 7-10 September 2009

39. Gawande U, Golhar Y (2018) Biometric security system: a rigorous review of unimodal and multimodal biometrics techniques. IJBM, InderScience 10(2):142–175

40. Sil N, Son D (2014) Fergus. Instance Seg. of Indoor Scenes Using a Coverage Loss, ECCV, Switzerland

41. Li GY, Yifan Q, Xingda (2019) "Deep Learning Approaches on Pedestrian Detection in Hazy Weather", IEEE Transaction on Industrial Electronics, IEEE Transactions on Industrial Electronics, vol 1, 1 November 2019

42. Wang X, Wang M, Li W (2014) Scene-specific pedestrian detection for static video. TPAMI 36(2):361–374

43. Tian Y, Luo P, Wang X, Tang X (2015) Pedestrian detection aided by deep learning semantic tasks, CVPR, pp 1-10, Boston, 8-10 June 2015

44. Xu C, Wang G, Yan S, Yu J, Zhang B, Dai S, Li Y, Xu L (2020) "Fast Vehicle and Pedestrian Detection Using Improved Mask R-CNN", Mathematical Problems in Engineering, vol 2020, Hindawi, pp 1-15, 2020

45. Han B, Wang Y, Yang Z, Gao X (2020) "Small-Scale Pedestrian Detection Based on Deep Neural Network", IEEE Transactions on Intelligent Transportation Systems, 21:(7), 2020

46. Wang H, Wang LY, Shengjin (2019) "Fast Pedestrian Detection With Attention-Enhanced Multi-Scale RPN and Soft-Cascaded Decision Trees", IEEE Transactions on Intelligent Transportation Systems vol 1, No 8, 2019

47. Sharif M, Khan MA, Akram T et al (2017) A framework of human detection and action recognition based on uniform segmentation and combination of Euclidean distance and joint entropy-based features selection. J Image Video Proc. 2017:89

48. Wojek C, Walk S, Schiele B (2009) "Multi-cue onboard pedestrian detection," IEEE Conference on Computer Vision and Pattern Recognition, 2009

49. Zhao L, Thorpe C (2000) Stereo and neural network-based pedestrian detection. IEEE Trans Intell Trans Syst 1(3):148–154

50. Dai J, He K, Sun J (2016) "Instance-aware semantic segmentation via multi-task network cascades", In: Computer Vision and Pattern Recognition (CVPR), 2016

51. Li Y, Qi H, Dai J, Ji X, Wei Y (2017) "Fully convolutional instanceaware semantic segmentation", In: Computer Vision and Pattern Recognition (CVPR), 2017

Coupled fixed point theorem in quasi metric space

Manjusha P. Gandhi[*]
Yeshwantrao Chavan College of Engineering
Wanadongri, Nagpur
India
manjusha_g2@rediffmail.com

Anushree A. Aserkar
Yeshwantrao Chavan College of Engineering
Wanadongri, Nagpur
India
aserkar_aaa@rediffmail.com

Abstract. In the present paper a unique common coupled fixed point theorem has been proven for quasi metric space with modified - ω distance function. This result is improvement, modification and extension in the study of quasi metric space. An example has been given to illustrate the work.
Keywords: fixed point, quasi-metric space, coupled fixed point, modified-ω distance.

1. Introduction and preliminaries

The fixed point theory is one of the important topics of functional analysis. The whole metric fixed point theory based on a very powerful theorem Banach Contraction principle [5]. Since then many researchers worked on it and develop the results in different directions.

Bhaskar and Lakshmikantham [6] initiated the concept of coupled fixed point in the following way:

Definition 1.1 ([6]). An element $(a, b) \in X \times X$ is called a coupled fixed point of mapping $J : X \times X \to X$ if $J(a, b) = a, J(b, a) = b$.

Further several researchers Lakshmikantham and Ciric [10], Choudhary and Kundu [8], Luong et al. [11], Razani and Parvaneh [12], Alsulami [3], Samet et al. [13], Alotaibi [2] extended the coupled fixed point theorems in partial order metric space under different constraints but it is not found in quasi metric space, so the authors are motivated towards the present work.

Remark 1. Every metric space is quasi metric space but the converse is not true.

---

[*]. Corresponding author

Remark 2. The results which are true for quasi metric space need not be true for metric space.

Wilson [16] introduced the concept of quasi metric space as here under:

Definition 1.2 ([16]). The function $q : X \times X \to [0, \infty)$ is a quasi-metric if it satisfies

(i) $q(a, b) = 0 \Leftrightarrow a = b$;

(ii) $q(a, b) \leq q(a, c) + q(c, b)$, for all $a, b, c \in X$.

The pair (X, q) is called quasi metric space.

The study of fixed point theorems on quasi metric space further continued by Aydi, et al. [4], Bilgili, et al. [7], Shatanawi, et al. [14], Shatanawi, et al. [15], Alegre, et al. [1].

Definition 1.3 ([4,9]). A sequence $\{a_l\}$ converges to $a \in X$ if $\lim_{l \to \infty} q(a_l, a) = \lim_{l \to \infty} q(a, a_l) = 0$.

Definition 1.4 ([9]). Let $\{a_l\}$ be a sequence in X. Then:

(i) $\{a_l\}$ is called left Cauchy if for any $\delta > 0, \exists N_0 \in N$, such that $q(a_l, a_m) < \delta \forall l \geq m > N_0$

(ii) $\{a_l\}$ is called right Cauchy if for any $\delta > 0, \exists N_0 \in N$, such that $q(a_l, a_m) < \delta \forall m \geq l > N_0$.

Definition 1.5 ([4,9]). $\{a_l\}$ is called Cauchy sequence if for any $\delta > 0, \exists N_0 \in N$ such that $q(a_l, a_m) \leq \delta \forall l, m > N_0$ or $\{a_l\}$ is right and left Cauchy.

Definition 1.6 ([1]). The modified -ω distance on (X, q) is a function $p : X \times X \to [0, \infty)$ which satisfies the following

(Q1) $p(a_1, a_2) \leq p(a_1, a_3) + p(a_3, a_2), \forall a_1, a_2, a_3 \in X$.

(Q2) $p : X \to [0, \infty)$ is lower semi continuous $\forall a \in X$.

(Q3) $\forall \varepsilon > 0 \exists \delta > 0$ such that $p(a_1, a_2) \leq \delta, p(a_2, a_3) \leq \delta \Rightarrow q(a_1, a_3) \leq \varepsilon \forall a_1, a_2, a_3 \in X$.

2. Main result

The aim of this paper is to establish coupled fixed point theorems in quasi metric space.

Theorem 2.1. *Let (X, q) be a complete quasi metric space equipped with an mw distance mapping p, also J and K: $X \times X \to X$ be two continuous functions such that the pair (J, K) satisfy*

(2.1) $p\{J(a, b), K(c, d)\} \le h \max\{p(a, J(a, b)), p(c, K(c, d))\},$

(2.2) $p\{K(a, b), J(c, d)\} \le h \max\{p(a, K(a, b)), p(c, J(c, d))\}.$

here $h \in [0, 1).$ Then J and K have unique common coupled fixed point.

Proof. Let $a_{2l+1} = J(a_{2l}, b_{2l}), b_{2l+1} = J(b_{2l}, a_{2l}),$

$$a_{2l+2} = K(a_{2l+1}, b_{2l+1}), b_{2l+2} = K(b_{2l+1}, a_{2l+1}).$$

Now, to prove that $p(a_l, a_{l+1}) = 0$ or $p(a_{l+1}, a_l) = 0$ and $p(b_l, b_{l+1}) = 0$ or $p(b_{l+1}, b_l) = 0.$

Case I. Consider $p(a_l, a_{l+1}) = 0$, for $l = 2n,$

$$\begin{aligned} p(a_{2n+1}, a_{2n+2}) &= p\{J(a_{2n}, b_{2n}), K(a_{2n+1}, b_{2n+1})\}, \\ &\le h \max\{p(a_{2n}, J(a_{2n}, b_{2n})), p(a_{2n+1}, K(a_{2n+1}, b_{2n+1}))\} \\ &= h \max\{p(a_{2n}, a_{2n+1}), p(a_{2n+1}, a_{2n+2})\}. \end{aligned}$$

(i) If $p(a_{2n}, a_{2n+1})$ is maximum, then $p(a_{2n+1}, a_{2n+2}) = 0.$

(ii) If $p(a_{2n+1}, a_{2n+2})$ is maximum, then $p(a_{2n+1}, a_{2n+2}) = 0,$

(2.3) $p(a_{2n+1}, a_{2n+2}) = 0.$

Now,

$$\begin{aligned} p(b_{2n+1}, b_{2n+2}) &= p\{J(b_{2n}, a_{2n}), K(b_{2n+1}, a_{2n+1})\} \\ &\le h \max\{p(b_{2n}, J(b_{2n}, a_{2n})), p(b_{2n+1}, K(b_{2n+1}, a_{2n+1}))\} \\ &= h \max\{p(b_{2n}, b_{2n+1}), p(b_{2n+1}, b_{2n+2})\}. \end{aligned}$$

(i) If $p(b_{2n}, b_{2n+1})$ is maximum then $p(b_{2n+1}, b_{2n+2}) = 0.$
(ii) If $p(b_{2n+1}, b_{2n+2})$ is maximum then $p(b_{2n+1}, b_{2n+2}) = 0,$

(2.4) $p(b_{2n+1}, b_{2n+2}) = 0.$

Now,

$$\begin{aligned} p(a_{2n+2}, a_{2n+1}) &= p\{K(a_{2n+1}, b_{2n+1}), J(a_{2n}, b_{2n})\} \\ &\le h \max\{p(a_{2n+1}, K(a_{2n+1}, b_{2n+1})), p(a_{2n}, J(a_{2n}, b_{2n}))\} \\ &= h \max\{p(a_{2n+1}, a_{2n+2}), p(a_{2n}, a_{2n+1})\}. \end{aligned}$$

(i) $p(a_{2n+1}, a_{2n+2})$ is maximum then $p(a_{2n+2}, a_{2n+1}) = 0$.
   (ii) If $p(a_{2n}, a_{2n+1})$ is maximum then $p(a_{2n+2}, a_{2n+1}) = 0$,

$$(2.5) \qquad\qquad p(a_{2n+2}, a_{2n+1}) = 0.$$

Similarly one can show that

$$(2.6) \qquad\qquad p(a_{2n}, a_{2n+2}) = 0, p(b_{2n}, b_{2n+2}) = 0$$

using Q1. From (2.1.5), (2.1.6) and Q3,

$$(2.7) \qquad q(a_{2n}, a_{2n+1}) = 0 \begin{cases} \therefore q(a_l, a_{l+1}) = 0 \Rightarrow a_l = a_{l+1} = J(a_l, b_l), \\ q(b_l, b_{l+1}) = 0 \Rightarrow b_l = b_{l+1} = K(b_l, a_l). \end{cases}$$

(a_l, b_l) is coupled fixed point.

Also, (2.1.8) $p(a_{2n}, a_{2n+1}) \leq p(a_{2n}, a_{2n+2}) + p(a_{2n+2}, a_{2n+1}) = 0$. From (2.1.3), (2.1.8) and Q3

$$(2.8) \qquad q(a_{2n}, a_{2n+2}) = 0,$$
$$q(a_{2n+1}, a_{2n+2}) \leq q(a_{2n+1}, a_{2n}) + q(a_{2n}, a_{2n+2}) = 0.$$

Similarly, $q(b_{2n+1}, b_{2n+2}) \leq q(b_{2n+1}, b_{2n}) + q(b_{2n}, b_{2n+2}) = 0$. Hence,

$$a_{2n} = a_{2n+1} = a_{2n+2} \Rightarrow a_l = a_{l+1} = a_{l+2}$$
$$\Rightarrow a_l = J(a_l, b_l) = K(a_{l+1}, b_{l+1}),$$

when $l \to \infty$, as J and K are continuous $a = J(a, b) = K(a, b)$.

Also, $b_{2n} = b_{2n+1} = b_{2n+2} \Rightarrow b_l = b_{l+1} = b_{l+2} \Rightarrow b_l = J(b_l, a_l) = K(b_{l+1}, a_{l+1})$, when $l \to \infty$, as J and K are continuous $\Rightarrow b = J(b, a) = K(b, a)$. Thus, (a, b) is common coupled fixed point of J and K.

Case II: When l is odd, $l = 2n + 1$,

$$p(a_{2n+1}, a_{2n+2}) = 0,$$
$$p(a_{2n+2}, a_{2n+3}) = p\{K(a_{2n+1}, b_{2n+1}), J(a_{2n+2}, b_{2n+2})\}$$
$$(2.9) \qquad \leq h \max\{p(a_{2n+1}, K(a_{2n+1}, b_{2n+1})), p(a_{2n+2}, J(a_{2n+2}, b_{2n+2}))\}$$
$$= h \max\{p(a_{2n+1}, a_{2n+2}), p(a_{2n+2}, a_{2n+3}))\}.$$

This implies

$$(2.10) \qquad\qquad p(a_{2n+2}, a_{2n+3}) = 0.$$

Also, it can be proved that

$$(2.11) \qquad p(a_{2n+3}, a_{2n+2}) = 0, p(b_{2n+2}, b_{2n+3}) = 0, p(b_{2n+3}, b_{2n+2}) = 0.$$

Now, by Q1

$$(2.12) \qquad p(a_{2n+1}, a_{2n+3}) \le p(a_{2n+1}, a_{2n+2}) + p(a_{2n+2}, a_{2n+3}) = 0.$$

From (2.1.12), (2.1.13) and Q_3

$$(2.13) \qquad\qquad q(a_{2n+1}, a_{2n+2}) = 0.$$

Also, $q(a_{2n+1}, a_{2n+3}) = 0$. Similarly, $q(b_{2n+1}, b_{2n+2}) = 0$ and $q(b_{2n+1}, b_{2n+3}) = 0$.
From (2.1.10), (2.1.11) and Q_3

$$q(a_{2n+1}, a_{2n+3}) = 0, a_{2n+1} = a_{2n+2} = a_{2n+3} \Rightarrow a_l = a_{l+1} = a_{l+2}$$
$$(2.14) \qquad \Rightarrow a_l = J(a_l, b_l) = K(a_{l+1}, b_{l+1}).$$

Similarly, one can prove that $\Rightarrow b = J(b, a) = K(b, a)$. Thus, (a, b) are common coupled fixed point of J and K.

Similarly, one can show that if $p(a_{l+1}, a_l) = 0$, (a, b) are common coupled fixed point of J and K. Now, assume that $p(a_l, a_{l+1}) \ne 0, p(a_{l+1}, a_l) \ne 0$. Then,

$$
\begin{aligned}
p(a_{2n+1}, a_{2n}) &= p((Ja_{2n}, b_{2n}), K(a_{2n+1}, b_{2n+1})) \\
(2.15) \qquad &\le h \max\{p(a_{2n}, J(a_{2n}, b_{2n})), p(a_{2n+1}, K(a_{2n+1}, b_{2n+1}))\} \\
&= h \max\{p(a_{2n}, a_{2n+1}), p(a_{2n+1}, a_{2n+2})\}.
\end{aligned}
$$

(i) If $p(a_{2n}, a_{2n+1})$ is maximum, then $p(a_{2n+1}, a_{2n+2}) \le hp(a_{2n}, a_{2n+1})$.

(ii) If $p(a_{2n+1}, a_{2n+2})$ is maximum, then $p(a_{2n+1}, a_{2n+2}) = 0$, which is contradiction.

Hence, $p(a_{2n+1}, a_{2n+2}) \le hp(a_{2n}, a_{2n+1})$. By similar process we can prove that

$$p(a_{2n}, a_{2n+1}) \le hp(a_{2n-1}, a_{2n}).$$

Also, we can prove

$$p(b_{2n+1}, b_{2n+2}) \le hp(b_{2n}, b_{2n+1})$$

and

$$p(b_{2n}, b_{2n+1}) \le hp(b_{2n-1}, b_{2n}).$$

Thus,

$$(2.16) \qquad p(a_l, a_{l+1}) \le hp(a_{l-1}, a_l) \text{ and } p(b_l, b_{l+1}) \le hp(b_{l-1}, b_l).$$

Now,

$$
\begin{aligned}
p(a_{l+1}, a_l) &= p(J(a_l, b_l), K(a_{l-1}, b_{l-1})) \\
(2.17) \qquad &\le h \max\{p(a_l, J(a_l, b_l)), p(a_{l-1}, K(a_{l-1}, b_{l-1}))\} \\
&= h \max\{p(a_l, a_{l+1}), p(a_{l-1}, a_l)\}, \\
p(a_{l+1}, a_l) &\le hp(a_{l-1}, a_l).
\end{aligned}
$$

Repeating l times

(2.18) $$p(a_{l+1}, a_l) \leq h^l p(a_1, a_0).$$

Also, one can prove

(2.19) $$p(a_l, a_{l+1}) \leq h^l p(a_0, a_1).$$

Similarly, we can prove that $p(b_{l+1}, b_l) \leq h^l p(b_1, b_0)$ and $p(b_l, b_{l+1}) \leq h^l p(b_0, b_1)$. Thus, as $l \to \infty, p(a_l, a_{l+1}) = 0, p(a_{l+1}, a_l) = 0, p(b_l, b_{l+1}) = 0, p(b_{l+1}, b_l) = 0$. Now, to prove $\{a_l\}$ and $\{b_l\}$ are Cauchy sequences, we need to prove $\lim_{s,t\to\infty} p(a_s, a_t) = 0$, for each $s, t \in N$.

Case I: If s is odd and t is even with $s < t$, then

$$\begin{aligned}
p(a_s, a_t) &= p(Ja_{s-1}, b_{s-1}), K(a_{t-1}, b_{t-1}) \\
&\leq h \max\{p(a_{s-1}, J(a_{s-1}, a_{s-1})), p(a_{t-1}, K(a_{t-1}, a_{t-1}))\} \\
&= h \max\{p(a_{s-1}, a_s), p(a_{t-1}, a_t)\} \\
&= hp(a_{s-1}, a_s).
\end{aligned}$$

Thus, we have $p(a_s, a_t) \leq h^s p(a_0, a_1)$.
Let $s, t \to \infty$. Then,

(2.20) $$\lim_{s,t\to\infty} p(a_s, a_t) = 0,$$

with $s < t$. Similarly $\lim_{s,t\to\infty} p(b_s, b_t) = 0$, with $s < t$.

Case II: If s is odd and t is even with $s > t$

$$\begin{aligned}
p(a_s, a_t) &= p(J(a_{s-1}, b_{s-1}), K(a_{t-1}, b_{t-1})) \\
&\leq h \max\{p(a_{s-1}, J(a_{s-1}, b_{s-1})), p(a_{t-1}, K(a_{t-1}, b_{t-1}))\} \\
&= h \max\{p(a_{s-1}, a_s), p(a_{t-1}, a_t)\} \\
&= hp(a_{t-1}, a_t).
\end{aligned}$$

Thus, $p(a_s, a_t) \leq h^t p(a_0, a_1)$.
Let $s, t \to \infty$. Then

(2.21) $$\lim_{s,t\to\infty} p(a_s, a_t) = 0,$$

with $s > t$. Similarly $\lim_{s,t\to\infty} p(b_s, b_t) = 0$ with $s > t$.

By similar argument, one can show for s even and t odd, for $s < t$ and $s > t$ $\lim_{s,t\to\infty} p(a_s, a_t) = 0$ and $\lim_{s,t\to\infty} p(b_s, b_t) = 0$.

Now, we show that $\{x_l\}$ is right Cauchy sequence. Consider the following cases:

(i) If $l, r \in N$ such that l is odd and r is even with $r > l$, then we have $\lim_{l,r\to\infty} p(a_l, a_r) = 0$ from (2.1.19).

(ii) If $l, r \in N$ such that l is even and r is odd with $r > l$, then we have $\lim_{l,r\to\infty} p(a_l, a_r) = 0$ from (2.1.21).

(iii) $l, r \in N$ such that l and r both are even with $r > l$, then we have $p(a_l, a_r) \leq p(a_l, a_{l+1}) + p(a_{l+1}, a_r)$. Thus, $\lim_{l,r\to\infty} p(a_l, a_r) = 0, l > r$.

(iv) If $l, r \in N$ such that l and r both are even with $r > l$ then, we have $p(a_l, a_r) \leq p(a_l, a_{r+1}) + p(a_{r+1}, a_r)$. Thus, $\lim_{l,r\to\infty} p(a_l, a_r) = 0, l > r$.

Hence, $\{a_l\}$ is right Cauchy sequence. With similar argument $\{b_l\}$ is right Cauchy sequence and also $\{a_l\}, \{b_l\}$ are left Cauchy sequences. Hence $\{a_l\}$ and $\{b_l\}$ both are Cauchy sequences.

Since (X, q) is complete quasi metric space, therefore $\lim_{l\to\infty} p(a_{2l}, a) = 0 = \lim_{l\to\infty} p(a, a_{2l})$

Now, $a = \lim_{l\to\infty} a_{2l+1} = \lim_{l\to\infty} J(a_{2l}, b_{2l}) = J(a, b)$ and $b = \lim_{l\to\infty} b_{2l+1} = \lim_{l\to\infty} J(b_{2l}, a_{2l}) = J(b, a)$. Thus, (a, b) is coupled fixed point of J and with similar argument it can be shown that (a, b) is coupled fixed point of K.

Hence, (a, b) is common coupled fixed point of J and K. To prove uniqueness first we have to prove $p(v, v) = 0$,

$$p(v, v) = p\{J(v, v), K(v, v)\} \leq h \max\{p(v, J(v, v)), p(v, K(v, v))\} = hp(v, v).$$

Thus, $p(v, v) = 0$.

Let (a, b) and (a', b') be two coupled fixed points of J and K, $J(a, b) = K(a, b) = a$ and $J(b, a) = K(b, a) = b$, $J(a', b') = K(a', b') = a'$ and $J(b', a') = K(b', a') = b'$.

Now,

$$p(a, a') = p\{J(a, b), K(a', b')\}, \leq h \max\{p(a, J(a, b)), p(a', K(a', b'))\}$$
$$= h \max\{p(a, a), p(a', a')\} = 0.$$

Thus, $a = a'$, similarly we can show that $b = b'$. This implies $(a, b) \equiv (a', b')$. $\square$

Hence, (a, b) is unique common coupled fixed point of J and K.

Corollary 2.2. *Let (X, q) be a complete quasi metric space equipped with an mw distance mapping p and $J{:}X \times X \to X$ be continuous function such that:*

(i) $p\{J(a, b), J(c, d)\} \leq h \max\{p(a, J(a, b)), p(c, J(c, d))\}$, where $h \in [0, 1)$. Then J has unique common coupled fixed point.

Proof. Consider $K = I$ (Identity map), we get the result. The following example validate our result. $\square$

Example 2.3. Let $X = (0, 3] p(a, b) = \frac{a+2b}{8}, q(a, b) = \frac{a+3b-2}{4}, J(a, b) = 4a + 3b - 15, K(a, b) = 3a + 2b - 10$. Here, q is quasi metric space, p is modified-ω distance function.

L.H.S. $= p\{J(a, b), K(c, d)\} = p(4a + 3b - 15, 3c + 2d - 10) = \frac{1}{8}(4a + 3b + 6c + 4d - 35)$

R.H.S. $= h \max\{p(a, J(a, b)), p(c, K(c, d))\} = h, \max\{p(a, 4a+3b-15), p(c, 3c+2d-10)\} = h \max\{\frac{9a+6b-30}{8}, \frac{7c+4d-20}{8}\} = \frac{h}{8} \max\{9a+6b-30, 7c+4d-20\}$. Condition (i) and (ii) of theorem are satisfied. Also, $J(2,3) = 2 = K(2,3), J(3,2) = 3 = K(3,2)$. Thus, $(2,3)$ is coupled common fixed point of J and K.

Conclusion. A unique common coupled fixed point theorem proved for quasi metric space.

Acknowledgement

References

[1] Aleire, J. Marin, *Modified ω distance on quasi metric spaces and fixed point theorems on complete quasi metric space*, Topol. Appl., 203 (2016), 120-129.

[2] A. Alotaibi, S.M. Alsulami, *Coupled coincidence points for monotone operators in partially ordered metric spaces,* Fixed Point Theory Appl., 44 (2011).

[3] S.M. Alsulami, *Some coupled coincidence point theorems for a mixed monotone operator in a complete metric space endowed with a partial order by using altering distance functions*, Fixed Point Theory Appl., 194 (2013).

[4] H. Ayadi, M.Jellali, E. Karapinar, *On fixed point results for α implicit contractions in quasi metric spaces and consequences,* Nonlinear Analysis Modelling and Control., 21 (2016), 40-56.

[5] S.Banach, *Sur les operations dans les ensemble abstraits et leur applications aux equations integrables,* Fund. Math., 3 (1922), 133-181.

[6] T. G. Bhaskar, V. Lakshmikantham, *Fixed point theorems in partially ordered metric spaces and applications,* Nonlinear Anal., 65 (2006), 1379-1393.

[7] N. Bilgili, E. Karapınar, B. Samet, *Generalized a-y contractive mapping in quasi metric spaces and related fixed point theorems*, J. Inequal. Appl., 36 (2014).

[8] B.S. Choudhury, A. Kundu, *A coupled coincidence point result in partially ordered metric spaces for compatible mappings*, Nonlinear Anal., 73 (2010), 2524-2531.

[9] M. Jleli, B. Samet, *Remarks on G-metric spaces and fixed point theorems*, Fixed Point Theory Appl., 210 (2012).

[10] V. Lakshmikantham, L. Ciric, *Coupled fixed point theorems for nonlinear contractions in partially ordered metric spaces*, Nonlinear Anal., 70 (2009), 4341-4349.

[11] N.V. Luong, N.X. Thuan, *Coupled fixed points in partially ordered metric spaces and application*, Nonlinear Anal., 74 (2011), 983-992.

[12] A. Razani, V. Parvaneh, *Coupled coincidence point results for (ψ,α,β)-weak contractions in partially ordered metric spaces,* J. Appl. Math., Article ID 496103 (2012).

[13] B. Samet, E. Karapınar, H. Aydi, V. Cojbašic Rajic, *Discussion on some coupled fixed point theorems*, Fixed Point Theory Appl., 50 (2013).

[14] W. Shatanawi, M.S. Noorani, H. Alsamir, *A fixed and common fixed point theorems in partially ordered quasi metric spaces*, J. Math. Comput. Sci., 16 (2012), 516-528.

[15] W. Shatanawi, A. Pitea, *Some coupled fixed point theorems in quasi-partial metric spaces*, Fixed Point Theory Appl., 153 (2013).

[16] W.A. Wilson, *On quasi-metric spaces*, Amer. J. Math, 53 (1931), 675-684.

n-Tuple Fixed Point Theorem in Bi-Complete *F*-quasi Metric Space

Manjusha P. Gandhi* [ID] and Anushree A. Aserkar [ID]

*Department of Applied Mathematics, Yeshwantrao Chavan College of Engineering, Hingna Road,
Wanadongri, Nagpur 441110, Maharastra, India*
*Corresponding author: manjusha_g2@rediffmail.com

Abstract. In the present paper, two theorems are discussed, one is fixed point theorem and another is *n*-tuple fixed point theorem for a new contractive condition in bi-complete *F*-quasi metric space. Also, an example is given to validate the result.

Keywords. Quasi metric space, *n*-tuple fixed point, Bi-complete

Mathematics Subject Classification (2020). 54H25, 47H10

1. Introduction

One of the most significant topic in functional analysis is fixed point theory. The whole fixed point theory based on very influential theorem Banach Contraction Principle [4]. Since then many researchers worked on it and develop results in different spaces like Metric space, Hilbert space, normed space, G-metric space, b-metric space, cone metric space etc. Further, fixed point theorems are extended in quasi-metric space.

Definition 1.1 ([16])**.** The function $q : X \times X \to [0, \infty)$ is a quasi-metric if it satisfies

  (i) $q(a, b) = 0 \Leftrightarrow a = b$, for all $a, b \in X$.

  (ii) $q(a, b) \le q(a, c) + q(c, b)$, for all $a, b, c \in X$.

The pair (X, q) is called quasi-metric space.

The study of fixed point theorems on quasi-metric space added by Aydi *et al.* [3], Bilgili *et al.* [6], Shatanawi *et al.* [14,15], and Alegre *et al.* [1].

Later, F-quasi metric space is defined as under

Definition 1.2 ([11]). (X, δ_q) is named as F-quasi metric space and δ_q is named as F-quasi metric, if a function $\delta_q : X \times X \to [0, \infty)$, a constant $B \in [0, +\infty)$ and a $f \in F$, so that

(δ_1) $\delta_q(x_1, x_2) = 0 \Leftrightarrow x_1 = x_2 \ \forall \ x_1, x_2 \in X$,

(δ_2) $\delta_q(x_1, x_2) > 0 \Rightarrow f(\delta_q(x_1, x_2)) \le f\left(\sum_{i=1}^{N-1} \delta_q(v_i, v_{i+1})\right) + B.$

For every $N \in \mathbb{N}$ with $N \ge 2$, $\forall \ x_1, x_2 \in X$ and for all $(v_i)_{i=1}^N \subset X$ with $(v_1, v_N) = (x_1, x_2)$.

The notion of coupled fixed point was initiated by Guo and Laxmikantham [10]. Berinde and Borcut [5] extended this theory to triple fixed point. Karapınar *et al.* [11,12] proved quadruple fixed point theorem in partial order metric space. This theory is further stretched for n-tuple fixed point theorems by Ertürk and Karakaya [7,8]. The n-dimensional theory is very useful in many engineering problems.

Definition 1.3 ([7]). Assume X be a non-empty set and let

$$F : \prod_{i=1}^n X^i \to X,$$

then $(x^1, x^2, \ldots, x^n) \in \prod_{i=1}^n X^i$ is termed as n-tuple fixed point if

$$x^1 = F(x^1, x^2, \ldots, x^n)$$
$$x^2 = F(x^2, x^3, \ldots, x^n, x^1)$$
$$x^3 = F(x^3, x^4, \ldots, x^n, x^1, x^2)$$
$$\vdots$$
$$x^n = F(x^n, x^1, \ldots, x^{n-1}).$$

The purpose of this paper is to establish the results on n-tuple fixed point which will be generalization of above results. We have proved n-tuple fixed point theorem in F-quasi metric space for a new contractive condition.

The following definitions are required to discuss to understand this paper.

Definition 1.4 ([2]). A function $f : (0, \infty) \to R$ is called non-decreasing function if $f(x_1) \le f(x_2)$, for all $x_1, x_2 \in [0, +\infty)$. Also f is said to be logarithmic-like when every positive sequence $\{x_n\}$ satisfies

$$\lim_{n \to \infty} x_n = 0 \Leftrightarrow \lim_{n \to \infty} f(x_n) = -\infty.$$

In the sequel F is set of functions f.

Definition 1.5 ([11]). Consider F-quasi metric space (X, δ_q). Then $\{x_n\}$ in X is known as right convergent sequence (left convergent sequence) to $x \in X$ if

$$\lim_{n \to \infty} \delta_q(x, x_n) = 0, \quad \lim_{n \to \infty} \delta_q(x_n, x) = 0.$$

Definition 1.6 ([11]). When a sequence $\{x_n\}$ in X is both right and left convergent, then it is said to be bi-convergent sequence.

Definition 1.7 ([11]). Let $\{x_n\}$ be sequence in F-quasi metric space (X, δ_q). Then $\{x_n\}$ is a right Cauchy sequence (left Cauchy sequence) if

$$\lim_{n,m\to\infty} \delta_q(x_n, x_m) = 0 \quad \lim_{n,m\to\infty} \delta_q(x_m, x_n) = 0.$$

$\{x_n\}$ is a called bi-complete Cauchy sequence if it is left and right both Cauchy sequences.

Definition 1.8 ([13]). The functions $J : X \times X \to X$ and $K : X \to X$ are commutative if

$$J(Kx, Ky) = K(J(x, y)), \quad \forall \ x, y \in X.$$

2. Main Result

Theorem 2.1. *Let (X, δ_q) be a bicomplete F-quasi Metric Space and $J, K : X \to X$ be two mappings which satisfy*

(2.1.1) *J and K are commutative,*

(2.1.2) *$J(X) \subset K(X)$, $K(X)$ is closed, $\forall \ x, y \in X$,*

(2.1.3) *$\phi(t) < t$, for $t > 0$,*

(2.1.4) *$\delta_q(Jx, Jy) \leq \phi(\delta_q(Kx, Ky))$, $\forall \ x, y \in X$.*

Then J and K have a unique common fixed point.

Proof. Let $x_0 \in X$. Then $x_1 \in X$ such that $Jx_0 = Kx_1$. By continuing this process, we can define the sequence $\{y_n\}$ in X such that

$$y_n = Jx_n = Kx_{n+1}, \quad \text{for } n = 0, 1, 2, \ldots.$$

Here J and K have common coincidence point.

To prove the unique coincidence point, consider u_1 and v_1 are two distinct coincidence points of J and K. Then $\exists \ u_2, v_2$ such that

$$\delta(u_2, v_2) > 0, \ Ju_1 = Ku_1 = u_2, \ Jv_1 = Kv_1 = v_2.$$

From (2.1.4)

$$\delta_q(u_2, v_2) = \delta_q(Ju_1, Jv_1) \leq \phi(\delta_q(Ku_1, Kv_1)) = \phi(\delta_q(u_2, v_2)) < \delta_q(u_2, v_2).$$

This is a contradiction, thus J and K have a unique coincidence point.

Consider $0 < \delta_q(Jx_0, Jx_1) < \varepsilon$, then

$$\begin{aligned}
\delta_q(Jx_n, Jx_{n+1}) &\leq \phi(\delta_q(Kx_n, Kx_{n+1})) \\
&< \delta_q(Kx_n, Kx_{n+1}) \\
&= \delta_q(Jx_{n-1}, Jx_n) \\
&\leq \phi(\delta_q(Kx_{n-1}, Kx_n)) \\
&< \delta_q(Kx_{n-1}, Kx_n) \\
&= \delta_q(Jx_{n-2}, Jx_{n-1}) \\
&\vdots \\
&= \delta_q(Jx_0, Jx_1) < \varepsilon.
\end{aligned}$$

Now, consider $(m,n) \in N$, $m > n$, therefore

$$\sum_{i=n}^{m-1} \delta_q(Jx_i, Jx_{i+1}) \le (m-1-n)\delta_q(Jx_0, Jx_1) < (m-1-n)\varepsilon < \varepsilon$$

Now, consider $f(B) \in F \times (0,\infty)$, so that (δ_2) is satisfied

$$(2.1.5) \quad f\left(\sum_{i=n}^{m-1} \delta_q(Jx_i, Jx_{i+1})\right) \le f(\varepsilon) < f(\varepsilon) - B, \ \forall \ n \in N$$

For $m > n \ge N$, using (δ_2) and (2.1.5)

$$\delta_q(Jx_n, Jx_m) > 0 \Rightarrow \delta_q(Jx_n, Jx_m) \le f\left(\sum_{i=n}^{m-1} \delta_q(Jx_i, Jx_{i+1})\right) \le f(\varepsilon)$$

Hence $\delta_q(Jx_n, Jx_m) < \varepsilon$

$\{y_n\} = \{Jx_n\}$ is a right Cauchy sequence.

Similarly, consider the pair (x_{i+1}, x_i), then by above process, one can prove that $\{y_n\}$ is also left Cauchy sequence and thus a Cauchy sequence.

Since (X, δ_q) is bi-complete metric space, therefore $\{y_n\}$ is convergent to $z \in X$.

Now, $\{Jx_n\} = \{Kx_{n+1}\} \subset K(X)$.

Therefore, we have $\lim_{n \to \infty} \delta_q(Kx_n, Kz) = 0$, because K is closed.

Now, to prove that J and K have z as coincidence point, assume that $\delta_q(Jz, Kz) > 0$. Then

$$f(\delta_q(Jz, Kz)) \le f(\delta_q(Jz, Jx_n) + \delta_q(Jx_n, Kz)) + B$$
$$\le f(\phi(\delta_q(Kz, Kx_n)) + \delta_q(Kx_{n+1}, Kz)) + B.$$

As $n \to \infty$

$$\lim_{n \to \infty} f(\phi(\delta_q(Kz, Kx_n)) + \delta_q(Kx_{n+1}, Kz)) + B \to -\infty.$$

which is a contradiction, therefore $\delta_q(Jz, Kz) = 0 \Rightarrow Jz = Kz$.

Therefore, z is coincidence point of J and K.

Therefore, $J(z) = K(z) = w$.

Now, $K(w) = K(K(z)) = J(F(z)) = J(K(z)) = J(w)$.

Hence w is another coincidence point of J and K, but J and K have unique coincidence point. Therefore,

$$z = w.$$

Therefore,

$$J(z) = K(z) = z.$$

Therefore, J and K have a single fixed point in common. $\qquad\square$

Lemma 2.1 ([9])**.** *Consider a F-quasi-metric space (X, δ_q). Then, the following assertions hold:*

(i) *(X^n, δ_q) is a F-quasi-metric space with*

$$\Delta_q((u_1, u_2, \ldots, u_n), (v_1, v_2, \ldots, v_n)) = \max(\delta_q(u_1, v_1), \delta_q(u_2, v_2), \ldots, \delta_q(u_n, v_n))$$

for $u_1, u_2, \ldots, u_n, \ v_1, v_2, \ldots, v_n \in X$.

(ii) *The mapping $a : X^n \to X$ and $b : X \to X$ contain an n tuple common fixed point iff the mapping $A : X^n \to X^n$ and $B : X^n \to X^n$ defined by*

$$A(u_1, u_2, \ldots, u_n) = (a(u_1, u_2, \ldots, u_n), a(u_2, \ldots, u_n, u_1), \ldots, a(u_n, u_1, u_2, \ldots, u_{n-1})),$$

$$B(u_1, u_2, \ldots, u_n) = (bu_1, bu_2, \ldots, bu_n),$$

possess a common fixed point in X^n.

(iii) *(X, δ_q) is bi-complete iff (X^n, Δ_q) is bi-complete.*

Theorem 2.2. *Let (X, δ_q) be a bi-complete F-quasi metric space. Also, assume $a : X^n \to X$, $b : X \to X$ be two mappings which satisfy*

(2.1.6) *$a(X^n) \subset b(X)$, $b(X)$ is closed, $\forall \ x, y \in X$*

(2.1.7) *$\delta_q(a(x_1, x_2, \ldots, x_n), a(y_1, y_2, \ldots, y_n)) \leq \phi \left\{ \dfrac{1}{n} (\delta_q(bx_1, by_1) + \delta_q(bx_2, by_2) + \ldots + \delta_q(bx_n, by_n)) \right\}$*

for all $(x_1, x_2, \ldots, x_n), (y_1, y_2, \ldots, y_n) \in X^n$.

(2.1.8) *$\Delta_q : X^n \times X^n \to [0, \infty)$ be defined by (2.1.1) and (2.1.3) of Theorem 2.1.*

Then a and b have a common n-tuple fixed point in X^n.

Proof. Assume $A : X^n \to X^n$ by $A(x_1, x_2, \ldots, x_n) = (a(x_1, x_2, \ldots, x_n), a(x_2, \ldots, x_n, x_1), \ldots, a(x_n, x_1, x_2, \ldots, x_{n-1}))$.

Also assume, $B : X^n \to X^n$ defined by

$$B(x_1, x_2, \ldots, x_n) = (bx_1, bx_2, \ldots, bx_n)$$

Using Lemma 2.1 (X^n, Δ_q) is bi-complete F-quasi metric space.

Also, $(x_1, x_2, \ldots, x_n) \in X^n$ is a common n-tuple fixed point of a and b iff A and B have a common fixed point.

Now,

$$\Delta_q(A(x_1, x_2, \ldots, x_n), A(y_1, y_2, \ldots, y_n)) = \Delta_q(a(x_1, x_2, \ldots, x_n), a(x_2, \ldots, x_n, x_1), \ldots, a(x_n, x_1, x_2, \ldots, x_{n-1}),$$
$$a(y_1, y_2, \ldots, y_n), a(y_2, \ldots, y_n, y_1), \ldots, a(y_n, y_1, y_2, \ldots, y_{n-1}))$$
$$= \max\{\delta_q(a(x_1, x_2, \ldots, x_n), a(y_1, y_2, \ldots, y_n)),$$
$$\delta_q(a(x_2, x_3 \ldots, x_n, x_1), a(y_2, \ldots, y_n, y_1)), \ldots,$$
$$\delta_q(a(x_n, x_1, x_2, \ldots, x_{n-1}), a(y_n, y_1, y_2, \ldots, y_{n-1}))\}.$$

Consider

$$\Delta_q(A(x_1, x_2, \ldots, x_n), A(y_1, y_2, \ldots, y_n)) = \delta_q(a(x_1, x_2, \ldots, x_n), a(y_1, y_2, \ldots, y_n)$$
$$\leq \phi \left\{ \frac{1}{n} (\delta_q(bx_1, by_1) + \delta_q(bx_2, by_2) + \ldots + \delta_q(bx_n, by_n)) \right\}$$
$$\leq \max \left\{ (\delta_q(bx_1, by_1), \delta_q(bx_2, by_2), \ldots, \delta_q(bx_n, by_n)) \right\}$$
$$= \Delta_q(B(x_1, x_2, \ldots, x_n), B(y_1, y_2, \ldots, y_n))$$

or

$$\Delta_q(A(x_1, x_2, \ldots, x_n), A(y_1, y_2, \ldots, y_n)) = \delta_q(a(x_2, \ldots, x_n, x_1), a(y_2, \ldots, y_n, y_1)$$
$$\leq \phi \left\{ \frac{1}{n} (\delta_q(bx_2, by_2) + \ldots + \delta_q(bx_n, by_n) + \delta_q(bx_1, by_1)) \right\}$$

$$\leq \frac{1}{n}(\delta_q(bx_2, by_2) + \ldots + \delta_q(bx_n, by_n) + \delta_q(bx_1, by_1))$$

$$\leq \max\{(\delta_q(bx_2, by_2), \ldots, \delta_q(bx_n, by_n), \delta_q(bx_1, by_1))\}$$

$$= \Delta_q(B(x_2, x_3, \ldots, x_n, x_1), B(y_2, y_3, \ldots, y_n, y_1)).$$

Proceeding in a similar way, one can prove

$$\Delta_q(A(x_1, x_2, \ldots, x_n), A(y_1, y_2, \ldots, y_n)) = \Delta_q(B(x_2, \ldots, x_n, x_1), B(y_2, \ldots, y_n, y_1)).$$

Thus by Lemma 2.1, a and b have a common n-tuple fixed point in X^n. □

Example 2.1. Let $X = [0, 1]$. Define $\delta_q : X \times X \to [0, \infty)$ by

$$\delta_q(x, y) = \begin{cases} 0, & x = y, \\ |y| + |x - y|, & \text{otherwise.} \end{cases}$$

δ_q is bi-complete F-quasi metric with $f(t) = \ln t$ and $B = 0$.

Consider $a : X^n \to X$ by $a(x_1, x_2, \ldots, x_n) = \dfrac{x_1 + x_2 + \ldots + x_n}{n}$.

Define $b : X \to X$ by $b(x) = \frac{x}{n}$.

Then a and b are commutative.

Also

$$\delta_q(a(x_1, x_2, \ldots, x_n), a(y_1, y_2, \ldots, y_n))$$

$$= |a(y_1, y_2, \ldots, y_n)| + |a(x_1, x_2, \ldots, x_n) - a(y_1, y_2, \ldots, y_n)|$$

$$= \frac{1}{n}[|y_1 + y_2 + \ldots + y_n| + |(x_1 - y_1) + (x_2 - y_2) + \ldots + (x_n - y_n)|]$$

$$= |by_1 + by_2 + \ldots + by_n| + |(bx_1 - by_1) + (bx_2 - by_2) + \ldots + (bx_n - by_n)|$$

$$= |\delta_q(bx_1, by_1) + \delta_q(bx_2, by_2) + \ldots + \delta_q(bx_n, by_n)|$$

$$\leq \phi\left\{\frac{1}{n}(\delta_q(bx_1, by_1) + \delta_q(bx_2, by_2) + \ldots + \delta_q(bx_n, by_n))\right\}.$$

All conditions of Theorem 2.2 are met, so a and b have common n-tuple fixed point.

Corollary 2.1. *Let (X, δ_q) be a bi-complete F-quasi metric space. Consider $J, K : X \to X$ be two arbitrary mappings which satisfy (2.1.1), (2.1.2), (2.1.3) and the condition below:*
(2.1.9) $\delta_q(Jx, Jy) \leq k\delta_q(Kx, Ky), \; \forall \; x, y \in X, \; k \in (0, 1)$.
Then J and K have a unique common fixed point.

Proof. Consider $\phi(t) = kt$ in Theorem 2.1, we get the result. □

Corollary 2.2. *Let (X, δ_q) be a bi-complete F-quasi metric space. Also, assume $a : X^n \to X$, $b : X \to X$ be two arbitrary mappings which satisfy (2.1.3), (2.1.6), (2.1.8) of Theorem 2.1 and*
(2.1.10) $\delta_q(a(x_1, x_2, \ldots, x_n), a(y_1, y_2, \ldots, y_n)) \leq \dfrac{k}{n}\{(\delta_q(bx_1, by_1) + \delta_q(bx_2, by_2) + \ldots + \delta_q(bx_n, by_n))\}$.
Then a and b have an n-tuple fixed point in common.

Proof. Consider $\phi(t) = kt$ in Theorem 2.1, we get the result. □

Remark 2.1. Corollary 2.1 and Corollary 2.2 are theorems proved by Ghasab *et al*. [9].

Remark 2.2. If $n = 4$ in Theorem 2.2, we will get quadruple fixed point.

Remark 2.3. If $n = 3$ in Theorem 2.2, we will get tripled fixed point.

Remark 2.4. If $n = 2$ in Theorem 2.2, we will get coupled fixed point.

Remark 2.5. If $n = 1$ in Theorem 2.2, we will get fixed point.

Acknowledgement

Competing Interests

The authors declare that they have no competing interests.

Authors' Contributions

All the authors contributed significantly in writing this article. The authors read and approved the final manuscript.

References

[1] C. Aleire and J. Marín, Modified w-distances on quasi-metric spaces and a fixed point theorem on complete quasi-metric spaces, *Topology and its Applications* **203** (2016), 32 – 41, DOI: 10.1016/j.topol.2015.12.073.

[2] O. Alqahtani, E. Karapınar and P. Shahi, Common fixed point results in function weighted metric spaces, *Journal of Inequalities and Applications* **2019** (2019), Article ID 164, DOI: 10.1186/s13660-019-2123-6.

[3] H. Ayadi, M. Jellali and E. Karapinar, On fixed point results for α-implicit contractions in quasi-metric spaces and consequences, *Nonlinear Analysis Modelling and Control* **21** (2016), 40 – 56, DOI: 10.15388/NA.2016.1.3.

[4] S. Banach, Sur les opérations dans les ensembles abstraits et leur application aux équations intégrales, *Fundamenta Mathematicae* **3** (1922), 133 – 181, URL: https://eudml.org/doc/213289.

[5] V. Berinde and M. Borcut, Triple fixed point theorems for contractive type mappings in partially ordered metric spaces, *Nonlinear Analysis: Theory, Methods & Applications* **74**(15) (2011), 4889 – 4897, DOI: 10.1016/j.na.2011.03.032.

[6] N. Bilgili, E. Karapınar and B. Samet, Generalized α-ψ contractive mapping in quasi-metric spaces and related fixed point theorems, *Journal of Inequalities and Applications* **2014** (2014), Article number: 36, DOI: 10.1186/1029-242X-2014-36.

[7] M. Ertürk and V. Karakaya, n-tuplet fixed point theorems for contractive type mappings in partially ordered metric spaces, *Journal of Inequalities and Applications* **2013** (2013), Article number: 196, DOI: 10.1186/1029-242X-2013-196.

[8] M. Ertürk and V. Karakaya, Correction: 'n-tuplet fixed point theorems for contractive type mappings in partially ordered metric spaces', *Journal of Inequalities and Applications* **2013** (2013), Article number: 368, DOI: 10.1186/1029-242X-2013-368.

[9] E.L. Ghasab, H. Majani, E. Karapinar and G.S. Rad, New fixed point results in *F*-quasi metric spaces and an Application, *Advances in Mathematical Physics* **2020** (2020), Article ID 9452350, DOI: 10.1155/2020/9452350.

[10] D. Guo and V. Laxmikantham, Coupled fixed points of nonlinear operators with applications, *Nonlinear Analysis: Theory, Methods & Applications* **11**(5) (1987), 623 – 632, DOI: 10.1016/0362-546X(87)90077-0.

[11] E. Karapınar and V. Berinde, Quadruple fixed point theorems for nonlinear contractions in partially ordered metric spaces, *Banach Journal of Mathematical Analysis* **6**(1) (2012), 74 – 89, DOI: 10.15352/bjma/1337014666.

[12] E. Karapınar and N.V. Luong, Quadruple fixed point theorems for nonlinear contractions, *Computers & Mathematics with Applications* **64**(6) (2012), 1839 – 1848, DOI: 10.1016/j.camwa.2012.02.061.

[13] V. Lakshmikanthm and L. Ćirić, Coupled fixed point theorems for nonlinear contractions in partially ordered metric spaces, *Nonlinear Analysis: Theory, Methods and Applications* **70**(12) (2009), 4341 – 4349, DOI: 10.1016/j.na.2008.09.020.

[14] W. Shatanawi, M.S. MD Noorani, H. Alsamir and A. Bataihah, Fixed and common fixed point theorems in partially ordered quasi-metric spaces, *Journal of Mathematics and Computer Science* **16** (2012), 516 – 528, URL: https://www.isr-publications.com/jmcs/1352/download-fixed-and-common-fixed-point-theorems-in-partially-ordered-quasi-metric-spaces.

[15] W. Shatanawi and A. Pitea, Some coupled fixed point theorems in quasi-partial metric spaces, *Fixed Point Theory and Applications* **2013** (2013), Article number: 153, DOI: 10.1186/1687-1812-2013-153.

[16] W.A. Wilson, On quasi-metric spaces, *American Journal of Mathematics* **53**(3) (1931), 675 – 684, DOI: 10.2307/2371174.

Isonumber based Iso-Key Interchange Protocol for Network Communication

Mamta S. Dani[1], Akshaykumar Meshram[2*], Rupesh Pohane[3] and Rupali R. Meshram[4]

*Corresponding Author:

[1, 2,*]Department of Applied Mathematics, Yeshwantrao Chavan College of Engineering, Nagpur-441110, M.S., India
[3]Department of Applied Mathematics, Suryodaya College of Engineering and Technology, Nagpur-440027, M.S., India
[4]Department of Mathematics, Kamla Nehru Mahavidyalaya, Nagpur-440024, M.S., India

Summary

Key exchange protocol (KEP) is an essential setup to secure authenticates transmission among two or more users in cyberspace. Digital files protected and transmitted by the encryption of the files over public channels, a single key communal concerning the channel parties and utilized for both to encrypt the files as well as decrypt the files. If entirely done, this impedes unauthorized third parties from imposing a key optimal on the authorized parties. In this article, we have suggested a new KEP term as isokey interchange protocol based on generalization of modern mathematics term as isomathematics by utilizing isonumbers for corresponding isounits over the Block Upper Triangular Isomatrices (BUTI) which is secure, feasible and extensible. We also were utilizing arithmetic operations like Isoaddition, isosubtraction, isomultiplication and isodivision from isomathematics to build iso-key interchange protocol for network communication. The execution of our protocol is for two isointegers corresponding two elements of the group of isomatrices and cryptographic performance of products eachother. We demonstrate the protection of suggested isokey interchange protocol against Brute force attacks, Menezes et al. algorithm and Climent et al. algorithm.

Keywords:

Cryptography, Block Isomatrix, Isomathematics, Isonumber, Isounit.

1. Introduction

Now a days, the security is main concern in large open network. To set up a private channel among two users' needs to interchange a mutual secret key [2]. It is feasible in limited and small network but not possible in large and broad networks like internet. The public-key cryptography (PKC) offers a technique to permit secret session keys to be interchange over an unprotected network in which each user holds key pair comprising of a non-secret key and a secret key such that only non-secret keys are published in network. Diffie–Hellman offered first feasible PKC in 1976 [3]. Number theory problems are the attraction in cryptographic researcher to build prominent PKC in which at least two user, user-I utilize the user-II non-secret key and encrypts the information

and then transmits to user-II. After getting the encrypted text, the user-II can decrypt the information with utilizing of his/her secret key [4].

Meshram C. [5-8] developed certain PKC schemes which are depends on solving discrete logarithm problem and integer factoring problem along with its generalization. Moreover offered specific designs for identity-based cryptography [09-15]. Blake I. and Climent J., independently study the Elliptic Curve discrete logarithm problem which is one of the main problems where PKC are constructed [16-17]. Meshram A. [18-20] proposed certain cryptographic schemes based on suzuki 2-group and dihedral group.

Recently, Meshram C. [21] introduce Quadratic Exponentiation Randomized PKC based on Partial Discrete Logarithm Problem. Meshram A. recommended $\mathcal{KEP}$ constructed on isoring isopolynomials coefficient [22]. Dani M. recommended $\mathcal{SISK}$ based $\mathcal{KEP}$ for protected transmission [23] and $\mathcal{KEP}$ based on $\mathcal{SIFK}$ [24]. Thatere A. recommended isoryptosystem constructed on $\mathcal{SIFK}$ [25].

2. Motivations and Organization

In this article, we have proposed an isokey interchange protocol based on isonumbers for corresponding isounits over $\mathcal{BUTI}$. The primary thought of this article is to examine, for two isointegers $\hat{a}$ and $\hat{b}$ with elements of the group of isomatrices $\widehat{\mathcal{H}}_1$ and $\widehat{\mathcal{H}}_2$, the cryptographic performance of products of the nature $\widehat{\mathcal{H}}_1^{\hat{a}} \widehat{\mathcal{H}}_2^{\hat{b}}$.

The rest of the article is coordinated in various sections. In section 3, we have reviewed the prerequisite background for article. Section 4, describes the suggested isokey Interchange Protocol. Section 5, investigate the security analysis of suggested isokey Interchange Protocol. Finally, in section 6, we have concluded the article.

3. Mathematical Background and Material

In this section, we have describes the definition such as Isomathematics, arithmetic operations in modern mathematics, arithmetic operations in Santilli's isomathematics, $\mathcal{BUTJ}$ and order of the elements.

3.1 Santilli's Isomathematics [26]

Isomathematics is a generalization of arithmetic operations in modern mathematics. Utilizing isomathematics, we have shown that, two multiplied by two is equal to twenty-eight (for inverse of isounit $\hat{T} = 7$).

3.2 Operations in Modern Mathematics

Addition, subtraction, multiplication and division are arithmetic operations in modern mathematics. In modern mathematics, "0" and "1" are additive unity and multiplicative unity respectively such that

$\rho + 0 = \rho$,
$\rho - 0 = \rho$,
$\rho^0 = 1$,
$\rho \times 1 = 1 \times \rho = \rho$,
$\rho \div 1 = \rho$,
$1 \div \rho = \dfrac{1}{\rho}$,
$\rho \times \sigma = \rho\sigma$,
$\rho \div \sigma = \dfrac{\rho}{\sigma}$ etc.

3.3 Operations in Santilli's Isomathematics

Isoaddition $\hat{+}$, isosubtraction $\hat{-}$, isomultiplication $\hat{\times}$ and isodivision $\hat{\div}$ are arithmetic operations in isomathematics and describe as follows;

$\rho \hat{+} \sigma = \rho + \hat{\mathcal{K}} + \sigma$,
$\rho \hat{-} \sigma = \rho - \hat{\mathcal{K}} - \sigma$,
$\rho \hat{\times} \sigma = \rho\hat{T}\sigma$, and
$\rho \hat{\div} \sigma = \left(\dfrac{\rho}{\sigma}\right)\hat{J}$.

Where, $i)$ $\hat{T}\hat{J} = 1, \hat{T}$ is called inverse of isounit $\hat{J} \neq 1$ and $ii)$ $\hat{\mathcal{K}}$ is called isozero.

3.4 $\mathcal{BUTJ}$

An isomatrices $\hat{\mathcal{H}}_{\hat{v}}(\mathcal{Z}_{\hat{q}})$ of size $v \hat{\times} v$, $\hat{\mathcal{H}}_{\hat{u}}(\mathcal{Z}_{\hat{q}})$ of size $u \hat{\times} u$ and $\hat{\mathcal{H}}_{\hat{u}\times\hat{v}}(\mathcal{Z}_{\hat{q}})$ of size $u \hat{\times} v$ for isoprime number $\hat{q}$, isonumbers $\hat{u}, \hat{v} \in \mathcal{N}\left(\mathcal{Z}_{\hat{q}}\right)$ and invertible isomatrices $\mathcal{L}_{\hat{u}}(\mathcal{Z}_{\hat{q}})$ of size $u \hat{\times} u$, $\mathcal{GL}_{\hat{v}}(\mathcal{Z}_{\hat{q}})$ of size $v \hat{\times} v$.

Define isomatrix $\hat{H} = \begin{bmatrix} \hat{\alpha} & \hat{\gamma} \\ \hat{0} & \hat{\beta} \end{bmatrix}$,

$\hat{\alpha} \in \hat{\mathcal{H}}_{\hat{u}}(\mathcal{Z}_{\hat{q}}), \hat{\beta} \in \hat{\mathcal{H}}_{\hat{v}}(\mathcal{Z}_{\hat{q}}), \hat{\gamma} \in \hat{\mathcal{H}}_{\hat{u}}\hat{\mathcal{H}}_{\hat{u}\times\hat{v}}(\mathcal{Z}_{\hat{q}})$,

with subset $\hat{\Theta} = \begin{bmatrix} \hat{\alpha} & \hat{\gamma} \\ \hat{0} & \hat{\beta} \end{bmatrix}$,

$\hat{\alpha} \in \mathcal{GL}_{\hat{u}}(\mathcal{Z}_{\hat{q}}), \hat{\beta} \in \mathcal{GL}_{\hat{v}}(\mathcal{Z}_{\hat{q}}), \hat{\gamma} \in \hat{\mathcal{H}}_{\hat{u}}\hat{\mathcal{H}}_{\hat{u}\times\hat{v}}(\mathcal{Z}_{\hat{q}})$

By utilizing property [28], we have compute isopowers of these $\mathcal{BUTJ}$ to find the order of the subgroup generated by a isomatrix $\hat{\mathcal{H}} \in \hat{\Theta}$.

For non negative isointeger $\hat{p}$ and isomatrix $\hat{\mathcal{H}} = \begin{bmatrix} \hat{\alpha} & \hat{\gamma} \\ \hat{0} & \hat{\beta} \end{bmatrix} \in \hat{\Theta}$,

Define $\hat{\mathcal{H}}^{\hat{p}} = \begin{bmatrix} \hat{\alpha}^{\hat{p}} & \hat{\gamma}^{(\hat{p})} \\ \hat{0} & \hat{\beta}^{\hat{p}} \end{bmatrix}$, where

$\hat{\gamma}^{(\hat{p})} = \begin{cases} 0 & if\ \hat{p}=0 \\ \sum_{\hat{j}=1}^{\hat{p}} \hat{\alpha}^{\hat{p}-\hat{j}}\hat{\gamma}\hat{\beta}^{\hat{j}-1} & if\ \hat{p} \geq 1. \end{cases}$

i) If $\hat{0} \leq \hat{d} \leq \hat{p}$ then $\hat{\gamma}^{(\hat{p})} - \hat{\alpha}^{\hat{d}}\hat{\gamma}^{(\hat{p}-\hat{d})} + \hat{\gamma}^{(\hat{d})}\hat{\beta}^{\hat{p}-\hat{d}}\hat{\gamma}^{(\hat{p})} = \hat{\alpha}^{(\hat{p}-\hat{d})}\hat{\gamma}^{(\hat{p})} + \hat{\gamma}^{(\hat{p}-\hat{d})}\hat{\beta}^{\hat{d}}$

ii) If $\hat{d} = 1$ then $\hat{\gamma}^{(\hat{p})} = \hat{\alpha}\hat{\gamma}^{(\hat{p}-1)} + \hat{\gamma}\hat{\beta}^{\hat{p}-1}$ or
$\hat{\gamma}^{(\hat{p})} = \hat{\alpha}^{\hat{p}-1}\hat{\gamma} + \hat{\gamma}^{(\hat{p}-1)}\hat{\beta}$

For isointegers $\hat{c}, \hat{e}$; define $\hat{c} + \hat{e} \geq \hat{0}$,
$\hat{\gamma}^{(\hat{c}+\hat{e})} = \hat{\alpha}^{\hat{c}}\hat{\gamma}^{(\hat{e})} + \hat{\gamma}^{(\hat{c})}\hat{\beta}^{\hat{e}}$.

3.5 Order of the elements

In this subsection [28-29], we have define the way to guarantee the maximum order of group generated by the isomatrix $\hat{\mathcal{H}} = \begin{bmatrix} \hat{\alpha} & \hat{\gamma} \\ \hat{0} & \hat{\beta} \end{bmatrix} \in \hat{\Theta}$.

Suppose that monic isopolynomial
$\hat{h}(\hat{y}) = \hat{c}_0 + \hat{c}_1\hat{y} + \cdots + \hat{c}_{\hat{w}-1}\hat{y}^{\hat{w}-1} + \hat{y}^{\hat{w}} \in \mathcal{Z}_{\hat{q}}[\hat{\gamma}]$.

i) If $\hat{h} \in \mathcal{Z}_{\hat{q}}$ is an irreducible isopolynomial, then the order of the isomatrix $\overline{\overline{\alpha}}$ is identical to the order of any root of $\hat{h}$ in $F_{\hat{q}^{\hat{w}}}$ and the order of $\overline{\overline{\alpha}}$ divides $\hat{q}^{\hat{w}} - 1$.

ii) If $\hat{h} \in \mathcal{Z}_{\hat{q}}$ is a primitive isopolynomial, the order of $\overline{\overline{\alpha}}$ is precisely $\hat{q}^{\hat{w}} - 1$.

To design of block isomatrices $\overline{\overline{\alpha}} = \begin{bmatrix} \overline{\overline{\alpha_1}} & \hat{0} & \hat{0} \\ \hat{0} & \overline{\overline{\alpha_2}} & \hat{0} \\ \hat{0} & \hat{0} & \overline{\overline{\alpha_k}} \end{bmatrix}$

suggested by Odoni et al. [30], for different primitive isopolynomials in $\mathcal{Z}_{\hat{q}}$ of degree $\hat{w}_{\hat{j}}$ and $\overline{\overline{\alpha}}_{\hat{j}}$ is the companion matrix of $\hat{h}_{\hat{j}}$, and $\hat{h}_{\hat{j}}$, for $\hat{j} = 1,2,\ldots,k$.

Since, order of each block $\overline{\overline{\alpha}}_i$ is $\hat{q}^{\hat{w}_{\hat{j}}} - 1$, so the order of $\overline{\overline{\alpha}}$ is $\text{lcm}(\hat{q}^{\hat{w}_1} - 1, \hat{q}^{\hat{w}_2} - 1, \ldots, \hat{q}^{\hat{w}_k} - 1)$.

For companion isomatrices $\overline{\overline{\alpha}}, \overline{\overline{\beta}}$ and
$\hat{h}(\hat{y}) = \hat{c}_0 + \hat{c}_1\hat{y} + \cdots + \hat{c}_{\hat{u}-1}\hat{y}^{\hat{u}-1} + \hat{y}^{\hat{u}}$,
$\hat{f}(\hat{y}) = \hat{e}_0 + \hat{e}_1\hat{y} + \cdots + \hat{e}_{\hat{v}-1}\hat{y}^{\hat{v}-1} + \hat{y}^{\hat{v}}$ be two primitive polynomials in $\mathcal{Z}_{\hat{q}}[\hat{\gamma}]$. For two invertible

isomatrices $\hat{\mathcal{R}}$ and $\hat{\mathcal{S}}$, define $\hat{\alpha} = \hat{\mathcal{R}}^{-1}\overline{\hat{\alpha}}\,\hat{\mathcal{R}}$ and $\hat{\beta} = \hat{\mathcal{S}}^{-1}\overline{\hat{\beta}}\,\hat{\mathcal{S}}$ such that the order of $\hat{\mathcal{H}}$ is lcm$(\hat{q}^{\hat{u}} - 1, \hat{q}^{\hat{v}} - 1)$.

4. Suggested Isonumber based Isokey Interchange Protocol

Suppose that $\hat{\mathcal{H}}_1 = \begin{bmatrix} \hat{\alpha}_1 & \hat{\gamma}_1 \\ \hat{0} & \hat{\beta}_1 \end{bmatrix} \in \hat{\Theta}$ with orders $\hat{z}_1$ and $\hat{\mathcal{H}}_2 = \begin{bmatrix} \hat{\alpha}_2 & \hat{\gamma}_2 \\ \hat{0} & \hat{\beta}_2 \end{bmatrix} \in \hat{\Theta}$ with orders $\hat{z}_2$, are two isometrix. For isonumbers $\hat{m}$; $\hat{n} \in \mathcal{N}$, define the following notation; $\hat{\alpha}_{\hat{m}\hat{n}} = \hat{\alpha}_1^{\hat{m}}\hat{\alpha}_2^{\hat{n}}, \hat{\beta}_{\hat{m}\hat{n}} = \hat{\beta}_1^{\hat{m}}\hat{\beta}_2^{\hat{n}}$, and $\hat{\psi}_{\hat{m}\hat{n}} = \hat{\alpha}_1^{\hat{m}}\hat{\gamma}_2^{(\hat{n})} + \hat{\gamma}_1^{(\hat{m})}\hat{\beta}_2^{\hat{n}}$.

If two clients Taylor and Eileen wish to interchange an isokey, they may implement the following algorithm:

1) Taylor and Eileen consent on isounit $\hat{I}, \hat{q} \in \mathcal{N}, \hat{\mathcal{H}}_1 \in \hat{\Theta}$ with orders $\hat{z}_1$ and $\hat{\mathcal{H}}_2 \in \hat{\Theta}$ with orders $\hat{z}_2$.

2) Taylor select two arbitrary isonumber $\hat{u}; \hat{v} \in \mathcal{N}$ such that $1 \le \hat{u} \le \hat{z}_1 - 1$, $1 \le \hat{v} \le \hat{z}_2 - 1$.

And numerate $\hat{\alpha}_{\hat{u}\hat{v}}, \hat{\beta}_{\hat{u}\hat{v}}, \hat{\psi}_{\hat{u}\hat{v}}$ for constructing $\hat{\psi} = \begin{bmatrix} \hat{\alpha}_{\hat{u}\hat{v}} & \hat{\psi}_{\hat{u}\hat{v}} \\ \hat{0} & \hat{\beta}_{\hat{u}\hat{v}} \end{bmatrix}$.

(3) Taylor refers $\hat{\psi}$ to Eileen.

(4) Eileen select two arbitrary isonumber $\hat{a}, \hat{b} \in \mathcal{N}$ such that $1 \le \hat{a} \le \hat{z}_1 - 1$, $1 \le \hat{b} \le \hat{z}_2 - 1$.

And numerate $\hat{\alpha}_{\hat{a}\hat{b}}, \hat{\beta}_{\hat{a}\hat{b}}, \hat{\psi}_{\hat{a}\hat{b}}$ for constructing $\hat{\chi} = \begin{bmatrix} \hat{\alpha}_{\hat{a}\hat{b}} & \hat{\psi}_{\hat{a}\hat{v}} \\ \hat{0} & \hat{\beta}_{\hat{a}\hat{b}} \end{bmatrix}$.

(5) Eileen refers $\hat{\chi}$ to Taylor.

(6) Then the isomatrices $\hat{\psi}$ is non-secret keys for Taylor and the isomatrices $\hat{\psi}$ is non-secret keys for Eileen.

(7) Taylor numerate $\hat{K}_{\text{Taylor}} = \hat{\alpha}_1^{\hat{u}}\hat{\alpha}_{\hat{a}\hat{b}}\hat{\gamma}_2^{(\hat{v})} + \hat{\alpha}_1^{\hat{u}}\hat{\psi}_{\hat{a}\hat{b}}\hat{\beta}_2^{\hat{v}} + \hat{\gamma}_1^{(\hat{u})}\hat{\beta}_{\hat{a}\hat{b}}\hat{\beta}_2^{\hat{v}}$.

(8) Eileen numerate $\hat{K}_{\text{Eileen}} = \hat{\alpha}_1^{\hat{a}}\hat{\alpha}_{\hat{u}\hat{v}}\hat{\gamma}_2^{(\hat{b})} + \hat{\alpha}_1^{\hat{a}}\hat{\psi}_{\hat{u}\hat{u}}\hat{\beta}_2^{\hat{b}} + \hat{\gamma}_1^{(\hat{a})}\hat{\beta}_{\hat{u}\hat{v}}\hat{\beta}_2^{\hat{b}}$.

Following proof shows that $\hat{K}_{\text{Taylor}} = \hat{K}_{\text{Eileen}}$.

If $\hat{K}_{\text{Taylor}} = \hat{\alpha}_1^{\hat{u}}\hat{\alpha}_{\hat{a}\hat{b}}\hat{\gamma}_2^{(\hat{v})} + \hat{\alpha}_1^{\hat{u}}\hat{\psi}_{\hat{a}\hat{b}}\hat{\beta}_2^{\hat{v}} + \hat{\gamma}_1^{(\hat{u})}\hat{\beta}_{\hat{a}\hat{b}}\hat{\beta}_2^{\hat{v}}$ and $\hat{K}_{\text{Eileen}} = \hat{\alpha}_1^{\hat{a}}\hat{\alpha}_{\hat{u}\hat{v}}\hat{\gamma}_2^{(\hat{b})} + \hat{\alpha}_1^{\hat{a}}\hat{\psi}_{\hat{a}\hat{v}}\hat{\beta}_2^{\hat{b}} + \hat{\gamma}_1^{(\hat{a})}\hat{\beta}_{\hat{u}\hat{v}}\hat{\beta}_2^{\hat{b}}$, then $\hat{K}_{\text{Taylor}} = \hat{K}_{\text{Eileen}}$.

As, $\hat{\psi} = \begin{bmatrix} \hat{\alpha}_{\hat{u}\hat{v}} & \hat{\psi}_{\hat{u}\hat{v}} \\ \hat{0} & \hat{\beta}_{\hat{u}\hat{v}} \end{bmatrix} = \hat{\mathcal{H}}_1^{\hat{u}}\hat{\mathcal{H}}_2^{\hat{v}}$,

$\hat{\chi} = \begin{bmatrix} \hat{\alpha}_{\hat{a}\hat{b}} & \hat{\psi}_{\hat{a}\hat{v}} \\ \hat{0} & \hat{\beta}_{\hat{a}\hat{b}} \end{bmatrix} = \hat{\mathcal{H}}_1^{\hat{a}}\hat{\mathcal{H}}_2^{\hat{b}}$

$\hat{\mathcal{H}}_1^{\hat{u}} = \begin{bmatrix} \hat{\alpha}_1^{\hat{u}} & \hat{\gamma}_1^{(\hat{u})} \\ \hat{0} & \hat{\beta}_1^{\hat{u}} \end{bmatrix}$,

$\hat{\mathcal{H}}_1^{\hat{a}} = \begin{bmatrix} \hat{\alpha}_1^{\hat{a}} & \hat{\gamma}_1^{(\hat{a})} \\ \hat{0} & \hat{\beta}_1^{\hat{a}} \end{bmatrix}$

$\hat{\mathcal{H}}_2^{\hat{v}} = \begin{bmatrix} \hat{\alpha}_2^{\hat{v}} & \hat{\gamma}_2^{(\hat{v})} \\ \hat{0} & \hat{\beta}_2^{\hat{v}} \end{bmatrix}$ and

$\hat{\mathcal{H}}_2^{\hat{b}} = \begin{bmatrix} \hat{\alpha}_2^{\hat{b}} & \hat{\gamma}_2^{(\hat{b})} \\ \hat{0} & \hat{\beta}_2^{\hat{b}} \end{bmatrix}$

Suppose that, $\hat{\mathcal{H}}_{\text{Taylor}} = \hat{\mathcal{H}}_1^{\hat{u}}\hat{\chi}\hat{\mathcal{H}}_2^{\hat{v}} = \begin{bmatrix} \hat{\alpha}_{\hat{a}} & \hat{K}_{\text{Taylor}} \\ \hat{0} & \hat{\beta}_{\hat{a}} \end{bmatrix}$ and $\hat{\mathcal{H}}_{\text{Eileen}} = \hat{\mathcal{H}}_1^{\hat{a}}\hat{\psi}\hat{\mathcal{H}}_2^{\hat{b}} = \begin{bmatrix} \hat{\alpha}_{\hat{a}} & \hat{K}_{\text{Eileen}} \\ \hat{0} & \hat{\beta}_{\hat{a}} \end{bmatrix}$

Then, $\hat{\mathcal{H}}_{\text{Taylor}} = \hat{\mathcal{H}}_1^{\hat{u}}\hat{\chi}\hat{\mathcal{H}}_2^{\hat{v}} = \hat{\mathcal{H}}_1^{\hat{u}}\hat{\mathcal{H}}_1^{\hat{a}}\hat{\mathcal{H}}_2^{\hat{b}}\hat{\mathcal{H}}_2^{\hat{v}} = \hat{\mathcal{H}}_1^{\hat{a}}\hat{\mathcal{H}}_1^{\hat{u}}\hat{\mathcal{H}}_2^{\hat{v}}\hat{\mathcal{H}}_2^{\hat{b}} = \hat{\mathcal{H}}_1^{\hat{a}}\hat{\psi}\hat{\mathcal{H}}_2^{\hat{b}} = \hat{\mathcal{H}}_{\text{Eileen}}$

Hence, $\hat{K}_{\text{Taylor}} = \hat{K}_{\text{Eileen}}$ hold i.e., the isokey interchange protocol is successful achieved.

5. Suggested Isonumber based Isokey Interchange Protocol

If foe incapable to find isounit then suggested isokey interchange protocol secure and if foe capable to find isounit then following attack is secure.

Brute force attacks: For large order for $\hat{\mathcal{H}}_1$ and $\hat{\mathcal{H}}_2$ as 1024 bits then Brute force attacks not applicable.

Menezes and Wu algorithm [31]: Since no isomatrix powers are published over network. Thus Menezes and Wu algorithm is not feasible for the suggested protocol.

Climent et al. algorithm [32]: For identity isomatrix $\mathcal{I}_{\hat{w}}$ of size $\hat{w}$ and null matrix $\hat{0}_{\hat{w}}$ of the same size, an equation

$\hat{\zeta}_{\hat{\mathcal{H}}}(\hat{\mu}) = \det(\hat{\mu}\mathcal{I}_{\hat{w}} - \hat{\mathcal{H}}) = \hat{c}_0 + \hat{c}_1\hat{\mu} + \hat{c}_2\hat{\mu}^2 \dots + \hat{c}_{\hat{w}-1}\hat{\mu}^{\hat{w}-1} + \hat{\mu}^{\hat{w}}$

is the characteristic equation for isomatrix $\widehat{\mathcal{H}} \in \mathcal{GL}_{\widehat{w}}\left(\mathcal{Z}_{\widehat{q}}\right)$.

Then

$$\widehat{\zeta}_{\widehat{\mathcal{H}}}\left(\widehat{\mathcal{H}}\right) = \hat{c}_0 + \hat{c}_1 \widehat{\mathcal{H}} + \hat{c}_2 \widehat{\mathcal{H}}^2 \ldots + \hat{c}_{\widehat{w}-1} \widehat{\mathcal{H}}^{\widehat{w}-1} + \widehat{\mathcal{H}}^{\widehat{w}} = \widehat{0}_{\widehat{w}},$$

Meanwhile two different characteristic equations for two different isomatrices, so the attack based on Cayley–Hamilton theorem is not feasible for the suggested protocol.

The inefficiency of this type of attack is guaranteed by Alvarez R et al [1].

6. Conclusion

In this article, we have suggested a new isokey interchange protocol based on isomathematics; utilizing isonumbers for corresponding isounits and for isointegers $\widehat{a}$, $\widehat{b}$; the behavior of isomatrix isoproducts of the type $\widehat{\mathcal{H}}_1^{\widehat{a}} \, \widehat{\mathcal{H}}_2^{\widehat{b}}$, where $\widehat{\mathcal{H}}_1$; $\widehat{\mathcal{H}}_2$ over $\mathcal{BUIJ}$ with a large sufficient order as, for example, 1024 bits. Large isoprime isonumbers are absence in suggested protocol which is one of the primary asset of this protocol. Moreover, Brute force attacks, Menezes and Wu algorithm and Climent et al. algorithm are infeasible in suggested isokey interchange protocol.

References

[1] Alvarez R., Tortosa L., Vicent J-F, Zamora A., "*Analysis and design of a secure key exchange scheme*," Information Sciences, 179 (12), pp. 2014-2021, (2009). DOI: 10.1016/j.ins.2009.02.008

[2] Alvarez R., *Aplicaciones de las matrices por bloques a los criptosistemas de cifrado en flujo*, Ph.D. Thesis Dissertation, University of Alicante, (2005). (https://rua.ua.es/dspace/bitstream/10045/13571/1/tesis_ralvarez.pdf)

[3] Diffie W., Hellman M., "*New directions in cryptography*," IEEE Transactions on Information Theory, 22, pp. 644–654, (1976). DOI: 10.1109/TIT.1976.1055638

[4] Ko S., Leem C. S., Na Y. J., Yoon C. Y., "*Distribution of digital contents based on non-secret key considering execution speed and security*," Information Sciences, 174 (3–4), pp. 237–250, (2005). DOI: 10.1016/j.ins.2004.08.011

[5] Meshram C., "*The Beta Cryptosystem*," Bulletin of Electrical Engineering and Informatics, 4 (2), pp. 155-159, (2015). (http://journal.portalgaruda.org/index.php/EEI/article/view/442)

[6] Meshram C. and Meshram S. A., "*PKC Scheme Based on DDLP*," International Journal of Information & Network Security, 2 (2), pp. 154-159, (2013). (http://ijins.iaescore.com/index.php/IJINS/article/view/17480)

[7] Meshram C. and Meshram S. A., "*A Non-secret key*

[8] Meshram C., "*A Cryptosystem based on Double Generalized Discrete Logarithm Problem*," International Journal of Contemporary Mathematical Sciences, 6 (6), pp. 285 – 297, (2011). (http://www.m-hikari.com/ijcms-2011/5-8-2011/meshramIJCMS5-8-2011.pdf)

[9] Meshram C. and Meshram S. A., "*An identity based cryptographic model for discrete logarithm and integer factoring based cryptosystem*" Information Processing Letters, 113 (10), pp. 375-380, (2013). DOI: 10.1016/j.ipl.2013.02.009

[10] Meshram C., "*An Efficient ID-based Cryptographic Encryption based on Discrete Logarithm Problem and Integer Factorization Problem*," Information Processing Letters, 115 (2), pp. 351-358, (2015). DOI: 10.1016/j.ipl.2014.10.007

[11] Meshram C. and Obaidat M. S., "*An ID-based Quadratic-Exponentiation Randomized Cryptographic Scheme*," IEEE International Conference on Computer, Information and Telecommunication Systems, pp.1-5, (2015). DOI: 10.1109/CITS.2015.7297722

[12] Meshram C., "*An efficient ID-based Beta Cryptosystem*," International Journal of Security and Its Applications, 9 (2), pp. 189-202, (2015). (http://article.nadiapub.com/IJSIA/vol9_no2/18.pdf)

[13] Meshram C., Powar P. L., Obaidat M. S. and Lee C. C., "*An IBE Technique using Partial Discrete Logarithm*," Procedia Computer Science, 93, pp. 735-741, (2016). DOI: 10.1016/j.procs.2016.07.282

[14] Meshram C., Meshram S. A. and Zhang M., "*An ID-based cryptographic mechanisms based on GDLP and IFP*," Information Processing Letters, 112 (19), pp.753-758, (2012). DOI: 10.1016/j.ipl.2012.06.018

[15] Meshram C. and Powar P. L., "*An Efficient Identity-based QER Cryptographic Scheme*," Complex & Intelligent Systems, 2 (4), pp. 285-291, (2016). DOI: 10.1007/s40747-016-0030-8

[16] Blake, Seroussi G., Smart N., "*Elliptic Curves in Cryptography*," London Mathematical Society, Lecture Notes. Series, vol. 265, Cambridge University Press, pp. 001-204, (1999). DOI: 10.1017/CBO9781107360211

[17] Climent J. J., Ferrandiz F., Vicent J. F., Zamora A., "*A non linear elliptic curve cryptosystem based on matrices*," Applied Mathematics and Computation, 174, pp. 150–164, (2006). DOI: 10.1016/j.amc.2005.03.032

[18] Meshram A., Meshram C. and Khobragade N. W., "*An IND-CPA secure PKC technique based on dihedral group*," Indian Journal of Computer Science and Engineering, 8 (2), pp.88-94, (2017). (http://www.ijcse.com/docs/INDJCSE17-08-02-024.pdf)

[19] A. Meshram, C. Meshram and N. W. Khobragade, "*An IND-CCA2 secure non-secret key cryptographic protocol using suzuki 2-group*," Indian Journal of Science and Technology, 10 (12), pp.01-08, (2017). DOI: 10.17485/ijst/2017/v10i12/111588

[20] Meshram A., Meshram C. and Khobragade N. W., "*Non-secret key cryptographic technique based on suzuki 2-group*," International Journal of Advanced Research in

Cryptosystem based on IFP and DLP," International Journal of Advanced Research in Computer Science, 2 (5), pp. 616-619, (2011). DOI: 10.26483/ijarcs.v2i5.823

Computer Science, 8 (03), pp.300-305, (2017). DOI: 10.26483/ijarcs.v8i3.3000

[21] Meshram C., Obaidat M. S. and Meshram A., "*New efficient QERPKC based on partial discrete logarithm problem*," 2020 International Conference on Computer, Information and Telecommunication Systems (CITS), Hangzhou, China, pp. 1-5, (2020), DOI: 10.1109/CITS49457.2020.9232533.

[22] Meshram A., Meshram C., Bagde S. D. and Meshram R. R., "*RIPIC based key exchange protocol*," Advances in Mathematics: Scientific Journal, 9 (12), pp. 11169–11177, (2020). DOI: 10.37418/amsj.9.12.97

[23] Dani M. S., Meshram A., Meshram C., and Wazalwar N. M., "*An efficient key exchange scheme using santilli'sisofields second-kind for secure communication*," Advances in Mathematics: Scientific Journal, 10(2), pp. 1131–1139, (2021). DOI: 10.37418/amsj.10.2.39

[24] Dani M. S., Meshram A. and Meshram C., "*Santilli'sisofields firstkind based key exchange protocol,*" Journal of Physics: Conference Series, 1913 (1), 012095, (2021). DOI: 10.1088/1742-6596/1913/1/012095

[25] Thatere A. B., Meshram A., Meshram C., Wazalwar N. M., "*SIFK based Isobeta Cryptosystem*," International Journal of Engineering Trends and Technology, 69 (7), pp. 76-79, (2021. DOI: 10.14445/22315381/IJETT-V69I7P211

[26] Santilli R. M., "*Isonumbers and genonumbers of dimension 1, 2, 4, 8, their isoduals and pseudoduals, and "hidden numbers" of dimension 3, 5, 6, 7*," Algebras, Groups and Geometries, 10, pp. 273-322, (1993). (http://www.santilli-foundation.org/docs/Santilli-34.pdf)

[27] Climent J. J., "*Propiedades espectrales de matrices:el indice de matrices triangulares por bloques, La raiz Perron de matrices cociclicas no negativas*," Thesis for Doctoral Degree, (1993). (http://www.cervantesvirtual.com/nd/ark:/59851/bmcmk686)

[28] Hoffman K., Kunze R., "*Linear Algebra*," Prentice-Hall, New Jersey, (1971). (https://www.cin.ufpe.br/~jrsl/Books/Linear%20Algebra%20-%20Kenneth%20Hoffman%20&%20Ray%20Kunze%20.pdf)

[29] Koblitz N., "*A Course in Number Theory and Cryptography*," Springer-Verlag, (1987). (http://almuhammadi.com/sultan/crypto_books/Koblitz.2nd Ed.pdf)

[30] Odoni R. W. K., Varadharajan V., Sanders P. W., "*Public key distribution in matrix rings*," Electronic Letters, 20, pp. 386–387, (1984). DOI: 10.1049/el:19840267

[31] Menezes A., Wu Y-H., "*The discrete logarithm problem in GLðn; qÞ,*" Ars Combinatoria, 47, pp. 22–32, (1997). (https://dblp.org/db/journals/arscom/arscom47.html#MenezesW97)

[32] Climent J. J., Gorla E., Rosenthal J., "*Cryptanalysis of the CFVZ cryptosystem*," Advances in Mathematics of Communications, 1, pp. 1–11, (2007). DOI: 10.3934/amc.2007.1.1

Mamta S. Dani is currently working as an Associate Professor with the Department of Applied Mathematics, Yeshwantrao Chavan College of Engineering Nagpur, India. She has more than 34 year teaching & research experience. Her current research interests include cryptography, network security and wireless communication.

Akshaykumar Meshram received the Ph.D. degree from R.T.M. Nagpur University, Nagpur, India. He is currently an Assistant Professor with the Department of Applied Mathematics, Yeshwantrao Chavan College of Engineering, Nagpur, India. His current research interests include cryptography, network security, soft computing, and wireless communications. He has published more than twelve scientific articles on the above research fields in international journals and conferences.

Rupesh Pohane is currently an Assistant professor with the department of Applied Mathematics, Suryodaya College of Engineering and Technology, India from last 10 years. He has done his M.Sc. Mathematics and B.ed. from Nagpur University, India. His current research interest includes cryptography, network security, black holes and relativity.

Rupali R. Meshram is an Assistant Professor with the Department of Mathematics, Kamla Nehru Mahavidyalaya Nagpur, India from last 03 years. She has done his M.Sc. Mathematics from Nagpur University, India. Her current research interest includes cryptography, boundry value problems and relativity.

RGN

Research Article

Numerical Solution of 2nd Order Boundary Value Problems with Dirichlet, Neumann and Robin Boundary Conditions using FDM

M. Adak*[1] and A. Mandal[2]

[1] *Department of Applied Mathematics and Humanities, Yeshwantrao Chavan College of Engineering, Nagpur, India*
[2] *Department of Civil Engineering, Visvesvaraya National Institute of Technology, Nagpur, India*
*Corresponding author: malabikaadak@yahoo.co.in

Abstract. In many fields of science and engineering, to determine the harmonic motion, damped and forced variation, current from electric circuit, 2nd order ODE is required to solve. Solving the ODE with complicated boundary condition that occur in engineering problems is a great challenges analytically. Therefore, numerical technique *finite difference method* (FDM) is very popular and important for solving the boundary value problems. In this article three different conditions as Dirichlet, Neumann and Robin (mixed) boundary conditions are applied in initial-boundary problem. FDM is used to solve ODE boundary value problems. Error calculation, stability, convergence are also explained. To test the accuracy numerical solutions are verified with analytical solution and error is calculated at each point for different mesh grid size as mesh grid size is decreased result will give the accuracy.

Keywords. Finite difference scheme, Dirichlet condition, Convergence, Neumann condition, Mixed condition, Stability

Mathematics Subject Classification (2020). 65M06, 65N06

1. Introduction

In science and engineering several problems are occurred in mathematically analyzing ordinary differential equations which are satisfying particular condition. Only a selected class of differential equations can be solved analytically. These problem consists differential equation and complicated conditions which not to be solved in practically, in general on can get some

closed form solution, and hence can use numerical methods for solving such differential equations. Some researchers studied in this field like Balagurusamy [5], Hildebrand [6], Jain [7], Levy [9], Sastry [11,12], Scheid [13] developed the FDM for determining the initial-boundary values problems. Second order, third order BVM with ordinary differential equation for Dirichlet boundary condition is solved by Lakshmi [8], Muhammad [9], Siddiqi [14], and Xu [15]. Adak [1–4] studied finite difference methods to solve partial differential equation with convergence of numerical techniques.

From previous research it is cleared that the most of boundary value problems with Dirichlet boundary condition are investigated. Hence, the main focus of this article, well-posed (Dirichlet boundary condition) as well as ill-posed (Neumann and Robin boundary condition) problems has been determined.

2. Boundary Value Problems

A *boundary value problem* (BVP) consists an ODE or PDE and specific *boundary condition* (BC) in physically.

We begin by discussing various types of boundary conditions that can be imposed. A BVP which only has one independent variable is an ODE but we consider BVP in dimensions we need to use PDE.

Throughout this article, linear non-homogeneous second order ODE is considered defined by

$$u'' + r(x)u' + s(x)u = t(x), \quad a < x < b. \tag{2.1}$$

Corresponding to ODE (2.1), there are three important boundary conditions. They are given by

Dirichlet Boundary Condition. If the values of the function are specified on the boundary in a BVP, this type of constraint is called Dirichlet boundary condition.

For example, $u(a) = \alpha$, $u(b) = \beta$ in domain $[a,b]$, where α and β are constant.

Neumann Boundary Condition. If the derivatives of the unknown function are specified on the boundary in a BVP, this type of constraint is called Neumann boundary condition.

For example, $u'(a) = \alpha$, $u'(b) = \beta$ in domain $[a,b]$, where α and β are constant.

Robin Boundary Condition. If a weighted combination at the function value and its derivative at the boundary is called Robin boundary condition or mixed boundary condition.

For example, $u'(a) + cu(a) = \alpha$, $u'(b) + du(b) = \beta$, where c and d are constants.

3. Finite Difference Approximation

In process of finite difference method to solve a BVP, derivatives are replaced by finite difference approximation in ODE with in the specific conditions. After simplifying finite difference approximations with initial-boundary conditions we get linear system of equations. Solving this system of equations desired solution of BVP is obtained.

The interval $[a, b]$ is discretized in x axis into n number of equally spaced subintervals with h for solving problem given by (2.1), so that

$$x_i = x_0 + ih, \quad i = 1, 2, 3, \ldots,$$

where $x_0 = a$, $x_n = b$.

At these points the corresponding value of u are denoted by

$$u(x_i) = u_i = u(x_0 + ih), \quad i = 0, 1, 2, \ldots, n.$$

Using Taylor's expansion, values of $u'(x)$ and $u''(x)$ at point $x = x_i$ is given by

$$u_i' = \frac{u_{i+1} - u_{i-1}}{2h} + O(h^2),$$

$$u_i'' = \frac{u_{i-1} - 2u_i + u_{i+1}}{h^2} + O(h^2).$$

The *ordinary differential equation* (ODE) (2.1) at point $x = x_i$ is denoted by

$$u_i'' + r_i u_i' + s_i u_i = t_i.$$

Substituting the expressions for u_i' and u_i'', we obtain

$$\frac{u_{i-1} - 2u_i + u_{i+1}}{h^2} + r_i \frac{u_{i+1} - u_{i-1}}{2h} + s_i u_i = t_i, \quad i = 1, 2, \ldots, n,$$

where $u_i = u(x_i)$, $s_i = s(x_i)$.

Error Calculation. We first find the exact solution. Solve the given differential equation, that means, determine CF (Complementary Function) and PI (Particular Integral). Then different type of errors can be calculated by

$$\text{Absolute Error (AE)} = |\text{Exact solution} - \text{Numerical solution}|,$$

$$\text{Relative Error (RE)} = \frac{|\text{Exact solution} - \text{Numerical solution}|}{\text{Exact solution}},$$

$$\text{Percentage Error (PE)} = \frac{|\text{Exact solution} - \text{Numerical solution}|}{\text{Exact solution}} \times 100.$$

Stability of Numerical Method. If the difference value of the numerical result and the exact result tends to zero as number of iteration tends to infinity, then numerical method is said to be stable.

Convergence of Numerical Method. In iteration of numerical technique, if each successive iteration result is progressively closer to the exact result, it is known as *convergence*. A numerical method is not always given converging results. Convergence should be satisfied certain conditions. If these conditions are not satisfied, it is known as *divergence*.

Consistency of Numerical Method. If the finite difference representation converges to the differential equation to solve problem with mesh size tends to very small value, then a numerical scheme is called consistent.

We have explained the method with three types of boundary conditions. In several practical problems, derivative of boundary conditions may be specified, and this requires finite approximation in case of boundary condition which are described above. The following examples illustrate FDM to obtain the solution of BVP.

4. Test Problems and Verification

Problem 1 (Dirichlet Boundary Conditions). *Solve the heat transfer ODE boundary value problem for a rod of length 1 unit. The governing equation is defined by $u'' + u + 1 = 0$, $0 \leq x \leq 1$, with BC $u(0) = 0$ and $u(1) = 0$. Determine the value of $u(0.5)$ using finite difference method with sub-interval $h = 0.5$ and $h = 0.25$. Also, calculate error at each point using FDM.*

Solution. *Case* I: Consider $h = 0.5$.

Here interval is $0 \leq x \leq 1$, i.e., $[0,1]$. We discretize the interval into subintervals with mesh size $h = 0.5$.

So $x_0 = 0$, $x_1 = x_0 + h = 0.5 = \frac{1}{2}$, $x_2 = x_0 + 2h = 1$.

There are only three values of x, so we have three points.

Dirichlet's boundary conditions are given by $u(0) = 0$ and $u(1) = 0$.

That means, $u(0) = u(x_0) = u_0 = 0$ and $u(1) = u(x_2) = u_2 = 0$.

We have to find $u(0.5) = u_1$.

The given differential equation is approximated as

$$\frac{u_{i-1} - 2u_i + u_{i+1}}{h^2} + u_i + 1 = 0.$$

$\Rightarrow \quad u_{i-1} - (2 - h^2)u_i + u_{i+1} = -h^2, \quad i = 1, 2, \ldots, n-1 \qquad (4.1)$

Using boundary conditions $u_0 = 0$ and $u_n = u_2 = 0$. Since number of sub-interval $n = 2$ and unknown point is 1, then take $i = 1$.

Eq. (4.1) becomes $u_0 - \left(2 - \frac{1}{4}\right)u_1 + u_2 = -\frac{1}{4}$.

Using BCS (*boundary conditions*), $u_0 = 0$ and $u_2 = 0$

$$u_1 = u(0.5) = \frac{1}{7} = 0.142854.$$

Exact Solution. To find exact solution of the given differential equation

$\quad u'' + u + 1 = 0$.

$\Rightarrow \quad (D^2 + 1)u = -1$.

$\quad$ AE $m^2 + 1 = 0$ or $m = \pm i$

$\quad$ CF $u_c = C_1 \cos x + C_2 \sin x$

$\quad$ PI $= \dfrac{1}{D^2 + 1}(-1) = -1$

The general solution is

$\quad u(x) = C_1 \cos x + C_2 \sin x - 1$. $\qquad (4.2)$

Using BCS $u(0) = 0$ in eq. (4.2), we get

$\quad C_1 = 1$.

Using BCS $u(1) = 0$ in eq. (4.2), we get

$\quad C_2 = 0.5463$.

Therefore, the obtained exact solution is given by

$$u(x) = \cos x + (0.5463)\sin x - 1.$$

The value of y at $x = 0.5$ is

$$u(0.5) = 0.139493.$$

Error at $x = 0.5$ is $|0.139493 - 0.142854| = 0.003361$.

Case II: $h = 0.25$.

Here interval is $0 \le x \le 1$, i.e., $[0,1]$. We discretize the interval into subintervals with mesh size $h = 0.25$.

So $x_0 = 0$, $x_1 = x_0 + h = 0.25$, $x_2 = x_0 + 2h = 0.5$, $x_3 = x_0 + 3h = 0.75$, $x_4 = x_0 + 4h = 1$.

Using $h = 0.25$, eq. (4.1) becomes

$$u_{i-1} - \frac{31}{16}u_i + u_{i+1} = -\frac{1}{16}, \quad i = 1, 2, \ldots, n-1. \tag{4.3}$$

Put $i = 1, 2, 3$ (unknown points) in eq. (4.3), system of linear equations is

$$u_0 - \frac{31}{16}u_1 + u_2 = -\frac{1}{16},$$

$$u_1 - \frac{31}{16}u_2 + u_3 = -\frac{1}{16},$$

$$u_2 - \frac{31}{16}u_3 + u_4 = -\frac{1}{16},$$

where $u_0 = 0$ and $u_4 = 0$ (due to BCS).

The above equations become

$$-\frac{31}{16}u_1 + u_2 = -\frac{1}{16},$$

$$u_1 - \frac{31}{16}u_2 + u_3 = -\frac{1}{16},$$

$$u_2 - \frac{31}{16}u_3 = -\frac{1}{16}.$$

Solving system of equations, we get

$$u_1 = y(0.25) = 0.10476,$$

$$u_2 = y(0.5) = 0.14031,$$

$$u_3 = y(0.75) = 0.10476.$$

Using eq. **(??)**, exact solutions at each point are

$$u_1 = y(0.25) = 0.1041,$$

$$u_2 = y(0.5) = 0.1395,$$

$$u_3 = y(0.75) = 0.1041.$$

Errors are 0.0006, 0.0008, 0.0006 at $x = 0.25, 0.5, 0.75$.

Since the ratio of two errors in *Case* I and *Case* II is about 4, it follows that the order of convergence is h^2. These results show that the accuracy of numerical method depends upon

the mesh size h which is selected. As h is decreased, the accuracy increases but the number of equation to be increased for solving.

Problem 2 (Neumann Boundary Conditions). *Solve the ill-posed BVP defined by $u''(x) - (1 - x)u'(x) + xu(x) = x$, $u'(0) = 0$ and $u(1) = 0$, using finite difference method with mesh size $h = \frac{1}{3}$.*

Solution. Here interval is $0 \le x \le 1$, i.e., $[0, 1]$.
Points are given by $x_0 = 0$, $x_1 = x_0 + h = \frac{1}{3}$, $x_2 = x_0 + 2h = \frac{2}{3}$, $x_3 = x_0 + 3h = \frac{3}{3} = 1$.
Therefore, $h = \frac{1}{3}$.
To solve the equation $u_i'' + (1 - x_i)u_i' + x_i u_i = x_i$ use finite difference approximation

$$\frac{u_{i-1} - 2u_i + u_{i+1}}{h^2} + (1 - x_i)\frac{u_{i+1} - u_{i-1}}{2h} + x_i u_i = x_i$$

$$\Rightarrow \quad (2 - h + x_i h)u_{i-1} - (4 - 2h^2 x_i)u_i + (2 + 1 - x_i h)u_{i+1} = x_i h^2$$

$$\Rightarrow \quad \left(\frac{5}{3} + \frac{x_i}{3}\right)u_{i-1} - \left(4 - \frac{2}{9}x_i\right)u_i + \left(3 - \frac{x_i}{3}\right)u_{i+1} = \frac{x_i}{9} \tag{4.4}$$

Given boundary conditions are

$$u'(0) = 0$$

$$\Rightarrow \quad u_0' = 0$$

$$\Rightarrow \quad \frac{u_1 - u_{-1}}{2h} = 0$$

$$\Rightarrow \quad u_1 = u_{-1}$$

$$u(1) = 0$$

$$\Rightarrow \quad u_3 = 0$$

Putting $i = 0, 1, 2$ (unknown points) in eq. (4.4), we get

$$\frac{5}{3}u_{-1} - 4u_0 + 3u_1 = 0$$

$$6u_0 - 7u_1 = 0 \quad \text{(because } u_1 = u_{-1}\text{)}$$

$$16u_0 - \frac{106}{3}u_1 + 26u_2 = \frac{1}{3}$$

$$17u_1 - \frac{104}{3}u_2 = \frac{2}{3}$$

Solving above three equations, we get the numerical approximations

$$u_0 = -8.342, \ u_1 = -7.15u_2 = -3.986.$$

Problem 3 (Robin Boundary Conditions). *Determine the temperature distribution from mixed BVP defined by $u''(x) - xu(x) = 0$, $0 \le x \le 1$, for $u(x_i)$, $x_i = 0$, $\frac{1}{3}$, $\frac{2}{3}$, with BC $u(0) + u'(0) = 1$ and $u(1) = 1$, using finite difference method.*

Solution. Here interval is $0 \le x \le 1$, i.e., $[0, 1]$.
Points are given by $x_0 = 0$, $x_1 = x_0 + h = \frac{1}{3}$, $x_2 = x_0 + 2h = \frac{2}{3}$, $x_3 = x_0 + 3h = \frac{3}{3} = 1$.
Therefore, $h = \frac{1}{3}$.

Mixed boundary conditions are given by $u(0) + u'(0) = 1$ and $y(1) = 1$.

That means, $u(0) + u'(0) = u(x_0) + u'(x_0) = 1$ and $u(1) = u(x_3) = u_3 = 1$.

We have to find u_0, u_1, u_2.

The given differential equation is approximated as

$$\frac{u_{i-1} - 2u_i + u_{i+1}}{h^2} = x_i u_i,$$

$$u_{i-1} - (2 + h^2 x_i) u_i + u_{i+1} = 0, \quad i = 0, 1, 2. \tag{4.5}$$

Putting $i = 0, 1, 2$ (unknown points) in eq. (4.5), we get

$$u_{-1} - 2u_0 + u_1 = 0, \quad \text{(because } x_0 = 0\text{)}$$

$$u_0 - \frac{55}{27} u_1 + u_2 = 0, \quad \left(\text{because } x_1 = \frac{1}{3} \right) \tag{4.6}$$

$$u_1 - \frac{56}{27} u_2 + u_3 = 0. \quad \left(\text{because } x_2 = \frac{2}{3} \right)$$

The first boundary condition is

$$u(0) + u'(0) = 1$$

$$\Rightarrow \quad u_0 + u'_0 = 1$$

$$\Rightarrow \quad u_0 + \frac{u_1 - u_{-1}}{2h} = 1 \quad \text{(use centre difference approximation)}$$

$$\Rightarrow \quad 2u_0 + 3(u_1 - u_{-1}) = 1$$

$$\Rightarrow \quad u_{-1} = \frac{2u_0 + 3u_1 - 2}{3}$$

The second boundary condition is

$$u(1) = u_3 = 1.$$

Using BCS, eqs. (4.6) become the system of linear equations given by

$$-2u_0 + 3u_1 = 1,$$

$$u_0 - \frac{52}{27} u_1 + u_2 = 0,$$

$$u_1 - \frac{55}{27} u_2 = -1.$$

Solving the above equations, we get the numerical approximations

$$u_0 = u(0) = \frac{13}{55} = 0.23636,$$

$$u_1 = u(1/3) = \frac{27}{55} = 0.49091,$$

$$u_2 = u(2/3) = \frac{39}{55} = 0.70909.$$

5. Conclusion

This study focused in various boundary conditions to obtain solutions of 2nd order initial-boundary value problem with ODE. Finite difference method is used for predicting harmonic motion, damped and forced variation, current from electric circuit. In this study, three problems

are consider in various boundary conditions. The numerical results are examined with analytical results with Dirichlet condition for checking accuracy of numerical method. From the results it is cleared that the numerical results are very closer with exact results. Results also show that if the mesh size is reduced finite difference method will give the better accuracy. Hence, this technique can be successfully applied in more complicated domain in future work.

Competing Interests

The authors declare that they have no competing interests.

Authors' Contributions

All the authors contributed significantly in writing this article. The authors read and approved the final manuscript.

References

[1] M. Adak and N.R. Mandal, Numerical and experimental study of mitigation of welding distortion, *Applied Mathematical Modelling* **34**(1) (2010), 146 – 158, DOI: 10.1016/j.apm.2009.03.035.

[2] M. Adak and C.G. Soares, Effects of different restraints on the weld-induced residual deformations and stresses in a steel plate, *The International Journal of Advanced Manufacturing Technology* **71** (2014), 699 – 710, DOI: 10.1007/s00170-013-5521-9.

[3] M. Adak and C.G. Soares, Residual deflections and stresses in a thick *T* joint plate structure, *Journal of Applied Mechanical Engineering* **5**(6) (2016), Article ID 1000233, 7 pages, URL: https://www.walshmedicalmedia.com/open-access/residual-deflections-and-stresses-in-a-thick-tjoint-plate-structure-2168-9873-1000233.pdf.

[4] M. Adak, Comparison of explicit and implicit finite difference schemes on diffusion equation, in: *ICACM2018: Mathematical Modeling and Computational Tools*, Springer Proceedings in Mathematics & Statistics, Vol. 320, 227 – 238, Springer, Singapore (2020), DOI: 10.1007/978-981-15-3615-1_15.

[5] E. Balagurusamy, *Numerical Methods*, McGraw Hill, New Delhi (1999).

[6] F.B. Hildebrand, *Introduction of Numerical Analysis*, McGraw Hill, New York (1956).

[7] M.K. Jain, S.R. Iyengar and R.K. Jain, *Numerical Methods for Scientific and Engineering Computation*, Wiley Eastern Limited, New Delhi (1985).

[8] R. Lakshmi and M. Muthuselvi, Numerical solution for boundary value problem using finite difference method, *International Journal of Innovative Research in Science, Engineering and Technology* **2**(10) (2013), 5305 – 5313.

[9] H. Levy and E.A. Baggott, *Numerical Solution of Differential Equations*, Dover, New York (1950).

[10] A.N. Muhammad, E. Al-Said and I.N. Khalida, Finite difference method for solving a system of third order boundary value problems, *Journal of Applied Mathematics* **2012** (2012), Article ID 351764, 10 pages, DOI: 10.1155/2012/351764.

[11] S.S. Sastry, *Engineering Mathematics*, 3rd edition, Vols. 1 and 2, Prentice-Hall of India, New Delhi (2004).

[12] S.S. Sastry, *Introductory Methods of Numerical Analysis*, 5th edition, PHI, New Delhi (2012).

[13] F. Scheid, *Theory and Problems of Numerical Analysis*, Schaum Series, McGraw Hill, New York (1968).

[14] S.S. Siddiqi and M. Iftikhar, Numerical solution of higher order boundary value problems, *Abstract and Applied Analysis* **2013** (2013), Article ID 427521, 12 pages, DOI: 10.1155/2013/427521.

[15] X. Xu and E. Zhou, Numerical solutions for the eighth-order initial and boundary value problems using the second kind Chebyshev wavelets, *Advances in Mathematical Physics* **2015** (2015), Article ID 964623, 9 pages, DOI: 10.1155/2015/964623.
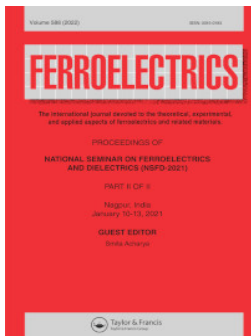
Dielectric relaxation study of aqueous glycol ethers with water using time domain reflectometry technique in the frequency range 10 MHz to 50 GHz

Zamir S. Khan, Arsala Khan, M. P. Lokhande, Avadhut Deshmukh & A. C. Kumbharkhane

Published online: 03 May 2022.

Submit your article to this journal ⎘

View related articles ⎘

View Crossmark data ⎘

Taylor & Francis
Taylor & Francis Group

Check for updates

Dielectric relaxation study of aqueous glycol ethers with water using time domain reflectometry technique in the frequency range 10 MHz to 50 GHz

Zamir S. Khan[a], Arsala Khan[b], M. P. Lokhande[c], Avadhut Deshmukh[d], and A. C. Kumbharkhane[d]

[a]Department of Physics, Anjuman College of Engineering and Technology, Nagpur, India; [b]Department of Physics, Yeshwantrao Chavan College of Engineering (YCCE), Nagpur, India; [c]Department of Physics & Electronics, GVISH, Amravati, India; [d]School of Physical Sciences, Swami Ramanand Teerth Marathwada University, Nanded, Maharashtra, India

ABSTRACT

The Complex permittivity spectra of glycol ether (GE) compounds such as ethylene glycol mono-methyl ether (EGME), ethylene glycol ethyl ether (EGEE) and ethylene glycol butyl ether (EGBE) with water mixture over entire concentration range and at 25 °C has been determined using Time Domain Reflectometry technique in the frequency range 10 MHz to 50 GHz. The complex permittivity spectra for GE–water were fitted in Cole–Davidson model. The Static dielectric constant (ε_0), Relaxation time (τ), effective Kirkwood correlation factor (g^{eff}), excess permittivity (ε_0^E) and Bruggeman factor (f_B) have been calculated by non-linear least square fit method. The intermolecular interactions between GE-water binary mixtures suggest the non-linear behavior of dielectric parameters. The contribution of hydrogen bonding interactions among the solute-solvent mixtures is confirmed by Excess properties and Bruggeman factor.

1. Introduction

Molecular interactions in the liquid and nature of rotational dynamic were provided by Dielectric Relaxation Spectroscopy (DRS) [1]. Glycol ethers (GE) is very interesting class of solvent having ether, that is, oxygen (–O–) and hydroxyl (–OH–) group. The hydroxyl group can act as proton donor as well as acceptor. Aqueous solutions of GE have a wide range of chemical, biological, pharmaceutical, industrial and condensed matter physics applications because GE and water molecules have the H-bond sites and they can enter into intra and intermolecular hydrogen bonding giving rise to different conformations [2–5]. Literature survey indicates that the glycol ethers has been studied in pure form and non-polar solvents such as dioxane, benzene and carbon tetrachloride but dielectric relaxation behavior of these systems in aqueous solution is scarce [6–8]. The molecules of these compounds have several hydrogen bonding sites which may leads to different conformations through intra and intermolecular interactions. The local structures of hydrogen bonding liquids are complicated due to molecular clusters and

network structures through the hydrogen bond. Ethylene glycol mono-methyl ether (EGME) with structural formula $CH_3OCH_2CH_2OH$ or 2-Methoxyethanol, or methyl cellosolve is used mainly as a solvent. It is a comprehensible, monotonous liquid with an ether-like smell.

It is in a group of solvents identified as glycol ethers which are prominent for their talent to liquefy a range of special types of substance compounds and for their miscibility with water and other solvents. It can be formed by the nucleophilic attack of methanol on protonated oxirine followed by proton transfer. Ethylene glycol mono-ethyl ether (EGEE) has structural formula $CH_3CH_2OCH_2CH_2OH$ or 2-Ethoxyethanol, it is also known Cellosolve or ethyl cello solve, is a solvent used widely in commercial and industrial applications. It is a comprehensible, monotonous, nearly fragrance-free liquid that is miscible with water, ethanol, diethyl ether, acetone and ethyl acetate. Ethylene glycol mono- butyl ether (EGBE) with structural formula $CH_3 (CH_2)_2CH_2OCH_2CH_2OH$ or 2-Butoxyethanol is an organic compound. As a comparatively nonvolatile, low-priced solvent of squat toxicity, it is worn in several conjugal and manufacturing products as of its properties as a surfactant.

The hydroxyl group is a functional group of alcohols whereas oxy-group is functional group of ethers. So the ether alcohols having general formula are R–O–R–OH. The homologous series of mono-alkyl ethers of ethylene glycol has general formula $C_nH_{2n+2}O_2$, where $n = 1, 2, 3$, and so on. Dielectric studies have been carried out extensively on alcohols and its water mixtures to understand strong intra and intermolecular interactions through hydrogen bond, which play an important role in biochemistry, results in a peculiar dynamical property. The hydrophilic/hydrophobic balances in glycol ethers make the dielectric relaxation study interesting. Recently dielectric relaxation study of polymers and binary mixtures of 2-methoxyethanol-water have been successfully carried out in our laboratory [9–12].

In the present study the complex permittivity spectra of Ethylene glycol mono-methyl ether (EGME), Ethylene glycol mono-ethyl ether (EGEE) and Ethylene glycol mono-butyl ether (EGBE) with water have been measured at 25 °C. The dielectric parameters such as static dielectric constant, relaxation time have been calculated. The dielectric behavior of these associating liquid have been discussed in terms of Bruggeman factor, Kirkwood correlation factor and excess properties.

2. Experimental

2.1. Materials

EGME, EGEE, and EGBE were obtained commercially (Merck, India) and were used without further purification. The water used in the preparations of mixtures was obtained by double distillation procedure. The binary mixture of GE and Water were prepared at different concentrations by volume fraction.

2.2. Measurement

The dielectric spectra were obtained by the time domain reflectometry (TDR) technique. The Tektronix Digital Serial Analyzer model number DSA8300 sampling mainframe
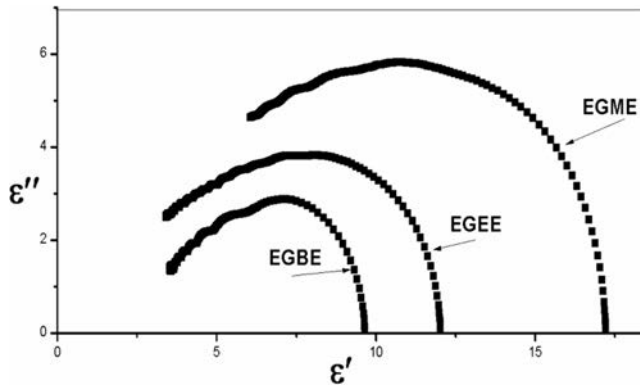
Figure 1. Cole–Cole plot for GE at 25 °C.

along with the sampling module 80E10B has been used. A repetitive fast pulse with 12 ps incident rise time was fed through coaxial cable having impedance 50 Ω. Sampling oscilloscope monitors change in step pulse after reflection from the end of line. Reflected pulse without sample R_1 (t) and with sample R_x (t) were recorded in time window of 5 ns and digitized in 2000 points. The Fourier transformation of the pulses and data analysis were done to determine complex permittivity spectra $\varepsilon^*(\omega)$ using nonlinear least square fit method [13, 14].

3. Results and discussion

Asymmetric shape of the loss peak was observed for the alcohol and its water mixtures, and the dielectric spectrum was described well by the Havriliak-Negami (HN) equation.

The HN equation gives the complex permittivity as [15].

$$\varepsilon^*(\omega) = \varepsilon_\infty + \frac{\varepsilon_0 - \varepsilon_\infty}{[1 + (j\omega\tau)^{1-\alpha}]^\beta} \tag{1}$$

where ε_0 is the static dielectric constant, ε_∞ is the permittivity at high frequency, τ is relaxation time. α and β are the symmetric and asymmetric distribution of relaxation times, respectively. The model can be fitted in three ways: (i) If $\alpha = 0$ and $\beta = 1$ then single Debye relaxation, (ii) $0 \leq \alpha \leq 1$ then it would be a Cole–Cole model of symmetric distribution of relaxation times and iii) $\alpha = 0$ and β varied such that $0 \leq \beta \leq 1$, this behavior is identified as Cole–Davidson (CD) asymmetric distribution of relaxation times.

The dielectric loss spectrum of pure water in this frequency range is usually described by a single Debye relaxation [12, 16].The Cole–Cole plot is shown in Fig. 1 (ε'' vs. ε') for pure GE at 25 °C. From Fig. 1 it is observed that the Cole–Cole Plots for the pure glycol ethers at 25 °C exhibit the skewed arc curve and the value of ε'' max is less than $(\varepsilon_0-\varepsilon_\infty)/2$ which indicate that the dielectric behavior deviate from the single Debye relaxation. This deviation is usually explained by assuming there is not just one relaxation time but a continuous distribution.

The complex permittivity spectra $\varepsilon^*(\omega)$ of the glycol ethers–water mixtures have been fitted in CD model using least squares fit method to determine the dielectric relaxation
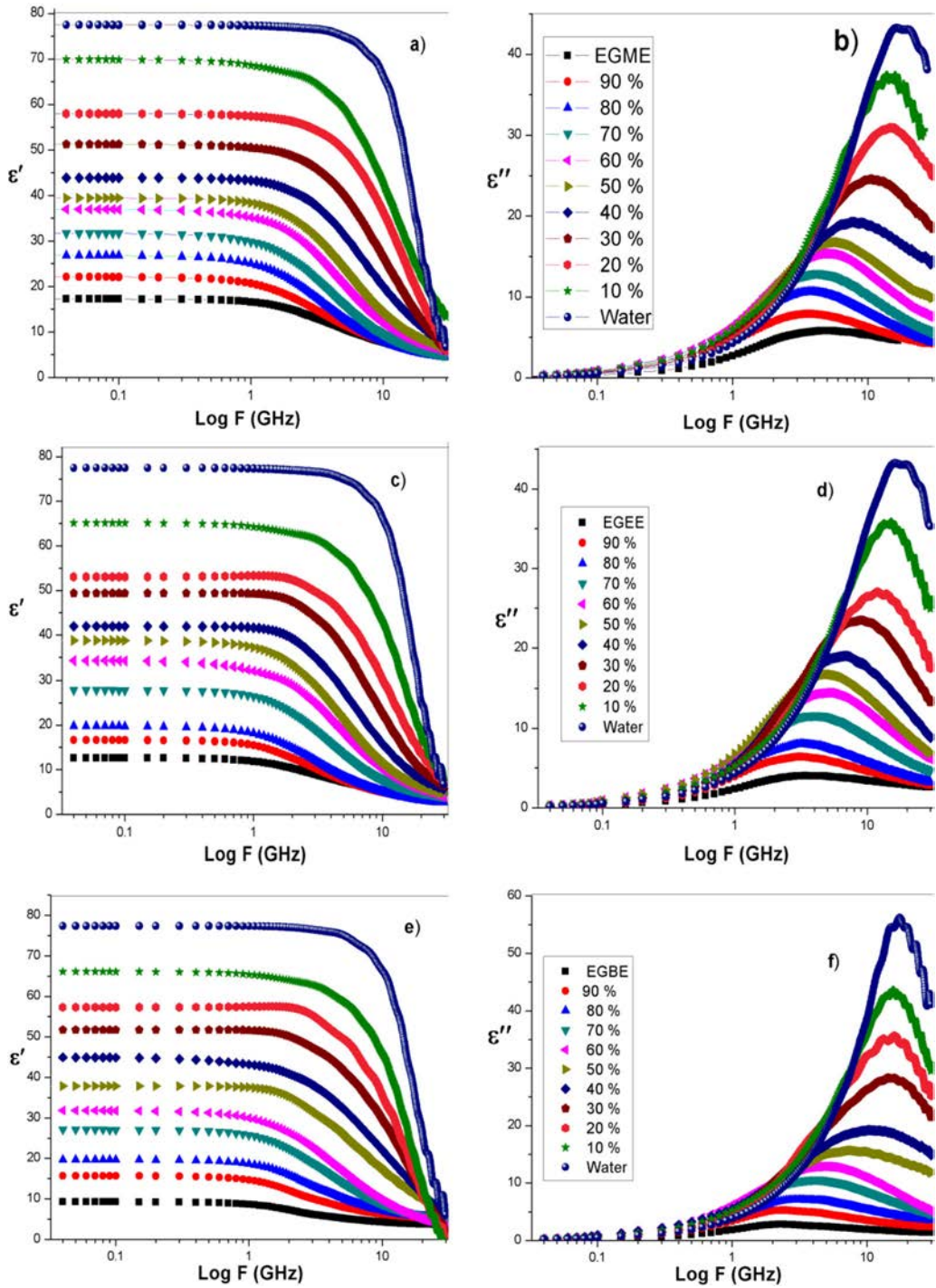
Figure 2. (a), (b), and (c) are the dielectric permittivity whereas (d), (e), and (f) are dielectric loss spectra for EGME, EGEE, and EGBE, respectively.

Table 1. Dielectric relaxation parameters for glycol ethers-water mixtures at 25 °C.

| V_w | EGME-Water | | |
	ε_0	τ(ps)	β
0.00	18.07 (1)	25.03 (18)	0.754 (2)
0.10	23.12 (8)	35.24 (32)	0.774 (4)
0.20	27.63 (6)	38.08 (18)	0.854 (1)
0.30	32.70 (7)	34.75 (16)	0.866 (1)
0.40	38.14 (8)	30.21 (14)	0.871(2)
0.50	41.04 (11)	24.47 (14)	0.850 (2)
0.60	44.84 (15)	18.15 (11)	0.925 (2)
0.70	50.99 (17)	15.37 (8)	1.000 (2)
0.80	56.79 (19)	13.05 (9)	1.000 (1)
0.90	66.01 (13)	11.36 (7)	0.927(2)
1.00	78.49 (69)	9.72 (17)	1.000 (1)
	EGEE-Water		
0.00	13.36 (4)	30.71(33)	0.704 (3)
0.10	17.48 (5)	42.88(33)	0.810 (2)
0.20	22.47 (5)	43.48(5)	0.850 (2)
0.30	28.74 (6)	38.97(7)	0.880 (1)
0.40	34.72 (3)	32.7(3)	0.913(8)
0.50	39.61 (4)	27.07(6)	0.918 (9)
0.60	43.12 (5)	22.44(5)	0.940 (1)
0.70	50.41 (5)	18.03(5)	0.956 (1)
0.80	53.46(10)	14.05(3)	1.020 (1)
0.90	63.18(12)	11.87(13)	1.090(1)
1.00	78.49(13)	9.72 (17)	1.000 (1)
	EGBE-Water		
0.00	9.91 (5)	40.35 (59)	0.686 (5)
0.10	17.02 (10)	47.02 (99)	0.706 (6)
0.20	21.04 (10)	51.06 (52)	0.761 (4)
0.30	28.17 (6)	46.76 (18)	0.844 (2)
0.40	31.98 (2)	39.41 (15)	0.914 (7)
			Cont.
0.50	39.01 (15)	32.44 (13)	0.945 (3)
0.60	44.01 (17)	26.14 (10)	0.959 (3)
0.70	49.93 (29)	21.15 (10)	1.112 (5)
0.80	55.64 (31)	17.41 (8)	1.170 (4)
0.90	61.78 (5)	14.39 (30)	1.230 (4)
1.00	78.5 (13)	9.72 (17)	1.000 (1)

Note: Numbers in bracket denotes uncertainties in the last significant digits obtained by the least square fit method. For example, 18.07(1) means 18.07 ± 0.01.

parameters. The dielectric permittivity spectra have been shown in Fig. 2(a–c) and dielectric loss spectra in Fig. 2(d–f) for EGME, EGEE, and EGBE, respectively, at 25 °C.

The corrected data have been fitted with the Havriliak–Negami (HN) equation. The values of the dielectric parameters at 25 °C are reported in Table 1.

3.1. Static dielectric constant (ε_0)

The values of dielectric constant at 25 °C for glycol ethers–water mixtures are plotted against volume fraction of water (V_W) shown in Fig. 3. The static dielectric constant increases for GE for addition of water. The values of dipole moment in gas phase for EGME, EGEE and EGBE are very similar but the static dielectric constants are in decreasing order such that EGME > EGEE > EGBE, as the chain length increases from EGME to EGBE the dielectric constant goes on decreasing.
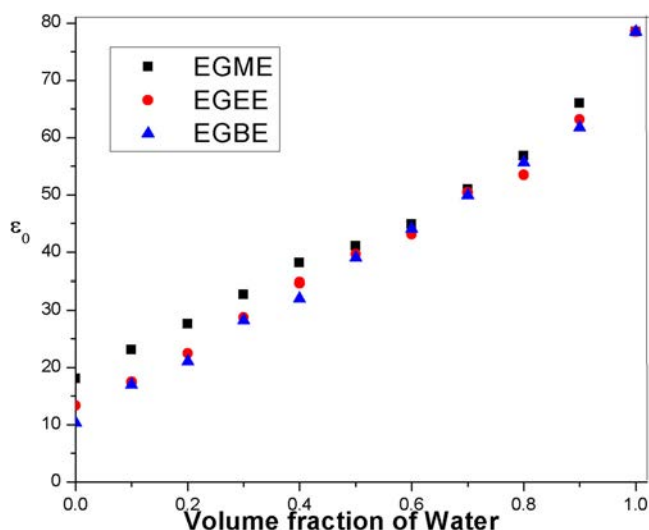
Figure 3. Static dielectric constant (ε_0) versus volume fraction of water (V_w) for glycol ethers-water mixtures.

In the present manuscript, we demonstrate huge manipulation of a hydroxyl group (–OH) on the Static dielectric constant (ε_0) value of a molecule. The value of ε_0 decreases with the increase in the number of carbon atoms in the chain of the molecule [17]. Water molecule does not have any carbon atom but EGME, EGEE, and EGBE molecule have carbon atoms. Therefore, the ε_0 value of EGME, EGEE, and EGBE should be very low as compared to water. It is observed that on the addition of glycol ether (GE) in water, the static dielectric constant increases and also increases with a decrease in temperature.

3.2. Dielectric relaxation time (τ)

The relaxation time is a function of molecular size and relaxation time τ increases from EGME to EGBE which are reported in Table 1. The values of relaxation time at 25 °C for glycol ethers–water mixtures are plotted against volume fraction of water (V_W) shown in Fig. 4. The relaxation time decreases for GE for addition of water. Fig. 4, relaxation time increases with an increase in volume fraction of water in GE and attains a maximum value at $V_W = 0.2$ of GE-water mixtures. Then with a further increase in the volume fraction of water in a binary mixture, there is a gradual decrease in relaxation time and reaches a minimum value. The variation of relaxation time provides information regarding the hydrophilic character of the solute particle. The molecular relaxation time is dependent on the chain length of the molecule, viscosity and temperature.

3.3. Kirkwood correlation factor

The information regarding the orientation of dipoles in polar liquids is given by Kirkwood correlation factor [11, 18]. For pure liquids, the value of Kirkwood factor is obtained by using Kirkwood–Froehlich equation:
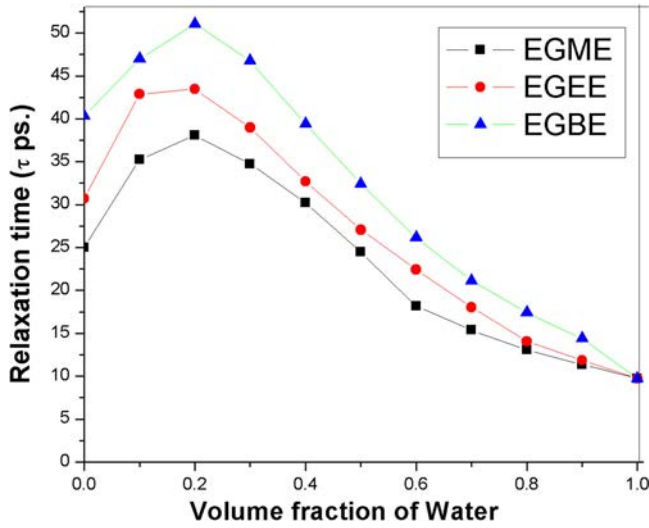
Figure 4. Relaxation time τ (ps.) versus volume fraction of water (V_W) for glycol ethers -water mixtures.
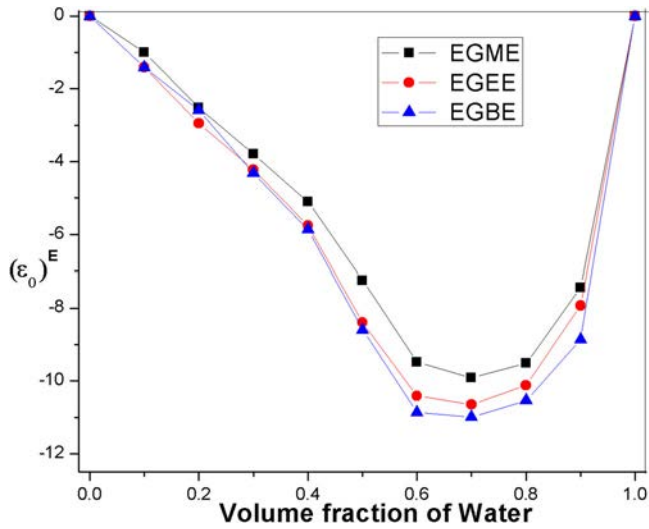
Figure 5. Excess permittivity $(\varepsilon_0)^E$ versus volume fraction of water (V_W) for glycol ethers -water mixtures.

$$g\mu^2 \frac{4\pi N\rho}{9kTM} = \frac{(\varepsilon_0 - \varepsilon_\infty)(2\varepsilon_0 + \varepsilon_\infty)}{\varepsilon_0(\varepsilon_\infty + 2)^2} \qquad (2)$$

where, g is the Kirkwood correlation factor, μ is the dipole moment of the liquid, N is the Avogadro's Number, ρ is the density of the liquid, ε_0 is the static dielectric constant, ε_∞ is the permittivity at high frequency, k is the Boltzmann constant, M is the molecular weight and T is the temperature. For the binary mixture, the effective correlation factor (g^{eff}) gives information of dipole–dipole correlation in associating binary mixture of polar liquids by the modified effective Kirkwood equation [19–21].

Table 2. Kirkwood correlation factor (g^{eff}) for glycol ether-water mixture at 25 °C.

V_w	EGME	EGEE	EGBE
0.0	1.64 (6)	1.45 (6)	1.36 (6)
0.1	1.80 (5)	1.48 (4)	1.41 (5)
0.2	1.88 (4)	1.56 (4)	1.50 (4)
0.3	1.98 (4)	1.84 (4)	1.79 (4)
0.4	2.05 (4)	1.98 (4)	1.92 (4)
0.5	2.09 (4)	2.05 (4)	2.01 (4)
0.6	2.17 (4)	2.10 (4)	2.11 (4)
0.7	2.25 (4)	2.20 (4)	2.18 (4)
0.8	2.42 (5)	2.35 (4)	2.30 (4)
0.9	2.50 (5)	2.40 (5)	2.37 (5)
1.0	2.82 (6)	2.82 (6)	2.82 (6)

$$\frac{4\pi N}{9kT}\left[\frac{\mu_w^2 \rho_w V_w}{M_w} + \frac{\mu_A^2 \rho_A \ (1-V_w)}{M_A}\right] \times g^{eff} = \frac{(\varepsilon_{0m} - \varepsilon_{\infty m})(2\varepsilon_{0m} + \varepsilon_{\infty m})}{\varepsilon_{0m}(\varepsilon_{\infty m}+2)^2} \tag{3}$$

where, g^{eff} is the effective Kirkwood correlation factor, μ_w is the dipole moment of water, μ_A is the dipole moment of GE, ρ_w, and ρ_A are the densities of the water and GE, respectively. V_w is the volume fraction of Water. The values of Kirkwood correlation factor for entire binary mixtures of glycol ethers–water are reported in Table 2. The g^{eff} values glycol ethers increases for addition of small amount of water. This value gives significance of association in the mixtures and orientation of dipoles in the liquids. The g^{eff} values for pure liquids, that is, for water, EGME, EGEE, and EGBE are 2.82, 1.64, 1.45, and 1.36, respectively. The significance of association effects according to decreasing order is as follows EGME > EGEE > EGBE. The g^{eff} values for water and glycol ethers are greater than unity, which suggest that the molecular dipoles have parallel orientation among themselves. Also water has higher correlation factor as compared to glycol ether indicates the strong intermolecular interaction in water molecules through hydrogen bonding whereas the g^{eff} for glycol ethers in pure form are such that, EGME > EGEE > EGBE.

3.4. Excess dielectric properties

The contribution of hydrogen bonds to the dielectric properties of the mixture is also studied in terms of the excess static dielectric permittivity. The excess permittivity (ε_0^E) can be written as [11, 22]

$$(\varepsilon_0)^E = \ (\varepsilon_0)_M - [(\varepsilon_0)_w V_w + \ (\varepsilon_0)_{GE}(1-V_W)] \tag{4}$$

The excess static dielectric constant $(\varepsilon_0)^E$ provides qualitative information about multimer formation in the mixture given as follows.

    i. The excess static dielectric constant $(\varepsilon_0)^E$ is equal to zero means there is no interaction between solute–solvent mixtures.

    ii. The values $(\varepsilon_0)^E <0$, means there is interaction between constituents of solute-solvent such that there is less contribution in the total number of effective dipoles in the mixture and $(\varepsilon_0)^E$ values get reduced.
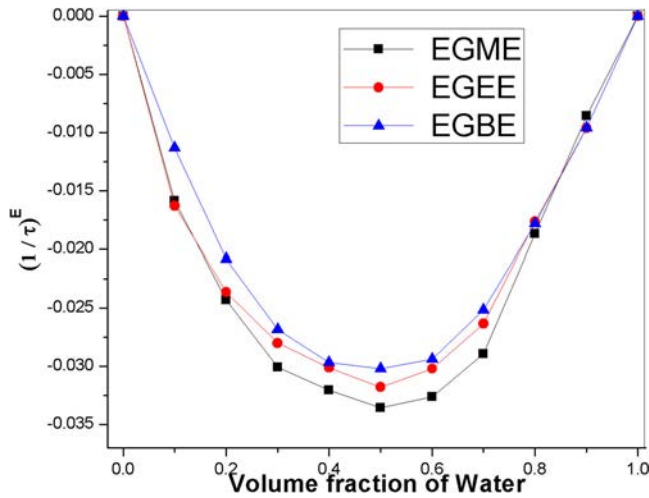
Figure 6. Excess inverse dielectric relaxation $(1/\tau)^E$ versus volume fraction of water for glycol ethers -water mixtures.

iii. When $(\varepsilon_0)^E > 0$, means there is interaction between solute-solvent mixtures such that there is increase in the number of effective dipoles contributed in the mixture and $(\varepsilon_0)^E$ values get increased.

where, the subscripts M and W represent mixture and water, respectively, and V_W represents the volume fraction of water in solute. The plot of excess permittivity Vs. the volume fraction of water (V_W) is shown in Fig. 5. The plot exhibits a pronounced minimum and it remains negative for the whole concentration range. These negative $(\varepsilon_0)^E$ values for GE–water mixtures show the experimental evidence of a molecular interaction among the unlike species through hydrogen bonding so that the total number of effective dipoles gets reduced. The magnitude of minima or maxima increases with the addition of the CH_2 group in the glycol ether molecule. It is attributed as the extensive volume contraction takes place due to strong solute-solvent interactions [23]. The pronounced minima of $(\varepsilon_0)^E$ value for EGME & EGEE are found approximately at $V_W \approx 0.6$ and for EGBE at $V_W \approx 0.8$ which gives the stable adduct formation as water: EGME & EGEE in the mole ratio of 1:2.3 and for water: EGBE in the mole ratio of 1:4. From Fig. 5 the minimum in ε_0^E values for EGBE > EGEE > EGME indicates as increase in chain length, the hetero-molecular H-bond interaction reduces the number of effective dipoles

3.5. Excess inverse relaxation time

The excess inverse relaxation property is useful for perception of cooperative domain in the mixture and may give affirmation for formation of multimers in the mixture due to intermolecular interaction. The excess inverse relaxation time is defined as [24, 25]

$$(1/\tau)^E = (1/\tau) - [(1/\tau)_w \ V_w + \ (1/\tau)_{EGME} \ (1 - V_w)] \tag{5}$$
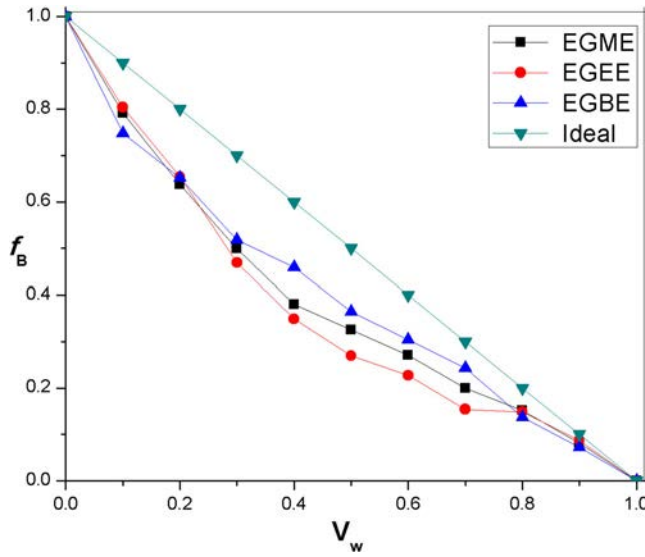
Figure 7. Bruggeman factor (f_B) versus volume fraction of water (V_W) at 25 °C.

where, $(1/\tau)^E$ is the excess inverse relaxation time which corresponds to broadening of dielectric spectral lines, the subscript w denotes the water, and V_w represents mole fraction of water in GE.

The information regarding dipolar rotational time from excess inverse relaxation time $(1/\tau)^E$ is as follows [13]

  i. $(1/\tau)^E = 0$ indicates that there is no interaction between the constituents of mixture, so their dipolar rotational time do not change.
 ii. $(1/\tau)^E > 0$ indicates that relaxation time effectively get reduced due to solute-solvent interaction resulting in faster rotational motion, that is, the field co-operates in the rotation of dipoles.
iii. $(1/\tau)^E < 0$ indicates that relaxation time effectively gets enhanced resulting in slower rotational field.

In this study, the values of excess inverse relaxation time $(1/\tau)^E$ are found to be negative for all concentration shown in Fig. 6, which indicates that the rotation of dipoles is slow due to solute-solvent interaction formed by the hydrogen bonded structures which produces a field in such a way that the effective dipole rotation is hindered. From the Fig. 6 the value of Excess inverse dielectric relaxation $(1/\tau)^E$ are EGME > EGEE > EGBE.

3.6. Bruggeman factor

The static permittivity of binary mixtures can be obtained by using the Bruggeman mixture formula [26].

$$f_B = \left(\frac{\varepsilon_{0m} - \varepsilon_{wat}}{\varepsilon_{oA} - \varepsilon_{wat}}\right)\left(\frac{\varepsilon_{oA}}{\varepsilon_{om}}\right)^{1/3} = 1 - V_w \tag{6}$$

where, ε_{0m}, ε_{0A}, and ε_{0wat} are the static dielectric constant of a mixture, solute (GE) and water respectively and V_w is the volume fraction of water in GE. Bruggeman showed the linear relationship between the Bruggeman factor (f_B) and volume fraction of water but the experimental values behaves non-linearly which is show in Fig. 7. The nonlinear relationship of the experimental values is explained by the modified Bruggeman expression which is given as [27]:

$$f_B = \left(\frac{\varepsilon_{0m} - \varepsilon_{0wat}}{\varepsilon_{0A} - \varepsilon_{0wat}}\right)\left(\frac{\varepsilon_{0A}}{\varepsilon_{0m}}\right)^{1/3} = 1 - [a - (a - 1)V_w]V_w \qquad (7)$$

where, "a" is the arbitrary parameter whose value is 1 which means the mixture is ideal that is there is no interaction between the solute and solvent. The calculated value of "a" for EGME, EGEE and EGBE–water mixture is determined using least square fit method and it is found to be 2.04, 1.83, and 1.70, respectively, at 25 °C. The larger value of "a" suggests that effective volume fraction of solute in water reduced very much.

4. Conclusion

The temperature dependent complex permittivity spectra of glycol ethers (GE) water mixture have been studied using Time Domain Reflectometry technique in the frequency range 10 MHz to 50 GHz. The dielectric permittivity spectra of GE-water are described by Cole-Davidson model. The negative values of Excess permittivity $(\varepsilon_0)^E$ for EGBE > EGEE > EGME indicates as increase in chain length GE-water mixture and shows an experimental confirmation of certain interaction among the unlike molecules through bonding. The value of effective Kirkwood correlation factor is EGME > EGEE > EGBE and greater than one which confirms the parallel alignment of molecules. The modified Bruggeman equation confirms the interaction between the constituents of mixture.

Acknowledgment

References

[1]   J. P. Martínez Jiménez et al., Dielectric behaviour and molecular polarization process in some polar- non polar mixtures: Alcohol + n-alkane, J. Mol. Liq. **139** (1-3), 48 (2008). DOI: 10.1016/j.molliq.2007.10.011.

[2]   S. S. Dhondge, C. P. Pandhurnekar, and D. V. Parwate, Density, speed of sound, and refractive index of aqueous binary mixtures of some glycol ethers at T) 298.15 K, J. Chem. Eng. Data **55** (9), 3962 (2010). DOI: 10.1021/je901072c.

[3]   S. S. Dhondge et al., Volumetric and viscometric study of aqueous binary mixtures of some glycol ethers at T = (275.15 and 283.15) K, J. Chem. Thermodynamics **43** (12), 1961 (2011). DOI: 10.1016/j.jct.2011.07.008.

[4]   L. I. Xinxue et al., Density, viscosity, and excess properties for binary mixture of diethylene glycol monoethyl ether + water from 293.15 to 333.15 K at atmospheric pressure, Chin. J. Chem. Eng. **17** (6), 1009 (2009). DOI: 10.1016/S1004-9541(08)60309-2.

[5]   H.-C. Ku, and C.-H. Tu, Densities and viscosities of seven glycol ethers from 288.15 K to 343.15 K, *J. Chem. Eng. Data* **45** (2), 391 (2000). DOI: 10.1021/je990281u.

[6]   Y. S. Joshi *et al.*, The dielectric relaxation study of 2(2-alkoxyethoxy)ethanol–water mixtures using time domain reflectometry, *J. Mol. Liq.* **163** (2), 70 (2011). DOI: 10.1016/j.molliq.2011.07.012.

[7]   J. B. Shinde *et al.*, Dielectric dispersion study of glycol ethers and their binary mixture with water, *Indian J. Pure App. Phys.* **56**, 301 (2018).

[8]   N. K. Karthick *et al.*, Hydrogen bond interactions in the binary solutions of ethyl acetate with nitrobenzene: Spectroscopic, theoretical and dielectric studies, *J. Mol. Liq.* **251**, 385 (2018). DOI: 10.1016/j.molliq.2017.12.064.

[9]   Z. S. Khan *et al.*, Dielectric relaxation study of aqueous ethylene glycol mono-methyl ether (EGME) with water using time domain reflectometry technique in the frequency range 10 MHz to 50 GHz, *J. Adv. Dielect.* **10** (03), 2050004 (2020). DOI: 10.1142/S2010135X20500046.

[10]   Y. S. Joshi, and A. C. Kumbharkhane, Study of heterogeneous interaction in binary mixtures of 2-methoxyethanol-water using dielectric relaxation spectroscopy, *J. Mol. Liq.* **161** (3), 120 (2011). DOI: 10.1016/j.molliq.2011.05.003.

[11]   Y. S. Joshi, and A. C. Kumbharkhane, Study of dielectric relaxation and hydrogen bonding in water + 2-butoxyethanol mixtures using TDR technique, *Fluid Phase Equilib.* **317**, 96 (2012). DOI: 10.1016/j.fluid.2012.01.005.

[12]   Y. S. Joshi, P. G. Hudge, and A. C. Kumbharkhane, Dielectric relaxation study of aqueous 2-ethoxyethanol using time domain reflectometry technique, *Indian J. Phys.* **85** (11), 1603 (2011). DOI: 10.1007/s12648-011-0176-6.

[13]   J. Hasted, *Aqueous Dielectrics* (Chapman and Hall: London, 1973). DOI: 10.1002/jobm.19760160714.

[14]   R. H. Cole *et al.*, Time domain reflection methods for dielectric measurements to 10 GHz, *J. Appl. Phys.* **66** (2), 793 (1989). DOI: 10.1063/1.343499.

[15]   S. Havriliak, and S. Negami, A complex plane analysis of α-dispersions in some polymer systems, *J. Polym. Sci. C Polym. Symp.* **14** (1), 99 (1966). DOI: 10.1002/polc.5070140111.

[16]   Z. Lu *et al.*, Dielectric relaxation in dimethyl sulfoxide/water mixtures studied by microwave dielectric relaxation spectroscopy, *J. Phys. Chem. A.* **113** (44), 12207 (2009). DOI: 10.1021/jp9059246.

[17]   R. J. Sengwa, V. Khatri, and S. Sankhla, Dielectric behavior and hydrogen bond molecular interaction study of formamide-dipolar solvents binary mixtures, *J. Mol. Liq.* **144** (1-2), 89 (2009). DOI: 10.1016/j.molliq.2008.10.009.

[18]   R. N. Mathpati *et al.*, Dielectric relaxation and hydrogen bonding interaction of polyethylene glycol dimethyl ether in water mixture, *Phys. Chem. Liq.* **58** (5), 664–674 (2020). DOI: 10.1080/00319104.2019.1633527.

[19]   J. G. Kirkwood, The dielectric polarization of polar liquids, *J. Chem. Phys.* **7** (10), 911 (1939). DOI: 10.1063/1.1750343.

[20]   P. J. Stiles, and J.-B. Hubbard, Polarization diffusion and dielectric friction in polar liquids, *Chem. Phys.* **84** (3), 431 (1984). DOI: 10.1016/0301-0104(84)85192-7.

[21]   R. J. Sengwa, comparative dielectric study of mono, di and trihydric alcohols, *Indian J. Pure App. Phys.* **41**, 295 (2003).

[22]   A. C. Kumbharkhane, S. M. Puranik, and S. C. Mehrotra, Dielectric relaxation studies of aqueous N,N-dimethylformamide using a picosecond time domain technique, *J. Solution Chem.* **22** (3), 219 (1993). DOI: 10.1007/BF00649245.

[23]   F. Franks, *Water a Comprehensive Treaties* (Plenum Press, New York, 1973, vol. II).

[24]   S. D. Deshmukh *et al.*, Investigation of intermolecular interactions between amide-amine binary mixtures through dielectric relaxation study, *Ferroelectrics* **519** (1), 23 (2017). DOI: 10.1080/00150193.2017.1362280.

[25]   K. L. Pattebahadur *et al.*, Dielectric characterization and molecular interaction behavior in amide–amide binary mixture, *Ferroelectrics* **519** (1), 33 (2017). DOI: 10.1080/00150193.2017.1362282.

[26]   D. A. G. Bruggeman, Berechnung verschiedener physikalischer Konstanten von heterogenen Substanzen. I. Dielektrizitätskonstanten und Leitfähigkeiten der Mischkörper aus isotropen Substanzen, *Ann. Phys.* **416** (8), 665 (1935). DOI: 10.1002/andp.19354160802.
[27]   S. M. Puranik, A. C. Kumbharkhane, and S. C. Mehrotra, The static permittivity of binary
       mixtures using an improved bruggeman model, *J. Mol. Liq.* **59** (2-3), 173 (1994). DOI: 10.
       1016/0167-7322(93)00665-6.

Effect of lanthanum dopant on pyroelectric characteristics of lead germanate (Pb$_5$Ge$_3$O$_{11}$) single crystals

J. R. Ghulghule

Published online: 26 Apr 2022.

Submit your article to this journal ⬚

View related articles ⬚

View Crossmark data ⬚

Taylor & Francis
Taylor & Francis Group

Check for updates

Effect of lanthanum dopant on pyroelectric characteristics of lead germanate (Pb$_5$Ge$_3$O$_{11}$) single crystals

J. R. Ghulghule

Department of Applied Physics, Y.C.C.E. Wanadongri, Nagpur, India

ABSTRACT

In this article, the behavior of pyroelectric coefficient and spontaneous polarization with temperature have been studied for pure (LG), 0.5 wt% (LG1) and 1 wt% (LG2) lanthanum doped lead germanate (Pb$_5$Ge$_3$O$_{11}$) single crystals. These crystals were grown by method of controlled cooling of the melt. The pyroelectric coefficient of grown crystals was measured over a temperature range 40–300 °C, which shows a change in sign negative to positive for LG and LG1 while for LG2 it shows only negative sign for a said temperature range. The observed results of pyroelectricity and spontaneous polarization in pure and doped materials are discussed. The comparative study of room temperature values of pyroelectric coefficient measured by various methods, spontaneous polarization and figure of merit is presented in this paper.

1. Introduction

Ferroelectric materials have become potentially useful for device applications. Out of numerous electrical, optical, and mechanical properties of these materials, the pyroelectric study is both of primary and applied interest. Ferroelectrics are pyroelectrics predominantly because of large temperature dependent of spontaneous polarization.

Pb$_5$Ge$_3$O$_{11}$ has become a desirable material for device application due to large spontaneous polarization and its reversibility. Being an optically active ferroelectric, it is useful for electro-optic devices. These crystals are uniaxial ferroelectric which undergoes second order phase transition at 177 °C, at which crystal symmetry changes from hexagonal, $P\bar{6}$ to trigonal, $P3$ [1–5]. An intense study has been carried out in this material by large number of researchers from past five decades, due to application of its physical properties in pure and applied sciences. This compound has a potential utility as pyroelectric material, in ferroelectric memory devices and for hologram recording and readout [6]. Several researchers have used various methods for study of pyroelectric effect in different materials.

In Chynoweth dynamic method [7], the crystal under study, heated by exposure to a strong light pulse, generates a pyroelectric current given by

---
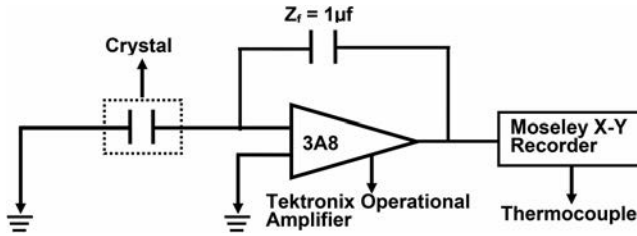
Figure 1. Measurement circuit for static method.

$$i = \frac{dP_S}{dt} = \left(\frac{dP_S}{dT}\right)\left(\frac{dT}{dt}\right) \tag{1}$$

where P_S the spontaneous polarization, t the time, T the temperature, and $\frac{dT}{dt}$ is the rate of change of temperature. This technique helps in evaluation of polarization, bias, space charge, and surface layers in the crystals.

Another method is static or charge integration method suggested by Glass [8].

It involves the continuous integration of charge developed on crystal faces as the temperature of the crystal is increased. The measurement circuit is shown in Fig. 1.

The charge on the feedback capacitor Z_f will then change the polarization of the crystal $[\Delta T]_{T_1}^{T_2}$ so that the output voltage of the operational amplifier is

$$V_{out} = \frac{[\Delta T]_{T_1}^{T_2}}{Z_f} \tag{2}$$

As crystal is heated, the output voltage is noted as a continuous function of temperature using X-Y recorder. The pyroelectric coefficient is obtained from the temperature derivative of this curve.

A direct technique was developed by Byer and Roundy [9] to measure the pyroelectric coefficient. This technique is more straight forward than the above two methods. According to them, the variation of spontaneous polarization of the crystal, occurs due to change in temperature, produces a displacement current I parallel to the polar axis given as

$$I = A \, P_C(T)\left(\frac{dT}{dt}\right) \tag{3}$$

where $P_C(T) = \left(\frac{dP}{dT}\right)$ is the pyroelectric coefficient evaluated at temperature T and A is the surface area normal to the polar axis. The pyroelectric coefficient is given by

$$P_C(T) = \frac{I}{A\,\left(\frac{dT}{dt}\right)} \tag{4}$$

Thus for constant value of $\left(\frac{dT}{dt}\right)$, a measured current I gives variation of $P_C(T)$ with T over a broad temperature range.

Thus when $\left(\frac{dT}{dt}\right)$ is held constant over a wide temperature range, a measurement of current I gives direct plot of $P_C(T)$ over that temperature range. For the measurement apparatus the equivalent circuit is shown in Fig. 2.
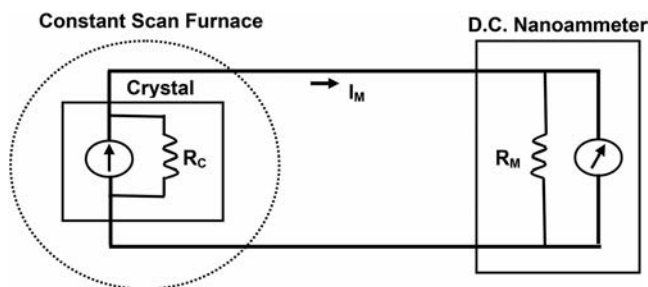
Figure 2. Measurement apparatus equivalent circuit.

A small amount of an appropriate additive significantly affects the crystallization process and physical properties of lead germanate crystals. Matsumoto et al. [10] showed that in lead germanate ceramics the substitution of Sr and Ba for Pb-site and Si for Ge-site gives enhanced values of pyroelectric coefficient than pure ceramic. Otto et al. [11] reported lowering of T_c and enhancement of pyroelectric coefficient due to the substitution of Cs^{1+} or Bi^{3+} at Pb^{2+} in lead germanate crystals. They further suggest that improved pyroelectric coefficients in doped crystals make them better sensitive so as to use as pyroelectric thermal detectors. Watton et al. [12] also reported increase in pyroelectric coefficient in Ba doped lead germanate single crystals.

The paper reports the effect of lanthanum dopant on the variation of pyroelectric coefficient and calculated spontaneous polarization with temperature.

2. Experimental

Pure $Pb_5Ge_3O_{11}$ (LG) single crystals were grown with controlled cooling of the melt using high grade materials PbO (99.9%, Aldrich USA) and GeO_2 (99.999%, ReachIM, USSR) in 5:3 molar ratio. The initial material was prepared by mixing the weighed PbO and GeO_2 in agate pestle mortar for about 3 h. The thoroughly mixed material was divided in to three parts. The first part was used to grow LG crystals. La_2O_3 (99.9%, Indian Rare Earths) was added as dopant in 0.5 wt% and 1 wt% in other two parts of starting material, to grow LG1 and LG2 crystals, respectively. The powders were thoroughly mixed and pallets were prepared using hydraulic press by applying a pressure of 1 ton/(in.)^2. The calcinations were done at 600 °C in a platinum crucible for about 6 h in a closed furnace in air. The platinum-rhodium-platinum 13% thermocouple was placed just near the crucible in maximum temperature region. Tablets of LG, LG1, and LG2 were recrushed to fine powder. The reacted material was heated in platinum crucible up to 750 °C and the molten material was maintained at thermal equilibrium for 4 h. At thermal equilibrium the temperature control was ±0.5 °C. The crucible rotation was introduced during thermal equilibrium and was continued up to 30 °C below melting points of respective compositions during cooling. A cooling rate of 1 °C/h was maintained in the vicinity of respective melting points. An appropriate cooling rate was maintained and precautions were taken to protect grown crystals from sudden thermal and mechanical stresses. The temperature was controlled by automatic temperature controller (457-D INDOTHERM MAKE with accuracy ±1 °C) during growth process.

Table 1. Comparison of measured pyroelectric coefficients in pure and doped $Pb_5Ge_3O_{11}$ by different methods.

Material	Pyroelectric coefficient in C/cm^2 K			References
	Dynamic method	Static method	Direct method	
LG (SC)	–	–	-2.2×10^{-8}	Our data
LG1 (SC)			-1.21×10^{-8}	
LG2 (SC)			-0.73×10^{-8}	
LG (SC)	–	–	1.1×10^{-8}	Watton et al. [12]
Ba:LG (SC)			2.0×10^{-8}	
Ba:LG (SC)			3.2×10^{-8}	
LG (SC)	–	–	1.1×10^{-8}	Otto et al. [11]
Cs,Bi:LG (SC)			1.9×10^{-8}	
Cs,Bi:LG (SC)			2.3×10^{-8}	
LG (SC)	–	–	1.17×10^{-8}	Matsumoto et al. [10]
LG (PC)			0.4×10^{-8}	
0.050 Ba:LG (PC)			0.6×10^{-8}	
0.100 Ba:LG (PC)			0.45×10^{-8}	
0.050 Sr:LG (PC)			0.74×10^{-8}	
0.100 Sr:LG (PC)			0.47×10^{-8}	
LG (PC)	–	–	0.2×10^{-8}	Kanduser et al. [15]
LG (PC)	–	–	1.6×10^{-8}	Nagata et al. [16]
LG (SC)	–	–	3.08×10^{-8}	Fadnavis and Katpatal [17]
0.1Nd:LG (SC)			-6.9×10^{-8}	
0.2Nd:LG (SC)			-5.70×10^{-8}	
LG (PC)	0.55×10^{-8}	–	–	Glass et al. [18]
LG (PC)	1.1×10^{-8}	–	–	Kremenchugskii and Roitsina [19]
LG (SC)	2.0×10^{-8}	2.1×10^{-8}	–	Borisenok et al. [20]
LG (SC)	–	1.8×10^{-8}	–	Monya et al. [21]

S.C. → Single crystals; P.C. → Ceramic.

The differential thermal analysis (DTA) confirmed melting points of LG, LG1, and LG2 as 730.2 °C, 733.1 °C, and 733.3 °C, respectively. This indicates that doping increased melting point in LG1 by 2.9 °C and in LG2 by 3.1 °C. It reveals the enhancement of solid state bonding as a result of doping. The X-ray diffraction study was carried for pure and doped compositions at room temperature in the range $\theta = 5°$–$95°$ using CuKα target and wavelength 1.54184 Å. A PHILIPS PW1700 (Holland) automated X-ray powder diffractometer was used. The system provided computerized data of 2θ, d values, and intensity values, which was compared with J.C.P.D.S. data given by Sugii et al. [13] and Nassu et al. [14]. Estimated lattice parameters for LG, LG1, and LG2, respectively, are ($a_0 = 10.232$ Å, $c_0 = 10.679$ Å), ($a_0 = 10.2274$ Å, $c_0 = 10.685$ Å), and ($a_0 = 10.2271$ Å, $c_0 = 10.674$ Å). These calculated values are comparable with the reported values for pure lead germanate ($a_0 = 10.251$ Å, $c_0 = 10.685$ Å) by Sugii et al. [13] in JCPDS data card No. 24-576 ($a_0 = 10.10$ Å, $c_0 = 10.34$ Å) by Nassu [14] in JCPDS data card No. 33-751 and by Bush et al. [6], ($a_0 = 10.226$ Å, $c_0 = 10.664$ Å) for brownish crystals and ($a_0 = 10.214$ Å, $c_0 = 10.649$ Å) for dark brown crystals. It is apparent that doping has changed the lattice parameters.

Crystals of LG, LG1, and LG2 used for measurement were cleaned, polished and a layer of air drying silver paste was coated on the surfaces. The crystal holder with highly insulating alumina blocks for separating two electrodes was fabricated for the measurements. Pyroelectric current at different temperatures was measured for both pure and doped crystals in the temperature range 40–300 °C with an interval of 10 °C, using Byer and Roundy [9] technique. SES Make nanoammeter (Model NM 122) was used during measurement. This instrument is essentially designed for very low current measurement
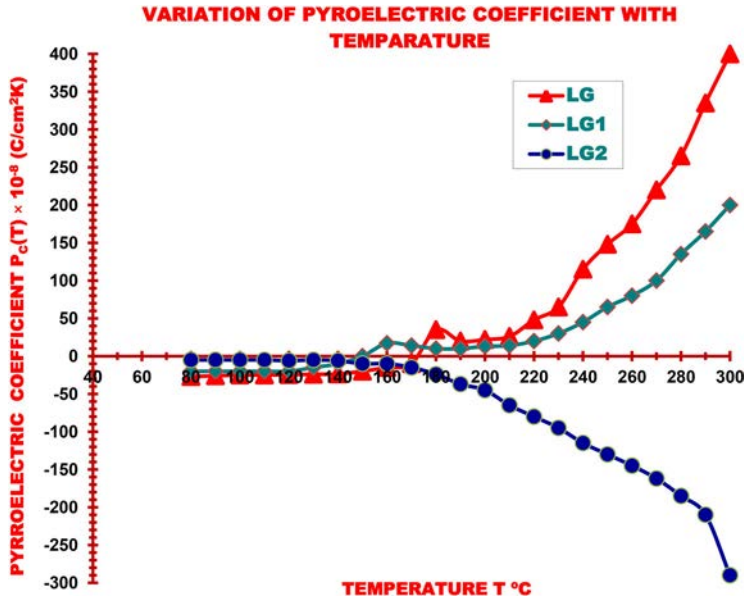
Figure 3. Variation of pyroelectric coefficient with temperature.

from high impedance source. For pyroelectric effect, during the measurements, the steady rates of heating and cooling were maintained at $1.4\,°C/min$ and $1.5\,°C/min$, respectively. The temperature was measured by Cr-Al thermocouple and controlled by automatic temperature controller (457-D INDOTHERM MAKE with accuracy $\pm1\,°C$) .

The pyroelectric coefficient was calculated using Eq. (4). As seen from Fig. 2, the equivalent circuit indicates that the measured current I_M equals I within 1% as long as $R_C > 100R_M$. Where R_C and R_M are the leakage resistance of crystal and input resistance of meter, respectively. Since $R_M \cong 10^5\Omega$ and $R_C \cong 10^{10}\Omega$, the correct pyroelectric current was measured.

Measurement techniques significantly influenced the value of pyroelectric coefficient. Table 1 compares the reported values measured by different techniques for lead germanate systems, which indicates that most of the investigators used direct measurement technique suggested by Byer and Roundy. It also shows the variation in magnitude of room temperature values, measured using different techniques by various investigators. Our measured room temperature values of $P_C(T)$ are comparable with the values reported by the most of the investigators.

3. Results and discussion

Figure 3 shows the variation of $P_C(T)$ with temperature for LG, LG1, and LG2 crystals for cooling cycle. It shows following observations.

- Room temperature pyroelectric coefficients are negative for pure and doped compositions.
- $P_C(T)$ shows change in sign for LG and LG1 with small peaks, respectively, at $180\,°C$ and $160\,°C$. However both are not observed for LG2 crystals.
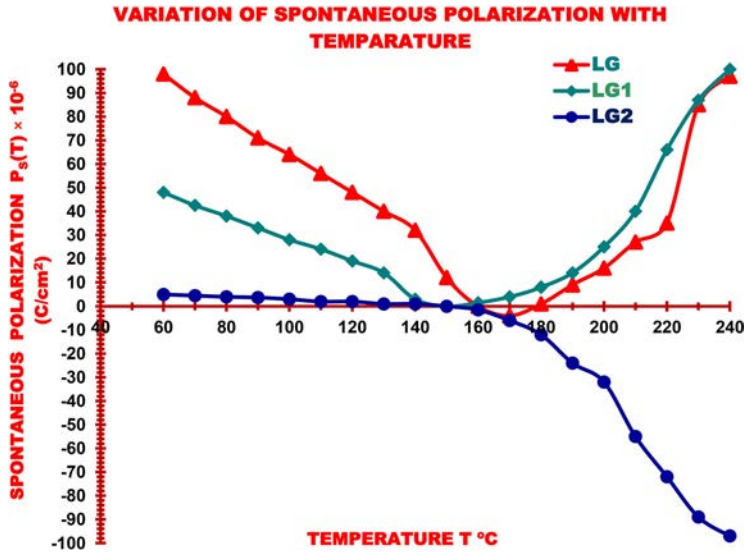
Figure 4. Variation of spontaneous polarization with temperature.

- Insignificant temperature dependence of $P_C(T)$ below respective transition temperatures of LG, LG1, and LG2.
- Significant temperature dependence of $P_C(T)$ above respective transition temperatures of LG, LG1, and LG2.
- Lanthanum dopant has reduced the magnitude of room temperature $P_C(T)$. This reduction increases with increasing doping concentration.

The spontaneous polarization $P_S(T)$ for LG, LG1, and LG2 at various temperatures is estimated using our data of pyroelectric coefficients and the following expression suggested by Matsumoto et al. [10].

$$P_S(T) = -2P_C(T)(T_C - T) \qquad (5)$$

where $P_C(T)$ is the pyroelectric coefficient while $P_S(T)$ is the spontaneous polarization at T (K) and T_C is the transition temperature.

Figure 4 shows the variation of estimated values of $P_S(T)$ with temperature for LG, LG1, and LG2 crystals during cooling cycle. It shows following significant features.

- Room temperature values of spontaneous polarization are positive for pure and doped samples.
- $P_S(T)$ approaches to zero value near corresponding transition temperatures of pure and doped compositions.
- Lanthanum doping has reduced the spontaneous polarization in LG1 and LG2 compared to LG in ferroelectric phase. This reduction becomes more with increasing the concentration of dopant.
- Above transition temperature LG1 shows marginal rise of $P_S(T)$ compared to LG, while in LG2 $P_S(T)$ increases in the negative direction.

Table 2. The comparison of our estimated values of spontaneous polarization in C/cm^2.

Material	Spontaneous polarization in C/cm^2	References
LG (SC)	6.73×10^{-6}	Our data
LG1 (SC)	3.21×10^{-6}	
LG2 (SC)	1.86×10^{-6}	
LG (SC)	4.4×10^{-6}	Matsumoto et al. [10]
Ba:LG (PC)	0.90×10^{-6}	
Sr:LG (PC)	0.50×10^{-6}	
LG (SC)	4.8×10^{-6}	Iwasaki et al. [1]
LG (SC)	4.0×10^{-6}	Nanamatsu et al. [2]
LG (SC)	4.6×10^{-6}	Lee et al. [22]
LG (SC)	4.3×10^{-6}	Blumberg and Kursten [23]
LG (SC)	6.153×10^{-6}	Kim et al. [24]
Sr:LG (SC)	5.521×10^{-6}	
Sr:LG (SC)	4.832×10^{-6}	
LG (SC)	-4.62×10^{-6}	Fadnavis and Katpatal [17]
0.1Nd:LG (SC)	9.66×10^{-6}	
0.2Nd:LG (SC)	7.12×10^{-6}	

S.C. → Single crystals; P.C. → Ceramic.

Table 2 shows the comparison of our estimated values of spontaneous polarization in pure and doped samples with reported room temperature values of lead germanate single crystals and ceramics. A comparison reveals that the order of magnitude of PS(T).

As recommended by Bhalla et al. [25], the resultant pyroelectric coefficient is the addition of primary as well as secondary pyroelectricity in the crystal. Hence

$$P_C(T) = P_C(T)_{PRIM} + P_C(T)_{SEC} \qquad (6)$$

The secondary component $P_C(T)_{SEC}$ in the crystal is given as

$$P_C(T)_{SEC} = e_{33}\alpha_3 + 2e_{31}\alpha_1 \qquad (7)$$

where e_{ij} are the piezoelectric stress coefficients and α_i are the expansion coefficients of a single crystal. Following Eq. (7), we calculated the secondary contribution of pyroelectric coefficient using reported values of e_{ij} and α_i in the literature of pure $Pb_5Ge_3O_{11}$. The estimated value comes out to be $0.154 \times 10^{-8} C/cm^2 K$. Presuming the contribution of $P_C(T)_{SEC}$ same for all the three compositions and is equivalent to our theoretically estimated value, the calculated $P_C(T)_{PRIM}$ for LG, LG1, and LG2 at room temperature are $-2.354 \times 10^{-8} C/cm^2 K$, $-1.364 \times 10^{-8} C/cm^2 K$ and $-0.884 \times 10^{-8} C/cm^2 K$, respectively. Thus the resultant primary pyroelectric coefficient comes out to be negative in all the three compositions.

The contribution of primary pyroelectricity below transition temperature is due to dipole relaxation, domain configuration, and domain wall motion. This will be decided by surface charge layers left behind by relaxing dipoles and moving domain walls. Pinning and clamping of domain wall will significantly affect the primary value. Because of the point defects due to lead/oxygen deficiency wall movement is hindered affecting this primary value.

The La^{3+} doped $Pb_5Ge_3O_{11}$ compositions belong to the system of hetrovalent impurity, causing enhancement of lead ion vacancy sites. These sites may result the increase in localized space charge formation, which can enhance pinning of domains at low temperature. The decrease in the magnitude of primary as well as total pyroelectric

Table 3. Comparison of characteristics of pyroelectric detector materials.

Material	Pyroelectric coefficient, $P_C(T)$ in C/cm^2 K	Dielectric constant, ε	Curie temperature, T_C (°C)	Figure of merit, $F_M = \frac{P(T)}{\varepsilon C}$ in C cm/J	References
TGS	4.0×10^{-8}	35	49	4.6×10^{-10}	Yokoo et al. [28]
LiTaO$_3$	2.3×10^{-8}	54	618	1.3×10^{-10}	
LiNbO$_3$	0.4×10^{-8}	30	1200	0.46×10^{-10}	
PbTiO$_3$	6.0×10^{-8}	200	470	0.94×10^{-10}	
SBN	6.5×10^{-8}	380	115	0.8×10^{-10}	
PVF$_2$	0.24×10^{-8}	11	120	0.9×10^{-10}	
LG (SC)	1.17×10^{-8}	50	177	1.17×10^{-10}	Matsumoto et al. [10]
LG (PC)	0.4×10^{-8}	30	177	0.67×10^{-10}	
0.050 Ba:LG (PC)	0.6×10^{-8}	32	157	0.94×10^{-10}	
0.100 Ba: LG (PC)	0.45×10^{-8}	37	145	0.61×10^{-10}	
0.050 Sr:LG (PC)	0.74×10^{-8}	35	149	1.06×10^{-10}	
0.100 Sr: LG (PC)	0.47×10^{-8}	39	126	0.60×10^{-10}	
LG	-2.2×10^{-8}	110	180	-1.0×10^{-10}	Our data
LG1	-1.21×10^{-8}	110	160	-0.55×10^{-10}	Our data
LG2	-0.73×10^{-8}	84	155	-0.43×10^{-10}	Our data

S.C. $\rightarrow$ Single crystals; P.C. $\rightarrow$ Ceramic.

coefficient at room temperature in LG1 and LG2 therefore can be attributed to pinning of domain in these compositions. Contribution due to space charge, release of trap charges and strain remain insignificant at room temperature. Except near the transition temperature, temperature dependent dipolar relaxation and domain wall motion also remain insignificant. Probably these two together are the origin of temperature independent pyroelectric coefficient below transition temperature as observed in Fig. 3.

With increase in temperature there is a change in reorientation of dipoles causing the change in polarization on the surface. Further above transition temperature probably two processes may contribute in pyroelectric behavior. (1) The release of trap charges at domain configuration, defect states and vacancy sites as envisaged by Aristove et al. [26] and Shur et al. [27] and (2) thermal and mechanical strain contributing in secondary pyroelectric phenomena. The secondary pyroelectric effect is a result of crystal deformation. Thermal expansion causes a strain that alters the electric displacement via piezoelectric process. Below transition temperature these factors remain insignificant as observed from nature of pyroelectric behavior. The creation of additional charge carriers in crystal lattice because of unknown impurities and release of accumulated charges at the interface between bulk and surface charge layer will also contribute toward pyroelectric coefficient on heating. All these parameters are probably contributing toward significant temperature dependent pyroelectric behavior in LG and LG1. However in LG2, above transition temperature, the pyroelectric coefficient increased in negative direction. Because of crystal deformation or structural changes occurring at that temperature, the contribution of thermal and mechanical strain within the crystal and release of trap charges may alter. Hence the net pyroelectric effect will be due to the resultant effect of total pyroelectricity and release of one type of trap charges.

The observed change of sign of pyroelectric coefficient in LG and LG1, probably due to alteration in the nature of liberated trap charges and their relative strength and contribution of primary and secondary pyroelectricity together. However, in LG2 the nature of released charges may remain same. Hence the change of sign is not observed.

An acceptable material for pyroelectric detector, should have high $P_C(T)$, high resistivity, small ε and low thermal capacity. Thus it is feasible to work out figure of merit, indicating the involvement of material properties in device performance. The voltage output V of the pyroelectric detector depends upon $P_C(T)$, C' the volume specific heat and ε. The figure of merit F_M of a pyroelectric detector for voltage responsivity is given by

$$F_M = \frac{P_C(T)}{\varepsilon C'} \tag{8}$$

The comparison of F_M of LG, LG1, and LG2, with reported other ferroelectrics [26] and lead germanate compositions [10], is shown in Table 3.

By considering the value of volume specific heat 2.0 J/K cm^3 of pure $Pb_5Ge_3O_{11}$ single crystal specified by Matsumoto et al. [10], F_M for LG, LG1, and LG2 can be estimated using Eq. (8). Lanthanum dopant has reduced the magnitude of F_M. The results further suggests that both $P_C(T)$ and F_M for pure and doped compositions are comparable with reported values of lead germanate and other materials except TGS. Furthermore TGS crystals are hygroscopic, hence show less thermal stability as reported by Blumberg et al. [23], which causes bad reproducibility.

However, our estimated values of $P_C(T)$ for pure and lanthanum doped compositions are independent of temperature in the low-temperature zone (Fig. 3). Therefore, our grown compositions can become more thermally stable compared to TGS and are considerable for fabrication of pyroelectric detector.

4. Conclusions

1. Single crystals of LG, LG1, and LG2 show pyroelectricity. Dopant has decreased the magnitude of the room temperature pyroelectric coefficient.
2. Temperature dependent $P_C(T)$ show change of sign in LG and LG1, which is not observed in LG2. The observed pyroelectric behavior in these compositions can be attributed to contribution of primary and secondary pyroelectricity as envisaged by Bhalla.
3. The estimated room temperature values of $P_S(T)$ are positive. Lanthanum dopant has reduced $P_S(T)$ in ferroelectric phase.
4. All three compositions (LG, LG1, LG2) may be used as thoughtful materials for pyroelectric detector, since they are more thermally stable compared to TGS in low-temperature zone.

References

[1] H. Iwasaki et al., 5PbO·3GeO$_2$ crystal; a new ferroelectric, *Appl. Phys. Lett.* **18** (10), 444 (1971). DOI: 10.1063/1.1653487.
[2] S. Nanamatsu et al., Ferroelectricity in $Pb_5Ge_3O_{11}$, *J. Phys. Soc. Jpn.* **31** (2), 616 (1971). DOI: 10.1143/JPSJ.31.616.
[3] H. Iwasaki et al., Ferroelectric and optical properties of $Pb_5Ge_3O_{11}$ and its isomorphous compound $Pb_5Ge_2SiO_{11}$, *J. Appl. Phys.* **43** (12), 4907 (1972). DOI: 10.1063/1.1661044.
[4] M. I. Kay, J. A. Gonzalo, and R. Maglic, The phase transition in sodium nitrite, *Ferroelectrics* **9** (1), 179 (1975). DOI: 10.1080/00150197508237721.

[5] Y. Iwata, Neutron diffraction study of the structure of paraelectric phase of $Pb_5Ge_3O_{11}$, *J. Phys. Soc. Jpn.* **43** (3), 961 (1977). DOI: 10.1143/JPSJ.43.961.

[6] A. A. Bush et al., Low-frequency relaxation processes in $Pb_5Ge_3O_{11}$ ferroelectric crystals, *Phys. Solid State* **46** (9), 1722 (2004). DOI: 10.1134/1.1799193.

[7] A. G. Chynoweth, Dynamic method for measuring the pyroelectric effect with special reference to barium titanate, *J. Appl. Phys.* **27** (1), 78 (1956). P. DOI: 10.1063/1.1722201.

[8] A. M. Glass, Investigation of the electrical properties of $Sr_{1-x}Ba_xNb_2O_6$ with special reference to pyroelectric detection, *J. Appl. Phys.* **40** (12), 4699 (1969). DOI: 10.1063/1.1657277.

[9] R. L. Byer and C. B. Roundy, Pyroelectric coefficient direct measurement technique and application to a nsec response time detector, *Ferroelectrics* **3** (1), 333 (1972). DOI: 10.1080/00150197208235326.

[10] K. Matsumoto et al., Dielectric properties of ceramic lead germanate derivatives, *Jpn. J. Appl. Phys.* **24** (S2), 466 (1985). DOI: 10.7567/JJAPS.24S2.466.

[11] H. H. Otto et al., Ferroelectric properties of lead germanate derivatives: $Pb_{5-x}M_xGe_3O_{11}$, m = $(Cs_{1/2}Bi_{1/2})$ and $(Nd_{2/3}\square_{1/3}$, *Ferroelectrics* **25** (1), 543 (1980). DOI: 10.1080/00150198008207066.

[12] R. Watton, C. Smith, and G. R. Jones, Pyroelectric materials: operation and performance in the pyroelectric camera tube, *Ferroelectrics* **14** (1), 719 (1976). DOI: 10.1080/00150197608236709.

[13] K. Sugii, H. Iwasaki, and S. Miyazawa, Crystal growth and some properties of $5PbO \cdot 3GeO_2$ single crystals, *Mater. Res. Bull.* **6** (6), 503 (1971). DOI: 10.1016/0025-5408(71)90029-8.

[14] K. Nassu, J. W. Shiever, D. C. Joy, and A. M. Glass, The crystallization of vitreous and metastable $Pb_5Ge_3O_{11}$, *J. Crystal Growth*, **42**, 574–578 (1977). DOI: 10.1016/0022-0248(77)90249-4.

[15] A. Kanduser et al., $Pb_5Ge_3O_{11}$ ceramic pyroelectric detector, *International Symposium on Applications of Ferroelectrics*, University of Illinois, USA, 6–8 Jun. 1990, pp. 388–390.

[16] K. Nagata et al., Properties of grain-oriented lead germanate ceramics, *Jpn. J. Appl. Phys.* **24** (S2), 744 (1985). DOI: 10.7567/JJAPS.24S2.744.

[17] S. A. Fadnavis and A. G. Katpatal, Nd^{+3} doped lead germanate—a good candidate for pyroelectric detector, *Ferroelectrics* **211** (1), 79 (1998). DOI: 10.1080/00150199808232335.

[18] A. M. Glass, K. Nassau, and J. W. Shiever, Evolution of ferroelectricity in ultrafine-grained $Pb_5Ge_3O_{11}$ crystallized from the glass, *J. Appl. Phys.* **48** (12), 5213 (1977). DOI: 10.1063/1.323604.

[19] L. S. Kremenchugskii and O. V. Roitsina, *Pyroelectric Radiation Detectors* [in Russian] (NaukevaDumka, Kiev 1979).

[20] V. A. Borisenok et al., Measurement of pyroelectric coefficient of some crystals by dynamic and Static method, *Sov. Phys. Crystallogr.* **33** (5), 780 (1988).

[21] V. G. Monya, E. V. Siyankov, and N. V. Tnerdokhlebov, *Physics of Active Dielectrics* [in Russian] (DGV, Dneproptrovsk 1981), p. 99.

[22] S. D. Lee, M. S. Jang, and J. H. Lee, Growth and electrical properties of lead germanate single crystals, *New Phys. (Korean Phys. Soc.)* **26** (3), 197–203 (1986).

[23] H. Blumberg and H. D. Kursten, Switching behaviour of $Pb_5Ge_3O_{11}$ single crystals, *Krist. Tech.* **14** (8), 985 (1979). DOI: 10.1002/crat.19790140813.

[24] J. H. Kim et al., Sr^{2+}-doping effect on the phase transition in $Pb_5Ge_3O_{11}$ single crystals, *Solid State Commun.* **88** (9), 727 (1993). DOI: 10.1016/0038-1098(93)90633-X.

[25] A. S. Bhalla, L. E. Cross, and R. W. Whatmore, Pyroelectric and piezoelectric properties of lithium tetraborate single crystal, *Jpn. J. Appl. Phys.* **24** (S2), 727 (1985). DOI: 10.7567/JJAPS.24S2.727.

[26] V. V. Aristov, L. S. Kokhanchik, and V. G. Monya, Investigations of domain contrast in $Pb_5Ge_3O_{11}$ with a scanning electron microscope, *Ferroelectrics* **70** (1), 15 (1986). DOI: 10.1080/00150198608221417.

[27] V. YaShur, V. V. Letuchev, and Y. A. Popov, Changes in the domain structure of lead germanate single crystal, *Sov. Phys. Solid State* **24** (11), 1957 (1982).

[28] T. Yokoo, K. Shibata, and Y. Kuwano, Application of pyroelectricity of $LiTaO_3$ for infrared detectors, *Jpn. J. Appl. Phys.* **24** (S2), 149 (1985). DOI: 10.7567/JJAPS.24S2.149.
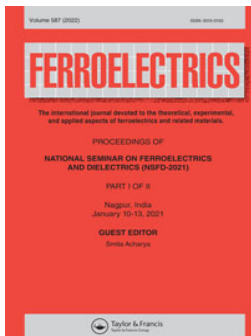
Effect of lanthanum oxide addition on physical, electrical and dielectric properties in lithium borosilicate glasses

V. Y. Ganvir, H. V. Ganvir & R. S. Gedam

Published online: 26 Apr 2022.

Submit your article to this journal ⎘

View related articles ⎘

View Crossmark data ⎘

Taylor & Francis
Taylor & Francis Group

Check for updates

Effect of lanthanum oxide addition on physical, electrical and dielectric properties in lithium borosilicate glasses

V. Y. Ganvir[a], H. V. Ganvir[a], and R. S. Gedam[b]

[a]Department of Applied Physics, Yeshwantrao Chavan College of Engineering, Nagpur, India;
[b]Department of Physics, Visvesvaraya National Institute of Technology, Nagpur, India

ABSTRACT

In the present study, lanthanum oxide doped lithium borosilicate glasses were synthesized using standard melt-quenching technique. The synthesized glass materials were characterized by XRD, FTIR, density calculation, Electrical and dielectric properties measurements. The amorphous nature of the studied glasses was established through XRD spectra. FTIR spectra were used to investigate the different functional groups. Improvements in density and molar volume values were reported as the La_2O_3 content increased, it can be attributed to higher molecular weight of La_2O_3. Numerous other physical parameters such as lanthanum ion concentration (N), internuclear distance (r_i), polaron radius (r_p), and field intensity (F) were determined using density values and are discussed in detail here. Electrical conductivity and dielectric measurements were carried out by impedance spectroscopy. The dynamical processes taking place in the glass system was studied by introducing conductivity and composition scaling. The dielectric constant (ε') and dielectric loss ($Tan\ \delta$) with frequency at various temperatures are extensively explored. There is a fairly good correlation among the physical parameters, FTIR, electrical conductivity and dielectric properties for the glasses studied in the present work.

1. Introduction

Borosilicate glasses are the most powerful glass system in terms of technical, industrial and science applications [1]. Glasses of this form are common in many applications ranging from chemical resistance for laboratory glassware, interface materials for encapsulation of hazardous nuclear waste, optical components, and sealing materials [2]. The ionic conductivity in glasses has been widely recognized in past few years and particular interest has been centered on lithium conducting glasses owing to their availability as strong and stable electrolytes in lithium batteries [3]. In addition, lithium borosilicate glasses are often used owing to their superior glass forming properties in comparison to many other conventional structures, they are an ideal host for rare earth oxides. [3]. Because rare earth oxide doped borosilicate glasses are known to have different unique properties, they may be used to produce devices with specific attributes [4].

Lanthanum Oxides (La_2O_3) constitutes 14.1% of total rare earth content resources [5]. Lanthanum oxide is expected to have the ability to modify glass network [5]. This

---

Table 1. Compositions of the glass samples.

Sample designation	Li_2CO_3	B_2O_3	SiO_2	La_2O_3
0-BSLI	30.00	60.00	10.00	0.0
0.5-BSLILA	30.00	59.57	9.93	0.5
1.0-BSLILA	30.00	59.14	9.86	1.0
1.5-BSLILA	30.00	58.71	9.79	1.5
2.0-BSLILA	30.00	58.29	9.71	2.0

is a very powerful rare earth among all REO ions for enhancing the variety of physical, electrical and optical properties of glasses and ceramics [6–8]. Therefore in order to expand the available knowledge concerning the REO doped glasses, the current study makes an effort to investigate how physical, electrical and dielectric properties are modified by adjusting the La^{3+} ions content in the SiO_2–Li_2O–B_2O_3 glass system.

2. Experimental

In present study, the glass formulation '30Li_2O-(70-X) [1/7 SiO_2:6/7 B_2O_3]-X La_2O_3' was prepared using the normal melt quenching process where 'X' ranged from 0 to 2 in the step of 0.5 mole percentage. The high quality processed raw materials including SiO_2, Li_2CO_3, B_2O_3 and La_2O_3 (Purity of more than 99.9 per cent of E-Merck make) were used in material preparation.

This mixture was blended in acetone for about 1 hour, and it was then placed in the platinum crucible for a period of 3 hours in an electric furnace at 1223–1273 K. This heated fluid was poured in an aluminum mold to get the perfect desired shape of the bulk glass samples. Then immediately, these quenched bulk glasses were moved to annealing furnace at 588 K for three hours to eliminate the thermal stress that developed while quenching and kept it until room temperature. The sample designations and precise composition of the different samples are mentioned in Table 1.

The X-ray diffraction patterns for the prepared glasses were recorded using X'pert pro-PANalytical. A 'Perkin Elmer Spectrometer' was used to obtain the FTIR spectra in the mid-infrared region. The density of the glass materials were determined using a SHIMADZU density measurement package based on Archimedes theory with toluene as dipping solution. For impedance measurements, the synthesized glass sample was cut into cylinders with a thickness of approximately 2.5 to 3 mm. The parallel faces of cylindrical-shaped glass samples were polished with silver paint to ensure good electrical interaction. Impedance measurements in the 20 mHz to 20 MHz band frequency range have been recorded at temperatures ranging from 423–673 K, based on the temperature of all samples collected on a 'Novocontrol make High Resolution dielectric analyzer'. This collected data used to provide insight on the electrical properties of La^{3+} doped LBS glasses.

3. Results and discussion

Figure 1 illustrates the X-ray diffractograms of the prepared glass samples, in which only humps are shown and no high peak thus illustrating the amorphous existence of glass samples [9,10].
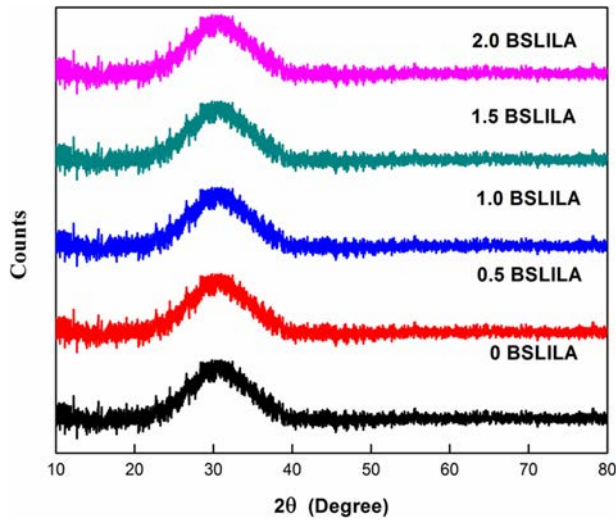
Figure 1. X-ray diffraction (XRD) spectra of BSLILA glass samples.

Figure 2 displays the FTIR spectra of La_2O_3 doped lithium borosilicate glass samples. The band at about $460\,cm^{-mo}$ is allocated to B-O-Si stretching and Si-O-Si vibrations and a band at about $550\,cm^{-m}$ is assigned to Si-O-Si stretching [11–13]. The band at $819\,cm^{-m}$ can be due to vibration of B-O bond in BO_4 unit. Band $943\,cm^{-mn}$ is allocated to B-O bond stretching in di borate group [11–13]. The existence of di-borate and tri-borate groups is confirmed by bands $\sim 1000\,cm^{-m}$ of an infrared absorption [11–13]. This feeble band possibly results from the torsional modes of the boron tetrahedrons. The region from $1200\,cm^{-m}$ to $1350\,cm^{-m}$ suggests that meta-borate, ortho-borate and pyro-borate units have high absorption in this area [11–13].

The observed FTIR spectra support the conversion of BO_3 to BO_4 with the inclusion of La_2O_3, as seen in Fig. 2. It is also found that bands at $819\,cm^{-m}$ moving slightly toward the lower wavenumber side of the spectrum and that band at $1121\,cm^{-m}$ is shifted toward the higher wavenumber side of the spectrum [11–13]. This shift in the band location affirms the structural changes and creation of the BO_4 units [11–13].

Figure 3 illustrates the compositional influence of density (ρ) and molar volume (V_M) on La_2O_3 comprising lithium borosilicate glasses. It is found that the density (ρ) and molar volume (V_M) rises with the addition of La_2O_3. The rise in density can be appreciated on the basis of the molecular weights of oxides used for glass preparation. Since La^{3+} ions ($Li_2O = 29.88\,gm/mol$, $B_2O_3 = 69.62\,gm/mol$, $La_2O_3 = 325.82\,gm/mol$, $SiO_2 = 60.09\,gm/mol$) have a greater molecular weight than other oxides in glasses, inclusion of La_2O_3 at the cost of B_2O_3 and SiO_2 improves the density of glass samples.

The rise in the molar volume due to the incorporation of La_2O_3 can be attributed to higher ionic radius of La^{3+} ions. Since La^{3+} ion has a greater ionic radius than other ions in its composition, it expands the glass structure and increases the molar volume. This introduces La^{3+} ions into the voids in the glass system, which opens the glass structure. This is evidenced by the FTIR result and the observed findings are consistent with the previous recorded studies, where density and molar volume of glasses increased with REOs [7,14].
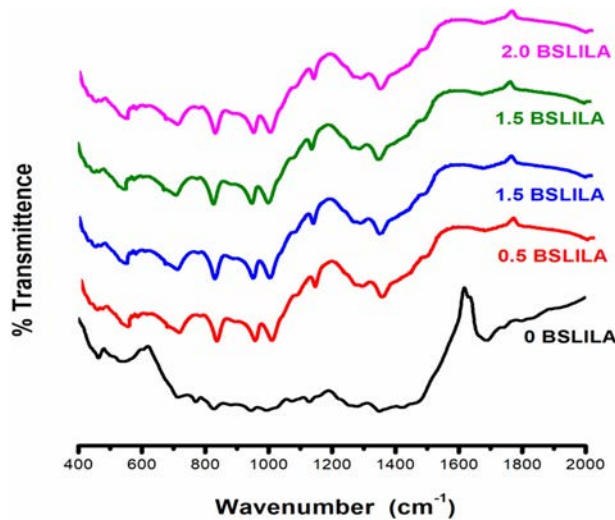
Figure 2. FTIR spectra of La_2O_3 doped lithium borosilicate glasses.
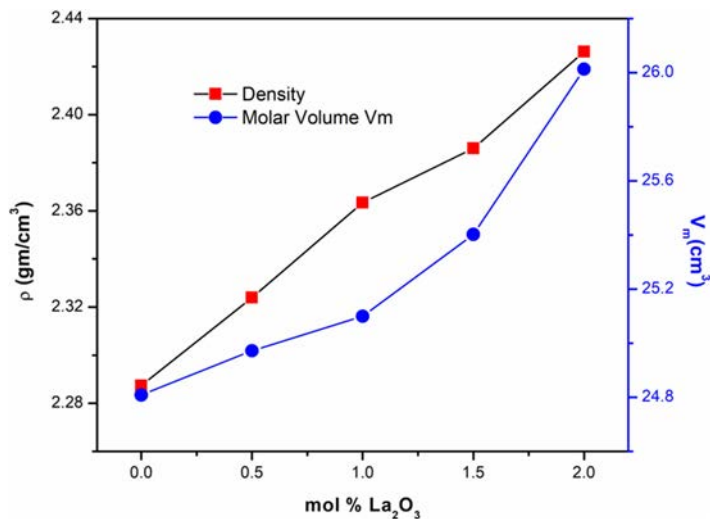
Figure 3. Variation of density and molar volume versus mol% La_2O_3.

Physical characteristics play a key role in appreciating the arrangement of the atoms in the glass network and in supplying useful knowledge on the structure of the glass. The standard formulae [6,7,9] were used to determine the lanthanum ions (N), the inter-nuclear distance (r_i), the polaron radius (r_p) and the field strength (F). Table 2 shows the estimated values for these physical parameters.

Table 2 reveals that the concentration of La^{3+} ions rises with a rise in La_2O_3 content. The incorporation of La^{3+} ions into interstices results in a reduction of the La-O inter-nuclear gap, thus growing the bond power. This contributes to higher field intensity around ions of La^{3+} [14,15].

Figure 4 displays the dc conductivity graph against temperature and is observed to satisfy the Arrhenius equation.

Table 2. Physical properties of lithium borosilicate glasses containing La$_2$O$_3$.

X mol %	Unit	0	0.5	1	1.5	2
P	(g/cm^3)	2.2873	2.3239	2.3634	2.3860	2.4262
V$_M$	(cm^3)	24.8081	24.9717	25.0991	25.4018	26.0129
N ($\times 10^{22}$)	(ions/cm^3)	–	1.2060	2.3997	3.5566	4.7218
r$_i$	(Å)	–	4.3607	3.4670	3.0408	2.7667
r$_p$	(Å)	–	1.7571	1.3969	1.2252	1.1148
F ($\times 10^{17}$)	(cm^{-2})	–	1.8463	2.9209	3.7970	4.5866
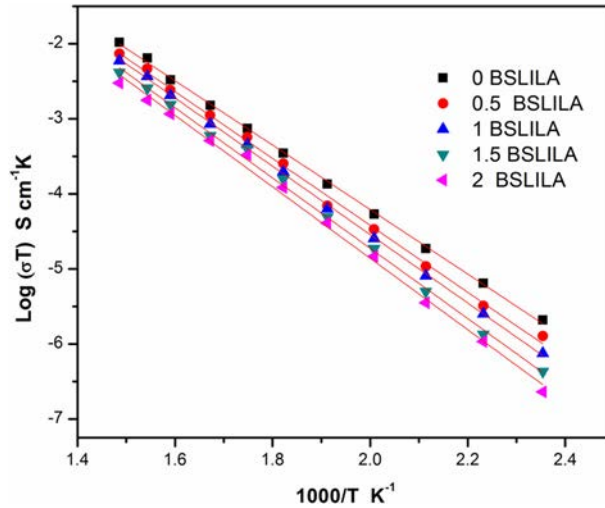
Figure 4. Variation of conductivity with temperature for La$_2$O$_3$ Doped lithium borosilicate glasses.

$$\sigma = \sigma_0 \exp\left(-\frac{E_a}{k_b T}\right) \tag{1}$$

where σ_0 is pre-exponential factor, E_a is activation energy, constant k_B is Boltzmann constant and T is temperature.

The slopes of these Arrhenius plots were used to determine activation energies. These activation energy data and conductivity at temperature 573 K have been depicted for different mol % of La$_2$O$_3$ in Fig. 5. These graphs demonstrate that with the addition of La$_2$O$_3$ the activation energy rises while the conductivity decreases. The lithium ion concentration was unchanged in the reported systems; thus, a drop in conductivity can be due to decreased empty sites for Li$^+$ ions. The decline in the number of empty sites could be attributed to the conversion of BO$_3$ into BO$_4$ units which is evidenced by the FTIR result. These findings are consistent with those obtained in borate, borosilicate and vanado-tellurite glasses [7,14,15].

The electric modulus model has been used to illustrate the relaxing behavior of studied glass system. Figure 6 shows the variance of the real part of electrical modulus component (M') with frequency for 1.5 mol % La$_2$O$_3$ glass samples.

It is evident from this figure, that the value of M' is closer to zero at low frequencies due to the absence of restoring forces for mobile Li + ions and M' rises as frequency rises [15,16]. Further M' achieves the maximal value conforming to $M\infty = (\varepsilon_\infty)^{-1}$
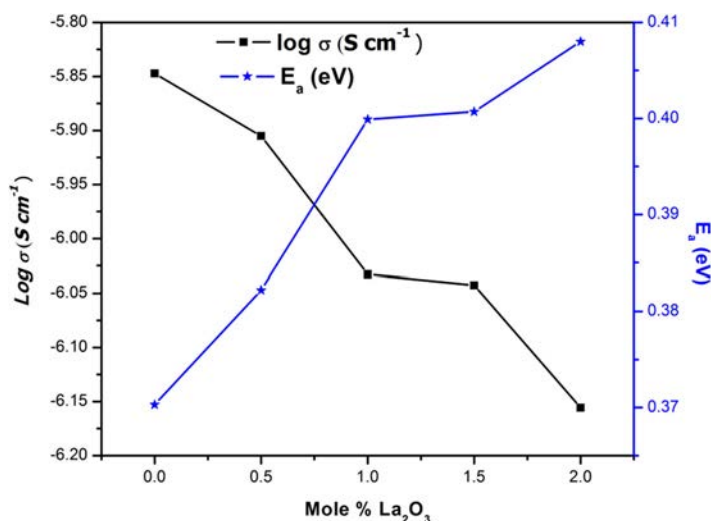
Figure 5. Variation of conductivity and activation energy with La_2O_3.
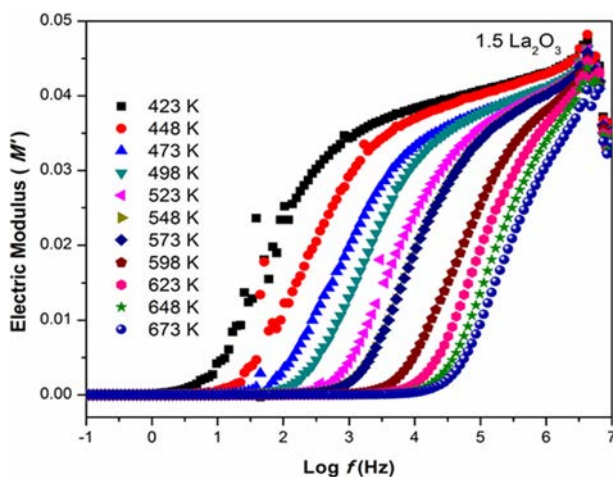
Figure 6. Variation of real part of electric modulus (M′) with frequency and temperature for 1.5 mol % La_2O_3 glass sample.

owing to relaxation processes [16,17]. The other samples in the analyzed sequence exhibit a similar qualitative pattern.

The plot of log of frequency versus the imaginary component of the equivalent electric modulus M″ has been presented in Fig. 7.

As can be shown from this figure, M″$_{Max}$ transitions to higher frequencies as the temperature increases. f_p denotes the center of relaxation peak and is often used to measure the relaxation period τ ($\tau = 1/2\pi fp$) under the condition $\omega_c\tau = 1$. The estimated relaxation period for 1.5 mole percent La_2O_3 is plotted against 1000/T in Fig. 8.

The activation energies $E_{a(DC)}$ and $E_{a(\tau)}$ are estimated using the Arrhenius equation for each sample in the series and are shown in Table 3. Due to the striking similarity
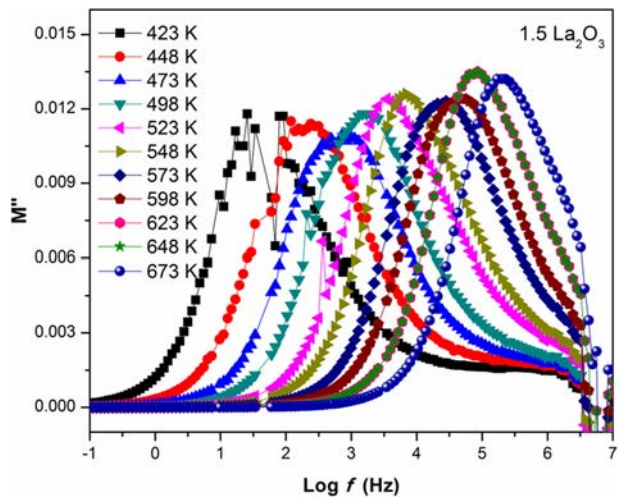
Figure 7. Variation of imaginary part of electric modulus (M") with frequency and temperature for 1.5 mol % La_2O_3 glass sample.
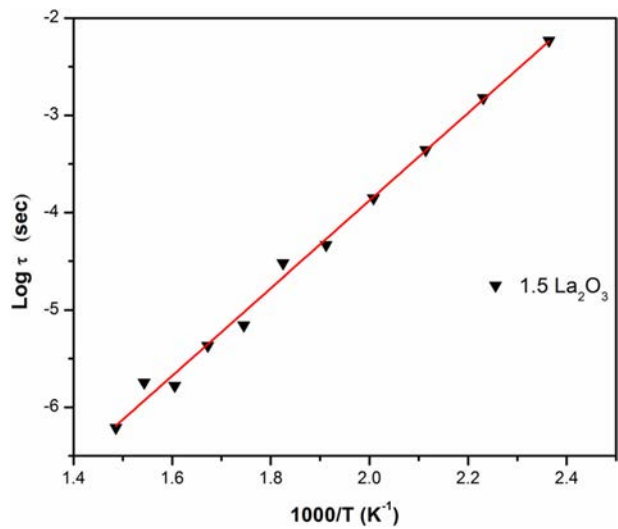
Figure 8. Variation of relaxation time with temperature for 1.5 mol% La_2O_3 glass sample.

Table 3. $E_{a(DC)}$ and $E_{a(\tau)}$ values for glass samples of BSLILA series.

Mole %	$E_{a(DC)}$ (eV)	$E_{a(\tau)}$ (eV)
0-BSLI	0.3703	0.3649
0.5-BSLILA	0.3822	0.3710
1-BSLILA	0.3999	0.3843
1.5-BSLILA	0.4007	0.3901
2-BSLILA	0. 4080	0.4010

between $E_{a(DC)}$ and $E_{a(\tau)}$, charge carriers will move across the same energy barrier during conduction and relaxation [14–16].

The outcome of a standardized plot using *Log (σ'/σ_{dc})* as the Y-axis parameter and *Log ($f/\sigma_{dc}T$)* as the X-axis parameter for a 1.5 mole percent La_2O_3 glass sample is seen
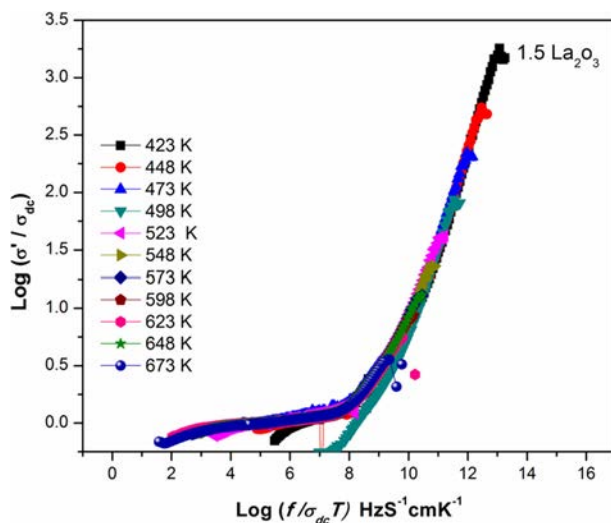
Figure 9. Conductivity scaling of 1.5 mol % La_2O_3 glass sample for different temperatures.
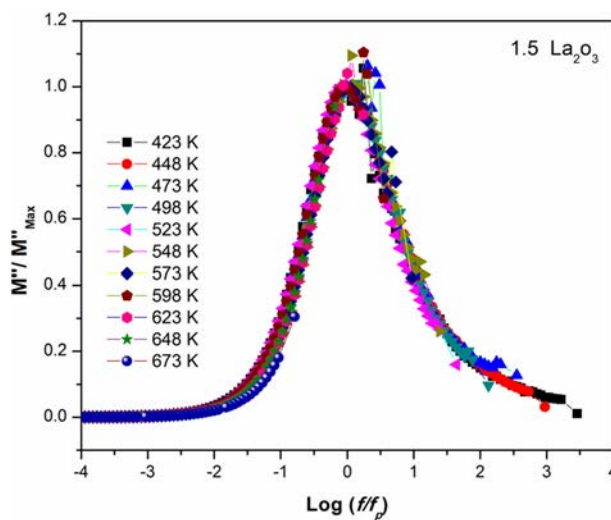
Figure 10. Imaginary component of electric modulus M''/M''_{max} as a function of Log f/fp for 1.5 mol % La_2O_3 glass sample at different temperatures.

in Fig. 9, where data for various temperatures converge on a single master curve. Similar nature graph is obtained for remaining glasses of the series.

The imaginary part of modulus is seen in Fig. 10 as a superimposed plot with scaled results. In this figure, the Y axis is scaled as (M''/M''_{Max}) and the X axis is scaled as Log Log (f/f_p). Figures 9 and 10 confirm that complex processes operating at various frequencies need almost the same thermal stimulation, implying that the conduction mechanism is temperature independent [16–22].

A mole percent factor was added to investigate the impact of composition on the conduction process. Y-axis is scaled with Log (σ'/σ_{dc}) and Log $(fx/\sigma_{dc}T)$ as a X-axis for
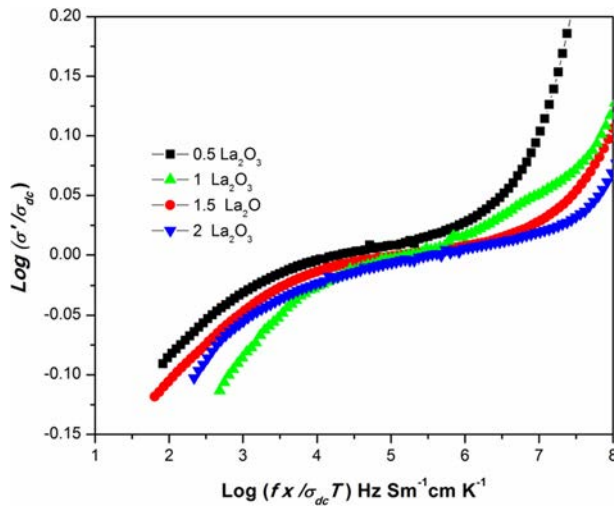
Figure 11. Scaling for different mol % La_2O_3 glass samples at 573 K.
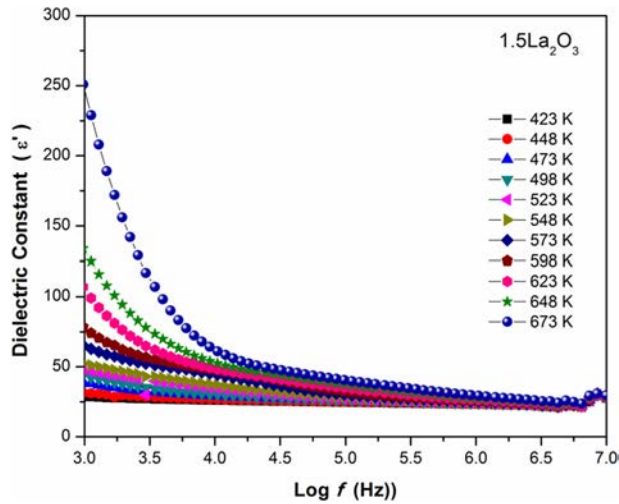
Figure 12. Dependence of dielectric constant (ε') on frequency of 1.5 mol % La_2O_3 glass sample for different temperature.

studied glass system. Figure 11 depicts data that does not constitute a single master curve. As a result of this research, it is established that the conduction process is compositional rather than temperature dependent [14–18].

The dielectric constant (ε') and dielectric loss (Tan δ) with a log of frequency for 1.5 mole percent La_2O_3 is presented in Figs. 12 and 13 (1.5 BSLILA). It is clear from these graphs that ε' and Tan δ decrease with increasing frequency and decreasing temperature. As can be seen from these results, the dielectric constant increases with decreasing frequency and increasing temperature, which is typical for oxide glasses [14–16]. The increase in ε' and Tan δ with temperature in the low frequency area may be a result of a decrease in bond capacity [14–16]. With the rise in temperature, dipolar polarization is influenced due to (i) improvement in orientational vibration caused by
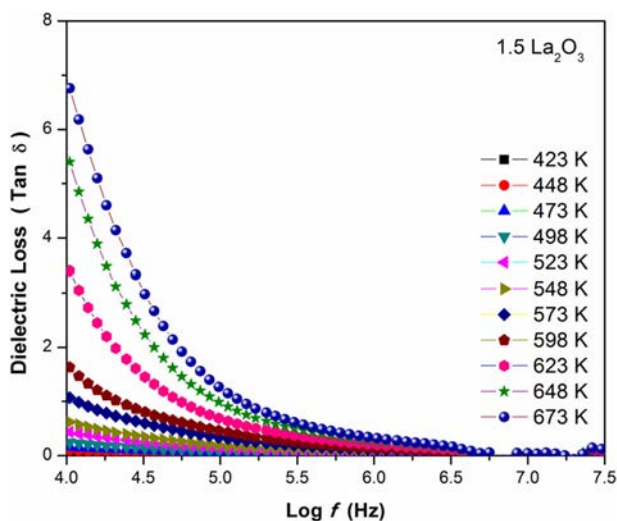
Figure 13. Dependence of dielectric loss (Tan δ) on frequency of 1.5 mol % La$_2$O$_3$ glass sample for different temperature.
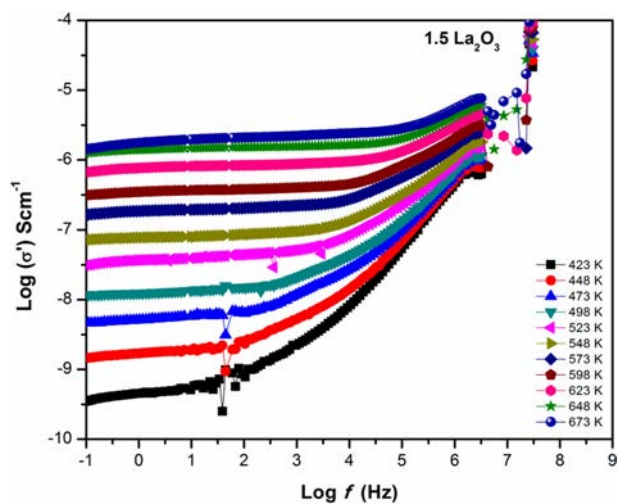
Figure 14. Variation of AC conductivity with frequency for 1.5 mol % La$_2$O$_3$ glass sample.

weakening intermolecular forces and (ii) a disruption in orientational vibration caused by thermal activation [14–16]. Charge accumulation occurs as a result of charge carriers hopping from low energy barrier sites to high energy barrier sites, resulting in enhanced net polarization and a high dielectric constant at low frequency [14–22]. At high frequencies, though, the failure of charge carriers to rotate quickly and appropriately results in a decrease in charge carrier oscillation, resulting in a decrease in dielectric constant and dielectric loss. Other glass samples of series exhibit comparable qualitative activity.

Figure 14 depicts the ac conductivity of a 1.5 mole percent La$_2$O$_3$ glass sample as a function of frequency at various temperatures (1.5 BSLILA).

This figure shows that ac conductivity rises with temperature at all frequencies, which is due to thermal activation. AC conductivity is temperature independent at low frequency and high temperature since the slope does not vary. However, at low temperature and high frequency, the slope changes, indicating that AC conductivity is frequency dependent. This change in the frequency independence of AC conductivity to frequency dependency indicates the initiation of the conductivity relaxing phenomenon [15,16]. Conductivity is frequency independent in the low frequency area owing to the arbitrary scattering of ionic charge, whereas conductivity exhibits dispersion at higher frequencies [14–16]. Related qualitative activity with other glass objects is detected.

4. Conclusion

The melt quench process was used to prepare La_2O_3 doped lithium borosilicate glasses. XRD study revealed that the formulated glass samples were amorphous in nature. The formation of BO_4^- units is confirmed by FTIR spectra. The increased density with addition of La_2O_3 is due to La_2O_3's higher molecular weight than other glass constituents. The measured values of various physical parameters, such as La^{3+} ion concentration (N), mean spacing between La^{3+} RE ions (r_i), polaron radius (r_p), and field intensity (F) of La-O bonds, endorse the variance of density (ρ) and molar volume (V_M). The addition of La_2O_3 in LBS glasses reduces the electrical conductivity. The normalized plot of Log (σ'/σ_{dc}) versus Log ($f/\sigma_{dc}T$) and M''/M''_{Max} versus Log (f/f_{Max}) of the obtained data demonstrates that complex processes occurring at different frequencies require nearly the same thermal activation energy. The Normalized plot of Log (σ'/σ_{dc}) versus Log ($fx/\sigma_{dc}T$) at 573 K demonstrates that the conduction process is compositional dependent and not temperature dependent. The dielectric constant (ε') and dielectric loss (Tan δ) of glasses decrease steadily with increasing frequency and decreasing temperature, which is due to electron hopping and bond energy difference in net polarization.

References

1. M. Neyret *et al.*, Ionic transport of alkali in borosilicate glass. Role of alkali nature on glass structure and on ionic conductivity at the glassy state, *J. Non. Cryst. Solids* **410**, 74 (2015). DOI: 10.1016/j.jnoncrysol.2014.12.002.
2. R. M. Mahani and S. Y. Marzouk, AC conductivity and dielectric properties of SiO_2–Na_2O–B_2O_3–Gd_2O_3 glasses, *J. Alloys Compd.* **579**, 394 (2013). DOI: 10.1016/j.jallcom.2013.05.173.
3. L. Maia, Electrical conductivity and relaxation frequency of lithium borosilicate glasses, *Solid State Ion.* **168** (1–2), 87 (2004). DOI: 10.1016/j.ssi.2004.02.016.
4. D. Manara, A. Grandjean, and D. R. Neuville, Structure of borosilicate glasses and melts: a revision of the Yun, Bray and Dell model, *J. Non-Cryst. Solids* **355** (50–51), 2528 (2009). DOI: 10.1016/j.jnoncrysol.2009.08.033.
5. S. S. Hajer *et al.*, Effect of lanthanum oxides on optical properties of zinc borotellurite glass system, *MSF.* **846**, 63 (2016). DOI: 10.4028/www.scientific.net/MSF.846.63.
6. V. Y. Ganvir and R. S. Gedam, Effect of La_2O_3 addition on structural and electrical properties of sodium borosilicate glasses, *Mater. Res. Express* **4** (3), 035204 (2017). DOI: 10.1088/2053-1591/aa66e4.
7. R. S. Gedam and D. D. Ramteke, Synthesis and characterization of lithium borate glasses containing La_2O_3, *Trans. Indian Inst. Met.* **65** (1), 31 (2012). DOI: 10.1007/s12666-011-0107-4.

8. S. R. Tiple et al., Effect of La_2O_3 on the electrical conductivity and thermal properties of proton conducting glasses, *AIP Conf. Proc.* **1512**, 600–602 (2013). DOI: 10.1063/1.4791180.

9. V. Y. Ganvir and R. S. Gedam, Influence of SM_2O_3 addition on electrical properties of lithium borosilicate glasses, *Integr. Ferroelectr.* **185** (1), 102 (2017). DOI: 10.1080/10584587.2017.1370346.

10. P. P. Pawar, S. R. Munishwar, and R. S. Gedam, Physical and optical properties of Dy3+/Pr3+ Co-doped lithium borate glasses for W-LED, *J. Alloys Compd.* **660**, 347 (2016). DOI: 10.1016/j.jallcom.2015.11.087.

11. S. Y. Marzouk et al., Linear and non-linear optics and FTIR characteristics of borosilicate glasses doped with gadolinium ions, *Opt. Mater. (Amst.)* **35** (12), 2077 (2013). DOI: 10.1016/j.optmat.2013.05.023.

12. P. P. Pawar et al., Physical, thermal, structural and optical properties of Dy3+ doped lithium alumino-borate glasses for bright W-LED, *J. Lumin.* **183**, 79 (2017). DOI: 10.1016/j.jlumin.2016.11.027.

13. V. K. Deshpande and A. P. Raut, Effect of gamma irradiation on the density, glass transition temperature and electrical conductivity of lithium borosilicate glasses with alumina addition, *J. Non. Cryst. Solids* **457**, 104 (2017). DOI: 10.1016/j.jnoncrysol.2016.11.028.

14. V. Y. Ganvir, H. V. Ganvir, and R. S. Gedam, Effect of Dy_2O_3 on electrical conductivity, dielectric properties and physical properties in lithium borosilicate glasses, *Integr. Ferroelectr.* **203** (1), 1 (2019). DOI: 10.1080/10584587.2019.1674947.

15. M. Prashant Kumar and T. Sankarappa, DC conductivity of rare earth ions doped vanado-tellurite glasses, *J. Non. Cryst. Solids* **355** (4–5), 295 (2009). DOI: 10.1016/j.jnoncrysol.2008.11.004.

16. D. D. Ramteke and R. S. Gedam, Study of Li_2O–B_2O_3–Dy_2O_3 glasses by impedance spectroscopy, *Solid State Ion.* **258**, 82 (2014). DOI: 10.1016/j.ssi.2014.02.006.

17. A. A. Bahgat, Study of dielectric relaxation in Na-doped Bi–Pb–Sr–Ca–Cu–O glasses, *J. Non-Cryst. Solids* **226** (1–2), 155 (1998). DOI: 10.1016/S0022-3093(97)00482-1.

18. E. K. Abdel-Khalek and A. A. Bahgat, Optical and dielectric properties of transparent glasses and nanocrystals of lithium niobate and lithium diborate in borate glasses, *Phys. B Condens. Matter* **405** (8), 1986 (2010). DOI: 10.1016/j.physb.2010.01.085.

19. B. Roling, Scaling properties of the conductivity spectra of glasses and supercooled melts, *Solid State Ion.* **105** (1–4), 185 (1998). DOI: 10.1016/S0167-2738(97)00463-3.

20. B. Roling et al., Carrier concentrations and relaxation spectroscopy: new information from scaling properties of conductivity spectra in ironically conducting glasses, *Phys. Rev. Lett.* **78** (11), 2160 (1997). DOI: 10.1103/PhysRevLett.78.2160.

21. P. Muralidharan, M. Venkateswarlu, and N. Satyanarayana, AC conductivity studies of lithium borosilicate glasses: synthesized by sol-gel process with various concentrations of nitric acid as a catalyst, *Mater. Chem. Phys.* **88** (1), 138 (2004). DOI: 10.1016/j.matchemphys.2004.06.032.

22. R. Pereira et al., Impedance spectroscopy study of SiO_2–Li_2O:Nd_2O_3 glasses, *J. Alloys Compd.* **597**, 79 (2014). DOI: 10.1016/j.jallcom.2014.01.151.

Taylor & Francis
Taylor & Francis Group

Check for updates

Mathematical simulation for the formulation of synthesis of PMN-PZN ceramics at different sintering temperature with reliability of density measurement

Mamta V. Takarkhede[a], Jayant P. Modak[b], Sheela. A. Band[c], Prerana M. Parakhi[d], and Leena C. Bhoyar[d]

[a]Department of Physics, JDCOEM, Nagpur, Maharashtra, India; [b]Department of Mechanical Engineering, JDCOEM, Nagpur, Maharashtra, India; [c]Department of Physics, YCCE, Nagpur, Maharashtra, India; [d]Department of Mathematics, JDCOEM, Nagpur, Maharashtra, India

ABSTRACT

This paper discusses the approach to formulate mathematical model (MM) for synthesis of any ceramic and to decide reliability of density measurement. In the research of basic science, the majority of operations are still executed manually which needs to be focused and develop a mathematical relation which simulate the real input and output data directly. The advantages and limitations of the developed mathematical models are identified and the models are classified in terms of range of application and goals. In this study, a generalized experimental data based model developed to simulate the contemporary techniques for the purpose of study, compression, inducing generalized approach for the mathematical model of ceramic synthesis. The findings indicate that the topic understudy is of great importance, as no such approach of experimental data based mathematical simulation is adopted for the formulation of synthesis of ceramics so far. Thus the results of this experimental research would be useful to industry for manufacturing of multilayer capacitors.

1. Objective of investigation

Current study was focused on mathematical model for characterization of ceramics of binary compositions 0.6PMN–0.4PZN synthesized by columbite method [1]. Lead based pervoskite ferroelectric relaxors like lead magnesium niobate $Pb(Mg_{1/3} Nb_{2/3})O_3$ (PMN) and lead zinc niobate $Pb(Zn_{1/3}Nb_{2/3})O_3$ (PZN) are attractive candidates for applications such as multilayer capacitors (MLC), actuators and medical ultrasonic transducers due to its high dielectric constant, broad dielectric maxima, high electrostrictive strain response and relative low firing temperature [2–6].

It is know that any mathematical model is a simulation process of any phenomenon. Mathematical model is vital process of the final system which is in reality a collection of conceptual, physical, mathematical, visualization, and possibly statistical sub-models [7]. Quantitative results from mathematical models can easily be compared with observational data to identify the strength of the model and weaknesses. To estimate
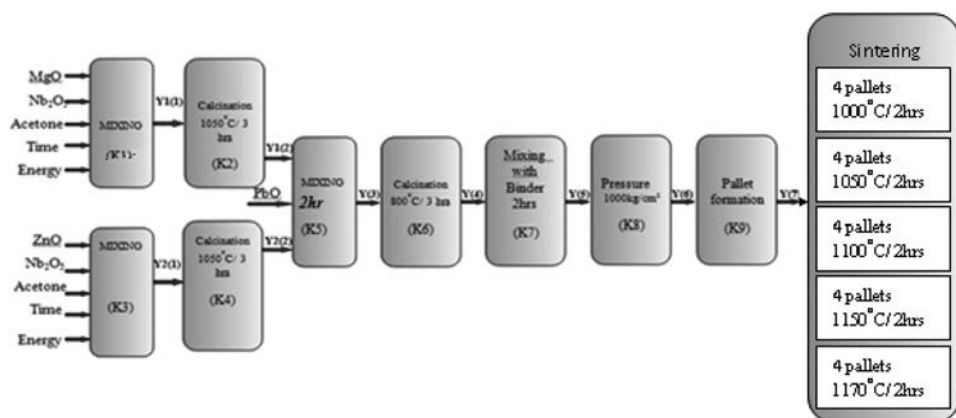
Figure 1. Block Representation of Synthesis Process of 0.6PMN-0.4PZN.

numerical output from mathematical model is to help to understand the model performance. In addition to assess the capability of model to simulate important features of the natural occurrence. By using this information back into the model development process will enhance model performance.

2. Experimental Investigations

In the present study, 0.6PMN-0.4PZN ceramic was prepared by Columbite method [1] which is the simple and most reliable among the several methods for synthesis of lead based ceramics to get reproducible dielectric properties. Steps involved in synthesis are described as below.

The raw materials like MgO, Nb_2O_5 are mixed together with acetone with proper stoichiometric in agate mortar for $1\,h = 3600\,s$ with manual energy [8] for human stiring $\approx 200\,Nm$ to get homogeneous mixture. This is based on the fact that normal human energy input rate is 0.124 hp in continuous duty. Similarly, raw materials like ZnO, Nb_2O_5 are mixed together with acetone in agate mortar for 1 h with energy almost same. After mixing both mixtures MN and ZN are calcinated in two different alumina crucibles simultaneously in furnace for 3 h at 1050 °C.

The dried MN or ZN and PbO were ground well separately for 2 hrs. in proper stoichiometric formula with acetone in an agate mortar with energy input of 400 Nm to get a homogeneous mixture. The homogeneous mixture was then calcined at calcination temperatures 800 °C for 2 h. Subsequently 1.7 wt% polyvinyl acetate (PVAc) as a binder was mixed with the calcined powder of PMN-PZN. Subsequently, homogeneous mixture was pressed into pellets 1–2 mm thickness and 1 cm diameter. The pellets were sintered in closed alumina crucible at temperatures between 1000–1170 °C for 2 h. The rate of heating during calcination and sintering was 10 °C per/min [9]. Later the Pellets were furnace cooled. Block Representation of Entire Process of Formation of 0.6PMN-0.4PZN is shown in Fig. 1.

2.1. Densities Measurement of PMN-PZN

Densities of the sintered pallets at temperatures between 1000–1170 °C were measured by Archimedes water displacement method. The density measurement was carried out

Figure 2. Density measurement.

by the Archimedes' water displacement method by Mettler Toledo XS105, R. T. M Nagpur University Campus, India (Fig. 2). In the present study, thickness and diameter of all the pellets were measured and theoretical density was calculated.

At room temperature, PMN exhibit cubic structure with lattice cell constant 'a'= 4.049 Å and theoretical density of PMN, PZN and 0.6PMN-0.4PZN are 8.1389 g/cm^3, 8.4771 g/cm^3 and 8.27411g/cm^3, respectively. Experimentally densities of the sintered specimens were measured by the Archimedes water displacement method. and relative density is calculated by

$$\% \text{ Relative density} = \frac{Experimental\ Density}{Theoretical\ Density} \tag{1}$$

3. Mathematical Simulation of Experimental Process

3.1. Nomenclature of Involved Variables

The variables which affect the synthesis of ceramic were selected. At preliminary stage, more parameters were selected based on the material and environmental parameters. Later on, to reduce the variables in number, some variables are clubbed together while some variables which seemed to be uncontrollable or least affecting, those parameters were discarded. Finally a set of attributes were selected as follows:

3.1.1. Transformation Factor

In Fig. 1, the block representing conversion of MgO, Nb$_2$O$_5$, acetone in already stated quantities were mixed at a certain input energy rate for certain duration which precipitated Y1(1) i.e. MN. This transformation process is stimulated by a transformation factor K(1). The magnitude of K(1) in terms of input physical quantity to the process and output physical quantity from the process is defined by transformation factor which in this case K(1). Likewise for every process, the transformation factors are estimated K2, K3, K4, K5, K6, K7, K8 and K9 are mentioned in respective block in Fig. 1.

3.2. Mathematical Model for Formation of MN and ZN

The mixing process under consideration for formation of MN and ZN presented in Fig. 3(a) and Fig. 3(b), respectively, in a block form. The input quantities for this process
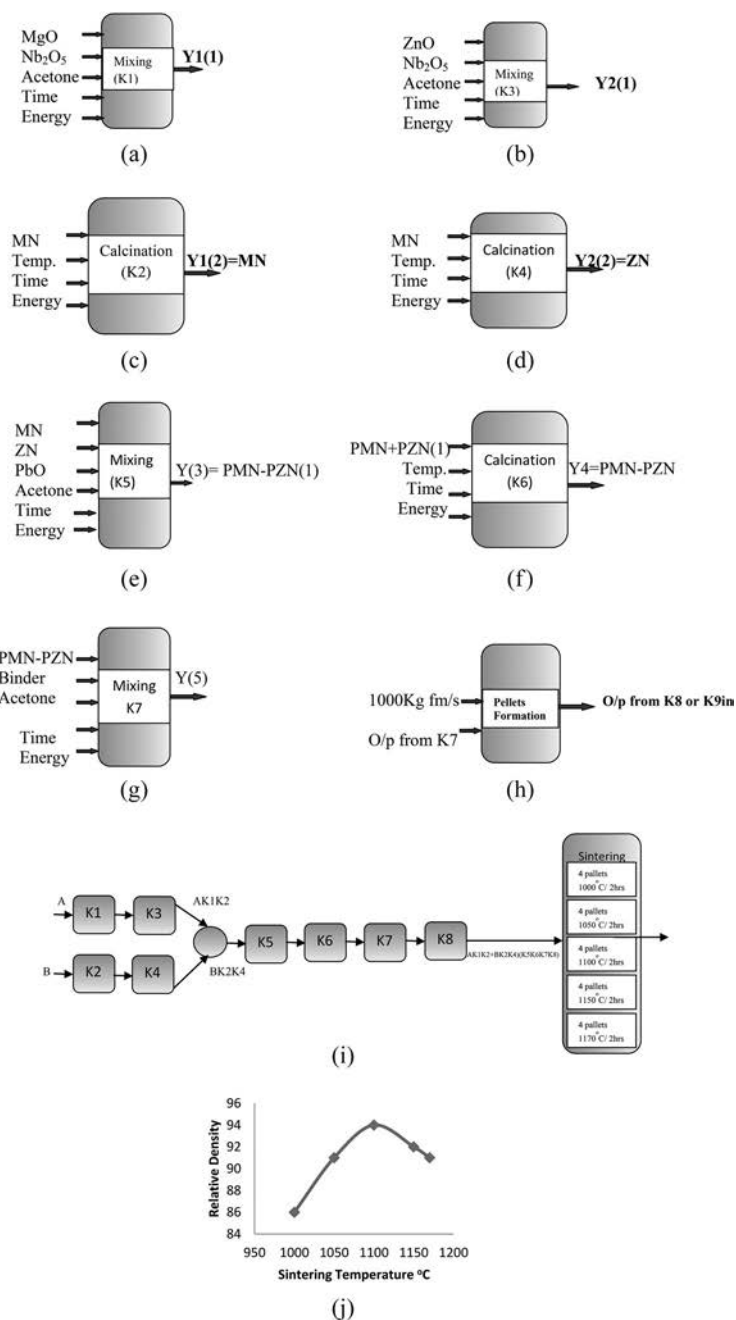
Figure 3. (a) and (b) Block Representation of Formation of Required MN and ZN. (c) and (d) Block Representation of Calcination of MN and ZN. (e) Block Representation of Formation of model of PMN-PZN. (f) Block Representation of Calcination of PMN-PZN. (g) Block Representation of formation of model for mixing with binder of PMN-PZN. (h) Block Representation of formation of model for Pallet Formation of PMN-PZN. (i) Block Representation of formation of model for sintering of PMN-PZN. (j) Graphical Representation relative density at sintering temperature of PMN-PZN.

Table 1. Nomenclature of involved variables.

S. No.	Variable	Symbol	Quantity
1	MgO	X	2.7079 gm
2	Nb_2O_5	Y	17.2929 gm(for MN)
			7.6562 gm (for ZN)
3	Acetone	Z	200 cc(for MN& ZN),
			400 cc(for PMN + PZN)
4	ZnO	X	0.2343 gm
5	MN	Y1(1)	3.7074 gm(for PMN + PZN)
6	ZN	Y2(2)	2.7985 gm(for PMN + PZN)
7	PbO	P	13.4939 gm (for PMN + PZN)
8	Polyvinyl acetate	Q	0.34 gm
9	Time	T	10,800 sec(for MN& ZN)
			7200 sec(for calcination and sintering)
10	Energy	E	7.2×10^5 Nm
11	Yield strength of steel(f/A)	S	20×10^3
12	Acceleration due to gravity	g	9.8m/s
13	Boiling point of water	Θ	100°C
14	Calcination Temperature	θ_1	1050°C
15	Calcination Temperature	θ_2	800°C
16	Sintering Temperature	θ_3	1000°C
17	Sintering Temperature	θ_4	1050°C
18	Sintering Temperature	θ_5	1100°C
19	Sintering Temperature	θ_6	1050°C
20	Sintering Temperature	θ_7	1070°C

are quantities of MgO, Nb_2O_5 and acetone for MN and ZnO, Nb_2O_5 and acetone for ZN. The mixing is done manually. Mixing process needs energy. Here it is human energy. The continuous duty human energy output is 0.13 hp [10]. It is assumed in this case, that the operator has worked at 0.3 hp level based on pulse rate rise during mixing operation. This comes to energy input rate for mixing as 200 Nm/s. This parameter K1 and K3 represent the extent, to which the input to this phenomenon precipitated the output as shown in Fig. 3.1, represents the phenomenon of mixing process in terms of each cause (independent variable) and effects (dependent variable). The quantity of the independent variables and dependent variables are already known through experimentation already presented in Tables 1 and 2. The magnitude of K1 and K3 are evaluated as detailed below. The time duration of mixing process is 1 h =3600 s. As a result of mixing process at the end of 1 h, one gets Y1(1), i.e., MN and Y2(1), i.e., ZN

Therefore this process can be represented in mathematical form as under [11]

$$Y1(1) = f_1(x, Y, Z, t, g, E) \tag{2}$$

Where f_1 states for function of "x, Y, Z, t, g, E"
Equation (1) can be put in dimensionless form as under

$$\frac{Y1(1)}{x} = f\left(\left(\frac{Z}{Y}\right), \left(\frac{E}{Y(gt)^2}\right)\right) \tag{3}$$

Assuming probable mathematical form of Eq. (2), it can be said that

$$\frac{Y(1)}{x} K1 \left(\frac{Z}{Y}\right) \left(\frac{E}{Y(gt)\hat{2}}\right) \quad i.e. \tag{4}$$

Table 2. Quantitative transformation factor and out-put for different processes are as follows: quantitative transformation factor is similar to transformation in actual system.

S. No.	Process	Out-put	Coefficient
1	Mixing of MgO, Nb_2O_5, Acetone $=$ MN	Y1(1)$=$MN(1)	K1
2	calcination MN	Y1(2)$=$MN	K2
3	Mixing of ZnO, Nb_2O_5, Acetone $=$ ZN	Y2(1)$=$ZN(1)	K3
4	calcination ZN	Y2(2)$=$ZN	K4
5	Mixing of MN, ZN, PbO, Acetone $=$ PMN-PZN	Y(3)$=$PMN-PZN(1)	K5
6	calcination PMN-PZN	Y(4)$=$ PMN-PZN	K6
7	Mixing of PMN-PZN with binder	Y(5) $=$PMN $+$ PZN $+$ Binder	K7
8	pallet formation of PMN-PZN	Y(6)$=$ Pallets (20)	K8
9	sintering PMN-PZN pallets	Y(7)	K9

Table 3. % Relative density (Yexpt) at different sintering temperature.

Sr.No .	Sintering temperature(^{o}C)	X (K9-Output)	% Relative density (Yexpt)
1	1000	4.6726×10^{-6}	86.000
2	1050	5.149×10^{-6}	91.000
3	1100	5.2588×10^{-6}	94.000
4	1150	5.764×10^{-6}	92.000
5	1170	5.794×10^{-6}	91.000

Table 4. Difference between calculated Y and Expt. Y.

S.No.	Density(Expt.Y)	Calculated Y	Difference between Expt Y and Calculated Y
1	86.000	85.99339124	-0.007
2	91.000	90.99312	-0.00688236
3	94.000	93.99305	-0.006949164

By using proper input quantities and performing above calculation of Eq. (4), K1 is found to be 35.38. Similarly mixing process of ZnO, Nb_2O_5 and acetone is represented as

$$Y2(1) = f2(X, \ Y, \ Z, \ t, \ g, \ E) \tag{5}$$

Equation (5) can be put in dimensionless form as under

$$\frac{Y2(1)}{X} = f\left(\frac{Z}{Y} \quad \frac{E}{Y(gt)\hat{2}}\right) \tag{6}$$

$$\frac{Y2(1)}{X} = K3\left(\frac{Z}{Y}\right)\left(\frac{E}{Y(gt)\hat{2}}\right) \tag{7}$$

And K3 is found to be 60.51.

3.3. Formation of Mathematical Model of Calcinations of MN and ZN

After mixing MN(1)$=$Y1(1) and ZN(1)$=$Y2 (1) are calcinated in alumina crucible separately in furnace for 3 hrs.(i.e.$=$ 10,800 s) at 1050 $^{\circ}$C (i.e., θ1). The coefficient of calcinations of MN process and output of calcinations of MN are designated as K2 and Y1(2)$=$MN respectively.

While for ZN, the coefficient of calcination of ZN process and output of calcinations are designated as K4 and Y2(2)$=$ZN, respectively. Energy input during 10,800 s is 1.3572×10^7

Table 5. Reliability of density at different temperature.

Equationn	Avg Error	Relability= (1-Avg Error)*100
1	−1.7E-13	100
2	0.010784	98.921
3	1.2E-13	100
4	−0.00246	100.2459
5	−3.8E-13	100

Therefore process can be represented in mathematical form as under.

$$Y1(2) = f (Y1(1), g, t, E, \theta 1) \tag{8}$$

$$Y2(2) = f (Y2(1), t, g, E, \theta) \tag{9}$$

Equations (8) and (9) can be put in dimensionless form by assuming calcinations coefficient K2 and K4 for calcinations process of MN and ZN respectively.

$$\frac{y1(2)}{Y1(1)} = K2\left(\frac{E}{Y1(1)(gt)\hat{2}}\right)\frac{\theta 1}{\theta} \tag{10}$$

$$\frac{y2(2)}{Y2(1)} = K4 \ \frac{E}{Y2(1)(gt)\hat{2}} \ \frac{\theta 1}{\theta} \tag{11}$$

The values of K2 = 13.593 and K4 = 2.19984 are found.

3.4. Formation of Mathematical Model of PMN-PZN

The dried MN = Y1(2) or ZN = Y2(2) and PbO = p were ground well manually for 2 h (=7200 s) in proper stoichiometric formula with acetone(400 cc = Z) in an agate mortar with energy E = 28.8 × 10^5 Nm to get a homogeneous mixture. Let us consider the mixing coefficient is K5 and its out is Y(3). Therefore, process can be represented in mathematical form as

$$Y(3) = f\left(Y1(2), \ \frac{Y2(2)}{p}, \ \frac{E}{Z(gt)\hat{2}}\right) \tag{12}$$

Equation (11) can be put in dimensionless form as under

$$\frac{Y(3)}{Y1(2)} = K5 \left[\frac{Y2(2)}{p} \ \frac{E}{Z(gt)\hat{2}}\right] \tag{13}$$

$$K5 = 179876.2875$$

3.5. Formation of Mathematical Model Calcinations of PMN-PZN

The homogeneous mixture was then calcined at calcinations temperatures 800 °C/2 h with calcinations coefficient K6 and its out is Y(4) with energy E = 0.9048 × 10^7.

$$\frac{Y(4)}{Y(3)} = K6\left(\frac{E}{Y(3)*g*t^2}\right) \ \frac{\theta 2}{\theta} \tag{14}$$

Therefore the result of above process i.e. K6 is 13.756.

3.6. Formation of Mathematical Model for Mixing with Binder of PMN-PZN

After that 1.7 wt. % polyvinyl acetate (PVAc) as a binder (Q) mixed with the calcined powder of PMN-PZN manually for $\frac{1}{2}$ h $= 1800$ s by using 100 cc Acetone. Let us assume that coefficient of mixing is K7 which is calculated as 1.1955 by using

$$\frac{Y(5)}{Y(4)} \ = \ K7 \ \left(\frac{Z}{Q}\right)\left(\frac{E}{Y4 \ (g.t)\hat{2}}\right) \tag{15}$$

3.7. Formation of Mathematical Model for Pellets Formation of PMN-PZN

$$O/p \ from \ K8 = \ O/p \ from \ K7 \ *(1000/Yield \ strength \ of \ steel)$$

Subsequently, homogeneous mixture of PMN-PZN was pressed into pellets with 1-2mm thickness and 1 cm diameter. Let us assumed that K8 is coefficient of pallet formation and its output is Y(6). Let Yield strength of steel is 1.454×10^3 kgf/cm^2 and 0.687 transfer function with Out-put From K8 is 0.0837453.

3.8. Formation of Mathematical Model for Sintering of PMN-PZN

The pellets were sintered in closed alumina crucible at different temperatures between 1000–1170 °C for 2 h. The rate of heating during calcination and sintering was 10 °C per/min [7]. Later the Pellets were furnace cooled. This process in a block diagram form can be represented as below.

The calculated values of A, B and K8 o/p are 8.877×10^{-4}, 1.7343×10^{-4} and 0.21834 respectively with relative density at different sintering temperature (1000–1170 °c) are in the range of 5.58×10^{-5} to 6.92×10^{-5}.

3.9. Density Reliability Model

It is observed that density of ceramics increases with increase in sintering temperature and decreased after 1150 °C as shown in Fig. (2).

The decrease in density at higher sintering temperature greater than 1100 °C is due to loss of PbO which result in conversion of pervoskite to pyrochlore .The decrease in density at higher sintering temperature greater than 1100 °C is due to loss of PbO which result in conversion of pervoskite to pyrochlore [12].The reliability of sintered pallets were calculated by using a formula

$$Reliability = (1 - Avg \ Error) * 100 \tag{16}$$

From above table let us take different combinations any values of densities i.e. (1,2,3); (1,2,4); (1,2,5); (1,3,2); (1,3,4); (1,3,5); (1,4,2); (1,4,3); (1,4,5); (1,5,2); (1,5,3) etc.

From this graph (2j) we get

$$Y = A_0 + A_1 X + A_2 X^2 \qquad (17)$$

Form first set of combination (1,2,3) following equations are formed [13]

$$86 = A_0 + A_1(4.6726 \text{ x } 10^{-6}) + A_2(2.18332 \text{ x } 10^{-11}) \qquad (18)$$

$$91 = A_0 + A_1(5.149 \text{ x } 10^{-6}) + A_2(2.65122 \text{ x } 10^{-11}) \qquad (19)$$

$$94 = A_0 + A_1(5.2588 \text{ x } 10^{-6}) + A_2(2.7655 \text{ x } 10^{-11}) \qquad (20)$$

On solving above equations we get

$$Ao = 727.58,$$

$$A1 = 27143618$$

$$A2 = 2.87052 \times 10^{13}$$

After that calculate values of Ycal by using above value of A0, A1, A2 using Eq. (17), i.e. $y = A_0 + A_1 X + A_2 X^2$,

$$\mathbf{Y} = 727.58 + (27143618)\mathbf{X} + (2.87052 \text{ x } 10^{13})\mathbf{X^2} \qquad (21)$$

Thus from Eq. (17)

$$\text{For } X = 4.6726 \times 10^{-6} \text{ we get } Y = 85.99339124 \qquad (22)$$

$$\textbf{For } X = 5.149 \times 10^{-6} \text{ we get } Y = 90.99312 \qquad (23)$$

$$\text{For } X = 5.2588 \times 10-6 \text{ we get } Y = 93.99305 \qquad (24)$$

In this way we have to find out the difference of all y by using different sets of combinations.

Then find the average error of each equation.

$$\text{Reliability} = (1 - \text{Avg Error}) * 100 \qquad (25)$$

Thus the result indicate that the study under consideration with 100% reliability (Tables 3–5).

4. Conclusion

We have successfully demonstrated the synthesis and mathematical modeling of 0.6PMN-0.4PZN ceramic at different sintering temperature. Through the mathematical interpretation, we have studied % reliability of density measurement. The errors in measurement are negligible. The findings stipulate that the topic understudy with 100% reliability. Thus the results of this experimental research would be useful to industry for manufacturing of multilayer capacitors.

Reference

[1]   S. L. Swartz, and T. R. Shrout, Fabrication of peroskite lead magnesium niobate, *Mat. Res. Bull* **17** (10), 1245 (1982). DOI: 10.1016/0025-5408(82)90159-3.

[2] A. A. Bokov, and Z. G. Ye, Recent progress in relaxor ferroelectrics with perovskite structure, *J. Mater. Sci.* **41** (1), 31 (2006). DOI: 10.1007/s10853-005-5915-7.

[3] B. N. Rolov, Effect of compositional fluctuations on unshrap phase transition, *Solid State (Engl. Transl)* **6**, 1676 (1965).

[4] C. A. Randall *et al.*, Classification and consequences of complex lead perovskite ferroelectrics with regard to B- site cation order, *J. Mater. Res.* **5** (4), 829 (1990). DOI: 10.1557/JMR.1990.0829.

[5] G. Robertas *et al.*, Broad distribution of relaxation times in 0.6PMN-0.4PZN relaxor ceramics, *Ferroelectrics* **353** (1), 3 (2007). DOI: 10.1080/00150190701367002.

[6] M. V. Takarkhede, and S. A. Band, Large dielectric response of 0.6PMN-0.4PZN relaxor ferroelectric ceramic for multilayer capacitors, *Ferroelectrics* **514** (1), 70 (2017). DOI: 10.1080/00150193.2017.1357955.

[7] J. P. Modak, and A. R. Bapat, Formulation of a generalized experimental model for a manually driven flywheel motor and its optimization, *Appl. Ergon.* **25** (2), 119 (1994). DOI: 10.1016/0003-6870(94)90075-2.

[8] K. Murrell, *Ergonomics, Man in His Working Environment* (Springer, Netherlands, 1965), Vol. 1, pp. 496.

[9] Y. I. Liou Cheng, and L. Wu, Effect of heating rate on the dielectric properties of PMN-PT relaxor ceramics, *J Am. Ceram. Soc.* **77** (12), 3255 (1994). DOI: 10.1111/j.1151-2916.1994.tb04579.x.

[10] P. B. Khope, and J. P. Modak, Development and performance evaluation of a human powered flywheel motor operated forge cutter, *In. J. Sci. Technol. Res.* **2** (3) 146–149 (2013).

[11] H. Schenck, *Theories of Engineering Experimentation* (McGraw-Hill Inc., New York, 1979)

[12] T. R. Shrout, and A. Halliyal, Preparation of lead-based ferroelectric relaxors for capacitors, *Am. Ceram. Soc. Bull.* **66**, 704 (1987).

[13] L. R. Harvill, and L. A. Pipes, *Applied Mathematics for Engineers and Physicists* (Dover Publications Inc., 2014).

A Case Report on Mucocutaneous Leishmaniasis

Sahil Kirade [a*†], Priyanka Meshram [a‡], Roshan Umate [b¥] and Hemlata Wasnik [c]

[a] *Florence Nightingale Training College of Nursing, Datta Meghe Institute of Medical Sciences, Sawangi (M), Wardha, Maharashtra, India.*
[b] *Jawaharlal Nehru Medical College, Datta Meghe Institute of Medical Sciences, Sawangi (M), Wardha, Maharashtra, India.*
[c] *Department of Applied Physics, Yeshwantrao Chavan College of Engineering, Nagpur, India.*

Authors' contributions

This work was carried out in collaboration among all authors. All authors read and approved the final manuscript.

Case Report

ABSTRACT

Mucocutaneous Leishmaniasis (ML) can have devastating consequences, although early detection can help avoid difficulties. This research aims to explore clinical markers that can detect ML early. The protozoal infection Leishmaniasis is caused by fungal pathogens. The skin and mucosa are affected by mucocutaneous leishmaniasis (MCL). India is home to species like Leishmania donovani and Leishmania major, which cause visceral and epidermal leishmaniasis, respectively.
The Main Diagnosis, Therapeutic Intervention and Outcome: Mucocutaneous Leishmaniasis was diagnosed after a physical examination and investigation by the doctor. Patient was treated antiepileptic drug and antianxiety drugs to reduce fear and anxiety.
Therapeutic Intervention: Antipyretics and antibiotics such as Tab. Paracetamol, Injection Ceftriaxone 1 gm IV (BD), Tablet Pantoprazole 40 Mg iv (OD), Inj. Ondansetron 4 mg iv (TDS) were given for 7 days in this instance with Narcolepsy.
Outcome: For fever, the patient was given medications prescribed by the doctor, such as paracetamol. In addition, the patient's condition improved as a result of the medical treatment. The patient's problems had subsided, and he reported feeling better.
Nursing Perspectives: To control fever, the patient was given medications prescribed by the doctor, such as paracetamol. In addition, the patient's condition improved as a result of the medical treatment. The patient's problems had subsided, and he was in better shape.

[†]*GNM 2nd Year;*
[‡]*Nursing Tutor;*
[¥]*Research Scientist;*
Corresponding author: E-mail: sahilkirade@gmail.com;

Conclusion: The patient was admitted to A.V.B.R. Hospital with a headache, breathing difficulties, muscle weakness, walking difficulties, reduced balance and coordination, and other symptoms. In this case of Mucocutaneous Leishmaniasis, the patient received the necessary treatment and medications. The condition of the patient had improved.

1. INTRODUCTION

Leishmaniasis is a parasite infection in tropical parts of the world and southern Europe. It's thought to be a tropical illness that has gone undiscovered (NTD). Leishmaniasis is caused by parasitic infection with Leishmania parasites, disseminated via the bite sand flies [1,2]. In Brazil and neighboring regions, leptospirosis (ATL) is a major public health issue. It is the second most popular protozoa-related disease, after malaria, and is found in 88 countries. Minas Gerais ranks eighth in Brazil and first in Southeastern Brazil in terms of reported instances. ATL transmission has been confirmed in 401 of the state's 853 communities. Between 2001 and 2006, 100 people died due to the disease [3,4].

ATL is a non-contagious viral infection caused by different types of Leishmania parasites that affect the skin and mucosae. It is predominantly a zoonotic illness that affects animals other than humans and can cause secondary infestation [5,6]. Nasal and or oral mucosae involvement is often more severe than cutaneous involvement. Furthermore, the psychological stigma associated with this condition has yet to be evaluated by health surveillance services, as only individuals who experience its repercussions may feel it. This disease's psychological, social, and behavioral repercussions are more important than the physical discomfort. The biological component that governs parasite spread is development time, and it is one of the primary drivers of the severity and consequences of mucosal ulcers [6,7]. The incubation time for ATL varies greatly. When the inoculation time is known, infection in closed communities has a time of incubation of 10 to 60 days. The cutaneous form of the illness predominates in 95 percent of reported cases, with the mucosal variety accounting for 3 percent to 5 percent of cases [8,9].

2. PATIENT INFORMATION

2.1 Patient-Specific Information

In A. V. B. R. H., a 29-year-old man was admitted on 06-07-21, with the chief complaint of loss of muscle control, breathlessness, or muscle weakness, fatigue or hallucinations, difficulty with gait, impaired balance and coordination, fever, headache, and chills, the doctor diagnosed a case of Mucocutaneous Leishmaniasis after a physical examination and investigation.

Medical History: On 06th July 2021, a 29-year-old male patient was admitted to the A. V. B. R. hospital. The patient had history of feeling very sick. He had been suffering from loss of muscle control, muscle paralysis, muscle weakness, weariness, or hallucinations for a few days and they were getting worse. He had fever, headache, chills, and breathlessness five days before admission, and he took illicit drugs at regular doses on his own.

Family History: He belongs to nuclear family. In the patient's family, there is no hereditary history like DM, Asthma, Hypertension, etc.

Psycho-Social History: He was mentally stable, conscious and oriented to date time and place. He had maintained a good relationship with doctors and nurses and other patients.

2.2 Clinical Finding

Physical Examination: Obesity is thought to be linked to the illness. Patients with cataplexy usually have atonia in their limbs and neck muscles, as well as a loss of deep tendon reflexes.

Important Clinical Findings: Blood Investigation: WBC:-<5000 cells/mm3. RBC: -20,000-40,000 (cells/mcL), IgM and IgG test Positive, Platelet count 12,000 cells/mm^3

Timeline: He took treatment in A. V. B. R. H. and got the proper treatment. Taking proper medication and now he has been good condition.

Therapeutic Interventions: Present case of took the Mucocutaneous Leishmaniasis, antipyretics are drugs that are administered to people who have a fever. Tablet Paracetamol BD, Injection Ceftriaxone 1gm IV (BD), Injection

Pantoprazole 40 Mg IV (OD), Injection Ondansetron 4mg Intravenous (TDS).

Nursing Perspectives: Fluid replacement (DNS and RL) is administered, and vital signs are monitored hourly. 2 hourly temperature chart was rigorously adhered to, as was the intake output chart. Tab. Antibiotics with paracetamol were prescribed by the doctor.

3. DISCUSSION

ML was discovered in people who had granulomatous nasal/oral lesions that aren't specific. A history of skin lesion or a scan showing skin leishmaniasis did not appear to be a good predictor of mucosal leishmaniasis diagnosis in the current study. In this study, 62% of the patients had no recollection of skin involvement and no possibly a scar from a prior lesion. This is significant information because it demonstrates the limited value of using the patient's bad history of prior leishmaniasis or the absence of a scar as markers not to consider the diagnosis hypothesis of mucous membrane leishmaniasis in a diagnosis of chronic rhinitis without a patient in a diagnose rhinitis without the need for a patient. As confirmed by the current work, we are left with immunological testing to help identify mucosal leishmaniasis because the parasite is not usually identified in skin lesions [10,11].

The major issue of the Health Department's Leishmaniasis Tegumentary Americana Surveillance Program, which aimed to reduce deformities caused by the disease, is early mucosal leishmaniasis detection [12,13].

The extended delay between the onset of symptoms and an etiology diagnosis of mucosal leishmaniasis may indicate a lack of training in most physicians on a right approach for mucous membrane leishmaniasis, either by the family physician or by the infectious disease specialist. (Who is frequently not trained to properly approach nasal complaints) or by the specialist (who frequently only performs a nasopharyngeal biopsy, which is non-conclusive in most cases in mucosal leishmaniasis) [14].

Diagnostic delays, which lasted six years in the current research, might be explained by the patients' failure to seek medical attention. Nonetheless, because persistent nasal blockage is a complaint that directly impacts an individual's quality of life and ability to work, it's improbable that the delay was due to a failure to seek medical help. Patients with LM have reported obtaining long-term treatment for chronic rhinitis without gaining a definitive etiological diagnosis [15]. Silveira et al. discovered that the period between the cutaneous lesion and oropharyngeal involvement was up to two years in 30.4 percent of patients and more than ten years in 50.0 percent in research conducted in the state of Paraná [16].

The Montenegro skin test, according to several studies, is the most widely used and reliable for screening persons with ATL suspicion, with over 90% sensitivity and specificity. A positive Montenegro test in an endemic location could imply prior leishmaniasis, prior the antigen used in the test is injected, asymptomatic parasite exposure (infection), allergy to the test dilution agent, or cross-reactivity with other disorders (Chagas, sporotrichosis, Virchowian leprosy, tuberculosis, chromo mycosis, and others). The validity of the results, like with any other screening test, will be determined by clinical history and the prevalence of illness in the community being examined. The lack of a link between papule diameter and symptom onset in this series' Dubrovnik test, as well as the mean papule diameter, is consistent with previous findings [5].

The indirect immunofluorescence search for antibodies should not be performed alone to diagnose ATL; it should be utilized in concert with other illnesses in the differential diagnosis, Montenegro test results, and other parasite methods. Patients with mucosal lesions had greater and longer-lasting titers of this reactivity, which could be used to track drug response in mucosal disease patients. We can better understand why antibody production is restricted when assessed using the immunofluorescence approach because leishmania is a parasite that enhances cell immunity. The Polymerase Chain Reaction (PCR) is an effective approach for detecting ATL, especially when the goal is to identify the species because it's difficult to separate parasites from epithelial lesions. Despite the fact that it is rarely employed in routine diagnostic procedures, the reaction has been used for research purposes. Adenoma's carcinoma, basal cell carcinoma, lymphomas, rhinophyma, rhinosporidiosis, entomophthoromycosis, Virchowian leprosy, tertiary syphilis, septal rupture or drug usage, rhinitis, sinusitis, sarcoidosis, Wegener Specimen [6]. Notification may be influenced by

social and cultural factors. In research conducted in Acre, an endemic location with significant public leishmaniasis prevention efforts, the period between symptom onset and medical intervention ranged from 2 to 9 months. A rigorous search for questionable cases and a well-functioning reporting system are most likely to blame for the increased occurrence of the mucosal form [14,15].

Patients may be treated as a result of spontaneous demand at healthcare facilities, an active search for patients in transmission zones - as suggested by epidemiological surveillance or the family healthcare team; or, ultimately, in high-risk areas with limited access to health services.

4. CONCLUSION

Finally, educational, social, economic, and geographic characteristics appear to be linked to the late identification of mucosal leishmaniasis. The otorhinolaryngological exam and the Montenegro test remain the most essential parts in the diagnosis, but they are frequently presumptive. More research employing novel techniques is needed to increase diagnostic accuracy to identify in mucosal lesions, the parasite or its components.

DISCLAIMER

The products used for this research are commonly and predominantly use products in our area of research and country. There is absolutely no conflict of interest between the authors and producers of the products because we do not intend to use these products as an avenue for any litigation but for the advancement of knowledge. Also, the research was not funded by the producing company rather it was funded by personal efforts of the authors.

CONSENT AND ETHICAL APPROVAL

As per international standard or university standard guideline Patient's consent and ethical approval has been collected and preserved by the authors.

COMPETING INTERESTS

Authors have declared that no competing interests exist.

REFERENCES

1. Albuquerque PL, Silva Júnior GB, Freire CC, Oliveira SB, Almeida DM, Silva HF, Cavalcante MD, Sousa AD. Urbanization of visceral leishmaniasis (kala-azar) in Fortaleza, Ceará, Brazil. Revista Panamericana de Salud Pública. 2009;26: 330-3.

2. Diniz JL, da Rocha Costa MO, Gonçalves DU. Mucocutaneous Leishmaniasis: Clinical markers in presumptive diagnosis. Brazilian Journal of Otorhinolaryngology. 2011 May 1;77(3):380-4.

3. Aitken C, Jeffries DJ. Nosocomial spread of viral disease. Clinical Microbiology Reviews. 2001 Jul 1;14(3):528-46.

4. Gaspari V, Zaghi I, Macrì G, Patrizi A, Salfi N, Locatelli F, Carra E, Re MC, Varani S. Autochthonous Cases of Mucosal Leishmaniasis in Northeastern Italy: Clinical Management and Novel Treatment Approaches. Microorganisms. 2020 Apr; 8(4):588.

5. Mota LA, de Miranda RC. Otorhinolaryngologic Manifestations in Leishmaniasis.

6. Gomes CM, de Paula NA, Morais OO, Soares KA, Roselino AM, Sampaio RN. Complementary exams in the diagnosis of American tegumentary leishmaniasis. Anais Brasileiros de Dermatologia. 2014 Sep; 89:701-9.

7. Fishman G. Patterns of victimisation and notification. Brit. J. Criminology. 1979;19:146.

8. Oryan A, Akbari M. Worldwide risk factors in leishmaniasis. Asian Pacific Journal of Tropical Medicine. 2016 Oct 1;9(10):925-32.

9. Abbafati C, Abbas KM, Abbasi-Kangevari M. Global burden of 369 diseases and injuries in 204 countries and territories, 1990–2019: A systematic analysis for the Global Burden of Disease Study 2019. The Lancet. 2020a;396:1204–1222.
Available:https://doi.org/10.1016/S0140-6736(20)30925-9

10. Abbafati C, Machado DB, Cislaghi B. D., 2020d. Global age-sex-specific fertility, mortality, healthy life expectancy (HALE), and population estimates in 204 countries and territories, 1950–2019: A comprehensive demographic analysis for the Global Burden of Disease Study 2019. The Lancet. 2019;396:1160–1203.
Available:https://doi.org/10.1016/S0140-6736(20)30977-6

11. James SL, Castle CD, Dingels ZV. Estimating global injuries morbidity and mortality: Methods and data used in the

Global Burden of Disease 2017 study. Injury Prevention. 2020a;26:I125–I153.
Available:https://doi.org/10.1136/injuryprev-2019-043531

12. James SL, Castle CD, Dingels ZV. Global injury morbidity and mortality from 1990 to 2017: Results from the global burden of disease study 2017. Injury Prevention. 2020b;26:I96–I114.
Available:https://doi.org/10.1136/injuryprev-2019-043494

13. Lozano R, Fullman N, Mumford JE. Measuring universal health coverage based on an index of effective coverage of health services in 204 countries and territories, 1990–2019: A systematic analysis for the Global Burden of Disease Study 2019. The Lancet. 2020;396:1250–1284.
Available:https://doi.org/10.1016/S0140-6736(20)30750-9.

14. Handler MZ, Patel PA, Kapila R, Al-Qubati Y, Schwartz RA. Cutaneous and mucocutaneous leishmaniasis: differential diagnosis, diagnosis, histopathology, and management. Journal of the American Academy of Dermatology. 2015 Dec 1;73(6):911-26.

15. Berbert TR, Mello TF, Wolf Nassif P, Mota CA, Silveira AV, Duarte GC, Demarchi IG, Aristides SM, Lonardoni MV, Vieira Teixeira JJ, Silveira TG. Pentavalent antimonials combined with other therapeutic alternatives for the treatment of cutaneous and mucocutaneous leishmaniasis: A systematic review. Dermatology Research and Practice. 2018 Dec 24;2018.

16. Silveira FT, Lainson R, Shaw JJ, De Souza AA, Ishikawa EA, Braga RR. Cutaneous leishmaniasis due to Leishmania (Leishmania) amazonensis in Amazonian Brazil, and the significance of a negative Montenegro skin-test in human infections. Transactions of the Royal Society of Tropical Medicine and Hygiene. 1991 Jan 1;85(6):735-8.

Peer-review history:
The peer review history for this paper can be accessed here:
https://www.sdiarticle5.com/review-history/81616

Research Article

Analysis of Spectroscopic, Morphological Characterization and Interaction of Dye Molecules for the Surface Modification of TiB$_2$ Nanoparticles

S. Mayakannan,[1] R. Rathinam [iD],[2] Rajasekaran Saminathan [iD],[3] R. Deepalakshmi,[4] Mahesh Gopal [iD],[5] J. Justin Maria Hillary [iD],[6] S. Nanthakumar,[7] V. Y. Ganvir,[8] and Pallavi Singh[9]

[1]*Department of Mechanical Engineering, Vidyaa Vikas College of Engineering and Technology, Tiruchengode, Namakkal, Tamilnadu, India*

[2]*Department of Chemistry, Sri Eshwar College of Engineering, Coimbatore, 641202 Tamilnadu, India*

[3]*Mechanical Engineering, College of Engineering, Jazan University, Jazan city, Jazan, Saudi Arabia*

[4]*Computer Applications, Department of Inter-Disciplinary Studies, The Tamil Nadu Dr. Ambedkar Law University, Chennai, Tamilnadu, India*

[5]*Department of Mechanical Engineering, Wollega University, P.O. Box. 395 Nekemte, Ethiopia*

[6]*Department of Mechatronics Engineering, Sri Krishna College of Engineering and Technology, Coimbatore, Tamilnadu, India*

[7]*Department of Mechanical Engineering, PSG Institute of Technology and Applied Research Neelambur, Coimbatore, 641062 Tamilnadu, India*

[8]*Department of Applied Physics, Yeshwantrao Chavan College of Engineering, Nagpur, India*

[9]*Department of Biotechnology, Graphic Era Deemed to be University, Dehradun, Uttarakhand, India*

Correspondence should be addressed to Mahesh Gopal; doctorgmahesh@gmail.com

Nanoparticles of titanium diboride (TiB$_2$) coated with a conductive polymer and subjected to an oxidizing agent was carried out in this research. TiB$_2$ nanoparticles coated with polypyrrole (PPy) were studied using XRD and TEM techniques. Nitrogen adsorption and desorption properties of nanoparticles are covered with modified polypyrrole to understand better the surface zone, structural features, and pore geometries of the nanoparticles. The water-based hazardous anionic Congo red (CR) dye was removed using polypyrrole-coated titanium diboride (PPy@TiB$_2$) nanoparticles. Numerous cutting-edge experimental techniques, including FTIR, FE-SEM, EDXS, and element mapping analysis, were used to confirm the CR color's adhesion to the PPy@TiB$_2$ nanoadsorbent study. While conducting batch experiments, coated TiB$_2$ nanoadsorbents with polypyrrole enhanced the adsorption behaviour. One of the factors evaluated in the adsorption tests was pH; another was contact time, and a third was dose. At pH $= 4$, 98.75% of Congo red dye was detached using 60 mg of PPy-coated TiB$_2$ nanoadsorbent. Several sorption-desorption cycles were performed on this nanoadsorbent to determine its reusability. An excellent adsorption capacity for water treatment is reported in PPy-coated TiB2 nanoadsorbent.

1. Introduction

Every continent has a textile industry, and this sector contributes significantly to global economic growth [1]. Due to the coloring, printing, and washing processes carried without the appropriate pretreatment measures, textile wastewater is increasingly dyed. There are various concentrations of colored components in textile wastewater, which contribute
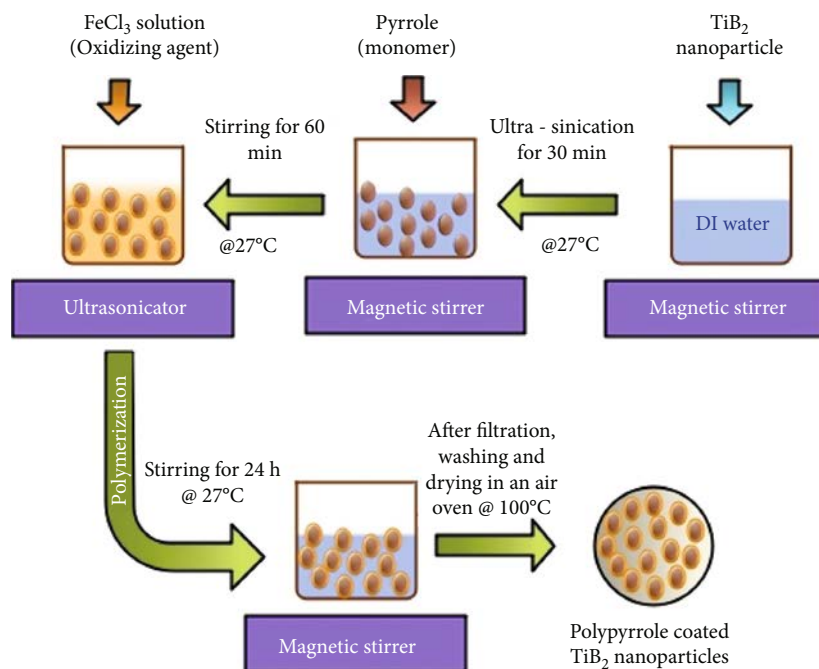
FIGURE 1: Diagram for the production of PPy@TiB$_2$.

(a)

(b)
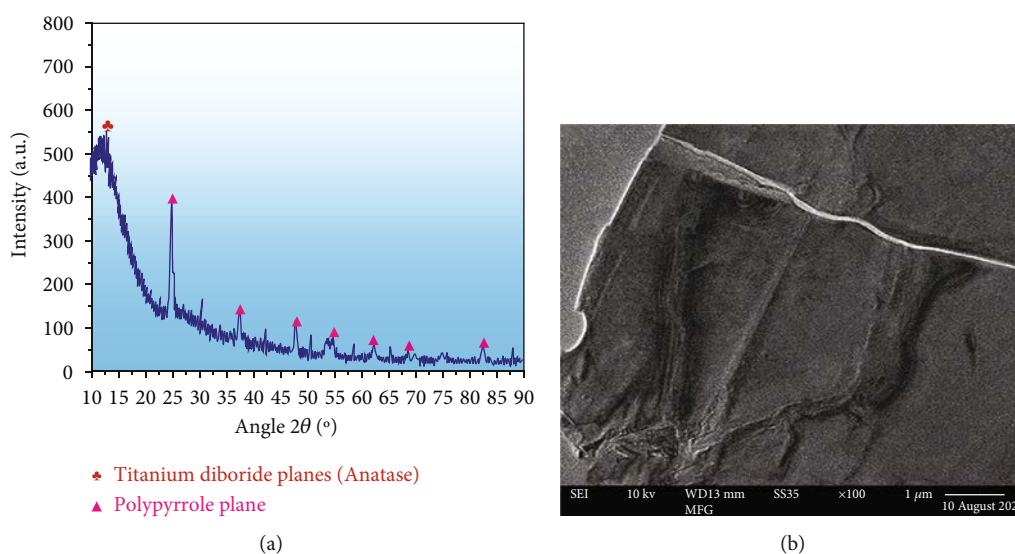
FIGURE 2: (a) XRD and (b)TEM analysis of PPy@TiB$_2$.

to its pollution [2]. Therefore, textile effluent is clean since it has a high concentration of pigment molecules. Due to CR's ability to convert to benzidine, the anionic synthetic diazo dye is carcinogenic. Because of its aromatic structure, CR dye is both physiochemically and thermally stable [3]. CR's color changes depending on the pH, turning red at a pH of less than 5. Toxic to humans and animals, industrial effluent contains significant levels of COD and BOD, suspended particles and colloids, salts, and some other hard materials [4]. To deal with textile wastewater treatment issues, energy, water, and chemicals are required. There are numerous advantages to adsorption over other water treatment methods that are investigated as a viable option [5].

Various adsorbent forms are tried, including polar and nonpolar adsorbents. High surface-area adsorbent materials have effectively extracted different dye compounds from textile effluent. Various essential uses for nanomaterials have also been demonstrated [6–8]. Nanoparticles of titanium diboride (TiB$_2$) were employed in multiple material science applications: high-performance solar cells and photocatalytic devices using TiB$_2$-based nanotubes or nanoflowers, TiB$_2$ nanoparticles, and a PVDF membrane covered with a TiB$_2$ layer amplified for photocatalytic wastewater purification [9–11]. A polymer matrix alters the material's properties, such as combining polypropylene, polypyrrole, polyamide, or polylactic acid. Environmental scientists have

(a)

(b)
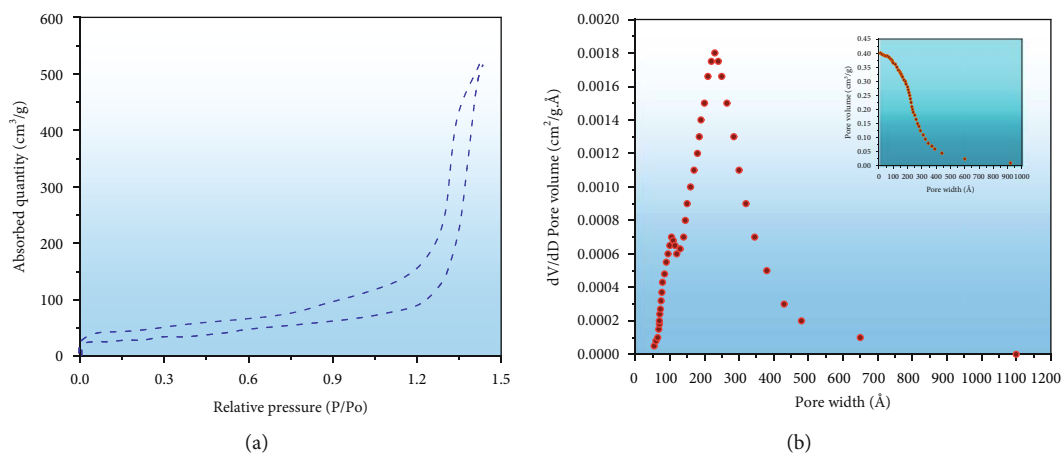
Figure 3: (a) Isotherm of N-adsorbed and desorbed of PPy@TiB$_2$ and (b) grain size dispersal plot and comparison of pore width and volume plot.
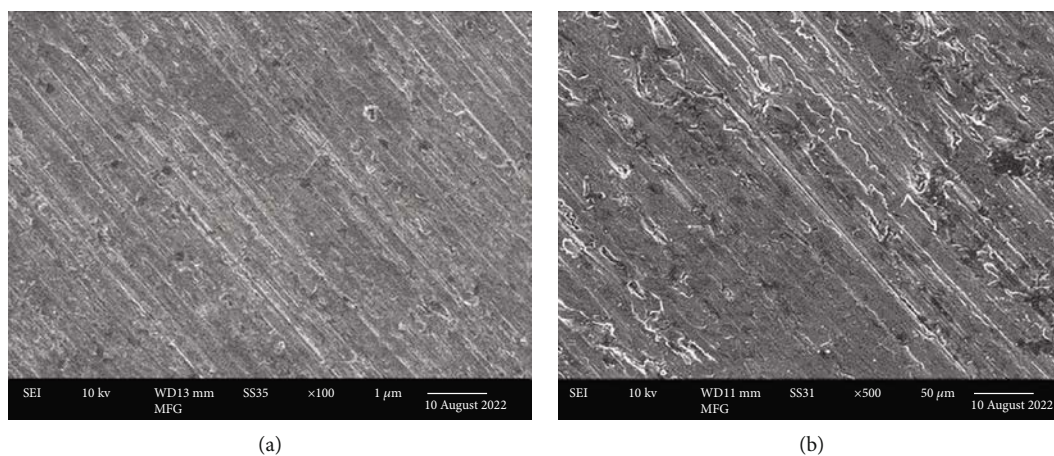

(a)

(b)

Figure 4: FESEM images of various magnifications of (a) PPy@TiB$_2$ and (b) CR-adsorbed PPy@TiB$_2$.
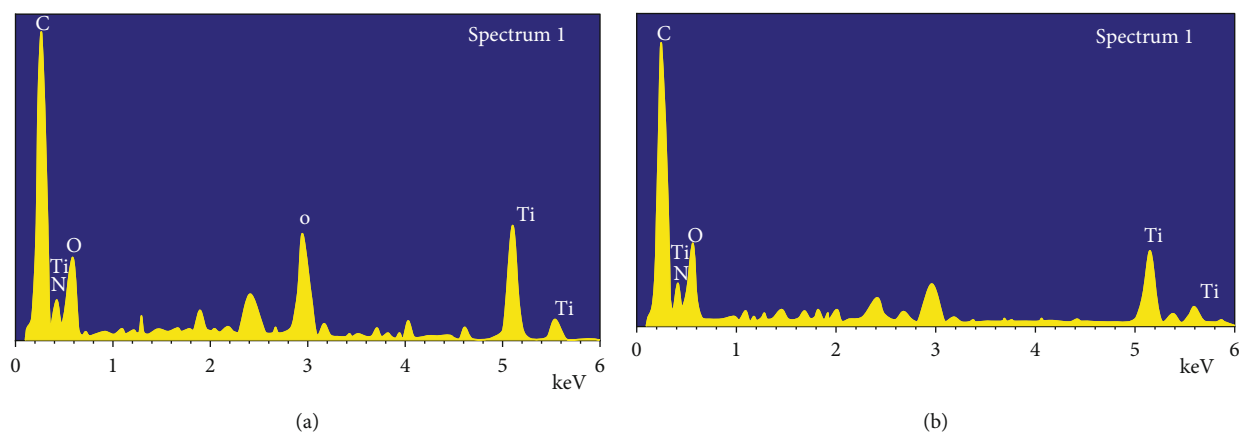

(a)

(b)

Figure 5: Energy dispersive X-ray analysis of (a) PPy@TiB$_2$ and (b) Congo red-adsorbed PPy@TiB$_2$.

been considering polymeric nanoadsorbents based on polypyrrole for several years.

The polymer has many properties that make it an ideal solution for water pollution problems [12]. Scientists have found that polypyrrole-based nanocomposites effectively clean the environment of heavy metal ions and radioactive pollutants, pigments, chemical compounds, and pesticides. Recent studies highlight photovoltaic efficiency, optical features, degradation capacity of photocatalytic materials, physical characteristics, and electric characteristics [13–15]. The

(a)

(b)
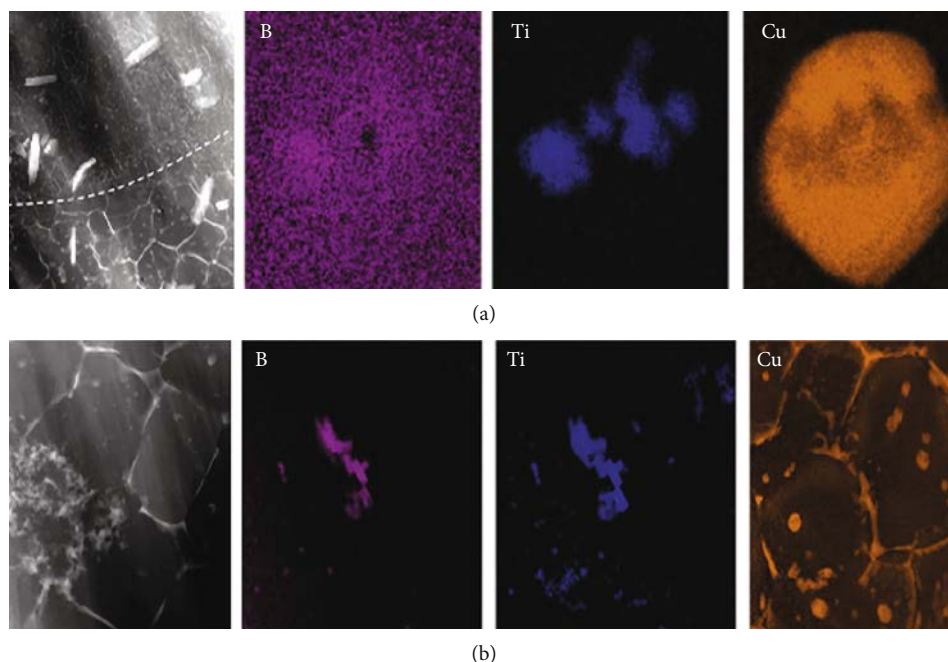
FIGURE 6: (a) PPy@TiB$_2$ and (b) process after Congo red-adsorbed PPy@TiB$_2$ elemental mapping analysis.

(a)

(b)
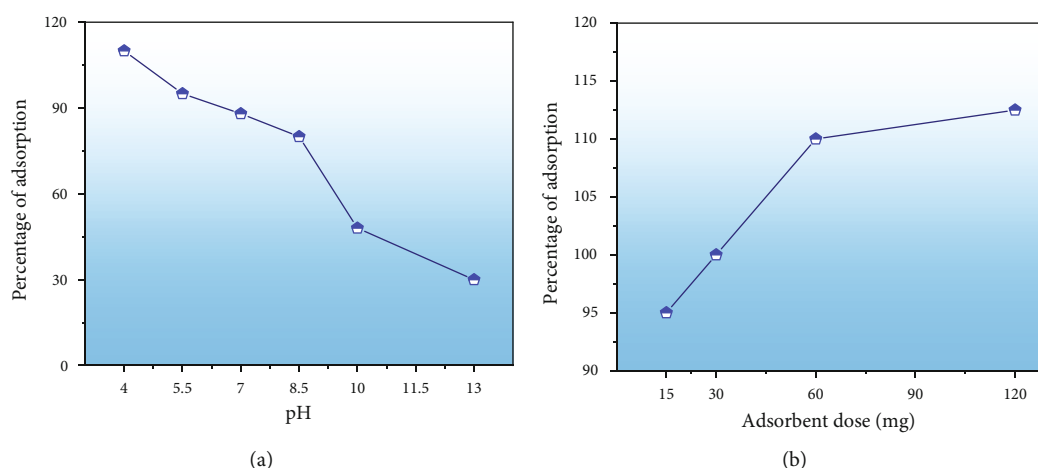
FIGURE 7: (a) Impact of pH and (b) impact of adsorbent dosage.

chemical polymerization production of polypyrrole-coated titanium diboride (PPy@TiB$_2$) has positively affected the environment. In the adsorption investigation, several traits and parameters were analyzed. Scientists have used the produced PPy@TiB$_2$ nanomaterial for wastewater dye removal due to its excellent performance and ease of reusing [16].

2. Experimentation

2.1. Methods and Materials. In the presence of a PPy monomer, a chemical polymerization approach is used to create a PPy@TiB$_2$ nanoadsorbent. There were 2 mL of pyrrole monomer and 30 minutes of ultrasonication at 27°C to prepare TiB$_2$ nanoparticles. The pyrrole monomer was allowed to adsorb on the TiB$_2$ nanoparticles' surfaces by swirling the dispersion for 60 minutes at 27°C [17, 18]. Iron was added to

the TiB$_2$ dispersion as an oxidizing agent to polymerize the pyrrole on the nanoparticles' surfaces. The mixture was stirred for an additional 24 hours at 27°C using an electric stirrer. A four-hour oven drying at 100°C removed the contaminants and unreacted oxidants after cleaning the PPy@TiB$_2$ nanoadsorbent with deionized water and acetone after polymerization. An illustration of TiB$_2$ nanoparticles coated with polypyrrole is indicated in Figure 1.

2.2. Characterization. PPy@TiB$_2$ nanoadsorbent including TEM, HR-TEM, and fast Fourier transform (FFT) were synthesized. TESCAN FE-SEM, elemental mapping, and EDX analyze the PPy@TiB$_2$ nanoadsorbent earlier and the subsequent adsorption. X-ray diffraction measurements were determined using Cu Kα radiation with a 10° to 90° (2Θ) wavelength range [19]. The nitrogen adsorption technique
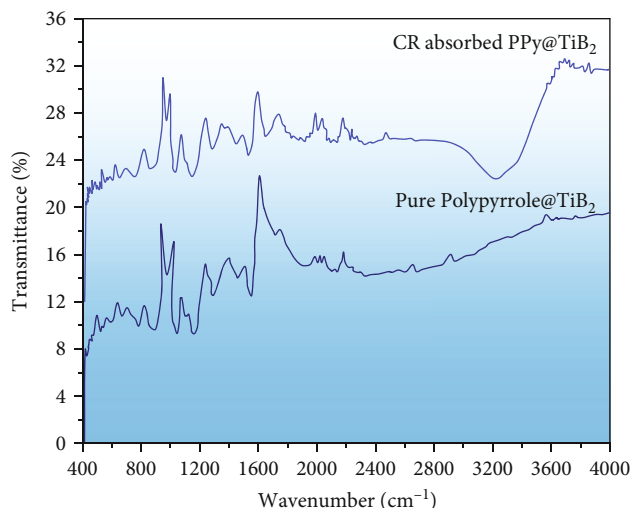
FIGURE 8: Image of attenuated total reflection-Fourier transform infrared spectroscopy.

measures pore size distributions and particular surface area. Using an FTIR spectrometer, it was necessary to conduct pre- and postadsorption studies on the nanoadsorbent, nano-PPy@TiB$_2$ [20].

2.3. Adsorption Studies. When removing Congo red (CR), batch experiments were carried out to test how the as-synthesized PPy@TiB$_2$ nanoadsorbent performed. The nanoadsorbent PPy@TiB$_2$ nanoadsorbent was studied to assess the effects of pH (acidity), contact time, and dosage on adsorption performance [21]. A pH experiment was conducted to check the PPy@TiB$_2$ nanoadsorbent-adsorbed CR at various pH levels (4 to 13). Adsorbent doses of 60 mg and 10 ppm of CR were used to test the adsorption performance. The synthetic nanoadsorbent was evaluated at various doses (15, 30, 60, and 120 mg) in a 10 ppm CR dye concentration to determine the effect of the dose [22]. Color concentrations were measured using a UV-V spectrophotometer during the batch adsorption trials. The formula used to calculate the percentage of CR dye that is eradicated is as follows [23, 24]:

$$\text{Percentage of Removal} = \frac{C_i - C_f}{C_i} \times 100 \qquad (1)$$

C_i starting concentration of Congo red color
C_f CR dye's ending concentration

3. Results and Discussions

3.1. Properties of PPy@TiB$_2$ Nanoparticles. Investigation of PPy@TiB$_2$ nanocrystalline adsorbent structure was done using XRD. As-synthesized PPy@TiB$_2$ is indicated in Figure 2(a). Results showed that TiB$_2$ nanoparticles in composite form with PPy polymer were anatase crystalline. There were no visible phases other than TiB$_2$ in Figure 2(a), which verify the XRD pattern of its different stages (rutile and brookite). It discovered that PPy@TiB$_2$ nanocomposite reduced the crystalline phase of TiB$_2$ and

PPy's amorphous nature by interacting with TiB$_2$. XRD data suggest that the surface morphology of TiB$_2$ nanoparticles with conducting polymer PPy was successful, as demonstrated by these results [25, 26]. Furthermore, TEM and HR-TEM analysis strongly support these findings.

Yet, Figure 2(b) shows the TEM patterns of the synthesized PPy@TiB$_2$. The TEM image of the synthesized PPy@TiB$_2$ showed that only the TiB$_2$ facet had PPy polymer deposited on it, regardless of the other aspect [27]. A patch of unilluminated PPy polymer showed TiB$_2$ nanoparticles scattered everywhere, while PPy polymer granules with TiB$_2$ nanoparticles interacted tightly. TiB$_2$'s high contrast made it distinct from PPy, which has lower contrast (Figure 2(b)). This nanoadsorbent formed using TiB$_2$ in the TEM image inset clearly showed the crystalline structure of the TiB$_2$ [28]. High resolution-TEM and FFT confirm that TiB$_2$ nanocomposite PPy@TiB$_2$ nanocomposite had an anatase crystalline phase as shown in supplemental Figures 3(a) and 3(b).

The surface, structural characteristics, and pore geometries of the PPy@TiB$_2$ nanospecific adsorbent were determined by the isotherm of nitrogen attachment shown in Figure 3(a). It reveals that saturation is observed at higher pressures, with a gradual increase in adsorption up to roughly 0.70 relative pressure (P/Po) [29]. Because of this, mesoporous adsorbents have a unique isotherm. The average pore diameters of the nanoadsorbent with 62.27 m$_2$/g surface area are 245.307 Å for adsorption and 216.698 Å for desorption using the nitrogen adsorption-desorption isotherm and the BJH technique [30]. In Figure 3(b), the average BET pore sizes for adsorption and desorption were 232.0041 Å and 247.2938 Å, respectively. According to IUPAC guidelines, mesoporous materials have pore diameters between 20 and 500 nm. Thus, the PPy@TiB$_2$ nanoadsorbent favours the mesoporous character of the material because of its pore sizes. Desorption is showed to be possible in Figure 3(a), where the desorption sum pore volume (0.385022 cm^3/gram) is greater than the adsorption sum pore volume (0.361217 cm^3/gram) at P/Po = 0.982. It shows that reversible desorption is conceivable. The regeneration results confirmed this tendency even more conclusively. A mesopore capillary condensation is present in the isotherm, in accordance with IUPAC's classifications of physisorption isotherm/hysteresis loops [31].

These images were taken at three different magnification levels and show the material's granular structure. As the magnification increased, the brightness decreased, indicating that the brightest particles were on the surface while the dullest particles were discovered deep within the layer (Figures 4(a) and 4(b)). It appeared like the character was uniform and smooth. Nanoparticles prepared before CR adsorption became more dispersed and bulkier in their microstructures.

Additionally, the components in the adsorbed PPy@TiB$_2$ were found out by FESEM-EDX analysis. As depicted in Figure 5, pure and CR-adsorbed PPy@TiB$_2$ samples have different elemental compositions. In the EDX spectra, carbon, oxygen, nitrogen, and titanium (Ti) are all visible (Figure 5(a)). Because of their relative atomic weights of

TABLE 1: Assignment of FTIR peaks in the pure and Congo red-adsorbed PPy@TiB$_2$.

FTIR peaks of PPy@TiB$_2$ (wavenumber cm^{-1})	Peaks role	FTIR peaks of Congo red-adsorbed PPy@TiB$_2$ (wavenumber cm^{-1})	Peaks role
1537.64	Carbon-carbon pyrrole bond stretching vibration	1521.56	Carbon-carbon pyrrole bond stretching vibration
1447.79	Conjugated C-N band for stretching	1436.68	Conjugated C-N band for stretching
1291.17	A band of conjugated deformation in the plane of C-H	1272.28	A band of conjugated deformation in the plane of C-H
1142.18	Conjugated carbon-nitrogen stretching vibrations	1136.32	Conjugated carbon-nitrogen stretching vibrations
1034.13	Nitrogen-hydrogen in the planar deformation band	1025.04	Nitrogen-hydrogen in the planar deformation band
992.25, 882.29, 780.08	Deformations of the pyrrole ring G-H in and out of the plane	988.32, 860.58, 754.42	Deformations of the pyrrole ring G-H in and out of the plane
664.89	Characteristic peak of TiB$_2$	649.33	Characteristic peak of TiB$_2$
478.71	Stretching mode for the titanium-boride bond	477.51	Stretching mode for the titanium-boride bond

(a)

(b)
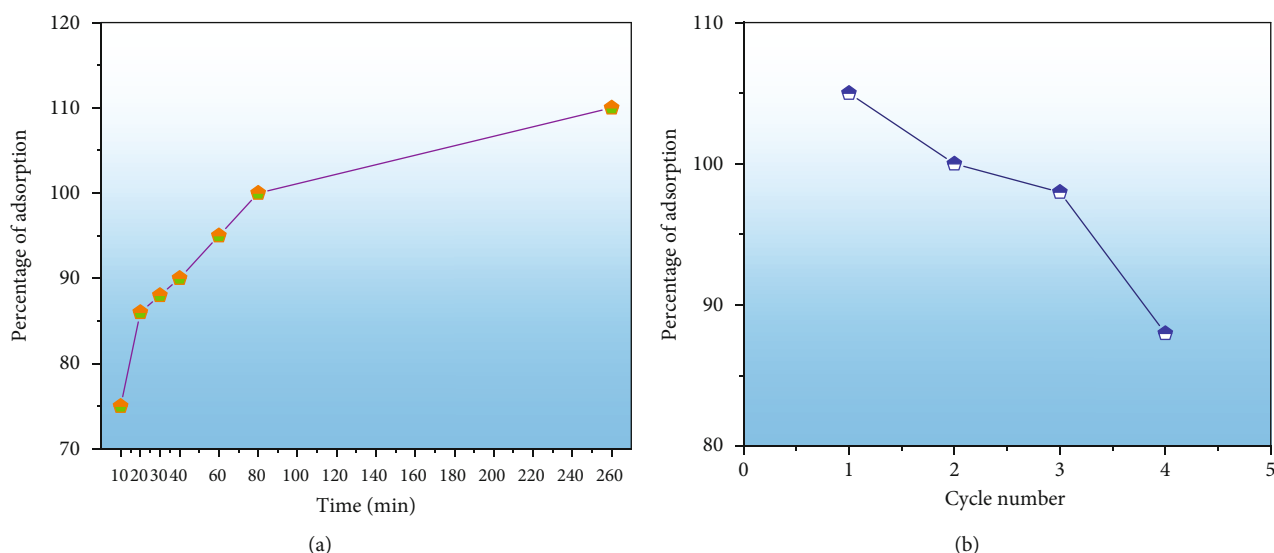
FIGURE 9: (a) Impact of contact duration and (b) regeneration capabilities of PPy@TiB$_2$ for Congo red dye adsorption.
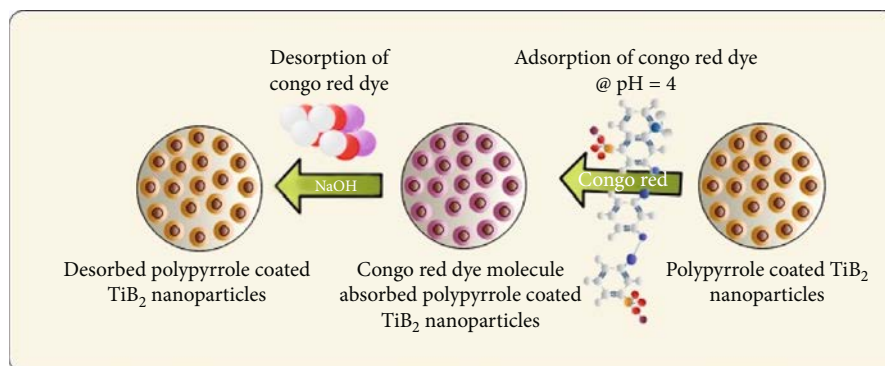
FIGURE 10: Diagram for adsorbed and desorbed mechanism of Congo red dye molecule on PPy@TiB$_2$.

50.75 and 28.21%, C and O atoms may have an effect on PPy@TiB$_2$'s adsorption to CR dye molecules. In Figure 5(b), Na, C, and O atoms with high atomic masses indicate as evidence that CR molecules adsorb onto PPy@-TiB$_2$. Elements in PPy@TiB$_2$ and CR-adsorbed PPy@TiB$_2$ were studied further by an elemental mapping experiment [32, 33]. Before and after CR dye adsorption on PPy@TiB$_2$, the elemental mapping is indicated in Figure 6. In the PPy@-TiB$_2$ nanoadsorbent, carbon, oxygen, nitrogen, and titanium were all evenly distributed. C, O, and Na distributions were validated by exposing the nanoadsorbent PPy@TiB$_2$ nanoadsorbent to CR molecules [32, 33].

3.2. Behaviour of Adsorption

3.2.1. Impact of pH. When the aqueous phase's pH alters, it alters both the binding sites and ionization processes in this experiment [34, 35]. Figure 7(a) illustrates the percentage of Congo red adsorption by PPy@TiB$_2$ at different pH values (4.0, 5.5, 7, 8.5, 10.0, and 13.0). The starting pH level of 4.0 (98.75%) had the highest adsorption rate, which decreased as the pH increased. Positively charged PPy@TiB$_2$ surface was inhibited by electrostatic contact with negatively charged CR (due to the presence of two –SO$_3$ groups) [36]. Both Congo red and PPy@TiB$_2$ became negatively charged as the pH increased and the adsorption percentage reduced [37].

3.2.2. Effect of Adsorbent Dose. The amount of PPy@TiB$_2$ used had a beneficial impact on the adsorption percentage (Figure 7(b)). The percentage of adsorption rate was increased to obtain the equilibrium state of maximum adsorption [38]. Adsorption on the PPy@TiB$_2$ surface increases when the dose increases as the number of adsorption sites increases. The optimum PPy@TiB$_2$ amount attains to be 0.05 gm due to this study.

The AT-FTIR spectrum of pure PPy@TiB$_2$ and that of CR-adsorbed PPy@TiB$_2$ is indicated in Figure 8. Band assignments and wavenumbers are shown in Table 1 for the two samples, including the pure TiB$_2$ and TiB$_2$+CR-adsorbed PPy@TiB$_2$ FTIR bands. Most peaks experienced a minor shift to the lower wavenumbers after CR dye adsorbs on PPy@TiB$_2$ [39]. Therefore, these shifting peak values make it clear that the CR dye was successfully adsorbing onto PPy@TiB$_2$.

3.2.3. Effect of Adsorption Time. In adsorption experiments, adsorption time is critical. CR adsorption is illustrated in various time intervals in Figure 9(a). During the first 30 minutes of the investigation, the percentage of CR slowly adsorbing into the PPy@TiB$_2$ grew dramatically, reaching a maximum (110%) after 260 minutes. CR adsorption was stable, indicating that it attains the equilibrium phase. For the nanoadsorbent PPy@TiB$_2$ nanoadsorbent, 260 minutes show the optimal duration for carbon dioxide adsorption. When PPy@TiB$_2$ is adsorbed, the diffusion process is evidenced by the gradual rise in the adsorbed percentage [40].

3.2.4. Regeneration Study. The exhausted adsorbent (Congo red-adsorbed PPy@TiB$_2$) was evaluated on how well it can revitalize in a regeneration study [41]. It is shown in Figure 9(b) that NaOH was used as a desorbing agent for four cycles. This PPy@TiB$_2$ nevertheless showed outstanding regeneration efficacy with an adsorption decrease from 98.75 to 97% in Figure 9(b). PPy@TiB$_2$ proves to be a valuable and economical material for removing CR. The reproducibility of PPy@TiB$_2$ for eliminating CR from textile wastewater was established.

3.2.5. Adsorption Mechanism. The dynamic, active sites on the PPy@TiB$_2$ surface allowed CR to adsorb on it. A schematic diagram of CR dye molecule adsorption and desorption onto PPy@TiB$_2$ nanoadsorbent is indicated in Figure 10. Chemical polymerization was employed to synthesize nanocomposite using TiB$_2$ nanoparticles. Dispersed TiB$_2$ nanoparticles were used to adsorb the Polypyrrole monomer. Then, the pyrrole-adsorbed TiB$_2$ dispersal is treated with the FeCl$_3$ solution as an oxidizing agent. Finally, CR adsorption was determined using the polymerized PPy@TiB$_2$ nanoadsorbent. Carbo-oxygen-nitrogen-titanium elements make up its surface. Adsorption of textile wastewater is made more accessible with the final polymer form's increased surface area and chemical functionality. This positive charge is created by protonating the PPy@TiB$_2$ surface functional groups at pH = 4. This positive charge is used to interact with CR's negative –SO$_3$ groups. Due to the negative CR's electrostatic attraction to the TiB$_2$ surface, the adsorption is reduced as pH rises, whereas deprotonation caused a decrease in surface charge density.

4. Conclusion

Chemical polymerization with pyrrole (monomer) and ferric chloride successfully converted tiny titanium diboride nanoparticles (oxidizing agent). Polypyrrole originates on the surface of TiB$_2$ nanocomposites. PPy@TiB$_2$ nanoparticles were formed, and CR molecules could adhere to them, according to spectroscopic, structural, and morphological studies. It discovered that pH = 4 260 minutes of contact hours, 60 mg of adsorbent, and a Congo red dye concentration of 10 ppm were the ideal adsorption conditions. After four cycles, a nanoadsorbent could maintain 90% of the CR color. The outcomes show that polypyrrole-coated titanium oxide nanoparticles are an effective treatment option for colored wastewater containing dye.

Data Availability

All authors confirmed that all necessary data are available in the manuscript.

Conflicts of Interest

The authors declare that they have no conflicts of interest.

References

[1] U. Sudhakara and J. Srinivasb, "Mechanical characteristics and corrosion behavior of friction stir AA5251-AA6063 butt

welds," *Materials Today: Proceedings*, vol. 15, pp. 132–137, 2019.

[2] Rajesh and P. Kaushik, "Micro structural behavior analysis of friction stir processed Al alloy AA6063/SIC," *The International Journal of Mechanical Engineering and Technology*, vol. 8, no. 11, pp. 991–998, 2017, [Online]. Available: https://www.scopus.com/inward/record.uri?eid=2-s2.0-85036561589&partnerID=40&md5=9100d82d683bd81f02d51a289c90ec1e.

[3] T. Teker, T. Kurşun, and T. Kurşun, "Weldability of AA6063 alloys by using keyhole gas tungsten arc welding technique," *Kovove Materialy-Metallic Materials*, vol. 52, no. 4, pp. 237–242, 2021.

[4] I. Sabry, A. M. El-Kassas, A.-H. I. Mourad, D. T. Thekkuden, and J. A. Qudeiri, "Friction stir welding of T-joints: experimental and statistical analysis," *Journal of Manufacturing and Materials Processing*, vol. 3, no. 2, 2019.

[5] R. Ramamoorthi, K. P. Yuvaraj, C. Gokul, S. J. Eashwar, N. Arunkumar, and S. A. T. Dheen, "An investigation of the impact of axial force on friction stir-welded AA5086/AA6063 on microstructure and mechanical properties butt joints," *Materials Today: Proceedings*, vol. 37, Part 2, pp. 3159–3163, 2021.

[6] Z. Ahmadi, M. Zakeri, M. Farvizi, A. Habibi-Yangjeh, S. Asadzadeh-Khaneghah, and M. Shahedi Asl, "Synergistic influence of SiC and C3N4 reinforcements on the characteristics of ZrB2-based composites," *Journal of Asian Ceramic Societies*, vol. 9, no. 1, pp. 53–62, 2021.

[7] N. Kaushik, S. Singhal, P. G. Rajesh, and B. N. Tripathi, "Experimental investigations of friction stir welded AA6063 aluminum matrix composite," *Journal of Mechanical Engineering Science*, vol. 12, no. 4, pp. 4127–4140, 2018.

[8] A. Sharma and D. B. Karunakar, "Effect of SiC and TiC addition on microstructural and mechanical characteristics of microwave sintered ZrB$_2$ based hybrid composites," *Ceramics International*, vol. 47, no. 18, pp. 26455–26464, 2021.

[9] S. A. A. Alem, R. Latifi, S. Angizi et al., "Development of metal matrix composites and nanocomposites via double-pressing double-sintering (DPDS) method," *Materials Today Communications*, vol. 25, p. 101245, 2020.

[10] S. A. Delbari, J. Lee, M. Sheikhlou et al., "Effect of iron nanoparticles on spark plasma sinterability of ZrB2-based ceramics," *Journal of the Australian Ceramic Society*, vol. 58, no. 4, pp. 1117–1128, 2022.

[11] E. S. Motailo, L. A. Lisyanskii, S. V. Vikhman, and D. D. Nesmelov, "Physical and mechanical properties of composite ceramics in the ZrB2–SiC–MoSi2 system," *Glass Physics and Chemistry*, vol. 47, no. 6, pp. 646–652, 2021.

[12] M. Shahedi Asl, Y. Azizian-Kalandaragh, Z. Ahmadi, A. Sabahi Namini, and A. Motallebzadeh, "Spark plasma sintering of ZrB2-based composites co-reinforced with SiC whiskers and pulverized carbon fibers," *International Journal of Refractory Metals and Hard Materials*, vol. 83, article 104989, 2019.

[13] T. Chen, W. Lu, Y. Fu, T. Chen, and W. Li, "Synthesis and characterization of chrom-free Zr-Ti-Ni pale green coating on AA6063 aluminium alloy," *Advanced Materials Research*, vol. 1053, pp. 414–420, 2014.

[14] V. A. Shcherbakov, A. N. Gryadunov, Y. N. Barinov, and O. I. Botvina, "Synthesis and properties of composites based on zirconium and chromium borides," *Russian Journal of Non-Ferrous Metals*, vol. 60, no. 2, pp. 179–185, 2019.

[15] B. Mohammadzadeh, S. Jung, T. H. Lee et al., "Characterization and FEA evaluation of a ZrB$_2$-SiC ceramic containing TaC for beam-column joint application," *Ceramics International*, vol. 47, no. 8, pp. 11438–11450, 2021.

[16] A. D. Sytchenko, S. B. Kabildina, and P. V. Kiryukhantsev-Korneev, "Effect of nitrogen concentration in a gas mixture on the structure and properties of Zr–B–(N) coatings obtained by the HIPIMS methods," *Russian Journal of Non-Ferrous Metals*, vol. 62, no. 6, pp. 785–793, 2021.

[17] S. Cheneke and D. Benny Karunakar, "The effect of solution treatment on aging behavior and mechanical properties of AA2024-TiB2 composite synthesized by semi-solid casting," *SN Applied Sciences*, vol. 1, no. 11, pp. 1–17, 2019.

[18] S. C. Lemessa and D. B. Karunakar, "Characterization and mechanical properties of 2024/Y2O3 composite developed by stir rheocasting," *Lecture Notes in Mechanical Engineering.*, vol. 1, pp. 439–453, 2020.

[19] S. Cheneke and D. B. Karunakar, "Microstructure characterization and evaluation of mechanical properties of stir rheocast AA2024/TiB2 composite," *Journal of Composite Materials*, vol. 54, no. 7, pp. 981–997, 2020.

[20] Y. R. Wang, C. J. Jin, and J. I. Song, "Mechanical characteristics of Al2O3, TiO2 and Al2O3-40.wt%TiO2 thermal coating on AISI 1045 matrix by nano-indentation test," *8th Asian-Australasian Conference on Composite Materials 2012, ACCM 2012 - Composites: Enabling Tomorrow's Industry Today,*, vol. 1, pp. , 2012639–645, 2012, [Online]. Available: https://www.scopus.com/inward/record.uri?eid=2-s2.0-84892991822&partnerID=40&md5=acf24a5e41c4f2209d799b3f515de0cd.

[21] C. Badini, P. Fino, M. Musso, and P. Dinardo, "Thermal fatigue behaviour of a 2014/Al$_2$O$_3$-SiO$_2$ (Saffil® fibers) composite processed by squeeze casting," *Materials Chemistry and Physics*, vol. 64, no. 3, pp. 247–255, 2000.

[22] O.-G. Lademo, O. S. Hopperstad, and M. Langseth, "An evaluation of yield criteria and flow rules for aluminium alloys," *International Journal of Plasticity*, vol. 15, no. 2, pp. 191–208, 1999.

[23] J. Feng, X. Du, Y. Sun, K. Zhao, Z. Shi, and M. Liu, "Effect of La–O–S complex inoculant on microstructure and mechanical characteristics of ductile iron," *Journal of Materials Science*, vol. 57, no. 8, pp. 5288–5297, 2022.

[24] S. Dharani Kumar and S. Sendhil Kumar, "Investigation of mechanical behavior of friction stir welded joints of AA6063 with AA5083 aluminum alloys," *Mechanics and Mechanical Engineering*, vol. 23, no. 1, pp. 59–63, 2019.

[25] T. S. Mahmoud, "Effect of friction stir processing on electrical conductivity and corrosion resistance of AA6063-T6 Al alloy," *Proceedings of the Institution of Mechanical Engineers, Part C: Journal of Mechanical Engineering Science*, vol. 222, no. 7, pp. 1117–1123, 2008.

[26] M. Abu-Okail, N. A. Alsaleh, W. M. Farouk et al., "Effect of dispersion of alumina nanoparticles and graphene nanoplatelets on microstructural and mechanical characteristics of hybrid carbon/glass fibers reinforced polymer composite," *Journal of Materials Research and Technology*, vol. 14, pp. 2624–2637, 2021.

[27] T. Kannan, B. Arulmurugan, L. Feroz Ali, and L. Rajeshkumar, "Performance analysis of AA3103 and AA6063 dissimilar weld joints by friction stir welding," *Songklanakarin Journal of Science & Technology*, vol. 44, no. 2, pp. 316–322, 2022, https://www.scopus.com/inward/record.uri?eid=2-s2.0-

8 5 1 3 2 8 9 7 8 7 2 & p a r t n e r I D = 4 0 & m d 5 = 28f9d950f7503bca3caec366bfa43639.

[28] T.-Y. Chen, W. Lu, W.-F. Li, and Y.-Q. Fu, "Synthesis of chrome-free coloring conversion coating on AA6063 aluminium alloy and its electrochemical properties," *Cailiao Gongcheng/Journal Materials Engineering*, vol. 43, no. 12, pp. 52–57, 2015.

[29] F. O. Edoziuno, A. A. Adediran, B. U. Odoni, O. G. Utu, and A. Olayanju, "Physico-chemical and morphological evaluation of palm kernel shell particulate reinforced aluminium matrix composites," *Materials Today: Proceedings*, vol. 38, pp. 652–657, 2021.

[30] O. S. I. Fayomi, O. P. Gbenebor, M. Abdulwahab, C. A. Bolu, and A. P. I. Popoola, "Structural modification, strengthening mechanism and electrochemical assessment of the enhanced conditioned AA6063-type Al-mg-Si alloy," *Journal of New Materials for Electrochemical Systems*, vol. 16, no. 1, pp. 59–64, 2013.

[31] D. Özyürek, T. Tunçay, and H. Kaya, "The effects of t5 and t6 heat treatments on wear behaviour of aa6063 alloy," *High Temperature Materials and Processes*, vol. 33, no. 3, pp. 231–237, 2014.

[32] G. N. Kumar, V. M. Reddy, Y. V. M. Reddy, and K. H. Reddy, "Study of abrasive wear behavior of AA 6063/TICP In-situ composites," *International Journal of Mechanical Engineering and Technology*, vol. 8, no. 5, pp. 42–52, 2017, [Online]. Available: https://www.scopus.com/inward/record.uri?eid=2-s2.0-8 5 0 1 9 5 5 0 6 2 6 & p a r t n e r I D = 4 0 & m d 5 = 0627f78d6d5367e54b06132b8dfa5740.

[33] P. Sureshkumar and V. C. Uvaraja, "Effect of ceramic and metallic reinforcement on mechanical, corrosion, and tribological behavior of aluminum composite by adopting design of experiment through Taguchi technique," *Journal of Tribology*, vol. 140, no. 5, 2018.

[34] N. Kaushik and S. Singhal, "Experimental investigations on microstructural and mechanical behavior of friction stir welded aluminum matrix composite," *International Journal of Engineering*, vol. 32, no. 1, pp. 162–170, 2019.

[35] O. S. I. Fayomi, I. G. Akande, A. P. I. Popoola, and H. Molifi, "Potentiodynamic polarization studies of cefadroxil and dicloxacillin drugs on the corrosion susceptibility of aluminium AA6063 in 0.5 M nitric acid," *Journal of Materials Research and Technology*, vol. 8, no. 3, pp. 3088–3096, 2019.

[36] T. Chen, W. Lu, W. Li, and Y. Fu, "Preparation and performace of a black-grey coating on AA6063 aluminium alloy," *Journal of Chinese Society for Corrosion and protection*, vol. 35, no. 2, pp. 177–182, 2015.

[37] T. Chen, Y. Fu, W. Lu, T. Chen, and W. Li, "Synthesis and characterization of chrom-free dark coating on AA6063 aluminium alloy with K2ZrF6," *Advanced Materials Research*, vol. 1053, pp. 421–428, 2014.

[38] S. Arnuri and S. N. Gurugubelli, "The effect of T8 heat treatment on wear behaviour and microstructure of 6063 aluminium alloy deformed by Cryo and RT ECAP," *Minerals, Metals and Materials Series*, pp. 1727–1741, 2021.

[39] A. Sabahi Namini, S. A. Delbari, M. Shahedi Asl, Q. V. Le, and M. Shokouhimehr, "Characterization of reactive spark plasma sintered (Zr,Ti)B2-ZrC-SiC composites," *Journal of the Taiwan Institute of Chemical Engineers*, vol. 119, pp. 187–195, 2021.

[40] E. R. Ferkhatly, A. V. Kovalska, and Y. I. Bogomol, "Microstructure and micromechanical properties of directionally crystallized composites of the B4C–(TixZr1 – x)B2 system," *Journal of Superhard Materials*, vol. 44, no. 2, pp. 111–116, 2022.

[41] V. A. Shcherbakov, A. N. Gryadunov, and M. I. Alymov, "Microstructural features of SHS-pressing ZrB2-B4C and TiB2-B4C composites," *Letters on Materials*, vol. 9, no. 1, pp. 11–16, 2019.

Artificial Intelligence and Live: Birth Occurrence Before *In vitro* Fertilization

Abhilasha S. Kharabe, Ranjit Ambad[1], Akash More[2], Lalit B. Damahe[3]

Clinical Embryology, Datta Meghe Medical College, [1]Department of Biochemistry, Datta Meghe Medical Collage, [3]Department of Biochemistry, Yeshwantrao Chavan College of Engineering, Nagpur, [2]Department of Clinical Embryology Jawaharlal Nehru Medical College, Datta Meghe Institute of Medical Sciences, Wardha, Maharashtra, India

Abstract

Millions of infertility-stricken couples rely on *in vitro* fertilization (IVF) every year in the hopes of establishing or expanding their families. Endometriosis, poor egg quality, a mother or father's genetic condition, ovulation issues, antibody disorders that destroy sperm or eggs, sperm inability to penetrate or survive in the cervical mucus and low sperm counts are all typical complications that lead to human infertility. Nonetheless, fertilization is not guaranteed with IVF. They hefty expense of IVF and the uncertainty of the outcome make it a difficult decision. Because there are so many problems and fertilization factors in the IVF procedure, it is difficult for fertility physicians to anticipate a successful pregnancy. In this study, the likelihood of a live birth was calculated using artificial intelligence (AI). This research focuses on predicting the likelihood that when the embryo gives birth to a living baby develops from a couple rather than a donor. We compare multiple AI methods, including both traditional machine and ensemble of algorithms human fertilization and embryology authority. The pregnancy success is determined by both male and female characteristics as well as living condition. In reproductive medicine, predicting the success of IVF treatment is a highly semantic issue. There is a strong need for developing systems to support the human mind since there are still differences in outcomes among reproductive centers and the literature is constantly being flooded with new approaches designed to predict the desired outcome. Since 1986, several approaches have been put out in an effort to make this prediction. The clinically relevant criteria IVF are used in this study to predict a successful pregnancy. As a result, AI has a potential future in decision-making for diagnosis, prognosis, and therapy. Medical practitioners can give live-birth advice at clinics based on their own expertise or the success record of the fertility center, which may or may not be acceptable in some instances. Making decisions with AI assistance may not be bad, but it is likewise not better). However, what autonomy really needs is learning knowledge that is pertinent to and significant to one's values. Having knowledge of a prediction's foundation (cleavage rate, symmetry, etc.) is irrelevant; the dangers, side effects, and benefits, as well as the level of confidence associated with them, are what matter assessments. This research will aid patients and doctors in making a definite decision based on a tool that predicts whether IVF therapy will be based on a patient's inherent quantifiable predictions, successful or failing. Couples will be counseled on their chances of having a live birth using this tool, which will help them mentally prepare for the pricey and time-consuming IVF procedure.

Keywords: Fertilization, infertility and *in vitro*, live birth

Introduction

Millions of infertility-stricken couples rely on *in vitro* fertilization (IVF) every year in the hopes of establishing or expanding their families. Infertility affects over 80 million couples throughout the world. After more than a year of unprotected intercourse, infertility might lead to "unsuccessful pregnancy." IVF is a method of reducing the number of failed embryos by fertilizing a fertilized egg from a woman's uterus with a sperm outside the body, i.e., a laboratory, to form an embryo that will then be implanted in a woman's uterus for development. Artificial insemination, which involves injecting sperm directly into the uterus, can lead to pregnancy in some cases. More than 5 million babies have been born as a result of

Address for correspondence: Dr. Ranjit Ambad,
Department of Biochemistry, Datta Meghe Medical College, Wanadongri,
Hingna, Nagpur, Maharashtra, India.
E-mail: ambad.sawan@gmail.com

How to cite this article: Kharabe AS, Ambad R, More A, Damahe LB. Artificial intelligence and live: Birth occurrence before *In vitro* fertilization. J Datta Meghe Inst Med Sci Univ 2022;17:495-8.
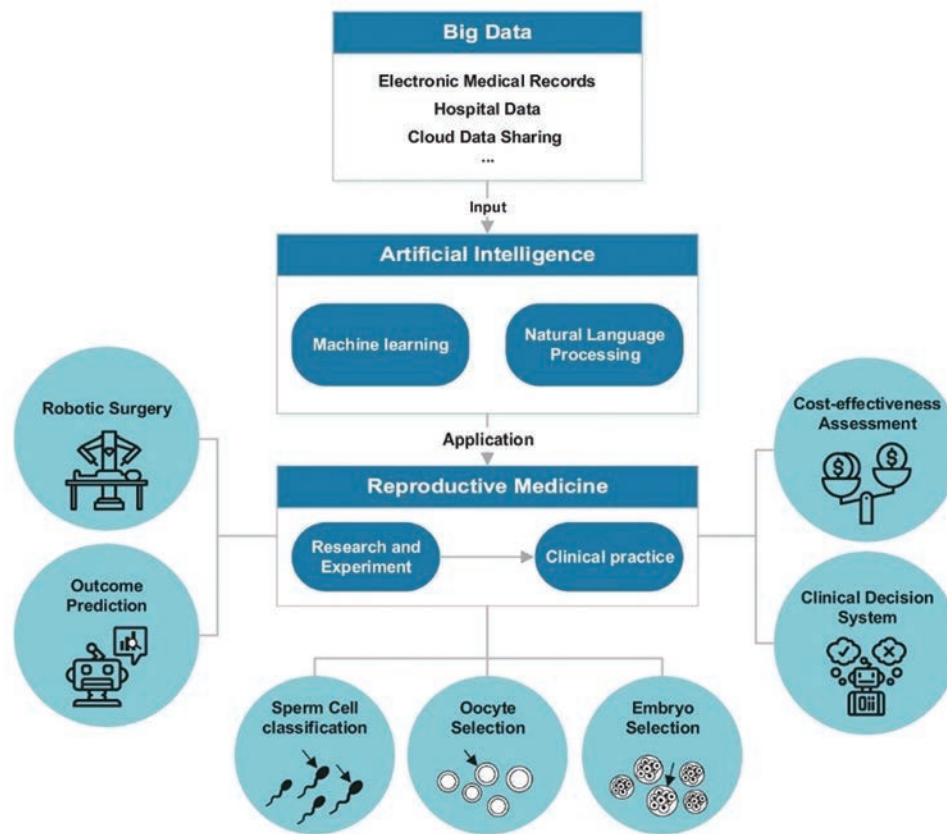
Figure 1: Diagrammatically shows AI in IVF and reproductive medicines.[11] AI: Artificial intelligence, IVF: *In vitro* fertilization

IVF worldwide, according to reports. Although the birth rate in the new cycle has often been used to test for congenital birth defects, it is very useful, as it allows couples and physicians to make strategic decisions about treatment over time, thanks to the success of IVF and intracytoplasmic sperm injection (ICSI), and the widespread use of embryo cryopreservation over the past two decades, published as a single normal person. The rate may be measured or differentiated based on a woman's age or type of infertility she has [Figure 1].

Nonetheless, Fertilization is not guaranteed with IVF. They hefty expense of IVF and the uncertainty of the outcome make it a difficult decision. Because there are so many problems and fertilization factors in the IVF procedure, it is difficult for fertility physicians to anticipate a successful pregnancy. In this study, the likelihood of a live birth was calculated using artificial intelligence (AI). This research focuses on predicting the likelihood when the embryo gives birth to a living baby develops from a couple rather than a donor. We compare multiple AI methods, including both traditional machine and ensemble of algorithms for human fertilization and embryology authority. The pregnancy success is determined by both male and female characteristics as well as living condition. The clinically relevant criteria in IVF are used in this study to predict a successful pregnancy. As a result, AI has a potential future in decision-making for diagnosis, prognosis, and therapy.

In reproductive medicine, predicting the success of IVF treatment is a highly semantic issue. There is a strong need for developing systems to support the human mind since there are still differences in outcomes among reproductive centers and the literature is constantly being flooded with new approaches designed to predict the desired outcome. Since 1986, several approaches have been put out in an effort to make this prediction.

AI, often known as machine intelligence, is a sort of intelligence displayed by machines. AI research in computer science is concerned with any technology that can understand its surroundings and act independently to achieve its objectives.

Discussion

A 30-year-old woman with a 2-year unexplained birth was 46% more likely to have a live baby after the first complete IVF cycle, and a 79% chance after three full cycles, according to pretreatment statistics. If she harvests five eggs and transfers one cracked embryo to her first full cycle, her chances of rising to 28% and 56%, respectively (excluding the remaining embryos to be frozen). Predicting a live birth is part of the difficulty of determining whether a woman gives birth based on the existing IVF data is a problem of binary separation. The aim of this study was to examine the various models that predict living births following a complete IVF cycle. The study focuses on predicting the chances of a live birth when the fetus grows

into a couple instead of a donor. The new cycle and the next ice cycle – the melting of a single cycle of ovarian stimulation is called the complete IVF cycle. For example, consider a 29-year-old woman with an AMH of 8.03 ng/ml and a body mass index of 21.97 who has been suffering from infertility for 2 years. Before she married, she had an abortion. After the first complete cycle of IVF, she now has a 65% chance of giving birth live. The selected criteria of the IVF Live Birth Occurrences, such as the women's age and the number of eggs. The current study used critical parameters, such as intrinsic and extrinsic datasets, that determine the success of the IVF procedure, to analyze and find the most reliable machine learning (ML) method to be used in the prediction of IVF Live Birth Occurrence.[1-13]

Studies that examine the effectiveness of AI models for embryo selection do so for one of two sorts of outcomes: Either (a) outcomes important to the patient, including a live delivery or a pregnancy with a fetal heartbeat, or (b) agreement with the current standard, in this case, evaluation by embryologists. The fact that a potentially viable embryo can result in either a live birth or no live birth, depending on other, nonembryo circumstances like the mother's health, is one of the difficulties with utilizing live birth as the meaningful outcome (ground truth).

The three-cycle package encourages couples to participate in multiple treatment cycles to increase the chances of having a healthy baby. After repeated treatment cycles, accumulated clinical pregnancies and live birth rates provide a more accurate measure of overall success rates and specific years. Calculate the appropriate growing number of live births to address the couple's primary concerns: how likely is IVF to produce a child? These congenital and recurrent birth rates can help IVF patients receive intensive counseling. Women who had up to three ICSI cycles had a much higher chance of having a live birth, according to the study. It also mentioned excellent cumulative birth rates for women under 35 years old, regardless of transfer day. If embryos are implanted on Day 5 for women 40 years or older, the age-related drop infertility is largely overcome, and cumulative live birth rate results are likely to be better. Our findings could have an influence on couples considering IVF therapy. AI algorithms, according to a group of reproductive experts, have the potential to help practitioners from worldwide standardize, automate, and improve IVF outcomes for the benefit of patients if properly designed. To make this happen, AI developers and health-care experts must work together.

In vitro fertilization and embryology in humans: Artificial intelligence

The embryo screening and selection technique is part of the IVF procedure. Its purpose is to choose the "best" embryos from a wider pool of fertilized oocytes, the majority of which will be unviable due to improper development or genetic defects. Indeed, it is commonly acknowledged that implantation rates in humans are difficult to predict, even after embryo selection based on morphology, time-lapse microscopic imaging, or embryo biopsy with preimplantation genetic testing. We will need to use new technology to improve embryo evaluation and selection while simultaneously increasing live birth rates.

Several AI-based systems for analyzing human embryos have lately emerged as objective, standardized, and efficient tools. AI-based technology can also help with other clinical aspects of IVF, such as evaluating a patient's reproductive potential and customizing gonadotropin stimulation regimes. Because AI can evaluate "huge" data, the ultimate goal will be to employ AI to review all embryological, clinical, and genetic data to provide patient-specific treatments.

This chapter gives an overview of current AI technologies in reproductive medicine, as well as their possible uses in the future.

When opposed to a solely human approach, the application of AI in IVF offers the potential to give a more objective, faster, and maybe more accurate evaluation of crucial milestones in the IVF process, making it more reproducible and repeatable. ML, a kind of AI that enables models to automatically learn and change as they are exposed to new data, can aid in embryo selection (whether images or other data). This is especially helpful when we have access to a lot of data but are unsure of how to utilize it to improve our forecasts or when we are unable to manually analyze all of the data to produce relevant information. Potential variables include morphological traits like fragmentation and cleavage of the embryonic cells' blastomeres, morphokinetic traits like the intervals between certain traits, and clinical traits like the woman's age or the reason of her infertility.

Studies that investigate the efficacy of AI models for embryo selection typically focus on one of two types of outcomes: (a) outcomes that are significant to the patient, such as a live birth or a pregnancy with a heartbeat, or (b) agreement with the current standard, in this case, evaluation by embryologists. One of the problems with using live birth as the relevant outcome is that a potentially viable embryo might result in either a live birth or no live birth, depending on other, nonembryo factors like the mother's health (ground truth).[14-17]

CONCLUSION

Millions of infertility-stricken couples rely on IVF every year in the hopes of establishing or expanding their families. Medical practitioners can give live-birth advice at clinics based on their own expertise or the success record of the fertility center, which is not always suitable. This study will aid patients and professionals in making better decisions by providing a tool that predicts whether IVF therapy will be successful or unsuccessful based on a patient's natural quantitative determinants. This software will inform couples about their chances of delivering a live delivery so they may mentally prepare before undergoing costly and time-consuming IVF therapy. The data may be gathered from a number of IVF clinics in various geographic

regions, and it includes information on a variety of races from across the world according to the scope of future work. A few lifestyle factors should be considered because they have an indirect impact on fertility. If data from people of various ethnicities and ages are collected, AI performance can be improved. A study of successful fertility can also be conducted, emphasizing the importance of each characteristic in IVF. Model performance can be improved using a variety of feature selection and dimensionality reduction strategies.

When opposed to a solely human approach, the application of AI in IVF offers the potential to give a more objective, faster, and maybe more accurate evaluation of crucial milestones in the IVF process, making it more reproducible and repeatable. Rapid recent developments in the field of computer vision, which enables massive volumes of picture data to be automatically evaluated by computers, hold significant potential for bettering embryo selection.

Decision-making aided by AI should be contrasted with current practices. Expert opinion nowadays is based on physiologically significant even if they are more widely communicated than decisions made using opaque models are not very reliable for forecasting a live delivery. Making decisions with AI assistance may not be bad, but it is likewise not better). However, what autonomy really needs is learning knowledge that is pertinent to and significant to one's values. Having knowledge of a prediction's foundation (cleavage rate, symmetry, etc.,) is irrelevant; the dangers, side effects, and benefits, as well as the level of confidence associated with them, are what matter assessments.

Studies that investigate the efficacy of AI models for embryo selection typically focus on one of two types of outcomes: (a) outcomes that are significant to the patient, such as a live birth or a pregnancy with a heartbeat, or (b) agreement with the current standard, in this case, evaluation by embryologists. One of the problems with using live birth as the relevant outcome is that a potentially viable embryo might result in either a live birth or no live birth, depending on other, nonembryo factors like the mother's health (ground truth).

Financial support and sponsorship

Conflicts of interest
There are no conflicts of interest.

References

1. Gurunath S, Pandian Z, Anderson RA, Bhattacharya S. Defining infertility – A systematic review of prevalence studies. Hum Reprod Update 2011;17:575-88.
2. McLernon DJ, Steyerberg EW, te Velde ER, Lee AJ, Bhattacharya S. Predicting the chances of a live birth after one or more complete cycles of *in vitro* fertilisation: Population based study of linked cycle data from 113873 women. BMJ 2016;355:i5735.
3. McLernon DJ, Steyerberg EW, Te Velde ER, Lee AJ, Bhattacharya S. An improvement in the method used to assess discriminatory ability when predicting the chances of a live birth after one or more complete cycles of *in vitro* fertilisation. BMJ 2018;362:k3598.
4. Vaughan D, Pan W, Yacoby Y, Seidler EA, Leung AQ, Doshi-Velez F, *et al*. The application of machine learning methods to evaluate predictors of live-birth in programmed thaw cycles. Fertil Steril 2019;112:e273.
5. Qiu J, Li P, Dong M, Xin X, Tan J. Personalized prediction of live birth prior to the first *in vitro* fertilization treatment: A machine learning method. J Transl Med 2019;17:317.
6. Gowramma GS, Nayak S, Cholli N. Evaluation of machine learning algorithms on the prediction of live birth occurrence. Int J Pharm Res Sch 2021;13:3243-51.
7. Engmann L, Maconochie N, Bekir JS, Jacobs HS, Tan SL. Cumulative probability of clinical pregnancy and live birth after a multiple cycle IVF package: A more realistic assessment of overall and age-specific success rates? Br J Obstet Gynaecol 1999;106:165-70.
8. Malizia BA, Hacker MR, Penzias AS. Cumulative live-birth rates after *in vitro* fertilization. N Engl J Med 2009;360:236-43.
9. Abuzeid MI, Bolonduro O, La Chance J, Abozaid T, Urich M, Ullah K, *et al*. Cumulative live birth rate and assisted reproduction: Impact of female age and transfer day. Facts Views Vis Obgyn 2014;6:145-9.
10. Swain J, VerMilyea MT, Meseguer M, Ezcurra D, Fertility AI Forum Group. AI in the treatment of fertility: Key considerations. J Assist Reprod Genet 2020;37:2817-24.
11. Zaninovic N, Rosenwaks Z. Artificial intelligence in human *in vitro* fertilization and embryology. Fertil Steril 2020;114:914-20.
12. Francolini G, Desideri I, Stocchi G, Salvestrini V, Ciccone LP, Garlatti P, *et al*. Artificial Intelligence in radiotherapy: State of the art and future directions. Med Oncol 2020;37:50.
13. Siristatidis C, Pouliakis A, Chrelias C, Kassanos D. Artificial intelligence in IVF: a need. Systems biology in reproductive medicine 2011;57:179-85. [doi.org/10.3109/19396368.2011.558607].
14. Rosenwaks Z. Artificial intelligence in reproductive medicine: A fleeting concept or the wave of the future? Fertil Steril 2020;114:905-7.
15. ESHRE Working group on Time-lapse technology, Apter S, Ebner T, Freour T, Guns Y, Kovacic B, *et al*. Good practice recommendations for the use of time-lapse technology†. Hum Reprod Open 2020;2020:hoaa008.8
16. Afnan MA, Rudin C, Conitzer V, Savulescu J, Mishra A, Liu Y, *et al*. Ethical implementation of artificial intelligence to select embryos in *in vitro* fertilization. In: Proceedings of the 2021 AAAI/ACM Conference on AI, Ethics, and Society. Virtual Event, USA. ACM, New York, NY, USA: 2021. p. 11.
17. European Society for Human Reproduction and Embryology. 2021. Available from: https://www.Eshre.Eu/PressRoom/Resources. [Last accessed on 2021 Jan 26].

Artificial Intelligence in Reproductive Medicine

Anistha Rajendra Bansod, Rakesh Kumar Jha[1], Akash More[2], Rupa A. Fadnavis[3]

Clinical Embryology, Datta Meghe Medical College, [1]Tutor, Department of Biochemistry, Datta Meghe Medical Collage, [2]Department of Clinical Embryology, Jawaharlal Nehru Medical College, Datta Meghe Institute of Medical Sciences Sawangi (Meghe) Wardha, [3]Computer Science and Engineering Assistant Professor, Yeshwantrao Chavan College of Engineering, Nagpur, Maharashtra, India

Abstract

Artificial intelligence (AI) refers to a computer-controlled system or device's ability to interpret and judge human tasks. AI has advanced significantly in a range of disciplines in recent years, from medical to experimental. With the assistance of someone who knows what they are doing, you can learn concepts and algorithms. The success of current efforts has contributed to learning because of the availability of huge datasets, accessibility, and computing capacity. Machine learning is the process of a computer extracting information from patterns and using those patterns to make predictions. Technology for assisted reproduction, many mechanical learning technologies have been employed to improve assisted reproductive technology performance, and they are now being used more frequently in health care. Despite the numerous hurdles, the integration of AI therapy will undoubtedly provide an important direction for the future development of medicine. We cover the work done on machine learning and AI in this overview, as well as how to keep the industries ahead of the curve, and, in terms of fertility therapists, the tests conducted on these industries and experiments address the issues as well as give light on the future direction and potential. We have accounted for all of these things in this post, keeping machine learning and AI expertise and concepts in mind. A review of the above-mentioned reproductive medicine experiments, as well as a review of AI future issues and trends, are thoroughly examined. AI trials in the medical industry will continue to rise as precision medicine develops and large data becomes more widely available. Despite its limits, present AI technology is ideally suited to addressing well-defined difficulties in a variety of therapeutic settings. Women who do not have children, such as infertility patients, could benefit from such a system, which could improve pregnancy outcomes and treatment. Similarly, to a married woman who, despite her best attempts, has been unable to conceive for many years, that type of woman can assist in conceiving. We realize that AI technology capabilities are expected to grow over time and that solutions can benefit by delivering high-quality health care more precisely and effectively in practice.

Keywords: Artificial intelligence, embryo, machine learning, oocytes, reproductive medicine, sperm

INTRODUCTION

The efficiency of robots to teach and evidence across the desert dividing line between animal and human natural intelligence is characterized as assisted reproductive technology (ART). Keeping all of this in mind, AI has swiftly advanced and has gradually crept into our personal and social lives. In just a few years, computers have gained significant computing power, data storage, and memory, and the ability to manage massive amounts of data. With this incredible accomplishment, I have been able to handle comprehensive learning work in a gradual manner.[1] Speech identification is an example of an AI application that is used in everyday life.[2] There is little doubt that these coverings will get faster, smarter, and more accessible, despite the fact that the current location of AI studies still has a long way to go.[3]

DISCUSSION

AI is widely used in a number of areas, such as sperm cell selection and precision imaging to increase treatment success rates, assess fetal and oocyte quality, and develop a viable and effective ART anticipation model. Further research is being done to identify positive symptoms of resistance to increase the rate of elimination and improve the ART

Access this article online

Quick Response Code:

Website:
www.journaldmims.com

DOI:
10.4103/jdmimsu.jdmimsu_279_22

Address for correspondence: Dr. Rakesh Kumar Jha,
Tutor, Department of Biochemistry, Datta Meghe Medical Collage
Wanadongri, Hingna, Nagpur, Maharashtra, India.
E-mail: vaishali.ten@gmail.com

How to cite this article: Bansod AR, Jha RK, More A, Fadnavis RA. Artificial intelligence in reproductive medicine. J Datta Meghe Inst Med Sci Univ 2022;17:499-503.
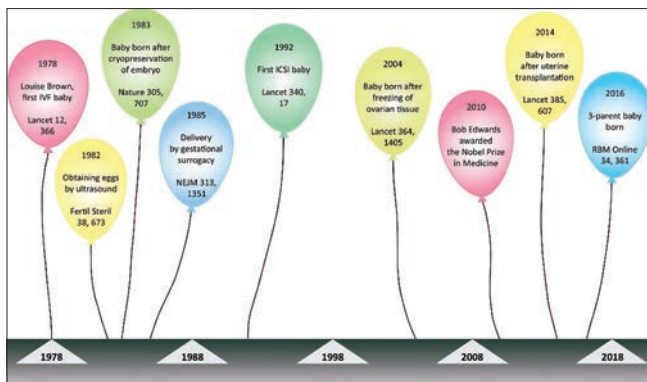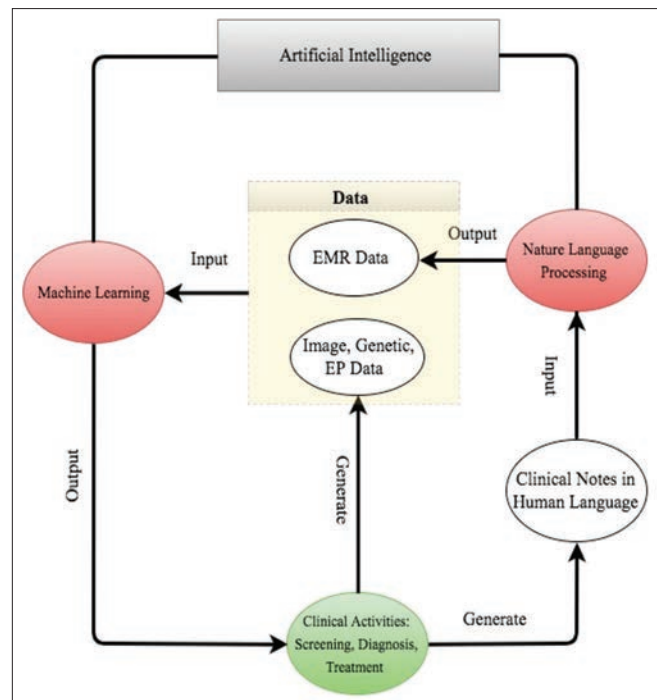
Figure 1: Very important part of human reproductive medicine, in the last 40 years

treatment environment. By allowing flexible separation of sperm, embryos, and oocytes, a well-structured AI component with image analysis can improve detection efficiency, reduce errors, and gain less manual classification. However, the main limitations of current studies range from the breadth and quality of data, which has a significant impact on the use of a trained model, application, and standard practice. Data used in most studies are limited, from a single source, and are lagging behind. Major clinical studies are still lacking to evaluate the external validity of algorithms and make extensive use of inadequate scientific resources to classify and predict, rather than to combine findings and conclusions. Anthical techniques, artificial intelligence (AI) in the treatment of infertility, are often limited and are usually spontaneous. He can see the need to improve on his or her testing and treatment, remote specialist medical systems, or the reproductive capacity of intelligence. In reproductive medicine, AI has a role [Figure 1].

Medications such as oocyte and embryo cryopreservation, assisted fertilization, prenatal testing, and embryonic stem cell technology have significantly improved clinical pregnancy rates in the 40 years since the birth of the first child *in vitro* fertilization (IVF), despite many complications. Stay.[4] The most important part of the success of IVF is the level of embryos, however, there are still gaps in methods for accurately determining the quality of eggs, sperm, and embryos. There are no embryo selection methods using one parameter or algorithm. As a result, predicting the chances of a successful pregnancy for each patient and understanding the cause of each failure is difficult. In reproductive medicine, AI-based methods may provide a solution to current problems. The goal of improving the treatment and prognosis of infertile patients using large amounts of data generated by complex diagnostic and therapeutic methods is the driving force behind the development of these applications. AI has the potential to improve clinical efficacy and efficiency, ultimately improving the ART treatment cycle.

AN OVERVIEW OF GENETIC ENGINEERING

Mechanical learning (ML), natural language processing (NLP), and robotic surgery are now the three most important types of

AI methods commonly used in medical systems. Features and predictions of disease outcomes.[5] In addition to structured data, the NLP method obtains and processes relevant information from randomized clinical data, such as electronic medical records (EMRs).[6,7] NLP converts informal data into structured data that a machine can understand and analyze using machine learning techniques.

ARTIFICIAL INTELLIGENCE IN HEALTH CARE

Reproductive medicine applications of artificial intelligence

Choosing sperm and analyzing sperm

The study of sperm is the initial stage in determining whether or not a couple is infertile. Anomalies in human sperm samples are reflected in sperm morphology. To assess a sample's prospective fertility, the ability to distinguish sperm cell morphology and track changes in sperm motility is critical. Computer-assisted sperm analysis (CASA) equipment is currently being used in human and animal studies as well as conventional analysis. Technology can detect the fullness of sperm cells and report moving percentages and kinematic data.[8] Due to the inherent lack of consideration and difficulty in assessing sperm formation in person, as well as a wide range of results obtained by different laboratories, automated image-based methods should be developed to provide meaningful and accurate results. In addition, idiopathic male factor infertility accounts for one-third of male infertility. [9] (this shows that existing sperm testing procedures cannot diagnose many of the causes of infertility. Using 2043 sperm tracks from the CASA system, researchers designed a random and quantitative way to differentiate mouse sperm movement patterns. 2017 was a year of change.[8] Human

sperm was treated in the same way. The total accuracy of this model is 89.92%, and it was enhanced using data from 425 human sperm. The researchers used dosage, total testicular volume, follicle-stimulating hormone, luteinizing hormone, complete testosterone, and ejaculate. The capacity to predict chromosomal irregularities with more than 95% accuracy. Deug drilling algorithms can also be used to improve predictions about seminal quality based on lifestyle data and environmental factors.[10] Using a list of questions and environmental parameters, two different sensory networks are designed to predict the fullness of human sperm and its flow. Despite the fact that this procedure appears to be less expensive than the more expensive laboratory tests, it can work in early detection.[11] Five AI algorithms were used to predict human reproductive ratings, and eight trait variants were used to determine acceptable traits that could more accurately predict male reproductive rates. properly remove noise. Finally, feature selection methods improved AI accuracy, as well as vector support and improved particle swarm optimizations, fit, and area under curve (AUC) level (94 and 0.932).

Oocytes are assessed and chosen

Oocyte levels play a major role in complete reproductive success, whether naturally or on ART. Pregnancy rates per oocyte currently detected are believed to be 4.5%.[12] Further knowledge of oocyte development skills will allow for the development of new IVF procedures and indicators for oocyte quality prediction and selection of the best IVF egg.[13] Most methods are designed to test and select an oocyte with the potential to develop, however, barriers such as a normal oocyte or embryo may obscure the aneuploidy and make further research needed to improve the precision and methods. As a result, applying AI selection methods for oocytes in IVF systems may open up new opportunities.[14] Photographs were taken of mouse oocytes as they grew *in vitro* from the germinal vesicle to the metaphase II phase for end-stage analysis. They used the particle image velocimetry method to calculate the cytoplasm motion velocity profile, and then analyzed data on the artificial neural network of differentiation to distinguish oocytes that are capable or inappropriate with 91.03% accuracy. In addition, a few studies have used noninvasive methods to quantify the developmental capacity of human oocytes. In addition, using AI to test human oocytes using end-of-life or to test genetic expression by transcriptomics or genomics may have a promising future and benefit from ART.[15]

Choosing an embryo

Fetal selection methods based on morphokinetic signals have recently been described. In addition, embryonic testing using a flexible monitoring system (Time lapse [TL]) provides continuous information on the embryonic growth stage and morphokinetics, although over time algorithms are still debated, and some researchers do not consider the evidence of fetal selection benefits (evidence).[16] In an incubator using the TL system, 800 human embryos with known implant data

have been tested repeatedly. They developed a model based on an examination of morphokinetic traits and an examination of embryo morphology in D3. Low-intensity artificial embryos can be eliminated using morphokinetics.

THE PROGNOSIS OF *IN VITRO* FERTILIZATION SUCCESS

Many infertile couples use ART to try to conceive a child. However, many infertile couples are under a lot of pressure because of the low rate of clinical pregnancy and the high cost per cycle. Physicians can streamline complementary therapies for infertile couples and enhance the effect of ART pregnancy by incorporating an effective IVF and AI predictive model[17] of the clinic. They used previous IVF/intracytoplasmic sperm injection records to predict the outcome with more than 80% AUC, indicating that more research is needed. The best predictions were the age of the woman, the number of mature embryos, and the level of serum estradiol/day of human chorionic gonadotropin treatment. The quality and size of the input database where the trained model limits even the best model in terms of performance. In a future study, efforts should be made to address these issues. The recognition of natural language.

NLP is a branch of AI that deals with the understanding and translation of a person's speech or text using the software. Combining machine learning, in-depth learning, and mathematical models allows the computer to capture the natural way people communicate. Indigenous language processing (NLP) is the subject of computer science — in particular, the branch of AI-computer computers' ability to understand the text and spoken words in a way that people can understand. NLP is an AI program that attempts to interpret human speech and extract useful insights into things like EMR data to aid in clinical decisions. Text processing and splitting are both parts of the NLP process.[18] However, instead of entering health information into a precise structure so that the computer can see the data, NLP allows doctors to write automatically.

Big data in the reproductive system involves studying a large number of patients and combining different types of data. Using AI to analyze this type of data has a lot of power to detect patterns that people do not see. EMRs are commonly used to store and share medical data. In reproductive medicine research, the use of EMRs is a good solution for data collection. Patient statistics, medical history, adverse events, physical examination, clinical laboratory findings, and tracking data are all digitally recorded in EMRs. By extracting important information from EMRs through NLP, we can obtain sufficient data for the following machine learning process.

LIMITATIONS AND DIFFICULTIES OF AI RESEARCH

Some AI barriers include developmental delays, which may vary depending on what you are trying to achieve. Influence performance and lack of knowledge about high technology.

Compatibility with various systems and platforms, as well as usability. The most prevalent problems that most businesses experience when attempting to implement AI

- Identifying the correct data set
- Data security and storage
- Infrastructure
- Integration of
- AI into existing systems
- AI model training and complex algorithms.

Image analysis of sperm cells and embryos, as well as predicting ART success, are two important areas for AI research. Early diagnosis, treatment, and forecasting technology are very poor. To encourage the use of AI in reproductive medicine, further research is needed. In some cases, AI technology has evaluated or performed more than skilled physicians, raising concerns that machine learning models will eventually replace physicians. We should think of AI as a tool to help doctors grow and improve their work. Simple and repetitive tasks can be handled by machine learning, saving time, and doctors effort.[19] In the meantime, clinicians should harmonize the results of machine learning models in clinical practice rather than following systemic recommendations thoughtlessly. Physicians should always check whether the model is structured in a logical way and whether it is in line with the actual clinical situation.[19] AI's role in reproductive medicine in the future.

An important guide to development in reproductive medicine is a data-based decision-making process. Through motivating programs and strengthening learning methods, it can be developed in real-time, supporting physicians in making better clinical decisions based on the patient's clinical information. Read, test, and summarize medical data using NLP to create large databases, and then use in-depth reading to read these data volumes to build models. Models are constantly being developed by comparing expert diagnoses and eventually used in AI-assisted diagnostics. The most important and important application is an AI-based medical diagnostic program, which can support physicians in resolving complex medical problems and serve as a useful medical tool. IBM's Watson is a well-known machine learning machine in health care.[18] It reveals cancer screening and treatment options. The method can help physicians make informed decisions and anticipate patient outcomes. The more information a patient provides, the more likely it is that an accurate result will be obtained.

The mechanization of IVF laboratories is also a promising area for development. Combining the technological advances in selective embryonic and embryonic stem cells, oocyte extraction by the mechanical removal of cumulus cells, oocyte formation, fertilization, embryonic culture, and monitoring embryonic development in a self-replicating machine can greatly enhance ART efficiency and effectiveness. As a result, the development of AI will benefit a large number of infertile couples.

Conclusion

We have accounted for all of these things in this post, keeping machine learning and AI expertise and concepts in mind. A review of the above-mentioned reproductive medicine experiments, as well as a review of AI future issues and trends, are thoroughly examined. AI trials in the medical industry will continue to rise as precision medicine develops and large data becomes more widely available. Despite its limits, present AI technology is ideally suited to addressing well-defined difficulties in a variety of therapeutic settings. Women who do not have children, such as infertility patients, could benefit from such a system, which could improve pregnancy outcomes and treatment. Similarly to a married woman who, despite her best attempts, has been unable to conceive for many years, that type of woman can assist in conceiving. We realize that AI technology capabilities are expected to grow over time and that solutions can benefit by delivering high-quality health care more precisely and effectively in practice.

Financial support and sponsorship
Nil.

Conflicts of interest
There are no conflicts of interest.

References

1. Diana M, Marescaux J. Robotic surgery. Br J Surg 2015;102:e15-28.
2. Abdel-Hamid O, Mohamed AR, Jiang H, Deng L, Penn G, Yu D. Convolutional neural networks for speech recognition. IEEE/ACM Trans Audio Speech Lang Process 2014:22;1533-45.
3. LeCun Y, Bengio Y, Hinton G. Deep learning. Nature 2015;521:436-44.
4. Esteva A, Kuprel B, Novoa RA, Ko J, Swetter SM, Blau HM, *et al.* Corrigendum: Dermatologist-level classification of skin cancer with deep neural networks. Nature 2017;546:686.
5. Darcy AM, Louie AK, Roberts LW. Machine learning and the profession of medicine. JAMA 2016;315:551-2.
6. Nadkarni PM, Ohno-Machado L, Chapman WW. Natural language processing: An introduction. J Am Med Inform Assoc 2011;18:544-51.
7. Mehta N, Devarakonda MV. Machine learning, natural language programming, and electronic health records: The next step in the artificial intelligence journey? J Allergy Clin Immunol 2018;141:2019-21.e1.
8. Goodson SG, White S, Stevans AM, Bhat S, Kao CY, Jaworski S, *et al.* CASAnova: A multiclass support vector machine model for the classification of human sperm motility patterns. Biol Reprod 2017;97:698-708.
9. Gudeloglu A, Brahmbhatt JV, Parekattil SJ. Medical management of male infertility in the absence of a specific etiology. Semin Reprod Med 2014;32:313-8.
10. Girela JL, Gil D, Johnsson M, Gomez-Torres MJ, De Juan J. Semen parameters can be predicted from environmental factors and lifestyle using artificial intelligence methods. Biol Reprod 2013;88:99.
11. Sahoo AJ, Kumar Y. Seminal quality prediction using data mining methods. Technol Health Care 2014;22:531-45.
12. Santos Filho E, Noble JA, Poli M, Griffiths T, Emerson G, Wells D. A method for semi-automatic grading of human blastocyst microscope images. Hum Reprod 2012;27:2641-8.
13. Kaser DJ, Racowsky C. Clinical outcomes following selection of human preimplantation embryos with time-lapse monitoring: A systematic review. Hum Reprod Update 2014;20:617-31.
14. Armstrong S, Bhide P, Jordan V, Pacey A, Farquhar C. Time-lapse systems for embryo incubation and assessment in assisted reproduction. Cochrane Database Syst Rev 2018;5:CD011320.
15. De Geyter C, Calhaz-Jorge C, Kupka MS, Wyns C, Mocanu E, Motrenko T, *et al.* ART in Europe, 2014: Results generated from

European registries by ESHRE: The European IVF-monitoring consortium (EIM) for the European society of human reproduction and embryology (ESHRE). Hum Reprod 2018;33:1586-601.

16. Hashimoto DA, Rosman G, Rus D, Meireles OR. Artificial intelligence in surgery: Promises and perils. Ann Surg 2018;268:70-6.

17. Kohli M, Prevedello LM, Filice RW, Geis JR. Implementing machine learning in radiology practice and research. AJR Am J Roentgenol 2017;208:754-60.

18. Danilov GV, Shifrin MA, Kotik KV, Ishankulov TA, Orlov YN, Kulikov AS, *et al.* Artificial intelligence in neurosurgery: A systematic review using topic modeling. Part I: Major research areas. Sovrem Tekhnologii Med 2021;12:106-12.

19. Gyawali B. Does global oncology need artificial intelligence? Lancet Oncol 2018;19:599-600.

Log in | Register   🛒 Cart

71 | 1
Views | Altmetric

Research Articles

Effective detection of COVID-19 outbreak in chest X-Rays using fusionnet model

Ganesh Keshaorao Yenurkar & Sandip Mal ✉ ⓘ

❝ Cite this article   ☑ https://doi.org/10.1080/13682199.2023.2173543   ⟳ Check for updates

📄 **Full Article**   🖼 **Figures & data**   📑 **References**   ❝ **Citations**   📊 **Metrics**   🖨 **Reprints & Permissions**   **Read this article**

ABSTRACT

The worldwide pandemic of coronavirus disease 2019 (COVID-19) triggers acute respiratory difficulties and breathing disorders in humans. The reverse transcription-polymerasssse chain reaction (RT–PCR) examination is generally done for the primary diagnosis of COVID-19. Though, it realizes a high false-alarm rate because the test is done during the first five days of disclosure. But still, the medical field hugely relies on the skill of healthcare professionals to interpret the results. Hence, an automatic chest X-ray-based COVID-19 detection system is more essential in recent times. To fulfil this requirement, a novel FusionNet Model is proposed in this paper for the precise classification of COVID-19 diseases. The CXR (Chest X-Ray) images are initially gathered from Cohen CXR Dataset and COVID-CT-MD dataset. The collected data is pre-processed through image resizing, ROI (Region of Interest) extraction, and noise filtering through Improved Anisotropic Filtering (IAF) to attain an enhanced image. The feature extraction process extracts the global and local features by adopting the Parallel Attention Layer (PAL) module. The optimal features are selected based on the Entropy Correlation score – ESA (Emperor Salp Algorithm) based feature selection process. Finally, the selected features are fed into the SoftMax classifier for COVID-19 detection from chest X-ray images. The implementation of the proposed model has been executed on Cohen CXR Dataset and COVID-CT-MD dataset using the Python platform. The classification accuracy of 99.82% is attained in the case of the Cohen CXR Dataset, and 99.02%. In the case of the COVID-CT-MD dataset is obtained in the proposed FusionNet model.

🔍 **KEYWORDS:** COVID-19 detection   global and local features   FusionNet   PAL module   Entropy score   optimal features   SoftMax

Disclosure statement

The authors have no conflicts of interest to declare that are relevant to the content of this article.

Data availability statement

Data sharing is not applicable to this article.

Notes on contributors

Ganesh Keshaorao Yenurkar

Ganesh Keshaorao Yenurkar currently working as an Assistant Professor in Computer Technology department of Yeshwantrao Chavan College of Engineering, Wanadongri Nagpur, India. He is currently pursuing the PhD degree of Computer Science & Engineering programme in the School of Computing Science and Engineering at VIT Bhopal University, Bhopal, India. He has completed his BE and MTech from Rashtrasant Tukdoji Maharaj Nagpur University, Nagpur (RTMNU, Nagpur) in the year of 2008 and 2013 respectively. He has a number of publications in international journals of repute. He has guided number of UG students, and his research interest includes Machine Learning, Deep Learning, Cloud Computing, and Data Science.

Sandip Mal

Dr. Sandip Mal is the Programme Chair of Computer Science & Engineering Programme in the School of Computing Science & Engineering, VIT Bhopal. He has done his PhD and MTech from the Department of Computer Science and Engineering, Birla Institute of Technology, Mesra. He is a recipient of a number of fellowships from different government organizations for his academic and research work. He served as an Assistant Professor at Central University of Jharkhand prior to joining VIT Bhopal. He has a number of publications in National/International journals of repute. He has guided a number of UG, PG and Research Scholars and his research interest includes Image Processing & Software Engineering.

Related research ⓘ

Recommended articles   People also read   Cited by

Competitive verse water wave optimisation enabled COVID-Net for COVID-19 detection from chest X-ray images ❯

Priyanka Shivaprasad More et al.
Computer Methods in Biomechanics and Biomedical Engineering: Imaging & Visualization
Published online: 20 Nov 2022

An efficient stacked ensemble model for the detection of COVID-19 and skin cancer using fused feature of transfer learning and handcrafted methods ❯

B.H. Shekar et al.
Computer Methods in Biomechanics and Biomedical Engineering: Imaging & Visualization
Published online: 7 Sep 2022

An efficient COVID-19 detection from CT images using ensemble support vector machine with Ludo game-based swarm optimisation ❯

Shiny Irene D et al.
Computer Methods in Biomechanics and Biomedical Engineering: Imaging & Visualization
Published online: 24 Jan 2022

Diagnosis of Covid-19 using Chest X-ray Images using Ensemble Model ❯

Information for

Authors

R&D professionals

Editors

Librarians

Societies

Opportunities

Reprints and e-prints

Advertising solutions

Accelerated publication

Corporate access solutions

Open access

Overview

Open journals

Open Select

Dove Medical Press

F1000Research

Help and information

Help and contact

Newsroom

All journals

Books

Keep up to date

Register to receive personalised research and resources by email

✉ Sign me up

BACKGROUND REMOVAL OF VIDEO IN REALTIME

Arya Khanorkar

Yeshwantrao Chavan College of Engineering, Nagpur, Maharashtra, (India).

Bhavika Pawar

Yeshwantrao Chavan College of Engineering, Nagpur, Maharashtra, (India).

Diksha Singh

Yeshwantrao Chavan College of Engineering, Nagpur, Maharashtra, (India).

Kritika Dhanbhar

Yeshwantrao Chavan College of Engineering, Nagpur, Maharashtra, (India).

Nikhil Mangrulkar

Yeshwantrao Chavan College of Engineering, Nagpur, Maharashtra, (India).

E-mail: mangrulkar.nikhil@gmail.com

ABSTRACT

Background removal for video is a computer-vision based system to remove the background from a video with ease. Creating a professional background when at home, i.e., not in a very professional environment, can be a tedious task. Not everyone has time to learn editing and the technicalities involved in having an entire setup for creating a sophisticated background and it is not practical that normal people buy green screens or blue screens just for their everyday formal meets. Our goal is to create a quick and easy solution to that by removing background in real time while also maintaining the quality of the call, having the additional benefit of adding custom backgrounds and enabling users to add effects like adjust lighting, contrast etc., we are combining all 4-5 steps in 1 single step. SelfieSegmentation module of Mediapipe helps us achieve this. The Selfie Segmentation API creates an output mask from an input image. The mask will be the same size as the input image by default. A float integer with a range of [0.0, 1.0] is assigned to each pixel of the mask. The higher the confidence that the pixel depicts a person, and vice versa, the closer the number is to 1.0.

KEYWORDS

Categories and Subject Descriptors: G.4 [Mathematics of Computing]: Mathematical Software - User Interfaces; H5.2 [Information Interfaces and Presentation]: User Interfaces - User-centered design; Interaction styles; Theory and methods.

Background Removal, Online Meetings, Professional Background, Streaming.

1. INTRODUCTION

This pandemic has made it clear that virtual meets are here to stay. They are the new normal. But often virtual meetups from home fail to create the professional atmosphere due to backgrounds in the video. The professionalism required can be achieved by proper background in videos and minimal disturbances. Unnecessary and visually unpleasing objects need to be removed. This can be achieved by background removal, changing background color and adding virtual backgrounds. Background removal can help avoid the cumbersome task of arranging a good backdrop in some cases even eliminates the use of green screens which are used by many youtubers. It helps add to the overall aesthetics and pleasantness of video conferences or even live streams.

The technique of mimicking human intelligence in robots programmed to think and behave like humans is known as artificial intelligence (AI). Computer vision is a branch of artificial intelligence (AI) that allows computers and systems to extract useful information from digital photos, videos, and other visual inputs and act or make recommendations based on that data. A computer vision technique called object detection is used to locate and identify objects in pictures and movies. Using this type of identification and localization, object detection can be used to count the items in a scene, locate and track them precisely, and accurately label them.

Image segmentation is the technique of dividing a digital image into numerous pieces for use in digital image processing and computer vision (sets of pixels, sometimes known as image objects). Various portions of a movie can be discovered using object detection and image segmentation, and different adjustments can be performed to each of the components. We'll use these ideas to remove the backdrop from a video using AI.

Open Broadcaster Software (OBS) helps you set your scene as a virtual camera to which we will be feeding our video directly in real time using pyvirtualcam and mediapipe. We'll use Google Meet to recognize OBS as a video source and output it as a virtual camera, resulting in enhanced quality of video calls.

2.   REVIEW OF LITERATURE

2.1   PRESENT SYSTEM

The apps that currently provide such a feature for removing the background of a video in real time tends to worsen the quality of the video and do not provide us with smooth edges of the main object which is not ideal for a professional use. Also, the process to remove or change the background in these apps consists of various steps to be followed, sometimes we are even required to cut the video call and rejoin with a changed background. Through our project we have tried to overcome these problems by providing a system which removes the background while maintaining a proper quality of the video with fps greater than 30. And we also provide an easy way to change the backgrounds by just clicking a button on the keyboard.

Grzegorz Szwoch, in his paper presented, implementation of a background subtraction algorithm using the OpenCL platform. The algorithm works using a live stream of video frames from an on-line surveillance camera. A host machine and a parallel computing device are used to execute the processing. The research focuses on optimizing OpenCL algorithm implementation for GPU devices by taking into consideration specific GPU architecture aspects including memory access, data transfers, and work group structure. The technique is designed to work on any OpenCL-enabled device, including DSP and FPGA platforms. Several algorithm optimizations are presented and tested on a variety of devices with variable processing power. The work's major goal is to figure out which optimizations are required for on-line video processing in the surveillance system.

A relatively inexpensive background subtraction method is proposed by Hasup Lee et al., in their study employing background sets with im-age- and color-space reduction. Background sets are used to

recognize objects from dynamic backdrops like waves, trees, and fountains. The image space is decreased to handle jittered and unstable frames, such as those from handheld mobile devices. The color space is shrunk to account for color noise, such as the scattered RGB values from a digital camera. To reduce expenses, a combination of color-space reduction and hash-table look-up operations is used. The results, when compared to other methods, suggest that the proposed technology is feasible: it may also be used in mobile or embedded environments.

S. Joudaki, et al., in their paper, they presented a comparison of numerous existing background subtraction methods, ranging from basic background subtraction to more complicated providential techniques. The purpose of this research is to provide an overview of the advantages and disadvantages of commonly utilized approaches. The approaches are compared based on how much memory they demand, how long they take to compute, and how well they handle different types of films. Finally, other criteria such as processing time and memory needs were used to compare the existing approaches. Baoxin Li, et al., in their paper they proposed a video background replacement algorithm, this is based on adaptive background modelling and background subtraction. It can be accomplished with a pre-recorded background scene image rather of a blue screen. Identifying statistical outliers in respect to a specific background is the challenge. A two- pass approach is utilized to modify initial segmentation based on statistics about a pixel's vicinity, which lowers false positives in the background area while raising detection rates for foreground objects. Experiments with real image sequences, as well as comparisons with other existing approaches, are shown to demonstrate the benefits of the proposed methodology.

S. Brutzer, et al., in their paper, presented one of the most important approaches for automatic video analysis, particularly in the field of video surveillance, is background subtraction. Despite their usefulness, reviews of recent background removal algorithms in relation to video surveillance challenges include several flaws. To address this problem, we must first identify the major obstacles to background subtraction in video surveillance. We then evaluate the performance of nine back-ground subtraction algorithms with post-processing depending on how well they over-come those challenges. As a result, a fresh evaluation data set is presented that includes shadow masks and precise ground truth annotations. This enables us to offer a thorough evaluation of the advantages and drawbacks of various background sub-traction techniques.

In their study, R. J. Qian et al., presented an algorithm for altering video backgrounds without a blue screen physically. Pre-recording a backdrop image of the scene free of any foreground objects is required for the operation. Based on the color difference between the pixels in an input frame and their corresponding pixels in the background image, the method computes a probability map that contains the likelihood for each pixel to be classified into the foreground or background. The probability map is further improved using anisotropic diffusion, which reduces classification mistakes without adding a lot of artefacts. The foreground pixels from the input frames are then feathered onto a brand- new background video or image based on the enhanced probability map to create the output video. The method requires only a little amount of CPU resources and is designed to work in real time. Experiment findings are also reported.

A. Ilyas, et al., in their paper, presented a Modified Codebook Model-Based Real Time Foreground-Background Segmentation. The initial step in object tracking is the essential process of segmenting the scene in real time into the foreground and background. beginning with the codebook approach. Authors suggested certain changes that show notable improvements in the majority of the typical and challenging conditions. For accessing, removing, matching, and adding codewords to the codebook as well as moving cached codewords into the codebook, they included frequency options. They also suggest an evaluation procedure based on receiver operating characteristic (ROC) analysis, precision and recall methodology, to impartially compare various segmentation techniques. Authors suggested expressing the quality factor of a method as a single value based on a harmonic mean between two related features or a weighted Euclidean distance.

Rudolph C. Baron, et al., in their paper, presented a solution for managing a video conference. When establishing a video conference with a second person, a first participant can choose from among

several stored virtual backgrounds and use that background. One or more characteristics of the first and/or second participant, one or more characteristics of the video conference, and/or similar considerations may be used to choose the virtual background. The virtual backgrounds can be used, for instance, to provide people outside of a company organization a desired perception, message, and/or the like while they communicate with its employees via video conferencing. The virtual background can incorporate static image data, live or recorded video feeds, static business entity web pages, and dynamic business entity web pages.

Jian sun, et al., Effective techniques and approaches in a video sequence isolate the focus from the background, according to their paper. In one instance, a system creates an accurate real-time backdrop cut of live video by reducing the background contrast while maintaining the contrast of the segmentation boundary itself. This method enhances the border between the foreground and background images. The live video may then combine the fragmented foreground with another background. An adaptive background color mixture model can be used by the system to distinguish foreground from background more effectively when there are changes in the backdrop, such as camera movement, lighting changes, and the movement of small objects in the background.

Juana E. Santoyo-Morales, et al., in their paper presented a Background sub-traction models based on a Gaussian mixture have been widely employed in a range of computer vision applications for detecting moving objects. Background sub-traction modelling, on the other hand, remains a challenge, especially in video sequences with dramatic lighting changes and dynamic backdrops (complex backgrounds). The goal of this research is to make background subtraction models more resilient to complicated situations. The following enhancements were proposed as a result: Redefining the model distribution parameters (distribution weight, mean, and variance) involved in the detection of moving objects; enhancing pixel classification (background/foreground) and variable update mechanisms using a new time-space dependent learning rate parameter; and c) substituting a new space-time region-based model for the pixel-based model that is currently used in the literature.

According to Yiran Shen et al., background subtraction is a typical first step in many computer vision applications, including object localization and tracking. Its objective is to pick out the moving parts of a scene that match to the important things. Researchers in the field of computer vision have been working to increase the reliability and accuracy of such segmentations, but most of their techniques require a lot of computation, making them unsuitable for our target embedded camera platform, which has a much lower energy and processing capacity. In order to create a new background subtraction method that overcomes this issue while retaining an acceptable level of performance, authors added Compressive Sensing (CS) to the often-used Mixture of Gaussian. The results imply that their technique can significantly reduce the eventual time taking.

Semi-supervised video object segmentation should be considered, which is the process of creating precise and consistent pixel masks for objects in a video sequence based on ground truth annotations from the first frame, according to a suggestion made by Jonathan Luiten et al. To do this, they provided the PReMVOS algorithm (Proposal- generation, Refinement and Merging for Video Object Segmentation). The method separates the problem into two steps to specifically address the difficult issues related to segmenting multiple objects across a video sequence: first, generating a set of precise object segmentation mask proposals for each video frame; and second, choosing and merging these proposals into precise and object tracks that are pixel-wise and consistently timed inside a video sequence.

Thuc Trinh Le, et. al., demonstrated a method for removing items from videos. The technique simply requires a few input strokes on the first frame that roughly delineate the deleted objects. Authors claims that this is the first method which enables semi-automatic object removal from videos with intricate backgrounds. The following are the main phases in their system: Segmentation masks are improved after setup and then automatically distributed throughout the film. Video inpainting techniques are then used to fill in the gaps. Authors claim that their system can handle several, potentially intersecting objects, complex motions, and dynamic textures. As a result, a computational

tool that can automate time-consuming manual tasks for editing high-quality videos has been developed.

Thanarat H. Chalidabhongse, et. al., in their paper, showed how to use color pictures to detect moving items in a static background scene with shading and shadows. They created a reliable and efficient background subtraction method that can deal with both local and global lighting variations, such as shadows and highlights. The approach is based on a proposed computational color model that distinguishes between the brightness and chromaticity components. This technology has been used to create real-world image sequences of both indoor and outdoor locations. The results, which demonstrate the system's performance, are also provided, as well as several speed-up techniques used in their implementation.

Yannick Benezeth, et. al., in their paper, presented comparison of different state-of-the- art background subtraction approaches is presented. On several movies containing ground truth, there have been developed and tested methods ranging from straightforward background subtraction with global thresholding to more complex statistical algorithms. The purpose is to lay a solid analytic foundation on which to highlight the benefits and drawbacks of the most extensively used motion detection methods. The approaches are compared in terms of their ability to handle various types of videos, memory requirements, and computing effort. A Markovian prior, along with several postprocessing operators, are also considered. Most of the films are from modern benchmark collections and highlight a range of issues, including low SNR, background motion in many dimensions, and camera jitter.

Yi Murphey, et. al., in their paper, describes their work on image content-based indexing and retrieval, which is an important technique in digital image libraries. Image features used for indexing and retrieval in most extant image content-based approaches are global, meaning they are computed over the full image. Background features can readily be mistaken for object features, which is the fundamental drawback of retrieval techniques based on global picture features. Users typically refer to the color of a particular object or objects of interest in an image while searching for photos using color attributes. The technique described in this article uses color clusters to analyze image backgrounds. After being identified, the background regions are deleted from the image indexing process, so they won't interfere with it anymore. Three main calculation processes make up the algorithm: fuzzy clustering, color picture segmentation, and background.

Zhao Fei Li, et. al., in their paper, presented background noise removal is a key stage in the picture processing and analysis process. Researchers use a variety of techniques to remove background noise from images. For instance, grey threshold techniques are frequently used to eliminate noises that have a strong contrast to the object of interest. However, there are a lot of noises in the grey scale that don't change as the interesting objects do. These noises cannot be reduced using the grey level-based noise removal technique, but the contour feature is excellent at doing so. The contour feature-based image background removal approach depends on the contour model. The contour characteristic of the interest items is modelled using a revolutionary method proposed in this study. A unique background noise with the same grey level as the background noise is completely eradicated using this method.

Thuc Trinh Le, et. al., demonstrated a method for eliminating objects from videos in their study. A few strokes in at least one frame are all that are needed for the technique to roughly delimit the items to be eliminated. These undeveloped masks are then polished and automatically broadcast throughout the video. The corresponding areas are synthesized again using video inpainting methods. Authors claim that their system is capable of navigating several, perhaps crossing objects, intricate motions, and dynamic textures. As a result, a computational tool has been created for editing high-quality videos that can take the place of laborious human work.

3.   PROPOSED TECHNIQUE

The main objective of the proposed technique is to create a simpler process of removing background from a live or saved video, to simplify the process of creating an aesthetic background. Our project

allows the user to completely remove the background or put a different background and be able to switch between multiple backgrounds or colors.

The main objective of our project is to eliminate the need to physically change the arrangement of room for a better and professional background. Thus, providing users an easy way of applying or changing backgrounds while they are in some online meet or live streams while maintaining the quality of the video.
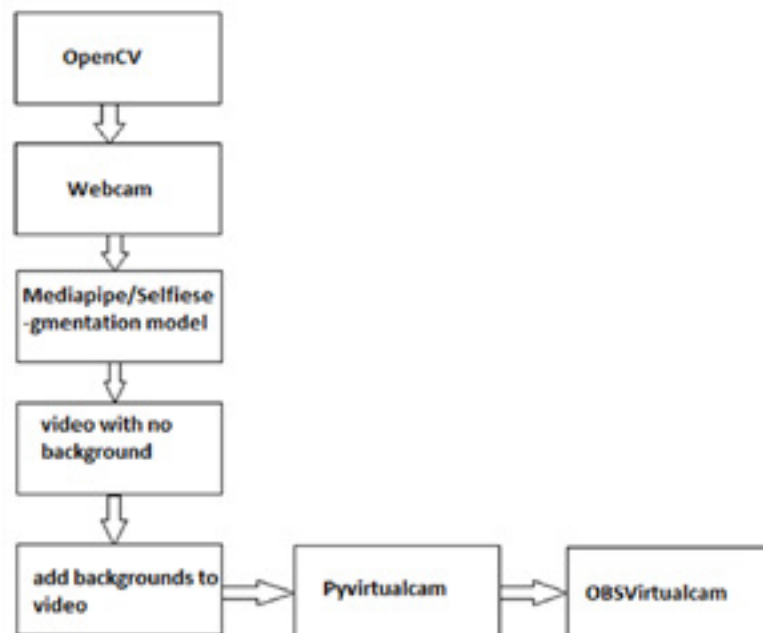
3.1   Flow of Proposed Technique

Fig. 1. Flowchart of the proposed system.

Fig. 1 shows the flow of the proposed system, starting with the accessing of the live video from webcam to the removal/changing of background and feeding the output to applications like google meet using OBS Virtual Camera.

3.2. IMPLEMENTATION

Our goal was to remove the background in real-time and with FPS more than 30.

3.2.1. STARTING THE WEBCAM

We should be able to access the webcam by simply running the code so that the video i.e., real time video can be directly taken as input. A computer vision library is called OpenCV (Open-Source Computer Vision). with a variety of image and video manipulation tools. The OpenCV library can be used to manipulate films in a variety of ways. To capture a video, you'll need a *VideoCapture* object. The index of the device or the video file's name is stored in *VideoCapture*. The device index is just a number that identifies which of the camera device is being used.

 Syntax: *capt = cv2.VideoCapture(0)*

Now a pop-up window will open if we have a webcam. We have set the frame size to 640X 480. Therefore, background-replacing images should be 640 x 480, which is the same size as the frame.

Creating a dataset for background images Make a folder called 'BackgroundImages' inside the project directory. You can download and store any image, or any number of images, in this directory.

3.2.2. BACKGROUND REMOVAL

We have used the *SelfieSegmentationModule* from *cvzone* package which uses OpenCV and *Mediapipe* libraries at its core and makes AI operations on videos and images very easy. *SelfieSegmentation* is a technique for removing the frame's background and replacing it with photos from our directory. It is based on MobileNetV3 but has been tweaked to be more efficient. It uses a 256x256x3 (HWC) tensor as input and outputs a 256x256x1 tensor as the segmentation mask. Before feeding it into the ML models, *MediaPipe SelfieSegmentation* automatically resizes the input image to the necessary tensor dimension. We use the webcam for input and frame width should be set to 640 x

480. Then we utilize the *cvzone* to execute *SelfiSegmentation*(), which carries out object identification, image segmentation, and ultimately background removal. The output frames can show the frames per second (fps) using the FPS() method.

 Syntax: seg = SelfiSegmentation() Setfps = cvzone.FPS()

 SelfieSegmentation() converts the image into RGB and sends it to the SelfieSegmentation model to process and then it checks if the image is colored; if yes it changes the color of the background and if not, it then changes the color of the image. As a result, we can see the background successfully removed.

3.2.3. STORE BACKGROUND IMAGES IN A LIST

Then, after creating a list of every image in the *BackgroundImages* folder, we iterate through it, reading each one and adding it to an empty list. At the beginning, the index is set at zero.

3.2.4. REPLACE BACKGROUND WITH DESIRED BACKGROUND

The frames are read from the camera using a while loop, and the background is then removed from the frames using the *seg.removeBG()* method and replaced with images from the directory. The camera's image *frame (img),* the directory's collection of photos, and with an index of image (*imgList[indexImg]*), are all passed to the seg.*removeBG()* function along with the threshold. To improve the edges, we additionally modify the threshold setting.

3.2.5. FUNCTIONALITY TO CHANGE BACKGROUND USING KEYBOARD SHORTCUTS

Using *cvzone.stackImages*, we stack the images and retrieve the output of the frames or background-replaced image. Then, by means of a straightforward if statement, we assign keys to change the background. The principle is to sequentially remove the indexes according to the key that was pressed to display the image for the resulting index. This lets you change the backgrounds quickly.

3.2.6. SEND THE FRAMES TO OBS VIRTUAL CAMERA

We then send the resulting frames to OBS Virtual Camera using *Pyvirtualcam().* It sends frames to a virtual camera from Python. The OBS virtual camera is detected by various platforms, and we have our very own background removal with whichever backgrounds, or no backgrounds, as required.

4. RESULTS AND DISCUSSIONS

With our proposed implementation, we successfully removed the background and add any other desired background in real time with FPS more than 30.

Fig. 2. Removal of background in real time.

Fig. 2. shows that the left half of the image has normal real-time video with backgroundand the right side has video with no background with FPS 34.
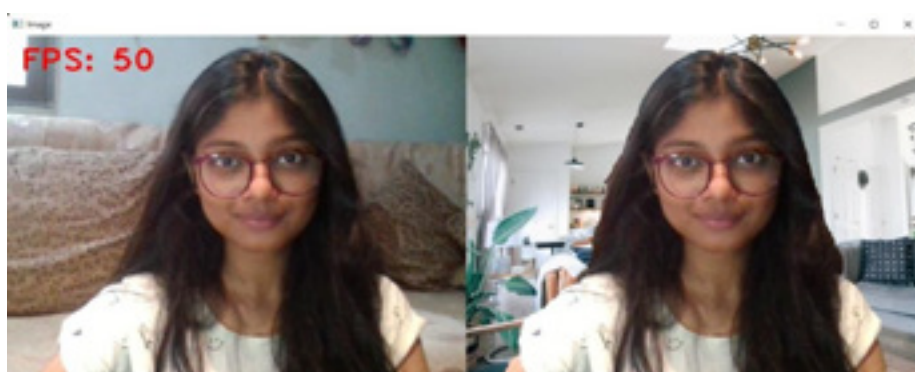

Fig. 3. Background changed in real time successfully with FPS = 50.

Fig. 3. shows that left side of the image has normal real-time video, and the right side hasvideo with desired background with FPS 50.
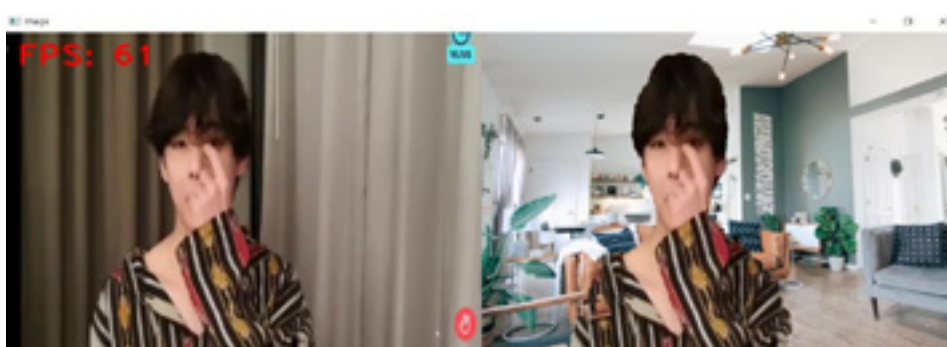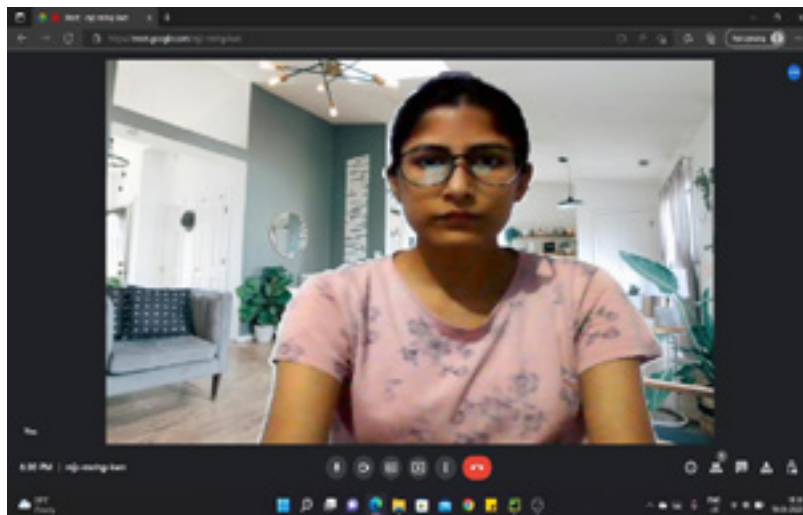

Fig. 4. Background changed of pre-recorded video successfully with FPS= 61.

Fig. 4. shows that left side of the image has normal pre-recorded video, and the right sidehas the video with desired background with FPS 61.

Fig. 5. Background changed in real time successfully on Google Meet.

Fig. 5. shows that we were able to change the background of our live video in a Google meet.

Fig. 6. Background changed in real time successfully and able to configure in Google Meet.

Fig. 6. shows that we were able to change the background of our live video as well as configure the features such as brightness, contrast, saturation, etc. of our real time videoin a Google meet.

4. CONCLUSION

We have implemented a computer-vision based system to remove the background from a video in real-time which enabled creating a professional background when not in a very professional environment. Our goal was to create solution for removing background in real time while also maintaining the quality of the call, having the additional benefit of adding custom backgrounds and enabling users to add effects like adjust lighting, contrast etc. We used *SelfieSegmentation* module of *Mediapipe* in this implementation. Our results shows that our technique successfully removed backgrounds from live videos as well as prerecorded videos at frame rate between 30 and 60. We also changed background of videos in reals time and prerecorded videos seamlessly. Our implementation also worked very well on streaming platforms like Google Meet.

REFERENCES

[1] A. ILYAS, M. SCUTURICI AND S. MIGUET, 2009, "Real Time Foreground-Background Segmentation Us - ing a Modified Codebook Model," 2009 Sixth IEEE International

Conference on Advanced Vi -deo and Signal Based Surveillance, pp. 454-459, doi: 10.1109/AVSS.2009.85.

[2] BAOXIN LI AND M. I. SEZAN, 2001, "Adaptive video background replacement," IEEE International Conference on Multimedia and Expo, 2001. ICME 2001., pp. 269-272, doi: 10.1109/IC ME.2001.1237708.

[3] G. SZWOCH, 2014, "Parallel background subtraction in video streams using OpenCL on GPU platforms," 2014 Signal Processing: Algorithms, Architectures, Arrangements, and Applications (SPA), pp. 54-59.

[4] H. LEE, H. KIM AND J. KIM, 2016, "Background Subtraction Using Background Sets With Image- and Color- Space Reduction," in IEEE Transactions on Multimedia, vol. 18, no. 10, pp.2093- 2 103 , doi: 10.1109/TMM.2016.2595262.

[5] JIAN SUN HEUNG-YEUNG, SHUM XIAOOU AND TANG WEIWEI ZHANG, 2009, "Background Removal In A Live Video," Assigned to Microsoft Technology Licensing, LLC.

[6] JONATHON LUITEN, PAUL VOIGTLAENDER AND BASTIAN LEIBE, 2019, "PReMVOS: Proposal-

[7] Generation, Refinement and Merging for Video Object Segmentation" In book: Computer Vision – ACCV 2018 (pp.565-580), DOI:10.1007/978-3-030-20870-7_35

[8] JUANA E. SANTOYO-MORALES AND ROGELIO HASIMOTO BELTRAN, 2014, "Video background

[9] Subtraction in Complex Environments" in Journal of Applied Research and Technology 12(3):527-427, DOI:10.1016/S1665-6423(14)71632-3

[10] R. J. QIAN AND M. I. SEZAN, 1999, "Video Background Replacement without a Blue Screen". Proc. of IEEE International Conference on Image Processing. Kobe, Japan.

[11] RUDOLPH C. BARON, ANDREW R. JONES, MICHEAL M. MASSIMI, KEVIN C. MCCONNELL, 2014, "Background Replacement for Video Conferencing", Application filed by International Business Machines Corp.

[12] S. BRUTZER, B. HÖFERLIN AND G. HEIDEMANN, 2011, "Evaluation of background subtraction techniques for video surveillance," CVPR 2011, pp. 1937-1944, doi: 10.1109/ CVPR.2011.59955 08.

[13] S. JOUDAKI, M. S. BIN SUNAR AND H. KOLIVAND, 2015, "Background subtraction methods in video streams: A review," 2015 4th International Conference on Interactive Digital Media (ICIDM), pp. 1-6, doi: 10.1109/IDM.2015.7516329.

[14] CHALIDABHONGSE, THANARAT & HARWOOD, DAVID & DAVIS, LARRY, 1999, "A statistical approach for real-time robust background subtraction and shadow detection", IEEE ICCV.

[15] THUC TRINH LE, ANDRÉS ALMANSA, YANN GOUSSEAU AND SIMON MASNOU, 2019, "Object removal from complex videos using a few annotations", in Computational Vidual Media 5(3) August 2019, DOI:10.1007/s41095-019-0145-0, Project: Video Inpainting

[16] THUC TRINH LE, ANDRÉS ALMANSA, YANN GOUSSEAU AND SIMON MASNOU, 2018, "Removing objects from videos with a few strokes" in Conference: SIGGRAPH Asia 2018 Technical Briefs, DOI:10.1145/3283254.3283276.

[17] YANNICK BENEZETH, PIERRE-MARC JODOIN, BRUNO EMILE, HÉLÈNE LAURENT AND CHRISTOPHE ROSENBERGER, 2010, " Comparative study of background subtraction algorithms" in Journal of Electronic Imaging 19(3):033003-033003, DOI:10.1117/1.3456695

[18] YI LU AND HONG GUO, 1999, "Background removal in image indexing and retrieval," Proceedings 10th International Conference on Image Analysis and Processing, pp. 933-938, doi: 10.1109/ICIAP.1999.797715.

[19] YIRAN SHEN,WEN HU, MINGRUI YANG AND JUNBIN LIU, 2012, "Efficient background subtraction for tracking in embedded camera networks" DOI:10.1145/2185677.2185698

[20] ZHAO FEI LIV AND JIANG QING WANG, 2014, "Image Background Removal by Contour Feature" in Advanced Materials Research 926-930:3050-3053, DOI:10.4028/www.scientific.net/ AMR.926-930.3050

Novel approach to Create Human Faces with DCGAN for Face Recognition

Roshni Khedgaonkar
and
Kavita Singh
and
Summy Mate
Yeshwantrao Chavan College of Engineering, Nagpur, India

Due to the remarkable data generation abilities of the generative models, many generative adversarial networks (GAN) models have been developed, and several real-world applications in computer vision and machine learning have emerged. The generative models have received significant attention in the field of unsupervised learning via this new and useful framework. In spite of GAN's outstanding performance, steady training remains a challenge. In this model, use of Deep Convolutional Generative Adversarial Networks is incorporated, Main aim is to produce human faces from unlabeled data. Face generation has a wide range of applications in image processing, entertainment, and other industries. Extensive simulation is performed on the Celera dataset. Key focus is to successfully construct human faces from the unlabeled data and random noise and achieved average loss of 1.115% and 0.5894% for generator and discriminator respectively.

---

1. INTRODUCTION

GANs (Generative Adversarial Networks) are gaining popularity in the research community of deep learning. Computer vision, natural language processing, time series synthesis, semantic segmentation, and other disciplines have all used GANs. GANs are machine learning-based generative model compared to other models like variational autoencoders. GANs have a number of advantages in managing estimation functions, producing needed samples quickly, removing deterministic bias, and integrating data. GANs have found considerable success in computer vision domain, particularly in the field of image generation, image translation, and image completion. The two greatest ones are that they are difficult to train and difficult to analyze. Regarding being difficult to train, the generator frequently fails to learn the entire range of datasets, and attaining Nash equilibrium for the discriminator and generator during training is challenging. In terms of evaluation, the main concern is how to best assess the dissimilarity between the target pr real distribution and the generated distribution pg. Unfortunately, accurate pr estimate is impossible. As a result, obtaining accurate estimates of the relationship between pr and pg is difficult Wang et al. [2021].

Firstly, uses of a Deconvolutional Neural Networks architecture for G was DCGAN(Deep Convolutional Generative Advisory Network) Zeiler and Fergus [2014]. Deconvolution is a method for visualizing the characteristics of a CNN that has demonstrated to be effective in the visualization of Convolution Neural Networks (CNNs) Yu et al. [2015]. DCGAN makes use of the deconvolution operation for G spatial up-sampling capability, allowing for the producing of high resolution images with GANs. DCGAN's architecture differs significantly from that of the original Fully Conditional GAN (FCGAN), allowing for higher resolution modelling and more stable training. As shown in fig 1. At the beginning, DCGAN replaces any pooling layers with stride and fractional-stride convolutions for the discriminator and generator, respectively. Second, batch

normalization is used by both the discriminator and the generator, which aids in the location of generated samples and real samples centering at zero, i.e., equivalent statistics for created samples and real samples. Finally, ReLU activation is applied in the generator for all layers except output, whereas LeakyReLU activation is used in the discriminator for all levels. As the generator gets gradients from the discriminator, Large-Scale Scene Understanding (LSUN) Deng et al. [2009], ImageNets Creswell et al. [2018], has been assembled are used to train DCGANs. Generally, DCGAN is giving effective result on minimum resolution and less diversified images, because of the optimization and limit model capacity used in DCGAN. Key focus is to create faces using latent vectors or random noise. This paper is organized in the following way. Section 2 discusses the overview of GAN. Section 3 Provides a proposed methodology, a detailed description of the techniques and methods used followed by result and then discussion in section 4, and the conclusion is shown in section 5.
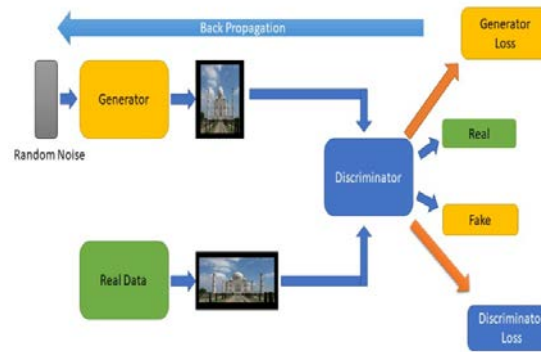
Figure 1. DCGAN working ProcessRadford et al. [2015]

2. OVERVIEW

Generative models are able to through instant action on region of image vision problems. Generative models are the traditional models where given preparing information p-data(x) from an unreadable information producing appropriation creates new examples information p-model(x) from a similar dissemination. The ultimate objective of any Generative Model is to draw comparable information tests (p-model(x) from the inclined genuine information conveyance p-data(x))Aslan et al. [2019]. GANs (Generative Adversarial Networks) are a resilient network used for unsupervised machine learning to establish a two ply min-max game, i.e., building up both players (networks) with their own goals. The generator network (G) is one participant, while the discriminator network (D) is the other (D). The first player (G) attempts to trick the second player (D) by creating exceptionally common-looking true pictures from arbitrary idle vector z, and the second player (D) improves in-recognizing genuine and produced information. Both organizations try to streamline themselves in the best possible way to achieve their individual goals because they both have goal capabilities, i.e., D needs to extend its cost worth, while G needs to limit its cost worthAslan et al. [2019].

Another category of convolutional neural organizations (CNN) called Deep Convolutional GAN (DCGAN). DCGAN was the main structure that practiced de-convolutional neural organizations (de-CNN) basic layout, which balances out GAN preparation. These systems are made up of two organizations: one acts as a CNN called the generator, while the other acts as a de-CNN called the discriminator Goodfellow et al. [2014]. A recently proposed category of design limitations remembered for CNN are:

—Remove all degrees of pooling layers with step convolutions.

—Both G and D should utilize Batch Normalization.

—Use ReLU and Leaky-ReLU in the generator and the discriminator organizations separately.

3. PROPOSED METHODOLOGY

Architecture

Deep learning(CNN) based DCGAN technique is being used in proposed approach. Because of its great accuracy, CNN are employed for picture categorization and recognition. A fully-connected layer, where all of the neurons are connected to one another and the output is processed, is produced by the CNN by using a hierarchical model. In the discriminator model, this paper defined our first convolution layer in which input to layer is an image of 3 channels (RGB channel). And after that 32 is the dimension of the convolution layer. In other words, applying 32 kernels to an input image or convolving to an input image. The filter size or convolution kernel size is 4*4. Then, used a stride of 2*2 which will move with 2 steps during the convolution process. Further, we applied batch normalization. A deep neural network is trained using the batch normalization approach, which standardizes the inputs to each layer for each mini-batch. The goal must be to keep the learning process stable and drastically cut down on the how many training iterations are needed to train deep networks. Scaling the layers output, precisely by standardizing the activations of every input variable per mini-batch, such as the activations of a previous layer's node. Then the use of 2*2 stride which will move with 2 steps during the convolution process same as before.

Further, the use of batch normalization layer, network training is fundamentally impacted by batch norm since, it renders the relevant optimization problems landscape suitably smooth. After that, defined a single completely linked layer that receives a 2048 input and gives outputs a single feature, then passed sigmoid function to output full connected layer because it has a range of values from 0 to 1. The optimal choice is sigmoid because anything only has a possibility of occurring between 0 and 1. The following stage is to distinguish between genuine misfortune and false misfortune. A Sigmoid layer and the Binary Cross Entropy (BCE) loss are combined. This adaption is more mathematically stable than using a simple Sigmoid followed by a BCE Loss. Since, the use of log-total trick for mathematical solidity by combining the activities into one layer. To distinguish the images during feedforward and backpropagation, assigned a zero to the counterfeit name and a one to the real brand. For smoothing the yield, 0.9 incentive Adam is being used for a sophisticated computation that may be used to refresh network loads iteratively based on preparation data instead of the usual stochastic angle plunge methodology. Kingma and Ba Kingma and Ba [2014] introduced Adam in the ICLR work "Adam: Adam combines the finest features of the AdaGrad and RMSProp improvement computations to create a calculation that can deal with insufficient slopes on noisy situations. Adam is a reasonably easy to construct character, and the default arrangement boundaries perform admirably in most situations. Alpha 0.0005 was utilized, which is also known as the learning rate or step size. For the first-moment estimates, we utilized beta1 is 0.1, the exponential decay rate, and beta2 is 0.99, the exponential decay rate for the second-moment estimations. The next stage is to train the whole Deep Convolution Neural Network. The training of both discriminator and generator is two-fold method. To begin, we use real photos to train our discriminator. The Celera dataset was used in this analysis. The images in this dataset span a wide range of postures and foundation issues. CelebA has a lot of variety, a lot of content, and a lot of feedback. The discriminator learns that this is how real images look by passing the real images through it. And generates a real loss for the said images Next during the first pass training random noise is passed through the generator where it generates fake images from it that are to be passed through the discriminator. The fact that these images are exactly the same size or dimensions as the discriminator input

capacity is crucial. After that, the discriminator calculates the loss for these fake images, which is known as fake loss. Backpropagation is then performed by combining these real and artificial losses. It is a method for modifying the loads of a neural network based on the previous error rate. When backpropagate we update the filter and weights of the fully connected layers based on the calculated losses. It is trained by passing latent vectors or random noise through a generator from which it generates fake images which are then passed through the discriminator but this time it generates a loss for fake images using flipped labels. The same back propagation process is then repeated to finish the training. All this training is done multiple times in the form of epochs. An epoch is essentially nothing but an iteration of the training cycle. Architecture structure of both generator and discriminator network is depicted fig 2 and fig 3 respectively.
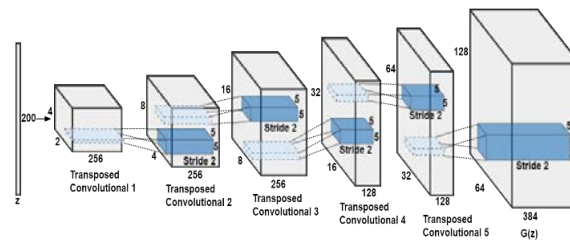
Figure 2. Architecture of Generator NetworkAslan et al. [2019]
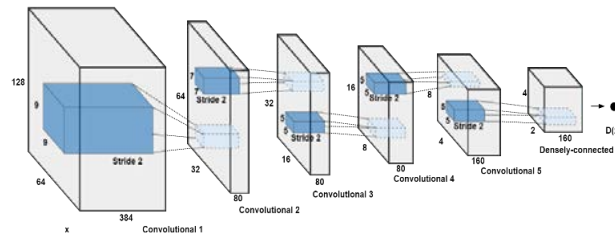
Figure 3. Architecture of Discriminator NetworkAslan et al. [2019]

4.   RESULT AND DISCUSSION

For experimentation, celebA dataset is use, plotting of face landmarks for input data is shown in fig 4. Considered types of layers, output shape and their parameters of generator and discriminator which is used to generated the images using un-labelled data and discriminator compared data with original face images shown in fig 5 and fig 6. The ability to transform un-labelled data into meaningful data and their potential to generate large amounts of results is nothing but power of DCGAN. If size of dataset increases then achieves great accuracy. As approach from fig 5 and fig 6 as analyze there is increase in little accuracy when epoch reached from 30 to 80. After running 80 epochs of the network the results shown in table 1 have been gathered. Fig 7 shows the graphical representation of average loss of Generator and discriminator

The dense layer is the typical layer of a neural network with many connections. It is the most typical and often utilised layer. Based on the results of the convolutional layers, a dense layer is utilised to categorise the images. Hence, the single dot is 1 and parameters is 8193.the summary of discriminator is shown in Table2. After the discriminator works complete then alternate way generator work starts from dense layer to convolutional 2D. The output shape of Dense layer is 8192 and parameters is 827392. Then after it reshape by 8x8x128. Conv2DTranspose is a

convolution operation whose kernel is learnt (just like normal conv2d operation) while training model. Hence, it given the output shape is 16x16x8. Again passed filter of 256, kernel size is 4 then generated output is 32x32x256. Same as next layer is having filter size is 512 and finally generated output size is 64x64x3."Table 3 tabulated the summary of generator.
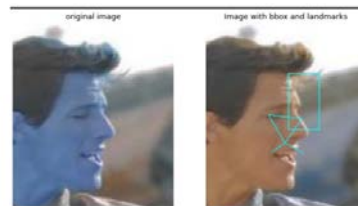

Figure 4. Image of plotting Lines on faces

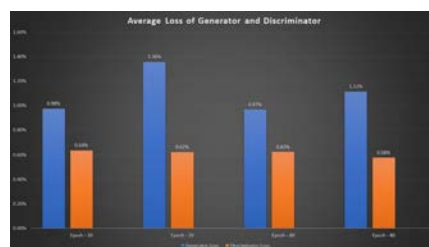

Figure 5. Generated Images after 30 epoch

Figure 6. Generated Images after 40 epoch

Figure 7. Graphical representation of average loss of Generator and discriminator

Epoch	Generator	Discriminator
Average Loss Epoch – 10	0.9761 %	0.6383 %
Average Loss Epoch – 20	1.3599 %	0.6244 %
Average Loss Epoch – 40	0.9685 %	0.6261 %
Average Loss Epoch – 80	1.1156 %	0.5894 %

Table I: Average and minimum Loss of Generator and Discriminator

Layer (type)	Output Shape	Param
conv2d_8 (Conv2D)	(32, 32, 64)	3136
lleaky_re_lu_12 (LeakyReLU)	(32, 32, 64)	0
conv2d_9 (Conv2D)	(16, 16, 128)	131200
leaky_re_lu_13 (LeakyReLU)	(16, 16, 128)	0
conv2d_10 (Conv2D)	(8, 8, 128)	262272
leaky_re_lu_14 (LeakyReLU)	(8, 8, 128)	0
flatten_2 (Flatten)	(8192)	0
dropout_2 (Dropout)	(8192)	0
dense_4 (Dense)	(1)	8193"

Table II: Summary of Discriminator

Layer (type)	Output Shape	Param
dense_5 (Dense)	(8192)	827392
reshape_2 (Reshape)	(8, 8, 128)	0
conv2d_transpose_6 (Conv2DTranspose)	(16, 16, 128)	262272
leaky_re_lu_15 (LeakyReLU)	(16, 16, 128)	0
conv2d_transpose_7 (Conv2DTranspose)	(32, 32, 256)	524544
leaky_re_lu_16 (LeakyReLU)	(32, 32, 256)	0
conv2d_transpose_8 (Conv2DTranspose)	(64, 64, 512)	2097664
leaky_re_lu_17 (LeakyReLU)	(64, 64, 512)	0
conv2d_11 (Conv2D)	(64, 64, 3)	38403

Table III: Summary of Generator

5. CONCLUSION AND FUTURE WORK

There are several networks present in machine learning but the use of DCGAN as a category of GAN is proposed for generation of face images. There is another category of GAN, Conditional GAN (cGAN) is to assists the discriminator in correctly classifying the input so that, it is difficult for the discriminator to complete. One of the most popular, effective, and successful types of GAN architecture is deep convolutional GAN. ConvNets (Convolutional Networks) are used to implement it rather than a multi-layered perceptron. The ConvNets use a convolutional stride and are built without max pooling which provides realistic possible images. Extensive simulation has been performed on CelebA face dataset using DCGAN, which achieved more accuracy as compared to cGAN is previous network model after that DCGAN launched. It is most useful for face generation and recognition for security purposes. Hence, the proposed approach found that DCGAN outperformed cGAN. There are many opportunities to expand the dataset using dataset as like we generated new faces by using dataset. Detect the number plate of bike so that we get the full information of that person when they do not follow the rules. If any criminal found on railway station camera can detect them as a criminal as like there are many applications used in

this field.

References

Aslan, S., Güdükbay, U., Töreyin, B. U., and Cetin, A. E. 2019. Deep convolutional generative adversarial networks based flame detection in video. *arXiv preprint arXiv:1902.01824*.

Creswell, A., White, T., Dumoulin, V., Arulkumaran, K., Sengupta, B., and Bharath, A. A. 2018. Generative adversarial networks: An overview. *IEEE signal processing magazine 35,* 1, 53–65.

Deng, J., Dong, W., Socher, R., Li, L.-J., Li, K., and Fei-Fei, L. 2009. Imagenet: A large-scale hierarchical image database. In *2009 IEEE conference on computer vision and pattern recognition*. Ieee, 248–255.

Goodfellow, I. J., Pouget-Abadie, J., Mirza, M., Xu, B., Warde-Farley, D., Ozair, S., Courville, A., and Bengio, Y. 2014. Generative adversarial networks.

Kingma, D. P. and Ba, J. 2014. Adam: A method for stochastic optimization. *arXiv preprint arXiv:1412.6980*.

Radford, A., Metz, L., and Chintala, S. 2015. Unsupervised representation learning with deep convolutional generative adversarial networks. *arXiv preprint arXiv:1511.06434*.

Wang, Z., She, Q., and Ward, T. E. 2021. Generative adversarial networks in computer vision: A survey and taxonomy. *ACM Computing Surveys (CSUR) 54,* 2, 1–38.

Yu, F., Seff, A., Zhang, Y., Song, S., Funkhouser, T., and Xiao, J. 2015. Lsun: Construction of a large-scale image dataset using deep learning with humans in the loop. *arXiv preprint arXiv:1506.03365*.

Zeiler, M. D. and Fergus, R. 2014. Visualizing and understanding convolutional networks. In *European conference on computer vision*. Springer, 818–833.

Roshni Khedgaonkar received her B.E. degree in computer science engineering from Anjuman College of Engineering and Technology,Nagpur in 2008. She is M.Tech. in Computer Science and Engineering from Yashvantrao Chavhan College of Engineering,Nagpur in 2012 and working as an Assistant professor in Yashvantrao Chavan College of Engineering, Nagpur. Her research interests are Image processing, Pattern recognition and Machine learning
E-mail: rskhedgaonkar@ycce.edu.

Dr. Kavita R Singh received the B.E degree in Computer Technology in 2000 from RGCERT, Nagpur University, Nagpur, India, and the Mtech. Degree in Computer Science and Engineering from Birla Institute of Technology, Ranchi, India, in 2007, and the Ph. D. degree in Computer Science from the Sardar Vallabhbhai National Institute of Technology (SVNIT), Surat, Gujarat, India. She is currently Associate Professor in Computer Technology Department, Yeshwantrao Chavan College of Engineering, Wanadongri, and Nagpur, India. Her current research interests include the area of Data structures, Database, Rough sets, Image Processing, Machine Learning, Pattern Recognition and Near Sets.
E-mail: singhkavita19@gmail.com.
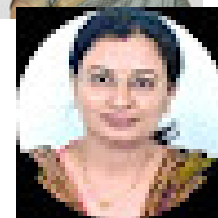
Mr. Sunny Mate received the B.E degree in Computer Science and Engineering, Nagpur University, Nagpur, India, and the Mtech. Degree in Computer Science and Engineering from Yashvantrao Chavhan College of Engineering,Nagpur
E-mail: sunnymate@gmail.com.
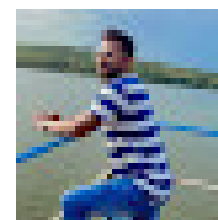
On the Real Time Object Detection and Tracking

Praful V. Barekar[1*], Kavita R. Singh[1], Shailesh D. Kamble[1], Bhagyashree V. Ambulkar[2]

[1]*Computer Technology Department, YeshwantraoChavan College of Engineering, Nagpur, India.*
[2]*Department of Computer Science, G. H. Raisoni Institute of Engineering and Technology, Nagpur, India*

Abstract

Object detection and tracking is widely used for detecting motions of objects present in images and video. Since last so many decades, numerous real time object detection and tracking methods have been proposed by researchers. The proposed methods for objects to be tracked till date require some preceding information associated with moving objects. In real time object detection and tracking approach segmentation is the initial task followed by background modeling for the extraction of predefined information including shape of the objects, position in the starting frame, texture, geometry and so on for further processing of the cluster pixels and video sequence of these objects. The object detection and tracking can be applied in the fields like computerized video surveillance, traffic monitoring, robotic vision, gesture identification, human-computer interaction, military surveillance system, vehicle navigation, medical imaging, biomedical image analysis and many more. In this paper we focus detailed technical review of different methods proposed for detection and tracking of objects. The comparison of various techniques of detection and tracking is the purpose of this work.

Keywords: Object Detection, Tracking, Segmentation, and Video processing

*Corresponding author Email: praful.barekar20@gmail.com

4th International eConference on Frontiers in Computer & Electronics Engineering and nanoTechnology
[ICFCEET] proceedings

Packrat Parsing with Dynamic Buffer Allocation

Nikhil Mangrulkar[1*], Kavita Singh[1], Mukesh Raghuwanshi[2]

[1]*Yeshwantrao Chavan College of Engineering, Nagpur, India.*
[2]*G. H.Raisoni College of Engineering & Management, Pune, India.*

Abstract

Packrat parsing is a type of recursive decent parsing with guaranteed liner time parsing. For this, memoization technique is implemented in which all parsing results are memorized to avoid repetitive scanning of inputs in case of backtracking. The issue with this technique is large heap consumption for memoization which out weigh the benefits. In many situations the developers need to make a tough decision of not implementing packrat parsing despite the possibility of exponential time parsing. In this paper we present our developed technique to avoid such a tough choice. The heap consumption is upper bounded since memorized results are stored in buffer, capacity of which is decided at runtime depending on memory available in the machine. This dynamic buffer allocation is implemented by us in Mouse parser. This implementation achieves stable performance against a variety of inputs with backtracking activities while utilizing appropriate size of memory for heap.

Keywords: Packrat parsing, Parsing Expression Grammars, parser generators, backtracking.

*Corresponding author Email: nmangrulkar@ycce.edu

1. Introduction:

A recursive descent parsing algorithm with backtracking needs to be designed carefully or else, backtracking would cause the time required for parsing to grow exponentially with the input length [1].Packrat parsing, introduced by B. Ford in 2002, is a technique for implementation of recursive descent parser along with backtracking [2]. The primary concept used in packrat parsing is of memoization which works by storing all intermediate results parsed at each distinct position in the input stream. Since each non terminal is called only once, packrat parsing avoids the possibility of exponential time for parsing. Packrat parsers are mainly used with Parsing Expression Grammars or PEGs which also introduced by B. Ford [3-4]. The Context Free Grammars (CFG) can produce multiple tree parse trees which makes it powerful and capable of representing natural languages, which is unnecessary for computer-oriented language since the programming languages are supposed to be deterministic. PEGs avoid ambiguity in grammars by not allowing the ambiguous productions in the rules at first place.

The linear time parsing guarantee given by Packrat parsers comes at a cost of large heap consumption as every intermediate result is stored in memory to avoid reevaluation. As pointed out by some of the researchers, this cost of heap consumption is so high that it nullifies the benefit offered by memoization [5]. This caused many developers to drop the idea of using memoization till recent years. Of late asthe memory available increased, few researchers implemented the PEG based parsers like Rats! and Mouse.

The purpose of this paper is to make optimal use of the resource available by using fixed minimum buffer size if the system on which program is executed is constrained for memory and if sufficient memory is available, use the portion of it for memoization.

Our idea behind dynamic memory allocation of Packrat parsing is based on the fact that if available resources; specifically, memory; is not used optimally, we are failing to take the advantage that Packrat parser offers. If the amount of memory available is not large enough and still large memory size is allotted for memoization, it may hamper the performance of system as CPU will get busy in paging and garbage collection. If too small size of memory is used for memoization even if amount of memory available is large enough, then we will be missing out on implementing linear time parsing.

We take an approach to allot the memory for storing the intermediate results optimally. If sufficient memory is available, some percentage of it will be used for memoization. If free space available is not enough, fix size of memory will be allotted for this purpose. Our experimental results demonstrated promising results.

2. Memoization

D. Michie et. al. [6] introduced the concept of memoization as a method for machine learning. By storing the calculated results, the machine "learned" it. Next time whenever same calculation was requested, the machinemerely "remembered" it by looking up the previously stored results. Stack data structure was used for storing those results which made look-up process linear. The results are merely pushed on top of the stack making insertions of results constant.

In packrat parsing, the results are stored in a matrix or similar data structure that provides constant time look-ups (when the location of the result is already known) and insertions [7]. For every encountered production this matrix is consulted; if the production has already occurred once the result is thereby already in the matrix and merely needs to be returned; if not, the production is evaluated, and the result is both inserted into the matrix and returned. Conventional recursive descent parsers that use backtracking may experience exponential parsing time in the worst case. This is due to redundant calculations of previously computed results caused by backtracking. However, memoization avoids this problem since the result only needs to be evaluated once. This gives packrat parsing a linear parsing time in relation to the length of the inputstring (given that the access andinsertion operations in the matrix are done in constant time).

4th International eConference on Frontiers in Computer & Electronics Engineering and nanoTechnology
[ICFCEET] proceedings

Nariyoshi Chida, *et. al.,* presented Linear Parsing Expression Grammars (LPEGs) in their work in 2017 [8]. LPEGs are a subcategoryof PEGs which are equivalent to DFAs. It is PEGs with syntax limited to right linear.For formulating LPEGsthey excluded patterns of recursive nonterminalswhich were followed by expressions. By this, the syntax of LPEGs became limited to right linear. Robert Grimm introduced Rats! as described in [9]. It translates grammar specification into programming language source code in Java. Redziejowski RR implemented aoperating system independent tool "Mouse" also written in Java[10]. This tool transcribes PEG into executable parser. In this tool they also provided a feature of providing semantics, because of which this tool is not only transcribing the PEGs but also can solve the expressions.

Kimio Kuramitsu presented Packrat parsing with elastic sliding window [11]. He mentioned that there are many claims available in literature that questions the benefits of memoization over its overhead. He also stated that few literatures also claims that plain recursive descent parsers are sufficiently competitive, or even faster than packrat parsers. He pointed out that the performance of Packrat parsing depends on two factors: i) Backtrack activity and ii) Effectiveness of Memoization. He has implemented technique based on sliding window protocol used in networks to handle unlimited length of incoming data. Author have used array data structure to implement the elastic window for memoization of size $W \times N$, where W is window size and N is number of non-terminals. Hashing based index is used to locate the memoized result in the array. From their experimental results they demonstrated that the heap consumption of their technique was less than the traditional Packrat parser. As elaborated [11]; the elastic sliding parsermaintained constant heap consumption, whereas simple Packrat parser had linear consumption.

Manish Goswami et. al.[12] implemented Packrat parsing based parser using Stack data structure. They modified the data structure sued by Packrat parsing based tool Mouse, which is originally implemented using array. They have compared their implementation with Rats!, an another tool based on Packrat parsing and the original Mouse tool. They showed that their modified implementation of Mouse parser performed better than both the other tools.

4. Parsing Expression Grammars:

Parsing Expression Grammars (PEGs) is a newer way of representing rules that can be used for defining syntax for machine-oriented languages. A prioritized choice operator '/' is used by PEGs for specifying possible expansions for a nonterminal. The '/' operator gives multiple patterns to be examined orderly, using the first effective match. A rule using PEGs can be defined by using form represented in Figure 1.

$$E \leftarrow xy \ / \ x$$

Figure 1: A Parsing Expression Grammar

In Figure 1 above, *E* is nonterminal which can be reduced if input matches *xy* or *x* which are terminals. Options at the right-hand side of rule can be a terminal, a non terminal or combination of both. To begin with, input will be checked for match with *xy* and only if there is no match, *x* will be checked for a possible match. For this '/' operator is used which as mentioned earlier, works as a priority operator, deciding the sequence of matching. It is worth mentioning here that if the first-choice symbol can reduce to nonterminal, the next options would not be checked in any case. Hence, it is required to decide the sequence of symbols in rule very carefully.PEG can be seen as a proper representation of a top-down parser.

4th International eConference on Frontiers in Computer & Electronics Engineering and nanoTechnology [ICFCEET] proceedings
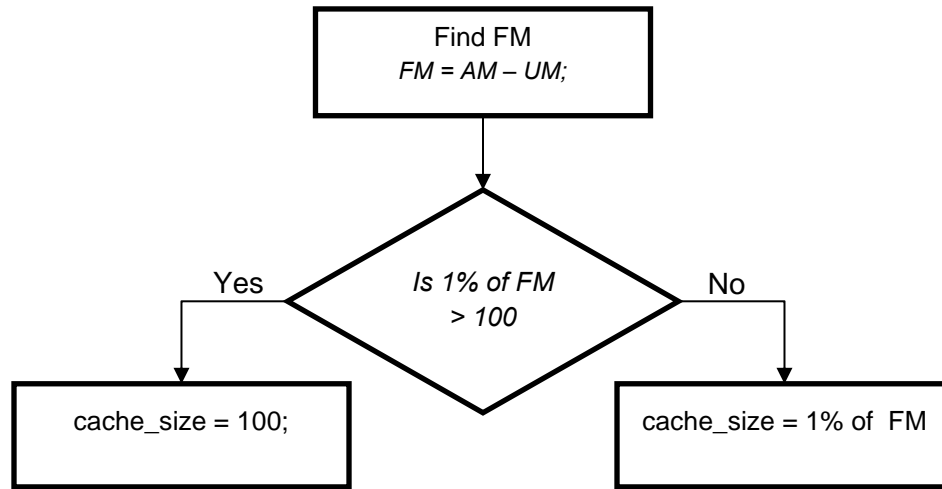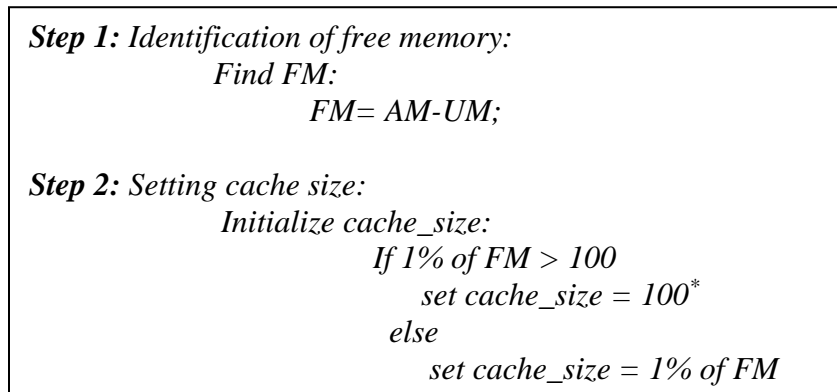
5. Methodology:

Figure 2: Graphical representation of our approach to decide minimum size of cache

Given below is our algorithm to select minimum size of cache.

> **Step 1:** *Identification of free memory:*
>   *Find FM:*
>   *FM= AM-UM;*
>
> **Step 2:** *Setting cache size:*
>   *Initialize cache_size:*
>   *If 1% of FM > 100*
>   *set cache_size = 100**
>   *else*
>   *set cache_size = 1% of FM*

Where, *FM* is free memory
     *AM*is Available Memory
     *UM*isUsed Memory

    Our algorithm is a two-step approach in which step 1 is to identify the free memory available in the system. Once the FM (free memory) is calculated, step 2 is to set the cache size. Here we check the amount of FM available. If 1% of FM is greater that 100 cache size, then maximum cache size is set to 100. If it is less than 100, 1% of FM is set as cache size. The value 100 has been taken into consideration based on the fact that parsing a sufficiently large input string would also not require more than 100 memorization. Also for every 1 byte of input about 400 bytes of memory is required for memorization which is the reason we are selecting only 1% of free memory to avoid excessive use of memory space for memorization. Because of our this approach, it is guaranteed that no more than 1% of free memory will be utilized for memorization if we are constrained for memory and if memory is available, we would take maximum benefit from it by storing every intermediate result.

6. Results and Discussion:

We have implemented our algorithm by modifying current Mouse tool. All the executions has been tested on system having Intel(R) Core(TM) i5-8265U CPU @ 1.60GHz and 8.00 GB (7.89 GB usable) RAM. Figure 3 shows the output generated by the program for "123 + 4567 + 789" as input given to the tool.

Figure 3: Output generated for input 123 + 4567 + 789

It can be observed in Figure 3 above, there were 3 situations where backtracking was done by the tool for the given input. Maximum backtracking required was of 4 places occurred after consuming input tokens "123+".

We are not presenting the performance comparison of our program with other tools like original Mouse and Modified Parser [11] as we need to compare the performance on systems with different size of RAM to verify the effectiveness of our approach. Our implementation is stable and is performing promisingly under varying size of input.

7. Conclusion:

Packrat parsing is a technique for implementing recursive descent parsers with backtracking which gives guaranteed linear time parsing. However, many researchers have questioned the effectiveness of packrat parsing due to overhead of large heap consumption for memorization. Dropping memorization because of this overhead is not a proper solution specially if there is availability of resources which could give us optimum utilization and guaranteed liner time parsing. This paper presented an approach to select the optimum size of heap to be used for storing memorized results. A two-step process is presented which ensures that if resources are available, they will be optimally utilized to provide best performance and along with guaranteed linear time parsing and, if the system is constrained for resource, bare minimum resource will be utilized for memorization to ensure memory is available for smooth functioning of the system.

Conflict of interest: The authors declare that they have no known competing financial interests or personal relationships that could have appeared to influence the work reported in this paper.

References

[1]. Birman A, Ullman JD. "Parsing algorithms with backtrack". In11th Annual Symposium on Switching and Automata Theory (swat 1970) 1970 Oct 28 (pp. 153-174). USA IEEE. https://doi.org/10.1109/SWAT.1970.18

[2]. Bryan Ford, "Packrat Parsing: a Practical Linear-Time Algorithm with Backtracking", Master's thesis, Massachusetts Institute of Technology, Department of Electrical Engineering and Computer Science, Cambridge, MA, USA, 2002. https://doi.org/10.1145/583852.581483
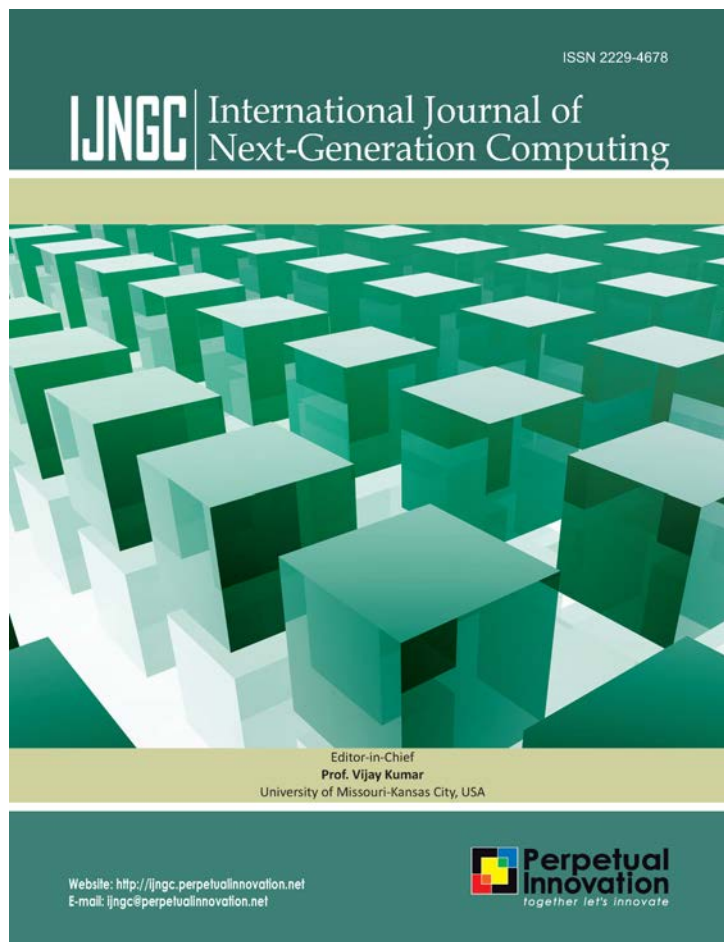
4th International eConference on Frontiers in Computer & Electronics Engineering and nanoTechnology [ICFCEET] proceedings

[3]. Ford B. "Parsing expression grammars: a recognition-based syntactic foundation". InProceedings of the 31st ACM SIGPLAN-SIGACT symposium on Principles of programming languages 2004 Jan 1 (pp. 111-122). https://doi.org/10.1145/982962.964011

[4]. B. Ford. "Packrat Parsing: Simple, Powerful, Lazy, Linear Time - Functional Pearl" In Proceedings of the ACM SIGPLAN International Conference on Functional Programming, ICFP, Pittsburgh, Pennsylvania, USA, 2002. ACM SIGPLAN Notices37/9 (2002) 36-47. https://doi.org/10.1145/583852.581483

[5]. Becket R, Somogyi Z. "DCGs+ memoing= packrat parsing but is it worth it?"InInternational Symposium on Practical Aspects of Declarative Languages 2008 Jan 7 (pp. 182-196). Springer, Berlin, Heidelberg.(LNCS, volume 4902). https://doi.org/10.1007/978-3-540-77442-6_13

[6]. MICHIE, D. "Memo Functions and Machine Learning". Nature 218 (1968) 19-22. https://doi.org/10.1038/218019a0

[7]. M. E. Lesk and E. Schmidt. UNIX Vol. II. chapter Lex; a Lexical Analyzer Generator,pages 375-387. W. B. Saunders Company, Philadelphia, PA, USA, 1990.

[8]. Nariyoshi Chida, Kimio Kuramitsu, "Linear Parsing Expression Grammars", Preprint Version, Sep 2017. https://doi.org/10.1007/978-3-319-53733-7_20

[9]. Grimm R. "Practical packrat parsing" Technical Report TR2004-854, New York University; 2004 Mar.

[10]. Redziejowski RR. "Mouse: from parsing expressions to a practical parser". InConcurrency Specification and Programming Workshop 2009 Sep.

[11]. Kuramitsu, Kimio. "Packrat parsing with elastic sliding window" Journal of information processing 23/4 (2015) 505-512. https://doi.org/10.2197/ipsjjip.23.505

[12]. Manish M. Goswami, M.M. Raghuwanshi, Latesh Malik, "Performance Improvement of Stack Based Recursive-Descent Parser for Parsing Expression Grammar", International Journal of Latest Trends in Engineering and Technology, 6/3 (2016) 302-309.

4th International eConference on Frontiers in Computer & Electronics Engineering and nanoTechnology [ICFCEET] proceedings

Improved League Championship Algorithm (ILCA) for Load Balancing in Cloud Computing

(https://ijngc.perpetualinnovation.net/index.php/ijngc/issue/view/45)

Download

🔒 PDF (https://ijngc.perpetualinnovation.net/index.php/ijngc/article/view/930/370)

Statistic

Downloads

Prof.Amol D Gaikwad
RTMNU Nagpur University YCCE

Dr.Kavita R. Singh
RTMNU Nagpur University

Abstract

You can't obtain the outcomes you need without planning, thus it's at the heart of cloud computing. This article's major goal is to decrease value-added time, increase resource utilisation, and make cloud services viable for a single activity. In recent years, metaheuristic algorithms have drew attention to the correct functioning of work scheduling algorithms among the many job scheduling techniques. With sports leagues, the algorithm based on the League Championship (LCA) is fascinating because it can be used to identify the best team/task for programming.This article uses the Improved League Championship Algorithm (ILCA) to schedule tasks, reducing deployment time, cloud usage, and cost. The ILCA is implemented through the Cloudsim simulator and the Java programming language with a nonpreventive planning strategy. ILCA also enhances economies of scale and minimises the value of using the cloud. As it has proven to be versatile in terms of time to manufacture, resource usage and economics, ILCA could be a good candidate for a cloud broker as it has proven to be versatile in terms of time to manufacture, resource usage and economics usage.

How to Cite

Gaikwad, A. ., & Singh, K. . (2022). Improved League Championship Algorithm (ILCA) for Load Balancing in Cloud Computing . *International Journal of Next-Generation Computing*, *13*(5). https://doi.org/10.47164/ijngc.v13i5.930

More Citation Formats ▾

References

1. Jena, T., Mohanty, J.R. (2017). GA-based customer conscious resource allocation and task scheduling in multi-cloud computing. Arab J Sci. Eng., 43(8): 4115- 4130. https://doi.org/10.1007/s13369-017-2766-x (https://doi.org/10.1007/s13369-017-2766-x) DOI: https://doi.org/10.1007/s13369-017-2766-x (https://doi.org/10.1007/s13369-017-2766-x)

2. Kalra, M., Singh, S. (2015). A review of metaheuristic scheduling techniques in cloud computing. Egyptian Informatics Journal, 16(3): 275-295. https://doi.org/10.1016/j.eij.2015.07.001 (https://doi.org/10.1016/j.eij.2015.07.001) DOI: https://doi.org/10.1016/j.eij.2015.07.001 (https://doi.org/10.1016/j.eij.2015.07.001)

3. Dubey, K., Kumar, M., Sharma, S.C. (2017) Modified HEFT algorithm for task scheduling in cloud computing. In Science Direct, Procedia Computer Science, 125: 725- 732. https://doi.org/10.1016/j.procs.2017.12.093 (https://doi.org/10.1016/j.procs.2017.12.093) DOI: https://doi.org/10.1016/j.procs.2017.12.093 (https://doi.org/10.1016/j.procs.2017.12.093)

4. Kashan, A.H. (2009) League championship algorithm: A new algorithm for numerical function optimization. 2009 International Conference of Soft Computing and Pattern Recognition, Published in IEEE Computer Society, pp. 43-48. https://doi.org/10.1109/SoCPaR.2009.21 (https://doi.org/10.1109/SoCPaR.2009.21) DOI: https://doi.org/10.1109/SoCPaR.2009.21 (https://doi.org/10.1109/SoCPaR.2009.21)

5. Abdulhamid, S.M., Latiff, M.S.A., Abdul-Salaam, G., Madni, S.H.H. (2016). Secure scientific applications scheduling technique for cloud computing environment using global league championship algorithm. PLoS ONE, 11(7): e0158102. https://doi.org/10.1371/journal.pone.0158102 (https://doi.org/10.1371/journal.pone.0158102) DOI: https://doi.org/10.1371/journal.pone.0158102 (https://doi.org/10.1371/journal.pone.0158102)

6. Ge, Y., Wei, G. (2010). GA-based task scheduler for the cloud computing systems. In: International Conference web Information System Mining, WISM 2010. pp. 181– 186. https://doi.org/10.1109/WISM.2010.87 (https://doi.org/10.1109/WISM.2010.87) DOI: https://doi.org/10.1109/WISM.2010.87 (https://doi.org/10.1109/WISM.2010.87)

7. Kaur, S., Verma, A. (2012) An efficient approach to genetic algorithm for task scheduling in cloud computing environment. I.J. Information Technology and Computer Science, 10: 74-79. https://doi.org/10.5815/ijitcs.2012.10.09 (https://doi.org/10.5815/ijitcs.2012.10.09) DOI: https://doi.org/10.5815/ijitcs.2012.10.09 (https://doi.org/10.5815/ijitcs.2012.10.09)

8. Liu, A., Wang, Z. (2008). Grid task scheduling based on adaptive ant colony algorithm. In: International conference on Management E-commerce E-government Grid, pp 415–418. https://doi.org/10.1109/ICMECG.2008.50 (https://doi.org/10.1109/ICMECG.2008.50) 358 DOI: https://doi.org/10.1109/ICMECG.2008.50 (https://doi.org/10.1109/ICMECG.2008.50)

9. Zhang, Z., Zhang, X. (2010). A load balancing mechanism based on ant colony and complex network theory in open cloud computing federation. In: 2nd International Conference on Industrial Mechatronics and Automation, pp 240–243. https://doi.org/10.1109/icindma.2010.5538385 (https://doi.org/10.1109/icindma.2010.5538385) DOI: https://doi.org/10.1109/ICINDMA.2010.5538385 (https://doi.org/10.1109/ICINDMA.2010.5538385)

10. Gupta A, Kapoor L, Wattal M. C2c (cloud-to-cloud): An ecosystem of cloud service providers for dynamic resource provisioning. InInternational Conference on Advances in Computing and Communications 2011 Jul 22 (pp. 501-510). Springer, Berlin, Heidelberg. DOI: https://doi.org/10.1007/978-3-642-22709-7_49 (https://doi.org/10.1007/978-3-642-22709-7_49)

11. Kennedy, J., Eberhart, R. (1995). Particle swarm optimization. Proceedings of ICNN'95 - International Conference on Neural Networks, Perth, WA, Australia, Australia. http://dx.doi.org/10.1109/ICNN.1995.488968 (https://dx.doi.org/10.1109/ICNN.1995.488968) DOI: https://doi.org/10.1109/ICNN.1995.488968 (https://doi.org/10.1109/ICNN.1995.488968)

12. Ramezani, F., Lu, J., Hussain, F.K. (2014). Task-based system load balancing in cloud computing using particle swarm optimization. Int J Parallel Program, 42:739–754. https://doi.org/10.1007/s10766-013-0275-4 (https://doi.org/10.1007/s10766-013-0275-4) DOI: https://doi.org/10.1007/s10766-013-0275-4 (https://doi.org/10.1007/s10766-013-0275-4)

13. Pooranian, Z., Shojafar, M., Abawajy, J.H., Abraham, A. (2015) An efficient meta-heuristic algorithm for grid computing. J Comb Optim (2015), New York. https://doi.org/10.1007/s10878-013-9644-6 (https://doi.org/10.1007/s10878-013-9644-6) DOI: https://doi.org/10.1007/s10878-013-9644-6 (https://doi.org/10.1007/s10878-013-9644-6)

14. Gąsior, J., Seredyński, F. (2013). Multi-objective parallel machines scheduling for fault-tolerant cloud systems. Algorithms and Architectures for Parallel Processing: Springer. pp. 247–256. https://doi.org/10.1007/978-3- (https://doi.org/10.1007/978-3-) 319-03859-9_21 DOI: https://doi.org/10.1007/978-3-319-03859-9_21 (https://doi.org/10.1007/978-3-319-03859-9_21)

15. Chen, Z.G., Du, K.J., Zhan, Z.H., Zhang, J. (2015). Deadline constrained cloud computing resources scheduling for cost optimization based on dynamic objective genetic algorithm. Evolutionary Computation (CEC), 2015 IEEE Congress on; 2015: IEEE. https://doi.org/10.1109/CEC.2015.7256960 (https://doi.org/10.1109/CEC.2015.7256960) DOI: https://doi.org/10.1109/CEC.2015.7256960 (https://doi.org/10.1109/CEC.2015.7256960)

16. Liu, X.F., Zhan, Z.H., Du, K.J., Chen, W.N. (2014). Energy aware virtual machine placement scheduling in cloud computing based on ant colony optimization approach. Proceedings of the 2014 Conference on Genetic and Evolutionary Computation; 2014: ACM. https://doi.org/10.1145/2576768.2598265 (https://doi.org/10.1145/2576768.2598265) DOI: https://doi.org/10.1145/2576768.2598265 (https://doi.org/10.1145/2576768.2598265)

17. The NASA Ames iPSC/860 log by CS Huji labs parallelworkload.

Home (https://ijngc.perpetualinnovation.net/index.php/ijngc)
Current Issue
(https://ijngc.perpetualinnovation.net/index.php/ijngc/issue/view/35)
Archives (https://ijngc.perpetualinnovation.net/index.php/ijngc/issue/archive)
About the Journal
(https://ijngc.perpetualinnovation.net/index.php/ijngc/about)
Announcement
(https://ijngc.perpetualinnovation.net/index.php/ijngc/announcement)

Editorial Team
(https://ijngc.perpetualinnovation.net/index.php/ijngc/about/editorialTeam)

EMPIRICAL ANALYSIS OF MACHINE LEARNING-BASED ENERGY EFFICIENT CLOUD LOAD BALANCING ARCHITECTURES: A QUANTITATIVE PERSPECTIVE

K.R.Singh

Yeshwantrao Chavan College of Engineering,Nagpur, Maharashtra, (India).
Indira Gandhi Delhi Technical University for Women, New Delhi, Delhi, (India).

A.D.Gaikwad

B Yeshwantrao Chavan College of Engineering,Nagpur, Maharashtra, (India).
Indira Gandhi Delhi Technical University for Women, New Delhi, Delhi, (India).

S.D.Kamble

Yeshwantrao Chavan College of Engineering,Nagpur, Maharashtra, (India).
Indira Gandhi Delhi Technical University for Women, New Delhi, Delhi, (India).

ABSTRACT

Design of energy efficient load balancing models in cloud environments requires in-depth analysis of the cloud architecture and nature of requests served by the cloud. Depending upon these parameters, machine learning models are designed which aim at assigning best possible resource combination to serve the given tasks. This assignment varies w.r.t. multiple task and cloud parameters; which include task time, virtual machine (VM) performance, task deadline, energy consumption, etc. In order to perform this task, a wide variety of algorithms are developed by researchers cloud designers. Each of these algorithms aim at optimizing certain load balancing related parameters; for instance, a Genetic Algorithm (GA) designed for optimization of VM utilization might not consider task deadline before task allocation to the VMs. While, algorithms aimed at performing deadline aware load balancing might not provide effective cloud-to-task-mapping before allocation of tasks. Thus, it becomes difficult for researchers to select the best possible algorithms for their cloud deployment. In order to reduce this ambiguity, the underlying text compares different energy efficient cloud load balancing algorithms; and evaluates their performance in terms of computational complexity, and relative energy efficiency. This performance evaluation is further extended via inter architecture comparison; in order to evaluate the most optimum load balancer implementation for a given energy efficient application. Thus, after referring this text, researchers and cloud system designers will be able to select optimum algorithmic implementations for their given deployment. This will assist in reducing cloud deployment delay, and improving application specific load balancer performance.

KEYWORDS

Cloud, Load, Balancing, Machine, Learning, Task, Deadline, Energy.

1. INTRODUCTION

Due to the current CoVID-19 pandemic, most businesses are forced to adopt the work-from home (WFH) model. This model has increased dependency of users on cloud-based services, thereby requiring cloud service providers to optimize their load-balancing models. These models are broadly categorized into 2 types; which are hardware load balancing, and elastic load balancing. The former type consists of optimizing performance of hardware components like virtual machines, servers, memory utilization, task optimization, and central processing unit (CPU) optimization.

While, the later type consists of network load balancers, application load balancers and hybrid load balancers. Hierarchical categorization of these algorithms can be observed from figure 1, from where it can be observed that network load balancing depends on VM and Server load balancing; application load balancing depends on memory, task and CPU load balancing; while classic (or hybrid) load balancing depends on all the hardware-based load balancing models. VM load balancing models aim at optimizing virtual machine performance by assigning tasks in such a manner that most VM resources are utilized, thereby improving hardware utilization efficiency.

This model does not take into consideration deadline constraints, memory constraints, etc. while modelling the load balancer. In contrast, memory-based load balancer models only take into consideration memory utilization; and aim at optimizing task storage without considering resource or CPU load values. Server load balancing algorithms assist in optimization server utilization while performing load balancing, while CPU load balancers aim at optimizing CPU utilization while load balancing. Moreover, task load balancing models aim at executing tasks under a given deadline without considering CPU load, memory or virtual machine efficiency values.
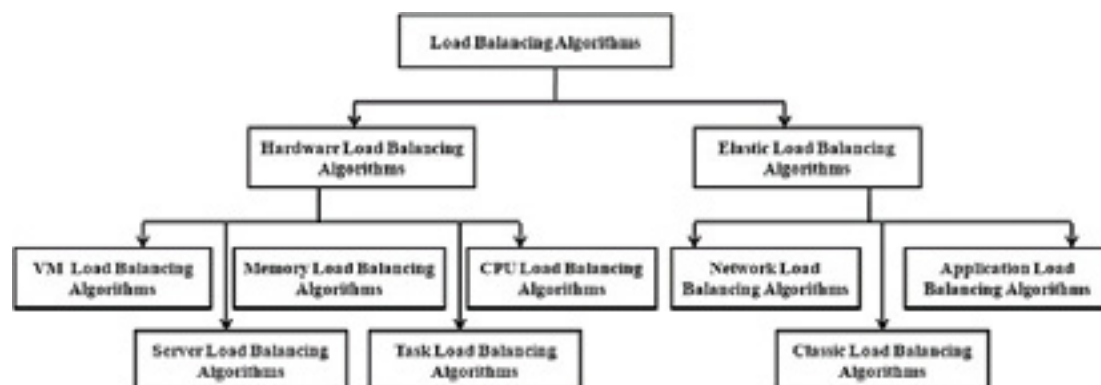

Figure1. Hierarchical categorization of load balancing models.

Elastic load balancers aim at optimizing a group of parameters during load balancing. For instance, network load balancers optimize virtual machine and server parameters; while application load balancers aim at optimization of memory, CPU load and task parameters. A combination of these parameters is optimized by classic load balancers, wherein depending upon the application; one or more cloud task parameters are optimized. An in-depth survey of these optimization models can be referred from the next section; wherein various machine learning models for load balancing are described. This is followed by statistical analysis of these models; their comparative evaluation. The evaluation assists in identification of best suited for models for any given application; which will assist researchers and system designers for high speed and high efficiency system design. Finally, this text concludes with some interesting observations about the reviewed algorithms; and recommends methods to improve them.

2. LITERATURE REVIEW

A wide variety of energy efficient cloud load balancing models have been proposed by researchers and cloud designers. These algorithms aim at improving energy efficiency via application of different machine learning models including but not limited to bio-inspired models, swarm-optimization models, neural networks, etc. The work in (Panda, Moharana, Das, and Mishra, 2019)[1] introduces such an energy efficient model that utilizes virtual machine consolidation in cloud environments.

The model aims at minimizing energy consumption during virtual machine (VM) migration process via threshold-based sleep scheduling. Here, virtual machines with lower load levels are put to sleep for specified clock cycles, thereby assisting in energy reduction. Due to this sleep scheduling, VMs with high loads are easily identified. This identification assists in assigning tasks to the sleep mode VMs, thereby reducing the probability of load imbalance. Description of the model can be observed from figure 2, wherein load balancing and VM migration processes are described.
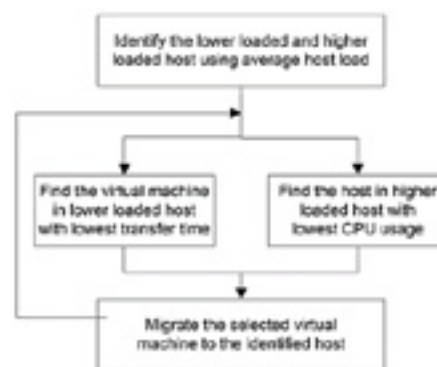

Figure2. Energy efficient VM migration and load balancing.

Figure 2. Energy efficient VM migration and load balancing (Panda et al., 2019)[1] Due to efficient migration of VMs, and proper load division, the model is able to reduce load imbalance levels by 15% energy consumption by 20% when compared with non-energy aware models. A similar model that uses dynamic energy efficient resource (DEER) allocation can be observed from (Rehman, Ahmad, Jehangiri, Ala'Anzy, Othman, Umar, and Ahmad, 2020)[2], wherein resource with minimum utilization is used for load balancing. This model also performs intelligent sleep scheduling, due to which an energy efficiency of 15% is achieved when compared with Dynamic Resource Allocation Strategy (DRAM) model. This model also reduces computational cost by 10% when compared with DRAM, thereby making is useful for real time load balancing applications. A load-based model that uses self-organizing maps (SOMs) can be observed from (Malshetty and Mathapati, 2019)[3], wherein cluster heads are created, and all load requests are handled by them.

The selected cluster heads are able to reduce computational load on centralized server, and select machines with minimum power consumption, thereby improving overall energy efficiency of the system. It is observed that the proposed model is able to reduce energy consumption by 18% and delay of processing by 10% when compared with Low-energy adaptive clustering hierarchy (LEACH) model. This approach can be compared with other models, a survey of these models can be observed from (Ala'anzy and Othman, 2019)[4], wherein effects load balancing & server consolidation are studied. The work compares algorithms like load-aware Global resource affinity management, advanced prediction-based minimization of load migration, multidimensional hierarchical VM migration, extended first fit decreasing algorithm, locusts inspired scheduling algorithm, etc.

It is observed that soft computing models outperform linear models in terms of energy efficiency & load balancing performance. An example of such a soft computing model can be observed from (Salem Alatawi and Abdullah Sharaf, 2020)[5], wherein Honey Bee optimization is combied with fuzzy logic for improved energy efficiency during load balancing. The model uses a fuzzy approach for host & VM selection, and then deploys a Honey Bee optimization model for load scheduling

between these components. Due to incorporation of VM energy levels, and task length in the fitness function (described in equation 1), the model is able to schedule tasks with good energy efficiency.

$$Fitness = \frac{T_{length} * T_{deadline}}{E_{vm}} \dots (1)$$

Where, T length T deadline are task length, and task deadline; while E vm is the per task execution energy of the VM. The model aims are reducing this fitness value in order to improve the energy efficiency, and execute tasks of the given length under the given deadline. The model is able to reduce energy consumption by up to 18% when compared with only fuzzy model, and up to 15% when compared with only the Honey Bee optimization model, thereby making it applicable for real time use. Execution of tasks with high energy efficiency must be accompanied with effective placement of VM services. This placement allows schedulers to select nearby VMs in order to execute tasks with high efficiency and low energy consumption. Example of such an architecture can be observed from (Alharbi, El-Gorashi, and Elmirghani, 2019)[6], wherein researchers have showcased the use of cloud-to-fog load balancing reduces energy consumption by 75% when compared with only-cloud load balancing architecture. This architecture can be observed from figure 3, wherein data from cloud is offloaded to fog nodes for efficient balancing.
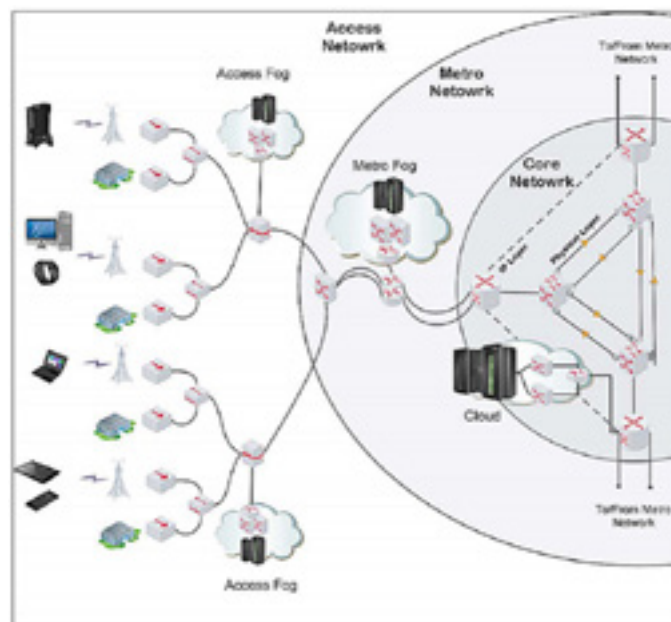

Figure3. Offloading data from single cloud to fog nodes for energy efficient load balancing [6].

Figure 3. Offloading data from single cloud to fog nodes for energy efficient load balancing [6] Due to offloading of tasks on fog nodes, the computational load is shared between different nodes, thereby assisting in faster task execution, and better energy efficiency. This efficiency can be further improved via addition of soft computing models. Such a model is defined in (Dong, Xu, Ding, Meng, and Zhao, 2019)[7], wherein glow worm swarm optimization (GSO) is used. The model combines clustering for extraction of large task resources, with sine cosine analysis (SCA) in order to modify the step size of GSO for energy adaptive scheduling. This modification in step size allows the GSO model to select load & energy optimized cloud resources for the given task.

The clustered input tasks are divided into edge group & cloud group; wherein each group has task elements based on CPU utilization and memory consumption. For instance, the edge group retains

tasks with high CPU utilization but low memory consumption, while the cloud group retains tasks with high memory consumption. This task division is governed using the following equation,

$$L\_group = \partial * L\_cpu + \emptyset * L\_memory \dots (2)$$

Where, L group is resource requirement for the given group, L cpu is resource requirement w.r.t CPU utilization, L memory is resource requirement w.r.t. memory utilization, while and are cloud and edge constants. The model is compared with First Fit Decreasing (FFD) & OTS models and it is observed that the GSO model has 25% better energy efficiency, 15% better throughput, and 18% better load balancing degree when compared with these algorithms. This efficiency can be further improved by performing computations on fog devices as observed from (Bhuvaneswari and Akila, 2019)[8], wherein comparison of different fog-based load balancing algorithms w.r.t. their energy performance is studied. Algorithms like ant colony optimization (ACO), max-min algorithm, active monitoring for load balancing (AMLB), and round robin (RR) are compared. It is observed that the ACO based soft computing model has 15% better efficiency when compared with RR, while AMLB when combined with ACO provides 25% better energy efficiency than individual algorithms. Another hybrid combination that uses ACO with support vector machines (SVM) can be observed from (Junaid, Sohail, Ahmed, Baz, Khan, and Alhakami, 2020)[9], wherein file type formatting (FTF) is used for load classification. Input requests are given to SVM model and depending upon file type at input, the model classifies load types into low power, medium power and high power. After this, the classified load is given to ACO, wherein VM to load mapping is performed using greedy heuristics. Flow of the model can be observed from figure 4, wherein training phases and testing phases can be seen with the final load balancing process. It is observed that the model performs SVM training on file formats, and provides the classified results to ACO. The ACO model internally maps suitable VMs to tasks for high energy efficiency. Due to this, the proposed SVMFTF model provides 8% better energy efficiency than random forest (RF), 6% than Naïve Bayes, 9% than k-nearest neighbours (kNN), and 4% than convolutional neural network (CNN) models.
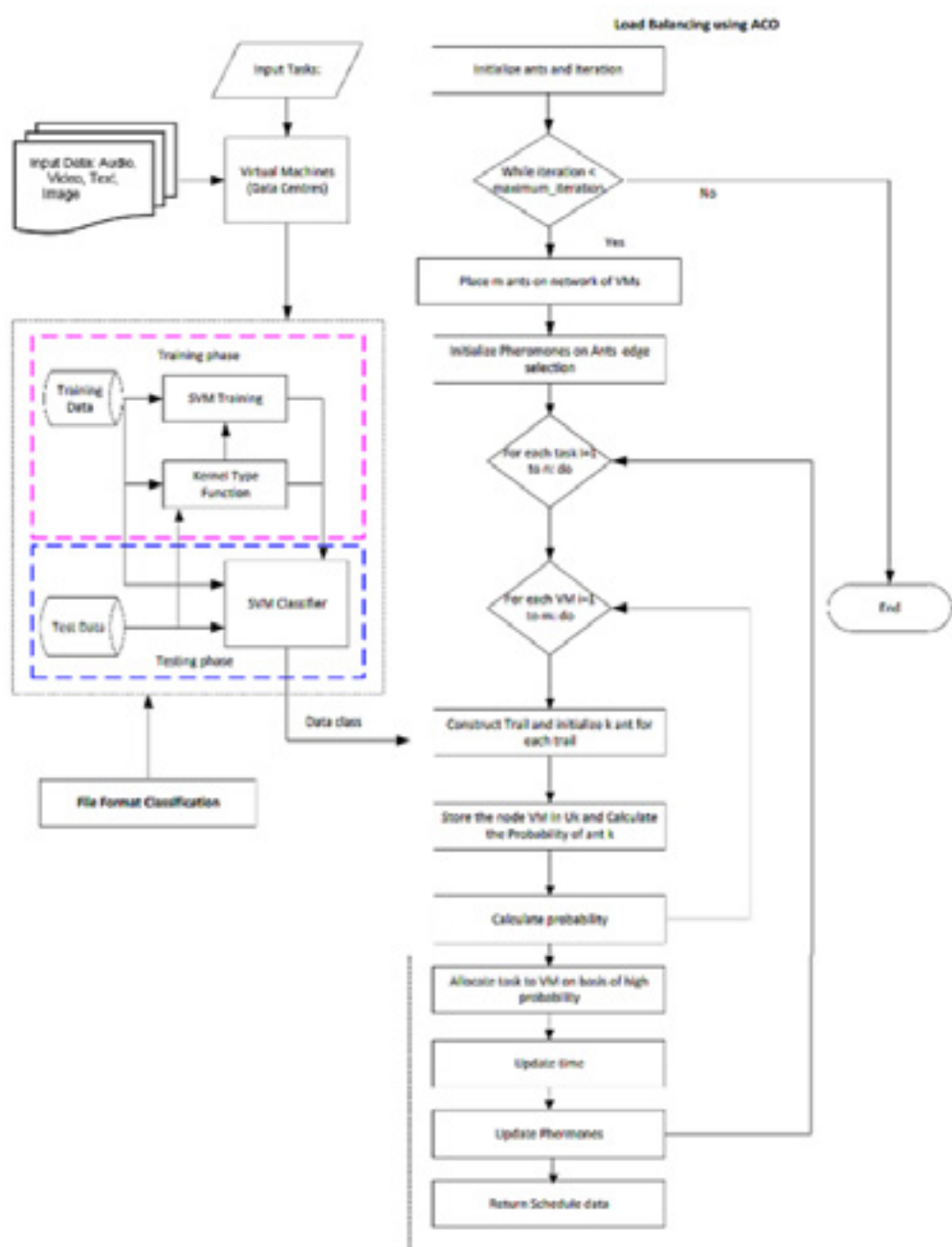
Figure4.SVMFTF model for energy efficient load balancing [9].

Figure 4. SVMFTF model for energy efficient load balancing [9] The model also showcases better throughput, and migration performance when compared with RF, Na¨ıve Bayes, kNN, CNN models. Specifically, the model provides 8% better throughput than RF, 3% better than Na¨ıve Bayes, 15% better than kNN, and 5% better than CNN; while it provides 10% better migration performance than RF, 4% better than Na¨ıve Bayes, 8% better than kNN, and 5% better than CNN models when compared on the same task set and cloud configurations . Comparison of this model can be done with other standard load balancing models as suggested in (Dey and Gunasekhar, 2019)[10], wherein models like first in first out (FIFO), fair scheduling, capacity scheduling, hybrid scheduling, longest approximate time to end scheduling, self-adaptive mapreduce scheduling, and context-aware scheduling for Hadoop are discussed. Each of these models are compared on parameters like Job Characteristics, Responsiveness, Resource Pool Configuration, Queue Characteristics, Parallelization of Tasks, Queue Responsiveness, Dynamic Priority, Locality Management, Remaining Burst Time, Task Priority, Context and Energy Efficiency. All these parameters are evaluated on the Planet Lab dataset, wherein it is observed that Robust Local Regression (RLR) methods like self-adaptive map-reduce scheduling, and context-aware scheduling outperform other methods by over 10% in terms of

energy efficiency. The same trend is observed for other parameters, due to the sophistication of the RLR methods, and in-depth analysis for the given tasks.

A similar study like [10] can be observed in (Kulshrestha and Patel, 2019)[11], wherein models like ALB, transport layer load balancer (TLLB), network layer load balancer (NLLB), VM provisioning on host, consolidation of VMs on host, and VM-level task scheduling are described. Out of these algorithm ALB outperforms other models in terms of energy efficiency by providing 8% better performance than TLLB, 5% better performance than VM provisioning, and 15% better performance than VM consolidation. An example the ALB scheme can be observed in (Zhang, Jia, Gu, and Guo, 2019)[12], wherein Matrix sparseness with normalizedWater-Filling (MSNWF) is described. This model is compared with Heterogeneous Network (HETNET), and OPT models, and it is observed that MSNWF provides 15% better energy efficiency than HETNET and 5% better energy efficiency than OPT. Thus, the MSNWF model can be used for high performance cloud load balancing applications, wherein along with efficiency of task scheduling, energy efficiency is also improved. This model performance can be further improved by integration of broker service policy for software as a service (SaaS) application. Modelling of such architectures requires high efficiency broker design, wherein any incoming task is first given to a broker for estimation of approximate processing site. This estimation allows the cloud VMs to pre-allocate resources for the task, thereby improving the task execution efficiency. In order to model such brokers, architectures like shortest job scheduling, Min-min, Max-min, Two-phase (OLB + LBMM), Modified active monitoring, Throttled Load Balancer, Genetic Algorithm, Honey Bee foraging algorithm, ACO, etc. are available (Jyoti, Shrimali, Tiwari, and Singh, 2020)[13]. It is observed that ACO and other soft computing models when utilizing fog and cloud computing, outperform other models in terms of energy efficiency. An example of such a model can be observed from (Lin, Peng, Bian, Xu, Chang, and Li, 2019)[14], wherein the soft computing models are deployed on cloud. The results of these models are VM-to-task mapping, which are executed either on the cloud infrastructure or offloaded to the fog device for better load balancing capabilities. The model for this architecture can be observed from figure 5, wherein offloading process is performed using different wireless standards.
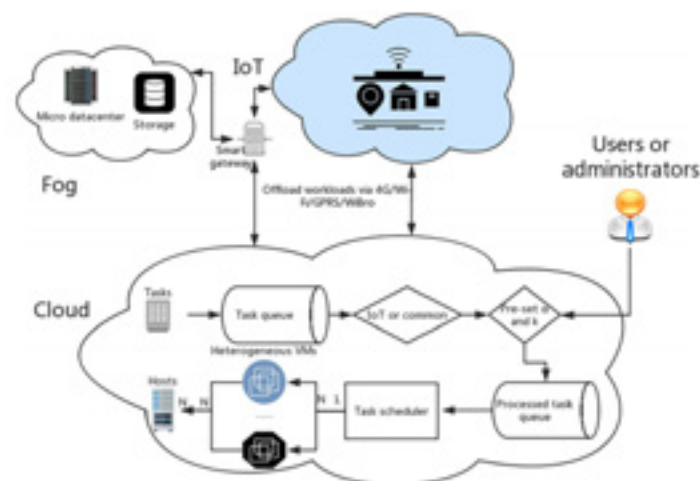

Figure5. Fog-cloud load balancing model with soft computing for efficient task mapping [14].

Figure 5. Fog-cloud load balancing model with soft computing for efficient task mapping [14] The model utilizes total amount of resource in host, total amount of resource in VM, estimated execution time of task, normalization of task average demand for resource, normal resource load of task, relative load of task for resource upon VM, task length, and task priority for scheduling. It is observed that the proposed soft computing model outperforms first come first serve by 15%, random assignment by 25%, trade-off by 8%, main resource load & time balancing by 16%, and main resource task balance by 9% in terms of energy efficiency. This is due to design of energy & task length aware fitness function design, which suggests that soft computing must be used for any kind of load balancing models. A similar model is proposed in (Mandal, Mondal, Banerjee, and Biswas, 2020)[15], wherein

service level agreement (SLA) is used for detection of task overload at different hosts. It uses a mapping ratio that consists of VM utilization and allocated resource characteristics in order to assign tasks to non-overloaded VMs. The value of this mapping ratio (Mapping r) can be observed from equation 3, wherein both the parameters are split into task & resource related characteristics.

$$Mapping_r = \frac{VM\_mips + VM\_RAM + VM\_BW}{T_{length} + T_{deadline}} \dots (3)$$

where in, VM mips, VM RAM & VM BW are VM specific capacity, available RAM & bandwidth while Tlength & Tdeadline are task related length & deadline parameters. It is observed that the proposed model outperforms minimum migration time MMT by 45%, maximum correlation MaxCorr by 35%, minimum utilization (MU) by 46%, and random selection RS by 34%, thereby making it highly useful for real time cloud deployments. Context-aware load balancing models have better efficiency than energy-aware, or task-length aware models because these models adaptively modify their internal rules depending upon the context of given task and condition of the VMs. Such a model that utilizes context information for energy efficient load balancing is described in (Royaee, Mirvaziri, and Khatibi Bardsiri, 2021)16], wherein automata ant colony based multiple recursive routing protocol (AMRRPL) is used. The model solves issues like bottlenecking, efficient parameter selection, effect of upstream nodes, and congestion which are inherent with load balancing. The model uses destination oriented directed acyclic graph (DODAG) in order to perform load balancing via laying out all possible VM-to-Task combinations on an acyclic graph. Due to use of DODAG the model is able to achieve an energy efficiency of 8% when compared with ERPL (enhanced RPL), and 45% when compared with HECRPL (hybrid energy efficient RPL) and its configurations. This model can be applied to various applications including software defined network (SDN), content delivery network (CDN), cost-based distribution (CBD) networks, etc. for highly energy efficient load balancing. An example of this application for CDN can be observed in (Gupta, Goyal, and Gupta, 2015)[17], wherein a reliability aware load balancer model is applied.

The model uses a modified version of Genetic Algorithm (GA) for task scheduling, and is able to obtain 15% better energy efficiency when compared with queue length-based load balancing (QLBLB) model. Another low power model that uses first of maximum loss scheduling algorithm (FOML) is described in (Liang, Dong, Wang, and Zhang, 2020)[18], wherein relationship between energy utilization & average completion time is used. The model selects VM with maximum energy utilization and assigns it to a task that has average completion time (when compared to all tasks in queue). This task is then deleted, and a new average completion task is evaluated and assigned to the next maximum energy utilization VM. This process makes sure that all the high energy consuming VMs are assigned to moderate sized tasks, while other VMs are assigned to large & small sized tasks. Flow of this model can be observed from figure 6, wherein ETC (extended time of completion) and ACT (average completion time) matrices are evaluated for the given set of tasks.
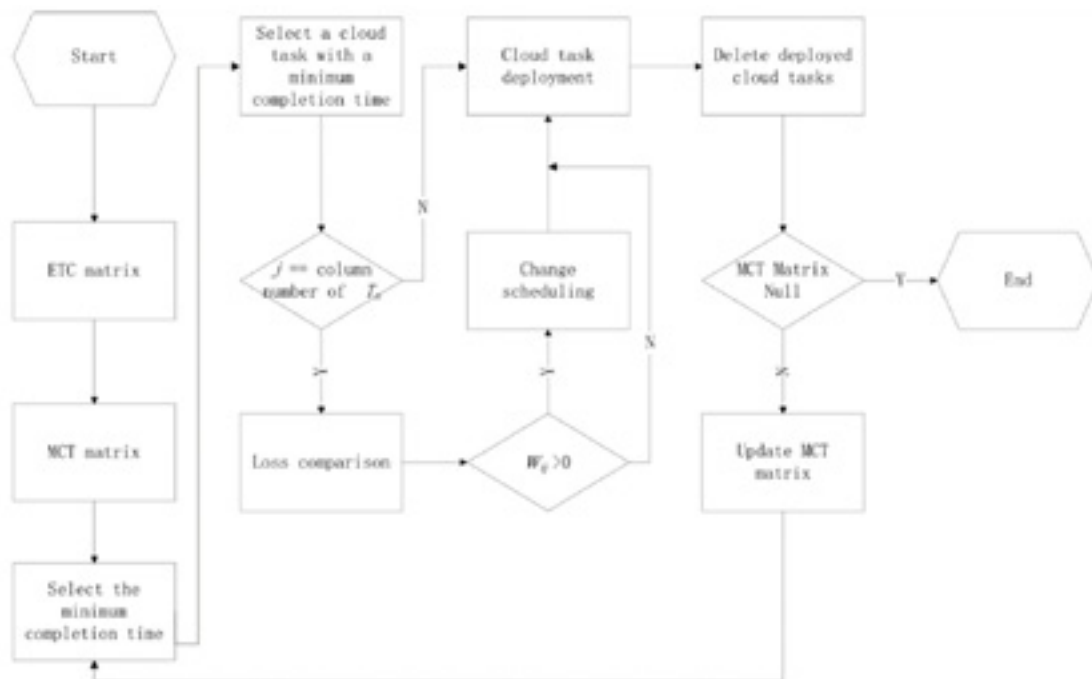
Figure6.Maximum energy utilization model for efficient task scheduling [18].

Figure 6. Maximum energy utilization model for efficient task scheduling [18] The FOML model is able to obtain 10% better energy utilization when compared with min-min model, 8% better utilization when compared with max-min model, 12% when compared with suffrage model, and 15% better than E-HEFT model, thereby making it highly effective for real time deployments.

Similar models are described in (Hadikhani, Eslaminejad, Yari, and Ashoor Mahani, 2020)[19], and (Sadeghi and Avokh, 2020)[20], wherein geographic information and Two-hop Routing Tree with Cuckoo search (CCTRT) models are defined. These models able to achieve 5% and 12% better energy efficiency when compared with E-HEFT model, thereby suggesting that the use of soft computing models is fundamental to design of energy efficient load balancing algorithms. The efficiency of these models can be further improved via use of predictive workload balancing, wherein the system is able to predict workloads depending upon task patterns, and pre allocate cloud & fog VMs for efficient execution. Architecture for such a system can be observed in (Jodayree, Abaza, and Tan, 2019)[21], wherein rule-based workload prediction is defined. It uses a combination of historical data analysis and random workload assignment in order to speed up workload balancing. Due to predictive analysis, the model is able perform host reduction and thereby reduce energy consumption by 10% when compared with random assignment algorithm.

This model can be further extended via use of deadline constrained task scheduling as suggested in (Ben Alla, Ben Alla, Touhafi, and Ezzati, 2019)[22], wherein a dynamic classifier is used to divide incoming tasks into priority queues, and each of these queues is processed using Fuzzy Logic and Particle Swarm Optimization model (FLPSO). The FLPSO model used in this approach is able to reduce energy consumption by 60% when compared with FCFS (first come first serve), 25% when compared with EDF (earliest deadline first), and 15% when compared with Differential Evolution (DE) with Multiple Criteria Decision Making (MCDM) algorithms. This comparison appears to be true for different VM and task combinations, thereby assisting in deploying the FLPSO model for a wide variety of cloud infrastructures.

This approach must be compared with other models like the ones mentioned in (Pourghebleh and Hayyolalam, 2020)[23] in order to evaluate its real time applicability and deployment capabilities.

Similar energy efficient models are discussed in (Rashid, Tripathi, Prakash, and Tripathi, 2019)[24], (Singh and Kumar, 2019a)[25] and (Kansal and Chana, 2018)[26] wherein load based energy efficiency, security aware energy efficiency, and migration aware energy efficiency models are

3C Empresa. Investigación y pensamiento crítico. ISSN: 2254-3376

Ed. 50 Vol. 11 N.º 2 August - December 2022

described. Each of these models utilize soft computing techniques like ACO, PSO, GA, and GSO in order to achieve high energy efficiency. A resource aware load balancing model can be observed in (Ahmed, Aleem, Noman Khalid, Arshad Islam, and Azhar Iqbal, 2021)[27], wherein heterogenous clustering is used in order to perform resource-based task mapping. The model performs job to resource mapping depending upon resource availability, and resource aware load balancing for obtaining higher utilization ratio. It uses a predictive model for classification and forecasting job device suitability & job time estimation matrix as observed from figure 7, wherein the overall model is described. The model extracts features including front end clang (percentage of tasks remaining), kernel features ratio of task length to current machine configuration), and static features (initial performance of machines and number of tasks) from tasks and provides them to Resource aware load balancing and hierarchical clustering (RALBHC) model for improvement of resource utilization.

The model is able to achieve an energy efficiency of 25% when compared with Max-min algorithm, 15% when compared with Minimum Completion Time, 8% when compared with Resource-Aware Scheduling Algorithm (RASA), and 10% when compared with Task-Aware Scheduling Algorithm (TASA). Another energy efficient model that uses equal load distribution for fog-to-cloud & cloudto-fog migration (EDCW) is described in (Kaur and Aron, 2020)[28], wherein linear programming (LP) is used. The use of LP results into equal distribution of tasks between fog node and cloud node, thereby assisting in improved load balancer performance. The model is able to achieve 15% better energy efficiency when compared with Round Robin model, and 8% better efficiency when compared with throttled model, thereby making it useful for low energy load balancing applications.

Similar energy-efficient models are proposed in (Escobar, Ortega, D´ıaz, Gonz´alez, and Damas, 2019)[29], (?, ?)[30], (Taboada, Aalto, Lassila, and Liberal, 2017)[31],(Kumar, Singh, and Mohan, 2021)[32], and (Singh and Kumar, 2019b)[33], where in parallel evolutionary algorithms, context-based load balancing, energy-aware load balancing, resource-efficient load-balancing, and secure load balancing models are described. These models make use of different soft computing methods in order to perform task-based & resource-based load balancing. The underlying models are able to reduce energy consumption via optimization of the fitness function, wherein resource energy, task length, task deadline, and resource performance parameters are used. A quantitative analysis of these models is described in the next section, wherein the underlying models are compared in terms of relative energy efficiency values, thereby assisting cloud system designers to identify energy-efficient load-balancing models for their deployment.
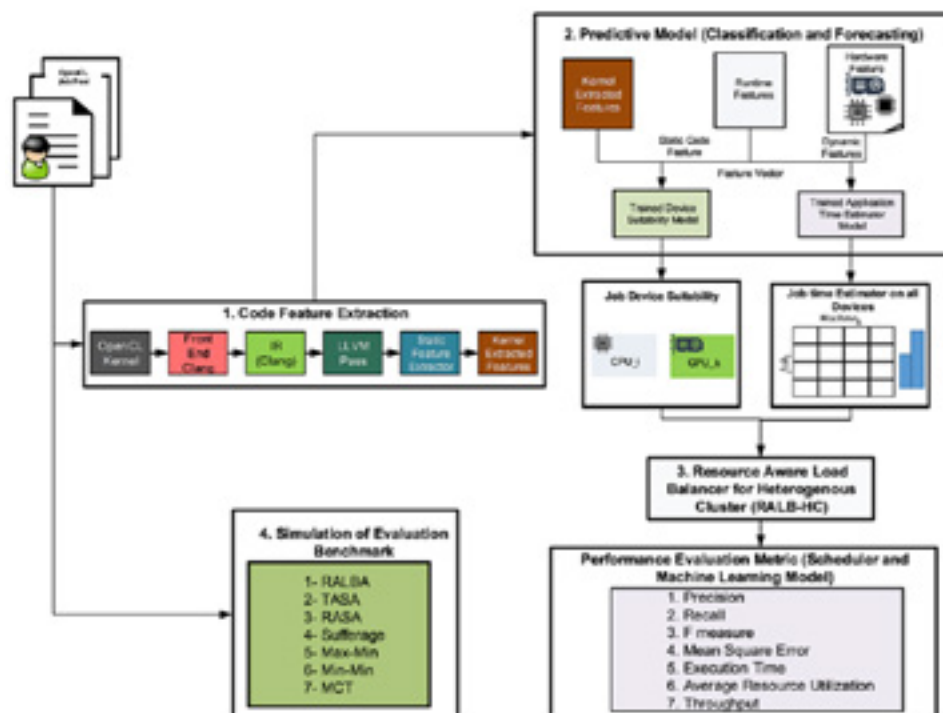
Figure7.Maximum energy utilization model for efficient task scheduling [18].

3. QUANTITATIVE ANALYSIS

From the literature, it is observed that the energy efficiency of different cloud load balancing algorithms is estimated using their relative percentages. This limits the quantitative comparison capability of these algorithms. In order to resolve this drawback, this section evaluates absolute percentage energy efficiency when compared with the basic first come first serve (FCFS) algorithm.

This process will allow researchers to estimate energy performance of reviewed algorithms, along with their computational complexity. The computational complexity is divided into fuzzy ranges of low (L), medium (M), high (H) and very high (VH). Maintaining a balance between energy efficiency and computational complexity is a must while designing load balancing models for cloud. The quantitative results are tabulated in table 1, wherein the aforementioned parameters are compared across different algorithms.Based on this analysis it can be observed that the FLPSO (Ben Alla et al., 2019)[22], AMRRPL (Royaee et al., 2021)[16], MU (Mandal et al., 2020)[15], SLA based model (Mandal et al., 2020)[15], EDF(?, ?)[22], and GSO SCA(Dong et al., 2019)[7] model outperform other models in terms of relative energy efficiency.This performance evaluation can also be observed from the visualization in figure 8, wherein different algorithms and their accuracies are compared. It can also be observed that CNN and other deep learning models are not used for energy efficient load balancing, because training of these models for dynamic loads is resource intensive, thereby requires large amount of power.

Model Used	Energy efficiency %	Computational Complexity
Threshold based sleep scheduling [1]	15	M
DEER [2]	12	M
DRAM [2]	8	M
Load based SOM [3]	22	H
Honey bee optimization [5]	25	H
Fuzzy logic [5]	15	M
Cloud to fog migration [6]	34	H
Single cloud [6]	18	M
GSO SCA [7]	33	M
FFD [7]	23	M
OTS [7]	15	L
ACO [8]	18	M
AMLB [8]	8	L
RR [8]	3	L
ACO FTF SVM [9]	12	H
RF [9]	5	M
Naïve Bayes [9]	8	M
kNN [9]	2	L
CNN [9]	0	VH
RLR [10]	15	H
NLLB [11]	10	M
MSNWF [12]	25	VH
HETNET [12]	15	H
Fog-cloud model [14]	15	H
Random assignment [14]	22	M
SLA based model [15]	48	H
MMT [15]	40	M
Max Corr. [15]	30	M
MU [15]	41	M
RS [15]	31	M
AMRRPL [16]	48	H
ERPL [16]	16	M
HECRPL [16]	5	M
FOML [18]	15	M
Min to Min [18]	6	L
E-HEFT [18]	23	M
CCTRT [20]	18	H
Rule based prediction [21]	15	M
FLPSO [22]	60	H
EDF [22]	48	M
DE [22]	26	M
MCDM [22]	31	M
RALBHC [27]	35	H
Max to Min [28]	18	M
RASA [28]	2	M
TASA [28]	25	M

Moreover, standard CNN models are also not available for this purpose, therefore it is a necessity that researchers should develop such models that aim towards energy efficiency. These models can then be extended via transfer learning or recurrent networks in order to incrementally tune their performance. Neural network models have very low energy consumption during evaluation, thus pre-training of models is further recommended.
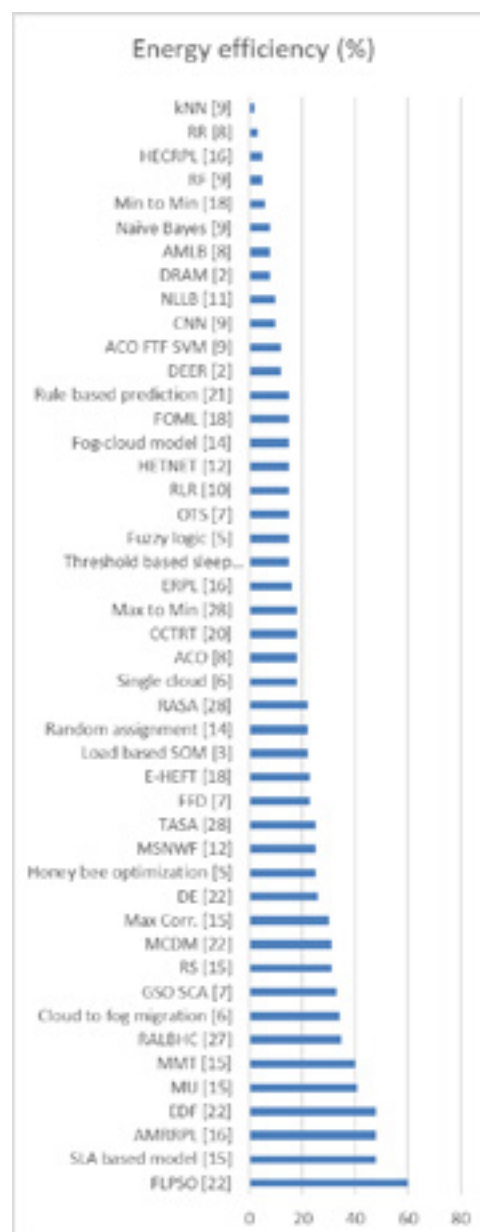
Figure8.Energy efficiency of different load balancing models.

4. CONCLUSION AND FUTURE SCOPE

The comparative quantitative analysis indicates that FLPSO (Ben Alla et al., 2019)[22], SLA based model (Mandal et al., 2020)[15], AMRRPL (Royaee et al., 2021)[16], EDF(Ben Alla et al., 2019)[22], MU (Mandal et al., 2020)[15], MMT [15], RALBHC (Ahmed et al., 2021)[27], Cloud to fog migration (Alharbi et al., 2019)[6], GSO SCA (Dong et al., 2019)[7], RS (Mandal et al., 2020)[15], MCDM (Ben Alla et al., 2019)[22], and Max Corr. (Mandal et al., 2020)[15] outperform linear models like kNN (Junaid et al., 2020)[9], HECRPL (Royaee et al., 2021)[16], CNN (Junaid et al., 2020)[9], and Rule based prediction (Jodayree et al., 2019)[21] in terms of energy efficiency.

Energy efficient models utilize soft computing techniques like PSO, ACO, GA, GSO, and Honey Bee Optimization in order to achieve this task via energy aware fitness function design. Deep learning models are not used for this purpose due to their energy intensive training process.

This limitation can be removed via using pre-trained CNN models that are optimized for energy efficient load balancing. Furthermore, existing models like SLA based model [15], AMRRPL (Royaee et al., 2021)16], EDF (Ben Alla et al., 2019)[22], MU (Mandal et al., 2020)[15], MMT [15], RALBHC (Ahmed et al., 2021)[27], etc. can be further improved via addition of soft computing for optimization

of energy consumption. These additions will enhance system performance and help the models to be tuned with high energy efficiency.

REFERENCES

[1] Ahmed, U., Aleem, M., Noman Khalid, Y., Arshad Islam, M., and Azhar Iqbal, M. 2021. RALB-HC: A resource-aware load balancer for heterogeneous cluster. Concurr. Comput. 33, 14 (July).

[2] Ala'anzy, M. and Othman, M. 2019. Load balancing and server consolidation in cloud computing environments: A meta-study. IEEE Access 7, 141868–141887.

[3] Alharbi, H. A., El-Gorashi, T. E. H., and Elmirghani, J. M. H. 2019. Energy efficient virtual machine services placement in cloud-fog architecture. In 2019 21st International Conference on Transparent Optical Networks (ICTON). IEEE.

[4] Ben Alla, S., Ben Alla, H., Touhafi, A., and Ezzati, A. 2019. An efficient energy-aware tasks scheduling with deadline-constrained in cloud computing. Computers 8, 2 (June), 46.

[5] Bhuvaneswari, D. and Akila, A. 2019. An energy efficient management in various fog platforms. In 2019 International Conference on Machine Learning, Big Data, Cloud and Parallel Computing (COMITCon). IEEE.

[6] Dey, N. S. and Gunasekhar, T. 2019. A comprehensive survey of load balancing strategies using hadoop queue scheduling and virtual machine migration. IEEE Access 7, 92259– 92284.

[7] Dong, Y., Xu, G., Ding, Y., Meng, X., and Zhao, J. 2019. A 'joint-me' task deployment strategy for load balancing in edge computing. IEEE Access 7, 99658–99669.

[8] Escobar, J. J., Ortega, J., D´ıaz, A. F., Gonza´lez, J., and Damas, M. 2019. Energyaware load balancing of parallel evolutionary algorithms with heavy fitness functions in heterogeneous CPU-GPU architectures. Concurr. Comput. 31, 6 (Mar.), e4688.

[9] Gupta, P., Goyal, M. K., and Gupta, N. 2015. Reliability aware load balancing algorithm for content delivery network. In Advances in Intelligent Systems and Computing. Advances in intelligent systems and computing. Springer International Publishing, Cham, 427–434.

[10] Hadikhani, P., Eslaminejad, M., Yari, M., and Ashoor Mahani, E. 2020. An energyaware and load balanced distributed geographic routing algorithm for wireless sensor networks with dynamic hole. Wirel. netw. 26, 1 (Jan.), 507–519.

[11] Jodayree, M., Abaza, M., and Tan, Q. 2019. A predictive workload balancing algorithm in cloud services. Procedia Comput. Sci. 159, 902–912.

[12] Junaid, M., Sohail, A., Ahmed, A., Baz, A., Khan, I. A., and Alhakami, H. 2020. A hybrid model for load balancing in cloud using file type formatting. IEEE Access 8, 118135–118155.

[13] Jyoti, A., Shrimali, M., Tiwari, S., and Singh, H. P. 2020. Cloud computing using load balancing and service broker policy for IT service: a taxonomy and survey. J. Ambient Intell. Humaniz. Comput. 11, 11 (Nov.), 4785–4814.

[14] Kansal, N. J. and Chana, I. 2018. An empirical evaluation of energy-aware load balancing technique for cloud data center. Cluster Comput. 21, 2 (June), 1311–1329.

[15] Kaur, M. and Aron, R. 2020. Equal distribution based load balancing technique for fog-based cloud computing. In Algorithms for Intelligent Systems. Springer Singapore, Singapore, 189–198.

[16] Kulshrestha, S. and Patel, S. 2019. A study on energy efficient resource allocation for cloud data center. In 2019 Twelfth International Conference on Contemporary Computing (IC3). IEEE.

[17] Kumar, J., Singh, A. K., and Mohan, A. 2021. Resource-efficient load-balancing framework for cloud data center networks. ETRI J. 43, 1 (Feb.), 53–63.

[18] Liang, B., Dong, X.,Wang, Y., and Zhang, X. 2020. A low-power task scheduling algorithm for heterogeneous cloud computing. J. Supercomput. 76, 9 (Sept.), 7290–7314.

[19] Lin, W., Peng, G., Bian, X., Xu, S., Chang, V., and Li, Y. 2019. Scheduling algorithms for heterogeneous cloud environment: Main resource load balancing algorithm and time balancing algorithm. J. Grid Comput. 17, 4 (Dec.), 699–726.

[20] Malshetty, G. and Mathapati, B. 2019. Efficient clustering in WSN-Cloud using LBSO (load based Self-Organized) technique. In 2019 3rd International Conference on Trends in Electronics and Informatics (ICOEI). IEEE.

[21] Mandal, R., Mondal, M. K., Banerjee, S., and Biswas, U. 2020. An approach toward design and development of an energy-aware VM selection policy with improved SLA violation in the domain of green cloud computing. J. Supercomput. 76, 9 (Sept.), 7374–7393.

[22] Panda, B., Moharana, S. C., Das, H., and Mishra, M. K. 2019. Energy aware virtual machine consolidation for load balancing in virtualized environment. In 2019 International Conference on Communication and Electronics Systems (ICCES). IEEE.

[23] Pourghebleh, B. and Hayyolalam, V. 2020. A comprehensive and systematic review of the load balancing mechanisms in the internet of things. Cluster Comput. 23, 2 (June), 641–661.

[24] Rashid, A., Tripathi, Y., Prakash, A., and Tripathi, R. 2019. Load aware energy-balanced data gathering approach in CRSNs. IET Wirel. Sens. Syst. 9, 3 (June), 143–150.

[25] Rehman, A. U., Ahmad, Z., Jehangiri, A. I., Ala'Anzy, M. A., Othman, M., Umar,

[26] A. I., and Ahmad, J. 2020. Dynamic energy efficient resource allocation strategy for load balancing in fog environment. IEEE Access 8, 199829–199839.

[27] Royaee, Z., Mirvaziri, H., and Khatibi Bardsiri, A. 2021. Designing a context-aware model for RPL load balancing of low power and lossy networks in the internet of things. J. Ambient Intell. Humaniz. Comput. 12, 2 (Feb.), 2449–2468.

[28] Sadeghi, F. and Avokh, A. 2020. Load-balanced data gathering in internet of things using an energy-aware cuckoo-search algorithm. Int. J. Commun. Syst. 33, 9 (June), e4385.

[29] Salem Alatawi, H. and Abdullah Sharaf, S. 2020. Toward efficient cloud services: An energy-aware hybrid load balancing approach. In 2020 International Conference on Computing and Information Technology (ICCIT-1441). IEEE.

[30] Singh, A. K. and Kumar, J. 2019a. Secure and energy aware load balancing framework for cloud data centre networks. Electron. Lett. 55, 9 (May), 540–541.

[31] Singh, A. K. and Kumar, J. 2019b. Secure and energy aware load balancing framework for cloud data centre networks. Electron. Lett. 55, 9 (May), 540–541.

[32] Taboada, I., Aalto, S., Lassila, P., and Liberal, F. 2017. Delay- and energy-aware load balancing in ultra-dense heterogeneous 5G networks. Trans. emerg. telecommun. technol. 28, 9 (Sept.), e3170.

[33] Zhang, X., Jia, M., Gu, X., and Guo, Q. 2019. An energy efficient resource allocation scheme based on cloud-computing in H-CRAN. IEEE Internet Things J. 6, 3 (June), 4968–4976.

AUTORS BIOGRAPHY

Dr. Kavita Singh has completed her doctoral degree from SVNIT, Surat in 2014 in biometrics. Her areas of expertise are Machine Learning, soft computing, computer vision, latex and Image Pro-cessing. She has more than 50 international paper publications in reputed conferences, book chapters and journals. She worked as reviewer, session chair for many international journals and conferences. She has delivered 20 talks on different topics in-cluding her expertise area. She worked as Principal Investigator for projects funded by AICTE under RPS Scheme. She has also a strong association with industries like IBM, Nvidia etc. She is currently working as Associate Prof. at Department of Computer Technology, YCCE, Nagpur.

Mr. Amol D Gaikwad has received his B.Tech degree in Computer Science and Engineering from RTMNU Nagpur University, Nag-pur and MTech. degree in Computer Science and Engineering Master of Technology degree from Yeshwantrao Chavan College of Engineering, Engineering (An Autonomous Institution Affili-ated to Rashtrasant Tukadoji Maharaj Nagpur University), Nag-pur, India. He is currently pursuing Ph.D. from from Yeshwan-trao Chavan College of Engineering, (An Autonomous Institu-tion Affiliated to Rashtrasant Tukadoji Maharaj Nagpur Univer-sity), Nagpur, India. His predominant research areas include High Performance Computing, Cloud Computing. He has pub-lished research papers in various reputed international confer-ences and journals. He is the life member of ISTE, India, IE, India.

Shailesh D. Kamble received Bachelor of Engineering degree in Computer Technology from Yeshwantrao Chavan College of Engineering, Nagpur, India under the Rashtrasant Tukadoji Ma-haraj Nagpur University, Nagpur, India. He received Master of Engineering degree from Prof Ram Meghe Institute of Technolo-gy and Research, formerly known as College of Engineering, Bandera under Sant Gadge Baba Amravati University, Amravati, India. He completed his doctoral degree from G.H. Raisoni Col-lege of Engineering (An Autonomous Institution Affiliated to Rashtrasant Tukadoji Maharaj Nagpur University), Nagpur, In-dia. He is working as the Associate Professor in Department of Computer Technology at Yeshwantrao Chavan College of Engi-neering, Nagpur, India. He is having 20 years of teaching and re-search experience. His current research interests include image processing, video processing and language processing. He is the author or co-author of more than 20 scientific publications in International Journal, International Conferences, and National Conferences. He is the life member of ISTE, India.

Dr. Rakhi D. Wajgi

A Case Report on Management and Outcomes of Dengue Fever with Urinary Tract Infection.

Authors	Vaishali Rokade, Pallavi Dhole, Aniket Pathade, RD Wajgi, Kanchan Bokade
Publication date	2022/6/1
Journal	International Journal of Early Childhood Special Education
Volume	14
Issue	4
Description	Dengue fever is a serious tropical infection that can cause hemorrhagic symptoms. Concurrent dengue infection, on the other hand, is to be expected and is a fascinating condition in tropical medicine. The authors discuss an intriguing instance of dengue fever with a urinary tract infection that was discovered by chance. Urinary tract infections are quite prevalent, affecting one out of every five women at some point in their lives. UTIs are more frequent in women, although they can also affect men, the elderly, and children. Urinary tract infections affect one to two percent of youngsters. Urinary tract infections account for 8 million to 10 million doctor visits each year. Patient specific information:- The patient is 32-year women admit in AVBRH. the chief complaint of high fever for 3 days, burning micturition, shivering, chills, lower abdominal pain. He was diagnosed as a Urinary tract infection with dengue fever. Main …
Scholar articles	A Case Report on Management and Outcomes of Dengue Fever with Urinary Tract Infection. V Rokade, P Dhole, A Pathade, RD Wajgi, K Bokade - International Journal of Early Childhood Special …, 2022 Related articles

Document details - Optimization of elliptic curve scalar multiplication using constraint based scheduling

→] Export   ⬇ Download   More... ›

Journal of Parallel and Distributed Computing

Volume 167, September 2022, Pages 232-239

Optimization of elliptic curve scalar multiplication using constraint based scheduling(Article)

Zode, P.,   Deshmukh, R.   ⚇

[a]Deptt. of Electronics Engg., Yeshwantrao Chavan College of Engg., Nagpur, India
[b]Center for VLSI and Nanotechnology, Visvesvaraya National Institute of Technology, Nagpur, India

Abstract

Elliptic Curve Cryptography is public key cryptography that features smaller keys, ciphertexts, and signatures and is faster than RSA at the same security level. Scalar multiplication is the main and the most compute-intensive operation in the generation of keys. Point Addition, Doubling and Inversion are the basic operations for scalar multiplication. Inversion is a very expensive operation as compared to multiplication, addition and squaring in the finite fields with an affine coordinate system. López-Dahab coordinates are the best alternative to reduce the inversion overhead in scalar computation. Area, Delay and Power trade-offs are the main constraints in hardware implementations of scalar multiplication. In this paper, optimization of elliptic curve scalar multiplication using constraint-based scheduling for the López-Dahab coordinate system is proposed. Data dependency graphs of point addition and doubling are modified for optimization of area and delay. The proposed architecture is implemented on Altera Stratix-II FPGA. The constraint is applied on the field multiplication operation and the considerable area is reduced. The proposed architecture computes scalar multiplication in 11.43 µs and takes 9856 ALMs. The performance comparison with state of the art shows that area is reduced by 41.21%, delay is reduced by 2.4% and Area-Delay-Product is improved. © 2022 Elsevier Inc.

Author keywords

Constraint based scheduling   Elliptic curve cryptography   López-Dahab coordinates   Public key cryptography
Scalar multiplication

Indexed keywords

Engineering controlled terms:	Curve fitting Economic and social effects Geometry Network security Scheduling
Engineering uncontrolled terms	Ciphertexts Co-ordinate system Constraint-based scheduling Elliptic curve Lopez-dahab coordinate Optimisations Point additions Proposed architectures Scalar multiplication Security level
Engineering main heading:	Public key cryptography

⚇ Zode, P.; Deptt. of Electronics Engg., Yeshwantrao Chavan College of Engg., Nagpur, India;

Cited by 2 documents

Basiri, M.M.A.
Efficient hardware implementations of Lopez–Dahab projective co-ordinate based scalar multiplication of ECC
(2023) *Analog Integrated Circuits and Signal Processing*

Patel, K. , Shah, M. , Prajapati, P.
High speed elliptic curve cryptography architecture for NIST recommended Galois field
(2022) *International Journal of Advanced Technology and Engineering Exploration*

View details of all **2** citations

Inform me when this document is cited in Scopus:

Set citation alert ›   Set citation feed ›

Related documents

Find more related documents in Scopus based on:

Authors ›   Keywords ›

SciVal Topic Prominence ⓘ

Topic:

Prominence percentile: ⓘ

Efficient carry select 16-bit square root adder with complementary metal-oxide semiconductor implementation

Pavitha Uppinakere sathyanarayan[1], Mamtha Mohan[1], Sandeep Kakde[2], Annam Karhik[3]
[1]Department of Electronics and Communication, M. S. Ramaiah Institute of Technology, Bengaluru, India
[2]Department of Electronics Engineering, Yeshwantrao Chavan College of Engineering, Nagpur, India
[3]Institute of Aeronautical Engineering, Dundigal, Hyderabad, India

Article Info

ABSTRACT

The adder is the maximum usually used mathematics block in programs inclusive of central processing unit (CPU) and virtual sign processing. As a result, it is important to expand a space-saving, low-strength, high-overall performance adder circuit. The hassle is diagnosed to layout mathematics sub structures with minimized strength dissipation, low area, and minimal time postpone of common-sense circuits. In conventional carry select adder (CSA), the time required to generate the sum output is less than other basic adder circuits but the principal difficulty is the location because the variety of transistors used to put in force the CSA circuit is fairly more. So, the area increases because of which the overall power consumption of the circuit will be more. If it's far viable to lessen the variety of transistors used withinside the structure of CSA adder, then, the strength intake of the circuit may be decreased or even the reaction time will improve. By lowering the area of the adder circuit, the suggested solution intends to reduce power consumption and latency.

Corresponding Author:

Pavitha Uppinakere sathyanarayan
Department of Electronics and Communication Engineering
M. S. Ramaiah Institute of Technology
MSRIT Post, Bengaluru 560054, India
Email: alihas@upm.edu.my

1. INTRODUCTION

The logical arithmetic unit is a very important subsystem within any numerical system. The layout of excessive pace and coffee strength Very large-scale integration (VLSI) architectures must be effective. Arithmetic processing units, which can be optimised for overall performance parameters together with pace and power consumption [1], [2]. Adders are key components of general use microprocessors and digital signal processors. Accordingly, optimal design of the adder units improves the overall performance of the system. The amount of space available is a critical consideration in the design of adders [3]. The enormous carry propagation delay [4] observed in traditional adder circuits, such as ripple carry adder and carries save adder, is the major speed constraint of adders. The fundamental benefit of carry select adder (CSA) is that it has shorter propagation delays. The format of high-tempo and low-power VLSI architectures goals inexperienced arithmetic processing units [5], which is probably optimized for the general overall performance parameters, namely, tempo and power consumption. Adders are the crucial aspect components in famous reason microprocessors and digital signal processors. They additionally locate use in lots of different capabilities which includes subtraction, multiplication and division. As a result, the optimum design of the adder units improves the overall performance of the system. Furthermore, for the packages consisting of the Reduced instruction set computer (RISC) processor design, wherein unmarried cycle execution of

commands is the important thing degree of overall performance of the circuits, use of a green adder circuit turns into necessary, to realise green gadget overall performance [6].

The main system construct is 16-bit modified adder circuit. The fundamental benefit of CSA is that it has shorter propagation delays. The targeted parameters are area, delay and power consumption. The modified CSA is improved by reducing the number of transistors used to implement the adder. To achieve the improvement, the binary excess converter (BEC) block of the modified CSA is replaced with improved BEC architecture. The improved BEC uses 3 transistor (3T) AND gate logic.

The main contribution of the paper is as shown in: i) Reduction in area, delay and power consumption, ii) The location is an important element that is to be taken into consideration withinside the layout of adders, iii) The principal pace predicament of adders arises from the massive bring propagation put off encountered withinside the traditional adder circuits, inclusive of ripple bring adder and bring shop adder. The principal benefit of CSA is its decreased propagation put off characteristics, and iv) The modified CSA is improved by reducing the number of transistors used to implement the adder.

The implementation of a 16-bit modified adder circuit is done in Cadence Virtuoso and simulated with Spectre 180 nm complementary metal oxide semiconductor (CMOS) technology with 1.8 V. The outcomes could be as compared with traditional CSA with admire to propagation delay, strength consumption, and transistor count. First the overall CSA adder architecture is divided into five stages with different input bits for each stage. The adder modified from the conventional one, which is proposed in the reference paper is implemented stage by stage. The basic blocks required for implementing each stage like root cause analysis (RCA), BEC and multiplexer (MUX) are generated using individual gates like XOR, and AND, which are made using transmission gates in Virtuoso Schematic Editor and each of their cell blocks are generated for further instantiation. After implementing and generating the modified adder, the improvement is made to the design and then the improved design is simulated. The functionality of both modified and improved are checked for similarity and the parameters like area, power and delay are compare to check for improvements.

The BEC block of the modified CSA is replaced with improved BEC architecture, which consists of 3T AND gate logic. The logic of the 3T AND gates is based on PMOS and NMOS pass transistors (PTL). The main benefit of employing this AND gate design is that it reduces the number of transistors, resulting in a smaller space.

2. RELATED WORK

The carry select adder (CSA) is one of the fastest adders available, and it's employed in many data-processing processors to execute quick arithmetic operations. It is obvious from the CSA's structure that there is room to reduce the CSA's area and power consumption. One of the maximum vital regions of studies in VLSI device layout is the development of area and strength green high-pace information course good judgment systems [7], [8]. The objective of the paper is to realize an efficient adder unit using novel architectural design. The paper improves upon the conventional carry select adder by replacing the ripple carry adder blocks with binary to excess-1 converter (BEC) blocks. Transmission gate (TG) is used to implement the adder logic. The use of TG and BEC reduce the number of transistors used and power dissipation.

In the main research field of VLSI system design [9], [10], the area and power reduction of the data path logic system play a major role. Fast additions and multiplications [11], [12] have continually been a essential requirement for excessive overall performance processors and systems. The sum of every bit role of the simple adder is sequentially generated and carried over to the following role. The circuit architecture is simple and space efficient. Therefore, each full adder can only start operating until the previous carry signal is ready, which slows down the calculation. CSLA [13], [14] is used in many computing systems to mitigate the problem of carry propagation delay and generate sums. The sum of each bit position of the basic adder is sequentially generated and carried over to the next position. There are many types of adder designs, each with its own strengths and weaknesses. The square root carry selective adder [15], [16] is constructed via way of means of compensating for delays because of the 2 convey chains and the block multiplexer sign from the preceding stage.

A ripple-carry adder [17], [18] and a multiplexer are usually used in a carry-select adder. When using a carry-select adder to add two n-bit values, two adders (and hence two ripple-carry adders) are used to do the calculation twice, once with the assumption that the carry-in will be zero and once with the assumption that it will be one. Following the calculation of the two outcomes [19 [20], the proper sum as well as the correct carry-out are picked using the multiplexer once the correct carry-in is known. Ripple carry adders [21], [22] have the maximum compact design, however they perform at a sluggish pace. The carry look ahead adder, on the alternative hand, has a quicker pace however takes up greater space. CLSA [23]

overcomes each the issue that the ripple carry adder and the carry look ahead adder cause. Rather than using dual ripple carry adders, a carry select adder may be built the use of a ripple-carry adder and an add-one circuit. Several adder structures [24] were proposed primarily based totally at the area, delay, and energy intake requirements. In analog design [25], the main parameters which are considered for the designs are area and power.

3.   PROPOSED METHODOLOGY AND IMPLEMENTATION OF SYSTEM BLOCKS

A ripple-carry adder and a multiplexer are usually used in a carry-select adder. When using a carry-select adder to add two n-bit values, two adders are used to do the calculation twice, once with the assumption that the carry-in will be zero and once with the assumption that it will be one. Figure 1 shows the main building blocks, for square root carry-select adder (SQRT CSA) which consists of multiplexer, exclusive OR (XOR) gate, half adder and full adder as shown in Figure 1(a).

3.1. Multiplexer

The 2:1 multiplexer (MUX) implemented using transmission gate (TG) that is used in the paper is proven withinside the Figure 1(b). A multiplexer is a circuit that combines two or more input lines with a single output line. In a simplest way, a multiplexer is a circuit with numerous inputs and a single output. The binary data is collected from the input lines and sent to the output line. One of these data inputs will be connected to the output based on the values of the selection lines.
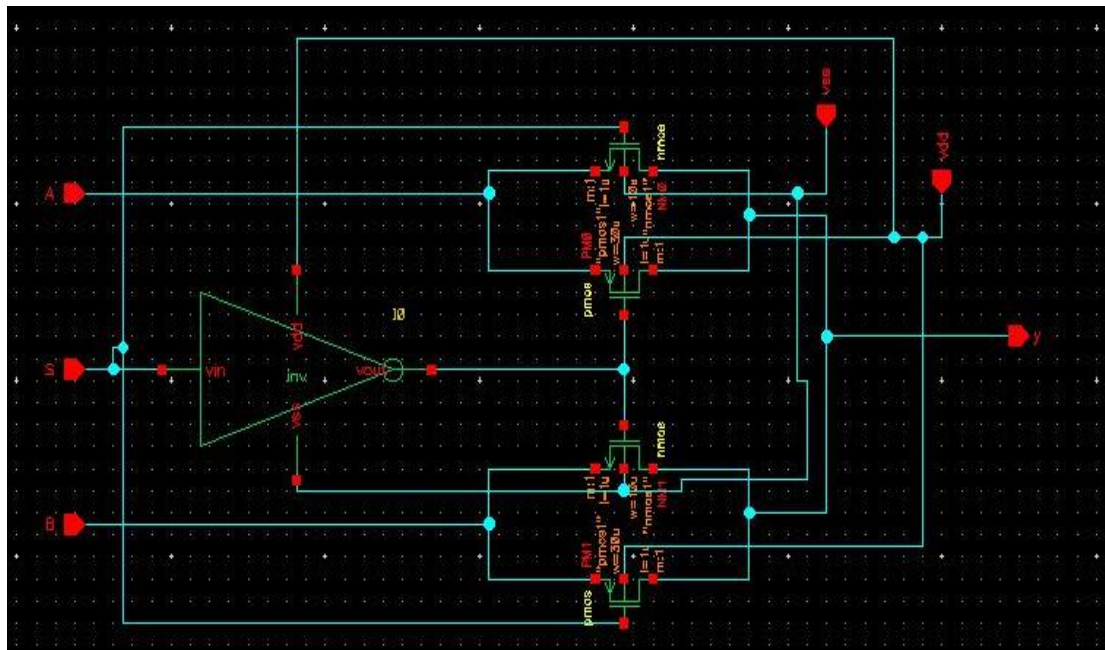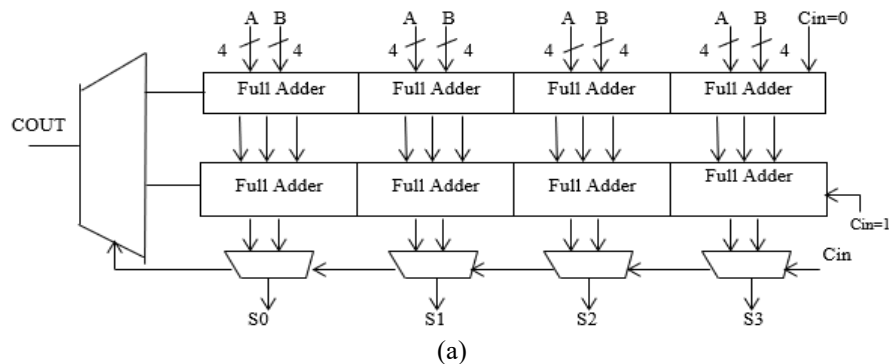

(a)

(b)

Figure 1. Top level block diagram, (a) carry select adder block diagram and
(b) 2:1 MUX using transmission gates

3.2. XOR gate

The XOR gate is implemented using transmission gate architecture as shown in Figure 2. It uses a total of 8 transistors, 2 transmission gates and 2 inverters. An XOR cell is created with two inputs, one output, supply and ground pins, which will be connected in the larger circuits.
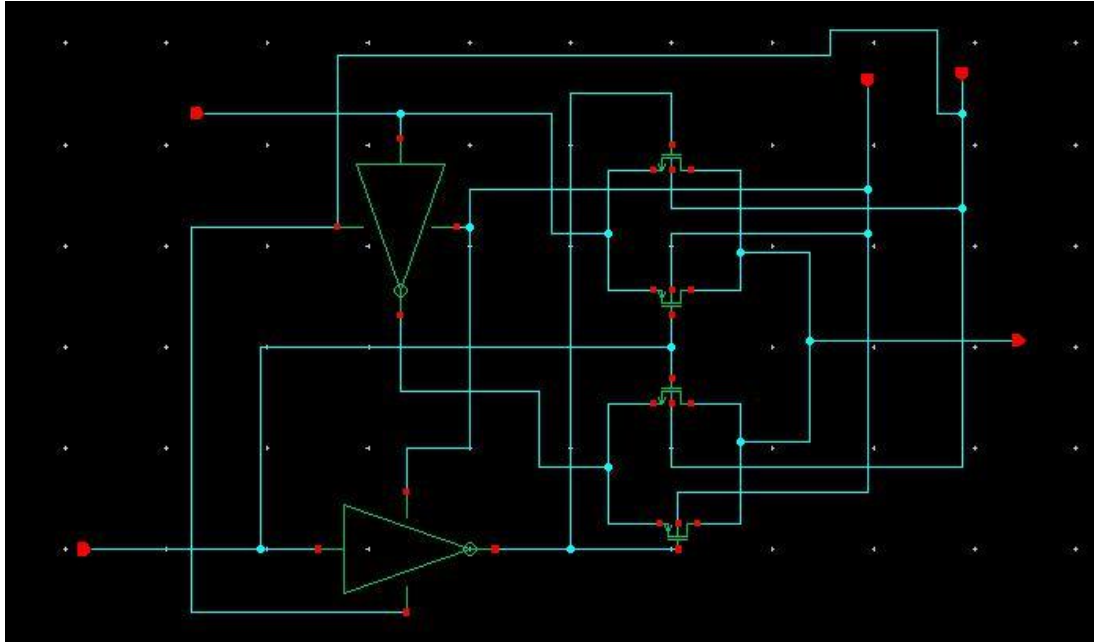

Figure 2. XOR gate using transmission gates

3.3. Half adder

A combination circuit known as a half adder is used to add two bits. The augend and addend bits are the input variables, whereas the sum and carry bits are the output variables. The half adder block is as shown in Figure 3 which is required in the design of CSA adder is implemented using transmission gates, using the XOR gates and AND gates which are as implemented using transmission gates as shown in previous blocks.
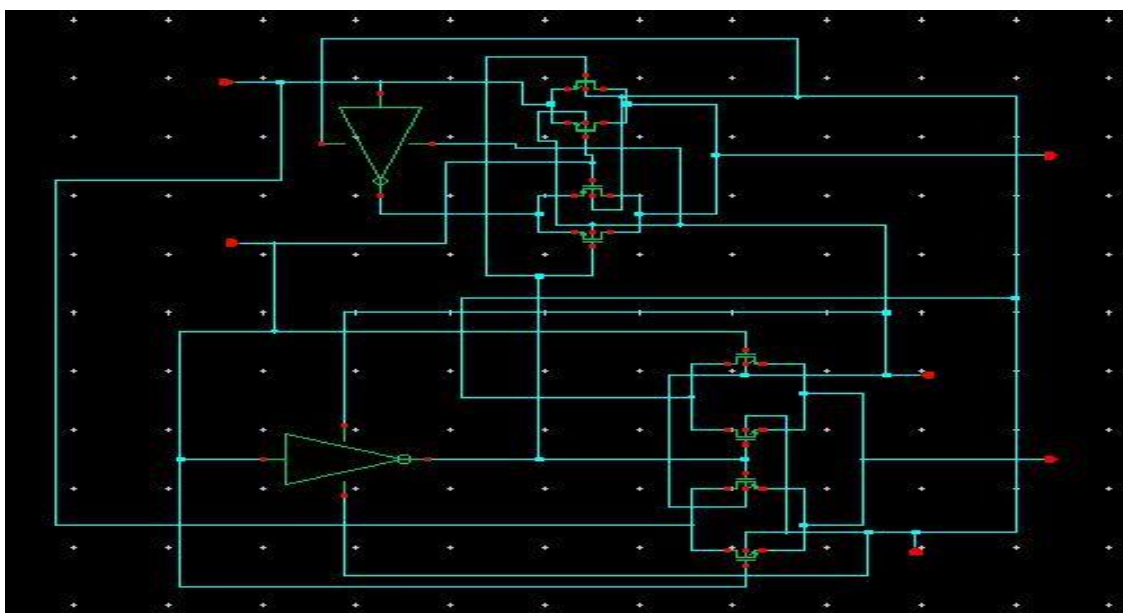

Figure 3. Half adder

Efficient carry select 16-bit square root adder with complementary ... (Pavitha Uppinakere sathyanarayan)

3.4. Full adder

The full adder is an adder that takes three inputs and outputs two results. Figure 4 shows 1-bit full adder and it is also implemented using transmission gates just like the half adder design. The first two inputs are A and B, with the third being a Cin input. The Boolean expressions for outputs of 1-bit full adder are given as:
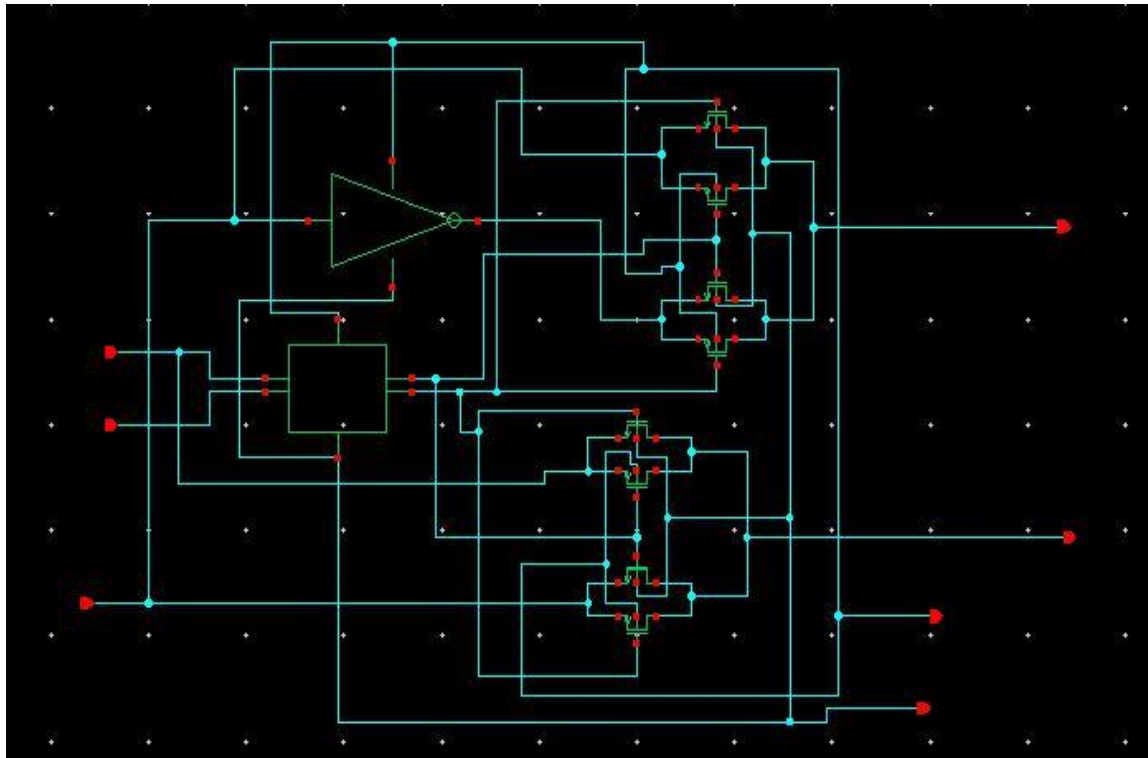
Sum=(A XOR B) XOR Cin
Carry=A * B+Cin *A + Cin * B

Figure 4. Full adder

3.5. Binary to excess 1 converter (BEC)

Figure 5 shows a 3-bit BEC. For stages with more bits, the same BEC architecture is changed to the required number of bits. The Boolean expressions of the 4-bit BEC is indexed as (observe the practical symbols ~ NOT, and AND, ^ XOR). BEC block is implemented by instantiating the XOR, Inverter and AND gate blocks generated before as per the BEC architecture discussed previously.

X0=~B0
X1=B0^B1
X2=B2^(B0 and B1)
X3=B3^(B0 and B1 and B2)

3.6. 6:3 Multiplexer

Figure 6 shows block diagram of 6:3 MUX and it is implemented using individual 2:1 MUX blocks which was generated before. Similarly, based on different inputs of different stages, the inputs of the MUX are changed. All the circuit level schematics are verified for functional simulations.

3.7. Stage 1

The first stage of the CSA adder has 2bit inputs as per the block diagram discussed before. There is no need for a multiplexer so it is made by cascading two 1bit full adders. The carry out generated by this stage is given as carry in for the next stage (stage 2).
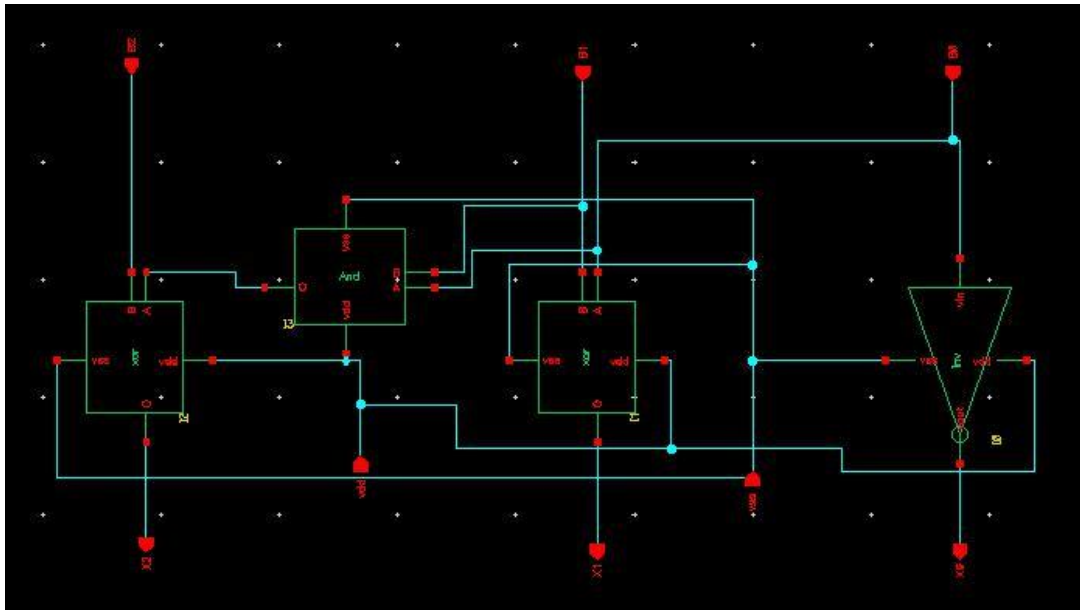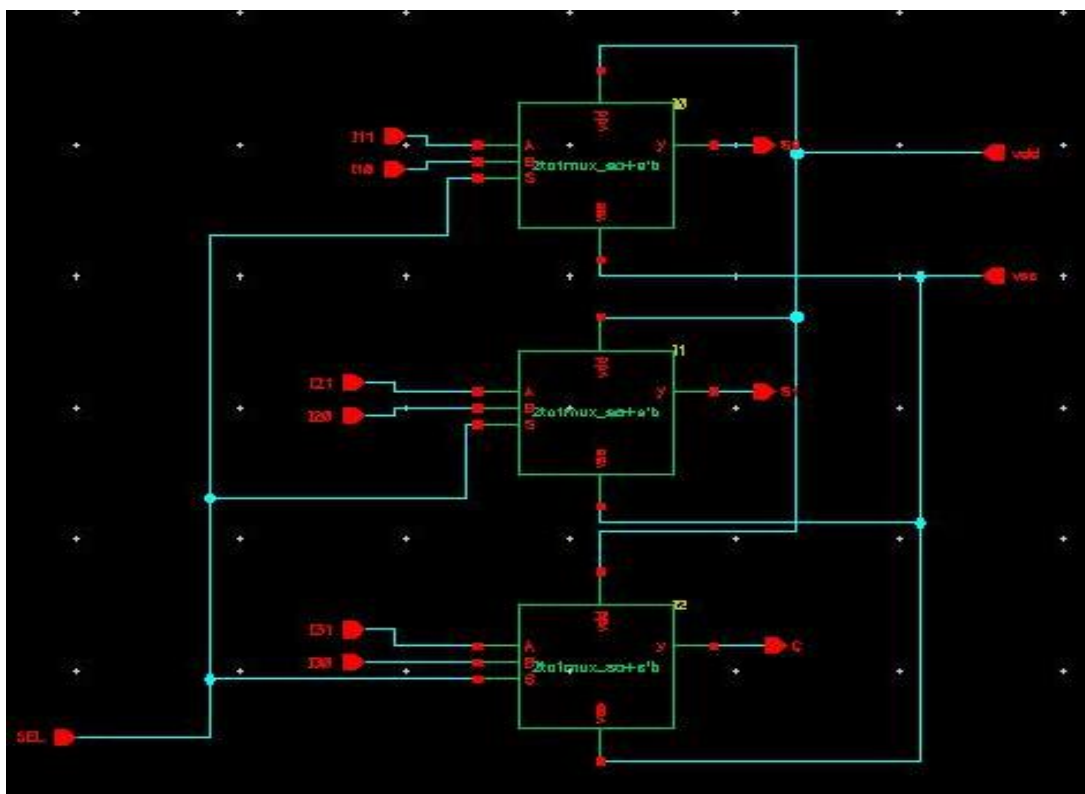
Figure 5. Binary to excess converter

Figure 6. 6:3 MUX

3.8. Stage 2

The 3:2 RCA block with carry in as 1 has been replaced by a BEC block with input 3 bits for the enhanced architecture of the SQRT CSA adder. Figure 7 shows Stage 1 of SQRT CSA and the modified stage is implemented in Virtuoso schematics is show in Figure 8. The modification reduces the number of transistors used for implementing the functionality of adding one to the output of the 3:2 RCA block for carry in of zero. The 6:3 MUX remains the same but, now instead of selecting between the outputs of two 3:2 RCA

blocks, it selects either the output of 3:2 RCA (Cin=0) if carry in of the Stage 2 is '0' or output of the 3bit BEC, if the carry of the stage is '1'.

Other stages of the CSA adder are modified same as that of stage 2, which is a 2-bit stage. For Stage 3 (3-bit inputs), a 4-bit BEC replaces the 4-bit RCA with carry in 1 and so on for other stages The combined 16-bit SQRT CSA is implemented using the individual stages generated before as shown in Figure 9.
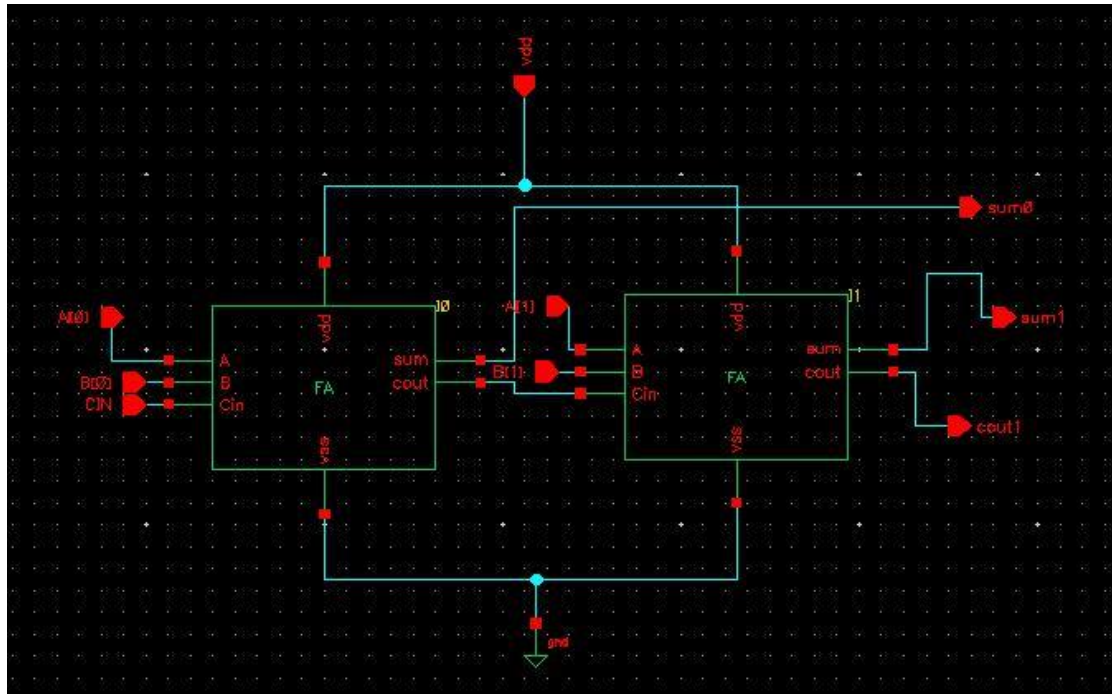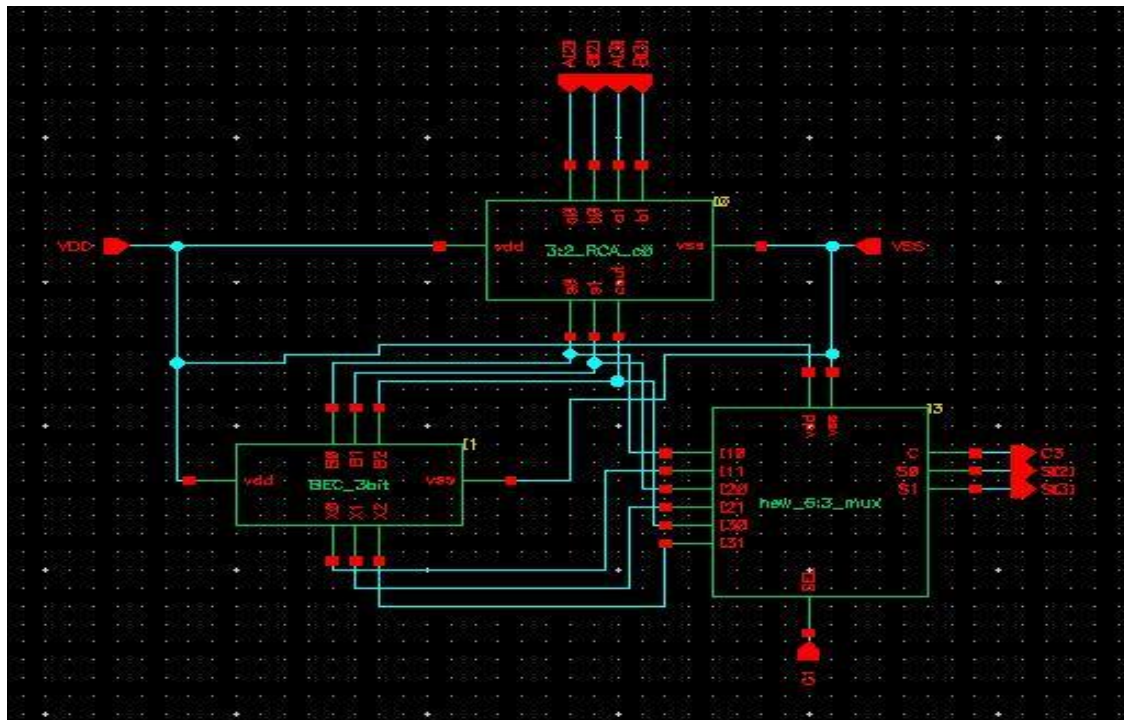

Figure 7. Stage 1 of SQRT CSA

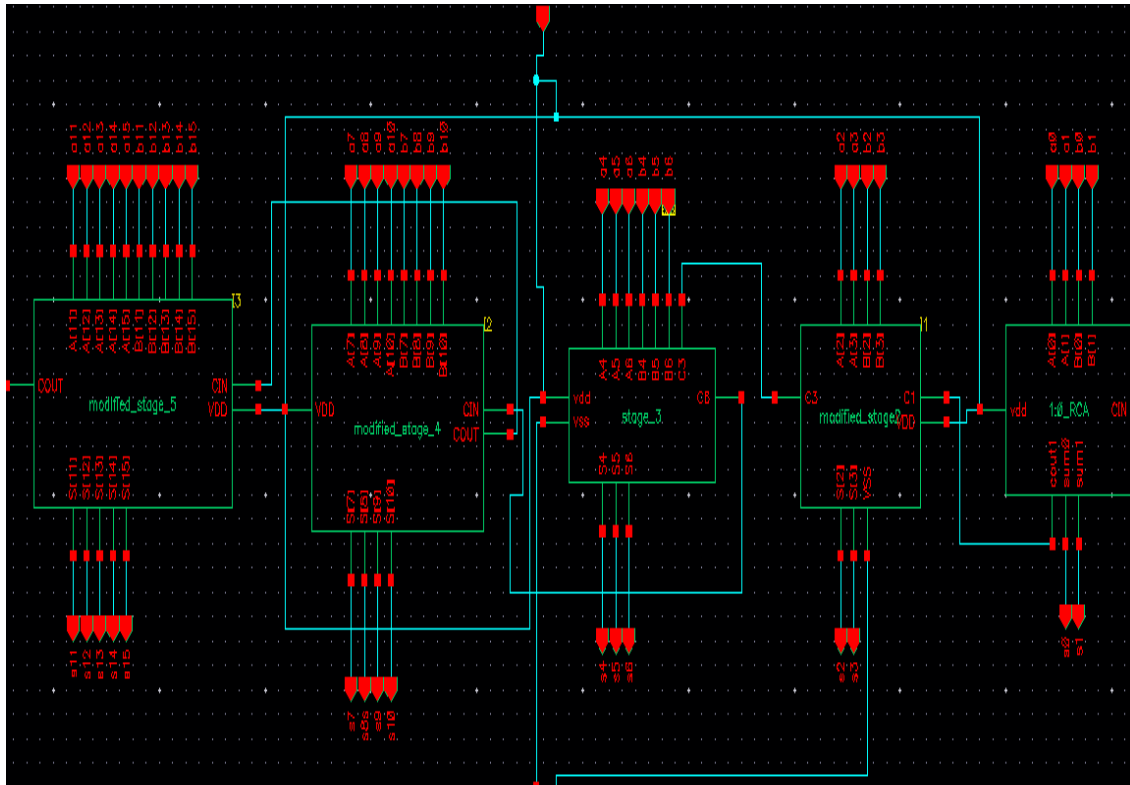Figure 8. Stage 2 of modified SQRT CSA

Figure 9. Combined 16-bit modified CSA adder

4. RESULTS AND DISCUSSION

4.1. Power calculations

Power consumption of each stage is calculated to check the performance. Maximum power consumption is calculated for individual stages in Cadence tool using following steps: i) While simulating the design in virtuoso analog design environment window select OUTPUT→save all. ii) In save all enable all options. iii) run simulation. iv) In waveform window select BROWSER→Results→Open results, select Waveform data, a window will pop up, here select *psf* file. v) In left side of waveform window, we can observe a browser. In browser double click on *Tran* option. Here we have current, voltage and power signals at various parts of the design. vi) Double click on *Pwr* option then we can observe wave of power signal in waveform window. vii) The maximum power consumption can be observed at the maximum peak of the waveform.

4.2. Improved design

Figure 10 shows an implementation of 3T AND gate. The changed CSA is progressed through decreasing the quantity of transistors used to put into effect the adder. To achieve the improvement, the BEC block of the modified CSA is replaced with improved BEC architecture.

The improved BEC uses 3 transistor (3T) AND gate logic. The logic of the 3T AND gates is based on PMOS and NMOS pass transistors (PTL). The main benefit of employing this AND gate design is that it reduces the number of transistors, resulting in a smaller space. The 3T AND gate used in BEC is designed using the same transistor parameters used for all the other gates in the adder. The cell blocks of the 3T AND is generated and used to improve the BEC. New BEC blocks are generated by replacing the conventional AND gates with improved AND gates. Improved 3-bit BEC is shown in Figure 11. All the stages of the modified adder are replaced with improved BEC with different input bits according to the stage. The overall transistor count, delay and power consumption of each stage is obtained for comparison.
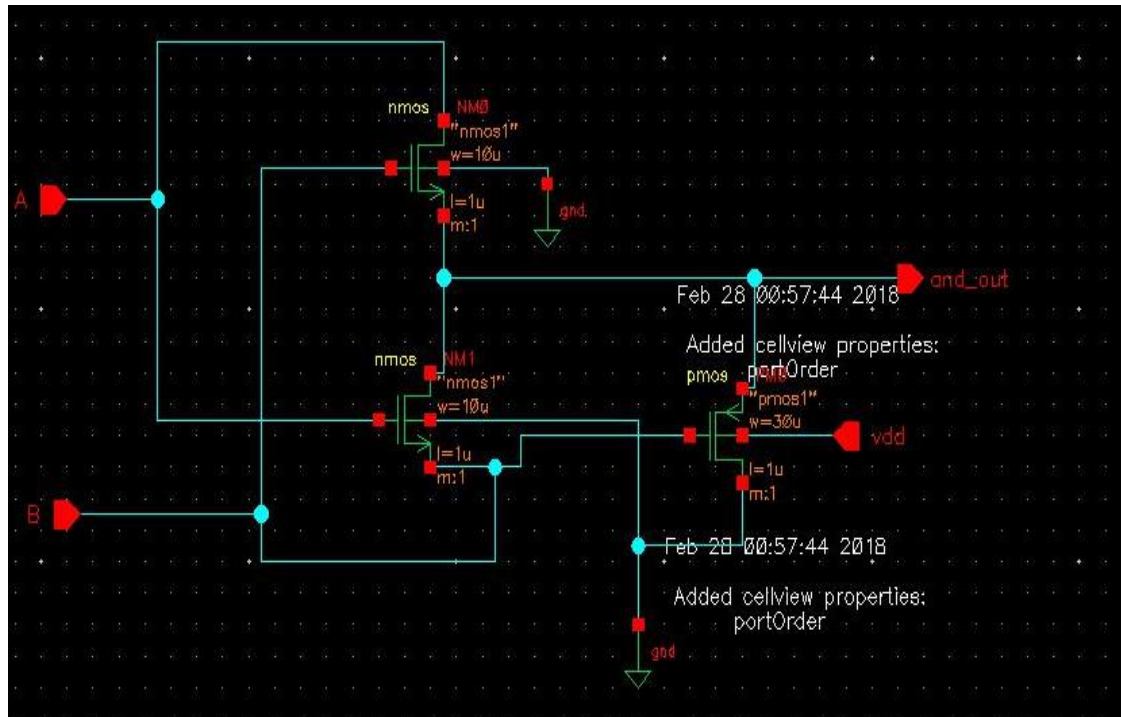
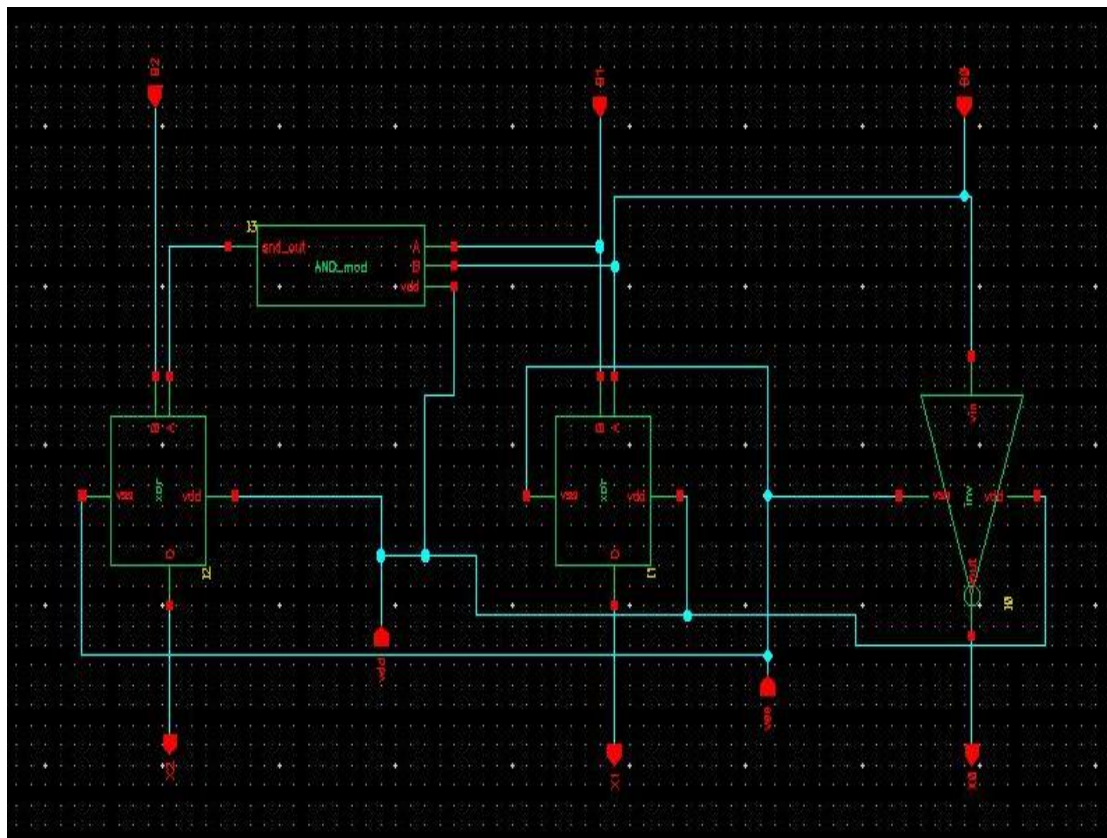Figure 10. Implementation of 3T AND gate

Figure 11. Improved 3-bit BEC

4.3. Simulation results

Table 1 shows simulation results of CSA and Table 2 shows simulation results of improved CSA The modified CSA adder stages are simulated in Spectre simulator 180 nm technology with 1.8 power supply. The parameters like transistor counts, power consumption and delay of each stage is recorded and compared and is as shown in Table 3. From the tables, it is clear that the numbers of transistors are less for improved stages and the delay is also less compared to the modified stages of CSA.

Table 1. Simulation results of CSA

Stages	Transistor count	Power mW	Delay nS
(2bit) Modified Stage1	40	8.099	1.09
(2bit) Modified Stage2	74	12.78	2.13
(3bit) Modified Stage3	116	18.85	3.92
(4bit) Modified Stage4	156	19.12	4.09
(5bit) Modified Stage5	196	21.70	6.01

Table 2. Simulation results of improved CSA

Stages	Transistor count	Power mW	Delay nS
(2bit) Improved Stage1	40	8.099	1.09
(2bit) Improved Stage2	71	12.28	1.08
(3bit) Improved Stage3	110	18.53	2.25
(4bit) Improved Stage4	147	19.65	3.21
(5bit) Improved Stage5	184	24.10	4.51

Table 3. Comparison with existing work

Features	Carry Selet Adder [5]		Proposed Work	
	Transistor count (area)	Delay (nS)	Transistor count (area)	Delay (nS)
(2bit) Improved Stage1	40	1.61	40	1.09
(2bit) Improved Stage2	74	1.85	71	1.08
(3bit) Improved Stage3	116	2.30	110	2.25
(4bit) Improved Stage4	156	3.43	147	3.21
(5bit) Improved Stage5	196	4.82	184	4.51

5. CONCLUSION

In this paper, 16-bit CSA adder is designed by using a 3T AND gate using 180 nm CMOS technology. The improvement done to the modified 16-bit CSA adder by using a 3T AND gate has improved the area and delay of the adder circuit. Since the adder circuit have application in signal processing and multiplexers, the use of improved CSA adder architecture as the sub components in such applications can improve the overall response time and area of the whole applications.

REFERENCES

[1] B. S. Premananda, A. Bajpai, G. Shakthivel, and A. R. Anurag, "Low power add-one circuit IPGL based high speed square root carry select adder," *Indian Journal of Science and Technology*, vol. 14, no. 9, pp. 776–786, Mar. 2021, doi: 10.17485/ijst/v14i9.343.

[2] Yajuan He, Chip-Hong Chang, and Jiangmin Gu, "An area efficient 64-bit square root carry-select adder for low power applications," in *2005 IEEE International Symposium on Circuits and Systems*, Dec. 2013, pp. 4082–4085, doi: 10.1109/ISCAS.2005.1465528.

[3] S. Manju and V. Sornagopal, "An efficient SQRT architecture of Carry Select adder design by common Boolean logic," in *2013 International Conference on Emerging Trends in VLSI, Embedded System, Nano Electronics and Telecommunication System, ICEVENT 2013*, Jan. 2013, pp. 1–5, doi: 10.1109/ICEVENT.2013.6496590.

[4] S. Sakthikumaran, S. Salivahanan, V. S. K. Bhaaskaran, V. Kavinilavu, B. Brindha, and C. Vinoth, "A very fast and low power carry select adder circuit," in *ICECT 2011 - 2011 3rd International Conference on Electronics Computer Technology*, Apr. 2011, vol. 1, pp. 273–276, doi: 10.1109/ICECTECH.2011.5941604.

[5] S. Akhter, S. Chaturvedi, and K. Pardhasardi, "CMOS implementation of efficient 16-Bit square root carry-select adder," in *2nd International Conference on Signal Processing and Integrated Networks, SPIN 2015*, Feb. 2015, pp. 891–896, doi: 10.1109/SPIN.2015.7095289.

[6] S. Khan, S. Kakde, and Y. Suryawanshi, "VLSI implementation of reduced complexity wallace multiplier using energy efficient CMOS full adder," in *2013 IEEE International Conference on Computational Intelligence and Computing Research, IEEE ICCIC 2013*, Dec. 2013, pp. 1–4, doi: 10.1109/ICCIC.2013.6724141.

[7] N. Malishetty, P. Malarmannan, P. Sivaprakash, M. Rohit, and J. Pradeep, "Design and implementation of modified square root carry select adder in QCA," *International Journal of Pure and Applied Mathematics*, vol. 119, no. 12, pp. 14427–14432, 2018.

[8]   S. Kakde, S. Khan, P. Dakhole, and S. Badwaik, "Design of area and power aware reduced complexity Wallace tree multiplier," in *2015 International Conference on Pervasive Computing: Advance Communication Technology and Application for Society, ICPC 2015*, Jan. 2015, pp. 1–6, doi: 10.1109/PERVASIVE.2015.7087207.

[9]   O. J. Bedrij, "Carry-select adder," *IRE Transactions on Electronic Computers*, vol. EC-11, no. 3, pp. 340–346, Jun. 1962, doi: 10.1109/IRETELC.1962.5407919.

[10]   S. Khan, S. Kakde, and Y. Suryawanshi, "Performance analysis of reduced complexity Wallace multiplier using energy efficient CMOS full adder," in *Proceedings - 2013 International Conference on Renewable Energy and Sustainable Energy, ICRESE 2013*, Dec. 2014, pp. 243–247, doi: 10.1109/ICRESE.2013.6927823.

[11]   B. Ramkumar, H. M. Kittur, and P. M. Kannan, "ASIC implementation of modified faster carry save adder," *European Journal of Scientific Research*, vol. 42, no. 1, pp. 53–58, 2010.

[12]   T. Y. Chang and M. J. Hsiao, "Carry-select adder using single ripple-carry adder," *Electronics Letters*, vol. 34, no. 22, pp. 2101–2103, 1998, doi: 10.1049/el:19981706.

[13]   Y. Kim and L. S. Kim, "64-Bit carry-select adder with reduced area," *Electronics Letters,* vol. 37, no. 10, pp. 614–615, 2001, doi: 10.1049/el:20010430.

[14]   J. M. Rabaey, Digtal integrated circuits-a design perspective, upper sadd. NJ: Prentice-Hall, 2001.

[15]   Y. Deodhe, S. Kakde, and R. Deshmukh, "Design and implementation of 8-bit vedic multiplier using CMOS logic," in *Proceedings - 2013 International Conference on Machine Intelligence Research and Advancement, ICMIRA 2013*, Dec. 2014, pp. 340–344, doi: 10.1109/ICMIRA.2013.71.

[16]   A. Z. Jidin and T. Sutikno, "FPGA implementation of low-area square root calculator," *Telkomnika (Telecommunication Computing Electronics and Control)*, vol. 13, no. 4, pp. 1145-1152, 2015, doi: 10.12928/telkomnika.v13i4.1894.

[17]   A. Bajpai, A. R. Anurag, G. Shakthivel, and B. S. Premananda, "Design of low power and high-speed 16-bit square root carry select adder using AL," in *2018 IEEE 3rd International Conference on Circuits, Control, Communication and Computing, I4C 2018*, Oct. 2018, pp. 1–4, doi: 10.1109/CIMCA.2018.8739724.

[18]   M. G. Ganavi and B. S. Premananda, "Design of low-power square root carry select adder and Wallace tree multiplier using adiabatic logic," in *Lecture Notes in Electrical Engineering*, vol. 545, pp. 767–781, 2019.

[19]   P. Meshram, "Designed implementation of modified area efficient enhanced square root carry select adder," *International Journal for Research in Emerging Science and Technology*, 2015, doi: 10.13140/RG.2.1.2228.6809.

[20]   M. Nam, Y. Choi, and K. Cho, "High-speed and energy efficient carry select adder (CSLA) dominated by carry generation logic," *Microelectronics Journal*, vol. 79, pp. 70–78, Sep. 2018, doi: 10.1016/j.mejo.2018.07.001.

[21]   I. S. Maan and A. K. Singla, "Design of low power and area efficient SQRT carry select adder using parallel prefix adder structure," *An International Journal of Engineering Sciences*, vol. 17, no. 1, pp. 296–302, 2016.

[22]   G. Savita, V. K. Magraiya, G. Kulshrestha, and V. Goyal, "Designing of low power 16-bit carry select adder with less delay in 45 nm CMOS process technology," *International Journal of Emerging Techno logy and Advanced Engineering*, vol. 3, no. 7, pp. 250–252, 2013.

[23]   M. Bahadori, M. Kamal, A. Afzali-Kusha, and M. Pedram, "An energy and area efficient yet high-speed square-root carry select adder structure," *Computers and Electrical Engineering*, vol. 58, pp. 101–112, Feb. 2017, doi: 10.1016/j.compeleceng.2017.01.021.

[24]   G. Jain, K. Vyas, V. K. Maurya, and M. Patel, "Comparative analysis of different architectures of MCML square root carry select adders for low-power applications," in *Advances in Intelligent Systems and Computing*, vol. 409, 2016, pp. 299–306.

[25]   P. Sireesha, G. R. Kumar, C. P. Bhargavi, A. Sowjanya, and P. Manga Rao, "Design and analysis of 32-bit high speed carry select adder," *Journal of Physics: Conference Series*, vol. 1916, no. 1, p. 012006, May 2021, doi: 10.1088/1742-6596/1916/1/012006.

BIOGRAPHIES OF AUTHORS

Pavitha Uppinakere sathyanarayan ⓘ 🔍 SC Ⓟ is currently working as a Assistant professor in E & C department, M S Ramaiah Institute of Technology, Bangalore. Her research interest includes Low Power VLSI, Face Recognition. She has obtained her B. E in E & C from VTU and M. Tech in VLSI and Embedded Systems from VTU, Belagavi in the year 2005 and 2010 respectively. Curresntly She is persuing Ph. D from VTU; Belagavi. She can be contacted at email: pavitha@msrit.edu.

Mamtha Mohan ⓘ 🔍 SC Ⓟ working as an Assistant Professor at M S Ramaiah Institute of Technology since 16 years. She completed M. Tech at BMS College of Engineering in 2003 and completed Ph. D from Jain university, Bangalore in 2019. She is a member of IEEE and ISTE. Her research interserts are Image Processing, Biomedical Engineering, Wireless Communication, optical Communication Netwroks, Computer Communication Netwroksand Data Structuress. She can be contacted at email: mamtha.m@msrit.edu.

Sandeep Kakde 🆔 📇 SC Ⓟ is presently working as Assistant Professor in Yeshwantrao Chavan College of Engineering, Nagpur. He has over nineteen years of industry and college experience, worked as a Senior Design Engineer at Bharat Electronics Limited, Bangalore, as a Senior Design Engineer in Sanyo LSI Technology India Private Limited, ITPL Park, Bangalore, deputed as a Senior Deign Engineer in Sanyo Semiconductors, Japan and as an Assistant Consultant in Tata Consultancy Services, Bangalore. He received his B.E. degree in Electronics Engineering Department from the Visvesvaraya Regional College of Engineering (renamed Visvesvaraya National Institute of Technology), Nagpur, India, in 2000; M. Tech degree in VLSI Design area from Electronics Engineering Department, Yeshwantrao Chavan College of Engineering, Nagpur, India and received Ph. D degree in Electronics Engineering from the University of Nagpur. He can be contacted at email: sandip.kakde@gmail.com.

Annam Karhik 🆔 📇 SC Ⓟ Research student in branch of ECE-Veltech Dr. RR & Dr. Sr University, Chennai. He obtained M.Tech (ECE) diploma from Mallareddy institute of technology & science (JNTUH), obtained B.Tech (ECE) from Vaageswari College of engineering (JNTUH). He Worked as Assistant professor in Institute of Aeronautical Engineering, Dundigal, Hyderabad. His regions of interest consists of Digital Signal Processing, Speech processing, Embedded Systems. He can be contacted at email: karthik011190@gmail.com.

Advances in Materials and Processing Technologies ›
Latest Articles

Research Article

Application of ANN modelling for optimisation of surface quality and kerf taper angle in abrasive water jet machining of AISI 1018 steel

Yogesh V. Deshpande ✉ ⓘD, Dinesh R. Zanwar, A. B. Andhare ⓘD & P. S. Barve
Accepted 28 Jun 2022, Published online: 11 Jul 2022

📄 **Full Article**   🖼 **Figures & data**   📑 **References**   ❝ **Citations**   📊 **Metrics**   🖶 **Reprints & Permissions**   **Read this article**

ABSTRACT

Abrasive water jet machining (AWJM) is the modern machining method used in various industrial applications. In this paper, an attempt has been made to determine optimum AWJM parameters using artificial neural network (ANN). Flow rate of abrasive, stand-off distance and traverse speed are used as input parameters for machining of AISI 1018 steel. Experimental data are used for training and testing of ANN. A feed forward ANN is established using the experimental data obtained during the AWJ machining of steel. Surface roughness (R_a) and kerf taper angle (Ө) are estimated, on the basis of ANN performance and regression analysis. The regression plots of both responses show more than 97% of agreement among the estimated values and experimental data. Later on, novel approach of model optimisation is executed using univariate analysis on inputs to ANN to get the optimal AWJM process parameters. Optimal response solution is obtained as surface roughness (R_a) = 2.46 μm and taper angle (Ө) = 1.25° at flow rate (A_f) = 450 g/min; stand-off distance (S_d) = 3 mm and traverse speed (T_v) = 85 mm/min. The study shows that the ANN is proficient tool for deciding the optimum AWJ machining parameters.

🔍 **KEYWORDS:** Abrasive water jet machining   surface quality   kerf taper angle   artificial neural network

Disclosure statement

No potential conflict of interest was reported by the author(s).

Data Availability Statement

The authors confirm that the data supporting the findings of this study are available within the article or its supplementary materials.

Related research ⓘ

People also read   Recommended articles   Cited by
1

Estimation and control of surface quality and traverse speed in abrasive water jet machining of AISI 1030 steel using different work-piece thicknesses by RSM >

Abhishek Madankar et al.
Australian Journal of Mechanical Engineering
Published online: 28 Jan 2021

Application of statistical and soft computational techniques in machining of Nickel based supper-alloy using cryogenically treated tools for estimation of surfa… >

Yogesh V. Deshpande et al.
Australian Journal of Mechanical Engineering
Published online: 30 Jan 2022

Experimental investigation and optimization of abrasive waterjet machining parameters for GFRP composites using metaphor-less algorithms >

Dharmagna R. Tripathi et al.
Materials and Manufacturing Processes
Published online: 12 Jan 2021

View more

Information for

Authors

R&D professionals

Editors

Librarians

Societies

Opportunities

Reprints and e-prints

Advertising solutions

Accelerated publication

Corporate access solutions

Open access

Overview

Open journals

Open Select

Dove Medical Press

F1000Research

Help and information

Help and contact

Newsroom

All journals

Books

Keep up to date

Register to receive personalised research and resources by email

✉ Sign me up

Copyright © 2023 Informa UK Limited   Privacy policy   Cookies   Terms & conditions   Accessibility

Registered in England & Wales No. 3099067
5 Howick Place | London | SW1P 1WG

Home   8   More ⌄   🔍   🔔¹   ✉   💬   👤

Article

Optimization of Elliptic Curve Scalar Multiplication using Constraint Based Scheduling

May 2022 · Journal of Parallel and Distributed C... 167(9) · Follow journal
DOI: 10.1016/j.jpdc.2022.05.006

Pravin Zode · Raghavendra Deshmukh

Request full-text   Share ⌄   More ⌄

Overview   Stats   Comments   Citations (1)   References (27)   Related research (10+)

Abstract

Elliptic Curve Cryptography is public key cryptography that features smaller keys, ciphertexts, and signatures and is faster than RSA at the same security level. Scalar multiplication is the main and the most compute-intensive operation in the generation of keys. Point Addition, Doubling and Inversion are the basic operations for scalar multiplication. Inversion is a very expensive operation as compared to multiplication, addition and squaring in the finite fields with an affine coordinate system. López-Dahab coordinates are the best alternative to reduce the inversion overhead in scalar computation. Area, Delay and Power trade-offs are the main constraints in hardware implementations of scalar multiplication. In this paper, optimization of elliptic curve scalar multiplication using constraint-based scheduling for the López-Dahab coordinate system is proposed. Data dependency graphs of point addition and doubling are modified for optimization of area and delay. The proposed architecture is implemented on Altera Stratix-II FPGA. The constraint is applied on the field multiplication operation and the considerable area is reduced. The proposed architecture computes scalar multiplication in 11.43 μs and takes 9856 ALMs. The performance comparsion with state of the art shows that area is reduced by 41.21 %, delay is reduced by 2.4% and Area-Delay-Product is improved.

Methods   ⤡

○   ○   ○

ECC
19 Method publications · 75
Method questions

View

📄 Top related publications

↗ Most cited
A Secure Biometrics-Based Authentication Key Exchange Protocol for Multi-Server TMIS using ECC

Article   Method details available

July 2018 · Computer Methods and Programs in Biomedicine

Mingping Qi · Jianhua Chen · Yitao Chen

91 Reads · 42 Citations

Propagation of radiosonde pressure sensor errors 1 measurements

Article   Method details available   Full-text avail

January 2014 · Atmospheric Measurement Tech

Ryan M. Stauffer · Gary A Morris · Anne Th Nicholas R. Nalli

285 Reads · 39 Citations

View more methods papers

👁 Public Full-texts

Request a copy of this research directly from the authors.   (Request full-text)

Similar research
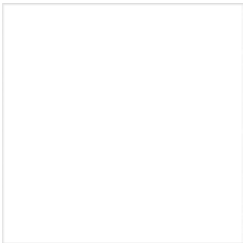
An Area Aware Accelerator for Elliptic Curve Point Multiplication

Preprint | File available

November 2020

👤 Malik Imran · 👤 Samuel Pagliarini · 👤 Muhammad Rashid

This work presents a hardware accelerator, for the optimization of latency and area at the same time, to improve the performance of point multiplication process in Elliptic Curve Cryptography. In order to reduce the overall computation time in the proposed 2-stage pipelined architecture, a rescheduling of point addition and point doubling instructions is performed along with an efficient use of required memory...

(Download)   Recommend   Follow   Share

+10

Innovative Dual-Binary-Field Architecture for Point Multiplication of Elliptic Curve Cryptography

Article | Full-text available

January 2021

IEEE Access

👤 Jiakun Li · 👤 Weijiang Wang · 👤 Jingqi Zhang · [...] · 👤 Shiwei Ren

High-performance Elliptic Curve Cryptography (ECC) implementation in encryption authentication severs has become a challenge due to the explosive growth of e-commerce's demand for speed and security. Point multiplication (PM) is the most common and complex operation in ECC which directly determines the performance of the whole system. This article proposes a 6CC-6CC (clock cycle) dual-fie...

(Download)   Recommend   Follow   Share
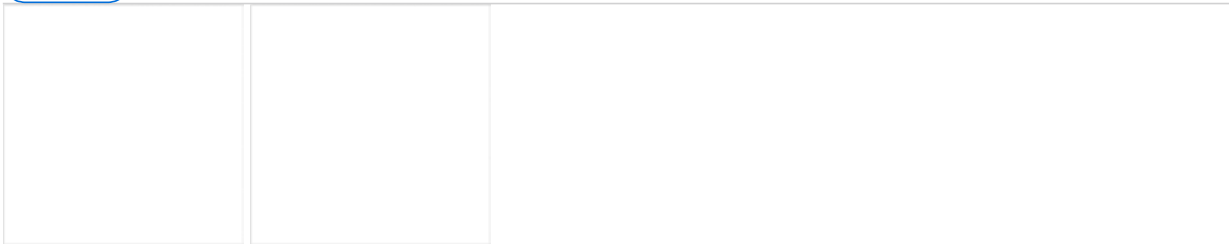
Architectural review of polynomial bases finite field multipliers over GF(2 m)

Conference Paper | Full-text available

March 2017 · 2017 International Conference on Communication, Computing and Digital Systems (C-CODE)

Malik Imran · Muhammad Rashid

In elliptic curve cryptography (ECC), hardware architectures of finite field (FF) multipliers are frequently proposed for polynomial as well as for normal bases representations over GF(2 m). Although the polynomial bases provide efficient FF multiplication as compared to normal bases, the performance of the entire elliptic cryptosystem mainly depends upon its FF multiplier. Consequently, this paper provides a...

Download   Recommend   Follow   Share

Elliptic Curve Cryptoprocessor Implementation on a Nano FPGA: Interesting for Resource-Constrained Devices

Article   Full-text available

December 2012

Hilal Houssain · Turki F. Al-Somani

Download   Recommend   Follow   Share

Implementation of GF(2m) Elliptic Curve cryptoprocessor on a Nano FPGA

Article   Full-text available

January 2011

Turki F. Al-Somani · Hilal Houssain

This paper presents an implementation of an Elliptic Curve Cryptography (ECC) cryptoprocessor on a Nano Field Programmable Gate Array (FPGA). Nano FPGAs offer groundbreaking possibilities in power, size, lead-times, operating temperature and cost. To the best of our knowledge, this is the first ECC implementation on Nano FPGAs. The proposed ECC cryptoprocessor was modeled using VHDL and...

Download   Recommend   Follow   Share

View more related research

ResearchGate

Company

About us

Blog

Careers

Resources

ResearchGate Updates

Help Center

Contact us

Business Solutions

Marketing Solutions

Scientific Recruitment

Publisher Solutions

Select Language

Powered by Google Translate

Management of a Patient with Glenn Shunt

Mayur Mandawkar[1*], Priyanka S Meshram[1] and Aniket Pathade[2]

*Correspondence: Mayur Mandawkar, Florence Nightingale Training College of Nursing, Sawangi Meghe, Wardha Datta Meghe Institute of Medical Sciences, Wardha, Maharashtra, India, Email: ✉

Author information +

⬇ View PDF   ⬇ Download PDF

Abstract

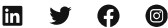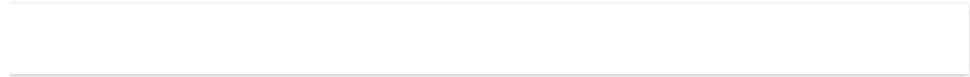Introduction: The Glenn and Fontan procedures are still the two most popular operations for those with a single ventricle. Some people may be difficult to treat because of their cardiopulmonary anatomy. This article describes the Glenn shunt procedure in a patient with a single pulmonary artery and a hereditary lung. Main diagnosis, therapeutic intervention, and outcome: After a physical examination and inquiry, the doctor diagnosed the patient with Ischemic Stroke and prescribed analgesics to relieve the pain. Antipyretic medications are used to lower fever. Therapeutic intervention: This patient was administered Glenn shunt antipyretics for 7 days, including Tab. paracetamol 500 mg (BD), Inj. Ceftriaxone 1 gm IV (BD), Inj. Pantoprazole 40 Mg iv (OD), and Inj. Ondansetron 4MG iv (TDS). Outcome: The patient was given medications prescribed by the doctor, such as paracetamol. In addition, the patient's condition improved as a result of the medical treatment. The patient's problems had subsided, and he was in better shape. Nursing perspectives: - DNS and RL were used to administer fluid replenishment. Check vital signs and blood pressure every hour. Maintaining the patient's intake and output chart, as well as ensuring that he or she gets enough rest and sleep. Administered drugs as directed by the doctor. Because the patient had a fever, he was given hydrotherapy. Conclusion: The patient was hospitalized to A.V.B.R.H. with bradycardia, exhaustion, weakness, gait trouble, impaired balance and coordination, fever, chills, headache, and other symptoms. In this case of heart illness, the patient received the necessary treatment and medication. The patient's health has improved.

Keywords

Glenn shunt • Pulmonary artery • Single lung • Single ventricle

Introduction

Despite breakthroughs in science, single ventricular heart abnormalities are rarely changed to biventricular anatomy in today's world. For individuals with single ventricular heart disease, the Glenn shunt followed by the Fontan operation remains the best therapy or rather palliation option. Despite breakthroughs in science, single ventricular heart abnormalities are rarely changed to biventricular anatomy in today's world. For individuals with single ventricular heart disease, the Glenn shunt followed by the Fontan operation remains the best therapy or rather palliation option [1].

In some cases, extracardiac anatomy can be convoluted, complicating surgical operations. A Glenn shunt procedure in a neonate with a single lung is described in this paper. In some cases, extracardiac anatomy can be convoluted, complicating surgical operations. A Glenn shunt procedure in a neonate with a single lung is described in this paper [2].

The unidirectional Cavo pulmonary connection, also known as the Glenn procedure, is used to eliminate the volume load from the circulation. There is no longer a large left-to-right volume overload after the bidirectional Cavo pulmonary connection, and hence the fundamental source of heart problems in the univentricular shunted circulatory is resolved. As a result, heart failure is rarely a significant hallmark of patients with a bidirectional Cavo pulmonary link. However, even after the circulatory revision, a fraction of patients who have this procedure may have persistent atrioventricular or semilunar valve insufficiency or cardiac failure. There are persistent heart failure findings in such patients, with respiratory symptoms, and failure to thrive is the most typical

---

Submit Manuscript →

📱 +447915608527

Awards & Nominations

📖 50+ Million Readerbase

GET THE APP

Journal Highlights

↪ Clinical Practice

↪ General Practice

↪ Generic Medicines

↪ Health Care

↪ Health Care Systems

↪ Health Informatics

↪ Health Services

↪ Healthcare Delivery System

↪ Healthcare Environment

↪ Healthcare Organizations and Systems

↪ Medical Practice

↪ Medical Services

↪ Medical Statistics

↪ Mental Health Nursing

↪ Mid-Wife Practice

↪ Nurse Practitioners

↪ Nursing Care

↪ Nursing Science

↪ Patient Care

↪ Preventive Medicine

manifestations of heart problems. The intensity of symptoms varies, just as it does with biventricular heart failure. Patients' exertional power is generally limited at this stage due to the mandatory cyanosis caused by the bidirectional Cavo pulmonary link, which can make determining the severity of heart failure difficult. Clinical judgment is required to determine the relative contributions of heart failure and cyanosis [3].

The Glenn operation requires babies to stay in the hospital for 1 to 2 weeks to recover. They are looked after and monitored 24 hours a day, seven days a week. They're also given medications to aid their hearts and blood flow. They'll continue to take some of these medications at home [4].

The care team instructs parents on how to care for their infant at home during this period. When babies are feeding well, growing well, and putting on weight, they can generally go home [5].

The care team instructs parents on how to care for their infant at home during this period. When babies are feeding well, growing well, and putting on weight, they can generally go home [6].

Following heart surgery, many children thrive and do well. They'll need to see a cardiologist regularly, as well as have EKGs, echocardiography, lab tests, and cardiac catheterizations on occasion. Cardiac catheterization is a procedure that allows cardiologists to examine and treat the heart's function [7].

Patient Information

A 5-year-old boy was admitted. After a physical examination and investigation, the doctor identified a case of Glenn's shunt with the predominant symptom of weariness, weakness (mostly in the lower extremities), problems with gait, decreased balance and coordination, fever, headache, chills, myalgias, and arthralgias.

Medical history: On Jun 20th, 2021, a patient was admitted to the A. V. B. R. hospital. The patient had a history of frequent alcohol consumption and Ischemic Stroke for 3 years. He had fever, headache, chills, myalgia, and arthralgia five days before admission, and he took acetaminophen at regular doses on his own.

He had diffuse stomach discomfort, frequent vomiting, hematemesis, epistaxis, and diarrhea on the fourth day of symptoms after his fever and headache had subsided. He had diffuse stomach discomfort, frequent vomiting, hematemesis, epistaxis, and diarrhea on the fourth day of symptoms after his fever and headache had subsided.

The present case had a history of Glenn shunt.

Family history: He belongs to a nuclear family. His father breadwinner of the family. In the patient's family, there is no hereditary history like DM, Asthma, and Hypertension, etc.

Psycho-social history: He was mentally stable, conscious, and oriented to date time, and place. He had maintained a good relationship with doctors and nurses as well as other patients also.

Clinical finding

Physical examination: The patient was awake and aware of the time, date, and location. His physique was average, and he kept himself clean. For three days, I've had a broad body soreness and a high fever (the highest recorded temperature was 39.4°C). He was determined to be aware (Glasgow Coma Scale 15), with a pulse of 100 beats per minute and blood pressure of 100/60 mmHg on physical examination. -20 breaths per minute no rash or active bleeding was present. Other general and systemic examinations revealed no abnormality. The diagnosis on admission was Glenn's shunt.

Important clinical findings: Blood Investigation: WBC: <5000 cells/mm^3. RBC: 20,000-40,000 (cells/mcL), IgM and IgG test: Positive, Platelet count: 12,000 cells/mm^3.

Timeline: He took treatment in A. V. B. R. H. and he got the proper treatment. Taking proper medication and now he has been in good condition.

Therapeutic interventions

Antipyretics for Ischemic Stroke, including Tab. paracetamol 500 mg (BD), Inj. Ceftriaxone 1 gm IV (BD), Inj. Pantoprazole 40 mg iv (OD), and Inj. Ondansetron 4 mg iv was prescribed in this instance (TDS). Antipyretics for Ischemic Stroke, including Tab. paracetamol 500 mg (BD), Inj. Ceftriaxone 1 gm IV (BD), Inj. Pantoprazole 40 mg iv (OD), and Inj. Ondansetron 4 mg iv was prescribed in this instance (TDS).

Nursing perspectives

DNS and RL check vital signs on an hourly basis to administer fluid replacement. The temperature chart was meticulously maintained every two hours, and the intake output chart was meticulously maintained. Antibiotics, tab. paracetamol, as prescribed by a physician. DNS and RL check vital signs on an hourly basis to administer fluid replacement. The temperature chart was meticulously maintained every two hours, and the intake output chart was meticulously maintained. Antibiotics, tab. paracetamol, as prescribed by a physician.

Discussion

The congenital cardiac disease affects about 2.5–3/1000 live births, with palliative treatments being one of the therapeutic options. Dr. William Glenn conducted the first Glenn shunt technique in 1958, and it is now a valuable palliative treatment for patients with single ventricle heart disease [4].

The congenital cardiac disease affects about 2.5–3/1000 live births, with palliative treatments being one of the therapeutic options. Dr. William Glenn conducted the first Glenn shunt technique in 1958, and it is now a valuable palliative treatment for patients with single ventricle heart disease. A phased approach is the conventional surgical therapy for single-ventricle congenital heart abnormalities. Palliative operations are required because of increased pulmonary vascular resistance [5].

A phased approach is the conventional surgical therapy for single-ventricle congenital heart abnormalities. Palliative operations are required because of increased pulmonary vascular resistance. It is required to prepare the patient for the Fontan procedure and to ensure that the patient survives [6].

The Glenn shunt is one of the most important milestones on the way to the Fontan operation. It's necessary to get the patient ready for the Fontan treatment and make sure he or she survives. The Glenn shunt is one of the most important milestones on the way to the Fontan operation. It lowers pulmonary vascular resistance and alleviates ventricular volume overload, allows for longterm life and stage palliation in single-ventricle heart defects, one-and-a-half ventricle physiology, and, in some cases, a bridge to two-ventricle restoration. Although having a single lung would not be a contraindication for the treatment, the pulmonary vascular state is one of the most important factors in achieving the best results, and the operation requires extra attention. Although having a single lung is not a contraindication for the treatment, pulmonary vascular status is one of the most important criteria for achieving the best results, and the operation deserves special care. Only a few cases of Fontan operation with a single lung have been documented in the literature. The main difference between patients with confluent pulmonary artery to the lungs and those with single lung was discovered to be the one-lung individuals decreased postoperative oxygen saturation [8].

The Fontan operation was successfully performed with an acceptable outcome in some patients even when only one lung was present. Glenn shunting to one lung has been shown to cause late problems such as congenital anomalies and impaired pulmonary functional ability in some longterm studies. Hypoxia, metabolic acidosis, and higher airway pressure can all lead to pulmonary vasoconstriction and high pulmonary vascular resistance. One-lung breathing is thus one of the most important events, and nitroglycerin, inhalation nitric oxide, and intravenous milrinone can be used to lower pulmonary vascular resistance. The pulmonary artery and lung of our patient were both single. We chose to conduct a Glenn shunt as a prelude to the Fontan treatment after a careful study of the case and the family's agreement. The operation was uncomplicated and straightforward; nevertheless, the patient required additional chest physiotherapy in the postoperative phase to maintain a 94% arterial oxygen level [9].

Conclusion

The Glenn shunt continues to provide excellent graded palliation and a bridge to two-ventricle correction in single-ventricle patients. The single-ventricle cohort had a lot of arrhythmias and pulmonary arteriovenous fistulas. The surviving patients' quality of life would be an essential outcome measure for further research.

References

1. Donofrio MT, Moon-Grady AJ, Hornberger LK, and Copel JA, et al. "Diagnosis and treatment of fetal cardiac disease: A scientific statement from the American Heart Association."*Circ*129 (2014): 2183-2242.
2. Chauvaud S, Fuzellier JF, Berrebi A, and Lajos P, et al. "Bi-directional cavopulmonary shunt associated with ventriculo and valvuloplasty in Ebstein's anomaly: benefits in high risk patients."*Eur J Cardiothorac Surg*13 (1998): 514-519.

3. Perry BD. "Childhood experience and the expression of genetic potential: What childhood neglect tells us about nature and nurture."*Brain Mind*3 (2002): 79-100.
4. Hoffman JI, Kaplan S. "The incidence of congenital heart disease."*J Am Coll Cardiol*39 (2002): 1890-1900.
5. Agresta F, Ansaloni L, Baiocchi GL, and Bergamini C, et al. "Laparoscopic approach to acute abdomen from the Consensus Development Conference of the Società Italiana di Chirurgia Endoscopica e nuove tecnologie (SICE), Associazione Chirurghi Ospedalieri Italiani (ACOI), Società Italiana di Chirurgia (SIC), Società Italiana di Chirurgia d'Urgenza e del Trauma (SICUT), Società Italiana di Chirurgia nell'Ospedalità Privata (SICOP), and the European Association for Endoscopic Surgery (EAES)."*Surg Endosc*26 (2012): 2134-2164.
6. Fujii Y, Sano S, Asou T, and Imoto Y, et al. "Outcomes of one-lung Fontan operation: a retrospective multicenter study in Japan." *Ann Thorac Surg*94 (2012): 1275-1280.
7. Iratwar S, Patil A, Rathod C, and Korde P, et al. "Ventriculosubgaleal shunt in children with hydrocephalus."*J Datta Meghe Inst Med Sci Univ*14 (2019): 115-118.
8. Anjankar S. "Urethral protrusion of the distal end of shunt."*J Pediatr Neurosci*13 (2018): 371-372.
9. Lamture Y, GajbhiYe V. "Migration of Thecoperitoneal Shunt into a Hernial Sac."*J Clin Diagn Res*13 (2019).

Categories

Business & Management

Clinical Sciences

Genetics & Molecular Biology

Medical Sciences

Pharmaceutical Sciences

Chemistry

Engineering

Immunology & Microbiology

Neuroscience & Psychology

Science & Technology

Guidelines

Author Guidelines

Editor Guidelines

Reviewer Guidelines

About Hilaris

About Us

Open Access

Contact Us

Terms

FAQs

Site Map

Follow Us

Facebook

Twitter

LinkedIn

Instagram

Youtube

Design of a Bulk Driven Gain Boosting Technique Operational Amplifier for Low Power and High Swing Applications.

- **Author(s):** KAKDE, SANDEEP; THAKARE, RAJESH; KAMBLE, SHAILESH; PATIL, MANOJ; U. S., PAVITHA

- **Abstract:** In this paper, a Bulk Driven Gain Boosting (BDGB) technique has been analyzed which is further employed in the design of a novel operational amplifier to enhance the gain and at the same time, a nested compensation technique is also used to improve the bandwidth without consuming extra power. The proposed operational amplifier circuit has been designed in sub threshold region and is biased with very less current at the first stage; an extra biasing circuit with gate to drain connected transistors is also designed to bias the last stage. The proposed configuration achieves open loop gain of 70dB, CMRR of 144dB, PSRR of 70dB and the unity gain bandwidth of 11MHz at 5pF load capacitance. The output swing is more than 650mV at 0.8V supply voltage consuming only 2.5μW static power. The gain/swing performance of the proposed low-voltage OPAMP would be therefore good enough not to require another amplifying stage in many high-speed, high swing and low-power applications.

For access to this entire article and additional high quality information, please check with your college/university library, local public library, or affiliated institution.

STUDY OF DIFFERENT CODING METHODS OF POLAR CODE IN 5G COMMUNICATION SYSTEM

Atish A. Peshattiwar

Reaserch Scholar Department of Electronics Engineering, Yeshwantrao Chavan College of Engineering, Nagpur, Maharashtra, (India).

E-mail: atishp32@gmail.com

Atish S. Khobragade

Professor, Department of Electronics Engineering, Yeshwantrao Chavan College of Engineering, Nagpur, Maharashtra, (India).

E-mail: atish_khobragade@rediffmail.com

https://doi.org/10.17993/3ctecno.2022.v11n2e42.90-99

ABSTRACT

Sure, most of you are aware that right now everyone is thinking or at least the industry and researchers are thinking about the next generation, the first generation of what will 5G be, and that a significant part of the 5G telecommunication standard has been finalised, in particular the error control codes that will be used in 5G telecommunication. One of the codes that will be used is called a Low-Density Parity Check code (or LDPC code for short), and the other is called Polar Code. These two famous and celebrated codes have distinct and fascinating histories. Both technologies are now capable of providing near-capacity results, making them formidable competitors in the race to become the 5G communication system's ultimate provider. In this paper, we zeroed in on the 5G Polar codes and their encoding methods.

KEYWORDS

5G Communication System, Channel Coding, LDPC Codes, Polar Codes, Coding Methods.

1. INTRODUCTION

The POLAR codes are a new type of capacity-achieving codes developed by Arkan [1]. Since 2008, polar codes have been the subject of increasing study and interest in both the academic and professional worlds. As part of the ongoing standardisation process for 5th generation wireless systems, the 3rd Generation Partnership Project (3GPP) has certified polar codes as the channel coding for uplink and downlink control information for the enhanced mobile broadband (eMBB) communication service (5G). Polar coding is one of the proposed encoding methods for the two new frameworks that 5G expects, namely extremely reliable low-latency communications (URLLC) and massive machine-type communications (mMTC).

Creating a polar code involves determining the values of channel dependability associated with each bit of information to be encoded. This id can be accomplished with a specific signal-to-noise ratio and code length. Due to the expected wide range of code lengths, transmission rates, and channel conditions in the 5G architecture, it is impractical to calculate separate reliability vectors for each possible parameter combination. A lot of work has gone into creating polar codes that are straightforward to implement, require little in the way of descriptive complexity, and provide adequate error-correction across a wide range of code and channel parameters.

In light of their impending widespread deployment, researchers would do well to take into account the one-of-a-kind codes created for 5G and their encoding procedure when evaluating error-correction performance and constructing encoders and decoders. Almost all works of contemporary literature fall short of this goal. Polar code properties have an immediate effect on decoder performance, and there may be substantial time and effort costs associated with encoding and decoding. Publications that focus on hardware and software implementations of the 5G standard may be able to increase their readership if they emphasise compliance with the standard.

An "industry standard" is a set of guidelines for providing a service that has been accepted by a number of different companies. In most cases, an agreement between multiple manufacturers to create products that are compatible with one another leads to a standardisation of details, which is the result of a commercial trade-off. A standard is a compromise between competing goals that ultimately results in a hodgepodge of techniques that, when combined, achieve satisfactory performance.

Here, we zeroed in on one particular 5G coding method—Polar Codes—to see what all the fuss is about. 2014 saw the introduction of new encoding schemes for the polar code [2] developed by kia niu.

The remainder of the paper is organised as follows. Polar code: the basics Section II focuses on encoding, while Section III discusses the more advanced design elements and ideas used in 5G decoding, such as SC, SCF, and SCL. In Section IV, we compare the results of our Latency and Throughput measurements, and in Section V, we draw some conclusions based on our findings.

2. 5G POLAR CODE ENCODING

The method employed by the 5G standard to encode polar codes is discussed at length here. In what follows, I'll be making use of the notation defined by the 3GPP technical specification [2]. Polar codes are used to transmit uplink control data over the physical uplink shared channel and uplink control channel. Both the payload on the physical broadcast channel and the downlink control information (DCI) on the physical down-link control channel (PDCCH) are encrypted using polar codes during the downlink transmission (PBCH). For the upper communication layers in 5G applications, the required rate $R = A/E$ is specified, where A is the amount of information bits.

A mother polar code of length N = 2n is required for this purpose. When the code is too long (or too short) for the specified code length E, it is punctured, shortened, or repeated until it is. Depending on the channel, the minimum and maximum code lengths N for the uplink and downlink are 32 and 512, 1024, respectively. An additional cap is imposed by the minimum allowable coding rate of 1/8. Figure 6 depicts the various encoding methods planned for use in the 5G polar codes design. The bits of information contained in vector a, denoted by the G code, will be conveyed using the payload of G code bits. Depending on the parameters of the encoding scheme, the message could be split into two parts, each of which would be encoded separately before being sent. For every AJ-bit segmented vector, a polar code-word of length E will be generated. There is an associated L-bit CRC for each AJ-bit vector. The resulting vector c is fed into an interleave, which requires K = AJ + L bits. To generate a mother polar code of length N, we need to know the expected coding rate R, the expected codeword length E, the relative bit channel reliability sequence, and the frozen set. While the remaining bits of the N-bit u vector are held steady, the interleaved vector cJ and any parity-check bits are added to the information set.

Using the generator matrix of the selected mother code, GN = G2n, we encode the vector u as d = u GN. Sub-block interleaving is then used to divide the encoded d into 32 blocks of the same length. Then, the circular buffer receives these blocks after they have been scrambled to produce y. For rate matching, the N-bit vector y is modified in some way (puncturing, shortening, or repeating) to yield the E-bit vector e. In the event that concatenation is necessary, the computed vector f is then ready to be modulated and transmitted as g.

Having the parameters A and E in play makes it clear that there is a cap on the effectiveness of the channel being used. While A 11 uses many different block codes, the uplink uses 12 A 1706. The agreed upon codeword length range is 18 E 8192, even though G 16384 may cause the payload length G to be longer. Segmentation could be used to do this, dividing the data bits into two polar codewords. . For PDCCH in the downlink, the maximum value of A is 140, but in this case, if A is 11, the message will be zero-padded until A = 12. Although E 8192 is employed for uplink, the presence of the CRC lower limits E to 25. There is only one valid PBCH passcode that utilises the combination of A = 32 and E = 864. These flags are the Input Bits Interleaver Activation (IBIL) signal and the Channel Interleaver Activation (CIA) (IIL). There are two kinds of PC helper bits, and NPC and nwm both provide the total number of them.

Fig. 1. Yellow, red, and orange blocks are used in downlink, uplink, and both, respectively, in the 5G polar codes encoding chain.

3. DECODING CONSIDERATION

Even though the 3GPP does not provide any decoding instructions, the final code structure provides some pointers on how to decode polar codes, which are commonly used in 5G. Figure 1 shows an encoding sequence; flipping the sequence facilitates decoding. The received encoded symbols are then padded and deinterleaved to the length of the mother polar code following a second block segmentation and deinterleaving operation for the uplink. A rate-matching algorithm will be used to determine the type of padding to be used, with punctuation requiring the addition of zeros, shortening requiring the use of saturated symbols, and repetition calling for the merging of symbols. The importance of properly handling the code's helper bits at this stage will be emphasised. After padding,

the number of encoded symbols is a power of two, which is readable by common polar code decoders [1]. Next, we consider SCL in light of these repercussions and current needs.

When the check for all active pathways fails, the list decoder triggers its early decoding termination feature; decoding continues when at least one active pathway succeeds. The decoder's BLER performance may, however, depend on how it deals with routes that have become unavailable. Keeping the unsuccessful paths in the list is the simple solution to keeping the number of active paths constant and simplifying the decoder design. After each bit estimate, one strategy is to immediately turn off failed paths. As a result, the BLER performs better, and the computational complexity and energy consumption of the decoder are reduced. However, this causes a variation in the total number of possible courses of action. Last but not least, distributed assistance bits could be thought of as dynamically frozen bits that supply the bit's value for the check. The BLER's efficiency is the same using this method as it was using the ineffective path deactivation. Since all surviving paths are guaranteed to get the work done, assistance bits do not have the same impact on the decoder's computational complexity or power consumption as dynamically frozen bits do. As an added bonus, they do not lead to dismissal in the midst of the work week.

However, the number of viable paths varies based on the computational complexity and power requirements of the decoder. Finally, distributed assistance bits can be viewed as dynamically frozen bits that supply the bit with the value the check requires. The BLER's efficiency is the same using this method as it was using the ineffective path deactivation. However, unlike dynamically frozen bits, which reduce computational complexity and power consumption of the decoder and lead to early termination, assistance bits do not guarantee that all remaining pathways will pass the check.

Native successive cancellation (SC) decoding of polar codes is also recommended in [1]. Like a left-biased depth-first binary tree search, its decoding time is linear in N log N. N bits are approximable at the leaf nodes, while the root node has soft information on the received code bits. Figure 4 depicts the decoding tree for a (8, 4) polar code, where black leaf nodes represent the information bits and white nodes represent the frozen bits. Figure 3 shows how the message flow can be defined recursively with a node at the tth stage as the starting point. The node receives 2t soft inputs from its parent node and uses them to generate 2t1 soft outputs _, which are then sent to the node's left child via the formula I = f I i+2t1); later, the node combines the 2t1 hard decisions it receives from the node's left child with to generate 2t1 soft outputs r for the Finally, it combines the 2t1 hard decisions r it received from its right child with to determine the 2t hard decisions it will send to its parent node, with I = I ri if I 2t1 and I = r i2t1 otherwise. When a leaf node is accessed, the soft information is used to make a hard decision regarding the value of the information bits; frozen bits are always decoded as zeros.

In particular, the channel model affects update rules f and g for left and right child nodes. In BEC, hard decisions can take on any value from 0 to 1, while soft values are limited to 0 and 1.
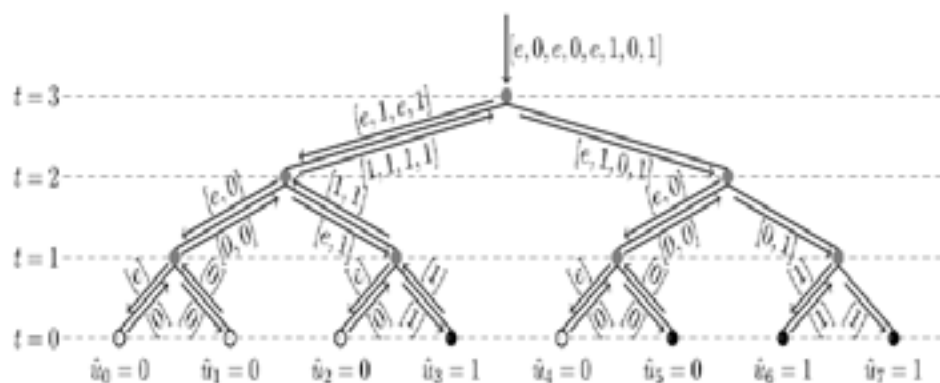
Fig. 2. White and black dots in the SC decoding of a (8, 4) polar code over a BEC stand for frozen and information bits.
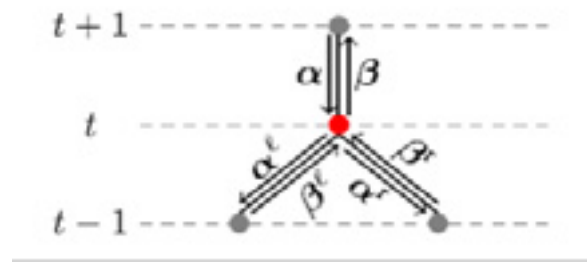
Fig. 3. SC decoding node.

3.1. DECODING FOR SUCCESSIVE-CANCELLATION (SC)

The SC decoding method, as first described [1], operates by sequentially traversing the graph representation of Fig. 2 while iteratively computing u from the noisy channel data. Do this from top to bottom and from right to left. It was first advised to calculate two bits at once in order to decrease time and boost throughput [3]. By utilising specialised, quicker decoding algorithms on selected network nodes [6] or even pruning the graph using a priori knowledge of the locations of the frozen bits [5], the SC technique was further improved. One candidate codeword is always considered, regardless of the SC algorithm version that is being used.
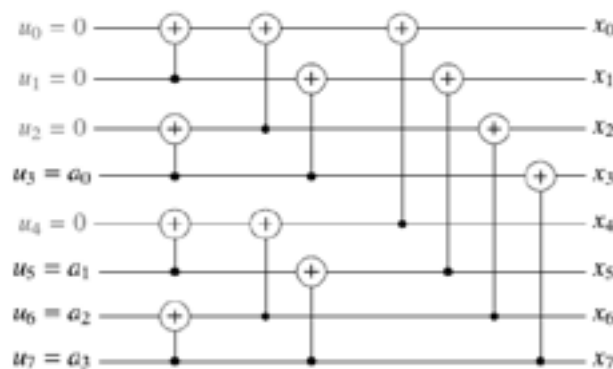
Fig. 4. Graph representation of a (8, 4) polar code.

3.2. PERFORMANCE OF SC DECODING

Fig. 5 compares the (2048, 1723) 10GBASE-T LDPC code's error-correction performance to polar codes running at the same rate. These results were obtained by modulating the binary-input additive white Gaussian noise (AWGN) channel with random codewords and binary phase-shift keying (BPSK). First, it must be stated that the (2048, 1723) polar code performs substantially poorer than the LDPC code. Up until Eb/N0 = 4.25 dB, the LDPC code works better than the PC(32768, 27568) polar code, which was intended to perform best for Eb/N0 = 4.5 dB. There is a growing performance difference over the LDPC code after that. The final polar error-rate curve, abbreviated PC*, is produced by combining the output of two polar codes (32768, 27568). (32768, 27568). The first, which has been in use up until this point, was constructed for 4.25 dB, whereas the second was designed for 4.5 dB. Polar codes can be easily decoded because of their predictable structure, which makes it easy to create a decoder that can decipher any polar code of a specific length. Therefore, polar code changes inside a system are easier than LDPC code modifications.

These findings demonstrate that a (32768, 27568) polar code built with an Eb/N0 of 4.5 dB or higher is required to surpass the (2048, 1723) LDPC one in the low error-rate zone and that this may be done even in high error-rate regions by combining numerous polar codes. Even though the polar code is longer than the LDPC code, its decoder is nevertheless built in a simpler manner. The performance difference between the (2048, 1723) code and the LDPC code with a list size of 32 and a 32-bit CRC is reduced by using the list-CRC technique [4], as illustrated in Fig. 2.

The use of some of these strategies to list decoding will need more study. Due to its serial nature, SC decoding has a limited throughput. ASIC decoders for (1024, 512) polar codes currently offer the fastest implementation, processing data at a rate of 48.75 Mbps while operating at 150 MHz [11]. The fastest decoder, on the other hand, can handle data at a rate of 26 Mbps for the (32768, 27568) code and is FPGA-based. Although it may be significantly increased by employing the SSC or ML-SSC decoding algorithms, this poor throughput renders SC decoders unusable for the bulk of systems.
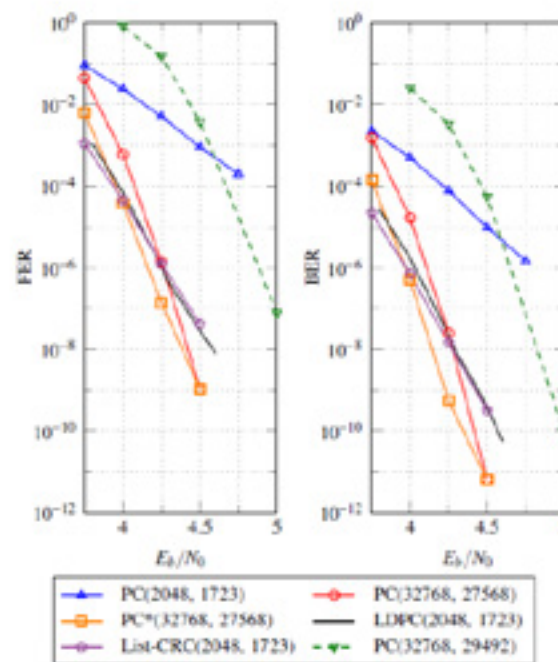
Fig. 5. Polar codes' error-correction performance is contrasted with an LDPC code of the same rate. In addition to a rate 0.9 polar code's functionality.

3.3. DECODING USING SUCCESSIVE-CANCELLATION FLIP (SCF)

Similarities exist between the SC algorithm and the SCF decoding technique [8]. At first, its operation is similar to that of SC decoding; however, in addition to decoding, it also keeps track of the bits that are the least reliable. A cyclic redundancy check must also be used to string together the polar code (CRC). The SCF decoder generates a full codeword candidate and checks if the computed CRC is the same as the expected one. When the CRC verification fails, the SC decoding process continues until the least reliable bit-decision is found. The SCF makes a contrasting conclusion and continues decoding SC. After two tries, if the CRC does not match the expected CRC, the bit-decision with the second-lowest confidence is swapped and the process is repeated. Until the CRC comparison is conclusive or until the maximum number of trials have been conducted, this technique is repeated.

3.4. DECODING OF THE SUCCESSIVE-CANCELLATION LIST (SCL)

As their names imply, the SCL algorithm [7] and the SC algorithm have some similarities. In contrast to SC decoding, the output of the SCL decoding method is a smaller set of up to L possible codewords. It considers both ui options for the locations I where data bits can be found. A path dependability metric computed during the method is used to filter out all but the L best pathways from the final list of survivors. At the end

of the decoding process, the estimated codeword is selected from among the L candidates based on which one has the highest route dependability score.

If a polar code and a CRC are paired, the projected CRC and computed CRC for each of the L candidates are compared. Out of all the candidates who pass the CRC, the decoded codeword is selected as the most trustworthy candidate. If all candidates fail the CRC, the technique simply selects the candidate with the highest route dependability.

3.4. LATENCY AND THROUGHPUT

To evaluate the latency boost from the novel algorithm and implementation, we compare two unrolled decoders with an LLR-based SC-list decoder developed in accordance with the technique described in [6] in Table I. The first unrolled decoder, also called the "unrolled SC-list," does not rely on any specific set of constituent decoders. The second is called "unrolled Dec-SPC-4," and it incorporates all of the component decoders we have covered so far while limiting the number of SPC decoders to four. When the SC-list decoder is unrolled, we find that decoding time is cut by more than half. Latency is reduced to between 63% (L = 2) and 18.9% (L = 32) of the unrolled SC-list decoder when the rate-0, rate-1, repetition, and SPC-4 constituent decoders are used. In comparison to SC-list decoding, the suggested decoding strategy and implementation yield a performance boost of between 18.4 and 11.9% for list sizes of 2 and 32, respectively.

The impact of the unrolled decoder is more noticeable for shorter lists, while the impact of the new constituent decoders is greater for longer lists.

When there is no limitation on the length of the individual SPC decoders, as in the case of "Unrolled Dec-SPC-4+" in Table I, the latency for the recommended decoder is also shown. Turning on these longer constituent decoders decreases latency by 14% and 18% for L = 2 and L = 8, respectively. We do not advise using SPC-8+ component decoders because of the drastic decrease in error-correction performance for L >= 8. Consequently, we do not guarantee the lag associated with such a decoder setup. The proposed decoder has a roughly linear decrease in throughput in function of L. At L = 32 and 433 s of latency, the data rate is 4 Mbps. Performance can be improved with adaptive decoding by using a Fast-SSC decoder prior to the list decode. The results of this method's throughput are shown for L = 8 and L = 32 in Table II. According to (17), when the throughput for L = 8 and 32 is equal, the effect of the list decoder on throughput diminishes, and the Fast-SSC performs better at 4.5 dB.

4. COMPARATIVE ANALYSIS

Table 1. Latency (in μsec) for various decoding methods of polar code.

Decoder	L		
	2	8	32
SC-List	558	1450	5145
Unrolled SC-list	193 (2.9×)	564(2.6×)	2294(2.2×)
Unrolled Dec SPC-4	30.4(18.4×)	97.5(14.9×)	433(11.9×)
Unrolled Dec SPC-4+	26.3(21.2×)	80.2(18.1×)	N/A

Table 2. When calculating 524,280 information bits, the suggested list decoder's information throughput and latency were compared to those of the ldpc decoders of [32].

Decoder	N	# of N-bit frames	Rate	Latency (ms)		Info. T/P (Mbps)
				Total	Per frame	
[32]	1944	540	1/2	17.4	N/A	30.1
proposed	1024	1024	1/2	13.8	0.014	38.0
[32]	1944	405	2/3	12.7	N/A	41.0
proposed	1024	768	2/3	10.0	0.013	52.4
[32]	1944	360	3/4	11.2	N/A	46.6
proposed	1024	683	3/4	8.78	0.013	59.6
[32]	1944	324	5/6	9.3	N/A	59.4
proposed	1024	615	5/6	6.2	0.010	84.5

5. CONCLUSION

This article will help the reader understand and implement the polar code encoding process in accordance with the 5G wireless systems standard, as well as simulate it for practise. This encoding chain exemplifies the 3GPP standards body's efforts to support a variety of code lengths and speeds while satisfying the various code criteria for the eMBB control channel, such as low description complexity and low encoding complexity. Insights into the consideration given to the receiver side during the standardisation process are provided. So long as cutting-edge hardware and decoders are used, the encoder was designed to allow for the decoder to be generated with a tolerable level of complexity and perform at the required latency. But now it is possible to optimise decoding complexity or improve error-rate performance by developing new decoding structures or principles.

We also investigated potential delays introduced by various decoding strategies, including successive cancellation (SC) decoding, successive cancellation flip (SCF) decoding, and successive cancellation list (SCL) decoding. Additionally, we conducted latency analyses to determine the relative merits of each decoding technique. Decoding algorithms can be tweaked to improve delay and throughput.

REFERENCES

[1] E. Arıkan, "Channel polarization: A method for constructing capacity- achieving codes for symmetric binary-input memoryless channels," IEEE Trans. Inf. Theory, vol. 55, no. 7, pp. 3051–3073, Jul. 2009 "Multiplexing and channel coding, v.15.3.0," 3GPP, Sophia Antipolis, France, Rep. 38.212, 2018.

[2] K. Niu, K. Chen, J. Lin, and Q. T. Zhang, "Polar codes: Primary concepts and practical decoding algorithms," IEEE Commun. Mag., vol. 52, no. 7, pp. 192–203, Jul. 2014.

[3] H. Vangala, E. Viterbo, and Y. Hong, "A comparative study of polar code constructions for the AWGN channel," Jan. 2015. [Online]. Available: arXiv:1501.02473

[4] R. Mori and T. Tanaka, "Performance of polar codes with the con- struction using density evolution," IEEE Commun. Lett., vol. 13, no. 7, pp. 519–521, Jul. 2009.

[5] I. Tal and A. Vardy, "How to construct polar codes," IEEE Trans. Inf. Theory, vol. 59, no. 10, pp. 6562–6582, Oct. 2013.

[6] P. Trifonov, "Efficient design and decoding of polar codes," IEEE Trans. Commun., vol. 60, no. 11, pp. 3221–3227, Nov. 2012.

[7] M. Mondelli, S. H. Hassani, and R. Urbanke, "Construction of polar codes with sublinear complexity," in Proc. IEEE Int. Symp. Inf. Theory (ISIT), Aachen, Germany, Jun. 2017, pp. 1853–1857.

[8] G. He et al., "Beta-expansion: A theoretical framework for fast and recursive construction of polar codes," in Proc. IEEE Glob. Commun. Conf. (GLOBECOM), Singapore, Dec. 2017, pp. 1–6.

[9] C. Condo, S. A. Hashemi, and W. J. Gross, "Efficient bit-channel relia- bility computation for multi-mode polar code encoders and decoders," in Proc. IEEE Int. Workshop Signal Process. Syst. (SiPS), Lorient, France, Oct. 2017, pp. 1–6.

[10] M. Mondelli, S. H. Hassani, and R. L. Urbanke, "From polar to Reed–Muller codes: A technique to improve the finite-length performance," IEEE Trans. Commun., vol. 62, no. 9, pp. 3084–3091, Sep. 2014.

[11] V. Bioglio, F. Gabry, I. Land, and J.-C. Belfiore, "Minimum-distance based construction of multi-kernel polar codes," in Proc. IEEE Glob. Commun. Conf. (GLOBECOM), Singapore, Dec. 2017, pp. 1–6.

[12] M. Mondelli, S. H. Hassani, and R. L. Urbanke, "Scaling exponent of list decoders with applications to polar codes," IEEE Trans. Inf. Theory, vol. 61, no. 9, pp. 4838–4851, Sept. 2015.

[13] J. Guo, M. Qin, A. G. I. Fábregas, and P. H. Siegel, "Enhanced belief propagation decoding of polar codes through concatenation," in Proc. IEEE Int. Symp. Inf. Theory (ISIT), Honolulu, HI, USA, Jun. 2014, pp. 2987–2991.

[14] U. U. Fayyaz and J. R. Barry, "Low-complexity soft-output decoding of polar codes," IEEE J. Sel. Areas Commun., vol. 32, no. 5, pp. 958–966, May 2014.

[15] A. Balatsoukas-Stimming, A. J. Raymond, W. J. Gross, and A. Burg, "Hardware architecture for list successive cancellation decoding of polar codes," IEEE Trans. Circuits Syst. II, Exp. Briefs, vol. 61, no. 8, pp. 609–613, Aug. 2014.

[16] A. Balatsoukas-Stimming, M. B. Parizi, and A. Burg, "LLR-based suc- cessive cancellation list decoding of polar codes," IEEE Trans. Signal Process., vol. 63, no. 19, pp. 5165–5179, Oct. 2015.

[17] C. Leroux, A. J. Raymond, G. Sarkis, and W. J. Gross, "A semi-parallel successive-cancellation decoder for polar codes," IEEE Trans. Signal Process., vol. 61, no. 2, pp. 289–299, Jan. 2013.

[18] B. L. Gal, C. Leroux, and C. Jego, "Software polar decoder on an embed- ded processor," in Proc. IEEE Workshop Signal Process. Syst. (SiPS), Belfast, U.K., Oct. 2014, pp. 180–185.

[19] O. Afisiadis, A. Balatsoukas-Stimming, and A. Burg, "A low-complexity improved successive cancellation decoder for polar codes," in Proc. IEEE Asilomar Conf. Signals Syst. Comput., Pacific Grove, CA, USA, Nov. 2014, pp. 2116–2120.

[20] C. Condo, F. Ercan, and W. J. Gross, "Improved successive cancellation flip decoding of polar codes based on error distribution," in Proc. IEEE Wireless Commun. Netw. Conf. (WCNC), Barcelona, Spain, Apr. 2018, pp. 19–24.

[21] I. Tal and A. Vardy, "List decoding of polar codes," IEEE Trans. Inf. Theory, vol. 61, no. 5, pp. 2213–2226, May 2015.

[22] S. A. Hashemi, A. Balatsoukas-Stimming, P. Giard, C. Thibeault, and W. J. Gross, "Partitioned successive-cancellation list decoding of polar codes," in Proc. IEEE Int. Conf. Acoust. Speech Signal Process. (ICASSP), Shanghai, China, Mar. 2016, pp. 957–960.

[23] S. A. Hashemi, M. Mondelli, S. H. Hassani, R. L. Urbanke, and W. J. Gross, "Partitioned list decoding of polar codes: Analysis and improvement of finite length performance," in Proc. IEEE Glob. Commun. Conf. (GLOBECOM), Singapore, Dec. 2017, pp. 1–7.

REVIEW ON DEEP LEARNING BASED TECHNIQUES FOR PERSON RE-IDENTIFICATION

Abhinav Parkhi

Reaserch Scholar, Department of Electronics & Telecommunication Engineering, YCCE, Nagpur, (India).

E-mail: abhinav.parkhi@gmail.com

Atish Khobragade

Professor, Department of Electronics Engineering, YCCE, Nagpur, (India).

E-mail: atish_khobragade@rediffmail.com

https://doi.org/10.17993/3ctic.2022.112.208-223

ABSTRACT

In-depth study has recently been concentrated on human re-identification, which is a crucial component of automated video surveillance. Re-identification is the act of identifying someone in photos or videos acquired from other cameras after they have already been recognized in an image or video from one camera. Re-identification, which involves generating consistent labelling between several cameras, or even just one camera, is required to reconnect missing or interrupted tracks. In addition to surveillance, it may be used in forensics, multimedia, and robotics.Re-identification of the person is a difficult problem since their look fluctuates across many cameras with visual ambiguity and spatiotemporal uncertainty. These issues can be largely caused by inadequate video feeds or low-resolution photos that are full of unnecessary facts and prevent re-identification. The geographical or temporal restrictions of the challenge are difficult to capture. The computer vision research community has given the problem a lot of attention because of how widely used and valuable it is. In this article, we look at the issue of human re-identification and discuss some viable approaches.

KEYWORDS

Person re-identification, Supervised Learning, Unsupervised Learning.

1. INTRODUCTION

T The process of Person Re-identification(Re-ID) has been thoroughly studied as a distinct person retrieval problem among non-overlapping cameras [1].Re-goal ID's is to determine whether a person of interest has ever been at a location at a different time that was captured by the same camera at a different time instant or even the same camera placed somewhere else [2].A photograph [3], a video clip [4], or even a written explanation [5] might be used to illustrate the subject.Person Re-ID is essential in smart surveillance technology with substantial academic effect and practical advantage due to the pressing need for community security and the growing number of security cameras.

The procedure of re-ID is difficult because of a variety of camera motions [6], poor picture resolutions [7, 8, 9, 10, 11, heterogeneous modalities [11, 12], complicated camera surroundings, background clutter [12], inaccurate bounding box creation, etc. These provide a lot of variations and uncertainty. Other elements that significantly increase the difficulties for realistic model deployment include the dynamically network of upgraded cameras [13], a massive gallery that offers effective restoration [14], group ambiguity [15], important domain change [16], unknown examining situations [17], and updating a model progressively [18], and changing clothes [19]. Re-ID still presents a problem as a result of these issues. This encourages us to carry out an extensive survey, establish a solid baseline for various Re-ID efforts,

and discuss a wide range of potential future paths. Person Although Re-ID is a difficult process, enhancing the semantic integrity of the analysis depends on it. Re-ID is crucial for programs that make use of single-camera surveillance systems. For instance, to find out if a person regularly visits the same place or if a different person or the same one picks up an abandoned box or bag. In addition to tracking, it has uses in robotics, multimedia, and more well-known technologies like automatic photo labeling and photo surfing [20].It is not difficult to comprehend the Person's Re-ID process. Being human, we always do it with ease. Our sights and minds have been conditioned to locate, identify, and then re-identify things and people in the actual world. Re-ID, which can be shown in Fig. 1, is the idea that a person who has been earlier seen would be identified as soon as they make an appearance using a specific description of the individual.

Even if hand-crafted features had some early success [21] and metric learning [22], the most advanced Re-ID algorithms currently available are constructed using convolutional neural networks (CNNs), which, when trained under supervision, need a significant amount of annotated (labelled) data to learn a stable embedding subspace. Recent deep learning approaches and detailed investigations on person Re-ID utilizing custom systemsprovided in [23], respectively. Large-scale dataset annotation for Re-ID is exceedingly labor intensive, time-consuming, and expensive, especially for techniques needing numerous bounding boxes for each individual to increase accuracy by making generalisations between two separate activities. One-shot learning and unsupervised learning are combined, for instance, in [24] and, which employ the Resnet50 [25] architecture with pre-trained networks on ImageNet [26]. Although it has been empirically demonstrated that pre-training and transfer learning significantly boost neural network performance, they are not appropriate for adjusting parameters across a wide range of domains or topologies. This article highlights the obstacles and unresolved problems in human re-identification and datasets, deep learning algorithms, and current research in these areas.

Figure

1.   Shows an example of a common DL workflow that involves following five stages (i) Data Collection (ii) Bounding Box Generation (iii)Data Annotation (iv) Model Training (v) Validation [67].

2. DEEP LEARNING MODERN RESEARCH

In today's Era, intelligent systems and tech sophisticated automation are the main focuses across a diverse range of domains, including smart cities, e-Health, enterprise intelligence, innovative treatment, cyber security intellectual ability, and many more [27].Particularly when it comes to security technologies as a wonderful approach to disclose complicated data structures in high dimensions, deep learning techniques have substantially improved in terms of effectiveness across a wide range of applications. In order to create intelligent data-driven systems that satisfy current expectations, DL techniques might be extremely important because to their exceptional learning capabilities from past data. DL has the ability to change both the world and how people live since it can automate procedures and learn from mistakes.

3. DEEP LEARNING TECHNIQUES

This section discusses the various deep neural network techniques. These strategies frequently use hierarchical structures with numerous levels of information processing to learn. Among the numerous hidden layers that are frequently observed in deep neural networks are the input and output layers. Reviewing the different training exercises available, that is (i) Supervised, an approach that is challenging and utilizes the use of tagged training data, and (ii) Unsupervised, an approach that examines unlabeled sets of data, is important before diving into the details of DL approaches.

3.1 SUPERVISED OR DISCRIMINATIVE LEARNING NETWORK

The term "supervised learning" refers to a process in which a supervisor doubles as an educator. The technique of instructing or training a computer system using labelled data is known as supervised learning. This suggests that the appropriate response has already been given to the given data. The machine is then given a new collection of examples so that the supervised learning algorithm may examine the training data (set of training examples) and provide an accurate output from labelled data.Discriminative deep architectures are frequently developed to give discriminative capability for pattern classification by modelling the posterior distributions of classes conditioned on observable data [29]. The three main categories of discriminative architectures are Multi-Layer Perceptron (MLP), Convolutional Neural Networks (CNN or ConvNet), Recurrent Neural Networks (RNN), and their variations. Here, we'll briefly discuss these techniques.

3.1.1 MULTI-LAYER PERCEPTRON (MLP)

The feed-forward artificial neural network known as the Multi-layer perceptron (MLP) [30] is a technique for supervised instruction (ANN). The deep neural network (DNN) or deep learning base architecture are other names for it. Several activation functions, often referred to as transfer functions, including ReLU (Rectified Linear Unit), Tanh, Sigmoid, and Softmax determine an MLP network's output [32].

The most popular technique for training MLP is back-propagation [31], a supervised learning method that is frequently referred to as the fundamental component of a neural network. Throughout the training phase, a variety of optimization techniques are employed liked Stochastic Gradient Descent (SGD), Limited Memory BFGS (L-BFGS), and Adaptive Moment Estimation (Adam).

3.1.2 CONVOLUTIONAL NEURAL NETWORK (CNN)

The commonly used deep learning architecture known as a convolutional neural network [33] was modelled after the visual brain of animals [34]. As seen in fig 2, Originally it had been used extensively for tasks involving object recognition, but it is currently also being investigated in areas such as object tracking [35], pose estimation [36], text detection and recognition [37], visual saliency detection [38], action recognition [39], scene labelling , and many more [40].

Since CNNs are particularly made to control the various 2D forms, they are frequently employed in visual identification, analyze clinical data, segmenting an image, processing language naturally, and many other applications [41].Several CNN versions, including visual geometry group (VGG) [42], AlexNet [43], Xception [44], Inception [45], ResNet [46], etc., may be used in various application sectors depending on their learning capacity.

1.   An illustration of Convolutional Neural Network.

3.1.3 RECURRENT NEURAL NETWORK (RNN)

Using sequential or time-series data, a different well-known neural network provides the result of one stage as input to the following step. The name for this neural network is recurrent neural network (RNN) [47]. Recurrent neural networks, like CNN and feed forward, learn from training input, but they stand out due to their "memory," which enables them to affect current input and output by consulting information from earlier inputs.While an RNN's output is reliant on what came before it in the sequence, a typical DNN assumes that inputs and outputs are independent of one another.However, because to the issue of declining gradients, standard networks with recurrence have difficulty in learning long data sequences. The popular recurrent network versions thatthe problems and perform effectively across a variety of real-life application areas are explored next.

3.1.4 LONG SHORT-TERM MEMORY (LSTM)

LSTMs are frequently used in video-based individual task re-ID and are capable of extracting temporal characteristics. Network for recurrent feature aggregation based on LSTM efficiently reduced interference brought on by background noise, shadowing, and recognition failure [48]. Among the first and shallowest LSTM nodes, it gathered cumulative discriminative characteristics. The temporal and geographical characteristics of the sections that include the probe pictures put were learned by the breakdown of a video sequence into multiple pieces [49]. The number of identical pedestrians in the sample is decreased by using this strategy, which also makes it simpler to identify similarity traits. Both of the aforementioned methods process each video frame independently.The duration of the video sequence typically has an impact on the characteristics that LSTM extracts. The RNN cannotcatch the temporalsignals of small details in the picture because it only creates temporal connections on high-level characteristics [50]. Therefore, research into a more effective technique for extracting spatial-temporal characteristics is still necessary.

3.1.5 GATED RECURRENT UNITS (GRUS)

A popular gating-based variation of the recurrent network techniques to monitor and regulate the flow of information between neural network units is the Gated Recurrent Unit (GRU) [51]. A reset gate and an update gate are all that the GRU has, as seen in Fig. 3, making it less complex than an LSTM.The primary difference between the two devices is the number of gates: an LSTM has three gates compared to a GRU's two (the reset and update gates). The GRU's characteristics allow dependencies from long data sequences to be collected adaptively without removing information from previous portions of the sequence.GRU is a little more compact approach as a consequence, often providing comparable results, and is significantly faster to compute [52].

Figure 3. A Gated Recurrent Unit's Basic Structure with a Reset and Update Gate.

3.2 UNSUPERVISED LEARNING NETWORK

DL approaches are widely used to explain the combined statistical parameters of the available data and the classes that they belong to, as well as the higher predictive properties or features for pattern recognition or synthesis [53].Since the methods under this category include frequently used to learn features or data generation and representation, they are fundamentally utilized for unsupervised learning [54]. Since generative modeling maintains the correctness of the discriminative model, it may be used as a preliminary step for supervised learning tasks as well. For generative learning or unsupervised learning, deep neural network algorithms including the Generative Adversarial Network (GAN), Autoencoder (AE), Restricted Boltzmann Machine (RBM), Self-Organizing Map (SOM), and Deep Belief Network (DBN), as well as its variations, are often utilized.

3.2.1 GENERATIVE ADVERSARIAL NETWORK (GAN)

.GANs make use of neural networks' capacity to train a function that can simulate a distribution as closely as feasible to the real thing. They are particularly capable of producing synthetic pictures with great visual fidelity and do not rely on prior assumptions about the distribution of the data. This important characteristic enables the application of GANs to any imbalance issue in computer vision tasks. GANs give a technique to alter the original picture in addition to being able to create a false image. There are several GANs with different strengths that have been published in the literature to address the imbalance issue in computer vision tasks. For example, a specific type of GANs called AttGAN [55], IcGAN [56], ResAttrGAN [57], etc., is frequently employed for tasks involving modifying face attributes.

GANs are comprised of two neural networks, as shown in Fig. 4. The discriminator D predicts the chance that a following sample will be taken from real data as opposed to data given by the generator G, which generates new data with features similar to the original data.The generator and discriminator in GAN modeling are then instructed to interact with one another.Healthcare, computer vision, data augmentation, video production, voice synthesis, epidemic prevention, traffic control, network security, and many more fields might all benefit from the utilization of GAN networks. In general, GANs have demonstrated to be a solid field of independent data expansion and a solution to problems requiring generative techniques.

2.   Generative Adversarial Networks Framework [58].

3.2.2 AUTO-ENCODER (AE)

A well-known auto-encoder (AE) unsupervised learning approach that makes use of neural networks to learn representations [59]. Data reduction describes the depiction of a set of data.High-dimensional data are often processed using auto-encoders. Three parts make up an autoencoder: an encoder, a code, and a decoder. The encoder creates the code that the decoder uses to reproduce the input by compressing it.Furthermore, generative data models have been learned using the AEs [60].Numerous unsupervised learning techniques, including dimension reduction, extraction of features, useful coding, dynamic modeling, noise removal, outlier or predictive modeling, etc., primarily rely on the auto-encoder. [59, 61]

3.2.3 KOHONEN MAP OR SELF-ORGANIZING MAP (SOM)

Another unsupervised learning method for constructing a low-dimensional (usually two-dimensional) representation of a higher-dimensional data set while preserving the topological structure of the data is the Self-Organizing Map (SOM) or Kohonen Map [62].SOM is a neural network-based method for dimension reduction in clustering [63].We can display huge datasets and identify likely clusters by using a SOM, which constantly moves a dataset's topological layout by bringing its neurons close to the data points inside the dataset.The input layer is the initial layer of a SOM, followed by the output layer, also known as the feature map, is the second layer. SOMs use competitive learning, which makes use of a neighboring function to preserve the topological properties of the input space, in contrast to other neural network models that use error-correction learning, such as Backpropagation with gradient descent [64].Sequence identification, sickness or health diagnosis, fault diagnosis, and virus or parasite attack detection are just a few of the many activities that SOM is frequently employed for [65].The main advantage of using a SOM is that it facilitates the discovery and recognition of patterns in high-dimensional data.

3.2.4 BOLTZMANN MACHINE WITH RESTRICTIONS (RBM)

A generative statistical neural network with the ability to learn a likelihood function over its inputs is the Restricted Boltzmann Machine (RBM) [66].Each node in a Boltzmann machine can be either visible or hidden and is linked to every other node.By understanding how the system functions normally, we can better comprehend anomalies. In RBMs, a subset of Boltzmann machines, there is a limit on the number of linkages between the accessible and deep layers [67].Due to this constraint, training techniques for Boltzmann machines in general can be more effective than those for Boltzmann machines, such as the gradient-based contrastive divergence algorithm [68]. Among the various uses of RBMs are data reduction, categorization, prediction, content-based- based filtering, pattern recognition, subject modelling, and many others.

3.2.5 DEEP BELIEF NETWORK (DBN)

A Deep Belief Network (DBN) [69] is a multiple-layer adaptive visuals model composed of so many unsupervised networks, such as AEs or RBMs, layered one on top of the other and using the hidden layer of each model as the input for the layer below it or connected sequentially.As a result, there are two types of DBNs: AE-DBNs, also called as stacked AE, and RBMDBNs, also known as stacked

RBMs.The AE-DBN consists of autoencoders, whereas Boltzmann machines with constraints constitute RBM-DBN, as was already indicated. The final objective is to create a descriptive divergence-based quicker unsupervised training method for every sub-network [70].The deep structure of DBN allows it to store a hierarchical representation of incoming data.Network architectures for unsupervised feed-forward are trained using unlabeled data as the basic tenet of DBN, and the networks are subsequently fine-tuned using marked input. DBN's potentially significant benefits over traditional shallow learning networks is its capacity to identify specific patterns, with strengthens logic and the ability to distinguish between true and wrong data [71].

Thus, the strategies for generative learning that were previously explored frequently allow us to use research method to build a new set of the data. Deep generative models of these kinds with supervised or discriminative learning methods may benefit from this preparation and to guarantee model correctness because improving classifier generalization through unsupervised representation learning.

4. CHALLENGES AND OPEN ISSUES

The fundamental difficulty with Re-ID is the variance in a person's appearance across multiple cameras. Re-ID is challenging to make self-operating for a variety of reasons.Re-ID networks usually consist of two essential parts:the capture of a unique individual description and the process of comparing two models to see if they match or don't match.The capacity to automatically recognize and track individuals in photos or videos is necessary in order to develop a distinctive person description.Numerous difficulties and problems are apparent, and they will guide future research in the area of person Re-ID.

4.1 RE-ID DEPENDING ON DEPTH

Depth photos capture the bones and contours of the body.Re-ID is made possible by this, which is crucial for applications involving individualized human contact in lighting and clothing variations [88]. In [72], a paradigm based on recurrent attention is put out to solve individual identification based on depth. Convolutional and recurrent neural networks are used to locate tiny, exclusionary localized parts of the body in a reinforcement learning framework.

4.2 RE-ID USING VISIBLE-INFRARED TECHNOLOGY

Visible-Infrared Re-ID handles the cross-modality matching between the noticeable and thermal pictures [88]. Because only infrared cameras can take photographs in low-light conditions, it is essential [73].Along with the cross- modality shared embedding learning [74] also looks into the classifier level discrepancy. Recent methods [75] decrease cross-modality disparity at both the picture and feature level by creating cross-modality person photographs and applying the GAN approach.[76] models the cross-modal reconstruction using a hierarchy elements. [77] presents a dual-attentive aggregate learning strategy to identify multi-level links.

4.3 CROSS-RESOLUTION RE-ID

Taking into consideration the major resolution variations [78], Cross-Resolution Re-ID [88] compares images with different resolutions.The high-resolution human pictures are produced in a cascaded fashion using a cascaded SR-GAN [79], which also incorporates the identification data. The adversarial learning method is used by Li et al. [80] to create representations of pictures that are independent of resolution.

4.4 LABEL NOISE FOR RE-ID

It is typically hard to eliminate label noise when there is an annotation issue [88]. To prevent label overfitting problems, Zheng et al. use a label smoothing algorithm [81]. To effectively learn a Re-ID model while avoiding label noise and the consequences of data with high characteristic ambiguity should be mitigated, a Distribution Net (DNet) is described in [82] that encodes the feature uncertainty.

For each identity, there aren't enough data for powerful Re-ID model training, unlike the generic classification issue [83]. It is also more challenging to learn the potent Re-ID model because of the unidentified new identities.

4.5 MULTI-CAMERA DYNAMIC NETWORK

The constantly updated multi-camera network [84], which necessitates model change for new cameras or probes, is another challenging issue. The Re-ID model may be updated and the representation can be tailored for different probing galleries employing an adaptive learning method with humans in the loop[85]. Active learning was a component of early research on continuous Re-ID in multi-camera networks [86]. [87] Introduces an approach for flexibility to adapt relying on the selective use of limited, non-redundant samples. Utilizing the ideal source camera theory and a geodesic flow kernel serve as the foundation for the development of a transitive inference strategy. An open-world person Re-ID system adds a number of contextual limitations (such Camera Topology) while dealing with large crowds and social interactions[88].

4.6 FEATURE LEARNING

High-level semantic representations of a person's traits, such their hair, gender, and age, can resist several environmental changes. For deep learning-based person Re-ID systems like those in [89], some research has used these traits to fill the gap between the photos and high-level conceptual data.Since it delivered on its predictions, feature recognition is one of the next possibilities.

4.7 ARCHITECTURE FOR AUTOMATED RE-ID

An advanced learning model's architectures must be manually created, which takes time, effort, and is prone to mistakes. The approach of automating architectural engineering, known as neural architecture search (NAS) [90], has recently been applied to address this issue. The study of NAS is currently receiving greater attention. Therefore, one of the essential aspects that must be considered in future research is the use of NAS for person Re-ID activities, as the majority of NAS techniques don't assure that there commended CNN is suitable for person Re-ID tasks.

4.8 ACCURACY VERSUS EFFICIENCY

Large models are typically employed to obtain the greatest accuracy, but they can be time and memory intensive, which reduces their usefulness, particularly when used to mimic real-time video monitoring systems. The majority of modern models did not consider CPU speed and memory capacity into account in order to increase accuracy. Authors who work in these fields must strike acompromise between processing speed and ranking accuracy.

4.9 LIGHTWEIGHT MODEL

The creation of a lightweight Re-ID model is another approach for dealing with the scalability problem. The issue of changing the network topology to create a light model is investigated [91, 92]. Another strategy is to employ model distillation. A system for multi-teacher customizable comparison reduction, for instance, is provided in [93], which in the absence of a primary data source, trains a user-specified lightweight student model from a number of teacher models.

5. DATASETS AND EVALUATION

Individuals' appearances vary greatly depending on Lighting, stances, view angles, scales, and camera resolutions may all vary while using different cameras. Visual ambiguities are further increased by elements like occlusions, a crowded background, and articulated figures. Therefore, it is crucial to gather data that successfully captures these aspects in order to create viable Re-ID approaches. In addition to good quality data that replicates actual circumstances, it is essential to compare and assess the Re-ID methodologies that are developed and find ways to enhance the methodology and databases.

5.1 DATASETS BASED ON IMAGES

Person re-ID using images, there have been a variety of datasets; the most common datasets are listed below.

VIPeR[94]: It is made up of 1,264 photos for 632 people and was taken by 2 non-overlapping cameras.

CUHK01 [95]: It is made up of 3,884 photographs for 971 individuals that were recorded by two separate cameras on a university campus.

Market-1501 [96]: It is comprised of 32,643 photos for each of the 1,501 people that make up the sample, which was taken from the front of a shop using 2 to 6 separate cameras.

DukeMTMC-ReID[97]: The dataset consists of 46,261 photos for 1852 individuals that were captured by 8 non-overlapping cameras on the Duke University campus.

Kinect-REID [98]: It has 71 person sequences that were recorded at the authors' department.

RGBD-ID [99]: There are four groups with various viewpoints, each with the same 80 people. It is produced on several days and has various aesthetic variants.

RegDB[100]: 412 people are represented by 4120 RGB photos and 4120 thermal photographs. Two types of cameras are used to capture them.

SYSU-MM01 [101]: It comprises of 491 people's 15,792 infrared photographs and 287,628 RGB photos. Six cameras, including two infrared cameras and four RGB cameras, are used to capture them from the writers' section.

5.2 DATASETS BASED ON VIDEOS

PRID2011 [102]: It is constituted of 24541 photos for 934 individuals from 600 recordings taken from two separate cameras in an airport's multi-camera network.

iLIDSVID[103]: It is made up of 600 movies shot by 2 non-overlapping airport cameras and 42495 photos for 300 people.

MARS [104]: The greatest video-based individual Re-ID dataset resides in this one. It is made up of around 1191003 photos for 1261 individuals from 200 recordings that were captured by 2 to 6 non-overlapping cameras.

RPIfield [105]: It consists of 601,581 images for 112 individuals, captured by 2 separate cameras on an open field at a college.

5.3 EVALUATION METRICS

Cumulative matching characteristics (CMC) [106] and mean average precision (mAP) are the two mostly used metrics for assessing Re-ID systems [107].

6. CONCLUSION

We have discussed the subject of human re-identification, as well as difficult problems and a summary of recent research in the discipline of person recognition, in this paper. Both closed set and open set Re-ID tasks have been taken into consideration. The approaches employed have been grouped, and their advantages and disadvantages have been covered. Additionally, we have outlined the benefits and drawbacks of the various Re-ID datasets. Popular Re-ID assessment methods are briefly discussed, along with potential expansions.In conclusion, person Re-ID is a broad and difficult field with much of space for growth and research.An effort is made in this work to give a concise overview of the Re-ID problem, its limitations, and related problems.

REFERENCES

(1)   Y.-C. Chen, X. Zhu, W.-S. Zheng, and J.-H.   Lai, "Person reidentification by camera correlation aware feature augmentation," IEEE   TPAMI, vol. 40, no. 2, 2018.

(2)   N. Gheissari, T. B. Sebastian, and R. Hartley,"Person reidentification using spatiotemporal appearance," in CVPR, 2006, pp. 1528–1535.

(3)   J. Almazan, B. Gajic, N. Murray, and D. Larlus,"Re-id done right: towards good practices for person re-identification," arXiv preprint arXiv:1801.05339, 2018.

(4)   T. Wang, S. Gong, X. Zhu, and S. Wang, "Person re-identification by video ranking," in ECCV, 2014.

(5)   M. Ye, C. Liang, Z. Wang, Q. Leng, J. Chen, and J. Liu, "Specific person retrieval via incomplete text description," in ACM ICMR, 2015, pp. 547–550.

(6)   S. Karanam, Y. Li, and R. J. Radke, "Person re-identification with discriminatively trained viewpoint invariant dictionaries," in ICCV, 2015, pp. 4516–4524.

(7)   X. Li, W.-S. Zheng, X. Wang, T. Xiang, and S. Gong, "Multi-scale learning for low-resolution person re-identification," in ICCV, 2015, pp. 3765–3773.

(8)   Y. Huang, Z.-J. Zha, X. Fu, andW. Zhang, "Illumination-invariant person re-identification," in ACM MM, 2019.

(9)   Y.-J. Cho and K.-J. Yoon, "Improving person re-identification viapose-aware multi-shot matching," in CVPR, 2016, pp. 1354–1362.

(10)   H. Huang, D. Li, Z. Zhang, X. Chen, and K. Huang, "Adversarially occluded samples for person re-identification," in CVPR, 2018, pp. 5098–5107.

(11)   A. Wu, W.-s. Zheng, H.-X. Yu, S. Gong, and J. Lai, "Rgb-infrared cross-modality person re-identification," in ICCV, 2017.

(12)   C. Song, Y. Huang, W. Ouyang, and L. Wang, "Mask-guided contrastive attention model for person re-identification," in CVPR, 2018, pp. 1179–1188.

(13)   A. Das, R. Panda, and A. K. Roy-Chowdhury, "Continuous adaptation of multi-camera person identification models through sparse non-redundant representative selection," CVIU, vol. 156, pp. 66–78, 2017.

(14)   J. Garcia, N. Martinel, A. Gardel, I. Bravo, G. L. Foresti, and C. Micheloni, "Discriminant context information analysis for post-ranking person re-identification," IEEE Transactions on ImageProcessing, vol. 26, no. 4, pp. 1650–1665, 2017.

(15)   W.-S. Zheng, S. Gong, and T. Xiang, "Towards open-world person re-identification by one-shot group-based verification," IEEE TPAMI, vol. 38, no. 3, 2015.

(16)   A. Das, R. Panda, and A. Roy-Chowdhury, "Active image pair selection for continuous person re-identification," in ICIP, 2015, pp. 4263–4267.

(17)   J. Song, Y. Yang, Y.-Z. Song, T. Xiang, and T. M. Hospedales, "Generalizable person re-identification by domain-invariant mapping network," in CVPR, 2019.

(18)   A. Das, A. Chakraborty, and A. K. Roy-Chowdhury, "Consistent re-identification in a camera network," in ECCV, 2014, pp. 330– 345.

(19)   Q. Yang, A. Wu, and W. Zheng, "Person re-identification by contour sketch under moderate clothing change." IEEE TPAMI, 2019.

(20) J. Sivic, C.L. Zitnick, R. Szeliski, Finding people in repeated shots of the same scene,Proceedings of the British Machine Vision Conference, 2006, pp. 909–918.

(21) M. Farenzena, L. Bazzani, A. Perina, V. Murino, and M. Cristani. Person re-identification by symmetry-driven accumulation of local features. In 2010 IEEE Computer Society Conference

(22) S. Liao and S. Z. Li. Efficient psd constrained asymmetric metric learning for person re-identification. In 2015 IEEE International Conference on Computer Vision (ICCV), pages 3685–3693, 2015.

(23) Liang Zheng, Yi Yang, and Alexander G. Hauptmann. Person re-identification: Past, present and future. ArXiv, abs/1610.02984, 2016.

(24) Yutian Lin, Xuanyi Dong, Liang Zheng, Yan Yan, and Yi Yang. A bottom-up clustering approach to unsupervised person re-identification. In AAAI, 2019.

(25) Kaiming He, Xiangyu Zhang, ShaoqingRen, and Jian Sun. Deep residual learning for image recognition, 2015.

(26)   J. Deng, W. Dong, R. Socher, L. Li, Kai Li, and Li Fei- Fei. Imagenet: A large-scale hierarchical image database. In 2009 IEEE Conference on Computer Vision and Pattern Recognition, pages 248–255, 2009.

(27) Sarker IH. Data science and analytics: an overview from datadrivensmart computing, decision-making and applications perspective.SN Comput Sci. 2021.

(28) Sarker IH. Machine learning: Algorithms,real-world applications and research directions. SN Computer. Science. 2021;2(3):1–21.

(29) Deng L. A tutorial survey of architectures, algorithms, and applications for deep learning. APSIPA Trans Signal Inf Process. 2014; p. 3.

(30) Pedregosa F, Varoquaux G, Gramfort A, Michel V, ThirionB,Grisel O, Blondel M, Prettenhofer P, Weiss R, Dubourg V, et al. Scikit-learn: machine learning in python. J Mach Learn Res.2011;12:2825–30.

(31) Han J, Pei J, Kamber M. Data mining: concepts and techniques. Amsterdam: Elsevier; 2011.

(32) Sarker IH. Deep cybersecurity: a comprehensive overview from neural network and deep learning perspective. SN Computer.Science. 2021;2(3):1–16.

(33) Ramachandran R, Rajeev DC, Krishnan SG, P Subathra, Deep learning an overview, IJAER, Volume 10, Issue 10, 2015, Pages 25433-25448.

(34)   D. H. Hubel and T. N. Wiesel, Receptive fields and functional architecture of monkey striate cortex, The Journal of physiology, 1968.

(35) J. Fan, W. Xu, Y. Wu, and Y. Gong, Human tracking using convolutional neural networks, Neural Networks, IEEE Transactions, 2010.

(36) A. Toshev and C. Szegedy, Deep -pose: Human pose estimation via deep neural networks, in CVPR, 2014.

(37)   M. Jaderberg, A. Vedaldi, and A. Zisserman, Deep features for text spotting, in ECCV, 2014.

(38) R. Zhao, W. Ouyang, H. Li, and X. Wang, Saliency detection by multicontext deep learning, in CVPR, 2015.

(39)   J. Donahue, Y. Jia, O. Vinyals, J. Hoffman, N. Zhang, E. Tzeng, and T. Darrell, Decaf: A deep convolutional activation feature for generic, 2014

(40) Nithin, D Kanishka and Sivakumar, P Bagavathi, Generic Feature Learning in Computer Vision, Elsevier, Vol.58, Pages202-209, 2015.

(41) LeCun Y, Bottou L, Bengio Y, Haffner P. Gradient-based learning applied to document recognition. Proc IEEE. 1998;86(11):2278–324.

(42) He K, Zhang X, Ren S, Sun J. Spatial pyramid pooling in deep convolutional networks for visual recognition. IEEE Trans PatternAnal Mach Intell. 2015;37(9):1904–16.

(43) Krizhevsky A, Sutskever I, Hinton GE. Imagenet classification with deep convolutional neural networks. In: Advances in neural information processing systems. 2012.

(44) Chollet F. Xception: Deep learning with depthwise separable convolutions. In: Proceedings of the IEEE Conference on computer vision and pattern recognition, 2017

(45) [45] He K, Zhang X, Ren S, Sun J. Deep residual learning for image recognition. In: Proceedings of the IEEE Conference on computervision and pattern recognition, 2016

(46) [46] Szegedy C, Liu W, Jia Y, Sermanet P, Reed S, Anguelov D, Erhan D, Vanhoucke V, Rabinovich A. Going deeper with convolutions.In: Proceedings of the IEEE Conference on computer vision and pattern recognition, 2015.

(47) Dupond S. A thorough review on the current advance of neural network structures. Annu Rev Control. 2019.

(48) Y. Yan, B. Ni, Z. Song, C. Ma, Y. Yan, X. Yang, Person reidentification via recurrent feature aggregation, Proceedings of the European Conference on Computer Vision, 2016.

(49) D. Chen, H. Li, T. Xiao, S. Yi, X. Wang, Video person reidentification with competitive snippet-similarity aggregation and co-attentive snippet embedding, Proceedings of the IEEE Conference on Computer Vision and Pattern Recognition, 2018, pp. 1169– 1178

(50) J. Li, S. Zhang, T. Huang, Multi-scale 3d convolution network for video based person re-identification, Proceedings of the AAAI Conference on Artificial Intelligence, volume 33, 2019, pp. 8618– 8625

(51) Chung J, Gulcehre C, Cho KH, Bengio Y. Empirical evaluation of gated recurrent neural networks on sequence modeling. arXiv preprint arXiv:1412.3555, 2014.

(52) Gruber N, Jockisch A. Are gru cells more specific and lstm cells more sensitive in motive classification of text? Front ArtifIntell. 2020;3:40.

(53) Deng L. A tutorial survey of architectures, algorithms, and applicationsfor deep learning. APSIPA Trans Signal Inf Process. 2014.

(54) Da'u A, Salim N. Recommendation system based on deep learning methods: a systematic review and new directions. Artif Intel Rev. 2020;53(4):2709–48.

(55) He Z, Zuo W, Kan M, Shan S, Chen X. AttGAN: Facial attribute editing by only changing what you want. IEEE transactions on image processing . 2019;28:5464–78.

(56) Perarnau G, van de Weijer J, Raducanu B, Álvarez JM. Invertible Conditional GANs for image editing. Conference on Neural Information Processing Systems . 2016.

(57) Tao R, Li Z, Tao R, Li B. ResAttr-GAN: Unpaired deep residual attributes learning for multi-domain face image translation. IEEE Access . 2019;7:132594–608.

(58) Moacir A. Ponti, Leonardo S. F. Ribeiro, Tiago S. Nazare,Tu Bui, John Collomosse "Everything you wanted to know about Deep Learning for Computer Vision but were afraid to ask" https://www.researchgate.net/publication/322413149

(59)   Goodfellow I, Bengio Y, Courville A, Bengio Y. Deep learning,vol. 1. Cambridge: MIT Press; 2016.

(60)   Liu W, Wang Z, Liu X, Zeng N, Liu Y, Alsaadi FE. A surveyofdeep neural network architectures and their applications. Neurocomputing.2017;234:11–26.

(61)   Zhang G, Liu Y, Jin X. A survey of autoencoder-based recommendersystems. Front Comput Sci. 2020;14(2).

(62)   Kohonen T. The self-organizing map. Proc IEEE.1990;78(9):1464–80.

(63)   [63] Sarker IH, Salah K. Appspred: predicting context-aware smartphone apps using random forest learning. Internet of Things. 2019;8:100106.

(64)   Han J, Pei J, Kamber M. Data mining: concepts and techniques. Amsterdam: Elsevier; 2011.

(65)   Kohonen T. Essentials of the self-organizing map. Neural Netw.2013;37:52–65.

(66)   [66] Marlin B, Swersky K, Chen B, Freitas N. Inductive principles for restricted boltzmann machine learning. In: Proceedings of the Thirteenth International Conference on artificial intelligence and statistics, p. 509–16. JMLR Workshop and Conference Proceedings, 2010.

(67)   Memisevic R, Hinton GE. Learning to represent spatial transformations with factored higher-order boltzmann machines. Neural Comput. 2010;22(6):1473–92.

(68)   Hinton GE, Osindero S, Teh Y-W. A fast learning algorithm for deep belief nets. Neural Comput. 2006;18(7):1527–54.

(69)   Hinton GE. Deep belief networks. Scholarpedia.2009;4(5):5947.

(70)   Hinton GE, Osindero S, Teh Y-W. A fast learning algorithm for deep belief nets. Neural Comput. 2006;18(7):1527–54.

(71)   Ren J, Green M, Huang X. From traditional to deep learning: fault diagnosis for autonomous vehicles. In: Learning control. Elsevier. 2021; p. 205–19.

(72)   A. Haque, A. Alahi, and L. Fei-Fei, "Recurrent attention models for depth-based person identification," in CVPR, 2016, pp. 1229–1238.

(73)   M. Ye, Z. Wang, X. Lan, and P. C. Yuen, "Visible thermal person re-identification via dual-constrained top-ranking," in IJCAI, 2018, pp. 1092–1099.

(74)   M. Ye, J. Shen, and L. Shao, "Visible-infrared person re-identification via homogeneous augmented tri-modal learning," IEEE TIFS, 2020.

(75)   Z. Wang, Z. Wang, Y. Zheng, Y.-Y. Chuang, and S. Satoh, "Learning to reduce dual-level discrepancy for infrared-visible person re-identification," in CVPR, 2019, pp. 618–626.

(76)   S. Choi, S. Lee, Y. Kim, T. Kim, and C. Kim, "Hi-cmd: Hierarchical cross-modalitydisentanglement for visible-infrared person reidentification," in CVPR, 2020, pp. 257–266.

(77)   M. Ye, J. Shen, D. J. Crandall, L. Shao, and J. Luo, "Dynamic dual-attentive aggregation learning for visible-infrared person reidentification," in ECCV, 2020.

(78)   X. Li, W.-S. Zheng, X. Wang, T. Xiang, and S. Gong, "Multi-scale learning for low-resolution person re-identification," in ICCV, 2015, pp. 3765–3773.

(79)   Z.Wang, M. Ye, F. Yang, X. Bai, and S. Satoh, "Cascaded sr-gan for scale-adaptive low resolution person re-identification." in IJCAI, 2018, pp. 3891–3897.

(80)   Y.-J. Li, Y.-C. Chen, Y.-Y. Lin, X. Du, and Y.-C. F. Wang, "Recover and identify: A generative dual model for cross-resolution person re-identification," in ICCV, 2019, pp. 8090–8099.

(81)   Z. Zheng, L. Zheng, and Y. Yang, "Unlabeled samples generated by gan improve the person re-identification baseline in vitro," in ICCV, 2017, pp. 3754–3762.

(82)   T. Yu, D. Li, Y. Yang, T. Hospedales, and T. Xiang, "Robust person re-identification by modelling feature uncertainty," in ICCV, 2019, pp. 552–561.

(83)   M. Ye and P. C. Yuen, "Purifynet: A robust person reidentification model with noisy labels," IEEE TIFS, 2020.

(84)   A. Das, A. Chakraborty, and A. K. Roy-Chowdhury, "Consistent re-identification in a camera network," in ECCV, 2014.

(85)   N. Martinel, A. Das, C. Micheloni, and A. K. Roy-Chowdhury, "Temporal model adaptation for person re-identification," in ECCV, 2016.

(86)   A. Das, R. Panda, and A. Roy-Chowdhury, "Active image pair selection for continuous person re-identification," in ICIP, 2015.

(87)   A. Das, R. Panda, and A. K. Roy-Chowdhury, "Continuous adaptation of multi-camera person identification models through sparse non-redundant representative selection," CVIU, vol. 15.2017.

(88)   Mang Ye, JianbingShen, Gaojie Lin, Tao Xiang, Ling Shao, Steven C. H. Hoi, Deep Learning for Person Re-identification:A Survey and Outlook, IEEE TRANSACTIONS ON PATTERN ANALYSIS AND MACHINE INTELLIGENCE-2021

(89)   C. Su, S. Zhang, J. Xing, W. Gao, and Q. Tian, ``Multi-type attributes driven multi-camera person re-identi_cation,'' Pattern Recognit., vol. 75, pp. 77_89, Mar. 2018.

(90)   T. Elsken, J. H. Metzen, and F. Hutter, ``Correction to: Neural architecture search,'' in Automated Machine Learning: Methods, Systems, Challenges, F. Hutter, L. Kotthoff, and J. Vanschoren, Eds. Cham, Switzerland: Springer, 2019.

(91)   W. Li, X. Zhu, and S. Gong, "Harmonious attention network for person re-identification," in CVPR, 2018, pp. 2285–2294.

(92)   K. Zhou, Y. Yang, A. Cavallaro, and T. Xiang, "Omni-scale feature learning for person re-identification," in ICCV, 2019, pp. 3702– 3712.

(93)   A. Wu, W.-S. Zheng, X. Guo, and J.-H. Lai, "Distilled person reidentification: Towards a more scalable system," in CVPR, 2019,pp. 1187–1196.

(94)   D. Gray, S. Brennan, and H. Tao, ``Evaluating appearance models for recognition, reacquisition, and tracking,'' in Proc. 10th Int. Workshop Perform. Eval. Tracking Surveill. (PETS), vol. 3, 2007, pp. 41_47.

(95)   W. Li, R. Zhao, and X. Wang, ``Human reidenti_cation with transferred metric learning,'' in Computer Vision_ACCV (Lecture Notes in Computer Science), vol. 7724. Berlin, Germany: Springer, 2013, pp. 31_44.

(96)   L. Zheng, L. Shen, L. Tian, S. Wang, J. Wang, and Q. Tian, ``Scalable person re-identi_cation:Abenchmark,'' in Proc. IEEE Int. Conf. Comput Vis. (ICCV), Dec. 2015, pp. 1116_1124.

(97)   E. Ristani, F. Solera, R. Zou, R. Cucchiara, and C. Tomasi, ``Performance measures and a data set for multi-target, multi-camera tracking,'' in Computer Vision_ECCV 2016 Workshops (Lecture Notes in Computer Science), vol. 9914. Cham, Switzerland: Springer, 2016, pp. 17_35.

(98)   F. Pala, R. Satta, G. Fumera, and F. Roli, ``Multimodal person re-identification using RGB-D cameras,'' IEEE Trans. Circuits Syst. Video Technol., vol. 26, no. 4, pp. 788_799, Apr. 2016.

(99)   I. B. Barbosa, M. Cristani, A. Del Bue, L. Bazzani, and V. Murino,``Re-identi_cation with RGB-D sensors,'' in Compute Vision_ECCV2012. Workshops and Demonstrations, A. Fusiello, V. Murino, andR. Cucchiara, Eds. Berlin, Germany: Springer, 2012, pp. 433_442.

(100) D. T. Nguyen, H. G. Hong, K. W. Kim, and K. R. Park, ``Person recognition system based on a combination of body images from visible lightand thermal cameras,'' Sensors, vol. 17, no. 3, p. 605, 2017.

(101) A.Wu,W.-S. Zheng, H.-X. Yu, S. Gong, and J. Lai, ``RGB-infrared crossmodality person re-identi_cation,'' in Proc. IEEE Int. Conf. Comput. Vis. (ICCV), Oct. 2017.

(102) M. Hirzer, C. Beleznai, P. M. Roth, and H. Bischof, ``Person re-identification by descriptive and discriminative classification,'' in Image Analysis (Lecture Notes in Computer Science), vol. 6688. Berlin, Germany:Springer, 2011, pp. 91_102.

(103) T. Wang, S. Gong, X. Zhu, and S. Wang, ``Person re-identification by video ranking,'' in Computer Vision_ECCV, D. Fleet, T. Pajdla, B. Schiele, and T. Tuytelaars, Eds. Cham, Switzerland: Springer, 2014,pp. 688_703.

(104) L. Zheng, Z. Bie, Y. Sun, J.Wang, C. Su, S.Wang, and Q. Tian, ``MARS: A video benchmark for large-scale person re-identi_cation,'' in Computer Vision_ECCV (Lecture Notes in Computer Science), vol. 9910. Cham, Switzerland: Springer, 2016, pp. 868_884.

(105) M. Zheng, S. Karanam, and R. J. Radke, ``RPI_eld: A new dataset for temporally evaluating person re-identi_cation,'' in Proc. IEEE/CVF Conf. Comput. Vis. Pattern Recognit. Workshops (CVPRW), Jun. 2018.

(106) X. Wang, G. Doretto, T. Sebastian, J. Rittscher, and P. Tu, "Shape and appearance context modeling," in ICCV, 2007.

(107) L. Zheng, L. Shen, L. Tian, S. Wang, J. Wang, and Q. Tian,"Scalable person re-identification: A benchmark," in ICCV, 2015,pp. 1116–1124.

Milind Narlawar

Management Of Bullous Pemphigoid with Diabetes Mellitus Type 2.

Authors	Pratiksha S Palsapure, Vaishali Balpande, Aniket Pathade, MS Narlawar, Samruddhi Gujar
Publication date	2022/6/1
Journal	International Journal of Early Childhood Special Education
Volume	14
Issue	4
Description	Introduction: It's an uncommon autoimmune disease that affects both men and women, albeit women have a higher prevalence. Presenting complaints and investigations: For six months, a woman in her 65th year patient has delivered a presentation dermatology department with the major complaint of fluid-filled sores all over her body. She had also been complaining of lesions with mild to severe scratching, irritation, and an occasional burning feeling over lesions for the past 6 months, and she was a recognised case of type 2 diabetes mellitus for which she had been taking medication for the past 6 to 7 years. The main Diagnosis, therapeutic intervention and outcomes: after a physical examination and inquiry, the doctor discovered a case of Bullous Phemphoid with a verified case of DM type 2. Inj. Insulin Mixtard 22U/16U, Tab. Defcort 12 Mg 2-1, Tab. Glicazide 80 Mg BD, Tab. Nicoglow 250 Mg OD, Tab …
Scholar articles	Management Of Bullous Pemphigoid with Diabetes Mellitus Type 2. PS Palsapure, V Balpande, A Pathade, MS Narlawar… - International Journal of Early Childhood Special …, 2022 Related articles

Effect of Different Inlet/Outlet Port Configurations on the Thermal Management of Prismatic Li-Ion Batteries

Gurjeet Singh[1]
Department of Mechanical Engineering,
Yeshwantrao Chavan College of Engineering,
Nagpur 441110, Maharashtra, India
e-mail: gurjeetpunia4@gmail.com

Hongwei Wu
School of Physics, Engineering and Computer
Science,
University of Hertfordshire,
Hatfield AL10 9AB, UK

The performance and life cycle of Li-ion batteries are governed by the maximum temperature and uniformity of temperature distribution in the battery pack, and an efficient thermal management system is highly desired to keep the operating temperature of the battery pack within safe operating limits. Air cooling has received extensive attention in the area of battery thermal management. However, performance intensification of air-cooling modules is essential while keeping the simplicity of design to satisfy the weight and space constraints of electric vehicle (EV) applications. In the current work, efforts have been made to design a simple and generalized air-cooling module for efficient thermal management of Li-ion batteries. The current work explored the effect of two common air flow configurations: side inlet and side outlet (SS) and side inlet and front outlet (SF), with different number of inlet/outlet ports (single inlet and single outlet, single inlet and two outlets, two inlets and single outlet, and two inlets and two outlets) on the thermal and hydraulic performance of Li-ion battery pack. Subsequently, a new design of battery module with an open outlet port is proposed. It is observed that the way fluid leaves the cooling module significantly influences the flow and temperature distribution uniformity of the battery pack. Significant improvement in the fluid flow distribution and lower temperature fluctuation are maintained by the SF designs as compared to the SS designs. Among all SS designs, only SS-Ib at $V_{in} \geq 5.6\,m/s$ and SS-IV at $V_{in} \geq 4.8\,m/s$ are found suitable for the thermal management of Li-ion battery pack, whereas all SF designs maintained desired T_{max} and ΔT_{max} conditions at $V_{in} \geq 4.8\,m/s$. Furthermore, the new design (SF-V) with an open outlet results in the reduction of T_{max} by $7\,°C$ and ΔT_{max} by 64.5% as compared to base design (SS-Ia) at the same pressure drop penalty.
[DOI: 10.1115/1.4055340]

Keywords: electric vehicles, lithium-ion battery, heat generation, flow nonuniformity, temperature fluctuation, air-cooling

1 Introduction

Environmental degradation by the rapid surge in the global carbon emissions over the past century has become a threat to the sustainable development all over the world. Utilization of natural energy resources, primarily fossil fuels (e.g., oil, gas, and coal), is the main contributor in the emission of greenhouse gases (GHGs), which are responsible for global warming. Although the Paris Climate Conference led to a new climate legal agreement for all countries to curb the global warming at $1.5–2\,°C$ [1], detrimental consequences of climate change cannot be avoided. Therefore, fulfilling current energy requirements in a sustainable manner is an ongoing challenge. It is observed that the worldwide consumption of oil is increased by 1.9×10^6 barrels per day and 66% of which is consumed alone by the transport sector [2]. The research area in the development and utilization of green energy and clean vehicles has received pre-eminent attention to curb the emissions of green house gases (GHGs) and avoid energy crisis. Clean vehicles, including pure electric vehicles (EVs), hybrid electric vehicles, plug-in hybrid electric vehicles, and fuel cell electric vehicles, compared to conventional internal combustion vehicles, are effective to reduce GHSs and pollutants emission [3–7]. It is estimated that using renewable electric power resources and EVs could reduce the GHS emissions up to 40% [8].

Furthermore, with the rising interest and focus on the EVs, it is expected that 30% of the new cars will be electrified by 2030 [9].

Battery module acts as a source of energy for the clean vehicles, and in this regard, lithium-ion (Li-ion) based batteries are proven to be more advantageous as compared to lead acid batteries due to their high energy density, low self-discharge rate, good stability, and high voltage. However, due to the electrochemical reaction inside the battery cell, the generated heat would affect the temperature distribution in the battery cells. The permissible temperature range during the discharging operation of Li-ion battery is $-20\,°C$ to $60\,°C$, whereas for the optimal performance, temperature range of $20–40\,°C$ must be maintained [10]. Furthermore, maintaining uniformity of temperature distribution among different cells is another important aspect, and high temperature difference among different battery cells may lead to different state of charge. Consequently, it results in electrical imbalance and performance degradation of the battery module. A maximum temperature difference lower than $5\,°C$ has to be maintained for the efficient performance of the battery pack.

Various thermal management techniques, such as air-cooling [10], liquid cooling [11–16], heat pipes [17–20], and phase change materials (PCMs) [21–25], have been studied in the last decade to dissipate the heat generation from Li-ion battery packs. It is found that the liquid cooling techniques are very effective to restrict the maximum temperature rise (T_{max}) and temperature difference among battery cells (ΔT_{max}) in the desirable range. However, it increases the complexity, weight, and cost of the cooling system. Furthermore, the liquid cooling using water is associated with the risk of short-circuits, and the use of hydrocarbons, such as silicon

---

[1]Corresponding author.

oil, is associated with high pressure drop. Use of PCMs has also received significant attention due to its simple design. Nevertheless, their capacity of dissipating heat is limited and is only applicable for low discharge rates [26]. Thermal management of Li-ion batteries using air-cooling has been widely explored due to their simple construction, light weight, less pumping power requirement, less price, and easy maintenance. In addition, space constraints in some applications, such as two wheelers, restrict the deployment of liquid cooling or PCM based cooling modules. Therefore, in such applications, air-cooling modules are expected to maintain the desired thermal–hydrodynamic environment. As a result, a lot of attention has been focused on the air-cooling modules over the last decade for its application in the cooling of Li-ion battery packs.

Mahamud and Park [27] numerically studied the cooling of cylindrical Li-ion cells using reciprocating air flow technique. It was noticed that for the reciprocating air flow arrangement the T_{max} and ΔT_{max} are reduced by 4 °C and 1.5 °C, respectively, as compared to the case of unidirectional air flow. They attributed it to the redistribution of heat and interruption of the boundary layers due to the periodic reciprocating flow. Na et al. [28] studied the two air flow arrangements: unidirectional air flow and reverse layered air flow, to cool the Li-ion battery cells of cylindrical shape. They observed that reversed flow arrangement could help to reduce the T_{max} and ΔT_{max} by 0.6 °C and 1.1 °C, respectively. Shahid and Agelin-Chaab [29] used a passive approach of secondary inlet plenum to achieve temperature uniformity in the 32 cylindrical cells of Li-ion battery pack. It was observed that the T_{max} and ΔT_{max} can be improved by 9% and 39%, respectively, for the best case as compared to the base case due to the enhanced mixing and turbulence in the air flow by addition of secondary plenum. Jiaqiang et al. [30] compared the thermal performance of Li-ion battery module with natural and forced air convection with different air inlet/outlet flow location strategies and addition of baffles. They noticed better temperature distribution and lower T_{max} for air inlet and outlet location on different sides as compared to the inlet and outlet location on the same wall. Fan et al. [10] studied three different configurations (aligned, staggered, and cross) of 32 high energy density cylindrical Li-ion battery cells. It was observed that the aligned configuration provided best cooling, whereas the staggered and cross configuration offered worse thermal performance and high pressure drop penalty. Wang et al. [31] studied the cooling performance of air-cooling system for large-scale Li-ion battery with 30 cylindrical 18,650 type cells. The battery is charged at 1 C rate and discharge at three variable rates of 1 C, 1.5 C, and 2 C. Two configurations of outlet ports are considered as case 1 (opening at top perpendicular to the inlet port) and case 2 (opening on opposite side of the inlet port). It was stated that temperature difference was lower for case 1 as compared to case 2. The cooling efficiency was found to be 73% and 62.3% for case 1 and case 2, respectively.

Fan et al. [32] simulated eight prismatic cells of Li-ion battery module in vertical orientation with equal spacing using air as a cooling media. They studied the effect of gap spacing between the cells and flowrate on the temperature distribution in the battery module. It was observed that the maximum rise in cell temperature reduced for lower gap and higher flowrate. Xie et al. [33] studied the effect of inlet plenum angle, outlet plenum angle, and gap size between the batteries on the thermal performance of an air-cooled system for cylindrical Li-ion batteries. It was found that the best thermal performance was obtained for 2.5 deg angles for both inlet and outlet plenums, and equal width of channels. The T_{max} and ΔT_{max} were found to be reduced by 12.8% and 29.7%, respectively, with the optimized method. Hong et al. [34] carried out 2D numerical simulations to study the forced air-cooling of Li-ion battery cells of rectangular shape. The T_{max} and ΔT_{max} are found to be beyond the safe working operation of the Li-ion battery. They explored different positions of the secondary vents near the outlet and found that the location of secondary vent strongly influences the temperature distribution of the battery module. Reduction in the T_{max} by 5 °C and ΔT_{max} by 60% was

observed for the best modified design as compared to the conventional design. Chen et al. [35] optimized the battery cell spacing to achieve homogenization in air flow distribution. Flow resistance network model [36] was used to calculate the air flow in the cooling channels, and flow distribution among channels could be improved by adding a modification factor so that the flow area of channels can be increased/decreased based on the existing low/high flowrate. It was noticed that for the best optimized design, T_{max} could be reduced by 4 °C, while temperature difference could reduce by 69% as compared to the conventional design. Furthermore, Chen et al. [37] studied the cooling performance of battery air-cooling module by optimizing the plenum angles and width of inlet and outlet port for U-type flow configuration. It was observed that the thermal performance of the battery cooling system could be significantly improved for the optimized width of inlet and outlet ports, whereas the plenum angles might not contribute to any performance improvement. Temperature difference and power consumption were reduced by 70% and 32%, respectively, for the best optimized design. Li et al. [38] carried out a combined experimental and numerical observation to study the cooling potential of air on copper mesh coupled double silica cooling plate for pouch Li-ion batteries. The effect of silica cooling plate thickness (0.5–2.5 mm), single/double silica cooling plates, air velocity, air inlet position, and number of cooling fans have been investigated. It was noticed that the T_{max} and ΔT_{max} decreased with the increase of the thickness of silica cooling plate, air inlet velocity, and number of fans. They recommended 1.5 mm as the optimum thickness for the silica cooling plate. The fan's position could offer better heat transfer when place at the front side as compared to the side position. Wang et al. [39] experimentally explored the effect of reciprocating air flow on the laminated Li-ion battery. To keep the ΔT_{max} below permissible limit of 5 °C, an aperiodic reciprocating air flow control strategy was designed which reversed the air flow as the temperature difference approached to 4.9 °C. Furthermore, enhancement in thermal performance could be achieved by increasing the air flowrate and with the usage of thinner air flow passage. Liu and Zhang [40] proposed a J-type flow configuration for the air-cooled thermal management of the Li-ion battery. The proposed configuration was made flexible by providing two ports at the outlet. The flow through both the outlets was controlled by two control valves. It was observed that J-type could result in significant improvement of the temperature uniformity. Furthermore, a surrogate-based optimization was performed to improve the performance of U, Z, and J-type configuration, and it was noticed that for the optimal case, the temperature rise could reduce by 35.3%, 46.6%, and 31.18%, respectively, for three designs. Effect of battery pack shape on temperature distribution inside the battery was studied by Kang et al. [41]. Two shapes of battery packs: square and rectangular, are obtained by different arrangement of cylindrical Li-ion battery cells for the combined numerical and experimental analysis. It was observed that the inner temperature distribution at the center and side could be different for both the packing. High temperature rise was noticed for the square battery pack at the center as compared to the rectangular pack. Zhang et al. [42] studied the effect of provided flow restrictors (spoilers) in the inlet manifold of Li-ion battery packs with eight prismatic cells. It was noticed that for the best number (five spoilers) and position of spoilers (fourth to eighth distributor section) the T_{max} and ΔT_{max} could be reduced by 1.86 °C and 2.77 °C, respectively, as compared to the base case (no spoilers). Furthermore, improvement in the thermal performance was also achieved by optimizing the height of spoilers and size of manifolds. Ma et al. [43] numerically studied the effect of installing silica cooling plates between the prismatic Li-ion battery cells and tampering of inlet manifold on the performance air-cooled Li-ion battery pack. It was stated noticed that with addition of silica plates, the T_{max} and ΔT_{max} reduced by 10 °C and 2.5 °C, respectively.

Moreover, considering the various advantages of the air-cooling systems over the other cooling modules, it became very

Table 1 Properties of Li-ion battery and air

Property	Battery	Air
Specific heat (J/kg/K)	900	1005
Thermal conductivity (W/m/k) (W/m/K)	240	0.0267
Density (kg/m³)	2700	1.165
Dynamic viscousity (Pa·s)	—	1.86×10^{-5}

critical to design an efficient air-cooling module so that the desired thermal characteristics of the Li-ion battery modules can be maintained. It was noticed that previous researchers have studied the effect of air flow direction, outlet vents, silica cooling plates, and flow configurations on the thermal performance of Li-ion battery packs. The comparative summary of various studies on the air-cooling battery packs with cylindrical and prismatic/pouch cells is provided in Table S1 available in the Supplemental Materials on the ASME Digital Collection. It was noticed that the methods of alternation in the air flow direction resulted in a complex design of cooling module due to the requirement of additional sensors and secondary blowers, whereas the method of installing silica cooling plates was expected to increase the overall weight and power consumption of the cooling pack. It was also observed that the desired conditions of $T_{\max}$ and $\Delta T_{\max}$ for the optimum thermal performance of Li-ion battery pack are only maintained in the studies of Hong et al. [34] and Liu and Zhang [40]. However, the applicability of both proposed methods is limited to their specific manifold designs (side inlet and side outlet) only. Moreover, in the current work, efforts have been made to design a simple and generalized air-cooling module for efficient thermal management of Li-ion batteries. The current work aims to

investigate the effect of two common air flow configurations: side inlet and side outlet (SS) and side inlet and front outlet (SF), with different number of inlet/outlet ports for the thermal management of Li-ion battery pack. Subsequently, a new design of battery pack with best thermal–hydrodynamic performance is proposed. Finally, the thermal performance of all the designs (suitable for maintaining the desired $T_{\max}$ and $\Delta T_{\max}$ conditions) is compared at same pressure drop penalty.

2 Geometric Description

In the current work, a Li-ion battery module consisting of 12 prismatic cells is considered. The dimensions of battery cells are: $L_{cell} = 151$ mm, $W_{cell} = 16$ mm, and $H_{cell} = 65$ mm. The properties of the battery and air are given in Table 1 [34]. In the current study, the effect of variable thermophysical properties is also investigated and provided in Supplementary Material S2 available in the Supplemental Materials on the ASME Digital Collection, and it is found that considering the constant thermophysical properties of air are sufficient to predict the thermal and hydrodynamic performance of the battery cooling modules. A 3D model of the battery pack for the base design is shown in Fig. 1. Air enters in the battery module from the lower end and leaves from the top end, as shown in Fig. 1. The distance between battery cells and distance of cells from the wall of battery case is kept as 3 mm. Other dimensions of the inlet and outlet manifolds are also given in Fig. 1. In the present study, two different categories of inlet and outlet flow arrangements: (1) SS and (2) SF designs are studied, as illustrated in Fig. 2. Furthermore, each category is divided based on the number of inlet and outlet ports. These cases can also be divided into single inlet and single outlet (SS-Ia, SS-Ib, and SF-I), single inlet and two outlets (SS-II and SF-II), two inlets
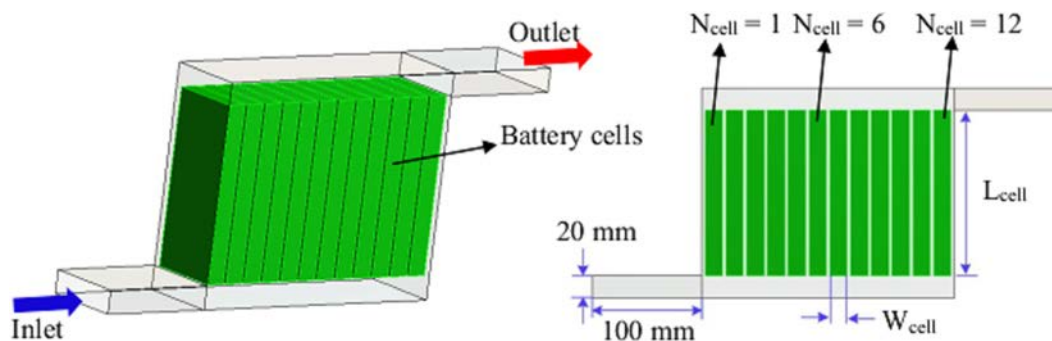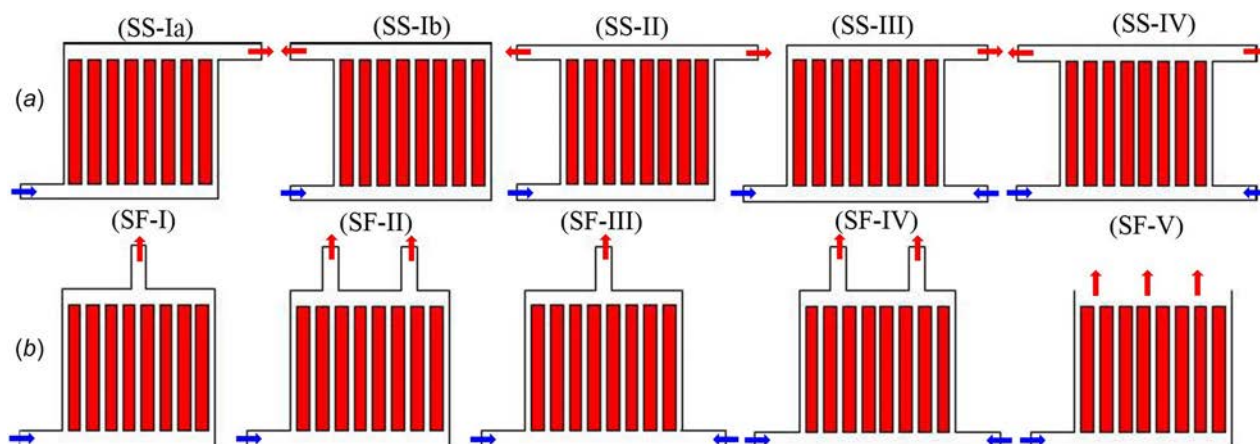

Fig. 1 Schematic 3D view of Li-ion battery pack for SS-I flow configuration

Fig. 2 Schematic of different inlet and out flow configurations: (a) side inlet and side outlet and (b) side inlet and front outlet designs

Table 2   Air inlet parameters

V_{in} (m/s)	Flow rate (m^3/s)	Re$_{in}$
2.4	0.007	4598
3.2	0.009	6131
4	0.011	7664
4.8	0.013	9196
5.6	0.016	10,729

and single outlet (SS-III and SF-III), and two inlets and two outlets (SS-IV and SF-IV).

For the different SS cases (Fig. 2(*a*)), designs SS-Ia and SS-IIb are considered to investigate the effect of the location of outlet port on the opposite and same walls, respectively, and in design SS-II, the effect of outlet port location is eliminated by providing two ports. In designs SS-III and SS-IV, the effect of addition of two inlet ports with respect to the combination of single outlet and two outlet ports is studied, respectively. In the SF designs, similar effect of adding two outlet ports for single inlet and two inlet ports is studied in the SF-II and SF-IV designs, respectively, and in designs SF-I and SF-III, effect of providing single and two inlet ports, respectively, is investigated for single outlet case. Furthermore, a new design (SF-V) is proposed in which effect of outlet port is removed by providing an open front outlet.

3 Numerical Modeling

3.1 Governing Equations. Heat transfer and fluid flow characteristics in the current numerical model are captured by solving generalized mass, momentum, and energy conservation equations. The following assumptions have been made for the simplification of the mathematical modeling:

(i) The effects of body and surface tension forces are neglected.
(ii) Effect of radiation and natural convection heat transfer is neglected.
(iii) Air is assumed to be continuum and incompressible.
(iv) Flow is assumed to be turbulent based on the value of Re.

The air flow is assumed to be in turbulent flow regime based on the Re values as given in Table 2, and k–ε model is used for the solution of the governing equations. k–ε is selected due to its good accuracy, convergence, and low memory requirements. Similar numerical modeling is also adopted by Refs. [34] and [35]. Following are the governing equations for the steady air flow with above mentioned assumptions.

3.1.1 Fluid Section

Mass conservation equation

$$\frac{\partial u_i}{\partial x_i} = 0 \tag{1}$$

Momentum conservation equations

$$\rho u_j \frac{\partial u_i}{\partial x_j} = -\frac{\partial P}{\partial x_i} + \frac{\partial}{\partial x_j}\left[(\mu + \mu_t)\frac{\partial u_i}{\partial x_i}\right] \tag{2}$$

$$\rho u_j \frac{\partial k}{\partial x_j} = \frac{\partial}{\partial x_j}\left[\left(\mu + \frac{\mu_t}{\sigma_k}\right)\frac{\partial k}{\partial x_j}\right] + \frac{\mu_t}{2}\left[\frac{\partial u_i}{\partial x_j} + \frac{\partial u_j}{\partial x_i}\right]^2 - \rho\epsilon \tag{3}$$

$$\rho u_j \frac{\partial \epsilon}{\partial x_j} = \frac{\partial}{\partial x_j}\left[\left(\mu + \frac{\mu_t}{\sigma_\epsilon}\right)\frac{\partial \epsilon}{\partial x_j}\right] + c_1\frac{\mu_t}{2}\left[\frac{\partial u_i}{\partial x_j} + \frac{\partial u_j}{\partial x_i}\right]^2 \frac{\epsilon}{k} - c_2\rho\frac{\epsilon^2}{k} \tag{4}$$

Energy conservation equation

$$\rho c_p u_j \frac{\partial T}{\partial x_j} = \frac{\partial}{\partial x_j}\left[\left(\lambda + \frac{\mu_t}{\sigma_T}\right)\frac{\partial T}{\partial x_j}\right] \tag{5}$$

where P, μ, λ, and c_p are Reynolds-averaged pressure, dynamic viscosity component, thermal conductivity, and specific heat, respectively. u_i and u_j denote Reynolds-averaged velocity components. Turbulent dynamic viscosity component (μ_t) is calculated by the following equation:

$$\mu_t = \rho C_\mu \frac{k^2}{\epsilon} \tag{6}$$

where $C_\mu = 0.09$.

The turbulent kinetic energy and dissipation rate of the turbulent kinetic energy are defined by k and $\in$, respectively. The typical values of the parameters C_1, C_2, σ_k, $\sigma_\in$, and σ_T are shown below

$$C_1 = 1.44, \quad C_2 = 1.92, \quad \sigma_k = 1.0, \quad \sigma_\in = 1.3, \quad \sigma_T = 0.85$$

3.1.2 Solid Section. Energy conservation equation

$$\frac{\partial}{\partial x_j}\left[\lambda_s \frac{\partial T_s}{\partial x_j}\right] + \phi_g = 0 \tag{7}$$

where subscript s denotes solid section and ϕ_g represents heat generation rate.

3.2 Boundary Conditions. Constant air velocity and temperature are assumed at the inlet of the cooling module. Different air velocities are used in the current work, as given in Table 2. The air inlet temperature is kept fixed at 300 K. All the outer walls are assumed to be adiabatic. The interface of battery surface and fluid sections is coupled, and heat generated in the battery cells are carried away by the forced air flow from the battery–fluid interface. No slip boundary condition is assumed at the interface. At the outlet of the cooling module, atmospheric pressure boundary condition is assigned. Heat generation (ϕ_g) inside the battery cells is assumed at constant rate of 41,408 W/m^3 [34].

3.3 Solution Procedure. All governing equations are solved by adopted the given boundary conditions by using ANSYS FLUENT 16.0. All the partial differential equations are discretized by using a finite volume method. Second order upwind scheme is used for the discretization of the momentum and energy equations. Pressure values are obtained by adopting standard discretization scheme. Pressure–velocity coupling is obtained by using the semi-implicit method for pressure linked equations algorithm. Convergence criteria is considered as 10^{-6} for the residuals of mass, momentum, and energy equations.

3.4 Grid Independence Analysis and Model Validation. Prior to the numerical simulations, a grid independence study has been carried to make the numerical model independent of grid size. In the current study, a 2D numerical model is used for the numerical simulation based on the observation of Hong et al. [34]. Hong et al. [34] compared the numerical results for the 3D and 2D numerical models with similar dimension of battery pack, and it is observed that 2D model is sufficient for the accurate estimation of fluid flow and heat transfer characteristics. In the current work, five different grid schemes have been studied, and the results of maximum temperature and overall pressure drop are given in Table 3. Nonuniform hexahedral grid elements are generated using ICEM with smallest grid element dimension as 0.1 mm near the walls. It is noticed that for grid elements of 26×10^5 and

Table 3 Grid independence test

No. of grid elements	T_{max} (°C)	AD (T_{max}) (%)	ΔP (Pa)	AD (ΔP) (%)
4.0×10^5	44.56	—	35.23	—
8.0×10^5	44.92	0.81	34.48	2.14
14×10^5	44.71	0.46	33.24	3.59
20×10^5	44.14	1.27	32.50	2.24
26×10^5	43.87	0.62	32.23	0.84
32×10^5	43.57	0.68	32.28	0.16
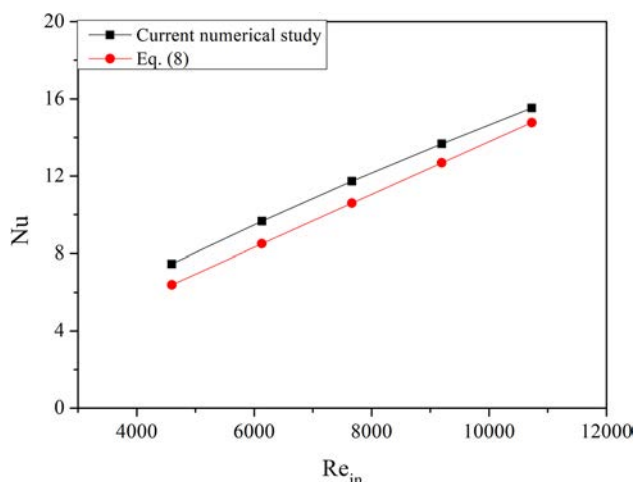
Fig. 3 Comparison of Nu for current numerical study and correlation of Nacke et al. [44]

32×10^5, absolute deviation (AD) between overall pressure drop and maximum temperature is less than 1%. Therefore, 26×10^5 grid elements are selected to save the computational time.

Validation of current numerical model is also carried out by comparing the results of Nu with the correlation of Nacke et al. [44] for the SS-Ia design. Results of Nu from current numerical study and Eq. (8) are compared in Fig. 3. Mean absolute deviation of 10.6% is noticed in calculation of Nu with respect to Eq. (8), which proves the accuracy of current numerical results

$$Nu = \left[\frac{RePr}{L/D_h}\right]^{1/3} \left(\frac{\mu_a}{\mu_{a,s}}\right)^{0.14} \tag{8}$$

4 Results and Discussion

In the current design, air enters from the common inlet port and then distributes across all channels around the battery cells and leaves through the outlet port. To measure the unevenness of air flow distribution in the battery pack, a velocity nonuniformity factor (α) is calculated as given by Eq. (9). Similar method is also used by Refs. [45] and [46] to estimate the flow maldistribution factor among the parallel channels

$$\alpha = \frac{V_{max} - V_{min}}{V_{avg}} \times 10 \tag{9}$$

where V_{max}, V_{min}, and V_{avg} represent the maximum, minimum, and average velocity of air in the channels

$$V_{avg} = \frac{\sum_{ch=1}^{ch=13} V_{ch}}{13} \tag{10}$$

To design a cooling system for the Li-ion battery pack, two prerequisite conditions are set based on the magnitude of maximum

temperature (T_{max}) and maximum temperature fluctuation ($\Delta T_{max} = T_{max} - T_{min}$) as given below:

First condition: $T_{max} \leq 40\,°C$
Second condition: $\Delta T_{max} \leq 5\,°C$

Therefore, a design which satisfies both the conditions is considered as suitable for the thermal management of Li-ion battery pack.

4.1 Air Flow Distribution

4.1.1 Comparison of Fluid Flow Distribution for SS Designs. Figures 4(a) and 4(b) compare the air velocity distribution in different channels and velocity nonuniformity factor, respectively, for different SS designs. Air velocity is calculated at the mid-length of the battery module in all channels. It is noticed that the air velocity is not uniform in all channels for the base design (SS-Ia). The velocity of air directly signifies the air flow distribution around the battery cells. It can be noticed from Fig. 4(a) that the air flowrate is lowest in the first channel (nearest to the inlet port), and it increases gradually as moving toward the right-side wall, and the flowrate is highest in the 13th channel (nearest to the outlet port). The velocity nonuniformity factor (α) is 67% for the SS-Ia design as shown in Fig. 4(b). The effect of nonuniform velocity distribution is also noticed on the temperature distribution of the battery cells, and it is found that T_{max} is 43.9 °C and ΔT_{max} is 8.1 °C for the battery pack. Thus, none of the conditions is satisfied for base design to obtain the optimum performance of the Li-ion battery pack.

In the present work, efforts have been made to limit temperature rise and fluctuation by following a very simplistic approach of changing the location of inlet and outlet ports. In the SS-Ia design, the flowrate is higher for the channels near the outlet port, whereas lower flowrate is noticed for the channels nearer to the inlet port. Therefore, to mitigate this anomaly of flow nonuniformity, both inlet and outlet ports are kept on the same side for the SS-Ib design. Similar approach is also adopted by Ref. 31. It is noticed that for the SS-Ib design, α is reduced by 56.6% as compared to the base case (SS-Ia). The location of inlet and outlet ports on the same side helped to increase the mass flow of air in the channels closer to the inlet port by restricting the flow across the far end channels. A minor rise of 1.8% in the pressure drop penalty is also observed (Table 4), which is insignificant as compared to the achieved uniformity in the flow distribution. Furthermore, the SS-II design is selected in such a manner that outlet ports are provided on both sides to remove the effect of outlet port location, while the location of inlet port is kept unchanged. It is noticed that α is reduced by 24.8% for the S-II design as compared to the design SS-Ia. Thus, the S-II design is not as advantageous as observed for the SS-Ib case. In the SS-Ib case, the flow through the far end channels is restricted due to the increased resistance to the fluid flow in the outlet manifold, whereas in the SS-II design, the flow from the far end channels can easily exit through the nearer outlet port (outlet port on right-side wall). Thus, no significant improvement in the flow distribution pattern is observed, and flow distribution of the SS-Ia and S-II designs are almost similar. However, a large reduction of 36.9% in the pressure drop penalty is observed for the SS-II design (Table 4), which highlights its potential to maintain better flow distribution characteristics at low pressure drop as compared to the SS-Ia design.

Contrary to the SS-II design, in the design SS-III, the effect of adding an additional inlet port is investigated, while position of the outlet port is kept same as that of SS-Ia design. It is found that similar to the SS-II case, the SS-III design also leads to the reduction of ~25% in the α. The flow distribution pattern of the SS-III design is entirely opposite than that of the SS-II design. In the SS-II design, the lower flowrate is observed in the channels near left-side wall while the flowrate is higher in the channels near the right-side wall. It is observed due to the high momentum of air flow toward the right-side wall in the inlet manifold for the S-II
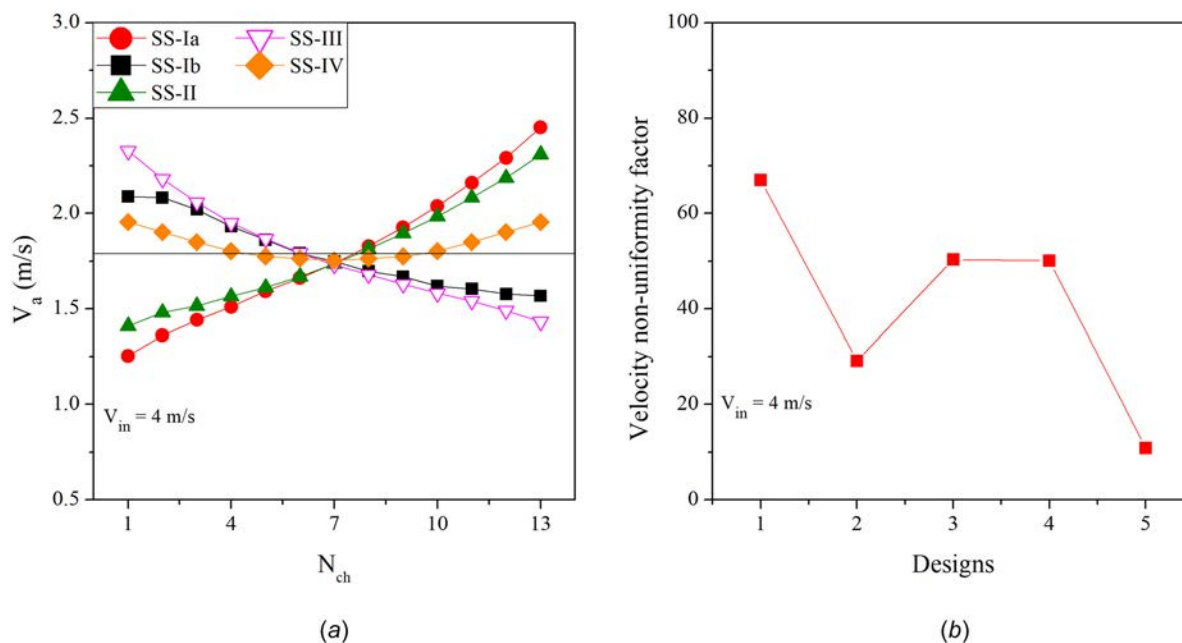
Fig. 4 Comparison of air flow distribution in the different SS designs: (a) velocity distribution and (b) velocity nonuniformity factor at V_{in} = 4 m/s

Table 4 Pressure drop for SS and SF design at V_{in} = 4 m/s

S. no.	SS design	ΔP (Pa)	SF design	ΔP (Pa)
1	SS-Ia	32.2	SF-I	35.3
2	SS-Ib	32.8	SF-II	22.2
3	SS-II	20.3	SF-III	37.4/inlet
4	SS-III	33.6/inlet	SF-IV	23.7/inlet
5	SS-IV	22.8/inlet	SF-V	19

design. After striking the side wall, the flow enters the neighboring channels, and the position of outlet port on the right-side wall further offers a low resistance path for fluid to exit, whereas for the channels near to the left-side wall, addition of an additional outlet port provides a free exit path and decreases the associated resistance in the outlet manifold. In the SS-III design, a striking effect is noticed in the inlet manifold due to positioning of the inlet ports on the opposite side walls. This impinging effect is expected to normalize the flow distribution in the inlet manifold, and its effect is also noticed on the reduction of α for the SS-III design. However, biased position of the outlet port on the right-side wall leads to nonuniformity in the flow distribution among different channels. Moreover, the biasness associated with location of the outlet port is removed in the SS-IV design by providing outlet port on both sides. It is found that for the SS-IV design, α is reduced by 84% as compared to that of SS-Ia design. Due to the symmetric location of both the inlet and outlet ports, the distribution of flow is also symmetric for the channels near the left and right-side walls. It can be clearly observed from velocity distribution of the SS-IV design that the flow is almost uniform in all channels. Nonetheless, cost and complexity of the cooling system increase for the SS-III and SS-IV designs due to the requirement of an additional inlet port which involves addition of either an additional fan on the second inlet port or dividing the inlet from the first fan into two symmetric pipes. On the other hand, the benefits offered by SS-II design are more alluring due to significant reduction in the pressure drop penalty as compared to the SS-III design.

4.1.2 Comparison of Fluid Flow Distribution for SF Designs. In the SF designs, the location of outlet port(s) is parallel to the length of the channels and location of inlet port is on the side

wall(s), as shown in Fig. 2(*b*). Therefore, to understand the effect of change in the location of outlet port from side outlet to the front outlet, the results of SF-I, SF-II, SF-III, and SF-IV designs are compared with the results of SS-Ia, SS-II, SS-III, and SS-IV designs, respectively. Figures 5(*a*) and 5(*b*) show the velocity distribution in different channels and α, respectively, for different SF designs. It is noticed that just by changing the location of outlet port from side outlet case (SS-Ia) to front outlet (SF-I), α is reduced by 63%. Likewise, the flow distribution uniformity is also significantly higher for other SF designs as compared to the SS designs (Figs. 4 and 5). It is noticed that $\alpha < 25\%$ for all the SF designs as shown in Fig. 5(*b*). It is evaluated that α is reduced by 57.2%, 64%, and 21.3% for SF-II, SF-III, and SF-IV designs as compared to the SS-II, SS-III, and SS-IV designs, respectively. Therefore, for similar number of inlet and outlet ports, it suggested to use front outlet port location as compared to the side outlet port location. However, the pressure drop penalty also increases as the outlet port location is changed to front wall(s) as compared to the outlet port location on the side wall(s) (Table 4). It is noticed due to increase of fluid flow resistance in the outlet manifold. The issue of high pressure drop penalty is eliminated for the newly proposed design with open outlet manifold, and it is noticed that the new design (SF-V) could offer significantly better flow distribution uniformity as compared to SS designs (except SS-IV) at very low pressure drop. The pressure drop and α is reduced by 40.1% and 64.6%, respectively, for the SF-V design as compared to the SS-Ia design which highlights the effectiveness of SF-V design to provide better fluid flow distribution at much lesser pressure drop.

Furthermore, among different SF designs, α is reduced by 12.7%, 27.1%, and 65.2% for SF-II, SF-III, and SF-IV designs, respectively, as compared to the SF-I case. It is found that similar to the SS-IV design (with two inlet and outlet port), the best flow distribution uniformity is maintained for the SF-IV design. Yet the reduction in α is ~65% for the SF-IV design as compared to the SF-I design, whereas for the SS-IV design α is reduced by ~84% as compared to the SS-Ia design. The design with two outlet ports and one inlet port (SF-II) offered only 12.7% improvement in the flow distribution uniformity as compared to the SF-I case, whereas the improvement for the SS-II is ~25% as compared to the SS-Ia. However, reduction in pressure penalty is ~37.1% for both SS-II and SF-II designs as compared to the
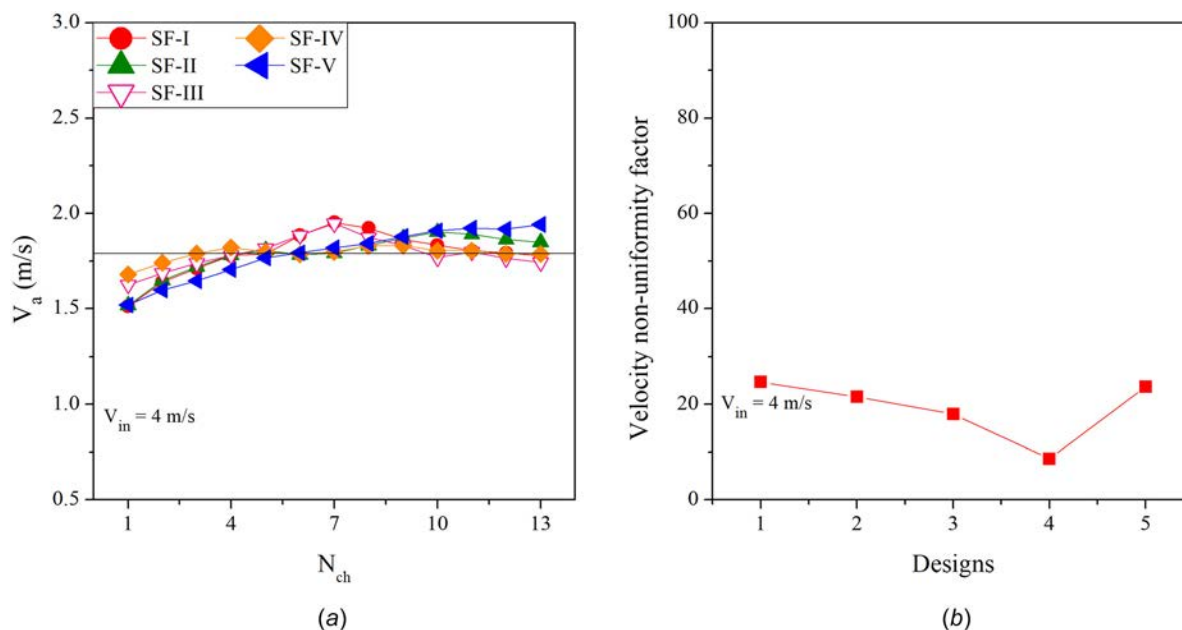
Fig. 5 Comparison of air flow distribution in the different SF designs: (*a*) velocity distribution and (*b*) velocity nonuniformity factor at V_{in} = 4 m/s

corresponding base designs (SS-Ia and SF-I, respectively). On the other hand, for the SF-III design α is reduced by 27.1% similar to the improvement for the SS-III design as compared to the corresponding base designs. Furthermore, for the new design (SF-V), no improvement in flow distribution uniformity is noticed; however, pressure drop penalty is reduced by 46% as compared to the SF-I design. Therefore, it is expected that the usefulness of the proposed new design can be best studied by maintaining same pressure drop for all designs, and it is reported in Sec. 4.4. In Sec. 4.2, temperature distribution for all the designs is compared.

4.2 Temperature Distribution

4.2.1 Comparison of Temperature Distribution for SS Designs. Temperature contours and average cell temperature (T_{avg}) distribution for different designs are compared in Figs. 6 and 7, respectively. Furthermore, in Fig. 8, T_{max} and ΔT_{max} are compared. It is noticed that among the SS designs, magnitude of T_{max} is highest for the SS-Ia design followed by SS-III and SS-II designs, whereas T_{max} is lowest for the SS-IV design followed by SS-Ib design as shown in Fig. 8(*a*). It is observed that due to high α for the SS-Ia design, the nonuniformity of temperature is also highest. As a consequence, formation of hotspot (high temperature zone) is observed for the cells closer to the left-side wall (Figs. 6(*a*) and 7(*a*)). The presence of an additional full channel near to the left-side walls (first channel) facilitates in enhancing the heat dissipation from the first battery cell and limits its temperature rise. Furthermore, the enhanced heat transfer effect due to the additional full channel is also propagated for the second battery cell as its temperature is also lower than that of the third battery cell (Fig. 7(*a*)). Similarly, the enhanced cooling effect is also noticed for the right-side channels, and the resultant lower temperature magnitude leads to lower average temperature of the battery pack. Furthermore, the temperature rise is also higher for the SS-II and SS-III designs (Fig. 8). The T_{max} and ΔT_{max} are reduced by 0.7 °C and 1.2 °C for the SS-II design as compared to the base design (SS-Ia). For the SS-III case, T_{max} and ΔT_{max} are reduced by 0.8 °C and 0.9 °C, respectively, as compared to the SS-Ia design. Moreover, pressure drop is reduced by 36.9% for the SS-II, whereas an additional fan or separate flow distribution network is needed for the SS-III design. Therefore, it can be concluded that apart from its simple and economically viable design, the SS-
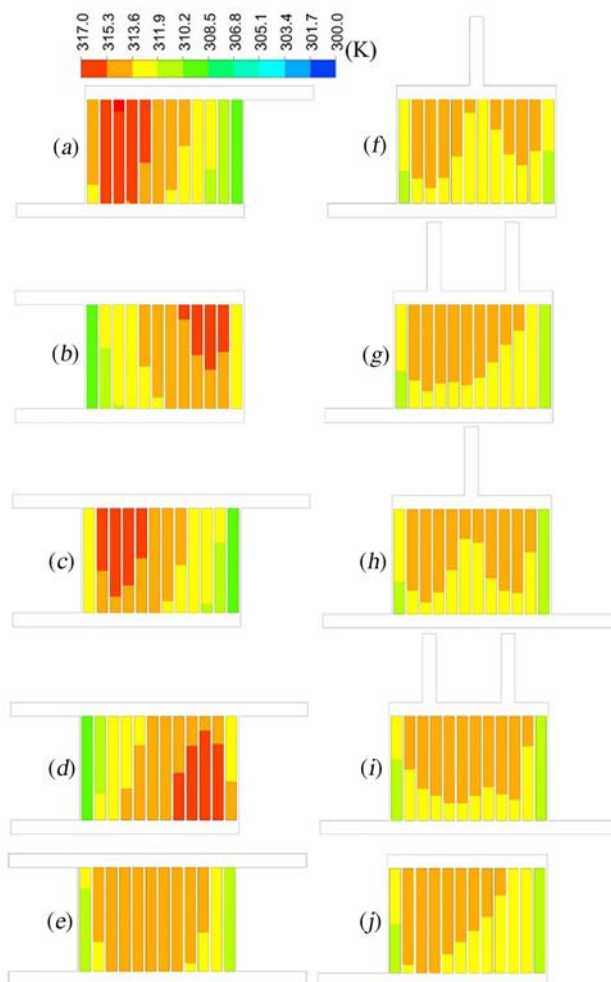
Fig. 6 Comparison of temperature contours for SS designs: (*a*) SS-Ia, (*b*) SS-Ib, (*c*) SS-II, (*d*) SS-III, (*e*) SS-IV and SF designs, (*f*) SF-I, (*g*) SF-II, (*h*) SF-III (*i*) SF-IV, and (*j*) SF-V at V_{in} = 4 m/s
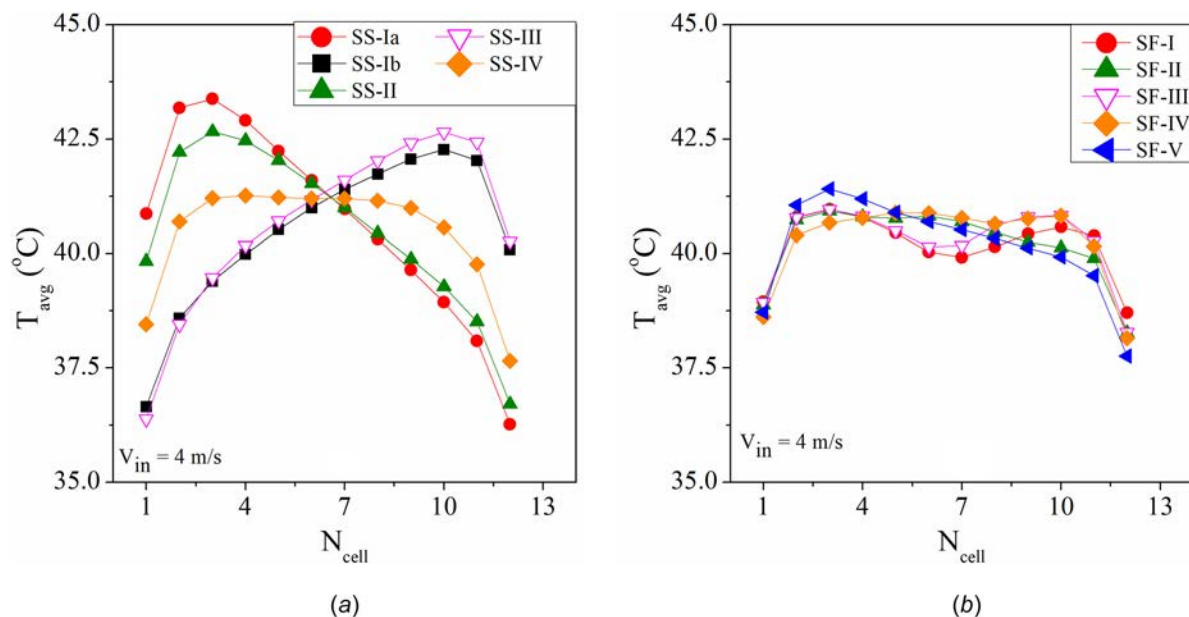
Fig. 7 Comparison of average temperature distribution for: (a) SS and (b) SF designs at V_{in} = 4 m/s
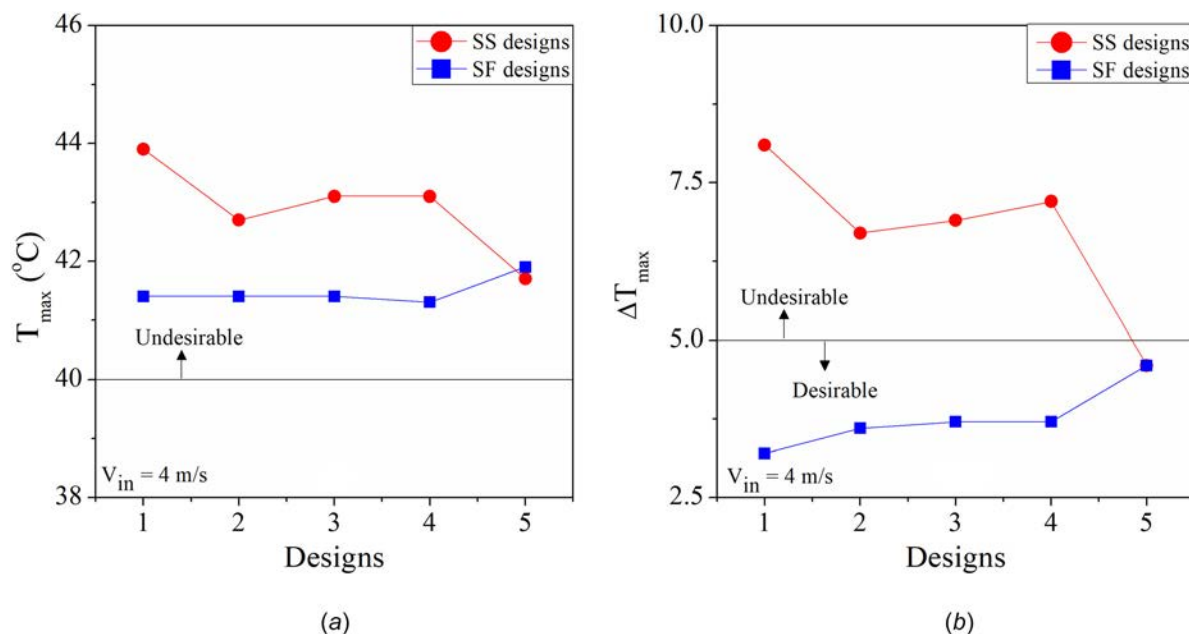
Fig. 8 Comparison of (a) T_{max} and (b) ΔT_{max} for SS and SF designs at V_{in} = 4 m/s

II case also maintained better thermohydraulic performance as compared to the SS-Ia and SS-III designs. Design SS-Ib leads to improvement in the air flow distribution and lowers the T_{max} and ΔT_{max} by 1.2 °C and 1.4 °C, respectively, as compared to the SS-Ia design. Therefore, the improvement in the thermal performance is better than that of SS-II and SS-III designs. Furthermore, for the SS-IV design, the effect of uniform fluid flow distribution can be clearly observed from the temperature contours (Fig. 6(e)), where the hotspots are significantly mitigated. It is found that T_{max} is reduced by 2.2 °C and ΔT_{max} is reduced by 3.5 °C (43% reduction) for the SS-IV design as compared to the SS-Ia design. Nonetheless, none of the SS designs can meet both of the desired conditions for the optimal thermal performance of the Li-ion battery pack (Fig. 8). Although design SS-IV can limit the $\Delta T_{max} < 5$ °C

as shown in Fig. 8(b), value of $T_{max} > 40$ °C makes it unfit under current boundary conditions.

4.2.2 Comparison of Temperature Distribution for SF Designs. The SF designs offer better air flow distribution which also results in better uniformity of temperature distribution (Figs. 6(f)–6(i)). It is noticed that just by changing the location of outlet port(s), ΔT_{max} is reduced by 2.4 °C, 1.8 °C, 1.7 °C, and 0.4 °C for the SF-I, SF-II, SF-III, and SF-IV designs as compared to the SS-Ia, SS-II, SS-III, and SS-IV designs, respectively. Furthermore, ΔT_{max} is reduced by 60%, 46.6%, 49%, and 19% for the SF-I, SF-II, SF-III, and SF-IV designs as compared to the SS-Ia, SS-II, SS-III, and SS-IV designs, respectively. The significantly higher deviation in the magnitude of V_{max} and V_{min} is responsible
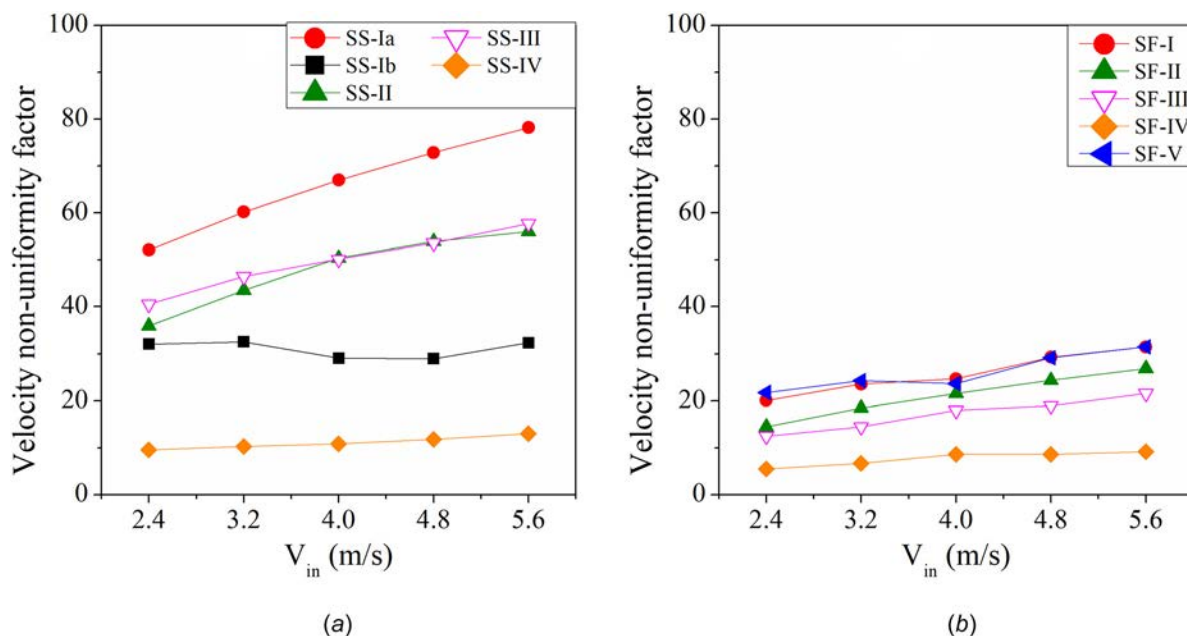
Fig. 9 Comparison of velocity nonuniformity factor for (*a*) SS and (*b*) SF designs at different V_{in}

for high temperature nonuniformity for the SS designs (except SS-IV). The deviation in the velocity distribution is considerably lower for the SF designs which lead to the reduction in the T_{max} and ΔT_{max}. Furthermore, it is noticed that $\Delta T_{max} < 5\,^{\circ}$C for all the SF designs which can be accredited to the better fluid flow distribution. Therefore, it can be concluded that the SF designs not only provide better fluid flow distribution for the battery pack but also maintain desired temperature difference among different battery cells. However, $T_{max} > 40\,^{\circ}$C for SF designs therefore, under current boundary conditions the SF designs are also not recommended for the thermal management of Li-ion battery pack. Furthermore, it is noticed that the presence of full first channel is advantageous in lowering the maximum temperature rise of the SS-Ia and SS-II designs, as shown in Fig. 7(*a*). Likewise, the 13th channel is responsible for lowering temperature rise of the SS-Ib and SS-III designs. However, the presence of full channels near the side walls (first and 13th channels) aggravates the issue of temperature nonuniformity for designs with uniform fluid flow distribution (SS-IV, SF-I, SF-II, SF-III, and SF-IV designs). Therefore, the temperature nonuniformity of these designs (SS-IV, SF-I, SF-II, SF-III, and SF-IV designs) can be further curtailed by proving only a half channel near the side walls. In Sec. 4.3, the effect of change in flow rate is studied on the thermal performance of the battery pack for different flow configurations.

4.3 Effect of Inlet Velocity. One of the simplest ways to control the temperature rise is increasing the inlet flowrate. However, due to the absence of any disturbance in the flow direction, its influence on the heat transfer enhancement is limited. Furthermore, increase in flowrate also comprises an additional pressure drop penalty and perhaps requires a special fan in certain cases. The change in flowrate also influences the flow distribution among different parallel channels; consequently, it alters the temperature distribution in the battery pack. In this section, the effect of change in air flowrate is studied on the velocity and temperature distribution for different designs.

Figure 9 compares velocity nonuniformity factor for all designs at different inlet air flow rates. In general, it is found that the α increases with the increase of V_{in}, whereas temperature nonuniformity decreases with the increase of V_{in}. It is also noticed that α increases from 52% to 78% for the SS-Ia design as V_{in} is increased from 2.4 m/s to 5.6 m/s. The increase in α is due to more momentum transfer toward the channels near to the right-side wall, and

the channels closer to the left-side wall received comparatively lesser flow which amplifies the velocity distribution nonuniformity. Surprisingly, better velocity distribution uniformity is maintained by the SS-Ib design for all flow rates, and α is maintained at 30 ± 2% for different flow rates which indicates the independency of velocity distribution on the magnitude of V_{in} for the SS-Ib. On the other hand, for the designs SS-II and SS-III, analogous to the SS-Ia design, the nonuniformity in velocity distribution rises significantly with the increase of flowrate. The velocity nonuniformity factor increases from 35.9% to 56% for SS-II and 40.5% to 57.7% for SS-III as the inlet velocity is increased from 2.4 m/s to 5.6 m/s. Although α increases from 9.6% to 13% as the inlet velocity is increased from 2.4 m/s to 5.6 m/s for the SS-IV design also, the uniformity in the velocity distribution is best at all inlet velocities among all SS designs. Moreover, uniformity in the air flow distribution is significantly higher for all SF designs as compared to the SS designs. Best flow distribution characteristics are noticed for SF-IV design, where α varies in the range of 5.5–9.2% as V_{in} is increased from 2.4 m/s to 5.6 m/s. Better flow distribution is maintained by SF-III ($\alpha = 12.5\%–21.6\%$) as compared to the SF-II ($\alpha = 14.5\%–26.9\%$) at different flow rates also. Among different SF designs, worst flow distribution results are noticed for the SF-I and SF-V designs.

Comparison of T_{max} and ΔT_{max} for different SS designs is shown in Fig. 10. It is noticed that for the SS-Ia design, $T_{max} < 40\,^{\circ}$C at highest studied flowrate (V_{in} 5.6 m/s); however, $\Delta T_{max} > 5\,^{\circ}$C for the entire studied flowrate range. Therefore, SS-Ia design is unable to provide the desired temperature uniformity for the cooling of Li-ion battery at the studied range of flowrate. Although shoot up of T_{max} is restricted with increase of flowrate, uniformity in the temperature distribution could not be maintained due to rise of α with increase of flowrate. Similar issue is also noticed for the SS-II and SS-III designs where desired temperature uniformity is not obtained due to significant rise of α with increase of flowrate. For the SS-Ib design, $\Delta T_{max} < 40\,^{\circ}$C for $V_{in} \geq 4.8$ m/s and ΔT_{max} is <5 $^{\circ}$C for $V_{in} = 5.6$ m/s; thus, SS-Ib design can be considered for EV cooling at $V_{in} \geq 5.6$ m/s. The independency of α from the V_{in} also makes SS-Ib design more suitable to be installed at higher flow rates for the effectual cooling of Li-ion battery pack. Furthermore, it is noticed that the desired T_{max} and ΔT_{max} are maintained by SS-IV at $V_{in} \geq 4.8$ m/s; therefore, $V_{in} \geq 4.8$ m/s is found to be the preferred V_{in} range to maintain optimum operating conditions for the Li-ion battery.
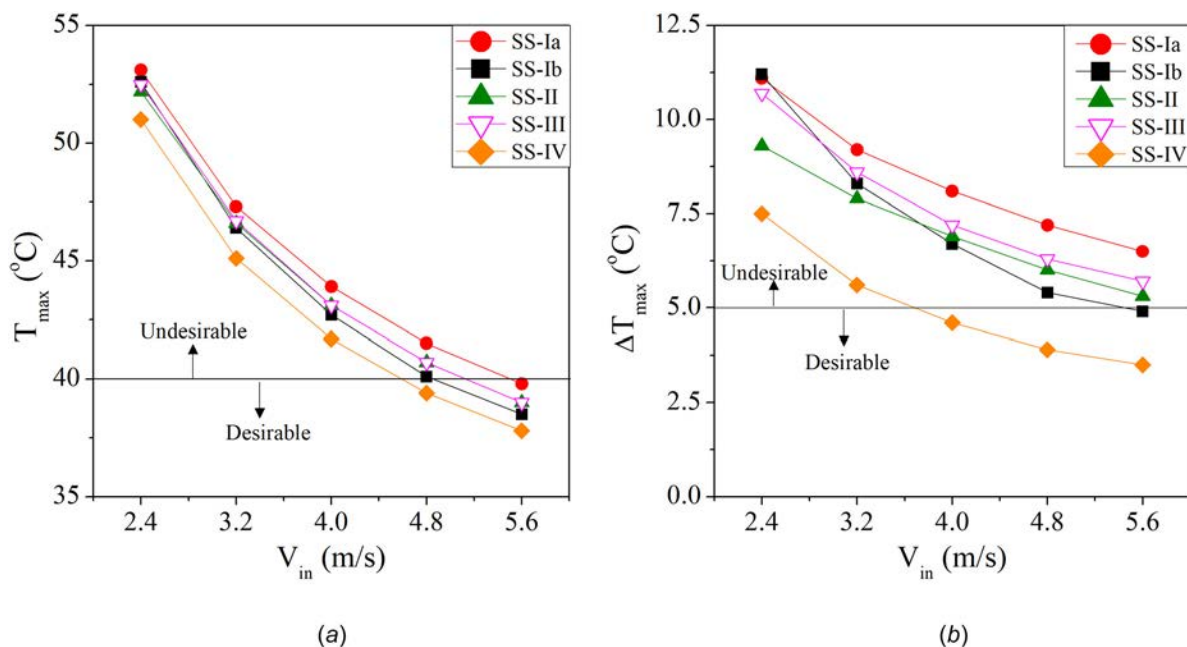
Fig. 10 Comparison of (*a*) T_{max} and (*b*) ΔT_{max} for SS designs at different V_{in}
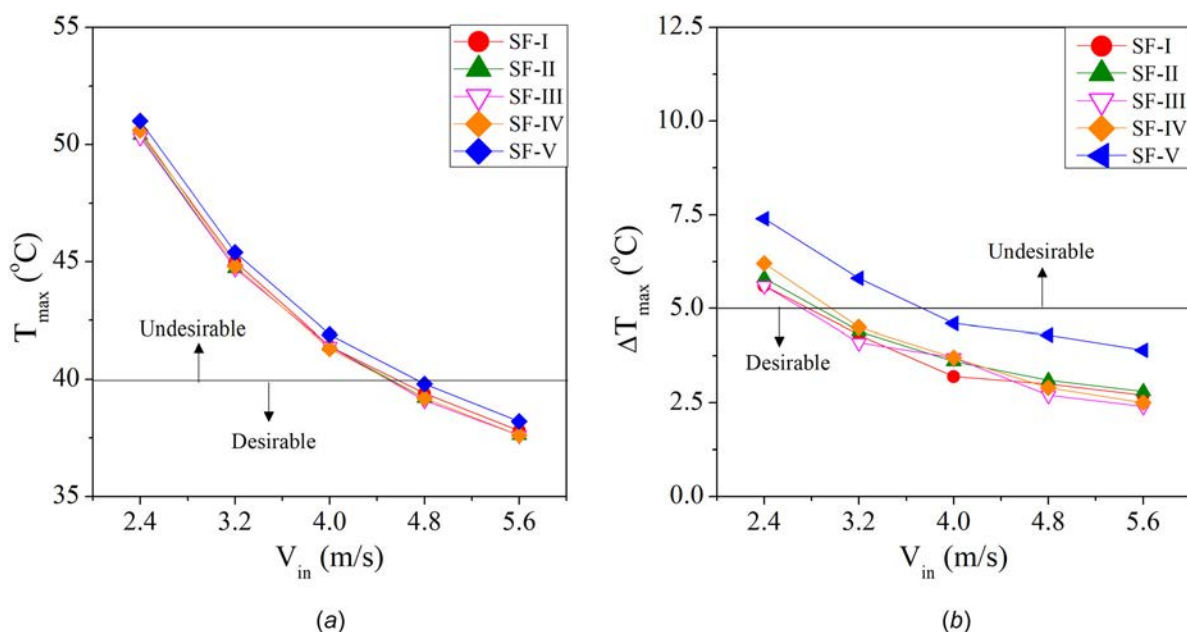
Fig. 11 Comparison of (*a*) T_{max} and (*b*) ΔT_{max} for SF designs at different V_{in}

Moreover, the perks of better flow distribution in the SF designs can be clearly observed from the T_{max} and ΔT_{max} profiles, as shown in Fig. 11. It is noticed that $T_{max} < 40\,^{\circ}C$ for all SF designs at $V_{in} \geq 4.8\,m/s$, and $\Delta T_{max} < 5\,^{\circ}C$ for all SF designs at $V_{in} \geq 4\,m/s$. Therefore, $V_{in} \geq 4.8\,m/s$ can be considered as a desired range for maintaining the favorable conditions of the T_{max} and ΔT_{max} to ensure an optimum performance of the Li-ion battery pack for all the SF designs. Furthermore, the designs: SF-II and SF-V, are found to be more alluring due to significantly lower pressure drop penalty as compared to other SF designs. Therefore, in Sec. 4.4, the performances of various designs are compared by keeping an almost same pressure drop penalty.

4.4 Comparison at Same Pressure Drop. The magnitude of pressure drop penalty controls the associated fluid flowrate, which

significantly influences the thermal performance of different designs. The performance of all the designs is compared at pressure drop penalty of $\sim 32\,Pa$ as occurred for the base case (SS-Ia) at $V_{in} = 4\,m/s$ as given in Table 4. As discussed earlier also, at this condition the desired favorable conditions are not maintained by the SS-Ia design. The same is expected for the SS-Ib design also as it is unable to maintain the desired characteristics even at slightly higher pressure drop. Furthermore, it is noticed that although the velocity distribution nonuniformity is mitigated for the SS-IV design, the desired thermal characteristics could not be met due to the lower overall flowrate because of higher associated pressure drop. Therefore, SS-IV design requires higher peristaltic power to achieve the desired temperature characteristics. Similarly, due to poor thermal performance and higher pressure drop per inlet port for the SS-III design as compared to the SS-IV (Table 4), the desired results are not expected. Therefore, among

Table 5 Comparison of thermal performance at similar pressure drop

Design	ΔP (Pa)	T_{max} (°C)	ΔT_{max} (°C)
SS-Ia	32.2	43.9	8.1
SS-II	32.1	39	5.3
SF-II	32.2	38.4	2.9
SF-V	32	36.9	2.8

the SS designs, only the results are compared for SS-II design at pressure drop of ~32 Pa. The SS-II design is selected due to its potential to maintain lower pressure drop at same flowrate as compared to the base case. Similarly, due to the higher pressure drop (Table 4) and unsuitability of the SF-I, SF-III, and SF-IV designs to meet the desired condition, their results are also not compared and only the results of the SF-II and SF-V are compared in this section.

In Table 5, the results of SS-Ia are compared with the SS-II, SF-II, and SF-V. It is noticed that for the SS-II design, the first condition of $T_{max} < 40\,°C$ is maintained, however, the $\Delta T_{max} > 5\,°C$ which limits its usability as an effectual cooling module configuration for the Li-ion battery pack. The higher temperature nonuniformity in the SS-II design is noticed due to presence of significant flow distribution nonuniformity. This problem is substantially reduced for the similar SF design (SF-II), and it can be observed that SF-II design successfully limits the rise of T_{max} and ΔT_{max} under the desired limits. Furthermore, the best results are noticed for the new proposed design (SF-V). It is observed that T_{max} is reduced by $7\,°C$ and ΔT_{max} by 65% for the SF-V design as compared to the SS-Ia at the same pressure drop. Thus, SF-V design is the best suited for the effectual air cooling of Li-ion battery pack in maintaining best thermal performance at minimal pressured drop penalty.

Nonetheless, SF-V design cannot be recommended for liquid cooling operations due to its inability to provide necessarily outlet port for the liquid collection. The liquid cooling or two-phase cooling is required for the heavy-duty applications where the air-cooling modules are inadequate to maintain the desired rates of heat dissipation. Therefore, SF-II design is suggested to be used in liquid cooling/phase change cooling modules. Furthermore, it will be exciting to study the applicability of current proposed design at variable battery discharge rates under unsteady rates of heat generation.

5 Conclusions

In the current work, effect of two common air flow configurations: SS and SF, with different number of inlet/outlet ports has been studied for thermal management of Li-ion battery pack with 12 prismatic cells. Subsequently, a new design of battery module with best thermal and hydrodynamic performance is proposed. Followings are the major conclusions from the current numerical work:

(1) It is noticed that the best flow distribution uniformity is provided by the design with two inlet and two outlet ports for both the SS and SF configurations. However, addition of two inlet ports increases the pressure drop and complexity of cooling module.

(2) The location of outlet port significantly influences the distribution of fluid in the channels, and the uniformity in the flow distribution is significantly higher for the SF designs as compared to the SS designs.

(3) It is more beneficial to add two outlet ports (SS-II design) as compared to the configurations of two inlet ports (SS-III design) for the SS case. Whereas, for the SF designs, addition of two inlet ports is found to be more advantageous as compared to addition of two outlet ports (SF-II).

(4) Nonuniformity in the velocity distribution increases with increase of flow rate except for SS-Ib design where the SS-Ib design maintained almost consistent fluid flow distribution trend for the studied range of flow rate.

(5) Among all SS designs, only SS-Ib at $V_{in} \geq 5.6$ m/s and SS-IV at $V_{in} \geq 4.8$ m/s are found suitable for the thermal management of Li-ion battery pack at the studied range of flow rate. Whereas all SF designs maintained desired T_{max} and ΔT_{max} conditions at $V_{in} \geq 4.8$ m/s.

(6) At same pressure drop, the best T_{max} and ΔT_{max} conditions are maintained by new proposed design (SF-V). The new design results in reduction of T_{max} by $7\,°C$ and ΔT_{max} by 64.5% as compared to base design (SS-Ia) at same pressure drop penalty; therefore, SF-V design is recommended as air-cooling modules for the effective thermal management of Li-ion battery packs.

Nomenclature

AD = absolute deviation
c_p = specific heat (J/kg/K)
EV = electric vehicle
H = height
L = length
N = number
Nu = Nusselt number
P = pressure (Pa)
Re = Reynolds number
T = temperature (°C)
V = velocity (m/s)
W = width

Greek Symbols

α = velocity nonuniformity factor
λ = thermal conductivity (W/m/K)
μ = dynamic viscosity (Pa·s)
ρ = density (kg/m³)

Subscripts

a = air
avg = average
ch = channel
in = inlet
max = maximum
min = minimum
s = solid

References

[1] United Nations Climate Change, 2015, "The Paris Agreement," United Nations Climate Change, Paris, France, accessed Feb. 4, 2022, https://unfccc.int/process-and-meetings/the-paris-agreement/the-paris-agreement

[2] Lin, B., and Xu, B., 2018, "How to Promote the Growth of New Energy Industry at Different Stages?," Energy Policy, **118**, pp. 390–403.

[3] Yu, H., Fan, J. L., Wang, Y., and Wang, J., 2018, "Research on the New-Generation Urban Energy System in China," Energy Procedia, **152**, pp. 698–780.

[4] Yang, D.-X., Qiu, L.-S., Yan, J.-J., Chen, Z.-Y., and Jiang, M., 2019, "The Government Regulation and Market Behavior of the New Energy Automotive Industry," J. Cleaner Prod., **210**, pp. 1281–1288.

[5] Thakur, A. K., Prabakaran, R., Elkadeem, M. R., Sharshir, S. W., Arıcı, M., Wang, C., Zhao, W., Hwang, J. Y., and Saidur, R., 2020, "A State of Art Review and Future Viewpoint on Advance Cooling Techniques for Lithium–Ion Battery System of Electric Vehicles," J. Energy Storage, **32**, p. 101771.

[6] Lu, M., Zhang, X., Ji, J., Xu, X., and Zhang, Y., 2020, "Research Progress on Power Battery Cooling Technology for Electric Vehicles," J. Energy Storage, **27**, p. 101155.

[7] Zichen, W., and Changqing, D., 2021, "A Comprehensive Review on Thermal Management Systems for Power Lithium-Ion Batteries," Renewable Sustainable Energy Rev., **139**, p. 110685.

[8] Wang, X., Li, B., Gerada, D., Huang, K., Stone, I., Worrall, S., and Yan, Y., 2022, "A Critical Review on Thermal Management Technologies for Motors in Electric Cars," Appl. Therm. Eng., **201**, p. 117758.

[9] IEA, 2022, "Global EV Outlook 2022," IEA, Paris, France, accessed Sept. 1, 2022, https://www.iea.org/reports/global-ev-outlook-2022

[10] Fan, Y., Bao, Y., Ling, C., Chu, Y., Tan, X., and Yang, S., 2019, "Experimental Study on the Thermal Management Performance of Air Cooling for High Energy Density Cylindrical Lithium-Ion Batteries," Appl. Therm. Eng., **155**, pp. 96–109.

[11] Karimi, G., and Dehghan, A., 2014, "Thermal Analysis of High-Power Lithium-Ion Battery Packs Using Flow Network Approach," Int. J. Energy Res., **38**(14), pp. 1793–1811.

[12] Beheshti, A., Shanbedi, M., and Heris, S. Z., 2014, "Heat Transfer and Rheological Properties of Transformer Oil-Oxidized MWCNT Nanofluid," J. Therm. Anal. Calorim., **118**(3), pp. 1451–1460.

[13] Huo, Y., and Rao, Z., 2015, "The Numerical Investigation of Nanofluid Based Cylinder Battery Thermal Management Using Lattice Boltzmann Method," Int. J. Heat Mass Transfer, **91**, pp. 374–384.

[14] Selvam, C., Lal, D. M., and Harish, S., 2016, "Thermal Conductivity Enhancement of Ethylene Glycol and Water With Graphene Nanoplatelets," Thermochim. Acta, **642**, pp. 32–38.

[15] Sidney, S., Dhasan, M. L., Selvam, C., and Harish, S., 2019, "Experimental Investigation of Freezing and Melting Characteristics of Graphene-Based Phase Change Nanocomposite for Cold Thermal Energy Storage Applications," Appl. Sci., **9**(6), p. 1099.

[16] Jilte, R., Kumar, R., and Ahmadi, M. H., 2019, "Cooling Performance of Nanofluid Submerged Versus Nanofluid Circulated Battery Thermal Management Systems," J. Cleaner Prod., **240**, p. 118131.

[17] Wang, S., Lin, Z., Zhang, W., and Chen, J., 2009, "Experimental Study on Pulsating Heat Pipe With Functional Thermal Fluids," Int. J. Heat Mass Transfer, **52**(21–22), pp. 5276–5279.

[18] Burban, G., Ayel, V., Alexandre, A., Lagonotte, P., Bertin, Y., and Romestant, C., 2013, "Experimental Investigation of a Pulsating Heat Pipe for Hybrid Vehicle Applications," Appl. Therm. Eng., **50**(1), pp. 94–103.

[19] Rao, Z., Huo, Y., and Liu, X., 2014, "Experimental Study of an OHP-Cooled Thermal Management System for Electric Vehicle Power Battery," Exp. Therm. Fluid Sci., **57**, pp. 20–26.

[20] Ye, Y., Saw, L. H., Shi, Y., and Tay, A. A., 2015, "Numerical Analyses on Optimizing a Heat Pipe Thermal Management System for Lithium-Ion Batteries During Fast Charging," Appl. Therm. Eng., **86**, pp. 281–291.

[21] Rao, Z., Huo, Y., Liu, X., and Zhang, G., 2015, "Experimental Investigation of Battery Thermal Management System for Electric Vehicle Based on Paraffin/Copper Foam," J. Energy Inst., **88**(3), pp. 241–246.

[22] Wang, Z., Zhang, Z., Jia, L., and Yang, L., 2015, "Paraffin and Paraffin/Aluminum Foam Composite Phase Change Material Heat Storage Experimental Study Based on Thermal Management of Li-Ion Battery," Appl. Therm. Eng., **78**, pp. 428–436.

[23] Jiang, G., Huang, J., Fu, Y., Cao, M., and Liu, M., 2016, "Thermal Optimization of Composite Phase Change Material/Expanded Graphite for Li-Ion Battery Thermal Management," Appl. Therm. Eng., **108**, pp. 1119–1125.

[24] Ping, P., Peng, R., Kong, D., Chen, G., and Wen, J., 2018, "Investigation on Thermal Management Performance of PCM-Fin Structure for Li-Ion Battery Module in High-Temperature Environment," Energy Convers. Manage., **176**, pp. 131–146.

[25] Zhang, J., Shao, D., Jiang, L., Zhang, G., Wu, H., Day, R., and Jiang, W., 2022, "Advanced Thermal Management System Driven by Phase Change Materials for Power Lithium-Ion Batteries: A Review," Renewable Sustainable Energy Rev., **159**, p. 112207.

[26] Qin, P., Liao, M., Zhang, D., Liu, Y., Sun, J., and Wang, Q., 2019, "Experimental and Numerical Study on a Novel Hybrid Battery Thermal Management System Integrated Forced-Air Convection and Phase Change Material," Energy Convers. Manage., **195**, pp. 1371–1381.

[27] Mahamud, R., and Park, C., 2011, "Reciprocating Air Flow for Li-Ion Battery Thermal Management to Improve Temperature Uniformity," J. Power Sources, **196**(13), pp. 5685–5696.

[28] Na, X., Kang, H., Wang, T., and Wang, Y., 2018, "Reverse Layered Air Flow for Li-Ion Battery Thermal Management," Appl. Therm. Eng., **143**, pp. 257–262.

[29] Shahid, S., and Agelin-Chaab, M., 2018, "Development and Analysis of a Technique to Improve Air-Cooling and Temperature Uniformity in a Battery Pack for Cylindrical Batteries," Therm. Sci. Eng. Prog., **5**, pp. 351–363.

[30] Jiaqiang, E., Yue, M., Chen, J., Zhu, H., Deng, Y., Zhu, Y., Zhang, F., Wen, M., Zhang, B., and Kang, S., 2018, "Effects of the Different Air Cooling Strategies on Cooling Performance of a Lithium-Ion Battery Module With Baffle," Appl. Therm. Eng., **144**, pp. 231–241.

[31] Wang, Y. W., Jiang, J. M., Chung, Y. H., Chen, W. C., and Shu, C. M., 2019, "Forced-Air Cooling System for Large-Scale Lithium-Ion Battery Modules During Charge and Discharge Processes," J. Therm. Anal. Calorim., **135**(5), pp. 2891–2901.

[32] Fan, L., Khodadadi, J. M., and Pesaran, A. A., 2013, "A Parametric Study on Thermal Management of an Air-Cooled Lithium-Ion Battery Module for Plug-In Hybrid Electric Vehicles," J. Power Sources, **238**, pp. 301–312.

[33] Xie, J., Ge, Z., Zang, M., and Wang, S., 2017, "Structural Optimization of Lithium-Ion Battery Pack With Forced Air Cooling System," Appl. Therm. Eng., **126**, pp. 583–593.

[34] Hong, S., Zhang, X., Chen, K., and Wang, S., 2018, "Design of Flow Configuration for Parallel Air-Cooled Battery Thermal Management System With Secondary Vent," Int. J. Heat Mass Transfer, **116**, pp. 1204–1212.

[35] Chen, K., Wang, S., Song, M., and Chen, L., 2017, "Structure Optimization of Parallel Air-Cooled Battery Thermal Management System," Int. J. Heat Mass Transfer, **111**, pp. 943–952.

[36] Liu, Z., Wang, Y., Zhang, J., and Liu, Z., 2014, "Shortcut Computation for the Thermal Management of a Large Air-Cooled Battery Pack," Appl. Therm. Eng., **66**(1–2), pp. 445–452.

[37] Chen, K., Song, M., Wei, W., and Wang, S., 2019, "Design of the Structure of Battery Pack in Parallel Air-Cooled Battery Thermal Management System for Cooling Efficiency Improvement," Int. J. Heat Mass Transfer, **132**, pp. 309–321.

[38] Li, X., He, F., Zhang, G., Huang, Q., and Zhou, D., 2019, "Experiment and Simulation for Pouch Battery With Silica Cooling Plates and Copper Mesh Based Air Cooling Thermal Management System," Appl. Therm. Eng., **146**, pp. 866–880.

[39] Wang, S., Li, K., Tian, Y., Wang, J., Wu, Y., and Ji, S., 2019, "Improved Thermal Performance of a Large Laminated Lithium-Ion Power Battery by Reciprocating Air Flow," Appl. Therm. Eng., **152**, pp. 445–454.

[40] Liu, Y., and Zhang, J., 2019, "Design a J-Type Air-Based Battery Thermal Management System Through Surrogate-Based Optimization," Appl. Energy, **252**, p. 113426.

[41] Kang, D., Lee, P.-Y., Yoo, K., and Kim, J., 2020, "Internal Thermal Network Model-Based Inner Temperature Distribution of High-Power Lithium-Ion Battery Packs With Different Shapes for Thermal Management," J. Energy Storage, **27**, p. 101017.

[42] Zhang, F., Lin, A., Wang, P., and Liu, P., 2021, "Optimization Design of a Parallel Air-Cooled Battery Thermal Management System With Spoilers," Appl. Therm. Eng., **182**, p. 116062.

[43] Ma, R., Ren, Y., Wu, Z., Xie, S., Chen, K., and Wu, W., 2022, "Optimization of an Air Cooled Battery Module With Novel Cooling Channels Based on Silica Cooling Plates," Appl. Therm. Eng., **213**, p. 118650.

[44] Nacke, R., Northcutt, B., and Mudawar, I., 2011, "Theory and Experimental Validation of Cross-Flow Micro-Channel Heat Exchanger Module With Reference to High Mach Aircraft Gas Turbine Engines," Int. J. Heat Mass Transfer, **54**(5–6), pp. 1224–1235.

[45] Kumar, R., Singh, G., and Mikielewicz, D., 2018, "A New Approach for the Mitigating of Flow Maldistribution in Parallel Microchannel Heat Sink," ASME J. Heat Transfer, **140**(7), p. 072401.

[46] Kumar, R., Singh, G., and Mikielewicz, D., 2019, "Numerical Study on Mitigation of Flow Maldistribution in Parallel Microchannel Heat Sink: Channels Variable Width Versus Variable Height Approach," ASME J. Electron. Packag., **141**(2), p. 021009.

Document details - Application of graph-theoretic approach for the evaluation of lean-six-sigma (LSS) critical-success-factors (CSFs) facilitating quality-audits in Indian small & medium enterprises (SMEs)

- **1 of 1**

- Export

- Download

- More...

Application of graph-theoretic approach for the evaluation of lean-six-sigma (LSS) critical-success-factors (CSFs) facilitating quality-audits in Indian small & medium enterprises (SMEs)(Article)

- Lande, M.,

- Seth, D.,

- Shrivastava, R.L.

- View Correspondence (jump link)

    - [a]Department of Mechanical Engineering, Vidya Pratishthan's Kamalnayan Bajaj Institute of Engineering and Technology (VPKBIET), Baramati, India

- [b]Department of Mechanical and Industrial Engineering, Qatar University College of Engineering, Doha, Qatar
- [c]Department of Mechanical Engineering, Y.C. College of Engineering, Nagpur, India

Abstract

Purpose: One of the major challenges for developing countries is the lack of mechanisms for the evaluation of critical success factors (CSFs) of quality initiatives, which hampers the journey toward sustainability. Lean Six Sigma (LSS) has been one of the most widely used initiatives supporting quality improvement with wastes reduction and facilitating sustainability. To expedite LSS and its spread, it is important to evaluate key CSFs. Accordingly, the purpose of this paper is to provide an approach for the evaluation of LSS-CSFs for Indian small and medium enterprises (SMEs). Design/methodology/approach: The paper uses a graph theoretic approach and demonstrates the evaluation of LSS-CSFs by proposing an index. The development of index is illustrated using a set of seven prioritized CSFs based on the literature review paper (Lande et al., 2016). Findings: This study guides about the translation of CSFs in the form of an index (number) and will benefit both researchers and practitioners, who wish to study the role of key CSFs for implementation and audit requirements for sustainability. Research limitations/implications: Authors remain confined only to Indian SMEs. Originality/value: LSS possesses the potential to enhance the performance of manufacturing SMEs, but its evaluation is not easy. This attempt for offering a useful evaluation scheme involving CSFs, in the areas of LSS in developing country contexts, is the first. The approach also facilitates both quality audits and benchmarking between different sets of CSFs. The approach is generalizable and can be extended in other areas. © 2019, Emerald Publishing Limited.

Author keywords

Critical success factorsGraph theoryIndianLean Six SigmaSmall and medium enterprises

---

Seth, D.; Department of Mechanical and Industrial Engineering, Qatar University College of Engineering, Doha, Qatar;

Document details - Simultaneous Scheduling of Machines, Tool Transporter and Tools in a Multi Machine Flexible Manufacturing System Without Tool Delay Using Crow Search Algorithm

- Export

- Download

- More...

Simultaneous Scheduling of Machines, Tool Transporter and Tools in a Multi Machine Flexible Manufacturing System Without Tool Delay Using Crow Search Algorithm(Article)

- Mareddy, P.L.,

- Narapureddy, S.R.,

- Dwivedula, V.R.,

- Prayagi, S.V.

- View Correspondence (jump link)

- ᵃElectrical Engg. Dept., Annamacharya Institute of Technology and Sciences, AP, Rajampet, 516125, India
- ᵇMechanical Engg. Dept., Annamacharya Institute of Technology and Sciences, AP, Rajampet, 516125, India
- ᶜSatya Institute of Technology and Management, AP, Vizianagarm, 535002, India

View additional affiliations_

Abstract

This paper deals with machines, tool transporter (TT) and tools simultaneous scheduling in multi machine flexible manufacturing system (FMS) with the lowest possible number of copies of every tool type without tool delay taking into account tool transfer times to minimize makespan (MSN). The tools are stored in a central tool magazine (CTM) that shares with and serves for several machines. The problem is to determine the lowest possible number of copies of every tool variety, allocation of copies of tools to job-operations, job-operations' sequencing on machines and corresponding trip operations of TT, including the dead heading trip and loaded trip times of TT without tool delay for MSN minimization. This paper proposes nonlinear mixed integer programming (MIP) formulation to model this simultaneous scheduling problem and crow search algorithm (CSA) built on the crows' intelligent behavior to solve this problem. The results have been tabulated, analyzed and compared © 2022. Jordan Journal of Mechanical and Industrial Engineering. All rights reserved

Author keywords

Crow search algorithmFmsMakespanNo tool delayOptimization techniquesScheduling of machinesTool transporter and tools

Indexed keywords

Engineering controlled terms:	Flexible manufacturing systemsInteger programmingLearning algorithms
Engineering uncontrolled terms	Crow search algorithmFmsMakespanMulti-machinesNo tool delayOptimization machineSearch AlgorithmsSimultaneous schedulingTool transporter and tool
Engineering main heading:	Scheduling

Shielded metal arc welding of AISI 409M ferritic stainless steel: study on mechanical, intergranular corrosion properties and microstructure analysis

Sachin Ambade
Department of Mechanical Engineering, Yeshwantrao Chavan College of Engineering, Nagpur, India

Chetan Tembhurkar
Mechanical Engineering Department, Priyadarshini College of Engineering, Nagpur, India

Awanikumar P. Patil
Department of Metallurgical and Materials Engineering, Visvesvaraya National Institute of Technology, Nagpur, India

Prakash Pantawane
Department of Manufacturing Engineering and Industrial Management, College of Engineering, Pune, India, and

Ravi Pratap Singh
Department of Industrial and Production Engineering, Dr BR Ambedkar National Institute of Technology, Jalandhar, India

Abstract

Purpose – The purpose of this study is on AISI 409 M ferritic stainless steel (FSS) which is developing a preferred choice for railway carriages, storage tanks and reactors in chemical plants. The intergranular corrosion behavior of welded SS 409 M has been studied in H_2SO_4 solution (0.5 M) with the addition of NH_4SCN (0.01 M) with different heat input. As this study is very important in context of various chemical and petrochemical industries.

Design/methodology/approach – The microstructure, mechanical properties and intergranular corrosion properties of AISI 409 M FSS using shielded metal arc welding were investigated. Shielded metal arc welding with different welding current values are used to change the heat input in the joints resulted in the microstructural variations. The microstructure of the welded steel was carefully inspected along the width of the heat-affected zone (HAZ) and the transverse-section of the thin plate.

Findings – The width of heat affected zone (3.1,4.2 and 5.8 mm) increases on increasing the welding heat input. Due to change in grain size (grain coarsening) as HAZ increased. From the microstructure, it was observed that the large grain growth which is dendritic and the structure become finer to increase in welding heat input. For lower heat input, the maximum microhardness value (388HV) was observed compared with medium (351 HV) and higher heat input (344 HV), which is caused by a rapid cooling rate and the depleted area of chromium (Cr) and nickel (Ni). The increase in weld heat input decreases tensile strength, i.e. 465 MPa, 440 MPa and 418 MPa for low, medium and high heat input, respectively. This is because of grain coarsening and chromium carbide precipitation in sensitized zone and wider HAZ. The degree of sensitization increases (27.04%, 31.86% and 36.08%) to increase welding heat input because of chromium carbide deposition at the grain boundaries. The results revealed that the higher degree of sensitization and the difference in intergranular corrosion behavior under high heat input are related to the grain growth in the HAZ and the weld zone.

Originality/value – The study is based on intergranular corrosion behavior of welded SS 409 M in H2SO4 solution (0.5 M) with the addition of NH4SCN (0.01 M) with different heat input which is rarely found in literature.

Keywords Microstructure, Hardness, SS 409M, SMAW, Hardness, HAZ, Intergranular corrosion

Paper type Research paper

1. Introduction

Ferritic stainless steel (SS) 409 M is modified version of AISI 409 M with a lower carbon content (0.03%) and with a very

low Ni percentage (<0.30%) using judicious balancing of ferritic stabilizing elements (Cr, Si, Ti) and austenitic stabilizers (Ni, Mn, C, N) applying Kaltenhausers relationship (Folkhard, 1988; Lakshminarayanan and Balasubramanian, 2012a),. The steel is becoming a preferred choice as utility grade construction material for railway carriages (and wagons), storage tanks and reactors in chemical plants because of its better strength, abrasion and corrosion resistance and easy fabrication (Folkhard, 1988; Lakshminarayanan and Balasubramanian, 2012a; Lakshminarayanan *et al.*, 2009; David *et al.*, 2003; Lippold and Kotechi, 2005; Lakshminarayanan *et al.*, 2008).

Steel possesses good weldability, which is used to reduce its mechanical properties, and is known to increase the risk of sensitization (Folkhard, 1988; Lakshminarayanan and Balasubramanian, 2012a; Lakshminarayanan *et al.*, 2009; David *et al.*, 2003; Lippold and Kotechi, 2005; Lakshminarayanan *et al.*, 2008). The coarse grain zone occurs due to heating the metal above critical temperature that lacks ductility and the formation of martensite which lowers ductility (Lakshminarayanan *et al.*, 2009). So, by using lower heat input or proper welding process, the excessive grain growth can be avoided (Lakshminarayanan *et al.*, 2009; Mohandas *et al.*, 1999; Vashishtha and Taiwade, 2014; Taiwade *et al.*, 2011).

It has been reported that the ferritic stainless steel (FSS) is more prone to intergranular corrosion than austenitic SS as FSS is having lower solubility in carbon and nitrogen due to this Cr precipitate formed easily in FSS (Lakshminarayanan and Balasubramanian, 2012a). Moreover, if the local concentration of chromium in the stainless-steel drops below 14 Wt.%, the steel is unable to develop passive layer on the surface making it more prone to corrosion. Sulfuric acids are widely used in chemical industries and possess corrosion problems. The role of thiocyanate in iron ions is known to be a complexing agent (Ogura *et al.*, 1976). The addition of thiocyanate increases the dissolution rate of chromium and hence increased corrosion rate. It has been reported that the authors Acha U. Ezeoke et. al. have shown the inhibition nature of KSCN at lower concentration (0.005 M) for mild steel in 0.5 M H_2SO_4 (Ezeoke *et al.*, 2012) Kotaro Ogura et. al also observed similar results. The dissolution rate with (0.01 M) or without SCN ions almost similar and has observed the passivating effect, but at higher concentration of SCN ions the rate of dissolution has increased resulting in depletion of passive film (Ogura and Sato, 1979). NH_4SCN is used as an oxidizer/inhibitor in testing the susceptibility of intergranular corrosion of stainless steel (ASTM G 108–94), and is known to inhibit the corrosion of metals and alloys (INCO, 1963). However, the role of NH_4SCN is complex as it sometimes increases the corrosion (acts as oxidizer) (Parvathavarthini and Dayal, 2002) and sometimes decreases corrosion (acts as an inhibitor) (INCO, 1963). It has also been reported by the researchers that the pitting charge magnitude in the presence of sulfur species increases in the following order $SO_4^{2-} < SO_3^- < S^{2-} < SCN^- < S_2O_3^{2-}$ (Vincent *et al.*, 2013). A 409 FSS required systematic investigation against the local breakdown and grain boundary regions for determining the Cr content and lowering the degree of sensitization of the steel (Emun *et al.*, 2018).

Welding is a crucial technique of steel fabrication and the chemical stability of the weld is sensitive to the thermal weld condition. The welding procedure for SS409M is already been well established but very few literatures available on intergranular corrosion behavior of 409 M FSS in acidic environments. The present investigation is along the effect of welding heat input on microstructure, mechanical and intergranular corrosion properties of FSS 409 M in sulfuric acid solution with NH_4SCN.

2. Materials and methods

The FSS AISI 409 M (referred to as test steel) of 3 mm thick was purchased from market. The chemical analysis (Wt.%) of the sample and electrode were obtained using direct reading optical emission spectrometer are presented in Table 1.

Three plate pieces of dimension $100 \times 150 \times 3 mm^3$ (length × width × thickness) were cut using wire-cut electrical discharge machine (EDM) (EZEECUT PLUS EZ-01 Electronica make). The welding was carried out by shielded metal arc welding (SMAW) were given Bead-on-Plate (BOP) welding and welding electrode E-308L was used (Lakshminarayanan *et al.*, 2009; Lakshminarayanan *et al.*, 2008). The welding was carried out with three different current 80 A (23 V), 90 A (24 V) and 100 A (25 V) on 409 M FSS. The welding plate fixture and welded plate is shown in Figure 1.

The heat inputs (Q) were estimated from current and voltage values using equation (1) (Vashishtha and Taiwade, 2014; Weman, 2003; Kou, 2003). The welding parameters for producing welded joints are presented in Table 2.

$$Q = (\eta VI/W) \tag{1}$$

Where, "*V*" = arc voltage in Volts (V), "*I*" = welding current in Amperes (A), "*w*" = welding speed in mm/s and arc efficiency (η) = 0.75 (Bihade *et al.*, 2013; Taiwade *et al.*, 2013).

The test samples were cut using wire cut EDM in perpendicular to welding direction from welded plates for microstructural examination. The specimens were grounded on SiC emery papers in the following sequences of the grits 180, 320, 600, 800, 1200, and final polishing were carried out

Table 1 Chemical analysis (Wt%) of the FSS 409 M and electrode

Material	C	Si	Mn	P	S	Cr	Ni	Fe
409M FSS	0.037	0.52	1.7	0.029	0.003	11.10	0.89	Bal.
ER308L Filler	0.01	0.8	1.7	0.015	0.01	18.0	10.0	Bal.

Figure 1 Welding plate fixture and welded plate

Table 2 Parameter for welding

Heat Input	Current (A)	Voltage (V)	Efficiency(η)	Speed (mm/s)	Heat Input (J/mm)
Low	80	23	0.75	3.6	383.33
Medium	90	24	0.75	3.2	506.25
High	100	25	0.75	3.0	625.0

on a velvet cloth with alumina powder of 0.75 μm. The polished samples were electrolytically etched in 90% ethanol plus 10% HCl at 6 V for 30 s using a potentiostat (Solartron-1285). Microstructural investigations were carried out using optical microscope (Zeiss Axiolab) at 200X magnification. For measuring the hardness of the weld, HAZ and base metal Vickers microhardness tester (MITUTOYO Japan) was used with 0.05 Kg load and dwell time of 20 s. The welded plates were sliced using wire cut EDM along transverse direction (perpendicular to welding direction) for preparing tensile testing specimens. Tensile testing specimen guidelines of ASTM E8 M-04 were followed as shown in Figure 2. The gauge lengths of tensile specimens were 50 mm, and they were broken in UTM (INSTRON 4467).

Prior to electrochemical test, the samples were cut at the weld joint and polished at series of emery papers. After polishing, the samples were ultrasonically cleaned in acetone and rinsed with distilled water at each stage. All the electrochemical tests were conducted on the polished flat square surface area of 100mm^2. For electrical connection, the test samples were pasted to copper strip (0.8 mm $\times$ 0.8 mm) using silver paste. The copper strip was then soldered to copper wire and mounted in araldite resins (Lakshminarayanan *et al.*, 2012) as shown in Figure 3. The double loop electrochemical potentio-kinetic reactivation (DLEPR) tests were performed in 0.5 M H$_2$SO$_4$ + 0.01 M NH$_4$SCN using potentiostat (Solartron-1285) at room temperature (30°C) to access degree of sensitization. Before electrochemical test, the solutions were de-aerated to free oxygen using dry nitrogen gas for 1 h. A standard three-electrode cell and corning round bottom flask with four necks was used for electrochemical tests. The electrochemical cell consists of first the working electrode (WE) where there is a test sample, second the platinum gauze electrode which is counter electrode (CE) and third the saturated calomel electrode used as reference electrode (RE) as per ASTM G5-94.

3. Results and discussion

Figure 4 represent optical micrograph of FSS in as received (AR) condition. Ferritic stainless-steel micrograph reveals single phase microstructure with well grown grains.

Figure 2 Tensile test specimen
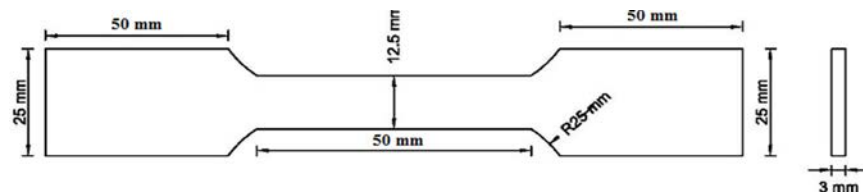
Figure 3 Sample for electrochemical study
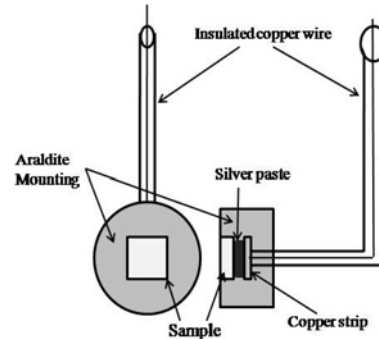
Figure 4 Microstructure of base metal
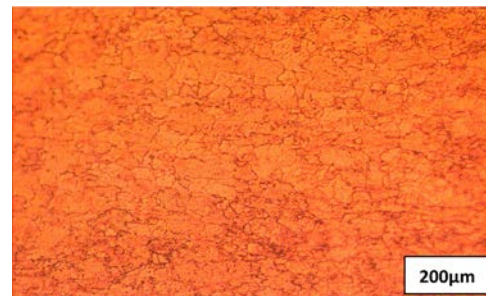
3.1 Microstructural examination

Figure 5 represents the microstructure of the welded specimens in different zones for low, medium and high heat input weld. In weld zone, the structure is dendritic. In low heat input weld, the dendrites are short but thicker. As heat input increase, the dendrites become thinner and longer. It is attributed to less nucleation and more lateral growth at low heat input and more nucleation and less lateral growth for high heat input weld. This is because shallow thermal gradient in low heat input weld allowed slower cooling and solidification. In high input weld, the thermal gradient is steep so the cooling rate is faster and longer dendrites are formed. In high heat input weld, the

Figure 5 Microstructures of various zones of weld produced on welding of FSS with various heat inputs (200 μm)

Zones	Low heat input	Medium heat input	High heat input
Weldment		WZ	WZ
Fusion line	HAZ WZ	HAZ WZ	HAZ WZ
HAZ	HAZ	HAZ	HAZ
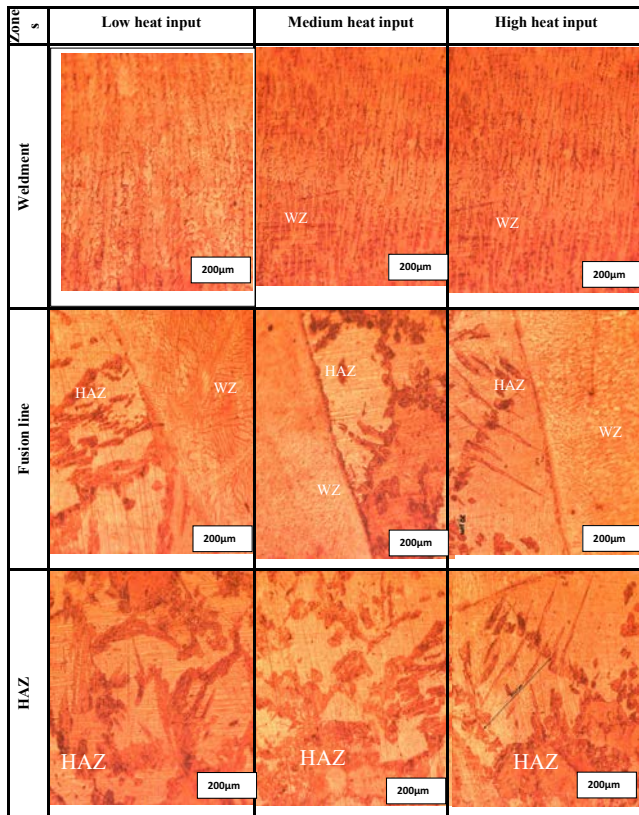
temperatures in weld pool are highest than low heat input weld. Higher temperature causes faster cooling and slower temperature causes slower cooling. Faster cooling causes more under cooling, and more under cooling causes more nucleation. When there are more nuclei, they will grow less in lateral direction so dendrites will be thinner. Faster cooling also causes dendrites to grow faster in the opposite direction in the direction of heat loss. So, dendrites will be longer and thinner in high input weld. Similarly, slower cooling causes less under

Table 3 Influence of welding heat input on width of HAZ

Welding Heat Input	Current (A)	Welding Heat (J/mm)	HAZ (mm)
Low Heat Input	80	383.33	3.1
Medium Heat Input	90	506.25	4.2
High Heat Input	100	625.0	5.8

cooling causes less nucleation. When there are less nuclei, they will grow more in lateral direction, so dendrites will be thicker. Slower cooling also causes dendrites to grow slower in the opposite direction in the direction of heat loss. So, dendrites will be smaller and thicker in low heat input weld. In the area around fusion zone, there is complete fusion between HAZ and weldment. In HAZ, there are bright and the dark regions marked with steaks, which is similar to martensitic structures. It is evident that the hardness in HAZ is more than the weld zone, this attributed to the presence of martensite (Lakshminarayanan and Balasubramanian, 2013; Lakshminarayanan and Balasubramanian, 2012b). It's also detected that the hardness at the fusion line is lower than HAZ. Lakshminarayanan *et al.* (2012) conveyed that the grain size of HAZ of EBW joint is lower than that of HAZ of GTAW. The study (Lakshminarayanan *et al.*, 2012) revealed that HAZ in both the welds has Widmanstatten ferrite along with martensite along the grain boundary. Also, the hardness (HV 0.05, 15 s) of GTAW weld joint is less than that of EBW joint. In all three joints, the heat affected zone (HAZ) hardness is more than that of the base metal due to the presence of martensite (Lakshminarayanan and Balasubramanian, 2013; Lakshminarayanan and Balasubramanian, 2012b; Du Toit *et al.*, 2006). The results of this study are thus in consistent with the results of Laxminarayanan (Lakshminarayanan *et al.*, 2012; Shanmugam *et al.*, 2009). Therefore, the higher hardness of HAZ is attributed to presence of martensite. Width of HAZ of welded test sample is estimated using optical microscope and image analyzer and presented in Table 3. It has been observed that the width of HAZ increases on increasing welding heat. As the heat input increases, the cooling rate decreases, and there is enough time for grain coarsening. This grain growth leads to wider HAZ for higher heat input. The wider HAZ region is attributed to the maximum temperature in the weld zone (Vashishtha and Taiwade, 2014; Taiwade *et al.*, 2013; Lakshminarayanan *et al.*, 2012).

3.2 Micro-hardness

Figure 6 shows the schematic of bead-on-plate weld and a horizontal dotted line across the base metal and HAZ along which the micro-hardness (HV) has been measured. Figure 7 shows the graph of variation in micro-hardness as a function of distance. From the figure it is seen that hardness in base metal is low and increases slowly until HAZ boundary is reached (Meena *et al.*, 2017). In HAZ, the micro hardness rapidly increases, reaches maximum value close to weld metal/HAZ interface and then decreases upto the end of HAZ. This is attributed to formation of martensite (Du Toit *et al.*, 2006; Amuda and Mridha, 2011). Figure 7 also shows that the

Figure 6 Schematic of bead-on-plate weld joint showing a line along which micro-hardness was measured
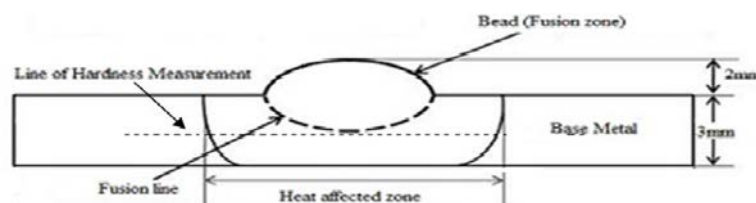
Figure 7 Variation of vickers micro-hardness (HV 0.05, 20 s) as a function of distance across FSS HAZ

hardness decreases gradually with the increasing welding heat input and lower hardness has been observed for high heat input weld. Micro-hardness varies from 201 to 344 HV for high heat input weld, 215 to 351 HV for medium heat input weld and 241 to 388 HV for low heat input weld. Maximum hardness of 388HV is noted for the low heat input weld, 351 HV for medium heat input weld and 344 HV for high heat input weld. These results are analogous with work of Vashishtha and Taiwade (2014), who found higher hardness in low heat input weld of low-Ni stainless steel. The attributed it to lower rate of cooling.

3.3 Tensile test and fractography

The tensile test results are shown in Table 4. The tensile strength of as received (AR) material was 549 MPa and that for low, medium and high input welding are 465 MPa, 440 MPa and 418 MPa, respectively. Thus, it is obvious that the tensile strength decreases when the welding current was increased.

Table 4 Influence of heat input on tensile strength and ductility

Samples	Current (A)	Welding Heat (J/mm)	Tensile strength (MPa)	% Elongation
As received	–	–	549	23.4
Low Heat Input	80	383.33	465	18.3
Medium Heat Input	90	506.25	440	15.1
High Heat Input	100	625.0	418	13.2

Figure 8 SEM micrograph of fractured surface of tensile specimens of FSS weld with varying heat input
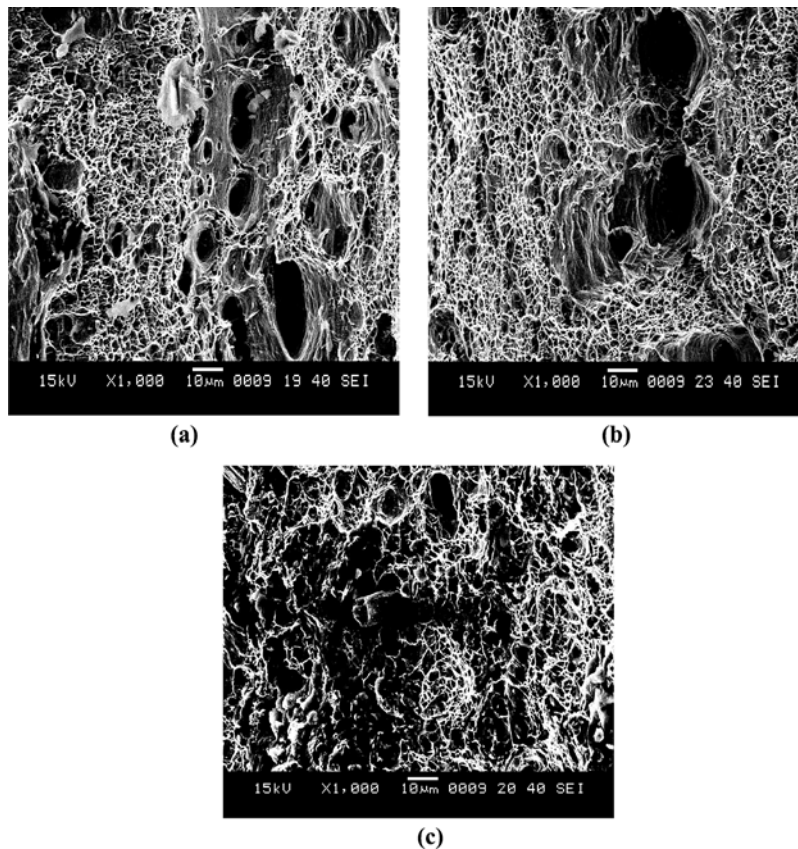
Figure 9 DLEPR curve for FSS a) AR, b) Low heat input, c) Medium heat input and d) High heat input

(a)

(b)

(c)

(d)
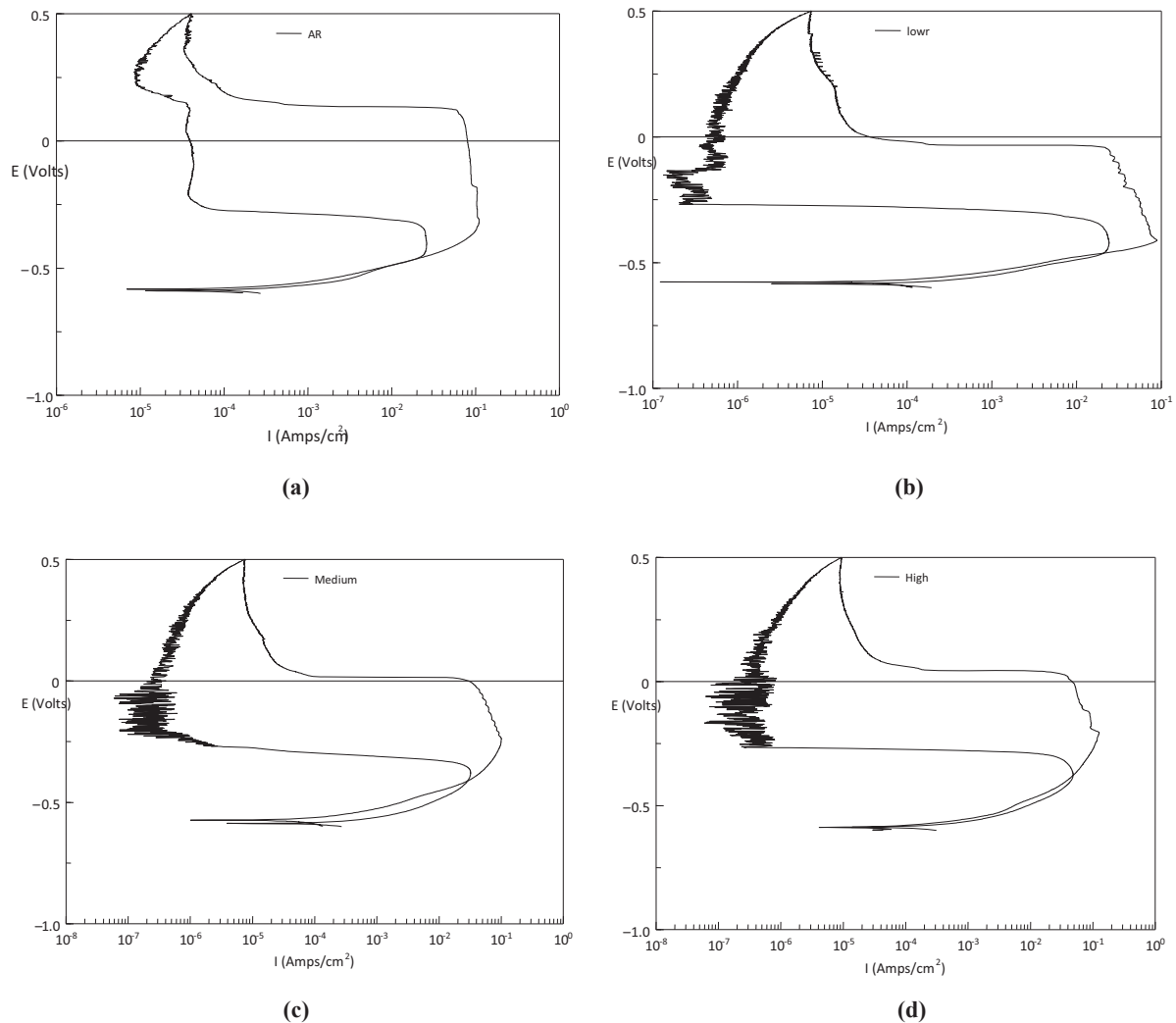
Similarly, percentage elongation decreases as welding current increases. It was noted that all tensile test samples failed in the heat-affected zone. This indicates that HAZ was the weakest portion of the tensile test specimen. The decrease in tensile strength with increasing the welding current is attributed to grain coarsening and chromium carbide precipitation in sensitized zone and wider HAZ. Figure 8 shows SEM fractographs of fractured surface. The fractured surface has a dimpled structure (Kuddus *et al.*, 2018), but the size of dimples decreases with increase in welding current. This is in agreement with our finding that increasing heat input causes drop in ductility. Our results are agreement with the results of Vashishtha and Taiwade (2014).

3.4 Dlepr (double loop electrochemical potentio-kinetic reactivation)

Figure 9 shows DLEPR curves for AR and HAZ sample of FSS welded with various welding current (or heat input). It is evident that both the activation (forward scan) and reactivation (reverse scan) part of the plot are very well defined. The maximum current density in forward as well as reverse scan is

derived from the plots and is presented in Table 5. From Table 5, it can be clearly seen from the %DOS value that the sensitization degree increases with the increase of heat input (Ambade *et al.*, 2021). This is because of the precipitation of carbide along grain boundaries due to welding heat (Tembhurkar *et al.*, 2021). The carbide precipitation is associated with Cr-depletion adjacent to grain boundary and therefore, it becomes more sensitive to grain boundary attack (Taiwade *et al.*, 2013; Lakshminarayanan and Balasubramanian, 2013; Lakshminarayanan and Balasubramanian, 2012b). The DOS increase with welding and on increasing welding heat input.

Table 5 Effect of welding current on degree of sensitization

Sample	Ia	Ir	DOS = Ir/Ia x 100 (%)
AR	0.1594	0.0261	15.96
Low Heat Input	0.088362	0.023898	27.04
Medium Heat Input	0.10059	0.032052	31.86
High Heat Input	0.12411	0.044781	36.08

4. Conclusions

- Width of heat affected zone (3.1, 4.2 and 5.8 mm) increases on increasing welding heat input. Due to change in grain size (grain coarsening) as HAZ increased.
- From the microstructure it was observed that the large grain growth which is dendritic and the structure become finer in order to increase in welding heat input.
- For lower heat input, the maximum microhardness value (388HV) was observed compared with medium (351 HV) and higher heat input (344 HV), which is caused by a rapid cooling rate and the depleted area of chromium (Cr) and nickel (Ni).
- The increase in weld heat input decreases tensile strength i.e., 465 MPa, 440 MPa and 418 MPa for low, medium and high heat input respectively. This is because of grain coarsening and chromium carbide precipitation in sensitized zone and wider HAZ.
- The degree of sensitization increases (27.04%, 31.86% and 36.08%) to increase welding heat input because of chromium carbide deposition at the grain boundaries.

References

Ambade, S., Sharma, A., Patil, A. and Puri, Y. (2021), "Effect of welding processes and heat input on corrosion behavior of ferritic stainless steel 409M", *Materials Today: Proceedings*, Vol. 41, pp. 1018-1023.

Amuda, M.O.H. and Mridha, S. (2011), "An overview of sensitization dynamics in ferritic stainless-steel welds", *International Journal of Corrosion*, Vol. 2011, p. 9, Research Article, Article ID 305793.

Bihade, M.S., Patil, A.P. and Khobragade, N.K. (2013), "Study of corrosion behavior of AISI SS 304L using electrochemical noise measurement", *Tiim*, Vol. 66, pp. 155-161.

David, S.A., Babu, S.S. and Vitek, J.M. (2003), *Welding: Solidification and Microstructure*, The Minerals, Metals & Materials Society

Du Toit, M., Van Rooyen, G.T. and Smith, D. (2006), "An overview of the heat affected zone sensitization and stress corrosion cracking behavior of 12% chromium type 1.4003 ferritic stainless steel", IIW Doc IX-H-640.

Emun, Y., Kuan, G., Kish, J. and Zurob, H. (2018), "Comparative corrosion evaluation of ferritic stainless steels utilized in automotive exhaust applications", SAE technical paper pp. 1-7.

Ezeoke, A.U., Adeyemi, O.G., Akerele, O.A. and Obi-Egbedi, N.O. (2012), "Computational and experimental studies of 4-Aminoantipyrine as corrosion inhibitor for mild steel in sulphuric acid solution", *International Journal of Electrochemical Science*, Vol. 7, pp. 534-553.

Folkhard, E. (1988), *Welding Metallurgy of Stainless Steels*, Spring- Verlag Wien, New York, NY.

INCO (1963), *Corrosion Resistance of the Austenitic Chromium-Nickel Stainless Steels in Chemical Environments*, INCO, New York, NY.

Kou, S. (2003), *Welding Metallurgy*, 2nd ed., John Wiley & Sons Inc., New York, NY.

Kuddus, A.I., Ambade, S.P., Bansod, A.V. and Patil, A.P. (2018), "Microstructural, mechanical and corrosion behaviour of dissimilar welding of Cr-Mn ASS and AISI 304 ASS by using 316L electrode", *Materials Today: Proceedings*, Vol. 5 No. 2, pp. 8307-8313.

Lakshminarayanan, A.K. and Balasubramanian, V. (2012a), "Sensitization resistance of friction stir welded AISI 409 M grade ferritic stainless steel joints", *The International Journal of Advanced Manufacturing Technology*, Vol. 59 Nos 9/12, pp. 961-967.

Lakshminarayanan, A.K. and Balasubramanian, V. (2012b), "Assessment of sensitization resistance of AISI 409M grade ferritic stainless steel joints using modified Strauss test", *Materials & Design*, Vol. 39, pp. 175-185.

Lakshminarayanan, A.K. and Balasubramanian, V. (2013), "Use of DLEPR test to asses sensitization resistance of AISI 409M grade ferritic stainless steel", *Journal of Materials Engineering and Performance*, Vol. 22 No. 8, pp. 2293-2303.

Lakshminarayanan, A.K., Balasubramanian, V. and Reddy, G. M. (2012), "On the fatigue behavior of electron beam and gas tungsten arc weldments of 409M grade ferritic stainless steel", *Materials & Design*, Vol. 35, pp. 760-769.

Lakshminarayanan, A.K., Shanmugam, K. and Balasubramanian, V. (2008), "Fatigue crack growth behavior of AISI 409M grades ferritic stainless steel welded joints using austenite ferritic and duplex stainless-steel electrodes", *ISIJ International*, Vol. 48 No. 11, pp. 1640-1646.

Lakshminarayanan, A.K., Shanmugam, K. and Balasubramanian, V. (2009), "Effect of autogenous arc welding processes on tensile and impact properties of ferritic stainless steel joints", *Journal of Iron and Steel Research International*, Vol. 16 No. 1, pp. 62-68.

Lippold, J.C. and Kotechi, D.J. (2005), *Welding Metallurgy and Weldability of Stainless Steels*, John Wiley & Sons, Vol. 101.

Meena, S.L., Butola, R., Murtaza, Q., Jayantilal, H. and Niranjan, M.S. (2017), "Metallurgical investigations of microstructure and micro hardness across the various zones in synergic MIG welding of stainless steel", *Materials Today: Proceedings*, Vol. 4 No. 8, pp. 8240-8249.

Mohandas, T., Reddy, M. and Mohammad, G.N. (1999), "A comparative evaluation of gas tungsten and shielded metal arc welds of a ferritic stainless steel", *Journal of Materials Processing Technology*, Vol. 94 Nos 2/3, pp. 133-140.

Ogura, K. and Sato, K. (1979), "Process of the activation of passive iron by thiocyanate ion", *Corrosion Science*, Vol. 19 No. 7, pp. 737-741.

Ogura, K., Ooeda, T. and Yosino, T. (1976), "The electrochemical bleaching of ferrc thiocyanate in acidic solution", *Electrochimica Acta*, Vol. 21 No. 11, pp. 1041-1043.

Parvathavarthini, N. and Dayal, R.K. (2002), "Influence of chemical composition, prior deformation and prolonged thermal aging on the sensitization characteristics of austenitic stainless steels", *Journal of Nuclear Materials*, Vol. 305 Nos 2/3, p. 209.

Shanmugam, K., Lakshminarayanan, A.K. and Balasubramanian, V. (2009), "Tensile and impact properties of shielded metal arc welded AISI 409M FSS joints", *Journal of Material Science Technology*, Vol. 25, pp. 181-186.

Taiwade, R.V., Patre, S.J. and Patil, A.P. (2011), "Studies on welding and sensitization of chrome-manganese austenitic stainless steel", *Transactions of the Indian Institute of Metals*, Vol. 64 No. 6, pp. 513-518.

Taiwade, R.V., Patil, A.P. and Dayal, R.K. (2013), "Effect of welding passes on heat affected zone and tensile properties of AISI 304 stainless steel ad chrome-manganese austenitic stainless steel", *Isij International*, Vol. 53 No. 1, pp. 102-109.

Tembhurkar, C., Kataria, R., Ambade, S., Verma, J., Sharma, A. and Sarkar, S. (2021), "Effect of fillers and autogenous welding on dissimilar welded 316L austenitic and 430 ferritic stainless steels", *Journal of Materials Engineering and Performance*, Vol. 30 No. 2, pp. 1444-1453.

Vashishtha, H. and Taiwade, R.V. (2014), "Welding behavior of low nickel chrome-manganese stainless steel", *ISIJ International*, Vol. 54 No. 6, pp. 1361-1367.

Vincent, S., Khan, A.F., Murty, B.S. and Bhatt, J. (2013), "Corrosion characterization on melt spun Cu60Zr20Ti20 on metallic glass: experimental case study", *Journal of Non-Crystalline Solids*, Vol. 379, pp. 4-53.

Weman, K. (2003), *Welding Processes Handbook*, Woodhead publishing Ltd., New York, NY.

Further reading

Loto, C.A. and Loto, R.T. (2012), "Electrochemical corrosion resistance evaluation of ferritic stainless steel", *International Journal of Electrochemical Science*, Vol. 7, pp. 11011-11022.

Murugan, S., Kumar, P.V., Raj, B. and Bose, M.S.C. (1998), "Temperature distribution during multipass welding of plates", *International Journal of Pressure Vessels and Piping*, Vol. 75 No. 12, pp. 891-898.

Van Niekerk, C.J. and Du. Toit, M. (2011), "Sensitization behavior of 11-12% Cr AISI 409 stainless steel during low heat input", *The Journal of the Southern African Institute of Mining and Metallurgy*, Vol. 111, pp. 243-250.

Corresponding author

Sachin Ambade can be contacted at: sachinamb2@rediffmail.com

Implementation of multi-objective Jaya optimization for performance improvement in machining curve hole in P20 mold steel by sinking EDM

Diwesh Babruwan Meshram
Department of Mechanical Engineering, Visvesvaraya National Institute of Technology, Nagpur, India and
Department of Plastic Technology, Central Institute of Petrochemicals Engineering and Technology, Korba, India

Vikas Gohil
Department of Mechanical Engineering, Bajaj Institute of Technology, Wardha, India

Yogesh Madan Puri
Department of Mechanical Engineering, Visvesvaraya National Institute of Technology, Nagpur, India, and

Sachin Ambade
Yeshwantrao Chavan College of Engineering, Nagpur, India

Abstract

Purpose – Machining of curved channels using electrical discharge machining (EDM) is a novel approach. In this study, an experimental setup was designed, developed and mounted on die-sinking EDM to manufacture curve channels in AISI P20 mold steel.

Design/methodology/approach – The effect of specific machining parameters such as peak current, pulse on time, duty factor and lift over material removal rate (MRR) and tool wear rate (TWR) were studied. Multi-objective optimization was performed using Taguchi technique and Jaya algorithm.

Findings – The experimental results revealed current and pulse on time to have the predominant effect over material removal and tool wear diagnostic parameters with contributions of 39.67, 32.04% and 43.05, 36.52%, respectively. The improvements in material removal and tool wear as per the various optimization techniques were 35.48 and 10.91%, respectively.

Originality/value – Thus, Taguchi method was used for effective optimization of the machining parameters. Further, nature-based Jaya algorithm was implemented for obtaining the optimum values of TWR and MRR.

Keywords Electro discharge machining, Curve hole, Material removal rate (MRR), Tool wear rate (TWR), Analysis of variance (ANOVA), Jaya algorithm

Paper type Research paper

1. Introduction

Electrical discharge machining (EDM) is one of the most widely used non-traditional machining technique. Because of its non-contact machining nature, it is independent of the material characteristics pertaining to the workpiece. Hence, it is extensively used to shape hard mold making workpieces, especially in aviation industries (Gohil and Puri, 2017). In the case of injection molding process of plastics, solidification of the product occurs by applying mold cooling. Mold cooling is intern achieved by flowing coolant (water) through channels made in mold. Cooling channels are commonly manufactured by creating multiple straight holes. In some situations, designers use straight holes instead of curve holes. Therefore,

the profile of a cooling channel renders a polygonal line. These straight holes restrict the degree of freedom in their shape and position. To solve these problems, it is requisite to design and develop a new method for machining curve channels and to put the process in real-world practice.

To achieve aforesaid objective, certain procedures have been developed for machining curve channels and can produce curved holes (Fukui and Kinoshita, 1989). The authors presented a unique L- and U-shape hole making process, which uses a modest mechanism (consist of a machining electrode, helical spring, shaft, pulleys, wires, fixtures, etc.) connected to conventional EDM. The device with tool electrode moves beside a curve path while performing EDM. A key feature of the device is that, it can machine a curve channel between two drilled holes perpendicular to each other. It was also reported that the upgraded device can cut U-shape and slant holes; those are impossible to make by traditional machining processes (Ishida and Takeuchi, 2002; Ishida and Takeuchi, 2008).

The author proposed a new experimental setup, wherein, the device was attached to the ram of the conventional EDM, which could be controlled by the computer (Nakajima *et al.* (2008). The tool electrode had a spherical shape that can travel along a straightforward and curve path. Ishida *et al.* further demonstrated a novel system for machining three-dimensional curve channels (Ishida *et al.*, 2004). The authors presented in-pipe flexible mechanism connected on a spark erosion machine. The mechanism was capable of maintaining a constant discharge gap while moving inside a curve hole fabricated by itself. The authors fabricated a micro robot, which machined a long-curved hole with EDM function (Kita *et al.*, 2010). To perform curve machining, an automatic discharge gap controller (ADGC) was devised and installed on the micro robot, which spontaneously and separately controlled the discharge gap in steady machining. Ishida *et al.* proposed and established a new apparatus, which could produce shapes, although limited, on the inside wall of a straight hole by EDM (Ishida *et al.*, 2008). The method was different from the all-existing devices for its capability to produce holes of variable cross sections. A new process is developed to machine a curve hole using spark machining (Takeuchi, 2002), consisting of a spring-based flexible mechanism that had an electrode at the end and a guide to provide machining direction. Recently, authors discussed created a semi-circular channel and optimized it through Taguchi method (Meshram and Puri, 2020). The author experimentally studied the electro discharge machining of AISI P20 steel in finish machining (Tamorim and Weingaertner, 2005). The authors studied the impact of dissimilar tool materials such as brass, copper and graphite on electro discharge machined surface (Dewangan *et al.*, 2014). The authors found that the brass tool was the appropriate choice for EDM of AISI P20 tool steel under straight polarity. The authors studied the impact of peak current pulses on machinability in spark erosion process (Muthuramalingam and Mohan, 2013). Taguchi technique is used to design the experiments and in optimization of material removal and tool wear in electro discharge turning method (Gohil and Puri, 2018). Further, the multiple regression model was estimated for identifying the relationship between the input machining parameter and output performance characteristics (Debnath *et al.*, 2018; Laxman and Raj, 2015; Meshram and Puri, 2019). The advanced Jaya algorithm was implemented for identifying the optimum values for output responses based on the input machining parameters. Comparative analysis was performed between the experimental and the Jaya algorithm values in curve hole EDM (Rao, 2016, 2019).

Although researchers have reported extensive research works on process optimization of EDM, there are very few works on curve hole machining using EDM. In view of the same, a novel curved channel machining approach was designed and developed for which the material removal rate (MRR) and tool wear rate (TWR) study were selected to optimize the parameter levels in machining curve channel. Further, parametric constraints of the process were evaluated and optimized using Taguchi methodology, regression modeling and using Jaya algorithm. A machined surface study has been evaluated by scanning electron microscope (SEM).

2. Materials and methods

2.1 Experimental setup and equipment

All experimental works were executed on RATNAPARKHI Make 500 × 300 ZNC electro discharge machine. A curve channel is machined in the AISI P20 mold steel workpiece and presented in Figure 1.

A specially designed and developed spindle was attached to the conventional EDM, as shown in Figure 2. A solid semicircular electrolytic copper tool was used to machine a curve channel. The actual experimental setup installed on the EDM machine is shown in Figure 3.

The experimental methodology suggested optimization on a trial-and-error basis, wherein the specific parameters set controlling the machining process were either fixed or varied as per the mandates and values presented in Tables 1 and 2, respectively.

Total 18 experiments were designed using the Taguchi method, and triplicate measurements were carried out, and the
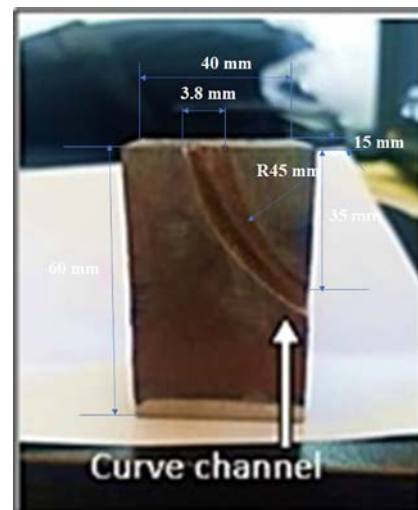
Figure 1 Curve machined work piece
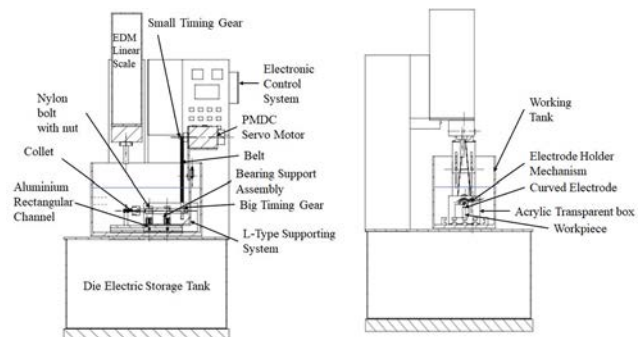

Figure 2 Experimental system for curve machining

Figure 3 Actual experimental setup for curve machining

Table 1 Machining factors and their levels

Factor	Levels	Values
Lift (lifting time), μs	2	1, 2
Ton (pulse-on time), μs	3	40, 60, 80
IP (peak current), A	3	8, 16, 24
DF (duty factor)	3	3, 6, 9

Table 2 Non-variable factors

Work material	AISI P20 mold steel
Electrode diameter	64 mm
Electrode material	Electrolytic copper
Machining time	20 min
Polarity	Straight
Dielectric	EDM oil
Density (g/cm^3)	7.86
Melting point ($^{\circ}$C)	2,600
Hardness, Rockwell C	30
Tensile strength, ultimate (Mpa)	965–1,030
Tensile strength, yield (Mpa)	827–862
Elongation at break	20%
Modulus of elasticity(Gpa)	205
Bulk modulus (Gpa)	140
Poisson's ratio	0.27–0.30
Shear Modulus (Gpa)	73
Thermal expansion	12.8×10^{-6}/$^{\circ}$C
Thermal conductivity ((W/(ms²K)).)	29

average values were deduced. Thus, in total, 54 experiments were performed as shown in Table 3.

Material removal and tool wear were estimated by calculating the rate of the same as follows:

$$\text{MRR (mg/min)} = \frac{W_i - W_f}{t} \times 1000 \quad (1)$$

$$\text{TWR (mg/min)} = \frac{W_i - W_f}{t} \times 1000 \quad (2)$$

In the present research, the main effects of parameters and the interaction of lift and IP, lift and Ton, and IP and Ton were

considered. Therefore, the degree of freedom (DOF) is calculated as follows:

$$
\begin{aligned}
\text{Degree of freedom} &= (\text{no. of parameters}) \times (\text{parameter levels} - 1)\\
&= (3) \times (3-1) = 6\\
\text{and} &= (1) \times (2-1) = 1\\
\text{Total DOF} &= 6 + 1 = 7
\end{aligned}
$$

Interaction of (Lift × Peak current), $(2-1) \times (3-1) = 2$
Interaction of (Lift × Pulse − on time), $(2-1) \times (3-1) = 2$
Interaction of (Peak current × Pulse − on time)$(3-1) \times (3-1) = 4$
     Total : $(2+2+4) = 8$
     Total DOF $= (7+8) = 15$

2.2 Data analysis

Figure 4 exhibits the effect of lift, Ton, IP and DF on MRR. It was observed that a negative correlation existed between the lift parameter and MRR, which may be because of the higher machining time available at Level 1. So does Ton, wherein, an increase in the Ton value leads to a significant decrease in MRR. This may be due to the unstable machining conditions beyond the first level of Ton time. However, IP is found to be directly proportional to MRR, which is expected for a higher current producing more intense discharges and in turn leading to melt and detachment of more material from the surface of work piece. Further, DF is inversely related to material removal because higher Ton and lower pulse off time (Toff) were available at Level 1 and lower Ton and higher Toff were available at Level 3. Figure 5 explains the effects of factors on signal to noise ratio analysis (SNRA) for MRR. As indicated, the effect of lift on MRR is less than other factors.

A similar method was implemented in the study of TWR. Figure 6 demonstrates the effect of lift, Ton, IP and duty factor over TWR. It was observed that the effect of duty factor had the least significant effect in comparison to the rest of the parametric constraints of lift, Ton and IP. Moreover, lift and Ton show an inverse relation to TWR. However, the peak current is directly proportional to TWR. This is because at higher current, more violent discharges are generated between the two electrodes, which holds responsible for high tool wear. Figure 6 indicates the plot of the main effects for SNRA–TWR. As it is clear from Figure 7, by rising the IP, the system becomes more sensitive, while sensitivity decreases with rise in lift and Ton. Experimentation and the corresponding results obtained are required to have an error analysis and consequent validation, for therein, statistical technique in analysis of variance (ANOVA) has been used because it helps in determining significant parameters and their effects. Application of ANOVA required the experimental data to be normally distributed for reducing statistical errors.

Figures 8 and 9 represent the normal probability plot of residuals for MRR and TWR, respectively. It was used to check the distribution of errors and the corresponding spread of the same from mean. If the error distribution was acceptable, the plot assumed the order of a straight line. As presented in Figures 8 and 9, the calculated p-value was greater than the 95% confidence interval (CI); error normality assumption rendered valid in the scenario [14].

Figures 10 and 11 show the graph of fitted values for material removal and tool wear, respectively. The random spread of data points about the abscissa confirmed that the errors are independently distributed with constant variance (Sivam *et al.*, 2013). In the above

Jaya optimization for performance improvement
Diwesh Babruwan Meshram et al.

World Journal of Engineering

Table 3 Experimental design using L18 OA

Run order	Lift	Ton	IP	Duty factor	TWR (mg/min)			MRR (mg/min)		
					Rep 1	Rep 2	Rep 3	Rep 1	Rep 2	Rep 3
1	1	1	1	1	0.963	1.053	1.131	13.130	14.382	13.933
2	1	1	2	2	1.877	1.787	1.894	17.933	18.820	22.194
3	1	1	3	3	1.967	2.134	2.302	23.967	19.573	21.914
4	1	2	1	1	0.633	0.821	0.942	11.533	12.644	12.206
5	1	2	2	2	1.267	1.194	1.420	14.900	15.259	15.669
6	1	2	3	3	1.540	1.871	1.625	15.240	15.192	13.336
7	1	3	1	2	0.067	0.053	0.1	2.967	3.845	4.431
8	1	3	2	3	0.933	0.933	0.844	7.406	8.160	7.552
9	1	3	3	1	1.267	1.594	1.217	14.467	16.473	14.760
10	2	1	1	3	0.800	1.147	0.877	5.943	6.920	8.402
11	2	1	2	1	1.583	1.573	1.286	20.350	19.333	18.755
12	2	1	3	2	1.367	1.768	1.462	17.967	18.336	18.883
13	2	2	1	2	0.533	0.790	0.463	5.750	6.706	7.960
14	2	2	2	3	0.700	0.691	0.711	5.477	5.247	6.182
15	2	2	3	1	1.389	1.097	1.037	16.121	15.572	15.641
16	2	3	1	3	0.133	0.262	0.295	0.633	1.403	2.196
17	2	3	2	1	0.733	0.588	0.892	13.413	12.897	13.637
18	2	3	3	2	0.970	1.086	0.730	10.133	11.716	12.236

Figure 4 Main effects plot (MRR)
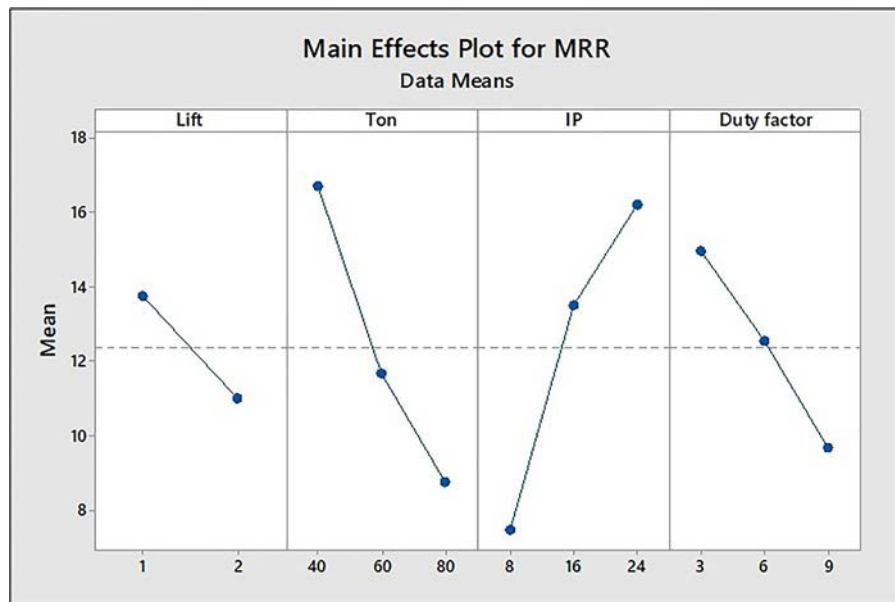
discussion, ANOVA assumptions are verified and not violated through these experiments, so ANOVA performed for inferences made will be valid.

Table 4 indicates the ANOVA table for MRR. It shows that lift, Ton, IP and duty factor have significant impact on MRR. In addition, their interaction also indicates p-value less than 0.05; thus, null hypothesis should be rejected, and the effects of relevant parameter held accountable.

Table 5 shows the ANOVA table for tool wear rate. Lift, Ton and IP have a substantial effect over tool wear. It was deduced that, the interaction of lift and Ton and lift and IP shows major effect over TWR; duty factor and interaction of Ton and IP have no effect on tool wear.

2.2.1 Regression analysis
Regression analysis was performed to find out the relationship between variable factors and output characteristics. Equation 3 represents the derived regression equation for MRR as follows:

$$MRR = 21.75 - 3.62\ Lift - 0.2194\ Ton + 1.292\ IP$$
$$- 1.124\ Duty\ factor + 0.0810\ Lift \times Ton$$
$$- 0.2491\ Lift \times IP - 0.00624\ Ton \times IP \qquad (3)$$

Figure 5 Main effects plot of S/N ratios (MRR)
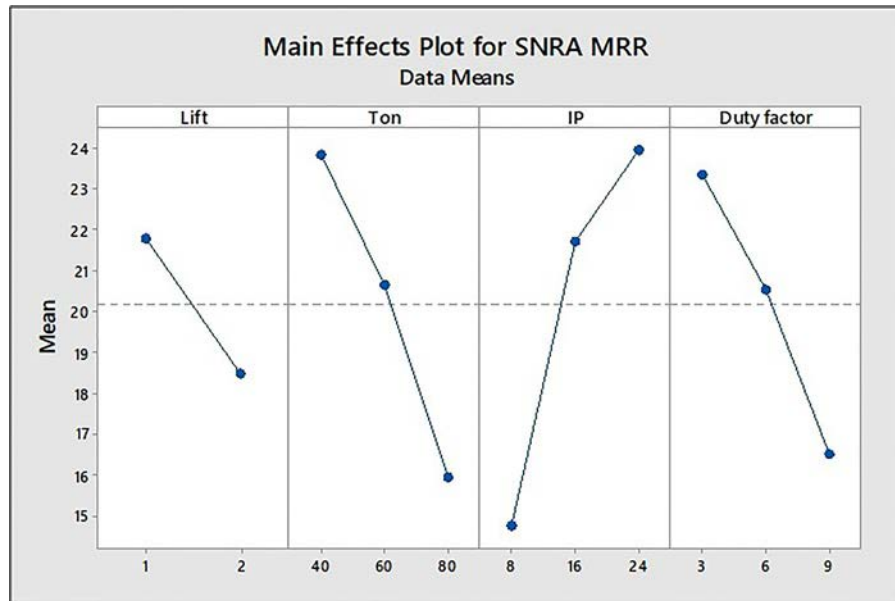
Figure 6 Main effects plot (TWR)
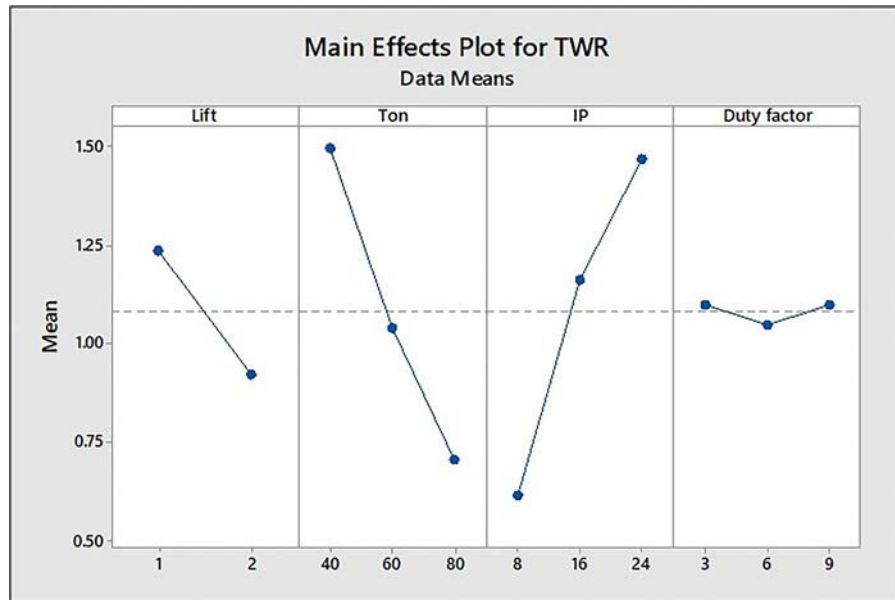
Table 6 shows the regression table indicating the values of R^2 and $R^2_{(adj.)}$. Both the values (R^2 and $R^2_{(adj.)}$) confirm that the model is fitted well. Further, ANOVA is conducted on the regression data and shown in Table 7. The p-value shows that the estimated model is significant at the 95% Cl.

Similarly, expression (4) derived for TWR is as follows:

$$TWR = 1.663 - 0.025 \ Lift - 0.02875 \ Ton + 0.1065 \ IP$$
$$- 0.0248 \ Duty \ factor + 0.00531 \ Lift \times Ton$$
$$- 0.03799 \ Lift \times IP + 0.000062 \ Ton \times IP \quad (4)$$

Table 8 shows the ANOVA coefficients of regression and their corresponding R^2 and $R^2_{(adj.)}$ values. Both the values were estimated close to 90%, which explains the lesser variance within and between the number of predictors in the model. The p-value shown in Table 9 indicated that the model fitted well within the 95% CI.

2.2.2. Signal to noise ratio analysis

SNRA is used to obtain the optimum condition. Application of Taguchi categories involves different response characteristics as higher the better (HB), lower the better (LB) and nominal the better (NB). In the present work, HB is selected to maximize the material removal, and LB is picked to minimize the tool wear. The solution to the said assumption is formulated in equations (5) and (6), respectively:

Figure 7 Main effects plot of S/N ratios (TWR)
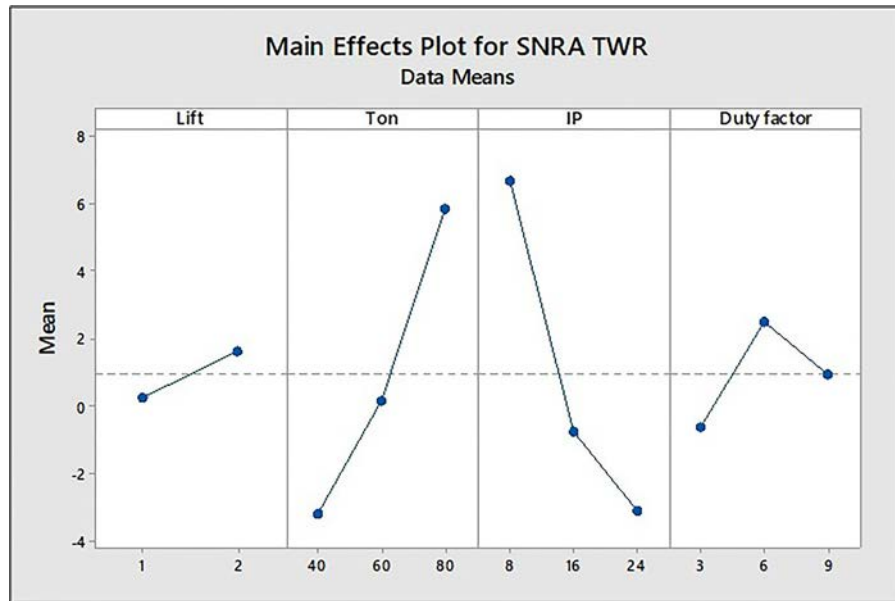
Figure 8 Probability plot of residuals (MRR)
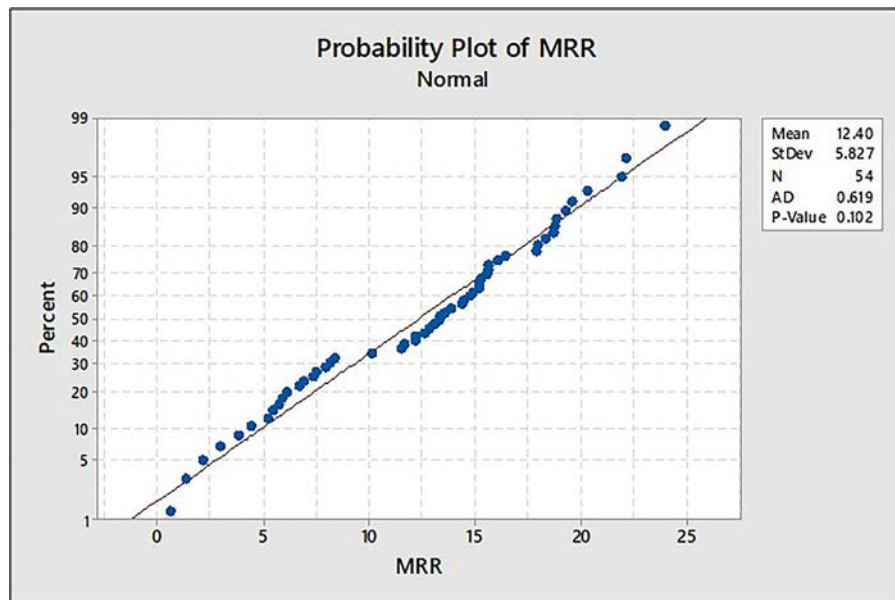
$$\eta_{HB} = -10\log\left[\frac{1}{n}\sum_{i=1}^{n}\left(\frac{1}{y_i^2}\right)\right] \quad (5)$$

$$\eta_{LB} = -10\log\left[\frac{1}{n}\sum_{i=1}^{n}y_{i^2}\right] \quad (6)$$

where η signifies the signal to noise ratio, y_i denotes the response value and n was the number of replications. Tables 10 and 11 show the signal to noise ratios obtained for material removal and tool wear for each parameter and their levels. The rationale of using the SNRA was to determine the order of parameters in which signals are predominant.

2.2.3 Jaya algorithm
Jaya algorithm is a nature-based algorithm that is used for obtaining the best value (closer to successes), and it moves from the worst values, i.e. avoid failure. This algorithm was developed by R. V Rao, which, being an advance algorithm, uses the regression equation as an objective function for minimization of TWR and minimization of MRR. The necessary requirement of this algorithm includes the number of machining parameters, the population size and the objective functions. The flowchart of the Jaya algorithm for curved hole machining is shown in Figure 12. TWR and MRR are optimized by minimizing and maximizing through "l" algorithmic iterations and assuming that there are m number of machining

Figure 9 Probability plot of residuals (TWR)
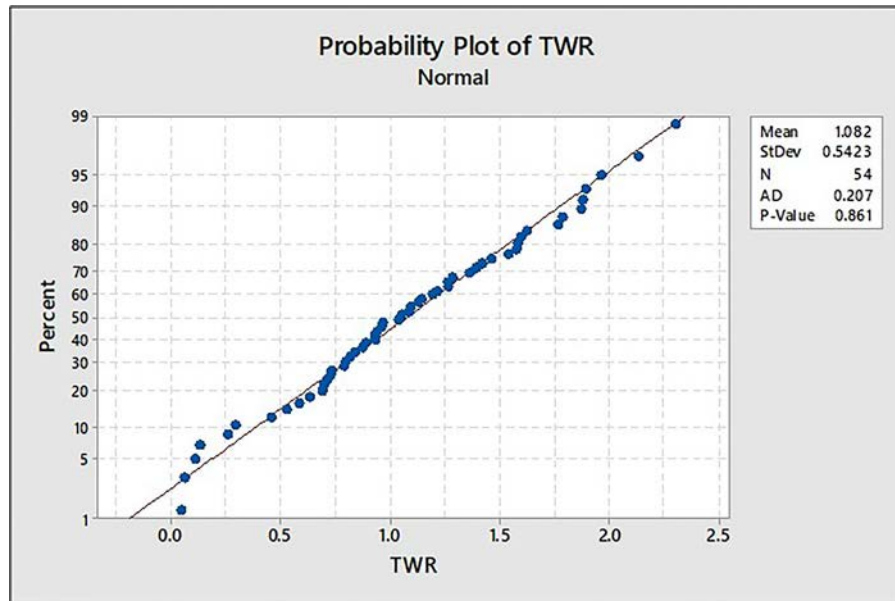
Figure 10 Plot of residuals versus fitted values (MRR)
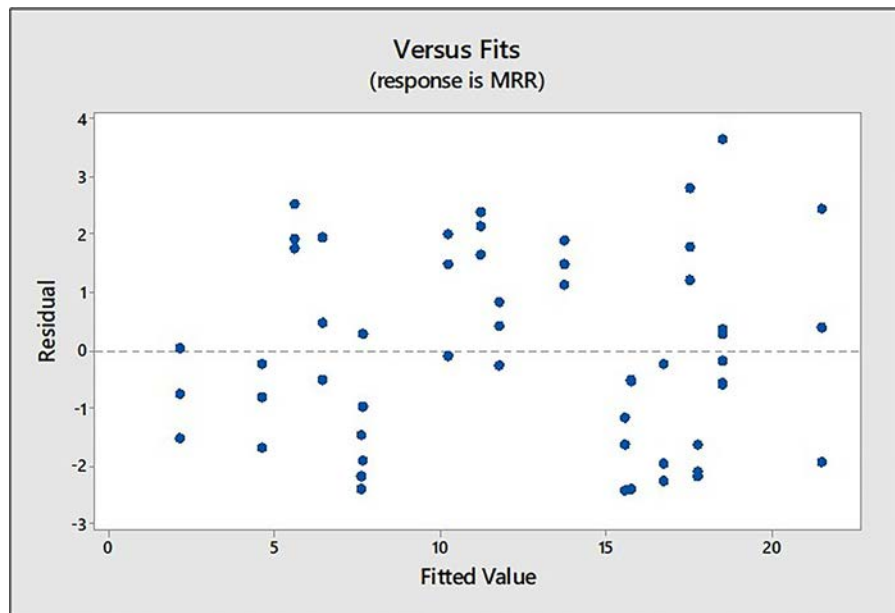
factors such as m = 1, 2…m (peak current, pulse on time, duty factor and lift) and n number of functional values ($n = 1,2…n$). The best objective function was found in the entire population and was represented as MRR-best, and the worst value is represented as MRR-worst. Next, assuming $E_{m,\,n,\,1}$ representing m^{th} factor for n^{th} population while running for l^{th} iteration factors, the algorithm may be mathematically represented as equation (8):

$$E'_{m,n,l} = E_{m,n,l} + r_{1,m,l}[(E_{m,best,l}) - E_{m,n,l}]$$
$$- r_{2,m,l}[(E_{m,worst,l}) - E_{m,n,l}] \qquad (8)$$

where $(E_{m,best,l})$ and $(E_{m,worst,l})$ are the best and worst values of the TWR or MRR, respectively, for the lth iteration with the machining factors. $E'_{m,n,l}$ is the iterated value of $E_{m,n,l}$, while $r_{1,m,l}$ and $r_{2,m,l}$ are two random number for m^{th} factor for the lth iteration between 0 and 1. Equation (8) was made of two sections; the first section, i.e. $E_{m,n,l} + r_{1,m,l}[(E_{m,best,l}) - |E_{m,n,l}|]$ representing closeness to the best solution, whereas second section $-r_{2,m,l}[(E_{m,worst,l}) - |E_{m,n,l}|]$ represents escaping from worst solution. $E'_{m,n,l}$ provided the optimized value for objective function for agreement; otherwise, $E_{m,n,l}$ was held as it is. For the next iteration, all accepted function

Jaya optimization for performance improvement
Diwesh Babruwan Meshram et al.

World Journal of Engineering

Figure 11 Plot of residuals versus fitted values (TWR)
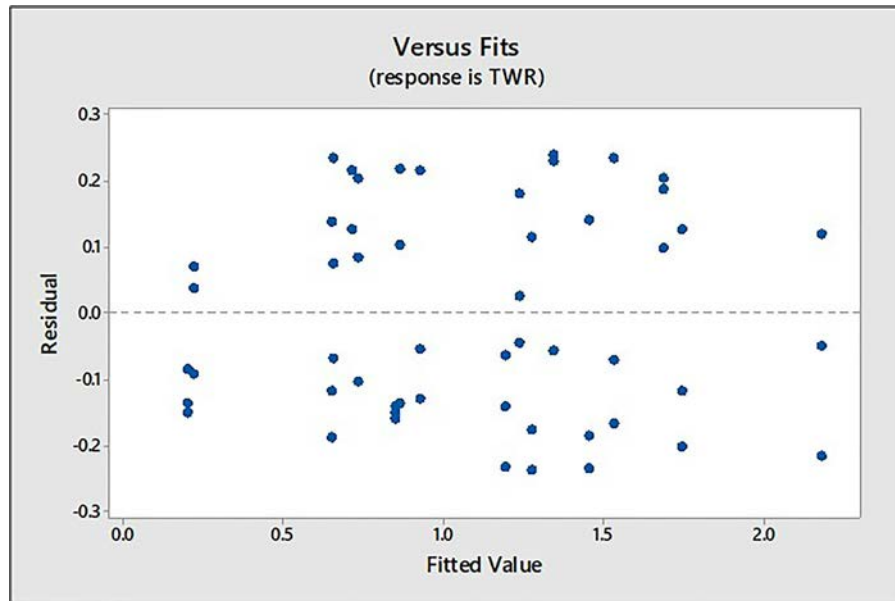
Table 4 ANOVA (MRR)

Source	DF	Adjusted SS	Adjusted MS	F-value	p-value
Lift	1	101.62	101.617	73.91	0.000
Ton	2	576.58	288.288	209.69	0.000
IP	2	713.89	356.946	259.63	0.000
Duty factor	2	156.96	78.481	57.08	0.000
Lift × Ton	2	46.67	23.336	16.97	0.000
Lift × IP	2	20.25	10.125	7.36	0.002
Ton × IP	4	36.03	9.007	6.55	0.000
Error	38	52.24	1.375		
Total	53	1799.66			

Table 5 ANOVA (TWR)

Source	DF	Adjusted SS	Adjusted MS	F-value	p-value
Lift	1	1.3317	1.33168	64.94	0.000
Ton	2	5.6924	2.84619	138.80	0.000
IP	2	6.7099	3.35496	163.61	0.000
Duty factor	2	0.0544	0.02722	1.33	0.277
Lift × Ton	2	0.1975	0.09877	4.82	0.014
Lift × IP	2	0.4232	0.21162	10.32	0.000
Ton × IP	4	0.1314	0.03284	1.60	0.194
Error	38	0.7792	0.02051		
Total	53	15.5850			

Table 6 Regression analysis (MRR)

Term	Coefficient	SE coefficient	T-value	p-value
Constant	21.75	4.22	5.15	0.000
Lift	−3.62	2.29	−1.58	0.121
Ton	−0.2194	0.0603	−3.64	0.001
IP	1.292	0.214	6.04	0.000
Duty factor	−1.124	0.121	−9.31	0.000
Lift × Ton	0.0810	0.0294	2.76	0.008
Lift × IP	−0.2491	0.0862	−2.89	0.006
Ton × IP	−0.00624	0.00240	−2.60	0.013
$S = 1.76131$	$R^2 = 92.07\%$	$R^2_{(adj.)} = 90.86\%$		

Table 7 ANOVA for regression analysis (MRR)

Source	DF	Adjusted SS	Adjusted MS	F-value	p-value
Regression	7	1,656.96	236.708	76.30	0.000
Residual error	46	142.70	3.102		
Total	53	1,799.66			

Table 8 Regression analysis (TWR)

Term	Coefficient	SE coefficient	T-value	p-value
Constant	1.663	0.407	4.08	0.000
Lift	−0.025	0.221	−0.11	0.912
Ton	−0.02875	0.00581	−4.95	0.000
IP	0.1065	0.0206	5.16	0.000
Duty factor	−0.0248	0.0117	−2.13	0.039
Lift × Ton	0.00531	0.00283	1.87	0.067
Lift × IP	−0.03799	0.00832	−4.57	0.000
Ton × IP	0.000062	0.000232	0.27	0.790
$S = 0.169938$		$R^2 = 91.48\%$	$R^2_{(adj.)} = 90.18\%$	

values were considered as input. Random numbers explore broad search space in the context of input factor. $E_{m,n,l}$ gives the absolute value to the required solution, improving the algorithm further.

3. Results and discussion

3.1 Confirmation runs

Confirmation runs were the concluding stage wherein the validations for the results from design of experiments (DOE)

technique were obtained. In the present work, two fresh experimental runs were designed with combinations indicated in Tables 10 and 11. The two new experiments run were A1B1C3D1

and A2B3C1D2 and were conducted to obtain MRR and TWR, respectively. Once optimal level of parameters was obtained, the finishing stage is to forecast and validate progress of the output responses. The estimated signal to noise ratio η_{opt} was calculated as:

$$\eta_{opt} = \eta_m + \sum_{j=1}^{k} (\eta_j - \eta_m) \tag{9}$$

η_m = Overall mean of signal to noise ratio;
η_j = Mean of signal to noise ratio at optimum level; and
k = Number of main design parameters.

Table 9 ANOVA for regression analysis (TWR)

Source	DF	Adjusted SS	Adjusted MS	F-value	p-value
Regression	7	14.2565	2.03664	70.52	0.000
Residual error	46	1.3284	0.02888		
Total	53	15.5850			

Table 10 S/N ratios larger is better (MRR)

Level	Lift	Ton	IP	Duty factor
1	21.80	23.84	14.74	23.38
2	18.49	20.65	21.73	20.55
3		15.94	23.97	16.51
Delta	3.32	7.90	9.23	6.87
Rank	4	2	1	3

Table 11 S/N ratios larger is better (TWR)

Level	Lift	Ton	IP	Duty factor
1	0.2627	−3.1976	6.6726	−0.6197
2	1.6144	0.1571	−0.7634	2.4974
3		5.8562	−3.0935	0.9381
Delta	1.3517	9.0538	9.7661	3.1171
Rank	4	2	1	3

Figure 12 Flowchart for Jaya algorithm
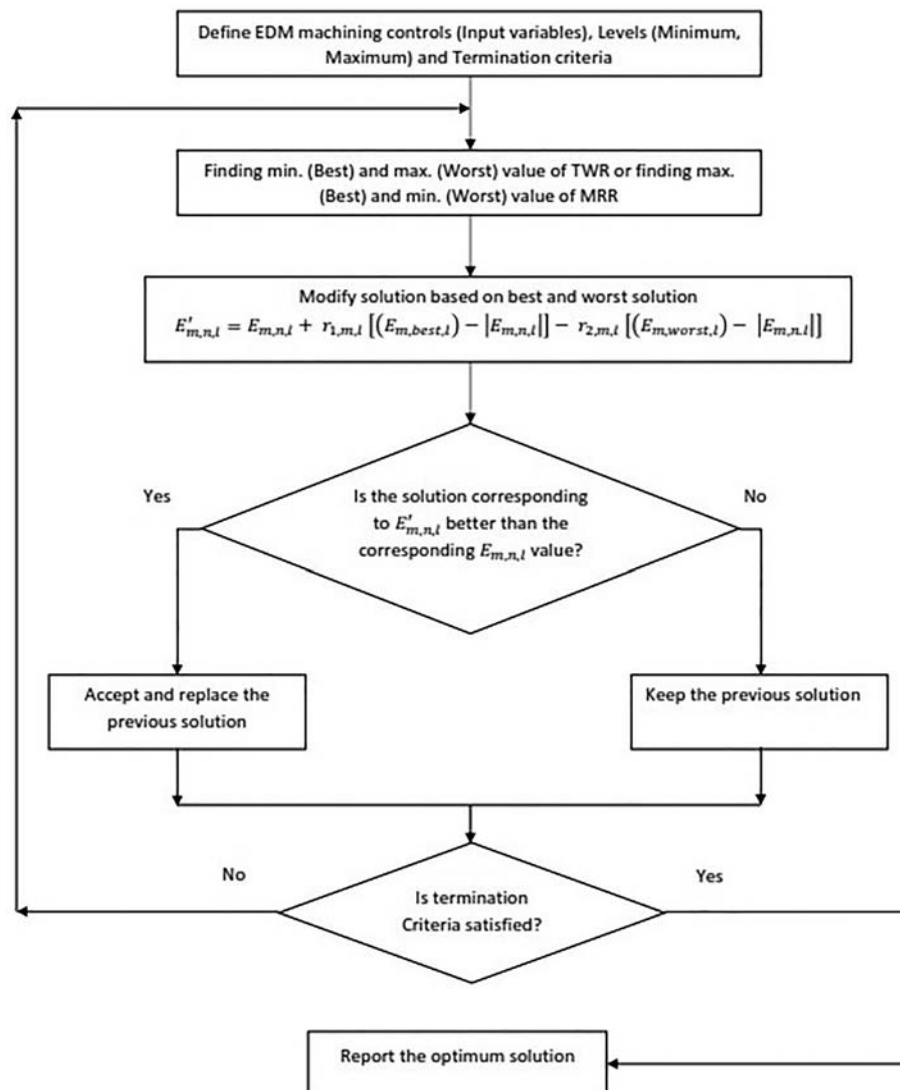
Table 12 Confirmation test outcomes (MRR and TWR)

		Optimal machining parameter		
Initial machining parameters		Prediction	Experiment	Improvement (%)
Levels	A2B2C2D2	A1B1C3D1	A1B1C3D1	
MRR (mg/min)	6.614	8.829	8.961	35.48
Levels	A2B2C2D2	A2B3C1D2	A2B3C1D2	
TWR (mg/min)	0.733	0.649	0.653	10.91

Figure 13 Response optimizer by Taguchi method

Figure 14 Response optimizer by regression model

The confirmation test results for MRR and TWR are shown in Table 12. The improvement in MRR and TWR is presented in Table 12. The test results are suitable and promises the efficiency of the Taguchi procedure for optimization.

3.2 Response optimizer
Further, the response optimizer was used to identify the optimum combination of input machining factors with the output responses through interactive plots. Figures 13 and 14

Table 13 Optimum values of control factors with machining response – TWR using Jaya algorithm

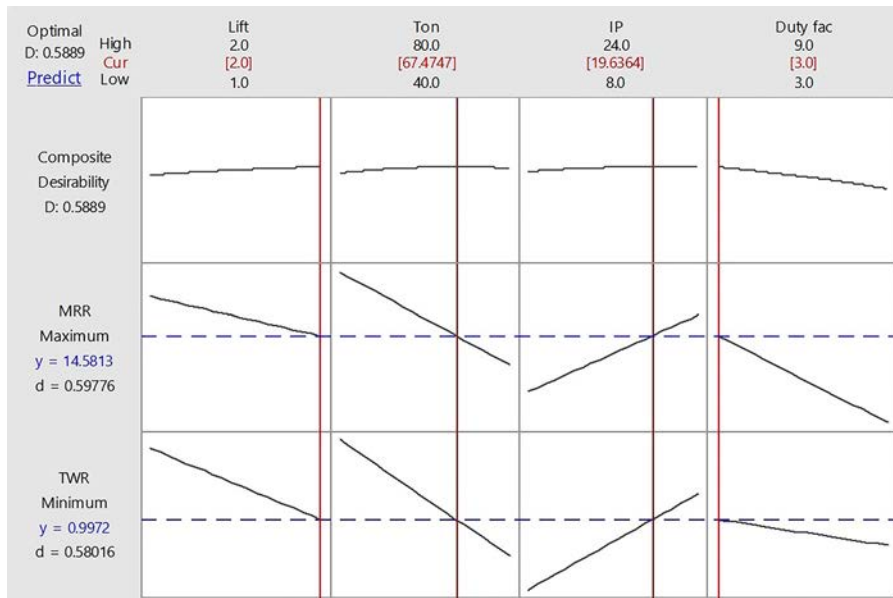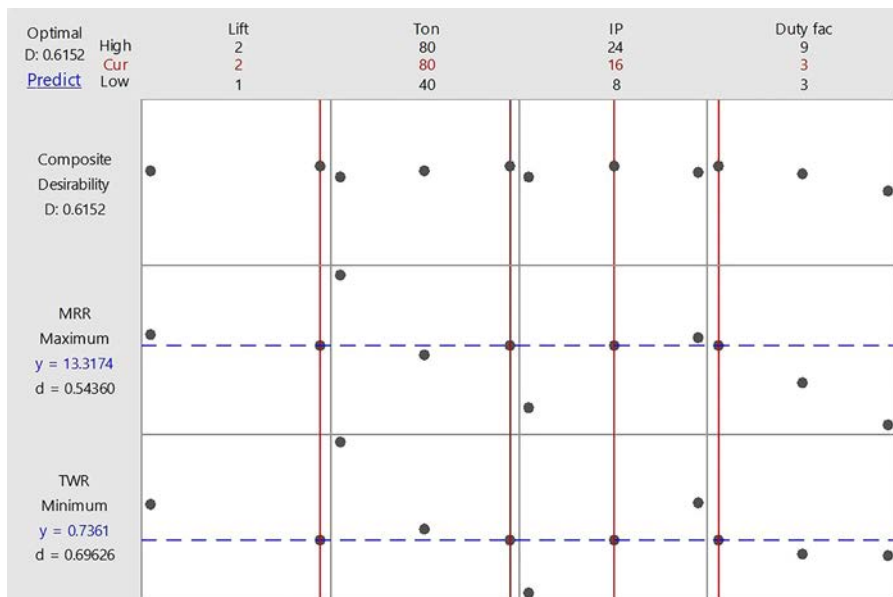| Sr. no.	Lift (Best)	Ton (Best)	IP (Best)	Duty factor (Best)	TWR (Best)	Sr. no.	Lift (Best)	Ton (Best)	IP (Best)	Duty factor (Best)	TWR (Best)
1	1.49	61.20	11.40	6.80	4.67	51	1.39	77.38	19.73	3.22	5.15
2	1.92	52.95	12.96	6.88	5.32	52	1.65	60.60	16.52	6.58	5.12
3	1.56	45.64	19.64	3.78	4.38	53	1.48	74.94	18.14	3.33	5.34
4	1.27	73.86	21.55	4.75	4.63	54	1.43	75.98	23.26	3.82	5.24
5	1.61	53.08	17.80	7.08	3.84	55	1.66	75.50	18.43	3.24	5.97
6	1.87	47.93	21.24	3.33	5.03	56	1.42	73.66	22.59	4.93	5.08
7	1.27	55.93	14.49	8.77	3.84	57	1.71	77.10	14.71	8.94	6.10
8	1.32	67.64	19.89	8.36	3.84	58	1.67	72.07	8.25	4.86	5.80
9	2.00	44.85	19.64	8.94	3.84	59	1.97	41.73	14.53	3.88	4.77
10	1.26	63.35	23.43	5.75	4.35	60	1.64	42.54	23.04	3.55	4.43
11	1.24	78.92	18.72	7.81	4.57	61	1.86	42.75	9.66	6.79	4.53
12	1.49	77.40	14.71	3.26	5.49	62	1.66	63.24	12.48	5.35	5.29
13	1.70	49.37	21.59	6.33	4.74	63	1.90	65.76	15.64	8.08	3.84
14	1.91	67.96	17.87	3.67	3.84	64	1.81	50.44	8.00	6.81	4.90
15	1.45	79.70	8.70	6.58	5.34	65	1.17	67.67	8.64	7.35	3.88
16	1.84	63.33	15.45	5.37	5.82	66	1.51	66.38	12.08	7.30	4.95
17	1.80	68.88	12.56	8.19	5.95	67	1.46	55.89	15.18	5.80	4.45
18	1.57	50.81	15.52	3.04	4.56	68	1.33	66.34	23.70	5.61	4.62
19	1.48	77.06	18.30	4.96	5.40	69	1.40	77.10	11.25	8.09	5.00
20	1.36	61.25	19.34	7.72	4.44	70	1.43	52.44	14.07	9.00	4.15
21	1.75	64.06	10.56	6.49	5.58	71	1.46	62.01	17.61	7.90	3.84
22	1.29	69.75	16.78	8.28	4.43	72	1.67	43.87	23.73	4.80	4.50
23	1.70	56.51	15.99	5.26	5.09	73	1.71	80.00	17.53	3.00	3.84
24	1.52	80.00	18.42	8.39	3.84	74	1.76	74.75	14.67	8.92	3.84
25	1.81	48.03	14.43	4.75	4.86	75	1.51	70.80	21.92	4.60	3.84
26	1.69	63.78	23.89	6.78	5.41	76	1.56	59.27	10.67	7.73	4.74
27	1.26	79.39	12.29	5.54	4.65	77	1.34	80.00	23.33	7.25	3.84
28	1.11	67.32	19.77	9.00	3.84	78	1.71	70.96	10.96	5.22	5.87
29	1.77	65.69	17.02	8.69	5.66	79	1.70	70.48	16.85	5.07	5.80
30	1.10	77.23	11.70	7.43	3.93	80	1.46	48.60	13.05	8.74	4.05
31	1.78	77.45	17.46	8.98	6.32	81	1.35	61.11	8.54	5.93	4.25
32	1.76	47.13	17.17	7.38	3.84	82	1.75	79.97	15.31	7.27	6.41
33	1.09	72.48	17.87	7.31	3.84	83	1.23	50.73	22.30	3.06	4.05
34	1.16	71.74	10.77	7.22	4.01	84	1.69	74.21	23.04	3.01	5.99
35	1.76	80.00	13.82	6.98	3.84	85	2.00	51.71	20.94	9.00	3.84
36	1.81	40.70	13.66	7.94	4.34	86	1.60	52.47	23.09	8.76	4.66
37	1.14	80.00	18.23	4.80	3.84	87	1.19	48.46	23.20	3.46	3.94
38	1.78	75.23	18.55	8.59	6.22	88	1.68	60.66	22.74	7.64	3.84
39	1.94	40.90	20.09	5.69	4.66	89	1.68	53.73	21.12	5.41	4.93
40	1.85	56.83	9.13	6.13	5.43	90	1.81	73.66	16.57	5.23	6.30
41	1.55	79.06	12.58	9.00	3.84	91	1.67	43.96	9.87	6.39	4.25
42	1.89	78.89	14.24	7.22	6.87	92	1.47	46.86	9.74	7.90	3.95
43	1.46	75.35	14.22	4.33	3.84	93	1.89	68.44	19.41	8.59	3.84
44	1.48	62.61	22.50	4.93	4.89	94	1.76	49.80	18.70	6.65	4.85
45	1.37	71.22	14.33	8.21	4.70	95	1.97	41.64	18.04	4.54	4.76
46	1.68	76.52	23.31	5.63	6.01	96	1.77	80.00	16.02	7.71	3.84
47	1.22	55.79	20.21	8.93	3.95	97	1.93	55.41	10.47	7.64	3.84
48	1.52	47.78	18.89	8.52	4.26	98	1.82	65.50	11.33	8.93	5.82
49	1.94	78.10	18.16	7.72	6.94	99	1.21	67.79	20.30	7.02	4.24
50	1.92	74.73	16.66	6.90	6.72	100	1.38	42.75	19.08	8.69	3.84

show the response plots by ANOVA and regression methods. The optimum combination per ANOVA are A = 2 μs, B = 80 μs, C = 16A and D = 3 with the maximum MRR = 13.134 (mg/min) and minimum TWR = 0.7361 (mg/min).

From the regression plots, the maximum MRR = 14.5813 (mg/min) and minimum TWR = 0.9972 mg/min with optimum combination being A = 2 μs, B = 67.4747 μs, C = 19.6364A and D = 3.

Table 14 Optimum values of control factors with machining response – MRR using Jaya algorithm

Sr. no.	Lift (Best)	Ton (Best)	IP (Best)	Duty Factor (Best)	TWR (Best)	Sr. no.	Lift (Best)	Ton (Best)	IP (Best)	Duty Factor (Best)	MRR (Best)
1	1.42	56.95	21.30	6.68	15.57	51	1.88	64.98	9.43	4.95	15.24
2	1.00	51.23	17.71	3.31	15.24	52	1.62	40.00	15.42	4.46	15.24
3	1.15	40.00	18.64	5.63	15.24	53	1.07	56.51	14.92	3.05	15.24
4	1.00	43.15	14.14	3.00	15.24	54	1.23	51.72	21.30	8.15	16.08
5	1.44	40.07	13.03	3.00	15.24	55	1.31	68.64	20.24	3.66	15.98
6	1.48	40.00	17.78	4.37	15.24	56	1.00	59.71	24.00	6.06	15.24
7	1.44	45.53	21.20	5.19	19.81	57	1.73	41.12	14.97	4.28	16.47
8	1.00	48.71	13.74	3.00	15.24	58	1.27	64.81	23.85	5.38	17.17
9	1.49	44.24	15.37	3.00	15.24	59	1.06	40.00	9.32	4.12	15.24
10	1.18	49.30	11.67	3.00	15.24	60	1.18	57.71	18.97	3.00	15.24
11	1.02	46.20	24.00	6.19	15.24	61	1.00	52.00	23.67	6.35	15.24
12	1.20	44.75	19.61	3.00	15.24	62	1.33	40.00	19.23	3.00	15.24
13	1.37	40.00	14.65	3.00	15.24	63	1.07	40.00	20.44	4.00	15.24
14	1.56	60.35	21.18	4.83	16.21	64	1.22	40.00	23.07	5.51	15.24
15	1.10	49.78	16.60	3.00	15.24	65	1.35	79.57	22.36	3.29	15.24
16	1.00	58.47	20.00	3.00	15.24	66	1.00	40.00	18.77	6.02	15.24
17	1.39	49.15	22.68	6.84	15.24	67	1.66	40.00	17.20	3.00	15.24
18	1.14	47.65	20.44	3.00	15.24	68	1.32	52.67	15.33	5.31	15.24
19	1.06	69.95	8.85	3.00	15.24	69	1.49	62.41	22.27	4.55	16.92
20	1.63	40.00	18.28	3.00	15.24	70	1.31	40.90	15.47	5.50	15.24
21	1.16	49.53	16.53	4.35	17.90	71	1.80	47.61	22.00	6.18	16.81
22	1.25	64.39	22.76	7.02	15.24	72	1.46	59.32	18.75	5.61	15.24
23	1.15	71.04	19.98	3.33	16.12	73	1.54	44.87	16.93	3.00	15.24
24	1.13	40.00	20.31	3.67	15.24	74	1.13	45.07	24.00	5.66	15.24
25	1.00	42.08	23.68	3.00	15.24	75	1.40	52.69	22.87	6.88	17.40
26	1.01	44.61	22.30	3.00	15.24	76	1.01	51.70	20.68	4.06	15.24
27	1.24	40.00	12.35	3.00	15.24	77	1.17	40.00	15.41	3.19	15.24
28	1.04	40.00	22.22	5.96	15.24	78	1.49	70.33	15.07	3.00	15.24
29	1.50	40.80	20.75	3.00	15.24	79	1.25	42.07	20.05	4.42	21.67
30	1.70	57.83	19.09	6.26	15.24	80	1.00	69.54	22.46	3.52	15.24
31	1.64	62.29	13.98	6.80	15.24	81	1.00	55.96	16.40	3.00	15.24
32	1.18	40.00	18.46	3.00	15.24	82	1.02	40.00	14.79	7.23	15.24
33	1.00	69.31	13.32	3.00	15.24	83	1.15	80.00	19.65	8.27	15.24
34	1.59	57.19	23.48	7.12	15.49	84	1.05	66.41	24.00	3.32	15.24
35	1.00	76.34	19.21	5.12	15.24	85	1.81	40.00	21.69	5.01	15.24
36	1.09	40.00	15.86	3.59	15.24	86	1.70	46.35	10.86	3.00	15.24
37	1.00	66.81	19.33	3.00	15.24	87	1.50	43.34	20.39	4.37	15.24
38	1.11	40.00	12.02	5.99	15.24	88	1.10	40.87	21.50	3.14	25.33
39	1.54	40.00	17.29	3.00	15.24	89	1.00	40.00	14.48	7.61	15.24
40	1.32	52.93	18.33	3.26	15.24	90	1.00	66.05	19.81	3.33	15.24
41	1.18	61.56	24.00	6.92	15.24	91	1.27	58.43	20.78	5.52	16.85
42	1.00	69.57	15.78	3.00	15.24	92	1.16	46.62	18.38	4.93	15.24
43	1.39	58.80	19.67	4.51	16.75	93	1.54	80.00	20.74	3.00	15.24
44	1.15	43.70	17.59	5.47	18.81	94	1.06	60.87	24.00	7.34	15.24
45	1.07	50.77	24.00	8.00	15.24	95	1.00	55.36	16.34	4.41	15.24
46	1.41	40.86	22.55	5.30	21.88	96	1.50	43.15	24.00	7.16	15.24
47	1.51	53.85	19.00	3.00	15.24	97	1.21	52.64	18.54	3.92	15.24
48	1.47	50.04	16.90	3.54	15.24	98	1.25	74.80	20.23	4.13	15.24
49	1.27	46.92	13.50	4.85	15.24	99	1.00	46.74	24.00	3.00	15.24
50	1.98	48.03	24.00	7.36	15.24	100	1.07	52.37	13.16	4.35	15.24

3.3 Multi-objective Jaya optimization

From the estimated results, it was found that the optimized best and worst vales for minimization of TWR and maximization of MRR were 7.2531 (mg/min), 6.3298 (mg/min) and 24.5332 (mg/min), 20.0168 (mg/min), respectively. Total 100 iterations and 20 runs are required for obtaining the desired optimum value. Based on the iterations performed, the optimum values of machining parameters for TWR (3.8447 (mg/min)) were $A = 1.08572$ μs, $B = 40.69722$ μs, $C = 8.0046A$ and $D = 3.0000$. Further, the best values of MRR (25.3341 (mg/min)) were estimated based on the machining factors to be $A = 1.98152$ μs, $B = 80.00002 \mu$s, $C = 24.0000A$ and $D = 8.2666$. Tables 13 and 14 show the estimated optimum values for the TWR and MRR, respectively.

## 3.4 Scanning electron microscope study for machined surface

The morphological analysis of curved hole machined is performed using an SEM machine (JEOL). It was found that the circular porous holes are observed for the eroded surface. The irregular grain structure and segregation effects of micro cracks were observed at $40\times$ magnification, as shown in Figure 15.

4. Conclusion

This paper presents a new concept of curve channel machining by EDM. An experimental setup was designed and developed to conduct experiments. The machining parameters were optimized to obtain higher MRR and lower TWR. The study was performed on AISI P20 mold steel because of its widespread applications in die and mold industry. On the basis of the experimental investigation, the following results were drawn:

- The highest significant parameter affecting material removal was identified as lift, IP, Ton and DF.
- Optimal factor setting to maximize material removal were identified and revealed that the MRR was accelerated from 6.614 to 8.961 mg/min.
- Tool wear was considerably affected by IP, Ton and lift in order of their effect.
- TWR was improved from 0.733 to 0.653 mg/min, thus showing a decrease of 0.08 mg/min.
- These investigational outcomes confirmed that the optimization of parameter levels by means of Taguchi technique was successful.

Figure 15 SEM image for curved hole machining
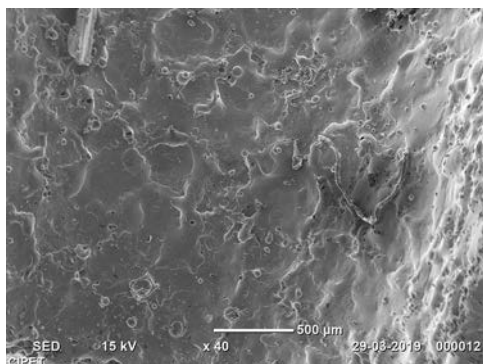
- In Minitab 17 statistical software, the response optimizer suggested that the estimated improvements in the TWR and MRR were found to be 92.16 and 85.42%, respectively.
- Jaya algorithm was successfully implemented for identifying the best optimum values for TWR and MRR along with the machining factors. (Maximum TWR= 7.2531 mg/min, maximum MRR= 24.5332 mg/min.)
- The workpiece material behavioral analysis of machined curved hole was studied by SEM.

References

Debnath, S., Rai, R.N. and Sastry, G.R.K. (2018), "A study of multiple regression analysis on die sinking EDM machining of Ex-Situ developed Al-4.5cu-Sic composite", *Materials Today: Proceedings*, Vol. 5 No. 2, pp. 5195-5201.

Dewangan, S., Biswas, C.K. and Gangopadhyay, S. (2014), "Influence of different tool electrode materials on EDMed surface integrity of AISI P20 tool steel", *Materials and Manufacturing Processes*, Vol. 29 Nos 11/12, pp. 1387-1394.

Fukui, M. and Kinoshita, N. (1989), "Developing a mole electric discharge digging machining", *CIRP Annals*, Vol. 38 No. 1, pp. 203-206.

Gohil, V. and Puri, Y.M. (2017), "Turning by electrical discharge machining: a review", *Proceedings of the Institution of Mechanical Engineers, Part B: Journal of Engineering Manufacture*, Vol. 231 No. 2, pp. 195-208.

Gohil, V. and Puri, Y.M. (2018), "Statistical analysis of material removal rate and surface roughness in electrical discharge turning of titanium alloy (Ti-6Al-4V)", *Proc IMechE, Proceedings of the Institution of Mechanical Engineers, Part B: Journal of Engineering Manufacture*, Vol. 232 No. 9, pp. 1603-1614.

Ishida, T. and Takeuchi, Y. (2002), "L-shaped curved hole creation by means of electrical discharge machining and an electrode curved motion generator", *The International Journal of Advanced Manufacturing Technology*, Vol. 19 No. 4, pp. 260-265.

Ishida, T. and Takeuchi, Y. (2008), "Creation of u-shaped and skewed holes by means of electrical discharge machining using an improved electrode curved motion generator", *International Journal of Automation Technology*, Vol. 2 No. 6, pp. 439-446.

Ishida, T., Kogure, S., Miyake, Y. and Takeuchi, Y. (2004), "Creation of long curved hole by means of electrical discharge machining using an in-pipe movable mechanism", *Journal of Materials Processing Technology*, Vol. 149 Nos 1/3, pp. 157-164.

Ishida, T., Nagasawa, H., Kita, M. and Takeuchi, Y. (2008), "Creation of cross-section changing hole with a hemisphere by means of electrical discharge machining", in Mitsuishi, M., Ueda, K. and Kimura, F. (Eds), *Manufacturing Systems and Technologies for the New Frontier*, Springer, London, pp. 365-368.

Kita, M., Ishida, T., Teramoto, K. and Takeuchi, Y. (2010), "Size reduction and performance improvement of automatic discharge gap controller for curved hole electrical discharge

machining", in Shirase, K. and Aoyagi S. (Eds), *Service Robotics and Mechatronics*, Springer, London, pp. 143-148.

Laxman, J. and Raj, K.G. (2015), "Mathematical modeling and analysis of EDM process parameters based on Taguchi design of experiments", *Journal of Physics: Conference Series*, Vol. 662, p. 12025.

Meshram, D.B. and Puri, Y.M. (2019), "Effective parametric analysis of machining curvature channel using semicircular curved copper electrode and OHNS steel workpiece through a novel curved EDM process", *Engineering Research Express*, Vol. 1 No. 1, p. 15014.

Meshram, D.B. and Puri, Y.M. (2020), "Optimized curved electrical discharge machining-based curvature channel", *Journal of the Brazilian Society of Mechanical Sciences and Engineering*, Vol. 42 No. 2, pp. 1-13.

Muthuramalingam, T. and Mohan, B. (2013), "Influence of discharge current pulse on machinability in electrical discharge machining", *Materials and Manufacturing Processes*, Vol. 28 No. 4, pp. 375-380.

Nakajima, T., Ishida, T., Kita, M., Teramoto, K. and Takeuchi, Y. (2008), "Development of curved hole machining method-size reduction of hole diameter", in Arai, E. and Arai, T. (Eds), *Mechatronics for Safety, Security and Dependability in a New Era*, Elsevier, New York, New York, NY, pp. 157-162.

Rao, R. (2016), "Jaya: a simple and new optimization algorithm for solving constrained and unconstrained optimization problems", *International Journal of Industrial Engineering Computations*, Vol. 7 No. 1, pp. 19-34.

Rao, R. (2019), *Jaya: an Advanced Optimization Algorithm and its Engineering Applications, International Journal of Industrial Engineering Computations*, Vol. 334, Springer International Publishing, Springer International Publishing AG, part of Springer Nature.

Sivam, S.P., Michaelraj, A.L., Kumar, S.S., Varahamoorthy, R. and Dinakaran, D. (2013), "Effects of electrical parameters, its interaction and tool geometry in electric discharge machining of titanium grade 5 alloy with graphite tool", *Proceedings of the Institution of Mechanical Engineers, Part B: Journal of Engineering Manufacture*, Vol. 227 No. 1, pp. 119-131.

Takeuchi, A. (2002), "A method to machine a curved tunnel with EDM", *International Journal of Electrical Machining*, Vol. 7, pp. 43-46.

Tamorim, F.L. and Weingaertner, W.L. (2005), "The influence of generator actuation mode and process parameters on the performance of finish EDM of a tool steel", *Journal of Materials Processing Technology*, Vol. 166 No. 3, pp. 411-416.

Further reading

Khachane, A. and Jatti, V. (2020), "Multi-objective optimization of EDM process parameters using Jaya algorithm combined with grey relational analysis, in Venkata Rao, R. and Taler, J. (Eds), *Advances in Intelligent Systems and Computing*, Vol. 949, Springer, Singapore, pp. 127-135.

Corresponding author

Diwesh Babruwan Meshram can be contacted at: diweshs@gmail.com

Effect of number of welding passes on the microstructure, mechanical and intergranular corrosion properties of 409M ferritic stainless steel

Sachin Ambade
Department of Mechanical Engineering, Yeshwantrao Chavan College of Engineering, Nagpur, India
Chetan Tembhurkar
Mechanical Engineering Department, Priyadarshini College of Engineering, Nagpur, India
Awanikumar Patil
Department of Metallurgical and Materials Engineering, Visvesvaraya National Institute of Technology, Nagpur, India, and
Diwesh Babruwan Meshram
Department of Mechanical Engineering, Visvesvaraya National Institute of Technology, Nagpur, India and
Department of Plastic technology, Central Institute of Petrochemicals Engineering and Technology, Korba, India

Abstract

Purpose – This paper aims to study the effect of number of welding passes on microstructure, mechanical and corrosion properties of 409 M ferritic stainless steel. Shielded metal arc welding (SMAW) process is used to weld two metal sheets of 409 M having 3 mm thickness as bead-on-plate with single, double and triple passes. Microstructures were observed at transverse section with the help of optical microscope and with increasing number of passes grain growth, and the width of heat-affected zone (HAZ) increases. The results of tensile tests revealed that as number of passes increases, there is reduction in tensile strength and ductility. Double loop electrochemical potentiokinetic reactivation (DL-EPR) test revealed that as number of passes increases, the degree of sensitization increases. This is due to the deposition of chromium carbides at the grain boundaries and the associated depletion of chromium.

Design/methodology/approach – Three welded plates of single, double and triple pass were welded by SMAW process. From three welded plates (single, double and triple passes), samples for microstructural examination were cut in transverse direction (perpendicular to welding direction) with the help of wire-cut electrical discharge machine (EDM). The welded plates were sliced using wire-cut EDM along transverse direction for preparing optical microscopy, tensile testing, microhardness and DL-EPR testing specimens.

Findings – From the microstructure, it was observed that the large grain growth, which is dendritic, and the structure become finer to increase in number of welding passes. As number of passes increases, the width of HAZ increases because of the higher temperature at the welded zone. The tensile strength decreases to increase the number of welding passes because of grain coarsening and chromium carbide precipitation in sensitized zone and wider HAZ. The maximum microhardness value was observed for single-pass weld as compared to double- and triple-pass welds because of the fast cooling rate. The degree of sensitization increases to increase the number of passes because of chromium carbide deposition at the grain boundaries.

Originality/value – The authors declare that the manuscript is original and not published elsewhere, and there is no conflict of interest to publish this manuscript.

Keywords 409M ferritic stainless steel, Shielded metal arc welding, Number of welding passes, Tensile test, Microhardness and degree of sensitization, Degree of sensitization, Microhardness

Paper type Research paper

1. Introduction

Ferritic stainless steels (FSS) are the most extensively used group of stainless steels because of their noble corrosion resistance compared to mild steel and is less expensive compared to

austenitic stainless steel (Lakshminarayanan et al., 2009a). AISI 409 M FSS primarily contains 0.03% C and 10.5% to 12.5% Cr apart from other elements (Lakshminarayanan et al., 2009b; Lakshminarayanan and Balasubramanian, 2012). The other elements such as 300 and 200 series stainless steel are known for their good resistance to corrosion in chloride environments (Lakshminarayanan and Balasubramanian, 2012; Du Toit and Van Niekerk, 2011). These elements are used for chemical processing equipment, solar water heaters, storage vessels and household appliances (Sathiya et al., 2007). Recently, 409 M FSS is a preferred choice to manufacture container and railway carriage and wagon (Vidyarthy and Dwivedi, 2017). For these applications, thin sheets require single-pass welding, and thick sheets require multi-pass welding. During multi-pass welding, the portion adjacent to weld joint, i.e. heat affected zone (HAZ), is heated as many times as the number of passes. Thus, it undergoes microstructural changes which were unlikely than from single pass welding. These microstructural changes alter mechanical properties and corrosion resistance. The grain coarsening takes place when the base metal is heated above a critical temperature (955°C), and due to rapid grain growth of the ferrite grains, which lacks ductility, and presence of small amount of martensite worsens the situation (Loto, 2019). Apart from this, chromium carbide precipitates at grain boundaries. The ASTM A763 and double loop electrochemical potentiokinetic reactivation (DL-EPR) tests are used to assess the intergranular corrosion behavior of 409 FSS (Scalise et al., 2014; Ramírez-López et al., 2017). The electrochemical impedance spectroscopy is a technique that is used to evaluate the electrochemical corrosion properties of 409 FSS (De Souza et al., 2017).

Cornelis et al. (Du Toit and Van Niekerk, 2011) welded AISI 409 FSS plates of 2 mm and 4 mm thickness plates by GTAW process. Authors observed that after testing for sensitization in 3.5% NaCl solution, the 2 mm plate observed sensitization at 0.1 to 0.25 kJ/mm heat input and for 4 mm thickness plate at heat input 0.2 to 0.9 kJ/mm. Gupta et al. (2019) welded 409 FSS with gas metal arc welding process using ER304L and ER308L fillers with heat inputs 0.3, 0.4 and 0.5 kJ/mm. Authors observed that the mechanical properties are superior for ER304L as compared to ER308L, and the grain size of weld metal was found to be minimum for 0.4 kJ/mm heat input. Lakshminarayanan et al. (2011) autogenously welded 409 M ferritic stainless by electron beam welded process. After experimentation, they found that there was change in microstructure as coarse ferrite grains were changed to fine equiaxed axial grains, and the mechanical properties obtained after welding were greater than the base metal. Several researchers have welded 409 M FSS by different welding processes, but the changes in microstructural, mechanical and corrosion properties were found better than the base metal. The single-pass welding changes the microstructure considerably as compared to double-pass welding. In multi-pass welding, HAZ is heated as many times as the number of welding passes. Each heating cycle can cause considerable changes in the microstructure and, consequently, considerable changes in the material properties. So, the present investigation aims to study the effect of number of welding passes on microstructure, mechanical and intergranular corrosion properties.

2. Materials and methods

The FSS (AISI 409 M) referred to as test steel, hereafter, was purchased from local market in form of 3 mm thick sheet. Its chemical composition was presented in Table 1.

Three plates of dimension $150 \times 100 \times 3 \text{ mm}^3$ (length $\times$ width $\times$ thickness) were cut from the material with the help of electrical discharge machine (EDM). These plates were given bead-on-plate (BOP) welding by shielded metal arc welding. Welding electrode E-308L of 3.15 mm diameter was used. To remove moisture, electrode was baked at 250°C in an oven for 45 min prior to welding. One to three passes welding were carried out at a constant speed by WPS-01certified welder. After each pass, 2 min rest was given to remove the slag and to change the electrode; in these, 2 min-weld joint cooled down considerably. The heat input (HI) of welding of all three passes was computed using equation (1). The welding parameters were presented in Table 2.

$$\text{HI} = (\eta \text{VI} / \text{w}) \tag{1}$$

where "V" is arc voltage, "I" is welding current, "w" is welding speed and "η" is welding efficiency and was taken as 0.7 (Ambade et al., 2020).

Three welded plates of single, double and triple pass were shown in Figure 1. From three welded plates (single, double and triple passes), samples for microstructural examination were cut in transverse direction (perpendicular to welding direction) with the help of wire-cut EDM. Precaution was taken to discard 5 mm part at the beginning and end of BOP weld. The samples were polished on series of wet polishing papers (180/320/400/600/800/1,200 grit) and finally polished on cloth smeared with alumina slurry (0.75 μm). The samples were electrolytically etched in 90% ethanol and 10% HCl for 30 s using a galvanostat (Solartron 1285). Microscopy was carried out on optical microscope (Zeiss Axiolab) at 200X magnification and scanning electron microscopy at 100X.

The welded plates were sliced using wire-cut EDM along transverse direction (perpendicular to welding direction) for preparing tensile testing specimens. For preparing tensile testing specimen, guidelines of ASTM E8 M-04 were followed as shown in Figure 2. The gauge lengths of tensile specimens were 50 mm, and they were broken in UTM (INSTRON 4467).

The fractured surfaces were examined using optical microscopy. DL-EPR tests used samples of dimension (10 mm $\times$ 10 mm). For electrical connection, the single-strand copper wire was soldered on copper strip of size 0.8 mm $\times$ 0.8 mm; then copper strip was pasted using silver paste on one surface of sample, and the other surface of sample was used for testing. The whole assembly was fixed in araldite solution. The sample of surface open was abraded on series of polishing paper (180 to 800 grit), and finally polished on cloth smear with 0.75 μm aluminum oxide (Al_2O_3) powder. A standard three-

Table 1 Chemical composition (Wt.%) of the FSS 409 M and electrode

Material	C	Si	Mn	P	S	Cr	Ni	Fe
409M FSS	0.043	0.52	0.327	0.029	0.003	11.607	0.136	Bal.
ER308L Filler	0.01	0.8	1.7	0.015	0.01	20.0	10.0	Bal.

Table 2 Welding parameter

Number of passes		Current (ampere)	Voltage (volts)	Efficiency(η)	Speed (mm/s)	Heat input (J/mm)
First	1st pass	90	22	0.7	3.21	431.78
Second	1st pass	90	22	0.7	3.21	431.73
	2nd pass	–	–	–	3.33	416.22
Third	1st pass	–	–	–	3.21	431.73
	2nd pass	90	22	0.7	3.33	416.22
	3rd pass	–	–	–	3.56	389.33

Figure 1 Welded plates for (a) single pass; (b) double pass and (c) triple pass
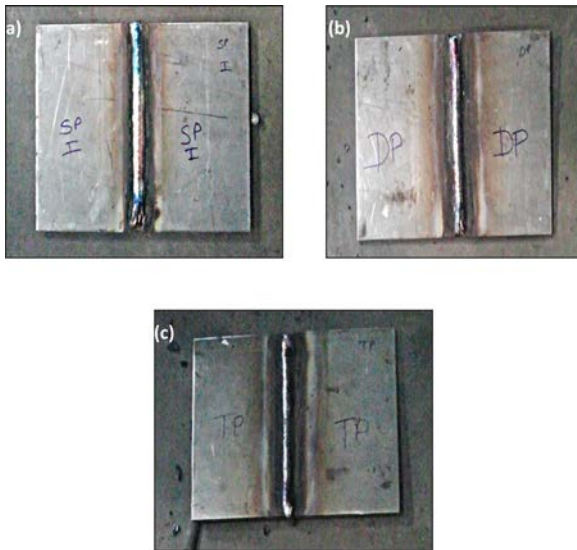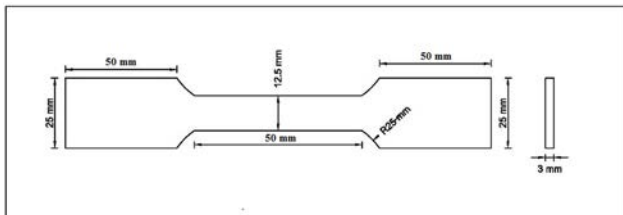

Figure 2 Tensile test specimen

electrode cell and cornered round-bottom flask with four necks was used for electrochemical tests. At room temperature, the DL-EPR tests were performed in test solution ($0.5\,M\,H_2SO_4 + 0.01\,M\,NH_4SCN$) using a potentiostat (Solartron-1285). Before start of DL-EPR test, the solutions were deaerated (oxygen free) by passing dry nitrogen gas for half an hour. The cell used working electrode (WE) as testing sample, counter electrode (CE) as platinum gauze electrode and reference electrode (RE) as saturated calomel electrode (SCE). In each DL-EPR test, testing specimens were electrostatically cleaned at $-1\,V$ (SCE) for 120 s, then permit time to attain constant open circuit potential (OCP) for 3,600 s. The DL-EPR tests were conducted at scan rate 1.667 mV/s. The potential range for forward scan was from $-650\,mV$ (SCE) to $+500\,mV$. The potential range for reversed scan was from $+500\,mV$ to $-650\,mV$ (SCE). The peak activation current density (I_a) was measured from forward scan and from reverse scan; the peak reactivation current density (I_r) was measured. Degree of sensitization (DOS) was evaluated from the ratio (I_r/I_a) $\times$ 100.

## 3. Results and discussion

3.1 Microstructural examination

Microstructure of test steel in as received (AR) condition is presented in Figure 3. It is obvious that test steel has single-phased microstructure. The microstructure shows well-grown grains. The structure is attributed to deformation by rolling during finishing stage of sheet production and appropriate mill annealing.

Microstructure of welded specimens from various zones and for single, double and triple passes are presented in Figures 4 and 5. In the weldment, the structure is dendritic and the structure becomes finer with increasing number of welding passes (Kolhe and Datta, 2008). It is attributed to more nuclei and consequently less growth of dendrites with increasing number of passes. In the area around fusion line, there is complete fusion between HAZ and weldment. In HAZ, there are bright and the dark areas,; there are features similar to martensitic or bainitic structures. In HAZ, grains become coarser with increasing number of passes.

Width of HAZ of welded specimens of all passes was measured optically and is presented in Table 3. It is seen that the width of the HAZ increased to increase the number of passes (Kolhe and Datta, 2008). It is attributed to higher temperature at welded zone. The higher temperature in welded

Figure 3 Microstructure of as received (AR) test steel

Figure 4 Optical micrograph of welded specimen
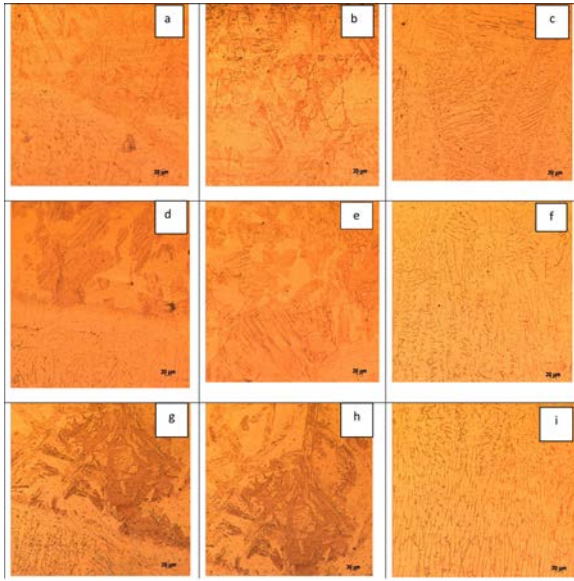
Notes: Single pass (a) interface: (b) HAZ: (c) fusion zone; Double pass (d) interface: (e) HAZ: (f) fusion zone; Triple pass (g) interface: (h) HAZ: (i) fusion zone.

Figure 5 SEM images of welded specimen at welded zone
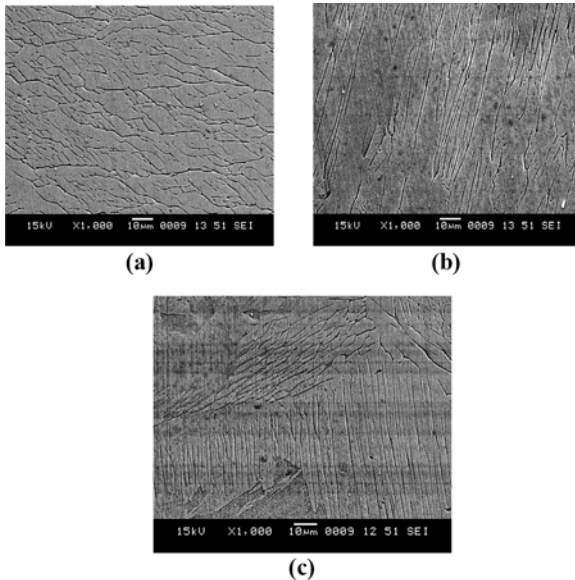
Notes: (a) Single pass; (b) double pass; (c) triple pass

zone allows more heat transfer by conduction for longer duration; as a consequence, the larger area is heated above critical temperature in triple-pass welding.

3.2 Tensile strength and fractography
The tensile strength of as received (AR) was 480 MPa and for single-, double- and triple-passes welding were observed as

Table 3 Width of HAZ

Welding passes	Passes	Heat input (J/mm)	HAZ (mm)
First	1st pass	431.73	3
Second	1st pass	431.73	5
	2nd pass	416.22	
Third	1st pass	431.73	8
	2nd pass	416.22	
	3rd pass	389.33	

441 MPa, 406 MPa and 362 MPa, respectively. Thus, it is evident that the tensile strength decreased as number of passes increased. This is due to the Creq/Nieq ratio, which leads to formation of chromium- (Cr) and nickel(Ni)-depleted region in the form of dendritic grain structure. It is also noted that all the tensile test samples failed at HAZ. This indicates that HAZ was the weakest portion of the tensile test specimen (Ahmed *et al.*, 2019). The decrease in tensile strength with increasing number of passes is attributed to grain coarsening and chromium carbide precipitation in sensitized zone and wider HAZ. Fractured surface of sample was examined in scanning electron microscopy (SEM). SEM fractography for single-, double- and triple-pass welding is shown in Figure 6. The fractured surface shows dimple structure. The dimple structure is associated with ductile fracture (Taiwade *et al.*, 2013). It was also seen that the size of dimple decreases as number of passes increased.

3.3 Micro hardness test
The microhardness was measured starting from the base metal and then across the HAZ. The variation in microhardness along the line for all passes is presented in Figure 7. It is evident that microhardness in HAZ area varies between 240 and 248 HV, 200 and 231 HV and 174 and 202 HV for single-,

Figure 6 SEM image of fractured surface of welded tensile test specimen
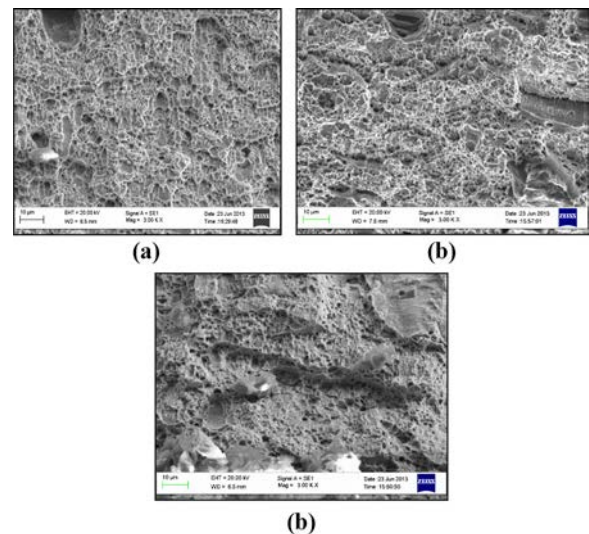
Notes: (a) Single; (b) double; (c) triple pass weld

Figure 7 Effect of number of passes on Vickers microhardness (HV 0.05, 20 s) as a function of distance from base to HAZ of welded plate

Figure 8 DL-EPR curve for various samples

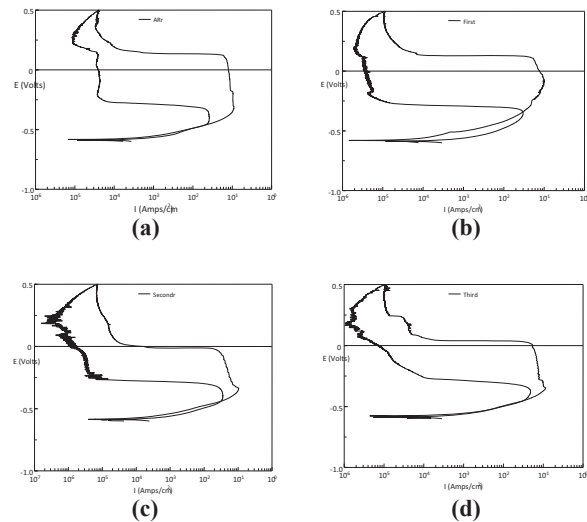**Notes:** (a) AR sample; (b) single pass; (c) double pass; (d) triple pass samples
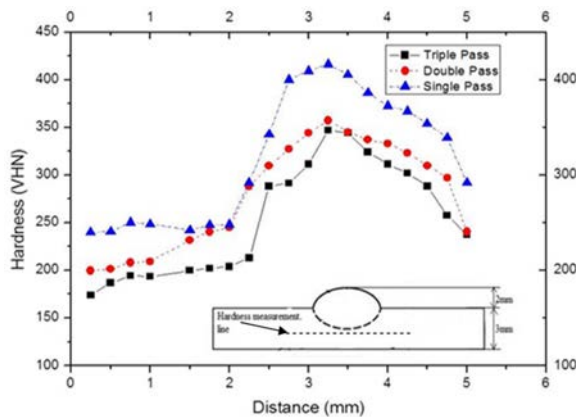
double- and triple-pass welding, respectively, whereas hardness of base metal is between 150 and 170 HV. It is evident that the base metal hardness increases slowly till it reaches HAZ (Lakshminarayanan *et al.*, 2009c). Then the microhardness in HAZ increases rapidly, and maximum microhardness was observed at a distance of 3.5 mm, i.e. close to fusion zone/HAZ interface. It was observed that the maximum hardness in HAZ is because of the formation of martensite in this zone (Lakshminarayanan and Balasubramanian, 2012; Doomra *et al.*, 2020). The maximum hardness of 416 HV was obtained for single pass, 358 HV for double pass and 347 HV for triple pass. A high heat input leads to more heating, higher temperature and heating for longer duration of heating. The coarser grains are responsible for lower hardness of HAZ in triple-pass weld (Taiwade *et al.*, 2013), and the grain size in the HAZ becomes coarser.

3.4 Double loop electrochemical potentiokinetic reactivation test

The DL-EPR tests were performed in test solution (0.5 M H_2SO_4 + 0.01 M NH_4SCN) using a potentiostat (Solartron-1285). Figure 8 shows DL-EPR curves for AR and HAZ sample of FSS welded with increasing number of passes. It is evident that both the activation (forward scan) and reactivation (reverse scan) part of the plot are very well defined. For the forward scan, the potential range will be −650 mV (SCE) to +500 mV. The potential range for reversed scan will be +500 mV to −650 mV (SCE). The peak activation current density (I_a) was measured from forward scan, and from reverse scan, the peak reactivation current density (I_r) was measured. DOS was evaluated from the ratio (I_r/I_a) × 100. The maximum current density was observed in forward and reverse scans and is derived from the plots and is presented in Table 4. It is evident from the per cent DOS values that degree of sensitization increased to increase the number of passes. This may be because of the martensitic formation (dark etched surface) in the microstructure as the number of passes increases, which increases the martensite formation, and it leads to the formation of chromium carbide precipitation in the HAZ (Lakshminarayanan *et al.*, 2011). As the temperature was increasing in the weld zone, the transformation of austenite to martensite takes place. The maximum amount of martensite

Table 4 Degree of sensitization of number of passes

Sample	Ia	Ir	DOS = Ir/Ia × 100 (%)
AR	0.1594	0.0261	15.96
First pass	0.1001	0.029617	29.61
Second pass	0.10319	0.035588	34.48
Triple pass	0.10998	0.048121	43.75

formation was observed at triple-pass welding. This is attributed to carbide deposition at grain boundaries due to welding heat (Lakshminarayanan and Balasubramanian, 2013). The carbide precipitation is associated with Cr depletion adjacent to grain boundary, and therefore, it becomes more sensitive to grain boundary attack (Ramírez-López *et al.*, 2017; Cavazos, 2006). The DOS increases with increasing number of welding passes and on increasing welding heat input (Amuda and Mridha, 2011).

It is evident that I_r value increases with increasing number of welding passes. I_r is indication of Cr-depleted area. The more Cr is depleted, the more will be I_r (Emun *et al.*, 2018). During double and triple pass, material is heated twice and thrice, respectively. This increases quality of Cr-carbide precipitation and thereby increases Cr-depleted area adjacent to grain boundary. It is evident that the per cent DOS increases with increasing number of passes (Taiwade *et al.*, 2013).

4. Conclusions

- From the microstructure, it was observed that the large grain growth, which is dendritic, and the structure become finer to increase the number of welding passes.
- As number of passes increases, the width of HAZ increased because of the higher temperature at the welded zone in which the transformation of austenite to martensite takes place.

- The tensile strength decreases to increase the number of welding passes because of grain coarsening and chromium carbide precipitation in sensitized zone and wider HAZ.
- The maximum microhardness value was observed for single-pass weld as compared to double- and triple-pass welds because of the fast cooling rate and the Cr- and Ni-depleted region.
- The degree of sensitization increases to increase the number of passes because of chromium carbide deposition at the grain boundaries.

References

Ahmed, M.M.Z., El-Sayed Seleman, M.M., Shazly, M., Attallah, M.M. and Ahmed, E. (2019), "Microstructural development and mechanical properties of friction stir welded ferritic stainless steel AISI 409", *Journal of Materials Engineering and Performance*, Vol. 28 No. 10, pp. 6391-6406, doi: 10.1007/s11665-019-04365-9.

Ambade, S., Sharma, A., Patil, A. and Puri, Y. (2020), "Effect of welding processes and heat input on corrosion behaviour of ferritic stainless steel 409M", *Mater. Today Proc*, No. xxxx, doi: 10.1016/j.matpr.2020.06.251.

Amuda, M.O.H. and Mridha, S. (2011), "Analysis of sensitization profile in medium chromium ferritic stainless steel (FSS) welds", *International Journal of Corrosion*, Vol. 2011 No. 1, pp. 17-22.

Cavazos, J.L. (2006), "Characterization of precipitates formed in a ferritic stainless steel stabilized with Zr and Ti additions", *Materials Characterization*, Vol. 56 No. 2, pp. 96-101.

De Souza, J.S., De Oliveira, L.A., Sayeg, I.J. and Antunes, R.A. (2017), "Electrochemical study of the AISI 409 ferritic stainless steel: passive film stability and pitting nucleation and growth", *Materials Research*, Vol. 20 No. 6, pp. 1669-1680.

Doomra, A., Sandhu, S.S. and Singh, B. (2020), "Effect of post weld heat treatment on metallurgical and mechanical properties of electron beam welded aisi 409 ferritic steel", *Metallurgical and Materials Engineering*, Vol. 26 No. 3, pp. 279-292.

Du Toit, M. and Van Niekerk, C.J. (2011), "Sensitization behaviour of 11-12% Cr AISI 409 stainless steel during low heat input welding", *J. South. African Inst. Min. Metall*, Vol. 111 No. 4, pp. 243-256.

Emun, Y., Quan, G., Kish, J. and Zurob, H. (2018), "Comparative corrosion evaluation of ferritic stainless steels utilized in automotive exhaust applications", *SAE Tech. Pap*, Vol. 2018–April No. July 2019,

Gupta, S.K.A.R., Raja, M., Vashista, M. Z. K. and Yusufzai, (2019), "Effect of heat input on microstructure and mechanical properties in gas metal arc welding of ferritic stainless steel", *Materials Research Express*, Vol. 6 No. 9, pp. 0-17.

Kolhe, K.P. and Datta, C.K. (2008), "Prediction of microstructure and mechanical properties of multipass SAW", *Journal of Materials Processing Technology*, Vol. 197 Nos 1/3, pp. 241-249.

Lakshminarayanan, A.K. and Balasubramanian, V. (2012), "Evaluation of microstructure and mechanical properties of laser beam welded AISI 409M grade ferritic stainless steel", *Journal of Iron and Steel Research International*, Vol. 19 No. 1, pp. 72-78, doi: 10.1016/S1006-706X(12)60050-8.

Lakshminarayanan, A.K. and Balasubramanian, V. (2013), "Use of DL-EPR test to assess sensitization resistance of AISI 409M grade ferritic stainless steel joints", *Journal of Materials Engineering and Performance*, Vol. 22 No. 8, pp. 2293-2303.

Lakshminarayanan, A.K., Balasubramanian, V. and Madhusudhan Reddy, G. (2011), "Microstructure and mechanical properties of electron beam-welded AISI 409M-grade ferritic stainless steel", *The International Journal of Advanced Manufacturing Technology*, Vol. 55 Nos 1/4, pp. 153-162.

Lakshminarayanan, A.K., Shanmugam, K. and Balasubramanian, V. (2009a), "Effect of autogenous arc welding processes on tensile and impact properties of ferritic stainless steel joints", *Journal of Iron and Steel Research International*, Vol. 16 No. 1, pp. 62-68, doi: 10.1016/S1006-706X(09)60012-1.

Lakshminarayanan, A.K., Shanmugam, K. and Balasubramanian, V. (2009c), "Effect of welding processes on tensile, impact, hardness and microstructure of joints made of AISI 409M FSS base metal and AISI 308L ASS filler metals", *Ironmaking & Steelmaking*, Vol. 36 No. 1, pp. 75-80.

Lakshminarayanan, A.K., Shanmugam, K. and Balasubramanian, V. (2009b), "Fatigue crack growth behavior of gas metal arc welded AISI 409 grade ferritic stainless steel joints", *Journal of Materials Engineering and Performance*, Vol. 18 No. 7, pp. 917-924.

Loto, R.T. (2019), "Effect of SO42− and Cl− anionic attack on the localized corrosion resistance and morphology of 409 ferritic stainless steel", *Results in Physics*, Vol. 12 No. October 2018, pp. 738-742, doi: 10.1016/j.rinp.2018.12.031.

Ramírez-López, M.C., Falcón-Franco, L.A., Curiel-López, F. F., Zambrano, R.P., Cabral-Miramontes, J.A., Gaona-Tiburcio, C. and Almeraya-Calderón, F. (2017), "Electrochemical reactivation of AISI 409 ferritic stainless steel sheet welded by laser process with application in aeronautical", *International Journal of Electrochemical Science*, Vol. 12 No. 6, pp. 4928-4939.

Sathiya, P., Aravindan, S. and Noorul Haq, A. (2007), "Effect of friction welding parameters on mechanical and metallurgical properties of ferritic stainless steel", *The International Journal of Advanced Manufacturing Technology*, Vol. 31 Nos 11/12, pp. 1076-1082.

Scalise, T.C., De Oliveira, M.C.L., Sayeg, I.J. and Antunes, R. A. (2014), "Sensitization behavior of type 409 ferritic stainless steel: confronting DL-EPR test and poractice W of ASTM A763", *Journal of Materials Engineering and Performance*, Vol. 23 No. 6, pp. 2164-2173.

Taiwade, R.V., Patil, A.P., Ghugal, R.D. and Patre, S.J. (2013), "Effect of welding passes on heat affected zone and tensile properties of AISI 304 stainless steel and chrome-manganese austenitic stainless steel", *ISIJ International*, Vol. 53 No. 1, pp. 102-109.

Vidyarthy, R.S. and Dwivedi, D.K. (2017), "Analysis of the corrosion behavior of an A-TIG welded SS 409 weld fusion zone", *Journal of Materials Engineering and Performance*, Vol. 26 No. 11, pp. 5375-5384.

Further reading

Chuaiphan, W. and Srijaroenpramong, L. (2014), "Journal of materials processing technology effect of welding speed on microstructures, mechanical properties and corrosion behavior of GTA-welded AISI 201 stainless steel sheets", *Journal of Materials Processing Technology*, Vol. 214 No. 2, pp. 402-408, doi: 10.1016/j.jmatprotec.2013.09.025.

Corresponding author
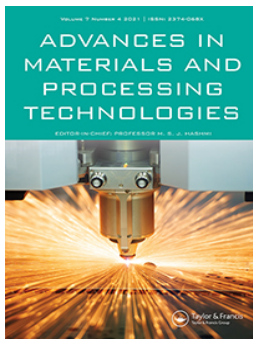
Sachin Ambade can be contacted at: sachinamb2@rediffmail.com

Experimental and finite element analysis of temperature distribution in 409 M ferritic stainless steel by TIG, MIG and SMAW welding processes

Sachin Ambade, Ravinder Kataria, Chetan Tembhurkar & Diwesh Meshram

Published online: 24 Jul 2022.

Submit your article to this journal ⟶

View related articles ⟶

View Crossmark data ⟶

Taylor & Francis
Taylor & Francis Group

Check for updates

Experimental and finite element analysis of temperature distribution in 409 M ferritic stainless steel by TIG, MIG and SMAW welding processes

Sachin Ambade [iD][a], Ravinder Kataria[b], Chetan Tembhurkar[c] and Diwesh Meshram [iD][d]

[a]Department of Mechanical Engineering, Yeshwantrao Chavan College of Engineering, Nagpur, India; [b]Department of Fashion Design, National Institute of Fashion Technology, Srinagar, India; [c]Department of Mechanical Engineering, Priyadarshini College of Engineering, Nagpur, India; [d]Department of Plastic Engineering, Central Institute of Plastics Engineering and Technology, Korba, India

ABSTRACT

In this study, three different arc welding processes, namely tungsten inert gas (TIG), metal inert gas (MIG) and shielded metal arc welding (SMAW) processes, are used to weld 409 M ferritic stainless steel. K-type thermocouples are located in the area of heat-affected zone by drilling blind holes in a plate at a distance of 3 mm and 7 mm from the weld line, revealing the contours of the temperature distribution of the weld. The experimental results are compared with the results of simulations using ANSYS by Goldak heat source model. The temperature is experimentally measured in the heat-affected region with the help of a thermocouple. The temperature distribution profile by the finite element method using ANSYS is compared with the experimental temperature distribution profile with the heat source. The experimental and simulation results for TIG, MIG and SMAW welding processes have been found to be excellent.

1. Introduction

Ferritic Stainless Steels (FSSs) contain 11–30% of Chromium (Cr) along with other alloying elements, especially molybdenum. The welding of the high-chrome FSSs has rapid grain growth at temperatures of more than 928°C [1]. The large grains absorb the smaller grains and grow more. The resulting thick grain structures are very sensitive to crack [2,3]. 409 M FSS can be used in various applications such as in automobile industries, shipbuilding industries, storage vessels, and so on [4]. 409 M FSS is becoming preferred choice in manufacturing of railway waggons and carriages [5,6]. The various researchers have simulated the welding process and compared with experimental results and observed a valuable solution to predict the thermal profile distribution in the weld.

Dean Deng et al. [7] welded modified 9Cr-1Mo steel pipes with three passes: first two by gas tungsten arc welding (GTAW) and one by gas metal arc welding (GMAW) by using TGS-9Cb and MGS-9Cb filler wire, respectively. The experimental and simulation

---

results are compared, and residual stresses are examined using ANSYS, which was utilised to determine the change in volumetric and yield strength in the material. For calculating the proportion of martensite and volumetric change during thermal expansion, ABAQUS codes were created. According to the results of simulation, change of volumetric and yield strength because of martensitic transformation has a great impact upon the residual strength of welding. Afzaal Malik et al. [8] welded low-carbon steel with GTAW. Goldak's heat source model was used to create Gaussian distributed moving heat source models, which disrupt the form and bounds of heat-affected zone (HAZ) and fusion zone (FZ). For 3D finite element simulations of the arc welding process, the authors employed APDL subroutines and MATLAB scripts to confirm the findings, which they compared to empirically. The results prove that welding speed, the parameters of total heat input and heat source affect the maximum temperatures in FZ and HAZ. Shanmugam NS et al. [9] used laser welding to weld T-joint of 304 ASS and the SYSWELD code used to describe the bead shape and thermal field during welding. The influence on welding was evaluated using different beam incidence angles of 30°, 45°, and 60°.The experimental results are compared to the simulation and it has been observed that there is a noble relationship between the experimental results and the simulation for bead width values and depth of penetration.

P Biswas, et al. [10] welded Cr Mn steel uses a two-sided fillet Submerged Arc Welding process and develops a 3D finite element model to move the distributed heat source and the results of simulation compared to the experimental results. The distributed heat source obtained after the simulation has almost a variation of 8% compared to the experimental results. The angular distortions are having a variation of 5 to 10% for the maximum distortions with experimental results. M. Abid et al. [11] simulated the single pass GMAW process by using the FE code ABAQUS and FORTRAN subroutine to predict the volumetric heat flux distribution using Goldak's double ellipsoidal heat source model. During pipe flange welding process in the HAZ of the pipe joints the temperature rises along the side of pipe relative to the values on the side of flange. A. H. Yaghi, et al. [12] fusion welded P92 steel pipe and simulation was carried out to find the residual stresses using ABAQUS. The findings of experimental temperature are compared to the finite element model using five thermocouples positioned at nodal positions on the pipe outer surface. Using the fusion zones in both the parent and deposited weld metal with experimental findings, it is discovered that the simulated results for the dispersed heat flux and the correctness of the results are verified.

In present investigation, the three welding processes, namely tungsten inert gas (TIG), metal inert gas (MIG) and shielded metal arc welding (SMAW), are used to weld 409 M FSS. The temperature is measured experimentally across heat affected zone with the help of thermocouples. The temperature distribution profile by finite element method using ANSYS are compared with the experimental temperature distribution profile along the heat source. The different researchers have compared single welding processes with the software's. But in this research, the three welding processes are compared with ANSYS software where this type of work has not been done previously.

2. Experimental work

2.1. Sample preparation

The dimensions of the sample are $300 \times 70 \times 3$ mm^3, as shown in Figure 1. The heat centre is moving perpendicular to the welding plate, with constant heating speed V. The three welding processes such as TIG, MIG and SMAW are performed. All welding process setup is arranged separately.

The chemical composition (% wt) of 409 M FSS is shown in Table 1. Tables 2 and 3 describe the welding parameters and Goldak heat source parameters, respectively.

The number of parameters b, c, a_f and a_r were designated for the shape of the power distribution. The data acquired for weld pool geometries from experiments and given good contract between real and modelled weld pool geometry as shown in Figure 2.

The K-type thermocouple is used to measure wide range of temperature. In the experiment, two K-type thermocouples of diameter 1.5 mm are used, fitted at blind drilled location of the plates as shown in Figure 3. The thermocouples are placed in HAZ at distances 3 and 7 mm from the weld line.

The temperature controller is used to visualise the temperature on or off welding processes with the help of K-type thermocouple. Temperature variation with time during welding is recorded by a video camera in the temperature controller.
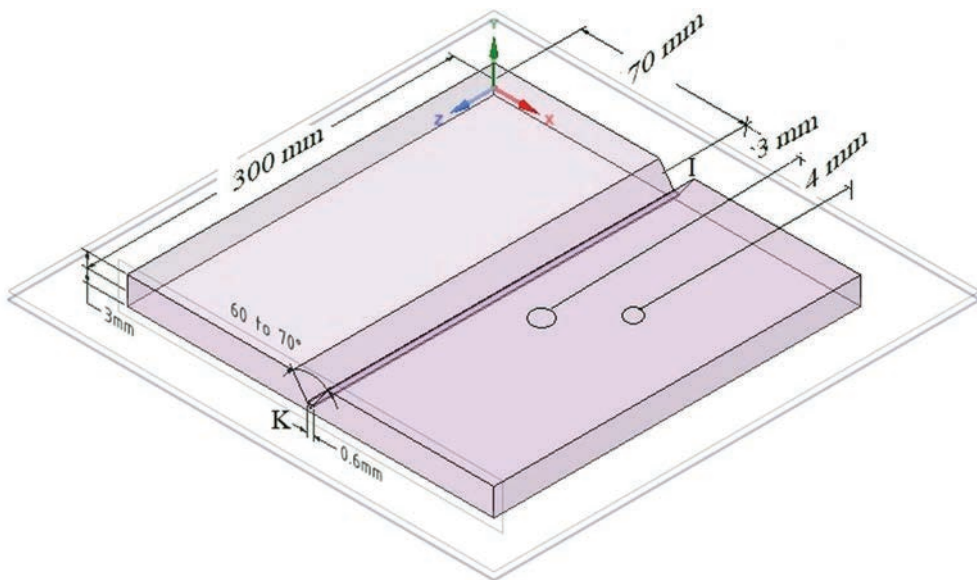
Figure 1. Schematic diagram of welding plate.

Table 1. Chemical composition (% wt) of 409 M FSS.

Sample	C%	Si%	Mn%	Cr%	Ni%	P%	S%	Nb%	Mo%	Al%	Cu%	Ti%	Fe%
409 M FSS	0.037	0.612	1.706	11.107	0.897	0.015	0.016	0.027	0.061	0.004	0.065	0.227	Bal.

Table 2. Parameter of welding process [13,14,18].

Welding Process	Current (I) (Ampere)	Voltage (V) (Volts)	Efficiency (η) (%)	Welding Speed (w) (mm/sec)	Heat input (H) = V × I × η / w (KJ/sec)
TIG	90	23	70	1.21	1.970
MIG	90	20	70	2.50	0.504
SMAW	90	24	70	3.00	0.504

Table 3. Goldak parameters of heat source.

Ellipsoidal Length		Heat Source		Fraction of Heat in Ellipsoidal	
Front (a$_f$) (mm)	Rear (a$_r$) (mm)	width (2b) (mm)	depth (c) (mm)	Front (f$_f$)	Rear (f$_r$)
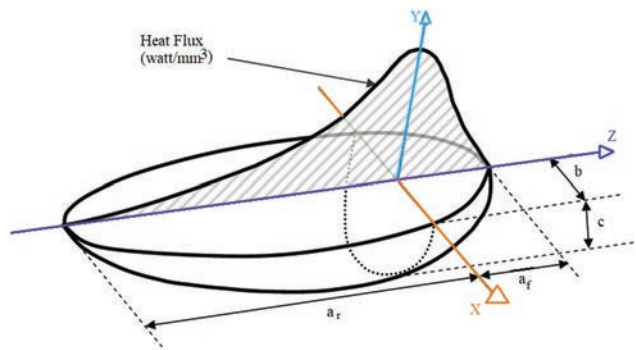
Figure 2. Goldak welding heat source model [27,28].

Figure 3. K-type thermocouple located at 3 mm and 7 mm from weld and temperature controller.

Figure 4. Element mesh.

2.2. Finite element analysis using ANSYS

The element mesh of the geometric model is shown in Figure 4. An element size of 1 mm is used in the heating zone, while 5 mm element size with spacing ratio 5 is used in the area far away from HAZ. Free mesh is performed in the middle zone. Finer meshes are adopted to study the effect of the mesh style on the result. In this case, three different element sizes 1 mm, 1.25 mm, 2.5 mm and 5 mm are modelled. All the elements are hexahedrons.

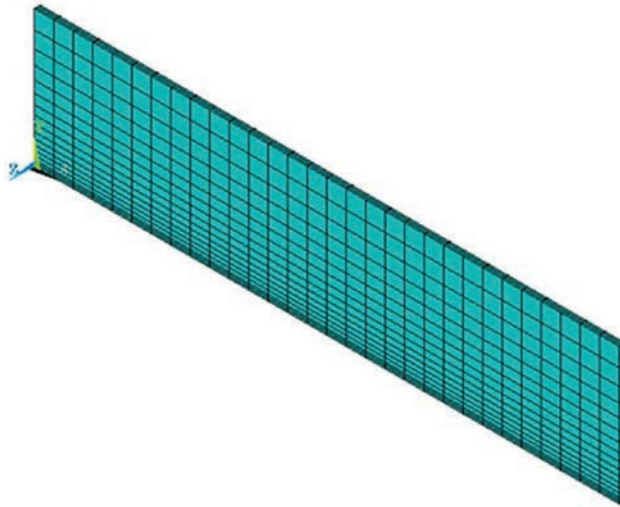The 3D finite element model was developed using ANSYS and used eight-noded, three-dimensional brick thermal element Solid 70. The structural analysis was carried out for the weld joint and the element Solid 70 can be automatically replaced by the equivalent structural element Solid 185 [15].

The birth and death technique was used in the ANSYS code where the death element effect does not actually remove the element, but first it was deactivated and birth element effect was obtained by reactivating the death element [16]. After converting the element type to structural type, proper boundary condition was applied.

2.3. Mechanical properties and boundary conditions

Once the element type is converted into structural type, proper structural boundary condition is supposed to be applied in the finite element model so that the structural analysis can be performed. The data are used in linear form. In this work, the welding process is simulated in ANSYS. The dimensions of the work piece are $300 \times 70 \times 3$ mm^3, as shown in Figure 1, in which the arc centre is moving along the x+ direction in line KI. The welding parameter performed in this work is varied with respect to the welding. The initial temperature is set to 28°C. Half of the model is created due to the symmetric properties of the plate geometry. Symmetric boundary condition is applied in the middle of the plate.

Twelve nodes at the bottom of the model which locate at the surface of plate except welding region are fixed in all degrees of freedom to avoid the rigid motion of the plate. While 12 more nodes in the other end with the corresponding locations are fixed as well.

2.4. Simulation approach in ANSYS

The quiet element technique is used in this work for the filler metal deposition. At the start, the nodal temperature of the filler metal elements is equal to the ambient temperature. The nodal constraints are removed at that time when the elements sequentially come under the influence of the heat source. The heat source is supposed to stay at least once on each element along the weld line for better computational results [17]. Equation 1 gives the appropriate time step used in the analysis to accomplish the task.

$$\text{Load step} = \frac{\text{Total Welding time (Sec)}}{\text{Number of Elements along the weld line}} \tag{1}$$

Therefore, a constant time step is used during the heating phase and the heat source moves with the specified welding speed quasi-stationary. However, the different time steps are used during the cooling phase. As the cooling of the weldment approaches to the ambient or equal to pre-heat temperature (if any), the time steps continuously increase.

3. Results and discussion

3.1. Experimental thermal profile of welding

The thermal profile is created by measurement of temperature through thermocouple with the help of temperature controller during welding at two points. One thermocouple is located at 3 mm perpendicular distance from the weld line and other one is located at 7 mm perpendicular distance from the weld line, but both points are 4 mm apart from
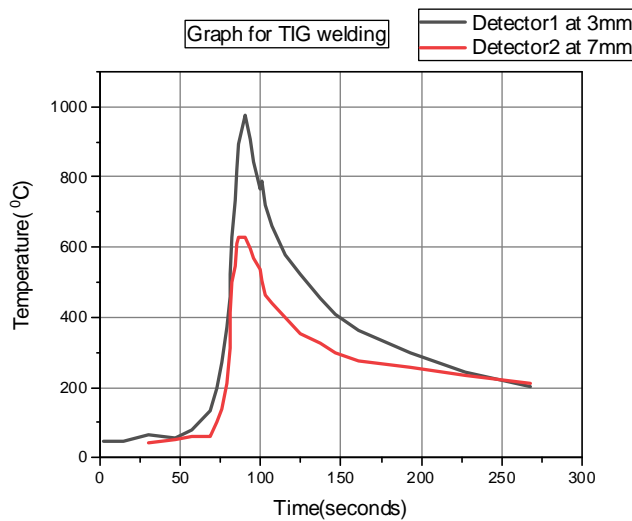
Figure 5. Experimental thermal profile of TIG welding.
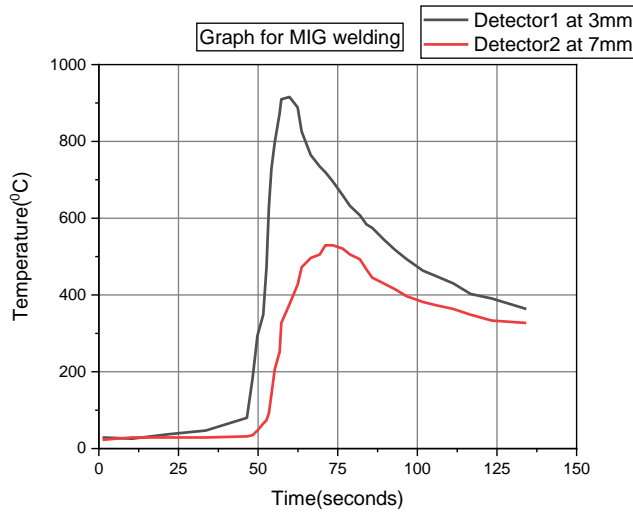
Figure 6. Experimental thermal profile of MIG welding.
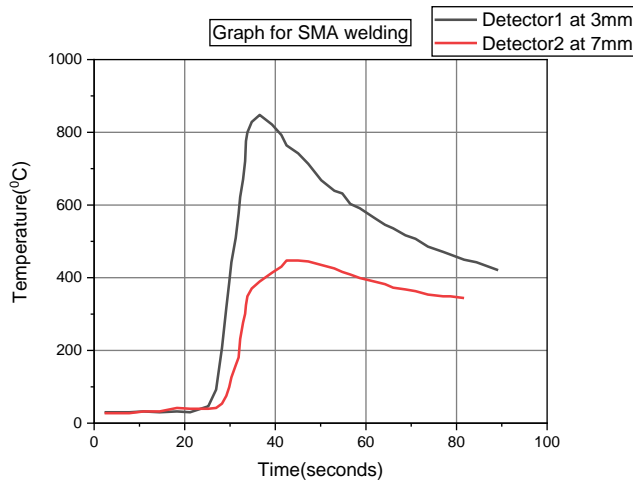
Figure 7. Experimental thermal profile of SMAW.

each other and in longitudinal direction at distances 150 and 145 mm from the start of the weld. Figures 5, 6 and 7 represent the experimental thermal profile of TIG, MIG and SMA welding, respectively.

The experimental thermal profile is created through data recorded between time and temperature which was measured by temperature controller during welding. For TIG, highest temperatures recorded by thermocouples were 998°C and 678°C at 3 mm and 7 mm distance from weld line, respectively, as shown in Figure 5. For MIG, the highest temperatures recorded were 910°C and 520°C at 3 mm and 7 mm distance from weld line, respectively, as shown in Figure 6. For SMAW, the highest temperatures recorded were 840°C and 430°C at 3 mm and 7 mm distance from weld line, respectively, as shown in Figure 7. It is observed that highest temperature was recorded for TIG by

thermocouples at 3 mm and 7 mm distance from weld line than MIG and SMAW. The mechanical properties of materials influence by heat input during welding processes [18–21]. The heat input for TIG welding is more as compared to MIG and SMAW as calculated in Table 2.

3.2. Thermal profile of welding by ANSYS

3.2.1. Tungsten inert gas welding

The Goldak double ellipsoidal heat source model along with quiet element technique for addition of filler metal is used for heat source and filler material modelling. The modelling of heat losses from the exposed surfaces by convection and radiation is considered in thermal analysis to predict the performance of TIG welding [22,23]. The combined heat transfer coefficient calculated and applied on all the applicable surfaces is 8.006 W m^{-2} k. The geometric parameters and joint geometry of two plates for welding by TIG process are shown in Tables 2 and 3, respectively.

The total heating time along the weld path of 300 mm with a torch speed of 1.21 mm/s is about 247.93 sec, and the complete welding sequence is divided into 30 load steps of 8.26 sec with equal space increment. For effective application of thermal load during the load step, the available stepped load option in ANSYS is used. And other additional four load steps of different time lengths are used for cooling of the weldment after extinguishing the arc. The total cooling time from the start of the cooling phase to the ambient temperature of 28°C is about 2850 sec (i.e. 47.5 minutes).

TIG welding, the temperature distribution along the plate of 300 mm at four varying times (16.68 sec, 125.1 sec, 241.86 sec and 2850 sec) as shown in Figure 8. The line adjacent to the welding line was found higher temperatures in the location of the heat source and found that the sudden temperatures rise before the heat source, were found in front of the flow heat source [24]. After the highest temperature reaches a certain point, the heat gradient behind the moving torch shows a cooling phenomenon. After cooling the temperature, distribution of weldment to almost uniform temperature is shown in Figure 8.

3.2.2. Metal inert gas welding

The Goldak double ellipsoidal heat source model along with quiet element technique for addition of filler metal is used for heat source and filler material modelling. The modelling of heat losses from the exposed surfaces by convection and radiation is considered in thermal analysis. The combined heat transfer coefficient is calculated and applied on all the applicable surfaces is 8.007 W m^{-2} k. The geometric parameters and joint geometry of two plates for welding by GMAW process are shown in Tables 2 and 3, respectively.

The total heating time along the weld path of 300 mm with a torch speed of 2.5 mm/s is about 120 sec, and the complete welding sequence is divided into 30 load steps of 4 sec with equal space increment. For effective application of thermal load during the load step, the available stepped load option in ANSYS is used. And other additional four load steps of different time lengths are used for cooling of the weldment after extinguishing the arc. The total cooling time from the start of the cooling phase to the ambient temperature of 28°C is about 2220 sec (i.e. 37 minutes).

(a) At time, t = 16.68 s

(b) At time, t = 125.1 s

(c) At time,t = 241.86 s
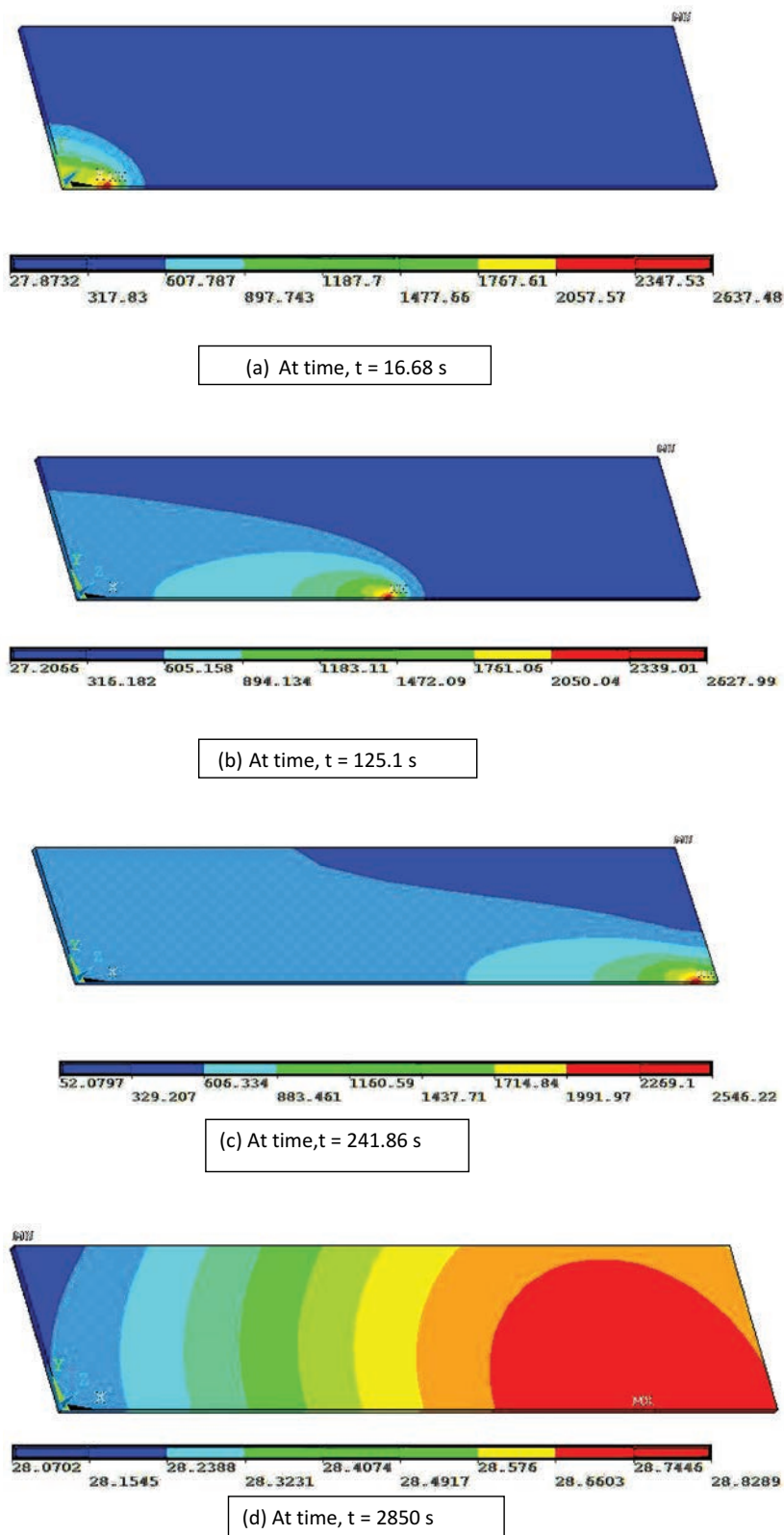

(d) At time, t = 2850 s

Figure 8. TIG welding process; the temperature profiles at four varying time steps.

Figure 9 shows the MIG welding process temperature distribution along a 300 mm plate at four different time intervals (8 sec, 60 sec, 116 sec, and 2340 sec). The highest temperatures of the weld line were found at the position of the heat source and sudden temperatures increase before the heat source was found in front of the smallest heat flow heat source. After the highest temperature reaches a certain point, the heat gradient behind the moving torch shows a cooling phenomenon. After cooling the temperature, distribution of weldment to almost uniform temperature is shown in Figure 9.

3.2.3. Shielded metal arc welding

The Goldak double ellipsoidal heat source model along with quiet element technique for addition of filler metal is used for heat source and filler material modelling. The modelling of heat losses from the exposed surfaces by convection and radiation is considered in thermal analysis. The combined heat transfer coefficient calculated and applied on all the applicable surfaces is 8.006 W m^{-2} k. The geometric parameters and joint geometry of two plates for welding by SMAW process are shown in Tables 2 and 3, respectively.

The total heating time along the weld path of 300 mm with a torch speed of 3 mm/s is about 100 sec, and the complete welding sequence is divided into 30 load steps of 3.34 sec with equal space increment. For effective application of thermal load during the load step, the available stepped load option in ANSYS is used. And other additional three load steps of different time lengths are used for cooling of the weldment after extinguishing the arc. The total cooling time from the start of the cooling phase to the ambient temperature of 28°C is about 2310 sec (i.e. 38.5 minutes).

Figure 10 shows, SMAW welding process the temperature distribution over the 300 mm plate at four different time intervals (8 sec, 60 sec, 116 sec, and 2340 sec). The highest temperatures of the weld line were found at the position of the heat source and sudden temperatures increase before the heat source was found in front of the smallest heat flow heat source. After the highest temperature reaches a certain point, the heat gradient behind the moving torch shows a cooling phenomenon [25]. After cooling the temperature, distribution of weldment to almost uniform temperature is shown in Figure 10.

3.3. Comparison of experimental results with finite element method

In Figure 11, Figure 12 and Figure 13, the experimental results are compared with simulation results performed by ANSYS and it shows good agreement between experimental results and finite element results of temperature distribution in welding. The results are compared at 3 mm and 7 mm away from the weld line along transverse direction of welding by three welding processes, i.e. TIG, MIG and SMAW. The temperature distribution relies on many parameters during welding which mostly affect the temperature distribution [26]. It is observed that in SMAW process, the required time for welding was less as compared to other two welding processes. The temperature distributions obtained through finite element analysis of MIG welding process and obtained from experimental measurements compared fairly well with a variation of only 10% for the peak temperatures as compared to TIG (15%) and SMA (18%) welding processes [10,27,28].

(b) At time, t = 60 s

(c) At time, t = 116 s

(d) At time, t = 2340 s
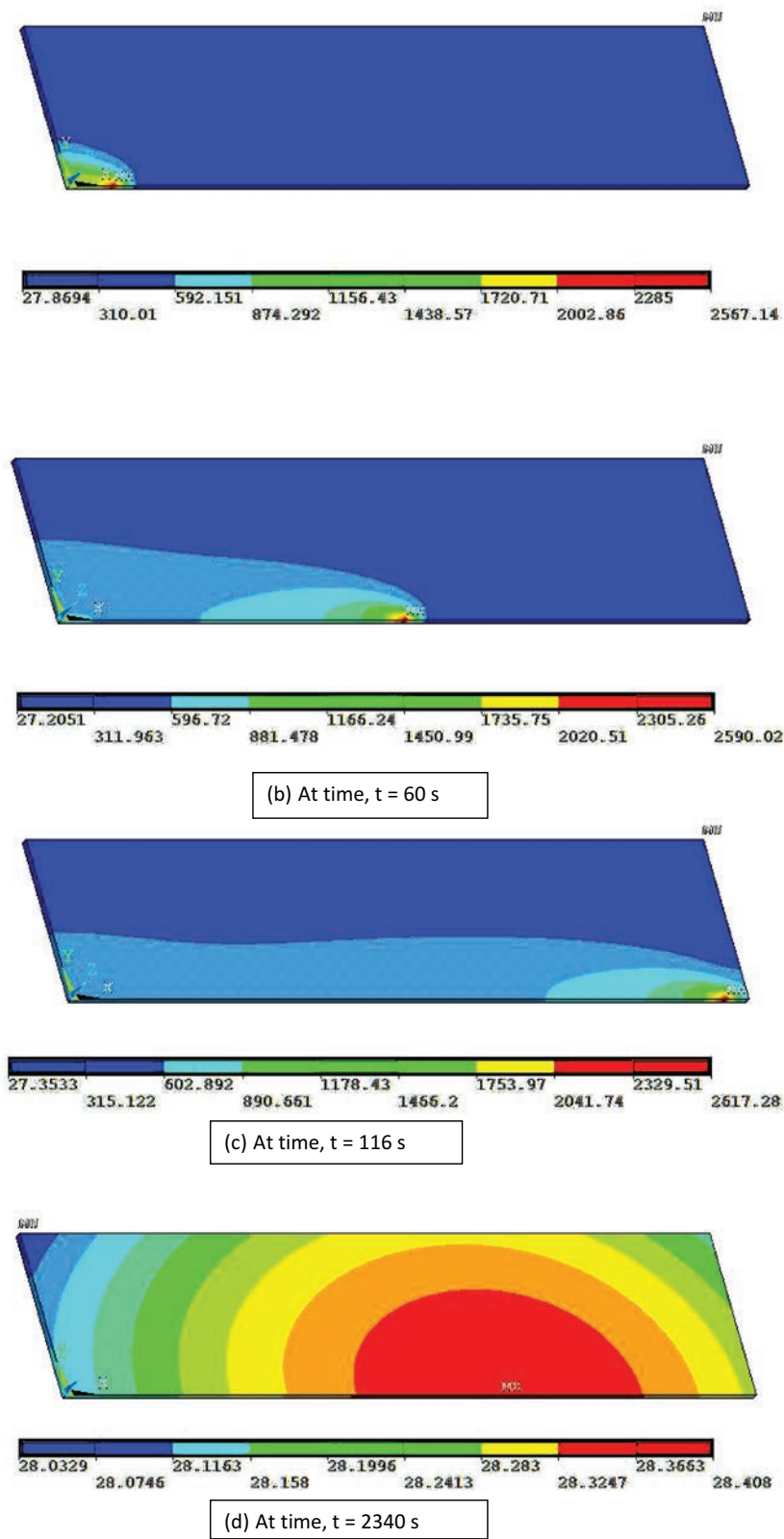
Figure 9. MIG welding process; the temperature profiles at four varying time steps.

(a) Time, t = 6.68 s

(b) Time, t = 50.1 s

(c) Time, t = 116 s

(d) Time, t = 2310 s
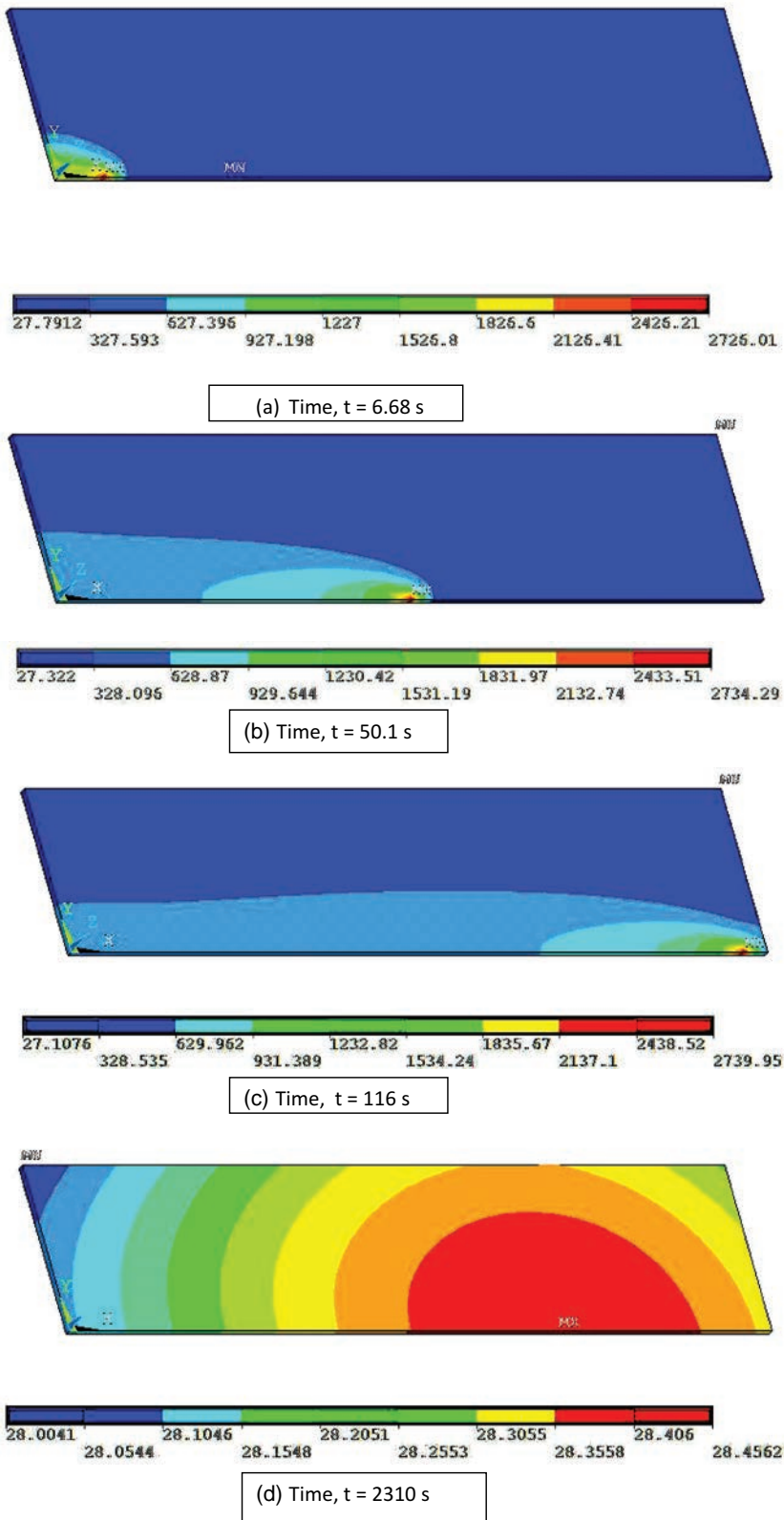
Figure 10. SMA welding process; the temperature profiles at four varying time steps.
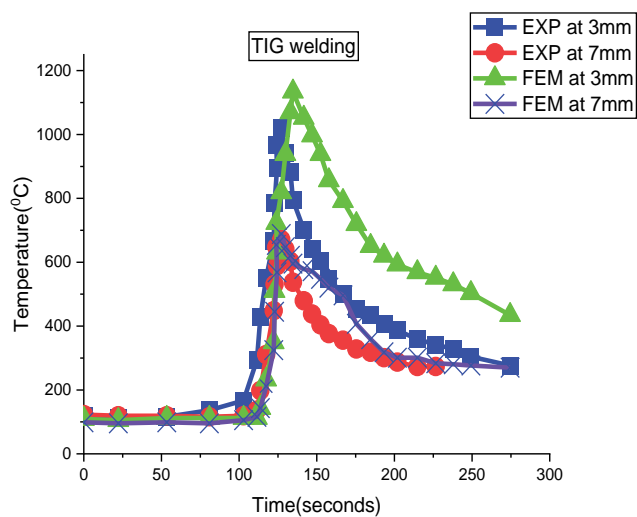
Figure 11. Comparison of temperature distribution in TIG.
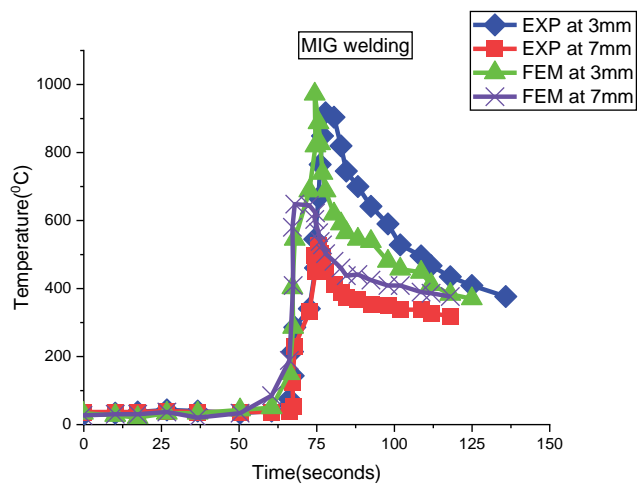
Figure 12. Comparison of temperature distribution in MIG.

4. Conclusions

The work is in consideration with three types of welding processes: GTAW, GMAW and SMAW. The temperature results from the finite element model are compared with the experimental temperature results.
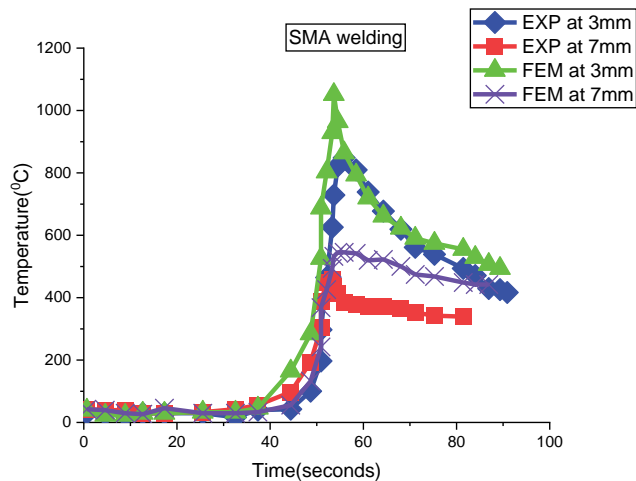
Figure 13. Comparison of temperature distribution of SMAW.

- The time required by welding processes in SMAW is 89 sec which is less than TIG (268 sec) and MIG which is 135 sec.
- From the simulation results, the time taken for heat source to start and end is less in SMAW (6.68–2310 sec) as compared to TIG (16.68–2850 sec) and MIG (8–2340 sec) welding processes.
- The weld temperature of TIG welding at 3 mm (998°C) and 7 mm (678°C) is highest as compared to the other welding processes.
- The experimental results are noble to the simulation results for TIG, MIG and SMAW welding processes.

Nomenclature

TIG	Tungsten inert gas
MIG	Metal inert gas
SMAW	Shielded metal arc welding
FEM	Finite element method
HAZ	Heat-affected zone
FZ	Fusion zone

Disclosure statement

No potential conflict of interest was reported by the author(s).

ORCID

Sachin Ambade http://orcid.org/0000-0002-2524-5798
Diwesh Meshram http://orcid.org/0000-0001-5584-3484

References

[1] Wang X, Song J, Sun M, et al. Microstructure and mechanical properties of 12 wt.% Cr ferritic stainless steel with Ti and Nb dual stabilization. Mater Des. 2009;30:49–56.
[2] Patra S, Ghosh A, Sood J, et al. Effect of coarse grain band on the ridging severity of 409L ferritic stainless steel. Mater Des. 2016;106:336–348.
[3] Lakshminarayanan AK, Shanmugam K, Balasubramanian V. Effect of welding processes on tensile and impact properties, hardness and microstructure of AISI 409M ferritic stainless joints fabricated by duplex stainless steel filler metal. J Iron Steel Res Int. 2009;16:66–72.
[4] Lakshminarayanan AK, Balasubramanian V. Understanding the parameters controlling friction stir welding of AISI 409M ferritic stainless steel. Met Mater Int. 2011;17:969–981.
[5] Weman K. . Welding processes handbook (Cambridge: Woodhead Publishing). 2012;.
[6] Hand book on stainless steel welding centre 2012.
[7] Deng D. FEM prediction of welding residual stress and distortion in carbon steel considering phase transformation effects. Mater Des. 2009;30:359–366.
[8] Malik MA, Qureshi ME, Dar NU. Numerical simulation of arc welding investigation of various process and heat source parameters. Fail Eng Mater Struct. 2007; 30:127–142
[9] Shanmugam NS, Buvanashekaran G, Sankaranarayanasamy K, et al. A transient finite element simulation of the temperature and bead profiles of T-joint laser welds. Mater Des. 2010;31:4528–4542.
[10] Biswas P, Mahapatra MM, Mandal NR. Numerical and experimental study on prediction of thermal history and residual deformation of double-sided fillet welding. Proc Inst Mech Eng Part B J Eng Manuf. 2010;224:125–134.
[11] Abid M, Qarni MJ. 3D Thermal finite element analysis of single pass girth welded low carbon steel pipe-flange joints. Turkish J Eng Environ Sci. 2009;33:281–293.
[12] Yaghi AH, Tanner DWJ, Hyde TH, et al. Finite element thermal analysis of the fusion welding of a P92 steel pipe. Mech Sci. 2012;3:33–42.
[13] Tembhurkar C, Kataria R, Ambade S, et al. Effect of fillers and autogenous welding on dissimilar welded 316L austenitic and 430 ferritic stainless steels. J Mater Eng Perform. 2021;30(2):1444–1453.
[14] Ambade S, Tembhurkar C, Patil A, et al. Effect of number of welding passes on the microstructure, mechanical and intergranular corrosion properties of 409M ferritic stainless steel. World J Eng. 2021. DOI:10.1108/wje-11-2020-0591
[15] Chen BQ, Hashemzadeh M, Guedes Soares C. Validation of numerical simulations with X-ray diffraction measurements of residual stress in butt-welded steel plates. Ships Offshore Struct. 2018;13:273–282.
[16] Darmadi DB, Tieu AK, Norrish J. A validated thermal model of bead-on-plate welding. Heat Mass Transfer. 2012;48:1219–1230.
[17] Ejaz Qureshi M, and Ullah Dar N. Numerical simulation of arc welding investigation of various process and heat source parameters. Failure of Engineering Materials & Structures, MED UET Taxila. 2007 30 127–142 .
[18] Lakshminarayanan AK, Shanmugam K, Balasubramanian V. Effect of welding processes on tensile, impact, hardness and microstructure of joints made of AISI 409M FSS base metal and AISI 308L ASS filler metals. Ironmaking Steelmaking. 2009;36(1):75–80.
[19] Das S, Vora J, Patel V, et al. Elucidating the effect of step cooling heat treatment on the properties of 2.25 Cr–1.0Mo steel welded with a combination of GMAW techniques incorporating metal- cored wires. Materials. 2021;14(20):6033.
[20] Brykov MN, Petryshynets I, Džupon M, et al. Microstructure and properties of heat affected zone in high-carbon steel after welding with fast cooling in water. Materials. 2020;13 (22):5059.
[21] Ambade S, Patil A, Tembhurkar C, et al. Effect of filler, autogenous and GTA welding on microstructure, mechanical and corrosion properties of low nickel Cr-Mn austenitic stainless steel. Adv Mater Process Technol. 2021; DOI:10.1080/2374068X.2021.1970989.

[22] Tomaz IDV, Colaço FHG, Sarfraz S, et al. Investigations on quality characteristics in gas tungsten arc welding process using artificial neural network integrated with genetic algorithm. Int J Adv Manuf Technol. 2021;113:3569–3583.

[23] Vora J, Patel VK, Srinivasan S, et al. Optimization of activated tungsten inert gas welding process parameters using heat transfer search algorithm: with experimental validation using case studies. Metals. 2021;11(6):981.

[24] Tembhurkar C, Kataria R, Ambade S, et al. Transient analysis of gta-welded austenitic and ferritic stainless steel. Lect Notes Mech Eng. 2020:59–65.

[25] Deogade SR, Ambade PSP, Patil A. Finite element analysis of residual stresses on ferritic stainless steel using shield metal arc welding. Int J Eng Res Gen Sci 2015;3:1131–1137.

[26] Vidyarthy RS, Dwivedi DK. Weldability evaluation of 409 FSS with A-TIG welding process. Mater Today Proc. 2019;18:3052–3060.

[27] Almeida DF, Martins RF, Cardoso JB. Numerical simulation of residual stresses induced by TIG butt-welding of thin plates made of AISI 316L stainless steel. Procedia Struct Integr. 2017;5:633–639.

[28] Goldak JA, and Akhlaghi M. A book of "Computational Welding Mechanics". Vol. XII (Springer) p. 321. 20 illus, Hardcover. 2005.

Document details - Optimization of green sand process for quality improvement in castings by using combination of Taguchi Techniques-GRA-PCA

- Export

- Download

- More...

Optimization of green sand process for quality improvement in castings by using combination of Taguchi Techniques-GRA-PCA(Article)

- Chaudhari, S.S.,

- Aloni, S.N.

- View Correspondence (jump link)

  - Yeshwantrao Chavan College of Engineering, Nagpur, 441110, India

Abstract

The castings produced by a sand casting process have multiple quality features. The quality of a casting always depends upon proper controlling of enormous parameters involved in the process as well as proper combination among these parameters, while some of the defects are found persisting and difficult to avoid. Controlling the process to avoid the rejections of cast components due to the presence of such persisting defects mainly depends on the right understanding of the parameters associated with it. In the work presented in this paper, the primary focus is on the optimization of essential parameters of the green sand process to minimize the occurrences of these persisting defects in gray iron automotive components through

experimental investigation using effective approach. The study applies the Taguchi's 'Design of Experiments' approach in combination with grey relational analysis (GRA) and principal component analysis (PCA) for determining the optimal level of parameters to minimize the defects Shrinkage porosity (SP), blowholes (BH), sand inclusion (SI), scabbing (SC) and low hardness (LH), which are persisting in the foundry industry producing cylinder heads and other castings required in the automotive, factory situated in central India. Optimal levels of parameters were determined by the single grey relational grade (GRG) obtained from GRA for overall improvement in multi-quality characteristics. PCA is used to determine the corresponding weighting values of each performance. The outcomes of this study assure that the approach used in this work, is useful to foundry industries to minimize the persisting casting defects. © 2022

Author keywords

Analysis of variance: ANOVAGreen sand processGrey relational analysis (GRA)Persisting casting defectsPrincipal component analysis (PCA)Process parametersTaguchi orthogonal array

Indexed keywords

Engineering controlled terms:	Design of experimentsFoundriesPrincipal component analysisProcess controlSar
Engineering uncontrolled terms	Casting defectGray relational analyseGreen sandGreen sand processGrey relatio defectPrincipal component analysePrincipal-component analysisProcess paramet
Engineering main heading:	Defects

Funding details

Document details - Performance evaluation of CNC turning process for tool tip temperature and tool wear by Taguchi method

- **1 of 1**

- Export
- Download
  - More...

Performance evaluation of CNC turning process for tool tip temperature and tool wear by Taguchi method(Article)

- Kamble, P.D.,
- Waghmare, A.C.,
- Askhedkar, R.D.,
- Sahare, S.B.,
- Patil, M.,
- Prayagi, S.V.
- View Correspondence (jump link)

- [a]Department of Mechanical Engineering, Yeshwantrao Chavan College of Engineering, Wanadongri 441110, Nagpur, India
- [b]Department of Mechanical Engineering, KDKCOE, Nagpur, India
- [c]Department of Mechanical Engineering, Ex-Professor, VNIT, Nagpur, India

[View additional affiliations](#)

Abstract

The performance of the CNC turning process is experimentally evaluated in this paper. The independent variables are feed rate, depth of cut, nose radius, tool type, and environmental condition. Three different levels of predictors are selected. The dependent variables are TTT (tool tip temperature) and TW (tool wear). The machine is run at 1337 RPM. The chatter in the spindle is included as an uncontrollable variable (Noise Factor) with three different values. The number of observations is calculated by Taguchi Method. The experimentation is conducted on CNC Spinner Lathe Machine. The responses are measured by a Non-contact laser gun and Canny Method in MATLAB software. The analysis is performed by Taguchi philosophy and ANOVA. The best setting for responses is identified by the main effect plot. The prediction of the output parameters at optimum levels is done by additive model. Minimum Tool Tip Temperature (50.545 °C) is achieved when Environmental condition is at high level (minimum quantity lubrication), Nose Radius is at low level (0.4 mm), Feed rate is

at low level (0.15 mm/rev), Depth of cut is at low level (0.5 mm) and tool type is at high level (CVD Coated insert). Minimum Tool Wear (0.0401 mm) is achieved when Environmental condition is at high level (minimum quantity lubrication), Nose Radius is at high level (1.2 mm), Feed rate is at high level (0.35 mm/rev), Depth of cut is at low level (0.5 mm) and tool type is at high level (CVD Coated insert). © 2022

Author keywords

Additive modelANOVAOptimizationTaguchi methodTool tip temperatureTool wearTurning process

Indexed keywords

Comparative analysis of different lattice topologies for cellular structure optimization in additive manufacturing

Chetan Mahatme [a],*, Jayant Giri [a], Rajkumar Chadge [a], Ashish Bhagat [b]

[a] *Yeshwantrao Chavan College of Engineering, Nagpur 441110, India*
[b] *Jawaharlal Nehru Medical College, DMIMS, Sawangi (M), Wardha 442001, India*

ARTICLE INFO

ABSTRACT

Cellular structures are prominent over solid structures in Additive manufacturing because of their inherent features like reduced weight, more strength, and porosity. A cylindrical component was designed and then different lattice topologies like grid, vin tile and hexagon were used to create the internal cellular structure. A comparative analysis was then carried out on these cellular structures based on different unit cell sizes, variable strut thickness, coefficient of volume reduction (VRC) and surface area coefficient (SAC). The effect of these parameters on mechanical properties was studied and correlated. These different cellular structures were then fabricated using PLA (Polylactic acid) material on a Makerbot Replicator + 3-D printer. These cellular structures were then simulated through FEA by providing loading and boundary conditions and the results were then evaluated and validated with experimentation work. The yielded results shown lowest stress and smallest of the deformation for vin tile lattice structure as compared to grid and hexagon lattice cellular structures. Physical experimentation results also validated the simulation outputs. This study was not limited to only creation of different cellular structures but it also compared how the structures behave mechanically through unit cell parameters like VRC and SAC. The cellular structures were tested virtually using FEA and physical experimentation was carried out on the 3-d printed samples. The results obtained through both the tests confirmed that vin tile cellular structure bears less stress and lowest deformation as compared to grid and hexagon cellular structures when subjected to same compressive loading conditions.

Copyright © 2022 Elsevier Ltd. All rights reserved.
Selection and peer-review under responsibility of the scientific committee of the International Conference on Recent Advances in Modeling and Simulations Techniques in Engineering and Science.

1. Introduction

Cellular structures are mostly seen in nature and are derived for designing various engineering applications. These structures have properties like they are lightweight in nature and use less material than solid structures. Structurally optimized and well adapted to their surroundings are the key features of these structures [1]. While designing these cellular structures the nature focused on reducing down the weight while using energy efficient ways to create them. The cellular structures available in nature are honeycombs, bone, wood, foam, etc.

Cellular structure are commonly used in industry and are prepared through manufacturing techniques like foaming, sintering, casting and vapor deposition method (VDM) [2]. These methods are conventional ones and are mostly suitable for creating simple cellular structures. The complex cellular structures can be prepared nowadays using modern manufacturing techniques like Additive Manufacturing (AM). It provides the means to create these complex geometries with variable density [3–7]. As in AM the base material is in powder or droplets of liquid form, it drastically reduces the material use and ultimately reduces the cost [8,9]. AM can be done through various techniques. [3–5,10–15]. AM materials include glass, metals, sand, polymers, etc. [3–5,14–16]. The layering resolution is also reaching to microns (<10μ). Advanced composite structures with complex geometries can also be manufactured now by using combination of AM materials i.e. polymer and powder simultaneously with complex topology [17,18].

Medical field application of cellular structures includes creation of scaffolds, implants for teeth and bone and engineered tissues

---

* Corresponding author at: Assistant Professor, Mechanical Engineering Department, Yeshwantrao Chavan College of Engineering, Nagpur 441110, India.
E-mail address: chetanmahatme@gmail.com (C. Mahatme).

[18,19]. Use of cellular structures for manufacturing bone implants consider various factors like pore size, internal connectivity of pores, volume reduction coefficient and permeability of the structure [20]. Various cellular structures were investigated in several studies for their mechanical performance. Variable density cellular structures and its optimization was proposed for AM by Zhang et al. [21], octahedral lattice structure was tested for various mechanical properties by Hedayati et al. [22]. Kalayu et al. mechanically investigated the performance of various cellular structures [23]. Mahatme et al. investigated the mechanical properties for vin tile lattice structure [24]. Giri et.al. investigated effect of process parameters in FDM process [25].

The work done here dealt with the comparative analysis of cellular structures created with different lattice topologies and different unit cell sizes and their structural performance under compressive loading conditions. The study is not limited to the structural performance under compressive loading but also considered key parameters like reduction of volume and overall surface area and their effect on the overall performance of the cellular structure. The cellular structures were also optimized through the optimization toolbox in Autodesk Netfabb and compared with the non-optimized structures. Finally, for evaluation of optimized as well as non-optimized cellular structures, they were tested experimentally as well as through FEA method.

2. Methodology

The procedure that was followed during this comparative study and the material used is explained in this section.

2.1. Cell structure

Cellular structures with different lattice topologies were created virtually and physically. The FEA analysis and physical compressive tests were performed on these cellular structures. Autodesk Netfabb software was used for designing the cellular structure as well as for FEA analysis. Fig. 1 shows the solid cylindrical component used for creating the different cellular structures.

2.2. Unit cell and different lattice topologies

For the purpose of comparative analysis, the Grid, Vin tile and hexagon lattice topologies were used. A dedicated 3-Dprinting software, Autodesk Netfabb was used for creating the cellular structures using these lattice topologies. A Solid cylindrical component (Fig. 1) was transformed into different cellular structures by inserting a lattice cell structure inside it. Combination of different lattice topologies with different unit cell sizes that were used for creating different cellular structures for comparison (Table 1). An example is shown in Fig. 2, where the grid lattice cell structure was incorporated in a cylindrical component.
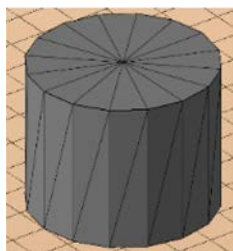
Fig. 1. Solid cylindrical component.

Table 1
Lattice topologies and Unit cell size combinations.

Lattice topologies	Size: Unit cell (mm)	Strut Thickness (mm)	Thickness (Threshold in mm)
Grid, Vin tile and Hexagon	$3 \times 3 \times 3$ to $7 \times 7 \times 7$	0.5, 1.0, 1.5	0.5

2.3. Parameters considered

The comparative analysis of cellular structures having different lattice topologies was mainly based on structural behaviour under compressive loading conditions. The other important parameters which were considered for evaluation of the different lattice structures were SAC and VRC. SAC stands for surface area coefficient and VRC stands for volume reduction coefficient. Both these parameters were equally important while comparing the cellular structures.

2.4. Fabrication of samples

The samples were fabricated using PLA (polylactic acid) material. Table 1 shows the combinations of geometrical variations that was used for creating the samples. The CAD file of solid component shown in Fig. 1 was converted into STL file and cellular structures were created using different lattice topologies shown in Table 1. The cellular structures were then checked for errors in Netfabb. Inbuilt repair scripts available in Netfabb was used to reduce down the triangulation errors of these cellular structures. These repaired cellular structures were then 3-D printed on Makerbot replicator+. The thickness of layer as 0.1 mm and infill density as 10% was kept common for all these cellular structures while printing. Physical compressive tests were performed on these samples as shown in Fig. 3. The layer resolution for 3-D printer was 0.1 mm.

2.5. FEA analysis and physical testing

The Finite Element Analysis was used to computationally simulate the physical conditions on the cellular structures. Simulation of physical conditions and theoretical analysis of structures behaviour was done through this technique. Same loading conditions were provided to all the samples and then their performance was compared. FEA analysis was done on Autodesk Netfabb. The mechanical performance of different cellular structures given in Table 1 was then compared on the basis of lattice and skin deformation and Maximum Von Mises Stress. The fabricated samples were then physically tested (Fig. 3) under same compressive loading conditions and FEA simulation results were compared for validation. Compressive testing was performed by using ASTM D1621 standard for Plastic and Elastomers. The standard requires the UTM to have enough force to compress the specimen by 13% of its height. For this universal testing machine of make FIE UTES-HGFL-60-C having maximum capacity of 600kN was used. The samples were then placed one-by one between the platens of the UTM as shown in Fig. 3(b). Position and orientation of the sample was same as in FEA simulation work. Gradual loading was then applied to the sample and the displacement and load were recorded through UTM display. For the compressive test υ was considered even in all directions.

3. Results and discussion

3.1. Results: FEA

Stress and displacement variation are shown in Fig. 4 for the cellular structures. Because of the variation in lattice structure
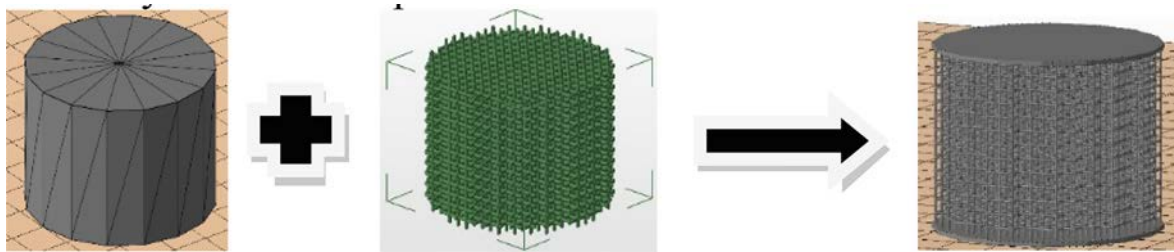
Fig. 2. Process of cellular structure design (Example: Grid lattice topology).
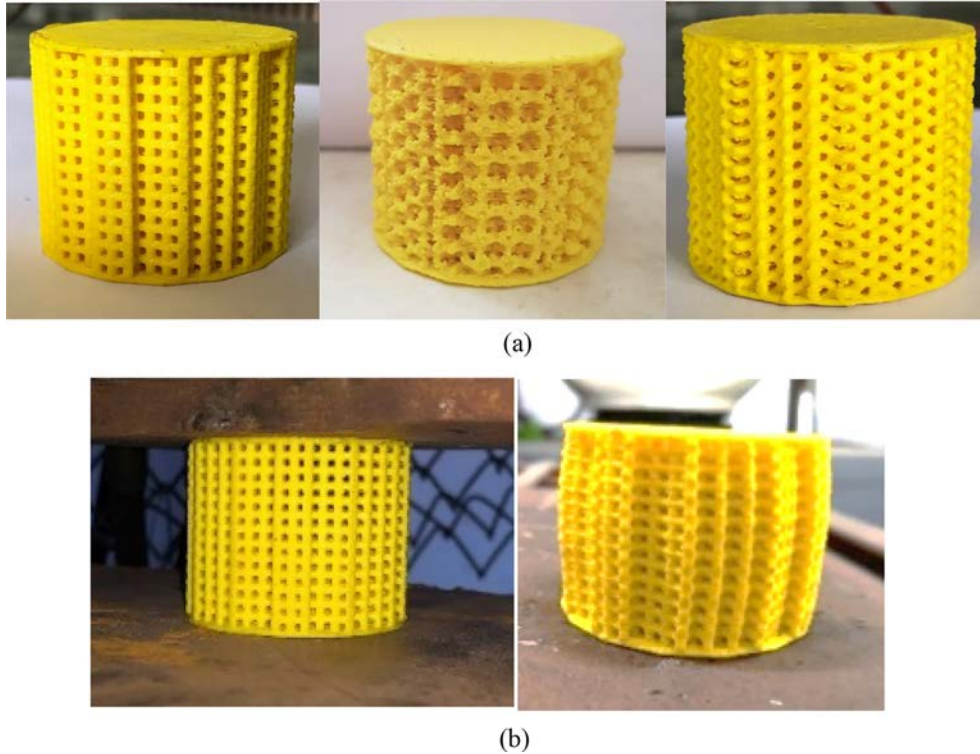
Fig. 3. UTM test setup (a) before starting the test (b) Hexagon: during and after test.

stress variation is prominently visible. Table 2 shows that the 3 × 3 × 3 mm unit cell size with 1.5 mm cell thickness proved to be more efficient in terms of minimum deformation and maximum stress bearing capacity. The Grid cellular structure with 3 × 3 × 3 mm unit cell size with 1.5 mm cell thickness showed deformation of 0.656188 mm while in Vin tile cellular structure 3 × 3 × 3 mm unit cell size with 1.5 mm cell thickness showed deformation of 0.185991 mm. For Hexagon cellular structure with 3 × 3 × 3 mm unit cell size with 1.5 mm cell thickness showed deformation of 0.17612 mm. This shows that the 3 × 3 × 3 mm unit cell size with 1.5 mm cell thickness proved to be more efficient in terms of minimum deformation and maximum stress bear-

ing capacity. The supremacy of this structure was also confirmed by the obtained VRC and SAC values. High VRC and SAC values for this sample indicated the high material reduction and more porous nature.

3.2. Structural optimization results

Cellular structures have inherent advantage of weight reduction and efficient structural optimization. Most of the work was done across the globe by various researchers in this field. The primary focus was to find optimized unit cell configuration so as to meet intended functional requirements. In this study Autodesk Netfabb
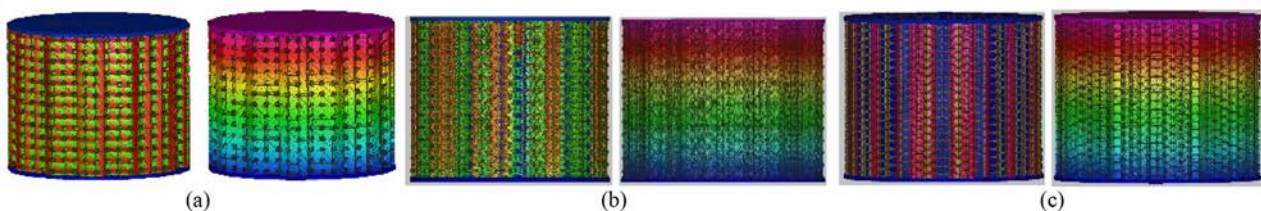
Fig. 4. Stress and displacement in unit cell (a) Grid 3 × 3 × 3–1.5 (b) Vin tiles 3 × 3 × 3–1.5 (c) Hexagon 4 × 4 × 4–1.5.

Table 2
FEA results.

Lattice topology	Size: unit cell (mm)	Strut thickness (mm)	SAC	VRC	Structure: non-optimized			
					Von mises stress (MPa)		Deformation (mm)	
					Lattice	Skin	Lattice	Skin
Grid	3 × 3 × 3	1.5	7.446	0.56	5.1329E + 07	2.76E + 06	0.656188	0.663963
Vin tile	3 × 3 × 3	0.5	10.299	0.267	8.8455E + 08	5.70E + 07	5.8538	5.872522
Hexagon	4 × 4 × 4	1.5	46.627	2.569	6.2832E + 07	1.72E + 06	0.401619	0.405083
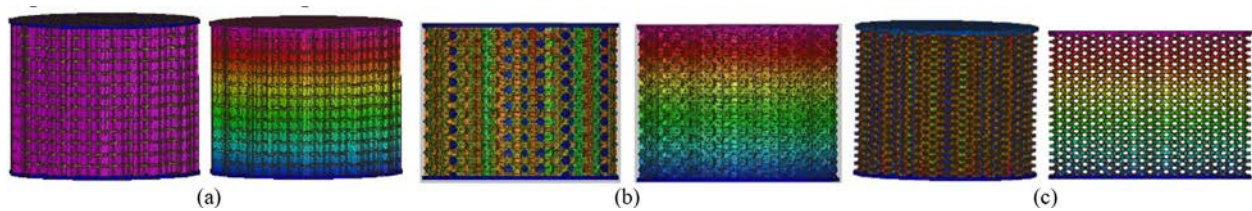
Fig. 5. Optimized structure (stress and deformation) (a) Grid 3 × 3 × 3–1.5 (b) Vin tiles 3 × 3 × 3–1.5 (c) Hexagon 4 × 4 × 4–1.5.

Table 3
Mechanical properties.

	Grid 3 × 3 × 3–1.5		Vin tile 3 × 3 × 3–1.5		Hexagon 4 × 4 × 4–1.5	
	Stress (max.) (MPa)	Deformation (max.) (mm)	Stress (max.) (MPa)	Deformation (max.) (mm)	Stress (max.) (MPa)	Deformation (max.) (mm)
Optimized	50.04	0.41	32.64	0.102	58.36	0.212
Non-optimized	51.32	0.656	37.76	0.185	62.83	0.401

software lattice optimization utility was used for structural optimization. The process flow followed was like this: 1. Defining unit cell and its parameters like strut thickness (max. min. and threshold). 2. Mesh generation and smoothness method. 3. Load and boundary conditions for FEA analysis. Autodesk Netfabb integrated ADS Nastran V12.1 (FEA solver) was used for performing the simulation. The lattice and skin were set for optimization in the solver. Maximum Optimization time and iteration were set to 10 min and 5 iterations. 1 mm was set as target maximum displacement. MiniOpt optimization algorithm was used and kernels were kept as it is. Hence KernelOpt was omitted for optimization.

Fig. 5 shows the simulation results for the Optimized cellular structure. In grid lattice structure, maximum Von Mises Stress was 2.5% less and maximum displacement 37.5% less than that of non-optimized cellular structure. Similar reductions were also observed in vin tile and hexagon lattice structures. These reductions in optimized cellular structures were because of stiffening of struts and strengthening of load bearing sections of the structures. The comparative results are as depicted in Table 3.

3.3. Mechanical properties: Comparison

As can be seen from Table 3, optimized cellular structures have less Von mises stress and smaller deformation as compared to non-optimized ones. This is because of the variable density internal structures. These variable density internal structures were generated during optimization process using MiniOpt Algorithm which is inbuilt in NASTRAN FEA solver integrated in Netfabb. The algorithm, through iterations, optimizes the structure by adding strength to the load bearing sections by varying the strut thickness, contributing to decrement in Von Mises stress and deformation. The results obtained in simulation study have pointed out that the optimized cellular structures are stiffer than the non-

optimized cellular structures when the unit cell parameters are kept constant.

4. Conclusions

In this study, we have designed various cellular structures using unit cell of grid, vin tile and hexagon lattice topology. The cellular structures were then structurally optimized and compared. For comparison purpose physical tests were performed on samples. FEA analysis was done and optimization methods were used for optimizing the structures. For validation of the simulation results, physical compression tests were also carried out on different samples on UTM. FEA simulation results and the physical compression test results were compared and they were in close agreement with each other.

It is seen from the result that the vin tile cellular structure with 3 × 3 × 3 mm unit cell size with 1.5 mm strut thickness had smallest of the deformation and lowest of the stress as compared to grid and hexagon lattice cell structures. Grid cellular structure with 3 × 3 × 3 mm unit cell size with 1.5 mm strut thickness and Hexagon 4 × 4 × 4 mm unit cell size with 1.5 mm strut thickness also showed promising results with less than 1 mm deformation but the von mises stress within those structures were far more than vin tile cellular structure. While comparing the structures on the basis of VRC and SAC with less than 1 mm deformation, vin tile cellular structure was once again superior to grid and hexagon structure. The study hence done a comparative evaluation of the grid, vin tile and hexagon cellular structures and their effectiveness when used for superior mechanical performance intended under compressive loading conditions.

The present study hints towards the selection of precise lattice structure for specified application for example while printing 3-D models of bones, mandible, etc. which requires better strength to

weight ratio and porosity. The present investigation also leads towards providing an insight for printing models for diversified domains such as prototypes for pre-surgical models, disruptive innovation-based models.

## CRediT authorship contribution statement

Chetan Mahatme: Conceptualization, Methodology, Software, Writing – original draft, Data curation. **Jayant Giri:** Software, Validation, Supervision. **Rajkumar Chadge:** Writing – review & editing. **Ashish Bhagat:** Visualization, Investigation.

Declaration of Competing Interest

The authors declare that they have no known competing financial interests or personal relationships that could have appeared to influence the work reported in this paper.

References

[1] T. Wester, Nature teaching structures, Int. J. Sp. Struct. 17 (2-3) (2002) 135–147, https://doi.org/10.1260/026635102320321789.

[2] J. Banhart, Manufacture, characterisation and application of cellular metals and metal foams, Prog. Mater. Sci. 46 (6) (2001) 559–632.

[3] I. Gibson, D.W. Rosen, B. Stucker (Eds.), Additive Manufacturing Technologies, Springer US, Boston, MA, 2010.

[4] J.-P. Kruth, M.C. Leu, T. Nakagawa, Progress in additive manufacturing and rapid prototyping, CIRP Ann. Manuf. Technol. 47 (2) (1998) 525–540.

[5] T. Wohlers, Wohlers Report 2011: Additive Manufacturing and 3D Printing, State of the Industry, Wohlers Associates, Ft Collins CO, 2011.

[6] J. Scott, N. Gupta, C.L. Weber, S. Newsome, T. Wohlers, T. Caffrey, Additive Manufacturing: Status and Opportunities, Science and Technology Policy Institute, Washington, DC, 2012, pp. 1–29.

[7] J. Conley, H. Marcus, Rapid prototyping and solid free form fabrication, ASME J. Manuf. Sci. Eng. 119 (4B) (1997) 811–816.

[8] C. Beyer, Additive manufacturing—implications of a breakthrough technology, ASME J. Manuf. Sci. Eng. (to be published).

[9] K.R. Haapala, F. Zhao, J. Camelio, J.W. Sutherland, S.J. Skerlos, D.A. Dornfeld, I. Jawahir, A.F. Clarens, J.L. Rickli, A review of engineering research in sustainable manufacturing, ASME J. Manuf. Sci. Eng. 135 (4) (2013) 041013.

[10] D.D. Gu, W. Meiners, K. Wissenbach, R. Poprawe, Laser additive manufacturing of metallic components: materials, processes and mechanisms, Int. Mater. Rev. 57 (3) (2012) 133–164.

[11] L.E. Murr, S.M. Gaytan, D.A. Ramirez, E. Martinez, J. Hernandez, K.N. Amato, P. W. Shindo, F.R. Medina, R.B. Wicker, Metal fabrication by additive manufacturing using laser and electron beam melting technologies, J. Mater. Sci. Technol. 28 (1) (2012) 1–14.

[12] P.J. Bartolo, Stereolithography: Materials, Processes and Applications, Springer, New York, 2011.

[13] P. Edwards, A. O'Conner, M. Ramulu, Electron beam additive manufacturing of titanium components: properties and performance, ASME J. Manuf. Sci. Eng. 135 (6) (2013) 061016.

[14] R.S. Amano, S. Marek, B.F. Schultz, P.K. Rohatgi, Laser engineered net shaping process for 316L/15% nickel coated titanium carbide metal matrix composite, ASME J. Manuf. Sci. Eng. 136 (5) (2014), https://doi.org/10.1115/1.4027758.

[15] J. Luo, H. Pan, E. Kinzel, Additive Manufacturing of Glass, ASME J. Manuf. Sci. Eng. (to be published).

[16] L.S. Dimas, G.H. Bratzel, I. Eylon, M.J. Buehler, Tough composites inspired by mineralized natural materials: computation, 3D printing, and testing, Adv. Funct. Mater. 23 (36) (2013) 4629–4638.

[17] Y. Li, N. Kaynia, S. Rudykh, M.C. Boyce, Wrinkling of Interfacial Layers in Stratified Composites, Adv. Eng. Mater. 15 (10) (2013) 921–926.

[18] D. Ali, S. Sen, Finite element analysis of mechanical behavior, permeability and fluid induced wall shear stress of high porosity scaffolds with gyroid and lattice-based architectures, J. Mech. Behav. Biomed. Mater. 75 (2017) 262–270, https://doi.org/10.1016/j.jmbbm.2017.07.035.

[19] V. Karageorgiou, D. Kaplan, Porosity of 3D biomaterial scaffolds and osteogenesis, Biomaterials 26 (27) (2005) 5474–5491, https://doi.org/10.1016/j.biomaterials.2005.02.002.

[20] S. Hollister, Porous scaffold design for tissue engineering, Nat. Mater. 5 (2006) 590, https://doi.org/10.1038/nmat1683.

[21] P.u. Zhang, J. Toman, Y. Yu, E. Biyikli, M. Kirca, M. Chmielus, A.C. To, Efficient design-optimization of variable-density hexagonal cellular structure by additive manufacturing: theory and validation, J. Manuf. Sci. Eng. 137 (2) (2015), https://doi.org/10.1115/1.4028724.

[22] A.A. Zadpoor, R. Hedayati, Analytical relationships for prediction of the mechanical properties of additively manufactured porous biomaterials, J. Biomed. Mater. Res. - Part A 104 (12) (2016) 3164–3174, https://doi.org/10.1002/jbm.a.35855.

[23] K.M. Abate, A. Nazir, Y.-P. Yeh, J.-E. Chen, J.-Y. Jeng, Design, optimization, and validation of mechanical properties of different cellular structures for biomedical application, Int. J. Adv. Manuf. Technol. 106 (3-4) (2020) 1253–1265.

[24] C. Mahatme, J. Giri, R. Chadge, S. Sonwane, Compression deformation analysis of cellular lattice structure for structural optimization in additive manufacturing, Mater. Today:. Proc. 47 (2021) 4214–4220, https://doi.org/10.1016/j.matpr.2021.04.463.

[25] J. Giri, A. Chiwande, Y. Gupta, C. Mahatme, P. Giri, (2021), Effect of process parameters on mechanical properties of 3d printed samples using FDM process, Mater. Today:. Proc. 47 (2021) 5856–5861, https://doi.org/10.1016/j.matpr.2021.04.283.
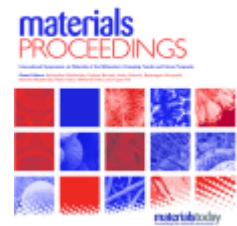
Experimental investigation of different electrical configurations and topologies for Photovoltaic system

Author links open overlay panelRajkumar
B. Chadge [a], Neeraj Sunheriya [a], Jayant
P. Giri [a], Naveen Shrivastava [b]
Show more
Add to Mendeley
Share
Cite

Abstract

The recent solar technology offers clean, economic andenvironment friendly energy applications to society. Photovoltaic (PV) modules are directly converted the incident solar radiations into electrical energy. These modules are connected in different electrical configurations and topologies. These configurations and topologies are decided as per the power requirement. The selection of variety of electrical configurationsand type of topologies arecritical for performance of the PV system. This research paper aims to Experimental investigationthe different PV array configurations (Series Parallel and Total cross Tied) with two different topologies (4SX5P and 5SX4P) in non-shading and partially shaded condition. It is observed that impedance of solar panel and input resistance playing important role in achieving maximum power output of PV system. The 4Sx5P topology shows the maximum power of 12 W is

observed at 8 am for uniform condition and 11.7 W is at 9:30 a.m. for partial shaded. Similarly 18.57 W at 9:15 a.m. for uniform condition and 15.26 W at 10:45 a.m. are observed for partial shaded condition of 5Sx4P topology. The power generated in both topologies is almost following the same pattern. From above graph it is clear that approximately 9–13% power variation was observed in uniform and partial shading condition for both the topologies.

Introduction

Energy is the most important factor for the economic as well as social and technological development of both developing and developed countries [1]. Mostly we are depending on different non renewable energy sources for satisfying our daily energy demand. In non-renewable energy sources fossil fuel are playing crucial role for managing these demands. But scarcity of fossil fuel, continuous price hike and environmental concern are the major bottle neck for usingthese for a long time. Detail literature review shows that lot of work was already carried out for minimizing the adverse effect of fossil fuels but these efforts are not enough as per different published reports on global disturbance. In recent year's renewable energy sources like solar energy, wind energy, bio gas and fuel cell technology are showing potential for bridging the gap of future energy demands with environmental concern. These energy sources having their own challenges and at the same time also providing different opportunities. Zero carbon emission, easy availability and environment friendlyare the important characteristics which attract lot of research on renewable energy sources.

Recently it is observed that solar technology is one of the most promising areas for future energy demand. Solar energy can be used in a direct or indirect way for producing the energy. In indirect utilization of solar energies like wind energy, hydro energy, ocean energy etc. observe that solar energy having secondary effect on production. Photoelectric and photo thermal are the direct conversion of energy from solar radiation. Photoelectric conversion direct directly converts the incident radiation into electrical energy while the photo thermal conversion directly convert the incident radiation into thermal energy. On grid, off grid and hybrid solar power plant are works on the principle of photoelectric conversion.

Solar water heater, solar cooker are working on the principle of solar photo thermal conversion.

The maximum achievable efficiency of polycrystalline silicon solar cells is 20–30%, which will further reduced by 5% due to the conventional series or parallel configurations. The present paper suggested the arrangement of some new configurations and their performance under non shaded and partially shaded conditions.

This paper based on the experimental investigation of photoelectric conversion. This conversion works on the principle of photoelectric effect. The silicon semiconductor materials are used for absorbing the incident radiations in Photoelectric effect. When these materials are exposed to light, the photons of light are absorbed by the semiconductor crystal which causes number of free electrons in the crystal. This resulted production of electricity. It is observed that when the radiations are incident on the silicon cell, some of the radiations are reflected, some are transmitted through the materials and remaining is absorbed by the material. These losses reduce the efficiency of the system. These silicon cells are arranged in different combination of solar panel or solar modules. These solar panels are electrically connected in different combination of topologies and configurations. These combinations are decided on the basis of project requirement and the applications. This selection played important role for enhancing the performance of the solar system.

Section snippets

Literature review

Solar panel is an array of number of PV cell. Cellsdirectly transform the sun's photons into electricity. These PV cells are available in different electrical and physical characteristics. Bansal et al. checked the detailed performance and done the degradation analysis on different type of PV power plants with different topologies. They found that HIT appears to be the most promising technology followed by pc-Si and a-Si technology for all conditions [2]. Jaiswal et al. presented an effectual

Experimental setup

The experimentation was carried out to determine an optimum PVarray configuration under different operating conditions. PV array configurations have been tested (SP and TCT) in two different topologies (4SX5P and 5SX4P). The tests have been carried out at the outdoor location of YCCE (latitude: 21.1110625), college campus Wanadongari, Nagpur.

The aluminum frame is fabricated with the PV solar modules dimensions. 20 poly-crystalline PV modules (60 W) were fitted in the frame. These modules are

Variation of power and time

All experiments are carried out from morning 6 a.m. to evening 6p.m. under actual atmospheric condition of the stated site. The fix load of 20 W was applied for all topologies.

Conclusions

Following are mentioned the conclusions of the investigations done on Solar PV Array by varying parameters.

This research work carried out SP and TCT array configuration with two different topologies (4SX5P and 5SX4P) in uniform and partially shaded condition. However all configurations can be taken at the same time to get better results. The impedance of solar panel and input resistance playing important role in achieving maximum power output of PV system. As soon as resistance increases the

Declaration of Competing Interest

The authors declare that they have no known competing financial interests or personal relationships that could have appeared to influence the work reported in this paper.

References (9)

- N. Bansal *et al.*

  Comparative investigation of performance evaluation, degradation causes, impact and corrective measures for ground mount and rooftop solar PV plants – a review

Sust. Energy Technol. Assess.

(2021)

- S. Pujan Jaiswal *et al.*

  Opportunities and challenges of PV technology in power system
  Mater. Today: Proc. DOI
  (2021)

- D. Kumar *et al.*

  A simplifiedsimulation model of silicon photovoltaic modules for performance evaluation at DifferentOperating conditions
  Optik
  (2020)

- Engin Karatepe *et al.*

  Development of a suitable model for characterizing photovoltaic arrays with shaded solar cells
  Solar Energy
  (2007)

There are more references available in the full text version of this article.

Cited by (2)

- The Effects of Non-Uniformly-Aged Photovoltaic Array on Mismatch Power Loss: A Practical Investigation towards Novel Hybrid Array Configurations
  2023, Sustainability (Switzerland)

- Optical Developments in Concentrator Photovoltaic Systems—A Review
  2023, Sustainability (Switzerland)
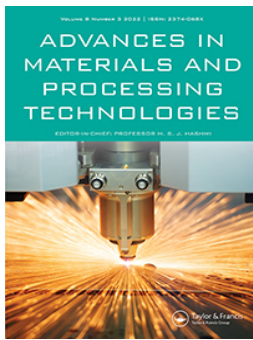
Effect of filler and autogenous welding on microstructure, mechanical and corrosion properties of low nickel Cr-Mn ASS

Sachin Ambade, Awanikumar P. Patil, Chetan K. Tembhurkar & Diwesh B. Meshram

Taylor & Francis
Taylor & Francis Group

Check for updates

RESEARCH ARTICLE

Effect of filler and autogenous welding on microstructure, mechanical and corrosion properties of low nickel Cr-Mn ASS

Sachin Ambade [ID][a], Awanikumar P. Patil [ID][b], Chetan K. Tembhurkar[c]
and Diwesh B. Meshram [ID][d]

[a]Department of Mechanical Engineering, Yeshwantrao Chavan College of Engineering, Nagpur, India;
[b]Department of Metallurgical and Materials Engineering, VNIT, Nagpur, India; [c]Department of Mechanical
Engineering, Priyadarshini College of Engineering, Nagpur, India; [d]Department of Plastics Engineering,
Central Institute of Plastics Engineering and Technology, Korba, India

ABSTRACT

This experimental study investigates the effects of welding low nickel Cr-Mn austenitic stainless steel with gas tungsten arc welding process with and without filler (autogenous) weld by varying the welding currents (120A, 130A and 140A). The microstructural examination of weld has been carried out with optical microscope and mechanical properties with Vickers microhardness and tensile tester. The corrosion behaviour of the welded joints are analysed by double loop electrochemical potentio-kinetic reactivation test to obtain degree of sensitisation. The microstructural examination of welded joints revealed that, as the welding current increases, the inter-dendritic spacing as well as the dendrite size increases. The tensile strength and hardness decrease with increasing welding current for 308 L filler and autogenous weld. The degree of sensitisation increases with increasing welding current for both the welds. The results reveal that the autogenous welds have higher tensile strength, higher hardness and lower degree of sensitisation as compared to welds with 308 L filler.

1. Introduction

In today's manufacturing world, Cr-Mn ASS (Chrome Manganese austenitic stainless steel) (200-series) is seen as the better economical and replacement of austenitic stainless steel (300-series). Many industrial applications such as aircraft, automotive, nuclear and food industry use 300-series austenitic stainless steel [1] due to its high tensile strength and corrosion resistance properties [2]. However, stainless steel (300-series) contains more nickel and the price of nickel is increasing drastically, breaking the backbone of manufactures and buyers [3]. So many mentioned industries are searching for alternative stainless steel which are cheaper and have reasonably good corrosion resistance and strength. Cr-Mn ASS grades containing manganese are seen as a substitute for nickel to balance the austenite phase [4]. The problems associated with welding in the austenitic stainless steels (ASS) are the sensitisation of the heat-affected zone of the weld, the weld

---

metal hot cracking and decreased corrosion resistance [5,6]. Since stainless steel does not dissipate enough heat, maintaining the good heat input when welding is critical. Therefore, proper selection of welding process is very important for better weld joint.

P.C. Pistorius and M. du Toit,2010 [7] suggested that it was possible to replace the 300-series ASS (304 ASS), by adding nitrogen, manganese and copper as in the 200-series ASS (201 ASS). R. V. Taiwade et.al, 2013 [8] investigated the effects of grain size on degree of sensitisation (DOS) of Cr-Mn ASS and found that the DOS decreases as the grain size of Cr-Mn ASS increases. N. N. Khobragade et al. 2013 [9] compared electrochemical behaviour of 304 ASS and low Cr-Mn ASS in different chloride-free and chloride concentration environments and found from polarisation plots, mott-schottky plots and electrochemical impedance spectroscopy (EIS), that 304 ASS is more corrosion resistant than Cr-Mn ASS.

H. Vashishtha et al. 2016 [10] examined the effect of shielded metal arc welding with E308, E309 and E310 fillers on Cr-Mn ASS and found that the weld produced with E308 filler has higher tensile strength and hardness but lower impact strength due to its higher delta ferrite contents. A.V.Bansod et al. 2016 [11] compared inetergranular corrosion susceptibility of Cr-Mn ASS in various thermal ageing conditions with 304 ASS and found that the Cr-Mn ASS are more vulnerable to intergranular corrosion than 304 ASS. H.Vashishtha et al. 2017 [12] welded high nitrogen ASS (201) with 304 ASS by SMAW and GTAW process using 308 L filler material at three different welding speeds. They found that on increasing welding speed micro hardness and ultimate tensile strength increases. They also found that width of heat affected zone decreases with increasing welding speed. Amuda M.O.H et al. 2017 [13] investigated the carbide precipitation in Cr-Mn ASS welds using GTAW process with different heat inputs and found that welds with heat input greater than 206 J/mm are more susceptible to carbide precipitation. A.V. Bansod et al. 2018 [14] welded Cr-Mn ASS by GTAW process with 308 L filler material with different heat inputs and found that with increasing heat input volume of delta-ferrite decreases heat-affected zone widens and corrosion resistance decreases.

Numerous researchers have focused on examining microstructures, mechanical and corrosion properties of austenitic stainless steel (300 series) weld joints and compared to Cr-Mn ASS [15]. The present experimental study deals with the performance of autogenous weld of Cr- Mn ASS and 308 L filler weld at different welding currents (120 A, 130 A and 140 A) and the changes in microstructural, mechanical and corrosion properties obtained in these joints. This study will be helpful to various industries such as aircraft, automobile and food industries as a better replacement of 300-series austenitic stainless steel.

2. Experimental work

2.1. Sample preparation

The chemical composition (wt %) of Cr-Mn ASS and 308 L filler material are shown in Table 1. Cr-Mn ASS was procured in the form of sheet and cut into the size of 150 × 75 x 3 mm using wire cut electrical discharge machine (EDM) and welded by GTAW along the longitudinal dimension. GTA welding parameters are shown in Table 2. Three welding currents 120A (low), 130A (medium) and 140A (high) were used in gas tungsten arc welding (GTAW)

Table 1. Chemical Composition (wt. %) of test materials.

Material	C	Si	Mn	P	S	Cr	Ni	M	Al	Cu	V	Nb	Ti	Fe
Cr-Mn ASS	0.096	0.550	10.118	0.058	0.010	15.102	0.289	0.001	0.001	0.950	0.059	0.004	0.007	Bal.
308 L Filler	0.01	0.8	1.7	0.015	0.01	20.0	10.0	0.1	-	0.15	-	-	-	Bal.

Table 2. GTA Welding parameters.

Welded plate	Current (I) (A)	Voltage (V)	Welding Speed (v) (mm/s)	Heat input per unit length (Q) (J/mm)
A	120	14	3.728	315.45
B	130	16	3.70	393.15
C	140	18	3.843	459.01
D	120	14	4.837	243.12
E	130	16	5.064	287.51
F	140	18	5.098	298.48

process on low Ni Cr-Mn ASS using 308 L filler material and without filler material (autogenous welding). The welded plate and schematic diagram is shown in Figure 1. For welding, 2% Thorium Alloyed Tungsten electrode (Red Band) of 1.6 mm diameter was used and the filler rod diameter was 2.4 mm. Samples for various studies were cut from the welded plates. The welded plates for 308 L filler and Autogenous weld at different currents is shown in Figure 2. The samples for microstructure examination were polished on series of emery paper (120 to 1000 grit) and then cloth polished with alumina powder (0.75 μm). The samples were cleaned ultrasonically in distilled water before etching. The sample was electrolytically etched with help of a potentiostat (Solartron-1285) in 10 wt% oxalic acid solution at a current density of 1 A/cm^2 for 90 sec as per A-262 Practice A test (ASTM standard) [16].

2.2. B) Tensile test

Tensile test samples were cut by wire cut EDM using ASTM E-8 standard with gauge length 25 mm, total length 100 mm, gripping length 30 mm from both sides and 10 mm width. The detailed geometry of samples is shown in Figure 3. The actual test samples cut from the welded sheets are shown in Figure 4. Tensile strength of samples was evaluated by universal testing machine (Instron 4467).

2.3. C) Sample for hardness testing

The hardness was measured by Micro Vickers hardness tester (Mitutoyo, Japan). Measurements were conducted on base metal-1, heat-affected zone (HAZ)-1, weld metal (WM), and heat-affected zone (HAZ)-2 and base metal-2 by taking load 0.3 Kg for 15 s. The hardness contour across the transverse section of weld metals was measured and compared.

2.4. D) Sample for DLEPR (Double Loop electrochemical potentiokinetic reactivation) test

ASTM G-108 standard was followed for DLEPR test. The samples of (10 mm x 10 mm x 3 mm) were cut from welded joint from each welded plate and were prepared in three steps. In first step, the insulated single strand copper wire was soldered on copper strip
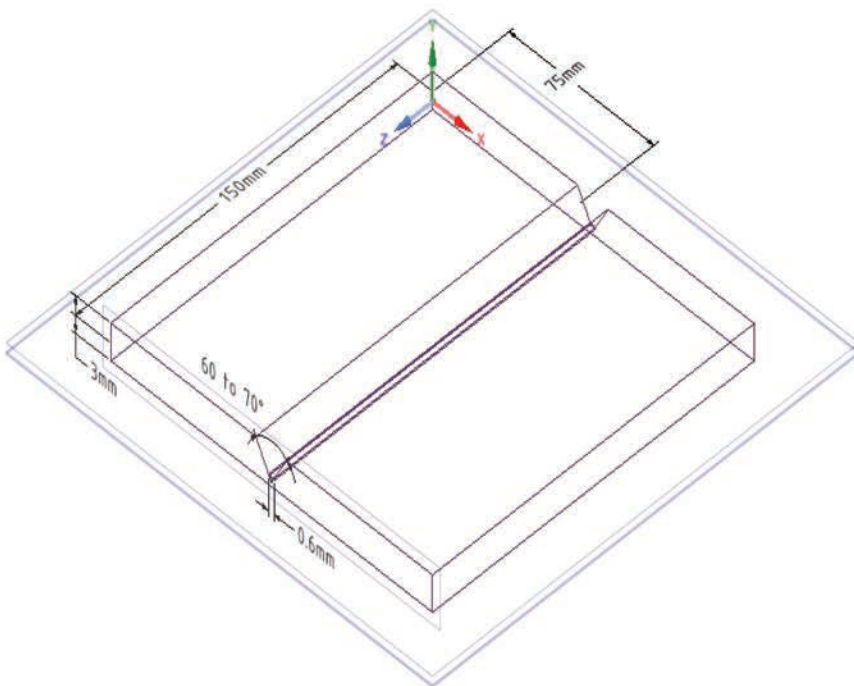
Figure 1. Welded plate and schematic diagram.

Figure 2. Plates welded with 308 L filler (A: 120A weld, B: 130A weld, C: 140A weld) and autogenous welding (D: 120A weld, E: 130A weld, F: 140A weld).

(All dimensions are in "mm")
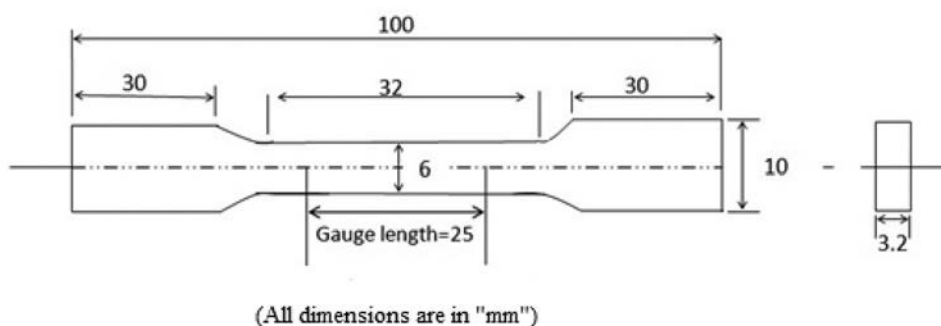
Figure 3. Specifications of the tensile test specimen.

(0.8 mm thickness). In the second step, copper strip piece was pasted by conductive silver paste to test sample. Then in third step, whole assembly was mounted in araldite solution to implant the soldered joints completely and to keep open one face of specimen as shown in Figure 5. Then, open face was polished on series of emery papers from 180 to 1000 grit and then cloth polished with alumina powder (0.75 μm). The samples were cleaned ultrasonically in distilled water before etching.

The solution of 0.5 M H_2SO_4 + 0.01 M NH_4SCN was prepared at room temperature for the DLEPR test [17,18]. The potentiostat (Solartron-1285) was used for DLEPR test. The electrochemical cell has three-electrode, first- counter electrode (platinum), second- reference electrode (saturated calomel electrode) and third- working electrode (Sample) as shown in Figure 5. The reported potential values are referenced to saturated calomel electrode (SCE).
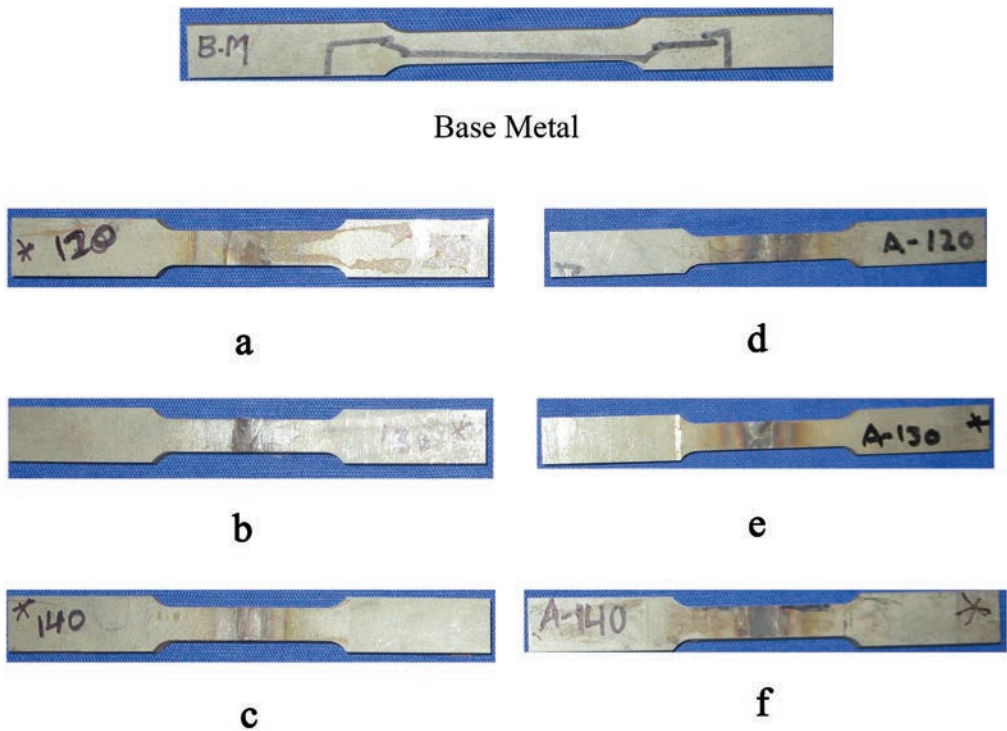
Figure 4. Tensile sample for GTAW (A: 120A weld, B: 130A weld, C: 140A weld) and Autogenous welding (D: 120A weld, E: 130A weld, F: 140A weld).
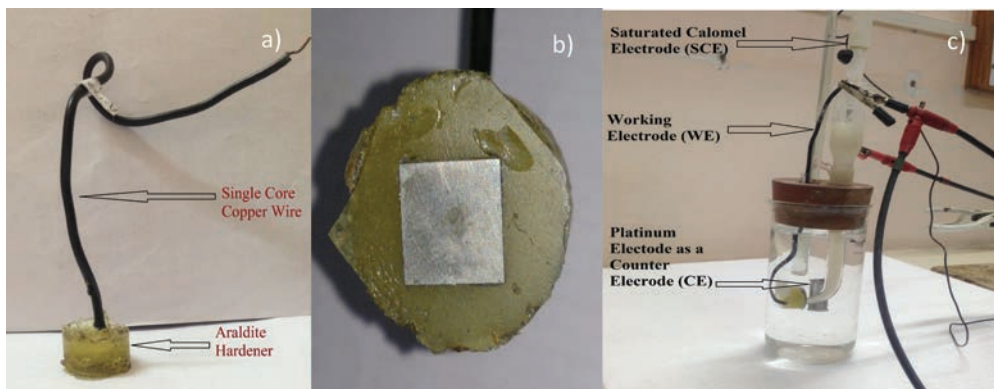
Figure 5. Sample and test set-up for electrochemical testing.

3. Results and discussion

3.1. Microstructural examination

Figure 6 shows the microstructure of the base metal (Cr-Mn ASS) used for welding. It shows equiaxed austenite grains and small amounts of carbide particles dispersed at austenite grains boundaries [15].
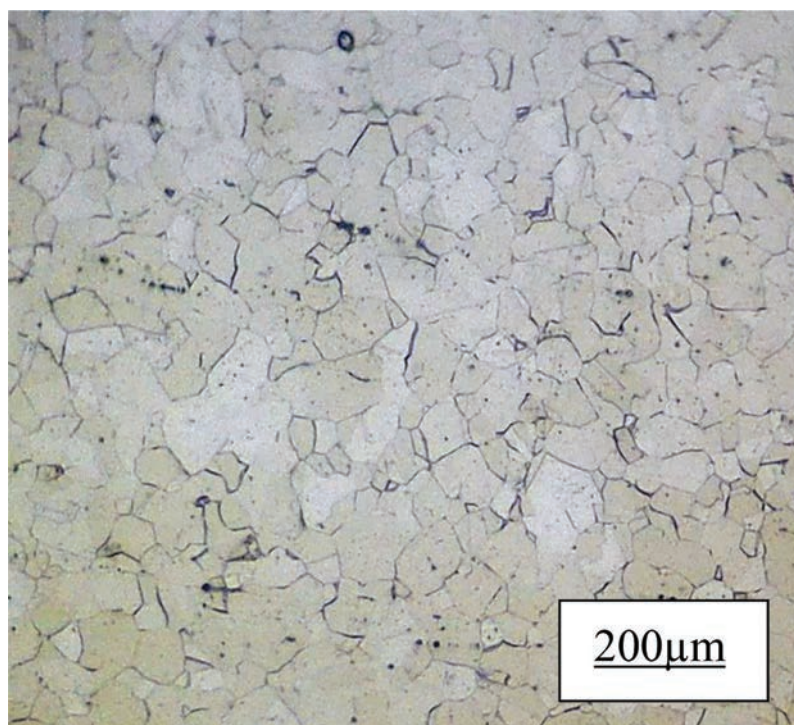
Figure 6. Microstructure of Cr-Mn austenitic stainless steel.
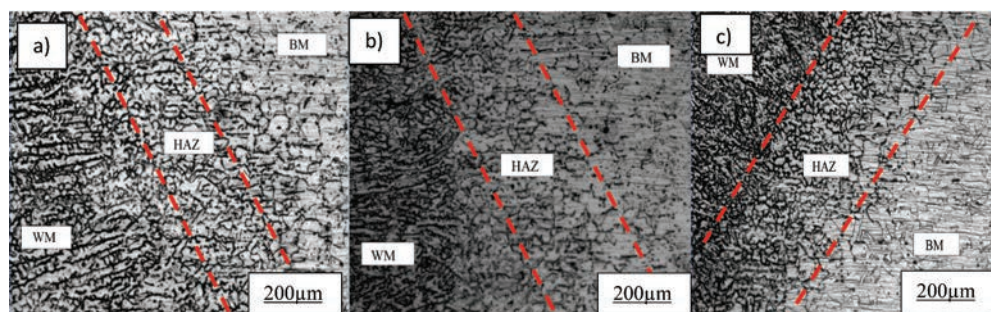
Figure 7. Microstructure of 308 L filler weld for a) low, b) medium and c) high heat input.

Figures 7 and 8 show microstructure of plates welded with filler (308 L) and without filler (autogenous weld) respectively. Each figure has three microstructures of weld joints. Each microstructure shows base metal (BM), heat-affected zone (HAZ) and weld metal (WM). It is evident that weld metal has dendritic microstructure, which is natural due to the process of solidification taking place in weld metal pool with cooling. It is also evident that the size of dendrites and interdendritic spacing and width of HAZ increases with increasing weld heat input. This is attributed to relatively higher temperature and large size weld pool of high heat input weld as compared to low and medium heat input weld [19]. Higher weld temperature and large size weld pool has more heat content, and it takes longer to cool down to
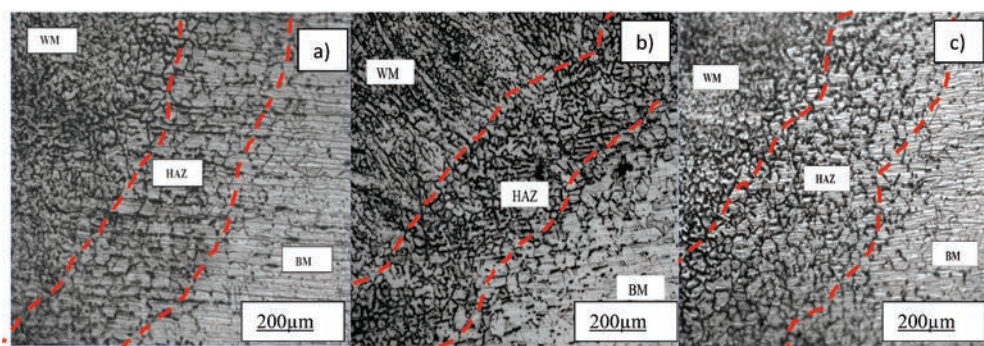
Figure 8. Microstructure of autogenous weld for a) low, b) medium and c) high heat input.

solidification temperature. As a consequence, the dendrites of high heat input weld get longer duration to grow and grow larger. At the same time, the higher weld metal pool temperature causes formation of less number of nuclei. The net result is that there are less number of nuclei and each nuclei grows into a large dendrite. Higher temperature in weld pool also causes more heat to be dissipated to base metal. As a consequence, the width of the heat-affected zone increases with increasing weld heat input. Extending the same logic to low heat input weld, it can be understood that relatively lower heat input causes relatively lower weld metal temperature, more nucleation and less growth of each dendrites, thus giving narrow HAZ. Smaller dendrites and smaller interdendritic spacing at low heat input weld. On comparing Figures 7 **and** 8, it becomes clear that the size of dendrite and width of HAZ of weld joint produced with filler metal is more. This suggests that the temperature of the weld with filler was relatively higher than the weld without filler. These results are in agreement with the work of Dayal et al. [20] explained that the width of HAZ is a function of welding parameters and physical properties of the base metal.

3.2. Tensile test

Results of tensile tests are presented in Figure 9 inform of stress-strain diagram. Ultimate tensile strength (UTS) is worked out from these plots and presented in Table 3. It is evident that the UTS of the weld with 308 L filler is less than that of the autogenous weld. It is noticed that the tensile specimens fractured at HAZ. It follows that the HAZ of weld with filler became weaker due to weld heat. It is also evident that the UTS decrease with increasing welding heat input for each type of weld. Increasing weld heat input, increases temperature of weld pool and as a consequence the HAZ is heated to high temperature, which may causing softening of the HAZ due to decreasing dislocation density of metal at HAZ. There may also be precipitation of chromium carbide ($Cr_{23}C_6$) at grain boundary due to heating.

3.3. Micro-hardness test

Microhardness profile across entire width of the weld joints produced with varying weld current (120A, 130A, and 140A) with or without filler is shown in Figure 10 **and** Figure 11, respectively. From the hardness profile it can be seen that the HAZ extend
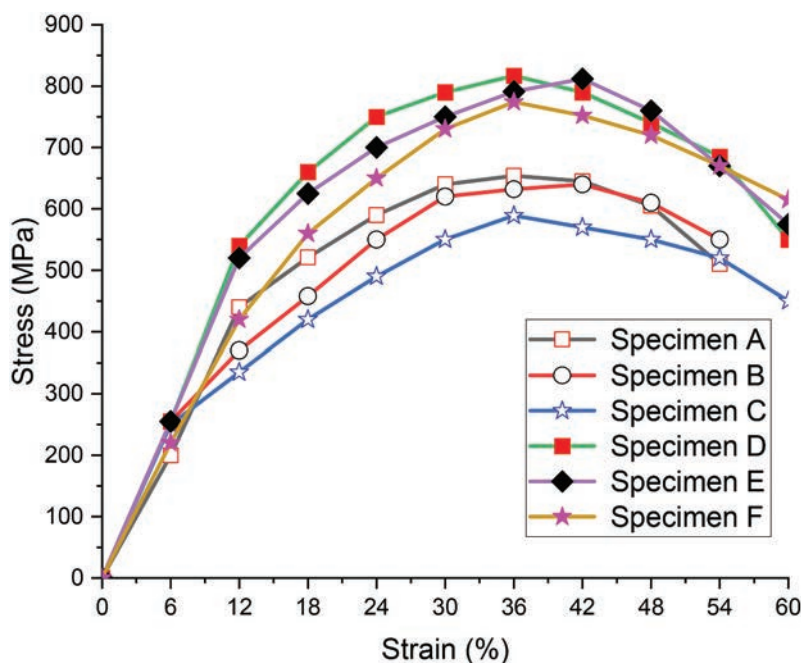
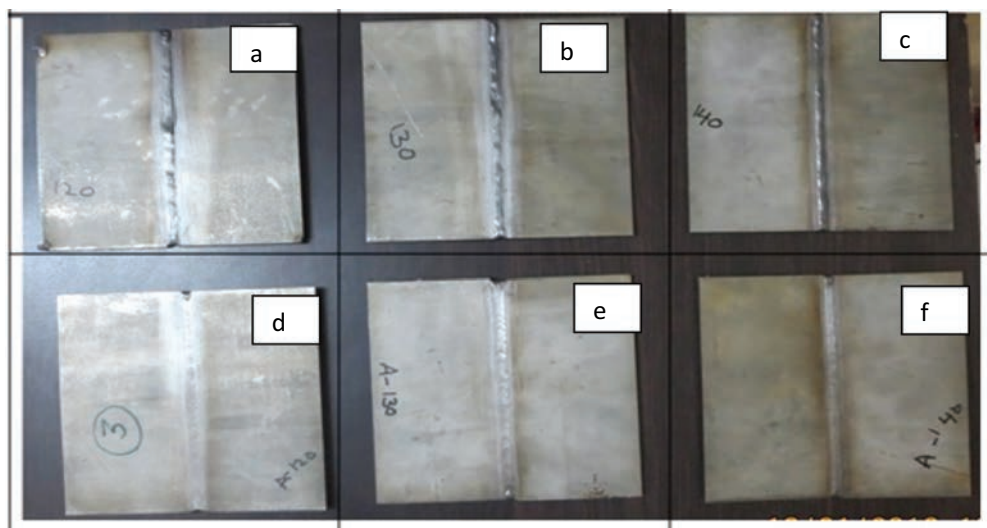**Figure 9.** Stress Strain diagram of GTAW for 308 L filler (A: 120A weld, B: 130A weld, C: 140A weld) and Autogenous welding (D: 120A weld, E: 130A weld, F: 140A weld).

**Table 3.** Tensile strength results for different welded samples.

Specimen	Welding Current (A)	Heat input per unit length (J/mm)	Ultimate tensile strength (MPa)
Base Metal (BM)	-	—	686.458
A	120	315.45	654.167
B	130	393.15	628.52
C	140	459.01	588.62
D	120	243.12	817.187
E	130	287.51	790.625
F	140	298.48	773.750

upto 3 mm on either side of the centre of the weld joint. It is evident in both the figure, that starting from base metal and going towards the centre of the weld metal, hardness decreases in general. There is an exception at the boundary of the base metal and HAZ, where the hardness increases sharply (like a spike). There is another exception of drop in hardness just before HAZ in weld with 140A current. Barring these exception, hardness in general decreases from the base metal to the centre of the weld metal. The drop in hardness becomes more steeper towards the centre of the weld metal. Let us see why the hardness of the weld metal is less than the base metal. The base metal has more carbon (0.096 wt %) as compared to the filler 308 L (0.01 wt %). The carbon is an interstitial element and produced lattice strain when dissolved in iron. Therefore, higher carbon in base metal naturally causes more lattice distortion. More lattice distortion in Cr-Mn ASS will impart it higher hardness as compared to 308 L filler metal. Secondly, during solidification of weld pool, cooling causes nucleation and growth of the nuclei. As
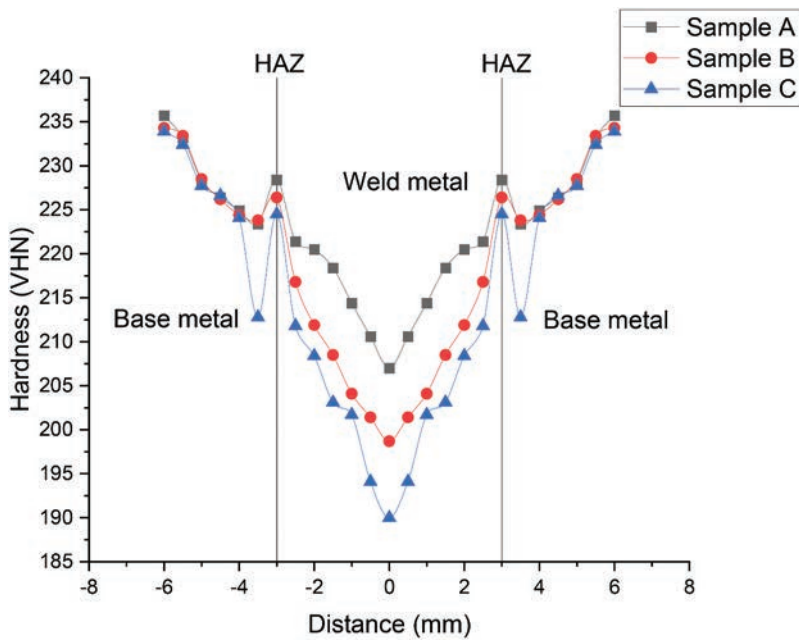
Figure 10. Microhardness profile of welded plate (including base metal, HAZ, weld metal, HAZ and base metal) for 308 L filler weld (A: 120A weld, B: 130A weld, C: 140A weld).
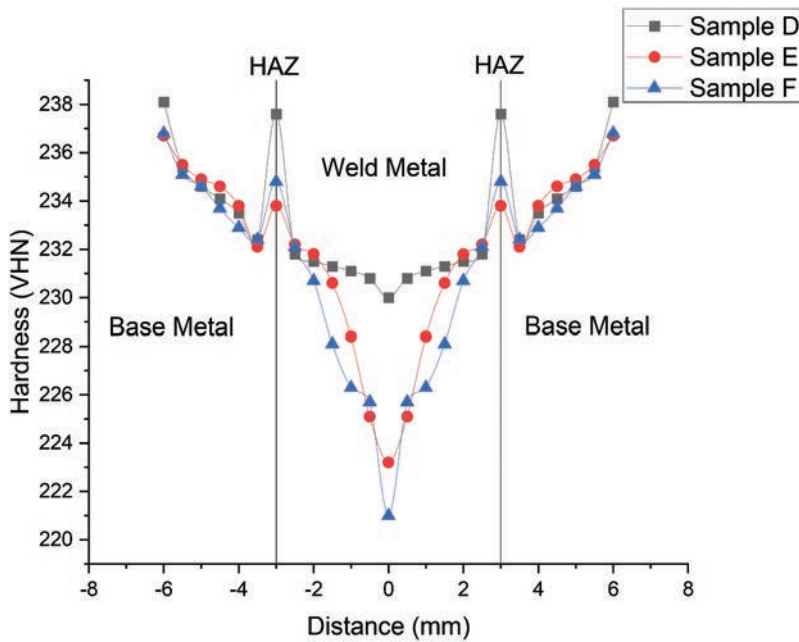
Figure 11. Microhardness profile of welded plate (including base metal, HAZ, weld metal, HAZ and base metal) for Autogenous weld (D: 120A weld, E: 130A weld, F: 140A weld).

Base Metal

a
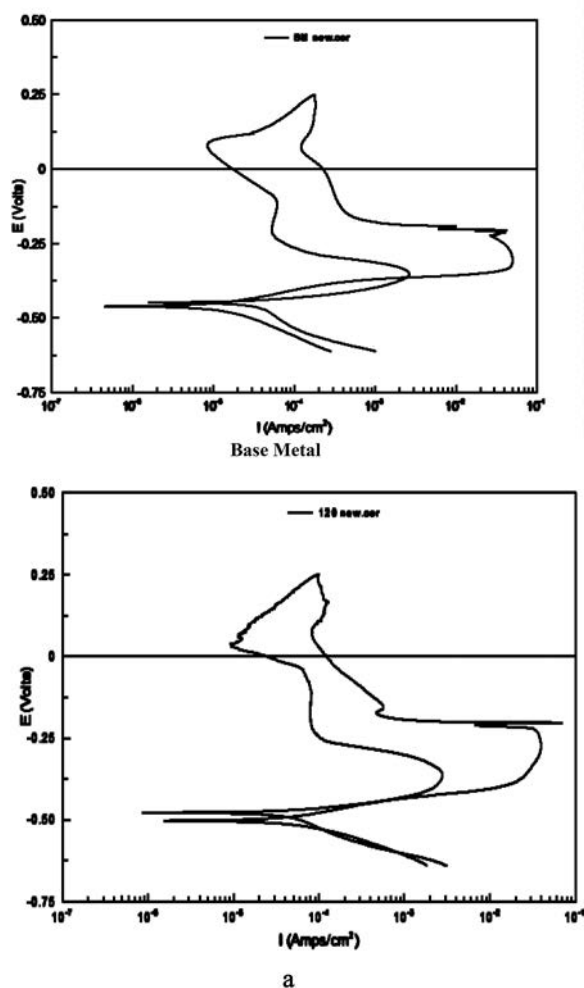
Figure 12a. DLEPR curves for Cr- Mn ASS Samples A: 120A weld.

a result, the size of the dendrites are influenced by weld heat input and time it takes to cool. It is evident from Figures 7 and 8 that the size of dendrites at weld metal increases with increasing welding heat input. It follows the larger the size of dendrites, the longer it gets to grow and therefore, the more should be the drop in hardness. This is what has been observed in Figures 10 and 11, that the drop in hardness of weld metal increases with increasing weld heat input. This is also in agreement with the results of tensile test (Figure 9 and Table 3). The stainless steels when heated or cooled in temperature range of 450–950°C suffer from the precipitation of chromium carbide at grain boundaries. The HAZ undergoes heating and cooling in the temperature range, and therefore, the spike in hardness at HAZ is attributed to the precipitation of chromium carbide at grain boundaries in HAZ. Lastly, let us see what causes sharp drop in hardness at base metal and HAZ boundary of 140A weld joint. It is attributed to the formation of more ferrite as ferrite to austenite transformation decreases at 140A weld, the excessive heat produced by the 140A welding. It follows that 140A current is not suitable for welding the Cr-Mn ASS.
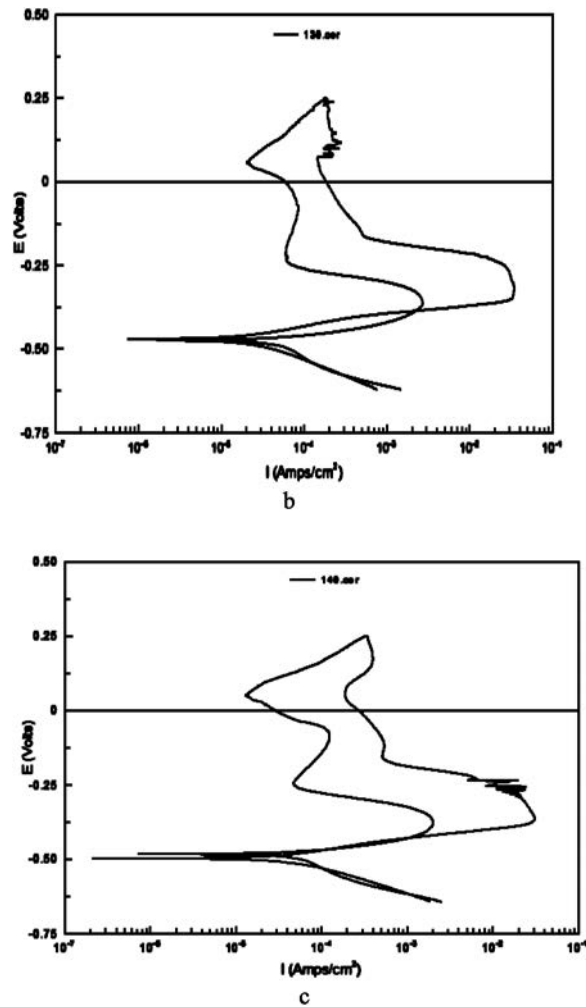
Figure 12b. B: 130A weld, C: 140A weld for 308 L filler and Samples.

3.4. Double Loop Electrochemical Potentiokinetic Reactivation (DLEPR) test

The results of DLEPR tests are shown in Figure 12. From the figures, the peak current densities of forward scan (i_a) and reverse scan (i_r) are noted. The i_r and i_a were then used to estimate % degree of sensitisation (% DOS). The % DOS value indicates susceptibility of the weld joint to intergranular corrosion (IGC). In this way, it is a measure of the extent of chromium carbide precipitated at the grain boundary due to slow heating or cooling in the temperature range of 450–950°C. The tests results are presented is Table 4. It is evident that % DOS of base metal is 2.66% i.e. it is susceptibility to IGC is almost negligible. It can be seen that on welding the % DOS of weld metal increases to 8.71% for weld with filler and to 8.48% for weld without filler. This suggests that the susceptibility of weld joint is more than that of base metal. It is also evident that % DOS increases with increasing

d

e
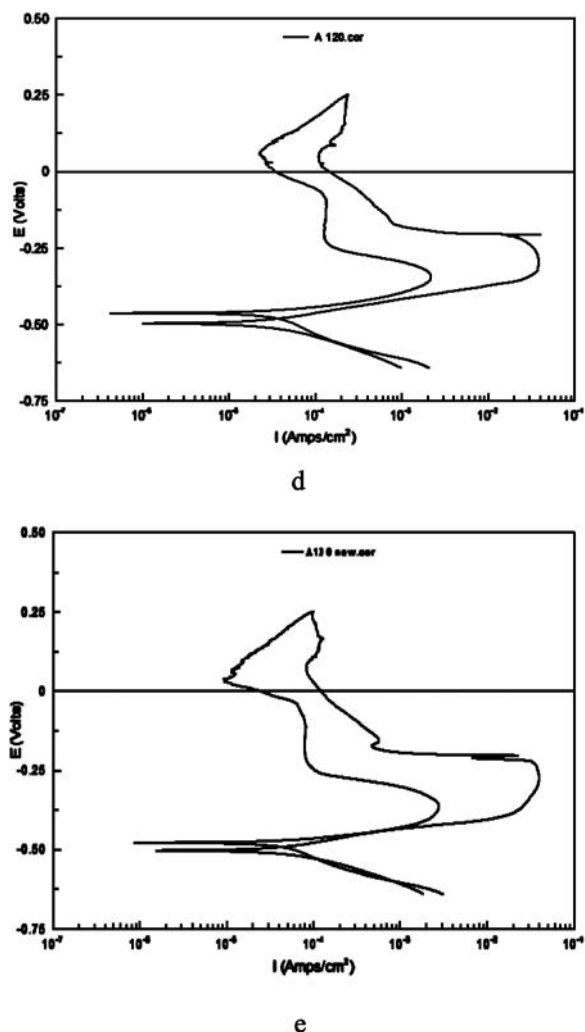
Figure 12c. D: 120A weld, E: 130A weld.

welding current [21]. Increasing welding current, increases temperature of the weld and therefore, it is likely that higher temperature retain for a longer time will case more chromium carbide and therefore, the more Chromium lean area at the grain boundary will be created. This chromium lean area makes the structure susceptible to IGC. So, the increasing % DOS with increasing welding current is attributed to more heating with increasing weld current. However, all the % DOS values are not very high. This is attributed to size of the dendrites being small. Fine grain size is less susceptible to IGC as compared to large grain size material [22].

4. Conclusions

(1)) The equiaxed grain structure of base metal ad its low % DOS value (2.66%) suggests that the base metal is in annealed condition and has not been cooled slowly (after annealing) in the temperature range of 450–900°C.
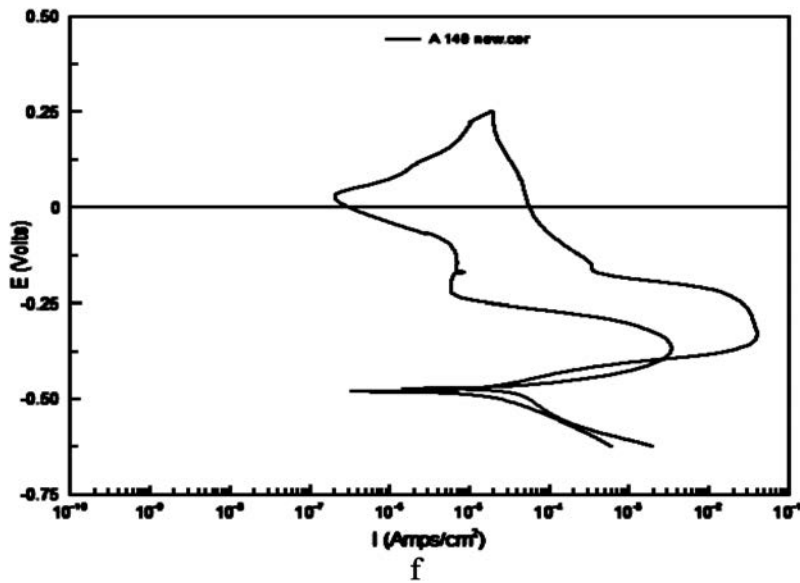
Figure 12d. F: 140A weld for autogenous welding.

Table 4. Degree of sensitisation for base metal and welded samples.

Sample	Peak activation current density, i_a (A/cm^2)	Peak reactivation current density, i_r (A/cm^2)	Degree of sensitisation, (DOS) = i_r/i_a x 100 (%)
Base Metal	0.097804	0.0026046	2.66
A	0.039447	0.0027982	7.09
B	0.034382	0.0026937	7.83
C	0.029015	0.0025275	8.71
D	0.038748	0.0021783	5.62
E	0.03932	0.002953	7.43
F	0.040093	0.0034035	8.48

(2)) The size of dendrites in weld metal decreases with increasing weld current from 120A to 140A, suggests that weld of higher weldig current cool faster.

(3)) The width of HAZ increases with increasing weld current. This suggests that higher weld current caused weld heat to be retained for longer duration allowing more heat to be conducted upto longer distances.

(4)) The size of dendrites for autogenous welding is relatively larger than that of weld with filler. This suggests that relatively more heat is generated in autogenous weld.

(5)) The maximum tensile strength was obtained for autogenous weld as compared to 308 L filler weld for low welding current (low heat input).

(6)) The hardness of weld metals for autogenous weld is highest as of 308 L filler weld and decreases with increase in current as ferrite to austenite transformation decreases for high heat input.

(7)) Values of % DOS for all the welds are quite low suggesting that the weld parameters do not make the weld joint susceptible to IGC. Results indicate that the weld without filler is less susceptible to IGC as compared to weld with 308 L filler.

Disclosure statement

No potential conflict of interest was reported by the author(s).

ORCID

Sachin Ambade Ⓘ http://orcid.org/0000-0002-2524-5798
Awanikumar P. Patil Ⓘ http://orcid.org/0000-0002-4511-7558
Diwesh B. Meshram Ⓘ http://orcid.org/0000-0001-5584-3484

References

[1] Ogundimu EO, Akinlabi ET, Erinosho MF. Study on microstructure and mechanical properties of 304 stainless steel joints by TIG-MIG hybrid welding. Surf.Rev.Lett. 2017;25:1850042.
[2] Hazra M, Srinivasa K, Madhusudhan G. Friction welding of a nickel free high nitrogen steel : influence of forge force on microstructure, mechanical properties and pitting corrosion resistance. Integr Med Res. 2013;3:90–100.
[3] Speidel MO. Nitrogen Containing Austenitic Stainless Steels Mat-wiss. u. Werkstoiftech. 2006; 37. 10:875–880
[4] John C, Lippold DJK. Welding Metallurgy and Weldability of Stainless Steels. USA: Wiley; 2005. p. 376.
[5] Lo KH, Shek CH, Lai JKL. Recent developments in stainless steels. Mater Sci Eng: R : Rep. 2009;65:39–104.
[6] Aydinol MK, Aydog GH. Determination of susceptibility to intergranular corrosion and electrochemical reactivation behaviour of AISI 316L type stainless steel. Corros Sci. 2006;48:3565–3583.
[7] Pistorius PC, Toit M. Applications and Uses LOW-NICKEL AUSTENITIC STAINLESS STEELS : METALLURGICAL CONSTRAINTS. The Twelfth International Ferroalloys Congress Sustainable Future, Helsinki, Finland. 2010;911–918.
[8] Taiwade RV, Patil AP, Ghugal RD, et al. Effect of Welding Passes on Heat Affected Zone and Tensile Properties of AISI 304 Stainless Steel and Chrome-Manganese Austenitic Stainless Steel. ISIJ Int. 2013;53:102–109.
[9] Khobragade NN, Khan MI, Patil AP. Corrosion Behaviour of Chrome – manganese Austenitic Stainless Steels and AISI 304 Stainless Steel in Chloride Environment. Trans Indian Inst. Met. 2014;67:263–273.
[10] Vashishtha H, Taiwade RV, Khatirkar RK, et al. Effect of austenitic fillers on microstructural and mechanical properties of ultra-low nickel austenitic stainless steel. Sci Technol Weld Joining. 2016;21(4):331-337.
[11] Bansod AV, Patil AP, Moon AP, et al. Intergranular Corrosion Behavior of Low-Nickel and 304 Austenitic Stainless Steels. J Mater Eng Perform. 2016;25:3615–3626.
[12] Vashishtha H, Taiwade RV, Sharma S, et al. Effect of welding processes on microstructural and mechanical properties of dissimilar weldments between conventional austenitic and high nitrogen austenitic stainless steels. J Manuf Process. 2017;25:49–59.
[13] Development M. ASSESSING SUSCEPTIBILITY TO CHROMIUM CARBIDE PRECIPITATION IN Cr-Mn AUSTENITIC STAINLESS. UNILAG J. Med. Sci. Technol. 2017;5:109–122.
[14] Bansod AV. Effect of heat on microstructural, mechanical and electrochemical evaluation of tungsten inert gas welding of low-nickel ASS. Anti Corrosion Methods Mater. 2018;65: 605–615.

[15] Chuaiphan W, Srijaroenpramong L. Effect of filler alloy on microstructure, mechanical and corrosion behaviour of dissimilar weldment between AISI 201 stainless steel and low carbon steel sheets produced by a gas tungsten arc welding. Adv Mater Res. 2012;581–582:808–816.

[16] Erog M, Aksoy M, Orhan N. Effect of coarse initial grain size on microstructure and mechanical properties of weld metal and HAZ of a low carbon steel. Mater Sci Eng: A. 1999;269:59–66.

[17] Tembhurkar C, Kataria R, Ambade S, et al. Effect of fillers and autogenous welding on dissimilar welded 316L Austenitic and 430 Ferritic Stainless Steels. J Mater Eng Perform. 2021;30:1444–1453.

[18] Ambade S, Tembhurkar C, Patil A, et al. Effect of number of welding passes on the microstructure, mechanical and intergranular corrosion properties of 409M ferritic stainless steel. World J Eng. 2021; DOI:10.1108/WJE-11-2020-0591

[19] Kuddus IA, Ambade S, Bansod A, et al. Microstructural, mechanical and corrosion behaviour of dissimilar welding of Cr-Mn ASS and AISI 304 ASS by using 316L electrode. Mater Today. 2018;5:8307–8313.

[20] Dayal RK, Parvathavarthini N, Raj B. Influence of metallurgical variables on sensitisation kinetics in austenitic stainless steels. Int Mater Rev. 2005;50:129–156.

[21] Ambade S, Sharma A, Patil A, et al. Effect of welding processes and heat input on corrosion behaviour of Ferritic stainless steel 409M. Mater Today Proc. 2021;41:1018–1023.

[22] Urade V, Ambade S. An overview of welded low nickel chrome-manganese austenitic and ferritic stainless steel. J Mater Sci Eng. 2016;5:1–6.

Simultaneous Scheduling of Machines, Tool Transporter and Tools in a Multi Machine Flexible Manufacturing System Without Tool Delay Using Crow Search Algorithm

Padma Lalitha Mareddy [a], Sivarami Reddy Narapureddy [b*], Venkata Ramamurthy Dwivedula [c], S.V. Prayagi [d]

[a] Professor,Electrical Engg. Dept.,Annamacharya Institute of Technology and Sciences, Rajampet, AP, India. 516125
[b] Professor,Mechanical Engg. Dept., Annamacharya Institute of Technology and Sciences, Rajampet, AP, India. 516125
[c] Principal ,Satya Institute of Technology and Management, Vizianagarm, AP, India. 535002
[d] Professor,Mechanical Engg. Dept., Yeshwantrao Chavan College of Engineering YCCE Nagpur, Maharashtra, India. 441110

Abstract

This paper deals with machines, tool transporter (TT) and tools simultaneous scheduling in multi machine flexible manufacturing system (FMS) with the lowest possible number of copies of every tool type without tool delay taking into account tool transfer times to minimize makespan (MSN). The tools are stored in a central tool magazine (CTM) that shares with and serves for several machines. The problem is to determine the lowest possible number of copies of every tool variety, allocation of copies of tools to job-operations, job-operations' sequencing on machines and corresponding trip operations of TT, including the dead heading trip and loaded trip times of TT without tool delay for MSN minimization. This paper proposes nonlinear mixed integer programming (MIP) formulation to model this simultaneous scheduling problem and crow search algorithm (CSA) built on the crows' intelligent behavior to solve this problem. The results have been tabulated, analyzed and compared.

1. Introduction

Manufacturing companies are expected to handle growing product complexities, shorter market time, new technologies, global competition threats, and quickly changing situation. FMS is setup to deal with manufacturing competition. FMS is an integrated production system consisting of multipurpose machine tools which are computer numerical controlled (CNC), linked to an automated material handling system (MHS) [1]. FMS aims to be flexible in manufacture without undermining the product quality. The flexibility of the FMS relies on the flexibilities of CNC machines, automated MHS, and control software. FMSs have been categorized into distinct kinds as per their workflow patterns, size, or manufacturing type. Four kinds of FMS are described from the planning and control point of perspective: single flexible machines (SFM), flexible manufacturing cells (FMC), multi-machine FMS (MMFMS), and multi-cell FMS (MCFMS) [2]. Advantages, such as reductions in cost, enhanced utilizations, decreased work-in-process, etc have already been proved by existing FMS implementations [3]. Use of resources is improved by scheduling tasks so as to reduce the MSN [4]. One way to achieve high productivity in

FMS is to solve scheduling problems optimally or near optimally.

Tool loading is a complicating issue in scheduling problems since the number of tool copies are limited and may be smaller than the number of machines due to economic restrictions. Job and tool scheduling is an important problem for production systems. Inefficient planning of job scheduling and tool loading may lead to under utilization of capital intensive machines, and high level of machine idle time [5]. Therefore, efficient scheduling of jobs and the tools enables a manufacturing system to increase machines' utilization and decrease their idle times. There are a number of studies on the machines and tools scheduling. Tang and Denardo [6] solved the problem of determining job sequence and tools which are placed before every job is processed on machine for minimization of tool switches. Chandra et al [7] proposed a practical approach for deciding the sequence of jobs and tools for minimization of the total set up and processing times to make sure that jobs are completed before their delivery dates. Song et al [8] mentioned heuristic algorithm for allocating tools and parts for minimization of tool switches between machines where every part needs to visit only one machine for its complete processing. Roh and Kim [9] examined allotment of part and tool, and scheduling issues for entire tardiness minimization under

its tool movement plan where every part needs to visit only one machine for its complete processing in FMS. Agnetis et al [1] addressed combined part and tool scheduling in FMC by placing tools in a CTM which are shared by machines using TT to minimize MSN and maximum delay. When two machines are in need of the same tool, the Tabu search algorithm is applied to address the disagreement. Tsukada and Shin [10] recommended distributed artificial intelligence approach for problems of tool scheduling and borrowing along with an approach to share the tool in FMS to deal the unexpected jobs' introduction in the dynamic situation. It is demonstrated that sharing of tool among distinct FMS cells helps to reduce tooling costs and improves the tools usage. Jun, Kim and Suh [11] recommended Greedy Search Algorithm for scheduling and supplying of tools, and determining the amount of additional tools required when FMS setup changes due to change in the product mix for MSN minimization in FMS. Keung, Ip and Lee [12] investigated machine allocation and job shop scheduling on the parallel machining workstation in tandem with different machines where tools are shared for minimization of tool switching cases and tool switches by means of GA approach. Ecker and Gupta [13] proposed an algorithm to task precedence relationships with the intend of sequencing tasks in order to minimize the overall time required for the tool changes on the SFM equipped with tool magazine, where every job requires one of the tools. Prabhaharan et al [14] addressed joint scheduling of operation and tool for MSN minimization by using preference dispatching rule and simulated annealing algorithms in the FMC with "m" indistinguishable work cells and the CTM. Karzan and Azizoğlu [15] addressed job sequencing and tool transporter movements problem on SFM with a limited tool magazine capacity. Branch-Bound algorithm and beam search technique are employed to obtain optimal or near optimal solutions for minimizing tool transporter movements between machine and tool crib area. Suresh Kumar and Sridharan [16] discussed simulation study conducted to analyze the impact of scheduling rules controlling part launch and tool request selection decisions of FMS. FMS was operating under tool movement along with part movement policy. Simulation study is employed to identify the best possible scheduling rule combinations for part launch and tool request selection to minimize mean flow time, tardiness and conditional mean tardiness. Ant Colony Optimization Algorithm was suggested by Udhay kumar and Kumanan [17] to produce optimal job and tool sequences to minimize makepan for FMS, and extended GT algorithms were used for active schedule creation. Udhaya Kumar and Kumanan [18] suggested un-traditional optimization algorithms like SA, ACO, PSO, and GA to produce the optimum jobs and tools sequence for tardiness minimization in FMS, and modified GT algorithms were used to generate efficient schedules. Aldrin Raj, et al [19] suggested 4 heuristics, including preference shipment rules, revised non-delay schedule generation algorithms with 6 dissimilar rules, revised GTA and Artificial Immune System algorithms for resolving machine and tools combined scheduling in FMS which consists of 4 machines and one CTM to minimize MSN. Özpeynirci [20] introduced a time-indexed mathematical model for machines and tools scheduling in FMS to minimize MSN. Costa, et al [21] have developed a hybrid GA that implements a local search enhancement scheme to resolve ' p ' parts on ' q ' machines scheduling undertaking tool

change activity triggered by tool wear. Sivarami Reddy et al [22] presented symbiotic organisms search algorithm (SOSA) to deal with machines and tools joint scheduling to produce best optimal sequences with a copy of every type of tools in a MMFMS that minimize MSN, and it is shown that SOSA outperforms the existing algorithms. Beezao et al [23] modeled and addressed the identical parallel machines problem with tooling constraints for minimizing MSN using an adaptive large neighborhood search metaheuristic(ALNS). It is demonstrated that ALNS outperformed other existing algorithms. Baykasoğlu and Ozsoydan [24] addressed automatic tool changer (ATC) indexing problem and tool changing problem concurrently in order to reduce non machining times in automatic machining centers using simulated annealing algorithm. Paiva and Carvalho [25] addressed job ordering and tool changing problem (SSP) to find out the jobs order and the tool loading order so as to minimize the tool changes. A methodology which employs graph representation, heuristic methods and local search methods is used for solving sequencing problem. Such techniques are integrated along with classical tooling approach to solve SSP in an algorithmic local search scheme. Gökgür et al [26] addressed constraint programming models in environments of parallel machines to solve tools scheduling and allotment problems with prearranged tools quantity in system due to financial limitations to minimize MSN. Job transport times and tool switch times among machines are not taken into account in the references reviewed above.

Sivarami Reddy et al [27] and Sivarami Reddy et al [28] solved machines and tools simultaneous scheduling problems without considering job transfer times and considering tool switch times among machines with a copy of every tool type (**SMTTATWACT**) for minimum MSN as an objective and shown that tool transfer times have significant effect on MSN.

Sivarami Reddy et al [29], Sivarami Reddy et al [30],and Sivarami Reddy et al. [31] addressed machines, AGVs and tools simultaneous scheduling with one copy of every tool type considering job transport times among machines, with and without considering tool transfer times among machines respectively to find out optimal sequences for MSN minimization in MMFMS.

Sivarami Reddy et al. [32] and Sivarami Reddy et al. [33] addressed concurrent scheduling of MCs and tools with a replica of each tool kind and alternate machines for minimization of MKSN.

The following are the other scheduling problems addressed in the literature. Al-Refaie et al. [34] devised a mathematical model for concurrent optimal patients' scheduling and sequencing in newly opened operating rooms under emergency events for maximization of patient's assignment over the empty available rooms. Abbas and Hala [35] proposed an optimization model to deal with quay crane assignment and scheduling problem considering multiple objective functions, such as minimization of handling makespan, maximization of number of containers being handled by each quay crane and maximization of satisfaction levels on handling completion times.

When operations of different jobs require the same tool at the same time, tool would be allocated for only one operation that causes other operations to wait for the tool in SMTTATWACT. This increases the MSN. Therefore it is important to address machines, TT and tools simultaneous scheduling with the lowest number of copies

of each tool kind which are much less than the number of machines without tool delay (SMATLNTC) by sharing the tools among machines to minimize MKSN in an FMS. As it causes no tool delay which in turn reduces MKSN with few additional copies for few tool types. The novelty of the research is addressing the SMATLNTC for minimization of MKSN first time, presenting nonlinear MIP model. CSA is employed to minimize MKSN of SMATLNTC and demonstrate its difference from other studies.

Automated tool sharing system presents technical solution to tools' high cost where different machines are able to employ same tool by dynamically moving the tool from machine to machine as tooling needs evolve. Because FMS is an interconnected manufacturing facility, it is important to concurrently schedule different components of FMS.

The job shop's scheduling problem [36], and the TT scheduling problem which are analogous to a problem of pick-up and delivery [37] are NP-hard problems. Combining them is a double interlinked NP-hard problem. Determining the lowest possible number of copies of every tool type for no tool delay and allocating them to the operations increases the scheduling problem complexity further, and it is also expected to improve the utilization of machines, TT and tools.

CSA is a metaheuristic developed by Askarzadeh [38]. It attempts to simulate the intelligent behavior of the crows to find the solution of optimization problems. It has been successfully applied to cope with engineering optimization problems [38-40, 27, 41-44, 29]. The advantages of the CSA over most other metaheuristic algorithms are that algorithm operations require two algorithm parameters, simple and easy to implement.

2. Problem and model formulation

Setup varies in FMS types and operations. Because having a common configuration is not feasible, the majority research focuses on defined production systems. Specification of the system, assumptions, criteria for objective and the problem addressed in this work are offered in the subsequent sections.

2.1. FMS Environment

Using common tool storage is typically followed in several manufacturing systems through one CTM serving multiple machines to cut down tool stocks. During the part's machining, demanded tool is shared from different machines or shipped from CTM by TT. CTM cuts down the tools copies required in system, and therefore cuts down tooling cost. Switching of tools and jobs between the machines will be carried out by TT and AGVs respectively. The FMS in this work is assumed to consist of four CNC machines, CTM with necessary tool types for all the machines and one copy of every type, a TT, two indistinguishable AGVs and each machine with ATC. There are loading and unloading (LU) stations where FMS releases parts for manufacturing and the completed parts are deposited and transported to the final storage facility respectively. To stock up the work-in-progress, an automatic storage and retrieval system (AS/RS) is

available. Figure 1 shows its configuration.
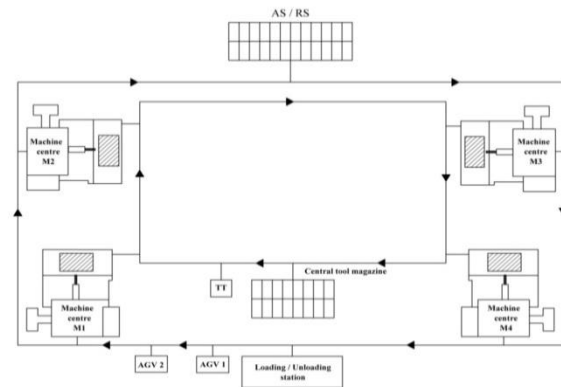
Figure 1. FMS environment

2.2. Assumptions

The following assumptions are made for the problem being studied

Initially all jobs, machines and TT are available for use.

Tool/ machine can perform one job only at any given time.

Operation's pre-emption on machine is barred.

The necessary machines and tools are identified before scheduling every operation.

Every job has operations' set with its own order and known processing times that also include setup times.

Initially, tools are stored in a CTM.

Transportation time of parts among machines is not taken into account.

At the time of jobs' arrival, the service life given to the tools will be sufficient to perform the operations allocated to the respective tools.

There is only one TT which moves the tools all through the system and tool switch times among machines are taken into account. A flow path layout for TT is given, travel times on each path segment are known and it moves along shortest predetermined paths.

TT starts from CTM initially, returns to CTM after all their assignments have been done and holds a single unit at a time.

The process planning information for determining the sequence of operations for optimizing tolerance stack-up is provided in terms of precedence constraints for each job. Thus, we assume that each job has prearranged operations order that cannot be altered.

2.3. Problem definition

Consider an FMS with a job set J of j job types $\{J_1, J_2, J_3 \dots , J_j\}$, m machines $\{M_1, M_2, M_3 \dots , M_m\}$, and total operations of job set $\{1,2,3.......N\}$ and k types of tools $\{t_1, t_2, t_3 \dots t_k\}$ with few copies of every type. A job's operations have a predetermined order of processing, and the order is known in advance. At most one operation at a time can be processed by a machine. Until its predecessor operation is complete, an operation cannot begin. The order of operations on a machine determines the setup requirements for a machine. The simultaneous scheduling problem is defined as determining the lowest possible number of copies of every variety of tools, allocation of copies of tools to job-operations and job-operations' sequencing on machines without tool delay, in addition to

determining each job's beginning and finishing times on every machine and tool copy and corresponding trip operations of TT, including the dead heading trip and loaded trip times of TT for MSN minimization in a MMFMS. The problem is stated in crisp, so unambiguous mathematical form is given in section 2.4.

2.4. Model formulation

In this section, nonlinear MIP model is introduced to clearly specify the crucial parameters and their effect on the FMS scheduling problem.

2.4.1. Notations

Decision variables

$$q_{rs} = \begin{cases} 1 & \text{if } c_r \text{ is less than } c_s, \text{ where } r \text{ and } s \text{ are operations of different jobs} \\ 0 & \text{otherwise} \end{cases}$$

$$y_{hi} = \begin{cases} 1 & \text{if the TT is assigned for dead heading trip between trip 'h' and trip 'i' where the demanded tool is available} \\ 0 & \text{otherwise} \end{cases}$$

$$y_{oi} = \begin{cases} 1 & \text{if the TT starts from CTM to accomplish trip 'i' as its first assignment} \\ 0 & \text{otherwise} \end{cases}$$

$$y_{ho} = \begin{cases} 1 & \text{if TT returns to the CTM after completing trip 'h' as its last assignment} \\ 0 & \text{otherwise} \end{cases}$$

$$ttw = \begin{cases} tttd_{o,u} & \text{if the TT starts from CTM to accomplish trip 'i' as its first accomplishment,} \\ 0 & \text{otherwise} \end{cases}$$

2.4.2. Mathematical model

In the formulation, machine and tool indices are not employed specifically as each job routing is available; the machine and tool indices are known for each operation index in I. Among operations and loaded trips there is one-to-one association. TT loaded trip for operation i is associated for every operation i. The destination of TT loaded trip' i' is a machine for which operation i is allocated and its origin is either a machine which is performing the operation using the tool required for operation i or a CTM. The tool needs to follow operations precedence constraints for the operations that belong to the same tool copy and same job i.e. RT_{kj}. The objective function for minimization of MSN is

Subscripts

j	index for a job
i, h, r, s	indices for operations
k	index for a tool
J	job set on hand for processing.
n_i	operations in job j.
N	$\sum_{j \in J} n_j$, total operations in job set J.
I	{1,2,-------N}, index set for operations.
I_j	{J_j +1, J_j +2,------J_j +n_j}, the indices' set in 'I' linked with job 'j', where 'J_j' is jobs' operations listed before job 'j' and J_1=0.
IS_i	$I - \{h; h \geq i, i, h \in I_j\}$ operations' index set without operation 'i' and same job's following operations to operation 'i'.
IP_h	$I - \{i; i \leq h, i, h \in I_j\}$ operations' index set without operation 'h' and same job's preceding operations to operation 'h'.
pt_i	operation 'i' processing time.
ct_i	operation 'i' completion time.
TL	the set of tool types to carry out the jobs' operations
TLCopy	set of copies of each tool variety.
R_k	indices set in I linked with tool type k in TL, $\forall k \in TL$
RT_{kj}	: $I_j \bigcap R_k$ the index set of operations in I common for tool k and job j $\forall k \in TL, \forall j \in J$
b_{kci}	Set of ready times of copies of tool type `k` at a machine for operation `i`, including tool copies' transfer time from other machines or CTM to this machine.
$TLRM_i$	$\min\{b_{kci}\}, \forall k \in TL, \forall c \in TLCopy, \forall i \in R_k$
ct_{ick}	operation i's completion time using copy c of tool type k, $\forall i \in I$, $\forall c \in TLCopy$, and $\forall k \in R_k$
u	first operation that uses tool k, $u \in R_k, \forall k \in TL$
v	preceding operation of i, $i, v \in R_k, \forall k \in TL$
L	number of TTs
a_j	job j ready time
TM_i	machine ready time for operation i
$tttl_i$	TT loaded trip 'i' travel time including load and unload times.
$tttd_{hi}$	TT empty trip 'i' travel time, trip commencing at a machine processing operation `h` and concluding at the machine processing operation `i` with the demanded tool.
$CTTTL_i$	TT loaded trip 'i' completion time
Q_i	: $\max(ct_{i-1}, TM_i), \quad \forall i \in I$

$Z = \min\left(\max\left(ct_i\right)\right), \quad \forall i \in I$ subject to	
$Z \geq ct_{N_j + n_j} \quad \forall j \in J$	(1)
$ct_i - ct_{i-1} \geq pt_i + tttl_i, \quad \forall i-1, i \in I_j, \forall j \in J$	(2a)
$ct_{N_j+1} \geq pt_{N_j+1} + tttl_{N_j+1}, \quad \forall j \in J$	(2b)
$ct_{ick} \neq ct_{hck}, i \neq h, \ \forall\, i, h \in R_k, \ \forall c \in TLCopy, \text{ and } \forall k \in TL$	(2c)
$(1 + H\,tagd_{rs})ct_r \geq ct_s + pt_r - H\,q_{rs}$ $(1 + H\,tagd_{rs})ct_s \geq ct_r + pt_s - H(1 - q_{rs})$ $\forall r \in I_j, \text{and } \forall s \in I_l \text{ where } j,l \in J, j<l$	(3)
$TM_i < TLRM_i, \ i \in I$ i` is the first scheduled operation on the machine	(4)
$Q_i - TLRM_i \geq 0 \quad \forall i \in I$	(5)
$y_{oi} + \sum_h y_{hi} = 1\ h \neq i, \quad i,h \in R_k, \ \forall k \in TL$	(6)
$y_{ho} + \sum_i y_{hi} = 1\ i \neq h, \ i,h \in R_k, \forall k \in TL$	(7)
$\sum_{i \in R_k}{}' y_{oi} \leq L \qquad \forall k \in TL$	(8)
$\sum_{i \in R_k} y_{oi} - \sum_{h \in R_k} y_{ho} = 0, \ \forall k \in TL$	(9)
$CTTTL_i - tttl_i \geq ct_v, \ \forall i,v \in R_k, i \neq u, \ \forall k \in TL$	(10)
$CTTTL_i - tttl_i \geq y_{oi}\,ttw + \sum_{h \in R_k, h \neq i} y_{hi}(CTTTL_h + tttd_{h,v})$ $\forall i \in R_k, \forall k \in TL, \ \text{if } h,i \in RT_{kj} \text{ then } i < h$	(11)
$CTTTL_u - tttl_u \geq \sum_{h,u \in R_k, h \neq u} y_{h,u}(CTTTL_h + tttd_{ho}), \ \forall k \in TL$	(12)
$\max(TM_i, CTTTL_i) \leq ct_i - pt_i, \ \forall i \in I$	(13)
$ct_i \geq 0, \ \forall i \in I$ $y_{hi} = 0,1 \quad i \neq h \quad i,h \in R_k, \forall i \in I$	

The 1st constraint specifies that MSN is greater than or equal to the completion time of last operation of all the jobs. The constraint 2a is the operations precedence constraints. The constraint 2b is the constraint for the completion time of first operations of jobs. The constraint 2c is the constraint for the operations that belong to the same tool copy.

H is a large positive integer in the 3rd constraint which ensures that no two operations allocated to the same machine can be concurrently performed. If operations 'r' and 's' that belong to distinct jobs need the same machine, then $tagd_{rs}$ is zero by definition. The 4th constraint defines that the machine ready time should be less than the TLRM$_i$ as the tool is to be shifted either from other machine or CTM if operation 'i' is the first scheduled operation on the machine. The 5th constraint defines that there will not be tool delay for operation i.

The 6th and 7th constraints express that tools are loaded and unloaded once for every operation respectively. The 8th constraint assures that every TT goes into the system at most one time. The 9th constraint keeps total TTs consistent in the system.

The 10th constraint states that TT loaded trip i can begin only when the preceding operation v is completed. The 11th constraint states that TT loaded trip i can begin only after TT dead heading trip is completed, and it is applicable if it is the first loaded trip of TT or TT loaded trips for operations other than the first operation of the tools. The 12th constraint states that TT loaded trip 'u' i.e. for first operation of a tool can begin only after completion of TT dead heading trip.

The 10th, 11th, and 12th constraints are connected to the starting times of TT loaded trips. Collectively, they declare that the TT loaded trip i cannot commence before the

maximum of dead heading trip to the preceding operation and the finish time of the preceding operation.

The 13th constraint specifies that the operation i cannot begin before maximum of the machine ready time and the TT loaded trip. However, this formulation is intractable due to its size and nonlinearity, thus meta-heuristic algorithm namely CSA is used to obtain near optimal or optimal solutions.

Since the MSN needs to be minimized, calculation of MSN and lowest possible number of tool copies for a given schedule needs to be developed. Flow-chart for such a computation is shown in Figure 2.

2.4.3. Input data

Since the FMS configurations differ from one to the other topologically, four different layout configurations shown in Figure 3 are considered as reported in Bilge and Ulusoy [45]. Job sets employed for this problem are the 1st ten job sets

employed by Aldrin Raj et al [19], which are also the standard problems provided by Bilge and Ulusoy [45] but with the additional information, such as tools to carry out the operations. These problems were developed for various levels of travel times to processing times' ratio (t/p). The 82 test problems were designed with 10 job sets, 2 AGVs and 4 layouts, 40 problems with t / p greater than 0.25 and 42 problems with t / p less than 0.25. Four separate layouts (LAOT 1, LAOT 2, LAOT 3 and LAOT 4) with three cases were taken into account for the estimation of the MSN with the growing processing times. The original processing times (OPT), twice the OPT and thrice the OPT had been used in case 1, case 2 and case 3 respectively. Case 1 and case 2 are taken into account for LAOT 1, LAOT 2 and LAOT 3 and all the cases are taken into account for LAOT 4. The three cases are classified into 2 sets with relatively high t / p ratio greater than 0.25(case 1) and relatively small t / p less than 0.25(case 2 and case 3).The above test problems with original travel times of TT are used for this problem.

The following data is offered as an input.

It is assumed that the flow path of tool transporter closely resembles flow path of the AGVs for any given layout, the average speed of tool transporter is 57 m/min, and travel time matrix of tool transporter including load and unload times of tool for various layouts is given in Table 1.

Number of jobs, each job's operations and job's maximum operations in job set.

Machine needed for every job operation (machine matrix),

Time needed to perform every job-operation on the machine (process time matrix), and

Tool for processing every job-operation (Tool matrix)

3. CSA

The crow flock behavior has many similarities with the process of optimization [38]. Crows conceal their surplus food in the environment's hiding places and get stored food when necessary. Crows are voracious to get better food sources, and they go after each other. If the crow notices another one is behind it, the crow attempts to deceive that crow by heading to a different location in the vicinity. The crows are searchers from an optimization view point, the environment is a search space. Every hiding place in environment is a corresponding viable solution, the food source's quality is an objective function, and the problem's global solution is the best food source. CSA tries to simulate crows ' behavior to get a solution to the problem of optimization

3.1. Implementation of CSA.

In this problem of simultaneous scheduling, CSA is employed to minimize MSN. In the suggested CSA, every parameter of solution vector has to represent job-operation, and the machine and tool that are allocated for job-operation. Therefore, job-operation, machine, and tool encoding is employed. The parameter's first item represents the job number and location in the order in which it happens in vector showing operation number. The parameter's second item indicates the machine allocated to process that operation, selected from machine matrix, and the parameter's third item represents tool allocated to perform the operation selected from tool matrix. Parameters in vector are same as job set's total operations. This coding is useful in checking precedent relationships between job's operations in the vector.
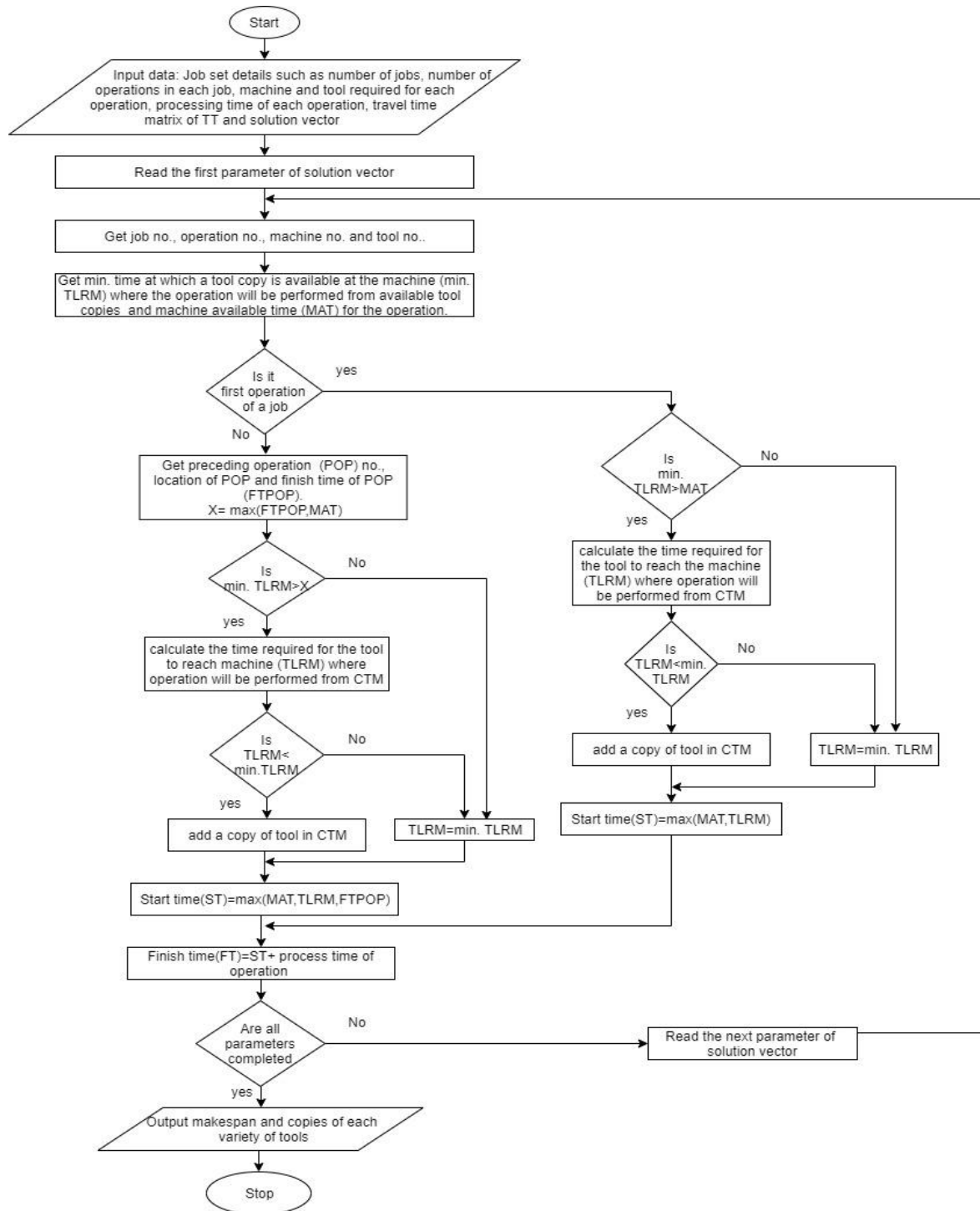
Figure 2. Flow chart for calculation of MSN and lowest possible number of tool copies for a given schedule.

Table 1. Travel time matrix of TT

Layout 1						Layout 2					
	To						To				
From	CTM	M1	M2	M3	M4	From	CTM	M1	M2	M3	M4
CTM	0	4	6	7	8	CTM	0	3	4	6	4
M1	8	0	4	6	7	M1	4	0	1	3	1
M2	7	4	0	4	6	M2	6	8	0	1	3
M3	6	6	4	0	4	M3	4	7	8	0	1
M4	4	7	6	4	0	M4	3	6	7	8	0
Layout 3						Layout 4					
	To						To				
From	CTM	M1	M2	M3	M4	From	CTM	M1	M2	M3	M4
CTM	0	1	3	7	8	CTM	0	3	6	7	10
M1	8	0	1	6	7	M1	13	0	3	4	7
M2	7	8	0	4	6	M2	14	10	0	6	4
M3	3	4	6	0	1	M3	8	6	4	0	4
M4	1	3	4	8	0	M4	10	10	8	4	0
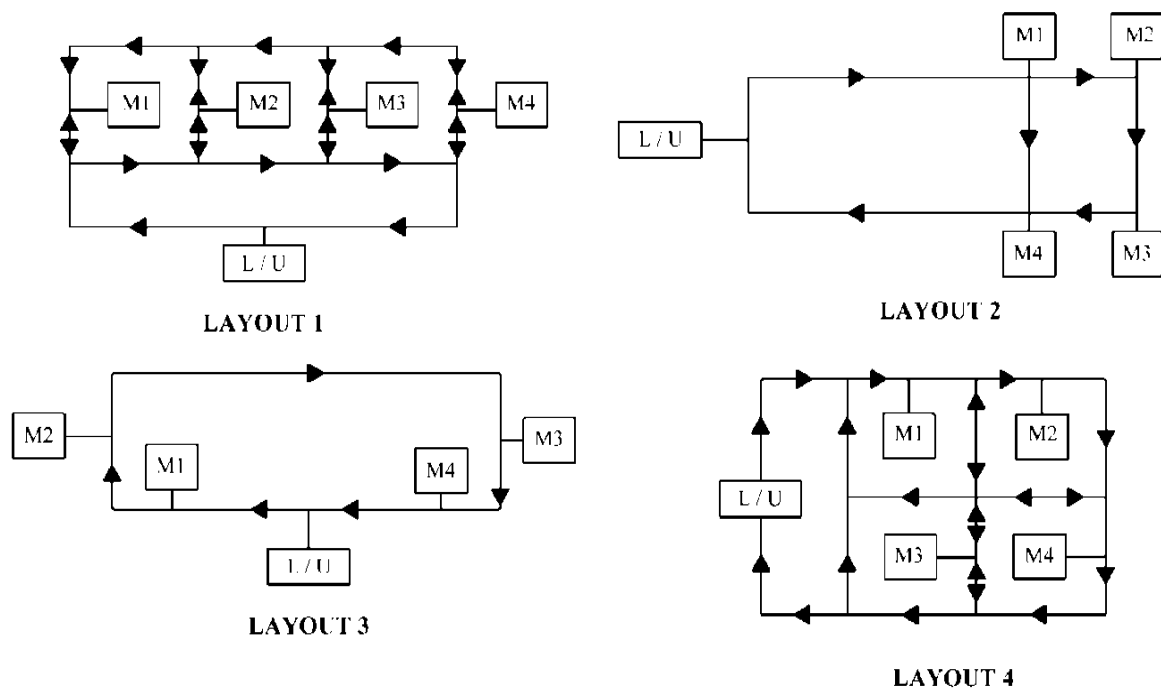
Figure 3. The layout configurations

3.1.1. Random solution generator (RSG)

RSG is devised to offer solutions for initial population. A solution vector is constructed parameter after parameter by this generator. An operation must be eligible for assigning to a parameter. An operation is said to be qualified once all of its predecessors are allocated. Qualifying operations are placed in a set for scheduling next. In the beginning, this set is made up by the first operations of each job. At every iteration one among the operations in the set is chosen arbitrarily and put next to the parameter in the vector. Then, machine and tool are picked up from machine matrix and tool matrix for the operation respectively and both are allotted to a parameter to end the vector. The set is kept up to date, and if the solution vector is not yet finished, the process will continue.

3.1.2. Limits function

It is used to ensure that the produced operations in a new solution are compatible with the precedence constraints requirement. If the precedence requirement constraints are not observed, the new solution will be corrected by the limits function so that the operations of the new solution vector will observe the precedence constraints requirement.

CSA's step-by-step implementation procedure is outlined below.

Step1: The problem and adjustable parameters be initialized.

MSN minimization is specified as an objective function. The decision variables are job-operations, machines, tools. The constraints are job-operations precedence requirements, copies of each tool variety and number of TTs. The CSA parameters, such as flock size (size of population), flight length(fl), probability of awareness (AP) and maximum iterations (iter$_{max}$) are set. Initialize iteration no to zero.

Step 2: Initialize positions.

N crows are arbitrarily situated as group mates in the search space.

This implies that N solutions are produced arbitrarily (located) through the use of RSG in the search space known as initial population.

$$\text{Initial population=} \begin{bmatrix} x_1^{1} & x_2^{1} & x_3^{1} \\ x_1^{2} & x_2^{2} & x_3^{2} \\ - & - & - \\ x_1^{N} & x_2^{N} & x_3^{N} \end{bmatrix}$$

where x_1^{i} is sequence of operations and x_2^{i} and x_3^{i} are machines and tools allocation to the corresponding job-operations respectively.

Step 3 : Assess objective function and initialize crows memory.

Each crow's position quality i,e MSN is computed by means of flow chart given in figure 2. The memory of every crow is initialized and crows are believed to have concealed their food in their original positions. That is solutions of the population and associated MSNs are recorded in memory.

Step 4: Crows make a fresh location in the search space as given below.

Crow i would like to make a new location, then it arbitrarily selects one among the crows, say the crow j, and pursues it to locate hidden food from the crow j. Crow i uses the following equation (14) to obtain new position.

$$x^{i,iter+1} = \begin{cases} x^{i,iter} + r_j X fl^{i,iter} X \left(m^{j,iter} - x^{i,iter} \right) \\ \quad a\ random\ position \end{cases}$$
$$r_j \geq AP^{i,iter} \quad (14)$$
$$otherwise$$

where r_j is a uniformly distributed random number between 0 and 1.

Fresh solution (new position) is obtained as per equation (14) for solution i (present position) in the population.

Step 5: Test if new positions (new solutions) are feasible.

If the new solution is infeasible, the use of limit functions will make it feasible. The crow modifies its location. That is the new solution of i (new location), which is to replace solution of i (present location).

Step 6: Update memory.

If the fresh solution MSN (fresh position of crow) is superior to the old solution MSN recorded in memory (crow's memory), fresh solution along with its MSN replaces the old solution and its MSN.

Repeat steps 4 to 6 for all members of the population.

Step 7: verify termination criterion.

Increment the iteration one by one. Repeat steps 4-6 till iteration no reaches iter$_{max}$. The best MSN position in the memory is identified as the optimization problem's solution when the termination requirement is met.

The initial population is generated arbitrarily by the use of RSG in the proposed methodology. Every vector of the solution consists of parameters equal to the job set operations. The data mentioned in section 2.4.3 is offered as an input. The code is written in MATLAB and offers a schedule for job-operations together with allocation of machines and tools to the corresponding job-operations for minimum MSN.

At every generation, all candidates of population are selected for replacement. Thus, NP competitions are provided to decide members for next generation.

Example: Job set 5 is considered that has five jobs and operations in job set are 13. Therefore, the solution vector with 13 parameters along with its job-operation, machine and tool based coding is given below.

333	114	141	324	532	322	232	442	433	511
221	114	233							

Randomly generated solution vector for the initial population is shown below.

114	333	522	442	121	232	144	413	231	344
233	521	312							

The generated solutions for initial population observe precedence constraints, therefore, they are feasible solutions.

Assessment: Each vector's MSN value in initial population is calculated and recorded together with vector in memory matrix.

Next generation: First vector in the population is considered as input vector and given below.

333 212 344 114 121 532 511 442 144 423 231 312 223

The above vector MSN is 66 and lowest possible tool copies are [3 2 1 1]

Generated random Value is 0.2059.Since the random value generated is lower than the probability of awareness (0.3), number other than 1 is produced at random and it is 200. The best of the 200th crow recorded in memory is taken and given below to generate new vector.

333 442 344 532 212 511 231 114 121 223 144 312 423

whose MSN is 75 and lowest possible tool copies are [2 2 1 1]

According to equation 14 new solution vector is generated and its feasibility is checked employing the Limit function. The fresh feasible vector generated is given below.

333 442 344 532 212 511 231 114 121 223 423 312 144

The new vector fitness value is assessed, and if it is superior than the input vector best fitness value in memory matrix, then the vector in the memory matrix is substituted by new vector. MSN of this vector is 70 and lowest possible tool copies are [2 2 1 1]

specified generations have been completed, the best sequence until now is given below.

114 532 333 212 344 121 442 521 144 423 231 312 223

whose MSN is 51 and lowest possible tool copies are [2 2 1 1]

First tool copy is represented with A, second tool copy is represented with B and so on. The above vector can be represented in the Job-operation, machine and tool copy form given below.

114A 532A 333A 212A 344A 212A 344A 121A 442B 511A 144A 423A231B 312B 223A

4. Results and discussions

The proposed approach has been applied on different population sizes varying from 2 to 12 times of operations in the job set, and it is found that when population size is 10 times of operations, better results are noticed. Different combinations of probability of awareness (AP) and flight length (fl) are employed, but a combination of 0.3 and 2 provided good results. Good results are obtained between 200 and 250 generations for most of the problems, so 250 generations are taken into account as the stopping criteria. The code written in MATLAB for *SMTTATWLNTC* is run on each job set discussed in section 2.4.3 for 20 times for MSN minimization. The best MSN from 20 runs is provided for every layout and job set, along with mean and standard deviation (SDV) for various cases in Table 2.

In Table 2, the non zero SDV in case 1 vary for LAOT 1 in the range [0.8127, 2.9105], for LAOT 2 in the range [0.5501, 2.0417], for LAOT 3 in the range[1.0501, 2.5644] and for LAOT 4 in the range [1.6051, 3.1473]; the non zero SDV in case 2 varies for LAOT 1 in the range [0.2236, 3.2911], for LAOT 2 in the range [1.2085, 3.4622], for LAOT 3 in the range [0.4474, 3.6158] and for LAOT 4 in the range [1.5761, 3.1289] and the non zero SDV in case 3 varies for LAOT 4 in the range [1.2732, 3.5700]. From Table 2 one interesting finding is that the SDV values are extremely small compared with the magnitude of the mean values. In fact, the coefficient of variation for non zero standard deviation varies in the range [0.001746, 0.3445]. Furthermore, the SDV is zero for 13 out of 85 problems. If one looks closer to the final solutions of 20 simulation experiments for these problems, one finds that distinct solutions with the same MSN value exist. It means many optima alternatives are there, and the suggested CSA is able to find them.

4.1. Gantt chart

The Gantt chart shows the feasibility of the job set 1 LAOT 2 of case 1 optimal solution for minimum MSN obtained by CSA. Below is given the job set 1 LAOT 2 of case 1 optimal solution vector.

113A 124A 212A 443A 532B 233B 424A 331A 511B 344A 221C 312A 141A

The solution above is given as Table 3 in the table form.

The operations assigned for every tool copy and machines are indicated in Gantt chart together with each operation's start and end times. The Gantt chart also shows empty trips, loaded trips and waiting time of TT. Figure 4 shows the above solution vector's Gantt chart. A five character word represents an operation. For instance, in operation 5132B, the 1st character '4' specifies the job number, the 2nd character '1' denotes the job-operation, the 3rd character '3' indicates the required machine, the 4th and 5th characters ' 2B ' denotes tool copy i,e tool type 2 and copy 'A' allocated to the job-operation.

In Figure 4, M4, M3, M2 and M1 denotes machines, T4A, T3A, T3B, T2A, T2B, T1A,T1B and T1C indicate tool copies and TT indicates tool transporter.

LTT xxxxx corresponds to TT loaded trips for operation xxxxx .

ETT xxxxx corresponds to TT empty trips for operation xxxxx.

WT xxxxx denotes TT waiting time to pick up the tool for operation xxxxx from machine.

Table 2. Best MSN of SMTTATWLNTC with mean and SDV for various job sets, layouts and cases

Job set number	Case 1											
	LAOT 1			LAOT 2			LAOT 3			LAOT 4		
	Best MSN	mean	SDV	Best MSN	mean	SDV	Best MSN	mean	SDV	Best MSN	mean	SDV
1	110	112.35	0.8127	87	87.75	0.5501	90	91.45	1.0501	123	125.75	1.2085
2	114	118.65	1.6944	94	95.7	1.3803	98	100.15	1.5985	135	137.3	1.7199
3	112	113.45	1.572	91	94.45	1.4318	95	98.75	1.5517	125	125.55	1.7614
4	109	111.65	1.4965	86	87.2	0.8335	85	86.95	1.4318	129	133.05	1.6051
5	96	96.85	1.0500	74	74.95	0.2286	74	75.95	2.5644	112	112.4	0.6806
6	107	107	0.0000	99	99	0.0000	100	100	0.0000	117	117	0.0000
7	107	112.95	2.6651	89	91.6	1.818	89	93.7	2.1546	121	128.6	4.4296
8	148	151.9	2.7511	135	137.25	1.2513	138	140.3	1.6575	167	173.6	2.6328
9	107	190.45	2.9105	104	106.2	1.3611	106	108.5	1.3955	135	138.3	1.6255
10	136	164.85	2.5808	141	144.8	2.0417	143	148.55	2.1879	179	183.85	2.5397
Job set number	case 2											
	LAOT 1			LAOT 2			LAOT 3			LAOT 4		
	Best MSN	mean	SDV	Best MSN	mean	SDV	Best MSN	mean	SDV	Best MSN	mean	SDV
1	149	150	0.5620	132	120	0.0000	135	135.4	0.5982	165	166.8	1.5761
2	166	169.8	2.6077	145	152.25	3.3067	147	153.75	3.3541	185	188.25	2.1491
3	162	168.95	2.9285	157	159.5	1.6702	152	159.1	2.5935	172	182.85	4.4636
4	144	146.25	1.7733	128	129.75	1.2085	128	130.35	0.8751	168	170.8	2.2804
5	128	128.05	0.2236	96	96	0.0000	105	105	0.0000	141	144.2	2.7067
6	188	188	0.0000	181	181	0.0000	182	182	0.0000	195	195	0.0000
7	160	163.75	2.0474	146	149.75	1.7733	132	132.2	0.4474	176	182	2.9558
8	268	266	0.0000	266	262	0.0000	265	265.15	0.4894	268	271	2.6557
9	186	191.5	2.7625	180	182.9	1.9708	181	183.4	1.818	200	204.3	2.3193
10	262	269.1	3.2911	249	259.75	3.4622	252	259.6	4.6158	273	284.9	5.1289
Job set number	case 3			-			-			-		
	LAOT 4			-			-			-		
	Best MSN	mean	SDV	-	-	-	-	-	-	-	-	-
2	241	248.3	3.57	-	-	-	-	-	-	-	-	-
3	241	245.1	2.0749	-	-	-	-	-	-	-	-	-
4	208	210.1	2.2455	-	-	-	-	-	-	-	-	-
5	177	177.4	1.2732	-	-	-	-	-	-	-	-	-
7	234	238.25	2.8447	-	-	-	-	-	-	-	-	-

Table 3. Optimal solution vector for job set 1 LAOT 2 of case 1

Job-operation	1-1	1-2	2-1	4-1	5-1	2-2	4-2	3-1	5-2	3-2	2-3	3-3	1-3
Machine number	1	2	1	4	3	3	2	3	1	4	2	1	4
Tool copy	3A	4A	2A	3A	2B	3B	4A	1A	1B	4A	1C	2A	1A

Jaya algorithm reported in Venkata Rao [46] is also applied on the above mentioned problems for various cases and layouts, and the results obtained are recorded along with the results obtained by employing CSA in Tables 4 and 5. When the MSN of both algorithms given in tables 4 and 5 are compared, it is observed that CSA is outperforming the Jaya algorithm.

The best MSN of **SMTTATWLNTC** with the best MSN of simultaneous scheduling of machines and tools with a copy of every tool type considering tool transfer time (**SMTTATWACT**) as reported in Sivarami Reddy et al [27] obtained by CSA and % reduction in MSN of former over later for various cases and layouts are given in Table 6. From Table 6, it is noticed that the % reduction in MSN of **SMTTATWLNTC** over **SMTTATWACT** varies in case1 for LAOT 1 from 0.00 to 20.74, for LAOT 2 from 0.00 to 19.38, for LAOT 3 from 0.00 to 18.46, for LAOT 4 from 0.00 to 4.26; in case 2 for LAOT 1 from 0.00 to 31.72, for LAOT 2 from 0.00 to 26.83, for LAOT 3 from 0.00 to 26.12 and for LAOT 4 from 0.00 to 19.35; and in case 3 for LAOT 4 from 5.85 to 13.

4.2. Convergence characterstics

Figure 5 shows CSA convergence characterstics for job set 4 LAOT 2 of case 1. The best value is 86, observed at 214 iteration and time per iteration is 0.429882 seconds.
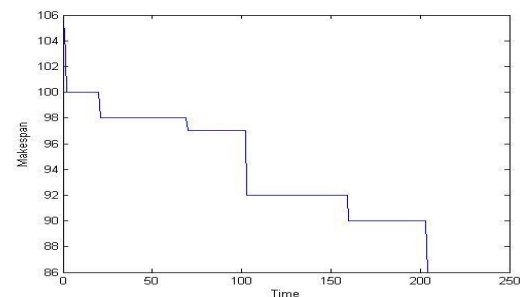
Figure 5. Convergence characteristics of CSA for job set 4, LAOT 2 of case 1
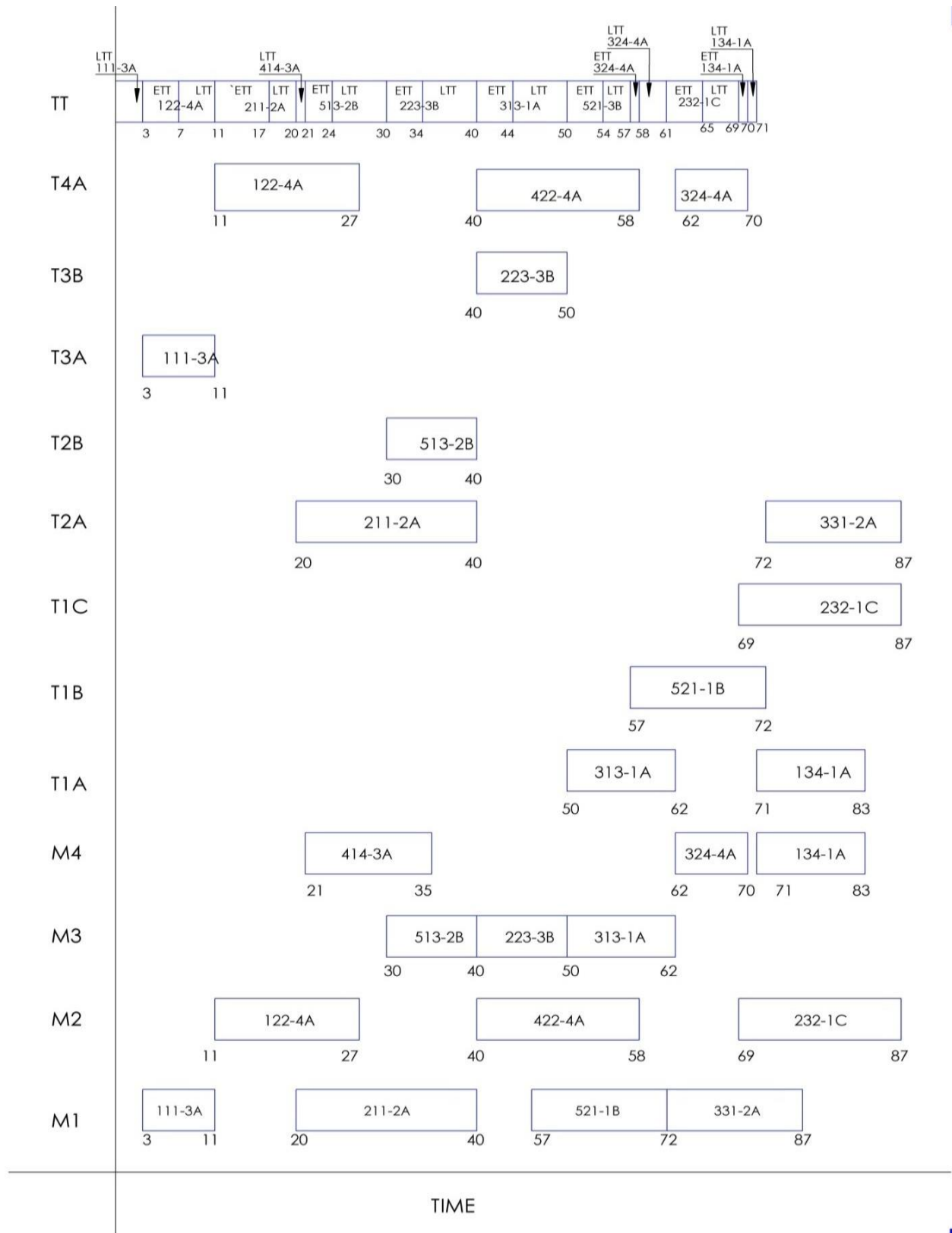
Figure 4. Gantt chart for job set 1, LAOT 2 of case1.

Table 4. Best MSN of SMTTATWLNTC obtained by CSA and Jaya algorithm for various layouts of case 1

					case 1					
					LAOT 1					
Job set number	Best MSN obtained by CSA	Lowest copies for each typeof tool for minimum MSN				Best MSN obtained by Jaya	Lowest copies for each typeof tool for minimum MSN			
		T1	T2	T3	T4		T1	T2	T3	T4
1	110	2	1	1	1	113	2	1	1	2
2	114	2	1	2	1	119	2	2	1	2
3	112	1	2	2	1	116	1	1	2	2
4	109	2	2	2	1	112	2	2	2	1
5	96	1	1	1	1	96	1	1	1	1
6	107	1	1	1	1	108	1	1	1	1
7	107	1	1	2	1	113	1	2	1	1
8	148	1	3	2	1	155	1	3	2	2
9	107	1	2	2	2	121	1	1	1	2
10	136	2	2	2	2	164	2	2	2	2
					LAOT 2					
Job set number	Best MSN obtained by CSA	Lowest copies for each typeof tool for minimum MSN				Best MSN obtained by Jaya	Lowest copies for each typeof tool for minimum MSN			
		T1	T2	T3	T4		T1	T2	T3	T4
1	87	3	2	2	1	88	2	1	1	2
2	94	2	2	1	2	97	2	2	2	1
3	91	2	2	3	2	95	2	2	2	2
4	86	2	2	2	1	88	2	3	2	1
5	74	2	1	2	1	75	1	2	2	1
6	99	1	1	1	1	99	1	1	1	1
7	89	2	1	3	2	94	1	2	2	2
8	135	1	2	3	1	137	2	2	3	2
9	104	2	2	2	3	108	2	3	1	3
10	141	2	2	3	2	147	1	2	3	2
					LAOT 3					
Job set number	Best MSN obtained by CSA	Lowest copies for each typeof tool for minimum MSN				Best MSN obtained by Jaya	Lowest copies for each typeof tool for minimum MSN			
		T1	T2	T3	T4		T1	T2	T3	T4
1	90	3	2	2	1	92	2	1	2	2
2	98	2	1	2	2	101	3	2	1	2
3	95	2	2	2	2	100	2	2	2	2
4	85	2	3	2	1	89	2	3	2	1
5	74	1	2	2	1	79	1	2	2	1
6	100	1	1	1	1	100	1	1	1	1
7	89	1	2	1	2	94	1	2	2	2
8	138	2	2	3	2	140	1	2	2	1
9	106	1	2	2	2	109	1	3	1	3
10	143	1	3	3	2	151	2	2	2	1
					LAOT 4					
Job set number	Best MSN obtained by CSA	Lowest copies for each typeof tool for minimum MSN				Best MSN obtained by Jaya	Lowest copies for each typeof tool for minimum MSN			
		T1	T2	T3	T4		T1	T2	T3	T4
1	123	1	1	1	1	128	2	1	1	1
2	135	2	1	1	1	137	1	1	1	1
3	125	1	1	1	2	129	1	1	2	1
4	129	1	2	1	1	134	1	1	2	1
5	112	1	1	1	1	113	1	1	1	1
6	117	1	1	1	1	117	1	1	1	1
7	121	1	1	1	1	130	1	1	1	1
8	167	1	1	2	1	174	1	2	2	1
9	135	1	1	1	2	139	1	1	1	2
10	179	1	1	1	1	183	2	2	2	2

Table 5. Best MSN of SMTTATWLNTC obtained by CSA and Jaya algorithm for various job sets, layouts of case 2 and case 3

		case 2								
		LAOT 1								
Job set number	Best MSN obtained by CSA	Lowest copies for each typeof tool for minimum MSN				Best MSN obtained by Jaya	Lowest copies for each typeof tool for minimum MSN			
		T1	T2	T3	T4		T1	T2	T3	T4
1	149	2	2	1	2	150	3	2	1	2
2	166	2	2	1	2	170	1	2	1	2
3	162	1	1	2	2	170	2	2	3	2
4	144	2	2	2	2	146	2	2	2	2
5	128	2	2	1	1	128	2	2	1	1
6	188	1	1	1	1	188	1	1	1	1
7	160	1	2	3	2	166	1	2	2	2
8	268	1	2	1	1	270	1	3	3	1
9	186	1	2	2	2	191	2	2	2	3
10	262	2	3	3	3	267	2	2	2	2
		LAOT 2								
Job set number	Best MSN obtained by CSA	Lowest copies for each typeof tool for minimum MSN				Best MSN obtained by Jaya	Lowest copies for each typeof tool for minimum MSN			
		T1	T2	T3	T4		T1	T2	T3	T4
1	132	2	2	1	2	132	2	2	1	2
2	145	2	2	2	2	152	2	2	2	2
3	157	2	2	3	2	158	2	2	3	2
4	128	2	2	2	2	129	1	2	2	2
5	96	1	2	1	1	107	1	2	2	1
6	181	1	1	1	1	181	1	1	1	1
7	146	2	2	2	3	151	2	2	2	2
8	266	1	2	2	1	266	1	3	3	2
9	180	2	2	2	3	184	2	3	2	3
10	249	2	3	3	2	262	2	3	2	2
		LAOT 3								
Job set number	Best MSN obtained by CSA	Lowest copies for each typeof tool for minimum MSN				Best MSN obtained by Jaya	Lowest copies for each typeof tool for minimum MSN			
		T1	T2	T3	T4		T1	T2	T3	T4
1	135	3	2	1	2	135	3	2	1	2
2	147	2	2	1	2	154	2	2	2	2
3	152	2	2	3	2	160	2	2	4	2
4	128	2	3	2	1	130	2	3	2	2
5	105	1	2	2	1	114	1	2	2	1
6	182	1	1	1	1	182	1	1	1	1
7	132	2	2	3	2	151	2	2	3	2
8	265	1	3	2	2	265	2	2	3	1
9	181	2	3	1	3	187	2	2	2	3
10	252	2	3	3	3	264	2	3	3	2
		LAOT 4								
Job set number	Best MSN obtained by CSA	Lowest copies for each typeof tool for minimum MSN				Best MSN obtained by Jaya	Lowest copies for each typeof tool for minimum MSN			
		T1	T2	T3	T4		T1	T2	T3	T4
1	165	2	1	1	2	167	2	1	1	2
2	185	2	2	1	2	187	1	3	2	2
3	172	1	1	2	2	186	1	1	2	2
4	168	2	2	1	1	170	1	1	2	1
5	141	2	1	1	1	146	2	2	1	1
6	195	1	1	1	1	196	1	1	1	1
7	176	2	2	1	2	184	1	2	1	1
8	268	1	2	2	2	272	1	2	3	2
9	200	2	3	1	2	209	1	2	2	3
10	273	2	2	2	2	265	2	2	2	2
		case 3								
		LAOT 4								
Job set number	Best MSN obtained by CSA	Lowest copies for each typeof tool for minimum MSN				Best MSN obtained by Jaya	Lowest copies for each typeof tool for minimum MSN			
		T1	T2	T3	T4		T1	T2	T3	T4
2	241	2	2	1	2	249	2	2	1	2
3	241	1	2	3	2	282	1	1	2	1
4	208	2	2	1	1	212	1	2	2	2
5	177	2	2	1	1	182	2	2	1	1
7	234	1	2	2	2	241	1	2	2	2

Table 6. Best MSN values of SMTTATWLNTC, SMTTATWACT and % reduction in MSN of former over later for various job sets, layouts and cases.

Job set number	case 1											
	LAOT 1			LAOT 2			LAOT 3			LAOT 4		
	MSN of SMTTATWLNTC	MSN of SMTTATWACT	% reduction	MSN of SMTTATWLNTC	MSN of SMTTATWACT	% reduction	MSN of SMTTATWLNTC	MSN of SMTTATWACT	% reduction	MSN of SMTTATWLNTC	MSN of SMTTATWACT	% reduction
1	110	116	5.17	87	95	8.42	90	95	5.26	123	123	0.00
2	114	120	5.00	94	100	6.00	98	104	5.77	135	137	1.46
3	112	118	5.08	91	102	10.78	95	106	10.38	125	131	4.58
4	109	116	6.03	86	98	12.24	85	99	14.14	129	131	1.53
5	96	96	0.00	74	77	3.90	74	82	9.76	112	112	0.00
6	107	107	0.00	99	99	0.00	100	100	0.00	117	117	0.00
7	107	113	5.31	89	95	6.32	89	99	10.10	121	126	3.97
8	148	160	7.50	135	151	10.60	138	149	7.38	167	172	2.91
9	107	135	20.74	104	129	19.38	106	130	18.46	135	141	4.26
10	136	171	20.47	141	165	14.55	143	166	13.86	179	182	1.65
Job set number	case 2											
	LAOT 1			LAOT 2			LAOT 3			LAOT 4		
	MSN of SMTTATWLNTC	MSN of SMTTATWACT	% reduction	MSN of SMTTATWLNTC	MSN of SMTTATWACT	% reduction	MSN of SMTTATWLNTC	MSN of SMTTATWACT	% reduction	MSN of SMTTATWLNTC	MSN of SMTTATWACT	% reduction
1	149	170	14.09	132	159	16.98	135	158	14.56	165	175	5.71
2	166	185	11.45	145	174	16.67	147	180	18.33	185	192	3.65
3	162	188	16.05	157	178	11.80	152	180	15.56	172	189	8.99
4	144	160	11.11	128	148	13.51	128	153	16.34	168	180	6.67
5	128	133	3.91	96	119	19.33	105	120	12.50	141	147	4.08
6	188	188	0.00	181	181	0.00	182	182	0.00	195	195	0.00
7	160	183	14.38	146	170	14.12	132	173	23.70	176	193	8.81
8	268	272	1.49	266	270	1.48	265	269	1.49	268	281	4.63
9	186	245	31.72	180	246	26.83	181	245	26.12	200	248	19.35
10	262	303	15.65	249	293	15.02	252	302	16.56	273	310	11.94
Job set number	case 3			-			-			-		
	LAOT 4			-			-			-		
	MSN of SMTTATWLNTC	MSN of SMTTATWACT	% reduction									
2	241	275	12.36	-	-	-	-	-	-	-	-	-
3	241	277	13.00	-	-	-	-	-	-	-	-	-
4	208	225	7.56	-	-	-	-	-	-	-	-	-
5	177	188	5.85	-	-	-	-	-	-	-	-	-
7	234	261	10.34	-	-	-	-	-	-	-	-	-

Conclusions

This paper introduces a nonlinear MIP model for machines, TT and tools simultaneous scheduling in MMFMS to minimize MSN with the lowest possible number of copies of every tool type without tool delay considering tool switch times between machines in MMFMS. This scheduling problem involves determining the lowest possible number of copies of every tool type for no tool delay, assigning of suitable tool copy for every job-operation, ordering and synchronization of those job-operations and associated trip operations of TT including the dead heading trip and loaded trip times of TT for minimum MSN. An algorithm for computation of MS and lowest possible number of copies of every variety of tools without tool delay is developed for a given schedule and Figure 2 shows its flow chart. The proposed algorithm is tested on the job sets mentioned in section 2.4.3. From the tables 2, it is quite evident that CSA is robust and able to find many optimal alternatives for the problems. From tables 4 and 5, it is noticed that CSA is outperforming Jaya algorithm. From Table 6, it is observed that impact of SMAATWLNTC on reduction in MSN over SMTTATWACT is significant. In future work with machines and tool scheduling, subsystems such as robots and automated storage and retrieval systems (AS/RS) may be integrated.

References

[1] Agnetis,Alessandro.Arianna Alfieri, Paolo, Brandimarte. Prinsecchi, Paolo. (1997). Joint Job/Tool Scheduling in a Flexible Manufacturing Cell with No On-Board Tool Magazine. Computer Integrated Manufacturing System, 10 (1), 61–68. https://doi.org/10.1016/S0951-5240(96)00023-7

[2] Saravanan, M., A,. Noorul Haq. (2008). Evaluation of scatter-search approach for scheduling optimization of flexible manufacturing systems. Int J Adv Manuf Technol, 38, 978–986. https://doi.org/10.1007/s00170-007-1134-5

[3] Chen, F. Frank. and Everett, E. AdamJr. (1991),The Impact of Flexible Manufacturing Systemson Productivity and Quality. IEEE Transactions on Engineering Management, 38(1)1, 33-45.

[4] Jyothi, S. D. (2012) Scheduling Flexible Manufacturing System Using Petri-nets and Genetic Algorithm. Project Report Indian Institute of Space Science and Technology, Thiruvananthapuram, https://www.semanticscholar.org › paper › SCHEDULING-FLEXIBLE-MAN...

[5] Shirazi, Rabia.& G. D. M. Frizelle. (2001). Minimizing the number of tool switches on a flexible machine: An empirical study. International Journal of Production Research, 39(15), 3547-3560, DOI: 10.1080/00207540110060888

[6] Tang, Christopher S. Eric V, Denardo. (1988). Models Arising from a Flexible Manufacturing Machine, Part I: Minimization of the Number of Tool Switches. Operations Research, 36(5), 767–777. https://doi.org/10.1287/opre.36.5.767

[7] Chandra, P. S. Li & M. Stan. (1993). Jobs and tool sequencing in an automated manufacturing environment. International Journal of Production Research, 31 (12), 2911-2925 .https://doi.org/ 10.1080/00207549308956907

[8] Song, Chang-Yong. Hark, Hwang. and Yeong-Daekim. (1995). Heuristic algorithm for the tool movment policy in Flexible Manufacturing systems. Journal of Manufacturing Systems, 14(3), 160-168. https://doi.org/10.1016/0278-6125(95)98884-9

[9] Roh, H.-K. and Y-D, Kim. (1997).Due-date based loading and scheduling methods for a flexible manufacturing system with an automatic tool transporter. International Journal of Production Research, 35 (11), 2989-3004, https:// doi.org/ 10.1080/ 002075497194255

[10] Tsukada,T.K. Kang. G. Shin. (1998). Distributed Tool Sharing in Flexible Manufacturing Systems. IEEE Transactions on Robotics and Automation, 14 (3), 379–389. DOI: 10.1109/70.678448

[11] Jun,Hong-Bae. Yeong-Dae, Kim. Hyo-Won, Suh. (1999). Heuristics for a Tool Provisioning Problem in a Flexible Manufacturing System with an Automatic Tool Transporter. IEEE Transactions on Robotics and Automation, 15(3), 488–496. DOI: 10.1109/70.768181

[12] Keung, K. W. W. H, Ip. and T. C. Lee. (2001). A genetic algorithm approach to the multiple machine tool selection problem. Journal of Intelligent Manufacturing, 12, 331–342. https://doi.org/10.1023/A:1011215416734

[13] Ecker, K.H. and J.N.D,Gupta. (2005). Scheduling tasks on a flexible manufacturing machine to minimize tool change delays. European Journal of Operational Research, 164, 627–638. https://doi.org/10.1016/j.ejor.2003.12.025

[14] Prabaharan,T. P. R,Nakkeeran, and N,Jawahar. (2006). Sequencing and Scheduling of Job and Tool in Flexible Manufacturing Cell. International Journal of Advanced Manufacturing Technology, 29 (3), 729–745. https://doi.org/10.1007/s00170-005-2567-3

[15] Karzan, Fatma Kilinç. and Meral, Azizoğlu.(2008). The tool transporter movements problem in flexible manufacturing systems. International Journal of Production Research,46(11), 3059–3084. https://doi.org/10.1080/00207540601070135

[16] Sureshkumar, N., and R.Sridharan.(2009). Simulation Modeling and Analysis of Tool Flow Control Decisions in a Flexible Manufacturing System. Robotics and Computer Integrated Manufacturing, 25, 829–838. https:// doi.org/ 10.1016/ j.rcim. 2008.12.004

[17] Udhayakumar, P. and S, Kumanan. (2010). Sequencing and scheduling of job and tool in a flexible manufacturing system using ant colony optimization algorithm. Int J Adv Manuf Technol, 50, 1075–1084. https://doi.org/10.1007/s00170-010-2583-9

[18] Udhayakumar, P. and S, Kumanan. (2012). Some metaheuristic approaches for optimising tardiness of job and tool in a flexible manufacturing system. Int. J. Advanced Operations Management, 4(3) , 219-252.https://doi.org/10.1504/IJAOM. 2012 .047683

[19] Aldrin Raj, J. Ravindran, D. Saravanan, M. and Prabaharan, T. (2014). Simultaneous scheduling of machines and tools in multimachine flexible manufacturing system using artificial immune system algorithm. International Journal of Computer Integrated Manufaturing, 27(5), 401–414. https://doi.org/ 10.1080/0951192X. 2013.834461

[20] Özpeynirci, Selin. (2015).A heuristic approach based on time-indexed modelling for scheduling and tool loading in flexibl manufacturing systems. Int J Adv Manuf Technol, 77, 1269–1274. https://doi.org/10.1007/s00170-014-6564-2

[21] Costa, A. F.A, Cappadonna, S, Fichera. (2016). Minimizing the total completion time on a parallel machine system with tool changes. Computers & Industrial Engineering, 91, 290–301.. https://doi.org/10.1016/j.cie.2015.11.015

[22] Sivarami Reddy, Narapu Reddy. Dwivedula, Venkata Ramamurthy. K, Prahlada Rao. M,Padma Lalitha. (2016). A Novel metaheuristic method for simultaneous scheduling of machines and tools in multi machine FMS. IET Digital Library International Conference on Recent Trends in Engineering, Science & Technology 2016, 1–6. ISBN-978-1-78561-785-0 DOI: 10.1049/cp.2016.1489

[23] Beezao, Andreza Cristina. Jean-Francüois, Cordeau. Gilbert Laporte,Horacio. Hidek, Yanasse. (2017).Scheduling identical parallel machines with tooling constraints. EuropeanJournal of Operational Research, 257(3), 834-844. doi: 10.1016/j.ejor.2 016.08.008

[24] Baykasoğlu, Adil. and Fehmi, Burcin Ozsoydan. (2017). Minimizing tool switching and indexing times with tool duplications in automatic machines. International Journal of Advanced Manufacturing Technology , 89,1775–1789.DOI 10.1007/s00170-016-9194-z

[25] Paiva Gustavo Silva. Marco Antonio M, Carvalho. (2017). Improved Heuristic Algorithms for the Job Sequencing and Tool Switching Problem. 88, 208-219. Computers and Operations Research, doi: 10.1016/j.cor.2017.07.013

[26] Gökgür, Burak.Brahim, Hnich. &Selin, Özpeynirci.(2018). Parallel machine scheduling with tool loading: a constraintprogramming approach. International Journal of Production Research. https://doi.org/10.1080/ 00207543. 2017. 1421781

[27] Sivarami Reddy, N. D.V,Ramamurthy. K, Prahlada Rao. (2018a).SimultaneousScheduling of Machines and Tools Considering Tool Transfer Times in Multimachine FMS Using CSA. International Conference on Intelligent Computing and Applications, Advances in Intelligent Systems and Computing 632, 421–432.

[28] Sivarami Reddy, N. D.V, Ramamurthy. and K, Prahlada Rao. (2018b). Simultaneous scheduling of jobs, machines and tools considering tool transfer times in multi-machine FMS using new nature-inspired algorithms. Int. J. Intelligent Systems Technologies and Applications, 17(1/2), , 70–88.

[29] Sivarami Reddy, N. D V, Ramamurthy. K, Prahlada Rao. & M. Padma Lalitha. (2019).Integrated scheduling of machines, AGVs and tools in multi-machine FMS using crow search algorithm, International Journal of Computer Integrated Manufacturing. DOI:10.1080/0951192X.2019.1686171 https:// doi.org/10.1080/0951192X.2019.1686171

[30] Sivarami Reddy, N. D. V, Ramamurthy. K, Prahlada Rao.& M, Padma Lalitha. (2021).Practical simultaneous scheduling of machines, AGVs, tool transporter and tools in a multi machine FMS using symbiotic organisms search algorithm. International

Journal of Computer Integrated Manufacturing, DOI: 10.1080/ 0951192X.2020.1858503   https://doi.org/10.1080/0951192X. 2020. 1858503

[31] Sivarami Reddy, N. D V,. Ramamurthy. M, Padma Lalitha.& K, Prahlada Rao.(2021b).Integrated simultaneous scheduling of machines, automated guided vehicles and tools in multi machine flexible manufacturing system using symbiotic organisms search algorithm.Journal of Industrial and Production Engineering.https://doi.org/10.1080/21681015.2021.1991014

[32] Sivarami Reddy N., Padma Lalitha M., S.P.Pandey, Venkatesh G.S.(2021c). Simultaneous scheduling of machines and tools in a multi machine FMS with alternative routing using symbiotic organisms search algorithm. Journal of Engg. ResearchDOI : 10.36909/jer.10653

[33] Sivarami Reddy N., Padma Lalitha M., D V. Ramamurthy, K Prahlada Rao. (2022). Simultaneous scheduling of machines and tools in a multi machine FMS with alternate machines using crow search algorithm., Journal of Advanced Manufacturing Systems https://doi.org/10.1142/S0219686722500305

[34] Al-Refaie et al. (2017).Optimal Scheduling and Sequencing of Operating Room Under Emergency Cases. Jordan Journal of Mechanical and Industrial Engineering 11(1), 21-26.

[35] Abbas, Al-Refaie. and Hala, Abedalqader. (2021). Optimal Quay Crane Assignment and Scheduling in Port's Container Terminals. Jordan Journal of Mechanical and Industrial Engineering, 15(2), 153-167.

[36] Lenstra, J.K.A.H.G,Rinnooy Kan. (1979).Computational complexity of discrete optimization problems. Ann. Discrete Math., vol. 4, 121–140.   https://doi.org/10.1016/S0167-5060(08)70821-5

[37] Lenstra, J.K. A.H.G,.Rinnooy Kan. (1981). Complexity of vehicle routing and scheduling problems. Networks, vol. 11, No. 2, 221–227. https://doi.org/10.1002/net.3230110211

[38] Askarzadeh,Alireza. (2016). A novel metaheuristic method for solving constrained engineering   optimization problems. Computers and Structures.169, 1– 12. https://doi.org/10.1016/j. compstruc.2016.03.001

[39] Oliva, Diego. , Salvador, Hinojosa. Erik, Cuevas. Gonzalo, Pajares. Omar, Avalos. Jorge, G«alvez. (2017). Cross entropy based thresholding for magnetic resonance brain images using Crow Search Algorithm. Expert Systems With Applications,79, 164-180. doi:10.1016/j.eswa.2017.02.042

[40] Sivarami Reddy, N. Dr.D.V,Ramamurthy. Dr. K, Prahlada Rao. and Dr. M, Padma Lalitha. (2017). Simultaneous Scheduling of Machines and Tools in Multi Machine FMS Using Crow Search Algorithm. International Journal of Engineering Science and Technology, 9(09S), 66–73.

[41] Sivarami Reddy,N. D.V,Ramamurthy. K,Prahlada Rao. (2018c). Simultaneous Scheduling of Machines and AGVs using Crow Search Algorithm. Manufacturing Technology Today, 17(09) ,12–22. ISSN: 0972-7396. www.i-scholar.in › index.php › MTT › search › authors › view › country=...

[42] Pankaj, Upadhyay. J.K, Chhabra.(2019). Kapur's entropy based optimal multilevel image segmentation using Crow Search Algorithm. Applied Soft Computing Journal105522, https://doi.org/10.1016/j.asoc.2019.105522.

[43] Anter Ahmed, M. Aboul Ella, Hassenian. Diego, Oliva.(2019).An improved fast fuzzy c-means using crow search optimization algorithm for crop identification in agricultural. Expert Systems With Applications, 118,340-354 doi: https://doi.org/10.1016/j.eswa.2018.10.009

[44] Spea Shaimaa, R. (2020). Solving practical economic load dispatch problem using crow search algorithm. International Journal of Electrical and Computer Engineering (IJECE) , 10(4), 3431-3440

[45] Bilge,Ümit.Gündüz, Ulusoy.(1995).A time window approach to simultaneous scheduling of machines and material handling system in FMS. Operations Research, 43, 1058−1070. https://doi.org/10.1287/opre.43.6.1058

[46] Venkata Rao, R.(2016). Jaya: A simple and new optimization algorithm for solving constrained and unconstrained optimization problems. International Journal of Industrial Engineering Computations , 7, 19–34.
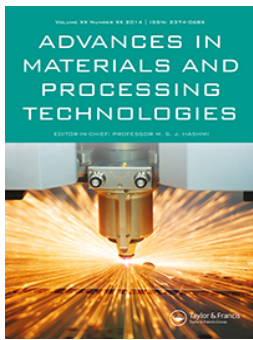
Novel curved trajectory machining using VOEDM process – experimental study and statistical optimisation thereof

Diwesh B. Meshram , Yogesh. M. Puri , Vikas K. Gohil & Sachin P. Ambade

Published online: 18 Jul 2020.

Submit your article to this journal ⌇

View related articles ⌇

View Crossmark data ⌇

Taylor & Francis
Taylor & Francis Group

RESEARCH ARTICLE

Novel curved trajectory machining using VOEDM process – experimental study and statistical optimisation thereof

Diwesh B. Meshram [a], Yogesh. M. Puri [a], Vikas K. Gohil [b]
and Sachin P. Ambade [c]

aDepartment of Mechanical Engineering Technology, Visvesvaraya National Institute of Technology, Nagpur,
India; bDepartment of Mechanical Engineering, Bajaj Institute of Technology, Wardha, India; cDepartment of
Mechanical Engineering, Yeshwantrao Chavan College of Engineering, Nagpur, India; dDepartment of
Mechanical Engineering, Visvesvaraya National Institute of Technology, Nagpur, India

ABSTRACT

This paper presents a novel Variable Oscillating EDM process through a mechanism provided on the Z-axis numerical control EDM for machining the curvature channel. The specific trajectory is machined inside the oil hardening non-shrinking steel workpiece through the curved copper electrode. In order to execute the experiments, critical input machining parameters (sparking current, pulse on time, pulse off time, and swing sensitivity) and output process characteristics (Electrode wear rate and material removal rate) are selected. Taguchi experimental design (L9) is used to design the experiments. The pulse off time has a significant effect on VOEDM process characteristics. Analysis of variance is used to identify the significant contributions of selected parameters. It identifies the major contributing factor to be the pulse off time for EWR (50.33%) and MRR (34.78%). The machining parameters optimised using regression analysis adopting a forward selection method. Finally, confirmation runs are performed to evaluate the results of optimal combination of machining parameters with output characteristics. The average experimental values at optimum conditions for achieving minimum EWR and maximum MRR are 0.000194mm^3/min and 0.000397mm^3/min, respectively. Further, SEM was used for analysing the material behaviour of workpiece. The experimental results confirm the validity and sustainability of the VOEDM process.

1. Introduction

Electrical discharge machining (EDM) is a spark erosion machining process in which the material is removed from the workpiece through a series of sparks from the electrode while being immersed in a liquid dielectric medium [1]. It is widely used in the manufacturing of complex geometry in hard material parts that are extremely difficult to machine [2]. Kunieda et al. discussed the recent trends that occurred in the EDM process by focussing

---

on a technology-driven system. Emerging areas related to the advance machining process were identified, and its applications are discussed [3]. EDM performance measure and EDM process parameters are the two crucial criteria selected in die-sinking EDM [4]. Further, the author also examined new areas of machining curved channel through EDM based on the specific set of rules. They also discussed the various mechanisms for machining the different trajectories. The primary focus was on the movement of the electrode on the workpiece in a specific direction of rotation [5].

In die-sinking EDM, the selection of electrode and workpiece is based on the customised application. Most of the research in this area has been concerned with the development of customised electrodes for improving the performance of EDM. Okada et al. used the curved hole EDM drilling technique wherein the electrode material was an Aluminium alloy [6]. Furthermore, the author discussed the behaviour of response characteristics by investigating machining parameters. The hardest material (Titanium alloy) had machined on the EDM with an alternative mechanism. Taguchi's design of experiment technique was implemented for the formulation of the experiments [7]. Aliakbari and Baseri used the rotary EDM process by employing a hollow electrode with the different combinations over X210Cr12 material. Material removal rate (MRR), Tool wear rate (TWR), surface roughness (SR), and overcut were also analysed and discussed [8].Researches have also been carried out by employing the curved copper electrode in machining the curved channel. Meshram et al. identified four output process characteristics during experimentation [9]. Das et al. reported the factors affecting and causing an increase in MRR by selecting the EN-31 tool steel workpiece material. They also successfully explained the applicability and benefits of adopting the methodology in manufacturing industries [10]. Industries require customised electrode and workpiece with regard to a specific application. The machining parameters analysis and performance improvement method using optimisation were explained by Gnanavel et al. [11]. The optimisation was used in machining a small channel by novel manufacturing process developed [12]. The author used a composite material as the workpiece and determined unique manufacturing process for analysing the machining parameters. They also reported that the multi-response optimisation was used for improving the process [13]. Marichamy et al. discussed a new approach to validate the output measurements on EDM by the Taguchi method [14]. Sivasankar et al. examined the methodological procedure utilised in EDM through the advanced modelling process. The predicted results indicate the sustainability of the model and its implementation [15].

Further, a new model, Taguchi-DEAR, was implemented for machining Titanium alloy (Ti-6Al-4 V) on EDM [16]. In the field of rapid manufacturing, complex geometry copper was manufactured for machining D2 steel. The author highlighted the very high efficiency of the EDM process in comparison to other conventional methods. Yet another approach in the EDM process has been the designing of electrodes with various geometries and utilising the machining parameters analysis [17]. Kumar et al. had conducted a detailed study related to the multi-objective optimisation of process characteristics. They adopted the nonlinear regression analysis for mathematical modelling [18]. Sonawane et al. discussed the results obtained by the confirmation of runs validated by multi-objective optimisation. MRR and other governing variables were identified, and its practical analysis was performed [19].

The replacement of copper electrode has also been an approach for reducing the problems arising during machining. Alternative materials have been suggested, and its

significant contribution to improving machining capabilities had been analysed [20]. The experiments were executed on P20 steel through copper electrode on a CNC EDM machine. The advanced regression model was considered for optimising the machining parameters. They suggested that the model helped in reducing the machining time and cost [21]. Minitab statistical software 16 was used for determining the regression equations for output characteristics and comparison between experimental values and values obtained by adopting optimisation techniques were performed [22].

Further, the complex relationships between EDM machining parameters and performance responses for SS-304 steel workpiece material were investigated based on the nonlinear identified problems. Support vector regression (SVR) was used for reducing the errors using the mathematical multi-objective model [23]. The concept of the Vikor index was discussed for optimisation in sustainable manufacturing through EDM. Multiple linear regression analyses formulate the mathematical correlation for the selected parameters [24]. Hybrid method was discussed by Baraskar et al. for high precision manufacturing components on EDM. Statistical analysis was executed by the design of experiment and multilinear regression analysis. Multi-objective optimisation method was adopted for the optimal solution [25].

In this paper, the curvature trajectory is machined by variable oscillating EDM (VOEDM) considering four variables; sparking current, pulse on time, pulse off time, and swing sensitivity. EWR and MRR were selected as the output performance characteristics. The concept of VOEDM process elaborates machining the curved trajectory through movement of curved electrode governed by the electronic control system. The forward-reverse motion of the curved electrode on the stationary workpiece results in generation of a series of sparks. The curved electrode contact area is variable, and its forward-reverse movement renders the oscillatory motion on the workpiece. Taguchi suggests a minimum of nine experiments required for the experimental investigation. The investigation was based on the critical input machining parameters with the desired range. Curved copper electrode and OHNS workpiece are the key combinations for the VOEDM process. The individual contribution to output characteristics is analysed by the ANOVA method. Further, the graphical plots (Main effect, residual and interaction) are used for measuring the variation observed with obtained results. Further, regression analysis is adopted for identifying the inter-relationship between the selected model. The major objective of this research study is to machine the curved channel using a defined trajectory with minimum EWR and maximum MRR. Confirmation runs and optimised plots are the key factors selected for obtaining accurate and factual results. Finally, it validates that the optimum values of EWR and MRR are within the range of confidence interval at 95%. The primary application of the VOEDM is developing the cooling channel of the plastic injection.

2. Materials and methods

2.1. VOEDM mechanism

The experiments were executed on Electronica 500 × 300 Z-axis Numerically Controlled (ZNC) EDM machine manufactured in Pune, India. VOEDM mechanism consisted of a drive motor, timing gears driven mechanism, bearing house assembly, nylon bolts,

Figure 1. Experimental setup for curved machining EDM process

nuts, Aluminium support for the bearing house assembly, and locking mechanism for the electrode as shown in Figure 1. The distinguishing features of the mechanism are as follows:

- Variable oscillating motion to the curved electrode.
- Locking mechanism for attaching different curvature electrodes.
- Flexibility in machining inside and outside the curved channel.
- Customised electronic control system (ECS) for implementation of the VOEDM process.

2.2. Configuration of the workpiece and curved electrode

The workpiece used for the experiments was oil-hardening non-shrinking steel (OHNS) applied in dies and mould manufacturing. The workpiece was shaped in rectangular

pieces of length 40 mm, width 12.5 mm and height 40 mm. The electrode was a semi-circular ring with a radius of 16.5 mm and a cross-sectional thickness of 3.2 mm. Experiments were conducted using nine pure copper electrodes with nine OHNS work-pieces. Every experiment required the individual curved electrode and workpiece to obtain accurate results. The chemical composition of OHNS workpiece was 0.94% (C), 0.99% (Mn), 0.49 (W), 0.99% (Cr), 0.39(V) and the copper curved electrode was 99% pure.

2.3. An experimental formulation for output characteristics

Both the end faces of the individual curved electrode were polished using fine-grade emery sheet, and the top face of the workpiece was ground using a surface-grinding machine. In order to measure the electrode wear rate (EWR) and material removal rate (MRR), it is necessary to obtain the initial weight of the workpieces and electrodes, which was obtained using METTLER Toledoc (Accuracy-0.19 g) SB-24001DR analytical balance. The machining time was 120 min for each experiment. The density of copper material and OHNS workpiece were selected as 8.96 g/cm^3 and 8.67 g/cm^3, respectively.

The EWR and MRR were calculated using the formula [26,27]:

$$EWR(mm^3/min)$$
$$= \frac{(Weight \ of \ the \ electrode(before)) - (Weight \ of \ the \ electrode(after))}{((Density \ of \ Cu \ electrode \ material) \times (Machining \ time))} \quad (1)$$

$$MRR(mm^3/min)$$
$$= \frac{(Weight \ of \ the \ Workpiece(before)) - (Weight \ of \ the \ Workpiece(after))}{((Density \ of \ OHNS \ electrode \ material) \times (Machining \ time))} \quad (2)$$

After completion of each experiment, the electrode was separated from the locking mechanism, and the workpiece unclamped. The tip of the curved electrode was appropriately aligned with the workpiece for generating the curvature trajectory through machining, and based on the input machining parameters, the output performance characteristics were analysed.

2.4. Taguchi experimental design

Taguchi experimental design was adopted for obtaining the different combinations of input machining parameters. Design of Experiments (DOE) was applied for the formulation of the planned experiments based on the selected levels [28,29]. The

Table 1. Process parameters and their levels.

Variables	Parameters		Levels and corresponding values of input		
			Level 1	Level 2	Level 3
A	IP	Sparking Current, IP (A)	5	20	35
B	T_{on}	Pulse on time, T_{on} (µs)	20	55	90
C	T_{off}	Pulse off time, T_{off} (µs)	1	5	9
D	SEN	Swing Sensitivity, SEN	1	51	99

Table 2. Experimental results for output performance characteristics.

Exp. no	IP (A)	T_{on} (µs)	T_{off} (µs)	SEN	EWR (mm^3/min)	MRR (mm^3/min)
1	5	20	1	1	0.000104	0.000269
2	5	55	5	51	0.000071	0.000336
3	5	90	9	99	0.000118	0.000394
4	20	20	5	99	0.000039	0.000288
5	20	55	9	1	0.000181	0.000528
6	20	90	1	51	0.000136	0.000422
7	35	20	9	51	0.000286	0.000336
8	35	55	1	99	0.000249	0.000278
9	35	90	5	1	0.000086	0.000336

chosen input machining parameters were sparking current (IP), pulse on time (T_{on}), pulse off time (T_{off}) and swing sensitivity (SEN) [30], identified from the available machining parameters on the ZNC EDM machine. The decided input machining parameters with three levels are indicated in Table 1. Based on the pilot study, it is forecasted that all selected parameters have a significant role in generating the curved trajectory during machining.

Further, orthogonal arrays were selected and constructed to facilitate experimental design using MINITAB 18 statistical software [31]. The required orthogonal array as per the given experimental condition is L$_9$, and performance outputs are discussed in Table 2. Equations (1 and 2) are used to calculate the values of EWR and MRR, respectively.

3. Results and discussion

3.1. Experimental analysis of obtained results

The innovative techniques used in the VOEDM process involved a smaller number of experimentation activities for optimising the output characteristics. By adopting the Taguchi method, the L9 orthogonal array was selected. The criterion depends on each row, indicating the combination of the input machining parameters with an aligned level, and the column shows the formation of the orthogonal array. In this study, MINITAB 18 statistical software was used to identify and analyse the various aspects related to optimisation. It also deals with graphical research based on the observation of standard experimental results. Table 3 provides the experimental results with S/N ratio for MRR and EWR.

Table 3. Experimental results with S/N ratio for the EWR and MRR.

Exp. no	EWR (mm^3/min)	S/N ratio	MRR (mm^3/min)	S/N ratio
1	0.000104	79.64542	0.000269	−71.4008
2	0.000071	83.01351	0.000336	−69.4626
3	0.000118	78.55371	0.000394	−68.0883
4	0.000039	88.1648	0.000288	−70.8016
5	0.000181	74.82909	0.000529	−65.5368
6	0.000136	77.34273	0.000423	−67.475
7	0.000286	70.85877	0.000336	−69.4626
8	0.000249	72.06709	0.000279	−71.096
9	0.000086	81.35403	0.000336	−69.4626
Average	0.000141	78.4255	0.000355	−69.1985

$$\eta = -10 \log \left[\frac{1}{n} \sum_{i=1}^{n} y_i^2 \right] \qquad (3)$$
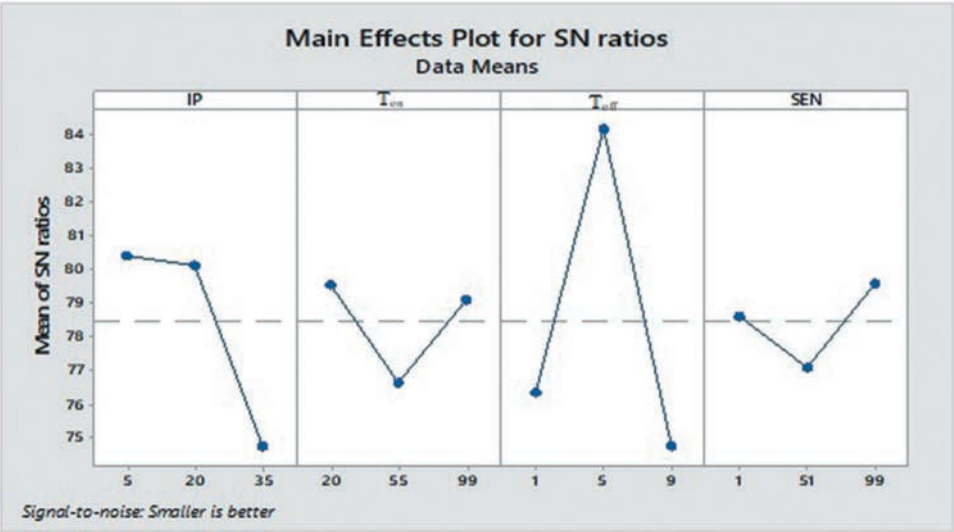

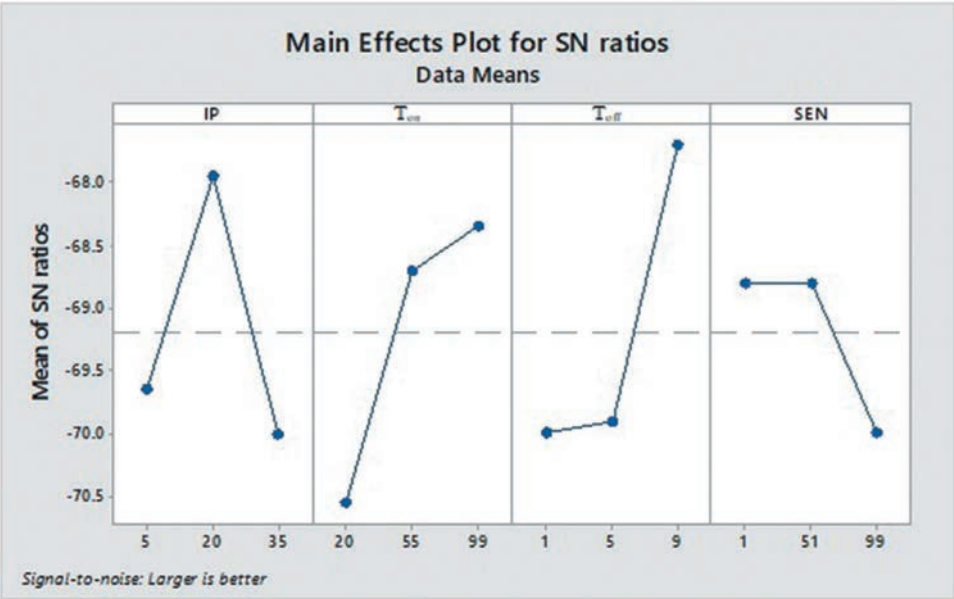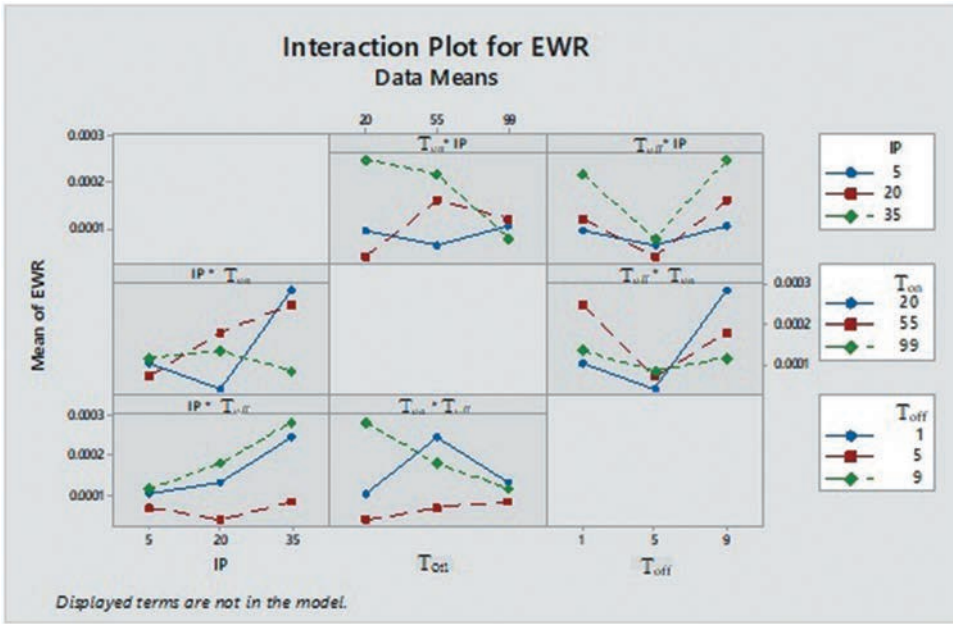Figure 2. Main effect plot for EWR

Figure 3. Main effect plot for MRR

Figure 4. Interaction plot for EWR

$$\eta = -10\log\left[\frac{1}{n}\sum_{i=1}^{n}\left(\frac{1}{y_i^2}\right)\right] \tag{4}$$

where η is the resultant S/N ratio (units: dB); n is the number of replications of each experiment; y_i is the input machining parameters of the ith experiment.

The VOEDM process served the main purpose so as to reduce EWR and increase MRR. The S/N ratio was distinguished and evaluated for EWR (Smaller is better) and MRR (larger is better) based on Equations (3 and 4) respectively. Figure 3 and Figure 4 show the main effect values plotted for input process characteristics.

3.1.1. Experimental effect of EWR by input machining parameters

From Figure 2, it was observed that IP increased from 5A to 35A, while EWR followed a decreasing trend. In relation to T_{on}, the increment from 20 µs to 55 µs led to a reduction in EWR, while further increment from 55 µs to 99 µs resulted in increasing EWR. When T_{off} changed from 1 µs to 9 µs through 5 µs, corresponding increment and decrement were observed in the EWR values, as was the case with the changes in SEN from 1 to 99 through 55. Furthermore, swing sensitivity was identified as the critical parameter in the VOEDM process.

3.1.2. Experimental effect of MRR by input machining parameters

Figure 3 depicts the main effect plot for MRR. It was observed that MRR increased with a change in IP values from 5A to 20A and further suffered a sudden decrease in the IP range of 20A to 35A. A continuous increasing trend of MRR was observed with a change in T_{on} from 20 µs to 99 µs through 55 and a small increase and a sudden increase in MRR

Table 4. ANOVA for EWR.

Source	DF	Seq SS	Adj SS	Adj MS	F-value	P-value	Contribution (%)
IP	2	0.000	0.000	0.000	5.78	0.066	36.90
Ton	2	0.000	0.000	0.000	0.26	0.779	8.00
T_{off}	2	0.000	0.000	0.000	7.88	0.041	50.33
SEN	2	0.000	0.000	0.000	0.15	0.863	4.78
Error	0	0.000	-	-	-	-	-
Total	8	0.000	-	-	-	-	100.00

Table 5. ANOVA for MRR.

Source	DF	Seq SS	Adj SS	Adj MS	F-value	P-value	Contribution (%)
IP	2	0.000	0.000	0.000	2.89	0.257	28.95
T_{on}	2	0.000	0.000	0.000	2.62	0.276	26.26
T_{off}	2	0.000	0.000	0.000	3.47	0.224	34.78
SEN	2	0.000	0.000	0.000	0.33	0.729	10.01
Error	0	0.000	-	-	-	-	-
Total	8	0.000	-	-	-	-	100.00

was observed for T_{off} from 1 µs to 5 µs and 5 µs to 9 µs, respectively. However, a decrease in MRR values was observed with the SEN values changing from 1 to 99 through 55.

3.2. Analysis of variance for experimental results

Analysis of variance (ANOVA) was used to determine the characteristic and relative importance of the machining variables [32,33]. ANOVA results evaluated and identified the individual contributions of the selected input variables from the total model,
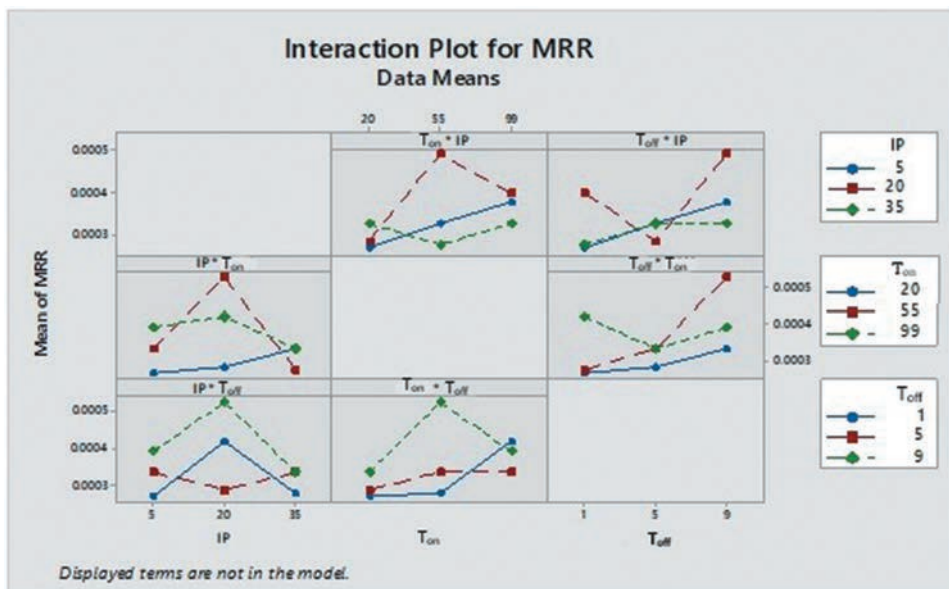
Figure 5. Interaction plot for MRR

including error. The S/N ratio is generally used to find the best set of controllable variables involved in the production process.

Tables 4 and 5 show the significant contributions of the different input machining parameters towards EWR and MRR. The general linear model (GLM) was used to fit the least square models, which consist of input and output values [34]. The stepwise method in GLM was adopted for EWR. SEN factor was included in every step for the required ANOVA table. The entire observed result was found to be conforming to 95% confidence level, and in both the cases, it was found out that the contribution of T_{off} (50.33%) and IP (36.90%) had a more significant impact on EWR. However, T_{on} (8.00%) and SEN (4.78%) had lesser contribution to EWR.

Similarly, it was observed that the greater influencing contribution to MRR was of T_{off} (34.78%) and IP (28.95%), while contributions of T_{on} (26.26%) and SEN (10.01%) was lesser.

Figures 4 and 5 indicate that all the significant parameters and their level are intersecting and contributing to the output characteristics, with the exception of SEN. The main aim was to determine the input variables IP, T_{on}, T_{off} and SEN to optimise EWR and MRR. Further, due to difficulty in establishing a relationship between the four input machining parameters for optimising two output characteristics; regression analysis was performed.

3.3. Regression model

Regression equation was used to obtain the relationship between input and output characteristics through a mathematical model. Hence, linear relationship was required

Table 6. Coefficients for regression analysis for EWR.

Term	Coeff	SE Coeff	T-value	P-value	VIF
Constant	−0.000141	0.000039	−3.6	0.173	
T_{on}	0.000005	0.000001	6.13	0.103	11.91
IP	0.000037	0.000006	6.51	0.097	74.21
T_{off}	0.00001	0.000008	1.3	0.418	10.8
SEN	−0.000005	0.000001	−4.24	0.148	28.08
$T_{on} \times IP$	0	0	−7.44	0.085	39.86
$IP \times T_{off}$	−0.000002	0.000001	−3.59	0.173	53.11
$T_{off} \times SEN$	0	0	1.86	0.314	16.32
S	R^2	$R^2_{(adj)}$			
0.0000241	98.94%	91.55%			

Table 7. Coefficients for regression analysis for MRR.

Term	Coeff	SE Coeff	T-value	P-value	VIF
Constant	0.000314	0.000059	5.29	0.119	
T_{on}	−0.000006	0.000003	−1.96	0.301	149.15
IP	0.00%	0.000003	0.27	0.832	16.85
T_{off}	0.000048	0.00001	4.73	0.133	14.56
SEN	0.000003	0.000001	3.11	0.198	20.65
$T_{on} \times T_{on}$	0	0	3.17	0.195	144.42
$T_{on} \times IP$	0	0	−2.77	0.221	27.82
$T_{off} \times SEN$	−0.000001	0	−4.81	0.131	37.85
S	R^2	$R^2_{(adj)}$			
0.0000259	98.78%	90.23%			

between the selected particular characteristics (Input and Output). The derived regression equation was obtained by forward selection method in regression model analysis with α = 0.25. The equation for the EWR Equation (5) and the MRR Equation (6) was as follows:

$$
\begin{aligned}
EWR = & -0.000141 + 0.000005\ T_{on} + 0.000037\ IP + 0.000010\ T_{off} \\
& - 0.000005\ SEN - 0.0000001\ T_{on} \\
& \times IP - 0.000002\ IP \times T_{off} + 0.0000001\ T_{off} \times SEN
\end{aligned}
\tag{5}
$$

$$
\begin{aligned}
MRR = & \ 0.000314 - 0.000006\ T_{on} + 0.000001\ IP + 0.000048\ T_{off} \\
& + 0.000003\ SEN + 0.0000001\ T_{on} \times T_{on} - 0.0000002\ T_{on} \\
& \times IP - 0.000001\ T_{off} \times SEN
\end{aligned}
\tag{6}
$$

The R2 value indicates that the forecast retains 98.94% and 98.78% of the variance in EWR and MRR, respectively. Tables 6 and 7 show that the selected regression models are the best-suited models that can be used with these parameters and parameter levels with respect to the R2(adj) test. R2(adj) was 91.55% and 90.23%, which accounts for the number forecasted in the model. Both values show that the data are well fitted.

From ANOVA results of EWR, the interaction effect of T_{on} and IP (45.22%) were found to be the major contributors to the VOEDM process. The significant contribution of IP (32.77%) and the interaction of IP and T_{off} (11.07%) indicated the primary effect on the EWR. The significant contributions to MRR were found to be by the interactions of T_{off} and SEN (28.25%). Again, T_{off} (25.21%) and T_{on} (18.93%) also signify a vital effect on
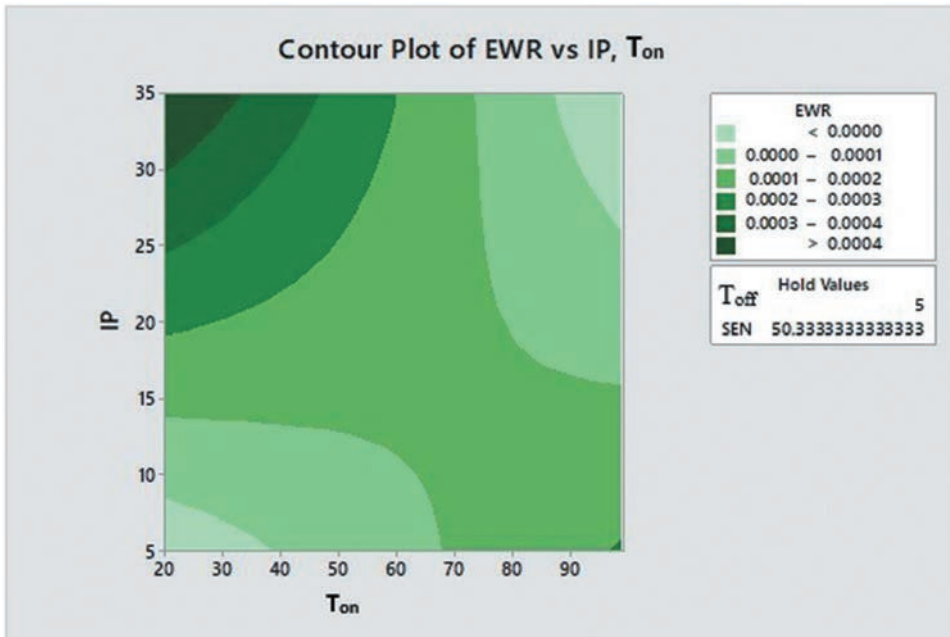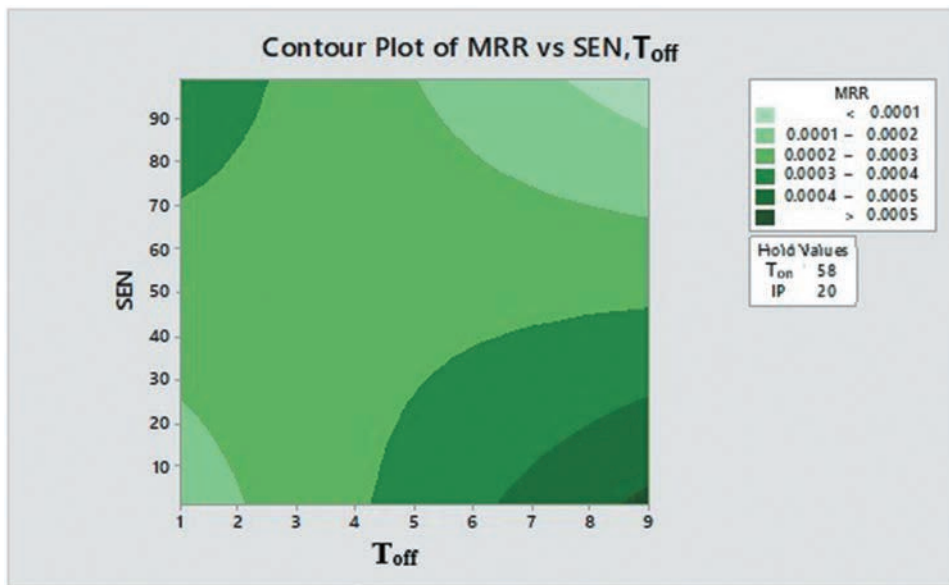

Figure 6. Contour plot for EWR

Figure 7. Contour plot for MRR

Table 8. Results of confirmation runs for EWR and MRR.

	Output characteristics	EWR	MRR
	Machining parameters combined with the level	A1B1C2D3	A3B1C1D3
	Average values of actual machining	0.00014	0.00036
ANOVA	Optimum Corresponding values	0.00023	0.00023
	Range of Confidence interval at 95%	(0.000094–0.000368)	(0.000031–0.000429
	Optimised plot	A3B1C1D3	
REGRESSION	Optimum Corresponding values	−0.0001	0.00053
	Range of Confidence interval at 95%	(−0.001194–0.000954)	(−0.000026–0.001090)
	Optimised plot	A1B2C1D3	
	Average experimental values at optimum conditions	0.00019	0.0004

the MRR. The obtained contribution justifies that the selected regression model was significant for optimising the output characteristics.

Figure 6 and 7 shows the contour plots for EWR and MRR. The values fall between the upper left and lower right, indicative of the effect of IP and T_{on} on EWR and the impact of SEN and $T_{off,}$ on MRR. The lower left and upper right parts signify over-cooked and under-cooked entrees.

3.4. Confirmation runs

The purpose of the confirmation runs is to validate the conclusions drawn during the analysis phase. Optimum levels of the input machining parameters were used for the prediction and confirmation of the improvement in output characteristics. Further, a new experiment was designed with a combination of parameters along with their levels A1B1C2D3 and A3B1C1D3 to obtain the EWR and MRR, respectively. The final step was to predict and verify the improvement in output characteristics.

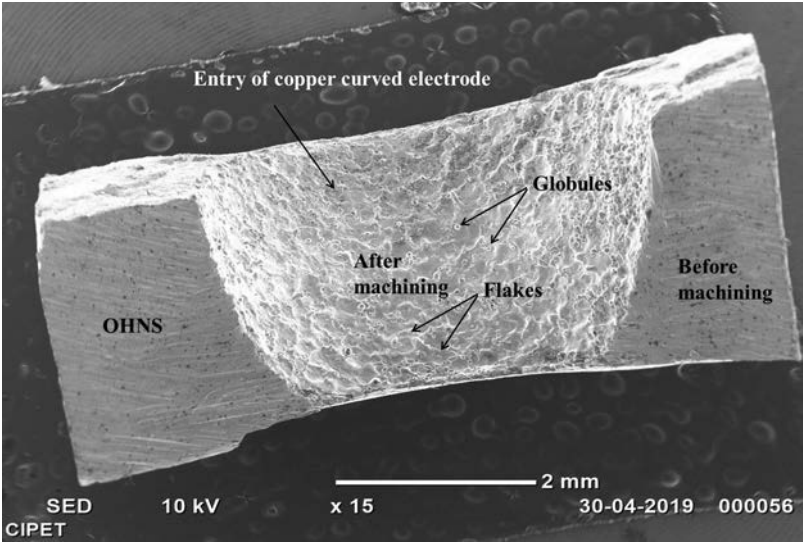**Figure 8. Actual curved machining with optimum machining parameters**

Figure 9. SEM image of curvature trajectory machined channel at optimum combination

The results of confirmation runs are presented in Table 8. The machining parameters obtained by applying the optimisation technique are experimentally executed, and the average values of the conformal experiment presented. All the obtained values were

accepted, and they were in the range of EWR and MRR, respectively. Figure 8 shows the curved channel machined through the novel VOEDM Process.

The actual average conformal experimental values at optimum conditions by regression analysis were validated by minimum value for EWR (0.000194 mm^3/min), which is found to be closer to experiment no.8. Again, the obtained maximum value of MRR (0.000397 mm^3/min) was found to be nearer to experiment no.6 of Table 2.

3.5. Curvature trajectory machined analysis

The OHNS material surface characterisation of the curved channel was analysed by a scanning electron microscope (SEM) [35], image captured at 80× magnification. Figure 9 shows the combined image of the workpiece material. It shows that before machining, the surface was plain, including white lines and black spots. After executing the VOEDM process, the surface was found to be containing small globes with the small flakes and voids. The surface variations occur due to the intensity of the spark that varies with the contact surface area of the electrode.

4. Conclusions

In this current research work, the actual curved trajectory is machined by variable oscillating electrical discharge machining (VOEDM) process. Our goal was to minimise the electrode wear rate (EWR) and maximise the material removal rate (MRR) in the VOEDM process. The main conclusion drawn from this research area is summarised as follows:

It was found that the pulse off time had a significant influence on EWR and MRR. Similarly, it was identified that the highest contributing machining factors were pulse off time and sparking current in output characteristics.

The interaction of selected input machining parameters was a statistically significant effect on EWR and MRR.

The regression model was applied and its significance was estimated by the regression coefficients. The interaction of pulse on time and sparking current; pulse off time, and sensitivity had the maximum effect on EWR and MRR, respectively.

The optimum combination of machining parameters for minimum EWR and maximum MRR was identified as follows: sparking current at level 3 (35A), pulse on time at level 1 (20 μs), pulse off time at level 1(1 μs) and swing sensitivity at level 3; sparking current at level 1 (5A), pulse on time at level 2 (55 μs), pulse off time at level 1 (1 μs), and swing sensitivity at level 3.

The actual average conformal experimental values at optimum conditions were obtained and it is suggested that the experiment no.8 and experiment no.6 were optimised for the best values of EWR and MRR, respectively.

The contour plots indicated that the statistical values were within limits for the output characteristics.

Finally, experimental results confirm the validity of the Taguchi method with regression analysis used for improving the machining performance and optimising the process characteristics in the VOEDM.

The improvement was justified and optimised. It was found that the EWR decreased by 37.58%, and MRR increased by 11.83% by proposing these statistical techniques in the developed VOEDM process.

In addition, SEM imagery was used for identifying the material surface characteristics.

Acknowledgments

Disclosure statement

No potential conflict of interest was reported by the authors.

ORCID

Diwesh B. Meshram http://orcid.org/0000-0001-5584-3484
Yogesh. M. Puri http://orcid.org/0000-0002-4523-0999
Vikas K. Gohil http://orcid.org/0000-0002-0747-7077
Sachin P. Ambade http://orcid.org/0000-0002-2524-5798

[1] Garg RK, Singh KK, Sachdeva A, et al. Review of research work in sinking EDM and WEDM on metal matrix composite materials. J Int J Adv Manuf Technol. 2010;50(5–8):611–624.

[2] Pawade MM, Banwait SS. A brief review of die sinking electrical discharging machining process towards automation. Am J Mech Eng. 2013;1(2):127–130.

[3] Kunieda M, Lauwers B, Rajurkar KP, et al. Advancing EDM through fundamental insight into the process. CIRP Ann Manuf Technol. 2005;54(2):64–87.

[4] Ho KH, Newman ST. State of the art electrical discharge machining (EDM). Int J Mach Tools Manuf. 2003;43(13):1287–1300.

[5] Meshram DB, Puri YM. Review of research work in die sinking EDM for machining curved hole. J Braz Soc Mech Sci Eng. 2016;39(7):2593–2605.

[6] Okada A, Yamaguchi A, Ota K. Improvement of curved hole EDM drilling performance using suspended ball electrode by workpiece vibration. CIRP Ann Manuf Technol. 2017;66(1):189–192.

[7] Gohil V, Puri YM. Experimental investigation on surface roughness in electrical discharge turning of Ti-6al-4v alloy. Trans FAMENA. 2017;40(4):1–10.

[8] Aliakbari E, Baseri H. Optimization of machining parameters in rotary EDM process by using the Taguchi method. Int J Adv Manuf Technol. 2012;62(9–12):1041–1053.

[9] Meshram DB, Puri YM. Effective parametric analysis of machining curvature channel using semicircular curved copper electrode and OHNS steel workpiece through a novel curved EDM process. Eng Res Exp. 2019;1(1):015014.

[10] Das MK, Kumar K, Barman TK, et al. Optimization of material removal rate in EDM using Taguchi method. Adv Mater Res. 2012;626:270–274.

[11] Gnanavel C, Saravanan R, Chandrasekaran M, et al. Restructured review on electrical discharge machining - A state of the art. IOP conference series: materials science and engineering, international conference on emerging trends in engineering research, Chennai, India.2017;183: 012015.

[12] Arrabiyeh PA, Dethloff M, Müller C, et al. Optimization of micropencil grinding tools via electrical discharge machining. ASME J Manuf Sci Eng. 2019;141(3):031005.

[13] Kandpal BC, Kumar J, Singh H. Optimization and characterization of EDM of AA 6061/ 10%Al2O3 AMMC using Taguchi's approach and utility concept. Prod Manuf Res. 2017;5(1):351–370.

[14] Marichamy S, Saravanan M, Ravichandran M, et al. Parametric optimization of EDM process on α–β brass using Taguchi approach. Russian J Non-Ferrous Metals. 2016;57 (6):586–598.

[15] Sivasankar S, Jeyapaul R. Modelling of an artificial neural network for electrical discharge machining of hot pressed Zirconium diboride-silicon carbide composites. Trans FAMENA. 2016;40(3):67–80.

[16] Vaddi V, Ch S, Pogaku V, et al. Optimization of electrical discharge machining of titanium alloy (Ti-6Al-4 V) using Taguchi-DEAR method. SAE Technical Paper 2018-28-0032. 2018.

[17] Singh J, Pandey PM. Process optimization for rapid manufacturing of complex geometry electrical discharge machining electrode. Proc Inst Mech Eng Part C. 2020;234(1):66–81.

[18] Kumar K, Agarwal S. Multi-objective parametric optimization on machining with wire electric discharge machining. Int J Adv Manuf Technol. 2012;62(5–8):617–633.

[19] Sonawane SA, Ronge BP, Pawar PM. Multi-characteristic optimization of WEDM for Ti-6Al-4V by applying grey relational investigation during profile machining. J Mech Eng Sci. 2019;13(4):6059–6087.

[20] Raj RSA, Sethuramalingam P. Analysis of multi objective optimisation using TOPSIS method in EDM process with CNT infused copper electrode. Int J Mach Mach Mater. 2017;19(1):76–94.

[21] Dang XP. Constrained multi-objective optimization of EDM process parameters using kriging model and particle swarm algorithm. Mater Manuf Processes. 2018;33(4):397–404.

[22] Prabhu S, Vinayagam B. Multiresponse optimization of EDM process with nanofluids using topsis method and genetic algorithm. Arch Mech Eng. 2020;63(1):45–71.

[23] Ubaid AM, Aghdeab SH, Abdulameer AG, et al. Multidimensional optimization of electrical discharge machining for high speed steel (AISI M2) using Taguchi-fuzzy approach. Int J Syst Assur Eng Manage. 2020;16:5788–5803.

[24] Mohanty UK, Rana J, Sharma A. Multi-objective optimization of electro-discharge machining (EDM) parameter for sustainable machining. Mater Today Proc. 2017;4(8):9147–9157.

[25] Baraskar SS, Banwait SS, Laroiya SC. Multiobjective optimization of electrical discharge machining process using a hybrid method. Mater Manuf Processes. 2013;28(4):348–354.

[26] Montgomery DC. Design and analysis of experiments. 9th ed. Wiley, New York;2017.

[27] Sultan T, Kumar A, Gupta RD. Material removal rate, electrode wear rate, and surface roughness evaluation in die sinking EDM with hollow tool through response surface methodology. Int J Manuf Eng. 2014;2014:1–16.

[28] Habib SS. Study of the parameters in electrical discharge machining through response surface methodology approach. Appl Math Modell. 2009;33(12):4397–4407.

[29] Wang CC, Chow HM, Yang LD, et al. Recast layer removal after electrical discharge machining via Taguchi analysis. J Mater Process Technol. 2009;209(8):4134–4140.

[30] Gaitonde VN, Manjaiah M, Maradi S, et al. Multiresponse optimization in wire electric discharge machining (WEDM) of HCHCr steel by integrating response surface methodology (RSM) with differential evolution (DE). In: Davim JP, editor. Woodhead publishing reviews: mechanical engineering series. Computational Methods and Production Engineering, Woodhead Publishing, Elsevier Inc.; 2017. p. 199–221.

[31] Minitab. 2020. (Version 18) [Software]. [cited 2020 Jan 28]. Available from: http://www. minitab.com/en-US/lp/free-statistical-software.aspx

[32] Yuvaraj T, Suresh P. Analysis of EDM process parameters on inconel 718 using the Grey-Taguchi and Topsis method. Strojniški Vestnik - J Mech Eng. 2019;65(10):557–564.

[33] Meshram DB, Puri YM. Optimized curved electrical discharge machining-based curvature channel. J Braz Soc Mech Sci Eng. 2020;42(2):1–15.

[34] Miller J, Haden P. Statistical analysis with the general linear model. In: Davim JP, editor. Woodhead publishing reviews: mechanical engineering series. Computational Methods and Production Engineering, Woodhead Publishing, Elsevier Inc.; 2017. p. 199–221.

[35] Mandal P, Mondal SC. Surface characteristics of mild steel using EDM with Cu-MWCNT composite electrode. Mater Manuf Processes. 2019;34(12):1326–1332.

Declaration by the Head of the Institution

I hereby declare that the data, information and support documents attached herewith are genuine and correct to my knowledge.

Dr. U.P. Waghe
Principal

Principal
Yeshwantrao Chavan
College of Engineering
Wanadongri Hingna Road,
NAGPUR-441110

SEAL